ARO 39143.4-MS-CF

MRS
MATERIALS RESEARCH SOCIETY
SYMPOSIUM PROCEEDINGS

Volume 537

GaN and Related Alloys

EDITORS
Stephen J. Pearton
Chihping Kuo
Alan F. Wright
Takeshi Uenoyama

GaN and Related Alloys

19991101 136

REPORT DOCUMENTATION PAGE

Form Approved
OMB NO. 0704-0188

Public reporting burden for this collection of information is estimated to average 1 hour per response, including the time for reviewing instructions, searching existing data sources, gathering and maintaining the data needed, and completing and reviewing the collection of information. Send comment regarding this burden estimates or any other aspect of this collection of information, including suggestions for reducing this burden, to Washington Headquarters Services, Directorate for information Operations and Reports, 1215 Jefferson Davis Highway, Suite 1204, Arlington, VA 22202-4302, and to the Office of Management and Budget, Paperwork Reduction Project (0704-0188), Washington, DC 20503.

1. AGENCY USE ONLY *(Leave blank)*	2. REPORT DATE	3. REPORT TYPE AND DATES COVERED
		Book

4. TITLE AND SUBTITLE

GaN and Related Alloys, MRS Symposium Proceedings, Volume 537

5. FUNDING NUMBERS

DAAG55-98-1-0478

6. AUTHOR(S)

Stephen J. Pearton, Chihping Kuo, Alan F. Wright, Takeshi Uenoyama (Editors)

7. PERFORMING ORGANIZATION NAMES(S) AND ADDRESS(ES)

Materials Research Society
Warrendale, PA 15086

8. PERFORMING ORGANIZATION REPORT NUMBER

9. SPONSORING / MONITORING AGENCY NAME(S) AND ADDRESS(ES)

U.S. Army Research Office
P.O. Box 12211
Research Triangle Park, NC 27709-2211

10. SPONSORING / MONITORING AGENCY REPORT NUMBER

ARO 39143.4-MS-CF

11. SUPPLEMENTARY NOTES

The views, opinions and/or findings contained in this report are those of the author(s) and should not be construed as an official Department of the Army position, policy or decision, unless so designated by other documentation.

12a. DISTRIBUTION / AVAILABILITY STATEMENT

Approved for public release; distribution unlimited.

12 b. DISTRIBUTION CODE

13. ABSTRACT *(Maximum 200 words)*

SEE PREFACE

14. SUBJECT TERMS	15. NUMBER IF PAGES
	16. PRICE CODE

17. SECURITY CLASSIFICATION OR REPORT	18. SECURITY CLASSIFICATION OF THIS PAGE	19. SECURITY CLASSIFICATION OF ABSTRACT	20. LIMITATION OF ABSTRACT
UNCLASSIFIED	UNCLASSIFIED	UNCLASSIFIED	UL

MATERIALS RESEARCH SOCIETY
SYMPOSIUM PROCEEDINGS VOLUME 537

GaN and Related Alloys

Symposium held November 30–December 4, 1998, Boston, Massachusetts, U.S.A.

EDITORS:

Stephen J. Pearton
University of Florida
Gainesville, Florida, U.S.A.

Chihping Kuo
Hewlett Packard Co.
San Jose, California, U.S.A.

Alan F. Wright
Sandia National Laboratories
Albuquerque, New Mexico, U.S.A.

Takeshi Uenoyama
Matsushita Electric Industrial Co., Ltd.
Kyoto, Japan



Materials Research Society
Warrendale, Pennsylvania

DTIC QUALITY INSPECTED 4

This work was supported in part by the Army Research Office under Grant Number ARO: DAAG55-98-1-0478. The views, opinions, and/or findings contained in this report are those of the authors and should not be construed as an official Department of the Army position, policy, or decision, unless so designated by other documentation.

Single article reprints from this publication are available through
University Microfilms Inc., 300 North Zeeb Road, Ann Arbor, Michigan 48106

CODEN: MRSPDH

Copyright 1999 by Materials Research Society.
All rights reserved.

This book has been registered with Copyright Clearance Center, Inc. For further information, please contact the Copyright Clearance Center, Salem, Massachusetts.

Published by:

Materials Research Society
506 Keystone Drive
Warrendale, PA 15086
Telephone (724) 779-3003
Fax (724) 779-8313
Web site: http://www.mrs.org/

Library of Congress Cataloging in Publication Data

GaN and related alloys : symposium held November 29–December 4, 1998, Boston, Massachusetts, U.S.A. / editors, Stephen J. Pearton, Chihping Kuo, Alan F. Wright, Takeshi Uenoyama
p. cm.—(Materials Research Society symposium proceedings, ISSN 0272-9172 ; v. 537)
Includes bibliographical references and index.
ISBN 1-55899-443-2
1. Gallium nitride—Congresses. 2. Semiconductors—Materials—Congresses. 3. Electroluminescent devices—Materials—Congresses. 4. Lasers—Materials—Congresses. 5. Epitaxy—Congresses. I. Pearton, Stephen J. II. Kuo, Chihping III. Wright, Alan F. IV. Uenoyama, Takeshi V. Materials Research Society symposium proceedings ; v. 537.
TK7871.G3G357 1999 99-15966
621.3815'2—dc21 CIP

Manufactured in the United States of America

CONTENTS

Preface

Acknowledgments

Materials Research Society Symposium Proceedings

PART I: GaN ELECTRONIC AND PHOTONIC DEVICES

*InGaN/GaN/AlGaN-Based LEDs and Laser Diodes G1.1.1
S. Nakamura, M. Senoh, S. Nagahama, N. Iwasa, T. Matushita, and T. Mukai

*Material Properties of GaN in the Context of Electron Devices G1.2.1
H. Morkoç, R. Cingolani, W. Lambrecht, B. Gil, H-X. Jiang, J. Lin, D. Pavlidis, and K. Shenai

*Near Defect-Free GaN Substrates G1.3.1
S. Porowski

*Dry and Wet Etching for Group III Nitrides G1.4.1
I. Adesida, C. Youtsey, A.T. Ping, F. Khan, L.T. Romano, and G. Bulman

*Contact Issues of GaN Technology G1.5.1
D. Qiao, L.S. Yu, S.S. Lau, G.J. Sullivan, S. Ruvimov, and Z. Liliental-Weber

*Pyroelectric and Piezoelectric Properties of GaN-Based Materials G1.6.1
M.S. Shur, A.D. Bykhovski, and R. Gaska

PART II: LASER DIODES AND SPECTROSCOPY

Characterization of InGaN/GaN-Based Multi-Quantum Well Distributed Feedback Lasers G2.2.1
D. Hofstetter, R.L. Thornton, L.T. Romano, D.P. Bour, M. Kneissl, R.M. Donaldson, and C. Dunnrowicz

Mechanisms of Optical Gain in Cubic GaN and InGaN G2.3.1
J. Holst, A. Hoffmann, I. Broser, T. Frey, B. Schöttker, D.J. As, D. Schikora, and K. Lischka

Carrier Dynamics of Abnormal Temperature-Dependent Emission Shift in MOCVD-Grown InGaN Epilayers and InGaN/GaN Quantum Wells G2.4.1
Y-H. Cho, B.D. Little, G.H. Gainer, J.J. Song, S. Keller, U.K. Mishra, and S.P. DenBaars

*Invited Paper

Mechanism for Radiative Recombination in $In_{0.15}Ga_{0.85}N$/GaN Multiple Quantum Well Structures G2.5.1
B. Monemar, J.P. Bergman, J. Dalfors, G. Pozina, B.E. Sernelius, P.O. Holtz, H. Amano, and I. Akasaki

*Spectroscopic Studies in InGaN Quantum Wells G2.7.1
S.F. Chichibu, T. Sota, K. Wada, S.P. DenBaars, and S. Nakamura

Composition Dependence of the Bandgap Energy of $In_xGa_{1-x}N$ Layers on GaN ($x \leq 0.15$) Grown by Metalorganic Chemical Vapor Deposition G2.8.1
J. Wagner, A. Ramakrishnan, D. Behr, M. Maier, N. Herres, M. Kunzer, H. Obloh, and K-H. Bachem

Optical Gain Spectra in InGaN/GaN Quantum Wells With the Compositional Fluctuations G2.9.1
T. Uenoyama

PART III: GROWTH AND CHARACTERIZATION

Hydrogen and Nitrogen Ambient Effects on Epitaxial Lateral Overgrowth (ELO) of GaN Via Metalorganic Vapor-Phase Epitaxy (MOVPE) G3.1.1
K. Tadatomo, Y. Ohuchi, H. Okagawa, H. Itoh, H. Miyake, and K. Hiramatsu

Pendeo-Epitaxy of Gallium Nitride and Aluminum Nitride Films and Heterostructures on Silicon Carbide Substrate G3.2.1
T. Gehrke, K.J. Linthicum, D.B. Thomson, P. Rajagopal, A.D. Batchelor, and R.F. Davis

Piezoelectric Effects in GaN/AlGaN Multiple Quantum Wells Probed by Picosecond Time-Resolved Photoluminescence G3.3.1
H.S. Kim, J.Y. Lin, H.X. Jiang, W.W. Chow, A. Botchkarev, and H. Morkoç

Nitridation of GaAs (001)-2x4 Surface Studied by Auger Electron Spectroscopy G3.4.1
I. Aksenov, Y. Nakada, and H. Okumura

Temperature Effect on the Quality of AlN Thin Films G3.7.1
M.P. Thompson, A.R. Drews, C. Huang, and G.W. Auner

Epitaxial Growth and Structural Characterization of Single Crystalline $ZnGeN_2$ G3.8.1
L.D. Zhu, P.H. Maruska, P.E. Norris, P.W. Yip, and L.O. Bouthillette

Cubic GaN Heteroepitaxy on Thin-SiC-Covered Si(001) G3.9.1
Y. Hiroyama and M. Tamura

*Invited Paper

Influence of Active Nitrogen Species on the Nitridation Rate of Sapphire G3.10.1
A.J. Ptak, K.S. Ziemer, M.R. Millecchia, C.D. Stinespring, and T.H. Myers

Structural Study of GaN(As,P) Layers Grown on (0001) GaN by Gas Source Molecular Beam Epitaxy G3.11.1
T-Y. Seong, I-T. Bae, Y. Zhao, and C.W. Tu

GaN Growth by Remote Plasma MOCVD: Chemistry and Kinetics by Real Time Ellipsometry G3.12.1
M. Losurdo, P. Capezzuto, and G. Bruno

Defects in GaN Pyramids Grown on Si(111) Substrates by Selective Lateral Overgrowth G3.13.1
Z. Mao, X. McKernan, C.B. Carter, W. Yang, and S.A. McPherson

Electrical and Photoelectrical Characterization of Deep Defects in Cubic GaN on GaAs G3.14.1
M. Lisker, A. Krtschil, H. Witte, J. Christen, D.J. As, B. Schöttker, and K. Lischka

Pressure Dependence of Optical Transitions in InGaN/GaN Multiple Quantum Wells G3.15.1
W. Shan, J.W. Ager III, W. Walukiewicz, E.E. Haller, M.D. McCluskey, N.M. Johnson, and D.P. Bour

Domain Structure of Thick GaN Layers Grown by Hydride Vapor Phase Epitaxy G3.16.1
T. Paskova, E.B. Svedberg, L.D. Madsen, R. Yakimova, I.G. Ivanov, A. Henry, and B. Monemar

Characterization of Be-Implanted GaN Annealed at High Temperatures G3.17.1
C. Ronning, K.J. Linthicum, E.P. Carlson, P.J. Hartlieb, D.B. Thomson, T. Gehrke, and R.F. Davis

Thermal Residual Stress Modeling in AlN and GaN Multilayer Samples G3.18.1
K. Wang and R.R. Reeber

Strong Piezoelectric Effects in Unstrained GaN Quantum Wells G3.19.1
R. Langer, J. Simon, O. Konovalov, N.T. Pelekanos, R. André, A. Barski, and M. Godlewski

Optical Absorption, Raman, and Photoluminescence Excitation Spectroscopy of Inhomogeneous InGaN Films G3.22.1
L.H. Robins, A.J. Paul, C.A. Parker, J.C. Roberts, S.M. Bedair, E.L. Piner, and N.A. El-Masry

Growth of Oriented Thick Films of Gallium Nitride From the Melt G3.23.1
J.S. Dyck, K. Kash, M.T. Grossner, C.C. Hayman, A. Argoitia, N. Yang, M-H. Hong, M.E. Kordesch, and J.C. Angus

p- and n-Type Doping of MBE Grown Cubic GaN/GaAs Epilayers G3.24.1
D.J. As, T. Simonsmeier, J. Busch, B. Schöttker, M. Lübbers, J. Mimkes, D. Schikora, K. Lischka, W. Kriegseis, W. Burkhardt, and B.K. Meyer

Cubic InGaN Grown by MOCVD G3.25.1
J.B. Li, H. Yang, L.X. Zheng, D.P. Xu, and Y.T. Wang

Optical Investigations of AlGaN on GaN Epitaxial Films G3.26.1
G. Steude, T. Christmann, B.K. Meyer, A. Goeldner, A. Hoffmann, F. Bertram, J. Christen, H. Amano, and I. Akasaki

Effects of Surface Preparation on Epitaxial GaN on 6H-SiC Deposited Via MOCVD G3.29.1
J. Elsner, Th. Frauenheim, M. Haugk, R. Gutierrez, R. Jones, and M.I. Heggie

Electron Beam Induced Impurity Electro-Migration in Unintentionally Doped GaN G3.30.1
M. Toth, K. Fleischer, and M.R. Phillips

Statistical Analysis of Local Composition and Luminescence in InGaN Grown by Molecular Beam Epitaxy G3.33.1
S. Einfeldt, T. Böttcher, D. Hommel, H. Selke, P.L. Ryder, F. Bertram, T. Riemann, D. Rudloff, and J. Christen

Ranges of Deposition Temperatures Applicable for Metalorganic Vapor Phase Epitaxy of GaN Films Via the Technique of Pendeo-Epitaxy G3.37.1
D.B. Thomson, T. Gehrke, K.J. Linthicum, P. Rajagopal, and R.F. Davis

Pendeo-Epitaxy—A New Approach for Lateral Growth of Gallium Nitride Structures G3.38.1
T.S. Zheleva, S.A. Smith, D.B. Thomson, T. Gehrke, K.J. Linthicum, P. Rajagopal, E. Carlson, W.M. Ashmawi, and R.F. Davis

Effects of Surface Preparation on Epitaxial GaN on 6H-SiC Deposited Via MOCVD G3.39.1
Z.Y. Xie, C.H. Wei, L.Y. Li, J.H. Edgar, J. Chaudhuri, and C. Ignatiev

High-Quality Hydrothermal ZnO Crystals G3.40.1
M. Suscavage, M. Harris, D. Bliss, P. Yip, S-Q. Wang, D. Schwall, L. Bouthillette, J. Bailey, M. Callahan, D.C. Look, D.C. Reynolds, R.L. Jones, and C.W. Litton

Disordering of InGaN/GaN Superlattices After High-Pressure Annealing G3.42.1
M.D. McCluskey, L.T. Romano, B.S. Krusor, D. Hofstetter, D.P. Bour, M. Kneissl, N.M. Johnson, T. Suski, and J. Jun

Synthesis of Nitrogen-Rich GaNAs Semiconductor Alloys and Arsenic-Doped GaN by Metalorganic Chemical Vapor Deposition G3.44.1
M. Gherasimova, B. Gaffey, P. Mitev, L.J. Guido, K.L. Chang, K.C. Hsieh, S. Mitha, and J. Spear

Si Delta Doped GaN Grown by Low-Pressure Metalorganic Chemical Vapor Deposition G3.49.1
J-H. Kim, G.M. Yang, S.C. Choi, J.Y. Choi, H.K. Cho, K.Y. Lim, and H.J. Lee

Influence of the First Preparation Steps on the Properties of GaN Layers Grown on 6H-SiC by MBE G3.50.1
R. Lantier, A. Rizzi, D. Guggi, H. Lüth, B. Neubauer, D. Gerthsen, S. Frabboni, G. Colì, and R. Cingolani

Effects of Susceptor Geometry on GaN Growth on Si(111) With a New MOCVD Reactor G3.53.1
Y. Gao, D.A. Gulino, and R. Higgins

Structure of AlN on Si (111) Deposited With Metalorganic Vapor Phase Epitaxy G3.56.1
E. Rehder, M. Zhou, L. Zhang, N.R. Perkins, S.E. Babcock, and T.F. Kuech

Influence of Doping on the Lattice Dynamics of Gallium Nitride G3.57.1
A. Kaschner, H. Siegle, A. Hoffmann, C. Thomsen, U. Birkle, S. Einfeldt, and D. Hommel

Molecular Beam Epitaxy of High Quality InGaN Alloys Using Ammonia: Optical and Structural Properties G3.59.1
N. Grandjean, J. Massies, M. Leroux, M. Laügt, P. Vennégues, S. Dalmasso, P. Ruterana, L. Hirsch, and S. Barrière

Properties of Epitaxial ZnO Thin Films for GaN and Related Applications G3.60.1
H. Shen, M. Wraback, J. Pamulapati, S. Liang, C. Gorla, and Y. Lu

Comparative Growth of AlN on Singular and Off-Axis 6H and 4H-SiC by MOCVD G3.61.1
S. Wilson, C.S. Dickens, J. Griffin, and M.G. Spencer

Gallium Nitride Growth Using Diethylgallium Chloride as an Alternative Gallium Source G3.62.1
L. Zhang, R. Zhang, M.P. Boleslawski, and T.F. Kuech

Piezoelectric Level Splitting in GaInN/GaN Quantum Wells G3.66.1
C. Wetzel, T. Takeuchi, H. Amano, and I. Akasaki

Photoluminescence Excitation Spectroscopy of Carbon-Doped Gallium Nitride G3.67.1
E.E. Reuter, R. Zhang, T.F. Kuech, and S.G. Bishop

GaN CVD Reactions: Hydrogen and Ammonia Decomposition and the Desorption of Gallium G3.68.1
M.E. Bartram and J.R. Creighton

Quantum-Confined Stark Effect and Recombination Dynamics of Spatially Indirect Excitons in MBE-Grown GaN-AlGaN Quantum Wells G3.69.1
P. Lefebvre, B. Gil, J. Allègre, H. Mathieu, N. Grandjean, M. Leroux, J. Massies, and P. Bigenwald

Enhanced GaN Decomposition at MOVPE Pressures G3.70.1
D.D. Koleske, A.E. Wickenden, R.L. Henry, M.E. Twigg, J.C. Culbertson, and R.J. Gorman

Defect States in SiC/GaN- and SiC/AlGaN/GaN-Heterostructures Characterized by Admittance and Photocurrent Spectroscopy G3.71.1
H. Witte, A. Krtschil, M. Lisker, J. Christen, F. Scholz, and J. Off

Microstructure of GaN Grown on (111) Si by MOCVD G3.72.1
D.M. Follstaedt, J. Han, P. Provencio, and J.G. Fleming

Ion Channeling Analysis of Gallium Nitride Implanted With Deuterium G3.73.1
W.R. Wampler and S.M. Myers

Optical Properties of Si-Doped $Al_xGa_{1-x}N/Al_yGa_{1-y}N$ (x = 0.24–0.53, y = 0.11) Multi-Quantum-Well Structures G3.74.1
H. Hirayama and Y. Aoyagi

Eptiaxial Growth of III-Nitride Layers on Aluminum Nitride Substrates G3.76.1
L.J. Schowalter, Y. Shusterman, R. Wang, I. Bhat, G. Arunmozhi, and G.A. Slack

Effect of Buffer Layer and III/V Ratio on the Surface Morphology of GaN Grown by MBE G3.77.1
E.C. Piquette, P.M. Bridger, R.A. Beach, and T.C. McGill

Relaxation Phenomena in GaN/AlN/6H-SiC Heterostructures G3.78.1
N.V. Edwards, A.D. Batchelor, I.A. Buyanova, L.D. Madsen, M.D. Bremser, R.F. Davis, D.E. Aspnes, and B. Monemar

Growth and Characterization of $B_xGa_{1-x}N$ on 6H-SiC (0001) by MOVPE G3.79.1
C.H. Wei, Z.Y. Xie, J.H. Edgar, K.C. Zeng, J.Y. Lin, H.X. Jiang, C. Ignatiev, J. Chaudhuri, and D.N. Braski

Optical and Structural Properties of Er^{3+}-Doped GaN Grown by MBE G3.80.1
R.H. Birkhahn, R. Hudgins, D.S. Lee, B.K. Lee, A.J. Steckl, A. Saleh, R.G. Wilson, and J.M. Zavada

PART IV: EPITAXIAL LATERAL OVERGROWTH AND SELECTIVE GROWTH

Selective Area Growth (SAG) and Epitaxial Lateral Overgrowth (ELO) of GaN Using Tungsten Mask G4.1.1
Y. Kawaguchi, S. Nambu, H. Sone, M. Yamaguchi, H. Miyake, K. Hiramatsu, N. Sawaki, Y. Iyechika, and T. Maeda

Epitaxial Lateral Overgrowth of GaN on SiC and Sapphire Substrates G4.3.1
Z. Yu, M.A.L. Johnson, J.D. Brown, N.A. El-Masry, J.F. Muth, J.W. Cook, Jr., J.F. Schetzina, K.W. Haberern, H.S. Kong, and J.A. Edmond

Fast Lateral Epitaxial Overgrowth of Gallium Nitride by Metalorganic Chemical Vapor Deposition Using a Two-Step Process G4.5.1
H. Marchand, J.P. Ibbetson, P.T. Fini, X.H. Wu, S. Keller, S.P. DenBaars, J.S. Speck, and U.K. Mishra

TEM Study of Defects in Laterally Overgrown GaN Layers G4.6.1
Z. Liliental-Weber, M. Benamara, W. Swider, J. Washburn, J. Park, P.A. Grudowski, C.J. Eiting, and R.D. Dupuis

Epitaxial Lateral Overgrowth of GaN With Chloride-Based Growth Chemistries in Both Hydride and Metalorganic Vapor Phase Epitaxy G4.7.1
R. Zhang, L. Zhang, D.M. Hansen, M.P. Boleslawski, K.L. Chen, D.Q. Lu, B. Shen, Y.D. Zheng, and T.F. Kuech

GaN: From Selective Area to Epitaxial Lateral Overgrowth G4.8.1
X. Li, S.G. Bishop, and J.J. Coleman

Process Routes for Low Defect-Density GaN on Various Substrates Employing Pendeo-Epitaxial Growth Techniques G4.9.1
K.J. Linthicum, T. Gehrke, D.B. Thomson, K.M. Tracy, E.P. Carlson, T.P. Smith, T.S. Zheleva, C.A. Zorman, M. Mehregany, and R.F. Davis

Homoepitaxial and Heteroepitaxial Gallium Nitride Grown by Molecular Beam Epitaxy G4.11.1
C.T. Foxon, T.S. Cheng, D. Korakakis, S.V. Novikov, R.P. Campion, I. Grzegory, S. Porowski, M. Albrecht, and H.P. Strunk

PART V: THEORY, DEFECTS, TRANSPORT, BANDSTRUCTURE

***Computational Materials Science, An Increasingly Reliable Engineering Tool: Anomalous Nitride Bandstructures and Device Consequences** G5.1.1
A. Sher, M. van Schilfgaarde, M.A. Berding, S. Krishnamurthy, and A-B. Chen

Absorption Coefficient and Refractive Index of GaN, AlN, and AlGaN Alloys G5.2.1
J.F. Muth, J.D. Brown, M.A.L. Johnson, Z. Yu, R.M. Kolbas, J.W. Cook, Jr., and J.F. Schetzina

Defect Complexes and Non-Equilibrium Processes Underlying the p-Type Doping of GaN G5.3.1
F.A. Reboredo and S.T. Pantelides

*Invited Paper

Role of the Substitutional Oxygen Donor in the Residual n-Type Conductivity in GaN G5.4.1
W.M. Chen, I.A. Buyanova, Mt. Wagner, B. Monemar, J.L. Lindström, H. Amano, and I. Akasaki

Interface Effects on the Persistent Photoconductivity in Thin GaN and AlGaN Films G5.5.1
O.P. Seifert, O. Kirfel, M. Munzel, M.T. Hirsch, J. Parisi, M. Kelly, O. Ambacher, and M. Stutzmann

Studies on Carbon as Alternative p-Type Dopant for Gallium Nitride G5.6.1
U. Birkle, M. Fehrer, V. Kirchner, S. Einfeldt, D. Hommel, S. Strauf, P. Michler, and J. Gutowski

*The Behavior of Ion-Implanted Hydrogen in Gallium Nitride G5.8.1
S.M. Myers, T.J. Headley, C.R. Hills, J. Han, G.A. Petersen, C.H. Seager, and W.R. Wampler

Spectroscopy of Proton Implanted GaN G5.9.1
M.G. Weinstein, M. Stavola, C.Y. Song, C. Bozdog, H. Przbylinska, G.D. Watkins, S.J. Pearton, and R.G. Wilson

A Critical Comparison Between MOVPE and MBE Growth of III-V Nitride Semiconductor Materials for Opto-Electronic Device Applications G5.10.1
M.A.L. Johnson, Z. Yu, J.D. Brown, F.A. Koeck, N.A. El-Masry, H.S. Kong, J.A. Edmond, J.W. Cook, Jr., and J.F. Schetzina

PART VI: SURFACES, THEORY, PROCESSING, DEVICES

Characteristic Temperature Estimation of GaN-Based Lasers G6.2.1
T. Honda, H. Kawanishi, T. Sakaguchi, F. Koyama, and K. Iga

GaN Nanotubes G6.3.1
S.M. Lee, Y.H. Lee, Y.G. Hwang, J. Elsner, D. Porezag, and T. Frauenheim

Characterization of Hot-Electron Effects on Flicker Noise in III-V Nitride Based Heterojunctions G6.4.1
W.Y. Ho, W.K. Fong, C. Surya, K.Y. Tong, L.W. Lu, and W.K. Ge

Characterization of Flicker Noise in GaN Based MODFETs at Low Drain Bias G6.5.1
W.Y. Ho, W.K. Fong, C. Surya, K.Y. Tong, W. Kim, A. Botchkarev, and H. Morkoç

Monte Carlo Simulation of Hall Effect in n-Type GaN G6.6.1
J.D. Albrecht, P.P. Ruden, E. Bellotti, and K.F. Brennan

*Invited Paper

Base Transit Time in Abrupt GaN/InGaN/GaN and AlGaN/GaN/AlGaN HBTs G6.7.1
S-Y. Chiu, A.F.M. Anwar, and S. Wu

Theoretical Studies of ZnO and Related $Mg_xZn_{1-x}O$ Alloy Bandstructures G6.8.1
W.R.L. Lambrecht, S. Limpijumnong, and B. Segall

Transport, Growth Mechanisms, and Material Quality in GaN Epitaxial Lateral Overgrowth G6.9.1
M.E. Coltrin, C.C. Willan, M.E. Bartram, J. Han, N. Missert, M.H. Crawford, and A.G. Baca

Electronic Structure and Optical Properties of $ZnGeN_2$ G6.11.1
S. Limpijumnong, S.N. Rashkeev, and W.R.L. Lambrecht

Electrical Characterization of Defects Introduced in n-GaN During High Energy Proton and He-Ion Irradiation G6.12.1
S.A. Goodman, F.D. Auret, F.K. Koschnick, J-M. Spaeth, B. Beaumont, and P. Gibart

Electrical Characterization of Sputter Deposition Induced Defects in n-GaN G6.13.1
F.D. Auret, S.A. Goodman, F.K. Koschnick, J-M. Spaeth, B. Beaumont, and P. Gibart

Photoluminescence of FS-GaN Treated in Alcoholic Sulfide Solutions G6.14.1
Y.V. Zhilyaev, M.E. Kompan, E.V. Konenkova, and S.D. Raevskii

Effect of Oxygen Ion Implantation in Gallium Nitride G6.15.1
W. Jiang, W.J. Weber, S. Thevuthasan, G.J. Exarhos, and B.J. Bozlee

Piezoelectric Field Effect on Optical Properties of GaN/GaInN/AlGaN Quantum Wells G6.20.1
J.S. Im, H. Kollmer, O. Gfrörer, J. Off, F. Scholz, and A. Hangleiter

Control of the Polarity and Surface Morphology of GaN Films Deposited on C-Plane Sapphire G6.23.1
M. Sumiya, T. Ohnishi, M. Tanaka, A. Ohtomo, M. Kawasaki, M. Yoshimoto, H. Koinuma, K. Ohtsuka, and S. Fuke

Thermal Annealing of InGaN/GaN Strained-Layer Quantum Well G6.25.1
M.C.Y. Chan, K-O. Tsang, E.H. Li, and S.P. DenBaars

XPS Study of Oxygen Adsorption on (3x3) Reconstructed MBE Grown GaN Surfaces G6.26.1
R.A. Beach, E.C. Piquette, and T.C. McGill

Thermal Stability of GaN Investigated by Raman Scattering G6.28.1
M. Kuball, F. Demangeot, J. Frandon, M.A. Renucci, N. Grandjean, and O. Briot

Electroluminescence Properties of InGaN/AlGaN/GaN Light Emitting Diodes With Quantum Wells G6.29.1
A.E. Yunovich, V.E. Kudryashov, A.N. Turkin, A.N. Kovalev, and F.I. Manyakhin

Electrical Characterization of MOVPE-Grown p-Type GaN:Mg Against Annealing Temperature G6.31.1
Shizuo Fujita, M. Funato, D-C. Park, Y. Ikenaga, and Shigeo Fujita

Rapid Thermal Processing of Implanted GaN Up to 1500°C G6.33.1
X.A. Cao, S.J. Pearton, R.K. Singh, C.R. Abernathy, J. Han, R.J. Shul, D.J. Rieger, J.C. Zolper, R.G. Wilson, M. Fu, J.A. Sekhar, H.J. Guo, and S.J. Pennycook

Extrinsic Performance Limitations of AlGaN/GaN Heterostructure Field Effect Transistors G6.35.1
P.P. Ruden, J.D. Albrecht, A. Sutandi, S.C. Binari, K. Ikossi-Anastasiou, M.G. Ancona, R.L. Henry, D.D. Koleske, and A.E. Wickenden

Behavior of W and WSi_x Contact Metallization on n- and p-Type GaN G6.39.1
X.A. Cao, F. Ren, J.R. Lothian, S.J. Pearton, C.R. Abernathy, J.C. Zolper, M.W. Cole, A. Zeitouny, M. Eizenberg, and R.J. Shul

Photoelectrochemical Etching of $In_xGa_{1-x}N$ G6.40.1
H. Cho, S.M. Donovan, C.R. Abernathy, S.J. Pearton, F. Ren, J. Han, and R.J. Shul

Modeling of a GaN Based Static Induction Transistor G6.41.1
G.E. Bunea, S.T. Dunham, and T.D. Moustakas

Contact Resistance of InGaN/GaN Light Emitting Diodes Grown on the Production Model Multi-Wafer MOVPE Reactor G6.42.1
R.W. Chuang, A.Q. Zou, H.P. Lee, Z.J. Dong, F.F. Xiong, R. Shih, M. Bremser, and H. Juergensen

Crystal Structure and Defects in Nitrogen-Deficient GaN G6.43.1
S. Oktyabrsky, K. Dovidenko, A.K. Sharma, V. Joshkin, and J. Narayan

Influence of Si-Doping on Carrier Localization of MOCVD-Grown InGaN/GaN Multiple Quantum Wells G6.44.1
Y-H. Cho, T.J. Schmidt, S. Bidnyk, J.J. Song, S. Keller, U.K. Mishra, and S.P. DenBaars

Theory of the Gain Characteristics of InGaN/AlGaN QD Lasers G6.45.1
A.D. Andreev and E.P. O'Reilly

Study of Thin Films Polarity of Group III Nitrides G6.46.1
K. Dovidenko, S. Oktyabrsky, J. Narayan, and M. Razeghi

Temperature Dependence of Bound Exciton Emissions in GaN G6.47.1
D.G. Chtchekine, G.D. Gilliland, Z.C. Feng, S.J. Chua, D.J. Wolford, S.E. Ralph, M.J. Schurman, and I. Ferguson

Room Temperature Laser Action in Laterally Overgrown GaN Pyramids on (111) Silicon G6.48.1
S. Bidnyk, B.D. Little, Y.H. Cho, J. Krasinski, J.J. Song, W. Yang, and S.A. McPherson

NiIn as an Ohmic Contact to P-GaN G6.49.1
D.B. Ingerly, Y.A. Chang, and Y. Chen

GaN p-n Structures Fabricated by Mg Ion Implantation G6.53.1
E.V. Kalinina, V.A. Solov'ev, A.S. Zubrilov, V.A. Dmitriev, and A.P. Kovarsky

Amplification Path Length Dependence Studies of Stimulated Emission From Optically Pumped InGaN/GaN Multiple Quantum Wells G6.54.1
T.J. Schmidt, S. Bidnyk, Y-H. Cho, A.J. Fischer, J.J. Song, S. Keller, U.K. Mishra, and S.P. DenBaars

Inductively Coupled Plasma Etching of III-Nitrides in Cl_2/Xe, Cl_2/Ar and Cl_2/He G6.56.1
H. Cho, Y.B. Hahn, D.C. Hays, K.B. Jung, S.M. Donovan, C.R. Abernathy, S.J. Pearton, and R.J. Shul

Focused Ion Beam Etching of GaN G6.57.1
C. Flierl, I.H. White, M. Kuball, P.J. Heard, G.C. Allen, C. Marinelli, J.M. Rorison, R.V. Penty, Y. Chen, and S.Y. Wang

Physics-Based Intrinsic Model for AlGaN/GaN HEMTs G6.58.1
S. Wu, R.T. Webster, and A.F.M. Anwar

Ensemble Monte Carlo Study of Electron Transport in Bulk Indium Nitride G6.59.1
E. Bellotti, B. Doshi, K.F. Brennan, and P.P. Ruden

Phonon Dynamics and Lifetimes of AlN and GaN Crytallites G6.65.1
L. Bergman, D. Alexson, R.J. Nemanich, M. Dutta, M.A. Stroscio, C. Balkas, and R.F. Davis

PART VII: LEDs, UV DETECTORS, AND OPTICAL PROPERTIES

Symmetry of Electrons and Holes in Lightly Photo-Excited InGaN LEDs G7.4.1
T.A. Kennedy, E.R. Glaser, W.E. Carlos, P.P. Ruden, and S. Nakamura

Fabrication of Smooth GaN-Based Laser Facets G7.5.1
D.A. Stocker, E.F. Schubert, K.S. Boutros, and J.M. Redwing

Uniformity and Performance Characterization of GaN p-i-n Photodetectors Fabricated From 3-Inch Epitaxy G7.6.1
R. Hickman II, J.J. Klaassen, J.M. Van Hove, A.M. Wowchak, C. Polley, M.F. Rosamond, and P.P. Chow

Monitoring and Controlling of Strain During MOCVD of AlGaN for UV Optoelectronics G7.7.1
J. Han, M.H. Crawford, R.J. Shul, S.J. Hearne, E. Chason, J.J. Figiel, and M. Banas

Generation Recombination Noise in GaN Photoconducting Detectors G7.8.1
M. Misra, D. Doppalapudi, A.V. Sampath, T.D. Moustakas, and P.H. McDonald

PART VIII: ELECTRONIC DEVICES AND PROCESSING

***Group-III Nitride Etch Selectivity in BCl_3/Cl_2 ICP Plasmas** G8.1.1
R.J. Shul, L. Zhang, C.G. Willison, J. Han, S.J. Pearton, J. Hong, C.R. Abernathy, and L.F. Lester

***Patterning III-N Semiconductors by Low Energy Electron Enhanced Etching (LE4)** G8.2.1
H.P. Gillis, M.B. Christopher, K.P. Martin, and D.A. Choutov

Normal and Inverted AlGaN/GaN Based Piezoelectric Field Effect Transistors Grown by Plasma Induced Molecular Beam Epitaxy G8.4.1
M.J. Murphy, B.E. Foutz, K. Chu, H. Wu, W. Yeo, W.J. Schaff, O. Ambacher, L.F. Eastman, T.J. Eustis, R. Dimitrov, M. Stutzmann, and W. Rieger

PART IX: QUANTUM DOTS AND PROCESSING

Piezoelectric Properties of GaN Self-Organized Quantum Dots G9.2.1
B. Daudin, F. Widmann, J. Simon, G. Feuillet, J.L. Rouvière, N.T. Pelekanos, and G. Fishman

Fabrication of Self-Assembling AlGaN Quantum Dot on AlGaN Surfaces Using Anti-Surfactant G9.4.1
H. Hirayama, Y. Aoyagi, and S. Tanaka

Scanning Tunneling Microscopy Studies of InGaN Growth by Molecular Beam Epitaxy G9.5.1
H. Chen, A.R. Smith, R.M. Feenstra, D.W. Greve, and J.E. Northrup

Ni/Si-Based Contacts to GaN: Thermally Activated Structural Transformations Leading to Ohmic Behavior G9.9.1
E. Kaminska, A. Piotrowska, J. Jasinski, J. Kozubowski, A. Barcz, K. Golaszewska, D.B. Thomson, R.F. Davis, and M.D. Bremser

*Invited Paper

PART X: NOVEL GROWTH, DOPING, AND PROCESSING

*Improvement of Crystalline Quality of Group III Nitrides on Sapphire Using Low Temperature Interlayers G10.1.1
H. Amano, M. Iwaya, N. Hayashi, T. Kashima, M. Katsuragawa, T. Takeuchi, C. Wetzel, and I. Akasaki

*GaN Homoepitaxy for Device Applications G10.2.1
M. Kamp, C. Kirchner, V. Schwegler, A. Pelzmann, K.J. Ebeling, M. Leszczynski, I. Grzegory, T. Suski, and S. Porowski

*Doping of AlGaN Alloys G10.4.1
C.G. Van de Walle, C. Stampfl, J. Neugebauer, M.D. McCluskey, and N.M. Johnson

*Etch Processing of III-V Nitrides G10.5.1
C.R. Eddy, Jr.

Damage-Free Photo-Assisted Cryogenic Etching of GaN as Evidenced by Reduction of Yellow Luminescence G10.6.1
J.T. Hsieh, J.M. Hwang, H.L. Hwang, and W.H. Hung

Focused Ion Beam Micromachining of GaN Photonic Devices G10.7.1
I. Chyr and A.J. Steckl

PART XI: RARE-EARTH DOPING AND OPTICAL EMISSION

*Luminescence From Erbium-Doped Gallium Nitride Thin Films G11.1.1
J.M. Zavada, M. Thaik, U. Hömmerich, J.D. MacKenzie, C.R. Abernathy, F. Ren, H. Shen, J. Pamulapati, H. Jiang, J. Lin, and R.G. Wilson

*RBS Lattice Site Location and Damage Recovery Studies in GaN G11.2.1
E. Alves, M.F. DaSilva, J.C. Soares, J. Bartels, R. Vianden, C.R. Abernathy, and S.J. Pearton

Visible and Infrared Rare-Earth Activated Electroluminescence From Erbium Doped GaN G11.3.1
M. Garter, R. Birkhahn, A.J. Steckl, and J. Scofield

Photoluminescence and Photoluminescence Excitation Spectroscopy of *In Situ* Er-Doped and Er-Implanted GaN Films Grown by Hydride Vapor Phase Epitaxy G11.4.1
S. Kim, X. Li, J.J. Coleman, R. Zhang, D.M. Hansen, T.F. Kuech, and S.G. Bishop

Optical Characterization of Erbium Doped III-Nitrides Prepared by Metalorganic Molecular Beam Epitaxy G11.6.1
U. Hömmerich, J.T. Seo, M. Thaik, J.D. MacKenzie, C.R. Abernathy, S.J. Pearton, R.G. Wilson, and J.M. Zavada

Optical and Structural Properties of AlGaN/GaN Quantum Wells Grown by Molecular Beam Epitaxy G11.7.1
N. Grandjean, J. Massies, M. Leroux, M. Laügt, P. Lefebvre, B. Gil, J. Allègre, and P. Bigenwald

Defect Luminescence in Heavily Mg Doped GaN G11.8.1
M.A. Reshchikov, G-C. Yi, and B.W. Wessels

Author Index

Subject Index

*Invited Paper

PREFACE

This proceedings volume is the permanent record of the Materials Research Society symposium entitled "GaN and Related Alloys," held November 30–December 4, 1998, at the MRS Fall Meeting in Boston, Massachusetts. The symposium covered the full spectrum of activity in the GaN and related materials arena. These semiconductors are finding applications in full-color displays, high-density information storage, white lighting for indoor or backlit displays, solar-blind UV detectors, high-power/high-temperature electronics, and for covert undersea communications. The symposium contained a plenary session with talks on laser diodes, electronic devices, substrates, etching, contacts, and piezoelectric and pyroelectric properties. This was followed by sessions on laser diodes and spectroscopy; conventional growth and characterization; epitaxial lateral overgrowth and selective growth; theory, defects, transport, and bandstructure; surfaces, theory, and processing; LEDs, UV detectors, and optical properties; electronic devices and processing; quantum dots; novel growth, doping, and processing; and finally, rare-earth doping and optical emission. One highlight was a panel discussion involving a report on high-temperature electronics in Japan and the U.S., conducted by a panel including university and government scientists (V. Dmitriev, P. Chow, S. DenBaars, M. Shur, E.R. Brown, J.C. Zolper, C.W. Litton, and J.M. Zavada).

The progress in laser diodes was highlighted shortly after the Meeting by the announcement of commercialization of this technology, and progress was reported in the growth of thick layers on patterned substrates by various methods, leading to lower overall defect concentrations and improved current-voltage and reliability characteristics. The rapidly increasing market for blue/green LEDs was noted by the entry of a number of new companies into the field. While these emitter technologies continue to be dominated by MOCVD material, there were exciting reports of UV detectors and HFET structures grown by MBE with device performance at least as good as by MOCVD. The understanding of carrier confinement mechanisms in lasers and LEDs continues to mature, and there is a much clearer picture of the effects of both defects and residual impurities such as H, C, and O.

This extremely well-attended symposium was the largest in this MRS series. Special mention should be made of the pre-symposium tutorial taught by Prof. M. Shur, which again broke all previous attendance records for MRS. The two poster sessions were also a source of information exchange, and proved very popular with attendees.

Stephen J. Pearton
Chihping P. Kuo
Alan F. Wright
Takeshi Uenoyama

December 1998

ACKNOWLEDGMENTS

The outstanding success of this symposium, both in terms of attendance and scientific quality, was due to the efforts of the authors and speakers who presented their technical work at the Meeting and composed the papers in this proceedings volume; the symposium organizers who put together the program and saw that it ran smoothly; and the following session chairpersons:

T. Uenoyama	S.F. Chichibu
A.F. Wright	M. Murakami
C. Kuo	J.M. Zavada
S.J. Pearton	C.R. Eddy
B.A. Monemar	M. Kamp
H. Morkoc	C.R. Abernathy
W.W. Chow	U. Hommerich
B.J. Skromme	A. Steckl

We also thank the staff of the Materials Research Society for providing the organization for the Meeting, and, most importantly, the sponsors listed below who provided financial (ARO) or in-kind (Sandia, HP, and Matsushita) support for the symposium:

U.S. Army Research Office (Dr. John Prater),
Grant DAAG55-98-1-0478
Hewlett-Packard
Matsushita Electric Industrial Co., Ltd.
Sandia National Laboratories

The editors of this volume extend their sincere appreciation to all who contributed to the success of the symposium.

MATERIALS RESEARCH SOCIETY SYMPOSIUM PROCEEDINGS

Volume 507— Amorphous and Microcrystalline Silicon Technology—1998, R. Schropp, H.M. Branz, M. Hack, I. Shimizu, S. Wagner, 1999, ISBN: 1-55899-413-0
Volume 508— Flat-Panel Display Materials—1998, G. Parsons, C-C. Tsai, T.S. Fahlen, C. Seager, 1998, ISBN: 1-55899-414-9
Volume 509— Materials Issues in Vacuum Microelectronics, W. Zhu, L.S. Pan, T.E. Felter, C. Holland, 1998, ISBN: 1-55899-415-7
Volume 510— Defect and Impurity Engineered Semiconductors and Devices II, S. Ashok, J. Chevallier, K. Sumino, B.L. Sopori, W. Götz, 1998, ISBN: 1-55899-416-5
Volume 511— Low-Dielectric Constant Materials IV, C. Chiang, P.S. Ho, T-M. Lu, J.T. Wetzel, 1998, ISBN: 1-55899-417-3
Volume 512— Wide-Bandgap Semiconductors for High Power, High Frequency and High Temperature, S. DenBaars, J. Palmour, M.S. Shur, M. Spencer, 1998, ISBN: 1-55899-418-1
Volume 513— Hydrogen in Semiconductors and Metals, N.H. Nickel, W.B. Jackson, R.C. Bowman, R.G. Leisure, 1998, ISBN: 1-55899-419-X
Volume 514— Advanced Interconnects and Contact Materials and Processes for Future Integrated Circuits, S.P. Murarka, M. Eizenberg, D.B. Fraser, R. Madar, R. Tung, 1998, ISBN: 1-55899-420-3
Volume 515— Electronic Packaging Materials Science X, D.J. Belton, M. Gaynes, E.G. Jacobs, R. Pearson, T. Wu, 1998, ISBN: 1-55899-421-1
Volume 516— Materials Reliability in Microelectronics VIII, J.C. Bravman, T.N. Marieb, J.R. Lloyd, M.A. Korhonen, 1998, ISBN: 1-55899-422-X
Volume 517— High-Density Magnetic Recording and Integrated Magneto-Optics: Materials and Devices, J. Bain, M. Levy, J. Lorenzo, T. Nolan, Y. Okamura, K. Rubin, B. Stadler, R. Wolfe, 1998, ISBN: 1-55899-423-8
Volume 518— Microelectromechanical Structures for Materials Research, S. Brown, J. Gilbert, H. Guckel, R. Howe, G. Johnston, P. Krulevitch, C. Muhlstein, 1998, ISBN: 1-55899-424-6
Volume 519— Organic/Inorganic Hybrid Materials, R.M. Laine, C. Sanchez, C.J. Brinker, E. Giannelis, 1998, ISBN: 1-55899-425-4
Volume 520— Nanostructured Powders and Their Industrial Application, G. Beaucage, J.E. Mark, G.T. Burns, D-W. Hua, 1998, ISBN: 1-55899-426-2
Volume 521— Porous and Cellular Materials for Structural Applications, D.S. Schwartz, D.S. Shih, A.G. Evans, H.N.G. Wadley, 1998, ISBN: 1-55899-427-0
Volume 522— Fundamentals of Nanoindentation and Nanotribology, N.R. Moody, W.W. Gerberich, N. Burnham, S.P. Baker, 1998, ISBN: 1-55899-428-9
Volume 523— Electron Microscopy of Semiconducting Materials and ULSI Devices, C. Hayzelden, C. Hetherington, F. Ross, 1998, ISBN: 1-55899-429-7
Volume 524— Applications of Synchrotron Radiation Techniques to Materials Science IV, S.M. Mini, S.R. Stock, D.L. Perry, L.J. Terminello, 1998, ISBN: 1-55899-430-0
Volume 525— Rapid Thermal and Integrated Processing VII, M.C. Öztürk, F. Roozeboom, P.J. Timans, S.H. Pas, 1998, ISBN: 1-55899-431-9
Volume 526— Advances in Laser Ablation of Materials, R.K. Singh, D.H. Lowndes, D.B. Chrisey, E. Fogarassy, J. Narayan, 1998, ISBN: 1-55899-432-7
Volume 527— Diffusion Mechanisms in Crystalline Materials, Y. Mishin, G. Vogl, N. Cowern, R. Catlow, D. Farkas, 1998, ISBN: 1-55899-433-5
Volume 528— Mechanisms and Principles of Epitaxial Growth in Metallic Systems, L.T. Wille, C.P. Burmester, K. Terakura, G. Comsa, E.D. Williams, 1998, ISBN: 1-55899-434-3
Volume 529— Computational and Mathematical Models of Microstructural Evolution, J.W. Bullard, L-Q. Chen, R.K. Kalia, A.M. Stoneham, 1998, ISBN: 1-55899-435-1
Volume 530— Biomaterials Regulating Cell Function and Tissue Development, R.C. Thomson, D.J. Mooney, K.E. Healy, Y. Ikada, A.G. Mikos, 1998, ISBN: 1-55899-436-X
Volume 531— Reliability of Photonics Materials and Structures, E. Suhir, M. Fukuda, C.R. Kurkjian, 1998, ISBN: 1-55899-437-8

MATERIALS RESEARCH SOCIETY SYMPOSIUM PROCEEDINGS

Volume 532— Silicon Front-End Technology—Materials Processing and Modelling, N.E.B. Cowern, D.C. Jacobson, P.B. Griffin, P.A. Packan, R.P. Webb, 1998, ISBN: 1-55899-438-6
Volume 533— Epitaxy and Applications of Si-Based Heterostructures, E.A. Fitzgerald, D.C. Houghton, P.M. Mooney, 1998, ISBN: 1-55899-439-4
Volume 535— III-V and IV-IV Materials and Processing Challenges for Highly Integrated Microelectonics and Optoelectronics, S.A. Ringel, E.A. Fitzgerald, I. Adesida, D. Houghton, 1999, ISBN: 1-55899-441-6
Volume 536— Microcrystalline and Nanocrystalline Semiconductors—1998, L.T. Canham, M.J. Sailor, K. Tanaka, C-C. Tsai, 1999, ISBN: 1-55899-442-4
Volume 537— GaN and Related Alloys, S.J. Pearton, C. Kuo, T. Uenoyama, A.F. Wright, 1999, ISBN: 1-55899-443-2
Volume 538— Multiscale Modelling of Materials, V.V. Bulatov, T. Diaz de la Rubia, R. Phillips, E. Kaxiras, N. Ghoniem, 1999, ISBN: 1-55899-444-0
Volume 539— Fracture and Ductile vs. Brittle Behavior—Theory, Modelling and Experiment, G.E. Beltz, R.L. Blumberg Selinger, K-S. Kim, M.P. Marder, 1999, ISBN: 1-55899-445-9
Volume 540— Microstructural Processes in Irradiated Materials, S.J. Zinkle, G. Lucas, R. Ewing, J. Williams, 1999, ISBN: 1-55899-446-7
Volume 541— Ferroelectric Thin Films VII, R.E. Jones, R.W. Schwartz, S. Summerfelt, I.K. Yoo, 1999, ISBN: 1-55899-447-5
Volume 542— Solid Freeform and Additive Fabrication, D. Dimos, S.C. Danforth, M.J. Cima, 1999, ISBN: 1-55899-448-3
Volume 543— Dynamics in Small Confining Systems IV, J.M. Drake, G.S. Grest, J. Klafter, R. Kopelman, 1999, ISBN: 1-55899-449-1
Volume 544— Plasma Deposition and Treatment of Polymers, W.W. Lee, R. d'Agostino, M.R. Wertheimer, B.D. Ratner, 1999, ISBN: 1-55899-450-5
Volume 545— Thermoelectric Materials 1998—The Next Generation Materials for Small-Scale Refrigeration and Power Generation Applications, T.M. Tritt, M.G. Kanatzidis, G.D. Mahan, H.B. Lyon, Jr., 1999, ISBN: 1-55899-451-3
Volume 546— Materials Science of Microelectromechanical Systems (MEMS) Devices, A.H. Heuer, S.J. Jacobs, 1999, ISBN: 1-55899-452-1
Volume 547— Solid-State Chemistry of Inorganic Materials II, S.M. Kauzlarich, E.M. McCarron III, A.W. Sleight, H-C. zur Loye, 1999, ISBN: 1-55899-453-X
Volume 548— Solid-State Ionics V, G-A. Nazri, C. Julien, A. Rougier, 1999, ISBN: 1-55899-454-8
Volume 549— Advanced Catalytic Materials—1998, P.W. Lednor, D.A. Nagaki, L.T. Thompson, 1999, ISBN: 1-55899-455-6
Volume 550— Biomedical Materials—Drug Delivery, Implants and Tissue Engineering, T. Neenan, M. Marcolongo, R.F. Valentini, 1999, ISBN: 1-55899-456-4
Volume 551— Materials in Space—Science, Technology and Exploration, A.F. Hepp, J.M. Prahl, T.G. Keith, S.G. Bailey, J.R. Fowler, 1999, ISBN: 1-55899-457-2
Volume 552— High-Temperature Ordered Intermetallic Alloys VIII, E.P. George, M. Yamaguchi, M.J. Mills, 1999, ISBN: 1-55899-458-0
Volume 553— Quasicrystals, J-M. Dubois, P.A. Thiel, A-P. Tsai, K. Urban, 1999, ISBN: 1-55899-459-9
Volume 554— Bulk Metallic Glasses, W.L. Johnson, C.T. Liu, A. Inoue, 1999, ISBN: 1-55899-460-2
Volume 555— Properties and Processing of Vapor-Deposited Coatings, M. Pickering, B.W. Sheldon, W.Y. Lee, R.N. Johnson, 1999, ISBN: 1-55899-461-0
Volume 556— Scientific Basis for Nuclear Waste Management XXII, D.J. Wronkiewicz, J.H. Lee, 1999, ISBN: 1-55899-462-9

Prior Materials Research Society Symposium Proceedings available by contacting Materials Research Society

Part I

GaN Electronic and Photonic Devices

InGaN/GaN/AlGaN-BASED LEDS and LASER DIODES

S. NAKAMURA, M. SENOH, S. NAGAHAMA, N. IWASA, T. MATUSHITA, T. MUKAI
R&D Dept., Nichia Chemical Industries LTD.,
491, Oka, Kaminaka, Anan, Tokushima 774-0044, Japan, shuji@nichia.co.jp

Cite this article as: MRS Internet J. Nitride Semicond. Res. 4S1, G1.1 (1999)

ABSTRACT

InGaN quantum-well-structure blue LEDs were grown on epitaxially laterally overgrown GaN (ELOG) and sapphire substrates. The output power of both LEDs was as high as 6 mW at a current of 20 mA. The LED on sapphire had a considerable amount of leakage current in comparison with that on ELOG. These results indicate that In composition fluctuation is not caused by threading dislocations (TDs), free carriers are captured by radiative recombination centers before they are captured by nonradiative recombination centers in InGaN, and that the dislocations form the leakage current pathway in InGaN. Red LED with an emission peak wavelength of 650 nm was fabricated by increasing the In composition and thickness of InGaN well layer. When the laser diodes (LD) was formed on the GaN layer above the SiO_2 mask region, the threshold current density was as low as 3 $kAcm^{-2}$. When the LD was formed on the window region, the threshold current density was as high as 6 to 9 $kAcm^{-2}$. There is a possibility that a leakage current due to a large number of TDs caused the high threshold current density on the window region. InGaN multi-quantum-well (MQW) structure LDs grown on the ELOG substrate showed an output power as high as 420 mW under RT-CW operation. The longest lifetime of 9,800 hours at a constant output power of 2 mW was achieved. The InGaN MQW LDs were fabricated on a GaN substrate. The fundamental transverse mode was observed up to an output power of 80 mW.

INTRODUCTION

All of III-V nitride-based light-emitting diodes (LEDs) [1-3] and laser diodes (LDs) [4,5] use an InGaN active layer instead of a GaN active layer because of the difficulty in fabricating highly efficient light-emitting devices using a GaN active layer. Highly efficient UV/blue/green/amber InGaN quantum-well structure LEDs have been fabricated directly on a sapphire substrate in spite of a high dislocation density of 1-10 x 10^{10} cm^{-2} originating from a large lattice mismatch between GaN and the sapphire substrate [1-3]. Due to the high efficiency of the LEDs grown on the sapphire substrates, the dislocations in InGaN do not appear to work as a nonradiative recombination center [6]. Epitaxially laterally overgrown GaN (ELOG) on sapphire was developed recently to reduce the number of threading dislocations in the GaN epitaxial layers [7,8]. Using the ELOG, the number of threading dislocations was reduced

Mat. Res. Soc. Symp. Proc. Vol. 537 © 1999 Materials Research Society

significantly in the GaN grown on the SiO_2 mask. Thus, there is a great interest in fabricating LEDs and LDs using the ELOG substrate which has a small number of dislocations in order to study the role of the dislocations in the InGaN-based LEDs and LDs. For the study, blue InGaN single-quantum-well (SQW) structure LEDs were fabricated on the ELOG and sapphire substrates [9]. The LDs were formed on the SiO_2 mask and window regions of the ELOG substrate [10]. Also, the LD was grown on the free-standing GaN substrate which was obtained by removing the sapphire substrate after growing a thick ELOG substrate [11]. In addition, present performance of InGaN-based LEDs and LDs are described.

BLUE LEDs ON ELOG AND SAPPHIRE SUBSTRATES

Selective growth of GaN was performed on a 2-μm-thick GaN layer grown on a (0001) C-face sapphire substrate. The 0.1-μm-thick silicon dioxide (SiO_2) mask was patterned to form 3-μm-wide stripe windows with a periodicity of 9 μm in the GaN <1-100> direction. Following the 7-μm-thick GaN growth on the SiO_2 mask pattern, the coalescence of the selectively grown GaN enabled the achievement of a flat GaN surface over the entire substrate. This coalesced GaN was designated the ELOG. We examined the defect density by plan-view transmission electron microscopy (TEM) observations of the ELOG substrates.

Figure 1 shows plan-view TEM image of the surface of the ELOG substrate with a thickness of 7 μm. The number of threading dislocations (TDs) on the SiO_2 mask area was lower than $1x10^6$ cm^{-2}, and that on the window area was approximately $3x10^7$ cm^{-2}. The TD density of conventional GaN which was grown directly on the sapphire substrate without the ELOG was of the order of $1x10^{10}$ cm^{-2} [6], the number of the TDs was reduced considerably when the ELOG substrate was used. After obtaining a 15-μm-thick ELOG substrate, an InGaN SQW blue LED structure was grown on the substrate in order to study a role of the dislocations. The LED structure was already described previously [9]. The characteristics of the LEDs were measured under a direct current (DC) at room temperature. For a comparison, blue LED with the same structure was also fabricated directly on the sapphire substrate without the ELOG.

Figure 2 shows a photograph of real LED on ELOG under a forward current of 3 mA. This photograph was taken using a microscope. The size of each LED chip is as large as 350 μm x 350 μm. Each LED chip includes many window and SiO_2 stripe regions periodically. No inhomgeneties of blue emission intensity over the entire surface of the p-type transparent Ohmic contact layer was observed. Thus, it is concluded that a large number of TDs of $3x10^7$ cm^{-2} on the widow region do not serve to decrease the efficiency of the LEDs. The ELOG and GaN on sapphire had average TD densities of $1x10^7$ cm^{-2} and $1x10^{10}$ cm^{-2}, respectively. Here, average TD density of the ELOG on sapphire was obtained by dividing the TD density of $3x10^7$ cm^{-2} on the window region by the ratio of (stripe periodicity of 9 μm)/ (window width of 3 μm) because the TD density on the SiO_2 stripe region was lower than $1x10^6$ cm^{-2}, as shown in Fig. 1.

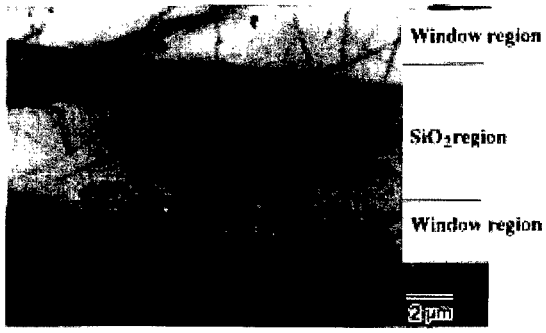


Fig. 1. Plan-view TEM image of the surface of the ELOG substrate with a thickness of 7 μm.

The output power of both LEDs at a current of 20 mA was 6 mW, which is equal to the external quantum efficiency of 11 %. In spite of a large number of dislocations, the LED on sapphire had the same output power as that on ELOG. Thus, the dislocation seems not to work as nonradiative recombination centers in the InGaN active layer. If the TDs work as nonradiative recombination centers, the output power of the LED on ELOG have to be much higher than that on sapphire due to a small number of average TD density.

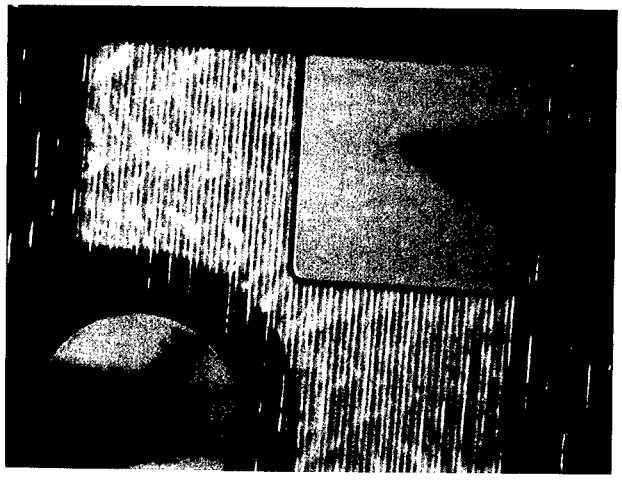


Fig. 2. Photograph of blue InGaN SQW LED on ELOG under a forward current of 3 mA.

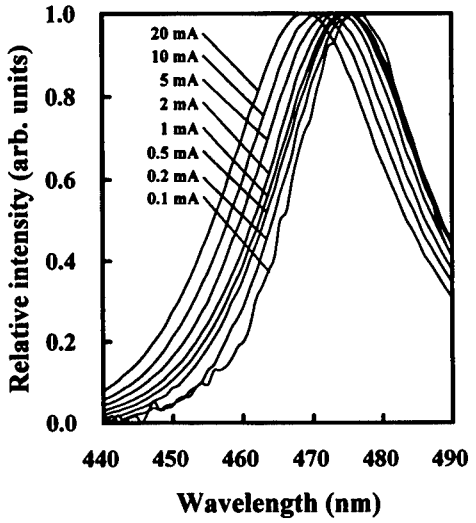


Fig. 3. Emission spectra of blue InGaN SQW LED grown on ELOG substrate at various forward currents.

Figure 3 shows the emission spectra of the blue InGaN SQW LEDs on ELOG at forward currents from 0.1 mA to 20 mA. At a current of 20 mA, the peak wavelength and the full-width at half maximum (FWHM) of the emission spectra of the LED on ELOG were 470 nm and 27 nm, respectively, and those on sapphire were 464 nm and 26 nm, respectively. The peak wavelength of the LED on ELOG is somewhat longer than that on sapphire probably due to a growth fluctuation. There is no significant difference between in the spectra of both LEDs. The broad spectral width is mainly due to an In composition fluctuation in the InGaN well layer [12-14]. This means that the size of the fluctuation is the same in both LEDs in spite of a large difference in the dislocation density. Thus, the In composition fluctuations are not related to the dislocations. In the spectra, the blueshift is easily observed due to a band-filling effect of the deep localized energy states. The blue LED on sapphire also showed the same blueshift with increasing the forward current. We measured the absorption spectra and electroluminescence (EL) of blue/green InGaN SQW LEDs grown on sapphire substrate in previous studies [12-14]. The entire EL appeared at the lower energy tail of the absorption spectra. The EL of blue and green LEDs originated from the carrier recombination at the deep localized energy states with a localization energy of 290 meV and 570 meV, respectively. The blueshift of the EL of the green SQW LEDs with increasing forward current was due to a band-filling effect of the localized energy states. Both LEDs showed the same peak wavelength dependence on the current, which implies the same blueshifts. Thus, the TDs are not directly related to the formation of the localized energy states. These localized states are probably formed by the In composition fluctuation in the InGaN well layer due to a natural phase

separation of InGaN during growth. Therefore, assuming that the localized states are formed by the In composition fluctuation in the InGaN well layer, the TD related composition fluctuation is eliminated because the TD density of the epilayer on the ELOG is relatively small.

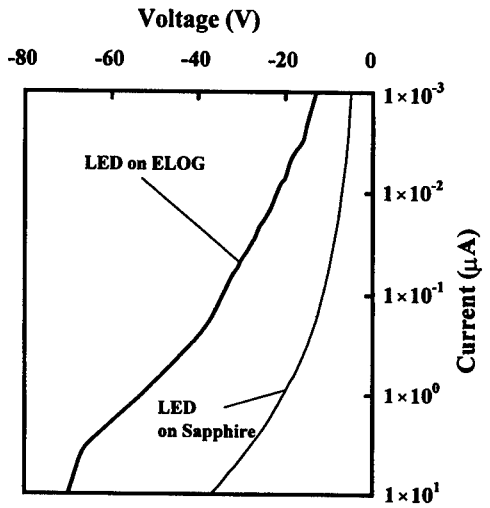


Fig. 4. I-V characteristics of blue InGaN SQW LEDs grown on ELOG and on sapphire substrates under reverse biased conditions.

Thus, the localization induced by the In composition fluctuations seem to be a key role of the high efficiency of the InGaN-based blue LEDs. When the electrons and holes are injected into the InGaN active layer of the LEDs, these carriers are captured by the localized energy states before they are captured by the nonradiative recombination centers caused by the large number of TDs [15]. It was reported that the TDs served as a nonradiative recombination center in GaN and InGaN [16,17]. These localized energy states can be formed only in InGaN films during the growth due to a phase separation of the InGaN. Assuming that the lateral spacing of the effective bandgap (potential) minimum due to the In composition determines the carrier diffusion length in InGaN, the diffusion length was estimated to be less than 60 nm from the spatially resolved CL spectrum mapping measurement [18]. It was also concluded that the efficiency of light emission was high as long as the minority carrier diffusion length was shorter than the dislocation spacing [18]. Considering about these previous results, the carrier diffusion length determined by the potential fluctuation due to InGaN phase separation must be less than the TD spacing in the InGaN layer in order to obtain high-efficient InGaN-based LEDs.

Figure 4 shows the reverse biased I-V characteristics of both LEDs. At a reverse bias voltage of -20 V, the reverse current of the LED on the ELOG was 0.009 μA, and that on sapphire was 1 μA. Under the reverse biased condition, the LED on sapphire had a considerable

amount of leakage current. This leakage current is probably caused by the TDs because the LEDs on sapphire have a considerable amount of leakage current and many TDs [19].

InGaN-BASED RED LEDs

We also fabricated red InGaN SQW LEDs by increasing the In composition and thickness of InGaN well layers in the above LED structure. The In composition and thickness of the InGaN well layer were changed to approximately 50 % and 40Å, respectively. Here, the In composition was determined assuming that the bowing parameter of InGaN was 1 eV [20]. However, recent studies revealed that the bowing parameter of InGaN is much higher than 1 eV [21,22]. In that case, the In content in the InGaN layer should be much smaller than the above values. The LED structure was grown directly on a sapphire substrate without ELOG. Figure 5 shows the emission spectrum of red InGaN SQW LED at a forward current of 5 mA. The peak wavelength is 650 nm (1.91 eV), which peak emission energy is almost equivalent to a band-gap energy of InN. When the current was changed from 5 mA to 80 mA, a large blueshift of the peak wavelength was observed from 650 nm to 580 nm. Because of low symmetry, the wurtzite system such as InGaN-based materials, displays pyroelectric and piezoelectric behavior [23-26]. The macroscopic polarization in the material comprising the active region of the SQW or MQW structure gives rise to a net electric field perpendicular to the plane of the well. This field, if strong enough, will induce a spatial separation of the electron and hole wave functions in the well. As the charge density becomes concentrated near the walls of the well, the wave function overlap decreases and the interband recombination rate decrease (the quantum-confined Stark effect (QCSE)). The blueshift of the electroluminecence (EL) of the InGaN SQW LEDs with increasing operating current can be explained by the QCSE resulting from piezoelectric fields [26], when the In composition and thickness of the InGaN well layer are large. However, a higher efficiency of the LEDs with increasing strain in the SQW upon increasing the In content in the InGaN well layers, was observed from UV to green LEDs [1,2,5]. These phenomena cannot be explained by only the QCSE. It may be that the localization effects induced by composition fluctuations must overcome these intrinsic limitations due to the piezoelectric field. Considering about previous works, the emission wavelength of the red LED dependence on the current (blueshift) is mainly dominated by the screening effects of the QCSE due to the large In composition and thickness of the InGaN well layer.

VIOLET LDs GROWN ON ELOG SUBSTRATES

The LDs with an InGaN MQW/GaN/AlGaN separate confinement heterostructure (SCH) was grown on above-mentioned ELOG substrate. To grow the thick AlGaN cladding layer with a high Al content required for optical confinement without any cracks, GaN/AlGaN modulation doped strained-layer superlattices (MD-SLSs) within the range of critical thickness instead of

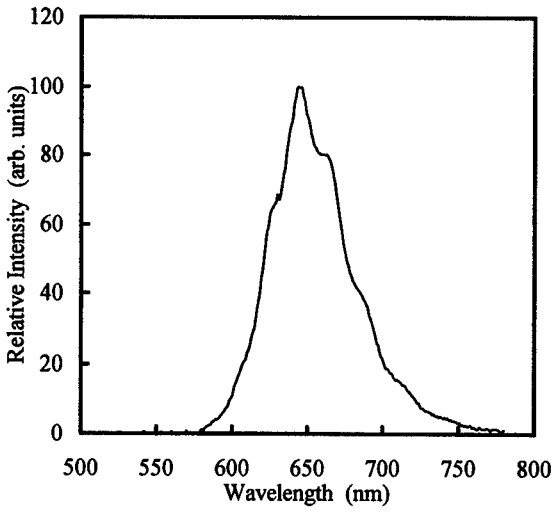


Fig. 5. Emission spectrum of red InGaN SQW LED grown on sapphire substrate.

thick AlGaN layers were used as cladding layers [10,11]. The LD structure was grown on the ELOG substrate with a thickness of 15 μm. The InGaN MQW LD device consisted of a 3-μm-thick layer of n-type GaN:Si, a 0.1-μm-thick layer of n-type $In_{0.1}Ga_{0.9}N$:Si, a $Al_{0.14}Ga_{0.86}N$/GaN MD-SLS cladding layer consisting of 120 25-Å-thick undoped GaN separated by 25-Å-thick Si-doped $Al_{0.14}Ga_{0.86}N$ layers, a 0.1-μm-thick layer of Si-doped GaN, an $In_{0.15}Ga_{0.85}N/In_{0.02}Ga_{0.98}N$ MQW structure consisting of four 35-Å-thick Si-doped $In_{0.15}Ga_{0.85}N$ well layers forming a gain medium separated by 105-Å-thick Si-doped $In_{0.02}Ga_{0.98}N$ barrier layers, a 200-Å-thick layer of p-type $Al_{0.2}Ga_{0.8}N$:Mg, a 0.1-μm-thick layer of Mg-doped GaN, a $Al_{0.14}Ga_{0.86}N$/GaN MD-SLS cladding layer consisting of 240 25-Å-thick undoped GaN separated by 25-Å-thick Mg-doped $Al_{0.14}Ga_{0.86}N$ layers, and a 0.05-μm-thick layer of p-type GaN:Mg. The 0.1-μm-thick n-type and p-type GaN layers were light-guiding layers. The n-type and p-type $Al_{0.14}Ga_{0.86}N$/GaN MD-SLS layers acted as cladding layers for confinement of the carriers and the light emitted from the active region of the InGaN MQW structure. The structure of the ridge-geometry InGaN MQW LD was almost the same as that described previously [5,10,11]. First, the surface of the p-type GaN layer was partially etched until the n-type GaN layer and the p-type $Al_{0.14}Ga_{0.86}N$/GaN MD-SLS cladding layer were exposed, in order to form a ridge-geometry LD. The laser cavity was formed parallel to the direction of the SiO_2 stripe. A mirror facet was formed by dry etching, as reported previously [5]. High-reflection facet coatings (90 %) consisting of 2 pairs of quarter-wave TiO_2/SiO_2 dielectric multilayers were used to reduce the threshold current. A Ni/Au contact was evaporated onto the

p-type GaN layer, and a Ti/Al contact was evaporated onto the n-type GaN layer. The electrical characteristics of the LDs fabricated in this way were measured under a direct current (DC). The structure of the LD is shown in Fig. 6.

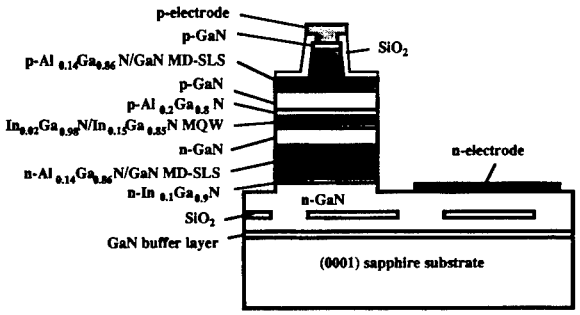


Fig. 6. Structure of the InGaN MQW-structure LDs with MD-SLS cladding layers grown on the ELOG substrate.

The ridge-geometry LDs were formed on the GaN layer above the SiO_2 region with low TDs of lower than $1x10^6$ cm^{-2} and the window region with a high TD density of $3x10^7$ cm^{-2}. The V-I characteristics and the light output power per coated facet of the LD with a cavity length of 450 μm and a ridge width of 4 μm as a function of the forward DC current (L-I) at RT were measured. When the LD was formed on the GaN layer above the SiO_2 mask region with low TDs, the threshold current was 53 mA, which corresponded to a threshold current density of 3 $kAcm^{-2}$. When the LD was formed on the window region with the high TD density, the LD had a threshold current density of 6 to 9 $kAcm^{-2}$, which was much higher than that of the LD formed on the SiO_2 mask. The higher threshold current density is probably caused by the large number of TD density of $3x10^7$ cm^{-2} at the window region. It was confirmed that the dislocation served as a leakage current pathway in InGaN as shown in Fig. 4. Thus, there is a possibility that a leakage current due to a large number of TDs caused the high threshold current density on the window region. Further studies are required to determine the exact reasons of the high threshold current density caused by TDs.

Figure 7 shows the results of a lifetime test for CW-operated LDs formed on the GaN layer above the SiO_2 mask region carried out at 20°C, in which the operating current is shown as a function of time under a constant output power of 2 mW per facet controlled using an autopower controller (APC). The LDs is survived 9,800 hours of operation. The LDs formed on the window region showed the lifetimes of 1,000-3,000 hours due to the high threshold current density of 6 to 9 $kAcm^{-2}$. The emission spectra of the LDs were measured under RT-CW operation at currents of 50 and 60 mA, as shown in Fig. 8. At a current of 50 mA, longitudinal modes with a mode

separation of 0.04 nm due to the cavity were observed. At a current of 60 mA, a single-mode emission was observed at an emission wavelength of 396.6 nm.

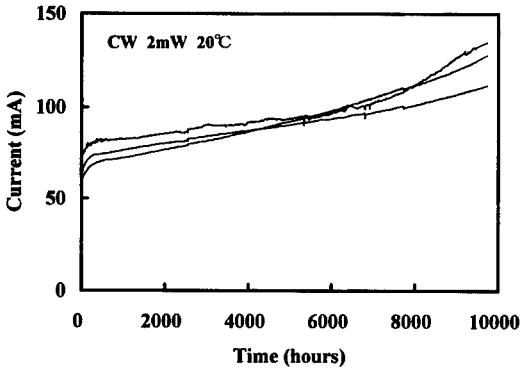


Fig. 7. Operating current as a function of time under a constant output power of 2 mW per facet controlled using an autopower controller. The InGaN MQW LDs with MD-SLS cladding layers grown on the ELOG substrate were operated under DC at 20°C.

High-power LDs were also fabricated on the ELOG substrate. After obtaining a 20-μm-thick ELOG substrate, the InGaN MQW LD structure was grown on the surface. The InGaN MQW LD structure was the same as described in Fig. 6 except for the active layer. The InGaN MQW structure was changed to an $In_{0.15}Ga_{0.85}N/In_{0.02}Ga_{0.98}N$ MQW structure consisting of two 40-Å-thick undoped $In_{0.15}Ga_{0.85}N$ well layers forming a gain medium separated by 100-Å-thick Si-doped $In_{0.02}Ga_{0.98}N$ barrier layers. The area of the ridge-geometry LD was 3 μm x 450 μm. A laser cavity was formed by cleaving the facets along {1-100} of the LD grown on the ELOG substrate after polishing the sapphire substrate to 70 μm. A facet coating (90 %) consisting of 2 pairs of quarter-wave TiO_2/SiO_2 dielectric multilayers was formed on one side of the facet. The output power of the LD was measured from the other side of uncoated facet.

Figure 9 shows the V-I characteristics and the light output power per uncoated cleaved facet of the LD grown on the ELOG substrate with a number of well of 2 as a function of the forward DC current (L-I) at RT. No stimulated emission was observed up to a threshold current of 40 mA, which corresponds to a threshold current density of 3 kA/cm^2. The slope efficiency was as high as 1.2 W/A per facet because the output power was measured from the uncoated cleaved mirror facet having low reflectivity. The differential quantum efficiency per facet was 39 %. The output power of the LDs was as high as 420 mW at an operating current of 490 mA. This

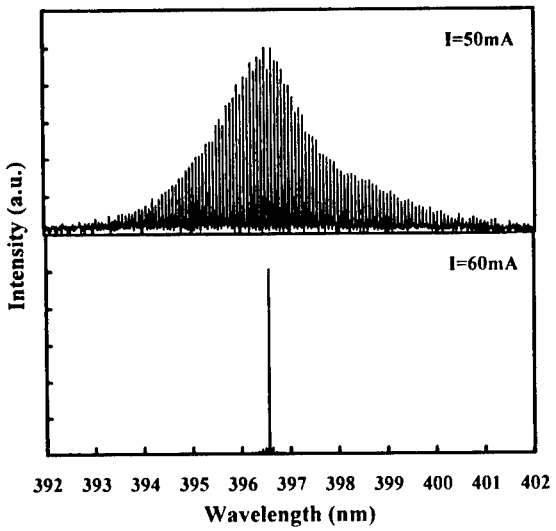


Fig. 8. Laser emission spectra measured under RT CW operation with currents of 50 mA and 60 mA.

output power is the highest ever reported for III-V nitride-based LDs under RT-CW operation. At an output power of 100 mW, a kink was observed in the L-I curve because the transverse mode change occurred at an output power of 100 mW. The emission spectra of the LDs were measured

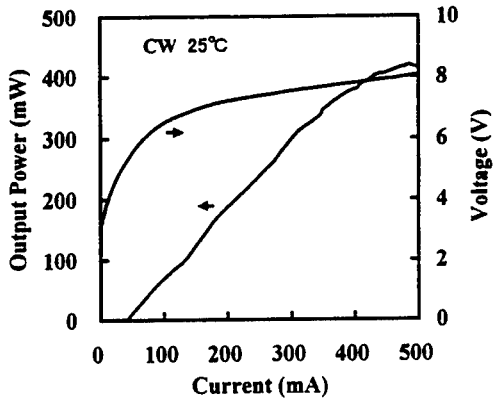


Fig. 9. Typical L-I and V-I characteristics of InGaN MQW LDs measured under CW operation at RT.

under RT-CW operation at output powers of 10 mW and 30 mW. At output powers of 10 mW and 30 mW, stimulated emission was observed at wavelengths of around 408.2 and 408.8 nm, respectively. The lifetime test of the high-power LD was carried out at an ambient temperature of 50°C and a constant output power of 30 mW controlled using the APC. The initial operating current was as high as 100 mA due to the high-temperature operation. A small increase in the operating current was observed with increasing operation time. After 250 hours of operation, the operating current increases dramatically. Thus, the lifetime of the LD was 250 hours.

LDs GROWN ON GaN SUBSTRATES

After obtaining a 20-μm-thick ELOG substrate, the wafer was removed from the MOCVD reactor. Next, GaN growth was carried out using a conventional hydride vapor phase epitaxy (HVPE) system using a horizontal quartz reactor because the growth rate of GaN is much higher when using the HVPE method. Undoped GaN growth was continued up to 200 μm. Then, the sapphire substrate was removed by polishing, in order to obtain a pure GaN substrate with a thickness of approximately 150 μm. Then, the InGaN MQW LD structure was grown on the surface of the 150-μm-thick GaN substrate by MOCVD. The InGaN MQW LD structure was the same as described in Fig. 6 except for the active layer. The InGaN MQW structure was changed to an $In_{0.15}Ga_{0.85}N/In_{0.02}Ga_{0.98}N$ MQW structure consisting of two 40-Å-thick undoped $In_{0.15}Ga_{0.85}N$ well layers forming a gain medium separated by 100-Å-thick Si-doped $In_{0.02}Ga_{0.98}N$ barrier layers. The area of the ridge-geometry LD was 3 μm x 400 μm. A laser cavity was formed by cleaving the facets along {1-100} of the LD grown on the GaN substrate. A facet coating (90 %) consisting of 2 pairs of quarter-wave TiO_2/SiO_2 dielectric multilayers was formed on one facet. The output power of the LD was measured from another uncoated facet.

Figure 10 shows the V-I characteristics and the light output power per uncoated cleaved facet of the LD grown on the GaN substrate as a function of the forward DC current (L-I) at RT. No stimulated emission was observed up to a threshold current of 80 mA, which corresponds to a threshold current density of 7 kA/cm^2. The slope efficiency was as high as 0.8 W/A per facet because the output power was measured from the uncoated cleaved mirror facet having low reflectivity. The differential quantum efficiency per facet was 26 %. The output power of the LDs was as high as 160 mW at an operating current of 300 mA. At an output power of 80 mW, a kink was observed in the L-I curve because the transverse mode change occurred at an output power of 80 mW.

Figure 11 shows near-field patterns (NFP) of the LDs taken by a charge-coupled device (CCD) camera through the optical microscope at output powers of 70 mW and 100 mW. The fundamental transverse mode was observed below the output power of 80 mW, as shown in Fig. 11(a). With increasing output power above 80 mW, the first-order transverse mode appeared, as shown in Fig. 11(b). This transverse mode change at an output power of 80 mW caused the

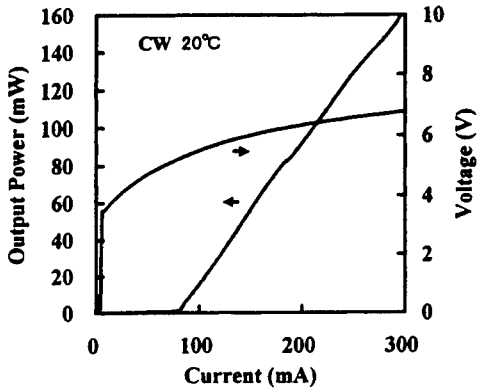


Fig. 10. Typical L-I and V-I characteristics of InGaN MQW LDs grown on GaN substrate measured under CW operation at RT.

kink in the L-I curve. In order to suppress the change, we must control the transverse mode to be a fundamental mode, by further narrowing the ridge width.

The emission spectra of the LDs were measured under RT-CW operation at output powers of 3 mW, 10 mW and 40 mW. At an output power of 3 mW, longitudinal modes with many sharp

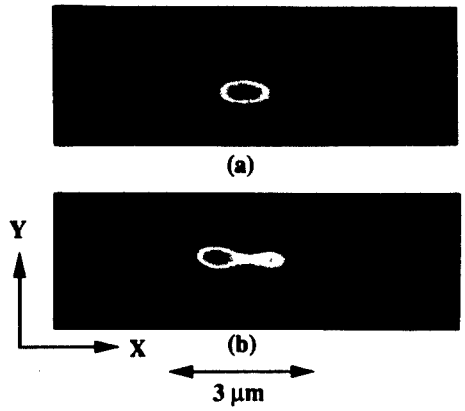


Fig. 11. Near-field pattern of InGaN MQW LDs at output powers of (a) 70 mW and (b) 100 mW under RT-CW operation. X and Y directions are parallel and perpendicular to the junction of the LD, respectively.

peaks due to a cavity with a length of 400 μm, were observed. At output powers of 10 mW and 40 mW, multimode emission was observed at wavelengths of around 410.5 and 411.3 nm, respectively. The lifetime test was performed under CW-operation at an ambient temperature of 50°C and a constant output power of 5 mW controlled using the APC. The initial operating

current was as high as 160 mA due to the high-temperature operation. After 180 hours of operation, the operating current increased dramatically. The lifetime was about 180 hours due to a high threshold current density of 14 $kAcm^{-2}$.

CONCLUSIONS

InGaN quantum-well-structure blue LEDs were grown on ELOG and sapphire substrates. The LED on sapphire had a considerable amount of leakage current in comparison with that on ELOG. These results indicate that In composition fluctuation is not caused by TDs, free carriers are captured by radiative recombination centers before they are captured by nonradiative recombination centers in InGaN, and that the dislocations form the leakage current pathway in InGaN. Red LED with an emission peak wavelength of 650 nm was fabricated by increasing the In composition and thickness of InGaN well layer. When the LD was formed on the GaN layer above the SiO_2 mask region, the threshold current density was as low as 3 $kAcm^{-2}$. When the LD was formed on the window region, the threshold current density was as high as 6 to 9 $kAcm^{-2}$. There is a possibility that a leakage current due to a large number of TDs caused the high threshold current density . The longest lifetime of 9,800 hours at a constant output power of 2 mW was achieved. InGaN MQW LDs were fabricated on a GaN substrate grown by HVPE. The fundamental transverse mode was observed up to an output power of 80 mW. These results indicate an imminent commercialization of the LDs in the near future.

REFERENCES

1. S. Nakamura, M. Senoh, N. Iwasa, S. Nagahama, T. Yamada, and T. Mukai, Jpn. J. Appl. Phys., **34**, L1332 (1995).
2. T. Mukai, D. Morita, and S. Nakamura, J. Crystal Growth, **189/190**, 778 (1998).
3. T. Mukai, H. Narimatsu, and S. Nakamura, Jpn. J. Appl. Phys., **37**, L479 (1998).
4. S. Nakamura, M. Senoh, S. Nagahama, N. Iwasa, T. Yamada, T. Matsushita, H. Kiyoku, and Y. Sugimoto, Y., 1996, Jpn. J. Appl. Phys., **35**, L74 (1996).
5. S. Nakamura, and G. Fasol, The Blue Laser Diode, (Springer-Verlag, Heidelberg, 1997).
6. S. D. Lester, F. A. Ponce, M. G. Craford, and D. A. Steigerwald, Appl. Phys. Lett., **66**, 1249 (1995).
7. A. Usui, H. Sunakawa, A. Sakai, and A. Yamaguchi, Jpn. J. Appl. Phys., **36**, L899 (1997).
8. O. H. Nam, M. D. Bremser, T. Zheleva, and R. F. Davis, R. F., 1997, Appl. Phys. Lett., **71**, 2638 (1997).
9. T. Mukai, K. Takekawa, and S. Nakamura, Jpn. J. Appl. Phys., **37**, L839 (1998).
10. S. Nakamura, M. Senoh, S. Nagahama, N. Iwasa, T. Yamada, T. Matsushita, H. Kiyoku, Y. Sugimoto, T. Kozaki, H. Umemoto, M. Sano, and K. Chocho, K., J. Crystal Growth, **189/190**, 820 (1998); Appl. Phys. Lett., **72**, 211 (1998); Jpn. J. Appl. Phys., **37**, L627 (1998).

11. S. Nakamura, M. Senoh, S. Nagahama, N. Iwasa, T. Yamada, T. Matsushita, H. Kiyoku, Y. Sugimoto, T. Kozaki, H. Umemoto, M. Sano, and K. Chocho, K., Jpn. J. Appl. Phys., **37**, L309 (1998); Appl. Phys. Lett., **72**, 2014 (1998).
12. S. Chichibu, T. Azuhata, T. Sota, and S. Nakamura, Appl. Phys. Lett., **69**, 4188 (1996).
13. Y. Narukawa, Y. Kawakami, Sz. Fujita, Sg. Fujita, and S. Nakamura, Phys. Rev. **B55**, 1938R (1997).
14. Y. Narukawa, Y. Kawakami, M. Funato, Sz. Fujita, Sg. Fujita, and S. Nakamura, Appl. Phys. Lett. **70**, 981 (1997).
15. S. Nakamura, Science, **281**, 956 (1998).
16. S. J. Rosner, E. C. Carr, M. J. Ludowise, G. Girolami, and H. I. Erikson, Appl. Phys. Lett., **70**, 420 (1997).
17. T. Sugahara, H. Sato, M. Hao, Y. Naoi, S. Kurai, S. Tottori, K. Yamashita, K. Nishino, L. T. Romano, and S. Sakai, Jpn. J. Appl. Phys., **37**, L398 (1998).
18. S. Chichibu, K. Wada, and S. Nakamura, Appl. Phys. Lett., **71**, 2346 (1997).
19. C. Sasaoka, H. Sunakawa, A. Kimura, M. Nido, A. Usui, and A. Sakai, J. Crystal Growth, **189/190**, 61 (1998).
20. K. Osamura, S. Naka, and Y. Murakami, J. Appl. Phys., **46**, 3432 (1975).
21. H. Amano, T. Takeuchi, S. Sota, H. Sakai, and I. Akasaki, Mat. Res. Soc. Symp. Proc., **449**, 1143 (1997).
22. M. D. McCluskey, C. G. Van de Walle, C. P. Master, L. T. Romano, and N. M. Johnson, Appl. Phys. Lett., **72**, 2725 (1998).
23. S. Chichibu, T. Azuhata, T. Sota, and S. Nakamura, Appl. Phys. Lett., **70**, 2822 (1997).
24. T. Takeuchi, S. Sota, M. Katsuragawa, M. Komori, H. Takeuchi, Amano, and I. Akasaki, Jpn. J. Appl. Phys., **36**, L382 (1997).
25. M. B. Nardelli, K. Rapcewicz, and J. Bernholc, Appl. Phys. Lett., **71**, 3135 (1997).
26. J. S. Im, H. Kollmer, J. Off, A. Sohmer, F. Scholz, and A. Hangleiter, Mat. Res. Soc. Symp. Proc., **482**, 513 (1998).

Material Properties of GaN in the Context of Electron Devices

H. Morkoç[1], R. Cingolani[1]*, W. Lambrecht[2], B. Gil[3], H.-X Jiang[4], J. Lin[4], D. Pavlidis[5], K. Shenai[6],

Cite this article as: MRS Internet J. Nitride Semicond. Res. 4S1, G1.2 (1999)

Abstract

Wide bandgap nitride semiconductors have recently attracted a great level of attention owing to their direct bandgaps in the visible to ultraviolet regions of the spectrum as emitters and detectors. However, this material system with its favorable heterojunctions and transport properties began to produce very respectable power levels in microwave amplifiers. If and when the breakdown fields achieved experimentally approaches the predicted values, this material system may also be very attractive for switching power devices. In addition to the premature breakdown, a number of scientific challenges remain including a clear experimental investigation of polarization effects. In this paper, transport properties as pertained to electronic devices and potential switching devices, and polarization effects will be treated.

Introduction:

Gallium nitride and its alloys with InN and AlN are important semiconductor materials with applications to emitters and detectors (visible to UV range) and high power/temperature electronics.[1,2,3,4,5,6] The production of commercial blue, green and yellow nitride LEDs, demonstration of CW injection lasers and UV detectors are truly extraordinary.[7,8,9] The large intrinsic dielectric breakdown fields, good thermal conductivity, and favorable transport properties make nitride semiconductors desirable for high power electronic devices.[10] For example, modulation doped FETs with a record power density of 6 W/mm have been reported at 10 GHz.[11]

Being non-centro-symmetric, nitrides exhibit large piezoelectric effects when under stress along the c direction. What is not as appreciated is the spontaneous polarization at heterointerfaces caused by the ionicity and uniaxial nature of the wurtzite. Polarization causes a sizable red shift (Stark Effect) in transition energies in InGaN/GaN [12,13] and AlGaN/GaN[14,15,16,17] quantum wells. Polarization and pyroelectric effects due to heterointerfaces in an ionic crystal, misfit and thermal strain, anisotropy, and temperature gradients have important ramifications in electronic devices,

1. Virginia Commonwealth University, P.O. Box 843072, Richmond, USA 23284-3072
* Permanent address: Dept. Material Science, University of Lecce, Lecce Italy
2. Department of Physics, Case Western Reserve University, Cleveland, OH 44106
3. Montpellier University II, 34095 Montpellier CEDEX 5 France
4. Kansas State University, Manhattan, Kansas 66506-2601
5. University of Michigan, Ann Arbor, MI 48109-2122
6. University of Illinois, Chicago, IL 60607-7053

Mat. Res. Soc. Symp. Proc. Vol. 537 © 1999 Materials Research Society

particulary in modulation doped FETs. For example, electric field caused by polarization effects can increase or decrease interfacial free carrier concentrations. As in the case of quantum wells, the literature interpretation of polarization effects in devices has so far been lumped into piezoelectric effects.[18,19].

Despite highly imperfect material, device performance in both emitters/detectors, and the microwave amplifiers has been truly outstanding. If the defects causing premature breakdown were reduced/eliminated, one would wonder whether it would be wrong at all to attempt to develop power/switching devices with large hold voltages and current handling capabilities. In this paper, performance advantages of nitrides in vertical high power devices will be visited along with the topical topic of polarization issues.

Transport Properties as Pertained to Electronic Devices

Transport properties of, namely n-type, GaN and to some extent its related binaries and alloys have been calculated and experimentally investigated. There are a few noteworthy features, among which are the high peak and saturation electron velocity in GaN that does not degrade with doping, and temperature nearly as much when compared to conventional compound semiconductors. Likewise, the low field mobility does not degrade with field as fast due to the large LO phonon energy. Very intriguing are the measured low field mobilities in modulation doped structures which are nearly twice as large as the predicted polar optical phonon limited mobility at room temperature. The optimistic view could be that certain scattering mechanisms are mitigated in such structures and that the bulk low field mobility in GaN at room temperature could be as high as some 2000 $cm^2V^{-1}s^{-1}$. If so, this would pave the way for much coveted very low power loss in GaN based amplifiers and switches. Also important are transport properties at low temperatures. The low temperature electron mobility in modulation doped structures is above 7,000 $cm^2V^{-1}s^{-1}$ s, and the electron velocity increases which provide basis for a compelling argument that cooled GaN based devices utilizing electron transport should be capable of offering much enhanced performance. Whether to cool or not to cool a given semiconductor device must be decided following an overall power/size optimization scheme of all the components that include the power supplies, supporting circuitry, and heat dissipation related hardware. Such optimization schemes often lead to suggestions that the system should be cooled to a certain temperature which bode well for GaN based modulation doped FETs.

Figures of merit for general power switching applications have been examined and it has been shown that power devices in wide energy bandgap materials provide several orders of magnitude improvement in power-handling capability[20]. Compared to Si, calculations for ideal GaN show that GaN offers more than two orders of magnitude improvement in electrical conductivity per unit area (σ_A), and nearly a factor of 10 improvement in maximum power switching frequency (f_{max}). Calculations have also been performed to determine thermal runaway limitations and results show that a SiC or a GaN PN junction diode can sustain 6X higher junction temperature rise compared to a silicon diode before catastrophic burnout occurs which shows potential for device operation above 600°C. Calculations have been performed to estimate performance improvements for SiC and GaN Schottky rectifiers. These results indicate that nearly a five-fold reduction in V_F can be expected for 200-V SiC and GaN Schottky rectifiers operating at a current

density of 100A/cm^2. Above 200V, silicon Schottky rectifiers are impractical because of high V_F and increased surface leakage currents. These results suggest the feasibility of fabricating high performance SiC and GaN Schottky rectifiers with $V_{BD} > 5000V$. In addition, for identical current-handling capability, SiC and GaN devices are expected to be an order of magnitude smaller in die size, thus offsetting any increase in wafer processing cost.

Heterojunction bipolar transistors based on nitride semiconductors are beginning to receive a good deal of attention for high power/switching applications. Arguments used above for rectifiers also apply for HBTs as the requirements for the collector region of an HBT are similar to those for rectifiers and switches. For example, for a given breakdown voltage, the GaN drift region can be either much thinner and/or doped much higher as compared to other semiconductors with smaller breakdown strengths (about a factor 30 compared to Si). This would result in low on resistances, and shorter transit times (nearly by two orders of magnitude as compared to Si), both of which are very much desirable. However, the caveat here is that GaN and related semiconductors have not yet demonstrates their intrinsic breakdown strengths, exhibiting instead premature breakdown. Here as well as above, the discussion is based on intrinsic breakdown strengths which is justifiable for prediction purposes and expecting natural advances in the technology of these materials that occur with time.

Polarization Effects

As alluded to earlier, observations support the presence of electric field in GaN-based heterostructures. The genesis is two fold: piezoelectric effects and the difference in spontaneous polarization between AlGaN and GaN even in the absence of strain. Spontaneous polarization was only recently fully understood, see King-Smith and Vanderbilt[21], Resta[22], and Bernardini and Fiorentini[23]. Nitrides lack inversion symmetry and exhibit piezoelectric effects when strained along [0001]. Piezoelectric coefficients are almost an order of magnitude larger than in traditional III-V, see Ref. 24, as shown in the table below. In addition, wurtzite GaN has a unique axis, thus allowing spontaneous polarization ($\mathbf{P}_0$ whose values are given below) even in the absence of strain. This manifests itself as polarization charge at hetero-interfaces.

	AlN	GaN	InN
e_{33} (C/m^2)	1.46	0.73	0.97
e_{31} (C/m^2)	-0.60	-0.49	-0.57
$\mathbf{P}_0$ (C/m^2)	-0.081	-0.029	-0.032
$[e_{31}-(C_{13}/C_{33})e_{33}]$ (C/m^2)	-0.86	-0.68	-0.90

Note that these are all in C/ m^2 and that 1C/m^2= 6.25*10^{14} e/cm^2

Let us compare the relative importance of spontaneous polarization to piezoelectric polarization. For a biaxially strained layer the effective piezoelectric polarization is given by

$$P_z^{piezo} = [e_{31}-(C_{31}/C_{33})e_{33}]\varepsilon_{\perp} \qquad (1)$$

Where $\varepsilon_{\perp} = \varepsilon_{xx} + \varepsilon_{yy}$ is the in-plane strain and C_{31} and C_{33} are elastic constants. The numerical values for $[e_{31}-(C_{31}/C_{33})e_{33}]$ are listed in the above table using the values for elastic constants from Kim et al.[25] and piezoelectric and spontaneous polarization data from Bernardini et al. For $Al_xGa_{1-x}N$ pseudomorphically strained on a relaxed GaN substrate, the strain $\varepsilon_{\perp}$ is expected to be proportional to x and given by $\varepsilon_{\perp} = 2x(a_{GaN}-a_{AlGaN})/a_{AlGaN}$, which is $0.0495x$ (using 3.112 Å for AlN c-plane lattice constant and 3.189 Å for GaN c-plane lattice constant, here x is in the range of 0 - 1 and depicts the AlN mole fraction in the alloy) and is tensile. The piezoelectric polarization is then $P^{piezo} = -4.26x * 10^{-2}$ C /cm^2 or $2.66x * 10^{13}$ e/cm^2 and points in the $[000\bar{1}]$ direction. The corresponding difference in spontaneous polarization between $Al_xGa_{1-x}N$ and GaN is also expected to be proportional to x and is given by $\Delta P^{spon} = -0.052x$ (C/m^2) or $3.25x * 10^{13}$ e /cm^2. Note that the two polarization effects have the same sign for Ga polarity and tensile strain in the alloy and point in the $[000\bar{1}]$ direction. For an $In_xGa_{1-x}N$ layer, the situation is rather different in that the differential spontaneous polarization between $In_xGa_{1-x}N$ and GaN is much smaller, $\Delta P^{spon} = -0.003x$ which translates to $1.88x * 10^{12}$ e /cm^2. Furthermore, the $In_xGa_{1-x}N$ layer on GaN would be under compressive stress $\varepsilon_{\perp} = -0.195x$ using 3.533Å and 3.189 Å for c-plane lattice constants for InN and GaN. Here x is in the range of 0 -1 and depicts the InN mole fraction, and $P^{piezo} = +0.176x$ or $1.1x * 10^{14}$ e/cm^2. For an InN mole fraction of 0.15, $P^{piezo} = 1.65 * 10^{13}$ e/cm^2. Here the piezoelectric polarization dominates and is opposite in direction but even larger in absolute magnitude. In the AlGaN case, the sign of the polarization is such that it produces a potential energy for electrons sloping down from the Ga face towards the N face. Here Ga and N faces correspond to polarities where the bonds (single) along the c-directions are from Ga cations to N anions, and N anions to Ga cations, respectively.

For a discussion of polarity as opposed to surface termination and definitions of Ga face, N face, see Hellman[26]. Thus for a structure with Ga polarity, the potential will slope down from the AlGaN surface towards the AlGaN/GaN interface and will help to drive free electrons towards the interface forming a 2DEG For example, if there is an Ohmic metal contact on the AlGaN surface, electrons will flow towards the 2DEG below that layer. The most favorable situation for enhancing sheet carrier concentration would occur for an InGaN (under compressive strain) quantum well on top of a relaxed n-GaN and below a AlGaN barrier (under tensile strain) with the entire structure having cation (Ga) polarity. In that case, the field will slope down towards the InGaN/AlGaN interface in the quantum well and will help localize the carriers in the 2DEG. Note that the piezoelectric polarizations estimated here are based on the theoretical values for perfectly insulating material. The field will be screened by the carriers present in each layer. For example, if carriers flow from a metal contact towards the 2DEG, then this will set up a counteracting field. The equilibrium self-consistent field is ultimately determined by the requirement that the chemical potential for electrons (i.e. the Fermi level) must be constant throughout the structure and thus depends on the doping and band bending in the substrate and possibly in each of the layers. At the least, one may expect these fields will be reduced by a factor corresponding to the macroscopic dielectric constant, i.e. a factor of order 10 but possibly larger if the layers acquire conductivity by free carriers. So, a more realistic expectation for the effects on sheet carrier concentration is of order 10^{11}-10^{12} e/cm^2.

In traditional device structures lacking polarization effects and for a uniform dopant concentration one obtains parabolically varying potentials with distance, whereas here there are linear terms due to the polarization on top of the parabolic terms. These linear terms lead to variations of the potential over a shorter distance scale determined by the thickness of the layers whereas the parabolic terms correspond to the space-charge regions. Thus the linear terms may help to localize carriers if the polarity of the structure is chosen properly. Some further words of caution about the above estimates are needed. If the AlGaN layers are not pseudomorphic but partially relaxed (by misfit dislocations for example), then the piezoelectric effect would be reduced but the spontaneous polarization would not. If the interfaces are not atomically sharp but exhibit a certain degree of interdiffusion then the differences in spontaneous polarization would be reduced as well if such grading occurs over a large thickness. Finally, if domains with inverted polarity exist then the overall polarization effects may be washed out. Also note that in a inverted structure with N polarity towards the surface, it may be possible to create a 2DHG (hole-gas) at the AlGaN/substrate GaN interface, but if a n-type GaN layer is placed on top, a 2DEG may form on top of the AlGaN layer.

Anisotropy in wide bandgap semiconductors is expected to cause thermal stimulus and thermal gradients. The latter is quite likely in devices where the junction temperatures are high against a relatively cool bulk. In such a case, the thermally induced electric field, pyroelectric effect, would be present with effects similar to those described above.[27] This phenomenon has not been studied in detail in nitride semiconductors. Contrary to this lack of attention, the electric field generated by thermal gradients, occurs readily in power devices, is comparable to the fields caused by applied voltages in nitride based FET like devices.

Polarization Effects in Device Like-Structures

While physics appears to be converging, reports on FETs appear to suggest that free carriers can be provided by polarization and that the experimental results agree with theory.[28,29] Results obtained in our laboratory, in conjunction with band discontinuities, with respect to polarization effects point to the importance of spontaneous polarization ordering of the barrier layer with respect to the smaller bandgap material, and polarization in general.[30,31,32] The polarization charge can be screened by to weakly bound and free carriers present in the system which may aid or hamper device effort. The complicating factor in nitrides is the lack of polarity control, Ga or N polarity, and lack of uniform polarity meaning presence of inversion domains.

As a result of polarization, the static potential at the GaN/AlN interface is different from that at the AlN/GaN interface giving rise to interface charge larger than the charge densities used in devices. A substantial level of effort has been expended toward determining band discontinuities, but the field is in desperate need of more in depth investigations in improved structures. The observed asymmetry in AlN/GaN and GaN/AlN interfaces caused by spontaneous polarization is within the experimental errors of Martin et al. Inversion domains combined with any strain in nitride based films lead to flipping PE fields with untold adverse effects on our ability to characterize the films let alone exploit this phenomenon for devices. Such flipping field would also cause much increased scattering of carrier as they traverse in the c-plane. Simply put, identical device structures with different polarity layers would have widely differing performance underscoring the importance that these issues will have to be investigated and reconciled. The

polarity mixing from one domain to the other causes the PE induced electric field to flip, causing a variation in the sheet carrier concentration along the channel of an FET like device. The same polarity mixing would have deleterious effects in the base of an HBT as well and depending on the polarity the induced field would either aid or impede minority carrier transit.

Polarization effects manifest themselves in quantum wells as Stark effect. Time resolved photoluminescence measurements performed in GaN/AlGaN MQWs indicated that temporal evolution of the A exciton peak undergoes a red shift as the recombination depletes the excess carriers. If one assumes that the red shift is due to polarization induced field, one can determine the intensity of the field. The picture may be more complex and or suffer from variation in samples as blue shift too has been observed which may have to do with interwell excitons and oblique excitons.[33] Though controversial, in lasers the injected carrier concentrations even at transparency are comparable to polarization induced charge, 10^{13} cm^{-2}, which means the PE induced field is screened. However, the PE effect reduces the gain at lower injection levels due, among others, to reduced oscillator strength.

Recent experimental results support that the built-in field originates primarily from the spontaneous polarization charge formed at the GaN/AlGaN interfaces with a minor contribution from the piezoelectric field induced by the strain (either lattice mismatch and thermal strain) as has been predicted. The experiments reveal that the fundamental transition of the quantum wells occurs at an energy *well* below the bulk GaN gap for well width larger than 3 nm (for the specific case of $GaN/Al_{0.15}Ga_{0.85}N$). Care was taken to assure that the transitions observed are intrinsic origin by performing two-photon absorption experiments with approximately half-gap excitation ($2\hbar\omega \approx E_{1e1h}$) and observing that linear and non-linear PL lead to same transition energies. The total polarization charge can be written as $P_{tot} = P_{piezo} + P_{spont.}$ where P_{piezo} is the piezoelectric charge caused by the lattice mismatch (lm) strain and by the thermal strain (ts) [$P_{piezo} = P_{lm} + P_{ts}$], whereas P_{spont} represents from the spontaneous polarizability of the GaN/AlGaN interface, as clearly demonstrated by the recent works of Bernardini et al. For an alternating sequence of wells (w) and barriers (b) the total electric field in the well can be calculated as

$$F_w = -4\pi L_b (P^w_{tot} - P^b_{tot}) / (L_w \varepsilon_b + L_b \varepsilon_w)$$

$$F_b = -4\pi L_w (P^b_{tot} - P^w_{tot}) / (L_b \varepsilon_w + L_w \varepsilon_b) \qquad (2)$$

Where ε is the dielectric constant of the particular layer. The piezoelectric charge induced by the in-plane lattice mismatch can be found from Eq. 1 using the in-plane strain for AlGaN/GaN as $\varepsilon_\perp = 2x(a_{GaN} - a_{AlGaN})/a_{AlGaN}$ where the AlGaN is pseudomorphically strained on a relaxed GaN substrate. Thick GaN buffer layers ensures that the GaN quantum wells are not under misfit strain. Moreover, since the $Al_{0.15}Ga_{0.85}N$ layers are thin and grow pseudomorphically,[34] they undergo a tensile in-plane strain $\varepsilon_\perp = 0.742\%$. This results in a piezoelectric polarization charge $P^w_{lm} = 0$ in the wells and $P^b_{lm} = -3.99 * 10^{12}$ ecm^{-2} in the $Al_{0.15}Ga_{0.85}N$ barriers. The thermal strain amounts to some 0.03%, resulting in an additional polarization charge of the order of $P^w_{ts} =$+

$2.57*10^{11}$ ecm^{-2}. For spontaneous polarization, we take the recent data of Bernardini et al. leading to P^{w}_{sp}= -1.81 $*10^{12}$ ecm^{-2} and P^{b}_{sp}= -7.64 $*10^{12}$ ecm^{-2}, the latter value being obtained by linear interpolation of the GaN and AlN values (P_{sp}= -5.09 $*10^{13}$ ecm^{-2} in AlN). The diffrential spontanous polarization between the $Al_{0.15}Ga_{0.85}N$ barrier and the GaN well is then -5.83$*10^{12}$ ecm^{-2}. By using these data and eq.(2) one can calculate the built-in field in the different samples, which turns out to vary in the range 1-3 MV/cm depending on the actual well width. Neglecting high-field effects and corrections for self-consistency, the red-shift caused by the built-in field in the wells is given by the quadratic Stark effect. [35,36]

The measured ground level transition energies and those calculated in the square well approximation with inclusion of the Stark shift are in very good agreement. The agreement between theoretical and experimental data is very reasonable, especially if we take into account that the nominal growth parameters were used in the calculations, without any fitting parameter.

The agreement between the calculated and measured data can in fact be substantially improved by the use of a self-consistent tight-binding (TB) model.[37] The tight-binding model is used to describe the electronic structure in the entire Brillouin zone, up to several eV above the fundamental gap, thus overcoming the well-known limitations of the envelope function approach. For the specific case of nitride semiconductors, the parameters of our empirical TB model were determined by fitting the band-structure of ref. 38. For the self-consistent calculations the electron and hole quasi-Fermi levels are calculated for a given photo-injected charge density. The resulting electron and hole distribution functions (n and p , respectively) are used to solve the Poisson equation. The Poisson equation is solved assuming zero-field at the boundaries. The obtained potential is thus inserted into the TB Schroedinger equation that is solved to get the energies and wavefunctions. The new quasi-Fermi levels are thus recalculated and the procedure is iterated until self-consistency is achieved. The agreement between the self-consistent calculations and the experimental data is very good both in terms of the trend and absolute values.

In conclusions, GaN and related materials exhibit transport characteristics that are very well suited for electronic devices based on electron transport as evidenced by the recent high power MODFETs with record power performance supplanted all the other competing semiconductors at microwave frequencies. Assumes that some day the intrinsic dielectric breakdown strength can be achieved, applicable figures of merit for switching/power device indicate that nitrides would be equally successful. Finally, recent theoretical and experimental investigations indicate that polarization induced charge is important in nitride semiconductors with device implications and that spontaneous polarization is dominant over strain induced piezoelectric polarization in typical GaN/AlGaN. This dominance would increase if the AlGaN grown on GaN relaxes in full or in part. However, the differential spontaneous polarization between GaN and InN is much smaller than that of GaN/AlN interfaces. Assuming that the InGaN on GaN is fully strained, the piezoelectric component of polarization would dominate. Full or partial relaxation of InGaN on GaN due to defects would reduce this polarization as well. For now, optical transitions in GaN/AlGaN quantum wells investigated support the assertion that spontaneous polarization is dominant and must not be lumped with piezoelectric polarization.

Acknowledgments: One of the authors, R.C. gratefully acknowledges Virginia Commonwealth University for hospitality. The work at Lecce is partially sponsored by INFM-Italia through Progetto Sud , and that at VCU by the Air Force Office of Scientific Research and Office of Naval Research under the direction of Drs. G. L. Witt, C.E. C. Wood, Y. S. Park and Mr. M. Yoder.

References:

[1] S.T. Strite and H. Morkoç, J. Vac. Sci. and Tech. B10, pp.1237-1266 (1992).

[2] H. Morkoç, S. Strite, G. B. Gao, M.E. Lin, B. Sverdlov, and M. Burns, J. Appl. Phys. Rev. 76, pp. 1363-1398 (1994).

[3] S. N. Mohammad and H. Morkoç, Progress and Prospects of Group III-V Nitride Semiconductors, Progress in Quantum Electronics, Vol. 20, No. 5/6, pp. 361-525, (1996).

[4] Group III Nitride Semiconductor Compounds, Edited by B.Gil, Clarendon Press, Oxford (1998), ISBN 0-19-850159-5.

[5] H. Morkoç, Wide Bandgap Nitride Devices, Springer, in press.

[6] S. Nakamura and G. Fosol, The Blue Laser, Springer Verlag, 1997.

[7] M. Razeghi and A. Rogalski, J. Appl. Phy. **79**, 7433 (1996).

[8] G. Y. Xu, A. Salvador, W. Kim, Z. Fan, C. Lu, H. Tang, H. Morkoç, G. Smith, M. Estes, B. Goldenberg, W. Yang, and S. Krishnankutty , Appl. Phys. Letts. 71, pp. 2154-2156 (1997).

[9] H. Morkoç, ìWurtzite GaN-Based Heterostructures by Molecular Beam Epitaxy, IEEE J.Selected topics in Quantum Electronics, Eds. Richard Miles and I. Akasaki, Vol. 4, Number 3, pp. 537-549 (1998).

[10] H. Morkoç, ìBeyond SiC III-V Nitride Based Heterostructures and Devices, in SiC Materials and Devices, Ed. Y. S. Park, Vol. 52, pp. 307-394, Academic Press (1998).

[11] S. T. Sheppard et al. presented at Device Research Conference, June 1998, Charlottesville, VA. Other GaN MODFETs references include: Y.-F. Wu, IEEE Electron Device Letters **19**, pp 50-53 (1998); A.T. Ping et al., IEEE Electron Device Letters **19**, pp 54-56 (1998).

[12] . T.Takeuchi, C.Wetzel, S.Yamaguchi, H.Sakai, H.Amano, I.Akasaki, Y.Kaneko, S.Nakagawa, Y.Yamaoka, and N.Yamada, Appl.Phys. Lett. 73, 1691 (1998)

[13] . J.S.Im, H.Kollmer, J.Off, A.Sohmer, F.Scholz, and A.Hangleiter, Phys. Rev. B57, R9435 (1998)

[14] . H. S. Kim, J. Y. Lin, H. X. Jiang, W.W. Chow, A. E. Botchkarev, and H. Morkoç, , Appl. Phys. Letts. In press.

[15] . M. Leroux, N. Grandjean, J. Massies, B. Gil, P. Lefebvre, and P. Bigenwald, Phys. Rev. B. in press;

[16]. Roberto Cingolani, A. Botchkarev, H. Tang, Hadis Morkoç, Giuliano Colì and Mauro Lomascolo, A. Di Carlo, and P.Lugli, Appl. Phys. Letts,.submitted.

[17] . A. Bykhovski, B. Gelmont, and M. Shur, Appl. Phys. Lett. 63, 2243, (1993).

[18] . E.T. Yu, G.J. Sullivan, P.M. Asbeck, C.D. Wang, D. Qiao, and S.S.Lau, Appl. Phys. Lett. **71**, 2794 (1997)

[19] . P.M. Asbeck, E.T. Yu, S.S. Lau, G.J. Sullivan, J. Van Hove and J. Redwing, Elec. Lett. **33**(14), 1230 (1997).

[20] . K. Shenai, R. S. Scott, and B. J. Baliga, *IEEE Trans. Electron Devices*, vol. 36, no. 9, pp.1811-1823, Sept. 1989.

[21] . R.D. King-Smith and D. Vanderbilt, Phys. Rev. B **47**, 1651 (1990).

[22]. R. Resta, Rev. Mod. Phys. **66**, 899 (1994),

[23]. F. Bernardini and V. Fiorentini, Phys. Rev. B. **57**, No 16, pp.1-4, 15 April (1998)

[24]. F. Bernardini, V. Fiorentini, and D. Vanderbilt, Phys. Rev. B **56**, R10024 (1997)

[25] . K. Kim, W. R. L. Lambrecht, and B. Segall Phys. Rev. B 56, 7018 (1997)

[26] . E.S. Hellman, in MRS Internet J. Nitride Semiconductor Research **3**, 11.

[27] . A.D. Bykhovski, V. V. Kaminski, M. S. Shur, Q. C. Chen, and M. A. Khan, Appl. Phys. Lett., **69**,3254, (1996).

[28] . P.M. Asbeck, E.T. Yu, S.S. Lau, G.J. Sullivan, J. Van Hove and J. Redwing, Electronics Lett. 33(14), 1230 (1997).

[29] . E.T. Yu, G.J. Sullivan, P.M. Asbeck, C.D. Wang, D. Qiao and S.S. Lau, Appl. Phys. Lett. **71**, 2794 (1997

[30] . G. A. Martin, S. Strite, A. Botchkarev, A. Agarwal, A. Rockett, H. Morko•, W. R. L. Lambrecht and B. Segall, Appl. Phys. Lett. 65, 610 (1994).

[31]. G. A. Martin, PhD. Thesis, ÒSemiconductor electronic band alignment at heterojunctions of wurtzite AlN, GaN and InNÓ, Department of Physics, University of Illinois, 1996.

[32] .G. A. Martin, A. Botchkarev, A. Agarwal, A. Rockett, H. Morko•, Appl. Phys. Lett. Vol. 68, 2541, (1996).

[33] . B. Gil, P. Lefebvre, J. Allègre, H. Mathieu, N. Grandjean, M. Leroux, J. Massies, P. Bigenwald, and P. Christol, Phys. Rev. B. in press.

[34] . T.Takeuchi, C.Wetzel, S.Yamaguchi, H.Sakai, H.Amano, I.Akasaki, Y.Kaneko, S.Nakagawa, Y.Yamaoka, and N.Yamada, Appl.Phys. Lett. 73, 1691 (1998)

[35] . G.Bastard, in ÒWave Mechanics Applied to Semiconductor HeterostructuresÓ, Edition de Physique, Paris , France, 1987

[36] . J.Singh, in "Semiconductor OptoelectronicsÓ (1995)

[37] . F.Della Sala, A.DiCarlo, P.Lugli, F.Bernardini, V.Fiorentini, R.Scholz, and J.M.Jancu, Appl. Phys. Lett., in press (1998)

[38] . J.M.Jancu, R.Scholz, F.Beltram, and F.Bassani, Phys. Rev. B57, 6493 (1995).

NEAR DEFECT FREE GaN SUBSTRATES

S. POROWSKI
High Pressure Research Center, Polish Academy of Sciences,
Sokolowska 29/37, 01-142 Warsaw, Poland, sylvek@unipress.waw.pl

Cite this article as: MRS Internet J. Nitride Semicond. Res. 4S1, G1.3 (1999)

The current status of GaN crystallization under high nitrogen pressure will be presented. Both conductive and semi-insulating GaN crystals will be characterized.

In particular the influence of Mg on the growth mechanisms will be discussed. The influence of Mg doping on morphology of Mg-doped crystals grown under pressure and Mg-doped homoepitaxial layers will be shown. It will be also shown that the addition of about 1 at.% of Mg into the solution improves significantly the structural quality of crystals reducing dislocation density at least by 3 orders of magnitude comparing to the crystals grown without an intentional doping. As it was estimated by selective wet etching and transmission electron microscopy the dislocation densities in the Mg-doped GaN is as low as 10 cm^{-1}. The introduction of Mg also lowers the optical absorption coefficients for energies below fundamental edge by 2 to 3 orders of magnitude what is explained by disappearance of defect related states in the gap.

The procedures for preparation of atomically flat epi-ready (000 1) surfaces without subsurface damage will be described. It will be shown that high quality homoepitaxial layers growing by monoatomic steps are possible on these substrates.

INTRODUCTION

The technology of GaN and its ternaries, GaAlN and GaInN is of crucial importance for blue optoelectronic devices. Progress in technology and basic research of GaN led to development of blue [1], green and yellow [2] light emitting diodes (LEDs), which are now commercially available from a number of sources. Also the low power laser diodes have been announced [3]. Still the stability and power of laser diodes are not satisfactory.

These results have been achieved using either sapphire or SiC substrates. Further progress can be attained by either developing more sophisticated layer growth techniques such as epitaxial lateral overgrowth (ELOG) or by developing GaN substrates. Essentially both methods rely on the same phenomenon, i.e. enforcing fast growth along (10$\underline{1}$0) direction in order to obtain large area substrate having reduced dislocation density. Due to absence of destabilizing factor of contact with the foreign substrate, the growth of single crystals is more promising technique.

Growth of GaN single crystals have been subject of the research for several years [4,5]. Using High Pressure Solution Growth (HPSG) method 100 mm^2 size GaN plate-like single crystals of good crystallographic quality have been obtained. Both n-type and semiinsulating (SI) crystals have been grown [6]. Also GaN surface preparation techniques have been developed, which include mechano-chemical polishing for active (N face) surface [7] of GaN platelets and Reactive Ion Etching (RIE) for inert (Ga face) surface.

GaN single crystal substrates were successfully used for MBE and MOCVD epitaxial growth. Homoepitaxial layers of very good crystallographic quality, resulting from good quality of the substrate and undisturbed epitaxial growth by flow of monoatomic steps. Recently, the dislocation-free multiquantum well (MQW) structures have been obtained.

In this paper we will discuss recent development of the growth of GaN single crystals. First the thermodynamic conditions for the growth of GaN crystals from the constituents: liquid Ga and N_2 under high pressure will be obtained. Then the physical properties, including

Mat. Res. Soc. Symp. Proc. Vol. 537 © 1999 Materials Research Society

crystallographic, optical and electric will be discussed. Subsequently the results of surface preparation techniques to GaN single crystals will be illustrated by results of microscopic and structural investigations. Finally the results of epitaxy both by MOCVD and MBE will be discussed.

PHYSICAL PROPERTIES OF Ga(l)-N_2-GaN SYSTEM AND GaN CRYSTAL GROWTH

Thermodynamic and kinetic properties of Ga(l)-N_2-GaN(s) system are determined mostly by strong bonding both in N_2 molecule and in GaN crystal. The transition between the initial state of liquid gallium and nitrogen N_2 and GaN crystal requires breaking the extremely strong bonding in N_2 molecule (bond energy 9.8 eV/molecule) and creation of GaN bonds. Strong bonding in GaN crystal (bond energy (9.32 eV/atom pair) leads to high melting temperature T^{M}_{GaN} ~ 2800 K [8]. The estimated N_2 equilibrium pressure for GaN is over 45 kbar [9]. Such pressures and temperatures are not accessible to present day crystal growth apparatus making necessary use of lower temperatures and lower nitrogen pressures. At present the large volume high gas pressure apparatus allows to obtain the nitrogen pressures up to 20 kbar.

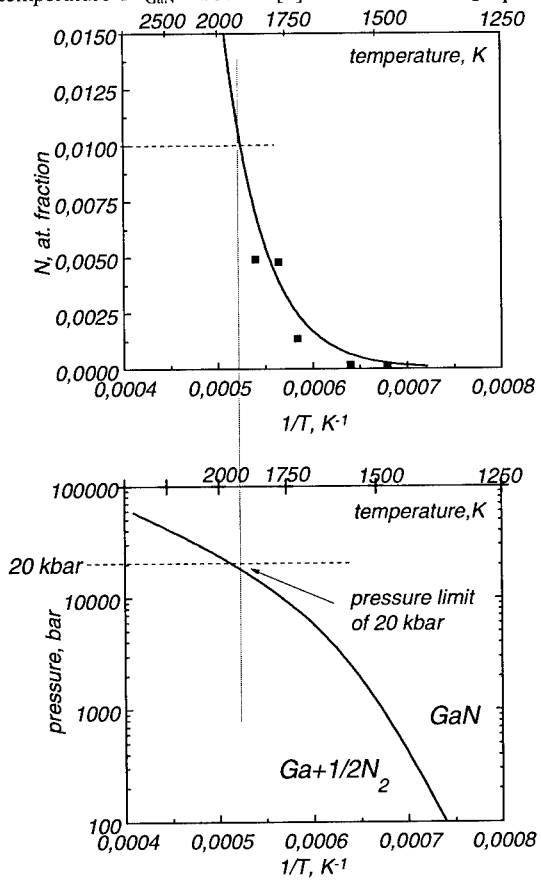


Fig 1. N_2(g) - Ga(l) - GaN(s) phase diagram: a - p-T coordinates [9]; b - x-T coordinates [10]

It is believed that GaN grows from nitrogen solution in liquid Ga. Thus the synthesis of GaN consists of several stages:

i/ adsorption of N_2 on liquid Ga surface

ii/ dissolution of nitrogen in liquid Ga and its diffusion to the cold zone

iii/ growth from solution

Recent quantum mechanical calculations have shown that adsorption of N_2 on liquid Ga surface leads to dissociation of N_2 molecule [11]. The energy barrier for this process is of the order of 4.2 eV which is less than half of the N_2 bonding energy. This indicates that the bonding between Ga and N atoms plays important role in the process. The estimate of the rate of the adsorption indicates that this process is not the rate limiting process in GaN crystallization at high pressures [6].

As it can be seen from Figure 1 nitrogen pressure about 20 kbar corresponds to nitrogen solubility in liquid gallium of the order of 1%. Lower temperatures correspond to lower nitrogen solubility, therefore by controlling the temperature

difference in the crucible we can control the difference of the nitrogen concentration and accordingly the supersaturation in the growth zone. Our growth results suggest that the nitrogen solubility and diffusion from the hot to cold zone of the gallium is the rate limiting step in the growth.

Due to relatively rapid dissolution of nitrogen in liquid Ga, in the beginning of the process GaN polycrystalline crust is created on the Ga surface. Some of the crust GaN crystals grow faster and inhibit the growth of neighboring crystals. Depending on the supersaturation and the temperature the two growth habits are obtained: needle-like habit which dominates for large supersaturation (large temperature difference) and plate-like habit which is prevalent for lower supersaturations (small temperature gradient in the crucible).

It has been found that morphology and quality of the GaN crystals depend crucially on the doping of growth solution. The morphology of the two principal surfaces of GaN platelets is different: one side is completely flat and the other is corrugated, with large number of multi-atomic steps, ridges and even growth hillocks. For undoped Ga solution the corrugated surface correspond to Ga face ((000$\bar{1}$) face) and the flat surface to N face (0001) [12,13]. The addition of Mg to liquid Ga changes the morphology of the plate - Ga face becomes completely flat and N face is corrugated [6]. Also the electric and optical properties are different - Mg doped crystal have very low concentration of free carriers and at room temperature these crystals are semiinsulating [6].

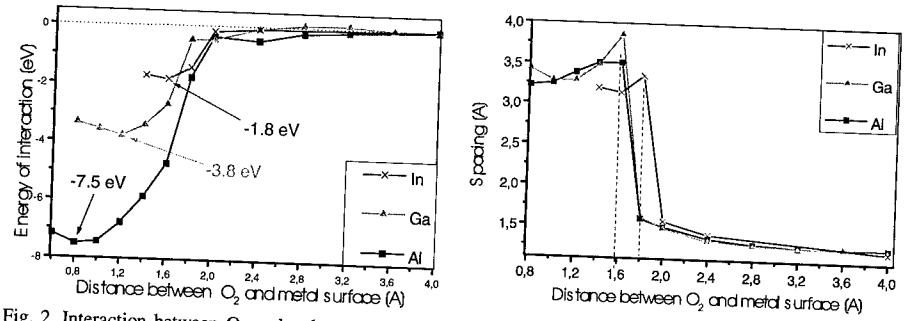
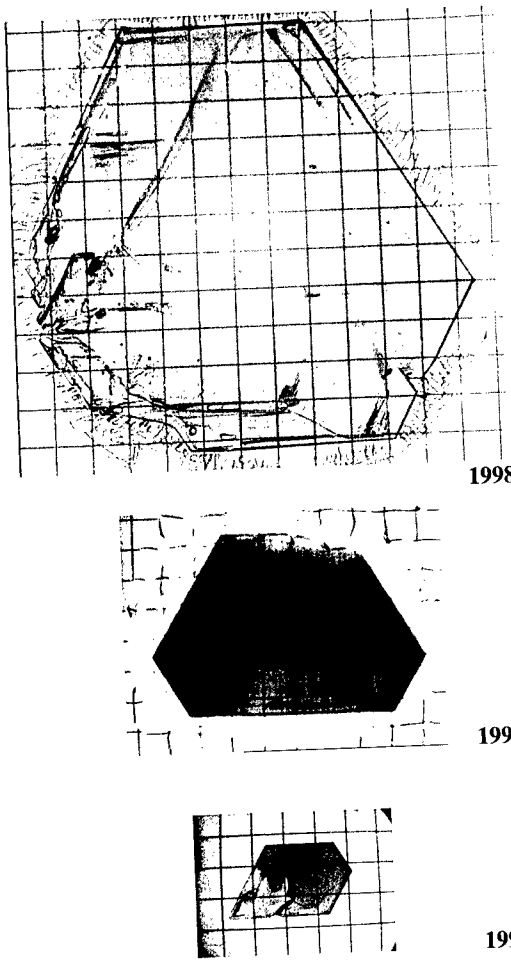


Fig. 2. Interaction between O_2 molecule and metal III group surface: a - excess energy, b - O - O distance in oxygen molecule dependence on the distance between the molecule and the metal surface.

High concentration of free electrons in GaN grown from undoped Ga is attributed either to nitrogen vacancies [14] or to oxygen substitutional impurity [15]. The incorporation of oxygen is related to its dissolution in liquid metal. This process has been investigated using quantum mechanical calculations. The results have been obtained using commercially available Dmol package distributed by Molecular Simulation Inc. within countrywide license in Poland [16] results of these calculations have been shown in Figure 2. In Figure 2a the excess energy of the oxygen molecule approaching the liquid metal group III surface is shown. As it can be seen, the adsorption of oxygen on liquid metal surface is barrierless process. This type of the adsorption energy curve is standard for the molecular adsorption. The nature of oxygen adsorption is different - the O_2 molecule disintegrates on the surface. On Figure 2 b the spacing between the oxygen atoms is presented as a function of the distance between the molecule and the metal surface. As it can be seen the distance between the oxygen atoms rapidly increases from 1.53 to above 3Å. This proves that adsorption leads to dissociation of oxygen molecule on the metal surface. Moreover, the barrierless character of the process indicates that the incorporation of oxygen is very efficient and that liquid gallium absorbs all oxygen from gaseous nitrogen.



The main problem in growth of high quality crystals is how to attain high growth rate and preserve the morphological stability of the surface. The growth rate can be increased either by higher equilibrium concentration of N in liquid Ga or by increase of the supersaturation. In our growth method we keep the supersaturation at the lowest possible level and increase the solubility by increasing the temperature of the liquid gallium. This leads to the increase of the growth rate and reduction of the destabilizing factor of high supersaturation The destabilizing influence of impurities is also reduced by preserving high purity of the process. This is achieved by initial annealing of the high pressure vessel in the temperature of 200°C and vacuum of 10^{-3} Torr.

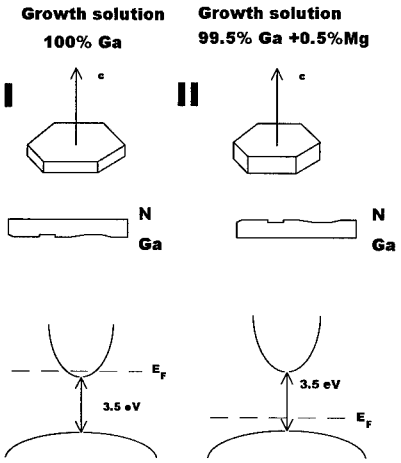
The improvement of the growth procedure led to considerable progress of GaN high pressure growth which is illustrated in Figure 3. The typical size of the undoped GaN crystal, obtained in 200h growth process is above 15 mm in length with the surface area above 100 mm^2.

The size of Mg - doped GaN crystals obtained in the process of the same duration is about 10 mm with the area of 80 mm^2. The size difference is related to reduction of the growth rate in the plane perpendicular to c axis for Mg-doped GaN crystals.

Fig. 3 Progress in GaN high pressure crystallization - increase of the size of GaN crystals in last 3 years,

PHYSICAL PROPERTIES OF PRESSURE GROWN GaN CRYSTALS

The HPSG method allows to grow both conductive and non-conductive crystals of GaN. The electrical properties depend on the solvent used for crystallization. As it is summarized in Fig. 4, GaN crystals grown from solutions in pure Ga, without an intentional doping, are highly conductive with Fermi level lying in the conduction band. The growth from solutions in Ga alloyed with small amount of Mg results in highly resistive crystals with Fermi level shifted into the gap. Fig. 5 shows temperature dependence of resistivity [17] for both types of crystals. It allows to compare the type of conductivity in undoped and Mg-doped crystals.



$n = 3 \div 6 * 10^{19}$ cm^{-3} LT - hopping

metallic conductivity T > 300K - p type

Fig. 4 Electric properties and morphology of GaN crystals: I - undoped, II - Mg - doped.

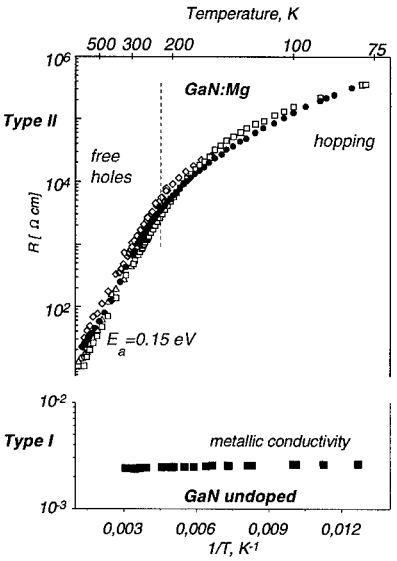


Fig. 5 Temperature dependence of resistivity of undoped and Mg-doped GaN crystals

GaN crystals grown from the solutions in pure gallium show metallic behavior in whole temperature range of 4.2 - 300K. High free electron concentration of 3-6 x 10^{19} cm^{-3} with mobilities of 30-90 cm^2/Vs [18, 17]] have been found (Table I). The main residual impurity detected in the crystals by SIMS [19] is oxygen. Its concentration was estimated to be in the range of 10^{18} - 10^{19} cm^{-3}. It is well established that oxygen is a single donor in GaN. However since the concentration of free electrons in the crystals is higher than the estimated concentration of the impurity the presence of an additional donor cannot be excluded. The N-vacancy as the additional source of free electrons is therefore often proposed [20,21].

Following the theory [20,22], highly probable native defects in GaN crystals which are highly n-type, are Ga-vacancies (V_{Ga}^{3-}). This is due to their low formation energy even at strongly Ga-rich conditions of crystallization. The presence of the negatively charged Ga vacancies at concentrations of 10^{18} cm^{-3} , in the n-type pressure grown GaN crystals, has been detected by positron annihilation experiments [23].

The addition of Mg into the growth solution drastically changes the electrical properties of GaN crystals. Their RT resistivity increases by orders of magnitude (Table I).

Table I Electrical properties of GaN crystals

crystal	conductivity type	ρ Ωcm, 300K	carrier concentration,cm^{-3}
GaN	metallic	10^{-3}-10^{-2}	3-6 x 10^{19}, n-type
GaN : Mg	hopping	10^4-10^6	----

The increase of electrical resistance in GaN:Mg crystals is related to drastic decrease of free electron concentration. The temperature dependence of resistivity for these samples at low temperatures up to about 250K, suggests hopping type of conductivity. At higher

temperatures the conductivity starts to be governed by the activation process leading to the creation of free holes in the valence band.

Also the optical absorption data [24] indicate that the free carrier concentration in the Mg-doped GaN is very low. The free carrier absorption which dominates the low energy part of the absorption spectra for the undoped GaN disappears completely for crystals grown from Mg containing solutions. For these crystals, the absorption coefficients for energies below the fundamental absorption edge are as low as 1-10 cm^{-1} as measured by Photothermal Deflection Spectroscopy . [25].

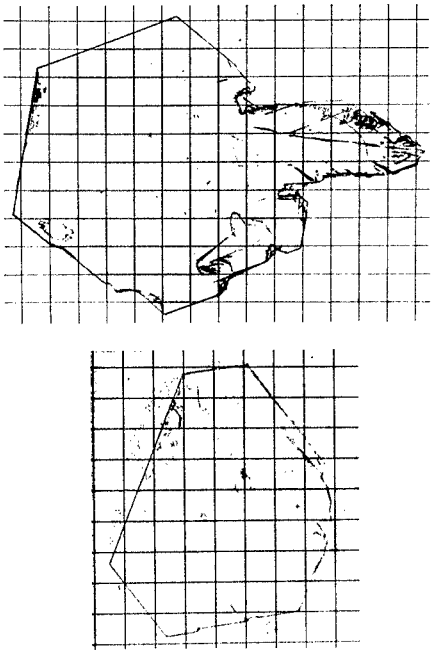


Fig 6 GaN undoped (top) and Mg-doped (bottom) single crystals. (grid spacing - 1mm).

The Mg impurity introduced into the growth solution does not change significantly the general habit of the crystals. In both cases they are hexagonal platelets with c-axis perpendicular to the hexagonal faces. Typical crystals of both types are shown in Fig. 6. The crystals with Mg are perfectly transparent and colorless whereas the conductive samples are usually slightly yellowish in color.

From the form of the crystals, it follows that the relative growth rates in directions perpendicular and parallel to the c-axis are similar however the crystals with Mg are generally thicker and require longer time to reach the same linear dimensions as the crystals grown without Mg.

One of the hexagonal faces of both types of crystals is usually flat. The opposite one often shows some macro-roughness (i.e. macrosteps) as a consequence of the unstable growth in one of the (0001) directions. As it was revealed [26] by wet etching [7] and confirmed by CBED measurements [12, 13], the flat surfaces of the conductive and non-conductive crystals correspond to opposite polar (0001) orientations of GaN.

For conductive GaN crystals the flat surface is always $(0001)_N$ face which is chemically active [7]. For the Mg-doped crystals this is always $(0001)_{Ga}$ face which is resistant to the wet etching in alkali water solutions.

The GaN crystals grown by HPSG method are of high structural quality as determined by X-ray diffraction (XRD) [27], transmission electron microscopy (TEM) [12, 28] and defect selective wet etching (etch pit density - EPD) techniques. The XRD data are summarized in Fig. 7. The X-ray rocking curves for symmetrical reflection are as narrow as 18-25 arcsec for almost all Mg-doped crystals and for best crystals grown without doping. For some of the conductive crystals the rocking curves splits onto few peaks indicating low angle (about 1 arcmin) grain boundaries. This is probably due to some inhomogeneity in distribution of residual donor impurities. The rocking curves for in-plane reflections are always very narrow what indicates that there is no twist mosaicity in all investigated crystals.

A number of GaN crystals have been studied by TEM [12,13,28] especially the samples used for optimization of surface preparation procedures and epitaxial growth of

layers and structures. In most observations the crystals were completely free of dislocations. Fig. 8 shows a 3μm. TEM cross-sectional view [28] of the GaN conductive crystal with GaN/AlGaN structure grown by MBE [29] on the active $(0001)_N$ surface. In this measurement no dislocations have been found over 100μm. area. It suggests that the dislocation density in the crystal is not higher than 10^4 cm^{-2}.

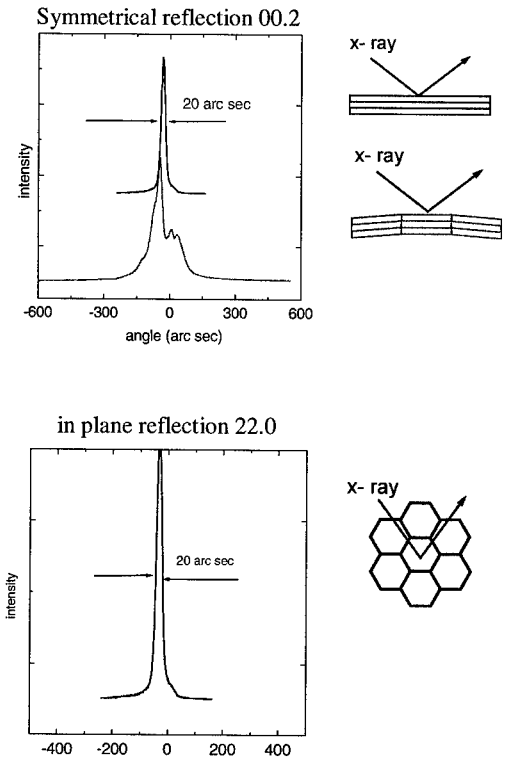


Fig.7 x-ray rocking curves of pressure GaN crystals

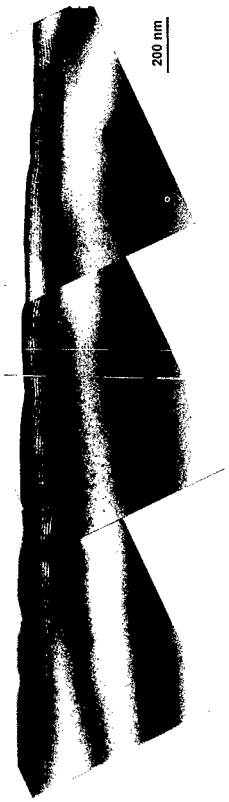


Fig. 8 TEM crossectional view of MQW structure grown on GaN substrate. Courtesy of M. Albrecht.

It was mentioned earlier that the Ga-side of GaN cannot be etched in alkali water solutions. However if molten KOH, NaOH or their molten eutectic are applied the defect selective etching of GaN heteroepitaxial layers and single crystals is possible. The method developed for GaN heteroepitaxial layers [7] has been applied to pressure grown GaN crystals doped with Mg. The number of the etch pits on heteroepitaxial GaN corresponded to defect density of 2 x 10^8 cm^{-2} whereas only very few such a pits have been found on the whole surface (few tens of mm^2) of GaN single crystal.

The estimations for dislocation density in pressure grown GaN crystals are summarized in Table II.

Table II Dislocation density in pressure grown GaN crystals

Type of crystal	Dislocation density, cm^{-2}
GaN, undoped, conductive	10^4
GaN:Mg, non-conductive	10^1 - 10^2

SURFACE PREPARATION

The surfaces of the pressure grown GaN crystals are often covered by the growth figures or surface layer resulting from the cooling of the system after crystallization at high temperature. Therefore to obtain epi-ready surfaces of GaN substrates it is necessary to subject them to the preparation procedures prior to epitaxial growth.

The mechanical polishing with diamond micropowders leads to the formation of highly damaged surfaces with scratches of 200 Å in depth. The thickness of the damaged layer under such mechanically polished surfaces is usually 2000 - 2500Å as it was shown by the RBS measurements [30] (Fig. 9).

It was shown that bulk GaN crystals (highly conductive, undoped) can be etched in aqueous solutions (10N - 1N) of KOH and NaOH [7]. However only one of the polar {0001} surfaces of bulk crystals is attacked by the applied etchants. The free etching of this surface $(000\underline{1})_N$ as it was identified by XPD [13]) is strongly anisotropic and results in the formation of numerous stable pyramids 100 - 200nm in height. As it was mentioned before for Mg-doped crystals also the $(000\underline{1})_N$.face is chemically active.

The same aqueous solutions (10N - 1N) of KOH and NaOH have been used for mechano-chemical polishing of the chemically active GaN surface [7]. When the mechano-chemical polishing procedure is applied, atomically flat surfaces of bulk GaN (RMS=0.1nm as estimated by AFM) are reproducibly obtained. The RBS measurements [30] (Fig.9) indicate that the applied procedure allows to remove the subsurface damage resulting from the mechanical polishing. It was confirmed by TEM studies of subsurface regions of mechano-chemically polished GaN crystals. One of the cross sectional TEM views of such a crystal is shown in Fig. 10.

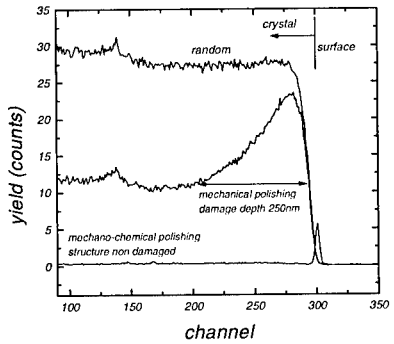
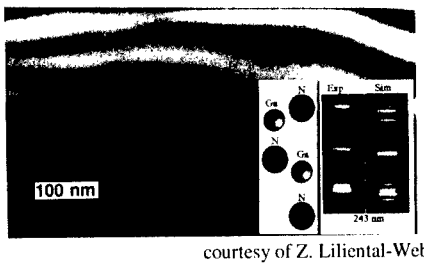


Fig. 9 RBS signals for polished GaN surfaces, Ref. 12



courtesy of Z. Liliental-Weber

Fig.10 Cross sectional TEM view of GaN crystal at the mechano-chemically polished surface. The insert shows CBED spectra used for polarity determination.

The procedures of the wet etching and mechano-chemical polishing with alkaline water solutions can be also applied for GaN heteroepitaxial layers but only to that which

shows tendency to develop hexagonal hillocks if grown by MOCVD. The orientation of this chemically active epitaxial GaN layers is the same as the orientation of chemically active surface of the conductive GaN crystals.

The surfaces of GaN crystals corresponding to the Ga-polarity faces cannot be prepared by the methods just described due to their chemical resistance to most chemicals, at room temperature. Therefore for these surfaces, the Reactive Ion Etching techniques are used for removing the subsurface damage introduced by the mechanical polishing. The application of RIE allows to remove the subsurface damage what was shown by TEM [28]. Some roughness remaining after the RIE treatment is usually removed at the first stages of epitaxial growth.

HOMOEPITAXY

Epitaxial growth of GaN layers and GaN-based structure was tried on both polar surfaces of pressure grown GaN crystals, by MOCVD [31, 32, 33, 34,] as well as by MBE with plasma [29] and ammonia [35] nitrogen sources.

The growth by propagation of monoatomic steps has been achieved by both methods on both polar surfaces. Fig. 11 shows the morphology of GaN homoepitaxial layer grown by MBE with NH_3 nitrogen source [gn] on the $(000\underline{1})_N$ prepared by mechano-chemical polishing. Such a sequence of atomic steps usually covers whole surface of GaN substrate. The only exception are the layers grown by MOCVD on $(000\underline{1})_N$ oriented substrates where the hexagonal growth hillocks are often observed. The origin of this morphological features was investigated by Weyher et al. [36].

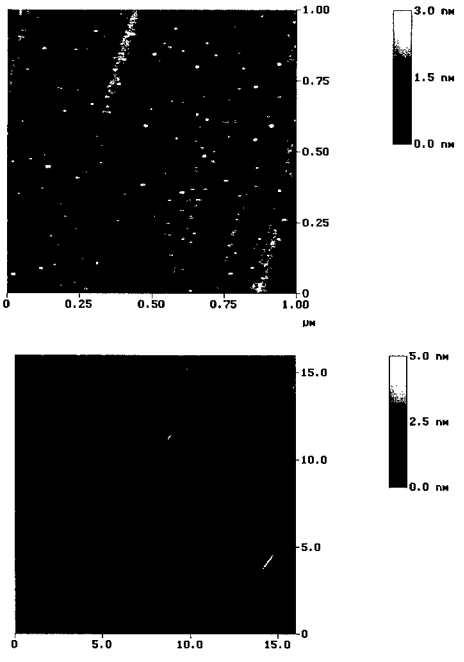


Fig. 11 AFM scans of GaN homoepitaxial layer grown on the active side of GaN crystal by MBE with ammonia N source [35]

On the other hand, the growth on the active, $(000\underline{1})_N$ surface by MBE with both NH_3 and plasma N-source results in smooth step flow morphology and almost perfect interfaces between the substrates and deposited layers. Sometimes some light element (probably oxygen) contaminant was found at the interface however it did not disturb the sequence of atomic planes as it was revealed by HREM [28]. It shows that the active surface of GaN is more sensitive to contamination's which often results in enhanced incorporation of impurities during epitaxy in comparison to the inert surface of the GaN substrates [37].

Probably also due to this reason the best photoluminescence spectra were obtained for layers deposited on the inert, Ga-side of GaN substrates [32, 33].

The donor bound exciton lines of the halfwidth below 0.5 meV have been measured on homoepitaxial GaN layers [32]. This confirms the good quality of homoepitaxial layers, resulting in the absence of the strain and extremely narrow excitonic lines.

The GaAlN/GaN multiquantum well (MQW) structures have been obtained using mechano-chemical (0001) surface preparation technique and plasma enhanced MBE growth method [29]. The results of TEM measurements indicate that the dislocation free area of the MQW extends over the range of 100 μm. [28]. This also indicates on very good crystallographic quality of the substrate surface

CONCLUSIONS

The results presented in this paper can be summarized by the following points:

1. Two types of GaN single crystals were obtained by HPSG method
   - a/ conductive - undoped Ga
     - max size - 18 mm
     - dislocation density ~ 10^4 cm^{-1}
   - b/ SI - Mg doped Ga
     - max size - 14 mm
     - dislocation density ~ 10^1 - 10^2 cm^{-2}
2. Surface preparation methods were developed
   - a/ $(0001)_N$ - mechanochemical polishing
   - b/ $(0001)_{Ga}$ - reactive ion etching
3. Atomic height step flow growth mode was achieved by MOCVD and MBE methods
4. Near dislocation-free epitaxial layers and MQW structures were grown by both MBE and MOCVD techniques.

ACKNOWLEDGMENT

The research presented in this paper has been supported by Poland's Committee for Scientific Research grant no 7 7834 95 C/2399. The quantum mechanical calculations have been made using Dmol software distributed by MSI Inc. in the framework of countrywide license supported by Committee for Scientific Research.

REFERENCES

[1] S. Nakamura, M. Senoh, T. Mukai, Jpn. J. Appl. Phys. 2, Lett. **32,** L8 (1993)
[2] S. Nakamura, M. Senoh , N. Iwasa, S. Nagahama, Jpn. J. Appl. Phys. 2, Lett. **34** L797 (1995)
[3] S. Nakamura, M. Senoh, S. Nagahama, N. Iwasa, T. Yamada, T. Matsushita, H. Kiyoku, Y. Sugimoto, Jpn. J. Appl. Phys.2, Lett. **35,** L74 (1996)
[4] S. Porowski, Mater. Sci. Eng. **B44**, 407 (1997)
[5] S. Porowski, I. Grzegory, J. Cryst. Growth 178, 174 (1998)
[6] S. Porowski, I. Grzegory, S. Krukowski, Mater. Res. Soc. Symp. Proc.
[7] J. L. Weyher, S. Müller, I. Grzegory, S. Porowski, J. Cryst. Growth **182**, 17 (1997)
[8] J. A. Van Vetchten, Phys. Rev. **B7** 1479 (1973)
[9] J. Karpinski, J. Jun and S. Porowski, J. Cryst. Growth **66** 1(1984)
[10] I. Grzegory, J. Jun, M. Bockowski, S. Krukowski, M. Wroblewski, B. Lucznik and S. Porowski, J. Phys. Chem. Solids **56**, 639 (1995)
[11] S. Krukowski, Z. Romanowski, I. Grzegory, S. Porowski, J. Cryst. Growth **189/190**, 159 (1998)
[12] Z. Liliental-Weber, C. Kisielowski, Ruvimov, I. Chen, J. Washburn, I. Grzegory, M. Bockowski, J. Jun, S. Porowski,. J. Electron. Mater. **25** 1545(1996)

[13] J-L. Rouviere, J. L. Weyher, M. Seelmann-Eggebert, S. Porowski, Appl. Phys. Lett. **73,** 668(1998)
[14] H.P. Maruska, J.J. Tjetjen, Appl. Phys. Lett. **15** (1969) 327
[15] Seifert., W., Franzheld, R., Butter, E., Sobotta, H., Riede V., Cryst. Res. & Technol. **18** (1983) 383
[16] B. Delley, J. Chem. Phys. **92**, 508 (1990)
[17] E. Litwin-Staszewska, to be published
[18] P. Perlin, J. Camassel, W. Knap, T. Talercio, J. C. Chevrin, T. Suski, I. Grzegory and S. Porowski, Appl. Phys. Lett. **67**, 2524 (1997)
[19] A. Barcz, T. Suski, unpublished
[20] P. Boguslawski, E. Briggs and J. Bernholz, Phys. Rev. **B51**, 17255, (1995)
[21] Wook Kim, A. E. Botchkarev, A. Salvador, G. Popovici, H. Tang and H. Morkoc, J. Appl. Phys. **82** (1), 1997
[22] J. Neugebauer and C. G. Van de Walle, Phys. Rev. **B50**, 8067, (1994)
[23] K. Saarinen, T. Laine, S. Kuisma, P. Hautojarvi, L. Dobrzyński, J. M. Baranowski, K. Pakuła, R. Stępniewski, M. Wojdak, A. Wysmołek, T. Suski, M. Leszczyński, I. Grzegory and S. Porowski, Phys. Rev Lett. **79**, 3030, (1997)
[24] S. Porowski, M. Bockowski, B .Lucznik, I. Grzegory, M. Wroblewski, H. Teisseyre, M. Leszczynski, E. Litwin-Staszewska, T .Suski, P. Trautman, K. Pakula and J.M. Baranowski, accepted for Acta Physica Polonica, 1997
[25] T. Suski, O. Ambacher, private communication
[26] I. Grzegory, private communication
[27] M. Leszczynski, I. Grzegory, H. Teisseyre, T. Suski, M. Bockowski, J. Jun, J.M.Baranowski, S. Porowski, J. Domagala, J. Cryst. Growth **169**, 235 (1996)
[28] M. Albrecht, private communication
[29] S. Porowski, I. Grzegory, M. Bockowski, M. Leszczynski, D Korakakis, A. Bell, I. Harrison, C. T. Foxon, M. Albrecht, H. P. Strunk, J. A. Davidson, P. Dawson, presented in
[30] M. Conway, J. S. Williams and C. Jagadish, private communication
[31] K. Pakula, A. Wysmolek, K. P. Korona, J. M. Baranowski, R. Stepniewski, I. Grzegory, M. Bockowski, J. Jun, S. Krukowski and S. Porowski, Solid State Commun. **97**, 919 (1996)
[32] M. Schauler, F. Eberhardt, C. Kirchner, V. Schweigler, M. Kamp, K.J. Ebeling, to be published
[33] P. Beaumont, to be published
[34] A. Zauner, to be published
[35] R. Held, G. Nowak, P. Cohen, S. Porowski, to be published
[36] J. L. Weyher, P. D. Brown, A. Zauner, S. Müller, D. Foord, P. R. Hageman, C. J. Humphreys, P. Larsen, I. Grzegory, S. Porowski, to be published
[37] M. Leszczynski, P. Prystawko, A. Sliwinski, T. Suski, E. Litwin-Staszewska, S. Porowski, Acta Phys. Pol. **A 94**, 427 (1998)

DRY AND WET ETCHING FOR GROUP III – NITRIDES

I. Adesida, C. Youtsey, A. T. Ping, F. Khan, L. T. Romano,* and G. Bulman**

Department of Electrical and Computer Engineering, University of Illinois, Urbana-Champaign, IL 61801
*Xerox PARC, Palo Alto, CA 94304
** CREE Research, Inc.,Durham, NC 27713

Cite this article as: MRS Internet J. Nitride Semiconductor Res. 4S1, G1.4 (1999)

ABSTRACT

The group-III nitrides have become versatile semiconductors for short wavelength emitters, high temperature microwave transistors, photodetectors, and field emission tips. The processing of these materials is significant due to the unusually high bond energies that they possess. The dry and wet etching methods developed for these materials over the last few years are reviewed. High etch rates and highly anisotropic profiles obtained by inductively-coupled-plasma reactive ion etching are presented. Photoenhanced wet etching provides an alternative path to obtaining high etch rates without ion-induced damage. This method is shown to be suitable for device fabrication as well as for the estimation of dislocation densities in n-GaN. This has the potential of developing into a method for rapid evaluation of materials.

INTRODUCTION

The success of the synthesis and growth of the wide bandgap group-III nitrides over the last decade has made the realization of a wide range of new devices possible. The bandgap energies of the III-nitrides range from 1.9 eV for InN to 3.4 eV for GaN to 6.2 eV for AlN. Using these materials, bright light emitting diodes (LEDs) and laser diodes (LDs) [1,2] operating at short wavelengths have been demonstrated. Indeed, LDs with InGaN/AlGaN active layers having lifetimes greater than 10,000 hours have been demonstrated making the commercialization of these devices a certainty. The excellent electron transport characteristics of GaN coupled with the wide bandgap, the chemical stability, and the availability of AlGaN/GaN heterostructures also make III-nitrides suitable for high power, high temperatures transistors. AlGaN/GaN heterostructure field effect transistors (HFETs) on sapphire operating at frequencies greater than 70 GHz have been demonstrated [3] and similar HFETs grown on SiC exhibiting power densities as high as 6.8 W/mm have also been fabricated [4]. Most recently, AlGaN/GaN heterojunction bipolar transistors have been demonstrated [5].

Improvements in the performance of these devices depend on the quality of epitaxial materials and the development of device processing technologies. In particular, effective etching techniques are essential for forming facets for GaN LDs, defining mesas for photodetectors, and gate recessing for HFETs. Group-III nitrides have high bond energies compared to conventional III-V semiconductors. The bond energies are 7.7 eV/atom for InN, 8.9 eV/atom for GaN, and 11.5 eV/atom for AlN compared to 6.5 eV/atom for GaAs. The high bond strengths and wide bandgaps make them essentially chemically inert and highly resistant to bases and acids at room temperature. Therefore a wide range of dry and wet etching techniques have been investigated for the processing of III-nitrides. Since bond strengths are high for the III-nitrides, external energy is required to initiate and sustain the dissociation of the bonds. Sources of external energy include energetic ions, energetic electrons, and optical radiation for different

Mat. Res. Soc. Symp. Proc. Vol. 537 © 1999 Materials Research Society

etching methods. In this paper, we present these etching methods and discuss the progress made in applying some of them to III-nitrides.

DRY ETCHING

Various methods of dry etching involving ion-assisted mechanisms have been applied to the processing of III-nitrides. They include ion milling [6,7], chemically assisted ion beam etching (CAIBE) [8,9,55], reactive ion beam etching (RIBE) [10], reactive ion etching (RIE) [11-15], electron-cyclotron-resonance reactive ion etching (ECR-RIE) [16-21], and inductively-coupled-plasma reactive ion etching (ICP-RIE) [22-27]. Optical excitation sources with photon energies higher than the bandgap energies of the semiconductors have been applied to both dry and wet etching methods. The photoassisted dry-etching method [28] involves optical radiation of the sample in the presence of reactive gases. Low energy electron-enhanced etching (LE4) [29] is a dry etching method where electrons with energies < 15 eV are the source of external energy.

Ion milling rely on physical sputtering to achieve etching but this method is not practical for nitrides because of low etch rates and high ion-induced damage [6,7]. Therefore, methods of dry etching involving chemical mechanisms in addition to physical sputtering are the most effective for device applications. Of these techniques, the CAIBE, RIE, ECR-RIE, and ICP-RIE have been the most widely investigated. Tools for ECR-RIE and ICP-RIE are high-density-plasma systems which use magnetic confinement of electrons to generate very high ion densities ($> 5 \times 10^{11}$ cm^{-3}). Although, the methods for coupling power to the plasma in these systems are different, the plasmas have similar properties. It should also be noted that in these systems the rf power generators for controlling the ion flux and for fixing the ion energy are different. This de-coupling allows for the delivery of large ion fluxes at low energies (or biases) onto samples. This enhances etch rates and prevents excessive lattice damage in comparison to conventional RIE.

Etch Rates and Profiles

The chemistries for the dry etching of III-nitrides are mostly halogen-based with the most prevalent being chlorine-based. A summary of some of these chemistries along with the etching methods and accompanying etch rates are presented in Table I. It should be noted that a direct comparison of the etch rates in Table I cannot be made since material quality and etching apparatus can differ significantly.

The plasma chemistries in Table I are identical to those utilized for conventional compound semiconductors. It should be expected that etch products for the group-III elements should therefore be similar in both cases. For nitrides etched in Cl-based gases, the etch-products are $GaCl_x$, $InCl_x$, and $AlCl_x$ for the Group III elements, while for nitrogen, it could be NCl_3 or perhaps free N_2. The volatility of these products is aided by ion bombardment. However, with the boiling point of $InCl_3$ being high at ~ 600 °C, other gas mixtures involving CH_4 have been investigated. The potential products for these mixtures are methyl- or ethyl-based metal-organics for the metals along with NH_3 for nitrogen. The boiling point of $(CH_3)_3Ga$, $(CH_3)_3In$, and $(CH_3)_3Al$ are < 150 °C, and are therefore, more readily volatile. Notwithstanding the similarities in terms of etch chemistries, we note that the high bond energies of the nitrides degrade their etch rates in comparison to those of other compound semiconductors.

The etch rates reported for GaN using RIE with various etch chemistries range from 17 to 100 nm/min [11-15]. Etch rates were found to depend strongly on the plasma self-bias voltage, and essentially independent of the chamber pressure for pressures less than 80 mTorr [13]. The higher etch rates were obtained at high plasma dc biases from -300 to -400 V. Anisotropic etch profiles were obtained in all cases but they were overcut which meant that physical mechanisms dominated the etching. In conventional RIE, physical and chemical components of etching cannot be independently

controlled. This impacts the shape of etch profiles significantly especially in the case of III-nitrides where high ion energy is required to break the bonds.

Table I. Summary of etch rates for various dry etching methods.

Gas Chemistry	Etching Technique	Etch Rate (nm/min)					
		GaN		AlN		InN	
Ar	Ion Milling	110	500 eV[6]	29	500 eV[7]	61	500 eV[7]
HCl [Ar ion]	CAIBE	190	500 eV[8]	--	---	--	---
Cl_2 [Ar ion]	CAIBE	210	500 eV[9]	62	500 eV[55]	--	---
HCl	RIBE	130	500 eV[10]	--	---	--	---
Cl_2	RIBE	150	500 eV[10]	--	---	--	---
SF_6	RIE	17	-400 V[11]	--	---	--	---
CHF_3, C_2ClF_5	RIE	45	500 W[12]	--	---	--	---
$SiCl_4$[w/Ar, SiF_4]	RIE	55	-400 V[13]	--	---	--	---
HBr [w/Ar, H_2]	RIE	60	-400 V[14]	--	---	--	---
BCl_3	RIE	105	-230 V[15]	--	---	--	---
$CH_4/H_2/Ar$	ECR-RIE	9	-250 V[16]	2.5	-300 V[16]	10	-300 V[16]
CCl_2F_2/Ar	ECR-RIE	20	-250 V[16]	18	-300 V[16]	18	-300 V[16]
BCl_3/Ar	ECR-RIE	30	-250 V[16]	17	-250 V[16]	17	-300 V[16]
HBr/H_2	ECR-RIE	70	-150 V[17]	65	-150 V[17]	17	-150 V[17]
$SiCl_4/Ar$	ECR-RIE	75	-280 V[18]	--	---	--	---
HI/H_2	ECR-RIE	110	-150 V[17]	120	-150 V[17]	100	-150 V[17]
$Cl_2/H_2/Ar$	ECR-RIE	200	-180 V[19]	110	-150 V[19]	150	-180 V[19]
IBr/Ar	ECR-RIE	300	-170 V[20]	160	-170 V[20]	325	-170 V[20]
ICl/Ar	ECR-RIE	1300	-275 V[21]	200	-275 V[21]	1150	-275 V[21]
Cl_2/N_2	ICP-RIE	65	-100 V[22]	39	-100 V[22]	30	-100 V[22]
Cl_2/SF_6	ICP-RIE	130	-250 V[23]	184	-250 V[23]	46	-250 V[23]
CH_4/H_2 /Ar	ICP-RIE	140	-620 V[24]	30	-100 V[24]	110	-480 V[24]
$Cl_2/Ar/H_2$	ICP-RIE	688	-280 V[25]	--	---	--	---
BCl_3/Cl_2	ICP-RIE	850	-120 V[26]	--	---	--	---
Cl_2/Ar	ICP-RIE	980	-450 V[27]	670	-450 V[27]	150	-100 V[22]
HCl	Photoassisted	0.004 nm/pulse[28]		--	---	--	---
H_2/Cl_2	LE4	50-70	1-15eV[29]	--	---	--	---

In CAIBE, an ion beam is directed onto a sample in a reactive gas ambient. The ion energy and beam current can be controlled while the flow of the reactive gas can also be controlled. Therefore, the physical and chemical etching components can be controlled independently. Adesida et al. [9] have characterized CAIBE etching using Ar/Cl_2. As shown in Fig. 1, the etch rates of GaN for 500 eV Ar and a flow of Cl_2 incident on GaN increases with ion beam density at room temperature in curve (b). Etch rates as high as 160 nm/min was achieved; this is enhanced in comparison to the etch rates obtained with Ar ion beam as shown in curve (a). The enhancement is due to the chemical component brought about by the presence of the chlorine atoms. Another enhancement is observed for CAIBE at 200 °C where it has been ascertained that the thermal energy contributed primarily to the chemical etching mechanisms. CAIBE etch rates as high as 100 nm/min for GaN at room temperature have also been reported by Kneissl et al. [30]. The trend for CAIBE etch rates of GaN has strong dependence on ion density and ion energy and moderate dependence on temperature and gas flow rate. The etch rates of $Al_xGa_{1-x}N$ diminished linearly from $x = 0$ to 1 at room temperature [9]. However, the etch rates for $x < 0.1$ were not

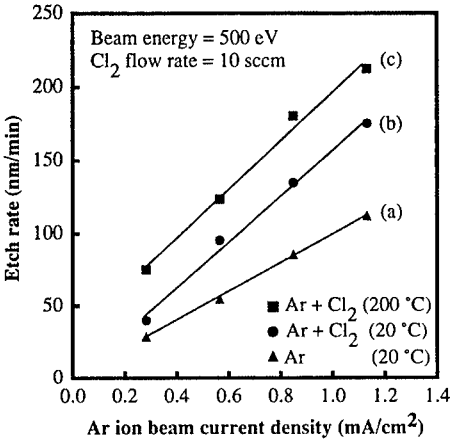


Fig. 1. Etch rate of GaN vs Ar ion current.

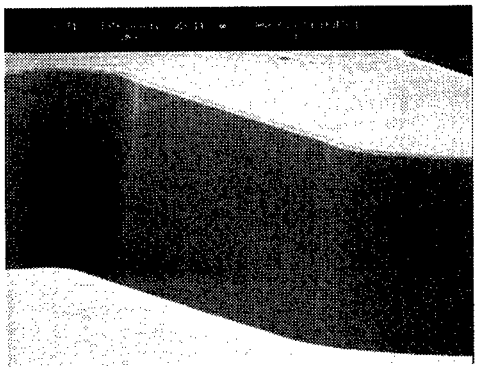


Fig. 2 GaN facet etched by CAIBE

significantly different, therefore heterostructures such as those utilized for lasers can essentially be etched at equi-etch rates. Ar/Cl_2 CAIBE etching produced anisotropic but only near-vertical etch profiles [9,31] at all substrate temperatures. The profiles were more vertical at higher temperatures due to increased chemical activities during etching [8,9]. In order to achieve the verticality necessary for laser facets, Binet [31] and Kneissl et al. [30] tilted and rotated their samples while etching. InGaN/AlGaN laser diodes with CAIBE-etched facets have been fabricated and demonstrated using this method by Kneissl et al. [30]. Highly vertical etch profiles have also been obtained by Ping et al. [8] using Ar/HCl CAIBE at 300 °C with no tilting of samples. An example of such a vertical etch-profile produced in an AlGaN/GaN heterostructure is shown in Fig. 2. The ultra-smooth sidewall demonstrated in Fig. 2 was obtained using a regrown oxide masking process [32]. The sidewall roughness was < 5 nm as measured in a scanning electron microscope.

High etch rates and highly anisotropic etch profiles have been obtained using high-density plasma reactive ion etching techniques. The high etch-rates produced by ECR-RIE and ICP-RIE methods are due to the higher plasma density available. The etch yields in the high-density plasma tools are the same as those in conventional RIE system, but the much larger ion fluxes in the former lead to higher etch rates. The higher efficiency of plasma generation also means that plasma can be generated and sustained in a higher vacuum environment than possible for conventional RIE tools. The independent biasing of the sample with 13.56 MHz generator provides for the control of the energy at which ions bombard the sample in high-density plasma etching tools. The directionality of low energy ions is preserved due to higher vacuum environment. This means that anisotropy can be achieved for etch profiles at lower ion energies.

A large body of work exists for ECR-RIE etching of III-nitrides [16-21]. Various chemistries involving chlorine and methane-based gases have been investigated as shown in Table I. Etch rates for GaN ranging from 20 to 200 nm/min have been obtained for operating pressures between 1 to 10 mTorr and ion energies < –300 V. Corresponding etch rates for InN and AlN are comparable or lower than for GaN. For example, etch rates of 200, 150, and 110 nm/min were reported for GaN, InN, and AlN, respectively, using $Cl_2/H_2/Ar$ plasma at a bias of -180 V [19]. The inclusion of H_2 in the plasma was found to increase etch rates and also improve surface morphology. This was achieved by the removal of nitrogen through the formation of NH_x products. In order to obtain even higher etch rates, novel gases such as ICl/Ar, IBr/Ar have been investigated [20,21]. High etch rates of 1300, 1150, and 200 nm/min in

ICl/Ar plasma have been obtained for GaN, InN, and AlN, respectively. Highly anisotropic profiles were routinely obtained using ECR-RIE.

Another high-density plasma source is the ICP-RIE. ICP-RIE sources are easier to scale up than ECR sources and are more economical to operate [25]. These factors have led to the investigation of ICP-RIE for III-nitrides in various plasmas [22-27]. As expected, high etch rates and etch profiles with high anisotropy have been demonstrated. Etch rates of GaN as high as 688 nm/min at –280 V [25] and 980 nm/min at –450 V [27] have been reported for $Cl_2/H_2/Ar$ and Cl_2/Ar plasmas, respectively. A GaN etch rate of 850 nm was obtained using BCl_3/Cl_2 plasma at –120 V and 30 mTorr [26]. Etch rates for InN, AlN, and various mole fractions of AlInN and AlGaN have also been reported [33]. Etch selectivities between these various materials have been reported for different gas mixtures including Cl_2/SF_6 [23]. Selectivities of 5 and 3 were reported for GaN on AlN and GaN on InN, respectively, using Cl_2/Ar at –250 V [34]. Corresponding selectivity results for Cl_2/SF_6 at – 250 V were < 1 for GaN/AlN and 4 for GaN/InN, respectively [23]. It would be expected that the formation of AlF or InF should retard the etching of the AlN, InN and the ternaries, however, the dc biases used for the etching were relatively high. The high dc bias cause physical sputtering of the etch-stopping material leading to low selectivity values. The best reported selectivity for GaN on AlN of 38 was obtained using Cl_2/Ar mixture at –20 V bias [27].

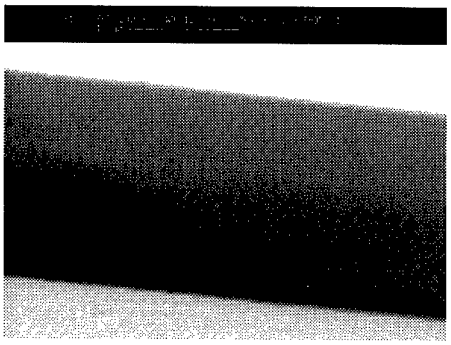


Fig. 3. InGaN/AlGaN laser facet etched by ICP-RIE

Highly anisotropic profiles with smooth sidewalls in GaN have been reported by Shul et al. [25]. A vertical etch profile with ultra-smooth sidewall in InGaN/AlGaN heterostructure obtained with a regrown oxide mask is shown in Fig. 3 [32]. This was obtained using Cl_2/Ar plasma at 2 mTorr and –160 V in a Plasmatherm SLR 790 ICP tool. These results have direct applications to laser facets.

Damage

Etch-induced damage can be manifested in different forms, all of which may affect the electronic and optical properties of devices fabricated on the etched materials. The forms in which damage can be categorized include: i) deposition of polymer, ii) creation of non-stoichiometric surfaces due to preferential depletion of one of the elements, iii) creation of near-surface lattice defects which can diffuse deep into the sample, and iv) implantation of etching species or hydrogen into the etched material. The few investigations that have been reported in this area measure electrical characteristics of the etched samples. Pearton et al. [35] performed Hall measurements on InN, InGaN, and InAlN exposed to Ar plasma under both ECR and conventional RIE conditions. It was found that the sheet resistances of the samples increased with increasing ion flux and ion energy. Ping et al. [36] investigated the Schottky characteristics of Pd on etched n-GaN layers. The samples were etched by RIE in $SiCl_4$ and Ar plasmas. Etching in $SiCl_4$ plasmas degraded the Schottky barrier heights significantly for self-bias voltages above -200 V. The barrier height decreased from 0.93 eV to 0.41 eV. A more severe degradation to 0.38 eV occurred for Ar plasma at –100 V. Annealing at 700 °C was able to restore the barrier height of the $SiCl_4$-etched sample.

The etch-induced degradation was utilized by Fang et al. [37] to improve the ohmic characteristics of Ti and Ti/Al on n-GaN layers. The samples were etched by RIE in BCl_3 prior to metal

deposition. It has also been found that etching with $SiCl_4$ RIE improved ohmic characteristics under all investigated conditions [38]. This can be explained by the depletion of nitrogen which leaves excess metallic Ga on the etched-surface. This change in stoichiometry renders the surface highly n-type, enhancing ohmic formation while degrading Schottky characteristics. The low bias etching that can be obtained using ICP-RIE and LE4 needs further investigations for realizing etched surfaces with low damage.

WET ETCHING

Wet etching is an important complement to dry etching methods by providing low damage etching, low cost, and complexity. Conventional wet etching of GaN, AlN, and InN has been studied in base and acid solutions [39-43]. Earlier studies [39] conducted on low quality GaN produced etch rates as high as 1 μm/min. However, recent studies by Mileham et al. [40] did not produce any measurable etching for high quality GaN. Slow etch rates have also been recorded for InN. Pearton et al. [41] found that InN etched very slowly in HCl/HNO_3 solutions. Guo et al. [42] reported etch rates of ~ 10 nm/min for InN using aqueous KOH and NaOH solutions at 60 °C. The etching of AlN was found to be highly dependent on the crystallinity of the sample [39]. Etch rates ranging from 10 to 1000 nm/min for AlN in KOH and AZ400K developer solution were reported by Mileham et al. [39,43]. The lower end of the etch rates were obtained for high quality crystalline AlN. It can be concluded that chemical stability exhibited by III-nitrides has resulted in very low etch rates with conventional wet etchants.

Photoelectrochemical wet etching

A recent development is the demonstration of photoelectrochemical (PEC) wet etching which has resulted in significantly higher etch rates for GaN [44-53]. The PEC process utilizes photogenerated electron-hole pairs to enhance oxidation and reduction reactions taking place in an electrochemical cell. The etching of n-GaN proceeds through surface oxidation followed by dissolution in aqueous solutions. This process is enhanced by the photogenerated holes by converting surface atoms to higher oxidation states. Increasing absorption of incident optical radiation with energy greater than the bandgap energy increase the supply of holes at the surface, thereby enhancing the etch rates.

Minsky et al. [44] first demonstrated PEC etching of n-GaN using KOH/H_2O and dilute HCl solutions. They utilized HeCd laser at 325 nm wavelength for illuminating n-GaN samples at light intensities of ~ 570 mW/cm^2. The GaN sample was connected to a Pt cathode during etching with no external bias applied. Etch rates of ~ 400 nm/min and 40 nm/min were obtained for the KOH and HCl solutions, respectively. No etching was observed in the absence of optical illumination. Youtsey et al. [45] have demonstrated the etching of n-GaN in KOH solutions using a broad-area Hg arc lamp. The electrochemical cell utilized by Youtsey et al. [45] is illustrated in Fig. 4. A Pt wire was used as the system cathode and a thin Ti (< 100 nm) metal was used as the mask. For a 0.04 M KOH solution

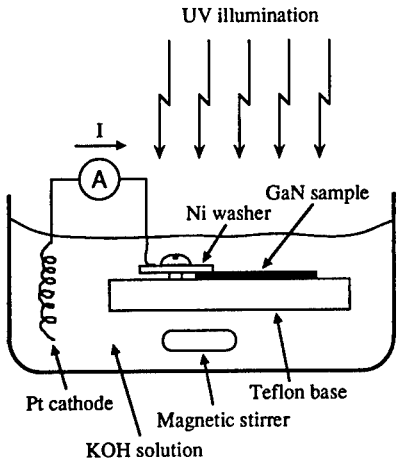


Fig. 4. Photoelectrochemical wet etching apparatus.

and for light intensities between 10 and 50 mW/cm^2, etch rates were proportional to the light intensity and varied from 50 to 300 nm/min. Highly anisotropic etch profiles as shown in Fig. 5 were obtained with the rough surfaces attributed to defects in the sample. However, under conditions of very low KOH concentrations (< 0.01 M) and high light intensities, anisotropic etch profiles with very smooth surfaces were obtained by Youtsey et al. [46]. The reaction kinetics in the latter etching is believed to be diffusion-controlled. Using similar etching procedure in KOH solutions, Cho et al. [47] reported etch rates greater than 100 nm/min and an activation energy of ~ 0.8 $kCal.mol^{-1}$ under diffusion-controlled kinetics.

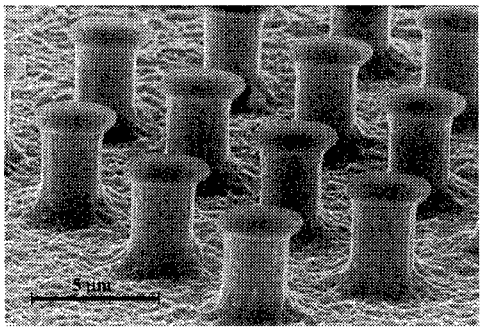


Fig. 5. Highly anisotropic GaN structures by PEC etching

Lu et al. [48] reported on photo-assisted anodic etching of n-GaN in solutions of tartaric acid/ethylene glycol at room temperature. Etch rates as high as 160 nm/min were obtained for Hg arc lamp illumination of ~ 60 mW/cm^2. Etch rates were found to be strongly dependent on the pH of the solutions. Peng et al. [49] have also reported on the strong pH dependence of etch rates of n-GaN in aqueous H_3PO_4 and KOH solutions. Etch rates as high as 120 nm/min were obtained for H_3PO_4 solution of pH =1 and KOH solution of pH = 14. Current-controlled PEC etching of n-GaN in KOH solutions under HeCd laser illumination has been reported by Rotter et al. [50]. Etch rates of up to 8 μm/hr were obtained with smooth "mirror-like" etched surfaces.

Youtsey et al. [51] have demonstrated selective PEC etching of n-GaN on p-GaN in KOH solutions. No etching was detected for the p-GaN. However, O et al. [52] have demonstrated the etching of p-GaN and InGaN in an LED structure using pulsed electrochemical methods in H_3PO_4/ethylene glycol/H_2O solutions.

In addition to the etching of GaN required for device fabrication, it has been shown that PEC can also reveal dislocations in n-GaN. Rotter et al. [50] observed etch pits with hexagonal symmetry and with a density in the range of 5 x 10^9 to 1 x 10^{10} cm^{-2}, corresponding to the dislocation density of the films. Perhaps, the most striking results reported so far in this area pertains to the nanometer-scale "whisker-like" features obtained using border-line diffusion-controlled etching conditions [53]. Figure 6 shows a scanning electron micrograph of "whiskers" obtained by etching n-GaN in 0.02 M KOH with a light intensity of 10 mW/cm^2. The whiskers have diameters of ~ 25 nm and lengths of ~200 nm. Taller whiskers have been produced, however, at heights approaching 1 um, they coalesce forming tree-like features. Figure 7 (a) shows a cross-sectional transmission electron micrograph (TEM) of the whiskers at low magnification. Both the whiskers and dislocations in the underlying unetched GaN are illustrated. At high magnification, propagation of dislocations from the unetched GaN into the etched whiskers is

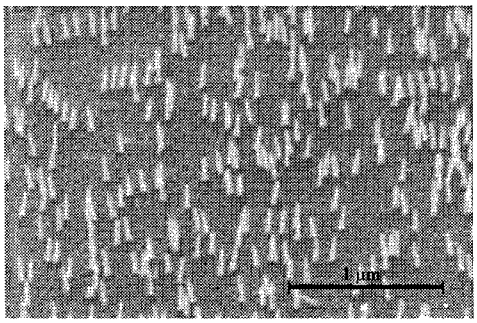


Fig. 6. Nanometer scale whiskers in GaN obtained by PEC etching.

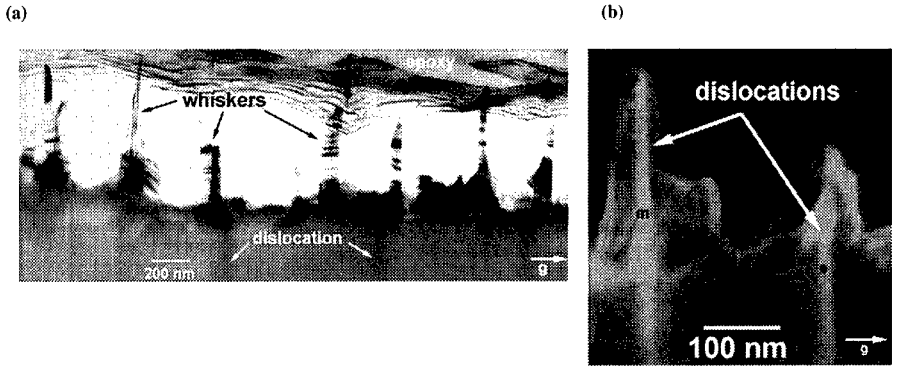


Fig. 7. (a) Cross-sectional TEM of etched GaN with whisker morphology, (b) higher magnification showing propagation of dislocations through the whiskers.

demonstrated in Fig. 7 (b). Both mixed (m) and edge (e) dislocations are associated with whisker formation as shown in the figure. The reduced etch rates at dislocations leading to whisker formation could arise due to a number of different effects [53]. Based on the mechanism of etching, it can be proffered that a spatially varying concentration of photogenerated holes exists on the GaN surface. Weimann et al. [54] have modeled dislocations as negative charged coulombic centers in explaining the low transverse Hall mobilities in n-GaN. These negative charge centers can become sinks for photogenerated holes thereby locally depressing the concentration of holes that can participate in the etching. This would result in the lateral selective etching of the crystalline over dislocation areas in the n-GaN.

As seen, under certain PEC etching conditions, dislocations are isolated on n-GaN. With the diameter of individual dislocation "whiskers" less than 50 nm, a plan view of a dislocation in a scanning electron microscope will be a spot or dot. Therefore an aerial image over a large area will result in the "star map" as shown Fig. 8. The counting of dots in a fixed area of the map yields the dislocation density of the material. Figure 8 shows the dislocation map of a high defect density MOCVD-grown n-GaN on SiC. The sample was etched in 0.004 M KOH under 30 mW/cm^2 light intensity for 15 min. The dislocation density is estimated from the figure to be 3.2 x 10^9 cm^{-2}. This estimation has been verified using TEM. It is seen that PEC method can be utilized for a rapid evaluation of dislocation densities in n-GaN materials. This method is less tedious than the conventional TEM method of assessing dislocation densities.

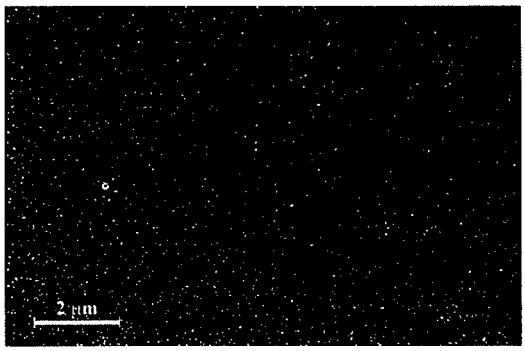


Fig. 8. 'Star map' of dislocations in GaN on SiC.

SUMMARY

Dry and wet etching methods for III-nitrides have been reviewed. Although the high bonding energies have constituted obstacles to the etching of the nitrides, high-density-plasma etching methods have yielded etch rates that are suitable for device fabrication. The low bias voltages enabled by these high-density-plasma etching methods should allow low damage etching of nitride surfaces. More efforts are required in this area to quantify the processing latitude provided by techniques such as the ICP-RIE. The photoelectrochemical etching method has been shown to be an emerging method for device fabrication and material characterization. The PEC was shown to have the potential of becoming a rapid evaluation tool for dislocations in n-GaN.

ACKNOWLEDGMENTS

This work was supported by at the University of Illinois by NSF grant No ECS 95-21671 and DARPA Grant No. F19628-96-C-0066; at CREE Research by DARPA Grant No. F19628-96-C-0066; and at Xerox by DARPA Grant No. MDA972-96-3-0014.

REFERENCES

[1] S. Nakamura, T. Mukai, and M. Senoh, Appl. Phys. Lett. 64, 1687 (1994).
[2] S. Nakamura, M. Senoh, S. Nagahama, N. Iwasa, T. Yamada, T. Matsushita, H. Kiyoku, and S. Sugimoto, Appl. Phys. Lett. 68, 2105 (1996).
[3] A. T. Ping, I. Adesida, K. Boutros, and J. Redwing, unpublished.
[4] S. Sheppard, K. Doverspike, W. Pribble, S. Allen, J. Palmour, L. Kehias, T. Jenkins, Paper V.B.–5, Device Research Conference (Charlolltesville, VA, 1998).
[5] L. McCarthy, P. Kozodoy, M. Rodwell, S. DenBaars, and U. Mishra, Compound Semiconductor 4 (8), 16 (1998).
[6] I. Adesida, A.T. Ping, C. Youtsey, T. Dow, M. Asif Khan, D.T. Olson, and J.N. Kuznia, Appl. Phys. Lett. 65, 889 (1994).
[7] S.J. Pearton, C.R. Abernathy, F. Ren, and J.R. Lothian, J. Appl. Phys 76, 1210 (1994).
[8] A.T. Ping, I. Adesida, and M. Asif Khan, Appl. Phys. Lett. 67, 1250 (1995).
[9] A.T. Ping, C. Youtsey, I. Adesida, M. Asif Khan, and J.N. Kuznia, J. Electron. Mat. 24, 229 (1995).
[10] J.-W. Lee, H.-S. Park, Y.-J. Park, M.-C. Yoo, T.-I Kim, H.-S. Kim, and G.-Y. Yeom, MRS Symp. Proc. 468, 373 (1997).
[11] D. Basak, M. Verdú, M.T. Montojo, M.A. Sánchez-García, F.J. Sánchez, E. Munoz, and E. Calleja, Semicond. Sci. Tech. 12, 1654 (1997).
[12] H. Lee, D.B. Oberman, and J.S. Harris Jr, Appl. Phys. Lett. 67, 1754 (1995).
[13] I. Adesida, A. Mahajan, E. Andideh, M. Asif Khan, D.T. Olson, and J.N. Kuznia Appl. Phys. Lett. 63, 2777 (1993).
[14] A.T. Ping, I. Adesida, M. Asif Khan, and J.N. Kuznia, Electron. Lett. 30, 1895 (1994).
[15] M.E. Lin, Z.F. Fan, Z. Ma, L.H. Allen, and H. Morkoç, Appl. Phys. Lett. 64, 887 (1994).
[16] S.J. Pearton, C.R. Abernathy, F. Ren, J.R. Lothian, P.W. Wisk, and A. Katz, J. Vac. Sci. Technol. A 11, 1772 (1993).
[17] S.J. Pearton, C.R. Abernathy, and C.B. Vartuli, Electron. Lett. 30, 1985 (1994).

[18] L. Zhang, J. Ramer, J. Brown, K. Zheng, L.F. Lester, and S.D. Hersee, Appl. Phys. Lett. 68, 367 (1996).
[19] R.J. Shul, S.P. Kilcoyne, M.H. Crawford, J.E. Parmeter, C.B. Vartuli, C.R. Abernathy, and S.J. Pearton , Appl. Phys. Lett. 66, 1761 (1995).
[20] C.B. Vartuli, S.J. Pearton, J.W. Lee, J.D. MacKenzie, C.R. Abernathy, and R.J. Shul, J. Vac. Sci. Technol. B 15, 98 (1997).
[21] C.B. Vartuli, S.J. Pearton, J.W. Lee, J. Hong, J.D. MacKenzie, C.R. Abernathy, and R.J. Shul, Appl. Phys. Lett. 69, 1426 (1996).
[22] H. Cho, C.B. Vartuli, S.M. Donovan, J.D. Mackenzie, C.R. Abernathy, S.J. Pearton, R.J. Shul, and C. Constantine, J. Electron. Mat. 27, 166 (1998).
[23] R.J. Shul, C.G. Willison, M.M Bridges, J. Han, J.W. Lee, S.J. Pearton, C.R. Abernathy, J.D. Mackenzie, S.M. Donovan, L. Zhang, and L.F. Lester, J. Vac. Sci. Technol. A 16, 1621 (1998).
[24] C.B. Vartuli, J.W. Lee, J.D. MacKenzie, S.M. Donovan, C.R. Abernathy, S.J. Pearton, R.J. Shul, C. Constantine, C. Barratt, A.Y. Poyakov, M. Shin, M. Skowronski, Mat. Res. Soc. Symp. Proc. 468, 393 (1997).
[25] R.J. Shul, G.B. McClellan, S.A. Casalnuovo, D.J. Rieger, S.J. Pearton, C. Constantine, C. Barratt, R.F. Karlicek Jr., C. Tran, and M. Schurman, Appl. Phys. Lett. 69, 1119 (1996).
[26] Y.H. Lee, H.S. Kim, G.Y. Yeom, J.W. Lee, M.C. Yoo, and T.I. Kim, J. Vac. Sci. Technol. A 16, 1478 (1998).
[27] S.A. Smith, C.A Wolden, M.D. Bremser, A.D. Hanser, R.F. Davis, and W.V. Lampert, Appl. Phys. Lett. 25, 3631 (1997).
[28] R.T. Leonard and S.M. Bedair, Appl. Phys. Lett. 68, 794 (1996).
[29] H.P. Gillis, D.A.Choutov, K.P. Martin, M.D. Bremser, and R.F. Davis, J. Electron. Mat. 26, 301 (1997).
[30] M. Kneissl, D.P. Bour, N.M. Johnson, L.T. Romano, B.S. Krusor, R. Donaldson, J. Walker, and C. Dunnrowicz, Apl. Phys. Lett. 72, 1539 (1998).
[31] F. Binet, J.Y. Duboz, N. Laurent, C. Bonnat, P. Collot, F. Hanauer, O. Briot, and R.L. Aulombard, Apl. Phys. Lett. 72, 960 (1998).
[32] F. Khan, C. Youtsey, and I. Adesida, unpublished.
[33] H. Cho, C. Vartulli, S. Donovan, C. Abernathy, S. Pearton, R. Shul, and C. Constantine, J. Vac. Sci. Technol. A16, 1631 (1998).
[34] R. Shul, C. Willison, M. Bridges, J. Han, J. Lee, S. Pearton, C. Abernathy, J. MacKenzie, S. Donovan, L. Zhang, and L. Lester, J. Vac. Sci. Technol. A16, 1631 (1998).
[35] S.J. Pearton, J.W. Lee, J.D. MacKenzie, C.R. Abernathy, and R.J. Shul, Appl. Phys. Lett. 67, 2329 (1995).
[36] A.T. Ping, A.C. Schmitz, M. Asif Khan, Q. Chen, J.W. Yang, and I. Adesida, J. Electron. Mater. 26, 266 (1997).
[37] Z. Fang, S.N. Mohammad, W. Kim, O. Aktas, A.E. Botchkarev, and H. Morkoç [*Appl. Phys. Lett.* (USA) vol.68 (1996) p.1672]
[38] A.T. Ping, Q. Chen, J.W. Yang, M.Asif Khan, and I. Adesida, J. Electron. Mater. 27, 261 (1998).
[39] Y. Morimoto, J. Electrochem. Soc.121, 1384 (1974).
[40] J.R. Mileham, S.J. Pearton, C.R. Abernathy, J.D. MacKenzie, R.J. Shul, and S.P. Kilcoyne, J. Vac. Sci. Technol. A14, 836 (1996).
[41] S. Pearton, C. Abernathy, F. Ren, J. Lothian, P. Wisk, and A. Katz, J. Vac. Sci. Technol. 11, 1772 (1993).
[42] Q.X. Guo, O. Kato, and A. Yoshida, J. Electrochem. Soc. 139, 2008 (1992).
[43] J.R. Mileham, S.J. Pearton, C.R. Abernathy, and J.D. MacKenzie, Appl. Phys. Lett. 67, 1119 (1995)
[44] M.S. Minskey, M. White, and E.L. Hu, Appl. Phys. Lett. 68, 1531 (1996).

[45] C. Youtsey, I. Adesida, and G. Bulman, Appl. Phys. Lett. 71, 2151 (1997).
[46] C. Youtsey, I. Adesida, L.T. Romano, and G. Bulman, Appl. Phys. Lett. 72, 560 (1998).
[47] H. Cho, K. Auh, R. Shul, S. Donovan, C. Abernathy, E. Lambers, F. Ren, and S. Pearton, J. Electron. Mater. (in press).
[48] H. Lu, Z. Wu, and I. Bhat, J. Electrochem. Soc. 144, L8 (1997).
[49] L. -H. Peng, C. Chuang, J. Ho, C. Huang and C.-Y. Chen, Appl. Phys. Let. 72, 939 (1997)
[50] T. Rotter, D. Uffmann, J. Ackermann, J. Aderhold, J. Stemmer, and J. Graul Mat. Res. Soc. Symp. Proc. 482 (1997).
[51] C. Youtsey, I. Adesida, and G. Bulman, J. Electron. Mater. 27, 282 (1998).
[52] J. O, P.S. Zory and D.P. Bour, SPIE Proc. 3002, 117 (1997).
[53] C. Youtsey, L.T. Romano, and I. Adesida, Appl. Phys. Lett. 73, 797 (1998).
[54] N.G. Weimann, L.F. Eastman, D. Doppalapudi, H.M. Ng and T.D. Moustakas, J. Appl. Phys. 83, 3656 (1998).
[55] A.T. Ping, M. Asif Khan, and I. Adesida, Semicond. Sci. Technol. 12, 133 (1997).

Contact Issues of GaN Technology

D. Qiao, L.S.Yu and S. S. Lau
Department of Electrical and Computer Engineering
University of California, San Diego
San Diego, CA 92093
lau@ece.ucsd.edu

G. J. Sullivan
Rockwell Science Center
Thousand Oaks, CA 91360

S. Ruvimov and Z. Liliental-Weber
Lawrence Berkeley National Laboratory
Berkeley, CA 94720

Cite this article as: MRS Internet J. Nitride Semicond. Res. 4S1, G1.5 (1999)

ABSTRACT

In this paper, we discuss the issue of fabricating reliable and reproducible ohmic contacts on AlGaN HFET structures. During the course of our investigation of fabricating contacts to HFETs, we found that the contact properties could vary significantly from one sample to another, even though they were nominally the same. This problem was prominently manifested in the ohmic contact behavior. The origin of this problem was traced back to the variation of the HFET structure during growth. In this paper, we report an attempt to fabricate reproducible ohmic contacts of these structures.

I. INTRODUCTION

Contact behavior is an important issue in device design and performance. In our laboratory, we have made an attempt to study the contact properties on GaN, AlGaN and AlGaN/GaN HFET structures in a systematic manner. We found that the Schottky barrier heights, ϕ_B^n, between n-GaN and n-$Al_{0.15}Ga_{0.85}N$ differ by about 0.3 eV. For example, the barrier height of Ni on GaN is ~0.95 eV and that on $Al_{0.15}Ga_{0.85}N$ is ~1.27 eV[1]. These are the average values (I-V and C-V) obtained on bulk samples, i.e., the layer thickness of GaN and AlGaN exceeds 1 μm. The barrier height of Ni on HFET structure i.e., $Al_{0.15}Ga_{0.85}N$ (300 Å)/3μm GaN (undoped), cannot be ascertained using the conventional I-V and C-V methods due

Mat. Res. Soc. Symp. Proc. Vol. 537 © 1999 Materials Research Society

to the presence of the piezoclectric donor charge at the AlGaN/GaN interface[2]. Internal photo emission is an alternative way to determine the Schottky barrier height of a metal/AlGaN/GaN heterostructure. In our laboratory, we have measured the barrier height of Ni of $Al_{0.15}Ga_{0.85}N$ (300 Å and 500 Å)/GaN using the internal photo emission technique and obtained a barrier height of ~1.30 eV, independent of the AlGaN layer thickness[3]. This value, well within the experimental scattering range, is considered to be consistent with the value obtained on bulk $Al_{0.15}Ga_{0.85}N$ samples. As the mole fraction of Al in the AlGaN top layer changes to 30%, the barrier height is seen to increase further to ~1.56 eV (see Table 1). These results suggest that the Schottky barrier of HFET structures is largely determined by the upper most AlGaN layer and that the barrier height appears to increase between 0.25 to 0.3 eV for every 15% increment in Al mole fraction in the AlGaN layer up to 30 % of Al. More work is needed to correlate the barrier height and the Al mole fraction in detail.

Table 1. Summary of Schottky barrier height[(a)]

Metal	Material	Ideality n factor	$q\phi_b$ (I-V) (eV)[(e)]	$q\phi_b$ (I-V) (eV)[(f)]	$q\phi_b$ (C-V) (eV)	$q\phi_b$ (photo) (eV)
Ni	Bulk AlGaN[(b)]	1.23	1.03	1.25	1.26	1.28
Ni	GaN	1.14	0.84	0.95	0.96	0.91
Ni	HFET[(c)]					1.31
Ni	HFET[(d)]					1.56
Ti	Bulk AlGaN[(b)]	1.08	0.79	0.84	1.10	
Ti	GaN	1.08	0.60	0.65	0.68	

[(a)]The data (I-V and C-V) are the average value from 15 diodes; the standard deviation is about 0.05 for both of the *n* factor and the barrier heights.

[(b)]Al mole fraction was 15% in the AlGaN samples.

[(c)]$Al_{0.15}Ga_{0.85}N$ (300 Å or 500 Å)/3μm undoped GaN.

[(d)] $Al_{0.3}Ga_{0.7}N$ (500 Å)/3μm undoped GaN.

[(e)] Calculated from Equation 1;

$$I = AA^*T^2 e^{-q\phi_b / kT}\left(e^{qV/nkT} - 1\right) \tag{1}$$

[(f)] Calculated from Equation 1 and corrected by equation 2;

$$\phi_{bc} = n\phi_b - (n-1)\frac{kT}{q}\ln\frac{N_c}{N_d} \tag{2}$$

We have also been investigating the ohmic behavior on the III-V nitrides. Of particular interest to us was understanding how to fabricate low resistance and reproducible ohmic contacts on HFET structures. During the course of the study, we found that the ohmic behavior varied significantly from one wafer to another, even though these wafers were nominally the same, i.e., n- $Al_{0.15}Ga_{0.85}N$ (300 Å)/ $Al_{0.15}Ga_{0.85}N$ (30 Å, undoped)/i-GaN(1 μm). Table 2 shows the results of the measured contact resistivity on four different wafers with nominally the same structure. The $n_s\mu$ product, extracted from Hall effect measurements, is the usual parameter that characterizes the HFET samples (see Table 2). For samples with a large value of $n_s\mu$ product, the contact resistance should be low, compared to samples with a small $n_s\mu$ value, at least in principle. This is because the $n_s\mu$ product is believed to indicate good electrical conduction in the channel region and should lead to low ohmic contact resistance. According to this idea, sample #4, in Table 2 should yield the lowest contact resistance, since it had the largest value of $n_s\mu$; and sample 2 with the smallest $n_s\mu$ should yield the largest contact resistance. Contact resistance measurement using the TLM method indicated that sample #4 had the highest contact resistivity (2.07E-3 $\Omega\cdot cm^2$), and sample #2 had a low contact resistivity of 4E-6 $\Omega\cdot cm^2$. This behavior was not expected and could not be explained by the $n_s\mu$ product value alone.

Table 2. Contact resistance and parameters of nominally the same AlGaN/GaN HFET structures ($Al_{0.15}Ga_{0.85}N$(300 Å)/GaN(1 μm)/sapphire)[a]

Samples	$n_s\mu$	R_c[b]	ρ_s[c]	R_s[d]	Al fraction in the AlGaN layer, %		Thickness of the AlGaN layer, Å	
	E16 $(V\text{-}s)^{-1}$	Ω·mm	$\Omega\cdot cm^2$	Ω/□				
					SIMS[e]	EDX[f]	SIMS	TEM[g]
#1	1.20	0.22	8.60E-7	830	9	11-15.2	220	210
#2	0.74	0.50	4.00E-6	990	10	~25.3	360	280
#3	1.09	3.73	2.05E-4	770	15	22-25.4	360	280
#4	1.34	15.25	2.07E-3	1190	22	30	600	340

[a]The contact metallization was Al(710 Å)/Ti(300 Å)/HFET annealed at 950 °C for 80 seconds in flowing N_2. The thickness of AlGaN and the Al fraction can vary significantly from one sample to another, even though they were nominally the same. These parameters can also vary but to a lesser extent when different analytical methods were used for the same sample.

[b]R_c: Contact resistance.

[c]ρ_s: Specific contact resistivity.

[d]R_s: sheet resistance.

[e]SIMS: Secondary ion mass spectroscopy.

[f]EDX: Energy dispersive x-ray.

[g]TEM: Transmission electron microscopy.

Structural and chemical analysis of the samples showed that these four nominally identical samples were in fact very different in the Al mole fraction and in thickness in the AlGaN layer. Sample #4 had an Al mole fraction of 22% (SIMS value, believed to be more accurate than

EDX) in the AlGaN layer with a thickness of 340 Å (TEM value, believed to be more accurate than SIMS). This sample had the largest contact resistivity (2E-3 $\Omega \cdot cm^2$). Sample #1 had an Al mole fraction of 9% in the AlGaN layer with a thickness of 210 Å, and yielded the smallest contact resistivity (8.6E-7 $\Omega \cdot cm^2$). Table 2 suggests that the contact behavior is primarily governed by the Al mole fraction and the thickness of the top AlGaN layer in these nominally identical samples. This observation led us to conclude that the control of the growth of the HFET samples is far from satisfactory. We, further, assume that sample non-uniformity is a common problem in almost all nitride growth systems.

II. APPROACHES TO FABRICATE LOW RESISTANCE-CONTACT IN A MORE CONSISTENT MANNER

We considered two approaches to improve the consistency of low resistance contact behavior in HFET structures where sample non-uniformity is expected. The first approach was to use Si implantation into the HFETs to increase the electron concentration to facilitate carrier tunneling across the contact[4-8]. We picked sample #4 (the worst case) in Table 2 as a test vehicle to examine the implantation approach; we assumed that if the contact behavior on sample #4 could be improved, then all other samples could be improved using the same approach. In using this approach, we divided sample #4 into two groups. For group 1 (samples #4C-1 and #4A-1), Si^{28} was directly implanted into the HFET structure at 40 keV with a dose of 1E16 cm^{-2}. The projected range, R_p, was estimated, using TRIM96, to be about 600 Å into the sample with a peak concentration of about 1.4E21cm^{-3}. After implantation, a layer of AlN, used as a capping layer for dopant activation, with a thickness of about 1800 Å was sputter-deposited onto the samples. For group 2 (samples #4C-2 and #4A-2), a layer of 1800 Å thick AlN was first deposited onto the samples, followed by Si implantation through the AlN layer at 120 keV with a dose of 1E16cm^{-2}. The estimated location of the peak concentration (6.2E20cm^{-3}) was about 340 Å into the HFET sample. The advantage of implanting through the AlN capping layer was the ability to place the R_p closer to the HFET surface region; the disadvantages include the loss of some implanted Si ions when the AlN capping layer is removed and the possibility of ion-mixing some Al into the AlGaN layer, thus changing the HFET top layer composition. Samples #4C-1, 4C-2, 4A-1 and 4A-2 were then annealed at 1150 °C for 30 seconds to activate the implanted Si, followed by removing the AlN capping layer using hot phosphoric acid. TLM patterns were then fabricated for contact resistance measurements. A conventional Al (710 Å)/Ti(300 Å)/HFET[9] metallization was e-beam deposited onto the two groups of implanted samples. The samples were coated with AlN (~1000 Å thick) as an encapsulation layer to prevent the oxidation during ohmic annealing.

It has been shown that Ti-based metallization schemes reduce contact resistance by forming a metallic $AlTi_2N$ layer with AlGaN, leaving an N-deficient AlGaN region, believed to be heavily n-type, beneath the $AlTi_2N$ contact layer[9]. Fig. 1(a) shows a cross-sectional electron microscopy image of sample #4C. The contact layer contains two sublayers of different contrast due to different Al/Ti ratio in the sublayers. EDX analysis indicates that the composition of the top sublayer is close to Al_3Ti, in good agreement with previous results, while the interfacial layer (with darker shading) is rich in Ti (with Ti/Al ~ 2). Table 3 shows the contact resistance for the conventional metallization (Al (710 Å)/Ti (300 Å)/HFET) on non-implanted samples (sample #4C), direct implanted samples (sample #4C-1) and implanted through the AlN (sample #4C-2).

Table 3. Contact Resistance for the conventional metallization (Al(710Å)/Ti(300Å))[(a)]

		R_c	ρ_s	R_s
		Ω·mm	Ω·cm^2	Ω/□
#4C	No implantation	15±3	(2.1±0.8)E-3	1200±300
#4C-2	120 keV, 1E16 cm^{-2}, implantation through AlN	4.9±0.2	(1.9±0.6)E-3	140±40
#4C-1	40 keV, 1E16 cm^{-2}, direct implantation	1.1±0.1	(1.4±0.4)E-4	90±15

[(a)]The implantation activation was done at 1150 °C for 30 seconds with an AlN capping layer in flowing N_2. The contact formation was done at 950 °C for 80 seconds.

It is clear that direct implantation and activation at 1150 °C for 30 seconds significantly reduced the sheet resistance of the HFET from 1200 Ω/□ to 90 Ω/□, in spite of the relatively low activation temperature of 1150 °C. As a result, the contact resistance R_c reduced from ~15 Ω·mm (non-implanted sample) to ~1.1 Ω·mm for directly implanted samples. This is because R_c is related to the sheet resistance by the following relationship:

$$R_c = \sqrt{\rho_s R_s}\,, \tag{3}$$

where R_c (Ω·mm) is the contact resistance, R_s (Ω/□) is the sheet resistance of the semiconductor beneath the contact and ρ_s (Ω·cm^2) is the specific contact resistivity at the metal/semiconductor interface. While the values of R_c for the implanted samples seemed to decrease substantially, depending on the implantation scheme, compared to those of non-implanted samples, the specific contact resistivity, ρ_s, did not decrease as impressively. This is primarily due to the inability of carrier tunneling through the remaining un-reacted AlGaN layer, using a relatively thin Ti(300Å) in the metallization scheme. Increasing the annealing time at 950 °C with and without an AlN capping layer did not improve the contact further beyond 80 seconds of annealing, apparently the reaction has reached an end point after 80 seconds of annealing.

To improve the specific contact resistivity, ρ_s, it is necessary to reduce the thickness of the un-reacted AlGaN layer for easier access to the GaN layer underneath. Based on this concept, we used a different Al(200 Å)/Ti(1500 Å) ratio for the contact formation. In this case, the Ti layer was much thicker and would consume more AlGaN to form $AlTi_2N$, thereby resulting in a much thinner (or none at all) un-reacted AlGaN for easy carrier tunneling. This scheme is referred to as the "advancing metallization" here. In the conventional scheme, 710 Å of Al reacts with 250 Å of Ti to form Al_3Ti at 250 °C to 300 °C, leaving an excess Ti layer 50 Å thick to react with the AlGaN layer. For samples with thicker AlGaN layers (≥300 Å) and with a high Al fraction (≥20%), the conventional Al(710 Å)/Ti(300 Å) metallization does not yield satisfactory contact resistance. There may be two possible reasons for this: (1) the chemical reactivity decreases with increasing Al fraction in the AlGaN layer, since AlN appears to be more stable at high temperatures than GaN; (2) for thick AlGaN with a high Al fraction, 50 Å of excess Ti is

not enough to consume most of the AlGaN top layer, leaving a relatively thick un-reacted AlGaN layer at the interface to hinder carrier tunneling due to its high Schottky barrier height and thickness.

Using the "advancing" scheme, Al and Ti react to form Ti_3Al (not Al_3Ti as in the conventional scheme) at 200-400 °C, leaving 850 Å of Ti in excess to fully react with the AlGaN layer to form the $AlTi_2N$ phase. This reaction would leave little or no AlGaN layer left in the HFET source and drain region, thus resulting in efficient carrier tunneling and much reduced specific contact resistivity, ρ_s.

Since the upper most contact layer is probably Ti_3Al (not Al_3Ti), a capping layer of AlN is required for the ohmic annealing at 950 °C for 10 minutes to prevent oxidation (5 minutes was found to be insufficient to react fully). Pure Ti capped with an AlN layer was not practical due to the ease of oxidation of un-reacted Ti after the removal of AlN even at room temperature in air. For the conventional Al(710 Å)/Ti(300 Å) scheme, the top Al_3Ti layers has been found to be stable when annealed at 950 °C for 80 seconds in N_2 with little oxidation.

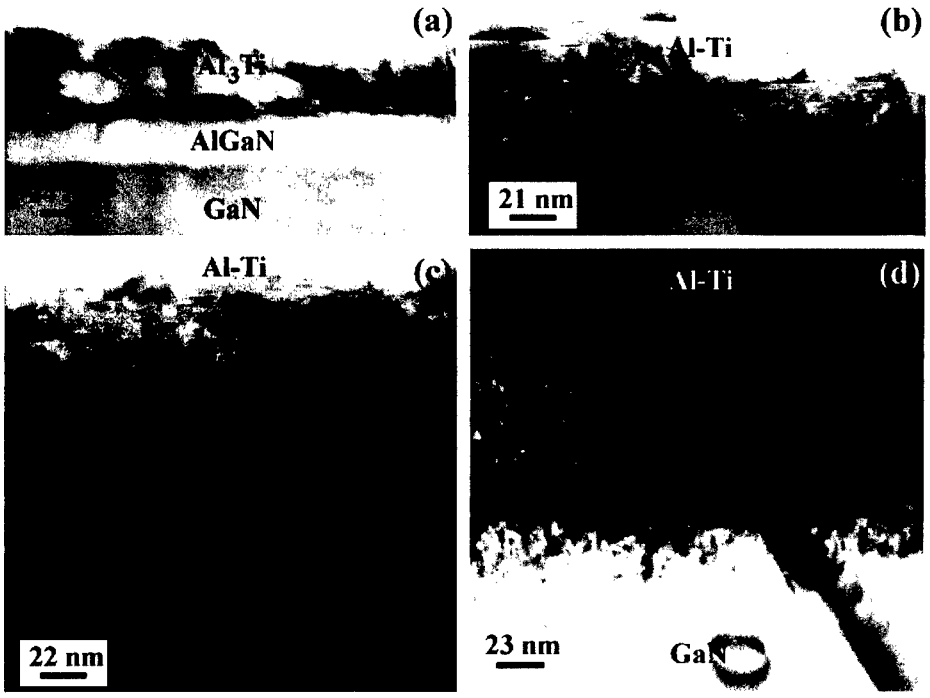


Fig. 1. TEM cross sectional view of samples (a) 4C, (b) 4A, (C) 4A-1 and (d) 4A-2.

Fig. 1 (b) shows the cross-sectional TEM image of the sample with the "advancing" Al(200 Å)/Ti(1500 Å) contact (#4A). It is clear that the AlGaN layer is partially and sometimes completely consumed due to the reaction with Ti. It also can be found that the reaction is enhanced at the dislocations intersecting the AlGaN layer. Fig. 1(c) shows the cross-sectional

TEM image of the sample with the "advancing" contact and the direct Si implantation prior to the metallization (#4A-1). Fig. 1(d) shows the image of the sample with the "advancing" contact and the Si implantation through a layer of AlN prior to the metallization (#4A-2). For these two samples, the contact layer contains two sublayers of different structure and composition, suggesting the reaction of the metal (presumably Ti) with AlGaN. The AlGaN layer is hardly visible on the TEM images of Figures 1(c) and (d) due to a high defect density in the HFET structure caused by the ion implantation. However, it seems that the AlGaN layer is less consumed in the samples #4A-1 (directly implanted) and #4A-2 (implanted through a layer of AlN) compared to sample #4A (not implanted). The damaged region, containing a high density of dislocation loops, is almost polycrystalline in the region close to the metal contact. This polycrystalline region differs in length and in average grain size for the direct and through-AlN implantation. The average grain size is about 50 Å and 110 Å for samples #4A-1 and #4A-2, respectively. TEM results suggest that both the sheet resistance, R_s, and the specific contact resistivity, ρ_s, may be affected by the remaining AlGaN layer and by the ion-implantation damage of crystalline lattice and possible diffusion of Ti through grain boundaries.

Table 4 summarizes the TLM results obtained on the samples with the "advancing" Al(200 Å)/Ti(1500 Å) metallization scheme. For the advancing scheme, the contact resistance and the specific contact resistivity were much smaller compared to those obtained with the conventional metallization scheme. The samples using a combination of direct implantation and the "advancing" metallization gave the lowest contact resistance, R_c, of 0.25 Ω·mm or 5.6×10^{-6} Ω·cm^2.

The drastic decrease in R_c is due to the reduction in sheet resistance R_s caused by the Si implantation and the reduction of ρ_s caused by the "advancing" metallization scheme. Both of these factors contribute to the reduction of R_c.

A comparison of Table 3 and Table 4 shows the advantage of using the "advancing" metallization scheme to reduce contact resistance. However, results shown in Table 2 indicate that the conventional Al(710 Å)/Ti(300 Å) system can form low resistance contacts quite readily on HFET structures with a thin AlGaN top layer and a low Al fraction.

Table 4. Contact Resistance for the "advancing" metallization (Al(200 Å)/Ti(1500 Å)) [(a)]

		R_c	ρ_s	R_s
		Ω·mm	Ω·cm^2	Ω/□
#4A	No implantation	1.8±0.3	(5±1)E-5	660±50
#4A-2	120 keV, 1E16 cm^{-2}, implantation through AlN	0.37±0.01	(1.0±0.1)E-5	129±3
#4A-1	40 keV, 1E16 cm^{-2}, direct implantation	0.25±0.01	(5.6±0.9)E-6	110±10

[(a)]The implantation activation was done at 1150 °C for 30 seconds with an AlN layer in flowing N_2. The contact formation was done at 950 °C for 10 minutes, with an AlN capping layer.

In summary, Si implantation into HFET structures was found effective in reducing the sheet resistance, R_S, of the structure. With annealing temperatures higher than 1150 °C, the sheet resistance is expected to decrease even more. The "advancing" metallization scheme of Al(200 Å)/Ti(1500 Å) reduced the specific contact resistivity, ρ_s. Combining direct implantation of Si and the "advancing" metallization, very low contact resistance (~0.25 Ω·mm) and low specific contact resistivity, ρ_s, (~5.6×10^{-6} Ω·cm^2) was achieved on HFET structures with an AlGaN layer at least as thick as 340 Å and with an Al fraction at least as large as 22%.

ACKNOWLEDGMENT

This study was supported by BMDO (Dr. K. Wu) monitored by the US Army Space and Strategic Defense Command. UCSD would like to acknowledge the National Science Foundation for support.

REFERENCES

[1]. L.S. Yu, D. J. Qiao, Q. J. Xing, S.S. Lau, K.S. Boutro and J.M. Redwing, Appl. Phys. Lett. **73**, 238 (1998).

[2]. C.H. Chen, S.M. Baier, D.K. Arch and M.S. Shur, IEEE Tran. Electron Device, **35**, 571 (1988).

[3]. E.T. Yu, X.Z. Dang, L.S. Yu, P.M. Asbeck, S.S. Lau, K.S. Boutros and J.M. Redwing, Appl. Phys. Lett. **73**, (1998).

[4]. J.C. Zopler, D.J. Rieger, A.G. Baca, S.J. Pearton, J.W. Lee, R.A. Stall, Appl.Phys. Lett. **69**, 538 (1996).

[5]. X.A. Cao, F. Ren, S.J. Pearton, A. Zeitouny, M. Eizenberg, J.C. Zolper, C.R. Aberbathy, J. Han, R.J. Shul and J.R. Lothian, Appl.Phys. Lett., **73**, 229(1998).

[6]. Jinwook Burm, Kenneth Chu, William A. Davis, William J. Schaff , Lester F. Eastman, Tyler J. Eustis, Appl.Phys. Lett., **70**, 464(1997).

[7]. J.C. Zolper, J. Han, R.M. Biefeld, S.B. Van Deusen, W.R. Wampler, D.J. Reiger, S.J. Pearton, J.S. Williams, H.H. Tan, and R. Stall, J. Electron. Mater., **27**, 179 (1998).

[8]. H. Kobayashi and W.M. Gibson, Appl. Phys. Lett., **73**, 1406, 1998.

[9]. S. Ruvimov, Z. Liliental-Weber, J. Washburn, D. Qiao and S.S. Lau, Appl. Phys. Lett. **73**, 2582 (1998).

PYROELECTRIC AND PIEZOELECTRIC PROPERTIES OF GAN-BASED MATERIALS

M. S. SHUR*, A. D. BYKHOVSKI*, R. GASKA**
*Department of Electrical, Computer, and Systems Engineering, Rensselaer Polytechnic Institute, Troy, NY 12180, USA, shurm@rpi.edu
**APA Optics, Inc., 2950 N. E. 84th Lane, Blaine, MN 55449, USA

Cite this article as: MRS Internet J. Nitride Semicond. Res. 4S1, G1.6 (1999)

Abstract

We review pyroelectric and piezoelectric properties of GaN-based materials. Pyroelectric effects in GaN have been studied in two different regimes: (i) uniform sample heating regime and (ii) under applied temperature gradient along the sample. The modeling results show that the pyroelectric coefficient, P_v, in GaN (for *c*-axis along the contacts) can reach $7x10^5$ V/m-K (compared to $P_v = 5x10^5$ V/m-K for the best-known high temperature pyroelectric/piezoelectric material $LiTaO_3$). This points to a high potential of GaN-based sensors for high temperature pyroelectronics. Piezoelectric effects strongly affect the performance of electronic and light-emitting devices based on III-N materials. Piezoelectrically induced charge in heterostructures can be as large as 3 to $4x10^{13}$ cm^{-2}. Hence, strong lattice polarization effects provide unique possibilities for utilizing GaN-based materials in high temperature piezoelectronics and for their applications in pyroelectric detectors.

Introduction

Recent improvements in material quality and contact technology for GaN-based materials system have led to a rapid progress in GaN devices. These devices include blue-green lasers[1], blue, green, and amber Light Emitting Diodes[2], Ultraviolet (UV) photodetectors[3,4], and AlGaN/GaN Heterostructure Field Effect Transistors [5-11]. Wide band gap, high peak and saturation velocities, high breakdown voltage and chemical inertness make AlN-GaN-InN based semiconductors an excellent material for solar-blind optoelectronics, and high-power, high-temperature electronics.

GaN-based materials are usually grown in the [0001] direction (when they have the wurtzite crystal structure) and in the [111] direction (when they have the zinc blende crystal structure). These are polar axes, and, therefore, GaN-based materials exhibit strong lattice polarization effects. These effects are uniquely suited for applications in high temperature piezoelectronics and for applications in pyroelectric sensors.

We report on preliminary studies of pyroelectric properties of GaN. Much (if not most) of the work in this area remains to be done, and we expect dramatic improvements in GaN-based pyroelectric sensors still to come. We discuss the piezoelectric properties of III-Nitrides and the application of the concept of "piezoelectric doping" to GaN-based Heterostructure Field Effect Transistors. We consider the issue of spontaneous polarization in wurtzite GaN, AlN, and InN. Finally, we discuss several unresolved issues and make projections of future progress in GaN-based piezoelectronic devices.

Pyroelectricity in gallium nitride thin films

The pyroelectric materials are capable to generate an electric charge in response to heat flow. Heat sources affect the sample temperature by means of thermal convection, thermal diffusion or radiation. Both the primary pyroelectric effect and the secondary pyroelectric effect (piezoelectric effect caused by temperature induced strain) contribute to the pyroelectric

Mat. Res. Soc. Symp. Proc. Vol. 537 © Materials Research Society

response in GaN. The primary pyroelectric effect is dominant under the condition of a fast heat transfer. Such conditions can be implemented, for example, when the sensor is immersed in medium with a small viscosity and /or high flow velocity. In such moving medium (for example, hot gas flow), a GaN-based sensor will generate a voltage response, which is proportional to the heat flow (and, hence, to the gas flow).

Secondary pyroelectricity is linked to strain related to thermal expansion. For example, a difference in thermal expansion coefficients between a substrate and a pyroelectric film produces strain in response to temperature changes, which, in turn, generates an electric charge as a result of the piezoelectric effect.

Our estimates show that the sensitivity of GaN pyroelectric sensors can be significantly improved. The modeling results indicate that the pyroelectric voltage coefficients in GaN (for *c*-axis along the contacts) can be as high as $7x10^5$ V/m-K [12] and exceed the $P_V = 5x10^5$ V/m-K for the best-known high temperature pyroelectric material $LiTaO_3$ [13].

Therefore, GaN-based sensors should be suitable for high temperature pyroelectronics and piezoelectronics. Moreover, we expect that the pyroelectric effect will be more pronounced in insulating AlN or in AlGaN with a large Al mole fraction..

Low pressure MOCVD was used to fabricate all our samples (for the details of the growth procedure, see [14]). The Hall electron concentration was approximately $5x10^{16}cm^{-3}$ and the Hall mobility was on the order of 350 cm^2/V-s. A typical sample resistance was close to 2 kΩ. GaN layers, 3 - 5 μm thick, had ohmic contacts on the basal plane.

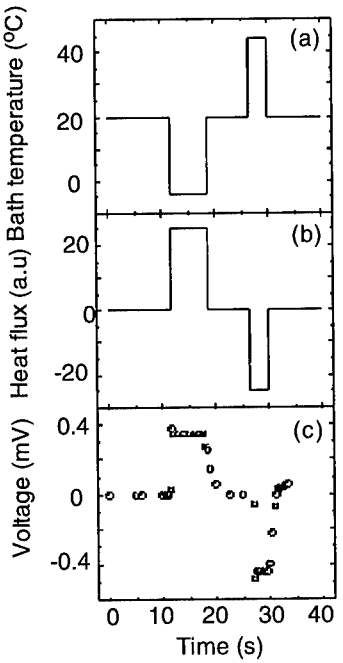


Fig. 1. Pyroelectric voltage versus time for uniform heating and cooling (after [15]).

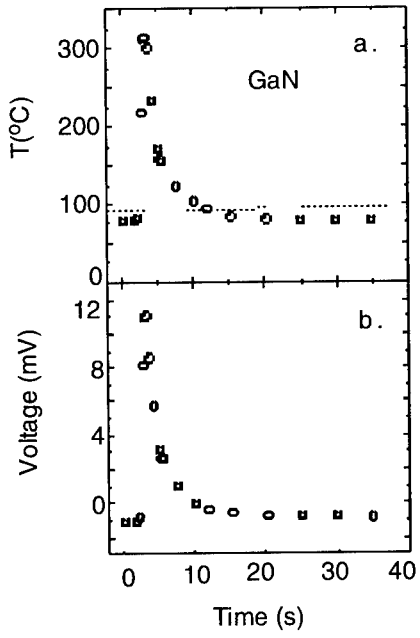


Fig. 2. Dynamics of contact temperature difference (a) and voltage response of GaN sample under non-uniform heating (b). Constant temperature of "cold" contact (94 °C) is shown by dotted line in Fig. 2 a.

Pyroelectric properties of GaN were studied in two different regimes: (i) under applied temperature gradient along the sample and (ii) uniform sample heating.

The pyroelectric voltage was measured in the GaN sample subjected to uniform (see Fig. 1) and non-uniform (Fig. 2) heating and cooling.[15] The time dependence of the voltage response in the GaN sample under applied temperature gradient is shown in Fig. 2. In these measurements, one contact was kept at a fixed temperature, which varied from 12 °C to 94 °C. The second contact was heated up to temperatures as high as 350 °C. The ambient temperature changed abruptly and a SmS-based thermoresistor monitored the sample temperature as a function of time. Cold and hot thermal shock experiments in the range from -100 °C to +300 °C used 96% ethyl or oil as a thermal bath. In these experiments, the heat transfer was caused mainly by free convection. Since the temperatures were relatively low, the radiative heat transfer was not important. Also, in uniform heating/cooling experiments, when the sample was dipped into the thermal bath, there was no appreciable temperature difference between the contacts, so that the sample did not act as a thermocouple.

Due to a relatively high thermal conductivity of sapphire, the temperature gradients in the sample could be neglected under the uniform heating/cooling conditions, and the lumped system analysis was valid. [16] The pyroelectric effect in these experiments can be described by the heat transfer equation, the equation of motion of a viscous fluid, and the equation for pyroelectric polarization. Both the sample temperature change, $T(t)$ - $T(0)$, and the heat flow affect the polarization. The temperature change is proportional to the thermal energy stored or dissipated.

In Reference [15], we described a model, which describes the time variation of the pyroelectric voltage. This model accounts for both primary and secondary pyroelectric effects. In order to compare the pyroelectric properties of GaN with those of other pyroelectric materials, we estimated the pyroelectric voltage coefficient of GaN:

$$P_v = \frac{dF}{dT}, \tag{1}$$

where F is the electric field in the sample caused by the pyroelectricity and T is temperature. In order to find the electric field, we solved Poisson's equation taking into account the pyroelectric polarization. For the primary pyroelectricity, such a solution yielded:

$$P_v = \frac{dP_s}{\varepsilon_s dT} \approx \frac{V(t_o)}{(T_o - T_\infty) r_d} \tag{2}$$

Here P_s is the spontaneous polarization, ε_s is the static dielectric permittivity of GaN, $V(t_0)$ is the peak voltage, T_0 is the initial sample temperature, T_∞ is the temperature of the ambiance, and r_d is the Debye length. From the experimental data given in Ref. [15], we estimated $P_v \sim 10^4$ V/m-K. This value is close to the values of P_v for pyroelectric ceramics, such as PZT and $BaTiO_3$. For the contacts along the c-axis, P_v might be close to 7×10^5 V/m-K.

Figures 3 and 4 compare the calculated and experimental time dependencies of the pyroelectric voltage and the sample temperature for cooling experiments. The temperature calculated using the free convection heat transfer mechanism (dominant under the conditions of this experiment) is in excellent agreement with the measured data.

Figure 4 shows the time dependence of the pyroelectric voltage for nearly the same temperature differences between the sample and the thermal bath but for the initial heat flows being different by approximately a factor of 3. These flows were estimated using the thermal boundary layer theory. As can be seen from the figure, the peak voltage increases proportionally to the thermal flux, in agreement with the theory.

Figures 3 and 4 show that the pyroelectric effect in GaN is a combination of fast and slow responses, in agreement with the proposed model. The fast response (jumps in Figs. 3, 4) is caused by the initial thermal flow, which is accounted for by the initial condition in the model described in Reference [15]. In the approximation used in [15], this response is instant.

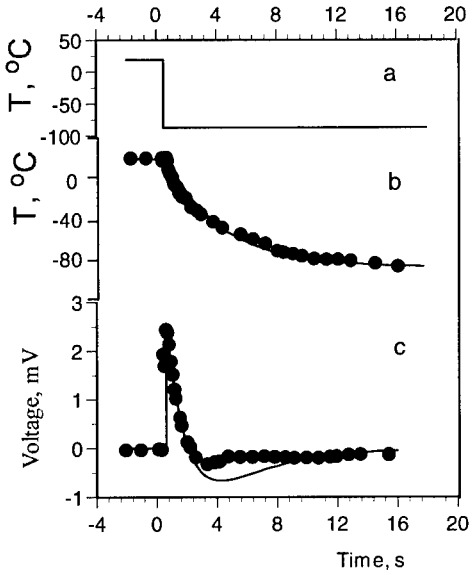


Fig. 3. Bath temperature (a), sample temperature (b), and pyroelectric voltage (c) versus time. Dots are measured data, solid curves are calculated. ΔT_o = 108 °C. (after [15]).

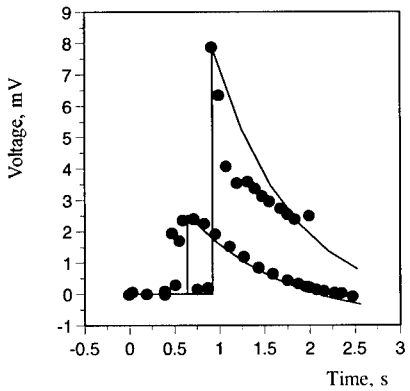


Fig. 4. Pyroelectric voltage as a function of time for conditions similar to that of Fig. 3. Circles are measured data, solid lines are calculated. Upper curve corresponds to initial thermal flux approximately three times larger than for bottom curve. ΔT_o = -105 °C (lower curve), ΔT_o = -99 °C (upper curve). (After [15].)

Figures 3 and 4 show that the pyroelectric effect in GaN is a combination of fast and slow responses, in agreement with the proposed model. The fast response (jumps in Figs. 3, 4) is caused by the initial thermal flow, which is accounted for by the initial condition in the model described in Reference [15]. In the approximation used in [15], this response is instant.

In practice, this time is determined by time that it takes to dip the sample into the thermal bath. The change of the sign of the effect and the minimum on the voltage versus time curve in Fig. 3 is a consequence of the two characteristic relaxation times, τ_T, and τ_s associated with the

slow response. The first relaxation time, τ_T, reflects the rate of the sample cooling due to free convection, and the second relaxation time, τ_s, reflects the pyroelectric charge relaxation. The time dependence of the pyroelectric voltage would have been different if free convection were not a dominant heat transfer mechanism (see [16]).

Figure 5 compares the experimental and calculated dependencies of the peak voltages on the sample temperature change, ΔT_o. The experimental points were measured using cold thermal shock experiments. As can be seen from the figure, the experimental data agree well with the theory [15]. These experiments showed that a GaN sample could be used as a heat flow counter. In order to check this idea further, we subjected the sample first to fast cooling and then to fast heating, within -4 °C to 43 °C temperature range. The absolute value of the temperature difference between the bath and the sample was about the same in each experiment. The sign of the voltage was determined by the direction of the thermal flow (in or out of the sample), and was proportional to the thermal flow (see Fig. 1). [15]

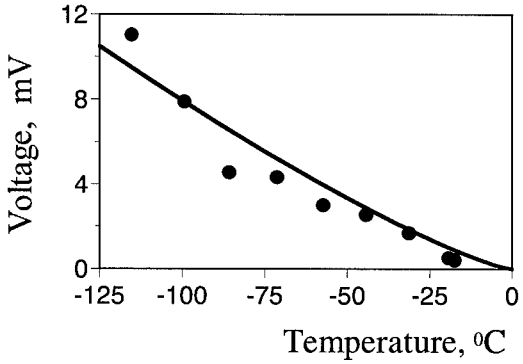


Fig. 5. Peak voltage as a function of difference between the final and initial sample temperatures. Circles are measured data, solid line is calculated (after [15]).

To characterize the ability of the GaN film to convert the thermal flow into the electricity, we introduced parameter $P_f = dF/dQ$, where F is the electric field, and Q is the heat flow. The model described in Reference [15] yields

$$P_f \approx \frac{V(t_o)}{Q(t_o)r_d} = \frac{\tau_T P_v}{\rho c_p} \qquad (3)$$

and

$$P_f = 0.0023 \ \frac{Vm^2}{W} \qquad (4)$$

Here ρ is the density and c_p is the heat capacity. If the GaN temperature increases by 1 °C in 1 s, then the generated electric field is $\rho c_p P_f \approx 60$ V/cm. Unlike the pyroelectric voltage coefficient, this parameter does not depend on heat flow.

As mentioned above, the studied GaN samples had contacts in the plane close to the basal plane. In this case, the collected pyroelectric charge (and the corresponding voltage drop) was proportional to a slight (3^o-4^o) misorientation between the growth direction and the c-axis. Nevertheless, the measured pyroelectric voltage coefficient of *n*-type GaN was on the order of 10^4 V/m-K. As mentioned above, this value is comparable to the values typical for pyroelectric ceramics. [13] III-Nitride samples having the contacts along the c-axis should allow one to collect more charge and to increase the sensitivity in 20 to 30 times. In addition, GaN exhibit strong pyroelectric effect at temperature above 300 °C, whereas such materials as $LiTaO_3$ and $PbTiO_3$

have the Curie temperature well below 300 °C and, thus, can not be used for high temperature applications.

Piezoelectric properties of III-Nitrides

Piezoelectric constants of GaN are 4-5 times larger than GaAs piezoelectric constants when they are compared using the wurtzite - zinc blende transformation procedure, see Table 1.[17]

Table 1. Piezoelectric constants. (After [12].)
InN constants estimated from ab initio calculations [20] and using optic phonon frequencies of InN.

e_{lm} (C/m^2)	e_{33}	e_{31}	e_{15}	e_{14}
GaN (electromechanical coefficients)	1	-0.36	-0.3	
GaN (mobility)	0.44	-0.22	-0.22	0.375
GaN (from optical phonons)	0.65	-0.33	-0.33	0.56
GaN (ab initio)	0.73	-0.49		
InN (from optical phonons)	0.43	-0.22	-0.22	0.37
InN (ab initio)	0.97	-0.57		
AlN (surface acoustic waves)	1.55	-0.58	-0.48	
AlN (ab initio)	1.46	-0.60		
SiC	0.2		0.08	
ZnO	1.32	-0.57	-0.48	
GaAs	-0.185	0.093	0.093	-0.16

This comparison is justified, since GaN has both wurtzite and zinc blende crystal structures. The value of e_{14} for GaN was extracted from the experimental data on the low field electron mobility using the analysis of the piezoelectric scattering mechanism in the two-dimensional electron gas (2DEG) in AlGaN/GaN heterostructures.[18] The analysis of the optical phonon frequencies of GaN also yields an estimate of e_{14} of GaN.[19] A similar estimate of e_{14} for InN implies that the piezoelectric effects in InN are stronger than in GaAs. The wurtzite GaN piezoelectric constants were also estimated from the GaN electromechanical coupling coefficients.[17] Finally, the piezoelectric constants of AlN, GaN and InN were predicted using ab initio calculations.[20] These calculations predict that piezoelectric constants in GaN-based materials are up to ten times larger than in other III-V semiconductors. Currently, it is difficult to determine which set of GaN piezoelectric constants is the most reliable. However, it is clear that these constants are comparable to those for AlN and ZnO and are much larger than for typical A_3B_5 materials, such as GaAs or InP.

Strongly pronounced piezoelectric properties play a key role in strained GaN-AlGaN and InGaN-GaN multilayer structures. The lattice-mismatch-induced strain generates polarization fields. In a GaN-AlN-GaN semiconductor-insulator-semiconductor (SIS) structure with the growth axis along a (0001) crystallographic direction, the strain-induced electric fields can shift the flat band voltage by 1.5 V and produce an accumulation region on one side and the depletion region on the other side of the AlN insulator. [21] As a consequence of the asymmetry in the space charge distribution, the capacitance-voltage (*C-V*) characteristics and the current-voltage (*I-V*) characteristics of the symmetrically doped SIS structures become asymmetrical. The degree of

the asymmetry depends on strain. This allowed us to develop *C-V* and *I-V* characterization techniques for SIS structures and FETs, extract critical thicknesses and demonstrate the gradual elastic strain relaxation process with an increase in strained layer thickness.[22,,24]

Piezoelectric properties affect the concentration and transport characteristics of 2D electrons confined in the triangular potential well at AlGaN/GaN heterointerface and might lead to accumulation or depletion regions at the heterointerfaces, depending on the polarity of the top surface.[25] An increase in the 2D-electron sheet carrier density caused by the piezoelectric effects is sometimes referred to as piezoelectric doping. These effects also cause a strain-induced energy band shift at the heterointerface. The surface charge density induced by the piezoelectric effect in AlGaN-GaN Heterostructure Field-Effect Transistors (HFETs) can be on the order of 10^{12} - 10^{13} cm^{-2}. [8, 26, 27] These results are very important for developing of a new class high power, high temperature electron devices, such as microwave power amplifiers and power switches.

Piezoelectric properties strongly affect the performance of light emitting devices based on III-N quantum well structures. They can dramatically change the selection rules for the interband transitions in III-Nitride quantum wells and multiple quantum wells (MQWs). Strain-induced electric field causes the spatial separation of electron and hole inside the quantum well.[28] As a result, the optical matrix element for the lowest conduction-band - first heavy hole transition can be dramatically reduced, and the transitions forbidden in strain-free structures can take place. Also, the strain-induced electric field causes a significant reduction of the apparent energy band gap.[29] This results in a red shift in optical spectra.[30] The red shift is more pronounced in wider quantum wells and for lower electron-hole concentrations. These effects were predicted [28,31] and confirmed by luminescence emission measurements.[30] Photoluminescence measurements in InGaN/GaN quantum wells under applied external electric field clearly demonstrated the important role of the built-in field in carrier recombination process.[32] A strain-induced modulation of optical transitions in quantum structures can be utilized for development of high-speed UV light modulators and fast switching light emitting devices.

In conventional GaAs-based Heterostructure Field Effect Transistors, the 2D-electron gas is induced by doping the wide band gap barrier layer or even the device channel. In AlGaN/GaN based heterostructures, strong piezoelectric effects allow one to induce the 2D-gas without doping. This technique of "piezoelectric doping" avoids the introduction of defects associated with conventional dopants. Electron sheet concentrations as high as $3x10^{13}$ cm^{-2} or more can be induced by the piezoelectric effect. [8, 26, 27]

The elastic strain relaxation and the piezoelectric doping in $Al_xGa_{1-x}N$-GaN HFETs were studied in References [24, 12]. We calculated the $Al_xGa_{1-x}N$/GaN band structure by solving Poisson's equation with the boundary conditions for the $Al_xGa_{1-x}N$ /GaN interface, which account for the piezoelectric effect:

$$\varepsilon_1 F_1 + P_1 + P_{s1} = \varepsilon_2 F_2 + P_{s2}, \qquad (5)$$

where ε_1 and ε_2 are the dielectric constants, and F_1, F_2 are the interface values of the electric field in $Al_xGa_{1-x}N$ and GaN, respectively, and P_1 is the piezoelectric polarization. The spontaneous polarizations of $Al_xGa_{1-x}N$ and GaN at zero strain, P_{s1}, P_{s2} are accounted for in Eq. (5). For the (0001) growth direction, P_1 is given by:

$$P_1 = \pm 2(e_{31} - e_{33}c_{31} / c_{33})u_{xx} \qquad (6)$$

The sign in Eq. (6) depends on the polarity of the structure (see a detailed discussion of this issue in [33]). Piezoelectric constants, e_{31}, e_{33} of $Al_xGa_{1-x}N$, were estimated using the linear interpolation between corresponding GaN and AlN piezoelectric constants. The strain in a heterostructure decreases once the layer thickness exceeds the critical thickness. The expression for the

deformation energy accounted for the dislocation stress components satisfying the free surface boundary condition and for the dislocation core energy and misfit strain. [24] A similar approach was developed for superlattices and semiconductor-insulator-semiconductor structures.[18]

In Ref. 24, the sheet electron density was calculated assuming that the spontaneous polarization at zero strain is negligible. In Ref. 12, the calculation of n_s was repeated using the spontaneous polarization values estimated in Ref. 20. Figures 6 a, b show the calculated strain and the sheet electron density, n_s, generated by the piezoelectric doping in $Al_xGa_{1-x}N$/GaN HFETs as a function of the Al molar fraction.[12] The calculation of n_s (solid lines in Fig. 6 b) accounted for the strain relaxation in HFETs with the AlGaN barrier thicknesses from 5 nm to 30 nm (Fig. 6 a). Dashed lines in Fig. 6 b correspond to fully strained structures. Also, n_s was calculated for the $Al_xGa_{1-x}N$ thickness, L, equal to the critical thickness, L_c , for a given Al concentration (see thick solid line in Fig. 6 b).

The results show that thinner $Al_xGa_{1-x}N$ layers with larger Al content should yield a higher piezoelectric doping. For example, the maximum piezoelectric doping for an unrelaxed heterostructure with $L = L_c = 5$ nm is $n_s \sim 3 \times 10^{13}$ cm^{-2}, which corresponds to $x \sim 0.6$. This is three times larger than the sheet electron density for $L = L_c = 20$ nm and $x = 0.2$.

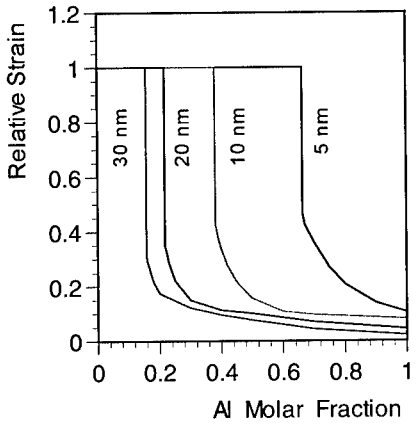


Fig. 6 a. Calculated strain as a function of Al molar fraction for various $Al_xGa_{1-x}N$ layer thicknesses equal to 5 nm, 10 nm, 20 nm and 30 nm.

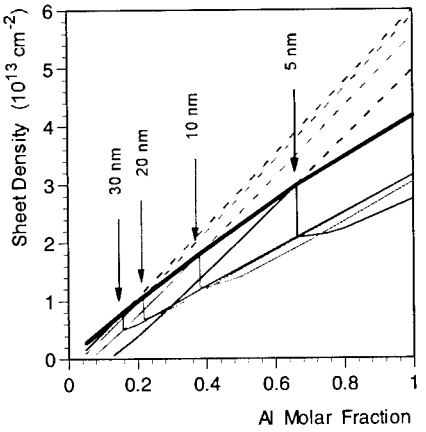


Fig. 6 b. The n_s induced by polarization in $Al_xGa_{1-x}N$-GaN heterostructures for various barrier thicknesses. Arrows show the onset of strain relaxation. Thick solid line shows n_s corresponding to critical thicknesses of AlGaN. [12]

We also measured the C-V characteristics of $Al_{0.25}Ga_{0.75}N$/GaN heterostructures with thicknesses of $Al_{0.25}Ga_{0.75}N$ ranging from 10 nm to 100 nm using standard mercury probe technique. We calculated the C-V characteristics accounting for strain by using Eq. (6) with strain u_{xx} adjusted to fit the experimental data (see Fig. 7). A similar approach was used in order to determine the elastic strain relaxation in GaN-AlN-GaN SIS structures. [22, 23] Figure 6 clearly shows that an increase in Al mole fraction in the AlGaN barrier leads to a higher built-in strain and piezoelectric doping of strained AlGaN/GaN heterostructures. A high value of n_s that can be achieved using the piezoelectric doping points to a high potential of piezoelectric doping as a possible substitute (or an important addition) to conventional impurity doping. The critical thickness of the $Al_xGa_{1-x}N$ barrier decreases with an increase in the Al molar fraction. This, in turn, reduces the depletion charge in the fully strained AlGaN barrier layer. Also, for $x > 0.4$,

$Al_xGa_{1-x}N$ usually becomes insulating. Therefore, in high-quality fully strained AlGaN/GaN heterostructures with high aluminum content, the dominant contributions to the electron gas sheet density should come from the piezoelectric doping as well as from the GaN channel doping. [11,34]

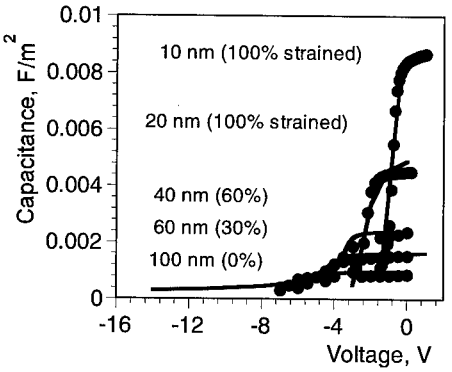


Fig. 7. Measured and calculated (solid lines) capacitance-voltage characteristics of $Al_{0.25}Ga_{0.75}$ N/GaN structures for different $Al_{0.25}Ga_{0.25}$ N layer thicknesses. Curve 1 is for 10 nm, curve 2 is for 20 nm, curve 3 is for 40 nm, curve 4 is for 60 nm, and 5 is for 100 nm. The structures 1, 2 are fully strained, 3, 4 and 5 correspond to elastic strain relaxation of 40%, 70% and 100%. Donor concentrations are N_d = $5x10^{17}$ cm^{-3} and 10^{17} cm^{-3} in $Al_{0.25}Ga_{0.75}N$ and GaN layers, respectively. (After [24])

The results obtained by other groups confirm the importance of the piezoelectric doping. Maeda et al. [35] calculated the maximum two-dimensional electron gas density in $Al_xGa_{1-x}N$/GaN HFETs by self-consistently solving Schrodinger's and Poisson's equations and accounting for the piezoelectric effect. The maximum 2D-electron gas density was defined as a critical density at which electrons start to spill over into the $Al_xGa_{1-x}N$ barrier. The calculated 2D-electron density was in the $2x10^{12}$ cm^{-2}-$1.2x10^{13}$ cm^{-2} range, depending on the Al molar fraction in the barrier layer, which varied in the range $0.15<x<0.3$, and on the degree of strain relaxation. These calculations assumed that strain relaxation could occur even in HFET with the Al content as low as $x = 0.15$ and $Al_xGa_{1-x}N$ thickness 15 nm.

Spontaneous Polarization

First-principle calculations [20] predict that spontaneous polarization in wurtzite III-Nitrides should be quite large. A large spontaneous polarization can cause a large internal electric field and strongly affect the band structure. However, the role of the spontaneous polarization depends on the mechanism of the screening of the internal electric field in the bulk of the pyroelectric material and/or at the heterointerfaces. In equilibrium, i.e. without strain or a heat flow, pyroelectric charges are usually compensated by either ambient charges or internal charges forming an equal and opposite dipole moment. An average (macroscopic) internal electric field in heterostructures and superlattices is usually compensated.[36]

In principle, an internal electric field caused by the pyroelectric charge might generate free electrons and holes even in an insulator due to band bending. However, inversion domains with polarization pointing in opposite directions might cancel the macroscopic electric field and reduce an overall energy of the structure (for the experimental evidence of inversion domains in GaN, see [37]). The analysis of the piezoresistive measurements in GaN-AlN-GaN SIS structures also provided evidence for the existence of the inversion domains in III-Nitrides.[38]

Another important screening mechanism is linked to the existence of a large number of surface and interface states in pyroelectrics. If the surface state density equals to P_s/q, the charges trapped in surface and/or interface states can cancel the spontaneous polarization, making an internal electric field vanish inside the film. Indeed, internal electric fields in pyroelectric materials are usually much smaller than predicted by the theory, which does not account for surface and interface states. [39], [40] Attempts to find even a trace of an internal electric field at the surfaces of a number of ferroelectrics did not yield any definite results.[39] The maximum value of a spontaneous polarization charge, ~10^{14} cm^{-2}, observed for all known ferroelectrics is equal to a maximum value of a density of slow and fast surface states in these materials.[39] The effect of the current-voltage characteristic collapse in some AlGaN-GaN heterostructures indicates the existence of a large number of interface states [41] [42], at least in some samples

The measurements of the current-voltage characteristics of GaN-AlN-GaN SIS structures seem to show that the effect of the spontaneous polarization is smaller than that of the polarization induced by the piezoelectric effect. [23] Hence, further theoretical and experimental studies are needed in order to elucidate a possible role played by spontaneous polarization in GaN-based structures.

Conclusions

GaN-based materials exhibit strong piezoelectric and pyroelectric effects. Both primary and secondary pyroelectric effects have been observed in GaN based structures. These effects are a combination of a fast response to an initial thermal flow and a slower response to heat dissipation or accumulation. The extracted pyroelectric voltage coefficients of GaN are comparable to those of the pyroelectric ceramics such as PZT or $BaTiO_3$. Also, GaN-based pyroelectric sensors should be capable of operating at very high temperatures, and, hence, have an advantage compared to more traditional pyroelectric sensors.

Piezoelectric effects in GaN and related materials can be used both for piezoelectric sensors and for "energy gap engineering" and "barrier engineering" in GaN-based transistors and other electronic and optoelectronic devices.

The demonstrated piezoresistive effect in GaN/AlN multilayer structures is 2 to 4 times larger than in SiC. [38] Hence, GaN-based structures can be used in pressure transducers and other electromechanical sensing elements.

However, all these applications are still emerging, and further theoretical and experimental studies are needed. A definite set of piezoelectric constants for GaN-based materials has to be established. The transient response of piezoelectric charge should be investigated in more detail. The role of spontaneous polarization, the role of surface and interface states, and of the inversion domains must be ascertained. The piezoelectric doping should be optimized. Further detailed theoretical and experimental studies of strain and dislocations in GaN-based structures are needed in order to better understand the observed stress-related effects and use these effects for the design of novel piezoelectronic and pyroelectronic devices.

New piezoelectronic and pyroelectronic device concepts will certainly emerge to take a full advantage of the unique properties of GaN-based materials. All in all, the recent research of wide band gap semiconductors with wurtzite crystal structure has opened a new dimension in semiconductor physics and device research. And the work has just begun.

Acknowledgment

The Office of Naval Research has supported this work (Project Monitors Dr. Colin Wood and Dr. John Zolper).

References

1 S. Nakamura, M. Senoh, S. Nagahama, N. Iwasa, T. Yamada, T. Matsushita, H. Kiyoku, Y. Sugimoto, Jpn. J. Appl. Phys., Part 2 (Letters), 35, 1B, L74-76 (1996). .

2 S. Nakamura, T. Mukai, and M. Senoh, J. Appl. Phys, 76 (12), 8189 (1994).

3 M. Razeghi, and A. Rogalski, J. Appl. Phys., 79(10), 7433 (1996).

4 M. S. Shur, and M. A. Khan, (1997 a). MRS Bulletin. 22, No. 2, 44-50.

5 J. Burm, K. Chu, W. J. Schaff, L. F. Eastman, M. A. Khan, Q. Chen, J. W. Yang, and M. S. Shur, IEEE Electron Device Letters 18, No. 4, 141 (1997).

6 B. J. Thibeault, B. P. Keller, Y. F. Wu, P. Fini, U. K. Mishra, C. Nguyen, N. Nguyen, and M. Le, *High Performance and Large Area Flip-Chip Bonded AlGaN/GaN MODFET.* (IEDM-97 Technical Digest, IEEE, San Francisco, 1997).

7 S. C. Binari, J. M. Redwing, G. Kelner, and W. Kruppa, Electronics Letters 33 (3), 242 (1997).

8 R. Gaska, J. Yang, A. Osinsky, A. D. Bykhovski, and M. S. Shur, Appl. Phys. Lett. **71** (25), 3673 (1997).

9 R. Gaska, Q. Chen, J. Yang, A. Osinsky, M. A. Khan, and M. S. Shur, IEEE Electron Device Letters. 18, No. 10, 492 (1997).

10 R. Gaska, J. Yang, A. Osinsky, M. A. Khan, and M. S. Shur, *Novel High Power AlGaN/GaN HFETs on SiC substrates,* (IEDM-97 Technical Digest, 1997), pp. 565-568.

11 M. S. Shur, and M. A. Khan, Physica Scripta, T69, 103 (1997).

12 M. S. Shur, A. D. Bykhovski, R. Gaska, and M. A. Khan, *GaN-based Pyroelectronics and Piezoelectronics*, in Semiconductor Homo- and Hetero-Device Structures, M. Francombe and C. E. C. Wood, Editors, Academic press, to be published.

13 J. Fraden, *Handbook of Modern Sensors*, (Springer, New York, 1996), p. 536.

14 M. A. Khan, J. N. Kuznia, J. M. Van Hove, Olson, D. T., Krishnankutty, S., and Kolbas, R. M. Appl. Phys. Lett. 58 (5), 526 (1991).

15 A. D. Bykhovski, V. V. Kaminski, M. S. Shur, Q. C. Chen, and M. A. Khan, Appl. Phys. Lett. **69**, 3254 (1996).

16 Y. Bayazitolu, and M. N. Ozisik, *"Elements of Heat Transfer"*, (McGraw-Hill Book Company, New York, 1988), pp. 18-22.

17 A. D. Bykhovski, B. L. Gelmont, and M. S. Shur, J. Appl. Phys. **81** (9), 6332 (1997).

18 M. S. Shur, B. Gelmont, and A. Khan, J. Electronic Materials 25, 777 (1996).

19 M. A. Littlejohn, J. R. Hauser, and T. H. Glisson, Appl. Phys. Lett. 26 (11), 625 (1975).

20 F. Bernardini, V. Fiorentini, and D. Vanderbilt, Phys. Rev. B 56(16), 10024 (1997).

21 A. Bykhovski, B. Gelmont, and M. S. Shur, J. Appl. Phys. 74(11), 6734 (1993).

22 A. Bykhovski, B. Gelmont, M. S. Shur, and A. Khan, Institute of Physics Conference Series Number 137, 691 (1994).

23 A. Bykhovski, B. Gelmont, M. S. Shur, and A. Khan, J. Appl. Phys. 77(4), 1616 (1995).

24 A. D. Bykhovski, R. Gaska, and M. S. Shur, Appl. Phys. Lett. 73 (24), 3577 (1998).

25 R. Gaska, J. Yang, A. D. Bykhovski, M. S. Shur, V. V. Kaminski, S. M. Soloviev, Applied Physics Letters 72 (1), 64-66 (1998).

26 P. M. Asbeck, E. T. Yu, S. S. Lau, G. J. Sullivan, J. Van Hove, and J. M. Redwing, Electron. Lett. 33, 1230 (1997).

27 E. T. Yu, G. J. Sullivan, P. M. Asbeck, C. D. Wang, D. Qiao, and S. S. Lau, Appl. Phys. Lett. **71** (19), 2794 (1997).

28 J. Wang, J. B. Jeon, Yu. M. Sirenko, and K. W. Kim, Photonics Technol. Lett. 9 (6), 728 (1997).

29 G. Martin, A. Botchkarev, A. Rockett, H. Morkoç, Appl. Phys. Lett. 68(18), 2541 (1996).

[30] A. Hangleiter, Jin Seo Im, H. Kollmer, S. Heppel, J. Off, F. Scholz, MRS Internet J. Nitride Semicond. Res. 3, 15 (1998).
[31] C. J. Sun, M. Z. Anwar, Q. Chen, J. W. Yang, M. A. Khan, M. S. Shur, A. D. Bykhovski, S. L. Weber, M. Smith, J. Y. Lin, and H. X. Xiang, Appl. Phys. Lett. 70, 2978 (1997).
[32] T. Takeuchi, C. Wetzel, S. Yamaguchi, H. Sakai, H. Amano, I. Akasaki, Y. Kaneko, S. Nakagawa, Y. Yamaoka, and N. N. Yamada, Appl. Phys. Lett. 73 (12), 1691 (1998).
[33] E. S. Hellman, MRS Internet J. Nitride Semicond. Res. 3, 11 (1998).
[34] M. S. Shur, and M. A. Khan, MRS Bulletin. 22, No. 2, 44-50 (1997).
[35] Maeda, N., Nishida, T., Kobayashi, N., and Tomizawa, M. (1998). Appl. Phys. Lett. 7 3(13), 1856-1858.
[36] E. L. Ivchenko, P. E. Pikus, *Superlattices and other heterostructures: symmetry and optical phenomena* (Springer Verlag, Berlin, New York 1995).
[37] L. T. Romano, J. E. Northrup, and M. A. O'Keefe, Applied Physics Letters. 69(16), 2394-2396 (1996).
[38] R. Gaska, J. Yang, A. D. Bykhovski, M. S. Shur, V. V. Kaminski, S. M. Soloviev, Appl. Phys. Lett. 71(26), 3817 (1997).
[39] V. M. Fridkin, *Ferroelectrics-Semiconductors* (Nauka, Moscow, 1976), p. 90.
[40] B. V. Selyuk, Ferroelectrics. 6, 37 –40 (1973).
[41] M. A. Khan, M. S. Shur, Q. C. Chen, and J. N. Kuznia, Electronics Letters 30, No. 25, 2175-2176 (1994).
[42] M. A. Khan, M. S. Shur, Q. C. Chen, J. N. Kuznia, and C. J. Sun, Electronics Letters 31, 398-400 (1995).

Part II

Laser Diodes and Spectroscopy

CHARACTERIZATION OF InGaN/GaN-BASED MULTI-QUANTUM WELL DISTRIBUTED FEEDBACK LASERS

Daniel Hofstetter*, Robert L. Thornton**, Linda T. Romano***, David P. Bour***, Michael Kneissl***, Rose M. Donaldson***, and Clarence Dunnrowicz***

*University of Neuchâtel, Institute of Physics, Rue A.-L. Breguet 1, 2000 Neuchâtel, Switzerland
Daniel.Hofstetter@iph.unine.ch
**MAXTEK Components Corporation, 13335 SW Terman Road, Beaverton, OR 97075-0428
***XEROX Palo Alto Research Center, 3333 Coyote Hill Road, Palo Alto, CA 94304

Cite this article as: MRS Internet J. Nitride Semicond. Res. 4S1, G2.2 (1999)

ABSTRACT

We present a device fabrication technology and measurement results of both optically pumped and electrically injected InGaN/GaN-based distributed feedback (DFB) lasers operated at room temperature. For the optically pumped DFB laser, we demonstrate a complex coupling scheme for the first time, whereas the electrically injected device is based on normal index coupling. Threshold currents as low as 1.1 A were observed in 500 μm long and 10 μm wide devices. The 3rd order grating providing feedback was defined holographically and dry-etched into the upper waveguiding layer by chemically-assisted ion beam etching. Even when operating these lasers considerably above threshold, a spectrally narrow emission (3.5 Å) at wavelengths around 400 nm was seen.

INTRODUCTION

Because of their reduced spot size, violet/blue semiconductor lasers are highly advantageous light sources in data scanning and optical storage applications. With the deployment of light emitters fabricated in the InGaN/GaN materials system, the development of an electrically pumped laser emitting light around 400 nm has experienced tremendous progress during the past couple of years. Under the lead of Nakamura et al., both pulsed and continuous wave operation of InGaN/GaN based devices have been demonstrated at room temperature [1], [2]. One of the main concerns in nitride lasers is the fabrication of high quality mirrors. Dry-etched mirrors with high reflective coatings seem to work pretty well in this material system [3]; however, these etched mirrors are typically not at the edge of the substrate, which complicates the access of the laser beam for most applications. In addition, usually a certain fraction of the optical mode gets diffracted into or reflected from the sapphire surface, leading to an asymmetric far-field with multiple emission lobes in the vertical direction [1], [4]. The use of distributed feedback for providing optical cavity formation could partly eliminate some of the mirror issues because no optical quality mirrors are required to achieve lasing action. Moreover, the longitudinal mode structure, which, due to the very close mode spacing in these devices, is very competitive and noisy, can be markedly improved by using the DFB mechanism for mode selection. A straight-forward way to explore this idea is the fabrication of optically pumped DFB lasers [5], [6].

In this article, we present the fabrication of an electrically injected InGaN/GaN-based DFB laser with a holographically defined, index-coupled 3rd order grating. Furthermore, we show some preliminary results on the fabrication of an optically pumped complex-coupled DFB laser. When compared to normal Fabry-Perot devices fabricated from the same material, we observe a

Mat. Res. Soc. Symp. Proc. Vol. 537 © 1999 Materials Research Society

comparable threshold gain, single mode behavior with a higher side mode suppression ratio, and a modehop-free tuning over a temperature range of more than 30 K.

FABRICATION

The fabrication of these devices relied on growing a 4 μm thick n-type GaN:Si layer on C-face sapphire. On top of this layer, we grew a 500 nm thick, n-doped $Al_{0.08}Ga_{0.92}N$:Si lower cladding layer, a 100 nm thick n-doped GaN:Si lower waveguiding layer, a 30 nm thick un-doped active region with five 3 nm thick $In_{0.15}Ga_{0.85}N$ quantum wells and 7 nm thick GaN barriers, and a 180 nm thick p-doped GaN:Mg upper waveguiding layer. For the electrically injected, index-coupled device, the 3rd order grating with a period of 240 nm was defined by a holographic exposure and dry-etched into the upper waveguiding layer by chemically-assisted ion beam etching. A numerical calculation of the coupling coefficient showed that the tooth shape of this 100 nm deep grating was a critical parameter. For our rectangular tooth geometry with rounded tops, the coupling coefficient was relatively weak, on the order of 5 - 10 cm^{-1}. Together with a cavity length of 1000 μm, this coupling strength corresponds to an effective reflectance of 15 - 30 %. After grating fabrication, we performed optical pumping experiments in order to confirm the matching between the grating resonance wavelength and the gain peak. Then, we proceeded with an epitaxial re-growth to complete the device structure. This re-growth consisted of a 300 nm thick p-doped $Al_{0.08}Ga_{0.92}N$:Mg upper cladding layer and a 100 nm thick p-type GaN:Mg contact layer.

Device processing for the electrically pumped devices involved the definition mesas to enable lateral n-type contacting of the devices, and evaporation of standard n- and p-metal Ti/Au layers. The p-metal contact stripes were 4, 10 or 20 μm wide, and thus defined the width of the gain region. A SiON layer was used to electrically isolate the non-contacted areas and the sidewalls of the mesas, thereby restricting gain to within a narrow stripe in the lateral direction. Following the SiON window etch, we evaporated another Ti/Au layer in order to provide the p-metal contact pads for the probe. Finally, the mirrors were etched, again by chemically-assisted ion beam etching. In order to ensure that these lasers would not accidentally oscillate as Fabry-Perot lasers, we dry-etched only one of the facets exactly vertical while leaving the other one at an angle of approximately 20 ° to the vertical.

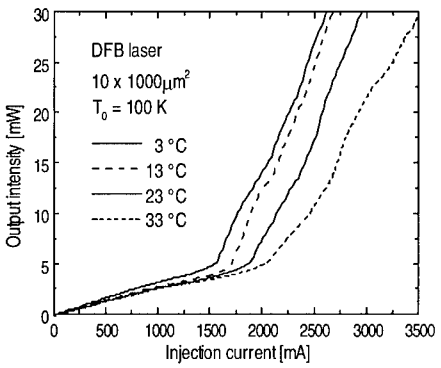


Fig. 1 - L-I-characteristics of an InGaN / GaN DFB laser with an active area of 10 x 1000 μm² at four different heatsink temperatures.

The fabrication of optically pumped complex-coupled DFB lasers relied on interrupting growth after the QW active region, and etching the grating with a depth of 45 nm through the QWs. Re-growth of 100 nm GaN and a 50 nm thick $Al_{0.08}Ga_{0.92}N$:Mg layer took place to complete the optical waveguide and a small fraction of the upper cladding layer. Because of the

resulting gain and refractive index variation, this coupling scheme should be much stronger than index coupling alone. Optically pumped lasers could then be fabricated by simply cleaving 6 mm wide and 10 mm long pieces.

ELECTRICALLY INJECTED DFB LASER

Measurements of the I-V- and L-I-characteristics were carried out under pulsed current conditions (500 ns pulse length, 0.05 % duty cycle) at room temperature. The lasers were probe contacted and tested on chip. At 1 mA forward current, the I-V-curve typically exhibited a "turn-on voltage" of 3.3 V, and for a 10 x 1000 μm^2 contact region, we observed a series resistance of 10 Ω. As shown in the L-I-curves of figure 1, we obtained, for the longest devices with 10 microns stripe width, pulsed threshold currents of 1550 mA at 3 °C and 2050 mA at 33 °C. From these measurements, we determined the T_0 value to be approximately 100 K.

The best threshold currents were obtained on lasers with 20 microns stripe width and 1000 µm cavity length. Values of 3200 mA for 20 microns wide devices were observed, corresponding to threshold current densities of 16 kA/cm^2. For shorter devices with 20 microns stripe width, we measured higher threshold currents of 4600 mA (threshold current density of 23 kA/cm^2). For the best devices, typical threshold voltages of $V(I_{th})$ = 16 V were seen.

High-resolution spectra of these lasers were measured using a grating spectrometer with a resolution of 0.5 Å (SPEX, d_{focal} = 1.26 m, w_{slit} = 50 µm). The laser output was focussed onto a quartz fiber using a microscope objective, and fed into the input slit of the spectrometer. By placing a 1024 element array photodetector into the output image plane, we were able to measure the spectrum in a spectral window of 10 nm width within 1 second.

In figure 2, we show high-resolution emission spectra at various current levels ranging from 1.01 x I_{th} and to 1.28 x I_{th}. While there is only one clean peak with a resolution limited width of 0.5 Å for lower injection currents, there appear to be multiple peaks with an overall width of 5 Å at higher injection levels. The fact that all additional features occurred at the long wavelength side of the main peak suggests that chirping due to device heating during the current pulse is responsible for this kind of broadening. From the spectral broadening at higher injection currents and the temperature tuning coefficient derived in the following paragraph, we were able to estimate the temperature increase during the pulse to be on the order of 20 - 30 K. Another possible reason for the spectral broadening at higher current levels is the onset of lasing in higher order lateral modes in these gain-guided structures. This explanation is supported by the fact that the L-I-curves show several kinks.

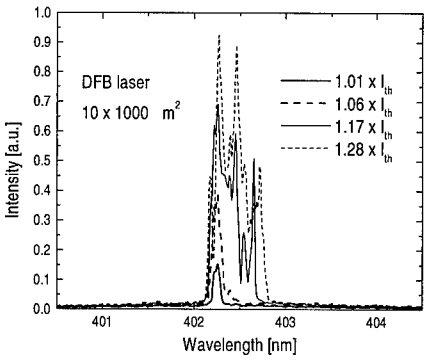


Fig. 2 - Emission spectra of an InGaN/GaN DFB laser at four different injection current levels ranging from 1.01 x I_{th} to 1.28 x I_{th}. All curves are drawn using the same vertical scale.

Emission spectra of a 1000 μm long DFB laser at four different heat-sink temperatures are shown in figure 3; they reveal laser oscillation in a single longitudinal mode with a sidemode suppression ratio of 15 dB and at a center wavelength of around 402 nm. Given the grating period of 240 nm and the above emission wavelength, we were able to calculate the effective refractive index of the propagating mode to be $n_{eff} = 2.52$. In order to maintain narrow emission spectra for this measurement, we adjusted the injection current to always be at 1.1 x I_{th}. The device remained in a single mode for temperatures ranging from 2 °C to 35 °C, which is a temperature range of more than 30 K; the temperature tuning coefficient was on the order of 0.014 nm/K. For Fabry-Perot type lasers fabricated on the same wafer, we measured a much larger average temperature tuning coefficient of 0.065 nm/K.

OPTICALLY PUMPED COMPLEX COUPLED DFB LASER

Cross-sectional transmission electron microscope (TEM) studies of both types of overgrowth reported in this article showed that no additional dislocations were created at the grating interface. This observation is in sharp contrast to InGaAsP/InP-based infrared DFB lasers, where the grooved interface serves as starting point for numerous dislocations [7]. However, we found also that only 3 out of 5 QWs were etched during the grating etch process; this conclusion confirmed that our device was a complex-coupled rather than a purely gain-coupled DFB laser. The reason for the insufficient etch-depth was mainly the lack of process control when trying to punch through all QWs without over-etching. From a calculation of the coupling strength for this complex-coupled sample, we estimated similar amounts of index- and gain-coupling (κ = 5 – 10 cm^{-1} each).

Optical pumping was carried out as described earlier using a pulsed 337 nm N_2 laser (r_{pulse} = 10 Hz, P_{peak} = 250 kW) whose stripe-shaped beam was attenuated by an appropriate number of glass slides. The output of the InGaN/GaN laser was fed into either a high resolution spectrometer (for linewidth measurements) or a low resolution grating spectrometer (for output intensity vs. current-curves). The pieces on which we performed these experiments were approximately 6 x 10 mm^2 in size, and all four facets were fabricated by scribing from the back and subsequent cleaving. Although this method resulted in a poor Fabry-Perot (FP) cavity and, in addition, the N_2 laser beam was pumping 30 – 40 % of the cavity length only, FP type laser emission could be observed as well as DFB laser emission. The orientation of the grating lines relative to the pump beam determined which emission would become the dominant one.

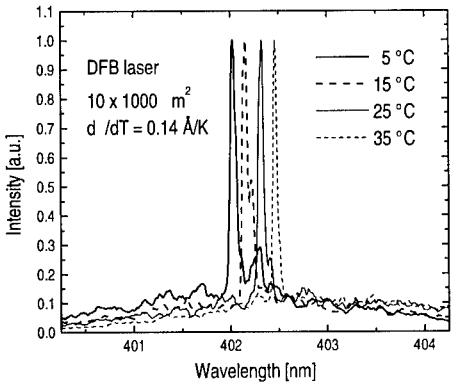


Fig. 3 - Emission spectra of the same device as in figure 2 at 1.1 x I_{th} and at different heat-sink temperatures. The temperature tuning coefficient obtained was 0.14 Å/K.

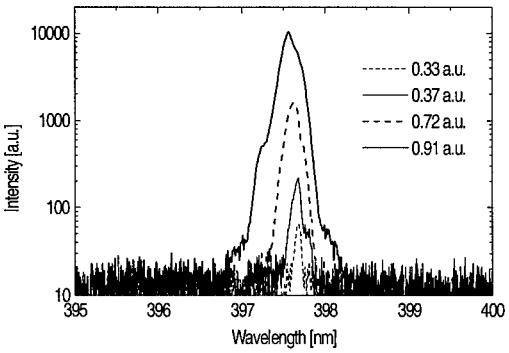


Fig. 4 - Emission spectra of an optically pumped complex-coupled DFB laser at different pump levels

Typical emission spectra of DFB type lasing are shown in figure 4. The emission peak stays at 397.5 nm from threshold all the way up to 0.9 a.u. pump intensity. It shifts somewhat towards shorter wavelengths at higher pump intensities. The reason for this wavelength shift is a slight reduction of the effective refractive index at high carrier density, which, at some point, overwhelms the index increase due to the relatively weak heating effects. The linewidth change from 1.5 Å right above threshold to 3.5 Å at 0.91 a.u. is likely due to lateral multimode operation and some chirping at high pump intensities. A similar series of low resolution emission spectra for the FP emission showed a peak wavelength of 395 nm with a typical linewidth of around 25 Å. In contrast to the DFB laser spectra, we see for the FP laser a pronounced red shift of the lasing peak when pumping at a higher intensity. While the DFB lasing wavelength is locked to the Bragg resonance wavelength, the emission of the FP follows the gain maximum, which, again due to device heating, shifts more rapidly towards longer wavelengths.

The far field of the DFB lasers reported in this article exhibited the usual interference effects due to the reflection from and the diffraction into the sapphire substrate. However, in the lateral direction, we observed a far field angle of approximately 10 ° above threshold, and a broad Lambertian characteristics below threshold. On Fabry-Perot lasers from similar material, we polished one mirror facet in order to get a far field measurement without the diffraction and refraction artifacts. Due to the insufficiently thick AlGaN lower cladding layer, the result of this measurement was very similar to what we reported earlier on optically pumped lasers [4]. It revealed two main emission lobes in the vertical direction and a number of weaker oscillations in between.

CONCLUSIONS

In conclusion, we have demonstrated electrically injected index-coupled and optically pumped complex-coupled InGaN/GaN-based DFB lasers. The best threshold current density observed was comparable to that of conventional Fabry-Perot type devices, and was on the order of 16 kA/cm^2. The T_0 value describing the T-dependence of the threshold current was approximately 100 K. The reason for the much better T_0 value measured on Fabry-Perot devices fabricated from the same material (T_0 = 150 K) is the increasing mismatch between the grating resonance wavelength and the gain maximum when heating or cooling the DFB lasers. The emission of the DFB laser was at a wavelength of 402 nm and occurred in a single longitudinal mode with a sidemode suppression ratio of 15 dB. The primary emission peak could be temperature tuned continuously between 2 and 35 °C at a rate of 0.14 Å/K. The optically pumped

device showed a narrow linewidth of 3.5 Å, even for pump intensities considerably above threshold, and almost no wavelength shift at higher pump intensities.

ACKNOWLEDGEMENTS

The authors would like to thank Fred Endicott and Greg Anderson for technical assistance, and Noble M. Johnson, Ross Bringans, Gary A. Evans (Southern Methodist University, Dallas, TX), and Peter S. Zory (University of Florida, Gainesville, FL) for helpful discussions. This work was supported by the Defense Advanced Research Projects Agency (DARPA contract number MDA 972-96-3-0014), and the Swiss National Science Foundation.

REFERENCES

[1] S. Nakamura, M. Senoh, S. Nagahama, N. Iwasa, T. Yamada, T. Matsushita, Y. Sugimoto, and H. Kiyoku, InGaN-based multi-quantum-well structure-laser diodes, Jpn. J. Appl. Phys., **35** (1), L74 – L76 (1996)

[2] D.P. Bour, H.F. Chung, W. Götz, B.S. Krusor, D. Hofstetter, S. Rudaz, C.P. Kuo, F.A. Ponce, M.G. Craford, and R.D. Bringans in *III-V Nitrides*, edited by T.D. Moustakas, I. Akasaki, B. Monemar, and F.A. Ponce (Mater. Res. Soc. Proc. **443**, Pittsburgh, PA, 1996) pp. 509 – 514

[3] M. Kneissl, D.P. Bour, N.M. Johnson, L.T. Romano, B.S. Krusor, R. Donaldson, J. Walker, and C.Dunnrowicz, Characterization of AlGaInN diode lasers with mirrors from chemically assisted ion beam etching, Appl. Phys. Lett., **72** (13), 1539 – 1541 (1998)

[4] D. Hofstetter, D.P. Bour, R.L. Thornton, and N.M. Johnson, Excitation of a higher order transverse mode in an optically pumped $In_{0.05}Ga_{0.95}N/In_{0.15}Ga_{0.85}N$ multiquantum well laser structure, Appl. Phys. Lett., **70** (13), 1650 – 1652 (1997)

[5] D. Hofstetter, M. Kneissl, D.P. Bour, C. Dunnrowicz, and R.L. Thornton, Demonstration of an InGaN/GaN-based optically pumped multi quantum well DFB laser using holographically-defined 3rd order gratings, Appl. Phys. Lett., **73** (14), 1918 – 1920 (1998)

[6] R. Hofmann, H.-P. Gauggel, U.A. Griesinger, H. Gräbeldinger, F. Adler, P. Ernst, H. Bolay, V. Härle, F. Scholz, H. Schweizer, and M.H. Pilkuhn, Realization of optically pumped second-order GaInN-distributed-feedback lasers, Appl. Phys. Lett., **69** (14), 2068 – 2070 (1996)

[7] S.N.G. Chu, T. Tanbun-Ek, R.A. Logan, J. Vandenberg, P.F. Sciortino, Jr., P. Wisk, and T.L. Pernell, Grating overgrowth and defect structures in distributed-feedback-buried hererostructure laser diodes, IEEE Journal of Selected Topics in Quantum Electronics, **3** (3), 862 – 873 (1997)

MECHANISMS OF OPTICAL GAIN IN CUBIC GAN AND INGAN

J. Holst, A. Hoffmann, I. Broser, T. Frey*, B. Schöttker*, D.J. As*, D. Schikora*, K. Lischka*, Technische Universität Berlin, Hardenbergstraße 36, 10623 Berlin, Germany, *Universität Paderborn, FB-6 Physik, D-33095 Paderborn, Germany

Cite this article as: MRS Internet J. Nitride Semicond. Res. 4S1, G2.3 (1999)

ABSTRACT

The epitaxial growth of zinc-blende (cubic) GaN and InGaN on GaAs with a common cleavage plane and readily high-quality, low-cost wafers may be considered as an alternative approach for the future realization of cleaved laser cavities. To obtain detailed information about the potential of cubic GaN and InGaN for device applications we performed optical gain spectroscopy accompanied by time-integrated and time-dependent photoluminescence measurements at 2 K and 300 K. From intensity-dependent gain measurements, the identification of the gain processes was possible. For moderate excitation levels, the biexciton decay is likely to be responsible for a gain structure at 3.265 eV in cubic GaN [10]. For the highest pump intensities, the electron- hole-plasma is the dominant gain process, providing gain values up to 200 cm^{-1}. Furthermore cubic GaN samples with different cavity lengths from 250 to 600 µm were cleaved to investigate the influence of the sample geometry on the gain mechanisms. In these samples increased gain values up to 150 cm^{-1} as well as lower threshold excitation densities were observed, indicating the potential of cubic GaN for device applications. The results of GaN will be compared with intensity-dependent gain measurements on InGaN samples, grown on GaAs with varying In-content. The observed gain mechanisms in cubic InGaN will be discussed in detail.

INTRODUCTION

The epitaxy of metastable, cubic GaN on GaAs (001) substrates has attracted some interest recently since c-GaN layers and the GaAs substrate have a common cleavage plane, they are considered to be well suited for the fabrication of laser cavities with cleaved facets [1-8]. Because of this application, high optical excitation experiments have been used to measure the gain in c-GaN/GaAs (001) grown by MBE [2] revealing some insight into involved recombination mechanisms [3]. The stimulated emission from c-GaN has been reported for MOCVD [4] and MOVPE [5] grown epilayers. In our previous work [10] we studied the gain spectra of c-GaN at 2 K and found that excitonic processes add to the gain at moderate excitation densities and many particle processes are effective for increased excitation intensities. The purpose of the present paper is to analyze the mechanisms of optical amplification and the efficiency of the stimulated emission in cubic GaN and InGaN layers.

Mat. Res. Soc. Symp. Proc. Vol. 537 © 1999 Materials Research Society

EXPERIMENTAL

Cubic GaN films with a phase purity better than 99.9% were grown on semi-insulating GaAs (001) substrates by RF-plasma assisted molecular beam epitaxy (MBE) at a substrate temperature of 720°C. Undoped epitaxial layers were grown under carefully controlled stoichiometric growth conditions[6]. Details of the growth procedure were reported in Ref.13. The optical properties of the c-GaN layers investigated under low and high excitation intensities are reported in Ref. 10. By cleaving we obtained c-GaN samples with cavity lengths of 550, 450 and 250 μm along the common (001) direction and performed high-excitation and gain measurements. The InGaN/GaN/GaAs (001) heterostructures were grown by plasma assisted MBE. The GaN buffer layers with a typical thickness in the range from 100-200nm were grown at T=720° C under carefully controlled stoichiometric conditions, exploiting Reflection High Energy Diffraction (RHEED) measurements of the surface reconstruction as an in-situ control of the composition of the layer surface during growth [7]. The InGaN layers had a thickness between 200-300 nm and were deposited at lower temperatures (T=610-680° C). During the InGaN epitaxy we used a Ga flux which was reduced by about 20% compared to that of the GaN layer deposition. The In flux was adjusted to establish a metal rich surface taking into account the extremely small and strongly temperature dependent sticking coefficient of In.

To obtain the high excitation density necessary for our investigations we used a dye laser pumped by an excimer laser, providing pulses with a duration of 15 ns at a rate of 30 Hz and a total energy of up to 20 μJ at 340 nm. The sample was mounted in a bath cryostat at 1.8 K. Gain measurements were performed using the variable-stripe-length method [8] . The excitation spot was focused onto a l x 50 μm^2 stripe, where l denotes the excitation length. The photoluminescence spectra were recorded from the top of the sample with a continuous-wave (cw) helium-cadmium laser.

RESULTS

Optical Amplification in cleaved c-GaN samples

Figure 1 shows the spectra of the edge emission from a cleaved sample with a cavity length of 450 μm at different excitation densities on a linear scale at 2 K. Above the threshold excitation of 1 MW/cm^2 a peak at 3.26 eV appears exhibiting a strong increase of the edge emission with excitation intensity and a strong polarization dependence. The emitted light is strongly TE polarized, as expected for an edge emitting cleaved facet. For higher densities up to 5 MW/cm^2 a slight shift to lower energies of the peak position is observed, indicating the increased carrier density in the sample. In Fig. 1a (inset of Fig. 1) the results of intensity dependent edge emission measurements for the 250, 450 and 550 μm c-GaN samples are summarized. For all the samples the same optical features were observed- a strongly polarization dependent stimulated emission peak occurs above a certain threshold, exhibiting a superlinear increase with increased excitation density.

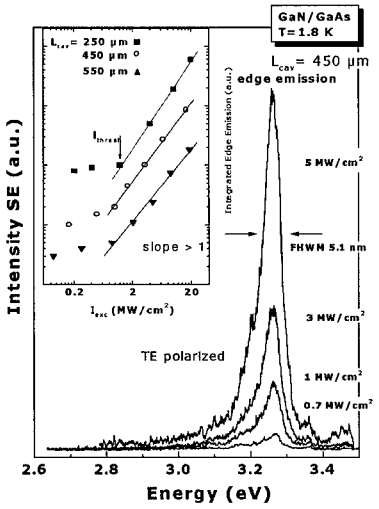


Fig. 1:Edge emission of a cleaved c-GaN sample (Inset: slope of excitation density versus integrated emission intensity for c-GaN samples with different cavity lengths)

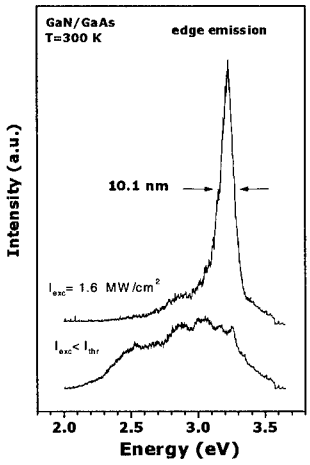


Fig. 2: Room temperature edge emission of a cleaved c-GaN sample with 450 µm cavity length

The threshold for the onset of stimulated emission increases with reduced cavity length L which is in accordance with the well known formula $I_{thres} \propto 1/L$ [9].

The room temperature spectrum of the edge emission of the cleaved sample is displayed in Fig. 2 and exhibits similar optical features as strong TE polarization and superlinear increase of edge emission. From these features the peak can attributed to the stimulated emission of c-GaN.

However, no Fabry-Perot modes are observed which are expected to be separated by about 0.4 meV. Imperfections of the cavity facets, excitation pulse variations and mode hopping are reasons to explain the unstructured stimulated emission spectra. We believe that the lateral confinement is caused by the interface sample-air on one side and the illuminated and nonilluminated parts of the sample on the other. The magnitude of the pump power locally changes the refractive index and therefore, a lateral confinement necessary for the feedback is provided [10]. This is confirmed by micro-photoluminescence measurements where it was found that the most part of the light is emitted from the cleaved facets of the samples.

To reveal more insight into the involved processes providing optical amplification gain measurements on the cleaved samples were performed and are shown in Fig. 3. At excitation densities of 1 MW/cm^2 the gain structure broadens and its peak position shifts to lower energies. This can be explained by the increased number of excited carriers in the sample, where the Coulomb interaction is screened and many particle effects are effective as gain process. The quasi Fermi-levels of the electrons and holes are shifted in the conduction and valence band, respectively.

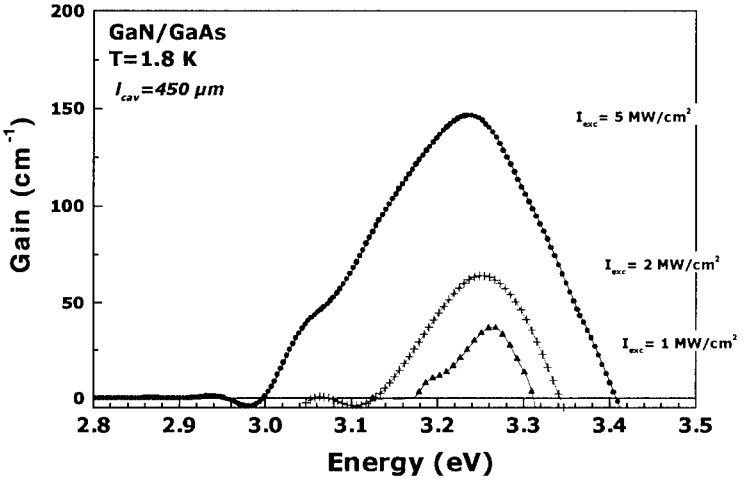


Figure 3: Gain spectra of a cleaved c-GaN sample with a cavity length of 450 µm at 2K

This results in the observed blue shift of the crossover gain-absorption on the high energy side with increasing excitation density. On the other hand the low energy side of the crossover gain-absorption is shifted to the red which is due to bandgap renormalization under high excitation densities. These are typical features of an electron-hole-plasma.

Optical Gain in c-InGaN

In Figure 4 low-temperature gain measurements of InGaN samples with varying In-content are shown. With increasing In-incorporation the gain structure shifts to lower energies and the gain values are increased. This is depicted in Fig. 4a where the obtained gain values for the samples

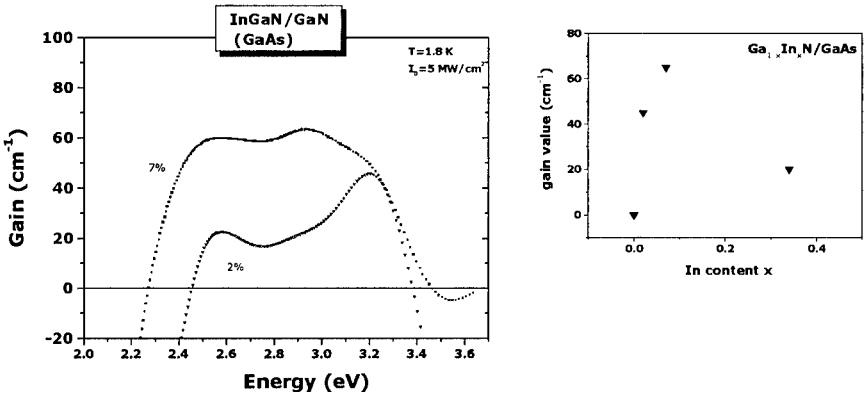


Fig. 4 : (left hand side) Gain spectra for $In_x Ga_{1-x} N$ with an varying In-content at a fixed excitation density (right hand side) Gain values for In-contents up to 50 %

with different In-content are shown. Samples with In-contents higher than 30 % exhibit lower gain values due to the reduced sample quality and the effects of In-clustering inhomogeneously distributed over the sample. The In-clustering is detrimental to the optical properties of InGaN as known from the hexagonal phase [11]. The optical gain of these "highly In-doped" InGaN samples occurs in the same energy range as for the InGaN samples with much lower In-contents as 7% in our case. This indicates the strong influence of the inhomogeneous distribution of In in these samples. The transition energy is very sensitive to the degree of compositional In-fluctuations in the samples.

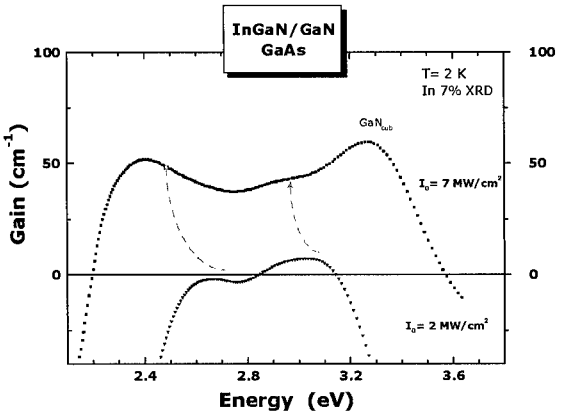


Fig. 5: Gain spectra of an InGaN sample with 7 % In for different excitation densities

Increasing the excitation density in the sample with 7% In-content the gain structures are shifted to the low energy side, see Figure 5. This is a typical feature of an electron-hole plasma, where the peak shifts into the lower energy spectral range and the gain structure broadens due to the increased number of excited carriers. It is interesting to note that at 2.4 eV optical gain is observed, indicating the strong shift of the emission into the green spectral range at significantly lower In-contents than in the hexagonal phase. This is due to the fact that a quantum-confined Stark effect due to piezoelectric fields is *not* expected the cubic phase. The absorption on the low energy side of the gain structures can be explained by the inhomogeneous distribution in the InGaN layers, which causes an increased number of defects. Additionally, another gain peak occurs at 3.23 eV which can be attributed from its energy position to be generated in the c-GaN layer.

CONCLUSION

In conclusion we reported on stimulated emission data and gain measurements of cleaved c-GaN samples. Excitonic processes as well as band filling processes dominate the optical gain at 2K. Above a threshold power density of 0.9 MW/cm^2 a stimulated emission peak was observed, exhibiting the typical optical features as polarization dependence and superlinear increase with pump intensity. For decreased cavity lengths the optical amplification and the threshold values increase. This indicates the influence of the cavity on the optical properties of highly excited c-GaN on GaAs. With a cleaved sample of 450 µm cavity room temperature stimulated emission is observed at 1.6 MW/cm^2. To our knowledge these are the lowest values reported for cleaved cubic GaN [12]. For the cubic InGaN samples a strong impact of the In-fluctuations on the optical gain is found. The energy position of the emission is very sensitive to the degree of In-

distribution. Due to the stronger bowing parameter and the lack of strong piezoelectric fields in cubic InGaN the emission is strongly shifted into the green spectral range at lower In-contents compared with the hexagonal phase. These results are promising and indicate the high potential for light-emitting device applications of this material system.

REFERENCES

[1.] D.J. As, D. Schikora, A. Greiner, M. Lübbers, J. Mimkes, and K. Lischka, Phys. Rev. B 54, R11118 (1996)
[2.] R. Klann, O. Brandt, H. Yang, H.T. Grahn, and K.H. Ploog, Appl. Phys. Lett. **70**, 1076 (1997)
[3.] J. Holst, L. Eckey, A. Hoffmann, I. Broser, B. Schöttker, D.J. As, D. Schikora, K. Lischka, Appl. Phys. Lett. **72,** 1439 (1998)
[4.] A. Nakadaira and H. Kanaka, Appl. Phys. Lett. 71, 812 (1997)
R. Klann, O. Brandt, H. Yang, H.T. Grahn, and K.H. Ploog, Appl. Phys. Lett. **70**, 1076 (1997)
[5.] J. Wu, H. Yaguchi, K. Onabe, Y. Shiraki, Appl. Phys. Lett. **73**, 1931 (1998)
[6.] D.J.As, F. Schmilgus, C. Wang, B. Schöttker, D. Schikora, and K. Lischka, Appl. Phys. Lett. **70**, 1311 (1997)
[7.] B. Schoettker, J. Kuehler, D.J. As, D. Schikora and K. Lischka, Material Science Forum Vols. 264-268 (1998), pp. 1173-1176
[8.] K. L. Shaklee, R. E. Nahory, R. F. Leheny, J. Lumin. **7**, 284 (1973)
[9.] J. I. Pankove, *Optical Processes in Semiconductors*, (Dover, New York, 1971)
[10.] I.K. Shmagin, J.F. Muth, R.M. Kolbas, S. Krishnankutty, S. Keller, U.K. Mishra, S.P. Den Baars, Appl. Phys. Lett. 81, 2021 (1997)
[11] J.S. Im, H. Kollmer, J. Off, A. Sohmer, F. Scholz, Phys. Rev. B **57,** 9435 (1998)

CARRIER DYNAMICS OF ABNORMAL TEMPERATURE-DEPENDENT EMISSION SHIFT IN MOCVD-GROWN InGaN EPILAYERS AND InGaN/GaN QUANTUM WELLS

Yong-Hoon Cho*, B. D. Little*, G. H. Gainer*, J. J. Song*,
S. Keller**, U. K. Mishra**, and S. P. DenBaars**

*Center for Laser and Photonics Research and Department of Physics
Oklahoma State University, Stillwater, OK 74078
**Electrical and Computer Engineering and Materials Departments
University of California, Santa Barbara, CA 93106

Cite this article as: MRS Internet J. Nitride Semicond. Res. 4S1, G2.4 (1999)

ABSTRACT

Temperature-dependent photoluminescence (PL) studies have been performed on InGaN epilayers and InGaN/GaN multiple quantum wells (MQWs) grown by metalorganic chemical vapor deposition. We observed anomalous temperature dependent emission behavior (specifically an S-shaped decrease-increase-decrease) of the peak energy (E_{PL}) of the InGaN-related PL emission with increasing temperature. In the case of the InGaN epilayer, E_{PL} decreases in the temperature range of 10 – 50 K, increases for 50 – 110 K, and decreases again for 110 – 300 K with increasing temperature. For the InGaN/GaN MQWs, E_{PL} decreases from 10 – 70 K, increases from 70 – 150 K, then decreases again for 150 – 300 K. The actual temperature dependence of the PL emission was estimated with respect to the bandgap energy determined by photoreflectance spectra. We observed that the PL peak emission shift has an excellent correlation with a change in carrier lifetime with temperature. We demonstrate that the temperature-induced S-shaped PL shift is caused by the change in carrier recombination dynamics with increasing temperature due to inhomogeneities in the InGaN structures.

INTRODUCTION

In spite of the recent rapid achievements in the area of InGaN-based light emitting devices, the fundamental mechanisms of spontaneous and stimulated emission are still in debate in these materials. Recently, it has been pointed out that strain-induced piezoelectric fields in InGaN/GaN quantum wells (QWs) may play an important role in the spontaneous recombination process [1,2]. On the other hand, recombination from localized band-tail states at potential fluctuations or even from quantum-dot-like deep traps originating from In-rich regions in the wells has also been proposed as a principal spontaneous emission mechanism in InGaN/GaN QWs [3-11]. The main difficulty in distinguishing between these two effects partly originates from the fact that both effects can explain - at least qualitatively - some experimental observations such as a large Stokes shift of the luminescence and an emission redshifting behavior with time [1-9]. More recently, a temperature-induced luminescence blueshift was observed in InGaN single QWs [10,11] and multiple QWs (MQWs) [6], which has been well explained by an involvement of band-tail states but can hardly be explained by the piezoelectric field effect alone. Therefore, a detailed understanding of the carrier dynamics and its relationship to the emission mechanism as a function of temperature are very important for both InGaN epilayers and InGaN/GaN MQWs.

Mat. Res. Soc. Symp. Proc. Vol. 537 © Materials Research Society

In this study, we report a systematic photoluminescence (PL) study of InGaN epilayers and InGaN/GaN MQWs as a function of temperature by means of PL, PL excitation (PLE), and time-resolved PL (TRPL) spectroscopy. As the temperature is increased, the peak energy position of the InGaN-related PL emission (E_{PL}) exhibits an S-shaped behavior (redshift-blueshift-redshift). In the case of the InGaN epilayer, E_{PL} decreases in the temperature range of 10 – 50 K, increases for 50 – 110 K, and decreases again for 110 – 300 K with increasing temperature. For the InGaN/GaN MQWs, E_{PL} decreases from 10 – 70 K, increases from 70 – 150 K, then decreases again from 150 – 300 K. This temperature-induced S-shaped PL shift is strongly affected by the change in carrier dynamics with increasing temperature for both the InGaN epilayer and the InGaN/GaN MQWs.

EXPERIMENT

The InGaN epilayers and the InGaN/GaN MQWs used in this study were grown on c-plane sapphire films by metalorganic chemical vapor deposition (MOCVD), following the deposition of a 1.8-μm-thick GaN buffer layer. For the InGaN epilayers, a 100-nm-thick InGaN layer was capped with a 50-nm-thick GaN layer. The MQW structures consisted of 12 MQWs with 3-nm-thick InGaN wells and 4.5-nm-thick GaN barriers, with a 100-nm-thick $Al_{0.07}Ga_{0.93}N$ capping layer. The growth temperatures of the GaN base layer, the MQW regions, and the AlGaN capping layer were 1050, 790, and 1040 °C, respectively. The In content of the InGaN layers was estimated to be about 18 % for both the epilayer and the MQWs by means of high-resolution x-ray diffraction measurements. We observed optically pumped stimulated emission from the MQW sample with a low threshold density (< 60 kW/cm^2) at room temperature. Details of the growth procedure and results of other structural and optical properties were reported elsewhere [12-15]. Additionally, the influence of Si doping in the GaN barriers of the MQWs on the optical properties is also given elsewhere [7]. PL spectra were measured as a function of temperature ranging from 10 to 300 K using the 325 nm line of a 20 mW cw He-Cd laser. PLE spectra were measured using the quasi-monochromatic light from a xenon lamp dispersed by a 1/2 m monochromator. TRPL measurements were carried out using a picosecond pulsed laser system consisting of a cavity-dumped dye laser synchronously pumped by a frequency-doubled modelocked Nd:YAG laser for sample excitation and a streak camera for detection. The overall time resolution of the system is better than 15 ps.

RESULTS AND DISCUSSIONS

Figure 1 shows 10 K PL and PLE spectra of the InGaN-related emission with a peak energy of ~ 2.99 and ~ 2.76 eV for (a) the InGaN epilayer and (b) the InGaN/GaN MQWs, respectively. A large Stokes shift of the InGaN emission between the PL peak energy and the band-edge obtained from the PLE spectra is clearly observed, which is mainly due to crystal imperfections such as In alloy fluctuations and/or interface roughness. We note that the observed Stokes shift for the MQWs is much larger than that of the epilayer, probably due to the influence of the MQW interfaces on the overall potential fluctuations. In general, the fundamental temperature-induced energy gap shrinkage of GaN, InGaN, and AlGaN can be described by the Varshni empirical equation [16]: $E_g(T) = E_g(0) - \alpha T^2/(\beta + T)$, where $E_g(T)$ is the bandgap transition energy at a temperature T, and α and β are known as the Varshni thermal coefficients. Previously, from photoreflectance studies, the parameters α = 8.32 (10) x 10^{-4} eV/K and β = 835.6 (1196) K for the GaN Γ_9^V - Γ_7^C ($In_{0.14}Ga_{0.86}N$) transition were obtained [17]. For simplicity, Varshni thermal coefficients obtained from the GaN and $In_{0.14}Ga_{0.86}N$ transitions [17] were used for the E_g estimation of the $Al_{0.07}Ga_{0.93}N$ and $In_{0.18}Ga_{0.82}N$ layers, respectively. The

temperature-dependent PL peak shift for the GaN and AlGaN layers was consistent with the estimated energy decrease of about 65 meV between 10 and 300 K, whereas the InGaN-related

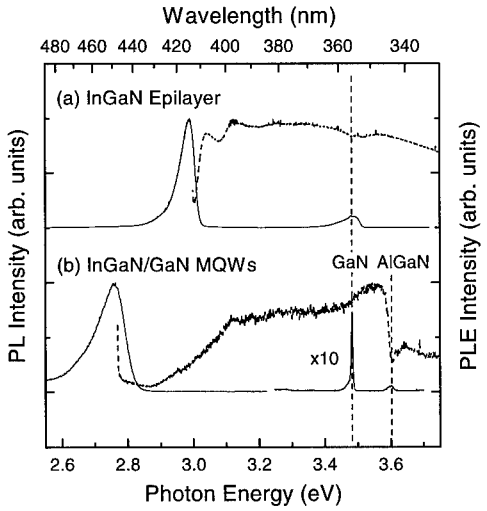


Figure 1. 10 K PL (solid lines) and PLE (dashed lines) spectra of (a) the InGaN epilayer and (b) the InGaN/GaN MQWs. A large Stokes shift of the PL emission from the InGaN layers with respect to the band-edge measured by PLE spectra is observed. Near-band-edge emission from the GaN and AlGaN layers was observed at 3.48 and 3.6 eV, respectively. The PLE contributions from the GaN layers [in (a) and (b)] and the AlGaN layer [in (b)] are clearly seen.

PL emission did not follow the typical temperature dependence of the energy gap shrinkage as will be shown later.

Figure 2 shows the evolution of the InGaN-related PL spectra for (a) the InGaN epilayer and (b) the InGaN/GaN MQWs over a temperature range from 10 to 300 K. As the temperature increases from 10 K to T_I, where T_I is 50 (70) K for the epilayer (MQWs), E_{PL} redshifts 10 (19) meV. This value is about five times larger than the expected bandgap shrinkage of ~ 2 (4) meV for the epilayer (MQWs) over this temperature range [17]. For a further increase in temperature, the PL peak blueshifts 22.5 (14) meV from T_I to T_{II}, where T_{II} is 110 (150) K for the epilayer (MQWs). By considering the estimated temperature-induced bandgap shrinkage of ~ 7 (13) meV for the epilayer (MQWs), the actual blueshift of the PL peak with respect to the band-edge is about 29.5 (27) meV over this temperature range. When the temperature is further increased above T_{II}, the peak positions redshift again. From the observed redshift of 45 (16) meV and the expected bandgap shrinkage of ~ 51 (43) meV from T_{II} to 300 K for the epilayer (MQWs), we estimate an actual blueshift of the PL peak relative to the band-edge to be about 6 (27) meV in this temperature range.

To elucidate the kinetics of carrier recombination, we performed TRPL measurements over the same temperature range. Figure 3 shows E_{PL}, the relative energy difference (ΔE) between E_{PL} and E_g at each temperature, and the decay times (τ_d) monitored at the peak energy, lower energy side, and higher energy side of the peak as a function of temperature. A comparison of these values clearly shows that the temperature dependence of ΔE and E_{PL} is strongly correlated with the change in τ_d. In both cases, we found an overall increase of τ_d with increasing temperature for $T < T_I$, in qualitative agreement with the temperature dependence of radiative recombination [18,19]. Moreover, in this temperature range, τ_d becomes longer with decreasing emission energy, and hence, the peak energy of the emission shifts to the low energy side as time proceeds. This behavior is a characteristic of localized carriers, which in this case is most likely related to alloy fluctuations (and/or interface roughness in the MQWs) [7,9]. We note that the observed longer lifetime for the MQWs compared to those reported by other groups is probably due to relatively larger degree of carrier localization caused by a larger number of QWs and/or

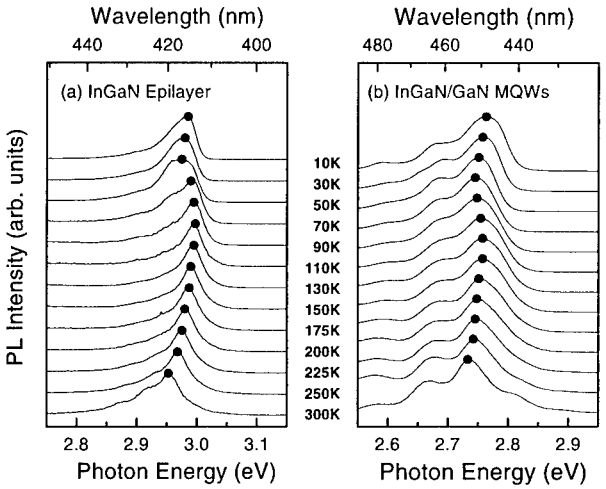


Figure 2. Typical InGaN-related PL spectra for (a) the InGaN epilayer and (b) the InGaN/GaN MQWs in the temperature range from 10 to 300 K. The main emission peak of both samples (closed circles) shows an S-shaped shift with increasing temperature. All spectra are normalized and shifted in the vertical direction for clarity. Note that the turnover temperature from redshift to blueshift occurs at about 50 and 70 K for the InGaN epilayer and the InGaN/GaN MQWs, respectively.

different growth conditions used in this work [3,7,20-22]. As the temperature is further increased beyond T_I, the lifetime of the epilayer (MQWs) quickly decreases to less than 0.1 (10) ns and remains almost constant between T_{II} and 300 K, indicating that non-radiative processes predominantly affect the emission in this range. This is further evidenced by the fact that there is no difference between the lifetimes monitored above, below, and at the peak energy for $T > T_I$, in contrast to the observations for $T < T_I$. This characteristic temperature T_I is also where the turnover occurs from redshift to blueshift for ΔE and E_{PL} with increasing temperature. Furthermore, in the temperature range between T_I and T_{II}, where a blueshift of E_{PL} is detected, τ_d dramatically decreases from 0.4 to 0.05 (35 to 8) ns for the epilayer (MQWs). Above T_{II}, where a redshift of E_{PL} is observed, no sudden change in τ_d occurs for either the epilayer or the MQWs.

From these results, the InGaN-related recombination mechanism for different temperature ranges can be explained as follows: (i) For $T < T_I$, since the radiative recombination process is dominant, the carrier lifetime increases, giving the carriers more opportunity to relax down into lower energy tail states caused by the inhomogeneous potential fluctuations before recombining. This behavior reduces the higher energy side emission intensity, and thus, produces a redshift in the peak energy position with increasing temperature. (ii) For $T_I < T < T_{II}$, since the dissociation rate is increased and other non-radiative processes become dominant, the carrier lifetime decreases greatly with increasing temperature and also becomes independent of the emission energies. Thus, due to the decreasing lifetime, these carriers recombine before reaching the lower energy tail states. This behavior gives rise to an apparent broadening of the higher energy side emission and leads to a blueshift in the peak energy. (iii) For $T > T_{II}$, since non-radiative recombination processes are dominant and the lifetimes are almost constant [in contrast to the case (ii)], the photogenerated carriers are less affected by the change in carrier lifetime so that the blueshift behavior becomes smaller. Note that the slope of ΔE is very sensitive to the change in τ_d with temperature for both the InGaN epilayer and the InGaN/GaN MQWs. Since this

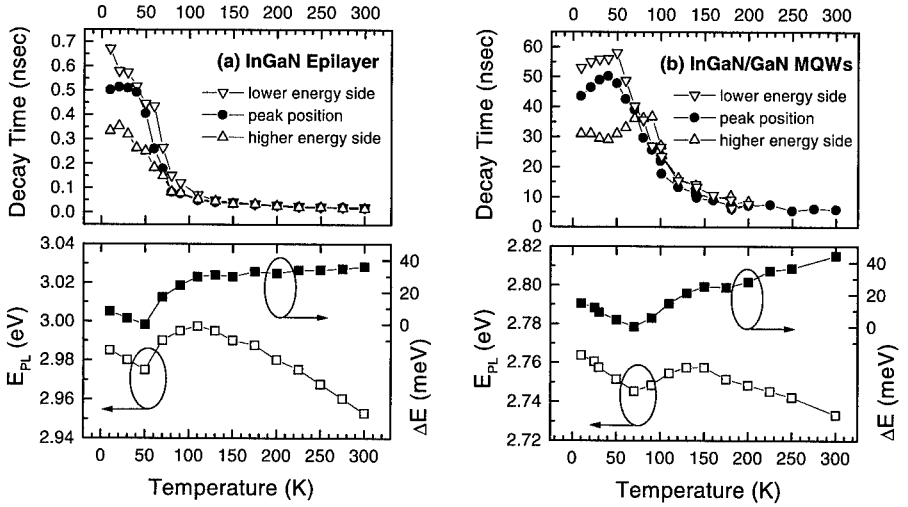


Figure 3. InGaN-related PL spectral peak position E_{PL} (open squares) and decay time τ_d as a function of temperature in (a) the InGaN epilayer and (b) the InGaN/GaN MQWs. ΔE (closed squares) represents the relative energy difference between E_{PL} and E_g at each temperature. The minimum value of ΔE is designated as zero for simplicity. Note that the lower energy side of the PL peak has a longer lifetime than the higher energy side below a certain temperature T_l, while there is no difference between lifetimes monitored above, below, and at the peak energy above T_l, where T_l is about 50 (70) K for the epilayer (MQWs). This characteristic temperature T_l is also where the turnover occurs from redshift to blueshift of the InGaN PL peak energy with increasing temperature.

blueshift behavior is smaller than the temperature-induced bandgap shrinkage in this temperature range, the peak position exhibits an overall redshift behavior. Consequently, the change in carrier recombination mechanism with increasing temperature causes the S-shaped redshift-blueshift-redshift behavior of the peak energy for the main InGaN-related emission. Therefore, the InGaN-related spontaneous emission features are significantly affected by different carrier recombination dynamics which vary with temperature, because of band-tail states arising from inhomogeneities such as large In alloy fluctuations, layer thickness variations in the MQWs, and/or defects. It should be noted that we observed similar temperature-induced S-shaped emission behavior for both the InGaN epilayers and the InGaN/GaN MQWs, even though τ_d of the latter is about two orders of magnitudes longer than that of the former. This strongly reflects the fact that the anomalous temperature-induced emission shift mainly depends on the change in carrier recombination dynamics rather than the absolute value of τ_d.

CONCLUSIONS

We have investigated the time-integrated and time-resolved PL properties of MOCVD-grown InGaN epilayers and InGaN/GaN MQWs over the temperature range of 10 to 300 K. The peak energy of the InGaN-related emission, E_{PL}, exhibited an S-shaped (redshift-blueshift-redshift) behavior with increasing temperature. The PL emission peak position and carrier lifetime as a function of temperature reveal that the InGaN-related emission is strongly affected by the change in carrier recombination dynamics with increasing temperature for both the InGaN epilayers and the InGaN/GaN MQWs. This anomalous temperature-induced emission behavior is attributed to band-tail states due to inhomogeneities in the InGaN-based material.

ACKNOWLEDGMENTS

This work was supported by AFOSR, ARO, ONR, DARPA, and KOSEF.

REFERENCES

1. T. Takeuchi, S. Sota, M. Katsuragawa, M. Komori, H. Takeuchi, H. Amano, and I. Akasaki, Jpn. J. Appl. Phys., Part 2 **36**, L382 (1997).
2. J. S. Im, H. Kollmer, J. Off, A. Sohmer, F. Scholz, and A. Hangleiter, Phys. Rev. B **57**, R9435 (1998); A. Hangleiter, J. S. Im, H. Kollmer, S. Heppel, J. Off, and F. Scholz, MRS Internet J. Nitride Semicond. Res. **3**, 15 (1998).
3. E. S. Jeon, V. Kozlov, Y. -K. Song, A. Vertikov, M. Kuball, A. V. Nurmikko, H. Liu, C. Chen, R. S. Kern, C. P. Kuo, and M. G. Craford, Appl. Phys. Lett. **69**, 4194 (1996).
4. S. Chichibu, T. Azuhata, T. Sota, and S. Nakamura, Appl. Phys. Lett. **69**, 4188 (1996).
5. P. Perlin, V. Iota, B. A. Weinstein, P. Wisniewski, T. Suski, P. G. Eliseev, and M. Osinski, Appl. Phys. Lett. **70**, 2993 (1997).
6. Y. H. Cho, G. H. Gainer, A. J. Fischer, J. J. Song, S. Keller, U. K. Mishra, and S. P. DenBaars, Appl. Phys. Lett. **73**, 1370 (1998).
7. Y. H. Cho, J. J. Song, S. Keller, M. S. Minsky, E. Hu, U. K. Mishra, and S. P. DenBaars, Appl. Phys. Lett. **73**, 1128 (1998); Y. H. Cho, J. J. Song, S. Keller, U. K. Mishra, and S. P. DenBaars, *ibid.* **73**, 3181 (1998).
8. P. Lefebvre, J. Allegre, B. Gil, A. Kavokine, H. Mathieu, W. Kim, A. Salvador, A. Botchkarev, and H. Morkoc, Phys. Rev. B **57**, R9447 (1998).
9. Y. Narukawa, Y. Kawakami, M. Funato, Sz. Fujita, Sg. Fujita, and S. Nakamura, Appl. Phys. Lett. **70**, 981 (1997); Y. Narukawa, Y. Kawakami, Sz. Fujita, Sg. Fujita, and S. Nakamura, Phys. Rev. B **55**, R1938 (1997).
10. P. G. Eliseev, P. Perlin, J. Lee, and M. Osinski, Appl. Phys. Lett. **71**, 569 (1997).
11. K. G. Zolina, V. E. Kudryashov, A. N. Turkin, and A. E. Yunovich, MRS Internet J. Nitride Semicond. Res. **1**, Art, 11 (1996).
12. S. Keller, A. C. Abare, M. S. Minsky, X. H. Wu, M. P. Mack, J. S. Speck, E. Hu, L. A. Coldren, U. K. Mishra, and S. P. DenBaars, Materials Science Forum **264 - 268**, 1157 (1998).
13. S. Bidnyk, T. J. Schmidt, Y. H. Cho, G. H. Gainer, J. J. Song, S. Keller, U. K. Mishra, and S. P. DenBaars, Appl. Phys. Lett. **72**, 1623 (1998).
14. T. J. Schmidt, Y. H. Cho, G. H. Gainer, J. J. Song, S. Keller, U. K. Mishra, and S. P. DenBaars, Appl. Phys. Lett. **73**, 560 (1998); *ibid.* **73**, 1892 (1998).
15. Y. H. Cho, F. Fedler, R. J. Hauenstein, G. H. Park, J. J. Song, S. Keller, U. K. Mishra, and S. P. DenBaars, J. Appl. Phys. (to be published).
16. Y. P. Varshni, Physica **34**, 149 (1967).
17. W. Shan, T. J. Schmidt, X. H. Yang, S. J. Hwang, J. J. Song, and B. Goldenberg, Appl. Phys. Lett. **66**, 985 (1995); W. Shan, B. D. Little, J. J. Song, Z. C. Feng, M. Schurman, and R. A. Stall, *ibid.* **69**, 3315 (1996).
18. B. K. Ridley, Phys. Rev. B **41**, 12 190 (1990).
19. J. Feldmann, G. Peter, E. O. Gobel, P. Dawson, K. Moore, C. Foxon, and R. J. Elliott, Phys. Rev. Lett. **59**, 2337 (1987).
20. C. I. Harris, B. Monemar, H. Amano, and I. Akasaki, Appl. Phys. Lett. **67**, 840 (1995).
21. C. K. Sun, S. Keller, G. Wang, M. S. Minsky, J. E. Bowers, and S. P. DenBaars, Appl. Phys. Lett. **69**, 1936 (1996).
22. J. S. Im, V. Harle, F. Scholz, and A. Hangleiter, MRS Internet J. Nitride Semicond. Res. **1**, 37 (1996).

MECHANISM FOR RADIATIVE RECOMBINATION IN $In_{0.15}Ga_{0.85}N$/GaN MULTIPLE QUANTUM WELL STRUCTURES

B Monemar, J P Bergman, J Dalfors, G Pozina, B E Sernelius, P O Holtz, H Amano*, and I Akasaki*,
Department of Physics and Measurement Technology, Linköping University, S-581 83 Linköping, Sweden
*Department of Electrical Engineering and Electronics, Meijo University, 1-501 Shiogamaguchi, Tempaku-ku, Nagoya 468, Japan

Cite this article as: MRS Internet J. Nitride Semicond. Res. 4S1, G2.5 (1999)

Abstract

We present a study of the radiative recombination in $In_{0.15}Ga_{0.85}N$/GaN multiple quantum well samples, where the conditions of growth of the InGaN quantum layers were varied. The piezoelectric field as well as short range potential fluctuations are screened via different mechanisms by donor electrons and excited electron-hole pairs. These effects account for a large part of the spectral shift with donor doping (an upward shift of the photoluminescence (PL) peak up to 0.2 eV is observed for a Si donor density of 2 x 10^{18} cm^{-3} in the well), with excitation intensity and with delay time after pulsed excitation (also shifts up to 0.2 eV). It appears like 2-dimensional screening of short range potential fluctuations is needed to fully explain the data. We suggest that excitons as well as shallow donors are at least partly impact ionized by electrons in the rather strong lateral potential fluctuations.

Introduction

InGaN/GaN multiple quantum well (MQW) structures provide the active medium for the violet III-nitride lasers [1]. The recombination processes in these structures therefore are of interest to determine. It has recently been claimed that the broad photoluminescence (PL) emission spectra in these structures are due to an inhomogeneously broadened envelope of excitonic emissions from "quantum dots (QDs)" [2]. These QDs are supposed to consist of regions of a size 3-5 nm having a bandgap much lower than the alloy matrix, due to segregation of In during growth [2]. Other recent work points towards the importance of the piezoelectric (PZ) field as the dominant mechanism governing the QW electronic structure and the recombination processes in these structures [3,4]. In the previous studies the In composition x in the QWs was typically smaller than 0.15, and the recombination processes were described in terms of QW excitons [2-4]. In this work we report on a study of the recombination dynamics in $In_xGa_{1-x}N$ MQWs over the temperature range 2 - 300 K. We conclude that both the PZ field and potential fluctuations are important at this In composition.

Samples and experimental procedure

The $In_xGa_{1-x}N$ MQW samples with 5 QWs were grown with MOCVD with an In fraction x about 0.15 for all samples studied in this work. The QW thickness was 3.0 nm, with a GaN barrier thickness of 6.0 nm. The detailed growth procedures have been described elsewhere [5]. The structural quality was investigated for selected samples. It was found that the interfaces of the QW were rather smooth, the lower GaN/InGaN interface was virtually atomically flat in high

Mat. Res. Soc. Symp. Proc. Vol. 537 © 1999 Materials Research Society

resolution TEM pictures, while the upper InGaN/ GaN interface had a short range fluctuation of about 1-2 monolayers.

The spectral PL experiments discussed here involve continuous wave (cw) laser excitation, as well as more advanced transient studies. For the transient PL measurements we had several UV laser systems available, tunable both above and below the GaN bandgap. For detection we employ photon counting techniques for the time domain 100 ps to 4 μs, and a streak camera for the faster time domain 15 ps to 2 ns. PLE spectra were obtained with a Xenon lamp and a monochromator as light source.

Transient photoluminescence spectra

We have investigated the transient behavior of the PL over a large time scale and a large dynamic range. The results for the shorter time scale will be reported separately [6]. The PL decay over a longer time scale (ns - μs) has been measured with photon counting technique over the entire spectral range covered by the PL emission. Typical results are shown in Figs 1(a) and 1(b) for selected samples at low temperature. In Fig 1 we compare the time resolved spectra of an undoped (a) and a doped sample (b) ($n = 2 \times 10^{18}$ cm^{-3}), respectively. It is noted that the spectra for the doped samples are considerably narrower, with the impression that the lower energy part of the spectrum in Fig 1 (a) is simply missing in the spectrum 1(b). This will be discussed further below. There is also a rather strong shift downwards for the peak energy with delay time, which is expected due to screening by the excited e-h pairs, and also due to spectral diffusion from carrier hopping before recombination.

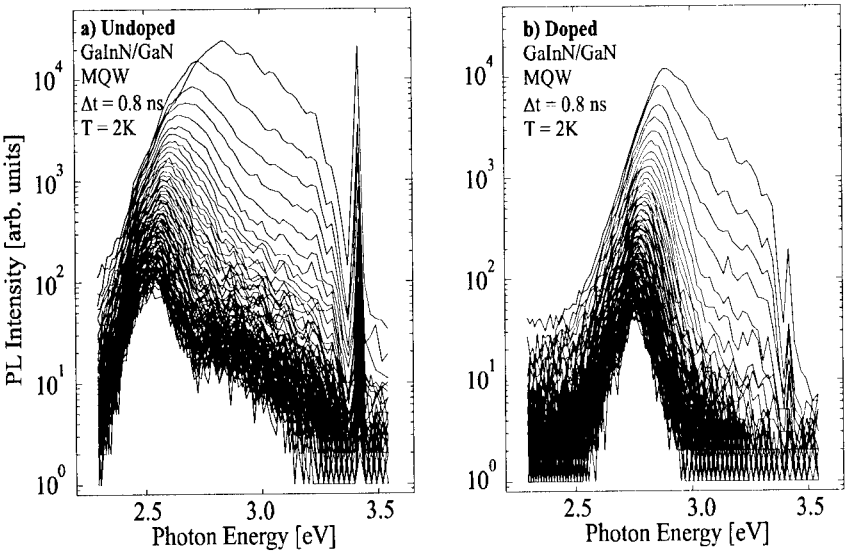


Fig. 1. Timeresolved PL spectra, with 0.8 ns between each spectrum, for two MQW samples obtained at 2 K with excitation at 3.6 eV. In a) are shown the spectra for a undoped sample while b) shows the corresponding data for a doped sample. Note the strong spectral shift between the two samples.

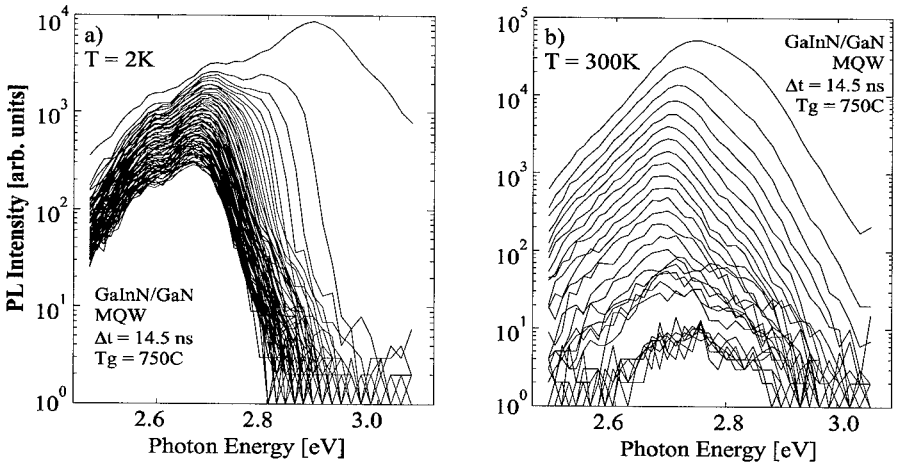


Fig. 2. Timeresolved PL spectra for an MQW sample with the InGaN layer grown at 750 C, obtained at 2 K (a) and at 300 K (b), respectively. The spectra at 300 K are broadened towards higher energy, and also have shorter decay time.

In Fig 2 we show a comparison of the timeresolved spectra at 2 K and 300 K for an MQW sample with the InGaN layers grown at 750 °C. The spectra are quite similar concerning downward shift with delay time, but the 300 K spectrum is broadened considerably and selectively on the high energy side, even at long delay times.

This may be understood by the presence of strong localization potentials in the system. Also, the decay is faster at 300 K, presumably due to the presence of a nonradiative recombination component at this temperature. The low temperature decay times are identified as the radiative decay times in the MQWs, since they are independent of the excitation power.

The values of the decay times are not welldefined at any temperature, since the decay curves are not exponential. Defining an effective decay time (measured as the time for a decrease of intensity by a factor 1/e of the initial value) we obtain a value about 150 ns at 2 K for the sample with the InGaN layer grown at 780 C [6]. The effective decay times are illustrated at three different temperatures in Fig 3. The temperature dependence of the decay times is not strong; in fact it seems like the radiative decay times are rather independent of temperature, so that the faster decay at 300 K is due to the presence of a nonradiative component at this temperature.

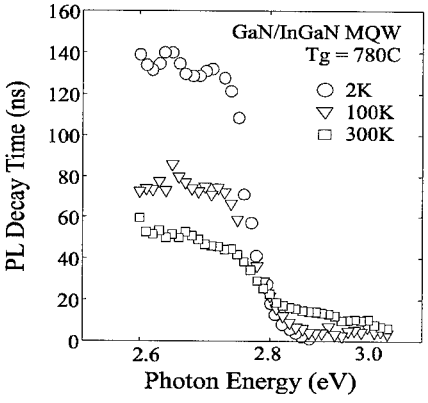


Fig. 3. Effective decay times as a function of detection photon energy for an undoped sample with the InGaN growth temperature 780 °C.

Discussion.

The shape of the broad PL spectrum from these InGaN MQWs does not give any direct information on the recombination mechanism. The considerably narrower PL peaks observed in similar systems with lower In composition can more consistently be ascribed to QW excitons [2,4,7]. We suggested earlier that due to the rather low fields necessary for impact ionization of excitons in these QWs, excitons may be largely transformed into separated electron-hole pairs when they encounter the strong local lateral fields due to the potential fluctuations in the QW [8]. Further, the importance of the piezoelectric field effects vs localization in potential fluctuations for the PL lineshape has to be determined.

The energy of the QW bandgap in our samples is estimated as 3.05 eV at 2 K [6]. The energy position of the broad PL peak is consistent with a downshift expected from a strong piezoelectric field across the QW [3]. The peak position observed for undoped MQW samples in low intensity stationary PL spectra (about 2.65 eV [6,8]), as well as in the timeresolved spectra at long time delay after the excitation pulse, are in good agreement with Ref. 3 for MQW samples with a similar In composition. The downshift from the estimated QW bandgap energy is about 0.4 eV. We therefore conclude that the PL peak position is consistent with a major effect of the piezoelectric field across the QW. The value of the PZ field necessary to explain the large downshift is about 1 MV/cm [3,4]. The width of the peak strongly indicates the presence of substantial potential fluctuations in the QWs, however.

The rather large upward shifts of the PL peak position with Si donor doping in the QWs [8], as well as with excitation intensity, points towards strong effects of carrier screening of the PZ field. We have simulated to what extent the donors or the excited carriers can screen out most of the PZ field. The most extreme screening effect would occur if one puts all the donor ions on one side and the electrons on the other side of the QW (this would be a gross overestimation of the ability of the carriers to screen the field). This screening would only reduce the potential drop across the well with 12%, for the highest Si doping concentration we have studied, $2x10^{18}$ cm^{-3}. A similar modeling with ordered electron-hole pairs at this density, as required to simulate the spectral shifts with intensity and delay time, gives a similar result. A doping (or excited electron-hole pair) concentration of the order 10^{19} cm^{-3} would be needed to reproduce the observed shifts (up to 200 meV upshift with Si doping at $2x10^{18}$ cm^{-3}), if these shifts were due to screening of the PZ field alone. To explain the screening effects in this case we need to assume rather strong potential fluctuations in the QWs, in addition to the PZ field.

We have made some simple modeling to find out if the doping induced blue shift of the PL spectrum [8] could be reproduced from lateral screening of potential fluctuations in the QW. In a 3D system we know that the screening increases with carrier concentration; the Thomas-Fermi screening length decreases. In a 2D system the Thomas-Fermi screening length is unaffected by a change in carrier concentration. However, the Thomas-Fermi screening length only describes the screening of a slowly varying potential or the resulting potential far away from the center of the potential. The higher the carrier concentration the better the system screens a rapidly varying potential or the core of the potential. This means that the effective depth of a potential well caused by fluctuations can vary with doping or carrier concentration. (In the present discussion we assume that the shallow donor electrons are ionized, e g by the strong fluctuating electric field in the QW).

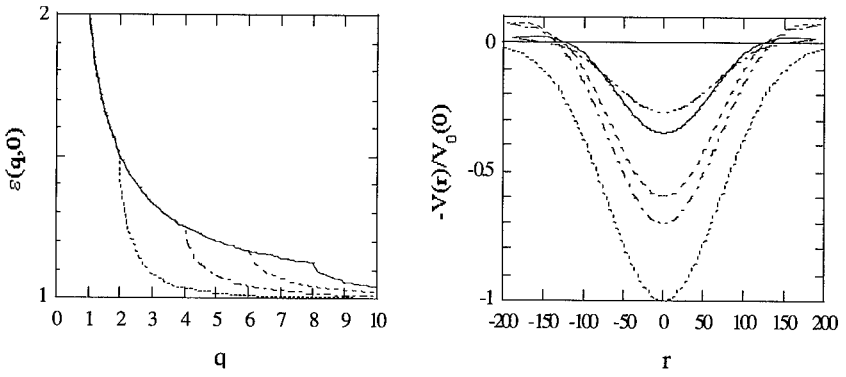


Fig. 4 (a). The general behavior of the static 2D dielectric function. Each curve is for a different carrier concentration. The dotted, dash-dotted, dashed and solid curves are for progressively higher carrier concentrations. All curves coincide for small momentum. Fig. 4 (b). The screening effect on a Gaussian potential of width 100 Å in one of the quantum wells. The dotted curve is the bare potential. The dash-dotted, dashed, full and dash-triple-dotted curves are for the carrier concentrations 2×10^{17} cm^{-3}, 4×10^{17} cm^{-3}, 2×10^{18} cm^{-3} and 1×10^{19} cm^{3}, respectively. All curves have been scaled to the value at the center of the unscreened potential.

The behavior of the 2D, low temperature, RPA dielectric function is shown in figure 4 (a), which represents the dielectric function for different electron concentrations. We see that all curves are equal for small momentum but deviates for large momentum. They start to deviate when the momentum exceeds the diameter of the Fermi-disk. The analytical expression for the dielectric function is:

$$\varepsilon(\mathbf{q},0)=\begin{cases}1+\dfrac{2me^2}{\hbar^2\kappa q}\,;\, q\le 2k_F\\[2ex] 1+\dfrac{2me^2}{\hbar^2\kappa q}\left(1-\sqrt{1-\left(2k_F/q\right)^2}\right)\,;\, q>2k_F\end{cases}$$

as derived in Ref. [9]. We have modeled a potential of the form $V(r)=V(0)e^{-\beta^2r^2}$, i.e., a Gaussian potential. We chose the parameter β to be 0.01 $Å^{-1}$. which means that the potential has a spatial extent of 100 Å . If we choose the unscreened depth of the potential as $V_0(0)$ = 386 meV we get the well depths equal to 272 meV, 232 meV and 134 meV, respectively for the densities $2x10^{17}$ cm^{-3}, $4x10^{17}$ cm^{-3} and $2x10^{18}$ cm^{-3}. (Fig. 4 (b). This corresponds to the blue shifts 38 meV and 100 meV as compared to the experimental values 40 meV and up to 200 meV, respectively, in going from $2x10^{17}$ cm^{-3} to $4x10^{17}$ cm^{-3} and from $4x10^{17}$ cm^{-3} to $2x10^{18}$ cm^{-3} [6,8].

In order to explain the large spectral shifts observed with doping we therefore need to assume that the unscreened potential fluctuations $V_0(r)$ in the QW are of a typical size 0.4 eV over a short distance of 100 Å. The partly screened potential seen in experiment may be considerably weaker, however. A typical fluctuation strength of about 0.2 eV seems to be needed to explain the observed strong shifts with doping in the QWs.

A major effect not taken into account in the simple screening model above is carrier transfer, which needs to be considered in a realistic model to explain the experimental data. Above the average electron concentration from the donors was considered. In practice, assuming the presence of rather short range potential fluctuations, carrier transfer processes (hopping) between different potentials may easily occur before recombination. The carriers will then have a tendency to be transferred to the lowest energy parts of the fluctuating potentials, selectively screening these. These potentials will experience a higher electron density, and thus be screened more effectively than by an average electron concentration. This transfer effect would explain part of the upshift of the PL peak with doping [8], and likewise the apparent absence of the low energy part of the PL spectrum in the timeresolved spectra in Fig 1 (b).

An argument for the dominance of free carriers in the recombination process is derived from the observed radiative decay times. For an excitonic process in a 30 Å QW the PZ field has been estimated to reduce the oscillator strength by about a factor 3 compared to the case of no PZ field [10]. Assuming an excitonic radiative lifetime (localized QW excitons) of < 1 ns at 2 K, the exciton decay time would not be more than 3 ns. Our observed values are of the order 100 ns, i e more than one order of magnitude larger, as expected if recombination between free (or separately localized) carriers dominate. It should be pointed out that in QWs with considerably smaller In composition, and consequently smaller potential fluctuations, the recombination is clearly dominated by excitons [3,4]. Also, the PL linewidth is then much smaller than reported in this work [3,4].

Summary

In $In_{0.15}Ga_{0.85}N$/GaN MQWs with a well thickness of 3 nm the peak PL photon energy is mainly determined by the piezoelectric field, while the width of the peak reflects the size of the screened potential fluctuations. We suggest that excitons and shallow donors in the QWs are largely impact ionized in the fluctuating lateral potential, so that the observed recombination is to a large extent due to separately localized electrons and holes up to room temperature. 2D screening needs to be considered to explain the PL peak shifts in donor doped MQWs.

References

1. S Nakamura and G Fasol, "The Blue Laser Diode", Springer Verlag, 1997.
2. Y Narukawa, Y Kawakami, Sz Fujita, Sg Fujita, and S Nakamura, Phys Rev **B55**, R1938 (1997)
3. T Takeuchi, S Sota, M Katsuragawa, M Komori, H Takeuchi, H Amano and I Akasaki , Jpn J Appl Phys **36**, L382 (1997)
4. A Hangleiter, J S Im, H Kollmer, S Heppel, J Off, and F Scholz, MRS Internet J Nitride Semicond Res **3**, 15 (1998)
5. See e g I Akasaki and H Amano, Jpn J Appl Phys **36**, 5393 (1997)
6 B Monemar, J P Bergman, J Dalfors, P O Holtz, G Pozina, H Amano, and I Akasaki, submitted Phys Rev B, 1998.
7 K C Zeng, M Smith, J Y Lin, and H X Jiang, Appl Phys Lett **73**, 1724 (1998)
8 J P Bergman, N Saksulv, J Dalfors, P O Holtz, B Monemar, H Amano, and I Akasaki, Mat Res Soc Proc **482**, 631 (1998)
9 F Stern, Phys. Rev. Lett. **18**, 546 (1967)
10 M B Nardelli, K Rapcewicz, and J Bernholc, Appl Phys Lett **71**, 3135 (1997)

SPECTROSCOPIC STUDIES IN InGaN QUANTUM WELLS

S. F. Chichibu,[*,**] T. Sota[***], K. Wada,[****] S. P. DenBaars,[*] S. Nakamura[*****]

[*]Materials and ECE Departments, University of California, Santa Barbara, CA 93106
[**]Institute of Applied Physics, University of Tsukuba, 1-1-1 Tennodai, Tsukuba, Ibaraki 305-8573, Japan
chichibu@ims.tsukuba.ac.jp
[***]EECE Department, Waseda University, 3-4-1 Ohkubo, Shinjuku, Tokyo 169-8555, Japan
[****]Department of Materials Science and Engineering, Massachusetts Institute of Technology, 77 Massachusetts Ave., Cambridge, MA 02139
[*****]Department of Research and Development, Nichia Chemical Industries Ltd., 491 Oka, Kaminaka, Anan, Tokushima 774-8601, Japan

Cite this article as: MRS Internet J. Nitride Semicond. Res. 4S1, G2.7(1999).

Abstract

Fundamental electronic modulations in strained wurtzite III-nitride, in particular $In_xGa_{1-x}N$, quantum wells (QWs) were treated to explore the reason why practical InGaN devices emit bright luminescences in spite of the large threading dislocation (TD) density. The emission mechanisms were shown to vary depending on the well thickness L and InN molar fraction x. The electric field across the QW plane, F, which is a sum of the fields due to spontaneous and piezoelectric polarization and the pn junction field, causes the redshift of the ground state resonance energy through the quantum confined Stark effect (QCSE). The absorption spectrum is modulated by QCSE, quantum-confined Franz-Keldysh effect (QCFK), and Franz-Keldysh (FK) effect from the barrires when, for the first approximation, potential drop across the well ($F\backslash L$) exceeds the valence band discontinuity, ΔE_V. Under large $F\backslash L$, holes are confined in the triangular potential well formed at one side of the well. This produces apparent Stokes-like shift in addition to the in-plane net Stokes shift on the absorption spectrum. The QCFK and FK further modulate the electronic structure of the wells with L greater than the three dimensional (3D) free exciton (FE) Bohr radius, a_B. When $F\backslash L$ exceeds ΔE_C, both electron (e) and hole (h) confined levels drop into the triangular potential wells at opposite sides of the wells, which reduces the wavefunction overlap. Doping of Si in the barriers partially screens the F resulting in a smaller Stokes-like shift, shorter recombination decay time, and higher emission efficiency. Finally, the use of InGaN was found to overcome the field-induced oscillator strength lowering due to the spontaneous and piezoelectric polarization. Effective in-plane localization of the QW excitons (confined excitons, or quantized excitons) in quantum disk (Q-disk) size potential minima, which are produced by nonrandom alloy potential fluctuation enhanced by the large bowing parameter and F, produces confined e-h pairs whose wavefunctions are still overlapped when $L<a_B$. Their Coulomb interaction is more pronounced for $F\backslash L<\Delta E_V$.

Introduction

Major developments of III-nitride semiconductors[1,2] have led to the commercial production[1] of blue and green single quantum well (SQW) light-emitting-diodes (LEDs) and to the demonstration of multiple quantum well (MQW) purplish-blue laser diodes (LDs).[1-10] The growth of nearly TD-free GaN has been realized by the lateral epitaxial overgrowth (LEO) technique,[11-16] and the device lifetime of the cw MQW LDs has been extended up to 10,000 hours using low TD density GaN on sapphire[14] and *pure* GaN substrates[15] prepared by LEO technique. InGaN alloys are attracting special interest because they are adopted as active

Mat. Res. Soc. Symp. Proc. Vol. 537 © 1999 Materials Research Society

regions of ultra-violet (UV),[17] blue,[1] green,[1] and amber[18] SQW LEDs and all MQW LDs[1-10] and they emit bright luminescences despite of the large TD density up to 10^{10} cm^{-3}.[19] The emission mechanisms in InGaN alloys are not yet fully understood due to complex material physics and engineering, such as large and anisotropic effective masses,[20] polarization due to the wurtzite crystal lattice,[21,22] and phase separating nature[23,24] due to large lattice, thermal, and chemical mismatches.

Several groups have assigned the spontaneous emission from InGaN QWs to the recombination of excitons localized at certain potential minima.[1,25-27] On the other hand, several groups have discussed the importance of the quantum confined Stark effect (QCSE)[28] due to the piezoelectric field (F_{PZ}) in strained wurtzite InGaN QWs.[2,25,29-31] In particular, the blueshift of the electroluminescence (EL) peak in InGaN SQW LEDs[1] with increasing drive current has been explained[1,25] by the combined effects of a reduction of QCSE due to Coulomb screening of F_{PZ}[2,25,29] and band-filling of the energy tail states.[1,25] Moreover, characteristic optical gain mechanisms were reported for InGaN LD wafers[25,32-34] although gain spectra which can be explained by the well-known e-h plasma (EHP)[35] lasing model were reported.[36-38] In order to obtain an insight into what dominates the emission properties of InGaN QWs for further optimization of blue LDs, it is necessary to investigate the effects of effective bandgap inhomogeneity and electric field in the QW separately and consistently.

In this article, several important physics which affect the emission properties of InGaN QWs are discussed. First, the influence of F was reexamined on AlGaN/GaN and GaN/InGaN strained QWs to conclude that there exists polarization-induced and junction high electric fields across the strained QWs. Presence of QW excitons is shown for the wells with $L<a_B$ even under high F. Next the presence of effective bandgap inhomogeneity, which produces certain quantum disk-size localized potential minima in InGaN, in practical LEDs is shown. Finally the origin of the QW exciton localization was investigated by comparing optical properties of InGaN QWs grown on dislocated GaN-base on sapphire and nearly TD-free GaN overgrown laterally on the SiO_2 mask.

Framework

Optical properties peculiar to wurtzite InGaN and III-nitride materials in comparison to familiar III-V semiconductors such as GaAs or InP known to date are summarized as follows:

(i) Nitrides have an excitonic character in their optical properties. Indeed, dominant resonance structures due to A and B FEs were found in both absorption and photoreflectance spectra of 3D GaN layers, and FE emission has been found even at RT,[39,40] since the exciton binding energy, E_b, is as large as 26 meV and a_B is as small as 3.4 nm.[20,39-43] It is also known that E_b is increased in QWs[44] due to confinement of wavefunctions.

(ii) The wurtzite structure has the highest symmetry compatible with the existence of spontaneous polarization. Moreover, strain-induced piezoelectric tensor of wurtzite has three nonvanishing independent components. In the absence of the external fields, the total macroscopic polarization, P, is the sum of the spontaneous polarization in the equilibrium structure, P_0, and of the strain induced piezoelectric polarization, P_{PZ}.

(iii) InGaN alloys have an immisible gap[23,24] and they usually show broad luminescence band.[1]

In following arguments follow these information.

Polarization in wurtzite lattice

Since III-nitride epilayers grown on sapphire (0001) or SiC $(0001)_{Si}$ substrates are along the c-axis, we shall consider only the polarization along the c-axis, $P_3=P_{0,3}+P_{PZ,3}$. Bernardini *et al.*[21] calculated $P_{0,3}$ in AlN, GaN, and InN as -0.081, -0.029, and -0.032 C/m^2, respectively. $P_{0,3}$ induces the electric field according to $F_{0,3}=-P_{0,3}/\varepsilon_0\varepsilon_r$, and is estimated to be 3.4 MV/cm for GaN, which is nearly 50 times the ionization field, F_i, of FEs in 3D GaN (7.6×10^4 V/cm).[39] From the

fact that FE emissions can be observed from 3D GaN even at RT,[39] $F_{0.3}$ should be smaller than F_i. This may be due to internal screening of the polarization since the layer is usually too thick and any kinds of internal charges contribute to screening. An expression for $P_{PZ,3}$ under the biaxial strain $(a-a_0)/a_0=\varepsilon_{xx}=\varepsilon_{yy}=-(C_{33}/2C_{31})\varepsilon_{zz}$ is given by $P_{PZ,3}=2(e_{31}-e_{33}C_{31}/C_{33})\varepsilon_{xx}$, where a is the lattice constant, a_0 is that of strain-free material, C_{ij} are the elastic stiffness constants, and e_{ij} are the piezoelectric constants. Bernardini *et al.*[21] reported the following values in units of C/m^2: e_{33}=1.46 and e_{31}=-0.60 for AlN; e_{33}=0.73 and e_{31}=-0.49 for GaN; e_{33}=0.97 and e_{31}=-0.57 for InN. For in-plane compressive strains usually found in InGaN, the direction of F_{PZ} is from Ga face to N face (surface to substrate) according to Hellman[22] if we consider the Ga surface growth (+C). The direction of $F_{PZ,3}$ is opposite to $F_{0.3}$ and the pn junction field F_{pn}. This means that total electric field F exists in the QW regions of practical devices is a sum of polarization-induced fields and the pn junction field, $F_3=F_{0.3}+F_{pn}-F_{PZ,3}$. Details of this will be discussed elsewhere, and we simply consider the effect of F on the band structures of strained QWs in this article.

Schematic band diagrams of InGaN QWs under an electric field

From the framework (i) and (ii), physical scenarios of the optical transitions in InGaN QWs are drawn as follows. Since the critical thickness of $In_xGa_{1-x}N$ ($0<x<0.15$) is reported to be greater than 40 nm,[2,29] coherent growth of InGaN is assumed. This strain causes F_{PZ} but excitons should also be significant. Therefore the problem treated here is the behavior of confined energy levels in QWs under F, as discussed for GaAs/AlGaAs QWs in the 1980's.[28,44,45] In QWs, FE absorption is observed even at RT under high F across the QW[28,44] due to quantum confinement of the wavefunctions which enhances the Coulomb interaction between the e-h pair to increase E_b.[44] Miller *et al.*[28] have observed an excitonic absorption in GaAs QWs, which was redshifted by 2.5 times the zero-field E_b for $F=10^5$ V/cm (50 times the F_i of 3D excitons). They have explained the redshift in terms of field modulation of quantized energy levels (QCSE).[28] We estimate[46] E_b in GaN / $Al_{0.1}Ga_{0.9}N$ QWs under F=0 as a function of L according to Bastard *et al.*[44] introducing finite barrier height. The obtained E_b value for L=3 nm is 47 meV and F_i is estimated to be 6.0×10^5 V/cm taking into account the shrinkage of e-h distance in z-direction down to 0.78 nm. E_b is 37 meV for L=6 nm.

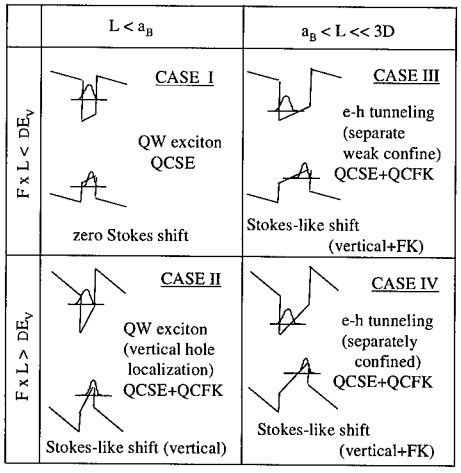


Fig.1 Schematic band diagrams of GaN/InGaN QWs under the electric field F. Each case represents the restrictions determined among F, L, ΔE_V, and a_B.

Taking the small fraction (1/4) of ΔE_V against the conduction band discontinuity ΔE_C into account,[47] schematic band diagrams of InGaN / GaN QWs are drawn in Fig. 1 for several cases; i.e. restrictions among FxL, ΔE_V, and a_B. Since the restriction $FxL>\Delta E_V$ breaks before breaking $FxL>\Delta E_C$ with increasing F or L, restrictions between FxL and ΔE_V and between L and a_B (quantum size effect) only are drawn in Fig.1. Note that in-plane (lateral) bandgap inhomogeneity is omitted.

In CASE I, both electron and hole wavefunctions are confined in the well and have unique quantized energy levels where zero Stokes-like shift is expected though the resonance energy slightly shifts to lower energy due to QCSE. In CASE II, at least the hole wavefunction drops into the triangular shape potential well at one side of the well, and

continuum states are formed at the rest of the potential slope inside the QW region. In addition the penetration of the barrier continuum wavefunction cannot be neglected. Therefore vertical component Stokes-like shift is produced. For the extreme situation of CASE II (pronounced CASE II), both the e-h wavefunctions drop into the triangular potential wells formed at opposite sides of the well resulting in z-directional separation. In CASE III and IV, the absorption tail would be modulated due primarily to QCSE[28] and QCFK.[45]

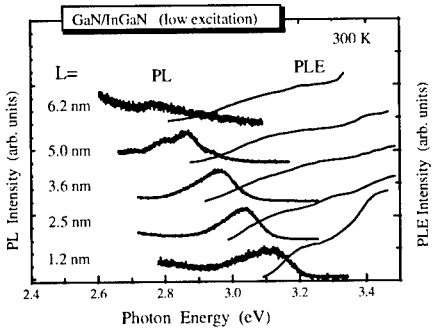


Fig.2 Low excitation PL and PLE spectra at RT of $In_{0.1}Ga_{0.9}N$ / GaN:Si MQWs for different well thickness, L. The apparent bandgap is defined as the energy where the PLE signal intensity drops to half the maximum.

Optical properties as a function of QW thickness

Low excitation PLE and PL spectra at RT of $In_{0.1}Ga_{0.9}N$/GaN MQWs with various L are shown in Fig. 2. The PL spectra exhibited a broad luminescence peak due to InGaN QWs, whose full width at half maximum (FWHM) was nearly 120 meV. The PL peak showed a redshift by 360 meV with increasing L from 1.2 to 6.2 nm, and the intensity decreased for L>3.6 nm ($L>a_B$). The PLE spectra exhibited broadened absorption tail except for the L=1.2 nm case. The broadening was pronounced for wells with $L>a_B$. These results agree with the scenario that the QW configuration changes from CASE I, II, to IV due to increasing L assuming constant x and F_{PZ}. The apparent bandgap energy determined as the energy where the PLE signal intensity drops to half the maximum, PL peak energies, and Stokes-like shifts are plotted as a function of L in Fig. 3. As expected, the apparent Stokes-like shift increased from nearly 50 meV to 220 meV. Since in CASE I, zero Stokes-shift is expected if the well had a homogeneous bandgap energy, the observed Stokes shift for CASE I ($L<a_B$) directly shows the presence of in-plane net Stokes shift due to localized energy states in the QW. Similar results were obtained at 4 K where the Stokes-shift was nearly 100 meV (L<2.5 nm). The observed blueshift of the high excitation PL peak indicates presence of high F across the wells.

In order to estimate F, confined energy levels and wavefunctions in $In_{0.1}Ga_{0.9}N$ QWs are calculated as functions of F, L, and n in the barrier by variational method neglecting E_b within the Hartree approximation by solving the Schrödinger equation and Poisson equation simultaneously and self-consistently. We did not fit the data but simply calculated and compared the relation between the low excitation PL peak energy and L (L<3.6 nm) in Fig. 3. As a result, the zero-field bandgap of the 3D InGaN well is obtained to be 2.92 eV and ΔE_C and ΔE_V are estimated to be about 400 and 100 meV, respectively. F is estimated to be nearly 3.5×10^5 V/cm which gives Stark shift of nearly 45 meV in the 3-nm-thick QW. Examples of the calculated quantized energy levels and e-h wavefunctions for InGaN under F=400 kV/cm are shown in Fig. 4. Under F=3.5×10^5 V/cm, F×L exceeds

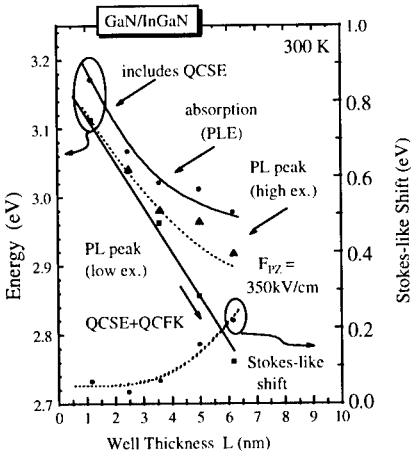


Fig.3 High and low excitation PL peak energies, apparent bandgap energy estimated from PLE spectra, and apparent Stokes-like shift of $In_{0.1}Ga_{0.9}N$ wells at RT as a function of L.

ΔE_V for L>3.4 nm. The hole confined level would already be formed in the triangular potential (CASE II) between 2.5 and 3.6 nm. Beyond this, the system belongs to CASE IV where the e-h are confined in opposite sides of the well, as shown in Fig. 4. This may explain the extremely long decay time τ in terms of reduction of the oscillator strength for large L at low temperature where nonradiative recombination is suppressed. At 4 K, τ was nearly 35 ns for L=5nm (>a_B). This may cause serious degradation of the emission intensity. Relatively shorter τ (0.97-4 ns) for L<2.5 nm at 4 K indicates that the overlap of the e-h wavefunction is still large because L is smaller than a_B. Note that the estimated F_i (6.0×10^5 V/cm) is larger than F (3.5×10^5 V/cm), which implies that Coulomb interaction between the e-h pair still remains. This kind of particles can be regarded as QW excitons.

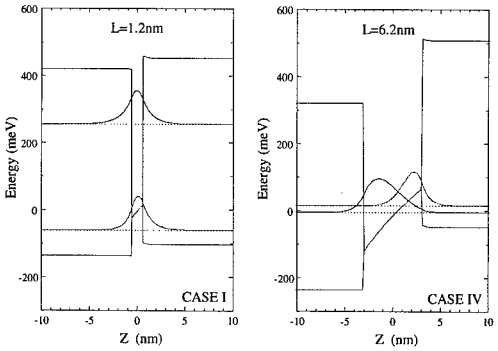


Fig.4 Quantized energy levels and wavefunctions of e-h pair in $In_{0.1}Ga_{0.9}N$ SQW under the condition of F=400kV/cm.

Optical properties as a function of InN molar fraction x

Next sample series have a 3-nm-thick InGaN SQW with various x, which correspond to CASE I, II, and pronounced CASE II. Note that change in x changes in ΔE_C, ΔE_V, and F_{PZ} simultaneously. The PLE spectra broadened and the PL peak energy showed pronounced redshift with increasing x, as shown in Fig. 5. The QW (x=0.03) exhibited a sharp onset of the PLE spectra at 3.3 eV, as is the case with L=1.2 nm in Fig. 2. If we assume a linear relation between F_{PZ} and x, F_{PZ} is estimated to be nearly 1.1×10^5 V/cm. The PLE spectra were taken at 10 K, and the sample is considered to belong to CASE I, as shown in Fig. 6. The appearance of the Stokes shift in the CASE I sample again indicates the presence of localized energy states. With increasing x, first the hole confined level drops into the triangular potential, as shown in Fig. 6 (400 kV/cm), and that of electron will also drop into the triangular potential at opposite side for higher x (pronounced CASE II). This scenario explain the broadness of the PLE spectra with increasing x. In addition, the spatial separation of the e-h pair normal to the QW plane may reduce the wavefunction overlap and

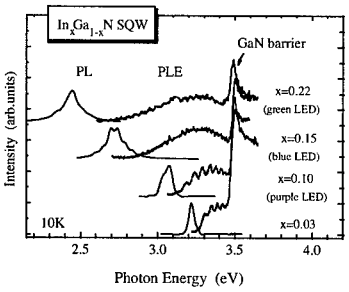


Fig.5 Low excitation PL and PLE spectra at 10 K of 3-nm-thick $In_xGa_{1-x}N$ / GaN:Si SQW structures with different InN molar fraction, x. The x values are estimated assuming coherent growth.

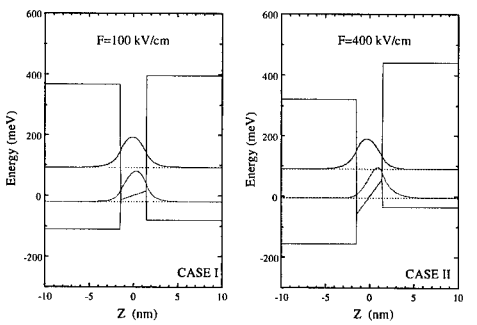


Fig.6 Quantized energy levels and wavefunctions of e-h pair in 3-nm-thick InGaN SQW under the condition of F=100kV/cm (x=0.03) and 400kV/cm (x=0.1).

increase the emission decay time with increasing x. However, as shown in Fig.6, the overlap of e-h wavefunction is still large.

Both the Stokes-like shift and the decay time had a critical x[25] of nearly 0.1 as shown in Fig. 7. This composition is considered to correspond to the point that the band diagram changes from CASE I to CASE II or pronounced CASE II where the absorption due to continuum states from barriers becomes remarkable. On the other hand, the degree of effective bandgap inhomogeneity suddenly increases by alloying In then increase monotonically with increasing x, judging from the values of PL FWHM, as shown in Fig. 7.

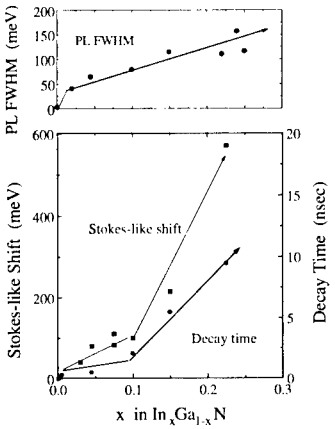


Fig.7 PL FWHM, apparent Stokes-like shift, and TR-PL decay time of 3-nm-thick $In_xGa_{1-x}N$ QWs as a function of x.

Coulomb screening effects by Si-doping of GaN barriers

One of the effective methods to screen polarization-induced F is by doping the wells or barriers. If the injected or doped charge density is enough to screen F_{PZ}, the pronounced CASE II QWs may recover wavefunction overlap.[25] Quantized energy levels and wavefunctions of a 3-nm-thick $In_{0.13}Ga_{0.87}N$ SQWs for F=0, F=500 kV/cm, and F=500 kV/cm with injected e-h pair density of 4×10^{12} cm^{-2} are shown in Fig. 8. As shown, the wavefunction overlap and the transition energy between the energy levels were recovered by the Si-doping. To confirm this experimentally, 3-nm-thick $In_{0.13}Ga_{0.87}N$ / GaN MQWs with different Si-doping concentrations in the GaN barriers were examined. F_{PZ} in the undoped MQW is estimated to be $5\text{-}6\times10^5$ V/cm.

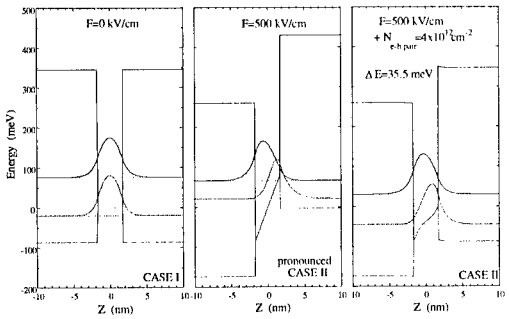


Fig.8 Quantized energy levels and wavefunctions of e-h pair in 3-nm-thick InGaN SQW under the condition of F=0kV/cm. F=500kV/cm, and F=500kV/cm and $N_{e\text{-}h\ pair}=4\times10^{12}cm^{-2}$.

The PL peak shifted to higher energy and the absorption tail in the PLE spectrum decreased by doping Si up to 10^{19} cm^{-3}, as shown in Fig. 9. The apparent resonance energy shifted to higher energy by 50 meV, which nearly agrees with Fig.8, and the apparent Stokes-like shift decreased from 220 meV to 120 meV. At the same time, the emission decay time τ decreased from 14 ns to 850 ps with increasing Si-doping. These results indicate that F_{PZ} was effectively screened, and the overlap of the e-h wavefunction was recovered. Note that screening of F_{PZ} reduces the slope of the conduction and valence bands within the QW to result in sharp onset of the absorption tail. This reduces the "vertical" component of the apparent Stokes-like shift. Of course, increased electron density due to the modulation doping may

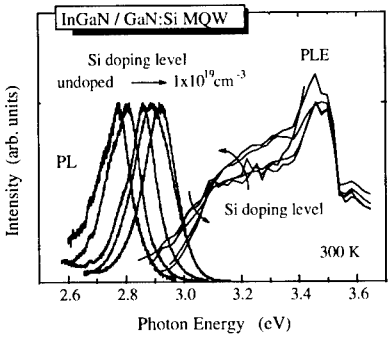


Fig.9 Low-excitation PL and PLE spectra at 300 K of $In_{0.13}Ga_{0.87}N$/GaN MQWs for different Si-doping concentrations (n). PLE edge was sharpened and the PL peak blueshifted with increasing n.

improve the radiative recombination rate, and the electrons will fill the energy tail states at the same time. The sample with the highest doping level showed the shortest τ=850 ps and the brightest emission. This value seems to be close to the intrinsic radiative recombination lifetime. The longer τ usually observed in the practical LEDs will be discussed later.

Why InGaN emits efficient luminescences / In-plane localization of QW excitons

Blue and green InGaN SQW LEDs show blueshift of the EL peak energy with increasing driving current.[1,25,48] This has been explained by combined effects of Coulomb screening of F_{PZ} and band filling of the localized energy states by QW excitons.[25] Really recently, Mukai *et al.*[49] reported that current and temperature dependences of the EL peak energy of 5.5-nm-thick $In_xGa_{1-x}N$ SQW LEDs change drastically at a critical emission peak wavelength of 375 nm. When x is very small, LEDs do not show any blueshifts but show temperature dependence. Conversely, when x is larger than corresponding emission peak of 375 nm, the LEDs show nearly temperature-independent but current density-dependent EL peak energy. Moreover, the output power of UV LEDs increase with increasing wavelength in UV region longer than 370nm where the self-absorption due to GaN base layer is already negligible. These results indicate that the emission mechanisms change with x, and those of GaN QW and InGaN QW are totally different.

Another supporting evidence of the importance of exciton localization in InGaN is shown in Fig. 10. Figure 10 shows the optical transmittance at 10 K and RT and high excitation PL spectra at RT of a 5-nm-thick GaN / $Al_{0.15}Ga_{0.85}N$ double-hetero (DH) structure grown on thick $Al_{0.3}Ga_{0.7}N$ base layer and those of 5.5-nm-thick $Al_{0.15}Ga_{0.85}N$ / InGaN / $Al_{0.1}Ga_{0.9}N$ DH structure (SQW UV-LED)[49] grown on thick GaN base. Since the former sample was grown on thick $Al_{0.3}Ga_{0.7}N$ to observe QW absorption spectrum, both GaN/AlGaN/AlGaN and InGaN/AlGaN/GaN QWs suffer from compressive biaxial strain. Then the F_{PZ} is opposite to the pn junction field. Against F_{PZ}, the GaN/AlGaN SQW exhibits an excitonic absorption peak up to RT, as predicted form the increase of E_b in QWs.[25,28,46,50] Therefore InGaN SQW would also show the excitonic character. Since the PL peak energy of InGaN/AlGaN SQW is higher than that of GaN/AlGaN SQW, the QW resonance energy of GaN/AlGaN should be smaller than that of InGaN/AlGaN structure, which means that QCSE due to F_{PZ} dominates the optical transitions in the binary GaN wells. Accordingly, the PL intensity of GaN/AlGaN SQW was far lower than that of InGaN/AlGaN, although the self-absorption due to the GaN base is remarkable for the particular UV-LED structure. Note that the PL peak energy agrees with the excitonic absorption peak at RT and excitons are delocalized for the GaN/AlGaN SQW, which is different from the results obtained from InGaN QWs.

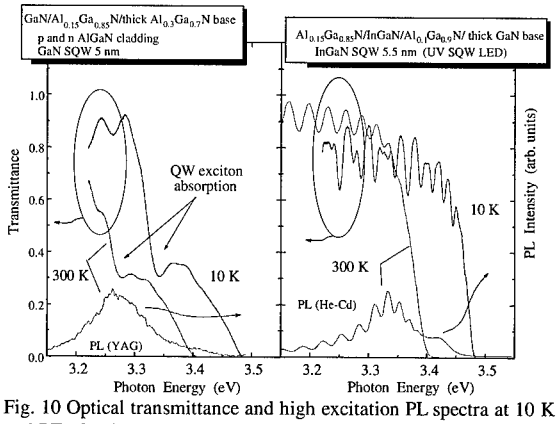


Fig. 10 Optical transmittance and high excitation PL spectra at 10 K and RT of a 5-nm-thick GaN / $Al_{0.15}Ga_{0.85}N$ DH structure grown on thick $Al_{0.3}Ga_{0.7}N$ base layer and those of 5.5-nm-thick InGaN / $Al_{0.1}Ga_{0.9}N$ DH structure (SQW UV-LED)[49] grown on thick GaN base.

Typical wide-area and spot-excitation CL spectra at 10 K of a 3-nm-thich $In_{0.1}Ga_{0.9}N$ SQW are shown in Fig. 11. Although the effect of the multiple interference fringes on the CL spectra is not negligible, wide area (10 μm$\times$10 μm) broad CL band (FWHM nearly 100 meV) consists of many sharp peaks (FWHM less than 20

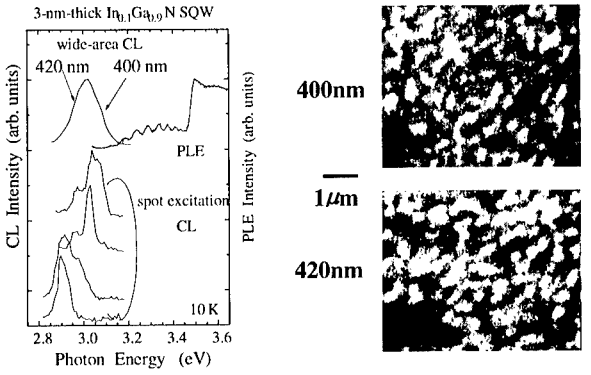


Fig.11 Wide-area (10 μmμ10 Xm) scanning and spot excitation CL spectra of 3-nm-thick $In_{0.1}Ga_{0.9}N$ SQW capped by a 6-nm-thick GaN. The broad CL peak (FWHM=100 meV) consists of several sharp emission peaks (FWHM=20 meV) having different peak energies. Monochromatic CL images taken at 400 and 420 nm showed primarily the complimentary relation. The resolution of the CL mapping is limited by the diffusion length, which was nearly 60 nm in lateral direction.

meV)[51] at 10 K. This clearly shows that the broad CL band consists of sharper emission peaks having various peak energies. Therefore, there exist several *structures* composed of an InN-rich part surrounded by a GaN-rich part in each spot area. This *structure* may be due to mesoscopic compositional undulation and it can act as quantum-disks (Q-disks),[52] dots, or segmented QWs having compositional and/or size inhomogeneity. Monochromatic scanning CL images of the same GaN-capped $In_{0.1}Ga_{0.9}N$ SQW taken at wavelengths of 400 nm and 420 nm are also shown in Fig. 11. A careful comparison between the two images using a triangular-shaped dark marker on the bottom-left corner indicated following results; (a) each bright (white in the figure) area consists of emissions from real spaces of about 60-400 nm in lateral size, (b) some dark areas in one figure correspond complementary to bright ones in the other figure, and (c) some areas exhibit both 400 and 420 nm CL emissions. These results can also be explained by the existence of compositional undulation whose lateral interval is smaller than 60 nm, which value is the spatial resolution of the system (diffusion length). Supporting evidences of the short diffusion length in InGaN QWs were reported by Rosner *et al.*[53,54] They showed less pronounced CL contrast in InGaN SQW compared to GaN.[54] Sato *et al.*[55] estimated the PL intensity as a function of TD density and also supported the short diffusion length model in InGaN QWs.[51] The result (c) indicates that the real area that emits CL is far smaller than the diffusion length (60 nm). Kisielowski *et al.*[56] and Ponce *et al.*[57] estimated the structural size of InN-rich clusters to be less than 10 nm and 20 nm, respectively. Such CL nanostructure was also found for compositions as low as x=0.03. This means that large FWHM of the PL peak and broadness of the PLE signal edge for the CASE I QWs represent the in-plane effective emission bandgap inhomogeneity. Note that e-h wavefunctions in the Q-disks are confined with respect to the z-direction, and Q-disks or Q-dots can improve the emission efficiency of QW excitons due to the lateral confinement in limited spaces, that can reduce nonradiative pathways. This is the reason why InGaN exhibits bright spontaneous emissions. Naturally, it overcomes disadvantages of using wurtzite materials due to the polarization-induced electric fields. The e-h wavefunctions are still overlapped even in the pronounced CASE II. The emission lifetime is affected by both the e-h pair separation due to F_{PZ} and in-plane localization for CASE II and pronounced CASE II. In Q-disks, the spontaneous emission lifetime becomes long since the emission is prohibited when the wave vector of exciton center-of-mass motion is above the critical energy.[52]

Origin of exciton localization

One of the possible origins of the in-plane bandgap inhomogeneity is an inhomogeneous distribution of F_{PZ} due to strain fluctuation. If we attribute the in-plane net Stokes shift to this, the potential fluctuation can be leveled by filling carriers to screen F_{PZ}. However, the FWHM of PL or EL in InGaN QWs does not

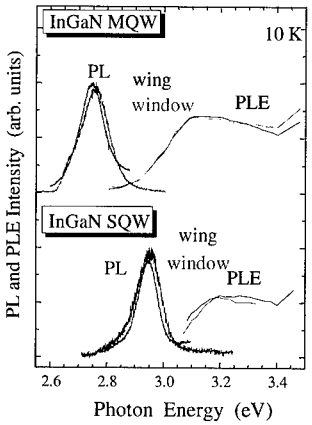


Fig. 12 PL and PLE spectra at 10 K obtained from InGaN SQW and MQW structures grown on LEO window and LEO wing regions.

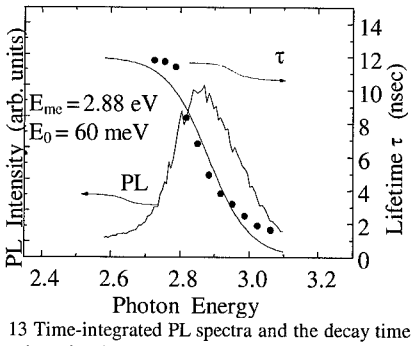


Fig. 13 Time-integrated PL spectra and the decay time τ as a function of emission energy at RT of InGaN MQW grown on the LEO wing.

change or even increase with increasing excitation level. Therefore, an intrinsic compositional inhomogeneity is the most probable. Keller *et al.*[58] found a spiral growth of InGaN initiated by the mixed character TDs. If such a growth mode accumulates In to the growth step edge, compositional inhomogeneity would be produced. To investigate this, optical properties of InGaN QWs were investigated as a function of TD density[59] using LEO technique. A series of InGaN QWs were grown on dislocated GaN grown from the SiO_2 mask opening (window) and nearly TD-free GaN laterally overgrown on SiO_2 from the opening (wing) at the same time in order to minimize run-to-run or place-to-place fluctualtion. Figure 12 shows PL and PLE spectra at 10 K of InGaN SQW and MQW structures grown on the window and wing. As shown, they showed exactly the same properties. The luminescence decay time τ measured by the time-resolved PL measurements was 6 ns at RT for the MQW structure, and was independent of TD density.[59] The low temperature PL lifetime was also independent of the TD density. In addition, the energy resolved τ of nearly TD-free InGaN MQW increased with decreasing the photon energy, as shown in Fig. 13. This is characteristics of the localized electronic system. The relation between τ and E was fitted using $\tau(E)=\tau_r/\{1+\exp[(E-E_{me})/E_0]$, where E_0=60 meV represents the depth in the tail states, E_{me}=2.88 eV is the energy similar to the mobility edge, and τ_r=12 ns is the radiative lifetime. These values are reasonable for the device-quality InGaN QW[1] systems with highly lattice mismatched nonrandom alloy broadening.

It should be noted that all the optical properties do not depend on TD density. Conversely, the in-plane net Stokes shift is affected by changing the barrier growth rate[60] and InN molar fraction of the QWs.[25] Therefore the in-plane effective bandgap inhomogeneity is caused by growth parameters, point defects, or thermodynamics rather than phase separation initiated by TDs. Anomalous temperature independence of the luminescence peak energy[1,25] cannot be explained only by an inhomogeneous F_{PZ}. Since the change in x changes F_{PZ}, the Q-disk size / segmented QW potential may, at least partly come from the nonrandom alloy potential fluctuation emphasized by the large bowing parameter in InGaN.[2,29,61]

For LDs, the effective bandgap inhomogeneity more than 50 meV is too large to obtain an uniform EHP in the well. Indeed, some InGaN MQW LDs showed EHP lasing in tail states.[25,26,32-34,62] This may cause the increase of threshold current density of InGaN LDs in terms of reduiction in differential gain.[62]

Summary

Importance of QW exciton localization into the energy tail states was explained in addition to high-field effects in InGaN QWs. This Q-disk size potential minima make the diffusion length short and effectively

keep carriers away from nonradiative pathways, which is a distinct difference between GaN and InGaN QWs. Strong F_{PZ} separate e-h pair into triangular potential wells formed at opposite sides of the well and apparent Stokes-like shift is dominated by F_{PZ} for CASE II, III, and IV. The oscillator strength of the separate e-h pair is very small for CASE III and IV. State-of-the-art InGaN LEDs and LDs generally have QWs with L = 2.5-3.5 nm and most of blue, green, and amber LEDs may belong to pronounced CASE II. However, the overlap of e-h wavefunctions is recovered by screening F_{PZ} by injecting carriers or doping Si, resulting in huge blueshift of the emission peak and a decrease of the apparent Stokes-like shift. Note that vertical e-h pair distance is still smaller than a_B, resulting in large overlap of their wavefunctions. Therefore the localized QW excitons have strong Coulomb interaction provided that $L<a_B$. In order to understand precise mechanisms of the bandgap inhomogeneity and carrier localization, and to obtain long wavelength LDs expanding from pure green to red wavelengths, fabrication and investigation of cubic zincblende InGaN QWs are mandatory to eliminate the modulation due to strain-induced piezoelectricity.

Acknowledgments

The authors are grateful to Professors U. Mishra, L. Coldren, J. Bowers, E. Hu, J. Speck, and K. Suzuki, and Drs. S. Keller, S. Fleischer, D. Cohen, J. Ibbetson, C. Bulutay, T. Azuhata, and T. Uenoyama for helpful discussions. The authors would like to thank A. Abare, M. Mack, M. Minsky, T. Deguchi, A. Shikanai, K. Torii, P. Kozodoy, M. Hansen, P. Fini, and H. Marchand for help in the experiments. The first author is thankful to Professor H. Nakanishi and Professor Y. Horikoshi for continuous encouragement.

References

[1] S. Nakamura and G. Fasol, *The Blue Laser Diode*, (Springer, Berlin, 1997).
[2] for a review, I. Akasaki, and H. Amano, Jpn. J. Appl. Phys. **36**, 5393 (1997).
[3] I. Akasaki, S. Sota, H. Sakai, T. Tanaka, M. Koike, and H. Amano, Electron. Lett. **32**, 1105 (1996).
[4] K. Itaya, M. Onomura, J. Nishio, L. Sugiura, S. Saito, M. Suzuki, J. Rennie, S. Nunoue, M. Yamamoto, H. Fujimoto, Y. Kokubun, Y. Ohba, G. Hatakoshi, and M. Ishikawa, Jpn. J. Appl. Phys. **35**, L1315 (1996).
[5] G. Bulman, K. Doverspike, S. Sheppard, T. Weeks, H. Kong, H. Dieringer, J. Edmond, J. Brown, J. Swindell, and J. Schetzina, Electron. Lett. **33**, 1556 (1997).
[6] A. Kuramata, K. Domen, R. Socjima, K. Horino, S. Kubota, and T. Tanahashi, Jpn. J. Appl. Phys. **36**, L1130 (1997).
[7] M. Mack, A. Abare, M. Aizcorbe, P. Kozodoy, S. Keller, U. Mishra, L. Coldren, and S. DenBaars, MRS Internet J. Nitride Semicond. Res. **2**, 41 (1997); J. Cryst. Growth **180/190**, 837 (1998).
[8] F. Nakamura, T. Kobayashi, T. Asatsuma, K. Funato, K. Yanashima, S. Hashimoto, K. Naganuma, S. Tomioka, T. Miyajima, E. Morita, H. Kawai, and M. Ikeda, J. Cryst. Growth **180/190**, 841 (1998).
[9] M. Kneissl, D. P. Bour, N. M. Johnson, L. T. Romano, B. S. Krusor, R. Donaldson, J. Walker, and C. Dunnrowicz, Appl. Phys. Lett. **72**, 1539 (1998).
[10] Yamada, Y. Kaneko, S. Watanabe, Y. Yamaoka, T. Hidaka, S. Nakagawa, E. Marenger, T. Takeuchi, S. Yamaguchi, H. Amano, and I. Akasaki, Proc. 10th IEEE Lasers and Electro-Optics Society Annual Meeting, San Francisco, USA, Nov. 10-13, 1997, PD1.2.
[11] application of LEO technique is introduced in several publications. For example, E. Bauser, *Thin film growth techniques for low dimensional structures*, eds. R. Farrow, S. Parkin, P. Dobson, J. Neave and A. Arrott (Plenum, New York, 1987), p. 171.
[12] A. Usui, H. Sunakawa, A. Sakai, and A. Yamaguchi, Jpn. J. Appl. Phys. **36**, L899 (1997); A. Sakai, H. Sunakawa, and A. Usui, Appl. Phys. Lett. **71**, 2259 (1997).
[13] T. Zheleva, O-H. Nam, M. Bremser, and R. Davis, Appl. Phys. Lett. **71**, 2472 (1997); O-H. Nam, M. Bremser, T. Zheleva, and R. Davis, Appl. Phys. Lett. **71**, 2638 (1997).

[14] S. Nakamura, M. Senoh, S. Nagahama, N. Iwasa, T. Yamada, T. Matsushita, H. Kiyoku, Y. Sugimoto, T. Kozaki, H. Umemoto, M. Sano, and K. Chocho, Jpn. J. Appl. Phys. **36**, L1568 (1997); Appl. Phys. Lett. **72**, 211(1998).
[15] S. Nakamura, M. Senoh, S. Nagahama, N. Iwasa, T. Yamada, T. Matsushita, H. Kiyoku, Y. Sugimoto, T. Kozaki, H. Umemoto, M. Sano, and K. Chocho, Jpn. J. Appl. Phys. **37**, L309 (1998).
[16] H. Marchand, J. Ibbetson, P. Fini, P. Kozodoy, S. Keller, S. DenBaars, J. Speck, and U. Mishra, MRS Internet J. Nitride Semicond. Res. **3**, 3 (1998); H. Marchand, X. H. Wu, J. Ibbetson, P. Fini, P. Kozodoy, S. Keller, J. Speck, S. DenBaars, and U. Mishra, Appl. Phys. Lett. **73**, 747 (1998).
[17] T. Mukai, D. Morita, and S. Nakamura, J. Cryst. Growth **189/190**, 778 (1998).
[18] T. Mukai, H. Narimatsu, and S. Nakamura, Jpn. J. Appl. Phys. **37**, L479 (1998).
[19] F. Ponce and D. Bour, Nature **386**, 351 (1997).
[20] M. Suzuki, T. Uenoyama, and A. Yanase, Phys. Rev. B **52**, 8132 (1995).
[21] F. Bernardini, V. Fiorentini, and D. Vanderbilt, Phys. Rev. B **56**, R10024 (1997).
[22] polarity problem has been reviewed in E. Hellman, MRS Internet J. Nitride Semicond. Res. **3**,11 (1998).
[23] A. Koukitsu, N. Takahashi, T. Taki, and H. Seki, Jpn. J. Appl. Phys. **35**, L673 (1996); I-hsiu Ho and G. B. Stringfellow, Appl. Phys. Lett. **69**, 2701 (1996).
[24] Osamura, S. Naka, and Y. Murakami, J. Appl. Phys. **46**, 3432 (1975); R. Singh, D. Doppalapudi, T. D. Moustakas, and L. Romano, Appl. Phys. Lett. **70**, 1089 (1997).
[25] properties of localized excitons in InGaN QWs are summarized in previous papers [S. Chichibu, T. Sota, K. Wada, and S. Nakamura, J. Vac. Sci. Technol. B **16**, 2204 (1998) and S. Chichibu, A. Abare, M. Mack, M. Minsky, T. Deguchi, D. Cohen, P. Kozodoy, S. Fleischer, S. Keller, J. Speck, J. Bowers, E. Hu, U. Mishra, L. Coldren, S. DenBaars, K. Wada, T. Sota, and S. Nakamura, European Mater. Res. Soc. 98 Spring Meeting, Session L-IV.1, Strasbourg, France, June 16-19 (1998); Mater. Sci. Eng. B (1998; unpublished)]; original papers are S. Chichibu, T. Azuhata, T. Sota, and S. Nakamura, Appl. Phys. Lett. **69**, 4188 (1996); **70**, 2822 (1997); **73**, 2006 (1998).
[26] E. Jeon, V. Kozlov, Y. Song, A. Vertikov, M. Kuball, A. Nurmikko, H. Liu, C. Chen, R. Kern, C. Kuo, and M. Crawford, Appl. Phys. Lett. **69**, 4194 (1996); A. Vertikov, A. Nurmikko, K. Doverspike, G. Bulman, and J. Edmond, *ibid* **73**, 493 (1998).
[27] Y. Narukawa, Y. Kawakami, Sz. Fujita, Sg. Fujita, and S. Nakamura, Phys. Rev. B **55**, R1938 (1997); Y. Narukawa, Y. Kawakami, M. Funato, Sz. Fujita, Sg. Fujita, and S. Nakamura, Appl. Phys. Lett. **70**, 981 (1997).
[28] D. A. Miller, D. S. Chemla, T. C. Damen, A. C. Gossard, W. Wiegmann, T. H. Wood, and C. A. Burrus, Phys. Rev. Lett. **53**, 2173 (1984); Phys. Rev. B **32**, 1043 (1985).
[29] T. Takeuchi, H. Takeuchi, S. Sota, H. Sakai, H. Amano, and I. Akasaki, Jpn. J. Appl. Phys. **36**, L177 (1997); T. Takeuchi, S. Sota, M. Katsuragawa, M. Komori, H. Takeuchi, H. Amano, and I. Akasaki, Jpn. J. Appl. Phys. **36**, L382 (1997); C. Wetzel, H. Amano, I. Akasaki, T. Suski, J. Ager, E. Weber, E. Haller, and B. K. Meyer, Mater. Res. Soc. Symp. Proc. **482**, 489 (1998).
[30] J. Bergman, N. Saksulv, J. Dalfors, P. Holtz, B. Monemar, H. Amano, and I. Akasaki, Mater. Res. Soc. Symp. Proc. **482**, 631 (1998).
[31] J. Im, H. Kollmer, J. Off, A. Sohmer, F. Scholz, and A. Hangleiter, Phys. Rev. B **57**, R9435 (1998).
[32] T. Deguchi, T. Azuhata, T. Sota, S. Chichibu, and S. Nakamura, Mater. Sci. Eng. B **50**, 251 (1997); T. Deguchi, A. Shikanai, K. Torii, T. Sota, S. Chichibu, and S. Nakamura, Appl. Phys. Lett. **72**, 3329(1998).
[33] G. Mohs, T. Aoki, M. Nagai, R. Shimano, M. K-Gonokami, and S. Nakamura, Solid State Commun. **104**, 643 (1997).
[34] S. Chichibu, D. Cohen, M. Mack, A. Abare, P. Kozodoy, M. Minsky, S. Fleischer, S. Keller, J. Bowers, U. Mishra, L. Coldren, D. Clarke, and S. DenBaars, Appl. Phys. Lett. **73**, 496 (1998).
[35] H. Haug and S. Koch, *Quantum Theory of the Optical and Electronic Properties of Semiconductors*, (World Scientific, Singapore, 1990); W. Chow, S. W. Koch, and M. Sargent III, *Semiconductor-Laser*

Physics, (Springer, Berlin, 1994); W. Chow, A. Wright, and J. Nelson, Appl. Phys. Lett. **68**, 296 (1996).
[36] G. Frankowsky, F. Steuber, V. Härle, F. Scholz, and A. Hangleiter, Appl. Phys. Lett. **68**, 3746 (1996).
[37] D. Wiesmann, I. Brener, L. Pfeiffer, M. Kahn, and C. Sun, Appl. Phys. Lett. **69**, 3384 (1996).
[38] M. Kuball, E. Jeon, Y. Song, A. Nurmikko, P. Kozodoy, A. Abare, S. Keller, L. Coldren, U. Mishra, S. DenBaars, and D. Steigerwald, Appl. Phys. Lett. **70**, 2580 (1997).
[39] S. Chichibu, T. Azuhata, T. Sota, and S. Nakamura, J. Appl. Phys. **79**, 2784 (1996); Proc. Int. Symp. On Blue Laser and Light Emitting Diodes (Ohmsha, Tokyo, 1996), pp.202; S. Chichibu, H. Okumura, S. Nakamura, G. Feuillet, T. Azuhata, T. Sota, and S. Yoshida, Jpn. J. Appl. Phys. **36**, 1976 (1997).
[40] B. Monemar, J. P. Bergman, H. Amano, I. Akasaki, T. Detchprohm, K. Hiramatsu, and N. Sawaki, Proc. Int. Symp. on Blue Laser and Light Emitting Diodes (Ohmsha, Tokyo, 1996), pp. 135.
[41] R. Dingle, D. D. Sell, S. E. Stokowski, and M. Ilegems, Phys. Rev. B **4**, 1211 (1971).
[42] B. Monemar, Phys. Rev. B **10**, 676 (1974).
[43] S. Chichibu, A. Shikanai, T. Azuhata, T. Sota, A. Kuramata, K. Horino, and S. Nakamura, Appl. Phys. Lett. **68**, 3766 (1996); A. Shikanai, T. Azuhata, T. Sota, S. Chichibu, A. Kuramata, K. Horino, and S. Nakamura, J. Appl. Phys. **81**, 417 (1997).
[44] G. Bastard, E. E. Mendez, L. L. Chang, and L. Esaki, Phys. Rev. B **26** (1982) 1974.
[45] D. A. B. Miller, D. S. Chemla, and S. Schmitt-Rink, Phys. Rev. B **33** (1986) 6976.
[46] E_b in GaN / $Al_{0.1}Ga_{0.9}N$ QW was calculated according to Ref. 44 using a variational method. We further consider the finite well potential. An usual variational function with two variational parameters was used as an envelop function of exciton, i.e. $\exp\{-[r^2/a^2+(z_e-z_h)^2/b^2]\}$, where a and b are the variational parameters, r is the absolute value of the relative position of electron and hole in the QW plane, and z_e (z_h) is the transformed z coordinate of the electron (hole).
[47] C. G. Van de Walle and J. Neugebauer, Appl. Phys. Lett. **70**, 2577 (1997).
[48] T. Taguchi, presented at the 43rd Spring Meeting of the Japan Society of Applied Physics and Related Societies, Asaka, Japan, Mar.29, 1996 (unpublished).
[49] T. Mukai, M. Yamada, and S. Nakamura, Jpn. J. Appl. Phys. **37**, L1358 (1998).
[50] C. Bulutay, N. Dagli, and A. Imamoğlu, IEEE J. of Quantum Electron. QE (1999) (unpublished).
[51] S. Chichibu, K. Wada, and S. Nakamura, Appl. Phys. Lett. **71**, 2346 (1997).
[52] M. Sugawara, Phys. Rev. B **51**, 10743 (1995).
[53] S. Rosner, E. Carr, M. Ludwise, G. Girolami, and H. Erikson, Appl. Phys. Lett. **70**, 420 (1997).
[54] J. Speck, H. Marchand, P. Kozodoy, P. Fini, X. Wu, J. Ibbetson, S. Keller, S. DenBaars, U. Mishra, and S. Rosner, Proc. 2nd Int. Symp. on Blue Laser and Light Emitting Diodes (Ohmsha, Tokyo, 1998), pp. 37.
[55] H. Sato, T. Sugahara, Y. Naoi, and S. Sakai, Jpn. J. Appl. Phys. **37**, 2013 (1998).
[56] their results are summarized in C. Kisielowski, Proc. 2nd Int. Symp. on Blue Laser and Light Emitting Diodes (Ohmsha, Tokyo, 1998), pp. 321.
[57] F. Ponce, S. Galloway, W. Goetz, and R. Kern, Mater. Res. Soc. Symp. Proc. **482**, 625 (1998).
[58] S. Keller, B. Keller, M. Minsky, J. Bowers, U. Mishra, S, DenBaars, and W. Seifert, J. Cryst. Growth **189/190**, 29 (1998).
[59] S. Chichibu, H. Marchand, S. Keller, P. Fini, J. Ibbetson, M. Minsky, S. Fleischer, J. Speck, J. Bowers, E. Hu, U. Mishra, S. DenBaars, T. Deguchi, T. Sota, and S. Nakamura, Proc. 2nd Int. Symp. on Blue Laser and Light Emitting Diodes (Ohmsha, Tokyo, 1998), pp. 604; Appl. Phys. Lett. **74**,(1999) (unpublished).
[60] S. Keller, S. Chichibu, M. Minsky, E. Hu, U. Mishra, and S. DenBaars, J. Crystal Growth (1998) (unpublished).
[61] M. Mcluskey, C. Van de Walle, C. Master, L. Romano, and N. Johnson, Appl. Phys. Lett. **72**, 2725 (1998).
[62] K. Domen, A. Kuramata, and T. Tanahashi, Appl. Phys. Lett. **72**, 1359 (1998).

COMPOSITION DEPENDENCE OF THE BAND GAP ENERGY OF $In_xGa_{1-x}N$ LAYERS ON GaN ($x \leq 0.15$) GROWN BY METAL-ORGANIC CHEMICAL VAPOR DEPOSITION

J. Wagner, A. Ramakrishnan, D. Behr, M. Maier, N. Herres, M. Kunzer, H. Obloh, and K.-H. Bachem

Fraunhofer-Institut für Angewandte Festkörperphysik, Tullastrasse 72, D-79108 Freiburg, Germany, wagner@iaf.fhg.de

Cite this article as: MRS Internet J. Nitride Semicond. Res. 4S1, G2.8 (1999)

ABSTRACT

We report on the composition dependence of the band gap energy of strained hexagonal $In_xGa_{1-x}N$ layers on GaN with $x \leq 0.15$, grown by metal-organic chemical vapor deposition on sapphire substrates. The composition of the (InGa)N was determined by secondary ion mass spectroscopy. High-resolution X-ray diffraction measurements confirmed that the (InGa)N layers with typical thicknesses of 30 nm are pseudomorphically strained to the in-plane lattice parameter of the underlying GaN. Room-temperature photoreflection spectroscopy and spectroscopic ellipsometry were used to determine the (InGa)N band gap energy. The composition dependence of the band gap energy of the strained (InGa)N layers was found to be given by $E_G(x)=3.43-3.28 \cdot x$ (eV) for $x \leq 0.15$. When correcting for the strain induced shift of the fundamental energy gap, a bowing parameter of 3.2 eV was obtained for the composition dependence of the gap energy of unstrained (InGa)N.

INTRODUCTION

There is considerable current interest in the (InGa)N alloy system because (InGa)N layers form the active region of most of the present green-to-violet light emitting devices based on group III-nitrides [1]. However, in spite of the technological importance of (InGa)N, so far published data on the composition dependence of the band gap energy of the (InGa)N alloy show significant scatter, with values for the bowing parameter ranging from 1.02 eV [2] to 3.5 eV [3]. For an accurate determination of the composition dependence of the (InGa)N band gap, the gap energy has to be derived from photoreflection (PR) [2] or spectroscopic ellipsometry (SE) [4] measurements rather than from photoluminescence (PL) data. This is because the (InGa)N near band-edge PL spectrum is Stokes-shifted relative to the band edge, leading to an underestimate of the gap energy [5]. The (InGa)N alloy composition should be assessed not only by X-ray diffraction but also by chemical analysis, as strain effects complicate the composition analysis by X-ray diffraction, requiring precise knowledge of the elastic parameters of the (InGa)N. (InGa)N layers grown on top of GaN have been found to be strained to the in-plane lattice parameter of the underlying GaN for layer thicknesses and compositions up to, at least, 100 nm and $x=0.15$, respectively [6,7].

In the present study pseudomorphically strained (InGa)N layers on GaN, grown by metal-organic chemical vapor deposition (MOCVD), were analyzed by PR spectroscopy and SE to determine the composition dependence of the (InGa)N band gap energy. Secondary ion mass spectroscopy (SIMS) and high-resolution X-ray diffraction (HRXRD) were used to assess the (InGa)N layers` composition and strain, respectively.

Mat. Res. Soc. Symp. Proc. Vol. 537 © 1999 Materials Research Society

EXPERIMENT

The hexagonal (InGa)N-on-GaN samples used in this study were grown by low-pressure MOCVD on c-plane 2´´ sapphire substrates. Details on growth can be found in Ref. 8. Data will be presented on a series of samples with varying In content ($x \leq 0.15$) and (InGa)N layer thicknesses ranging from 15 to 60 nm, grown on top of a 2 to 3 μm thick GaN layer. The (InGa)N composition was determined by SIMS using appropriate standards calibrated by energy dispersive X-ray analysis (EDX).

Selected samples were further analyzed by HRXRD using both the symmetric 00.6 and the asymmetric 10.5 reflections, in order to determine the *c* and *a* lattice parameters parallel and perpendicular to the growth axis. Fig. 1 shows a plot of *c* versus *a* for (InGa)N layers with a thickness of 30 nm as well as for the underlying GaN. All the *a* lattice parameters obtained for the (InGa)N are close to that of the GaN layer, indicating that the (InGa)N layers are under biaxial in-plane compression due to pseudomorphic growth. The GaN layer itself is also under slight compression due to the thermal mismatch with respect to the sapphire substrate. Using linear interpolations between the *c* and *a* lattice parameters of unstrained GaN [9] and InN [10], the composition dependent lattice parameters of unstrained (InGa)N are obtained, shown in Fig. 1 by the short-dashed line. Based on the elastic parameters given by Wright [11], the effect of in-plane biaxial compressive or tensile strain on *c* and *a* can be calculated, as

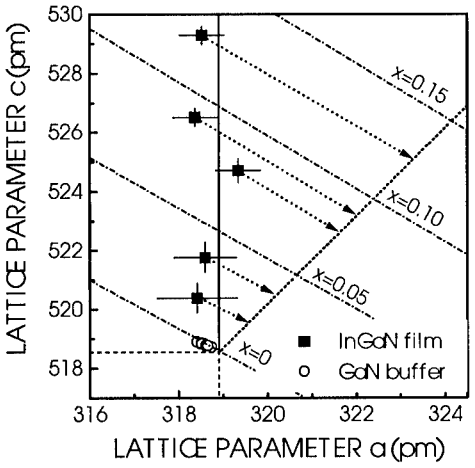


Fig. 1: c versus a lattice parameters as determined by HRXRD for 30 nm thick $In_xGa_{1-x}N$ layers on GaN (filled squares) with different In content x. Error bars are indicated. For comparison c and a lattice parameters of the underlying GaN are also shown (open circles). The full vertical line marks the a lattice parameter of unstrained GaN. The short-dashed line indicates the calculated c-versus-a relation for unstrained (InGa)N. For further details see text.

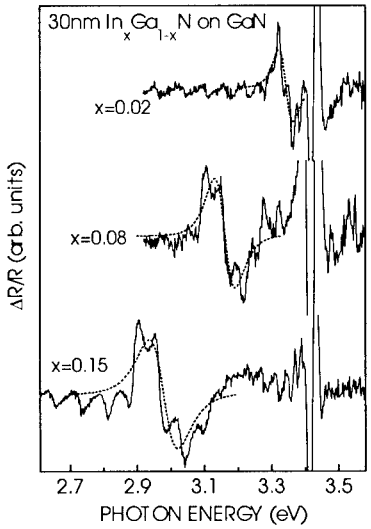


Fig. 2: Room-temperature PR spectra of 30 nm thick $In_xGa_{1-x}N$ layers on GaN with various In contents x given in the figure. Dashed curves indicate fits to the (InGa)N fundamental gap resonance.

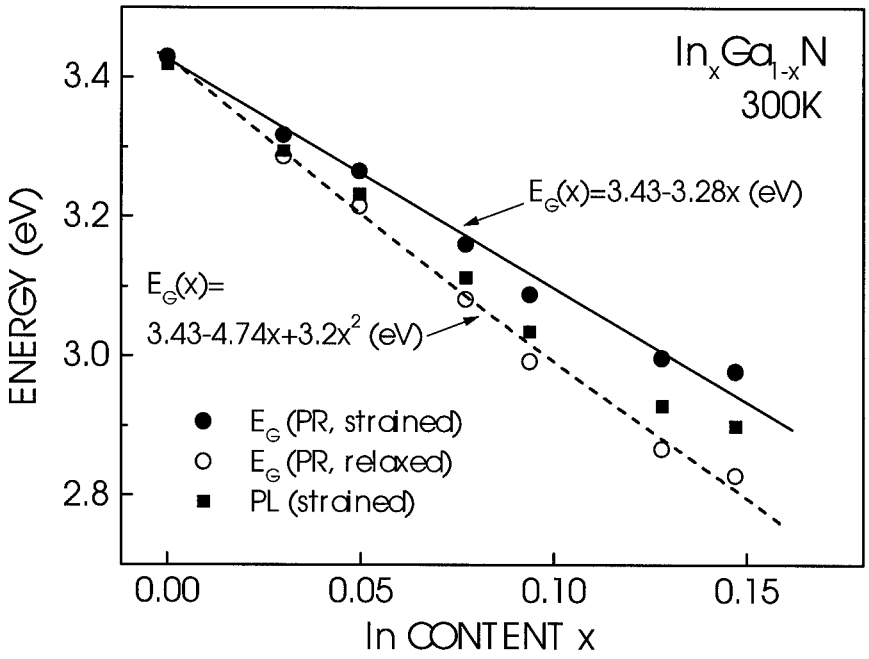


Fig. 3: Composition dependence of the room-temperature band gap energy of strained $In_xGa_{1-x}N$ layers on GaN as obtained by PR spectroscopy (filled circles), and after correction for the strain induced band gap shift (open circles, see text). (InGa)N alloy composition was determined by SIMS. The full and dashed curves indicate linear and quadratic fits to E_G for strained $In_xGa_{1-x}N$ and for numerically relaxed $In_xGa_{1-x}N$, respectively. For comparison, room-temperature PL peak positions are also shown (filled squares).

indicated by the dash-dotted lines for In contents of x=0, 0.05, 0.10, and 0.15. To extract information on the In content of the present strained (InGa)N layers, the measured data have to be projected parallel to the dash-dotted lines onto the *c*-versus-*a* curve for unstrained (InGa)N (short-dashed line), as indicated by arrows. The (InGa)N alloy composition deduced in this way agrees for x<0.1 within 10% with the SIMS data. For the highest In contents the HRXRD analysis yields a somewhat lower In content than SIMS, e.g. x=0.124 (HRXRD) versus x=0.147 (SIMS). Considering the large uncertainties in the (InGa)N elastic parameters required for the HRXRD based analysis of the alloy composition for strained (InGa)N, the SIMS data are used throughout the remaining paper.

RESULTS AND DISCUSSION

Room-temperature PR spectra are plotted in Fig. 2 for three different $In_xGa_{1-x}N$-on-GaN samples with an (InGa)N layer thickness of 30 nm and In contents of x=0.02, 0.08, and 0.15. Besides the very intense and spectrally sharp fundamental gap resonance of GaN at 3.43 eV, the corresponding resonance of the (InGa)N is well resolved at lower energies as a derivative-like structure. The (InGa)N resonance shows a low-energy shift and a significant broadening with increasing In content. Its line shape is somewhat distorted by Fabry-Perot interference

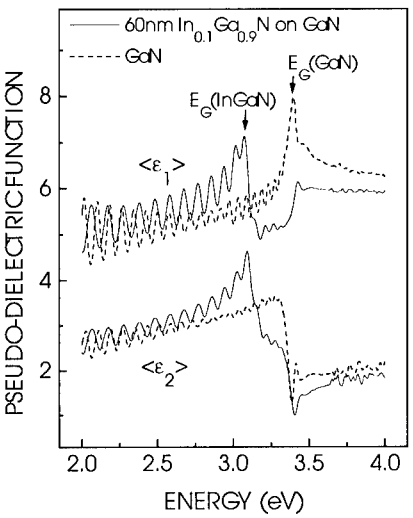


Fig. 4: Real $<\varepsilon_1>$ and imaginary part $<\varepsilon_2>$ of the pseudo-dielectric function spectrum of a 60 nm thick $In_{0.1}Ga_{0.9}N$ layer on GaN and, for comparison, of a GaN reference sample. Data were derived from room-temperature SE measurements performed at an incident angle of 75° and a polarizer-azimuth of 30°.

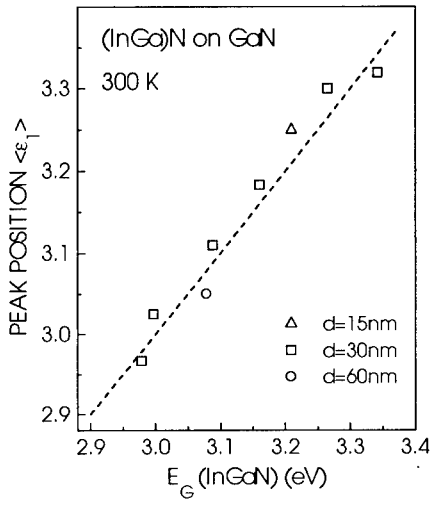


Fig. 5: Energy position of the (InGa)N related peak in the $<\varepsilon_1>$ spectrum versus (InGa)N band gap energy derived from PR measurements. Data are shown for different (InGa)N layer thicknesses d given in the figure. The dashed line indicates a one-to-one correspondence.

oscillations. The band gap energy of the (InGa)N was deduced from a fit to the PR resonance [12], as shown by the dashed curves. The resulting band gap energies E_G are plotted in Fig. 3 versus the In content determined by SIMS (full circles). The experimental data can be fitted by the linear relationship $E_G(x)=3.43-3.28\cdot x$ (eV) ($x\leq 0.15$), as indicated by the full line in Fig. 3. There is fair agreement with the composition dependence of the (InGa)N band gap energy reported by McClusky et al. [3] ($E_G(x)=3.42-3.93\cdot x$ (eV)), which was obtained from optical transmission experiments on 0.25 μm thick $In_xGa_{1-x}N$ layers ($x\leq 0.12$) strained to the in-plane lattice parameter of the underlying GaN. For comparison the PL peak energy at room-temperature is also plotted in Fig. 3 (filled squares). There is an increasing Stokes-shift between the band gap energy derived from the PR measurements and the PL peak energy upon increasing the In content. Alloy fluctuations [5] and the confined Stark effect due to piezoelectric fields [14] have been discussed as possible mechanisms responsible for this Stokes-shift.

As pointed out by McClusky et al. [3], the strain induced shift ΔE of the (InGa)N band gap has to be subtracted from the present $E_G(x)$ data obtained on pseudomorphic (InGa)N films on GaN, to obtain the composition dependence of the band gap energy of unstrained (InGa)N. Using the relationship for the strain induced band gap shift $\Delta E=1.02\cdot x$ (eV) given in Ref. 3, the expected band gap energies of unstrained (InGa)N have been calculated, which are shown in Fig. 3 by open circles. Taking a value of 1.89 eV for the room-temperature band gap energy of InN [15], the present data on the composition dependence of the band gap energy of unstrained (InGa)N can be fitted by $E_G(x)=3.43-4.74\cdot x+3.2\cdot x^2$ (eV). The bowing parameter of 3.2 eV com-

pares favorably well with that of 3.5 eV calculated in Ref. 3 for x=0.125. There is also consistency with a very recent study by Wetzel et al. [16], which reports on the basis of a combined HRXRD and PR spectroscopic analysis a bowing parameter of 3.8 eV for unstrained $In_xGa_{1-x}N$ ($x<0.2$).

It has been shown recently that SE measurements allow a determination of the (InGa)N band gap energy too [4]. Fig. 4 shows the real $\langle\varepsilon_1\rangle$ and imaginary part $\langle\varepsilon_2\rangle$ of the pseudo-dielectric function of a 60 nm thick $In_{0.1}Ga_{0.9}N$-on-GaN layer. For comparison the pseudo-dielectric function spectrum of a high-quality bulk-like GaN reference layer is also shown, which is very similar to that reported in Ref. 17 for hexagonal GaN. A pronounced peak in $\langle\varepsilon_1\rangle$ and minimum in $\langle\varepsilon_2\rangle$ at 3.40 eV marks the superposition of the A and B excitonic transitions at the fundamental band gap of GaN [18,19]. At the high-energy side of this peak a shoulder appears in $\langle\varepsilon_1\rangle$ which is tentatively assigned to the C excitonic transition. The oscillations observed in the pseudo-dielectric function spectrum for photon energies below the fundamental energy gap are caused by Fabry-Perot interferences due to multiple internal reflections in the epitaxial layer. In the $\langle\varepsilon_1\rangle$ spectrum of the (InGa)N-on-GaN sample, the fundamental gap interband transition of the GaN is attenuated. A new peak appears in both $\langle\varepsilon_1\rangle$ and $\langle\varepsilon_2\rangle$ at about 3.07 eV, which is in the transparency region of the GaN. The new peak is assigned to the fundamental gap interband transition of the $In_{0.1}Ga_{0.9}N$.

This assignment is confirmed by a direct comparison of the energy position of the (InGa)N related peak in the $\langle\varepsilon_1\rangle$ spectrum with the band gap energy derived from the PR measurements. In Fig. 5 the (InGa)N peak position in $\langle\varepsilon_1\rangle$ is plotted versus the (InGa)N band gap energy for (InGa)N-on-GaN samples with In concentrations up to x=0.15 and (InGa)N layer thicknesses of 15, 30, and 60 nm. There is an almost one-to-one correspondence between these two quantities with the peak in $\langle\varepsilon_1\rangle$ being on the average only slightly higher in energy than the band gap.

CONCLUSION

The composition dependence of the band gap energy of strained $In_xGa_{1-x}N$ on GaN ($x\leq0.15$) has been studied by PR spectroscopy and SE, using SIMS in combination with HRXRD for an accurate determination of the (InGa)N layers` composition and strain. The composition dependence of the band gap energy of (InGa)N strained to the in-plane lattice parameter of the underlying GaN was found to be given by $E_G(x)=3.43-3.28\cdot x$ (eV). After correction for the strain induced band gap shift, a bowing parameter of 3.2 eV was obtained for the composition dependence of the band gap of unstrained (InGa)N.

ACKNOWLEDGMENTS

Ch. Hoffmann and U. Kaufmann are thanked for performing the EDX analysis and for stimulating discussions, respectively. Continuous interest and encouragement by G. Weimann is gratefully acknowledged. Work was supported by the German Ministry for Education and Research.

REFERENCES

1. S. Nakamura and G. Fasol, *The Blue Laser Diode* (Springer, Berlin, 1997).
2. W. Shan, B. D. Little, J. J. Song, Z. C. Feng, M. Schurmann, and R. A. Stall, Appl. Phys. Lett. **69**, 3315 (1996).
3. M. D. McClusky, C. G. Van de Walle, C. P. Master, L. T. Romano, and N. M. Johnson, Appl. Phys. Lett. **72**, 2725 (1998).

4. J. Wagner, A. Ramakrishnan, D. Behr, H. Obloh, M. Kunzer, and K.-H. Bachem, Appl. Phys. Lett. **73**, 1715 (1998).
5. S. Chichibu, T. Azuhata, T. Sota, and S. Nakamura, Appl. Phys. Lett. **70**, 2822 (1997).
6. H. Amano, T. Takeuchi, S. Sota, H. Sakai, and I. Akasaki, Mat. Res. Soc. Symp. Proc. Vol. **449**, 1143 (1997).
7. F. Scholz, J. Off, A. Kniest, L. Görgens, and O. Ambacher, in Proceedings of E-MRS Spring Meeting 1998, Symposium L *Nitrides and Related Wide Band Gap Materials* (to appear in Mat. Sci. Eng. B).
8. H. Obloh, D. Behr, N. Herres, C. Hoffmann, M. Kunzer, M. Maier, S. Müller, W. Pletschen, B. Santic, P. Schlotter, M. Seelmann-E., K.-H. Bachem, U. Kaufmann, Proc. 2nd Int. Conf. Nitride Semicond. (Tokushima, Japan, 1997), p. 258.
9. C. M. Balkas, C. Baskeri, and R. F. Davis, Powder Diffraction **10**, 266 (1995).
10. K. Kubota, Y. Kobayashi, and K. Fujimoto, J. Appl. Phys. **66**, 2984 (1989).
11. A. F. Wright, J. Appl. Phys. **82**, 2833 (1997).
12. D. E. Aspnes, Surf. Sci. **37**, 418 (1973).
13. C. M. Herzinger, P. G. Snyder, B. Johs, and J. A. Woollam, J. Appl. Phys. **77**, 1715 (1995).
14. T. Takeuchi, S. Sota, M. Katsurgawa, M. Komori, H. Takeuchi, H. Amano, and I. Akasaki, Jpn. J. Appl. Phys. **36**, L382 (1997); J. S. Im, H. Kollmer, J. Off, A. Sohmer, F. Scholz, and A. Hangleiter, Mat. Res. Soc. Symp. Proc. Vol. **482**, 513 (1998).
15. T. L. Tansley and C. P. Foley, J. Appl. Phys. **59**, 3241 (1986).
16. C. Wetzel, T. Takeuchi, S. Yamaguchi, H. Katoh, H. Amano, and I. Akasaki, Appl. Phys. Lett. **73**, 1994 (1998).
17. T. Kawashima, H. Yoshikawa, S. Adachi, S. Fuke, and K. Ohtsuka, J. Appl. Phys. **82**, 3528 (1997).
18. A.J. Fischer, W. Shan, J.J. Song, Y.C. Chang, R. Horning, and B. Goldenberg, Appl. Phys. Lett. **71**, 1981 (1997).
19. A.A. Yamaguchi, Y. Mochizuki, H. Sunakawa, and A. Usui, J. Appl. Phys. **83**, 4542 (1998).

Optical Gain Spectra in InGaN/GaN Quantum Wells with the Compositional Fluctuations

Takeshi Uenoyama
Central Research Laboratories, Matsushita Electric Industrial Co., Ltd.,
3-4 Hikaridai, Seikacho, Sourakugun, Kyoto 619-0237, Japan,
Fax: +81-774-98-2586/Tel: +81-774-98-2511/E-mail: takeshi@crl.mei.co.jp

Cite this article as: MRS Internet J. Nitride Semicond. Res. 4S1, G2.9 (1999)

The compositional fluctuations of the In content were found in InGaN/GaN quantum wells and it caused the localized states by the potential fluctuation. We have evaluated the optical gain of GaN based quantum well structures with localized states. The localized states are treated as the subband states of the quantum disk-like dots in the well. It was found that the inhomogeneous broadening played an important role in the optical gain and that it should be reduced to use the benefit of the localized states for laser oscillations.

Introduction

A short wave length is one of the essential requirements of laser diodes (LDs) for high-density storage devices. Recently, continuous-wave operation of the InGaN multi-quantum-well LDs with a life time of more than thousand hours has been achieved [1]. However, there is a key issue, such as high threshold carrier density, to lead them to commercial production. So far, we evaluated the optical gain of the wurzite GaN/AlGaN quantum well lasers and derived that the threshold current density of the GaN/AlGaN LDs would be estimated very high compared to conventional GaAs/AlGaAs quantum well LDs. It is caused by the large density of states due to the strong electronegativity and the weak spin-orbit coupling of the N atom in group-III nitrides. To overcome the problem, we proposed the strain effects [2] and the incorporation of the GaAs or GaP in the well layer to reduced the density of states.

On the other hand, the well layer of InGaN/GaN quantum wells has the compositional fluctuations of the In contents. These fluctuations would induce the localized states due to the random potentials. Since the radiative recombination attributed to the localized excitons by the alloy fluctuation in InGaN/GaN quantum wells were measured recently [3,4], it becomes important to study the relation between the localized states and the optical gain. We evaluated the optical gain coefficient, including the broadening in the spectra by the transitions between the localized states.

Mat> Res, Soc. Symp. Proc. Vol. 537 © 1999 Materials Research Society

Formalism

Let us describe the localized states caused by the compositional fluctuations. We assume that the potential fluctuations in the well are written by the quantum-disk like potentials and that they are randomly distributed without any correlation among them, as shown in Fig. 1. The Hamiltonians H^i for the electronic states for the electron (i=e), the heavy hole (i=hh) and the light hole (i=lh) is given by

$$H^i = h^i(z) - \frac{\hbar^2}{2m_i}\frac{\partial^2}{\partial \mathbf{r}^2} + U(\mathbf{r}, z),$$

where

$$h^i(z) = -\frac{\hbar^2}{2m_i}\frac{\partial^2}{\partial z^2} + V^i_{QW}(z), (\mathrm{i} = \mathrm{e}, \mathrm{hh}, \mathrm{lh}),$$

$$U(\mathbf{r}, z) = \begin{cases} 0 & \text{if } |z| > \frac{L}{2} \\ \sum_j v(\mathbf{r} - \mathbf{r}_j, R_j, u_j) & \text{otherwise} \end{cases}$$

$v(\mathbf{r} - \mathbf{r}_j, R_j, u_j)$ are the potentials by the compositional fluctuations at $\mathbf{r}_j$ in the two dimensional system, where R_j and u_j are the radius and the potential depth of the quantum-disk, respectively, as shown in Fig.2. Then, the eingenfunctions of the localized state can be approximated as

$$\Psi^i_{j,n,m}(\mathbf{r}, z) = \phi^i_{j,n}(\mathbf{r})\zeta^i_m(z),$$

where

$$\left(-\frac{\hbar^2}{2m_i}\frac{\partial^2}{\partial \mathbf{r}^2} + v(\mathbf{r} - \mathbf{r}_j, R_j, u_j)\right)\phi^i_{j,n}(\mathbf{r}) = E^i_{j,n}\phi^i_{j,n}(\mathbf{r}),$$

$$h^i(z)\zeta^i_m(z) = E^i_{z,m}\zeta^i_m(z).$$

$\phi^i_{j,n}(\mathbf{r})$ and $\zeta^i_m(z)$ are the eigenfunctions in the lateral directions and z direction, respectively. Using the above eingenfunctions, the optical gain spectrum is given by

$$g(\omega) = \sum_{i,n,m,k}(1 - f(E^e_{n,k}) - f(E^h_{m,k}))\frac{1}{\pi}\frac{\left|\langle\zeta^e_n|\zeta^h_m\rangle\right|^2\Gamma_s}{(\omega - E^e_{n,k} - E^h_{m,k})^2 + \Gamma_s^2}$$

$$+ \sum_{i,n',m',n,m,k}(1 - f(E^e_{j,n'}) - f(E^h_{j,m'}))\frac{1}{\pi}\frac{\left|\langle\zeta^e_n|\zeta^h_m\rangle\right|^2\left|\langle\phi^e_{n'}|\phi^h_{m'}\rangle\right|^2\Gamma_l}{(\omega - E^e_{j,n'} - E^h_{j,m'})^2 + \Gamma_l^2}$$

where Γ_s and Γ_l are the energy widths of the broaden spectra for the continuum state transition and the localized state one, respectively. Γ_s is mainly caused by the carrier-carrier scattering and Γ_l is caused by the inhomogeneities of R_j and u_j of the potential.

Results and Discussions

Figure 3 (a) and (b) show the potential profiles and the bound state energies by the compositional fluctuations. The energy depths are 80 meV for the electron and 50 meV for the holes. The radii of the disks are assumed to be 20• and 50•, respectively. The effective masses are 0.2 m_0 for electron, 1.1m_0 for heavy hole and 0.17 m_0 for light hole, respectively. The quantum well length is 40•. In the case of R=20•, the number of the bound states are a few and it is almost like quantum-dots. However, the bound states become condensed, especially for the holes when the radius is more than R=50•. Then, these states become like band tailing by introducing the homogeneous or inhomogeneous broadening.

Figure 4 (a) and (b) show the carrier density dependence of the optical gain spectra of quantum wells with the random potentials in the case of Fig. 3 (a) and (b), respectively. The densities of the quantum disks are 1×10^{11} cm^{-2} in Fig. 4 (a) and Fig. 4 (b), respectively. We assumed here that the broadening energies, Γ_s and Γ_l, are same as 6 meV. It corresponds to the scattering rate of about 0.1 psec.

In the case of R=20•, there is only one peak from the localized state transition although there are two bound states in the valence band. This is due to the orthogonarity between the wavefunctions of n=1 and n=2. The gain appears from the localized state transition, increasing the carrier density. It becomes more than 1000 cm^{-1} at 4×10^{12} cm^{-2}. Note that the maximum gain is obtained at the localized state transition, which can be used for the laser oscillations.

On the other hand, in the case of R=50•, the gain appears from the localized state transitions. However, the maximum gain tends to move to the continuum state transitions, increasing the carrier density. Consequently, the advantage of using the localized states for laser oscillation becomes weak as long as the density of the localized states are around 1×10^{11} cm^{-2}.

Figure 5 shows the optical gain spectra for the case of Fig. 4 (b) at 6×10^{12} cm^{-2}, with the various broadening Γ_l s. When the broadening becomes small as 2 meV, the gain spectrum gets sharp and large. However, when it becomes broaden as 20 meV, the gain peak gets so broaden that there are no more benefit for laser oscillations. Therefore, in order to use the localized states in terms of the quantum disks or dots, the inhomogeneity of the structures should be reduced.

Then, we have estimated the energy broadening by the carrier-carrier scattering in terms of the intraband transitions. Since the population inversion needs many carriers in the cavity, the carrier-carrier scattering would be dominant mechanism of the relaxation in the subband. The relaxation time or rate is given by the imaginary part of the self-energy of the electron and the hole. The localized electrons or holes are also scattered by the carriers around them in the continuum states. Then, the spectra of the transitions attributed to the localized states become broaden, as well, but this is not one by the inhomogeneity of the structures of the localized states. The relaxation times of the localized electron and the continuum one at $n=2\times10^{12}$ cm^{-2}, u=80 meV and R=50• were 0.089 psec and 0.080 psec, respectively. They correspond to the energy broadening of 7.6 meV and 8.2 meV, respectively. The detail explanation of the calculation will

be discussed elsewhere [5]. Then, the energy broadening of the localized state is comparable of the continuum one. Therefore, in order to use the quantum-dot like structures for the reduction of the threshold current density, the homogeneity of their structures are definitely necessary.

Summary

In this paper, we investigated the relation between the optical gain spectra and the localized states by the compositional fluctuation in the InGaN/GaN quantum well structures. The relation between the energy widths in the broaden spectra by the localized states and the continuum ones is important. Since the broadening by intraband transitions is manly due to the carrier-carrier scattering, we estimated them quantitatively by using the many-body approach and found that the broadening of the localized state and the continuum one are comparable. In order to use the localized states positively for laser oscillations, the reduction of the inhomogeneity of the energies is necessary.

References

1. S. Nakamura, presented at the 2nd Intl. Conf. on Nitride Semiconductors, S-1 Oct. 27-31, Tokushima, (1997).
2. M. Suzuki, and T. Uenoyama, Jpn. J. Appl. Phys. **35**, L953, (1996).
3. S. Chichibu, T. Azuhata, T. Sota and S. Nakamura, presented at 38th Electronic Material Conference, W-10, June 26-28, Santa Barbara, (1996); Appl. Phys. Lett. **69**, 4188 (1996); ibid. . **70**, 2822 (1997).
4. Y. Narukawa, Y. Kawakami, Sz. Fujita, Sg. Fujita and S. Nakamura, Phys. Rev. **55**, R1938 (1997); Appl. Phys. Lett. **70**, 981 (1997).
5. T. Uenoyama, to be published.

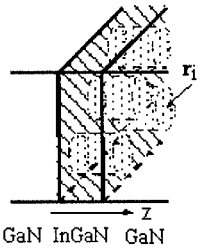


Fig. 1 InGaN/GaN quantum well

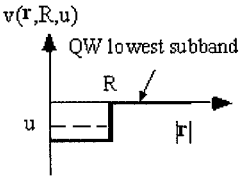


Fig. 2 Potential profile due to the compositional fluctuations.

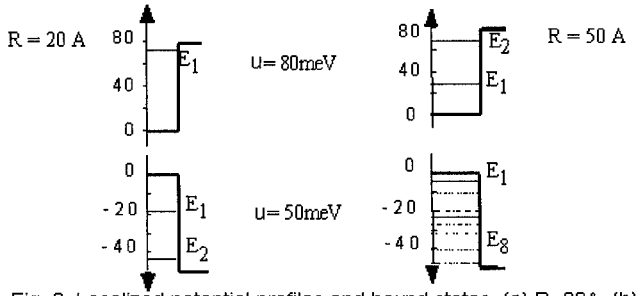


Fig. 3 Localized potential profiles and bound states. (a) R=20A, (b)

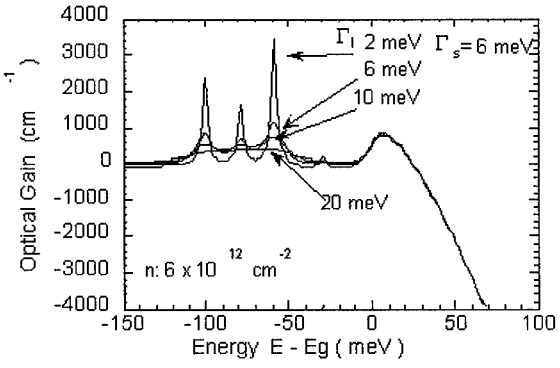


Fig.5. Optical gain spectra for the case of R=50 Å at 6×10^{12} cm^{-2}, with the various broadening Γ_is.

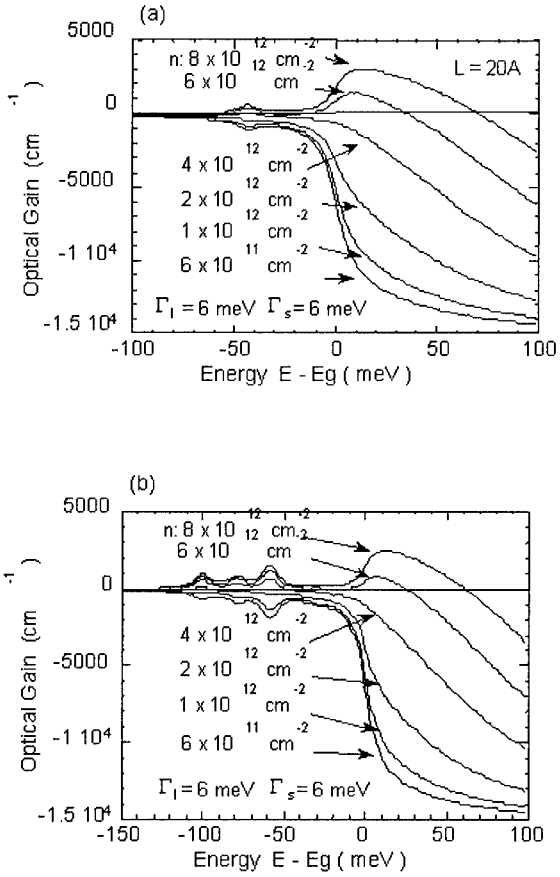


Fig. 4. Carrier density dependence of the optical gain spectra of quantum wells with the random potentials. R=20 Å (a) and R=50 Å (b)

Part III

Growth and Characterization

HYDROGEN AND NITROGEN AMBIENT EFFECTS ON EPITAXIAL LATERAL OVERGROWTH (ELO) OF GaN VIA METALORGANIC VAPOR-PHASE EPITAXY (MOVPE)

Kazuyuki Tadatomo, Yoichiro Ohuchi, Hiroaki Okagawa, Hirotaka Itoh,
*Hideto Miyake and *Kazumasa Hiramatsu
Mitsubishi Cable Industries, Ltd., Central Research Laboratory, Japan
Hideto Miyake, Kazumasa Hiramatsu
** Dept. of Electrical & Electronic Eng. Mie University, Japan*

Cite this article as: MRS Internet J. Nitride Semicond. Res. 4S1, G3.1 (1999)

Ambient gas effect on the epitaxial lateral overgrowth (ELO) of GaN via metalorganic vapor-phase epitaxy (MOVPE) on a MOVPE-grown GaN (0001) / sapphire (0001) substrate with a SiO_2 stripe mask has been studied by means of field-emission scanning electron microscopy (SEM) and high-resolution X-ray diffraction (XRD) analysis. Different ambient gases of nitrogen, hydrogen and their mixture (mixture ratio, hydrogen : nitrogen = 1 : 1) affect the lateral overgrowth rate, the surface morphology and the crystalline tilting of ELO-GaN layers. XRD revealed that the ELO-GaN layer on the SiO_2 mask aligned along the $<1\bar{1}00>$ direction exhibited anisotropic crystalline tilting toward $<11\bar{2}0>$. For ELO-GaN growth in nitrogen ambient, the growth rate of the (0001) facet decreases, the lateral overgrowth rate increases and the tilting of the ELO-GaN layer increases, while no smooth surface is obtained, in comparison with ELO-GaN growth in hydrogen ambient. For the mixture ambient, a smooth surface with a fast lateral overgrowth rate is achieved and the dislocation density is not more than 10^7 cm^{-2}, which is comparable to that in hydrogen ambient.

1. Introduction

Recently, high-performance optical devices such as light-emitting diodes (LEDs) and laser diodes (LDs) in green and ultraviolet regions have been developed using GaN, AlGaN and InGaN compound semiconductors [1, 2]. These GaN-related devices are usually fabricated on a sapphire substrate, because there is no large-scale substrate for GaN heteroepitaxial growth. Due to the large differences in lattice constant, thermal expansion coefficient and chemical nature between GaN and sapphire, many threading dislocations are formed from the GaN or AlN buffer layer on the sapphire substrate, and the dislocation density has been reported to be of the order of 10^9 -10^{10} cm^{-2} [3]. Although high-brightness LEDs have been realized in spite of the high dislocation density, the reduction of the dislocation density is desired to improve the performance and reliability of these devices. The epitaxial lateral overgrowth (ELO) technique based on the selective area growth (SAG) has recently attracted considerable attention, since the fabrication of blue-violet laser diodes on the ELO-GaN layer using this technique resulted in the achievement of a long lifetime of more than 10,000 hours [4].

The SAG in MOVPE on GaN/sapphire and AlGaN/sapphire with SiO_2 stripe patterns was published for the first time in 1994 by Kato et al. [5], followed by that on GaN/sapphire [6]. Intensive studies on SAG have revealed that the ELO effectively reduces the dislocation density [4, 7-11]. The crystalline properties and the growth mechanism of ELO-GaN can be affected by mask patterns such as stripe direction [10-13] and growth conditions such as growth temperature [10], source gases [10], growth pressure and ambient gas. However, the effects of ambient gas remain unclear. We investigate the effects of hydrogen gas, nitrogen gas and their mixture in an atmospheric MOVPE on ELO-GaN.

Mat. Res. Soc. Symp. Proc. Vol. 537 © 1999 Materials Research Society

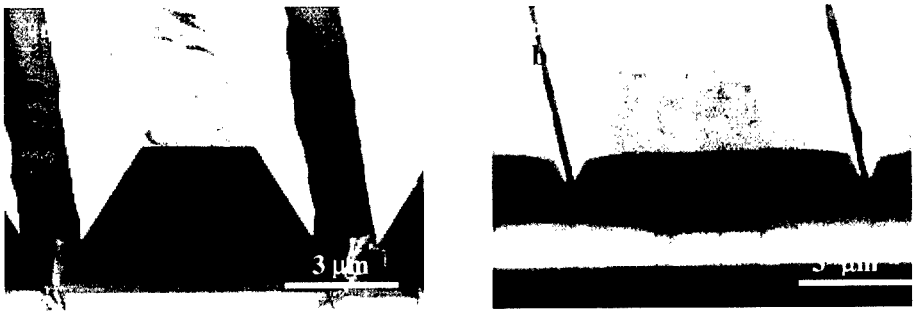


Figure 1 SEM images of GaN on SiO_2 stripe pattern along the <1$\bar{1}$00> direction at a growth time of 30 min in (a) hydrogen ambient and (b) nitrogen ambient.

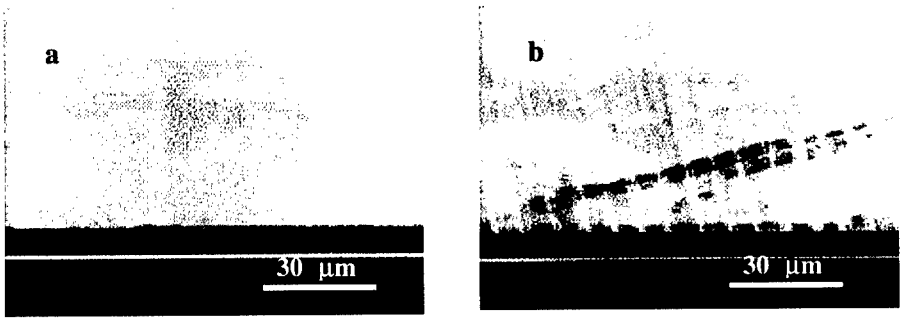


Figure 2 SEM images of GaN layer grown by ELO on SiO_2 stripe pattern along the <1$\bar{1}$00> direction (a) at a growth time of 120 min in hydrogen ambient and (b) at a growth time of 180 min in nitrogen ambient.

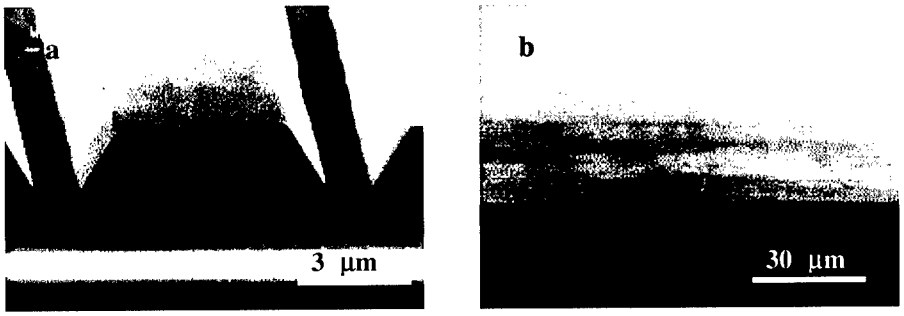


Figure 3 SEM images of GaN layer grown by ELO on SiO_2 line pattern along the <1$\bar{1}$00> direction in the mixture ambient at growth times of (a) 30 min and (b) 120 min.

2. Experimental

A conventional atmospheric MOVPE apparatus with a horizontal reactor was used. A 3-μm-thick undoped MOVPE-grown GaN on sapphire using a low-temperature GaN buffer layer was used as the substrate. A SiO_2 stripe pattern with a 4 μm window width and a 4 μm mask width was aligned along the $<11\bar{2}0>$ or $<1\bar{1}00>$ direction of the underlying GaN layer. After a 100-nm-thick SiO_2 film was deposited by a radio-frequency (RF) sputtering, the SiO_2 stripe pattern was fabricated by standard photolithographic processes and reactive ion etching (RIE). The growth temperature of GaN as measured by a thermocouple in the heating system was 1000°C. The growth rate of GaN at our standard conditions was 3.5μm/hr. The ambient gas in the ELO process was hydrogen, nitrogen or their mixture (mixture ratio, hydrogen : nitrogen = 1 : 1), and was controlled by a carrier gas for metalorganic materials. However, because of using hydrogen for bubbling of metalorganic materials, small amount of hydrogen (4.2 %) was mixed with the ambient gases in all ELO processes.

The growth rates of the lateral face and the c-facet of ELO-GaN were estimated from the field-emission scanning electron microscopy (SEM) images and the growth times.

In order to measure the dislocation density in the ELO-GaN layers, we observed the pits on an $In_{0.2}Ga_{0.8}N$ layer (100 nm-thick) grown on an ELO-GaN layer. The growth pit density (GPD) on the InGaN layer is considered to correspond to the dislocation density of the underlying ELO-GaN layer [14].

In order to investigate the crystallographic structure of the ELO-GaN layers, ω-scan X-ray diffraction (XRD) measurements were performed on the ELO-GaN (0004) plane as a function of ϕ (ϕ: the rotation angle of the sample about its surface normal), and reciprocal space mapping measurements were also carried out using a high-resolution X-ray diffractometer (Philips X' Pert MRD).

3. Results and Discussions

Figures 1(a) and (b) show SEM images of GaN on the $<1\bar{1}00>$ stripe pattern in hydrogen ambient and nitrogen ambient at a growth time of 30 min, respectively. In hydrogen ambient, a (0001) facet is observed on top, and off-facets are observed on the side walls. On the other hand, the ELO-GaN grown on the $<11\bar{2}0>$ stripe pattern in hydrogen ambient had triangular cross sections with only the $\{1\bar{1}01\}$ facet on the side walls at the same growth time. The lateral overgrowth rate on the $<1\bar{1}00>$ stripe pattern was faster than that on the $<11\bar{2}0>$ stripe pattern [14]. The lateral overgrowth rate in nitrogen ambient is enhanced remarkably in contrast with that in hydrogen ambient, as shown in Figure 1(b). The ELO-GaN grown on the $<11\bar{2}0>$ stripe pattern in nitrogen ambient at the same growth time had trapezoidal cross sections with a (0001) facet on top and the $\{1\bar{1}01\}$ facet on the side walls. In nitrogen ambient, the rate of lateral overgrowth on the $<1\bar{1}00>$ stripe pattern was also faster than that on the $<11\bar{2}0>$ stripe pattern. Nitrogen ambient improves the lateral overgrowth rate and suppresses the (0001) facet growth rate.

The fast growth rate of the (0001) facet results in the line structure of GaN with only the $\{1\bar{1}01\}$ facet on the side walls. The improvement of the (0001) facet in the case of nitrogen ambient indicates that the growth rate of the side walls in nitrogen ambient is slightly faster than that in hydrogen ambient. A larger amount of source materials might be consumed on the side walls in the case of nitrogen ambient. Consequently, the amount of source materials supplied to the (0001) facet is reduced, resulting in the improvement of the (0001) facet.

Figures 2(a) and (b) show SEM images of the ELO-GaN layer on the $<1\bar{1}00>$ stripe pattern in hydrogen ambient at a growth time of 120 min, and in nitrogen ambient at a growth time of 180 min, respectively. The ELO-GaN layer grown in hydrogen ambient is smooth, while that grown in nitrogen

ambient is undulated, corresponding to the mask pattern. The ELO-GaN layer with a smooth surface was not obtained on the <11$\bar{2}$0> stripe pattern for both nitrogen and hydrogen ambients.

In order to increase the lateral overgrowth rate similar to that like in nitrogen ambient and to improve surface morphology of the ELO-GaN layer similar to that in hydrogen ambient, their mixture ambient was employed for the growth. Figure 3 shows SEM images of GaN grown on the <1$\bar{1}$00> stripe pattern at growth times of 30 min and 120 min, respectively. A smooth surface was likewise obtained, similar to that in hydrogen ambient. Table 1 shows the rate of lateral overgrowth and (0001) facet in each ambient. The lateral overgrowth rate in nitrogen ambient (4.3 μm/hr) is faster than that in hydrogen ambient (2.6 μm/hr), while the (0001) facet growth rate in nitrogen ambient (2.1 μm/hr) is slower than that in hydrogen ambient (5.5 μm/hr). From this result, it is found that the lateral overgrowth rate is enhanced by using the mixture ambient.

Table1 Lateral growth rate and (0001) facet growth rate of ELO-GaN on the <1$\bar{1}$00> stripe pattern in hydrogen ambient, nitrogen ambient and their mixture ambient.

	Lateral growth rate (μm/hr)	(0001) facet growth rate (μm/hr)
H_2 ambient	2.6	5.5
H_2+N_2 ambient	3.0	4.0
N_2 ambient	4.3	2.1

Table 2 Dislocation density of ELO-GaN grown in the mixture.

On mask		On window
ELO region	Coalescence region	
$< 10^7$ cm^{-2}	6×10^7 cm^{-2}	4×10^8 cm^{-2}

Figure 4 shows the distribution of pits on InGaN surface grown on the ELO-GaN in the mixture ambient, where the dots were obtained from the SEM image, and the bars indicate the positions of SiO_2 masks under the ELO-GaN. The pit density can be seen in the coalescence regions on the masks and in the window regions. The density of dislocations above the masks decreased significantly, but dislocations were observed in the coalescence regions on the center of the masks. The dislocation densities obtained from the SEM image are less than 10^7 cm^{-2} above the masks and 4×10^8 cm^{-2} above the window regions, respectively, as shown in Table 2. These are of the same order as the dislocation density in hydrogen ambient [!4].

Figure 5 shows the full-widths at half maximum (FWHMs) of the XRD rocking curves for the (0004) plane as a function of ϕ. It is found that the FWHMs of the ELO-GaN layer are dependent on ϕ. The maximum FWHMs are observed at ϕ=90° and 270° (<11$\bar{2}$0>), corresponding to the lateral overgrowth direction, and the minimum FWHMs are observed at ϕ=0° and 180° (<1$\bar{1}$00>), corresponding to the SiO_2 stripe pattern. It is considered that the FWHM reflects the crystallographic tilting of the ELO-GaN layer. The FWHMs of a 4-μm-thick undoped GaN grown by MOVPE without ELO in hydrogen ambient is not dependent on ϕ as shown in Figure 5 (Ref. H_2). Although the ELO process using hydrogen ambient reduces the dislocation density of the GaN layer, it introduces the anisotropic crystallographic tilting. The anisotropic tilting is drastically enhanced in nitrogen ambient, but the tilt angle is smaller than that reported by Sakai et al. [15]. The mechanism of this phenomenon is under study.

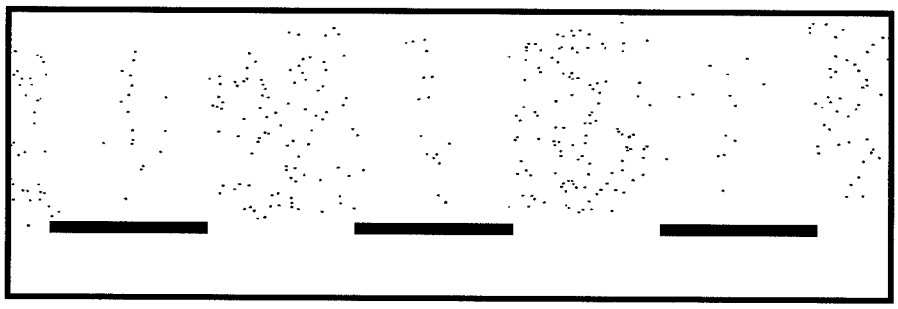


Figure 4 Distribution of pits on InGaN grown on GaN layer by ELO in the mixture ambient. Bars indicate the positions of SiO_2 masks under the ELO-GaN.

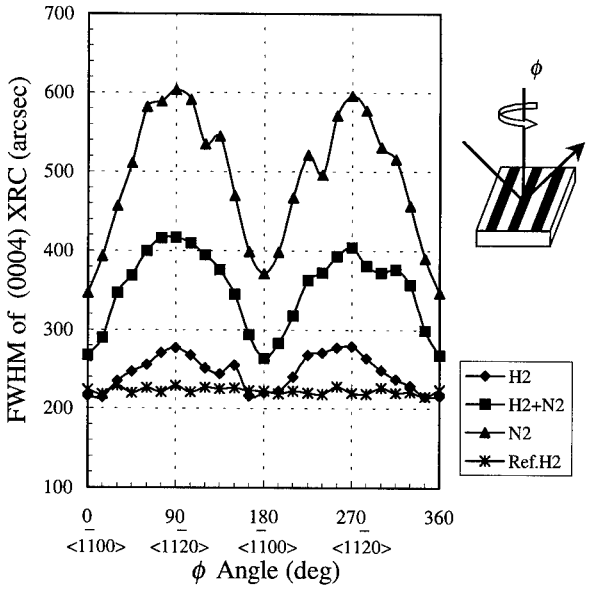


Figure 5 The FWHMs of XRD rocking curves for the (0004) GaN plane as a function of ϕ. Ref. H_2 indicates GaN on sapphire without ELO in hydrogen ambient.

4. Conclusion

We investigated the effects of hydrogen ambient, nitrogen ambient and their mixture ambient on ELO-GaN via atmospheric MOVPE. In hydrogen ambient, the ELO-GaN with a smooth surface was obtained using the <1$\bar{1}$00> stripe pattern, but the layer became rough on the <11$\bar{2}$0> stripe pattern. In nitrogen ambient, lateral overgrowth rate was very fast especially on the <1$\bar{1}$00> stripe pattern, but it was difficult to realize a smooth ELO layer surface. The mixture ambient allowed us to realize the fast lateral overgrowth rate and the smooth surface simultaneously. The reduction of the dislocation density in the ELO region was confirmed in the case of the mixture ambient. XRD analysis revealed the anisotropic crystallographic tilting of ELO-GaN toward the <11$\bar{2}$0>, which corresponds to the lateral growth direction. Nitrogen ambient enhanced the tilting of ELO-GaN.

5. Acknowledgements

The authors would like to acknowledge the encouragement and support of Tadao Tachibana, Kouichi Suzuki and Keisuke Imai of Mitsubishi Cable Industries, Ltd.

[1] S. Nakamura, T. Mukai and M. Senoh, Appl. Phys. Lett. 64 (1994) 1687.
[2] S. Nakamura, M. Senoh, S. Nagahama, N. Iwasa, T. Yamada, T. Matsushita, H. Kiyoku and Y. Sugimoto, Jpn. J. Appl. Phys. 35 (1996) L74.
[3] S. D. Lester, F. A. Ponce, M. G. Craford and D. A. Steigerwald, Appl. Phys. Lett. 66 (1995) 1249.
[4] S. Nakamura, M. Senoh, S. Nagahata, N. Iwasa, T. Yamada, T. Matsushita, H. Kiyoku, Y. Sugimoto, T. Kozaki, H. Umemoto, M. Sano and K. Chocho, Proc. 2nd Int. Conf. on Nitride Semicond. (Tokushima, 1997) 444.
[5] Y. Kato, S. Kitamura, K. Hiramatsu and N. Sawaki, J. Crystal Growth 144 (1994) 133.
[6] X. Li, A. M. Jones, S. D. Roh, D. A. Turnbull, E. E. Reuter, S. Q. Gu, S. G. Bishop and J. J. Coleman, Mat. Res. Soc. Symp. Proc. 395 (1996) 943.
[7] A. Usui, H. Sunakawa, A. Sakai and A. Yamaguchi, Jpn. J. Appl. Phys. 36 (1997) L899.
[8] T. S. Zheleva, O.-H. Nam, M. D. Bremser and R. F. Davis, Appl. Phys. Lett. 71 (1997) 2472.
[9] O.-H. Nam, M. D. Bremser, T. S. Zheleva and R. F. Davis, Appl. Phys. Lett. 71 (1997) 2638.
[10] D. Kapolnek, S. Keller, R. Vetury, R. D. Underwood, P. Kozodoy, S. P. DenBaars and U. K. Mishra, Appl. Phys. Lett. 71 (1997) 1204.
[11] H. Matsushima, M. Yamaguchi, K. Hiramatsu and N. Sawaki, Proc. 2nd Int. Conf. on Nitride Semicond. (Tokushima, 1997) 492.
[12] J. Park, P. A. Grudowski, C. J. Eiting and R. D. Dupuis, Appl. Phys. Lett. 73 (1998) 333.
[13] B. Beaumont, P. Gibart, M. Vaille, S. Haffouz, G. Nataf and A. Bouille, Proc. 2nd Int. Conf. on Nitride Semicond. (Tokushima, 1997) 412.
[14] K. Hiarmatsu, H. Matsushima, T. Shibata, N. Sawaki, K. Tadatomo, H. Okagawa, Y. Ohuchi, Y. Honda and T. Matsue, Mat. Res. Soc. Symp. 482 (1998) 257.
[15] A. Sakai, H. Sunakawa and A. Usui, Appl. Phys. Lett. 73 (1998) 481.

Pendeo-Epitaxy of Gallium Nitride and Aluminum Nitride Films and Heterostructures on Silicon Carbide Substrate

T. Gehrke, K. J. Linthicum, D. B. Thomson, P. Rajagopal, A. D. Batchelor *, R. F. Davis
Department of Materials Science and Engineering
* Analytical Instrumentation Facility
North Carolina State University
Box 7907
Raleigh, NC 27695-7907

Cite this article as: MRS Internet J. Semicond. Res. 4S1, G3.2 (1999)

ABSTRACT

Pendeo-epitaxy of individual GaN and $Al_xGa_{1-x}N$ films and single- and multi-layer heterostructures of these materials have been achieved on a columnar GaN seed layer using metallorganic vapor phase epitaxy. These structures have been characterized using scanning electron microscopy and atomic force microscopy. The RMS roughness value of the grown side wall plane $(1\bar{1}20)$ of these structures was 0.099 nm.

INTRODUCTION

Recent topics of focused research in the III-Nitride community have been the selective area growth coupled with lateral epitaxial overgrowth (LEO) and the application of this tandem process route to reduce the dislocation density of GaN films by several orders of magnitude in the overgrown areas. A new form of selective and lateral growth, namely 'pendeo (from the Latin: to *hang* or be *suspended*) -epitaxy' has been recently pioneered in our group [1-3], to achieve large area growth of III-N films having a continuous low dislocation density over the entire surface. This process route is based on the growth of GaN off a side wall and the ability to laterally overgrow a mask that has been employed to stop vertical propagation of line and planar defects. Additional details of this procedure and the initial results of this research have been reported previously [4,5].

In this paper we report the growth via pendeo-epitaxy of layered thin film structures consisting of GaN and $Al_xGa_{1-x}N$. The following sections describe the experimental procedure necessary to achieve layered structures by this technique in detail and discuss the results and conclusion of this study.

EXPERIMENTAL PROCEDURE

Layered structures containing GaN and $Al_xGa_{1-x}N$ have been grown on a 0.5 μm to 1.0 μm thick GaN seed layer grown on a high temperature, 100 nm thick AlN buffer layer previously deposited on a 6H-SiC(0001) substrate. All layers were grown using a cold-wall, vertical pancake style, RF-inductively heated metalorganic vapor phase epitaxy (MOVPE) system. The AlN buffer layers and the hexagonal GaN seed layers were each grown within the susceptor temperature ranges of 1080°C-1120°C and 980°C-1020°C, respectively, at a total pressure of 45 Torr. Triethylaluminum (20-25μmol/min), triethylgallium (23-29μmol/min), and NH_3 (1.5 slm) precursors were used in combination

Mat. Res. Soc. Symp. Proc. Vol. 537 © 1999 Materials Research Society

with a H_2 (3 slm) diluent. A 100 nm thick silicon nitride layer, employed as a growth mask for blocking the continued threading dislocations during the pendeo-epitaxial growth stage, was deposited using a plasma enhanced chemical vapor deposition (PECVD) system. A 150 nm layer of nickel was subsequently deposited as an etch mask and patterned in $\langle 1\bar{1}00 \rangle$ oriented stripes using standard photolithography techniques. Two different masks were used to produce (a) 2μm wide stripes with a spacing of 3μm, and (b) 3μm wide stripes with a spacing of 7μm. An inductively coupled plasma (ICP) etching system was employed to achieve the desired microstructures via (a) RF-sputtering of the exposed nickel stripes in an Ar-plasma and (b) ICP-etching of columnar forms in the GaN seed layers using a combination of Cl_2 and BCl_3. Etching was continued into the SiC substrate, which completely exposed each GaN column. Residual Ni was removed after etching by dipping in HNO_3. The samples were cleaned sequentially in tricloroethylene, acetone, methanol, and hydrochloric acid. The pendeo-epitaxial growth of the GaN and the $Al_xGa_{1-x}N$ layers were achieved within the susceptor temperature range of 1050-1100°C and 1080-1120°C, respectively, and at a total pressure of 45 Torr. Triethylgallium (23-27 μmol/min) and NH_3 (1.5 slm) precursors were again used in combination with a H_2 diluent (3 slm). The introducing of triethylaluminum at flow rates of 2.5 μmol/min and 5.8 μmol/min, respectively, into the growth chamber produced $Al_xGa_{1-x}N$ layers contained an Al concentration of approximately 5% and 10%.

A JEOL 6400 FE scanning electron microscope (SEM) and an Digital Instruments, Inc. Dimension 3000 atomic force microscope (AFM) operating in the tappingMode™ with an Olympus tapping mode etched silicon probe were employed for microstructural characterization.

RESULTS AND DISCUSSION

Figure 1 shows a schematic flow diagram of the process route for achieving pendeo-epitaxial growth of continuous layers of (c) GaN or (e) $Al_xGa_{1-x}N$. The intermediate steps in this approach can also be used to achieve the growth of (d) a double layer heterostructure of GaN and $Al_xGa_{1-x}N$, and a subsequent growth of (e) a continuous coalesced layer of $Al_xGa_{1-x}N$ or (f) a layered double heterostructure of GaN/ $Al_xGa_{1-x}N$ /GaN.

Each of the microstructures depicted in Figure 1 has been realized in this research, as shown in Figure 2. The scanning electron micrographs in the latter figure illustrate (a) the $\langle 1\bar{1}00 \rangle$ oriented columnar forms in a GaN seed layer, (b) simultaneous lateral growth of GaN from the side walls lateral overgrowth of the silicon nitride mask during pendeo-epitaxy, (c) a continuous, coalesced layer of GaN, (d) a bi-layer structure of GaN and $Al_{10}Ga_{90}N$, (e) a continuous coalesced layer of $Al_{10}Ga_{90}N$, and (f) a layered structure of GaN/$Al_{10}Ga_{90}N$/GaN.

The GaN layer shown in Figure 2(d) was grown for 35 min at a susceptor temperature of 1075°C and for 2 min at a susceptor temperature of 1090°C. The additional layer of $Al_{10}Ga_{90}N$ was grown for 20 min at 1090°C. This alloy layer appears in the scanning electron micrographs as a slightly darker cap atop the GaN layer. To produce the heterostructure shown in Figure 2(e) a thin GaN layer was grown for 2 min at a susceptor temperature of 1070°C and for 2 min at 1090°C. The $Al_{10}Ga_{90}N$ was deposited using three growth steps at the susceptor temperatures and times of 1090°C and 2 min, 1110°C and 50 min, and 1090°C and 30 min. The second step was

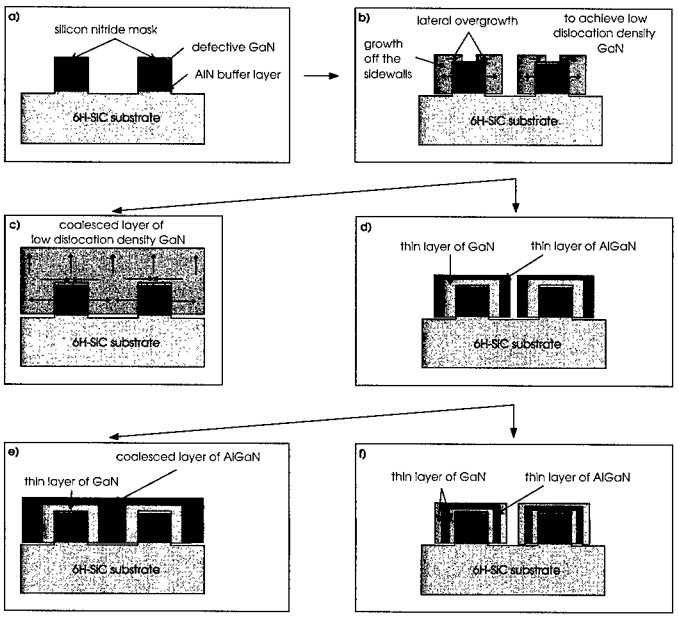


Figure 1. Schematic flow diagram showing the steps from (a) the etched columnar forms in the GaN seed layers to (b) lateral growth off the side walls of the seed layer and lateral overgrowth over the silicon nitride mask, to the growth of either (c) a continuous coalesced GaN film, or (d) a discrete bi-layer of GaN and $Al_xGa_{1-x}N$ from which further growth results in either (e) a continuous coalesced layer of $Al_xGa_{1-x}N$ or (f) a multi-layered structure of GaN and $Al_xGa_{1-x}N$ layers.

employed to force the $Al_{10}Ga_{90}N$ to grow laterally and coalesce; the third step was used to grow the film vertically. The growth rate of $Al_{10}Ga_{90}N$ films was markedly lower at both 1090°C and 1110°C than that of the GaN at any temperature employed in this study. A multi-layered structure shown in Figure 2(f) was also realized using several different growth parameter.

The first layer of GaN was grown at susceptor temperatures of 1075°C for 3 min and 1090°C for 2 min. The subsequent layer of $Al_{10}Ga_{90}N$ was grown using susceptor temperatures of 1090°C for 10 min and 1075°C for 5 min. The temperature during the $Al_{10}Ga_{90}N$ growth was not increased to 1110°C to limit the lateral growth. The additional layer of GaN was grown at a susceptor temperature of 1075°C for 10 min. The scanning electron micrograph in Figure 2(f) shows 60° interface planes between each layer. During the GaN growth the angled planes were growing out to the $(11\bar{2}0)$ plane to form the side walls of the structure.

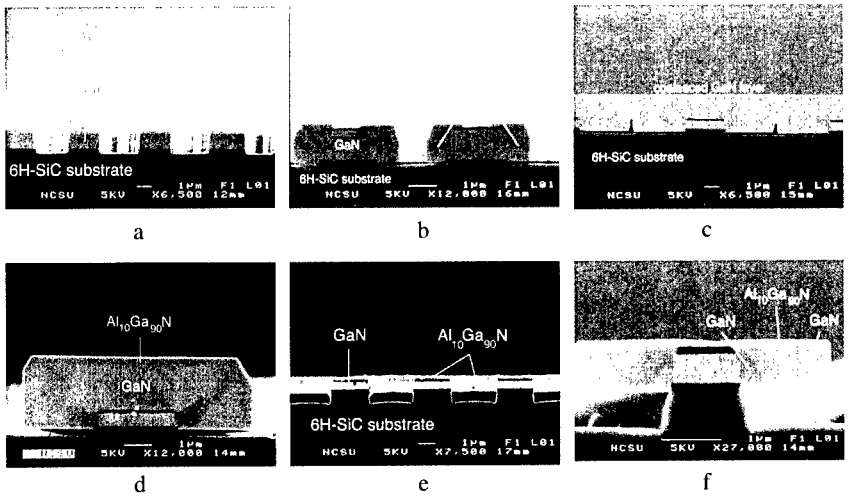


Figure 2. Scanning electron micrographs of (a) etched columnar forms in a GaN seed layer, (b) lateral and vertical growth phenomena during pendeo-epitaxy, (c) a continuous coalesced layer of GaN, (d) a discrete bi-layer structure of GaN and $Al_{10}Ga_{90}N$, (e) a continuous coalesced layer of $Al_{10}Ga_{90}N$, and (f) a multi-layered structure of GaN/$Al_{10}Ga_{90}N$/GaN.

The bi-layer structure in Figure 3 consists of a GaN layer grown at susceptor temperatures of 1075°C for 35 min and 1090°C for 2min and a capping layer of $Al_5Ga_{95}N$ grown for 20 min at a susceptor temperature of 1090°C. This structure possessed extremely smooth (0001) top and $(11\bar{2}0)$ side wall surfaces, as shown in the AFM images in Figure 4. The RMS roughness values of the (0001) plane and the $(11\bar{2}0)$ side walls were 0.548 nm and 0.099 nm, respectively.

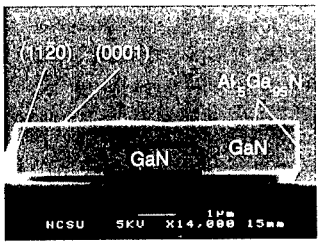


Figure 3. Scanning electron micrograph of a bi-layer structure of GaN and $Al_5Ga_{95}N$ used for AFM measurements.

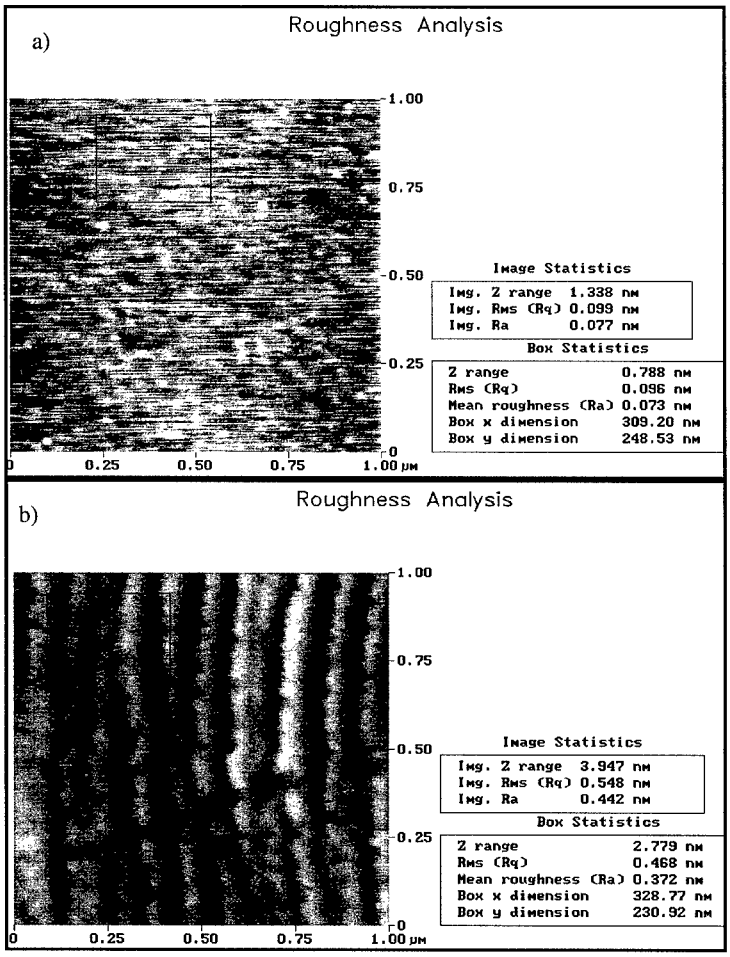


Figure 4.
Atomic force micrographs of:
a) the surface of the side walls represented by the $(1\bar{1}20)$ plane,
b) the top surface of the structure represented by the (0001) plane.

CONCLUSIONS

Pendeo-epitaxial growth of layered structures of GaN and $Al_xGa_{1-x}N$ has been achieved. The process steps for growing continuous coalesced GaN and $Al_xGa_{1-x}N$ layers have been discussed in detail. According to this steps the process routes for growing layered structures of GaN and $Al_xGa_{1-x}N$ have been introduced and discussed. The top surface and side walls of this structures have been characterized by atomic force microscopy and a RMS roughness of 0.548 nm and 0.099 nm, respectively, has been reported.

ACKNOWLEDGMENTS

The authors express their appreciation to Cree Research, Inc. for supplying the SiC wafers. This work was supported by the Office of Naval Research under the contract # N00014-96-1-0765, N00014-98-1-0384 with C. Wood as technical monitor, and N00014-98-1-0654 with J. Zolper as technical monitor.

REFERENCES

1. K. J. Linthicum, T. Gehrke, D. B. Thomson, K. M. Tracy, E. P. Carlson, T. Smith, T. S. Zheleva, R. F. Davis, Mat. Res. Soc. Symp., this volume
2. D. B. Thomson, T. Gehrke, K. J. Linthicum, P. Rajagopal, T. S. Zheleva, R. F. Davis, Mat. Res. Soc. Symp., this volume
3. T. S. Zheleva, D. B. Thomson, T. Gehrke, K. J. Linthicum, P. Rajagopal, S. Smith, R. F. Davis, Mat. Res. Soc. Symp., this volume
4. K. J. Linthicum, T. Gehrke, D. B. Thomson, E. P. Carlson, P. Rajagopal, T. Smith, R. F. Davis, Appl. Phys. Lett., submitted Nov. 1998
5. T. S. Zheleva, D. B. Thomson, K. J. Linthicum, S. Smith, R. F. Davis, J. of Electr. Mat., submitted Nov. 1998

PIEZOELECTRIC EFFECTS IN GaN/AlGaN MULTIPLE QUANTUM WELLS PROBED BY PICOSECOND TIME-RESOLVED PHOTOLUMINESCENCE

H. S. Kim [a)†], J. Y. Lin[†], H. X. Jiang [b) †], W. W. Chow*, A. Botchkarev**, and H. Morkoç**

[†] Department of Physics, Kansas State University, Manhattan, KS 66506-2601
* Sandia National Laboratories, Albuquerque, NM 85718-0601
** Department of Electrical Engineering and Physics, Virginia Commonwealth University, Richmond, Virginia 23284-3072

Cite this article as: MRS Internet J. Nitride Semicond. Res. 4S1, G3.3 (1999)

ABSTRACT

Piezoelectric effects in GaN/AlGaN multiple quantum wells (MQWs) have been directly probed by picosecond time-resolved photoluminescence (PL) spectroscopy. The time-resolved PL spectra of the 40 Å well MQWs reveal that the PL transition peak position is in fact blueshifted at early delay times due to the collective effects of quantum confinement of carriers, piezoelectric field, and Coulomb screening. However, the spectral peak position shifts toward lower energies as the delay time increases and becomes redshifted at longer delay times. By comparing experimental and calculation results, we have obtained a low limit of the piezoelectric field strength to be about 560 kV/cm in the 40 Å well GaN/$Al_{0.15}Ga_{0.85}N$ MQWs.

INTRODUCTION

The group III-nitride semiconductors have attracted much attention recently due to many important applications, such as blue/UV light emitting diodes (LEDs), laser diodes (LDs), and high-temperature/high-power electronic devices [1]. As demonstrated by GaN LDs, LEDs, and GaN based electronic devices, many GaN based devices must take advantage of multiple quantum well (MQW) structures such as GaN/AlGaN and InGaN/GaN MQWs. In order to optimize the device design, it is necessary to study and understand the physical properties of nitride MQWs as well as the MQW structural effects on the device performance. Recent work on the III-nitride alloy systems and MQWs has shown that localized excitons dominate the optical transitions in these systems at low temperatures[2-4]. And, it has been proposed and shown that piezoelectric fields due to lattice mismatch-induced strain in InGaN/GaN MQWs [5,6] and GaN/AlGaN QWs [6-9] are the primary reason for the large redshift of the photoluminescence (PL) emission peak. Indeed the piezoelectric field in strained layers has been used to modify the operating characteristics of devices fabricated from these materials [9-11].

EXPERIMENT

Time-resolved PL (TRPL) studies have been carried out for a set of GaN/AlGaN MQW samples grown under identical conditions with well thickness varying from 20 to 50 Å . These MQW samples were grown by reactive molecular beam epitaxy (MBE) on sapphire (Al_2O_3) substrates with a 1.5 μm $Al_xGa_{1-x}N$ (x=0.15) buffer layer. The MQWs are composed of ten periods of alternating GaN wells and 200 Å $Al_xGa_{1-x}N$ (x≈0.15) barriers. All samples were nominally undoped and the GaN epilayers grown under similar conditions were semi-insulating.

Mat. Res. Soc. Symp. Proc. Vol. 537 © 1999 Materials Research Society

For PL measurements, samples were attached to copper sample holders and placed inside a closed-cycle He refrigerator with a temperature variation from 10 to 300 K. Excitation pulses with pulse width of about 7 ps at a repetition rate of 19 MHz were provided by a cavity-dumped dye laser (Coherent 702-2CD) with Rhodamine 6G dye solution, which was pumped by a yttrium-aluminum-garnet (YAG) laser (Coherent Antares 76) with a frequency doubler. The output from the dye laser was frequency doubled again to provide a tunable wavelength in the ultraviolet (UV) region. The laser output after the second doubler has an average power of about 30 mW and the laser beam size on the sample was about 50 μm in diameter. The overall spectral resolution was about 0.2 meV and the time resolution of the detection system was about 25 ps.

RESULTS AND DISCUSSIONS

CW Spectra

Low-temperature (10 K) cw PL spectra for four representative $GaN/Al_xGa_{1-x}N$ MQW samples with well thickness L_w = 20 Å , 30 Å , 40 Å , and 50 Å are presented in Fig. 1(b), 1(c), 1(d), and 1(e) , respectively. For comparison, the PL spectrum of a GaN epilayer grown under the similar conditions is also shown in Fig. 1(a). For the GaN epilayer, the dominant transition at 3.485 eV at 10 K is due to the recombination of the ground state of A exciton [12-15]. In the 20 Å well MQW sample, the excitonic transition peak position at 10 K (3.548 eV) is blueshifted with respect to the epilayer by an amount of 63 meV, which is due to the well-known effects of quantum confinement of electrons and holes as well as the strain. Its transition energy (3.548 eV) is comparable to the bandgap of GaN under 0.4% compressive strain, which is expected for GaN embedded between $Al_{0.15}Ga_{0.85}N$ layers [7]. In the 30 Å and 40 Å well MQW samples, the cw transition peak positions at 10 K are redshifted with respect to the GaN epilayer by an amount of 13 and 45 meV, respectively. The origin of this redshift will be discussed later in relation with the results of the time-resolved PL (TRPL) spectra. On the other hand, the PL spectrum of the 50 Å well MQW sample exhibits a fairly complex behavior. The transition peak at higher emission energies (3.656 eV) in this sample is due to an optical transition in the AlGaN barrier regions [3]. The temperature dependence of the cw PL spectra of these samples has been measured. Figure 2 shows cw emission spectra of the 40 Å well MQW samples measured at four

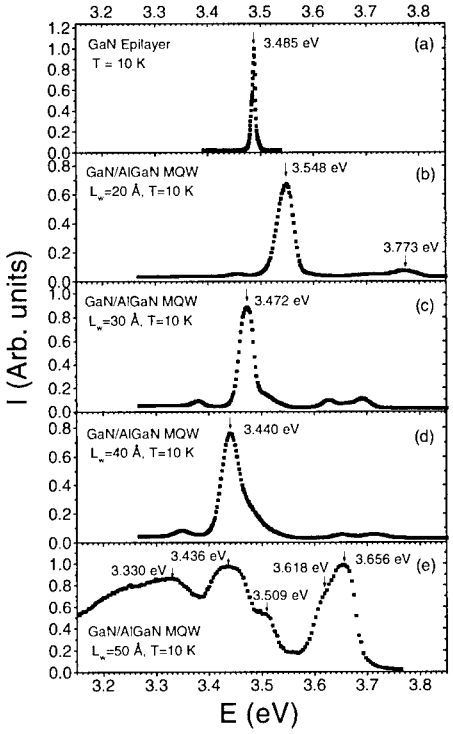


FIG. 1. Low-temperature (10 K) cw PL spectra of nominally undoped $GaN/Al_xGa_{1-x}N$ MQW samples with well thickness (b) L_w = 20 Å , (c) 30 Å , (d) 40 Å , (e) 50 Å, and (a) GaN epilayer grown under identical conditions as the MQW samples taken under the same experimental conditions.

representative temperatures T = 10, 100, 200, and 300 K, respectively. We observed two emission lines (3.440 and 3.480 eV at T = 10 K) with the lower-energy emission line being the dominant one at low temperatures. The higher-energy emission line may be related with higher

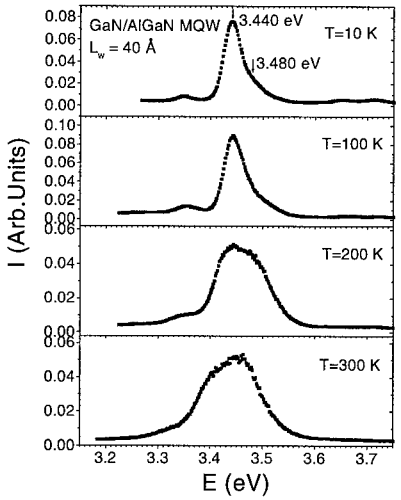


FIG. 2. CW PL spectra of nominally undoped 40 Å well $GaN/Al_xGa_{1-x}N$ MQWs measured at four representative temperatures T = 10, 100, 200, and 300 K.

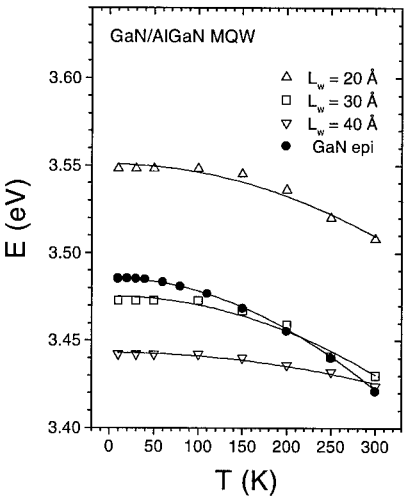


FIG. 3. The temperature dependence of the PL spectra peak positions of the dominant emission lines of $GaN/Al_xGa_{1-x}N$ MQW samples with well thickness L_w= 20 Å , 30 Å , and 40 Å. The solid lines are the least-squares fit of data with Eq. (1).

subband transitions and becomes dominant at higher temperatures (T=300 K). The temperature dependence of the PL peak position of the dominant emission line in the L_w = 20 Å , 30 Å , and 40 Å MQWs has been plotted in Fig. 3. For comparison, the temperature dependence of the PL spectral peak of a GaN epilayer grown under the similar conditions is also shown in Fig. 3. The temperature dependence of the dominant emission peak positions can be fitted by the temperature dependence of the bandgap energy using the empirical equation [16],

$$E_0(T) = E_0(0) - \alpha T^2/(\beta + T), \qquad (1)$$

where $E_0(0)$ is the transition energy at T=0 K and α and β are constants referred to as Varshni thermal coefficients. The solid curves in Fig. 3 are the least-squares fit of data by using Eq. (1). The fitted values for the GaN epilayer and MQWs with L_w = 20 Å , 30 Å , and 40 Å are $E_0(0)$ = 3.486 eV, 3.551 eV, 3.475 eV, and 3.443 eV; α = 0.0016 eV/K, 0.0010 eV/K, 0.0011 eV/K, and 0.0011 eV/K; $\beta = 1.89\times10^3$ K, 2.01×10^3 K, 2.01×10^3 K, and 5.41×10^3 K, respectively. The parameters obtained from the GaN epilayer and the 20 Å and 30 Å well MQWs are comparable to the parameters ($E_0(0)$ = 3.486 eV, $\alpha = 8.32\times10^{-4}$ eV/K, and β = 835.6 K) obtained by Shan et. al. [14] for a MOCVD GaN epilayer using the photoreflectance measurement. The value of β for the 40 Å well MQWs is anomalously larger

than those for the GaN epilayer. It is clear that for the 20 Å well MQW sample, the exciton peak position is blue shifted with respect to the epilayer at all temperatures. On the other hand, with respect to the GaN epilayer, the PL emission peaks in the 30 Å and 40 Å well MQW samples are redshifed with the amount of shift decreasing with temperature and become blue shifted at 300 K. Such a behavior is related to the effect of piezoelectric fields in these MQWs to be discussed in more detail next.

Time-resolved PL spectra

Time-resolved emission spectroscopy was employed to study the dynamics of optical transitions in GaN/$Al_xGa_{1-x}N$ MQWs. Figure 4 shows the TRPL spectra of the main emission lines of the 40 Å well MQW samples measured at T = 10 K for several representative delay times. The arrows in Fig. 4 indicate the spectral peak positions at different delay times. The dotted line indicates the position of the excitonic transition peak in the GaN epilayer grown under similar conditions. Several features can be observed for the 40 Å well MQW samples as

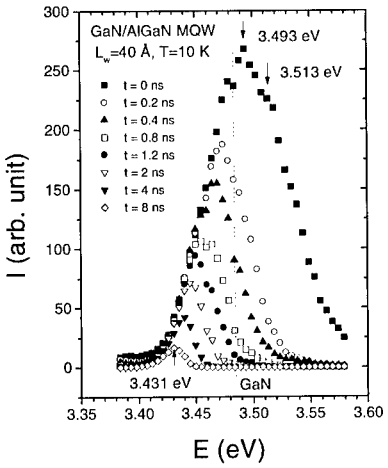


FIG. 4. Time-resolved PL spectra of the main emission lines measured at T = 10 K for 40 Å well MQWs for several representative delay times. Here, the delay time t_d = 0 has been chosen at the position of maximum intensity in the luminescence temporal responses. The arrows indicate the spectral peak positions at different delay times. The dotted lines indicate the position of the excitonic transition peak in GaN epilayers grown under similar conditions.

shown in Fig. 4. First, in contrast to the cw PL spectra shown in Fig.1(d), the spectral peak position at delay time t_d=0 (3.493 eV) is blueshifted with respect to the emission line in the GaN epilayer (3.485 eV). Second, the linewith of the emission line decreases with delay time. Third, the peak position of the emission line markedly shifts toward lower energies with an increase of delay time. For comparison with different well thicknesses, we have plotted in Fig. 5 the delay time dependence of the peak position E_p of different MQWs. In the case of 40 Å and 50 Å well MQW samples, E_p shift toward lower energies for more than 60 meV from t_d=0 to t_d=7 ns. The large amounts of redshift occurred in the early delay times, i.e., in the first 1 ns for 40 Å MQWs and in the first 200 ps for 50 Å MQWs.

The TRPL results can be explained well by the collective effects of piezoelectric field and photo-excited carrier screening. It is well established that piezoelectric fields are present in the well regions of the GaN/AlGaN MQWs and heterojunctions due to the lattice mismatch between GaN and AlGaN as well as the large value of the piezoelectric constant in GaN. Under

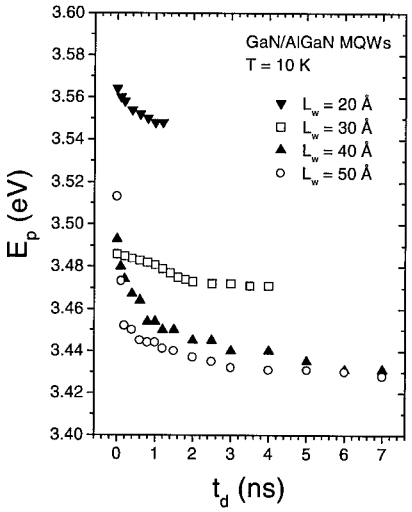


FIG. 5. The peak position E_p of the main emission line as functions of delay time t_d measured at T=10 K for the 20 Å, 30 Å, 40 Å, and 50 Å well $GaN/Al_xGa_{1-x}N$ MQW samples.

the influence of the piezoelectric field, optically excited carriers drift apart. The electrons (holes) move toward the direction opposed to (along) the piezoelectric field and the field induced by these spatially separated charge carriers will screen the piezoelectric field. On the other hand, the screening field due to the spatially separated charge carriers decreases with delay time because of the radiative recombination of electrons and holes. At t_d=0, the screening field induced by the photoexcited electrons and holes is strongest, which reduces or partially balances out the piezoelectric field. As the delay time increases, carriers recombine radiatively and the screening field gradually diminishes and the original piezoelectric field restores. Thus the total amount of shift from t_d=0 to $t_d \rightarrow \infty$ effectively corresponds to the variation of the electron and hole energy levels in the presence of the piezoelectric field with and without carrier screening, respectively. From this the piezoelectric field strength can also be estimated. By comparing experimental and calculation results, a lower limit value of the piezoelectric field strength of about 560 kV/cm in $GaN/Al_{0.15}Ga_{0.85}N$ MQWs as well as the electron and hole wave functions have been obtained for a 40 Å well MQW [8].

CONCLUSIONS

From cw PL spectra at low temperature (10 K), we observe that the exciton transitions for 20 Å MQWs are blue shifted with respect to the GaN epilayer and the PL emission peak positions for 30 Å, 40 Å, and 50 Å well MQWs are redshifted with respect to the GaN epilayer. On the other hand, the time-resolved PL spectra of the 30 Å, 40 Å, and 50 Å well MQWs reveal that the excitonic transition is in fact blueshifted at early delay times due to quantum confinement of carriers and the spectral peak position shifts toward lower energies as the delay time increases and becomes redshifted at longer delay times. It has been demonstrated that the results described above are due to the presence of the piezoelectric field in the GaN wells of GaN/AlGaN MQWs subject to elastic strain together with screening of the photoexcited carriers and Coulomb interaction. Our results show that TRPL spectroscopy is a powerful tool for studying and understanding the piezoelectric effects on optical properties of GaN MQWs and heterostructures.

ACKNOWLEDGMENTS

The research at Kansas State University is supported by ARO, BMDO, DOE (96ER45604/A000), and NSF (DMR-95-28226 and INT-97-29582). The research at the Virginia Commonwealth University is supported by ONR and AFOSR. The research at Sandia National Laboratories is supported in parts by DOE under contract No. DE-AC04-94AL85000.

H. S. Kim acknowledges support by RINS (BSRI-97-2406) in Gyeongsang National University.

REFERENCES

a) On leave from Department of Physics, Gyeongsang National University, Chinju, Korea.
b) e-mail : Jiang@phys.ksu.edu

1. H. Morkoç, S. Strite, G. B. Gao, M.E. Lin, B. Sverdlov, and M. Burns, J. Appl. Phys. **76**, 1363 (1994).
2. M. Smith, G. D. Chen, J. Y. Lin, H. X. Jiang, M. Asif Khan, and Q. Chen, Appl. Phys. Lett. **69**, 2837 (1996).
3. M. Smith, J. Y. Lin, H. X. Jiang, A. Salvador, A. Botchkarev, W. Kim, and H. Morkoç, Appl. Phys. Lett. **69**, 2453 (1996).
4. E. S. Jeon, V. Kozlov, Y. K. Song, A. Vertikov, M. Kuball, A. V. Nurmikko, H. Liu, C. Chen, R. S. Kern, C. P. Kuo, and M. G. Craford, Appl. Phys. Lett. **69**, 4194 (1996).
5. T. Takeuchi, S. Sota, M. Katsuragawa, M. Komori, H. Takeuchi, H. Amano, and I. Akasaki, Jpn. J. Appl. Phys. Part 2 **36,** L382 (1997).
6. A. Hangleiter, J. S. Im, H. Kollmer, S. Heppel, J. Off, and F. Scholz, MRS Internet J. Nitride Semicond. Res. **3**, 15 (1998).
7. Jin Seo Im, H. Kollmer, J. Off, A. Sohmer, F. Scholtz, and A. Hangleiter, Phys. Rev. B**57**, R9435 (1998).
8. H. S. Kim, J. Y. Lin, H. X. Jiang, W. W. Chow, A. Botchkarev, and H. Morkoç, Appl. Phys. Lett. **73**, 3426 (1998).
9. E. T. Yu, G. T. Sullivan, P. M. Asbeck, C. D. Wang, D. Qiao, and S. S. Lau, Appl. Phys. Lett. **71**, 2794 (1997).
10. R. Gaska, T. W. Yang, A. Osinsky, A. D. Bykhovski, and M. S. Shur, Appl. Phys. Lett. **71**, 3673 (1997).
11. E. S. Hellman, MRS Internet J. Nitride Semicond. Res. **3**, 11 (1998).
12. G. D. Chen, M. Smith, J. Y. Lin, H. X. Jiang, S. H. Wei, M. Asif Khan, and C. J. Sun, Appl. Phys. Lett. **68**, 2784 (1996).
13. D. C. Reynolds, D. C. Look, W. Kim, A. Özgür, A. Botchkarev, A. Salvador, H. Morkoç, and D. N. Talwar, J. Appl. Phys. **80,** 594 (1996).
14. W. Shan, T. J. Schmidt, X. H. Yang, S. J. Hwang, J. J. Song, and B. Goldenberg, Appl. Phys. Lett. **66**, 985 (1995).
15. K. C. Zeng, J. Y. Lin, H. X. Jiang, A. Salvador, G. Popovici, H. Tang, W. Kim, and H. Morkoç, Appl. Phys. Lett. **71**, 1368 (1997).
16. Y. P. Varshni, Physica **34**, 149 (1967).

NITRIDATION OF GaAs (001)-2x4 SURFACE STUDIED BY AUGER-ELECTRON SPECTROSCOPY

Igor Aksenov [*], Yoshinobu Nakada [**] and Hajime Okumura [***]

[*] Joint Research Center for Atom Technology (JRCAT) - Angstrom Technology Partnership, Higashi 1-1-4, Tsukuba, Ibaraki 305, Japan, aksenov@jrcat.or.jp

[**] Mitsubishi Materials Corporation, 1-297 Kitabukuro, Omiya, Saitama 330, Japan

[***] Electrotechnical Laboratory, Umezono 1-1-4, Tsukuba, Ibaraki 305, Japan

Cite this article as: MRS Internet J.Nitride Semicond.Res.4S1, G3.4 (1999)

ABSTRACT

Auger electron spectroscopy (AES) was used to investigate the processes taking place during the initial stages of nitridation of GaAs (001) surface. The analysis of the AES results combined with that of RHEED show that the processes taking place during nitridation greatly differ depending on the nitridation temperature. At low temperatures ($\leq$ 200°C) nitridation is hindered by kinetic restrictions on atomic migration, whereas at high temperatures ($\geq$ 500°C) the process of nitridation takes place simultaneously with the etching of the surface. However, for intermediate temperatures (300°C ~ 400°C) the results indicate that a complete monolayer of N atoms may be formed on the substrate during the initial stage of nitridation. The post-nitridation annealing of the samples nitrided at the intermediate temperatures results in the formation of a crystalline GaN layer, the line shape of the AES signals from which is identical to that for a GaN reference sample.

INTRODUCTION

GaN compound is difficult to grow on the technologically well-established substrates, i.e. Si and GaAs, which is due to the significant lattice mismatch of GaN with those materials. One of the methods of overcoming that difficulty is to grow a thin "low-temperature" buffer layer on the top of GaAs, which is amorphous and which crystallizes upon thermal annealing, leading to relaxation of the lattice mismatch. The subsequent MBE growth of the GaN compound on the top of that buffer layer results in a good quality cubic phase GaN [1]. However, a deeper understanding of the mechanisms governing initial stages of nitridation and subsequent nitride growth is vital for improvement of device performance. The formation of Ga-N and As-N bonds on the GaAs (001) surface during nitridation has been verified by X-ray photoelectron spectroscopy (XPS) [2,3], the results showing chemical shifts of the core levels of Ga, As and N caused by the nitridation process, with the formation of a disordered Ga-As-N phase in the subsurface region of the substrate. However, all XPS experiments have been carried out *after* nitridation by either transferring the nitrided sample from the "nitridation" chamber to the "XPS" chamber or by switching between nitridation and measurement cycles in the same chamber. It is important to note the inborn limitations of this experimental protocol since there is no guarantee that the surface conditions during measurements will be the same as those directly after the nitridation.

In the present study we used AES to investigate the processes taking place during the initial stages of interaction of active nitrogen species with the GaAs (001)-2x4 surface at various surface temperatures in the range from room temperature (RT) to 600°C. The measurements have been carried out *simultaneously* with the nitridation process, providing, thereby, an insight into the process of nitridation not hindered by the "post-nitridation" relaxation effects.

Mat. Res. Soc. Symp. Proc. Vol. 537 © 1999 Materials Research Society

EXPERIMENT

An experimental machine combining a differentially pumped electron beam column, a hemispherical electron energy analyzer for AES, as well as an RF plasma source for generation of active nitrogen species, has been constructed. Differential pumping of the column allows us to make AES measurements in the process of supplying active nitrogen to the surface, when the pressure in the chamber goes up to 10^{-4} Torr (base pressure is 2×10^{-10} Torr). The surface studied was an MBE-regrown GaAs (001) surface exhibiting (2x4) surface reconstruction, and the nitridation rate was controlled by using a mass flow controller, through which a flow of 1 ccm/s of the N_2 gas was introduced into the N-source. The substrate temperature during nitridation (T_s) was kept constant at various levels, i.e. at T_s = RT, 200°C, 300°C, 400°C, 500°C and 600°C. To characterize the bonding and composition of the buffer layer growing during the nitridation process, the Auger signals of Ga-LMM, As-LMM and N-KLL transitions at about 1070, 1230 and 380 eV, respectively, have been used. No traces of impurities, such as oxygen and carbon, have been detected on the original surface and at the beginning of the nitridation processes, although some oxygen ($\leq$ 2%) tends to appear after prolonged (~2 h) exposures to nitrogen flux.

RESULTS

Spectral Shape of the Auger Signals and the Core Level Shifts

The detailed non-differentiated spectra of N, Ga and As Auger transitions for various N- exposures are shown in Fig. 1 for T_s = 300°C. It can be seen that the signals exhibit, in addition to the dominant peak, a shoulder on the high kinetic energy (KE) side of the spectra. The experimental spectra can be deconvoluted into Voigt doublets (not shown), with the energy separation between the Voigt peaks constituting each doublet corresponding to the splitting of the LMM- and KLL-multiplets taking place due to the difference in the total relaxation energy of two core holes created during the Auger process. In addition, the As-signal during nitridation also exhibits a shoulder at the low-KE side of the spectra, this shoulder becoming more pronounced with decrease in the nitridation temperature. On the basis of the previous XPS results the above shoulder has been attributed to the surface AsN species, and the disappearance of this peak at higher temperatures is caused by desorption of the AsN species from the surface [2,3]. The N-originated spectra during nitridation also exhibit a shoulder at the low-energy side of the spectra separated by ~ 2.0 eV from the main N-KLL peak (Fig. 1),

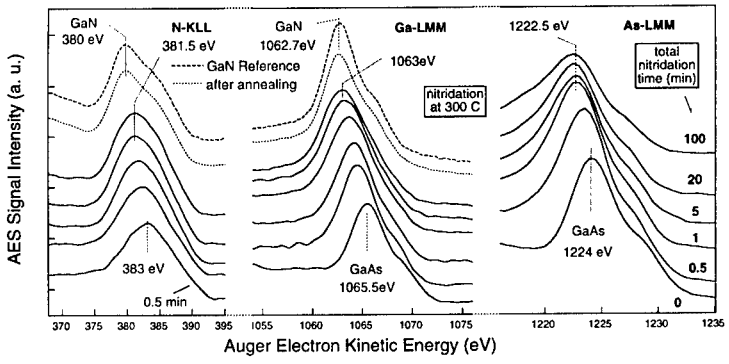


Fig. 1. Detailed Auger spectra from N-KLL, Ga-LMM and As-LMM transitions for various nitrogen exposures for the nitridation temperature T_s = 300°C, together with that of N and Ga taken after subsequent annealing at 630°C for 5 min (dotted curves) and those for a thick (~1.5 μm) MBE-grown GaN reference sample (dashed curves).

which disappears at higher temperatures just like the low-KE side shoulder on the As-originated spectra. This shoulder has been assigned to the N-originated signal from As-N bonds in the AsN species, in accordance with XPS results [3].

It can be seen from Fig. 1 that the spectral positions of the peaks exhibit shifts to lower KE as the nitridation proceeds. It has been found that the magnitude of these shifts depends on the nitridation temperature. Dependencies of the apparent energy shift of the peak of Ga-signal on nitrogen exposure for various nitridation temperatures are shown in Fig. 2. It can be seen that the magnitude of the shift increases with increase in the nitridation temperature in the range RT $\leq T_s \leq$ 300°C, levels off for 300°C $\leq T_s \leq$ 400°C, and starts to decrease for $T_s \geq$ 500°C. Therefore, the dependence of the magnitude of the shift on T_s is not monotone, but exhibits a maximum for the nitridation temperature in the range 300°C - 400°C. The situation is similar for As- and N-signals, where the most pronounced low-KE shifts (-1.5 eV) have also being observed for T_s in the range 300°C - 400°C, whereas nitridation at the lower or higher T_s results in the smaller shifts [4]. Annealing of the samples at 600-650°C results in the additional low-KE shifts for all signals, as well as in a drastic decrease on the intensity of As-signal due to the desorption of As from the surface. It is important to note that after annealing both the spectral position and the spectral shape of the Ga- and N-originated signals for the samples nitrided at the surface temperature 300°C $\leq T_s \leq$ 400°C (and only for T_s in that range) becomes *identical* to that of the GaN reference sample (Fig. 1). It is also important that annealing results in a complete disappearance of the As-signal from the surface only for the samples nitrided at 300°C $\leq T_s \leq$ 400°C, whereas the samples annealed after nitridation at higher or lower T_s still exhibit some As in the subsurface region (~2-5%) even after prolonged annealing.

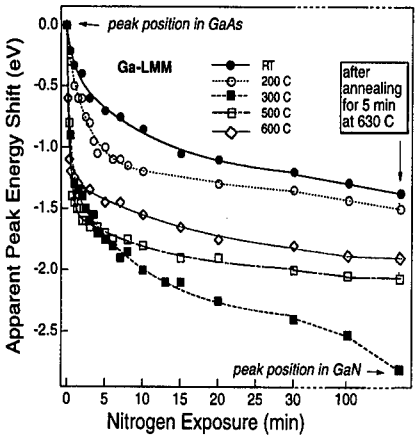


Fig. 2. Dependencies of the energy shifts of the peak of Ga-transition on N-exposure for various substrate temperatures together with that after subsequent annealing at 630°C for 5 min. The data for 400°C is similar to that for 300°C and is not shown.

In general there may be two factors determining the shift of the Auger spectra taken from the surface of a semiconductor. The first one is a chemical shift reflecting change in a chemical environment and the second is a shift of the Fermi level due to band bending. As it has been verified by XPS studies [2,3], nitridation of the GaAs (001) surface results in the formation of the disordered Ga-As-N compound as incoming N atoms substitute for the As atoms. The formation of the Ga-As-N phase leads to the broadening of the Auger signals and is partly responsible for the observed shifts in the spectra. Since the ionicity of the Ga-N bonds is higher than that of the Ga-As bonds due to an increased charge transfer from Ga to anion as arsenic is substituted by nitrogen, we can expect a shift of the core levels of Ga to higher binding energies (BE) and, therefore, a low-KE shift of the Ga-LMM Auger transition, which is in accordance with the experimental results. Since the low-KE shift of the spectra is mostly pronounced during the first 2 - 5 min of nitridation, we believe that the nitridation of the surface takes place mostly during this short time interval, after which it is much slowed down as N atoms begin to substitute As atoms in the back-bonds.

Comparing N-As bonds with the Ga-As ones we can see that the direction of charge transfer is reversed, the charge being transferred from As atom in the N-As bonds. Therefore, the formation of the N-As bonds should result in a low-KE shift of the As-originated signal, which is observed experimentally, but only for the nitridation temperatures $T_s \leq$ 400°C. At higher temperatures the As-originated signal, while shifting a little towards low-KE during the first 2 min of nitridation, exhibits a small shift towards high-KE as the nitridation proceeds. Therefore, we believe that the shift of the As-signal is determined by an interplay of two (or several) effects.

Careful analysis of the above results, together with those for the N-originated signal, indicate that, whereas nitridation at low temperatures (T_s < 300°C) results only in the chemical shift of the Auger signals under consideration, that for the temperatures $T_s \geq 300$°C leads to both the chemical shift and a shift caused by the band bending effect. It remains unclear why the band bending effect is the most pronounced at the temperatures in the range 300°C - 400°C. One possible explanation may be that a uniform layer of GaN (possibly creating a heterojunction with GaAs) is formed on the surface at these nitridation temperatures, which, however, is not formed upon nitridation at lower or higher temperatures due to kinetic restrictions on atomic migration (with the resulting island-like structures on the surface) or roughening of the surface due to etching effects for lower and higher temperatures, respectively.

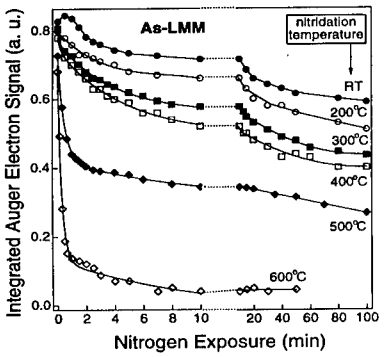


Fig. 3. Dependencies of As-signal intensities on the N-exposure for various temperatures.

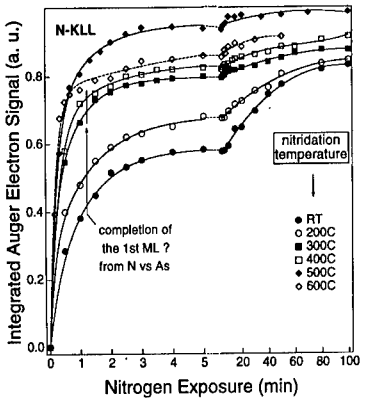


Fig. 4. Dependencies of N-signal intensities on the N-exposure for various temperatures.

Dependencies of the Auger Intensities on Nitrogen Exposure

Figs. 3, 4 show the dependencies of the integrated intensities $I(t)$ for the As- and N-originated Auger signals on the nitrogen exposure time t during nitridation. Since the spectra of all three elements exhibit a change in their spectral shape as the nitridation proceeds, we could not use the peak-to-peak values of the differentiated Auger signals to determine intensities of the signals. Instead, the areas of non-differentiated signals have been used for quantitative evaluation of the nitridation process, the areas having been determined by a trapezoidal integration with the cosine background correction. The data for the intensities the As- and N-originated signals has been normalized to that of the Ga-originated signal prior to the nitrogen exposure, the intensity of which at any nitridation temperature was taken as 1.0.

It can be seen from Figs. 3, 4 that, as the nitridation proceeds, the intensity of the As-signal decreases, whereas that of the N-signal increases. At the same time, the intensity of Ga-signal does not exhibit any drastic changes (not shown). It can also be seen that the intensities of the As- and N-originated signals exhibit the most drastic changes during the first several min (or even seconds, depending on the temperature) of nitridation, after which the signals level off at the levels strongly dependent upon the nitridation temperature. The magnitude of the changes in the intensities of the N- and As-originated signals greatly exceeds that for the Ga-originated signal, which is consistent with the substitutional (anion exchange) nature of the nitridation process, when N atoms substitute for those of As, whereas Ga atoms mostly retain their positions in the subsurface region.

An increase in the nitridation temperature results in a drastic decrease in the intensity of the As-signal due to the increase in the desorption rate of As and in a drastic increase in the

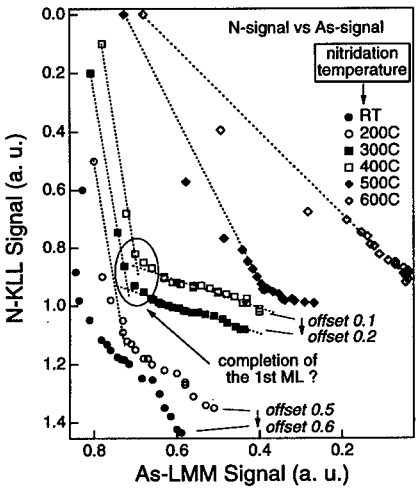


Fig. 5. Intensities of the N-signal as a function of that for the As-signal for various temperatures. Ellipse shows the position of breaks on the curves which probably arise due to the completion of the first monolayer. Notice the offsets of the curves.

intensity of the N-signal. However, it should be noted that, although the rate of an increase in the intensity of the N-signal (related to the sticking coefficient) for the highest nitridation temperature studied (600°C) during the initial 40 sec of nitridation exceeds that for 500°C, further nitridation results in the leveling off the signal for T_s = 600°C at the level *lower* than that for T_s = 500°C. The last phenomenon can be explained by taking into account an increased desorption rate of the nitrogen species from the nitrided surface at T_s = 600°C, which is accordance with the results of Makimoto *et al*. [6].

The dependencies of intensities of both As- and N-signals (not shown) are exponential-like smooth curves exhibiting no apparent breaks. However, plots of intensities of the N-originated signal (adsorbate) against that of the As-originated one (substrate), shown in Fig. 5, exhibit pronounced breaks, but *only* for the data taken for nitridation temperatures T_s = 300°C and 400°C (see ellipse in Fig. 5). A break in an adsorbate signal *vs* substrate signal dependence usually occurs at the completion of a monolayer (ML) [5]. Therefore, the breaks on the curves shown in Fig. 5 are believed to correspond to the completion of the first ML of N atoms.

The position of the break-points in Fig. 5 corresponds to the nitridation time of about 1.5 min and is shown as a vertical line on the $I_N(t)$ dependencies in Fig. 4. It can be seen from the examination of this figure that no apparent breaks are discernible in the $I_N(t)$ dependencies after 1.5 min of nitridation, which seems to contradict the results shown in Fig. 5. The above discrepancy, however, can be explained by taking into account possible changes of sticking probability of the active nitrogen species [7]. Indeed, whereas gradual changes in the value of the sticking probability result in the smoothing of the $I_{As}(t)$ and $I_N(t)$ dependencies, it will not affect the plot of I_N *vs* I_{As} since the time-variable is eliminated in this plot.

RHEED Results

Nitridation results in drastic changes of the initial (2x4) RHEED pattern, these changes depending on the nitridation temperature. At low temperatures $T_s \leq$ 200°C, once the nitrogen plasma is struck the GaAs reconstruction features fade out, the intensity of the diffracted beam being transferred to the background (not shown). The (2x4) reconstruction of the initial surface is destroyed after 1.5 min of nitridation with an appearance of (1x1) pattern from the unreconstructed surface, which, in its turn, disappears after 3 min of nitridation, giving rise to no pattern except for a smooth background, indicating that a disordered GaAsN layer is formed in the subsurface region. Thermal annealing of the samples at 630°C results in an appearance of an arc pattern, indicating an appearance of preferred orientations in the disordered layer. The crystallization, however, is not complete since the diffraction features retain their arc-like character even after prolonged annealing.

The situation is different for T_s in the range 300°C-400°C. Similar to the above case, nitridation during the first several min results in the formation of the disordered layer. However, after approximately 10 min of nitridation that disordered layer begins to re-crystallize, which is evidenced by an appearance of diffuse spots in the RHEED pattern corresponding to the lattice spacing of GaN (4.5 Å). The thermal annealing then results in an appearance of the sharp spotty RHEED pattern characteristic of a mixture of cubic and hexagonal GaN phases, the cubic phase being dominant [1].

An increase in the nitridation temperature up to $T_s \geq 500^{\circ}C$ results in a different progression. Upon striking the nitrogen plasma the (2x4) reconstruction quickly (after ~20 sec) changes to a sharp streaked (3x3) pattern. However, the surface retains the (3x3) reconstruction for only 10 sec, after which the (3x3) features fade giving rise to the (1x1) pattern from the unreconstructed surface. The (1x1) pattern, in its turn, also fades as the nitridation proceeds, but after further 2 min of nitridation the GaN-originated spots, superposed on the blurred (1x1) streaked pattern from GaAs, become discernible in the pattern. As we proceed with nitridation, the intensity of the GaN-originated spots increases, whereas that of the GaAs-originated streaks decreases, the streaks becoming indiscernible after about 5 min from the beginning of nitridation. At the same time, however, a blurred spots corresponding to the (004)- and (115)-diffraction features from the GaAs phase appear in the pattern, the intensity of this spots increasing as we proceed with nitridation. Diagonal lines between the diffraction spots also appear in the pattern, which is due to the formation of the (111) facets caused, in its turn, by the etching of the substrate by impinging nitrogen species [1]. Annealing of the samples at 650 - 700°C results in a disappearance of the GaAs-originated spots in the pattern. Therefore, we believe that at high nitridation temperatures the GaAs islands are formed on the top of the nitrided GaN layer due to out-diffusion of arsenic, substituted by nitrogen, from the GaAs substrate. These islands desorb from the surface at the temperatures higher than 650°C due to the desorption of arsenic.

CONCLUSIONS

In conclusion, the results presented above show that the processes taking place during nitridation of the GaAs (001) surface greatly differ depending on the nitridation (surface) temperature. On the one hand, at low temperatures ($T_s \leq 200^{\circ}C$) nitridation is hindered by kinetic restrictions on the atomic migration, and we believe that nitridation occurs through the formation of islands or "simultaneous multilayers" which do not cover the underlying surface completely. Disordered GaAsN phase is formed in the subsurface region, and that phase can not be completely re-crystallized even after prolonged annealing.

On the other hand, at high temperatures ($T_s \geq 500^{\circ}C$) the process of nitridation takes place simultaneously with the etching of the surface (at different portions of the surface) due to decomposition of the substrate under an impinging N-flux, leading to the growth of the (111) facets and resulting in the rough interface between the GaN and GaAs phases. It seems that the N atoms agglomerate to the nitrided portions of the surface to form GaN islands, whereas the surface portions which are not nitrided initially are etched by exposing the (111) facets.

However, for intermediate nitridation temperatures ($300^{\circ}C \leq T_s \leq 400^{\circ}C$) it was found that the disordered GaAsN phase, formed at the initial stage of nitridation, partly crystallizes even without annealing. Moreover, AES results indicate that one monolayer of N atoms (partly mixed with arsenic) may be formed on the substrate during the initial stage of nitridation. The formation of the complete ML of GaN results in the band bending, which leads to the most pronounced low kinetic energy shifts of the Auger signals for the nitridation temperatures in this range. The post-nitridation annealing of the samples nitrided at the intermediate temperatures results in the formation of a crystalline GaN layer, the line shape of the AES signals from which is identical to that for a thick GaN reference sample.

REFERENCES

1. H. Okumura, K. Ohta, G. Feuillet, K. Balakrishnan, S. Chichibu, H. Hamaguchi, P. Hacke, and S. Yoshida, J. Cryst. Growth **178,** 113 (1997).
2. A. Masuda, Y. Yonezawa, A. Morimoto, and T. Shimizu, Jpn. J. Appl. Phys. **34**, 1075 (1995).
3. X.-Y. Zhu, M. Wolf, T. Huett, and J. M. White, J. Chem. Phys. **97**, 5856 (1992).
4. I. Aksenov, Y. Nakada, and H. Okumura, Jpn. J. Appl. Phys. **37**, L972 (1998).
5. C. Argile and G. E. Rhead, Surf. Sci. Rep. **10,** 277 (1989).
6. T. Makimoto and N. Kobayashi: Appl. Surface Sci. **100/101**, 403 (1996).
7. I. Aksenov, Y. Nakada, and H. Okumura, J. Appl. Phys. **84**, 3159 (1998).

TEMPERATURE EFFECT ON THE QUALITY OF AlN THIN FILMS

Margarita P. Thompson*, Andrew R. Drews***, Changhe Huang**, Gregory W. Auner**

*CH&MSE Dept., Wayne State University, Detroit, MI 48202
**ECE Dept., Wayne State University, Detroit, MI 48202
***Physics Dept., Scientific Research Laboratories, Ford Motor Company, Dearborn, MI 48121

Cite this article as: MRS Internet J. Nitride Semicond. Res. 4S1, G3.7 (1999)

Abstract

AlN thin films were deposited at various substrate temperatures via Plasma Source Molecular Beam Epitaxy. The films were grown on 6H-SiC (0001) substrates. Reflection High Energy Electron Diffraction and Atomic Force Microscopy showed a dramatic change in the surface morphology of the film grown at 640°C. This is attributed to a change in the growth mechanism from pseudomorphic at lower temperatures to three-dimensional at higher than 640°C temperatures. Photoreflectance measurements showed an absorption shift toward 200 nm as the deposition temperature increases which is attributed to the change in the growth mechanism at higher temperatures. X-Ray Diffraction was unable to conclusively determine the AlN (0002) peak due to a significant diffuse intensity from the SiC (0002) peak. A MIS structure was created by depositing Pt contacts on the film grown at 500°C. I-V measurements showed that the Pt/AlN contact is Schottky.

Introduction

AlN is a group III-V nitride wide bandgap semiconductor. Its bandgap, the largest among the III-V nitrides, gives AlN an array of interesting properties including: high degree of hardness, high thermal and chemical stability, and high thermal conductivity [1-3]. One major area where these properties can find application is in the construction of high-power, high-temperature devices which can operate in harsh conditions. Of particular interest is the possibility for using AlN as an insulator in SiC-based MIS structures [4]. Such devices can operate at temperatures as high as 550°C while ordinary Si-based devices fail at around 120°C. At the same time AlN/SiC-based devices will be less susceptible to radiation damage.

However, prior to designing AlN-based devices, a number of materials issues need to be resolved. Two important problems are: i) finding a technique and optimal growth conditions for depositing stoichiometric AlN films of high purity and low defect density; ii) finding a substrate material which closely matches the lattice parameter and thermal expansion coefficient of AlN.

Here we report a systematic study of the effect of substrate temperature on the crystal quality of AlN thin films grown on 6H-SiC (0001) substrates via Plasma Source Molecular Beam Epitaxy (PSMBE). Our understanding of the growth mechanisms of AlN in the PSMBE system at various temperatures is presented.

Mat. Res. Soc. Symp. Proc. Vol. 537 © 1999 Materials Research Society

Experiment

All AlN films were deposited on pieces from a single 6H-SiC (0001) wafer which was obtained from Advanced Technology Materials in 1994. The substrate was n-type with carrier concentration of 4.8×10^{18} cm^{-3}. The films were deposited on the Si-face of the substrate. 6H-SiC was chosen as a substrate for AlN growth because of: (i) their close lattice parameter and thermal expansion coefficient match, and (ii) to study the properties of AlN/SiC MIS structures. Each substrate was ultrasonically degreased for 20 minutes in acetone and methanol in succession, followed by a one-minute etch in 10% (by volume) HF for removing any SiO_x from the surface. Prior to deposition, each substrate was preheated in the PSMBE system above 850°C for one hour for degassing. Deposition of AlN films was accomplished using a unique technique developed in our laboratory called Plasma Source Molecular Beam Epitaxy (PSMBE). The PSMBE system has a new and innovative deposition source which includes a magnetically enhanced, r. f. powered hollow cathode, lined with high purity aluminum. A mixture of high purity argon and nitrogen is supplied to the hollow cathode, where a plasma consisting of high energy aluminum, argon, and nitrogen is formed. A flux containing predominantly Al^+ and N^+ ions of energies around 1 eV leaves the hollow cathode source. This flux is further accelerated by negative bias applied to the substrate. The PSMBE system is described in detail elsewhere[5].

AlN films were grown at 440°C, 500°C, 560°C, 640°C, and 800°C using a substrate bias voltage of -15 eV which is optimum for our PSMBE system. All films had a thickness of approximately 2000 Å as measured by a piezoelectric thickness monitor. The films were characterized *in-situ* by Reflection High Energy Electron Diffraction (RHEED) and *ex-situ* by Atomic Force Microscopy (AFM), X-Ray Diffraction (XRD), and optical reflectance. The AFM characterization was performed using a Digital Instruments Nanoscope III operating in contact mode with standard Si_3N_4 tips. The films were characterized by XRD in a Scintag X1 θ-θ diffractometer using Cu radiation. The samples were supported on a zero-background quartz plate and data were collected either in symmetric (Bragg-Brentano) scans or in rocking scans. For optical reflection measurements a Lambda 900 UV/Vis/NIR Spectrometer with range 180-3,000 nm was used. For electrical measurements, Pt electrodes were deposited in a dc-magnetron sputtering system on the sample grown at 500°C. Blanket electrodes were deposited on the bottom surface of the SiC substrates and top circular contacts with a diameter of 1 mm were deposited on the films surface through a hard mask. C-V characterization was performed using a HP4192A LF impedance analyzer at frequencies of 1 MHz. I-V measurements were performed on a HP4140B pico-ammeter with a dc-voltage source. A heated chuck was used to reach temperatures up to 300oC.

Results and Discussion

AFM revealed a number of scratches on the substrates surface. The depth of the more profound scratches was around 2 nm as determined by AFM. Following a degassing procedure lasting one hour at 850°C, RHEED studies of the 6H-SiC substrates gave patterns with streaks which is an indication of relatively smooth surfaces with terraces and steps.

As-grown AlN films did not display similar streaking, but rather oblong spots, indicative of facetted islands on the surface. The RHEED pattern from the film deposited at 640°C consists of round spots which shows that the surface is rough and the pattern is due to transmission through surface asperities rather than reflection from the surface. Figure 1 shows AFM images

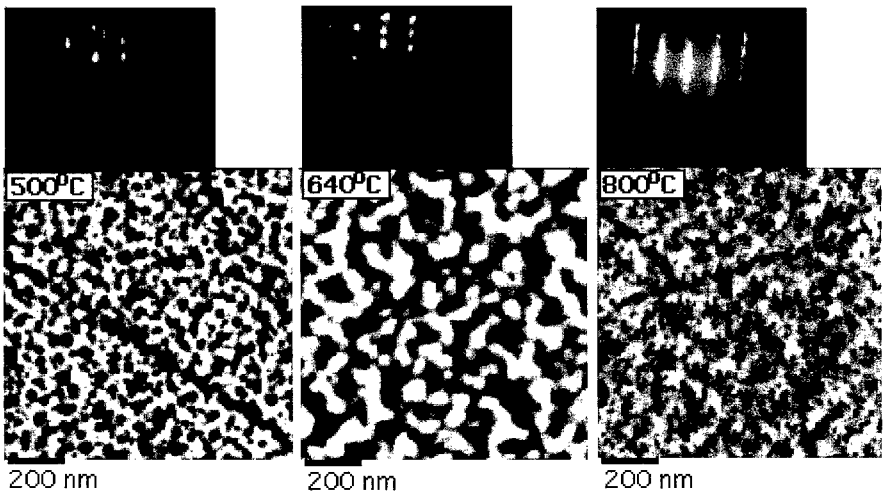


Figure 1. AFM images and RHEED patterns of the films grown at 500°C, 640°C, and 800°C. The film deposited at 640°C has the greatest roughness and the largest surface features.

and RHEED patterns of the films grown at 500°C, 640°C, and 800°C. The film grown at 640°C has the greatest roughness and the largest substrate features among all the films. The films grown at temperatures lower than 640°C have small surface features very similar to the 500°C film. The film deposited at 800°C shows unusually shaped features. From the surface analysis one can conclude that at around 640°C a change in the growth mechanism occurs. At lower temperatures the depositing species do not have enough energy for lateral movement on the surface. The growth is pseudomorphic which results in smooth but strained films. At around 640°C the growth changes to three-dimensional and the film grows in columns. As the deposition temperature increases the films get smoother. This model is in agreement with our previous studies [5, 6] on the temperature effect on the quality of AlN films deposited on silicon, sapphire, and Lely grown substrates.

Symmetric XRD scans on all the samples displayed significant intensity from the SiC (0002) peak near $2\theta=35.7^{\circ}$ that severely overlaps the AlN (0002) peak, despite the intentional 3.5° off-cut of the substrates. Figure 2a represents a symmetric scan on the AlN film grown at 800°C. An increased intensity around AlN (0002) peak at around $2\theta=36^{\circ}$ can be observed. However, rocking scans about the SiC (0002) peak (Fig.2b) showed that the substrates are not single crystals, and typically contain a spread in orientation of about 4 degrees. Figure 2b shows a rocking curve about the 6H-SiC (0002) peak of another piece from the same wafer illustrating a miscut, larger than the specified one, as well as the wide orientation spread. In addition to the strong crystalline peaks seen in the rocking scans a significant fraction of the SiC (0002) intensity is diffuse. Due to this diffuse "halo" we are unable to conclusively determine whether we have observed the AlN (0002) peak. However, RHEED data indicates textured AlN growth.

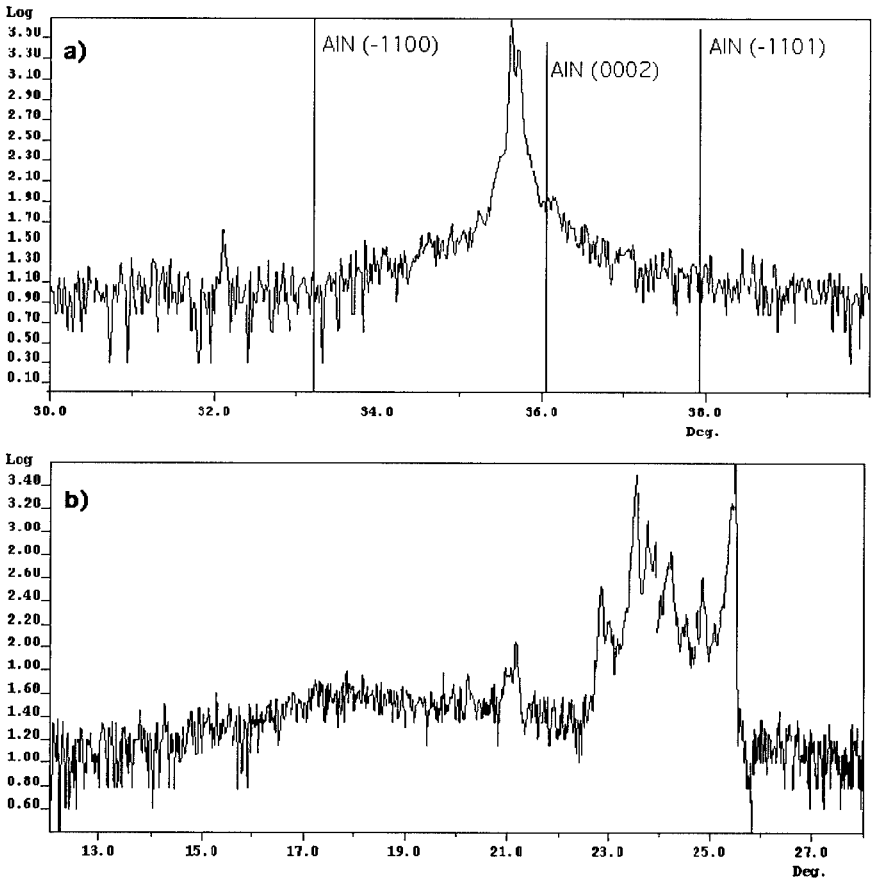


Figure 2. a) A symmetric XRD scan on the film grown at 800°C and the standard AlN (-1100), (0002), and (-1101) peaks. b) Rocking scan about the 6H-SiC (0002) peak.

Figure 3 shows photoreflectance measurements for all five films in the wavelength interval between 180 and 800 nm. All reflectance curves are characterized with one large peak in the interval 209-230 nm depending on the growth temperature. The films grown at temperatures lower than 640°C indicate a peak reflectivity of 37-40% in the range 209-216 nm with a decrease in reflectance at lower wavelengths probably due to absorption at the AlN bandgap. In high quality AlN, absorption should occur at around 200 nm which corresponds to an energy of 6.2 eV. The absorption of the films grown at lower temperatures is shifted to lower wavelengths due to a strained growth. At growth temperatures of 640°C and higher, the shift in absorption is observed towards 200 nm which, to our understanding, is due to a change in the growth mode which causes strain relaxation in the film. This conclusion is in agreement with the surface analysis data discussed above.

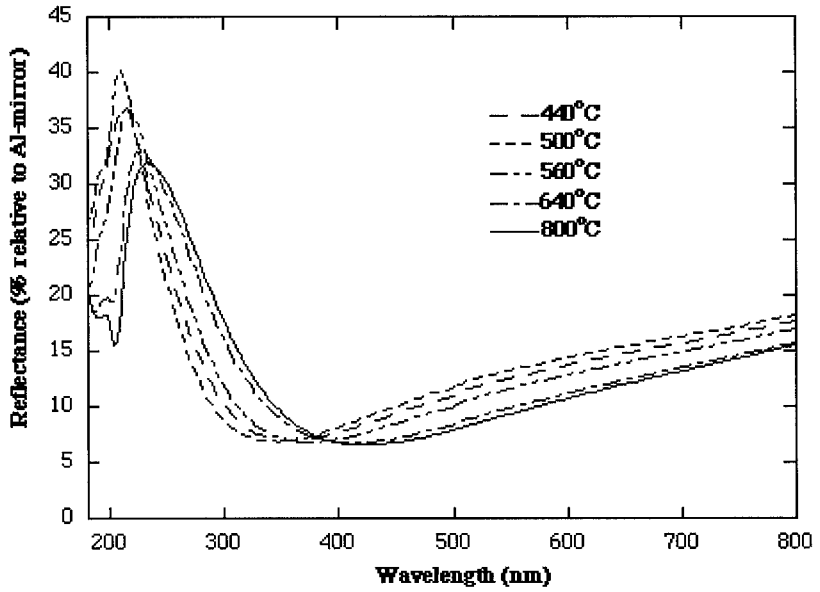


Figure 3. Photoreflectance measurements for all AlN films.

Capacitance-voltage (C-V) and current-voltage (I-V) measurements were performed at room temperature and 300°C on the film grown at 500°C. Due to the shorting of the contacts on all of the other samples, C-V and I-V measurements could only be performed on the film grown at 500°C. We believe that the contact shorting in the other samples is caused by small crystallites on the substrate surface which were visible under optical microscope. This is an example of the critical impact of the substrate surface quality on the performance of device structures. C-V measurements are shown in Figure 4a. A small hysteresis loop was observed both at room temperature and 300°C, which is an indication of the presence of trapping centers. Another feature of the C-V curve is the presence of a shoulder at room temperature and 300°C. However, at 300°C this shoulder is shifted toward lower voltages. Figure 4a also shows that the C-V curve measured at 300°C is shifted in the negative bias direction compared to the curve obtained at room temperature. This observation is similar to that reported by Tin et al. [4]. They attribute this shift to the activation of fixed positively charged states in the AlN layer at the film/substrate interface at elevated temperatures. The I-V characteristics at room temperature and 300°C are shown in Figure 4b. The sample has high leakage currents at both temperatures. Although the leakage current at 300°C is slightly higher it did not damage the sample. The I-V curves were repeatable even after multiple cycles of heating to 300°C and cooling back to room temperature. The high leakage current as well as the hysteresis loop in the C-V curves may be due to high defect density in the film grown at 500°C. RHEED, AFM and optical reflection measurements confirm that the defect density of this film is high. In addition, the SiC crystallites protrude through the film to within a very close distance to the contacts. Thus, the distance between a contact and the SiC substrate at the points of protrusion could be only a few

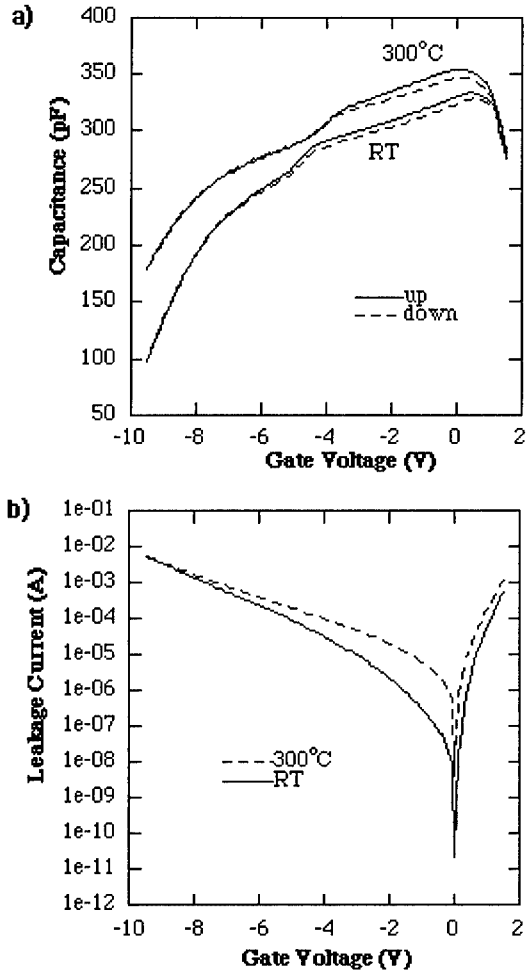


Figure 4. a) Capacitance-Voltage and b) Current-Voltage curves for the AlN film deposited at 500°C.

hundred Å which may partly account for the high leakage current. The defect density in the samples grown at higher temperatures is expected to be smaller and we would expect better C-V and I-V characteristics.

Conclusions

A systematic study of the effect of deposition temperature on the AlN crystalline quality was performed. Surface analysis including RHEED and AFM showed that around 640°C the growth mode changes from pseudomorphic to three dimensional. Temperatures higher than 640°C tend to give smoother films. Due to a high diffuse intensity of the SiC (0002) peak, XRD

scans could not conclusively determine that the higher intensity at $2\theta=36^{\circ}$ is due to the AlN (0002) peak. Photoreflectance measurements showed an absorption shift toward 200 nm as the deposition temperature of the films increased. Electrical measurements on the film deposited at 500°C showed that the Pt/AlN contacts are Schottky. C-V measurements showed a small hysteresis loop both at room temperature and 300°C. The C-V curve at 300°C was shifted toward lower negative voltages.

Acknowledgments

The authors wish to acknowledge support for this research by the National Science Foundation (Grant No. DGE-9870720) and the Institute for Manufacturing Research at WSU. We would also like to acknowledge Dr. Guang-Zhao Mao, Jie Xu, and Quiang Zhao for their support and contribution in conducting the experiments.

References

1. S. Strite and H. Morkoç, J. Vac. Sci. Technol. B 10 (1992) 1237
2. J. H. Edgar, J. Mater. Res. 7 (1992) 235
3. Robert F. Davis, Proceedings of the IEEE 79 (1991) 702
4. C. C. Tin, Y. Song, T. Isaacs-Smith, J. Electron. Mater. 26 (1997) 212
5. G. W. Auner, T. D. Lenane, F. Ahmad, R. Naik, P. K. Kuo, Z. Wu, "Epitaxial growth of AlN by plasma source molecular beam epitaxy", M. A. Prelas et al., "Wide Band Gap Electronic Materials" 329, (1995) Kluwer Academic Publishers, Printed in Netherlands
6. M. Lekova, G. W. Auner, F. Jin, R. Naik, V. Naik, Mat. Res. Soc. Symp. Proc. 449 (1997) 245

EPITAXIAL GROWTH AND STRUCTURAL CHARACTERIZATION OF SINGLE CRYSTALLINE $ZnGeN_2$

L.D. Zhu*, P.H. Maruska*, P.E. Norris*, P.W. Yip**, L.O. Bouthillette**

*NZ Applied Technologies, 8A Gill Street, Woburn, MA 01801, zhu@nzat2.tiac.net
**Air Force Research Laboratory, 80 Scott Dr., Hanscom AFB, MA 01731

Cite this article as: MRS Internet J. Nitride Semicond. Res. 4S1, G3.8(1999)

Abstract

A new nitride semiconductor, single crystalline $ZnGeN_2$ has been successfully grown by MOCVD for the first time. The epitaxial $ZnGeN_2$ is found to be of hexagonal wurtzite lattice without ordering of the zinc and germanium atoms in the pseudomorphic Group III sublattice. Lattice constants of the $ZnGeN_2$ are a = 3.186 ± 0.007 A, c = 5.174 ± 0.012 A, which gives c/a = 1.624.

Introduction

After three decades of fundamental research, Group III-nitrides research and development activity is in a renaissance. Bright and efficient blue and green LEDs are in the marketplace, InGaN/GaN/AlGaN heterostructure laser diode research is progressing at a rapid pace. Many other optoelectronic and high temperature electronic devices are being contemplated[1]. These achievements are attributed mainly to the breakthroughs in the course of GaN research, such as first synthesis of GaN[2], HVPE growth of single crystalline GaN[3], first demonstration of GaN LED, invention of buffer layer technology, success in p-type conversion, as well as epitaxial lateral over growth.

Compared to the conventional III-V semiconductors, Group III-nitrides system has some inherent limitations. In Group III-arsenides and phosphides, there are choices to construct lattice matched dissimilar band gap heterostructures to design various optoelectronic and electronic devices with excellent crystal quality. However, lattice mismatch between GaN and AlN, GaN and InN is as large as 2.4% and 11.3%, respectively. The large mismatch forces the use of low Al composition AlGaN, which causes carrier overflow in GaN/AlGaN heterojunctions. Increasing Al composition results in cracking of the AlGaN layer beside the increased resistivity. The situation in InGaN seems even more serious. The huge atomic size differences are the cause of instability in the alloy and results in phase separation. This fact limits utility of InGaN for use in photonic devices with longer wavelengths beyond green as well as other devices requiring high In composition or thick InGaN layers. Another limiting factor in GaN/AlGaN system is the low p-type conductivity. Resistivity of p-GaN is around 0.2 Ω-cm, and it is higher for p-AlGaN. This is a heating source as well as origin of parasitic RC time constant in high power laser diodes and HBTs.

To explore the potential of wide band gap semiconductors with a broad horizon, we noticed a set of nitride semiconductors which can be expressed as II-IV-N_2 compound system. Early in1957 Goodman pointed out that by ordered substitution of Group II and Group IV atoms for the Group III atoms in the III-V compounds a new ordered semiconducting II-IV-V_2 compounds could be prepared[4]. Crystallographically, this set of compounds evolves from the tetrahedral diamond structure with the Group V atom surrounded by two Group II and two

Mat. Res. Soc. Symp. Proc. Vol. 537 © 1999 Materials Research Society

Group IV atoms and the Group II or IV atom surrounded by four Group V atoms tetrahedrally. This coordination obeys the four electrons per site rule, and the atomic bonding in the crystal is of covalent nature. The transfer from III-V to II-IV-V_2 compounds brings about new properties of the materials such as band gap, electronic band structure, and non-linear optical properties caused by the drop in symmetry due to superlattice formation. Chalcopyrite II-IV-As_2 and II-IV-P_2 compounds are relatively extensively investigated in search of superior thermoelectric and non-linear optic materials[5]. An outstanding achievement in chalcopyrite research is the nonlinear optical applications of $ZnGeP_2$ and $CdGeAs_2$[5]. There is little work on II-IV-N_2, even including powder synthesis, perhaps due to the need for high temperature and pressure[6,7]. The goal of our research is an exploration of single crystalline II-IV-N_2 materials in conjunction with Group III-nitrides and SiC research.

Experiment

The initial growth experimentation was carried out by microwave plasma enhanced activated nitrogen MOCVD. However, most of the materials reported here have been grown by ammonia source MOCVD. The growth reactor is a water cooled stainless steel vertical chamber, in which the wafer can be rotated to ensure film thickness uniformity. The precursors used as zinc and germanium sources are diethylzinc and germane. Activated nitrogen was supplied from ammonia. Ammonia flow rate was kept at 180 mmole/minute, and total flow rate of diethylzinc and germane was varied around 30 mmole/minute. Corresponding $[NH_3]/([DEZ] + [GeH_4])$ ratio is 5000. Crystalline deposition could be obtained with the growth temperature from 550°C to 700°C. During the growth the chamber was kept at a pressure in a range of 40-500 Torr. The substrate used to grow $ZnGeN_2$ was c- and r-plane sapphire, and $ZnGeN_2$ was grown via an intermediate GaN seed layer.

Surface morphology of the epitaxial films were examined by photomicroscopy, scanning electron microscopy and atomic force microscopy. Crystallinity of the $ZnGeN_2$ layers was investigated by x-ray diffraction θ–2θ scans, double crystal x-ray rocking curve analysis and reflection high energy electron diffraction images.

Results

The epitaxial $ZnGeN_2$ layer is smooth, shiny, and the color looks yellowish by visual examination. A scanning electron microscope picture of the surface shows, sometimes, shiny particulates, the size and amount of which is dependent on the DEZ to GeH_4 molar ratio, suggesting that it is accumulation of extra zinc. Atomic force microscopy was utilized to examine the surface microscopic structure and roughness. Inclined height images of $ZnGeN_2$ layers grown on c- and r-plane sapphire substrates are shown in Figs. 1a and 1b, respectively. A common feature in the two microscopic pictures is a spike shaped morphology, which demonstrates that the growth is columnar from discontinuous seed islands, similar to the grain or domain structure of GaN on Sapphire. However, there is a distinct difference in the two surfaces. The crystal domains of $ZnGeN_2$ layer on r-plane sapphire is more fine and uniform in size and height with RMS value of 10.4 nm, while $ZnGeN_2$ film on c-plane sapphire is composed of larger and flatter domains with RMS value of 17.1 nm, even though there are some tall and rounded columns. These features can also be confirmed from phase images of the two surfaces shown in Figs.2a and 2b. An interesting feature in Fig. 2b compared to Fig.2a is domain orientation in plane. This feature is consistent with the conclusion about epitaxial crystallographic relationship derived from x-ray diffraction analysis given below.

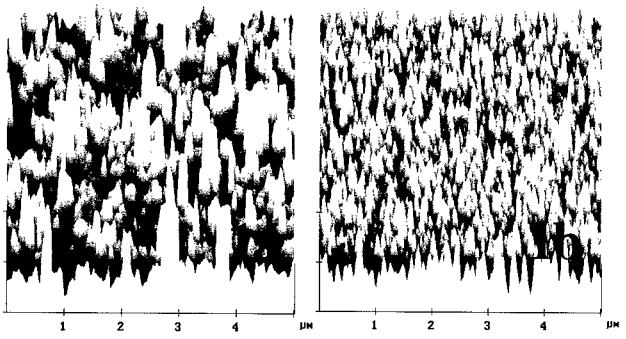


Fig.1. AFM height images of $ZnGeN_2$ surfaces grown on c-sapphire(1a) and r-sapphire(1b).

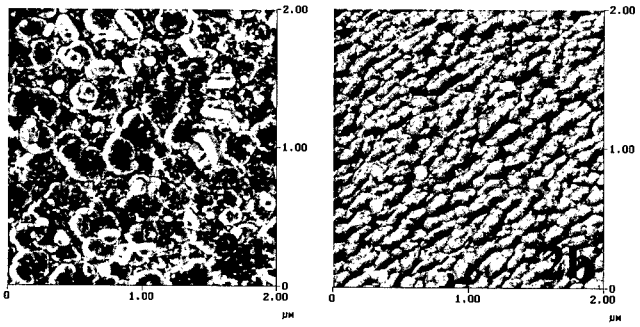


Fig.2. AFM phase images of $ZnGeN_2$ surfaces grown on c-sapphire(2a) and r-sapphire(2b).

Chemical composition ratios were determined by energy dispersive spectroscopy (EDS) measurement. Nitrogen K-line, zinc L-line and germanium L-line were used for the measurement. GaN and bulk $ZnGeP_2$ were used for calibration of the equipment. Zinc to germanium ratio in the solid can be controlled in 0.97-1.00 range by monitoring [DEZ] to [GeH_4] ratio in the gas phase at a given growth temperature. It is found that there is a self stoichiometric mechanism in a limited range of growth parameters. Detailed results in this aspect will be published elsewhere.

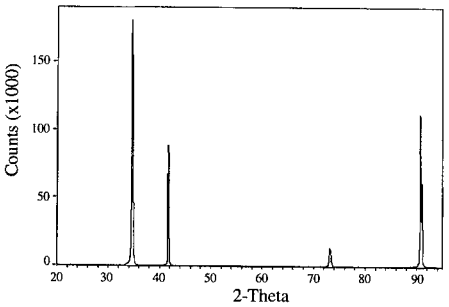


Fig. 3. X-ray diffraction θ–2θ spectrum of $ZnGeN_2$ grown on c-sapphire substrate.

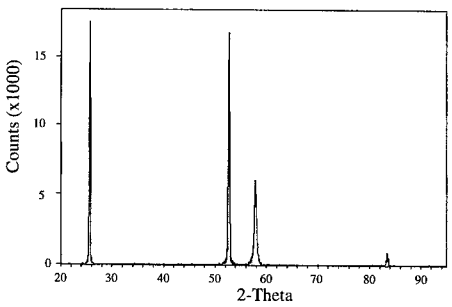


Fig. 4. X-ray diffraction θ–2θ spectrum of $ZnGeN_2$ grown on r-sapphire substrate.

Crystallinity of the $ZnGeN_2$ epitaxial layers were characterized using x-ray θ–2θ scan measurement. A typical x-ray diffraction spectrum of a $ZnGeN_2$ layer grown on c-plane sapphire substrate is shown in Fig. 3. The strong peak at 2θ=34.65° and second peak at 2θ=73.10° are from the epitaxial layer. Another typical θ–2θ scan on a $ZnGeN_2$ layer grown on r-plane sapphire is shown in Fig. 4. The only prominent diffraction peak coming from the epitaxial layer is at 2θ=57.80°. Because these diffraction spectra are almost indistinguishable from that of corresponding GaN on c- or r-plane sapphire, a further scrutinizing is needed to identify the crystallinity of the $ZnGeN_2$ layers. In this regard, two kinds of experiment have been carried out: one is growth of the same GaN intermediate layers as the actual ones and comparing the x-ray diffraction intensities; the other is reflection high energy electron diffraction study with very low incident angle to characterize the surface epitaxial layer. With a fixed diffractometer settings, the x-ray diffraction intensity counts of the intermediate GaN layers on c- and r-plane sapphires are 10000 for the (0002) diffraction and 300 for the (11-20) diffraction, respectively, while the corresponding counts from the $ZnGeN_2$ layers, chemical compositions of which have been confirmed by EDS in the range of measurement error, are 180,000 for the 2θ=34.65° diffraction (Fig.4) and 16,000 for the 2θ=57.80° diffraction (Fig.5), respectively. These experiments prove that the $ZnGeN_2$ layers are single crystals and the crystal structure is the same as GaN, wurtzite structure, and lattice constants of the two materials are almost indistinguishable. The other experiment to verify single crystalline nature of the $ZnGeN_2$ layers is reflection high energy electron diffraction (RHEED) study using JEOL 100-CX. The electron beam impingement angle was 1°, and the beam energies used were 20 and 100 keV. A RHEED pattern, taken with 100 keV, of a $ZnGeN_2$ sample grown on c-plane sapphire is shown in Fig. 5. The bight spot pattern is due to $ZnGeN_2$, while the dim fine points come from the sapphire substrate. The beam angle was essentially orthogonal to the c-axis of the film, leading to a (10-10) RHEED pattern, which is rectangular. This pattern assures that the $ZnGeN_2$ layer is an excellent single crystal with wurtzite lattice.



Fig. 5. RHEED pattern of $ZnGeN_2$ grown on c-sapphire substrate.

Improper seed layer preparation results in a polycrystalline $ZnGeN_2$ layer, which results in extra diffraction peaks. Our x-ray diffraction data obtained from single and polycrystalline epitaxial layers are compared in table I with that of Maunaye and Lang [6], who synthesized polycrystalline $ZnGeN_2$ powder in1970. From x-ray diffraction studies of the powder material they claimed that zinc and germanium atoms are ordered in the otherwise hexagonal sublattice, resulting in a monoclinic lattice structure with the deformed angle 118.88°. The data in table I clearly indicate that the split diffraction peaks due to the ordering in the powder crystal are degenerated in our epitaxial crystals. The diffraction line angles of the epitaxial $ZnGeN_2$ are

between the corresponding split lines of the powder. These data lead to a conclusion that in the epitaxial $ZnGeN_2$ single crystal, zinc and germanium atoms are disordered, resulting in a hexagonal wurtzite lattice.

Table I Comparison of x-ray diffraction data of synthesized powder and epitaxial $ZnGeN_2$ crystals

Synthesized powder $ZnGeN_2$		Epitaxial film $ZnGeN_2$	
monoclinic index	2θ	2θ	hexagonal index
0 0 1	32.28		
-1 0 1	32.84	32.40	1 0 -1 0
0 2 0	34.54	34.65	0 0 0 2
0 1 1	36.74		
-1 1 1	37.23	36.77	1 0 -1 1
1 0 1	57.22		
-1 0 2	58.24	59.91	1 1 -2 0

This phenomenon can be understood from the crystallographic relationship in the epitaxy. In the growth of $ZnGeN_2$ on c-plane sapphire substrate, the relationship is $ZnGeN_2\{0001\}$// sapphire{0001}, $ZnGeN_2\{11\text{-}20\}$//sapphire{10-10}. This is a configuration putting Zn-N or Ge-N molecular unit on lattice points and centers of the triangles in the close packed sapphire c-plane. There is a rotation symmetry around the perpendicular c-axis in this configuration and the freedom for zinc and germanium atomic ordering has been lost. For $ZnGeN_2$ layer grown on r-plane sapphire, the epitaxial relationship is $ZnGeN_2\{11\text{-}20\}$//sapphire{1-102}. The c-axis of the $ZnGeN_2$ is located in the plane of the rectangular sapphire surface lattice which brings about a mirror symmetry for the Zn and Ge atomic arrangement. This results in a loss of freedom for the ordering, which exists in the freely nucleating high temperature powder synthesis.

Lattice constants of the epitaxial $ZnGeN_2$ crystal, determined from the x-ray diffraction data, are $a = 3.186 \pm 0.007$ A, $c = 5.174 \pm 0.012$ A, which gives $c/a = 1.624$. The error mainly comes from the strain and defects existing in the $ZnGeN_2$ layers with different thickness and composition deviation.

This crystal structurally matches to GaN nearly perfectly. Lattice mismatch for c-plane growth is 0.09% on GaN, 15.98% on sapphire. For r-plane sapphire, three rectangular $ZnGeN_2$ two dimensional lattices can be accommodated on the rectangular surface lattice of the sapphire. If the c-axes are in the same direction as with epitaxial relationship $ZnGeN_2\{1\text{-}100\}$//sapp.{11-20}, lattice mismatches are 0.89% in $ZnGeN_2$ c-direction and 15.98% in other direction. If $ZnGeN_2$ c-axis is rotated 90° as with the relationship $ZnGeN_2\{11\text{-}20\}$//sapp.{11-20}, corresponding mismatches are 7.6% and 8.7%, respectively. Both arrangements are favorable compared to the growth on c-sapphire, and the 90° rotation arrangement has about half strain energy compared to the other one.

Crystal quality of the $ZnGeN_2$ was manifested by x-ray rocking curve FWHM of 24 arc minutes for 1 mm thick $ZnGeN_2$, as shown in Fig. 6.

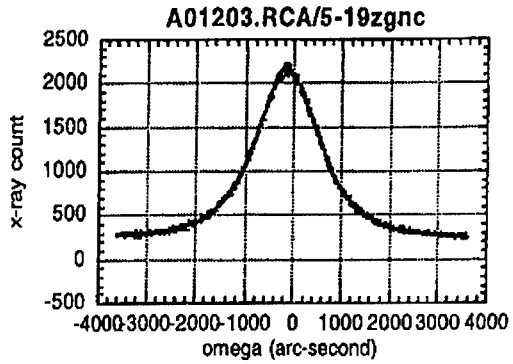


Fig. 6. X-ray double crystal diffraction rocking curve of a $ZnGeN_2$ epi-layer.

Conclusions

Single crystalline $ZnGeN_2$ has been successfully grown on sapphire and GaN/sapphire substrates by low pressure MOCVD for the first time. Precursors are DEZ, GeH_4 and ammonia. Appropriate growth temperature was in the range of 550-700°C. Chemical composition of the compound was monitored by EDS and adjusted to stoichiometric by varying $[DEZ]/[GeH_4]$, $[NH_3]/\{[DEZ]+[GeH_4]\}$ ratios in the gas phase. It is found that there is a self stoichiometric growth mechanism in a limited range of conditions. Single crystalline nature of the epitaxial $ZnGeN_2$ was verified by x-ray diffraction and RHEED. X-ray double crystal rocking curve FWHM was 24 arc minutes for a 1 mm thick $ZnGeN_2$ layer. Zn and Ge atoms are disordered in the epitaxial crystal, resulting in hexagonal wurtzite structure. Lattice constants of the $ZnGeN_2$ are $a = 3.186 \pm 0.007$ A, $c = 5.174 \pm 0.012$ A, with $c/a = 1.624$.

Acknowledgment

NZ Applied Technologies gratefully acknowledges the support of the Air Force Office of Scientific Research under Contract F49620-96-C-0048 and contract monitor Major Michael Prairie. Brian Demczyk and John Larkin at Hanscom AFB are acknowledged for the RHEED study.

References

1. J.I. Pankove, The satellite Workshop of the 2nd Int. Conf. on Nitride Semicond. (Nov.1, 1997 Tokushima, Japan) p.1.
2. W.C. Johnson, J.B. Parsons, and M.C. Crew, J. Phys. Chem., **36**, 2561 (1932).
3. H.P. Maruska and J.J. Tietjen, Appl. Phys. Lett., **15**, 367 (1969).
4. C.H.L. Goodman, Nature, **179**, 828 (1975).
5. J.L. Shay and J.H. Wernick, Ternary Chalcopyrite Semiconductors: Growth, Electronic Properties, and Applications, Pergamon Press, 1975.
6. M. Maunaye et J. Lang, Mater. Res. Bull., **5**, 793 (1970).
7. T. Endo, Y. Sato, H. Takizawa, M. Shimada, J. Mater. Sci. Lett., **11**, 424 (1992).

CUBIC GaN HETEROEPITAXY ON THIN-SiC-COVERED Si(001)

Yuichi Hiroyama , Masao Tamura

Joint Research Center for Atom Technology - Angstrom Technology Partnership,
1-1-4 Higashi, Tsukuba, Ibaraki 305-0046, Japan

Cite this article as: MRS Internet J. Nitride Semicond. Res. 4S1, G3.9(1999)

We have investigated the growth conditions of cubic GaN (β-GaN) layers on very thin SiC-covered Si(001) by using gas-source molecular beam epitaxy as functions of SiC layer thickness, Ga-cell temperature and substrate temperature. Under the present SiC formation conditions on Si substrates by carbonization using C_2H_2 gas, the SiC layers with the thickness between 2.5 and 4 nm result in the epitaxial growth of β-GaN on thus SiC-formed Si substrates. At the highest GaN growth rate of 110 nm/h (a Ga-cell temperature of 950 °C), β-GaN layers grown at a substrate temperature of 700 °C show a nearly flat surface morphology and the fraction of included hexagonal GaN becomes negligible when compared to the results of β-GaN layers grown under other conditions of Ga-cell and substrate temperatures. Thus obtained β-GaN films have good performance in photoluminescence intensity although the FWHM of band-edge recombination peak is still wider (137 meV) than the reported values for the β-GaN on 3C-SiC and GaAs.

INTRODUCTION

The combination of optoelectronic III-nitrides and highly advanced Si technology has the potential to be a key technology for fabricating optoelectronic integrated circuits. The luminescence in the blue and ultraviolet regions of GaN has attracted a lot of interest from many scientists and engineers. It has been reported that cubic GaN (β-GaN) epitaxial films can be grown on GaAs(001) and 3C-SiC(001) substrates by chemical vapor deposition (CVD) [1] or gas-source molecular beam epitaxy (MBE) [2, 3]. The successful growth of β-GaN on Si, however, has been reported only by a group from Boston University [4]. In a previous paper we reported that thin cubic SiC(β-SiC) formation on Si(001) substrates is effective for the epitaxial growth of β-GaN on Si(001) [5]. We confirmed that thin SiC layers not only play the role as a buffer layer to reduce the large lattice mismatch between Si and β-GaN but also as a mask to protect the Si substrates against the irradiation of the active nitrogen, *e.g.*, the nitrogen radicals and atomic nitrogen those were supplied during GaN growth.

The SiC formation by using a carbonization technique on Si substrates has been studied as an initial process of heteroepitaxy of SiC on Si [6]. Carbonization using hydrocarbons is a very easy way to obtain SiC layers on Si substrates; in the conventional CVD the carbonization was performed by using C_3H_8 [7] as a source gas and at very high processing temperatures between 1000 and 1300 °C. On the other hand, it was reported that SiC was obtained at lower temperatures (750 - 1000 °C) using acetylene (C_2H_2) [8], although pit formation in Si substrates was also observed. However low temperature carbonization is desired not only for avoiding the high-density pit formation as much as possible but also for device fabrication. In this paper we report the optimum SiC formation and β-GaN growth conditions, such as V/III ratios and substrate temperatures by RF-activated MBE. We also discuss the quality of β-GaN layers.

EXPERIMENT

Hydrogen-terminated Si(001) substrates were placed into a preparation chamber (having a base pressure of about 5×10^{-8} Torr) which was connected to an MBE growth chamber (base pressure of about 5×10^{-11} Torr). The Si substrates were heated up to 850 to 950 °C for 1 to 10 min under a C_2H_2 pressure of 5×10^{-7} to 5×10^{-5} Torr in order to form SiC layers. The SiC-formed Si(001) substrates were then cooled down to room temperature and immediately transferred to the MBE growth chamber . They were then annealed at 1000 °C for 1 min and cooled

Mat. Res. Soc. Symph. Proc. Vol. 537 © 1999 Materials Research Society

down to a growth temperature of 600 to 900 °C. GaN films were grown using RF-MBE under the following growth conditions: the nitrogen gas flow rate was set at 2 sccm and the RF-power was set at 300 W. Gallium molecular beam was supplied to the substrate by using a Knudsen-cell operating at 850 to 1000 °C.

The surface morphology and the quality of GaN films were characterized by using in-situ reflection high energy electron diffraction (RHEED) and cross-sectional transmission electron microscopy (XTEM) as well as x-ray diffraction (XRD) measurements. Photoluminescence (PL) measurements were also carried out using a 325 nm beam from a He-Cd laser.

THIN SiC LAYER FORMATION

Figure 1 shows high-resolution XTEM (HRXTEM) micrographs of the substrates carbonized at 950 °C for 10 min under various C_2H_2 pressures. For a C_2H_2 pressure of 5×10^{-7} Torr small SiC islands were formed on the Si. A RHEED pattern of the as-grown SiC layer showed three-dimensional diffused spots, as seen in the inset of Fig. 1(a). For a C_2H_2 pressure of 5×10^{-6} Torr the surface morphology of the SiC became flat (Fig. 1(b)), and a streaky RHEED pattern was observed. The film thickness of the SiC was approximately 4 nm. With a higher C_2H_2 pressure of 5×10^{-5} Torr an approximately 5-nm-thick SiC layer was formed. The clear spotty pattern shown in the inset of the Fig. 1(c) indicates that the surface flatness of the SiC was more degraded than that of the SiC grown at a pressure of 5×10^{-6} Torr. As shown in Fig. 1(b), the spacing between two {111} planes of the SiC layer was approximately 0.25 nm by referring to the spacing of 0.31 nm between {111}Si and was almost the same as that of bulk β-SiC. This indicates that the misfit between SiC and Si was almost completely relaxed by the generation of misfit dislocations in the SiC layer.

Figure 2 shows HRXTEM micrographs of Si substrates carbonized at 950 °C under a C_2H_2 pressure of 5×10^{-6} Torr for (a) 1 min and (b) 3 min. As seen in Fig. 2(a), a 1-nm-thick SiC layer was formed. The RHEED pattern of the SiC was more diffused than that of the thicker SiC layers. After carbonization for 3 min the thickness of the SiC layer was approximately 3 nm and the surface morphology was two-dimensional (Fig. 2(b)). Further growth of the SiC layer was saturated at 4 nm with the carbonization time up to 10 min as shown in Fig. 1(b). This thickness saturation of the SiC layer is known to be due to the suppression of the out-diffusion of Si atoms from the substrates during the SiC formation [9]. The GaN films grown on the substrates of Figs. 1(b), 1(c) and 2(b) became single-crystal cubic GaN films, while the films grown on the substrates shown in Figs. 1(a) and 2(a) became polycrystal structures having mixed phases of cubic and hexagonal GaN. Therefore, in order to avoid the degradation of the Si substrate as much as possible during the SiC formation, we employed the SiC formation conditions by short time heating for 3 min under a medium C_2H_2 pressure of 5×10^{-6} Torr.

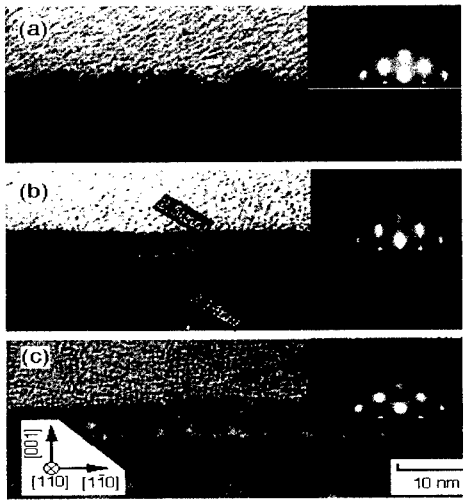


Figure 1. HRXTEM micrographs of the substrates carbonized at 950 °C for 10 min under various C_2H_2 pressures of (a) 5×10^{-7}, (b) 5×10^{-6} and (c) 5×10^{-5} Torr.

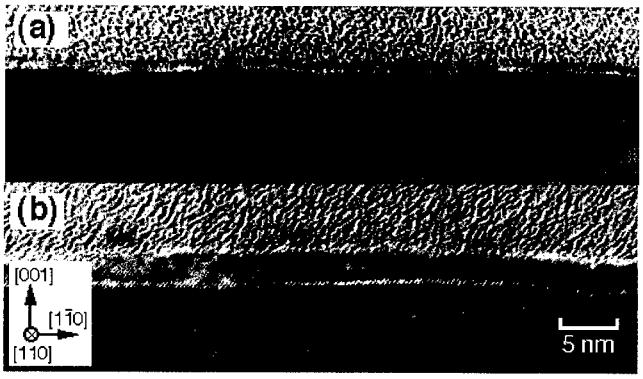


Figure 2. HRXTEM micrographs of Si substrates carbonized at 950 °C under a fixed C_2H_2 pressure of 5×10^{-6} Torr after annealing for (a) 1 and (b) 3 min.

GENERAL FEATURE OF GaN GROWTH

Figure 3 shows the GaN film growth rate as a function of Ga-cell temperatures (T_{Ga}) and substrate temperatures (T_{sub}). In the case of a constant T_{sub} the growth rate increased exponentially with the increase of T_{Ga} until it reached a saturation value of 110 nm/h at a T_{Ga} of 950 °C. This tendency was observed for all the T_{sub} cases from 600 to 800 °C. The growth rate at a T_{Ga} of 1000 °C was almost the same as that at 950 °C. This shows that the film growth at a T_{Ga} below 950 °C was dominated by the amount of Ga-flux (Ga-limited growth) and that the film growth at a T_{Ga} higher than 950 °C was dominated by the amount of N-flux (N-limited growth). Furthermore, in the case of a constant T_{Ga} below 930 °C the growth rate decreased with the increase of T_{sub}. This indicates that there was some loss of Ga by desorption during the growth with increased T_{sub}. With T_{Ga} of 950 °C and T_{sub} of 800 °C we concluded that the growth conditions of GaN were close to the stoichiometric conditions.

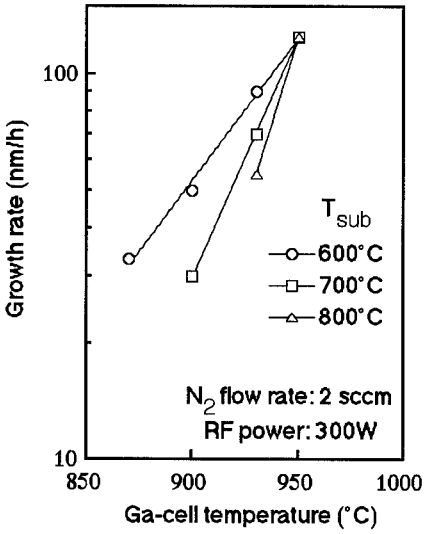


Figure 3. GaN film growth rate as a function of T_{Ga}.

Figure 4 shows RHEED patterns of GaN grown with different T_{sub} and T_{Ga} for [110] incidence of electron beams. All the patterns show that the GaN films basically have a β-GaN structure, except for that grown at a T_{sub} of 900 °C. For a T_{Ga} of 870 °C the diffused ring-like pattern indicates that the grown layer consisted of grains that rotated on the (001) plane. For a T_{Ga} of 900 °C the ring-like pattern was obtained at a T_{sub} of 500 °C. With the increase of T_{sub} the pattern became sharper but showed extra weak spots due to the twin formation at a T_{sub} of 700 °C. For a higher T_{Ga} of 930 °C spotty patterns from β-GaN were observed for all the T_{sub}. However, in the case of a T_{sub} of 600 and 800 °C, extra spots were included. At the highest T_{Ga} of 950 °C, spotty patterns were slightly elongated longitudinally for T_{sub} of 700 and 800 °C, which showed that the growing surface was rather flat. However, the spotty patterns at 900 °C mainly originated from a hexagonal structure together with clear rings due to the polycrystal formation.

CRYSTAL QUALITY

Figure 5 shows XTEM micrographs of the GaN grown at 600 °C for 1 hour with different T_{Ga}. At a T_{Ga} of 870 °C a columnar structure was clearly observed due to a large rotation angle of each column and the quality was much poorer than that of the higher T_{Ga} case. At a T_{Ga} of 900 °C the size of each column was larger than that at 870 °C and the boundary became unclear. At a T_{Ga} of 950 °C no columnar structure was observed and a nearly flat surface was obtained. With a higher T_{Ga}, for example, 1000 °C, the film growth rate did not increase as mentioned before and a Ga droplet formation on the surface became obvious due to the significant amount of excess Ga. These results suggest that the slightly Ga-rich conditions are favorable for the growth of β-GaN on thin-SiC-covered Si(001).

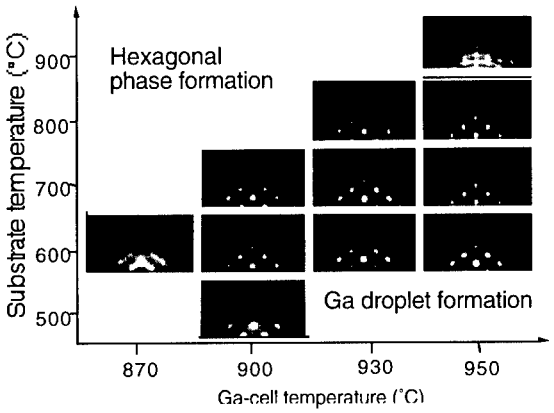


Figure 4. RHEED patterns of GaN grown at different T_{sub} and T_{Ga} for [110] incidence of electron beams.

Figure 6 shows XTEM micrographs of GaN films grown with various T_{sub}. The T_{Ga} was kept at 950 °C. In Fig. 6(a) and 6(b) no clear columnar structures were observed, although a number of stacking faults and twin

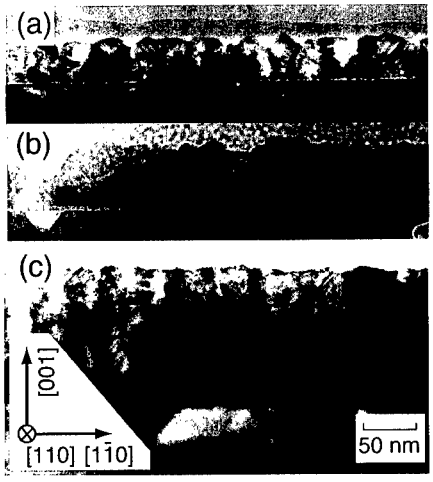


Figure 5. (upper) XTEM micrographs of the GaN grown at 600 °C for 1 hour with different T_{Ga}, (a) 870, (b) 900 and (c) 950 °C.

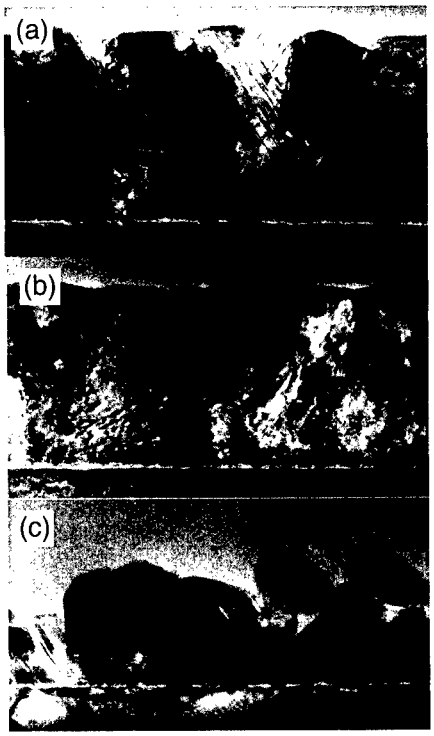


Figure 6. (right) XTEM micrographs of GaN films grown with T_{sub} of (a) 700, (b) 800 and (c) 900 °C. Ga-cell temperature was kept at 950 °C.

boundaries were formed. At a T_{sub} of 900 °C, the quality of the GaN film became considerably worse, which coheres with the result of Fig. 4. This may be due to the enhancement of Ga desorption from the growing surface.

Long-time growth of GaN films was then carried out at T_{sub} of 700 and 800 °C. The T_{Ga} was fixed at 950 °C. The RHEED pattern of the 1.1-μm-thick film grown at 700 °C for 10 hours showed almost the same pattern as that after growth for 1 hour. On the other hand, the RHEED pattern of the sample grown at 800 °C for 10 hours showed the appearance of many extra spots, which indicated mixing of a hexagonal phase. From these results we concluded that the optimum T_{sub} and T_{Ga} are respectively 700 and 950 °C.

An XRD spectrum of the thick GaN had only one peak at $2\theta = 40.06°$ translating to the lattice spacing of (002)GaN as 2.25Å, which indicates that the grown GaN film was a single phase of β-GaN. The full width at half maximum (FWHM) of the (002)GaN peak was 27 min. As listed in the ref. [10], the reported FWHMs of β-GaN on GaAs and 3C-SiC was distributed in the range between 16 and 76 min.

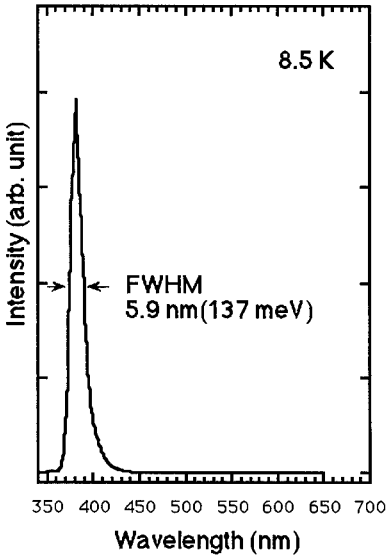


Figure 7. 8K PL spectrum of 1.1 μm-thick GaN.

Figure 7 shows an 8 K PL spectrum of a 1.1 μm-thick β-GaN film grown under the optimum conditions; T_{Ga} and T_{sub} were at 950 and 700 °C, respectively. The PL spectrum was dominated by a near band-edge peak at 381 nm (3.25 eV). The FWHM of the 381 nm peak was approximately 5.9 nm (130 meV). The FWHM of our β-GaN is wider than those obtained by Okumura et al. for β-GaN on a 3C-SiC substrate using ECR-MBE (19 meV at 4.2 K) [10] and by As et al. for β-GaN on a GaAs substrate using RF-MBE (24 meV at 2 K) [11]. The intensity of the yellow band between 500 and 700 nm, which is typically observed for hexagonal GaN, was 1000 times lower than that of the near band-edge peak at 381 nm. The donor-acceptor (D-A) recombination peak, reported to be around 400 nm for MOCVD [12] and gas-source MBE using hydrazine [10] and ammonia [13], was not observed in our β-GaN.

CONCLUSIONS

We investigated the optimum growth conditions for obtaining cubic GaN on SiC-covered Si(001) by using RF-MBE. We found that SiC layers between 2.5 and 4 nm thick became flat and that single-crystal cubic GaN films could be grown on thus formed SiC layers. Under optimized growth conditions it was found, by XTEM observations and XRD measurements, that GaN has a flat surface and the amount of hexagonal GaN is negligibly small. The PL spectrum was dominated by a near band-edge peak at 381 nm whose FWHM was 5.9 nm.

ACKNOWLEDGEMENTS

The authors thank Dr. Tomoyoshi Mishima and Dr. Seiichi Isomae in Hitachi Central Research Laboratory for PL and XRD measurements. They also thank Dr. Masakazu Ichikawa and all members of the Ichikawa group o the JRCAT for fruitful discussions. This work, partly supported by NEDO, was performed in the JRCAT under the joint research agreement between ATP and NAIR.

REFERENCES

[1] M. Mizuta, S. Fujieda, Y. Matsumoto, T. Kawamura, Jpn. J. Appl. Phys. **25**, L945 (1986).
[2] M.J. Paisley, Z. Sitar, J.B. Posthill, RF. Davis, J. Vac. Sci. Technol. **A7**, 701 (1989).
[3] H. Okumura, S. Misawa, S. Yoshida, Appl. Phys. Lett. **59**, 1058 (1991).
[4] For example, T.D. Moustakas, T. Lei, R.J. Molnar, Physica **B185**, 36 (1993).
[5] Y. Hiroyama and M. Tamura, Jpn. J. Appl. Phys. **37**, L630 (1998).
[6] P. Pirouz, F. Ernst, T.T. Cheng, Mater. Res. Soc. Proc. **116**, 57 (1988).
[7] S. Nishino, J.A. Powell, H.A. Will, Appl. Phys. Lett. **42**, 460 (1983).
[8] H. Nagasawa and Y. Yamaguchi, J. Cryst. Growth **115**, 612 (1991).
[9] A.J. Steckl and J.P. Li, Thin Solid Films **216**, 149 (1992).
[10] H. Okumura, K. Ohta, G. Feuillet, K. Balakurishnan, S. Chichibu, H. Hamaguchi, P. Hacke, S. Yoshida, J. Cryst. Growth **178**, 113 (1997).
[11] D.J. As, F. Schmilgus, C. Wang, B. Schöttker, D. Schikora, K. Lischka, Appl. Phys. Lett. **70**, 1311 (1997).
[12] J.N. Kuzunia, J.W. Yang, Q.C. Chen, S. Krishnankutty , M. Ashif Khan, Appl. Phys. Lett. **65**, 2407 (1994).
[13] H. Okumura, S. Yoshida, T. Okahisa, Appl. Phys. Lett. **64**, 997 (1994).

INFLUENCE OF ACTIVE NITROGEN SPECIES ON THE NITRIDATION RATE OF SAPPHIRE

A.J. Ptak[*], K.S. Ziemer[**], M.R. Millecchia[*], C.D. Stinespring[**], and T.H. Myers[*,†]
[*] Department of Physics, [**] Department of Chemical Engineering, West Virginia University, Morgantown, WV 26506; [†]tmyers@wvu.edu

Cite this article as: MRS Internet J. Nitride Semicond. Res. 4S1, G3.10 (1999)

ABSTRACT

The operating regimes of two rf-plasma sources, an Oxford CARS-25 and an EPI Unibulb, have been extensively characterized. By changing the exit aperture configuration and using an electrostatic deflector, the Oxford source could produce either primarily atomic nitrogen, atomic nitrogen mixed with low energy ions, or a large flux of higher energy ions (>65 eV) as the active species in a background of neutral molecular nitrogen. The EPI source produced a significant flux of metastable molecular nitrogen as the active species with a smaller atomic nitrogen component. Nitridation of sapphire using each source under the various operating conditions indicate that the reactivity was different for each type of active nitrogen. Boron contamination originating from the pyrolytic boron nitride plasma cell liner was observed.

INTRODUCTION

GaN has been grown by many techniques, each with its own form of active nitrogen species. Molecular beam epitaxy (MBE), using either electron cyclotron radiation (ECR) or radio frequency (rf) plasma sources, represents a particularly complex case since these sources produce ions of various energies, atoms, and potentially, nitrogen molecules in a metastable state. The reactivity of the individual species may play a crucial role in growth kinetics, particularly in the formation of point defects. One measure of the reactivity of a given species is indicated by its efficiency at the nitridation of sapphire, a common step in the nucleation process of GaN. The different reactivity of the various species is evident from the wide range of nitridation times observed [1,2,3,4]. We report the results of a study determining the active species from two rf-plasma sources under different operating conditions, and assess the relative reactivity of the various nitrogen species based on nitridation rates for sapphire.

RF-PLASMA SOURCE CHARACTERIZATION

Two rf-plasma sources were used to produce various species of nitrogen for the nitridation of sapphire. These sources were an Oxford Applied Research (Oxfordshire, England) CARS-25 source and an EPI Vacuum Products (St. Paul, MN) Unibulb source. The Oxford source featured a removable pyrolytic boron nitride (PBN) aperture plate allowing use of different hole configurations. We investigated plates with 1, 9, 37, and 255 holes. As the number of holes increased, the size of the holes was decreased proportionately in order to maintain the overall conductance of the plate. The EPI source contained the standard Unibulb configuration with a 400-hole aperture resulting in an approximately 50% increase in conductance.

The sources were mounted in a UHV chamber in direct line of sight to an Extrel quadrupole mass spectrometer for characterization. The mass spectrometer's repeller grid was biased separately to allow a determination of ion energies in the flux. Additionally, a stainless

Mat. Res. Soc. Symp. Proc. Vol. 537 © 1999 Materials Research Society

steel electrostatic deflector plate was positioned below the nitrogen source that could be biased to deflect ions out of the flux. The sources were operated under conditions producing a maximum growth rate for GaN in previous MBE growth experiments. Characterization results are summarized in Table I.

The Oxford source with the single-hole aperture produced a significant flux of high-energy ions, both molecular and atomic, similar to an ECR source [5]. The large, high-energy ion flux precluded accurate measurement of a neutral atomic nitrogen concentration. Reducing the aperture hole size also reduced the ion content in the flux as well as the total ion energy, probably due to wall interactions, as indicated in Table I. In essentially all the cases, the concentration of atomic nitrogen ions was two to three times that of molecular ions. The atomic nitrogen ions were also typically 5 to 10 eV more energetic, with both distributions peaked near the maximum energies. The maximum ion energy range listed in Table I is representative of the difference between molecular and atomic ionic species. Use of the 9, 37, or 255-hole aperture led to a varying mixture of atomic nitrogen and ions. Similar results have been reported for apertures used on an ECR source.[6] Atomic nitrogen accounted for 2-6% of the total nitrogen flux, with the ion content reduced to less than 0.1%. Another source parameter, the incorporation efficiency, was determined by measuring the nitrogen actually incorporated in GaN based on the growth rates from separate MBE growth experiments compared to the total nitrogen impinging on the growing layer. Measured growth rates were the right magnitude to be due to the atomic nitrogen, and too large to be due to the ions. While the incorporation efficiency scaled well with atomic nitrogen concentrations, it is clear that a significant fraction of the atomic nitrogen is not incorporated into the growing layer.

Several significant differences were observed for the EPI source. First, the total ion content was significantly reduced, to less than 3×10^{-5} percent of the total flux, with the remaining ions having energies less that 3 eV. Second, the incorporation efficiency was significantly larger, particularly when considering the measured atomic nitrogen concentration. During the characterization of the plasma sources, the mass spectrometer ionizer energy was set high enough to ionize both molecular and atomic nitrogen (typically >15 eV), but too low to crack a significant portion of molecular nitrogen into atomic nitrogen (>28 eV). During the EPI source characterization, considerable molecular nitrogen ions were produced with an ionizer

Table I. Results of rf-plasma source characterization.

SOURCE	APERTURE		Ion Content (%)	Max. Ion Energy (eV)	Atom Efficiency (%)[a]	GaN Incorporation Efficiency (%)[b]
	Hole Diameter (mm)	Number of Holes				
OXFORD CARS-25[d]	3.0	1	5	>65	[c]	——
	1.0	9	0.1	40 - 50	5 - 6	0.48
	0.5	37	0.05	15 – 25	3 - 4	0.32
	0.2	255	0.03	8 - 12	2 - 3	0.23
EPI Unibulb[e]	0.2	400	$< 3 \times 10^{-5}$	< 3	2 – 3	7.2

[a] atomic N out/total N into source x100% [b] N incorporated in GaN/total N into source times 100% [c] not measurable [d] 600W, 6 SCCM [e] 600W, 2 SCCM

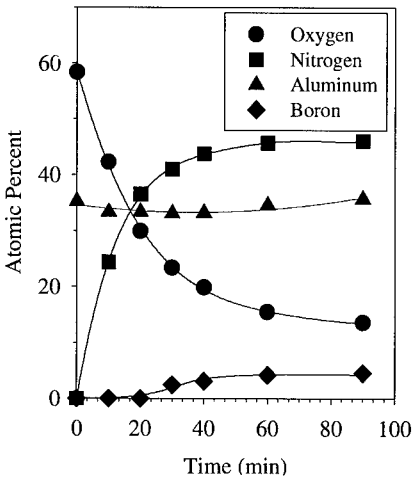


Figure 1. Auger analysis of Al, O, N, and B during nitridation of Al_2O_3 using the Oxford source with a single hole aperture. The solid lines are guides to the eyes.

energy approximately 6 eV lower than normally necessary to ionize molecular nitrogen. This energy difference corresponds to the $A^3\Sigma_u^+$ metastable state of the nitrogen molecule, and indicates this source produces a significant amount of nitrogen metastables. The presence of the metastables complicated the source characterization somewhat, but we were able to determine an atomic nitrogen efficiency of about 2-3%. This source has proven quite effective at incorporation of nitrogen in GaN, with growth rates at least an order of magnitude too large to be due to the atomic nitrogen based on comparison with the Oxford source. Since the ion content is negligible, the most likely active nitrogen species remaining is the molecular nitrogen metastable.

NITRIDATION OF SAPPHIRE

Nitridation experiments were performed in the same chamber as the rf-plasma source characterization using a heated sample stage. Nitridation at low temperature was chosen to accentuate differences in the reactivity of the various species. Nitridation did not occur at room temperature for any source configuration, but proceeded at a reasonable rate at 400°C, which was used for all the nitridation experiments. The nitridation chamber was connected to a separate chamber where Auger measurements could be performed using a Phi 545 Scanning AES Microprobe with Model 110A Cylindrical Electron Optics. Scans were performed with a 3 keV incident electron beam, a beam current of 2 μA and a nominal spot size of 3 μm.

Figure 1 details Auger analysis made during a nitridation run using the Oxford source with the single-hole aperture. The analysis uses elemental sensitivity factors [7], and is representative of the number of atoms of each species present within the Auger sampling depth. All of the nitridations performed with the Oxford source gave similar results, but with different time scales for differing conditions. Yeadon *et al.* have shown [8] that AlN and Al_2O_3 are immiscible and nitridation proceeds by the formation of an AlN overlayer on the Al_2O_3. Atomic force microscopy of a sapphire surface nitrided under similar conditions to that of the sample of Fig. 1 indicated a flat, featureless surface. Thus in order to quantitatively compare the nitridation rates, we used a standard model [9] for oxygen signal attenuation by an AlN overlayer normalized by the total Al signal to estimate AlN thickness. The model used a measured oxygen sensitivity factor relative to aluminum from Al_2O_3 and electron inelastic mean free paths based on the model by Tanuma *et al.* [10] The relative shift in Al signal strength between Al_2O_3 and AlN has been taken into account in the model. The model did not include backscatter correction factors, and so the calculated thickness values should be treated as approximate.

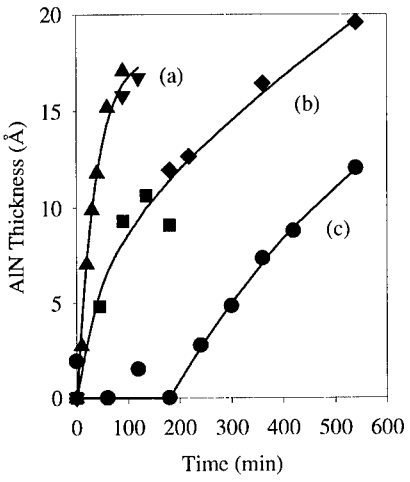


Figure 2. AlN overlayer thickness as a function of time for (a) ▵and ▿, single-hole aperture; (b) □ and ◇, 9-hole aperture with ions deflected; and (c) ○, 9-hole aperture without ion deflection. The solid lines are guides to the eye.

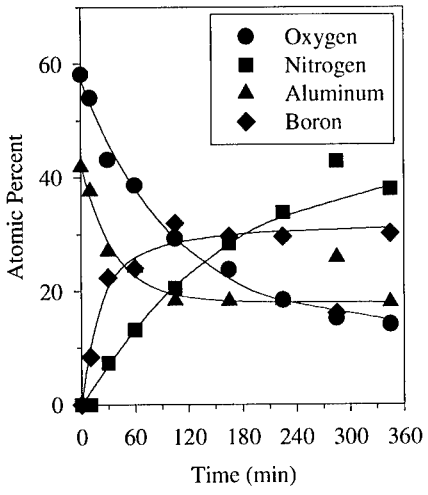


Figure 3. Auger analysis of Al, O, N, and B during nitridation using the EPI source.

Figure 2 summarizes AlN overlayer thickness as a function of time for three configurations of the CARS-25 source. Fig. 2(a) corresponds to the nitridation of two samples using the single-hole aperture, with a large flux (5%) of high-energy molecular and atomic nitrogen ions. This condition is similar to an ECR source, and results in a relatively rapid nitridation with a rate of about 0.3Å/min for the first 10Å. Fig. 2(c) is representative of the 9-hole aperture results. There appears to be an initiation stage lasting approximately 180 minutes, followed by AlN formation at a rate of about 0.03–0.04Å/min. The active flux from this source configuration is a mixture of both atomic nitrogen (5-6%) and nitrogen ions (0.1%). Fig. 2(b) represents the same configuration, but now the electrostatic deflector plate was used to remove the ions from the flux. Note the nitridation began immediately, and maintained a rate approximately three times (0.1Å/min) that shown in Fig. 2(c).

The trends shown in Fig.2 indicate that both energetic nitrogen ions and atomic nitrogen are quite reactive, with some indication that the energetic ions are the more reactive species. This is particularly evident for larger AlN thickness. Of equal interest is that a flux of lower energy ions apparently suppresses the nitridation process. A likely mechanism is that atomic nitrogen is adsorbed on the growing surface in a weakly bound state. The incoming ions (and possibly atoms) interact with this adsorbed nitrogen forming molecular nitrogen that quickly desorbs, removing these atoms from participating in the nitridation process. The initiation stage represents a period where the adsorbed nitrogen is very weakly bound to the sapphire surface and easily removed. Based on the rapid onset of AlN growth once initiated, it is likely that once AlN

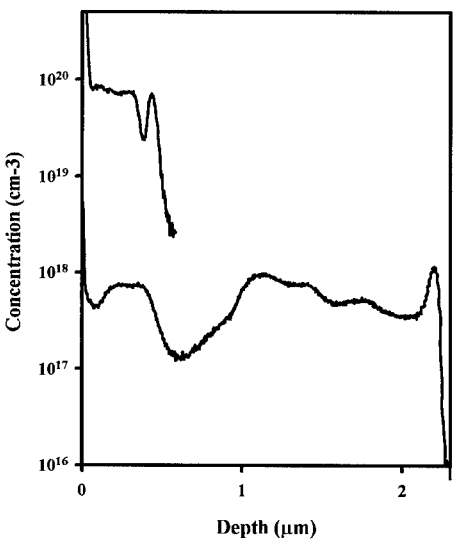


Figure 4. SIMS of B GaN grown using (a) the OXFORD source and (b) the EPI source.

is formed, the nitrogen is more strongly bound to the surface and the nitridation process then proceeds.

Figure 3 summarizes Auger analysis of nitridation using the EPI source. The results were substantially different from that observed with the Oxford source. While boron was observed for all nitridation conditions, the Auger analysis indicates significantly more boron on the Al_2O_3 surface exposed to the EPI source. The results imply that an overlayer of BN was formed within the first 20 minutes of nitridation, followed by an apparent cessation of BN formation. During this initial stage, both the Al and O Auger signals reduced in proportion, consistent with BN overlayer coverage without AlN formation. Surprisingly, both the B and the Al signal then became constant, while the O signal decreased and the N signal continued to increase. The latter is suggestive that AlN is now forming. Since the B signal also remains constant, it is feasible that $Al_{1-x}B_xN$ may actually be forming. The short predicted mean free paths for B (7Å) and Al (6Å) Auger electrons compared to that of O (11Å) or N (14Å) would result in a constant B and Al signal with the others still changing. Assuming that only AlN formation is occurring, modeling interprets an AlN growth rate during this second stage of 0.07Å/min, consistent with the atomic nitrogen concentration in the flux coupled with the lack of ions. This latter result may indicate that the nitrogen metastables believed to be present are relatively non-reactive, at least as far as nitridation is concerned. Interpretation of this set of Auger measurements, however, is certainly complicated.

The results depicted in Fig. 3 are suggestive that the flux from the EPI source has a significantly larger B content than the Oxford source, likely due to the degradation of the pyrolytic boron nitride (PBN) liner. In actuality, this result is more indicative of the efficacy of metastable nitrogen for group III-nitride layer growth. Fig. 4 summarizes the B content for two GaN layers measured using secondary ion mass spectrometry (SIMS) (Charles Evans and Associates). Fig. 4(a) represents the B concentration in a layer grown using the Oxford source with the 9-hole aperture, yielding an average B concentration of about $8x10^{19}$ cm^{-3}. Similar results were obtained for the other aperture sets, and also after replacing the PBN liner in the Oxford source. The EPI source actually emitted significantly less B, with incorporation levels in the mid-10^{17} to $1x10^{18}$ cm^{-3} range, as shown by Fig 4(b). The variation in B concentration for each trace corresponds to different source rf-powers, with the lowest corresponding to 200W and the highest to 600W. A similar difference in B incorporation has also been reported to occur with these sources for nitrogen doping of ZnSe and CdTe [11].

Thus, a likely interpretation of the rapid BN layer formation indicated by the results in Fig. 3 is that $A^3\Sigma_u^+$ nitrogen molecules are particularly efficacious for III-N growth. This is indicated both by the rapid BN overlayer formation, and by the significant increase in nitrogen incorporation efficiency observed for MBE growth. Enhanced growth using nitrogen

metastables is clearly demonstrated by the large (~2.3 μm/hr) growth rates we have obtained with the EPI rf-plasma source.

CONCLUSIONS

Nitridation of sapphire was investigated using two rf-plasma sources to determine the reactivity of various types of active nitrogen. The Oxford CARS-25 source, in conjunction with an electrostatic deflector plate, could provide an active nitrogen flux consisting of high energy ionic molecular and atomic nitrogen, a mixture of atomic nitrogen and lower energy ions, or predominantly atomic nitrogen. The EPI Unibulb source produced a significant amount of metastable molecular nitrogen. The nitridation rate for high-energy ions was ~0.3Å/min for the first 10Å, about three times faster than nitridation by atomic nitrogen at a similar concentration. The mixed atomic nitrogen/low energy ion condition showed an initiation stage that lasted for ~180 minutes, followed by nitridation at a rate of 0.03-0.04Å/min. This initiation stage may be due to formation and desorption of molecular nitrogen from the sapphire surface. Metastable nitrogen does not appear to be very reactive for nitridation, but does appear efficacious for the growth of group III-nitrides. Boron contamination was observed from both sources at levels significant enough to warrant further investigation.

ACKNOWLEDGEMENTS

This work was supported by ONR Grant N00014-96-1-1008 and monitored by Colin Wood. We would like to acknowledge continuing useful conversations with P. I. Cohen, R. M. Feenstra, N. Newman and C. E. C. Wood.

REFERENCES

[1] C. Heinlein, J. Grepstad, T. Berge, and H. Riechert, Appl. Phys. Lett. **71**, 3, (1997)
[2] C. Heinlein, J. Grepstad, S. Einfeldt, D. Hommel, T. Berge and A. Grande, J. Appl. Phys **83**, 6023 (1998).
[3] M. E. Lin, B. N. Sverdlov, and H. Morkoç, J. Appl. Phys. **74**, 5038 (1993).
[4] T. D. Moustakas, T. Lei, and R. J. Molnar, Physica B **185**, 36 (1993).
[5] R. J. Molnar and T. D. Moustakas, J. Appl. Phys. **76**, 4587 (1994).
[6] I. Berishev, E. Kim and A. bensaoula, J. Vac. Sci. Technol. **A16**, 2791 (1998).
[7] Handbook of Auger Electron Spectroscopy, Perkin-Elmer, Physical Electronics Division (Eden Prairie, MN, 1995).
[8] M. Yeadon, M. T. Marshall, F. Hamdani, S. Pekin, and H. Morkoç, J. Appl. Phys. **83**, 2847 (1998).
[9] Analysis followed standard procedures such as outlined in D. Briggs and M.P. Seah, Practical Surface Analysis Vol. 1, John Wiley and Sons (Chichester, England, 1990), p. 207.
[10] S. Tanuma, C.J. Powell, and D.R. Penn, Surf. Interface Anal., **17** 911 (1991).
[11] M. Moldovan, L.S. Hirsch, A.J. Ptak, C.D. Stinespring, T.H. Myers, and N.C. Giles, J. Elec. Mat, **27**, 756 (1998).

STRUCTURAL STUDY OF GaN(As,P) LAYERS GROWN ON (0001) GaN BY GAS SOURCE MOLECULAR BEAM EPITAXY

Tae-Yeon Seong,[a),c)] In-Tae Bae,[a)] Y. Zhao,[b)] and C.W. Tu[b)]

[a)]Dept. of Materials Science and Engineering, Kwangju Institute of Science and Technology (K-JIST), Kwangju 500-712, Korea, [c)]Electronic mail: tyseong@kjist.ac.kr
[b)]Dept. of Electrical and Computer Engineering, University of California, San Diego, La Jolla, CA 92093-0407

Cite this article as: MRS Internet J. Nitride Semicond. Res. 4S1, G3.11 (1999)

ABSTRACT

Transmission electron microscope (TEM) and transmission electron diffraction (TED) examination has been performed to investigate microstructural properties of gas source molecular beam epitaxial GaN(As,P) layers grown on (0001) GaN/sapphire at temperatures in the range 500 – 760 °C. As for the GaNAs, we report the observation of ordering with a space group *P*3m1 in the layer grown at 730 °C. The layers grown at temperatures below 600 °C are polycrystalline, whist the 730°C GaNAs layer has epitaxial relation to the GaN substrate. It is also shown that the GaNAs layers experience a structural change from a zinc-blende phase to a wurtzite phase, as the growth temperature increases. As for the GaNP, it is shown that the layers grown at temperatures ≤ 600 °C experience phase separation resulting in a mixture of GaN-rich and GaP-rich GaNP with zinc-blende structure. However, the layers grown at temperatures ≥ 730 °C are found to be binary zinc-blende GaN(P) single crystalline materials. The layers grown at temperatures ≥ 730 °C consist of two types of micro-domains, i.e., $GaN(P)_I$ and $GaN(P)_{II}$; the former having twin relation to the latter.

I. INTRODUCTION

Gallium nitride-based materials are of technological importance because of their applications in short wavelength optical devices, e.g. blue-green light emitting diodes (LEDs) and violet laser diodes (LDs). Due to a large bowing parameter, addition of As or P to gallium nitride could lead to the practical engineering of specific semiconductors having a wide range of wavelengths from ultra violet to larger than 2 μm.

Calculations based upon bulk thermodynamics indicated that a large miscibility gap exists for a GaN-GaP system where phase separation may occur by spinodal decomposition during layer growth.[1] The presence of such a miscibility gap would be a major obstacle for the successful growth of ternary GaNP alloy layers. Iwata et al.[2], investigating gas source molecular beam epitaxial (GSMBE) growth of $GaN_{1-x}P_x$ ($x \leq 0.015$), showed that phase separation occurred for a high PH_3 flow rate condition. Bi and Tu investigated GaN_xP_{1-x} layers grown on GaP substrates at temperatures in the range 500 – 610 °C by GSMBE using a N radical beam source.[3] They showed that GaN_xP_{1-x} with a maximum N concentration of 16% was obtained, but no phase separation was observed.

In this article, we describe structural results obtained from transmission electron microscope (TEM) and transmission electron diffraction (TED) studies of GaN(As,P) layers grown on (0001) GaN at temperatures ranging from 500 to 760 °C.

Mat. Res. Soc. Symp. Proc. Vol. 537 © 1999 Materials Research Society

II. EXPERIMENT

The GaN(As,P) layers were grown on MOVPE (0001) GaN/sapphire substrates in a modified GEN II MBE system. Pure elemental Ga was used as the group III source and thermally cracked phosphine was used as the group V source. PH_3 flow rate was 3 sccm. A N radical beam source (Oxford Applied Research Model MPD21) was used to produce active N species and the RF power was fixed at 300 W. AsH_3, cracked at 1000 °C, provided the As_2 flux and its flow rate was between 0 and 3 sccm. The growth temperature ranged from 500 to 760 °C and the growth rate was 0.9 monolayer/s.

For electron microscope examination, [11-20] and [01-10] cross-section and [0001] plan-view thin foil specimens were prepared using standard procedures and finished by Ar^+ ion thinning with the specimens cooled to ~77K. TEM, TED, and high resolution electron microscope (HREM) examination was performed in a JEM 2010 instrument operated at 200kV.

III. RESULTS AND DISCUSSION

A. The Growth of GaNAs Layers

TED examination was made of orthogonal [2-1-10] and [01-10] cross-section samples to investigate the structural properties of the GaNAs layers, which were grown at temperatures in the range 500 – 730 °C. Fig. 1 shows a [01-10] TED pattern taken from a region of the thin foil specimen including the 500 °C GaNAs layer and the GaN substrate. The pattern exhibits wurtzite GaN spots and diffuse rings. The ring pattern is characteristic of polycrystalline materials. The polycrystalline material was identified from the measured spacings of the diffuse rings, assuming that the wurtzite GaN substrate spots correspond to undistorted materials with the bulk GaN lattice parameters, i.e., $a = 0.3189$ nm and $c = 0.5185$ nm.[4] Measurements show that the rings are attributed to the zinc-blende $GaN_{1-x}As_x$ ($x \approx 0.012$), where the lattice parameter of the zinc-blende GaN material was assumed to be 0.452±0.001 nm.[5-7]

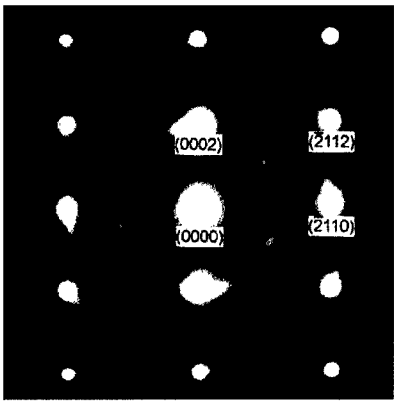


Fig.1. A [01-10] TED pattern obtained from a region of the thin foil specimen including the 500 °C GaNAs layer and the GaN substrate.

A TEM {-11-1} dark field (DF) image was obtained from the [2-1-10] cross-section sample of the 500 °C layer to investigate microstructure. The image showed the columnar grains which are inclined ~27° from the $[0001]_{GaN}$ direction. The grains varied in width from 3.5 to 6.5 nm and in length from 7.5 to 38 nm.

Fig. 2 shows a cross-section [01-10] TED pattern (~5° away from the exact pole) taken from the GaNAs layer grown at 730 °C. The pattern exhibits sharp wurtzite GaNAs spots (using the GaN substrate spots as a reference), indicating the epitaxial growth of a wurtzite material. A [0002] DF image obtained from the 730 °C layer illustrated the growth of a single-crystalline layer with defects providing the main contrast.

Another interesting feature is the presence of forbidden extra spots in the [01-

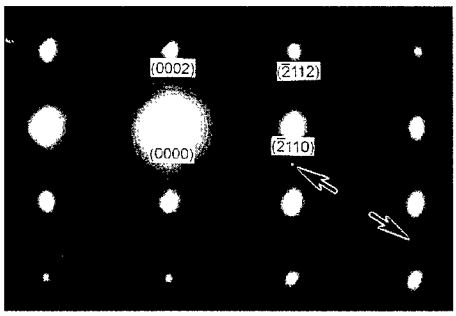


Fig.2. A [01-10] TED pattern obtained from the GaNAs layer grown at 730 °C.

10] TED pattern (Fig. 2) obtained from the GaNAs layer grown at 730 °C. The pattern was obtained by tilting the specimen ~5° toward the [2-1-1-4] direction. Such tilting was employed to get the superlattice spots excited, since they were extremely weak at the exact [01-10] pole. There are superlattice spots half way between the rows of the fundamental spots parallel to the [0001] direction, as indicated by the arrows. This is consistent with the existence of an ordered structure in the layer along the [0001] direction with a periodicity twice that of the wurtzite structure. The mixed group V atom sublattice of the ordered GaNAs layer consists of alternating N-rich and As-rich (0001) planes. Similar ordering was observed in the mixed group III-nitride layers.[8,9] Ruterana et al.[9], investigating MOVPE InGaN layers grown on (0001) sapphire reported evidence for the formation of such ordering with a space group *P*3m1. However, no superlattice-related structures were demonstrated.

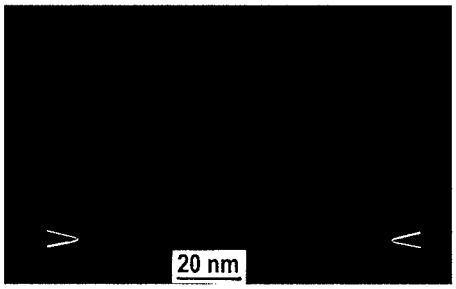


Fig. 3 A TEM DF image of the 730 °C layer taken using the forbidden (-211-1) spot.

Fig. 3 shows a DF image obtained from the 730 °C layer, which was recorded using the forbidden (-211-1) spot. The DF image revealed ordered domains as the small blobs. However, the contrast of the images was extremely weak. The interface between the overlayer and the substrate is indicated by the arrows. The domains varied in width from ~1.8 to ~4.5 nm and in length from ~4 to ~10 nm, and were randomly distributed throughout the layer. The details will be published elsewhere.[10]

B. The Growth of GaNP Layers

TED examination was made of orthogonal [01-10] and [2-1-10] cross-section specimens to investigate the structural properties of the $GaN_{1-x}P_x$ layers that were grown at temperatures in the range 500 – 760 °C. Fig. 4 shows a [01-10] TED pattern from a 500 °C layer and the GaN substrate. The pattern exhibits the wurtzite GaN spots and weak diffraction spots that are associated with the rings of diffuse diffracted intensity. The TED pattern shows that two different phases are present in the overlayer. The phases were identified from the measured spacings of the diffuse rings, assuming that the wurtzite GaN substrate spots correspond to undistorted materials with the bulk GaN lattice parameters, i.e., a = 0.3189 nm and c = 0.5185 nm.[4] Measurements show that the rings are attributed to zinc-blende $GaN_{1-x}P_x$ ($x \approx 0.91$ and 0.01), where the lattice parameter of the metastable zinc-blende GaN material was assumed to be 0.452±0.001 nm.[5-7]

A similar TED pattern was obtained from the layer grown at 600 °C. The characteristics of the pattern are similar to those of the 500 °C layer. However, some of the spots are associated

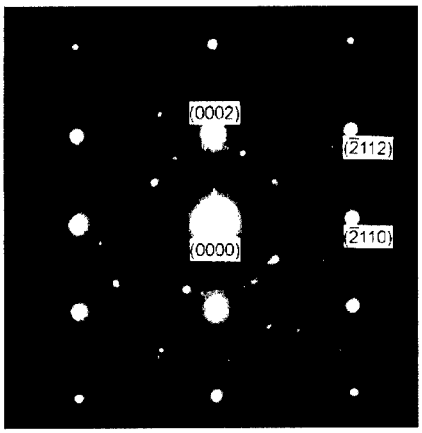


Fig. 4. A [01-10] TED pattern obtained from the layer grown at 500 °C.

with diffuse streaks approximately parallel to the $[-2112]_{GaN}$ direction. Such streaks are attributed to inclined grains. In a similar manner, measurements show that the overlayer consists of two phases of zinc-blende $GaN_{1-x}P_x$ ($x \approx 0.88$ and 0.03).

Fig. 5(a) shows a TED pattern from solely the 750 °C layer, being indexed in Fig. 5(b). The TED results show that [-111] and [110] of the zinc-blende overlayer are parallel to the c-axis and [2-1-10] of the wurtzite GaN substrate, respectively. The pattern from the overlayer exhibits two characteristic features: i) elongation of the diffracted spots; ii) presence of the two sets of <110> patterns. The elongation of the spots can be attributed to some degrees of irregularity in the size of the GaN(P) domains. (The 'GaN(P)' means that P is dissolved into binary zinc-blende GaN.) It is worth noting that there are two different types of zinc-blende crystal domains in the overlayer, i.e., $GaN(P)_I$ (indicated by 'open circle') and $GaN(P)_{II}$ (indicated by 'solid square') (Fig. 5(b)). The unit cell of the $GaN(P)_{II}$ domains is rotated counterclockwise by ~71° about the $[2\text{-}1\text{-}10]_{GaN}$ direction with reference to that of the $GaN(P)_I$ domains. This rotation causes the $(-111)_I$ and $(1\text{-}11)_{II}$ planes of the two domains to be parallel to each other, i.e., one having twin relation to the other. Measurements show that the lattice parameter of the $GaN(P)_I$ (or $GaN(P)_{II}$) is fairly close to the zinc-blende GaN, indicating that the phase is a binary alloy.

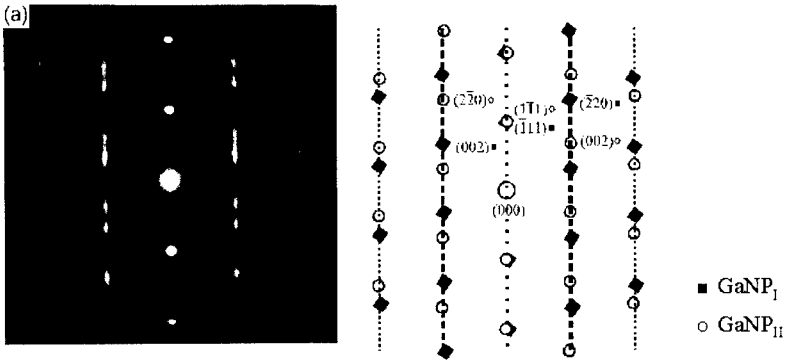


Fig. 5. (a) A TED pattern obtained from solely the 750 °C layer, which is indexed in (b).

TEM bright field and DF images were obtained to observe the microstructures and phases of the $GaN_{1-x}P_x$ layers grown at temperatures between 500 and 760 °C. For the 500 °C layer, the grains of the GaP-rich phase varied in width from ~26 to ~123 nm and in height from ~33 to ~73 nm, while those of the GaN-rich phase varied in width from ~17 to ~156 nm and in height from

~20 to ~40 nm. For the 600 °C layer, the GaP-rich grains varied in width from ~23 to ~50 nm and in height from ~23 to ~150 nm, while the GaN-rich grains varied in width from ~17 to ~50 nm and in height from ~16 to ~116 nm.

Fig. 6 shows a DF image obtained from the cross-section sample of the 750 °C layer, which was recorded using the (-11-1) spot of the $GaN(P)_I$. The image reveals fine needle-like contrast (termed here 'micro-domains') lying parallel to the layer surface. The micro-domains vary in thickness from ~0.8 to ~2.5 nm and in length from ~2 to ~10 nm. A HREM image is shown enlarged in the inset right top, clearly illustrating the twin relation between the two domains of $GaN(P)_I$ and $GaN(P)_{II}$.

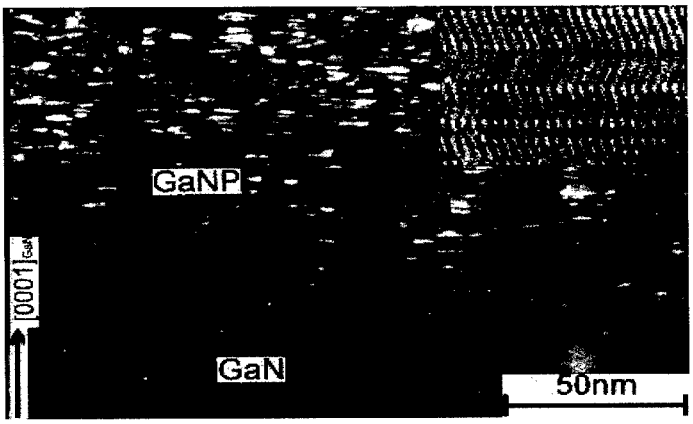


Fig. 6. A TEM dark field image obtained from the cross-section sample of the 750 °C layer, which was recorded using the (-11-1) spot of the $GaN(P)_I$.

GaN is a polytype material having two crystal structures of wurtzite and zinc-blende. The formation energies of the two phases are similar, although the wurtzite structure was calculated to be more stable than the zinc-blende.[11] This indicates that the crystal structure can be readily influenced by growth conditions. [7,12,13] It is worth noting that the only difference between the zinc-blende and wurtzite structures is the stacking sequence of the close-packed atomic layers. We found that GSMBE growth of pure GaN on (0001) GaN/sapphire at 730 °C led to a wurtzite phase. These results show that P plays an important role in the formation of the zinc-blende phase. Thus, the occurrence of the twin domains may be explained in terms of the uneven distribution of P at the growing surface. Local fluctuations in the P concentrations may cause a fault in the stacking order of the atomic layers, resulting in a number of twins and stacking faults, and hence the twin domains.

VI. CONCLUSION

GaN(As,P) layers grown on (0001) GaN/sapphire at temperatures ranging from 500 to 760 °C were examined by TEM and TED to investigate structural behaviour. For the GaNAs layers, ordering with a space group *P*3m1 was found to occur in the 730 °C layer. The layers grown at temperatures ≤ 600 °C were polycrystalline, whist the growth at 730 °C led to an epitaxial GaNAs layer. For the 500 °C layer, the grains were of width 3.5 – 6.5 nm and of length 7.5 – 38

nm. It was also shown that the layers grown at temperatures ≤ 600 °C had a zinc-blende structure, while the 730 °C layer grew in a wurtzite form. As for the GaNP layers, it is shown that for growth at temperatures ≤ 600 °C, phase separation occurred resulting in the formation of GaN-rich and GaP-rich GaNP phases. However, growth at temperatures ≥730 °C led to a binary single crystal material, containing two types of micro-domains, i.e., $GaN(P)_I$ and $GaN(P)_{II}$. The domains have twin relation to each other and vary in thickness from ~0.8 to ~2.5 nm and in length from ~2 to ~10 nm.

ACKNOWLEDGEMENTS

The authors would like to thank Korea Ministry of Science and Technology (MOST) for financial support. The work at UCSD was supported by BMDO (Dr. Kepi Wu) monitored by USASMDC.

REFERENCES

1. G. B. Stringfellow, J. Cryst. Growth **27**, 21 (1974).

2. K. Iwata, H. Asahi, K. Asami and S. Gonda, J. Cryst. Growth **175/176**, 150 (1997).

3. W.G. Bi and C.W. Tu, Appl. Phys. Lett. **63**, 3506 (1993).

4. S.M. Sze, *Physics of Semiconductor Devices*, 2nd ed. (John-Wiley & Sons, New York, 1981).

5. D. Chandrasekhar, D.J. Smith, S. Strite, M.E. Lin, and H. Morkoç, J. Cryst. Growth **152**, 135 (1995).

6. A. Trampent, O. Brandt, H. Yang, and K.H. Ploog, Appl. Phys. Lett. **70**, 583 (1997).

7. I.-T. Bae, T.-Y. Seong, Y.J. Park, and E-K Kim, (unpublished).

8. D. Korakis, K.F. Ludwig, and T.D. Mustakas, Appl. Phys. Lett. **71**, 72 (1997).

9. P. Ruterana, G. Nouet, W. Van der Stricht, I. Moerman, and L. Considine, Appl. Phys. Lett. **72**, 1742 (1998).

10. T.-Y. Seong, I.-T. Bae, C.-J. Choi, Y. Zhao and C. W. Tu, Electrochem. & Solid-State Lett., **2** 94 (1999).

11. C-Y. Yeh, Z.W. Lu, S. Froyen and A. Zunger, Phys. Rev. B **46**, 10086 (1992).

12. S. Strite and H. Morkoc, J. Vac. Sci. Technol. **B 10**, 1237 (1992).

13. Y. Xin, P.D. Brown, R.E. Dunin-Borkowski, C.J. Humphreys, T.S. Cheng, and C.T. Foxon, J. Crystal. Growth, **171**, 321 (1997).

GaN GROWTH BY REMOTE PLASMA MOCVD: CHEMISTRY AND KINETICS BY REAL TIME ELLIPSOMETRY

M. Losurdo, P. Capezzuto and G. Bruno
Plasma Chemistry Research Center-CNR, via Orabona 4- 70126 Bari, Italy, cscpml18@area.ba.cnr.it

Cite this article as: MRS Internet J. Nitride Semicond. Res. 4S1, G3.12(1999)

ABSTRACT

Cubic and hexagonal GaN layers have been grown on GaAs (001) and α-Al_2O_3 (0001) substrates, respectively, by remote plasma metalorganic chemical vapor deposition (RP-MOCVD). In situ spectroscopic ellipsometry is used to monitor in real time the chemistry and kinetics of the GaN growth. The subtrate/GaN interface formation is highlighted and the effect of the substrate plasma nitridation on the initial growth stage is discussed.

INTRODUCTION

There have been numerous recent publications on the effects of the two growth steps, i.e., substrate nitridation followed by the growth of a low temperature nucleation layer, upon the material properties of GaN epilayers grown by both molecular beam epitaxy (MBE) and metalorganic chemical vapor deposition (MOCVD) [1,2]. And, it has been shown that slight differences in the substrate nitridation and/or the growth of the GaN buffer layer prior to GaN epigrowth results in different GaN growth mechanisms [3,4]. Although the number of experimental studies conducted to date is already significant, it is not yet possible to establish an all-embracing theory of the influence of the surface properties upon the GaN growth chemistry and kinetics. And, it is widely recognized that a deeper understanding of the fundamental surface kinetics governing nitride growth is necessary to move from the "GaN art" to the "GaN science". While the investigation of the GaN growth mechanism is ongoing for MBE systems, where a variety of in situ diagnostic techniques can be used, such as reflection high energy electron diffraction (RHEED), low energy electron diffraction (LEED), X-ray photoelectron spectroscopy (XPS), some difficulties are encountered for the MOCVD process, where high pressure and reactive environment prevent from the use of the above techniques.

In this paper, the remote plasma MOCVD (RP-MOCVD) of GaN buffer layers grown on both α-Al_2O_3 and GaAs substrates, also pre-nitrided by N_2 plasmas, is discussed. Particular emphasis is placed on the in situ real time control of the growing surface and of the substrate/GaN interface by spectroscopic ellipsometry (SE), which is a non-invasive and non-intrusive optical technique compatible with the MOCVD environment. Ellipsometry data are used to depict the chemistry and kinetics of the initial stage of the GaN growth.

EXPERIMENT

The deposition system used in this study is the remote plasma MOCVD apparatus specifically designed for the growth and treatment of III-V materials [5] at reduced pressure (0.1 - 10 Torr) and reduced temperature. A unique feature of this apparatus is the presence of an in situ phase modulated ellipsometer (UVISEL-ISA Jobin-Yvon) compatible with the reactive environment of MOCVD reactors and, hence, able to monitor in real time the chemistry and kinetics of surface modifications with a sub-monolayer resolution. The substrates used for the growth were GaAs (001) and α-Al_2O_3 (0001). The remote r.f. (13.56 MHz) plasma source was

Mat. Res. Soc. Symp. Proc. Vol. 537 © 1999 Materials Research Society

used to produce H-atoms for the substrates cleaning, and N-atoms for the nitridation process and GaN growth. The H_2 remote plasma cleaning was operated at P = 1 Torr, r.f. power = 60 Watt and at a surface temperature of 250°C and 350°C for GaAs (001) and α-Al_2O_3 (0001), respectively. The subsequent nitridation by N_2-H_2 (3% in H_2) plasmas was operated at a pressure of 0.2 Torr, a r.f. power of 200 Watt and at a temperature of 250°C and 800°C for GaAs and α-Al_2O_3, respectively. GaN layers were grown at 600°C by trymethylgallium and N_2/H_2 (=1000/3 sccm) plasma at a pressure of 1 Torr and a r.f. power of 200 W. Single wavelength ellipsometry (SWE) was used, in terms of the ellipsometric angles Ψ and Δ [6], to monitor in real time the surface kinetics, and, at the growth end, ellipsometric spectra (SE) of the pseudodielectric function, $\langle\varepsilon\rangle = \langle\varepsilon_1\rangle + i\langle\varepsilon_2\rangle$, were acquired in the energy range 1.5 - 5.5 eV. In order to determine the chemical and optical properties of surfaces, ellipsometric data were modeled by optical models based on the Bruggeman effective-medium approximation (BEMA) [6] and references for the used dielectric functions are given in ref. [7]. Optical emission spectroscopy (OES) was used to control the N-atom density interacting with the growth surface. Ex situ atomic force microscopy (AFM) and X-ray diffraction (XRD) measurements were also performed to validate the ellipsometric approach.

RESULTS AND DISCUSSION

Figure 1 shows typical SWE real time (Ψ,Δ) trajectories recorded at 3 eV during GaN growth on both α-Al_2O_3 (0001) and GaAs (001) substrates previously nitrided. An easily provided information is the GaN layer thickness which is controlled in real time.

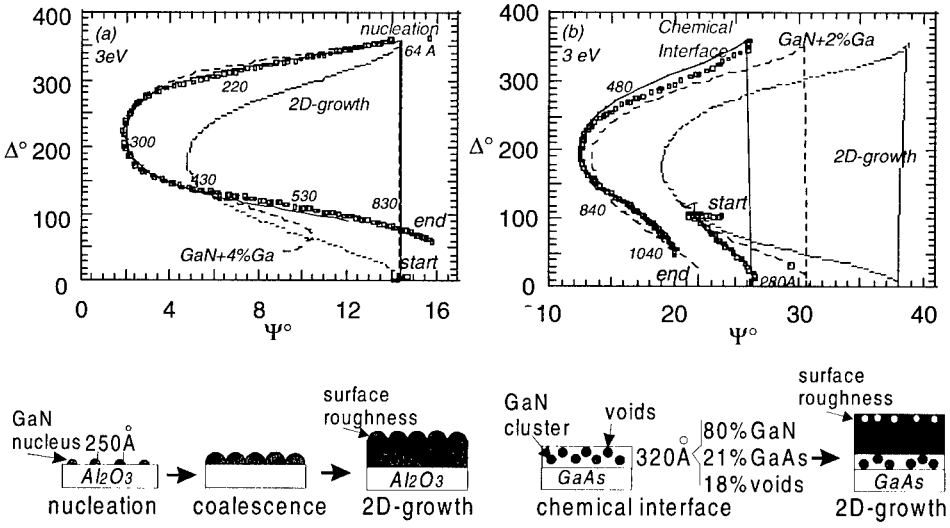


FIGURE 1. Time evolution of the optical response in the (Ψ,Δ) space at 3 eV during GaN growth on *(a)* α-Al_2O_3 and *(b)* GaAs. Points are for experimental data; full line is for the best-fit model which is, for GaN on α-Al_2O_3, nucleation followed by 2D-homogeneous growth and, for GaN on GaAs, chemical interface appearance followed by 2D-homogeneous growth. Simulated trajectories by different models (see text) are also reported for comparison.

For a better understanding of the (Ψ,Δ) data, it has to be considered that at 3 eV (below energy gap value, where the GaN absorption is almost zero) a closed and cyclical trajectory should be recorded for a well ordered and pure GaN layer. Thus, deviations from this ideal cyclical curve are indicative of non-homogeneous growth dynamics and/or defected absorbing layers. For the (Ψ,Δ) trajectories simulation, different models have been considered such as the 2D-homogeneous growth, the nucleation followed by homogeneous growth and the stoichiometry deviation in terms of Ga enrichment. Among these models, only the "nucleation followed by homogeneous growth with roughness" model fits the whole experimental trajectory in fig. 1(a). Specifically, the growth process of the GaN epilayer on α-Al_2O_3 can be distinguished into two regimes, i.e., an initial hemispherical nucleation regime followed by the GaN bulk growth (see scheme in fig. 1a). The nucleation density on the starting surface produces a mean separation of ~250 Å between nuclei, whose radius increases according to the the law R(t) = 1.8(Å/sec)·t until they come into contact. As soon as the complete nuclei coalescence is obtained, the homogeneous GaN growth starts with a steady-state growth rate of about 1 Å/sec and a gradual roughening of the growing surface also confirmed by SE modeling (see below) and AFM measurements.

For the GaN growth on GaAs (fig. 1b), the regression analysis fit evidences the appearance of a chemical interface between the substrate and the GaN film. For the interface formation regime, free fit parameters include the volume fractions of the interface components and the thickness of the interface layer. The simulation shows that the interface layer is modeled as a three-component GaAs/GaN/voids composite whose composition varies with time, i.e., the GaN volume fraction increases at the expense of GaAs until 100% GaN is reached. Then, the GaN bulk 2D-growth starts, and the GaN layer thickness increases linearly with time at about 1 Å/sec. The voids content at the interface simulates either the presence of structural defects and the grain boundaries.

Figure 2 shows the experimental SE spectra, at room temperature, of the real, $\langle\varepsilon_1\rangle$, and imaginary, $\langle\varepsilon_2\rangle$ part of the pseudodielectric function of the GaN buffer layers recorded at the end of the growth. In the figure, the solid lines are for the fitting results according to the models shown in the inset. A two-layer model (substrate/bulk GaN/surface roughness) provides the best fit for the SE spectrum of GaN grown on α-Al_2O_3. The surface roughness developed during the growth is simulated by an outer layer which is a mixture of GaN+voids as depicted in fig. 2.

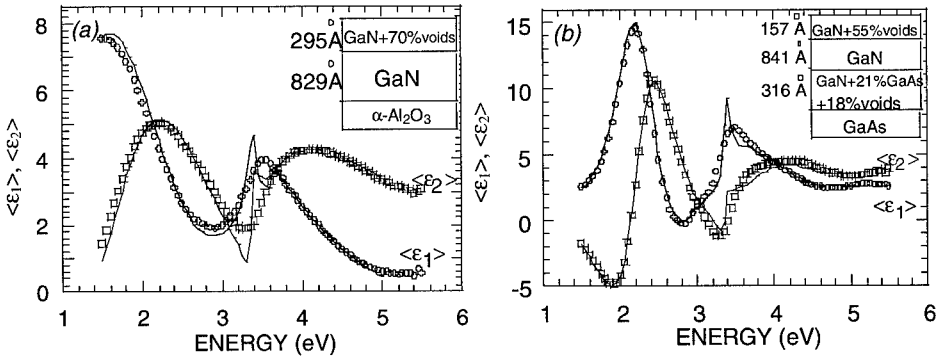


FIGURE 2. Real, $\langle\varepsilon_1\rangle$, and imaginary, $\langle\varepsilon_2\rangle$ part of the pseudodielectric function of the GaN layers grown on *(a)* α-Al_2O_3 and *(b)* GaAs. The best-fit curves (full line) by the BEMA models shown in the inset are also reported. The standard deviations are of ± 1% on constituents volume fraction and of ± 10% on layer thickness.

The best-fit model for the SE spectrum of GaN on GaAs employs a three-layer model (substrate/interface/bulk GaN/surface roughness) that accounts for the growth dynamics of fig. 1b: at first the interface formation between GaAs substrate and GaN film, and then the bulk GaN film growth. The evolution of the interface composition is approximated in the SE model by an average value (BEMA mixture of GaN+21% GaAs+18% voids). The comparison of the fit and experimental data in both GaN/α-Al_2O_3 and GaN/GaAs evidence the absence of a sharp excitonic transition, so indicating a very defective GaN buffer layer. Interestingly, cathodluminescence (CL) measurements have shown a very low intensity of the near-band edge emission and a well evident deep level emission at around 550 nm. Also, AFM images have shown a grain-like morphology with an average diameter of ~500 Å. These features have already been described by Tarsa et al.[8] and, they are, accordingly, related to the growth dynamics under N-stable conditions.

Thus, the amount of N-atoms impinging on the growing films is a crucial parameter for the GaN growth. In the present RP-MOCVD apparatus, the performance of the nitrogen remote plasma source has been evaluated by OES measurements, performed in the afterglow at the substrate position. There, the OES spectra are dominated by the N_2 1st positive system [7], which indicates a considerable amount of N-atoms and of electronically and vibrationally excited N_2 molecules impinging on the growth surface. Any contribute of ions is absent and the importance of this can be understood by considering that the ionized portion of the N_2 plasma beam has been suggested to have detrimental effect on the GaN film morphology and crystallinity [9].

Figure 3 shows the XRD measurements for GaN on both α-Al_2O_3 (0001) and GaAs (001) substrates from which the crystallographic structure has been derived. The XRD pattern of GaN grown on GaAs shows only the (002) and (004) reflections, so demonstrating this film to be purely cubic and (001) oriented monocrystalline. The FWHM of the (002) reflection is 22 min for a film ~100 nm thick, and this FWHM value is, to our knowledge, among the narrowest reported so far [10,11]. The GaN (002) reflection at 39.95° corresponds to the GaN with a lattice constant of 4.509 Å, which is in good agreement with the calculated value of 4.503 Å [12]. Also, from XRD, there is no evidence of a ternary alloy $GaAs_xN_{1-x}$ at the interface, and a detailed analysis of the (002) peak shape, which is sensitive to compositional disorder, suggests that, indeed, phase separation of GaAs and GaN [11] does seem to occur at the interface, in agreement with the ellipsometric data. Here, it is important to underline that, in the present case, the pure cubic phase is grown without arsenic background pressure in the initial stage as reported by others [10,11,13].

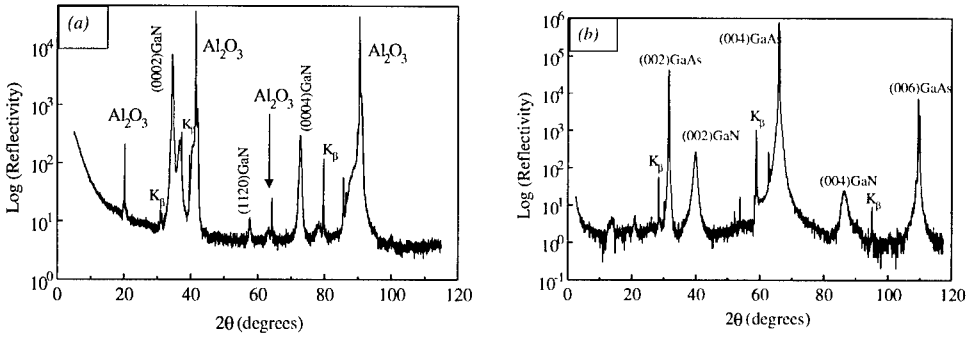


FIGURE 3. Typical XRD patterns of *(a)* GaN/α-Al_2O_3 (0001) and *(b)* GaN/GaAs(001) samples.

In the present case, we have grown pure cubic GaN on a plasma nitrided GaAs surface differently from other workers [14,15] who obtained hexagonal GaN on nitrided GaAs. This capability of our method is probably related to the fact that the remote plasma nitridation of the GaAs substrate occurs in absence of ion bombardment and under controlled conditions, so giving a very smooth (RMS = 3.1 Å) and homogeneous nitrided layer of 130 Å in thickness [7,16], which acts as a template for the subsequent growth of the cubic phase. However, from the SE analysis of the GaN layer grown at 600°C (see model in fig. 2b), there is no memory of the layer coming from the pre-nitridation of the GaAs surface at 250°C, i.e., the nitrided layer can not be discriminate after growth. This is, probably, because of its recrystallization and partial decomposition of the underlying GaAs surface during rise to growth temperature of 600°C, thus resulting in the "new" 316 Å interface layer of (GaN+21%GaAs+18%voids).

The XRD pattern of GaN grown on the (0001) plane of α-Al_2O_3 (fig. 3a) shows the main peak at 34.55° corresponding to the (0002) reflection from wurtzite GaN with a lattice constant in the c-direction of 5.18 Å [12]. This confirms that the film is grown with its c-plane parallel to the substrate. The (0002) peak has a FWHM value of 8.6 min, which is well comparable with the best value of ~ 5 min reported in literature [17]. The feasibility of our system for the deposition of GaN buffer layer is the consequence of the α-Al_2O_3 nitridation which has been performed under real time control by ellipsometry. In fact, α-Al_2O_3 nitridation leads to different surface chemistry and morphology depending on exposure time [18,19]. Figure 4 shows the time evolution of the $\langle\varepsilon_2\rangle$ value during α-Al_2O_3 nitridation. The decrease of $\langle\varepsilon_2\rangle$ is indicative of nitrogen incorporation, and the SE spectrum (spectrum B) recorded at the $\langle\varepsilon_2\rangle$ minimum can be modeled by a thin (~7 Å) layer of a BEMA mixture of AlN+10% Al_2O_3 which, however, can optically simulate an $AlNO_x$ layer also. AFM measurements of this Al_2O_3 nitrided surface show an atomically flat surface with a RMS value of 1.6 Å. For longer exposure time (>10 min in the figure), the $\langle\varepsilon_2\rangle$ trend reverses as a consequence of roughening and of free aluminum formation, this last also confirmed by XPS measurements. The formation of free Al, besides roughening [19], could be the reason why long nitridation time results in a degradation of GaN layer quality [18,19].

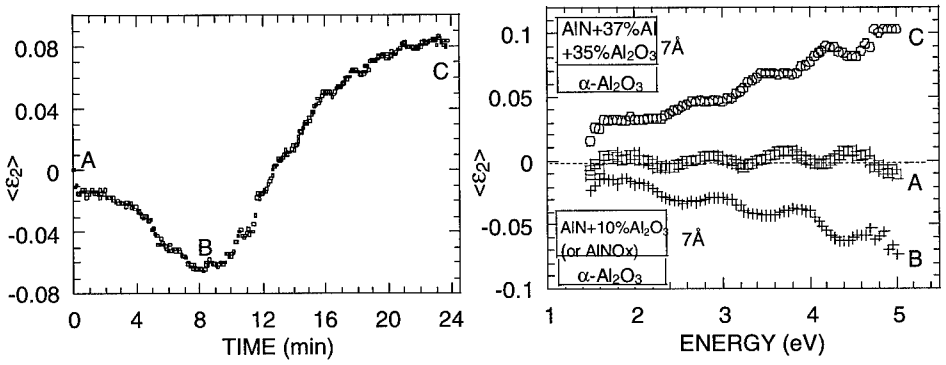


FIGURE 4. Time evolution of the $\langle\varepsilon_2\rangle$ value at 4.5 eV during α-Al_2O_3 nitridation (on the left) and SE spectra (on the right) at significant points of (A) H_2 plasma cleaned α-Al_2O_3 surface, (B) 8 min nitrided α-Al_2O_3 surface, and (C) 25min nitrided and damaged α-Al_2O_3. The inset shows the best-fit BEMA models of spectra B and C.

Thus, the real time control by SE of the α-Al_2O_3 nitridation has allowed the GaN growth to start soon after the minimum in $\langle\varepsilon_2\rangle$ (end-point of nitridation) has been reached.

CONCLUSIONS

In conclusion, spectroscopic ellipsometry has been applied as a real-time probe for the remote plasma MOCVD of GaN film in order to understand and optimize GaN growth and substrates nitridation processes. Ellipsometry has been shown to provide information on the end-point of the substrate (GaAs and α-Al_2O_3) nitridation, on the substrate/GaN film interface and on the growth kinetics. The RP-MOCVD growth of GaN under N_2 remote plasma preactivation conditions results in cubic GaN on GaAs and in hexagonal GaN on α-Al_2O_3.

ACKNOWLEDGEMENT

Financial support from Progetto Finalizzato Materiali e Dispositivi per Elettronica a Stato Solido (MADESS) of the National Council of Research (CNR) is acknowledged.

REFERENCES

[1] S. Nakamura, Jpn. J. Appl. Phys. **30**, L1705 (1991).
[2] T.D. Moustakas, T. Lei, R.J. Molnar, Physica **B**, 185, 36 (1993).
[3] K. Wang, D. Pavlidis, J. Singh, J. Appl. Phys. **80**, 1823 (1996).
[4] B. Daudin, F. Widmann, G. Feuillet, Y. Samson, M. Arlery, J.L. Rouviere, Phys. Rev. B, **56**, R7069 (1997).
[5] G. Bruno, P. Capezzuto, M. Losurdo, Phys. Rev. B, **54**, 17175 (1996).
[6] D.E. Aspnes, J. Phys. (Paris) Colloq. **10**, 3 (1983)
[7] M. Losurdo, P. Capezzuto, G. Bruno, E.A. Irene, Phys. Rev. B, **58**, 1 (1998).
[8] E.J. Tarsa, B. Heying, X.H. Wu, P. Fini, S.P. DenBaars, J.S. Speck, J. Appl. Phys. **82**, 5472 (1997)
[9] S. Gwo, H. Tokumoto, S. Miwa, Appl. Phys. Lett. **71**, 362 (1997).
[10] H. Yang, O. Brandt, M. Wassermeier, J. Behrend, H.P. Schonherr, K.H. Ploog, Appl. Phys. Lett., **68**, 244 (1996).
[11] T.S. Cheng, L.C. Jenkins, S.E. Hooper, C.T. Foxon, J.W. Orton, D.E. Lacklison, Appl. Phys. Lett., **66**, 1509 (1995).
[12] J.H. Edgar, *Properties of Group III Nitrides*, EMIS Datareviews Series No. 11, INSPEC, London, United Kingdom, 1994.
[13] O. Brandt, H. Yang, B. Jenichen, Y. Suzuki, L. Daweritz, K.H. Ploog, Phys. Rev. B, **52**, R2253 (1992).
[14] A. Kikuchi, H. Hoshi, K. Kishino, Jpn. J. Appl. Phys. **33**, 688 (1994).
[15] O. Brandt, H. Yang, A. Trampet, M. Wassermeier, K.H. Ploog, Appl. Phys. Lett, 71, 473 (1997).
[16] M. Losurdo, P. Capezzuto, G. Bruno, P.R. Lefebvre, E.A. Irene, J. Vac. Sci. Technol. B, **16**, 2665 (1998).
[17] O. Ambacher, J. Phys. D: Appl. Phys. **31**, 2653 (1998).
[18] S. Keller, B.P. Keller, Y.F. Wu, B. Heying, D. Kapolnek, J.S. Speck, U.K. Mishra, S.P. DenBaars, Appl. Phys. Lett. **68**, 1525 (1996)
[19] K. Uchida, A. Watanabe, F. Yano, M. Kouguchi, T.Tanaka, S. Minagawa, J. Appl. Phys. **79**, 3487 (1996).

Defects in GaN Pyramids Grown on Si(111) Substrates by Selective Lateral Overgrowth

ZHIGANG MAO*, STUART MCKERNAN*, C. BARRY CARTER*, WEI YANG** and SCOTT A. McPHERSON**
*Department of Chemical Engineering and Materials Science, University of Minnesota, MN55455-0132, U.S.A.
**Honeywell Technology Center, 12001 State Hwy. 55, Plymouth, MN 55441, U. S. A

Cite this article as: MRS Internet J. Nitride Semicond. Res. 4S1, G3.13 (1999)

ABSTRACT

Selective lateral growth of GaN is a promising technique for producing high quality material for microelectronic and optoelectronic devices. Single-crystal GaN/AlN layers have been grown on Si(111) substrates and subsequently used as the seeding layer for selective lateral overgrowth. GaN pyramids are formed above holes patterned in a Si_3N_4 mask. Transmission electron microscopy (TEM, which also denotes the microscope) of these structures shows that the GaN pyramid, GaN seed layer, and AlN buffer layer in the samples have the following epitactic relationship with respect to the Si substrate: $[11\bar{2}0]_{GaN} \parallel [11\bar{2}0]_{AlN} \parallel [\bar{1}10]_{Si}$ and $(0001)_{GaN} \parallel (0001)_{AlN} \parallel (111)_{Si}$. In the core of the pyramid (at or above the seed windows), dislocations thread through the pyramid perpendicular to the interface plane with very high density. Some of these threading dislocations, which originate from the GaN/AlN seed layer, form 90° bends and half loops at the edge of the pyramid core. In the lateral growth part of the GaN pyramid, the dislocation density is relatively low. The majority of dislocations thread through the pyramid parallel to the interface plane. Planar defects, usually parallel to the interface plane, were observed near the interface. The defect density decreases with the distance away from the interface, so that the top several microns of material maybe completely defect free. The mechanism of the growth of GaN pyramids is discussed and related to this defect structure.

INTRODUCTION

III-V nitrides have been extensively investigated for applications in microelectronic and optoelectronic devices because of their wide direct bandgap and good thermal, chemical, and mechanical stability. Selective growth is an important techniques in the fabrication of field effect transistors (FETs) [1] and semiconductor micro-device structures such as quantum wires and dots [2]. Selective growth can also be used to examine the growth mechanisms and the selective epitaxy of GaN.

Selective lateral growth of GaN on sapphire and SiC substrates has been reported recently [3]. The growth of single crystal GaN films on these substrates is well documented. Si is the substrate of choice due to its low cost, large size, and the potential for the integration of GaN-based optoelectronic devices with Si-based electronics.

In the present report, the microstructure and the lateral epitaxy mechanism of selectively grown GaN pyramids within windows in Si_3N_4 masks on Si(111) substrates have been studied by TEM.

EXPERIMENTAL DETAILS

The GaN growth was conducted in a low-pressure metal-organic chemical-vapor deposition (MOCVD) system with a vertical reactor. A Si(111) wafer was etched in $HF:H_2O$, rinsed and dried immediately before loading. The system was evacuated before the pressure was regulated at 10 Torr with a constant H_2 flow. The susceptor was inductively heated to 1150 °C and the Si wafer was baked at this temperature for 10 minutes under the H_2 flow. The AlN buffer layer deposition was initiated by flowing triethylaluminum (TEA) and ammonia (NH_3) into the reactor. The AlN buffer layer was grown for 20 minutes, resulting in a thickness of 100 nm. A thin GaN layer was then grown with triethylgallium (TEG) for 30 minutes, resulting in a thickness of about 200 nm. The wafer was then deposited with a 100 nm Si_3N_4 masking layer by plasma-enhanced chemical-vapor deposition (PECVD). Arrays of openings of 5 μm diameter and 20 μm center-

Mat. Res. Soc. Proc. Vol. 537 © 1999 Materials Research Society

center pitch were formed using photolithography and reactive ion etching (RIE). The wafer was reloaded into the MOCVD system for the lateral overgrowth. The system pressure was 76 Torr. The growth started as soon as the susceptor temperature reached 1050 °C, by flowing ammonia and TEG into the reactor. The total time for the lateral overgrowth was 3 hours.

The cross-sectional specimen was prepared using the usual 'sandwich' techniques: two pieces of the sample with the same orientation were glued face-to-face with epoxy. After mechanical grinding and dimpling of the cross-sectional specimen to a thickness of ~10 μm, the specimen was further thinned by ion-beam milling to electron transparency. The specimens were then examined in a Philips CM30 TEM operating at 300 kV. The analysis of the composition was carried out using an Edax PV9900 XEDS (X-ray energy dispersive spectrum) system attached to the CM30 TEM.

EXPERIMENTAL RESULTS AND DISCUSSION

Observation by scanning electron microscopy (SEM) indicates that each pyramid has predominantly six $\{10\bar{1}1\}$ facets [4]. These facets are identical to those of the pyramids grown on sapphire and SiC substrates [3]. Visible-light microscopy (VLM) of these specimens[4] can reveal the interface between the pyramids and the substrate, and show some fine structures in the center of the pyramids. There is a difference in the contrast between the center part and the lateral part of the pyramids. This difference could be associated with local differences in the defect density and growth mechanism. The height and width of the pyramids are ~15 μm.

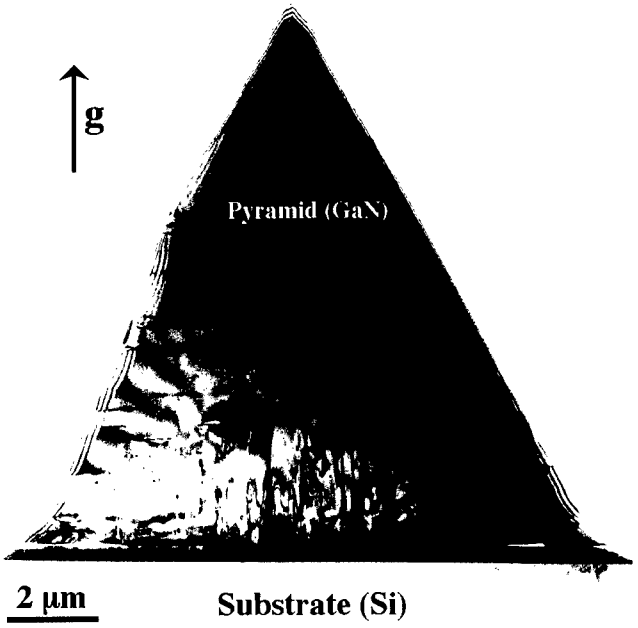


Figure 1 A low-magnification bright-field (BF) image of the cross-sectional specimen showing a pyramid. **g** = 0002.

Figure 1 is a low-magnification bright-field (BF) image of the cross-sectional specimen. A selectively grown GaN pyramid on Si substrate was clearly revealed in this image. In the center of the GaN pyramid (at and above the window area), dislocations thread through the pyramid nearly

perpendicular to the interface plane and the dislocation density is quite high. In the lateral growth part of the pyramid, the dislocations thread through the pyramid parallel to the interface plane. It is apparent that the density of the defects in the lateral part is lower than the core part (at and above the window area) of the pyramid and decreases with the distance away from the interface. Planar defects, usually parallel to the interface plane, were also observed near the interface. The mask (having a low average atomic number, *Z*) is revealed by the bright line between the pyramid and the substrate in the mass-thickness contrast TEM image of the cross-sectional specimen in figure 2. The size of the window in the mask is ~5 μm. The base of the pyramid is 15 μm wide from this image, consistent with the observations of VLM. The GaN pyramids clearly extend laterally well beyond the window. The contrast in the image also confirms that there is a layer between the Si_3N_4 mask and the substrate. At high magnifications, this layer is revealed to contain the expected two layers with thicknesses of 150 nm and 125 nm, respectively. The thickness of the mask is about 80 nm [4].

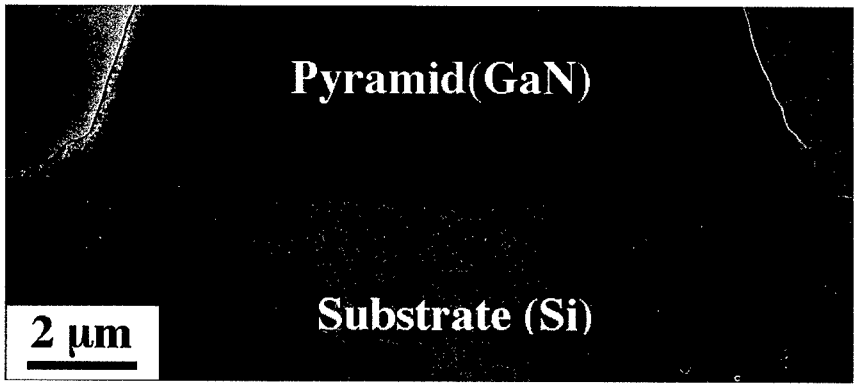
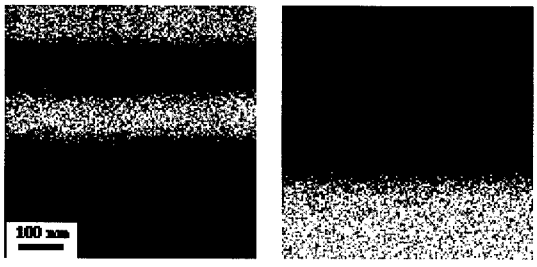


Figure 2 A low-magnification mass-thickness contrast TEM image of the cross-sectional specimen showing the mask.



(a) (b)

Figure 3 The X-ray composition map across the interface region. (a) Ga, (b) Si.

The composition map across the interface is given in Figure 3. The images show the corresponding X-ray composition maps for the elements Ga and Si. They confirm that the pyramid and seed layer are GaN, and the substrate is Si. Selected-area diffraction (SAD) patterns from the interface area, the GaN pyramid, and the substrate confirm that the GaN pyramid, the GaN layer, and the AlN buffer layer are all monocrystalline, with an epitactic relationship with respect to the Si substrate: $[11\bar{2}0]_{GaN} \parallel [11\bar{2}0]_{AlN} \parallel [\bar{1}10]_{Si}$ and $(0001)_{GaN} \parallel (0001)_{AlN} \parallel (111)_{Si}$ [4].

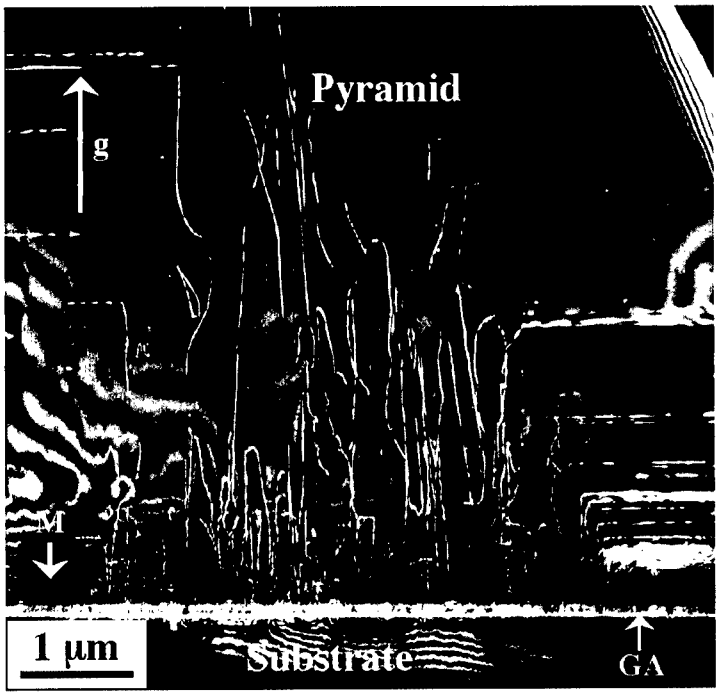


Figure 4 A weak-beam dark-field (WBDF) image taken near the [11$\bar{2}$0] GaN zone axis with **g**/4**g**, **g** = 0002. In the figure, "M" represents Si_3N_4 mask, "GA" represents the GaN seed layer and the AlN buffer layer.

A representative distribution of the dislocations within the core part in the pyramid is shown in Figure 4. This weak-beam dark-field (WBDF) image is taken near the [11$\bar{2}$0] GaN zone axis with the **g**/4**g** condition, **g** = 0002. In the figure, "M" represents the Si_3N_4 mask, "GA" represents the GaN seed layer and the AlN buffer layer. Planar defects parallel to the interface plane were clearly revealed near the interface in the lateral growth part of the pyramid. Convergent-beam electron diffraction (CBED) was attempted in order to determine if there was polarity change (inversion) across the boundaries of the planar defects. However, no unambiguous determination could be obtained due to the very high density of the defects in this area.

Further WBDF images were taken from the lateral growth part of the pyramid in order to analyse the dislocation characteristics. Representative images are shown in Figure 5. There are four defects in the WBDF images. These defects (dislocations or dislocation loops) are indicated as *A*, *B*, *C*, and *D* in the figures at different conditions. Figure 5(a) with **g**/5**g**, **g** = 1$\bar{1}$01, and (b) **g**/5**g** **g** = 000$\bar{2}$. In Figures 5(a), the electron beam is nearly parallel to the GaN [11$\bar{2}$0] zone axis and in (b) the GaN [01$\bar{1}$0] zone axis. The thickness fringes terminated at the ends of the dislocations can be used to determine the Burgers vector of the dislocations with Ishida's method [5,6]. All the thickness fringes terminated at the left-hand ends of the dislocations are indicated by arrows. Defects *A*, *C*, and *D* are dislocations, while defect *B* could have an associated dislocation half loop. By using these thickness fringes, together with **g**·**b** contrast analysis [6], the Burgers vectors of dislocations*A*, *B*, *C*, and *D* were determined to be $^1/_3$[$\bar{2}$110], $^1/_3$[1$\bar{2}$10], $^1/_3$[$\bar{1}\bar{1}$20], and $^1/_3$[1$\bar{2}$10], respectively. The line directions of dislocations *A*, *C*, and *D* were determined to be $^1/_3$[2$\bar{1}\bar{1}$0], [$\bar{1}$ 010], and $^1/_3$[2$\bar{1}\bar{1}$0], respectively [4], by trace analysis [6]. It is clear that the dislocations observed could be either pure screw or mixed dislocations with a 30° or 60° angle between the Burgers vector and the dislocation line.

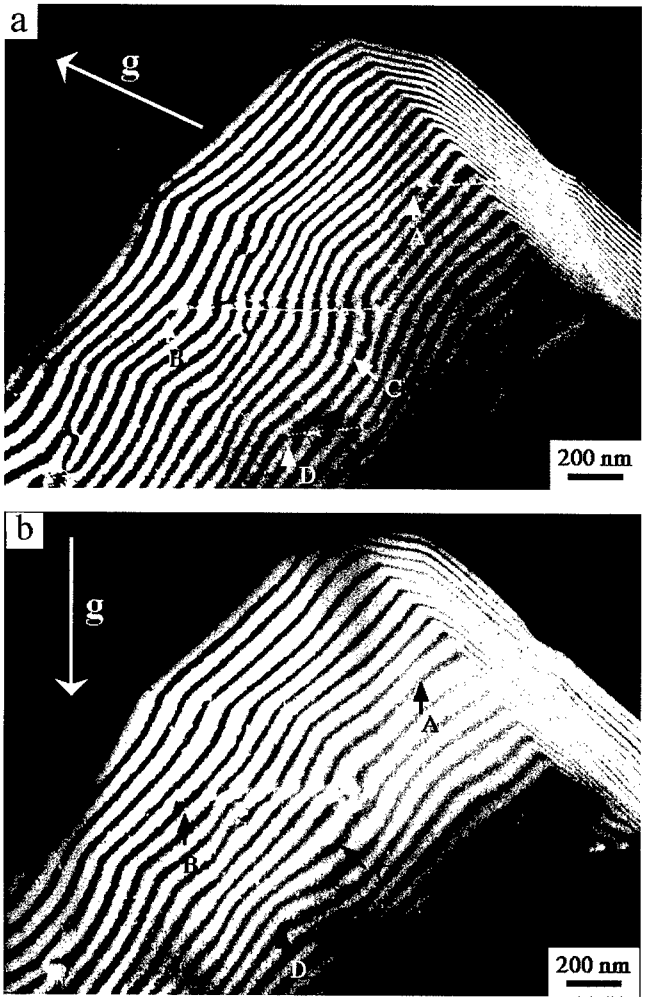


Figure 5 Weak-beam dark-field images with (a) **g**/5**g**, **g** = $1\bar{1}01$ and (b) **g**/5**g**, **g** = $000\bar{2}$. In (a), the electron beam is nearly parallel to the GaN $[11\bar{2}0]$ zone axis, in (b) the GaN $[01\bar{1}0]$ zone axis.

CONCLUSIONS

Based on the TEM observation, the following conclusions can be drawn:

- The GaN pyramid, GaN seed layer, and AlN buffer layer in the samples have the following epitactic relationship with respect to the Si substrate: $[11\bar{2}0]_{GaN} \parallel [1\bar{1}\bar{2}0]_{AlN} \parallel [\bar{1}10]_{Si}$ and $(0001)_{GaN} \parallel (0001)_{AlN} \parallel (111)_{Si}$.
- In the core of the pyramid (at or above the seed windows), dislocations thread through the pyramid perpendicular to the interface plane with very high density. Some of these threading

dislocations, which originated from the GaN/AlN seed layer, were found to form 90° bends and half loops at the edge of the pyramid core. The Burgers vector of these half loops is of [0001] type.

- At the lateral growth part of the GaN pyramid, the dislocation density was relatively low. The majority of dislocations thread through the pyramid parallel to the interface plane. The Burgers vectors of most dislocations are $^1/_3<11\bar{2}0>$, they could be either pure screw or mixed dislocations with a 30° or 60° angle between the Burgers vector and the dislocation line. Dislocation half loops with Burgers vector $^1/_3<11\bar{2}0>$ was also observed. All these defects lie on the (0001) plane.

- Planar defects mostly parallel to the interface plane were observed near the interface.

- The defect density decreases with the distance away from the interface, the top several microns of material being completely defect free.

ACKNOWLEDGMENTS

This research has been supported by AFOSR (under contract AF/F 48620-95-1-0360), Supplementary support was provided by Honeywell Technology Center and NSF under grant DMR-9522253. The microscopes are part of the CIE Characterization Facility

REFERENCE

1 H. Asai, S. Adachi, S. Ando, K. Oe, *J. Appl. Phys.*, **55**, 3868 (1984)
2 T. Fukai, S. Ando, Y. K. Fukai, *Appl. Phys. Lett.*, **57**, 1209 (1990)
3 T. S. Zheleva, O-H. Nam, M. D. Bremser, R. F. Davis, *Appl. Phys. Lett.*, **71**, 2472 (1997)
4 Z. Mao, S. McKernan, C. B. Carter, W. Yang, S. A. McPherson, submitted, (1998)
5 Y. Ishida, H. Ishida, K. Kohra, H. Ichinose, *Phil. Mag. A*, **42**, 453 (1980)
6 D. B. Williams, C. B. Carter, *Transmission Electron Microscopy-A Textbook for Materials Science,* Plenum Press, New York, (1996)

ELECTRICAL AND PHOTOELECTRICAL CHARACTERIZATION OF DEEP DEFECTS IN CUBIC GaN ON GaAs

M.LISKER[*], A.KRTSCHIL[*], H.WITTE[*], J.CHRISTEN[*], D.J. AS[**], B. SCHÖTTKER[**], K. LISCHKA[**]

[*] Institute of Experimental Physics, University of Magdeburg, PO Box 4120, D-39016 Magdeburg, Germany

[**] FB 6- Physics, University of Paderborn, Warburger Str. 100, D-33095 Paderborn, Germany,

Cite this article as: MRS Internet J. Nitride Semicond. Res. 4S1, G3.14 (1999)

Abstract

Nominally undoped cubic GaN epilayers deposited by rf-plasma assisted molecular beam epitaxy on semi-insulating GaAs substrates were investigated by electric and photoelectric spectroscopical methods. As a consequence of the existence of deep levels in the GaAs-substrate itself, special care has to be taken to separate the contributions of the substrate from that of the cubic GaN epilayer in the various spectra. Two different contact configurations (coplanar and sandwich structures) were successfully used to perform this separation. In the cubic GaN epilayer a trap with a thermal activation energy of (85±20)meV was found by thermal admittance spectroscopy and thermal stimulated currents. Optical admittance spectroscopy and photocurrent measurements furthermore revealed defects at E_G-(0.04-0.13) eV, E_G-(0.21-0.82) eV and two additional deeper defects at 1.91 Ev and 2.1 eV, respectively. These defect related transitions are very similar to those observed in hexagonal GaN.

Introduction

Cubic GaN layers grown on GaAs are of high interest for production of devices such as cleaved fabry perot type blue cavities using the substrate facets /1/. Furthermore, reaching very high p-type doping levels is feasible for cubic GaN /2/. However, for all applications based on cubic GaN the exact knowledge of defects in the layers is essential for optimization of devices. Therefore, intensive investigations on defects in GaN grown with MBE on semiinsulating (SI)-GaAs substrates were made with photoluminescence (PL), cathodoluminescence (CL) and temperature dependent Halleffect measurements (TDH). Some donor-acceptor-pair transitions were found in PL at 3.15eV /3/ involving a donor at 25meV and an acceptor at 130meV, as well as at 3.178eV and 3.056eV /4/. An acceptor bound exciton transition at 3.088 /4/ involves an acceptor at an activation energy of 212meV. In p-type undoped c-GaN grown under N-rich conditions an acceptor at an activation energy of 0.445eV was observed with TDH /5/, whereas in n-type undoped c-GaN-layers grown under Ga-rich conditions a shallow donor at an activation energy of 26meV and an deep donor at an activation energy of 0.6eV were found /5/. A further deep CL peak was observed at 2.4eV in undoped c-GaN /1/.

Mat. Res. Soc. Symp. Proc. Vol. 537 © 1999 Materials Research Society

However, the electrical and photoelectric characterization of cubic GaN /SI-GaAs involves some principle problems. SI-GaAs itself contains many deep levels which must be isolated in the GaN/GaAs heterostructure spectra, complicating the analysis of the GaN layers.

The aim of our works is the detection and isolation of deep levels in n- and p-type GaN layers and to separate them from the defects in the SI-GaAs substrate using thermal and photoelectric techniques by using different contact arrangements and different excitation energies.

Experimental

Cubic GaN (c-GaN) films with a phase purity better than 99.9% (estimated by both X-ray diffraction and Raman measurements) were grown on SI-GaAs substrates orientated in (001) direction by rf-plasma-assisted molecular beam epitaxy (MBE) at a substrate temperature of 720°C. Details of the nucleation process and growth parameters were described in /6/. All samples were nominally undoped. However, in c-GaN the type of conductivity can be influenced by the growth conditions and both p- and n-type GaN layers with low carrier concentrations were obtained /5/. Three different kinds of GaN- layers were investigated. 1.) The first group were nominally undoped p-type GaN-layers with carrier concentrations of $(1\text{-}5)\times10^{16}cm^{-3}$ and Hall mobilities between 220 and 300 cm^2/Vs (samples signed as P1 and P2), 2.) an nominally undoped, p-type GaN- layer on top at a p-type GaAs buffer layer (signed B1), and 3.) n-type GaN layers, nominally undoped or slightly Si-doped with carrier concentrations below $10^{14}cm^{-3}$ and mobilities of a few $100cm^2/Vs$ (signed as N1 and N2). The SI-GaAs substrate is identical for all heterostructures investigated.

Ohmic contacts were prepared on SI-GaAs after cleaning and chemically etching by evaporating the layer system Ni(5nm)/Ge(20nm)/Au(50nm) and subsequent annealing (see also /7/). On the GaN-surface the contacts was realized by evaporating of Al and followed by annealing for ohmic and a sputtered Pt layer for Schottky contact. In coplanar contact arrangement the ohmic as well as the Schottky-contact are on the GaN surface whereas the sandwich measurements were performed between the ohmic contact on the GaAs substrate and the Schottky contact on the GaN side. All Schottky contacts show rectifying behavior up to a frequency of 100kHz. The contacts on the GaN layer have a diameter of 1 mm.

The samples were characterized by thermal admittance spectroscopy (TAS), thermal stimulated currents (TSC), by DC-photocurrent spectroscopy (PC) and by optical admittance spectroscopy (OAS). The measurements were made in the temperature range from 80K to 450K. The admittance investigations were realized in the range of modulation frequency between 20Hz and 1MHz. The optical excitation in TSC measurements was performed with a laser at a wavelength of 675nm and a mercury-tungsten-lamp with an optical band pass filter ((330±30)nm).

OAS and PC investigations were performed in the wavelength region from 300nm to 3000nm using monochromator systems with Xe-lamp and W-lamps. The OAS and TAS experimental technique and the evaluation methods are described in detail elsewhere /8/. Furthermore, the use of OAS and PC to evaluate defect transitions in hexagonal GaN layers is described in /9/. Details for the investigation of defects in hexagonal GaN using TAS are given in /10/ and in /7/ for TAS and TSC investigations of GaAs.

Results and Discussion

Fig. 1 shows TAS spectra of the sample P2 measured in sandwich and coplanar contact arrangements. The main defect L1 with E_A=(530±30)meV in the spectrum of the sandwich arrangement is probably the well known deep level EL3 in the GaAs substrate /7/.

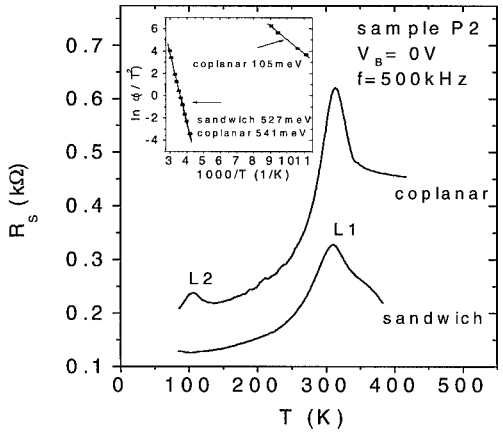


Fig. 1 : TAS spectra of the sample P2 in coplanar and sandwich contact arrangement. The corresponding Arrhenius plots are shown in the insert.

However, a further peak L2 at 100K with a thermal activation energy of (105±15) meV exclusively shows up in coplanar contact arrangement. Thus, we conclude that this defect L2 is located within the GaN layer. In another sample a level with an activation energy of (89±20)meV was observed by TAS in coplanar contact arrangement in the same temperature range.

For the separation of the deep levels we also performed TSC measurements with different excitation energies while the GaN layer is excited by UV-light with a wave length of (330±30) nm, a laser at 675nm mainly stimulates the GaAs substrate (low absorption coefficient in the GaN-layer). A comparison of both TSC spectra in Fig. 2 shows, that the defect level at about 120K with E_A= (85±15) meV only appears after UV-excitation. Therefore, we conclude that this level is located within the GaN layer and is the same trap L2 found with TAS as mentioned above.

In our photoelectrical measurements (OAS, PC) the deep levels in the GaAs substrate were detected also. However, the spectral ranges of the transitions in GaAs and GaN were well distinguishable as shown in Fig. 3. The relative signals from the GaAs substrate and from the GaN layer could be changed by using sandwich or coplanar contact arrangement similar as in the case of TAS measurements. The OAS spectrum of a sandwich arrangement were dominated by the near band gap peak (NBG) of the GaAs substrate. But using coplanar contacts the GaN spectrum exhibited more features and some additionally transitions stemming from the GaN layer, which were hardly observed in the sandwich structure.

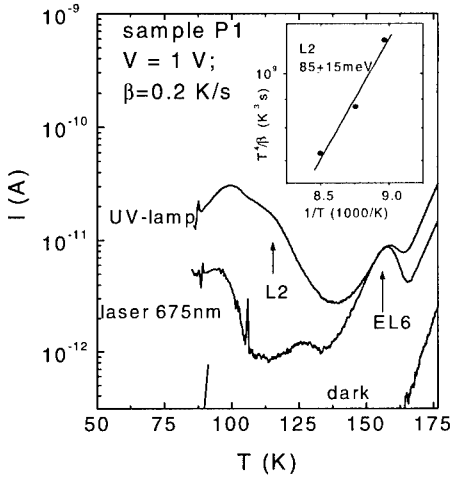


Fig. 2 : TSC spectrum of sample P1 with different light excitations (UV-lamp and 675nm laser). The inset shows the Arrhenius plot of the UV-induced trap.

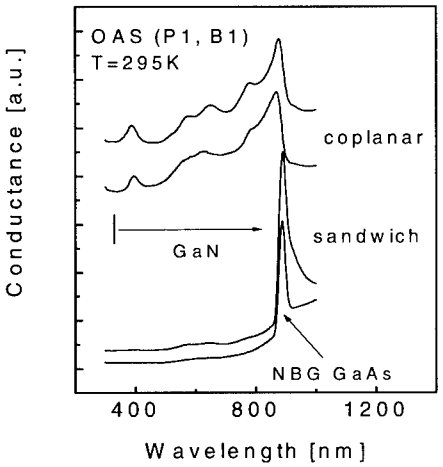


Fig. 3 : OAS spectra of the samples P1 and B1 in sandwich and coplanar contact arrangements.

Fig. 4 gives an example of the OAS spectrum of the sample P2. For the GaN samples P1, P2 and B1 all defect-band-transitions found were summarized in Table I.

In the near band gap region transitions involving shallow levels up to E_G-130meV appear which are comparable with the defects measured by TAS and TSC. Furthermore, the band between 3.0 and 2.2eV consist of deep level-opposite band- transitions and is adequate to the "blue band" in hexagonal GaN /9/. Some of these deep levels were also detected by PL -

measurements (see /4/ and /5/). The yellow band at 2.1eV and the 1.9eV band show the existence of very deep levels.

Table I : Summary of defect -band-transitions of cubic GaN/ SI-GaAs heterostructures found with OAS and PC at room temperature. A value of 3.23eV was assumed as the gap energy at 295K /11/.

E_{ph} (eV)	designation	interpretation	references
3.1 -3.2	near band gap (NBG)	E_G-(0.04 - 0.13)	130meV acceptor /3/
3.3 - 2.5	blue band (BB)	E_G-(0.21±0.03)	212meV acceptor /4/
		E_G-(0.33±0.03)	
		E_G-(0.57±0.05)	0.6eV donor /5/
2.41 - 2.44 and 2.15 - 2.18	yellow band (YB)	E_G-(0.82±0.05) yellow band	2.4eV CL-peak /1/, /12/
1.9 - 1.94	deep defect-band transition (DB)	deep defect	

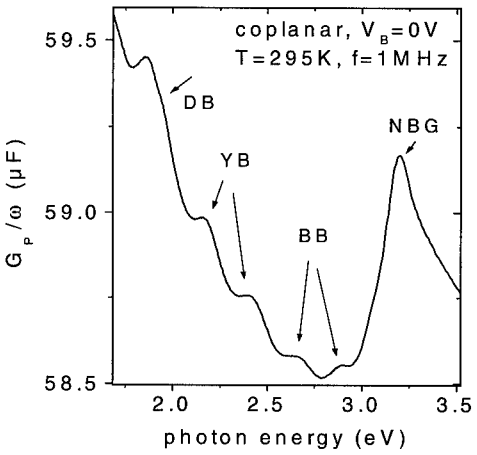


Fig. 4 : OAS spectrum of sample P2 in coplanar contact arrangement (the transition energies are listed in Table I). The meaning of the abbreviations is: NBG near band gap region: BB blue band region: YB yellow band region; DB deep defect-band transition.

It is important to note, that the OAS spectra of cubic GaN were very similar to those of hexagonal GaN as described in /9/. The spectral features in both crystallographic phases of GaN were nearly the same, only the optical transition energies were lightly shifted. We therefore conclude, that the origin and the formation mechanism of the deep defects in cubic GaN are similar to those in hexagonal GaN layers. This is further supported by DLTS measurements on hexagonal GaN by FANG et al. /13/ how reported DLTS traps similar to those seen here, especially in the 0.2eV range. However, due to the phase purity of our sample, which is better

than 99.9% and the optical shift to lower energies, we can exclude that the traps are generated by the h-GaN component.

In conclusion, we have investigated nominally undoped cubic GaN layers grown by rf-plasma assisted MBE on SI-GaAs using thermal and optical admittance spectroscopy (TAS and OAS) and thermal stimulated currents (TSC) measurements. By comparing coplanar and sandwich contact arrangements we could separate the GaAs-substrate related defects from the defects in the cubic GaN epilayer. Although in TAS and TSC the deep levels of the GaAs substrate (EL2, EL3 and EL5) are observed in all spectra, a defect with a thermal activation energy between 85meV and 105 meV can clearly be located in the cubic GaN films. OAS measurements showed defect-to band transitions in a wide range of transition energies. Besides two deep defects at 2.1 eV and 1.9 eV, defects in the range of E_G-(0.21-0.82)eV and shallower defects at E_G-(0.04-0.13) eV were also observed. The OAS-spectra of cubic GaN layers were very similar to those of hexagonal GaN, indicating the same nature of defect formation mechanism.

Acknowledgment

This work was financially supported by the Deutsche Forschungsgemeinschaft under contract numbers WI 1619/1-1, AS 107/1-1 and by the Kultusministerium Sachsen-Anhalt contract number 002KD1997.

References

/1/ D.J.As, C.Wang, B.Schöttker, D.Schikora, K.Lischka : Mater. Res. Soc. Symp. Proc. 482, 661 (1997)
/2/ O.Brandt, H.Yang, H.Kostial, K.L.Ploog : Appl. Phys. Lett. 69, 2707 (1996)
/3/ D.J.As, F.Schmilgus, C.Wang, B.Schöttker, D.Schikora, K.Lischka : Appl. Phys. Lett. 70, 1311 (1997)
/4/ J.Wu, H.Yaguchi, K.Onabe, R.Ito, Y.Shiraki : Appl. Phys. Lett. 71, 2067 (1997)
/5/ D.J.As, D.Schikora, A.Greiner, M.Lübbers, J.Mimkes, K.Lischka : Phys. Rev. B. 54, R8381 (1996)
/6/ D.Schikora, M.Hankeln, D.J.As, K.Lischka, T.Litz, A.Waag, T.Buhrow, F.Henneberger : Phys. Rev. B 54, R11118 (1996)
/7/ M.Lisker, A.Krtschil, H.Witte, O.Großer, J.Christen, M.Jurisch, U.Kretzer : Inst. Phys. Conf. Ser. 160, 413 (1997)
/8/ J.Barbolla, S.Duenas, L.Bailon : Sol. State Electron. 35, 285 (1992)
/9/ A.Krtschil, M.Lisker, H.Witte, J.Christen, U.Birkle, S.Einfeldt, D.Hommel : in print Mater. Science and Engineering B (1998)
/10/ A.Krtschil, H.Witte, M.Lisker, J.Christen, U.Birkle, S.Einfeldt, D.HommeL : J. Appl. Phys. 84, 2040 (1998)
/11/ G.Ramirez-Flores, H.Navarro-Contreras, A.Lastras-Martinez, R.C.Powell, J.E.Greene : Phys. Rev. B 50,8433 (1994)
/12/ C. Wang, D. J. As, B. Schöttker, D. Schikora, and K. Lischka: to be published in Semiconductors Science and Technology (February 1999)
/13/ Z.-Q. Fang, D.C.Look, W.Kim, Z.Fan, A.Botchkarev, H.Morkoc : Appl. Phys. Lett. 72, 2277 (1998)

PRESSURE DEPENDENCE OF OPTICAL TRANSITIONS IN InGaN/GaN MULTIPLE QUANTUM WELLS

W. Shan,* J.W. Ager III,* W. Walukiewicz,* E.E. Haller,* M.D. McCluskey,**
N.M. Johnson,*** and D.P. Bour***

*Materials Sciences Division, Lawrence Berkeley National Laboratory, Berkeley, CA 94720
**Department of Physics, Washington State University, Pullman, WA 99164
***Xerox Palo Alto Research Center, Palo Alto, CA 94304

Cite this article as: MRS Internet J. Nitride Semicond. Res. 4S1, G3.15(1999)

Abstract: The effect of hydrostatic pressure on optical transitions in InGaN/GaN multiple quantum wells (MQWs) has been studied. Photoluminescence (PL) and photomodulated transmission (PT) measurements were performed under applied pressure to examine the pressure dependence of optical transitions associated with confined states in MQWs. The PL emission from the MQWs was found to shift linearly to higher energy with applied pressure but exhibit a significantly weaker pressure dependence compared to epilayer samples with similar bandgap energies. Similar pressure coefficients obtained by PT measurements rule out the possibility of PL resulting from deep localized states. We show that the difference in the compressibility of InGaN and of GaN induces a tensile strain in the compressively strained InGaN well layers that partially compensates the applied hydrostatic pressure. This mechanical effect is the primary factor for the smaller pressure dependence of the optical transitions in the InGaN/GaN MQWs. At pressure above 100 kbar, the PL signal in MQWs samples is quenched, indicating that the carriers involved in the radiative recombination processes in the well layers originate primarily from the adjacent GaN layers.

INTRODUCTION

The $In_xGa_{1-x}N$ alloy system and related heterostructures such as quantum wells (QWs) are attracting much attention because of their scientific and technological importance. This has been manifested by recent breakthroughs in the development of high-efficiency blue light emitting diodes and laser diodes using $In_xGa_{1-x}N$/GaN QW structures as active media materials. A large number of studies on the optical properties of InGaN epilayers and InGaN/GaN QW structures have been reported. In particular, recent pressure-dependent photoluminescence (PL) studies on bulk-like $In_xGa_{1-x}N$ epitaxial layers have found that the pressure coefficients of the PL emission from InGaN epilayers do not substantially differ from that of GaN.[1,2] In addition, the pressure coefficient of GaN grown epitaxially on sapphire does not differ from that of bulk GaN,[3] suggesting that the highly defective region near the GaN/sapphire interface plastically deforms under applied pressure. The pressure dependent measurements are consistent with theoretical predictions of the pressure dependence of the band gap.[4] Recent pressure-dependent studies of the optical properties of $In_xGa_{1-x}N$/GaN QWs have found that the pressure coefficients of luminescence emission depend on QW sample structure and the In concentration.[5,6] One explanation of these results is that highly localized states, with small pressure coefficients, could be involved in the emission processes in the QWs.

Here we present a high-pressure study of optical transitions in an $In_{0.15}Ga_{0.85}N$/GaN multiple quantum well (MQWs) sample. Both photomodulated transmission (PT) and photoluminescence (PL) measurements were performed. A comparison between the pressure

Mat. Res. Soc. Symp. Proc. Vol. 537 © 1999 Materials Research Society

dependence of the absorption process probed by PT and that of the emission process measured by PL provides direct insights into the nature of the electronic states involved.

EXPERIMENT

The $In_{0.15}Ga_{0.85}N$/GaN MQW sample used in this work is a laser diode structure prepared by metalorganic chemical vapor deposition. It consists of a 10-period $In_{0.15}Ga_{0.85}N$/GaN superlattice grown on a 4-μm thick GaN layer deposited on a sapphire substrate, and it is capped by a 0.2-μm GaN:Mg *p*-type layer. The thicknesses of the well and the barrier are 18 and 62 Å, respectively. These values were derived from X-ray diffraction (XRD) measurements of the superlattice period (80 Å) and the ratio of the well/barrier growth times (35/120). The averaged In concentration was determined by Rutherford backscattering spectrometry. The MQW structure is pseudomorphically strained to the underlaying GaN layers.[7]

Photomodulation measurements were performed in a transmission geometry using a 150W xenon lamp as probing light source and a chopped HeCd laser beam (3250 Å) as modulating light. PL signals resulted from excitation by the laser and were dispersed by a 1-M double-grating monochromator. Application of hydrostatic pressure was accomplished by mounting small sample chips with sizes of ~200×200 μm^2 into gasketed diamond anvil cells. A small ruby chip was also placed in the DAC for pressure calibration. All the spectra reported in this work were recorded at room temperature (295 K).

RESULTS AND DISCUSSION

Fig.1 shows PT spectra taken from the $In_{0.15}Ga_{0.85}N$/GaN MQW sample and two thick epilayer samples ($In_{0.15}Ga_{0.85}N$ and $In_{0.11}Ga_{0.89}N$) at ambient pressure. The derivative-like spectral signatures denoted as E_0 in the spectra are associated with the optical transitions across the band gap of the respective samples. Note that the quantum confinement effects on the electron and hole states in the MQW have shifted the band gap of $In_{0.15}Ga_{0.85}N$ to an energy approximately equal to that of bulk $In_{0.11}Ga_{0.89}N$. The second derivative-like spectral feature (denoted as E_1) in the PT spectrum of the MQW is due to transitions from ionized Mg acceptor states to the conduction band edge in the *p*-type GaN cladding layer. As commonly observed in InGaN alloys and related heterostructure samples, the MQW sample exhibits fairly broad PT and PL spectral lineshapes. A Stokes shift of the PL peak energy (2.99 eV) relative to the transition energy (E_0) was observed.

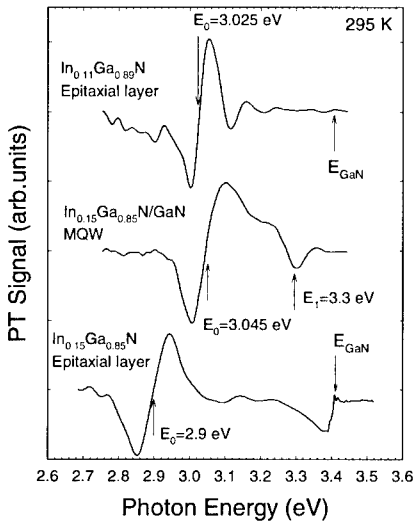


Fig. 1. PT spectra of an $In_{0.15}Ga_{0.85}N$/GaN MQW sample and two ($In_{0.15}Ga_{0.85}N$ and $In_{0.15}Ga_{0.85}N$) epilayer samples at ambient pressure

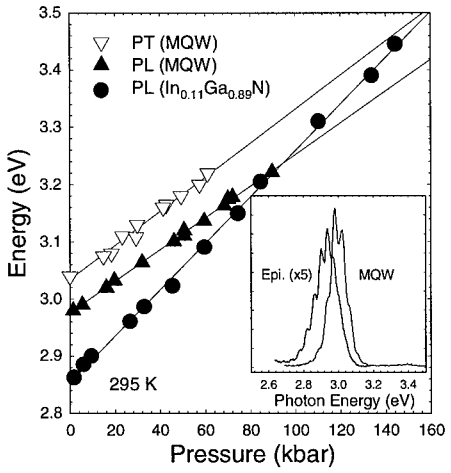


Fig.2. Shift of the PT transition and PL emission energies for the MQW sample and the $In_{0.11}Ga_{0.89}N$ epilayer sample as a function of applied pressure. The solid lines are the linear fits to the data. The inset shows the PL spectra of the samples at ambient pressure.

The pressure induced energy shifts for the E_0 transition and PL peak if the MQW sample, along with the PL emission from the thick $In_{0.11}Ga_{0.89}N$ epilayer, are plotted in Fig.2. The inset of the figure shows a comparison of the PL spectra taken from these two samples. The solid lines in the figure are least-squares fits to the experimental data using the linear-fit function

$$E(P)=E(0)+\alpha P, \qquad (1)$$

where the energy E is in eV and the pressure P is in kbar. The pressure coefficients for the E_0 transition and the PL emission in MQWs were determined to be 3.0×10^{-3} eV/kbar and 2.8×10^{-3} eV/kbar, respectively. A best fit to the PL data of the $In_{0.11}Ga_{0.89}N$ sample yields a pressure coefficient of 4.0×10^{-3} eV/kbar. The pressure dependence of the interband E_0 transition and the PL emission in the MQW sample is much weaker than that of thick, bulk-like $In_{0.11}Ga_{0.89}N$ epitaxial layer. Although weaker pressure dependences of PL emissions in InGaN/GaN quantum wells were previously reported,[1,2] this is the first time that a significantly smaller pressure dependence of an interband absorption in InGaN/GaN MQWs has been observed. The fact that the pressure coefficient obtained by PT measurements is very similar to that derived from PL measurements infers that the possibility of the PL transition involving deep localized states can be ruled out safely and it further demonstrates that the PL process originates from the effective-mass band-edge states in the MQW sample.

Application of hydrostatic pressure to strained QWs consisting of barrier and well materials with very different bulk moduli will lead to uniaxial strains that make the barriers and the wells experience different effective hydrostatic and axial pressure components.[8,9] Since the MQW structure used in this work was grown on a thick GaN layer, and the GaN barriers are much thicker than the $In_{0.15}Ga_{0.85}N$ wells, the deformation of the well layers is dominated by the compression of the stiffer GaN under hydrostatic pressure. The bulk modulus of InN (~125 GPa)[10] is approximately half of that of GaN (~210-237 GPa).[10-12] A linear interpolation gives a bulk modulus of $In_{0.15}Ga_{0.85}N$ about 7% smaller than that of GaN. Under hydrostatic pressure conditions, a tensile strain will be induced in the compressively strained $In_{0.15}Ga_{0.85}N$ well layers in the MQW structure to compensate the applied hydrostatic pressure because $In_{0.15}Ga_{0.85}N$ has a larger compressibility. As a result, the $In_{0.15}Ga_{0.85}N$ layers effectively experience a smaller hydrostatic pressure and an additional (0001) uniaxial stress. The relative volume change with applied pressure can be estimated using the Murnaghan equation of state:[13]

$$P=(B_0/B_0')[(V_0/V)^{B_0'}-1]. \quad (2)$$

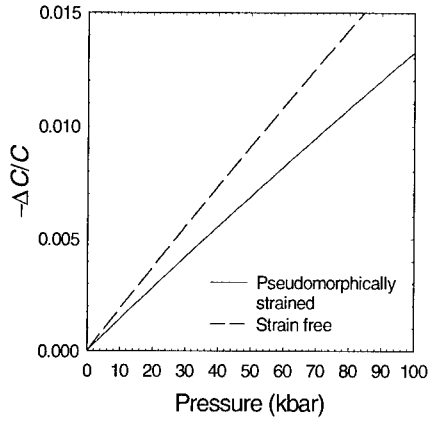


Fig.3. Relative change of the c-lattice constant of an $In_{0.15}Ga_{0.85}N$ layer pseudomorphically strained to GaN (solid line) and a strain-free $In_{0.15}Ga_{0.85}N$ layer (dashed line) as a function of pressure.

Here B_0 is the bulk modulus and B_0' is its pressure derivative ($=dB/dP$). For a crystal with wurtzite structure, the relative volume change can be related to the variation of lattice parameters a and c as:

$$\Delta V/V=2\Delta a/a+\Delta c/c. \quad (3)$$

The relative changes of the lattice parameters can further be related through the elastic stiffness coefficients as:

$$\Delta c/c=-2(C_{13}/C_{33})\Delta a/a. \quad (4)$$

Under the conditions that the $In_{0.15}Ga_{0.85}N$ well layers remain pseudomorphically strained to GaN at high pressures, the variation of the a-lattice parameter of the well layers has to match the change of the a-lattice constant of GaN under pressure. Using the first-order (linear) approximation, the relative changes of the c-lattice constant as a function of applied hydrostatic pressure for a pseudomorphically strained to GaN and strain-free (free standing) $In_{0.15}Ga_{0.85}N$ layer can be expressed as:

$$\Delta c/c= P/B_0^{InGaN} - P/[B_0^{GaN}(1- C_{13}/C_{33})^{GaN}], \quad (5)$$

and

$$\Delta c/c= P/[B_0^{InGaN}(1- C_{33}/C_{13})^{InGaN}], \quad (6)$$

respectively. The calculated results are given in Fig.3. The numerical values of C_{13}=108 GPa and C_{33}=399 GPa for GaN and C_{13}=94 GPa and C_{33}=200 GPa for InN were used, and no fitting parameters were invoked in the calculations. As is shown in the figure, the overall effect of mechanical strain is to make a strained $In_{0.15}Ga_{0.85}N$ layer sandwiched by stiffer GaN layers be compressed less than a free-standing layer at a given externally applied hydrostatic pressure. The effective pressure experienced by the well layers is only about 74% of the applied pressure. A pressure coefficient of $3.7\text{-}4.0\times10^{-3}$ eV/kbar can be derived from this purely mechanical correction. Fig.4 shows this mechanical correction to the experimental data. Therefore, we attribute the difference in the compressibility of $In_{0.15}Ga_{0.85}N$ from that of GaN to be the major factor responsible for the significantly weaker pressure dependence of the confined transition in our MQW sample.

We also found the PL intensities from the MQWs and the $In_{0.11}Ga_{0.89}N$ sample experienced a sudden drop as the applied pressure rises above 100 kbar, whereas their luminescence intensities did not change much at pressures below 100 kbar, as shown in Fig.5. While the PL intensity of the epilayer sample was found to decrease by a factor of four, the PL signal from the MQW in fact was quenched completely at pressures beyond 100 kbar. This

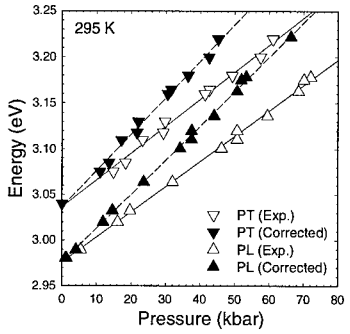


Fig.4. Comparison of the PT and PL transition energy shifts in the MQW sample as a function of pressure after the mechanical correction to the experimental data.

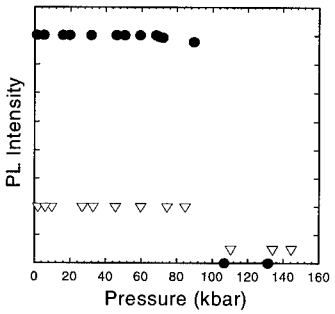


Fig.5. Change of PL intensities with pressure for the MQW sample (solid circles) and the $In_{0.11}Ga_{0.89}N$ sample (open triangles).

observation provides direct evidence that the PL emission from the MQW sample is dominated by contributions from the carriers photo-generated in the GaN cladding, barrier and underlying layers. After being generated in the GaN layers, electrons and holes diffuse into the well regions, and thermalize down to the lowest confined states, respectively, where they radiatively recombine to produce PL emissions. At pressures beyond 100 kbar, the band-gap energy of GaN becomes larger than the photon energy of the excitation laser line (3.81 eV), so that very few carriers could be generated in the GaN layers. At that point, the PL emission from the MQW collapsed, indicating that the carriers created directly in the very-thin well layers do not contribute noticeably to the PL signal at room temperature. The residual PL emission in the epilayer sample above 100 kbar is primarily due to its large thickness.

CONCLUSIONS

We found that both PT and PL spectral features corresponding to the transition associated with the confined states in an $In_{0.15}Ga_{0.85}N$/GaN MQWs exhibit a significantly smaller pressure dependence as compared to bulk-like thick InGaN epitaxial-layer samples. The very similar pressure coefficients obtained by monitoring two different transition processes, *i.e.*, absorption (PT) and recombination (PL), rule out the possibility of PL resulting from localized states deep in the band gap. The difference in the compressibilities of $In_{0.15}Ga_{0.85}N$ and GaN, which induces a tensile strain in the $In_{0.15}Ga_{0.85}N$ well layers, partially compensating the externally applied hydrostatic pressure, was found to be primarily responsible for the smaller pressure dependence obsserved for the confined transition in the MQW sample. An abrupt decrease of PL intensity in the MQW and $In_{0.11}Ga_{0.89}N$ samples was also observed at pressures above 100 kbar. The loss of the supply of photo-carriers from GaN layers above 100 kbar is found to be responsible for the sudden drop of the PL intensity in the epilayer sample and the quenching of the PL signal in the MQW sample at room temperature because the band gap of GaN exceeds the photon energy of the excitation light source.

ACKNOWLEDGEMENTS

The authors gratefully acknowledge the technical support by Professor P.Y. Yu and helpful discussions with P. Perlin. This work at LBNL was supported by the Director, Office of Energy Research, Office of Basic Research, Materials Sciences Division of the U.S. Department of Energy under Contract No.DE-AC03-76SF00098.

REFERENCES

1. W. Shan, J.J. Song, Z.C. Feng, M. Schurman, and R.A. Stall, Appl. Phys. Lett. **71**, 2433(1997).

2. W. Shan, J.W. Ager III, W. Walukiewicz, E.E. Haller, M.D. McCluskey, N.M. Johnson, D.P. Bour, Phys. Rev. B**58**, R10191(1998).

3. D.L. Camphausen and G.A.N. Connell, J. Appl. Phys. **42**, 4438(1971).

4. N.E. Christensen and I. Gorczyca, Phys. Rev. **B**50, 4397(1994).

5. P. Perlin, V. Iota, B.A. Weinstein, P. Wisniewski, T. Suski, P.G. Eliseev, and M. Osinski, Appl. Phys. Lett. **70**, 1993(1997).

6. P. Perlin, C.Kisielowski, V. Iota, B.A. Weinstein, L. Mattos, J. Kruger, E.R. Weber, and J.W. Yang, Appl. Phys. Lett. **73**, 2778(1998).

7. M.D. McCluskey, C.G. Van de Walle, C.P. Master, L.T. Romano, and N.M. Johnson, Appl. Phys. Lett. **72**, 2725(1998).

8. B. Gil, D.J. Dunstan, J. Calatayud, H. Mathieu, and J.P. Faurie, Phys. Rev. B**40**, 5522(1990).

9. J.A. Tuchman and I.P. Herman, Phys. Rev. B**45**, 11929(1991).

10. M. Ueno, M. Yoshida, A. Onodera, O. Shimomura, and K. Takemura, Phys. Rev. **B49**, 14(1994).

11. M. Leszczynski, T. Suski, P. Perlin, H. Teisseyre, I. Crzegory, M. Bokowski, J. Jun, S. Porowski, and J. Major, J. Phys. D**28**, A149(1995).

12. A. Polian, M. Grimsditch, and I. Grzegory, J. Appl. Phys. **79**, 3343(1996).

13. F.D. Murnaghan, Proc. Natl. Acad. Sci. **30**, 244(1944).

DOMAIN STRUCTURE OF THICK GaN LAYERS GROWN BY HYDRIDE VAPOR PHASE EPITAXY

T. Paskova, E.B. Svedberg, L.D. Madsen, R. Yakimova, I.G. Ivanov, A. Henry and B. Monemar

Department of Physics and Measurement Technology, Linköping University, S-581 83 Linköping, Sweden

Cite this article as: MRS Internet J. Nitride Semicond. Res. 4S1, G3.16(1999)

ABSTRACT

The crystal structure and surface morphology of hydride vapour phase epitaxy grown thick (12-105 μm) GaN layers have been investigated as a function of growth rate using several structure sensitive techniques like atomic force microscopy (AFM), x-ray diffraction (XRD) in ω-2θ and ω-rocking curve measurements as well as low temperature photoluminescence (PL). PL and XRD measurements reveal rather narrow lines: full width at half maximum (FWHM) values of the strongest donor-bound exciton line are in the range from 6.0 to1.8 meV and ω-2θ FWHM values are between 80 and 23 arcsec indicating good structural quality of the films. The ω-rocking curves show a single peak for the thinnest films with a FWHM of 250 arcsec and multiple peaks with FWHM of about 250-350 arcsec in thicker films indicating the formation of several high-quality domains when increasing either thickness or growth rate. Optical microscopy and AFM images reveal a domain type of morphology and also show an appearance of spiral hillocks in layers grown at growth rates exceeding a critical value. We interpret these results as dominating 2D multilayer growth at low growth rates, and competing 2D multilayer and spiral growth mechanisms at high growth rates.

INTRODUCTION

The growth of GaN is challenging, in part due to the independent optimisation of many growth parameters, and also due to the constraint of heteroepitaxy. Typically, sapphire or SiC substrates are used for substrates, although they are not lattice matched to the GaN layers. Thick hydride vapour phase epitaxial (HVPE) GaN layers on sapphire offer great potential as an alternative substrate for subsequent nitride growth. Studies by other researchers suggest that the application of thick GaN films for homoepitaxial growth of MOVPE GaN films may lead to improved optical and crystalline characteristics of the material [1,2]. From this point of view, it is very important to reach higher growth rates in HVPE growth while maintaining acceptable quality of the material. It has been found by other authors that the properties of thin GaN layers (several μm) are very different from those of thicker layers (over 20 μm), but while the thin MOVPE grown GaN layers have been intensively studied recently, there are a limited number of reports focused on thick films [2-5]. The growth mechanism of HVPE grown GaN is not fully understood at present, also its influence on the material properties is still far from complete.

In this study, we have examined the optical and structural properties as well as the morphology of the HVPE GaN layers as a function of growth rate in order to gain insight into the growth mechanism and its relationship to the structural characteristics.

Mat. Res. Soc. Symp. Proc. Vol. 537 © 1999 Materials Research Society

EXPERIMENTAL

All samples used in this study were grown under atmospheric pressure in a horizontal HVPE system. The sources for the V and III elements were NH_3 and metal Ga, respectively. HCl was used for reacting with Ga at ~850 °C to form GaCl. The NH_3 and HCl were injected separately and mixed at 1060 °C. The substrate was held at 1080 °C and at a distance of 75-85 mm from the gas mixing point. All samples were grown on a-plane sapphire without a buffer layer. In order to ensure a uniform nucleation, the substrates were nitridated in 20% NH_3 atmosphere for 10 minutes. Two series of GaN samples were investigated. In the first series the growth time was varied at constant growth rate, and in the second series, the growth rate was the variable parameter while the growth time remained constant. The growth conditions are presented in Table I.

Table I. Growth conditions for two groups of GaN samples.

	Growth temperature (°C)	N_2 flow rate (ml/min)	NH_3 flow rate (ml/min)	HCl flow rate (ml/min)	Growth rate (μm/h)	Growth time (min)
Series 1	1080	1000	400	24	~48	15 - 120
Series 2	1080	1000	400	10 - 30	20 - 105	60

The layer thicknesses and interfaces were revealed by cleaving or by making a cross-sectional cut of the sample. An optical microscope with Nomarski interference contrast was utilised for studying the surface morphology. AFM measurements were performed with a Nanoscope IIIa instrument operated in tapping mode using Si tips. Photoluminescence experiments were performed in a helium bath cryostat at 2 K, using the 244 nm wavelength of a frequency-doubled Ar^+ ion laser. The excitation power was about 7 mW over a spot approximately 100 μm in diameter. The luminescence was dispersed by a single monochromator (JY HR460) with a resolution of 0.4 Å and detected by a UV sensitive CCD camera. The XRD measurements were performed with a Philips MRD system with a Cu radiation source operated at 40 kV and 40 mA. The triple axis configuration was utilised in the HRXRD measurements by using a Ge (220) monochromator and an analyzer crystal in front of the detector. The triple axis mode provides high resolution, typically better than 12". The both PL and XRD methods at the excitation wavelengths used probe the uppermost several micrometers region of the layers.

RESULTS AND DISCUSSION

Figure 1 presents a typical PL spectrum of GaN film over the spectral range of 3.35 to 3.55 eV. All PL spectra indicate strong exciton emissions at 3.470 - 3.496 eV. The major peak is due to transitions associated with neutral donor bound exciton (DBE) at 3.478 eV. Well-defined free-exciton lines (A and B) can be seen in the spectrum at 3.486 eV and 3.494 eV, respectively. The peaks due to the transitions associated with neutral acceptor bound excitons (ABE_1) at 3.474 eV and (ABE_2) at 3.461 eV can also be seen. The defined FWHM of the DBE line ranges from 6.0 to 1.8 meV for all samples studied. These results show that the nominally undoped HVPE-grown GaN samples have a good optical quality.

In order to investigate the effect of growth rate on the crystalline quality of the layers, we determined the FWHM of the DBE line in the PL spectra as well as FWHM of (0002) reflection in XRD pattern using both ω-2θ and ω measurements. Their dependencies on the film thickness of GaN layers grown for different times at the same growth conditions are shown in Fig.2(a). Figure 2(b) presents these characteristics as a function of the growth rate. Information about the variation in the lattice parameter (i.e., degree of strain) [6] and the

dislocation distribution in the layers can be provided via the ω-2θ rocking curves. The FWHM obtained through a conventional ω-scan is due primarily to the variation in the mosaic spread.

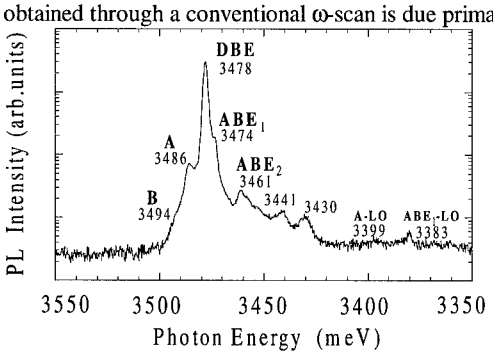


Fig.1 Low temperature (2K) PL spectrum of 80 μm thick GaN layer. The FWHM of the DBE peak is 2.3 meV.

Figure 2(a) shows, that increasing film thickness leads to an exponential decrease of the PL and ω-2θ linewidths. In changing the thickness from 15 to 96 μm, the FWHM of the exciton PL peak varies from 6.0 to 2.1 meV and ω-2θ FWHM values vary from 84 to 30 arcsec. These values indicate that the crystalline quality of the surface region of thick GaN HVPE films rivals the best GaN MOVPE layers. The narrowest ω-linewidth is 250 arcsec obtained for GaN layers with a thickness of 12 μm, one of the best values reported for GaN epitaxial layer grown without a buffer layer. Up to a critical thickness (d_{crit}) of about 42-48 μm, the (0002) reflection appears as a single peak (Fig.3a) in a ω-scan. The ω-FWHM value increases from 250 to 1000 arcsec with increasing thickness up to the d_{crit} . It is apparent that there is an increase in mosaic spread in thinner layers despite that the amount of stress in the layers decreases. In the thicker layers (over than d_{crit}), multiple peaks appear in the ω-scans (Fig.3b). A fitting procedure determined that each peak is comprised of several subpeaks with a FWHM values in the order of 250-350 arcsec, indicating the formation of several high quality domains.

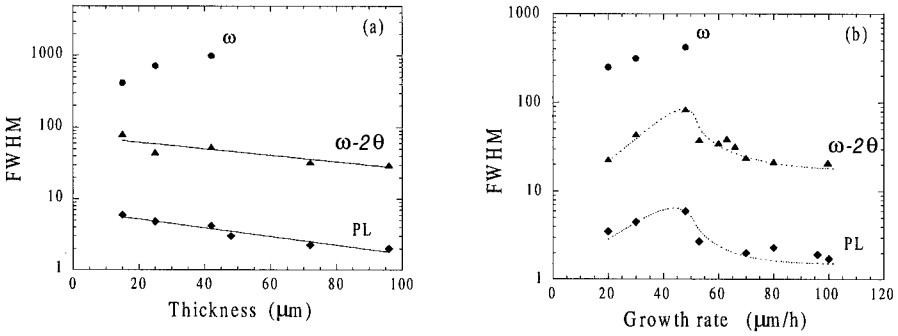


Fig.2 PL (meV) ana X-ray (arcsec) linewidths of GaN layers as a function of thickness (a) and growth rate (b). The dotted lines in Fig.2(b) are presented only as a guide to the eye and do not necessarily represent the specific functional relationship.

The dependence of the ω-FWHM on both the thickness and the growth rate are similar. At the same time, the dependencies of FWHM of both PL line and ω-2θ line versus growth rate show a more complicated behaviour (Fig.2b). In the beginning, increasing the growth rate results in a broadening of both linewidths. At further increasing the growth rate, both a

multipeak appearance in the ω-scans and a dip in the PL and ω-2θ dependencies are simultaneously observed. The narrowing of these lines is indicative of improvement of crystalline quality of the material. It seems that there is a critical growth rate value R_{crit} at which the behaviour of all dependencies is changed.

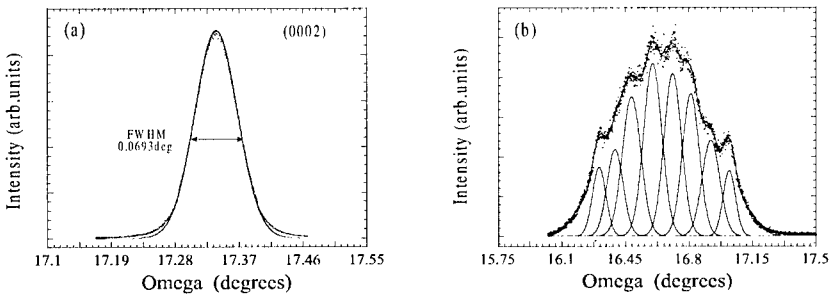


Fig.3 X-ray ω-scans of 12 μm (a) and 70 μm (b) thick GaN layers.

The surface topography images of the layers obtained by the optical microscopy show hillock type surfaces as illustrated by Fig.4 (a) and (b). The hillocks have a six-fold symmetry which is a typical feature for hexagonal crystals. The domains appear as single islands on the surface of the 12 μm thick GaN layer. Some of them are in the initial stage of development and some of them are further developed. The islands widen with increasing layer thickness and coalesce. Enlargement of a single island is limited by other islands and correspondingly when they meet boundaries are created. It is known that the boundaries have a high density of structural defects and they are an efficient source for more significant imperfections. In thinner films the increasing of both domain size and number results in broadening of the ω-curve. Further development of the hillock structure leads most probably to a domain appearance at the critical thickness of about 45 μm and to a tilting of the domains which can be seen as multipeaks in ω-scan. The domains might be formed over columnar structure crystallities which are expectable for heteroepitaxial growth without a buffer [7] and we directly observed in our layers by cathodoluminescence imaging [8].

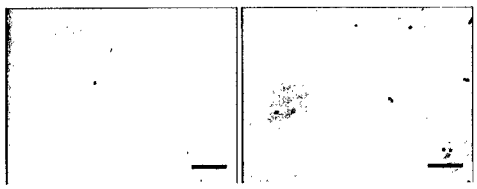


Fig.4 Optical micrographs of the growth surface of GaN layers with thickness of 12 μm (a) and 70 μm (b) grown at the same growth rate (25 μm/h). The marker represents 200 μm.

In the optical microscope, the surfaces of the domain-facets appear smooth. However, when the facets are imaged by AFM the presence of steps are revealed which are 30-80 nm wide and 5-6 Å high (Fig.5). As mentioned by Molnar *et al.* [2] this is indicative of a step-flow mode of growth. The step height corresponds to what one would expect for monoatomic steps (c = 5.19 Å). All samples grown at growth rate lower that R_{crit} (about 60 μm/h) show such kind of morphology independent of thickness. The morphology of our thinner HVPE-

GaN layer is similar to that observed by Rihrer *et al.* [9] for 2.8 μm thick MOVPE grown GaN layers. However more pronounced domain structure is typical for our layers and taking into account that locally the growth remains two-dimensional on the top of each terrace or island, the HVPE growth can be considered in terms of a 2D multilayer model [10] with high lateral/vertical growth ratio.

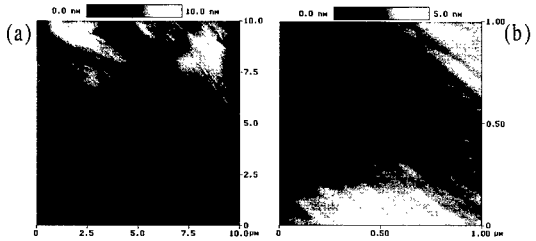


Fig.5 AFM micrographs of the surface of 70 μm thick GaN layer grown at 30 μm/h growth rate.

The morphology of GaN epilayers grown at higher growth rates exceeding the critical value was found to be completely different than for layers grown at lower growth rate. It is evident, even in optical microscope (Fig.6), that the domain facets are comprised of a huge number of small features.

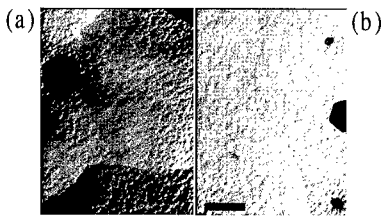


Fig.6 Optical microphotographs of two GaN layers grown at growth rate of 70 μm/h (a) and 80 μm/h (b). The marker represents 50 μm.

AFM images of thick layers (Fig.7) grown at 80 μm/h reveal the microstructure and show a presence of well-formed terraced hillocks. Two dimensional images of the layer surface (Fig.7b) reveal perfect flatness of every terraced step and very sharp boundaries between them with a height of ~13nm. Terrace-bunching resulting in hillocks mediated by a screw dislocation in the centre was evident. Using higher magnification (Fig.7c) we can see that the microstucture of every terrace was formed by step-flow mode growth with a height of ~10-13 Å.

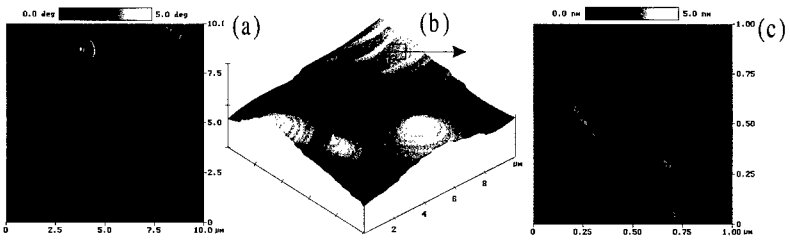


Fig.7 AFM micrographs of GaN layer grown at high growth rate (80 μm/h).

The growth mechanism of HVPE GaN layers grown at high growth rate is not exactly known; however the spiral growth model based on the existence of screw dislocations seems to be involved too. The 2D multilayer growth which is believed to be responsible for the background domain formation continues to be the favourite layer creator. However, at such high growth rates there is a comparative contribution of the spiral growth mode. The pronounced effect of the spiral growth might be related to a critical supersaturation of growth environment with GaCl. At low NH_3/HCl ratio of 15:1 used (compared to commonly used 40:1 [3]), Ga droplets might be formed which can lead to the observed morphological features. In general, at growth rates exceeding the R_{crit} value both growth mechanisms operate in a competitive way and the lateral/vertical growth ratio seems to be much lower than at low growth rate.

The 2D multilayer growth is the common growth mechanism for heteroepitaxy. Moreover for a system with high lattice mismatch between the substrate and the layer, islanding driven by an increasing strain component in the total system free energy usually leads to relaxation of the system [10]. So, the simultaneous operation of both mechanisms: 2D multilayer as a base and spiral growth which provides steps and enhances nucleation sites in the vicinity might explain the high growth rate approached as well as the improvement of structural characteristics with increasing the growth rate.

CONCLUSION

Thick HVPE-GaN epitaxial layers grown at growth rates between 20 and 105 μm/h were investigated. The layers exhibit in general a domain type structure with a slight misorientation. It was found that the domains are of high crystalline quality based on the values of structural characteristics. The HVPE growth of thick GaN layers proceeds via two growth mechanisms: 2D multilayer growth and spiral growth mechanism. The first one is completely dominant at low growth rate. At higher growth rate, both growth mechanisms operate in a competitive way.

REFERENCES

1. T. Detchprohm, K. Hiramatsu, N. Sawaki, I. Akasaki, J. Cryst. Growth **145**, 192 (1994).
2. R.J. Molnar, W. Götz, L.T. Romano, N.M. Johnson, J. Cryst. Growth **178**, 147 (1997).
3. K. Naniwae, S. Itoh, H. Amano, K. Itoh, K. Hiramatsu, I. Akasaki, J. Cryst. Growth **99**, 381 (1990).
4. Yu. Melnik, A. Nikolaev, I. Nikitina, K. Vassilevski, V. Dmitriev, in *Nitride Semiconductors,* edited by F.A. Ponce, S.P. DenBaars, B.K. Meyer, S. Nakamura, S. Stride (Mat. Res. Soc. Symp. Proc. **482**, Boston, MA 1997) pp.269-276
5. A. Usui, in *Nitride Semiconductors,* edited by F.A. Ponce, S.P. DenBaars, B.K. Meyer, S. Nakamura, S. Stride (Mat. Res. Soc. Symp. Proc. **482**, Boston, MA 1997) pp.233-244
6. N. Itoh, K. Okamoto, J. Appl. Phys. **63**, 1486 (1988).
7. I. Akasaki, H. Amano, Y.Koide, K.Haramatsu, N. Sawaki, J. Cryst. Growth **98**, 209 (1989).
8. E.M. Goldys, T. Paskova, I.G. Ivanov, B. Arnaudov, B. Monemar, Appl. Phys. Lett. **73** (24) (1998).
9. G.S. Rohrer, J. Payne, W. Qian, M. Skowronski, K. Doverspike, L.B. Rowland, D.K. Gaskill, in *GaN and Related Materials,* edited by F.A. Ponce, R.D. Dupuis, S. Nakamura, J.A. Edmond (Mat. Res. Soc. Symp. Proc. **395**, Boston, MA 1995) pp.381-386.
10. J.E. Greene, presented lecture at the Second Workshop on Science and Technology of Thin Films, Trieste, Italy, 1996 (unpublished)

CHARACTERIZATION OF Be-IMPLANTED GaN ANNEALED AT HIGH TEMPERATURES

C. RONNING*, K.J. LINTHICUM, E.P. CARLSON, P.J. HARTLIEB, D.B. THOMSON, T. GEHRKE, AND R.F. DAVIS
North Carolina State University, Department of Materials Science and Engineering, Box 7919, Raleigh, NC, 27695, USA
*University of Göttingen, II. Physical Institute, Bunsenstr. 7-9, D-37073 Göttingen, Germany

Cite this article as: MRS Internet J. Nitride Semicond. Res. 4S1, G3.17 (1999)

ABSTRACT

Single crystalline (0001) gallium nitride layers were implanted with beryllium and subsequently annealed within the range of 300-1100 °C for 10-60 minutes under a flux of atomic nitrogen obtained using a rf plasma source. The nitrogen flux protected the GaN surface from decomposition in vacuum at high temperatures. SIMS measurements revealed that no long range diffusion of the implanted Be occurred at 900 or 1100 °C. XRD spectra showed defect-related peaks in the as-implanted samples; these peaks disappeared upon annealing at 900 °C and higher for 10 minutes. Photoluminescence (PL) measurements showed one new line at 3.35 eV which provided strong evidence for the presence of optically active Be acceptors.

INTRODUCTION

Doping of semiconductors by ion implantation offers advantages in comparison to doping during film growth. (i) The concentration as well as the lateral and depth distributions of the dopants are precisely controllable, and (ii) almost all elements can be implanted with sufficiently high purity. However, this process is compromised by the radiation damage which has to be removed via annealing treatments. In the case of gallium nitride (GaN), this essential annealing procedure for dopant activation is very difficult due to the decomposition of the GaN surface for temperatures above 900 °C [1-3]. Annealing temperatures (T_A) of around 1300 °C for >5 minutes are necessary for GaN to fulfil the rule of thumb claiming that implanted semiconductors should be annealed up to 2/3 of the melting point for satisfying electrical activation [3-5].

At this writing, three special annealing procedures for temperatures above 900 °C have been investigated with limited success: (i) Rapid thermal annealing (RTA). During this process GaN is heated up to high temperatures and cooled down within a few seconds. Decomposition is a time dependent diffusion process, and in this small time frame significant decomposition of the implanted layer starts only for temperatures over 1150 °C [6,7]. (ii) N_2-overpressure. Annealing under N_2-overpressure in the kbar range opposes the surface decomposition, but only a slightly higher temperature limit of 1250 °C can be realized due to the exponential rise of the N vapor pressure as a function of temperature [8]. (iii) Polycrystalline AlN cap. An AlN layer, sputter deposited after the implantation, on top of the GaN layer was used to protect decomposition during annealing. Depending on the crystalline quality of the AlN annealing temperatures of 1300 °C for 30 sec. and good results were reached but only for some selected samples [5,9].

In this article we introduce a new annealing technique which allows the annealing of GaN at a temperature of 1100 °C for at least 1 hour. We have applied this technique to Beryllium implanted GaN, because achievement and control of substantial activation of p-type dopants in GaN remains a critical issue vis a` vis improved performance of devices fabricated in

Mat. Res. Soc. Symp. Proc. Vol. 537 © 1999 Materials Research Society

this material. The most commonly used p-type dopant is magnesium (Mg) which substitutes on Ga sites and has an ionization energy of ~ 0.25 eV. One-to-two orders of magnitude higher atomic concentration of Mg must be incorporated into GaN to achieve the desired hole concentration at room temperature [10]. This incorporation reduces the hole mobility due to the enhanced carrier-impurity scattering processes [11]. Beryllium (Be) is a more promising candidate for p-type doping given its measured lower ionization energy of ~ 0.15 eV [12,13].

EXPERIMENTAL

One-to-two μm thick epitaxial, monocrystalline and undoped GaN films were grown on on-axis n-type, Si-face α(6H)-SiC(0001) substrates at 1000 °C and 45 Torr using a vertical, cold-wall, RF inductively heated MOVPE deposition system [11]. A 0.1 μm high-temperature mono-crystalline (1100 °C) AlN-buffer layer was deposited prior to the GaN growth. Deposition was performed using triethylaluminum (TEA) and triethylgallium (TEG) in combination with 1.5 SLM of ammonia (NH_3) and 3 SLM of H_2 diluent.

Beryllium was twice implanted at 100 keV and 200 keV to create a broad depth distribution of this element. The dose ratio between the two implantation energies was 2/3 to adjust the maximum impurity concentration of both implantations. TRIM simulations gave a mean ion range of 276 nm (FWHM = 175 nm) and 472 nm (FWHM = 1060 nm), respectively, for the two energies [14]. The total implantation dose ranged between 10^{13} cm^{-2} and $2.5x10^{14}$ cm^{-2}.

All implanted samples were first sequentially annealed in a tube furnace under vacuum at 300, 600 and 900 °C for 10 minutes. The samples were transferred into a MBE chamber for annealing at higher temperatures. Heating of the samples was performed under a flux of atomic nitrogen obtained using a rf plasma source (300 W, Model RF 4.5, SVT Associates). The atomic nitrogen flux protected the GaN surface at 1100 °C for at least 1 hour using a distance between sample and rf source of around 40 cm.

Secondary ion mass spectroscopy (SIMS) was performed by the Analytical Instrumentation Facility at NC State University using a Cameca IMS-6f. Samples were analyzed with a 200 nA, 10 keV O^- primary beam. Two dimensional ω-2θ X-ray diffraction (XRD) pattern were measured using a Philips X'Pert-MRD system with a resolution of 0.001°. Photoluminescence measurements (PL) were performed after each annealing step at 14 K by exciting the GaN samples with a He-Cd laser (3.81 eV). Hall measurements were done after the deposition of Ni(50 nm)-Au(100nm) contacts.

RESULTS AND DISCUSSION

Figure 1 shows SIMS-profiles of implanted Be with a dose of 10^{13} cm^{-2} before and after annealing at 900 °C and 1100 °C for 15 minutes. Both implantation profiles of the 100 keV and 200 keV implantation are clearly visible and in good agreement with TRIM calculations [14]. Within the experimental resolution, no long range diffusion was observed after annealing. This observation is in agreement with Ref. [15], where also no redistribution was observed up to 800 °C. This

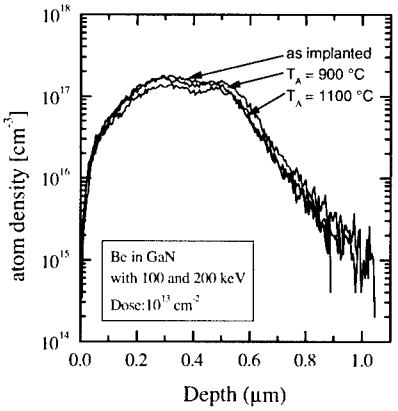


Figure 1: SIMS profiles of Be implanted in GaN, unannealed and annealed to 900 °C and 1100 °C for 15 minutes.

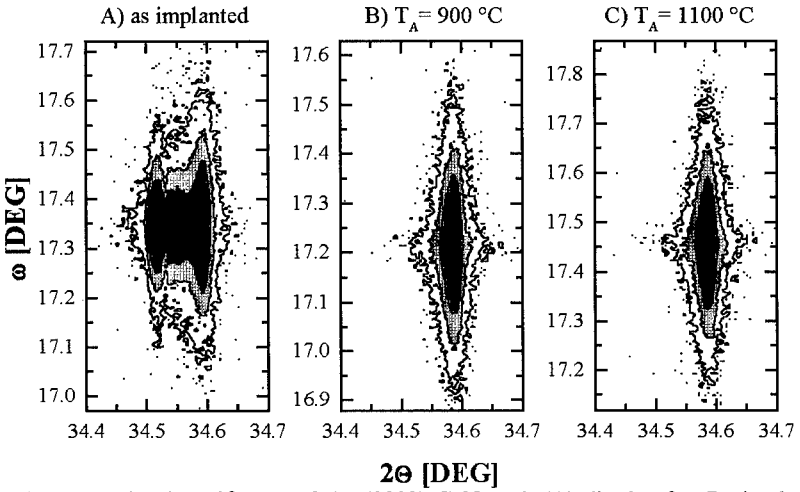


Figure 2: XRD 2-axis ω-2θ map of the (0002) GaN peak (A) dirctly after Be implantation with a dose of $2.5x10^{14}$ cm^{-2} and after subsequent annealing to a temperature of 900 °C (B) and 1100 °C (C) for 10 minutes. (Note: contour plots have log-scale).

excellent thermal stability of Be in GaN indicates a strong bonding of Be in the lattice. Therefore, diffusion of Be into GaN from an external source is not practical and ion implantation or epitaxial growth are the only possibilities to introduce Be into GaN.

Figure 2A displays a two dimensional ω-2θ X-ray diffraction (XRD) pattern of the GaN (0002) peak of a Be-implanted sample with a dose of $2.5x10^{14}$ cm^{-2}. Note: A vertical section of figure 2 is a rocking curve. No significant broadening of the rocking curve was observed compared to the non-implanted situation, but one remarkable characteristic is that a few new peaks appeared at the left side of the (0002) peak after the implantation process. The intensity of these peaks increased at the expense of the main (0002) peak with growing implantation dose. This effect has already been observed [16] and can easily be attributed to an expansion of the GaN crystal lattice by interstitials created during the implantation process. This strong defect related peaks disappeared already upon annealing at 900 °C for 10 minutes (Figure 2B) resulting into a spectrum which is comparable to the non-implanted spectrum. Consequently, no improvement was observed for a higher annealing temperature of 1100 °C (Figure 2C). We can conclude that in the view of XRD the GaN lattice is already fully recovered after annealing at a temperature of 900 °C.

The low temperature PL spectra of a Be-implanted GaN sample with a dose of $5x10^{13}$ cm^{-2} are summarized in Fig. 3. No PL lines were observed directly after ion implantation for this dose, but they were observed in the case of lower implantation doses. After annealing to a temperature of 900 °C for 15 minutes PL lines have been detected. However, the intensity of the band edge luminescence is several orders of magnitude lower in comparison to as-grown, unimplanted GaN samples. The weak luminescence line at 3.467 eV (commonly labeled as I_2) in Fig. 3 originates from recombinations of free excitons and/or excitons bound to shallow donors. The LO-phonon replicas for this line could not be observed in the implanted samples due to its low intensity; however, their positions at 3.384 eV and 3.292 eV were determined from the as-grown, unimplanted GaN grown on the same SiC-wafer. This results in a phonon energy of about 85 ± 5 meV for our samples, which is in agreement with values in the literature [17]. The

second luminescence peak at 3.444 eV is most likely related to defects created during the implantation procedure, as this line also was observed with varying intensities after implantation of Li, Si, Ge, In and Er [18]. We believe that this line is produced by nitrogen vacancies due to donor-band (eD) transitions, because it appears also in unimplanted GaN samples depending on the growth conditions.

One Be related transition with low intensity was observed at 3.35 eV. The intensity of this line varied as a function of the lateral quality of the GaN sample. We attribute this line to band-acceptor (eA) recombinations. For this case, the ionization energy of Be acceptors was calculated to be 150 ± 10 meV [12]. Dewsnip and co-workers [13] also observed a new line in GaN samples doped with Be during growth at 3.376 eV. However, they calculated the ionization energy to be 90-100 meV due to the assumption that this line is a donor-to-acceptor transition. Temperature dependent PL measurements showed different intensity behaviors of the lines at 3.444 eV and 3.35 eV; therefore, we can exclude that the line at 3.35 eV is a phonon replica of the 3.444 eV line. Furthermore, we never observed the line at 3.35 eV after implantation of Li, Si, Ge, In and Er into GaN even when the line at 3.444 eV was present [18]. These observations prove that the line at 3.35 eV is only related to the implanted Be acceptors.

Figure 3 also shows the recorded PL spectra for the same Be implanted GaN sample as a function of annealing temperature. Conflicting with the XRD-results, the implanted material was only partly recovered in view of PL at an annealing temperature of 900 °C, which is in agreement with Ref. [19]. After annealing to 1100 °C for 15 minutes a strong recovery of the PL lines occurred and was further improved after the 1 hour anneal. The intensity of the I_2-line grew more than two orders of magnitude and reached about 80 % of the intensity of the pre-implanted samples. However, the defect-related line at 3.444 eV is still visible and the Be-related line did not grow after the 1100 °C, 1 hour anneal. We can conclude that in view of the PL the implanted GaN is almost recovered after the 1100 °C, 1 hour annealing step, but point defects (invisible to XRD) are still present and may create Be-defect complexes, which are responsible for the low optical activation of Be acceptors.

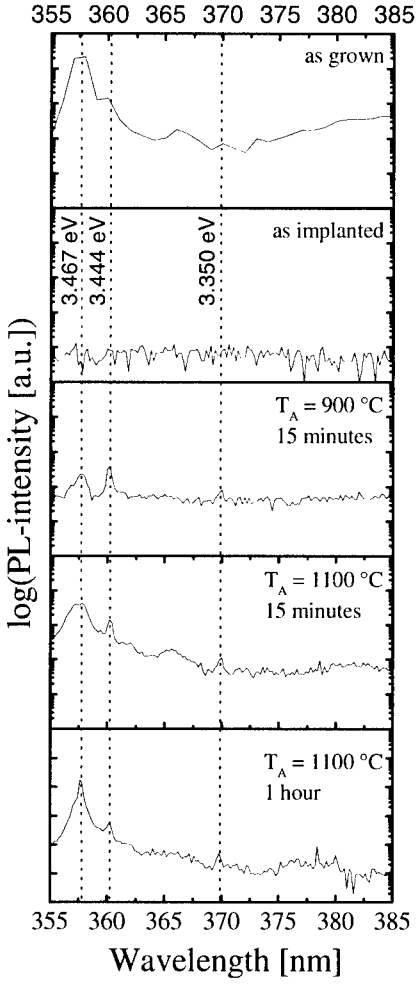


Figure 3: Photoluminescence spectra measured at 14 K of GaN. Spectra were recorded in the situations: as-grown, as-implanted with Be, and after annealing to several temperatures for different times. The implantation energies were 100 keV and 200 keV and the total implantation dose $5x10^{13}$ cm^{-2}.

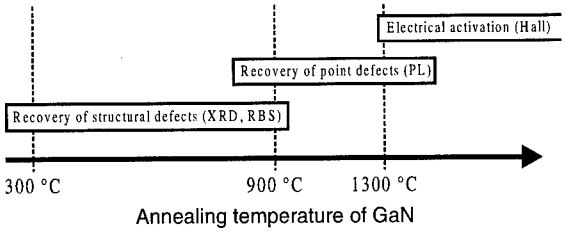


Figure 4: Fundamental recovery processes in ion implanted GaN and their detection methods as a function of annealing temperature (15 minutes).

Hall effect measurements were carried out after annealing to 1100 °C (1 hour) and deposition of Ni-Au contacts. All samples were too resistive for the determination of carrier concentrations or mobilities due to the remaining defects, which are creating compensating deep levels in the band gap.

CONCLUSIONS

We have summarized in Figure 4 the fundamental recovery processes in ion implanted GaN as a function of annealing temperature. The crystal structure of GaN is very resistant to ion bombardment due to the high ionicity of the Ga-N bond. This results in very high doses for amorphization [16]. However, structural defects can be readily created with medium implantation doses (10^{14}-10^{15} cm^{-2}), which can be detected by XRD or RBS-channeling [20]. These defects (mainly interstitials) lead to a lattice expansion which can be removed/recombined upon annealing to 900 °C. The recovery of point defects, visible by PL, starts around 800 °C and is not completed at a temperature of 1100 °C. Around 80 % of the free exciton line is recovered at this point. Based on primary observations on Mg-implanted GaN [21], we predict that after annealing to 1300 °C the GaN crystal is completely recovered and macroscopic electrical activation of the implanted impurities takes place.

We introduced in this article a new annealing procedure under a flux of atomic nitrogen obtained using a rf plasma source. In contrast to the N_2-overpressure technique [8] where the loss of nitrogen is prevented by the hydrostatic pressure, the atomic nitrogen flux protects the GaN surface by an exchange of nitrogen between solid and gas phase. An increase of the flux density by reducing the distance or increasing the power should result in the possibility to anneal GaN even to higher temperature as 1100 °C.

ACKNOWLEDGMENTS

The authors would like to thank D.P. Griffis and G.M. Guryanov for doing the SIMS measurements and Cree Research, Inc. for supplying the SiC substrates for this research. The implantations were conducted by ImplantSciences, Wakefield, MA (USA). This work was supported by the ONR under Contract N00014-92-J-1477 (M. Yoder, technical monitor). C.R. is grateful for funding by the DFG (Ro 1198/2-1). R. Davis was supported in part by the Kobe Steel, Ltd. Professorship.

REFERENCES

1. S.W. King, J.P. Barnak, M.D. Bremser, K.M. Tracy, C. Ronning, R.F. Davis, R.J. Nemanich, J. Appl. Phys. **84**, 5248 (1998).

2. C.B. Vartuli, S.J. Pearton, C.R. Abernathy, J.D. MacKenzie, E.S. Lambers, J.C. Zolper, J. Vac. Sci. & Techn. B **14**, 3523 (1996).

3. O. Ambacher, J. Phys. D: Appl. Phys. **31**, 2653 (1998).

4. J.H. Edgar (ed.), Group III Nitrides, London, INSPEC (1994).

5. J.C. Zolper, S.J. Pearton, J.S. Williams, H.H. Tan, R.J. Karlicek, R.A. Stall, Mater. Res. Soc. Proc. Vol. **449**, 981 (1997).

6. H.H. Tan, J.S. Williams, J. Zou, D.J.H. Cockayne, S.J. Pearton, J.C. Zolper, R.A. Stall, Appl. Phys. Lett. **72**, 1190 (1998).

7. S. Strite, P.W. Epperlein, A. Dommann, A. Rockett, R.F. Broom, Mater. Res. Soc. Proc. Vol. **395**, 795 (1996).

8. S. Strite, A. Pelzmann, T. Suski, M. Leszczynski, J. Jun, A. Rockett, M. Kamp , K. J. Ebeling, MRS Internet J. Nitride Semicond. Res. **2**, 15 (1997).

9. J.C. Zolper, J. Han, R.M. Biefeld, S.B. van Deusen, W.R. Wampler, S.J. Pearton, J.S. Williams, H.H. Tan, R.J. Karlicek, R.A. Stall, Mater. Res. Soc. Proc. Vol. **468**, ? (1997).

10. U. Kaufmann, M. Kunzer, M. Maier, H. Obloh, A. Ramakrishnan, B. Santic, P. Schlotter, Appl. Phys. **72**, 1326 (1998).

11. T.W. Weeks, Jr., M.D. Bremser, K.S. Ailey, E.P. Carlson, W.G. Perry, R.F. Davis, Appl. Phys. Lett. **67**, 401 (1995); J. Mat. Res. **11**, 1011(1996).

12. C. Ronning, E.P. Carlson, D.B. Thomson, R.F. Davis, Appl. Phys. Lett. **73**, 1622 (1998).

13. D.J. Dewsnip, A.V. Andrianov, I. Harrison, J.W. Orton, D.E. Lacklison, G.B. Ren, S.E. Hooper, T.S. Cheng, C.T. Foxon, Semicond. Sci. Technol. **13**, 500 (1998).

14. J.F. Ziegler, J.P. Biersack, and U. Littmark, *The stopping and ranges of ions in solids*, (Pergamon Press, New York, 1985).

15. R.G. Wilson, S.J. Pearton, C.R. Abernathy, and J.M. Zavada, Appl. Phys. Lett. **66**, 2238 (1995).

16. C. Liu, B. Mensching, K. Volz, B. Rauschenbach, Appl. Phys. Lett. **71**, 2313 (1997).

17. S. Fischer, C. Wetzel, E.E. Haller, B.K. Meyer, Appl. Phys. Lett. **67**, 1298 (1995).

18. E.P. Carlson, C. Ronning, R.F. Davis, unpublished.

19. C. Ronning, M. Dalmer, M. Deicher, M. Restle, H. Hofsäss, M.D. Bremser, R.F. Davis, Mat. Res. Soc. Proc. Vol. **468**, 407 (1997), and Ref. therein.

20. N. Parikh, A. Suvkhanov, M. Lioubtchenko, E.P. Carlson, M.D. Bremser, D. Bray, R.F. Davis, J. Hunn, Nucl. Instr. Meth. B **127/128**, 463 (1997).

21. C. Ronning, A. Stötzler, E.P. Carlson, P. Rajago, R.F. Davis, unpublished.

THERMAL RESIDUAL STRESS MODELING IN AlN AND GaN MULTI LAYER SAMPLES

Kai Wang and Robert R. Reeber

Department of Materials Science and Engineering
North Carolina State University, Raleigh, NC 27695-7907

Cite this article as; MRS Internet J. Nitride Semicond. Res. 4S1, G3.18 (1999)

ABSTRACT

Thermal residual stresses can detrimentally affect the electronic and optical properties of epitaxial films thereby shortening device lifetime. Based on our earlier work on thermal expansion of nitrides, we provide a finite element modeling analysis of the residual stress distribution of multilayered GaN and AlN on 6H-SiC. The effects of thickness and growth temperatures are considered in the analysis.

INTRODUCTION

Group III-nitride based semiconductors have direct band gaps that can provide blue or ultraviolet light-emitting devices and high temperature optoelectronics. Recent work [1-3] has highlighted some of the difficulties and successes with their thin film device fabrication. Processing such devices often relies on the high temperature growth of epitaxial layers on different substrates with different coefficients of thermal expansion. Residual stresses introduced by cooling or heating may detrimentally affect device long term performance and lifetime.

The stress-strain distribution in these electronic composite structures can be calculated from the temperature dependence of their thermoelastic properties. The results provide a guide for optimizing interfacial processing.

For an axially symmetric problem without a body force, the equilibrium equations of the system are:

$$\frac{1}{r}\frac{\partial(r\sigma_{rr})}{\partial r} - \frac{\sigma_{\theta\theta}}{r} - \frac{\partial\sigma_{rz}}{\partial z} = 0 \qquad (1)$$

$$\frac{\partial\sigma_{rz}}{\partial r} + \frac{\partial\sigma_{zz}}{\partial z} + \frac{\sigma_{rz}}{r} = 0 \qquad (2)$$

Where the σ_{ij} are the components of the stress tensor for a coordinate system (r, θ, z). After assuming displacements U and V along the r and z directions respectively, the strain tensor is

Mat. Res. Soc. Symp. Proc. Vol. 537 © 1999 Materials Research Society

$$
\begin{aligned}
e_{rr} &= \frac{\partial U}{\partial r} \\
e_{\theta\theta} &= \frac{U}{r} \\
e_{zz} &= \frac{\partial V}{\partial z} \\
e_{rz} &= \frac{\partial U}{\partial z} + \frac{\partial V}{\partial r}
\end{aligned}
\tag{3}
$$

Hooke's law is then

$$
\begin{bmatrix} \sigma_{rr} \\ \sigma_{\theta\theta} \\ \sigma_{zz} \\ \sigma_{rz} \end{bmatrix} = \begin{bmatrix} C_{11} & C_{12} & C_{13} & 0 \\ C_{12} & C_{11} & C_{13} & 0 \\ C_{13} & C_{13} & C_{33} & 0 \\ 0 & 0 & 0 & C_{44} \end{bmatrix} \begin{bmatrix} e_{rr} - \overline{\alpha_{\perp}}\Delta T \\ e_{\theta\theta} - \overline{\alpha_{\perp}}\Delta T \\ e_{zz} - \overline{\alpha_{\parallel}}\Delta T \\ e_{rz} \end{bmatrix}
\tag{4}
$$

Where $\overline{\alpha_{\perp}}$ and $\overline{\alpha_{\parallel}}$ are the mean coefficients of thermal expansion along the a- and the c-axes and the C_{ij} are the elastic constants. For a hexagonal crystal, there are five independent elastic constants.

A 2-D code, PDEase2, developed by SPDE, Inc. and distributed by Macsyma, is applied to calculate the stress-strain distributions of multilayer GaN/AlN or GaN/SiC structures. This code permits calculation of the stress/strain distribution for a cylindrically symmetrical system as shown in Fig. 1,

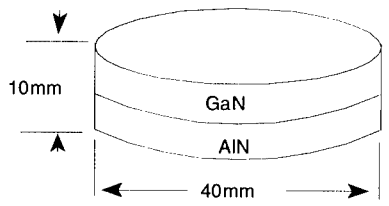


Figure 1. Geometry of the disk-shaped sample.

where the two layers are separated by a sharp interface. The GaN layer is either on top of AlN or SiC. For simplicity, a linear elastic continuum model for anisotropic samples was utilized. The c-axis is assumed to be perpendicular to the interface.

Thermoelastic property measurements for AlN and GaN have been reviewed [4] and high temperature thermal expansion was calculated semiempirically. These results, plus work on -SiC thermal expansion [5], permit us to calculate the stress-strain distributions for disk-shaped samples. The mean thermal expansion between 298°K and high temperatures are provided in Fig. 2. The lattice mismatches for the a-axis between GaN and SiC and for AlN and SiC are also plotted. Their elastic constants were chosen from Polian *et al.* [6], McNeil *et al* [7]. and Kamitani *et al* [8] and tensile strengths from Kosolapova's handbook [9].

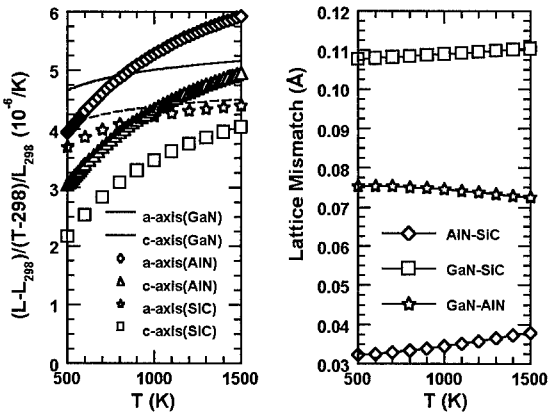


Figure 2. Mean thermal expansion and lattice mismatch.

The samples are assumed cooled to 298°K from a growth temperature of 1300°K. Selected materials properties are listed in Table 1. Residual stress distributions are calculated from the thermoelastic properties. The effects of thickness and growth temperatures are considered in the analysis.

Table 1. Selected thermoelastic properties of GaN, AlN and SiC

		GaN	AlN	SiC
Thermal Expansion ($10^{-6}K^{-1}$)	a-axis	5.11	5.72	4.34
(298~1300°K)	c-axis	4.47	4.75	3.74
	C_{11}	390.0	410.5	501
	C_{12}	145.0	148.5	111
Elastic Constants	C_{13}	106.0	98.9	52
(GPa)	C_{33}	398.0	388.5	553
	C_{44}	105.0	124.6	163
Young's Modulus (GPa)		302.7	329.7	444
Poisson's Ratio		0.26	0.239	0.164

RESULTS

Fig. 3(a) through 3(c) provide r-z plane stress distributions for a disk-shaped GaN on AlN sample. In fig. 3(a), the distribution of axial stress σ_{zz}, is peripherally concentrated along the sample and is tensile in GaN and compressive in AlN. Fig. 3(b) provides the shear stress σ_{rz} distribution. The shear stresses concentrate along the interface and also close to the edge. Fig. 3(c), the radial stress σ_{rr} distribution, is primarily a GaN/AlN interfacial stress. The σ_{rr} is compressive in GaN and tensile for AlN. The maximum calculated tensile stresses are 139.7MPa for GaN and 146.3MPa for AlN.

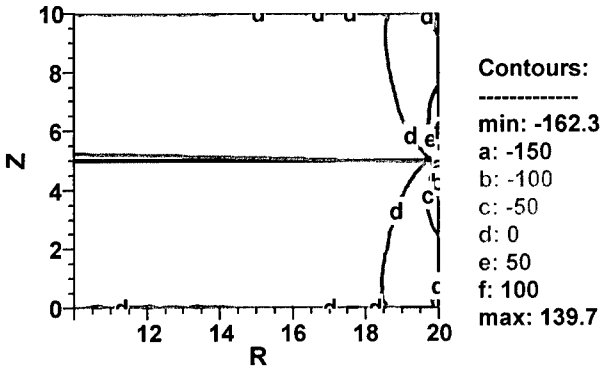


Figure 3(a). Distribution of σ_{zz}.

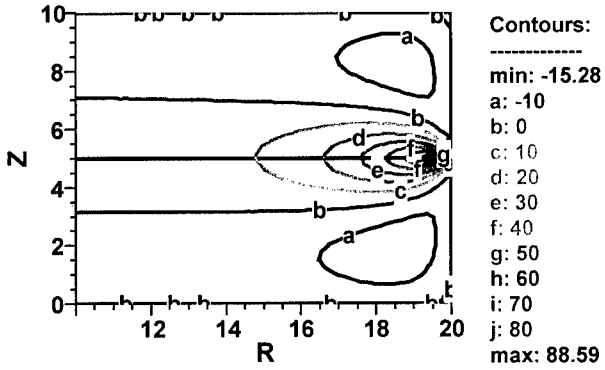


Figure 3(b). Distribution of σ_{rz}.

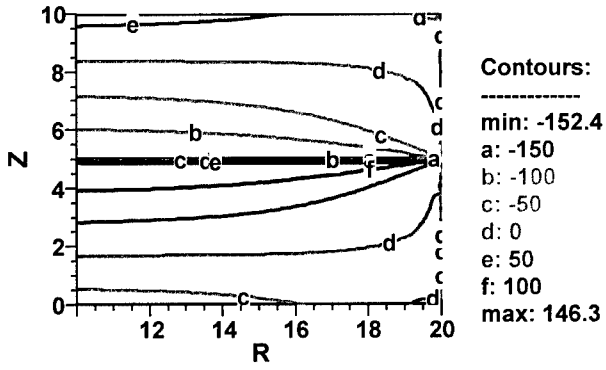


Figure 3(c). Distribution of σ_{rr}

The stress distributions for a disk-shaped GaN on 6H-SiC sample were also calculated. The distributions are similar to that of GaN on AlN sample except that the signs of the stresses are reversed. This is because the thermal expansion for SiC is smaller than GaN. The axial σ_{zz}, is peripherally concentrated along the sample and is compressive in GaN and tensile in SiC. The maximum σ_{zz} is 149MPa in GaN and 298MPa in SiC. The radial stress σ_{rr} distribution is also primarily a GaN/SiC interfacial stress. The σ_{rr} is tensile in GaN and compressive in AlN. The maximum σ_{rr} is 200 for GaN and 211MPa for SiC.

The thickness dependence of the maximum residual stresses was also calculated. The residual stresses do not change much except for the tensile radial stress in GaN. This varies from about 200MPa to 350MPa in GaN and indicates, within a thin layer of GaN grown on SiC, that the maximum tensile stress decreases with the GaN thickness. The maximum axial tensile stress fluctuates between 290MPa to 400MPa in SiC.

Figure 4 illustrates the temperature dependence of the maximum residual stress in a GaN on SiC substrate. The residual stresses increase with increasing growth temperature.

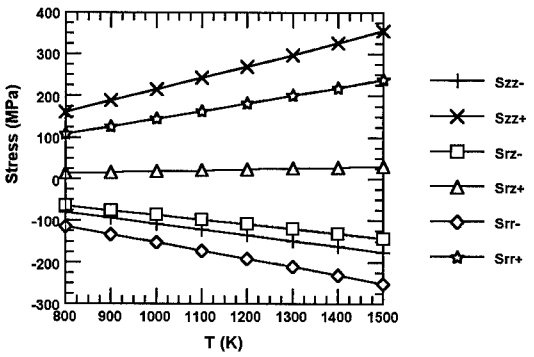


Figure 4. Growth temperature dependence of residual stresses in GaN over SiC sample.

Finally, we have calculated the maximum residual stress distribution for an AlN over SiC substrate grown at 1300°K. The distributions of the residual stresses are similar to that of the GaN on SiC except the maximum stresses are larger than in the GaN on SiC sample. This is easily understood as the differences of thermal expansion between AlN and SiC are larger than equivalent differences between GaN and SiC. The maximum tensile stress is 370MPa in AlN and 519MPa in SiC. The maximum compressive stress is 279PMa in AlN and 382MPa in SiC.

DISCUSSION AND CONCLUSIONS

Our calculations indicate that the residual stresses primarily concentrate along the interface and at the edge of the multilayered samples. The tensile strength indicated for a SiC single crystal is within the range of 180 to 200MPa [9]. GaN and AlN tensile strengths are expected to be smaller than SiC. Comparing the maximum residual stresses and the strength data of the

materials studied, we see that the residual tensile stresses in SiC and AlN are larger than their strength. Similar results are expected for GaN. This should cause cracking and other defects during processing as has been observed [2]. The effect of these residual stresses on the band gap can be illustrated by a simple calculation. Assume that the maximum stress is in the order of 400MPa in GaN. Since the band gap pressure coefficient is about 4.2×10^{-5} eV/MPa in GaN[10], the small shift of the band gap due to this stress is about 0.017eV. Increasing the thickness of GaN on SiC will slightly reduce the radial residual stress at the interface. Raising the growth temperature for GaN on SiC introduces higher residual stresses at room temperature. The residual stress reduction for AlN on SiC with decrease in growth temperature has been observed [11] experimentally as a decrease in crystal roughness from 1473°K to 1323°K.

In summary, we have performed a finite element modeling analysis of the residual stress distribution of multilayered GaN and AlN unbuffered on 6H-SiC. The effects of layer thickness and growth temperatures are analyzed. Residual stresses if unrelaxed during cooling probably introduce cracks and other defects. The effect of the stresses on the band gap is estimated and is minimal. More calculations should be performed on growing GaN and AlN on other substrates with different growth conditions and with varying thickness buffer layer. Such calculations can provide insights for optimizing the processing conditions of these important nitrides.

ACKNOWLEDGMENTS

This work was supported by the Army Research Office through Grant No. DAAH04-93-D-0003. Part of the work was performed while K. Wang held a National Research Council -Army Research Office Research Associateship.

REFERENCES

1. T. W. Weeks, Jr., M. D. Bremser, K.S. Ailey, E. Carlson, W. G. Perry, E. L. Piner, N.A. El-Masry, R. F. Davis, J. Mater. Res. **11**, 1011(1996).
2. I. Akasaki and H. Amano, J. Cryst. Growth **175/176**, 29(1997).
3. S. Nakamura, Science **281**, 956(1998).
4. K. Wang and R. R. Reeber in *Nitride Semiconductors*, edited by F. A. Ponce, S. P. DenBaars, B. K. Meyer, S. Nakamura, and S. Strite (Mat. Res. Soc. Symp. Proc. **482**, Boston, MA, 1997) pp. 863-868.
5. R. R. Reeber, Thermal expansion of α-SiC, in preparation(1998).
6. A. Polian, M. Grimsditch, I. Grzegry, J. Appl. Phys. **79**, 3343(1996).
7. L. E. McNeil, M. Grimsditch, R. H. French, J. Am. Ceram. Soc. **76**, 1132(1993).
8. K. Kamitani, M. Grimsditch, J. C. Nipko, C.-K. Loong, M. Okada, I. Kimura, J. Appl. Phys. **82**, 3152(1998).
9. T. Ya. Kosolapova, Handbook of High Temperature Compounds: Properties, Production, Applications, (Hemisphere Publishing Corporation, New York, 1990), pp. 507-525.
10. S. Strite and H. Morkoç, J. Vac. Sci. Technol. **B10**, 1237(1992).
11. L. B. Rowland, R. S. Kern, S. Tanaka, R. F. Davis, J. Mater. Res. **8**, 2310(1993).

Strong piezoelectric effects in unstrained GaN quantum wells

*R. Langer *, J. Simon*, O. Konovalov*, N.T. Pelekanos*, R. André**, A. Barski*, M. Godlewski****

*Département de Recherche Fondamentale sur la Matière Condensée, CEA/Grenoble, SP2M/PSC, 38054 Grenoble, Cedex 9, France

** Laboratoire de Spectrométrie Physique, CNRS, Université J. Fourier, 38402 Saint Martin d'Hères, France

*** Institute of Physics, Polish Academy of Sciences, 02-668 Warsaw, Al. Lotnikow 32/46 Poland

Cite this article as: MRS Internet J. Nitride Semicond. Res. 4S1, G3.19 (1999)

Abstract

Optical properties of GaN/AlGaN single quantum well (SQW) and multi quantum well (MQW) structures grown by nitrogen plasma assisted MBE on MOCVD-grown GaN/sapphire have been characterised by low temperature photoluminescence. Photoluminescence (PL) peaks corresponding to emission from very narrow (10 Å wide) SQWs are blue shifted with respect to the bulk GaN emissions but reveal strong red shift for wider SQWs (40 and 60 Å wide). Structural properties of SQW and MQW structures have been characterised by X-ray reciprocal lattice mapping in order to determine the strain conditions and composition of ternary AlGaN alloys. The results clearly demonstrate that in all structures under investigation the ternary (barrier) alloys are fully strained to underlying MOCVD-grown GaN/sapphire substrates. Despite of the fact that GaN quantum wells (QW) are unstrained, photoluminescence experiments clearly reveal the presence of extremely strong electric fields in the QW regions, which can be attributed to the interplay of the piezoelectric-type polarisation in the well and barrier layers due to Fermi level alignment.

Mat. Res. Soc. Symp. Proc. Vol. 537 © 1999 Materials Research Society

Introduction

GaN/AlGaN QWs are subject of intense investigations due to their potential for electronic and opto-electronic applications. Many recent publications report on the properties of GaN/AlN and GaN/AlGaN heterostructures, superlattices and/or multi QW structures [1,2,3,4]. Recently, a strong piezoelectric field has been found in GaN/AlGaN heterostructures with strained QW regions which was attributed to strain induced phenomena [1]. We report here the results on GaN/AlGaN SQW and MQW structures grown by Radio Frequency Molecular Beam Epitaxy (RFMBE) on MOCVD-grown GaN/sapphire. In order to demonstrate that the strong electric field is present in unstrained quantum wells, the total thickness of AlGaN barriers in all our samples was kept below the critical thickness and hence the AlGaN layers are strained. Our structures are pseudomorphic with the GaN/sapphire substrate and the GaN QW's are strain free.

Experimental

The GaN/AlGaN SQW structures studied have a single GaN QW of 10 and 40 Å thickness embedded between 1000 Å thick AlGaN barriers. The Al fraction in the barriers was about 17-20 %, as determined independently from PL and X-rays experiments. MQW structures of 20, 40 and 60 Å thick GaN wells have been grown for two different Aluminium concentrations in GaAlN barriers respectively of 10 and 20 %. The sample growth was performed in a RIBER MBE 2300 chamber. Standard Knudsen cells were used for Gallium and Aluminium evaporation and the active nitrogen was generated by a commercial (ADDON) radio frequency (RF) cell. Growth was performed at a relatively low substrate temperature of 650°C. The composition of the GaAlN films was adjusted by varying the beam equivalent pressure of the Gallium and Aluminium fluxes. The thickness of the layers was controlled by RHEED oscillations. MBE growth was performed on 1.5 μm thick GaN layers grown by MOCVD on sapphire. The oxide on this MOCVD grown GaN surface can easily be removed by acid etching (regal water) and short heating (~ 650°C) prior to growth. A well-defined RHEED pattern and intense RHEED oscillations show that the treated MOCVD surface is smooth on an atomic scale. To completely get rid of the eventual influence from a surface oxide or from a contamination layer, we interpose a few 1000 Å thick GaN layer.

PL time resolved measurements were performed at 2K with pulsed excitation (of ns length) above QW band gap energy and photon counting system with multi-channel analyser for PL detection.

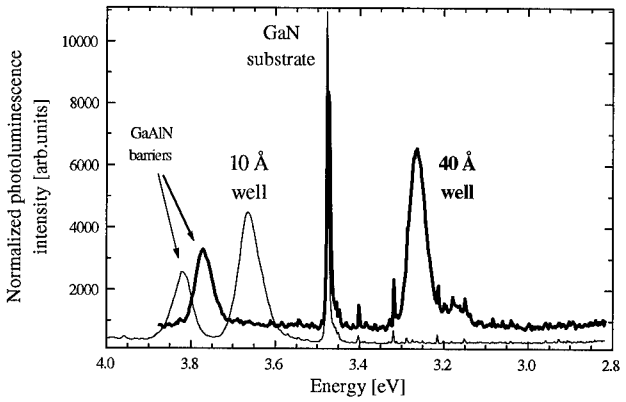


Fig1: Low temperature photoluminescence of 10 Å and 40 Å thick GaN quantum wells in AlGaN barriers with an aluminium concentration of 17.2% and 20.6% respectively.

Results and discussion

Low temperature (2 K) PL spectra, shown in Figure 1, are dominated by 3.47 eV band gap emission of the underlying 1.5 μm thick MOCVD-grown epilayer and of MBE-grown (few times 1000 Å thick) buffer layer. PL emission of ternary AlGaN barrier layers is also seen on the high-energy side of the emission spectra. In addition to barrier and substrate emissions, a SQW emission is also resolved with its LO-phonon replica. Assuming QW confinement effects only, SQW PL should show a blue-shift with respect to the GaN substrate emission, which should increase with a decreasing QW width. However, as shown in Figure 1, only the PL of 10 Å wide SQW is blue-shifted by about 150 meV. For 40 Å thick SQW's a pronounced red-shift of the PL lines is observed from the expected PL position. This red-shift of the PL can be explained by a strong internal electric field present in the structure [5], as will be discussed later. In order to determine the influence of Aluminium concentration in barriers on the PL line positions, two samples with different Aluminium concentrations have been grown. The first sample consisted of 20, 40 and 60 Å thick quantum wells separated by 100 Å GaAlN barriers with the Aluminium concentration of 10 %. The second sample has the same structure but the Aluminium concentration was increased to 20 %. Low temperature PL spectra of our MQW structures are shown in Figure 2. Only the emission from 20 Å thick well in the low Aluminium content sample is blue-shifted with respect to the GaN substrate emission. All emissions from 40 and 60 Å thick

wells are detected below the GaN emission. This phenomenon is clear evidence for a strong electric field present in our structures, which increases with the Aluminium concentration in barriers.

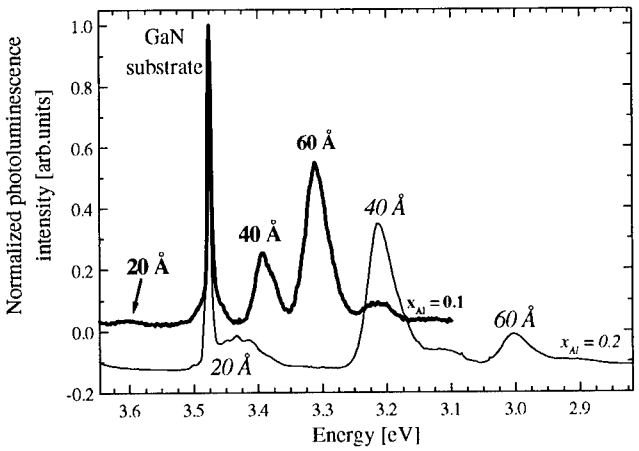


Fig2: Low temperature photoluminescence of two samples with 20 Å, 40 Å and 60 Å thick GaN quantum wells and 100 Å thick AlGaN barriers with an aluminium concentration of 17.2% and 20.6% respectively.

In order to determine the origin of this field the strain present in our samples has to be investigated. Strain could be precisely determined by X-rays reciprocal lattice mapping. Results of such experiments are shown in Figure 3 for the 40 Å thick SQW. X-rays mapping around the (-2 0 2) Bragg peak of the GaN substrate is shown. These measurements clearly demonstrate that the AlGaN alloy has the same in-plane lattice parameter (represented by the (h, k) axis in reciprocal units of Al_2O_3) as the GaN substrate. Both 1000 Å thick GaAlN barriers are thus fully strained to GaN. Similar conclusions can be drawn from reciprocal space mappings for all other QW's structures under investigation.

For totally pseudomorphic samples, one can precisely determine the Aluminium fraction in GaAlN barriers. From the in-plane lattice parameter and from the lattice parameter along the growth axis, using Vegard's law for the lattice parameter and a linear interpolation between

Poisson ratios for GaN [6] and AlN [7], we determine the Al fraction in all our samples, which agrees with our estimations from PL studies.

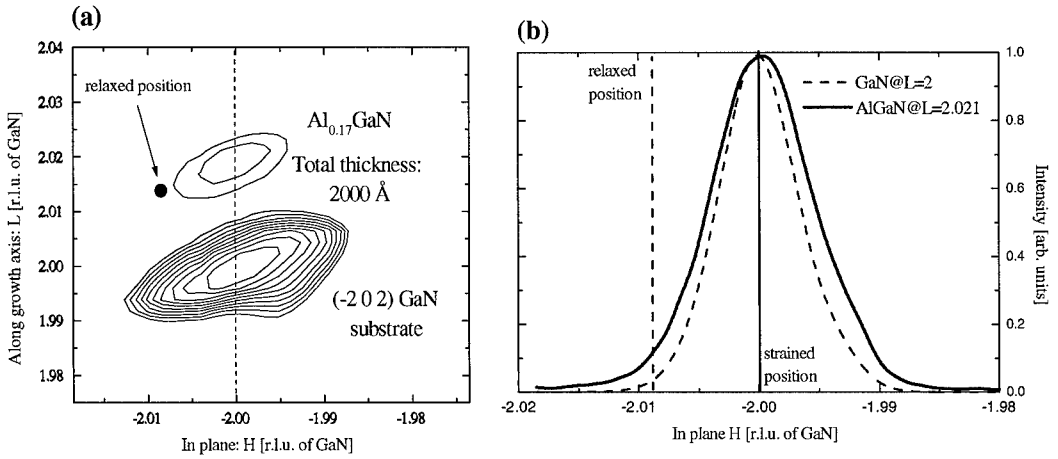


Fig3 (a): X-ray cartography of GaN single quantum well 40 A thick embedded in 1000 Å thick AlGaN barriers around (-2 0 2) Bragg peak of GaN substrate. The AlGaN barriers have the same in-plane lattice parameter than the GaN substrate. This is shown very precisely on the in plane scans (b) where the in-plane lattice parameter is represented by the H-axis in reciprocal lattice units of GaN

Despite of the fact that GaN QW's are not strained in our samples, we observed a dramatic dependence of QW PL on a QW width and on Aluminium concentration in barriers. This can be related to strong piezoelectric effects introducing strong internal electric fields to the structure. This hypothesis is further confirmed by PL kinetics measurements. For 40 and 60 Å wide SQW the PL intensity decay is highly non exponential and in μs range. In fact such slow PL kinetics resembles that of the yellow emission band and dramatically varies from the PL kinetics of excitons from GaN substrate. Those excitons show PL decay times in the range of 100 ps. Slow PL kinetics in GaN/AlGaN QW system can be explained by a strong reduction of radiative

recombination probability caused by electric field induced spatial separation of electrons and holes in a wide QW. Strong piezoelectric effects also explain why SQW emission is relatively weak when compared to the substrate emission. As was mentioned above, the internal electric field strongly reduces radiative recombination rates of QW's.

In conclusion, the present studies demonstrate strong piezoelectric effects in GaN/AlGaN QW structures with strained AlGaN barrier layers but with strain free GaN QW's. We believe that this is related to the large piezoelectric constants predicted for GaN and GaAlN [8].

References

[1] J. S. Im, H. Kollmer, J. Off, A. Sohmer, F. Scholz, A. Hangleiter, Phys. Rev. B 57, R9435 (1998).

[2] D. Korakakis, K. F. Ludwig, T. D. Moustakas, Appl. Phys. Lett. 72, 1004 (1998).

[3] K. C. Zeng, J. Y. Lin, H. X. Jiang, A. Salvador, G. Popovici, H. Tang, W. Kim, H. Morkoc, Appl. Phys. Lett. 71, 1368 (1997).

[4] M. A. L. Johnson, Shizuo Fujita, W. H. Rowland, K. A. Bowers, W. C. Hughes, Y. W. He, N. A. El-Masry, J.W. Cook, J. F. Schetzina , J. Ren, J. A. Edmond , J. Vac. Sci. Technol. B 14, 2349-2353 (1996).

[5] R. Langer, J. Simon, O. Konovalov, N.T. Pelekanos, A. Barski, M. Leszczynski, MRS Internet J. Nitride Semicond. Res. 3, 46 (1998).

[6] C. Kisielowski, J. Krüger, S. Ruvimov, T. Suski, J. W. Ager, E. Jones, Z. Lilienthal-Weber, M. Rubin, M. D. Bremser, R. F. Davis, Phys. Rev. B 54, 17745 (1996).

[7] L.E. McNeil, M. Grimsditch, R.H. French, J. Am. Ceram. Soc. 76, 1132-1136 (1993).

[8] F. Bernardini, V. Fiorentini, D. Vanderbilt, Phys. Rev. B 56, R10024 (1997).

OPTICAL ABSORPTION, RAMAN, AND PHOTOLUMINESCENCE EXCITATION SPECTROSCOPY OF INHOMOGENEOUS InGaN FILMS

L.H. Robins,* A.J. Paul,* C.A. Parker,** J.C. Roberts,** S.M. Bedair,**

E.L.Piner,*** N.A. El-Masry***

*National Institute of Standards and Technology (NIST), Gaithersburg, MD 20899
**Electrical and Computer Engineering, North Carolina State University, Raleigh, NC 27695
***Materials Science and Engineering, North Carolina State University, Raleigh, NC 27695

Cite this article as: MRS Internet J. Nitride Semicond. Res. 4S1, G3.22 (1999)

ABSTRACT

$In_xGa_{1-x}N$ films with x=0.06 to x=0.49 were characterized by optical transmittance, Raman, and photoluminescence excitation spectroscopies. Previous microstructural characterizations detected phase separation only in films with x>0.2. The transmittance data suggest that compositional inhomogeneity is also present in the lower-x films (x<0.2). Both Raman and photoluminescence excitation spectra show features that correlate with compositional inhomogeneity and phase separation in the films with x>0.2. The composition dependence of the Raman spectra, from x=0.28 to x=0.49, is consistent with an increase in the size of the phase-separated regions with increasing x.

INTRODUCTION

A new generation of short-wavelength optoelectronic devices is being developed from thin films of the group III nitrides (Al,Ga,In)N. The active layers of visible-emitting devices[1] are usually composed of $In_xGa_{1-x}N$. The growth of $In_xGa_{1-x}N$ layers is complicated by the tendency of GaN-InN alloys to phase separate, which was first observed[2] by Osamura *et. al.* in 1975 with x-ray diffraction (XRD) of annealed polycrystalline samples, and more recently by Singh[3] *et. al.* with XRD and optical absorption, and Piner[4] *et. al.* with XRD, transmission electron microscopy (TEM) and selected area diffraction (SAD). Doppalapudi[5] *et. al.*, using TEM and SAD, found evidence for long-range atomic ordering as well as phase separation in MBE-grown $In_xGa_{1-x}N$ films. The driving force for the phase separation and atomic ordering is the 10% difference between the relaxed Ga-N and In-N bond lengths. Ho and Stringfellow[6] predicted the solid phase miscibility gap of $In_xGa_{1-x}N$ with a modified valence-force-field model.

The theoretical prediction, and confirming experimental observations, of phase separation in the $In_xGa_{1-x}N$ system suggests the following inter-related questions. First, how does the phase separation affect the optical properties of the material? Second, is there a non-destructive optical characterization method that can be used to detect the occurrence of phase separation? We address these questions by performing optical transmittance, Raman, and double spectrally resolved photoluminescence excitation (DSR-PLX) spectroscopy of MOCVD-grown $In_xGa_{1-x}N$ films with x=0.06 to x=0.49, that were previously analyzed[4] for phase separation. Each of these techniques is found to provide different information about the structure of the samples.

Mat. Res. Soc. Symp. Proc. Vol. 537 © 1999 Materials Research Society

EXPERIMENT

$In_xGa_{1-x}N$ films were grown on (0001) sapphire substrates using a specially designed metal-organic chemical vapor deposition (MOCVD) reactor and growth conditions that have been described elsewhere (E.L. Piner[4] *et. al.* and references therein). An AlN buffer layer and then a AlGaN graded to GaN prelayer were grown on each substrate before the $In_xGa_{1-x}N$ layer; the $In_xGa_{1-x}N$ layer thickness is estimated to be 0.3 μm to 0.5 μm, and the AlGaN/GaN prelayer thickness is estimated to be 0.1 μm. The growth temperature for the $In_xGa_{1-x}N$ layer was between 690°C and 780°C. The In fraction, x, was controlled by varying the growth temperature and the hydrogen gas flow rate. Eleven films were examined, with x=0.06 to x=0.49 as determined from the shift of the 0002 XRD peak relative to pure GaN and InN, assuming a linear x-dependence of the lattice constant.

All optical measurements were performed at room temperature. Transmittance spectra of the samples were measured with a Cary model 14 spectrophotometer.[7] Metal-grid neutral density filters were inserted into the spectrophotometer reference channel to extend the lower end of the measured transmittance range to ~$3x10^{-5}$.

Raman spectra were excited by the 514.53 nm (2.409 eV) and 457.94 nm (2.707 eV) lines of an Argon ion laser and recorded by a Princeton Instruments intensified photodiode array detector attached to a Spex Triplemate monochromator.[7] The wavelength resolution of the monochromator was 0.10 nm, corresponding to a wavenumber resolution of 3.7 cm^{-1} for the Raman spectra excited at 514.53 nm, and 4.7 cm^{-1} for the Raman spectra excited at 457.94 nm. The wavenumber accuracy was ~0.2 cm^{-1}, calibrated with Ar, Kr and Xe line sources.

In the DSR-PLX experiment, PL was excited by a wavelength-tunable source, and the PL intensity within a selected wavelength band was monitored as the excitation energy was scanned. The measurement was then repeated for several different emission wavelength bands, so that several excitation spectra were obtained for each sample, corresponding to different emission wavelengths (or photon energies). The excitation source was a 300 watt xenon arc lamp coupled to a Spex model 1680 double monochromator.[7] The wavelength resolution of the spectrometer was 2 nm; the corresponding energy resolution varied from 0.006 eV at 1.9 eV, to 0.02 eV at 3.5 eV. Each emission band was selected by a bandpass interference filter, taken from a set of seven filters with center wavelengths every 50 nm from 450 nm to 750 nm and full bandwidths of 40 nm. To more completely remove the scattered excitation, each bandpass filter was paired with a longpass filter that had a cut-on wavelength slightly shorter than the bandpass center wavelength. The emitted PL was detected by a S20 type photomultiplier tube. The excitation source was mechanically chopped at 200 Hz, enabling lock-in detection of the PL signal.

The wavelength (or photon energy) dependence of the DSR-PLX source intensity was measured with a NIST-calibrated[8] silicon photodiode. By correcting for the wavelength dependence of the source intensity, the DSR-PLX spectra were normalized to a scale proportional to the number of emitted photons per exciting photon; the absolute quantum efficiency was not measured.

RESULTS AND DISCUSSION

Fig. 1 shows optical transmittance spectra of five samples, plotted on a semilog scale. For most of the samples, log(transmittance) decreases approximately linearly with energy above an absorption edge. The absorption edge energy decreases with increasing x. All the samples show a second absorption edge at 3.4 eV, the band gap of pure GaN. The 3.4 eV feature is attributed to the GaN prelayers. The x-dependence of the primary absorption edge energy is plotted in Fig. 2, together with a linear fit to the data. The x=0.06 and x=0.18 samples are not shown in Fig. 2 because their absorption edge energies could not be determined accurately due to

the large widths of the edges. The x=0.49 sample is shown in Fig. 2, but is excluded from the linear fit because the absorption edge energy does not decrease from x=0.43 to x=0.49.

The band gap reported[9] for pure InN is 1.9 eV. It is thus surprising that the observed absorption edge of these samples reaches 1.9 eV at x=0.36, and decreases below 1.9 eV for the samples with $x \geq 0.4$. The unexpectedly large shift of the absorption edge with x for all samples (including those with $x<0.2$) can be compared with the previous SAD and TEM measurements, which showed spinodal decomposition only for $x>0.2$. We tentatively attribute the large absorption edge shift to compositional inhomogeneity on the cation sublattice, i.e. clustering of Ga and In atoms, although other defect structures such as nitrogen vacancies cannot be ruled out. The possible observation of inhomogeneity in the $x<0.2$ films by absorption spectroscopy, but not by SAD or TEM, suggests that absorption is sensitive to inhomogeneity on a shorter length scale than the other techniques.

Raman spectra of the $x \geq 0.28$ samples, obtained with 2.409 eV or 2.707 eV excitation, are shown in Fig. 3. (Raman spectra could not be observed for the $x<0.28$ samples because of strong interfering luminescence in the Raman region. The interfering luminescence was weaker in the $x \geq 0.28$ samples, and was subtracted from the spectra shown in Fig. 3 by a curve-fitting method.) The dominant component of these spectra is the A_1(LO) mode. For comparison, the A_1(LO) frequencies of pure GaN and InN are shown in Fig. 3 as dashed lines. The separation between the Raman peaks measured at the two excitation energies, as well as the width of each peak, is seen to increase with increasing x. To better display the trends in the data, the full widths at half maximum of the A_1(LO) peaks are plotted as functions of x in Fig. 4(a), and the separation between the centers of the peaks measured at the two excitation energies is plotted as a function of x in Fig. 4(b). The broadening with increasing x [Fig. 4(a)] is tentatively attributed to an increase in compositional inhomogeneity. The separation between the peaks [Fig. 4(b)] is tentatively attributed to selective excitation of portions of the inhomogeneous sample with different compositions, and different A_1(LO) frequencies, at each excitation energy. In the resonant Raman effect, the scattering intensity is enhanced when the incident photon energy is near the band gap. In our experiment, each excitation energy (2.409 eV and 2.707 eV) is equal to the $In_xGa_{1-x}N$ band gap for a specific composition $x(E_{exc})$; we thus suggest that the Raman intensity is enhanced from portions of the sample with $x \approx x(E_{exc})$.

DSR-PLX spectra were obtained from samples with x=0.06, x=0.19, x=0.28, x=0.36 and x=0.43. Each PLX spectrum has a sigmoidal shape: the excitation efficiency (number of emitted photons per excitation photon), denoted η, increases from a lower value η_{low} to a higher value η_{high} within a specific energy range. To characterize the PLX spectra in a simple way, we define the threshold energy E_0 as the energy corresponding to the midpoint of the increase in excitation efficiency, i.e. $\eta(E_0)=0.5(\eta_{low} + \eta_{high})$. A model function was fitted to the data to obtain values for E_0. DSR-PLX spectra from the x=0.06 and x=0.28 samples are shown in Figs. 5(a) and 5(b), where each DSR-PLX spectrum is labeled with the center photon energy of the detected emission band; the data are plotted as solid lines; the model functions are plotted as dashed lines; and the calculated E_0 are marked by open circles. The value of E_0 is almost independent of emission energy in the x=0.06 [Fig. 5(a)] and x=0.19 samples. In contrast, E_0 shifts by a large amount with emission energy in the x=0.28 [Fig. 5(b)], x=0.36, and x=0.43 samples.

The DSR-PLX results are summarized in Fig. 6, where E_0 is plotted as a function of emission energy for each of the five samples. The data show in Fig. 6 confirm that the samples fall into two groups; for x=0.06 and x=0.19, E_0 is almost independent of emission energy, but for $x \geq 0.28$, E_0 has a strong dependence on emission energy, decreasing by about 1 eV as the emission energy decreases from 2.73 eV to 1.90 eV. Note that the first group corresponds to the samples that appears to be single-phase ($x<0.2$), while the second group corresponds to the samples that appear to be phase-separated ($x>0.2$) by SAD and TEM.

Several features complicated the analysis of the DSR-PLX spectra. Firstly, many of the spectra could not be measured to low enough excitation energy to accurately determine η_{low}, and uncertainty in η_{low} leads to uncertainty in E_0. This uncertainty was taken into account in the error analysis (error bars on E_0 in Fig. 6). Secondly, several spectra contain a distinct peak between 2 eV and 2.5 eV. A peak in this region was also observed in PLX spectra of an uncoated sapphire substrate, shown in Fig. 5(c), and is thus attributed to impurity centers in the substrate. The substrate peak was subtracted as part of the data analysis used to determine E_0. Finally, a derivative-like feature near 2.9 eV occurs in several spectra; other measurements suggest that this feature is a instrumental artifact.

Although both Raman and DSR-PLX spectra appear to be sensitive to compositional inhomogeneity, there is an important difference between them. The Raman spectra vary noticeably with x in the higher-x samples (Fig. 4), while the DSR-PLX spectra show little change from x=0.28 to x=0.43 (Fig. 6). To explain these results, consider the physical properties examined by the two techniques. Raman scattering probes optical phonon frequencies, which are sensitive to intermediate-range (~10 nm) structural order. DSR-PLX, on the other hand, probes interband electronic transitions, which are determined mostly by short-range order. We suggest that the size of the phase-separated regions increases from x=0.28 to x=0.49, and this increase has a greater effect on the phonon frequencies (Raman) than on the interband electronic transitions (PLX). The previous TEM observations[4] support our hypothesis: TEM images showed a distinct "tweed" appearance, indicating spinodal decomposition on a relatively large length scale, for the x=0.49 sample, but not for the x=0.28 sample.

CONCLUSIONS

Transmittance, excitation-wavelength dependent Raman, and double spectrally resolved photoluminescence excitation (DSR-PLX) spectroscopies were used to characterize $In_xGa_{1-x}N$ films with x=0.06 to x=0.49. The transmittance data suggest that compositional inhomogeneity is present even in the lower-x samples (x<0.2), in which inhomogeneity was not detected by microstructural methods (TEM, SAD, and XRD). Both Raman and DSR-PLX show "spectral signatures" that correlate with compositional inhomogeneity and phase separation in the higher-x samples (x>0.2). The composition dependence of the Raman spectra, from x=0.28 to x=0.49, is consistent with an increase in the size of the phase-separated regions with increasing x. In contrast, the DSR-PLX spectra show little change from x=0.28 to x=0.43.

ACKNOWLEDGEMENTS

The work at North Carolina State University was supported by ONR (University Research Initiative) under grant N00014-92-J_1477 and ARO/ARPA under grant DAAH04-96-1-0173.

[1] L. Sugiura, J. Nishio, M. Onomura, S. Nunoue, K. Itaya, and M. Ishikawa, in *Nitride Semiconductors*, edited by F.A. Ponce, S.P. DenBaars, B.K. Meyer, S. Nakamura, and S. Strite (Mater. Res. Soc. Proc. 482, Warrendale, PA, 1998), p. 1157-1167

[2] K. Osamura, S. Naka, and Y. Murakami, J. Appl. Phys. **46**, 3432 (1975)

[3] R. Singh, D. Doppalapudi, T.D. Moustakas, and L.T. Romano, Appl. Phys. Lett. **70**, 1089 (1997)

[4] E.L. Piner, N.A. El-Masry, S.X. Liu and S.M. Bedair, in *Nitride Semiconductors*, ibid., p. 125-130

[5] D. Doppalapudi, S.N. Basu, K.F. Ludwig, Jr. and T.D. Moustakas, J. Appl. Phys. **84**, 1389 (1998)

[6] I. Ho and G.B. Stringfellow, Appl. Phys. Lett. **69**, 2701 (1996)

[7] The use of trade names or brand names does not imply endorsement of the product by NIST.

[8] T.C. Larason, S.S. Bruce and C. L. Cromer, J. Res. Natl. Inst. Stand. Technol. **101**, 133 (1996)

[9] S. Strite and H. Morkoc, J. Vac. Sci. Technol. B **10**, 1237 (1992)

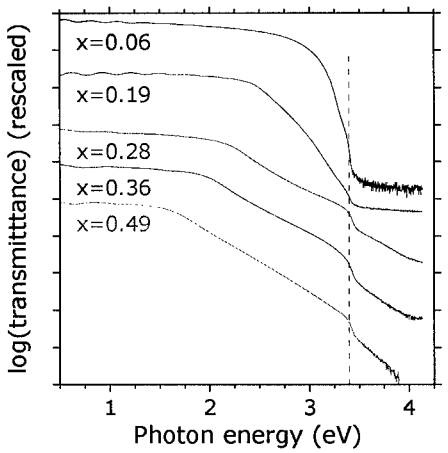


Fig. 1. Transmittance spectra of $In_xGa_{1-x}N$ samples with varying In fraction (x). Vertical line: GaN absorption edge at 3.4 eV.

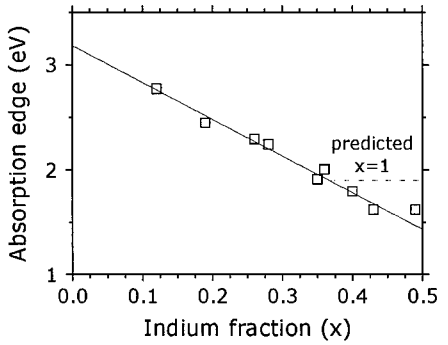


Fig. 2. Shift of absorption edge with In fraction. Solid line: best fit, excluding x=0.49. Dashed horizontal line: predicted absorption edge of pure InN (x=1).

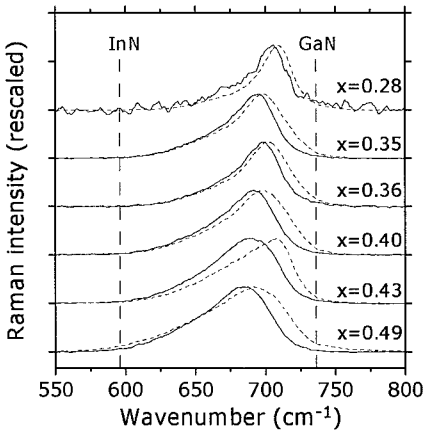


Fig. 3. Raman spectra of $In_xGa_{1-x}N$ samples. Solid lines: 2.409 eV excitation; dashed lines: 2.707 eV excitation; vertical dashed lines: $A_1(LO)$ frequencies of pure InN and GaN.

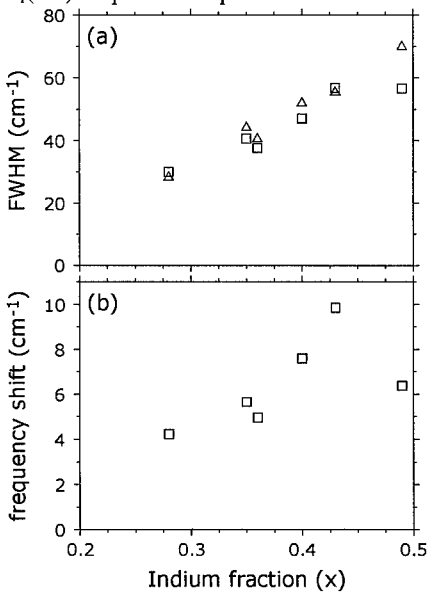


Fig. 4. x dependence of (a) FWHMs of Raman peaks excited at 2.409 eV (squares) and 2.707 eV (triangles); (b) separation between centers of Raman peaks excited at 2.409 eV and 2.707 eV.

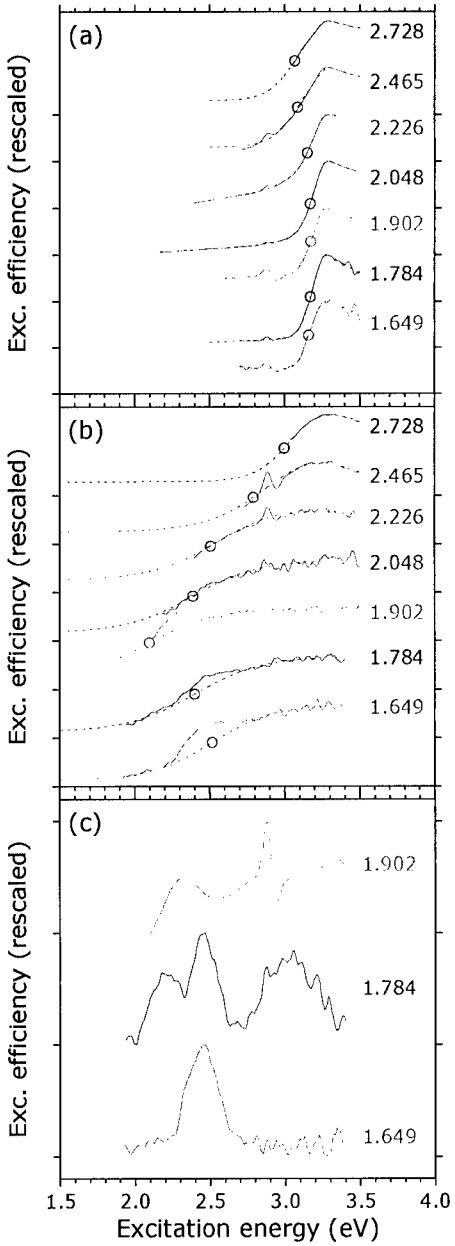


Fig. 5 (left). Double spectrally resolved photoluminescence excitation (DSR-PLX) spectra of (a) x=0.06 sample, (b) x=0.28 sample, and (c) sapphire substrate. For each spectrum, a label indicates the center of the detected emission energy band (eV), and the excitation threshold E_0 (midpoint of the transition from low to high excitation efficiency) is marked by an open circle.

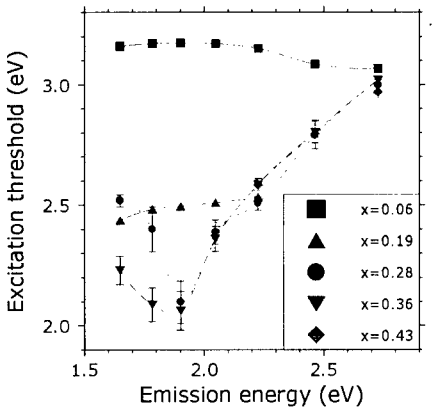


Fig. 6. Variation of excitation threshold energy of DSR-PLX spectra with emission energy, for five samples with differing In fractions (x). Interpolating curves that connect the data points have no theoretical significance.

GROWTH OF ORIENTED THICK FILMS OF GALLIUM NITRIDE FROM THE MELT

Jeffrey S. Dyck, Kathleen Kash, Michael T. Grossner*, Cliff C. Hayman*, Alberto Argoitia*,#, Nan Yang**, Moon-Hi Hong**, Martin E. Kordesch***, and John C. Angus*

Dept of Physics, jsd3@po.cwru.edu
*Dept of Chemical Engineering
**Dept of Materials Science and Engineering

Case Western Reserve University, Cleveland, OH 44106

***Dept of Physics and Astronomy, Ohio University, Athens, OH 45701

Cite this article as: MRS Internet J. Nitride Semicond. Res. 4S1, G3.23 (1999)

ABSTRACT

While significant strides have been made in the optimization of GaN-based devices on foreign substrates, a more attractive alternative would be homoepitaxy on GaN substrates. The primary motivation of this work is to explore the growth of thick films of GaN from the melt for the ultimate use as substrate material. We have previously demonstrated the synthesis of polycrystalline, wurtzitic gallium nitride and indium nitride by saturating gallium metal and indium metal with atomic nitrogen from a microwave plasma source. Plasma synthesis avoids the high equilibrium pressures required when molecular nitrogen is used as the nitrogen source. Here we report the growth of thick oriented GaN layers using the same technique by the introduction of (0001) sapphire into the melt to serve as a substrate. The mechanism of this growth is not established, but may involve transport of the metal as a liquid film onto the sapphire and subsequent reaction with atomic nitrogen. The films were characterized by x-ray diffraction, scanning electron microscopy, transmission electron microscopy, and Raman spectroscopy. X-ray diffraction showed that the GaN films were oriented with their c-axes parallel to the sapphire c-axis. The TEM analysis confirmed the orientation and revealed a dislocation density of approximately 10^{10} cm^{-2}. The E_2 Raman active phonon modes were observed in the GaN films.

INTRODUCTION

In spite of remarkable achievement in the growth and processing of gallium nitride and related III-nitride semiconductor devices, improvement of the crystalline quality of heteroepitaxially grown GaN films is still an important issue. Extended structural defects, such as dislocations, are a problem in films grown on sapphire and SiC substrates, even with the aid of buffer layers. Vertical conduction through the substrate and buffer layers is also an issue for devices. Significant reduction in the concentration of threading dislocations has recently been achieved through the use of epitaxial lateral overgrowth (ELOG) on (0001) sapphire and SiC substrates [1,2]. However, the ideal solution to these problems would be homoepitaxy on high quality, bulk GaN substrates.

The search for a viable method for production of GaN substrates remains open. Bulk growth techniques have succeeded in growing low-dislocation ($<10^6$ cm^{-2}) material at very high pressure (> 15 kbar), but the area of the crystallites remains about 1 cm^2 [3,4]. This size

Mat. Res. Soc. Symp. Proc. Vol. 537 © 1999 Materials Research Society

limitation has inspired several groups [5,6] to pursue hydride vapor phase epitaxy (HVPE) as a quasi-bulk approach to GaN growth yielding growth rates as high as 100 μm/hr. However, cracking is a common problem for HVPE growth of thick GaN overlayers over large areas, e.g., 2 inch (0001) sapphire wafers.

In our initial experiments, we showed that GaN and InN can be grown at sub-atmospheric pressures without the aid of a substrate from the reaction of liquid metal and activated nitrogen derived from a microwave plasma source [7-10]. While the optical quality of these crystals is quite good as determined by photoluminescence and Raman spectroscopy, the crystallite size is typically on the order of 100 μm, with some crystals as large as 1 mm.

The nitrogen saturated melts exhibit a strong tendency to wet the crucible. In some cases, the wetting was so extreme that the entire melt left the well of the crucible and formed solid nitride on the upper surfaces of the crucible [11]. This "spreading-wetting" phenomenon is a striking feature of group III metal/nitrogen melts and has been observed in Ga/N and Al/N systems by several prior investigators [12-15]. In order to promote controlled, oriented nucleation of the solid nitride from the melt, we introduce a substrate. The substrate provides a template for controlled nucleation provided the crystallization takes place at the interface between the substrate and the metal-nitrogen melt. Oriented growth will depend critically on the details of the temperature and concentration gradients as well.

In this paper, we present preliminary results on the growth of thick films of oriented GaN from the melt through the introduction of a substrate into the melt. The primary motivation of this work is to explore low pressure growth from the melt as a means to obtain thick single crystal films for use as substrates.

GROWTH METHOD

Previously, polycrystalline, wurtzitic gallium nitride and indium nitride were synthesized *without a substrate* by saturating gallium or indium metal with atomic nitrogen from a microwave plasma source. Details of this growth method have been published elsewhere [7], but we provide a brief overview here for completeness. In the case of GaN growth, high purity Ga metal was heated in vacuum to a temperature 900°C and exposed to a nitrogen plasma operating at 5 torr and 400W of microwave power at 2.45 GHz. The metal source was pre-treated with a hydrogen plasma immediately prior to the nitridation to remove contaminants from the surface. A polycrystalline crust of GaN formed on the surface of the Ga during cooling of the melt.

In the present work, the growth technique is a variation on this basic nitridation procedure, with the differences primarily being the geometry and inclusion of a substrate. A c-plane sapphire substrate was situated to provide the metal-nitrogen melt a template against which to wet. For this paper, we present the growth of two different samples, A and B. The heater for these experiments was a RF inductively coupled graphite susceptor held at 900°C. The crucible for sample A was situated on top of a protective molybdenum plate on the susceptor and the crucible temperature was 700-

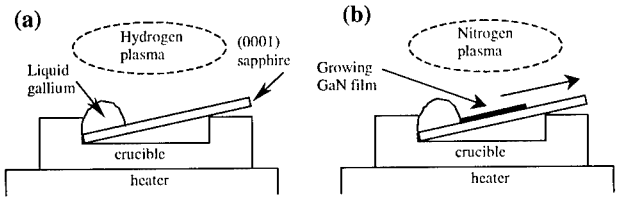


Figure 1. Schematic drawings of growth configuration. (a) The metal and substrate are first exposed to a hydrogen plasma to clean the surfaces. (b) After exposure to nitrogen plasma, a thin liquid metal film moves across the substrate and is converted to GaN.

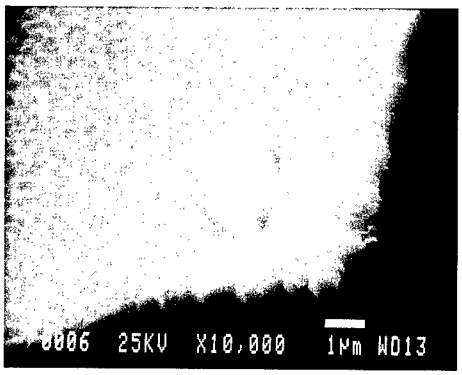


Figure 2. SEM image of a portion of a GaN layer that has peeled away from the (0001) sapphire substrate.

800°C. For sample B, the crucible was embedded in the heater so its temperature was 900°C. Prior to deposition, the sapphire was degreased in boiling organic solvents, rinsed in deionized water, and blown dry with nitrogen. The substrate and 99.99999% pure Ga source metal were heated under vacuum to a temperature of 700-900°C and exposed to the hydrogen plasma pre-treatment before replacing the hydrogen flow with nitrogen (see Figure 1). For sample A, after several minutes of plasma nitridation at the growth temperature, a dull film was visually observed to move up the substrate. Total nitridation time for sample A was 2 hours. For sample B, after several minutes of plasma nitridation at the growth temperature, a thin, reflective metal film was visually observed to move up the substrate and to subsequently darken and form a solid. Total nitridation time for sample B was 45 minutes.

RESULTS AND DISCUSSION

Sample A was smooth, mirror-like, and transparent. X-ray Diffraction (XRD) showed that the primary reflections were from the (0002) and (0004) planes of wurtzitic GaN, indicating a preferred orientation with the c-axis perpendicular to the surface. A Scanning Electron Microscope (SEM) image of a portion of the film that peeled away from the substrate is shown in Figure 2. In order to characterize the structural quality of the film, Transmission Electron Microscope (TEM) analysis was performed. The TEM image of sample A in Figure 3 shows that the film has a columnar structure with a high density of stacking faults and a 0.5 – 0.7 deg. texturing. The overall film thickness is about 1 μm. The selected area diffraction pattern (SADP) taken along the $[11\bar{2}0]_{GaN}$ zone axis shown in Figure 4 indicates that the basic

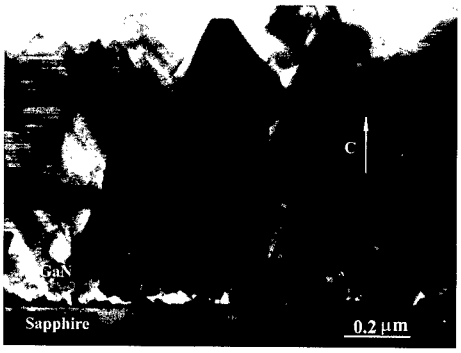


Figure 3. TEM image of GaN film sample A. The arrow marks the direction of the c-axis of the sapphire substrate.

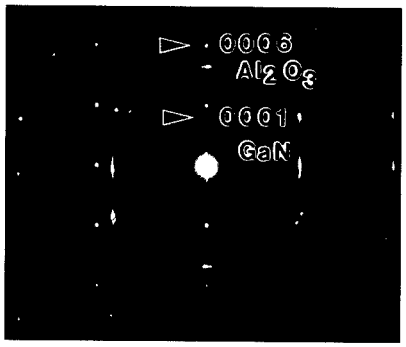


Figure 4. Selected area diffraction pattern of GaN film sample A taken along the $[11\bar{2}0]$ zone axis.

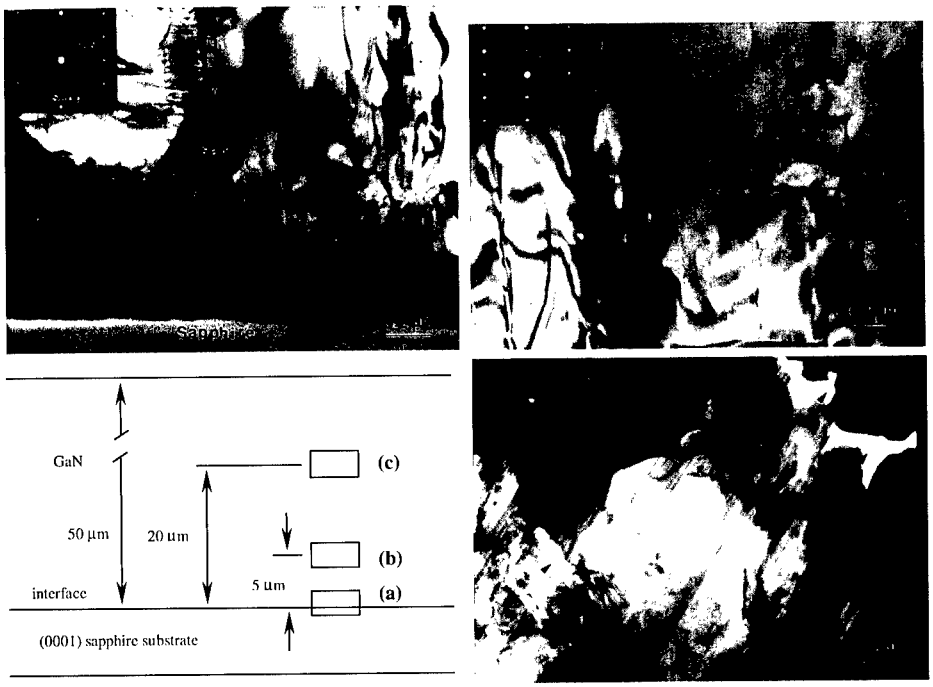


Figure 5. Cross-sectional TEM images of a 50 µm thick area of GaN film on (0001) sapphire substrate sample B near the (a) interface, (b) about 5 µm from the interface, and (c) about 20 µm from the interface. The inserts are selective area diffraction patterns taken along the $[11\bar{2}0]$ zone axis.

orientational relationship is $(0001)_{GaN}//(0001)_{Sapp.}$ and $[11\bar{2}0]_{GaN}//[1\bar{1}00]_{Sapp.}$ No Raman spectra could be obtained from this film.

Parts of sample B had a rough, gray surface and some areas were shiny, yellow, and transparent. Figure 5(a) shows a TEM image of the region near the substrate. The region extending from the interface to about 0.6 µm from the interface shows a typical tooth-like grain structure with a mean width of 0.2 µm. The c-axes of all grains are within 10° of the normal to the interface indicating a textured structure. Above this region, the quality of the GaN grains suddenly improved. The orientational relationship indicated in the inserted SADP is $(0001)_{GaN}//(0001)_{Sapp.}$ and $[11\bar{2}0]_{GaN}//[1\bar{1}00]_{Sapp.}$ A TEM image of a region about 5 µm away from the sapphire interface is shown in fig. 5(b). This area is composed of single crystal GaN with the c-axis perpendicular to the interface (see below). A contrast micrograph (not shown here) shows that most of the defects are threading edge-dislocations and basal screw-dislocations with the Burgers vector $\mathbf{b}=1/3[11\bar{2}0]_{GaN}$. Dislocation densities are of the order of $10^{10}/cm^2$. The inset is a SADP taken along the $[11\bar{2}0]$ zone axis. This image is typical of the film up to about 15-20 µm from the interface. Figure 5(c) shows a micrograph 20 µm away from the interface between the GaN film and the sapphire substrate. Here, the material is polycrystalline and the orientational relationship with the sapphire is lost. In addition, there is a high density of stacking faults and several holes are observed. Due to the high density of stacking faults, the SADP

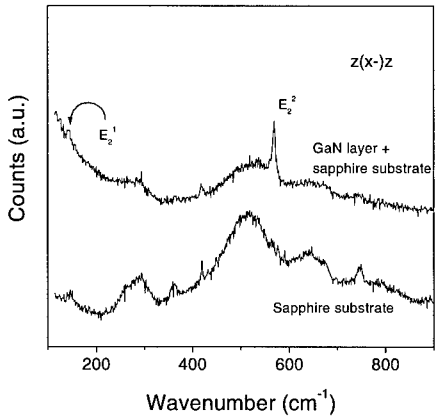


Figure 6. Raman spectrum of GaN film on c-plane sapphire substrate sample B and the spectrum from the substrate before deposition.

clearly shows streaks along the c-axis direction. The average thickness of the film is approximately 100 μm.

Raman spectra were taken in the z(x-)z configuration from a shiny yellow area of the film. From this scattering geometry, the allowable symmetry modes are E_2 and A_1(LO). The E_2 high and low modes are easily observable in Figure 6.

For sample A, grown at the lower temperature, the growth rate was 0.5 μm/hr. Sample B, grown at 900 °C, had a growth rate of over 100 μm/hr, which is similar to that achievable by HVPE. While the defect density of these films is high, these preliminary results are promising considering the growth was carried out on sapphire without an intentional buffer layer.

While the growth mechanism is still unclear, several points can be made. The GaN can be formed either from the vapor or by crystallization from the melt, and, likely, both mechanisms play a role. The vapor pressure of the liquid Ga and the nitrogen activity are high enough to support the growth rates observed. We propose that the initial textured growth at the interface may be vapor growth of GaN, and the rapid change to single crystal material marks the point at which wetting and growth from the melt begins. The upper portion of the film is polycrystalline. This loss of single crystallinity can occur for a number of reasons; for example, onset of interface instability.

CONCLUSIONS

Thick films of GaN are grown on (0001) sapphire by conversion of a layer of gallium metal by a nitrogen plasma. The films are highly oriented with $(0001)_{GaN}//(0001)_{Sapp.}$ and $[11\bar{2}0]_{GaN}//[1\bar{1}00]_{Sapp}$. For a sample grown at an overall rate of 100 μm/hr, dislocation densities are 10^{10} cm^{-2} for the single crystal region of the film and strong Raman active optical phonon modes are observed. These preliminary results indicate that direct conversion of nitrogen saturated gallium melts to the solid nitride may be an alternative for growth of thick GaN films for use as substrates.

ACKNOWLEDGMENTS

Supported by the Office of Naval Research and the Ohio Board of Regents. The assistance of Pirouz Pirouz and Juyong Chung with the electron microscopy is gratefully acknowledged.

REFERENCES

[#] Present address: OCLI, Santa Rosa, CA 95407.

1. O.H. Nam, M.D. Bremser, T.S. Zheleva, and R.F. Davis, *Appl. Phys. Lett.* **71**, 2638 (1997).

2. A. Sakai, H. Sunakawa, and A. Usui, *Appl. Phys. Lett.* **71**, 2259 (1997).

3. S. Porowski and I. Grzegory, *J. Cryst. Growth* **178**, 174 (1997).

4. S. Krukowski, Z. Romanowski, I. Grzegory, and S. Porowski, in *III-V Nitride Materials and Processes II*, edited by C.R. Abernathy, W.D. Brown, D.N. Buckley, J.P. Dimsukes, M. Kamp, T.D. Moustakas, S.J. Pearton and F. Ren (Electrochemical Society Symp. Proc. **97-34**, Paris, 1997) pp. 189-200

5. S.T. Kim, Y.J. Lee, D.C. Moon, C.H. Hong, and T.K. Yoo, *J. Cryst. Growth* **194**, 37 (1998).

6. R.J. Molnar, W. Gotz, L.T. Romano, and N.M. Johnson, *J. Cryst. Growth* **178**, 147 (1997).

7. A. Argoitia, C.C. Hayman, J.C. Angus, L. Wang, J.S. Dyck, and K. Kash, *Appl. Phys. Lett.* **70**, 179 (1997).

8. J.C. Angus, C.C. Hayman, E.A. Evans, and A. Argoitia, Proc. *III-V Nitride Materials and Processes II*, edited by C.R. Abernathy, W.D. Brown, D.N. Buckley, J.P. Dismukes M. Kamp, T.D. Moustakas, S.J. Pearton, and F.Ren, (Electrochem. Soc. Symp. Proc. **97-34**, Pennington, NJ, 1997) pp. 201-208.

9. J.C. Angus, A. Argoitia, C.C. Hayman, L. Wang, J.S. Dyck, and K. Kash in *Gallium Nitride and Related Materials II*, edited by C.R. Abernathy, H. Amano, and J.C. Zolper (Mater. Res. Soc. Symp. Proc. **468**, Pittsburgh, PA, 1997) pp. 149-154.

10. J.S. Dyck, K. Kash, K. Kim, W.R.L. Lambrecht, C.H. Hayman, A. Argoitia, M.T. Grossner, W. Zhou, and J.C. Angus in *Nitride Semiconductors*, edited by F.A Ponce, S.P. DenBaars, B.K. Meyer, S. Nakamura, and S. Strite (Mat. Res. Soc. Symp. Proc. Vol. **482**, Pittsburgh, PA, 1998) pp. 549-554.

11. J.S. Dyck, K. Kash, C.C. Hayman, A. Argoitia, M.T. Grossner, J.C. Angus, and W. Zhou, *J. Mat. Res.* (accepted for publication) 1998.

12. R.A. Logan and C.D. Thurmond, *J. Electrochem. Soc.* **119**, 1727 (1972).

13. R. Madar, G. Jacob, J. Hallais, and R. Fruchart, *J. Cryst. Growth* **31**, 197 (1975).

14. D. Elwell, R.S. Feigelson, M.M. Simkins, and W.A. Tiller, *J. Cryst. Growth* **66**, 45 (1984).

15. C. Toy and W.D. Scott, *J. Mat. Sci.* **32**, 3243 (1997).

P- AND N-TYPE DOPING OF MBE GROWN CUBIC GaN/GaAs EPILAYERS

D.J. As,* T. Simonsmeier, * J. Busch,* B. Schöttker,* M. Lübbers,* J. Mimkes,*
D. Schikora,* K. Lischka,* W. Kriegseis,** W. Burkhardt,** B.K. Meyer**

* Universität Paderborn, FB-6 Physik, Warburger Straße 100,
D-33095 Paderborn, Germany, d.as@uni-paderborn.de
** Universität Giessen, I. Physik. Inst. , Heinrich-Buff-Ring 16,
D-35392 Giessen, Germany

Cite this article as: MRS Internet J. Nitride Semicond. Res. 4S1, G 3.24 (1999)

ABSTRACT

P-type doping with Mg and n-type doping with Si of cubic GaN (c-GaN) epilayers is reported. Cubic GaN films are grown by rf-plasma assisted MBE on semi-insulating GaAs (001) substrates at a substrate temperature of 720°C. Elemental Mg and Si are evaporated from thermal effusions cells. Secondary ion mass spectroscopy (SIMS), low temperature photoluminescence (PL) and temperature dependent Hall-effect measurements are used to study the incorporation, optical and electrical properties. A Mg related shallow donor-acceptor transiton at 3.04 eV with an acceptor activation energy of E_A= 0.230 eV is observed by low temperature PL. At Mg concentrations above 10^{18} cm^{-3} the dominance of a broad blue band indicates that also in c-GaN Mg is incorporated at different lattice sites or forms complexes. Si-doped c-GaN epilayers are n-type with electron concentrations up to $5*10^{19}$ cm^{-3}. The incorporation of Si follows exactly the vapor pressure curve of Si, indicating a sticking coefficient of 1 for Si in c-GaN. With increasing Si-concentration the intensity of the near-band luminescence continuously increases and broadens.

INTRODUCTION

Cubic GaN (c-GaN) epilayers grown by molecular beam epitaxy (MBE) show outstanding electrical and optical features [1,2], demonstrating the high potential of c-GaN for the realization of blue emitting laser diodes. Gain measurements in undoped cubic material reveal gain values which are comparable to that of the best hexagonal GaN (h-GaN) [3]. Particularly, epitaxially grown layers of c-GaN lend themselves to the production of cleaved laser cavities and optically excited stimulated emission from such cleaved facetts has already been observed [4]. In order to fabricate almost any device it is necessary to carry out controlled doping of GaN in order to realize both n-type and p-type GaN material. In hexagonal GaN the principal p-type dopant is Mg and n-type dopant is Si.

In this paper we summarize recent doping experiments of cubic GaN epilayers by Mg and Si. Secondary ion mass spectroscopy (SIMS), low temperature photoluminescence (PL) and temperature dependent Hall-effect measurements are used to study the incorporation, the optical and electrical properties of Mg- and Si-doped samples.

Mat. Res. Soc. Symp. Proc. Vol. 537 © 1999 Materials Research Society

EXPERIMENTAL

Cubic GaN films are grown by rf-plasma assisted MBE on semi-insulating GaAs (001) substrates at a substrate temperature of 720°C. The growth rate is about 0.07 µm/h and the thickness of the layers is about 1 µm, respectively. Elemental Mg and Si are evaporated from commercial effusion cells at source temperatures between 260°C and 450°C, and 750°C and 1150°C, respectively. The concentration and depth distribution of Mg is measured by secondary ion mass spectroscopy (SIMS) using Mg implanted calibrated standards for quantification, and an O^{2+} primary beam of 6 keV. Photoluminescence (PL) measurements are performed in a He bath cryostat at 2 K. Luminescence is excited by the 325 nm line of a cw HeCd UV laser with a power of 3 mW and measured in a standard PL-system. Hall-effect measurements are performed using square shaped samples (Van der Pauw geometry) in a cryostat between 240 K to 380 K, at a magnetic field of 0.3 T and with the sample in the dark.

RESULTS AND DISCUSSION

Mg doping of cubic GaN

The 2 K photoluminescence spectra of cubic GaN epilayers grown at different Mg source temperatures T_{Mg} is shown in Fig.1. The lowest spectrum is that of an undoped reference sample grown before introducing Mg into the chamber. The near band edge luminescence of the reference sample is dominated by an excitonic transition X at 3.26 eV and an omnipresent donor-acceptor pair transition (D^0,A^0) at 3.15 eV [5]. The nature of the involved shallow donor and acceptor is not identified up to now. The corresponding binding energies are 25 meV and 130 meV, respectively. Mg-doping at source temperatures T_{Mg} below 300°C results in the appearence of a donor acceptor transition (D^0,A^0_{Mg}) at 3.04 eV. At about 60 K this transition thermalizes to the corresponding band acceptor transition (e, A^0_{Mg}) at about 3.07 eV. The donor participating in this line has the same ionization energy as the one observed in the undoped sample. From the energetic position an acceptor activation energy of $E_{Mg} = 0.230$ eV is estimated. This energy level is in excellent agreement with recent theoretical calculations of Mg_{Ga} for c-GaN [6] and is somewhat lower than that for the corresponding value of 0.265 eV for h-GaN [7]. Detailed characteristics of the temperature and intensity dependence of the PL spectra will be presented elsewhere. At Mg concentrations higher than 10^{18} cm^{-3} (T_{Mg} higher than 350°C) the low energy side of the spectrum will be dominated by a broad blue emission band centered at about 2.8 eV, which is modulated due to interference fringes of the PL light (upper curves in Fig.1). The nature of this deep transition is unknown up to now, however it seems that also in c-GaN Mg is incorporated at different lattice sites or forms complexes at high Mg flux. A recent publication on h-GaN attributes this blue band to Mg-V_N complexes [8]. Rapid thermal annealing experiments in N_2 atmosphere (30 s) show that the responsible defect for the blue band is thermally stable up to an annealing temperature of 1100°C.

The full squares in Fig.2 show the amount of incorporated Mg measured by SIMS versus the beam equivalent pressure of Mg (BEP_{Mg}). The Mg concentration remains below about $5*10^{18}$ cm^{-3} and is nearly independent on the arrival rate of supplied Mg, which varied by four orders of magnitude. This behaviour is similar to that observed

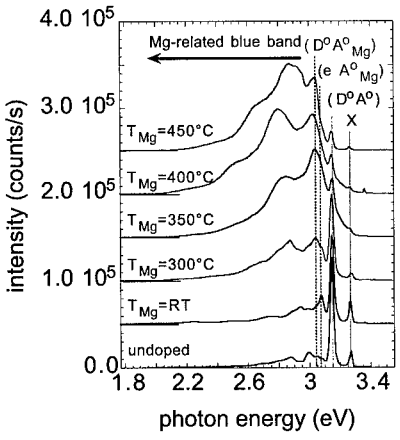


Fig. 1: Low temperature 2 K photo-luminescence spectra of Mg doped cubic GaN epilayers grown by different Mg source temperature T_{Mg}. (X excitonic transition, (D°,A°) omnipresent donor-acceptor pair transition). The dashed lines indicate the shallow Mg-related transitions (D°,A°$_{Mg}$) and (e,A°$_{Mg}$). The dashed arrow below 2.95 eV indicates the deep Mg-related blue band, which is modulated due to interference fringes of the PL light.

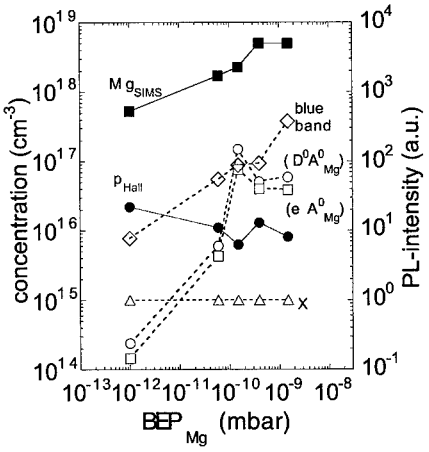


Fig. 2: Integral PL intensity of various observed transitions (open symbols), Mg concentration measured by SIMS (full squares), and free hole concentration p_{Hall} at room temperature versus beam equivalent pressure (BEP_{Mg}) of the offert Mg flux.

for MBE growth of hexagonal GaN [9] and GaAs [10] and is expected to be due to the high vapor pressure of Mg. Depth profile measurements show a homogenious distribution of Mg within the top epilayer and an accumulation of Mg by one order of magnitude at the GaN/GaAs interface [11]. This may be due to the increased number of structural defects near the interface incorporated as a result of the large lattice mismatch between substrate and epilayer.

Hall-effect measurements of the Mg-doped cubic GaN epilayers show p-type conductivity without postgrowth treatments. For the sample grown at a Mg source temperature of T_{Mg} = 300°C the measured free hole concentration p_{Hall} and hole mobility at room temperature is about $3*10^{16}$ cm^{-3} and 215 cm^2/Vs, respectively. This low hole concentration is expected due to the high ionization energy of Mg ($[Mg]_{SIMS}$ = $1.7*10^{18}$cm^{-3}). Under the assumption of compensation the temperature dependence of the concentration of free holes yields for the shallow Mg acceptor an activiation energy of E_{Mg}= 0.110 ± 0.020 eV [12]. The corresponding value for hexagonal GaN is 160 ± 5 meV [13]. In both cases the thermal activation energies are much lower than the optical

activation energies. The reason for this may be either due to a strong electron lattice coupling [14] since the Bohr radius of the "shallow" effective mass like acceptor state is only 6.3 Å or due to potential fluctuations [15]. The room temperature free hole concentration p_{Hall} versus the beam equivalent pressure of Mg (BEP_{Mg}) is depicted in Fig.2 by full circles. In contradiction to the Mg concentration measured by SIMS no increase of p_{Hall} vs. BEP_{Mg} is seen, indicating that an additional compensating donor may be incorporated during Mg-doping.

This assumption is constrained by our PL-measurements. Using Gaussian functions for the different transitions to fit the measured spectra, the integral intensities of the different PL-lines are estimated and also depicted in Fig. 2 versus BEP_{Mg} (open symbols). Both the shallow transitions, (D^0, A^0_{Mg}) and (e, A^0_{Mg}), as well as the deep blue band show a clear increase with increasing Mg-flux. Therefore all three transitions are related to the incorporation of Mg into c-GaN. However, whereas the shallow transitions seems to saturate at higher Mg-flux, this is not the case for the blue band. Since the measured hole concentration is nearly independent of the supplied Mg amount we conclude that the blue band may act as a compensating deep donor center. This conclusion is in agreement with similar observations made in h-GaN [16]. For p-type GaN theoretical calculations also show that Mg_i, Mg_N or Mg-V_N may act as compensating deep donors. Since the formation energies of all these Mg-related defects are low enough they may be possible candidats for the blue band in GaN.

Si-doping of cubic GaN

The optical properties of Si doped cubic GaN are shown in Fig. 3. At 2 K the spectrum of the sample grown with the lowest Si-flux (source temperature T_{Si}= 750°C) is dominated by the excitonic transition X at 3.26 eV and the omnipresent donor-acceptor pair transition (D°,A°) at 3.15 eV [5]. With increasing Si flux a clear shift to higher energies of the (D°,A°) and an increase of the full width at half maximum (FWHM) is observed. For samples grown at T_{Si} > 1025°C both lines merge to one broad band. This behavior is similar to the one observed in the well known case of GaAs heavily doped with Si or Te and can well be described by electron-impurity interactions (band tailing), shrinkage of the band gap due to exchange interaction among free carriers and conduction band filling effects [17, 18]. A detailed analysis of the PL-spectra will be published elsewhere.

For Si doped cubic GaN epilayers the free electron concentration at room temperature (measured by Hall-effect) is depicted in Fig. 4 as a function of the Si-effusion cell temperature (full triangles). One clearly sees that the free electron concentration nearly exactly follows the Si-vapor pressure curve (full line in Fig.4) [19]. This indicates a constant sticking coefficient of Si at the growth temperature chosen. Nearly all Si atoms are incorporated at Ga sites and act as shallow donors. Temperature dependent Hall-effect measurements further show that c-GaN grown at 720°C and a Si source temperature $T_{Si} \geq$ 1025°C are totally degenerated with a maximum free electron concentration of $5*10^{19}$ cm^{-3} and an electron mobility of 75 cm^2/Vs, respectively. This clearly demonstrates the ability of controlled n-type doping of cubic GaN by Si up to concentrations which are necessary for the fabrications of laser diodes.

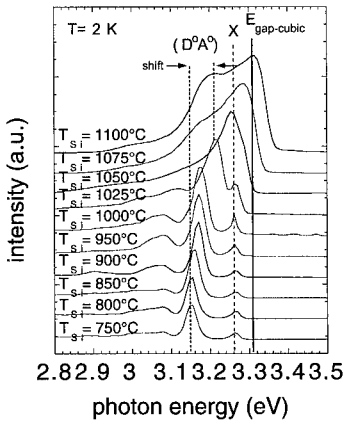


Fig. 3: Low temperature PL spectra of Si doped cubic GaN epilayers grown with different Si source temperatures T_{Si} .With increasing Si source temperature the (D°,A°) transition broadens and shifts to higher photon energies.

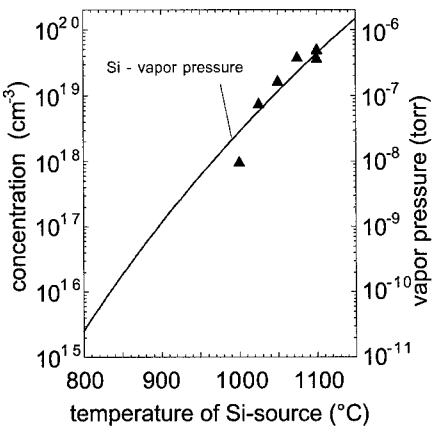


Fig. 4: Room temperature free electron concentration measured by Hall-effect (full triangles) versus Si source temperature. The full line represents the vapor presure curve of Si after [19].

CONCLUSIONS

Cubic GaN films grown by rf-plasma assisted MBE on semi-insulating GaAs (001) substrates are doped by Mg and Si, yielding p- and n-type conductivity, respectively. A Mg related shallow donor-acceptor transition at 3.04 eV with an optical acceptor activation energy of E_A= 0.230 eV is observed by low temperature PL. At Mg concentrations above 10^{18} cm^{-3} a broad blue band dominates the PL spectra and indicates that also in cubic GaN Mg is incorporated at different lattice sites or forms complexes. Hall-effect measurements show that this complex may act as a compensating donor. Si-doping follows exactly its vapor pressure curve, indicating a constant sticking coefficient in the investigated temperature range. With increasing Si-concentration a continuous increase and broadening of the near-band luminescence is measured. Si-doped c-GaN epilayers are n-type with electron concentrations up to $5*10^{19}$ cm^{-3}.

ACKNOWLEDGEMENTS

The authors acknowledge the support of their work by "Deutsche Forschungsgemeinschaft", project number As (107/1-1).

REFERENCES

1. D.J. As, D. Schikora, A. Greiner, M. Lübbers, J. Mimkes, and K. Lischka, Phys. Rev. B **54** (16), R11118 (1996)
2. D. Schikora, M. Hankeln, D.J. As, K. Lischka, T. Litz, A. Waag, T. Buhrow and F. Henneberger: Phys. Rev. **B 54** (12), R8381 (1996)
3. J. Holst, L. Eckey, A. Hoffmann, I. Broser, B. Schöttker, D.J. As, D. Schikora and K. Lischka: Appl. Phys. Lett. **72** (12), 1439 (1998)
4. J. Holst, A. Hoffmann, I. Broser, B. Schöttker, D.J. As, D. Schikora and K. Lischka: submitted to Appl. Phys. Lett.
5. D.J. As, F. Schmilgus, C. Wang, B. Schöttker, D. Schikora, and K. Lischka: Appl. Phys. Lett. **70** (10), 1311 (1997)
6. J. Neugebauer, C.G. Van de Walle, MRS Symp. Proc. Vol. **395**, 645 (1996)
7. M. Leroux, B. Beaumont, N. Grandjean, J. Massies, P. Gibart: MRS Symp. Proc.Vol. **449**, 695 (1997)
8. U. Kaufmann, M. Kunzer, M. Maier, H. Obloh, A. Ramakrishnan, B. Santic, P. Schlotter, Appl. Phys. Lett. **72** (11) 1326 (1998)
9. S. Guha, N.A. Bojarczuk, and F. Cardone, Appl.Phys.Lett. **71** (12), 1685 (1997)
10. C.E.C.Wood, D. Destimone, K.Singer, and G.W.Wicks, J.Appl.Phys. **53**, 4230 (1982)
11. D.J. As, T. Simonsmeier, B. Schöttker, T. Frey, D. Schikora, W. Kriegseis, W. Burkhardt, and B.K. Meyer, Appl.Phys. Lett. **73** (13), 1835 (1998)
12. D.J. As, Phys. Stat. Sol. (b) **210**, 2. Dec. (1998)
13. W. Kim, A. Salvador, A.E. Botchkarev, O. Aktas, S.N. Mohammad, and H. Morcoc, Appl. Phys. Lett. 69 (4), 559 (1996)
14. B.K. Ridley, in *"Quantum Processses in Semiconductors"*, 2nd Ed., Clarendon Press, Oxford, 1988, p.235
15. D.J. Dewsnip, J.W. Orton, D.E. Lacklison, L. Flannery, A.V. Andrianov, I. Harrison, S.E. Hooper, T.S. Cheng, C.T. Foxon, S.N. Novikov, B. Ya Ber, and Yu A. Kudriavtsev, Semicond. Sci. Technol. **13**, 927 (1998)
16. L.Eckey, U.von Gfug, J.Holst, A.Hoffmann, B.Schineller, K.Heime, M.Heuken, O.Schön, R.Beccard, J. of Crystal Growth **189/190**, 523 (1998)
17. A.P. Abramov, I.N. Abramova, S. Yu. Verbin, I. Ya. Gerlovin, S.R. Grigorév, I.V. Ignatév, O.Z. Karimov, A.B. Novikov, and B.N. Novikov, Semiconductors **27** (7), 647 (1993)
18. J. De-Sheng, Y. Makita, K. Ploog, H.J. Queisser, J. Appl. Phys. **53** (2), 999 (1982)
19. J.L. Souchiere, Vu Thien Binh, Surface Science **168**, 52 (1986)

CUBIC InGaN GROWN BY MOCVD

J.B. Li, Hui Yang, L.X. Zheng, D.P. Xu, Y.T. Wang

National Research Center for Opto-electronic Technology, Institute of Semiconductors, CAS, Beijing 100083, China

Cite this article as: MRS Internet J. Nitride Semicond. Res. 4S1, G3.25 (1999)

Abstract

We report on the growth of high-quality cubic phase InGaN on GaAs by MOCVD. The cubic InGaN layers are grown on cubic GaN buffer layers on GaAs (001) substrates. The surface morphology of the films are mirror-like. The cubic nature of the InGaN films is obtained by X-ray diffraction (XRD) measurements. The InGaN layers show strong photoluminescence (PL) at room temperature. Neither emission peak from wurtzite GaN nor yellow luminescence is observed in our films. The highest In content as determined by XRD is about 17% with an PL emission wavelength of 450 nm. The FWHM of the cubic InGaN PL peak are 153 meV and 216 meV for 427 nm and 450 nm emissions, respectively. It is found that the In compositions determined from XRD are not in agreement with those estimated from PL measurements. The reasons for this disagreement are discussed.

Introduction

The III-V nitrides have long been viewed as a promising system for semiconductors device applications in the blue and ultraviolet (UV) wavelengths in much the same manner that their highly successful As-based and P-based cousins have been exploited in the infrared (IR), red, and green wavelengths. Although most devices have been based on hexagonal films, cubic GaN is of significant interest [1-5]. Cubic GaN has been grown on substrates that have a cubic lattice, such as GaAs[2,6-8], Si[9], 3C-Sic[6-10], and MgO[11]. In our work, Cubic GaN is grown on GaAs substrates. Because GaAs substrates are conductive and easily cleaved, they will simplify the device fabrication process, thus decrease the device cost. So cubic GaN grown on GaAs has an exciting prospect for fabricating blue and geen LED as well as LDs. Now the quality of cubic phase GaN grown on GaAs have reached to a new level. The full width at half-maximum (FWHM) of room-temperature photoluminescence (PL) for GaN crystal is reported as about 46 meV[12], which approaches that of high quality hexagonal GaN film.

InGaN is a direct band material which has the band gap energy varying from 1.92 ev for InN to 3.2ev for cubic GaN. It is a very important material for use as an active layer for blue-green LED and LDs. However, InGaN is thermally unstable which causes difficulties in growing high quality and high indium concentration InGaN. In our letter, we have grown high quality cubic phase $In_xGa_{1-x}N$ on GaAs substrate by MOCVD. The indium composition x has been achieved as high as 0.17 with an emission wavelength of 450 nm.

Experimental procedure

Our cubic phase GaN is grown by MOCVD on GaAs substrate, using H_2 as carrier gas, high purity NH_3 as N source, triethylgallium (TEGa) as Ga source, and trimethylindium (TMIn) as

Mat. Res. Soc. Symp. Proc. Vol. 537 © 1999 Materials Research Society

indium source, respectively. The reaction chamber maintains low pressure (76 torr) during growth. A GaN buffer layer was first deposited at 550 °C for 2 min, then the GaN epilayer with a thickness of 0.7 μm was deposited at a temperature of 850 °C. Finally, the InGaN layer with a thickness of 0.3 μm was deposited on the GaN layer. X-ray diffraction (XRD) were used to determine the lattice constant and In content of InGaN films. The XRD measurements are performed using a synchrotron radiation with a wavelength of 1.535 Å. Room-temperature photoluminescence (PL) measurements were performed on all samples using a computer-controlled PL system. The excitation source is a He-Cd laser which operates at a wavelength of 325 nm and produces 25 mw of output power. A setup of a monochromator and a photomultiplier is used for PL measurements.

Result and Discussion

Figure 1 shows XRD profiles for several samples (ω/2θ mode). The positions of GaN (002) and (004) peaks are at 19.98 ° and 42.92 °, respectively. The InGaN diffraction peaks of (002) and (004) are separated clearly from GaN diffraction peaks of (002) and (004). It indicates the cubic phase InGaN films have been achieved. No diffraction peaks correspond to hexagonal phase GaN and InGaN are observed. Different diffraction-peak positions of InGaN indicate different indium composition x for InGaN films. Using Vegard's law and assuming a lattice constant of InN to be 0.498 nm, we calculated the indium alloy composition x from the lattice constant of InGaN crystals determined by XRD. The x values for different samples are indicated in Fig. 1. The highest In composition we have achieved here is 17%. The InGaN films show mirror-like surfaces.

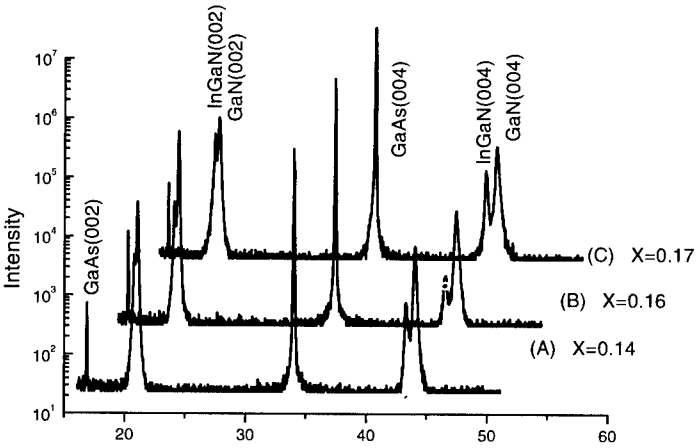


Figure 1. X-ray diffraction profiles (ω/2θ mode) for cubic InGaN films.

Figure 2 shows the room temperature PL spectra for the samples shown in Fig. 1. Except the cubic GaN band edge emission at 387 nm, in all the spectrum, there is a strong peak at 427 nm to 450 nm which we assign to cubic InGaN band edge emission. The FWHM for PL peaks of our InGaN films range from 153 mev to 220 mev, with emission wavelength range from 427nm to 450nm. The InGaN peaks in the spectra are quite narrow even compared with hexagonal InGaN. The GaN peak is relatively weak reflecting a strong absorption from the 0.3 μm thick InGaN film. The yellow band in our samples are also very weak. The quality of the films becomes better while the indium composition x decreased as indicated by the changes of FWHM.

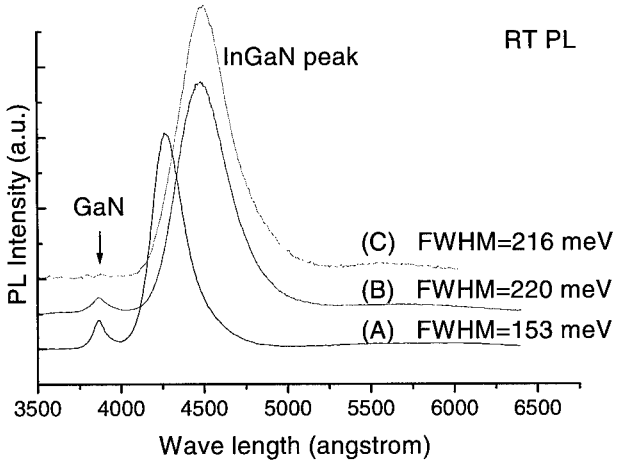


Figure 2. PL spectra of InGaN samples.

We have plotted the PL peak energies of our InGaN samples as a function of the In composition, as shown in Fig. 3. The dashed lines in the figure are linear connections between the two points corresponding to GaN (3.2eV) and InGaN (1.9eV to 2.2eV). We can see that the bandgap energy of our InGaN films are well bellow these lines. There are two possibilities for this discrepancy. One is that the In composition is not uniform in the InGaN films. The In composition drawn in the figure is an average value of our sample determined by XRD. It might be not uniform in the samples and much larger than average in some part of the samples. These high In content parts contribute to the PL leading to a longer wavelength than average. In this case, the In composition of the In-rich part might have a value as large as 0.45. The other possibility is that the In composition is uniform in the films while the bandgap energies of the InGaN are not linearly depend on x. There is bowing behavior in the relationship between the bandgap energy and In composition, as indicated by the solid curve in Fig. 2. Further investigation on this issue are required.

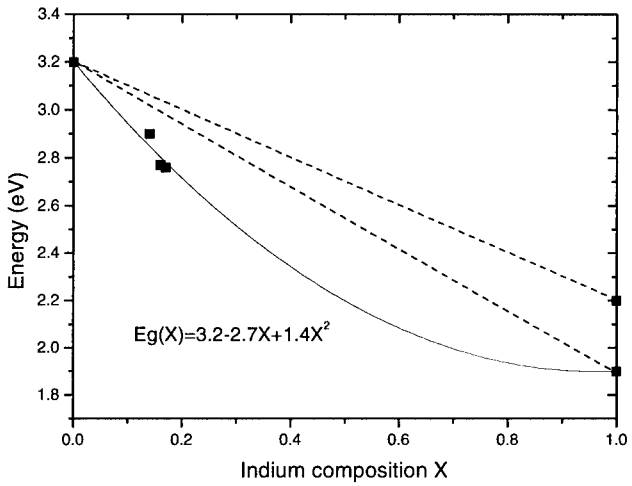


Figure 3. Bandgap energy v.s. indium composition of cubic InGaN. The dashed lines are linear connections between the points corresponding to GaN (3.2eV) and InGaN (1.9eV to 2.2eV). The solid curve is drawn according to the equation shown in the figure.

Summary

High In content cubic InGaN films have been grown on GaAs substrates by MOCVD. The cubic InGaN and cubic GaN (002) and (004) peaks in XRD profiles can be clearly separated. The lattice constant and In composition of InGaN can then be determined. All the cubic InGaN films show very strong room-temperature PL. The cubic InGaN sample emitting at 450 nm wavelength has a FWHM of only 220 meV, which shows the cubic InGaN film is of high quality.

Acknowledgement

The XRD measurements were carried out in Beijing Synchrotron Radiation facility, Institute of High Energy Physics, CAS, Beijing, China.

References

[1] S. Strite, H.Morkoc, J. Vac. Sci. Technol. B 10 1227 (1992).
[2] Fujieda, Y. Matsumoto, Jpn. J. Appl. Phys. 30 L1665 (1991).
[3] S. Yoshida, H. Okumura, S. Misawa, E. Sakuma, Surf. Sci. 267, 50(1992).
[4] A. Kikuchi, H. Hoshi, K. Kishino, Jpn. J. Appl. Phys. 33, 688(1994).
[5] S. Bharatan, K. S. Jones, C. R. Abernathy, S. J. Pearton, F. Ren, P. W. Wisk, J. R. Lothian, J. Vac. Sci. Technol A 12, 1094 (1994)

[6] H. Okumura, S. Yoshida, T. Okahisa, Appl. Phys. Lett. 64, 2997(1994)
[7] J. W. Yang, J. N. Kuznia, Q. C. Chen, M. Asif. Khan, T. George, M. De Graef, S. Mahajan, Appl. Phys. Lett. 67, 3759(1995)
[8] H. Hong, K. Wang, D. Pa Vidis, J. Electron. Mater. 24, 213(1995)
[9] T. Lei, T. D. Moustakas, R. J. Graham, Y. He, S. J. Berkowitz, J. Appl. Phys. 71, 4933(1992)
[10] M. J. Paisley, Z. Sitar, J. B. Posthill, R. F. Davis, J. Vac. Sci. Technol. A 7, 701(1989)
[11] R. C. Powell, N. E. Lee, Y. W. Kim, J. E. Greene, J. Appl. Phys. 73, 189(1989)
[12] Hui Yang, L.X. Zheng, J.B. Li, X.J. Wang, D.P. Xu, Y.T. Wang, and X.W. Hu, submitted to Appl. Phys. Lett.

OPTICAL INVESTIGATIONS OF AlGaN ON GaN EPITAXIAL FILMS

G. Steude[1], T. Christmann[1], B.K. Meyer[1], A. Goeldner[2], A. Hoffmann[2], F. Bertram[3], J. Christen[3], H.Amano[4], and I. Akasaki[4]
[1]1.Physikalisches Institut, Universitaet Giessen, 35952 Giessen, Germany,
[2]Institut für Festkoerperphysik der TU Berlin, Hardenbergstr. 36, D-10623 Berlin, Germany,
[3]Otto von Guericke Universitaet Magdeburg, PF 4120, D-39016 Magdeburg, Germany
[4]Department of Electrical and Electronic Engineering, 1-501 Shiogamaguchi, Tempaku-ku, Nagoya 468, Japan

Cite this article as: MRS Internet J. Nitride Semicond. Res. 4S1, G3.26(1999)

ABSTRACT

We have investigated $Al_xGa_{1-x}N$ /GaN heterostructures ($0<x<0.22$) grown by metal organic vapor phase epitaxy on sapphire with photoluminescence (PL), reflexion and cathodo-luminescence experiments. The energetic positions of the free A-exciton in GaN and AlGaN as a function of the alloy compositions are deduced from temperature dependent PL and from reflexion measurements. We obtain a small bowing parameter and no evidence for a Stokes shift between absorption and emission. The $Al_xGa_{1-x}N$ films induce additional compressive strain on the underlying GaN film. Compositional inhomogeneities are present, but the fluctuations are too small to be important for carrier localisation. The broadening of the luminescence line width in the alloy can be described by statistical disorder of a random alloy.

INTRODUCTION

A wide field of applications can be expected from opto-electronic devices based on the group-III nitrides, AlN, GaN and InN. Together with their ternary alloys they can cover the visible to ultraviolet spectral range. In order to optimize the device performance especially the properties of the ternary alloys have to be understood and controlled. Since the lattice mismatch between AlN and GaN is 2.4 % and for InN on GaN it is 11 %, strain effects (i.e. pseudomorphic versus strain relaxed growth) play an important role. They can lead to compositional fluctuations and eventually to phase separations. Also the influence of piezo electric field effects on the luminescent properties cannot be neglected.
We have recently reported on the excitonic luminescence of $Al_xGa_{1-x}N$ on GaN heterostructures and derived the excitonic band gap dependence on the Al molar fraction ($x<0.22$) at room temperature[1]. The deviation from a linear dependence was small and we obtained the non-linear contribution (bowing parameter) to be 0.6 eV. At low temperatures bound exciton emission dominates[2]. The free A-exciton emission was only observable at elevated temperatures ($T>100K$).
We have extended these investigation towards reflexion, transmission and absorption spectroscopy using calorimetric detection (CRS, CTS, CAS) to conclude on the absence or presence of a Stokes shift between absorption and emission. Cathodoluminescence experiments were used to resolve eventual compositional inhomogeneties.

Mat. Res. Soc. Symp. Proc. Vol. 537 © 1999 Materials Research Society

EXPERIMENTAL DETAILS

The films were grown by MOVPE on sapphire (0001) substrates. In a first step a 2 µm thick GaN film was grown on a 30 nm low temperature deposited AlN buffer. On this GaN layer $Al_xGa_{1-x}N$ films with thicknesses between 350 and 650 nm were grown. The AlN molar fraction varied between 0 and 0.22. More details especially about the determination of the composition can be found in ref.[3] Details of the set up for calorimetric detection of reflexion, transmission and absorption spectroscopy can be found in ref.[4]4 K cathodoluminescence (CL) measurements were performed in a fully computerized scanning electron microscope. The spatial resolution is better then 50 nm. In the CL wavelength image (CLWI) mode the local emission wavelength is mapped at any point of a rectangular area which is scanned by the electron beam. For further details see ref.[5] The luminescence was excited with an Excimer laser at 248 nm.

RESULTS AND DISKUSSION

In fig.1 the photoluminescence spectra of $Al_xGa_{1-x}N$ epilayers with Al contents from 6 to 22 % are shown. Apart from the shift of the peak position with increasing Al content one also observes a considerable increase in the linewidth, which is caused by alloy broadening (see below). In all cases the free A-exciton and neutral donor bound exciton of the underlying GaN layer could be detected (see inset in fig.1). One notes that the line positions shift blue as a function of the Al composition which means that additional biaxial compressive strain is induced in the GaN layers.
In the $Al_xGa_{1-x}N$ layers at temperatures around 100 K the free A-exciton emission appeared which then was observed up to 500 K, the highest temperature wich could be achieved in our cryosystem. The temperature dependence of the excitonic gap was fitted by the following formula[6,7]:

$$E(T)=E(0) - \kappa/\{\exp(\Theta_E/T)-1\} \qquad (1)$$

with κ=0.38 and Θ_E=618 K ± 30 K. The parameters were the same for all five samples (as one example see fig.2). In PL at low temperatures bound exciton emission and not free exciton

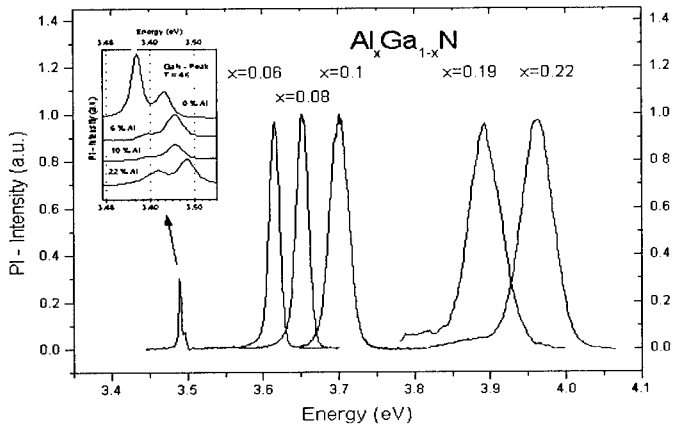


Fig.1: Photoluminescence of $Al_xGa_{1-x}N$ epilayers and of the underneath GaN films (inset).

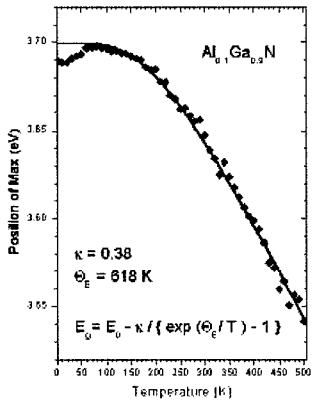


Fig.2: Measured band gap of $Al_{0.1}Ga_{0.9}N$ vs temperature. The drawn line is a fit to the experimental data (see text).

emission dominates. One notes that the data points deviate at temperatures below 50 K from the fitted line. The excitons are now localized at neutral donors and there is an energetic difference between free and bound exciton emission, the localization energy. In order to obtain the free exciton line position at low temperatures we extrapolated from the high temperature behaviour to the low temperature behaviour using equ.1.

In fig.3 we present a CAS spectrum of a sample with 6% Al content. The measurement temperature was 47 mK. One can identify the signals from the A- and B-excitons of the underlying GaN at the band gap energy of around 3.5 eV. At higher energies the signal from the A-exciton of the AlGaN film can be seen. In fig.3 (inset) we compare the line positions of the free A-exciton from calorimetric measurements and PL. One notes an almost perfect agreement. Small differences might be caused by compositional inhomogeneities which we tried to resolve by CL measurements.

In fig.4 we present CLWI of the film with an Al content of x=0.06. On a scale of 10 x 20 μm^2 the spectral position of the luminescence is mapped. In the wavelength image spectra are measured spot by spot and the peak positions found are translated into a colour scale. Blue means emission at 341.5 nm and yellow at 342.5 nm. One can certainly see inhomogeneities on the scale of micrometers (fig.4.b). One should, however, have in mind that the energetic positions differ only by some 5 to 10 meV. In the integrated intensity picture (fig.4.c) areas of bright emission (yellow) and low emission efficiency (blue) can be distinguished. The blue areas are caused by structural imperfections on the surface such as scratches. They can also be identified in the scanning electron microscope (SE) image (fig.4.a). If all spectra are added up, the averaged spectrum results (fig.4.d). The CL results were very similar for all five $Al_xGa_{1-x}N$ films, and it is worth to note that the film with x=0.22 had very much the same scatter in line positions (10 to 15 meV) as the film with x=0.06.

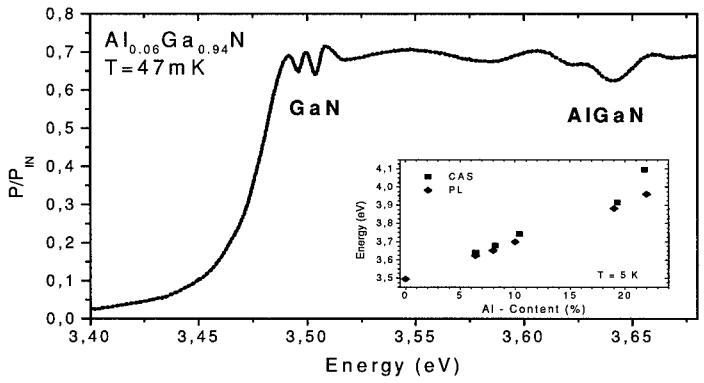


Fig.3: Calorimetric absorption spectrum of a $Al_{0.06}Ga_{0.94}N$ epilayer. In the inset the free A-exciton line position as a function of Al composition is shown.

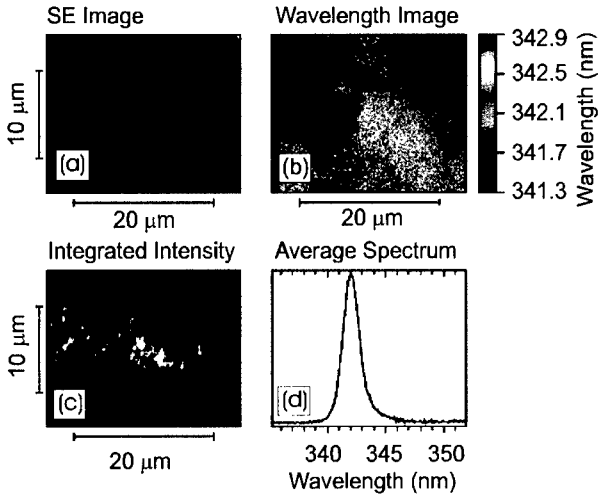


Fig.4: Catodoluminescence results on a $Al_{0.06}Ga_{0.94}N$ epilayer (a) secondary electron image; (b) wavelength image; (c) integrated intensity; (d) averaged spectrum.

This demonstrates that in $Al_xGa_{1-x}N$/GaN single heterostructures compositional inhomogeneities are less pronounced compared to InGaN/GaN.

Well resolved spectra of the A- and B-excitons in the underneath GaN films could be observed independent of the Al content by calorimetric spectroscopy. Their energetic positions as a function of the Al contents are shown in fig.5. There is a clear blue shift for both excitons, the energetic distance from A to B increases from 9 meV for x=0.06 to 11 meV for x=0.22. In the photoluminescence experiments only the A-exciton transition could be determined, the data are in agreement with the calorimetric measurements. From refexion and luminescence one can conclude that the top $Al_xGa_{1-x}N$ layer adds additional compressive strain to the underneath GaN film.

Strain modifies via the deformation potentials the eigen frequency of the phonons which can be measured by Raman spectroscopy. From the shift of the Raman lines in biaxially compressively strained films compared to the unstrained value the amount of built-in elastic strain can be quantified. Since the polar modes of E1 and A1 symmetry have a directional dispersion, the LO phonons interact with the vibrations of free carriers, and since the E2(low) has only a very small pressure coefficient, the E2(high) is the only usable mode for determination of the strain. Its shift is given by:

$\Delta\omega_{E2(high)} = 4.2\ cm^{-1}/GPa \cdot \sigma_{xx}$ with σ_{xx} the respective component of the strain tensor. We used the room temperature intrinsic value of $\omega_{E2(high)} = 567\ cm^{-1}$, which was determined for free-standing GaN films. There is a shift of the Raman line from the intrinsic value as as function of Al molar fraction. It is around 0.8 wavenumbers for x=0.06 and around 1.4 wavenumbers for x=0.218. These experimental findings could be quantified by using a two layer model (neglecting thermal mismatch) and taking into account the elastic constants of $Al_xGa_{1-x}N$ (interpolating between GaN and AlN). Details will be published elsewhere[8].

Besides the energetic shift of the excitonic emission with increasing Al-content the linewidth of the bound exciton luminescence line increases from 14 meV for x=0.06 to 35 meV for x=0.22. This can be explained by alloy brodening. We compare the experimental values with a calculation based on a model introduced by Schubert et al.[9] The broadening is caused by a statistical occupation of the cation places Ga by Al and the alloy disorder is seen by the exciton. Therefore we need to consider the exciton volume and its Bohr radius. The alloy broadening is given by:

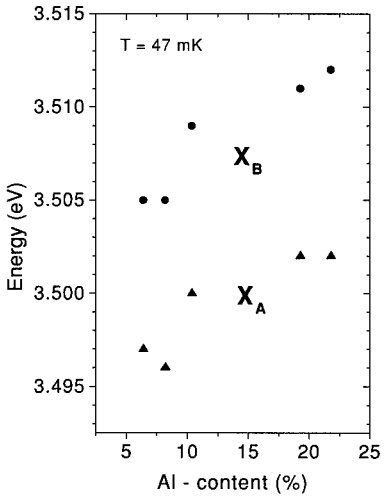


Fig.5: Line positions of the free A- and B-excitons in GaN as a function of Al content in $Al_xGa_{1-x}N$ on GaN epitaxial films.

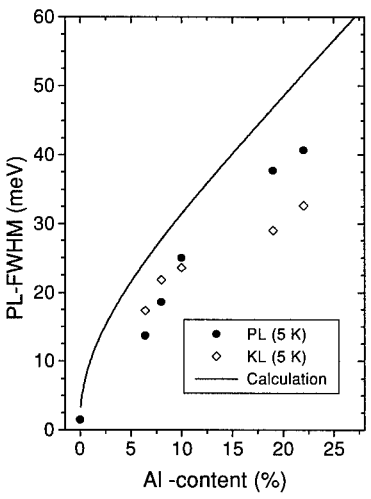


Fig.6: Alloy broadening of the photo-luminescence line width (PL: full circles; CL: hollow diamonds). The drawn line shows a calculation using equ.(2).

$$\Delta E_{exc} = 2.36\ \sigma_E = 2.36\ dE_g/dx\ \{x(x-1)/KV_{exc}\} \qquad (2)$$

dE_g/dx is the variation of the energy gap with composition, for which we used the analytical expression $E_g(x) = E_{g,GaN} + (c-b)x + bx^2$ with $c=E_{g,AlN} - E_{g,GaN}$ and b=0.6 eV. For the band gaps we used 3.48 eV (GaN) and 6.2 eV (AlN). K is the cation density. The factor 2.36 accounts for Gaussian broadening. The exciton volume is calculated from the Bohr radius for which we took 28 Å in GaN and 19 Å in AlN.

In fig. 6 we compare experiment and calculation. The maximum of broadening is reached for 70 % Al content (not shown in fig.6) which is related to the considerable increase of the electron effective mass towards AlN and the decrease of the dielectric constant. Due to the decreasing Bohr radius in $Al_xGa_{1-x}N$ the excitons will see much more alloy disorder.

In CL measurements (open diamonds) slightly different line widths are observed due to fact that the exciting spot size is smaller. In any case the experimental data are below the calculated. We have to have in mind, however, that we are dealing in the experiments with donor bound excitons and not with free excitons for which the Bohr radius concept is valid. For neutral acceptor bound excitons which were treated in the framework of the pseudo-donor model the influence of alloy broadening could be calculated. However, this model cannot been transfered to neutral donor bound excitons, since it requires the knowledge which particle of the exciton, electron or hole is bound first. Theoretical arguments suggest that the difference in linewidth of a bound exciton and a free exciton at low temperatures may not be significant.

Our experimental results confirm that alloy broadening in this statistical model accounts for the line width and clustering is negligible at least for the composition range investigated. It is also in line with the wavelength imaging by CL presented in fig.4.

From X-ray data it was already concluded that $Al_xGa_{1-x}N$ grew coherently on GaN resulting in a tensile stress in the $Al_xGa_{1-x}N$ layers. It should, however, be less than 0.5% since strained and

unstrained $Al_xGa_{1-x}N$ layers have practically the same composition dependence of the band gap[10]. Our data support these conclusions. There is no evidence for a Stokes shift between absorption and emission and the bowing parameter is small. In $Al_xGa_{1-x}N$ for the alloy composition range $0<x<0.22$ which is also the technological relevant one for the realisation of blue laserdiodes variations in recombination energies are less than 15 meV. For x=0.22 this translates into composition variations of less than 2%. The films showed free exciton emission at room temperature and with very good precision its position on alloy composition can be approximated with a linear dependence for $0<x<0.22$ to be $E_g(GaN) + 2.15\ x$ (eV).

SUMMARY

In conclusion we reported on photoluminescence, calorimetric spectroscopy and cathodoluminescence of $Al_xGa_{1-x}N$ on GaN layers for alloy compositions $0<x<0.22$. Small compositional inhomogeneities could be resolved, but will play a minor if not negligible role in carrier localisation. The luminescence linewidth increases in the alloy as expected for a random alloy. In contrast to InGaN/GaN pseudomorphic $Al_xGa_{1-x}N$/GaN single heterostructures with $x<0.22$ show a small bowing parameter[11]. There is an overall agreement in line positions of free exciton absorption and emission. Additional compressive strain is added to GaN layers by growing AlGaN films on top.

References

[1] G. Steude, D.M. Hofmann, B.K. Meyer, H. Amano, and I. Akasaki, physica status solidi (b) **205**, R7 (1998)

[2] G. Steude, D.M. Hofmann, B.K. Meyer, H. Amano, and I. Akasaki, physica status solidi (a), **165**, R3 (1998)

[3] T. Takeuchi, H. Takeuchi, S. Soat, H. Sakai, H. Amano, and I. Akasaki, Jpn. J. Appl. Phys. **36**, L177 (1997)

[4] L. Podlowski, A. Hoffmann, I. Broser, J. Cryst. Growth **117**, 698 (1992).

[5] J. Christen, M. Grundmann, D. Bimberg, J. Vac. Sci. Technol. **B9**, 2358 (1991).

[6] P. Lautenschlager, M. Garriaga, S. Logothetidis, and M. Cardona, Phys. Rev. B **35**, 9174 (1987).

[7] G. D. Cody, in *Semiconductors and Semimetals*, edited by J.I.Pankove, (Academic, New York, 1984), Vol. 21 B, pp 11-79.

[8] G. Steude, B.K. Meyer, A. Hoffmann, F. Bechstedt to be published

[9] E.F. Schubert, E.O. Göbel, Y. Horikoshi, K. Ploog and H.J. Queisser, Phys. Rev. B **30**, 813 (1984)

[10] D.K. Wickenden, C.B. Bargeron, W.A. Byrden, J. Miragliova, and T.J. Kistenmacher, Appl. Phys. Lett. **65**, 2024 (1994)

[11] M.D. McCluskey, C.G. Van de Walle, C.P. Master, L.T. Romero, and N.M. Johnson, Appl. Phys. Lett. **72**, 2725 (1998)

Extended Defects in GaN: a Theoretical Study

J. Elsner, Th. Frauenheim, M. Haugk, R. Gutierrez
Fachbereich Physik, Universität GH Paderborn, D-33098 Paderborn

R. Jones
Department of Physics, University of Exeter, Exeter, EX4 4QL, UK

M. I. Heggie
CPES, University of Sussex, Falmer, Brighton, BN1 9QJ, UK

Cite this article as: MRS Internet J. Nitride Semicond. Res. 4S1, G3.29 (1999)

Abstract

We present density–functional theory studies for a variety of surfaces and extended defects in GaN. According to previous theoretical studies[1] $\{10\bar{1}0\}$ type surfaces are electrically inactive. They play an important role in GaN since similar configurations occur at open–core screw dislocations and nanopipes as well as at the core of threading edge dislocations. Domain boundaries are found to consist of four–fold coordinated atoms and are also found to be electrically inactive. Thus, except for full–core screw dislocations which possess heavily strained bonds all investigated extended defects do not induce deep states into the band–gap. However, electrically active impurities in particular gallium vacancies and oxygen related defect complexes are found to be trapped at the stress field of the extended defects.

1. Introduction

GaN has recently been the subject of considerable interest due to its optoelectronic properties. In particular the wide band gap (3.4 eV for wurtzite GaN) makes blue light applications feasible. Defect–induced electronic states in the band gap can significantly alter the optical performance. This fact becomes extremely important in laser devices, where parasitic components in the emission spectrum are highly undesirable. Moreover, point defects could be trapped in the stress field of extended defects giving rise to charge accumulated in the vicinity. The resulting electrostatic field leads to electron scattering which will severely affect the electron mobility (see Look and Sizelove[2] for a recent model). Therefore, there is considerable interest in understanding the microstructure of extended defects in GaN and their interaction with point defects.

In this paper we present the geometries, energetics and electrical properties of extended defects in GaN using an *ab initio* local density–functional (LDF) cluster method, *AIMPRO*, and a self–consistent charge density–functional tight–binding method *SCC–DFTB*. The latter can be used in large supercells and enables the formation energy of the defects to be found. Details of the methods and their application to GaN and oxygen related defect complexes in GaN have been given previously[3–5] and will not be repeated here.

Mat. Res. Soc. Symp. Proc. Vol. 537 © 1999 Materials Research Society

2. Threading Dislocations in GaN

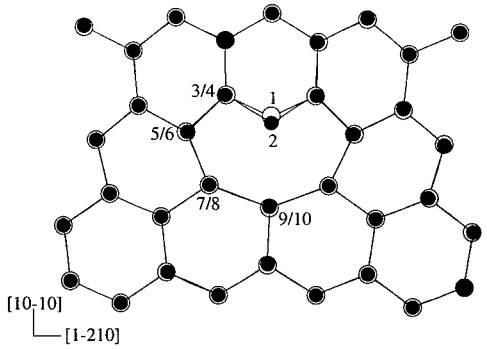
A. Threading Screw Dislocations

We consider first a screw dislocation with a full core[3]. Full core screw dislocations have recently been observed by Xin *et al.* using the high resolution Z-contrast imaging technique[6]. The presence of atoms so close to the dislocation axis leads to severely strained bond lengths distorted by as much as 0.4 Å. Consequently it is not surprising that such dislocations possess deep gap states ranging from $E_v + 0.9$ to $E_v + 1.6$ eV and shallow states around $E_c - 0.2$ eV. An analysis of these gap states revealed that the states above E_v are localised on N core atoms, whereas those below E_c are localised on both Ga and N core atoms. The strong distortion of the bonds of the core atoms leads to a high line energy within our calculations.

A similar calculation was then carried out with the hexagonal core of the screw dislocation removed giving a core with a narrow opening of ≈ 7.2 Å. The atoms on the walls adopt three fold coordinations similar to those found on the $(10\bar{1}0)$ surface. Thus Ga (N) atoms develop sp^2 (p^3) hybridisations which lower the surface energy and clean the gap from deep states[1]. Removing further material from the core resulted in a significantly higher line energy. Thus our calculations allow only diameters very much smaller than the diameter of nanopipes and we suppose that their formation is not due to Frank's mechanism.

B. Threading Edge Dislocations

The relaxed core of a threading edge dislocation with Burgers vector $a[1\bar{2}10]/3$ is shown in Fig. 1. It consists of a line of Ga and N atoms which have 3-fold coordination. With respect to the perfect lattice the distance between columns (1/2) and (3/4) [and the equivalent on the right] are 9 % contracted while the distance between columns (9/10) and (7/8) [and the equivalent on the right] are 13 % stretched. This atomic geometry for the threading edge dislocation has recently been confirmed by Xin *et al.*[6] using atomic resolution Z-contrast imaging. Consistent with our calculation they determined a contraction (stretching) of 15 ± 10 % of the distances between the columns at the dislocation core. See table 1 for the details of the geometry. The three-fold coordinated Ga (N) atoms (labelled 1 and 2 in Fig. 1 move in such a way to enhance sp^2 and p^3 hybridisation, respectively. This leads to empty Ga lone pairs pushed towards E_c, and filled lone pairs on N atoms lying near E_v, in a manner identical to the $(10\bar{1}0)$ surface. Thus threading edge dislocations are then also electrically inactive except possibly for shallow levels. It seems that the small bond distortions within the core makes it energetically uneconomic for the core of the threading edge dislocation to be open. We obtain a line energy for the edge dislocation which is by more than a factor of two lower than that found for the screw dislocation. This is mainly due to the lower elastic energy arising from the shorter Burgers vector.



Top view (in [0001]) of the relaxed core of the threading edge dislocation ($\mathbf{b} = \frac{1}{3}[1\bar{2}10]$). This geometry has recently been confirmed using the atomic resolution Z–contrast imaging technique[6]. The three fold coordinated atoms 1 (Ga) and 2 (N) adopt a hybridasation similar to the $(10\bar{1}0)$ surface atoms.

Table 1: Bond lengths, min-max (average) in Å and bond angles, min-max (average) in ^{o} for the most distorted atoms at the core of the threading edge dislocation ($\mathbf{b} = \frac{1}{3}[1\bar{2}10]$). Atom numbers refer to Fig. 1.

Atom	bond lengths	bond angles
1 ($Ga_{3x coord.}$)	1.85-1.86 (1.85)	112-118 (116)
2 ($N_{3x coord.}$)	1.88-1.89 (1.86)	106-107 (106)
3/4 ($Ga/N_{4x coord.}$)	1.86-1.95 (1.91)	97-119
5/6 ($Ga/N_{4x coord.}$)	1.92-2.04 (1.97)	100-129
7/8 ($Ga/N_{4x coord.}$)	1.94-2.21 (2.06)	94-125
9/10 ($Ga/N_{4x coord.}$)	1.95-2.21 (2.11)	100-122

In AlN, Wright *et al.*[7] have found, using a supercell geometry, that edge dislocations have an empty band of levels $\sim E_c - 2$ eV, while in n-type material, the core contains V_{Al} defects. The very much larger band gap of this material might be responsible for the differences of the properties of the edge dislocations from those in GaN.

To summarise, the density functional calculations reveal that the threading screw dislocations in their pure, i.e. impurity free form can exist with full cores and narrow open cores with diameters up to ≈ 7.2 Å. While full core screws are electrically active, open core screws induce no deep gap states. Threading edge dislocations in wurtzite GaN are stable with full cores and electrically inactive. However, the strained and 'dangling' bonds present in their cores could permit impurities and intrinsic defects to be trapped there.

3. Interaction of Oxygen with dislocations

A. Oxygen and Open Core Screw Dislocations

There is experimental evidence that oxygen acts as a donor in bulk GaN[8] and total energy calculations show that O sits on a N site[9]. Since the internal surfaces of screw dislocations are very similar to those of the low energy $(10\bar{1}0)$ surface, we investigated[10] the likely surface sites for oxygen replacing N atoms. We found that the energy of a neutral O_N defect is 0.8 eV lower at the relaxed $(10\bar{1}0)$ surface. This shows that there is a tendency for O to segregate to the surface. The added oxygen has an additional electron occupying a state near E_c. The defect has therefore a high energy and would attract acceptors resulting in a neutral complex. One possible acceptor, other than added dopants, would be a gallium vacancy (V_{Ga}) which acts as a triple acceptor and has been calculated to have a low formation energy in n–type GaN[11,12]. Consequently, we suppose that the surface oxygen concentration could be sufficiently large, and the oxygen atoms sufficiently mobile, that the three N neighbours of V_{Ga} at the $(10\bar{1}0)$ surface are replaced by O forming the V_{Ga}–$(O_N)_3$ defect.

Our calculations[10] showed that V_{Ga}–$(O_N)_3$ is more stable at the surface than in the bulk by 2.15 eV. Two O neighbours of the surface vacancy lie below the surface and each is bonded to three Ga neighbours, but the surface O is bonded to only two subsurface Ga atoms in a normal oxygen bridge site. The defect is electrically inactive with the O atoms passivating the vacancy in the same way as VH_4 in Si.

The question then arises as to the influence of the defect on the growth of the material. Growth over the defect must proceed by adding a Ga atom to the vacant site but this leaves three electrons in shallow levels near the conduction band resulting in a very high energy. This suggests that the defect can stabilise the surface and thus inhibit growth. From this we can conclude that such defects lead to the formation of nanopipes if we assume that during growth of the epilayers, either nanopipes with very large radii are formed which gradually shrink when their surfaces grow out, or there is a rapid drift of oxygen to a preexisting nanopipe. In either case the concentration of oxygen and V_{Ga}–$(O_N)_3$ defects increases at the walls of the nanopipe. The maximum concentration of this defect would be reached if 50% (100%) of the first (second) layer N atoms were replaced by O and further growth then would be prevented. It is, however, likely that far less than the maximum concentration is necessary to stabilise the surface and make further shrinkage of the nanopipe impossible. Provided oxygen could diffuse to the surface fast enough, the diameter and density of the holes would be related to the initial density of oxygen atoms in the bulk. This model requires that the walls of the nanopipe are coated with oxygen although the initial stages of formation of the pipe are obscure.

In conclusion, we have shown that oxygen has a tendency to segregate to the $(10\bar{1}0)$ surface and forms stable and chemically inert V_{Ga}–$(O_N)_3$ defects. These defects increase in concentration when the internal surfaces grow out. When a critical concentration of the order of a monolayer is reached, further growth is prevented. This model leads to nanopipes with $(10\bar{1}0)$ walls coated with GaO and supports the suggestions of Liliental-Weber *et al.* that nanopipes are linked to the presence of impurities[13].

B. Oxygen and Edge Dislocations

The V_{Ga}–$(O_N)_3$ defect considered above is electrically inactive at a $(10\bar{1}0)$ surface site but defects like V_{Ga}–$(O_N)_2$ and V_{Ga}–O_N act as single and double acceptors, respectively. If these were trapped in the strain field of a dislocation, then we would expect the dislocation to appear electrically active[5]. Indeed we find the energy of V_{Ga}–$(O_N)_n$ to be much lower at the dislocation core than in the bulk. This is because a neighbouring pair of three-fold coordinated Ga and N atoms are removed from the core and an O atom is inserted into the N site. The oxygen atom then lies in bridge site between two Ga atoms in a normal bonding configuration. Assuming Ga–rich growth conditions, O in equilibrium with Ga_2O_3 and n–type material the resulting formation energies of these defects lie between -2 and -3 eV. Thus the core of the dislocation will spontaneously oxidise if oxygen is mobile. In any event, we anticipate that the core will contain electrically active donor and acceptor pairs possibly giving rise to a negatively charged dislocation line. This is in agreement with recent temperature–dependent Hall–effect measurements[2].

In conclusion, the density functional calculations show that in wurtzite GaN the stress field of threading edge dislocations is likely to trap gallium vacancies and oxygen as well as their complexes resulting in a negatively charged dislocation line in n–type material.

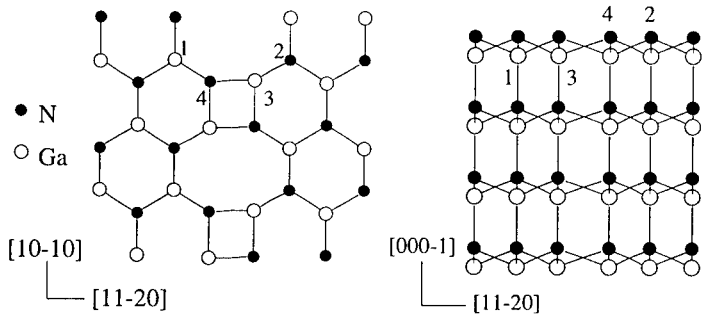
4. Domain boundaries on $\{11\bar{2}0\}$ planes

In addition to dislocations, two kinds of domain boundaries have also been observed[14–19]. They lie on $\{11\bar{2}0\}$ and $\{10\bar{1}0\}$ planes and following Xin *et al.*[19] are denoted by DB–I and DB–II respectively. Domain boundaries are either described in terms of a double position boundary (DPB) [otherwise termed a stacking mismatch boundary (SMB)] consisting of a different stacking sequence across the boundary, or an inversion domain boundary (IDB) which is characterised by a polarity inversion across the boundary. Domain boundaries of type DB–II have been explored extensively using transmission electron microscopy (TEM)[14,15,17,16] and theoretically by Northrup *et al.*[20] using the scf–LDA method with a plane wave basis.

In contrast to DB–II type boundaries which originate at the epilayer substrate interface the DB–I type boundaries found in a GaN sample grown by molecular beam epitaxy (MBE) on GaP extend only a short distance along the c–axis[19]. A high resolution Z–contrast image down [0001] reported by Xin *et al.*[21] shows clearly that DB–I has a *horizontal* displacement of $R_h = 1/2\langle 10\bar{1}0\rangle$. This configuration which is also called prismatic stacking fault is composed of four– and eight– fold rings along the fault. For an illustration see Fig. 2.

We investigated several models[22] corresponding to this horizontal displacement and found a double position boundary to possess the lowest domain wall energy. This double position boundary has an additional vertical displacement of $1/2\langle 0001\rangle$ giving a total displacement of $1/2\langle 10\bar{1}1\rangle$ as derived from TEM by Xin *et al.*[19] and is therefore denoted by DPB*–I. All atoms along the boundary are four–fold coordinated and form Ga–N bonds across the boundary (see Fig. 2). Since Ga–N bonds are very strong DPB*–I has a clearly defined spacing of $\sim$ 1.90 Å between the $\{11\bar{2}0\}$ planes at the boundary. Some of the bonds are quite distorted which makes that DPB*–I induces shallow electronic states $\sim$ 0.35 eV above VBM in the band gap. However, these states are not deep enough to be responsible for

the yellow luminescence which is centred at ≈ 2.2 eV and observed in n type GaN. On the other hand point defects may segregate to the DPB*-I boundary and change the electrical properties. We evaluated the formation energy of V_{Ga}^{3-} at the domain boundary and found it to be lower by 1.1 eV at pos. 3 with respect to a position in a bulk like environment. This suggests that if Ga vacancies diffuse easily in GaN a lot of them will be trapped at DPB*-I where they would introduce deep acceptor states and can act as electron traps, in agreement with recent electron energy loss spectroscopy (EELS) measurements by Natusch *et al.*[23].



Top view along [0001] (*left*) and side view along $[10\bar{1}0]$ (*right*) of the DPB*-I structure which has a total displacement of $1/2\langle 10\bar{1}1\rangle$. DPB*-I is found to possess the lowest wall energy of domain boundaries on $\{11\bar{2}0\}$ planes. Atom numbers 1 (2) refer to Ga (N) atoms in eight–fold rings close to the boundary, whereas atom numbers 3 (4) refer to Ga (N) atoms in four–fold rings with bonds across the boundary.

5. Summary

We have presented density-funcitonal calculations for a variety of extended defects observed in wurtzite GaN. All stable structures consist of four–fold coordinated atoms or possess pairs of three–fold coordinated Ga and N atoms which adopt energetically favorable sp^2 and p^3 positions as at the $\{10\bar{1}0\}$ surface. Apart from full–core screw dislocations which have very strained bonds and therefore induce deep states into the band gap, all other extended defects seem to possess only shallow gap states. However, point defects and impurities are likely to be trapped in the stress fields and could alter the electrical properties.

REFERENCES

1. J. E. Northrup and J. Neugebauer, Phys. Rev. B **53**, 10477 (1996).
2. D.C. Look and J.R. Sizelove, submitted to PRL 1998.
3. J. Elsner, R. Jones, P.K. Sitch, V.D. Porezag, M. Elstner, Th. Frauenheim, M.I. Heggie, S. Öberg and P.R. Briddon, Phys. Rev. Lett. **79**, 3672 (1997).
4. M. Elstner, D. Porezag, G. Jungnickel, J. Elsner, M. Haugk, Th. Frauenheim, S. Shuhai and G. Seifert, Phys. Rev. B **58**, 7260 (1998).
5. J. Elsner, R. Jones, M. Haugk, Th. Frauenheim, M.I. Heggie, S. Öberg and P. R. Briddon, Phys. Rev. B **58**, 12571 (1998).
6. Y. Xin, S. J. Pennycook, N. D. Browning, P. D. Nelist, S. Sivananthan, F. Omnès, B. Beaumont, J.-P. Faurie and P. Gibart, Appl. Phys. Lett. **72**, 2680 (1998).
7. A. F. Wright and J. Furthmüller, Appl. Phys. Lett. **72**, 3467 (1998).
8. C. Wetzel, T. Suski, J. W. Ager, E. R. Weber, E. E. Haller, S. Fischer, B. K. Meyer, R. J. Molnar and P. Perlin, Phys. Rev. Lett. **78**, 3923 (1997).
9. J. Neugebauer and C.G. Van de Walle, Festkörperprobleme **35**, 25 (1996).
10. J. Elsner, R. Jones, M. Haugk, R. Gutierrez, Th. Frauenheim, M. I. Heggie, S. Öberg and P. R. Briddon, Appl. Phys. Lett. in press (1998).
11. J. Neugebauer and C. Van de Walle, Appl. Phys. Lett. **69**, 503 (1996).
12. P. Bogulawski, E.L. Briggs and J. Bernholc, Phys. Rev. B **51** R17255 (1995).
13. Z. Liliental-Weber, Y. Chen, S. Ruvimov and J. Washburn, Phys. Rev. Lett. **79**, 2835 (1997).
14. Z. Sitar, M. J. Paisley, B. Yan, and R. F. Davis, Mater. Res. Soc. Symp. Proc. **162**, 537 (1990).
15. S. Tanaka, R. Scott Kern, and R. F. Davis, Appl. Phys. Lett. **66**, 37 (1995).
16. D. J. Smith, D. Chandrasekhar, B. Sverdlov, A. Botchkarev, A. Salvador, and H. Morkoc, Appl. Phys. Lett. **67**, 1830 (1995).
17. B. N. Sverdlov, G. A. Martin, H. Morkoc, and D. J. Smith, Appl. Phys. Lett. **67**, 2063 (1995).
18. J.-L. Rouvière, M. Arlery, A. Bourret, R. Niebuhr, and K. Bachem, Inst. Phys. Conf. Series **146**, 285 (1995).
19. Y. Xin, P. D. Brown and C.J. Humphreys, Appl. Phys. Lett. **70**, 1308 (1997).
20. J. E. Northrup, J. Neugebauer and L. T. Romano, Phys. Rev. Lett. **77**, 103 (1996).
21. Y. Xin, S. J. Pennycook, N. D. Browning, P. D. Nellist, S. Sivananthan, J.-P. Faurie and P. Gibart, *Nitride Semicond.* **482** 781, edited by F.A. Ponce, S.P. Den Baars, B.K. Meyer, S. Nakamura, S. Strite, Mat. Res. Soc., Pennsylvania (1998).
22. J. Elsner, M. Kaukonen, M. I. Heggie, M. Haugk, Th. Frauenheim and R. Jones, Phys. Rev. B in press (1998).
23. M.K.H. Natusch, G.A. Botton, R.F. Broom, P.D. Brown, D.M. Tricker and C.J. Humphreys, *Nitride Semiconductors* **482** 763, edited by F.A. Ponce, S.P. Den Baars, B.K. Meyer, S. Nakamura, S. Strite, Mat. Res. Soc., Pennsylvania (1998).

ELECTRON BEAM INDUCED IMPURITY ELECTRO-MIGRATION IN UNINTENTIONALLY DOPED GaN

M. Toth*, K. Fleischer** and M. R. Phillips*

*Microstructural Analysis Unit, University of Technology, Sydney, PO Box 123, Broadway, NSW 2007, Australia, matthew.phillips@uts.edu.au
** On leave from Technical University of Berlin

Cite this article as: MRS Internet J. Nitride Semicond. Res. 4S1, G3.30 (1999)

Abstract

Electron beam induced electromigration of O_N^+ and H^+ impurities in unintentionally n-doped GaN was investigated using cathodoluminescence (CL) kinetics profiling, CL imaging of regions pre-irradiated with a stationary electron beam, and wavelength dispersive x-ray spectrometry (WDS). The presented results (i) illustrate induced impurity diffusion in wide bandgap semiconductors, (ii) provide experimental evidence for the $(V_{Ga}\text{-}O_N)^{2-}$ model of yellow luminescence in GaN with low Si content[1], (iii) confirm the roles of O in frequently reported bound exciton and donor-acceptor pair emissions and (iv) suggest the involvement of O_N^+ and hydrogenated gallium vacancies in a blue emission in autodoped GaN.

Introduction

CL is light emitted due to recombination of e-h pairs generated by energetic electrons. CL kinetics profiles can be obtained by recording the CL signal as a sample is irradiated with the electron beam in a scanning electron microscope (SEM). Electron beam irradiation of an uncoated semiconductor or insulator produces a positive region at the beam impact point due to a loss of charge through the emission of secondary electrons. The positive region (of <50nm) is followed by a negative region produced by the electrons injected into the sample[2]. During electron beam irradiation CL intensity can change due to (i) diffusion of radiative or nonradiative centers in or out of the electron interaction volume, (ii) competitive recombination due to differences in recombination efficiencies between different luminescent centers, (iii) trapping of injected charge and consequent distortion of the interaction volume[2] and (iv) buildup of electron beam induced contamination on the sample surface and consequent CL absorption.

Experimental Procedure

The sample used in this study was an unintentionally n-doped 4μm epilayer of wurtzite GaN grown at 1040°C on a 25nm GaN buffer layer by metal-organic chemical vapor deposition. The buffer was grown at 550°C on a c-plane sapphire substrate. Trimethylgallium and ammonia were used as precursors. CL and WDS measurements were performed using an Oxford Instruments MonoCL2 scanning CL spectroscopy and imaging system and a Microspec WDS system both installed on a JEOL35C SEM with a liquid helium cold stage. The CL signal was dispersed by a 1200 lines/mm grating blazed at 500nm and detected using a Hamamatsu R943-02 peltier cooled PMT. Optical absorption measurements were performed using a Hitachi U3400 UV-VIS-NIR spectrometer. CL kinetics profiles were obtained by blanking the electron beam, driving the sample to a previously unirradiated region and by recording the CL signal as a function of time as the sample was irradiated with a stationary electron beam ("spot mode"). To

Mat. Res. Soc. Symp. Proc. Vol. 537 © 1999 Materials Research Society

minimize beam-induced effects during data acquisition, CL spectra and images were obtained using the minimum beam currents and dwell time (200μs per pixel) needed for satisfactory S/N ratios. CL spectra have been corrected for system response. Noise in CL kinetics profiles and asymmetries in beam induced features in CL images are contributed to by a strong dependence of ion diffusion on the local charge trap density (impurity and defect concentration). The features discussed below represent typical, reproducible behavior.

CL spectroscopy of GaN

CL spectra obtained using a beam energy (E_b) of 15keV and beam currents (I_b) of 0.5nA at 300K and 0.14nA at 4K are shown in figure 1(a). The room temperature spectrum consist of a near-edge emission at 3.4eV and the yellow luminescence (YL) centered on 2.07eV (FWHM = 540meV). The liquid He spectrum contains a donor-bound exciton (DX) peak[3] at 3.46eV (FWHM = 20meV) with a phonon replica at 3.39eV. The DX peak is contributed to by a free exciton (FX) emission not resolved as an individual peak in the spectrum[3]. A donor-acceptor pair (DAP) emission with 2 LO phonon replicas[3] are observed at 3.25, 3.16 and 3.07eV respectively. A blue luminescence (BL) is positioned at approximately 2.8eV while the YL is centered at 2.24eV (FWHM = 450meV). The features below 1.75eV are second order peaks. The DAP emission has been reported to be associated with O donors[4]. Ripples in the BL and YL bands are caused by the microcavity effect[5].

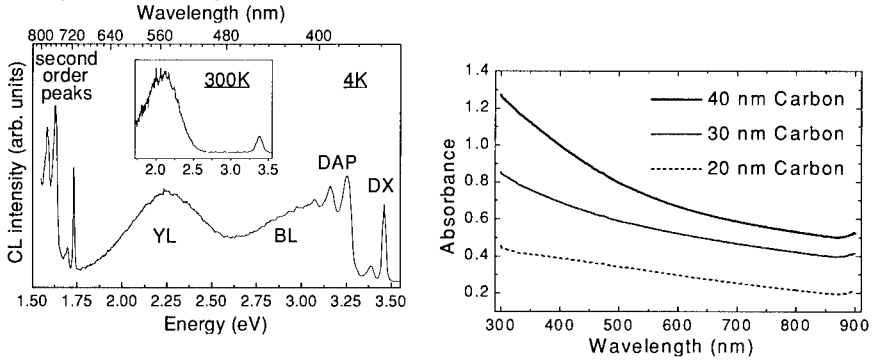


Figure 1. (a) CL spectra (E_b=15keV, corrected for system response) of autodoped GaN obtained at 4K (I_b=0.14nA, band pass=1nm) and 300K (inset, I_b=0.5nA, band pass=2.5nm). The high intensity of the second order peaks is a system response correction artifact. (b) Optical absorption spectra of 20, 30 and 40nm C films deposited under identical conditions.

YL has been attributed to a shallow donor-deep acceptor transition[6]. The most energetically favorable native deep acceptor in n-type GaN is the gallium vacancy (V_{Ga}^{3-}). V_{Ga}^{3-} can form a complex with the nearest neighbor O_N^+ and a less stable complex with the second nearest neighbor Si_{Ga}^{+1}. $(V_{Ga}\text{-}O_N)^{2-}$ and $(V_{Ga}\text{-}Si_{Ga})^{2-}$ complexes have low formation energies and are expected to play significant roles in YL generation[1,7].

Electron beam irradiation in an SEM can induce a C contamination layer on the specimen surface[11]. The contamination preferentially absorbs the blue end CL and hence modulates CL spectra and kinetics profiles. Optical absorption spectra of 20, 30 and 40nm C films are shown in figure 1(b). The observed decrease in the absorbance with increasing wavelength is used to explain some features of CL kinetics profiles presented in the following sections.

WDS kinetics of GaN

High concentrations of O_N^+ (approximately 10^{18} - 10^{20} cm^{-3})[13] can occur in n-type GaN, particularly in samples with low Si_{Ga}^+ content[1]. To determine the dominant impurity in the sample, $O_{K\alpha}$ and $Si_{K\alpha}$ lines were measured using WDS. Si was not detected under any conditions. WDS spectra showing the $O_{K\alpha}$ and $N_{K\alpha}$ lines acquired in spot mode before and after a 30min irradiation are shown in figure 2(a). The spectra were acquired using a beam energy of 25keV and a beam current of 300nA to obtain a sufficiently strong $O_{K\alpha}$ signal. The $O_{K\alpha}$ peak increased and the $N_{K\alpha}$ decreased during the irradiation. The $N_{K\alpha}$ decay is caused by x-ray absorption in a C contamination layer induced on the sample surface by the electron beam[11]. The $O_{K\alpha}$ increase is attributed to O_N^+ electro-diffusion from the surface and bulk towards the negative region of the electron interaction volume.

To verify that the $O_{K\alpha}$ increase is not related to the contamination layer, the spot mode $O_{K\alpha}$ and $C_{K\alpha}$ kinetics profiles shown in figure 2(b) were acquired from the sample. The $C_{K\alpha}$ intensity increased at a faster rate and, unlike the $O_{K\alpha}$, saturated after approximately 1400s. Oxygen contamination from residual gaseous O_2 is unlikely, as the SEM chamber pressure was approximately 2 x 10^{-6} Torr during irradiation experiments and (ii) the chamber was vented with dry nitrogen.

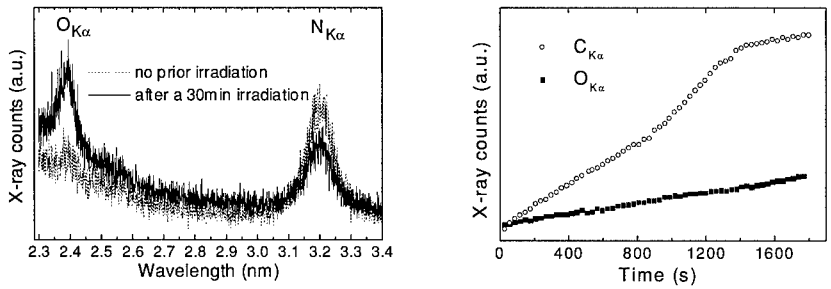


Figure 2. Qualitative WDS analysis of autodoped GaN (spot mode, E_b=25keV, I_b=300nA). (a) raw WDS spectra showing the $O_{K\alpha}$ and $N_{K\alpha}$ lines before and after a 30min irradiation, (b) $O_{K\alpha}$ and $C_{K\alpha}$ kinetics profiles. Si was not detected in the sample.

CL kinetics at room temperature

Room temperature CL kinetics profiles of the 3.4eV, BL and YL emissions are shown in figure 3(a). CL images of a region pre-irradiated using a stationary electron beam acquired using the above emissions are shown in figure 4. The room temperature kinetics profiles in figure 3(a) are dominated by the effects of H^+ and O_N^+ diffusion into and within the electron interaction volume. H^+ and O_N^+ impurities diffuse from the positive, near-surface region into the negative region of the interaction volume. The H^+ ions are most likely to originate at hydrogenated gallium vacancies and dangling bonds at the surface since interstitial hydrogen acts as an acceptor and has a high formation energy in n-type GaN[8]. The concentration of hydrogenated gallium vacancies hence decreases near the surface and increases in the bulk due to H^+ re-capture. Up to four H^+ ions can be incorporated at a gallium vacancy[12]. H^+ causes the vacancy energy levels to split and shift towards the valence band[12]. Outside the interaction volume,

O-related bonds are broken by short wavelength (UV) CL and O_N^+ impurities diffuse towards the negative region of the interaction volume.

At 25keV most of the detected BL and YL emissions originate approximately 300nm below the surface where the e-h pair generation rate maximizes[10]. Self-absorption of the near-edge emission causes most of the detected 3.4eV signal to be generated approximately 80nm below the surface[10], in the vicinity of the H depleted region. Radiative recombination in the H depleted region is reduced by (competitive) nonradiative surface recombination. In figure 3(a), O_N^+ diffusion causes the increase in the 3.4eV and BL emissions over the first 30s of irradiation and the long term increase in YL intensity. The 3.4eV intensity increases because of competitive recombination with YL; O_N^+ diffusion reduces the $(V_{Ga}\text{-}O_N)^{2-}$ complex contribution to YL generation in the vicinity of the positive near-surface region where most of the detected 3.4eV signal originates. The YL intensity increases because O_N^+ diffuses from the positive near-surface layer and from outside the interaction volume into the region where YL generation maximizes. The O rich region is seen as the large bright features in the CL images in figure 4. The dark contrast in the center each oxygen rich region appears when the 3.4eV emission starts to decrease (after 30s in figure 3(a)). This contrast and the decay in the 3.4eV kinetics profile are caused by accumulation of a C contamination layer and consequent CL absorption at the sample surface around the beam impact point. The C absorption effect is most pronounced at 3.4eV and decreases with increasing CL wavelength (BL and YL), in consistence with the C absorption spectra in figure 1(b).

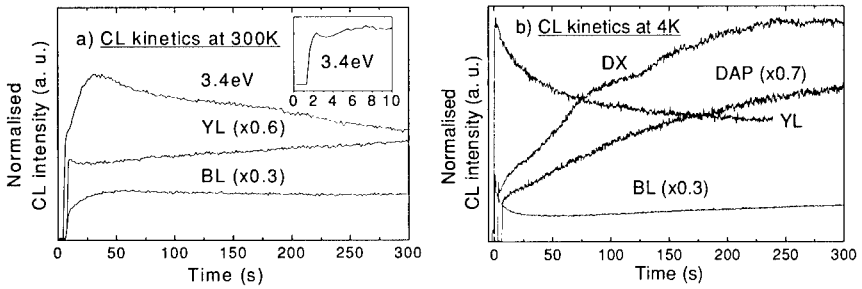


Figure 3. CL kinetics (E_b=15keV) of (a) 3.4eV, BL and YL emissions at 300K (I_b=3nA) and (b) DX, DAP, BL and YL emissions at 4K (I_b=6nA). The inset in (a) shows detail of the first 10s of the 3.4eV emission obtained using a lower electron dose (I_b=1.2nA).



Figure 4. CL images (T=300K, E_b=15keV, I_b=0.8nA, horizontal field width = 95μm) of a region pre-irradiated in 4 places using a stationary electron beam. The images were acquired using the: (a) 3.4eV, (b) BL and (c) YL emissions. Each spot irradiation was performed for approximately 10min (I_b=5nA).

H^+ diffusion causes the initial rapid, short lived decay of the 3.4eV (inset of figure 3(a)) and YL emission intensities. The 3.4eV decay reflects competitive recombination with YL centers activated by H^+ removal from gallium vacancies near the surface. The extent of the H^+ diffusion effect in spot mode kinetics profiles was found to vary across the sample due to a heterogeneous H^+ distribution in the sample. The variations in H concentration are probably caused by impurity congregation at extended defects and by deviations from thermodynamic equilibrium conditions during growth.

Electro-diffusion of both H^+ and O_N^+ into the negative region of the interaction volume, where most of the BL and YL signals are generated, causes the BL intensity to increase (figure 3(a)). We suggest a transition from a hydrogenated gallium vacancy to O_N^+ as a potential recombination path for BL generation. Under this assumption, the initial rapid increase in BL due to H^+ diffusion is caused by (i) effective creation of BL centers due to H passivation of gallium vacancies and (ii) a reduction in the concentration of competitive YL centers in the region where a majority of the BL signal is generated. The BL intensity maximizes after approximately 30s of irradiation and slowly decays due to BL absorption in the C contamination layer.

CL kinetics at base temperature

CL kinetics profiles of the DX, DAP, BL and YL emissions obtained at 4K are shown in figure 3(b). CL images obtained at 4K using the DX, DAP, BL and YL emissions after a 700s spot mode irradiation are shown in figure 5.

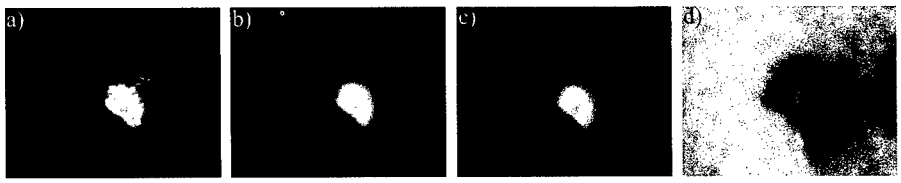


Figure 5. CL images (T=4K, E_b=15keV, I_b=0.2nA, horizontal field width = 42.5μm) of a region irradiated in spot mode (I_b=6nA) for 700s acquired using the: (a) DX, (b) DAP, (c) BL and (d) YL emissions.

At 4K the kinetics profiles change at lower rates and the impurity diffusion effected regions in CL images are smaller than at 300K due to a reduction in the thermal energy of the sample. The base temperature kinetics profiles differ from their room temperature counterparts due to the presence of the DX and DAP emissions. The DX and DAP emissions are not present at 300K due to thermal ionization of O_N. The DX and DAP kinetics profiles increase during irradiation because of O_N^+ diffusion into the negative region of the interaction volume. The generation profiles of the detected DX and FX signals maximize approximately 80nm below the surface due to self-absorption. The exponential nature of self-absorption of near-edge luminescence limits the O_N^+ diffusion contribution to the increase in DX intensity due to the nonlinear relationship between O_N^+ concentration in the negative region of the interaction volume and the measured increase in DX intensity. The apparent increase in DX intensity is contributed to by the FX emission which increases in the vicinity of the H^+ and O_N^+ depleted near-surface region due to a reduction in the concentration of competitive DX, DAP, YL and BL centers. The increase in DAP intensity due to O_N^+ diffusion is consistent with the suggestion that O_N^+ is the donor is involved in the DAP transition[4]. The rapid decrease in BL and YL intensities

during irradiation at 4K is probably caused by competitive recombination with DAP, DX and FX centers.

At 4K, the O_N^+ diffusion effected regions are small enough and the S/N ratio in the CL images is sufficiently high to resolve an O_N^+ depleted region around the O_N^+ enriched region in the BL and YL images. The dark contrast (figure 5(c) and (d)) indicates where the surplus O_N^+ has diffused from. The absence of a dark ring in the DX image is caused by an increase in the FX emission in the O_N^+ depleted region. Its absence in the DAP image can be explained by the acceptor distribution, assuming that the acceptor concentration is much lower than that of O_N^+. This assumption is plausible in light of the low O_N^+ and $(V_{Ga}\text{-}O_N)^{2-}$ formation energies in n-type GaN[1,7]. The DAP center concentration is hence governed by the concentration of the (negative) acceptors which diffuse away from the negative region of the interaction volume at an apparently low rate. The acceptor involved in the DAP transition has been suggested to be C^4, consistent with first principles calculations which show the C_N^- shallow acceptor to be the most energetically stable C state in n-type GaN[1].

Conclusion

Time resolved CL and WDS analysis of autodoped GaN was used to provide experimental evidence for the $(V_{Ga}\text{-}O_N)^{2-}$ model of yellow luminescence in GaN with low Si content[1], confirm the roles of O_N^+ in frequently reported bound exciton and donor-acceptor pair emissions and to suggest the involvement of O_N^+ and hydrogenated gallium vacancies in a blue emission in autodoped GaN.

We gratefully acknowledge Dr G. Li and Dr J. Zou for providing the sample used in this study.

References

1. J. Neugebauer and C. G. Van de Walle, Appl. Phys. Lett. 69 (4), 503 (1996).
2. J. Cazaux, J. Appl. Phys. 59 (5), 1418 (1986).
3. J. W. Orton and C. T. Foxon, Rep. Prog. Phys. 61, 1 (1998).
4. M. Leroux, B. Beaumont, N. Grandjean, P. Lorenzini, S. Haffouz, P. Vennegues, J. Massies and P. Gibart, Mat. Sc. & Eng. B 50, 97 (1997).
5. K. Knobloch, P. Perlin, J. Krüger, E. R. Weber, and C. Kisielowski, MRS Internet Journal of Nitride Semiconductor Research 3, 4 (1998).
6. P. Perlin, T. Suski, H. Teisseyre, M. Leszczynski, I. Grzegory, J. Jun, S. Porowski, P. Boguslawski, J. Bernholc, J. C. Chervin, A. Polian and T. D. Moustakas, Phys. Rev. Lett. 75 (2), 296 (1995).
7. T. Mattila and R. M. Nieminen, Phys. Rev. B 55 (15), 9571 (1996).
8. J. Neugebauer and C. G. Van de Walle, Phys. Rev. Lett. 75 (24), 4452 (1995).
9. M. Toth and M. R. Phillips, Scanning, (20), 425 (1998).
10. K. Fleischer, M. Toth, M. R. Phillips, J. Zou, G. Li and S. J. Chua, submitted for publication.
11. J. I. Goldstein, D. E. Newbury, P. Echlin, D. C. Joy, A. D. Romig, Jr., C. E. Lyman, C. Fiori and E. Lifshin, *Scanning Electron Microscopy and Microanalysis*, 2nd ed. (Plenum Press, New York and London, 1992), p. 514.
12. C. G. Van de Walle, Phys. Rev. B 56 (16), 10020 (1997).
13. G. Popovici, W. Kim, A. Botchkarev, H. Tang and H. Morkoc, Appl. Phys. Lett. 71 (23), 3385 (1997)

STATISTICAL ANALYSIS OF LOCAL COMPOSITION AND LUMINESCENCE IN InGaN GROWN BY MOLECULAR BEAM EPITAXY

S. Einfeldt,* T. Böttcher,* D. Hommel,* H. Selke,** P. L. Ryder,**
F. Bertram,*** T. Riemann,*** D. Rudloff,*** J. Christen ***

* Institute of Solid State Physics, University of Bremen,
PO Box 330440, 28334 Bremen, Germany
** Institute of Materials Physics and Structural Research, University of Bremen,
PO Box 330440, 28334 Bremen, Germany
*** Institute of Experimental Physics, University of Magdeburg,
PO Box 4120, 39016 Magdeburg, Germany

Cite this article as: MRS Internet J. Nitride Semicond. Res. 4S1, G3.33(1999)

Abstract

InGaN layers grown by molecular beam epitaxy are investigated in terms of their compositional homogeneity using transmission electron microscopy and cathodoluminescence spectroscopy performed with high spatial resolution. Strong fluctuations of the indium content were found in bulk-like layers, which could be partially reduced by modulating the indium flux during growth, i. e. by nominally growing a short period GaN/InGaN superlattice. For indium compositions above $x \cong 0.1$ this approach fails. Strained InGaN in quantum wells exhibits lateral fluctuations on an atomic scale and on a scale of several hundred nanometers. The results are discussed in view of the origin of inhomogeneous indium incorporation.

Introduction

Although the ternary alloy InGaN is established as the active material in optoelectronic devices operating in the short wavelength region, its epitaxial growth raises significant problems making it a subject of numerous investigations. The large lattice mismatch between InN and GaN is the reason for a miscibility gap in the phase diagram of InGaN, which could result in a demixing into phases of different composition during growth [1,2]. Moreover, the binding energy is significantly lower for InN compared to GaN, such that the thermal decomposition of InGaN causing the formation of indium droplets on the growth surface is a possible source of lateral variations of the composition [3]. Furthermore, compositional fluctuations arise from lattice relaxation of strained InGaN films on GaN due to V-shaped defects [4] and the composition pulling effect [5].

Direct evidence of compositional fluctuations in InGaN bulk-like layers and quantum well structures was given by spatially resolved measurements of optical and structural properties utilizing cathodoluminescence (CL) spectroscopy [6] and transmission electron microscopy (TEM) [7,8]. In this paper the attempt is started to distinguish between possible reasons for these fluctuations is with the object to draw conclusions for the optimization of expitaxial growth. Therefore, InGaN/GaN heterostructures were grown under different conditions and investigated by CL and TEM.

Experimental

Epitaxial growth was performed in a standard molecular beam epitaxy (MBE) system equipped with Knudsen cells for gallium and indium and a radio frequency plasma source (EPI Unibulb) operated with pure nitrogen gas. C-plane sapphire substrates were first nitridated using the nitrogen

Mat. Res. Soc. Symp. Proc. Vol. 537 © 1999 Materials Research Society

plasma followed by the growth of a GaN layer of variable thickness. Its growth temperature was 650°C for small layer thicknesses of 30 nm, 750°C for thicker layers and 830°C for cladding layers of quantum wells. InGaN was always grown at 650°C.

Cross-sectional specimens for TEM were prepared by mechanical grinding to about 5 μm thickness followed by xenon ion milling at 5 kV. TEM experiments were carried out on a Philips EM420 operating at 120 kV and equipped with a scanning TEM system and an energy-dispersive X-ray (EDX) spectrometer. Using a 10 nm electron probe the local chemical composition was deduced from the intensity ratio of the indium L- and gallium K-lines applying the standardless thin film method. Frequency distributions of the indium content were typically determined from EDX mappings of 256×200 points over a lateral length of 3 μm. Since the EDX mappings contain significant noise due to a limited integration time for each measured point, the real magnitude of compositional fluctuations is overestimated using the width of these distributions. Digital analysis of high resolution TEM lattice images (DALI) was applied to obtain mappings of the local lattice parameter c in InGaN/GaN quantum wells [9]. Assuming a Poisson ratio of 0.51 and neglecting relaxation of the fully strained wells the lattice parameters were converted into a local indium content. Since only relative variations of the indium content will be discussed, possible deviations from these assumptions are not relevant.

CL was measured in plan-view configuration usually at 5 K using a modified, high-resolution scanning electron microscope. Scanning the focused electron beam over an area of (2 μm × 3 μm) to (13 μm × 20 μm), a local spectrum was recorded at each of the 256×200 points. Typical changes of local spectra were found on a lateral length scale of a few hundred nanometer for all samples under investigation. The set of more than 50.000 local spectra was used to derive an integral (averaged) spectrum and a frequency distribution of the peak energies in the local spectra.

Results

Figure 1 illustrates the variation of the local composition in a typical bulk-like InGaN layer of 1 μm thickness on a thin GaN layer which in the following is referred to as conventionally grown. Based on X-ray diffraction (XRD) measurements the mean indium mole fraction of this samples amounts to $x = 0.08$. In ref. 10 the laterally averaged indium content was shown to decrease up to a layer thickness of 300 nm and to remain constant up close to the surface. This fact is confirmed by the two frequency distributions of the local indium content shown in Figure 1a, whose maxima are clearly shifted against each other. The large width of both distributions reflects the strong lateral fluctuation of the composition discussed in ref. 6. However, a quantization of the fluctuations should not be deduced from Figure 1a due to significant noise in the used EDX mapping. Since the band gap of InGaN naturally depends on the indium content, the energy of the near-band gap luminescence changes laterally across the sample which was shown in ref. 6 as well. Thus the frequency distribution of peak energies of the local CL spectra presented in Figure 1b is closely related to the local indium distribution. Obviously the distribution is broad and asymmetric as could be expected from Figure 1a. The superposition of all local spectra results in a large full width at half maximum (FWHM) of 0.35 eV for the peak in the integral spectrum shown in Figure 1b.

In the following possible origins of fluctuations will be discussed. The first parameter under consideration is the crystal perfection of InGaN. Extended defects are known to act as points of local lattice relaxation and by this can increase the local indium content without increasing strain energy. The defect density in InGaN is limited by the crystal perfection of the GaN grown below which improves with its layer thickness. Therefore, InGaN was grown under comparable conditions on GaN buffer layers of up to 1 μm thickness. Without showing results in this paper similar lateral fluctuations were found even for the thickest GaN buffer layers. In conclusion, if defects are the relevant source for compositional fluctuations, MBE growth of thick GaN layers does not sufficiently reduce their density to effectively improve the compositional homogeneity of InGaN.

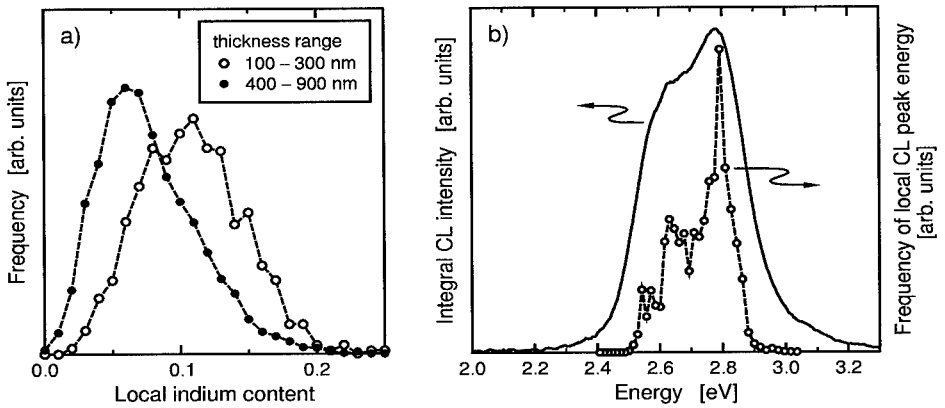


Figure 1: Conventionally grown $In_{0.08}Ga_{0.92}N$ (1000 nm) on GaN (30 nm): a) Frequency distribution of the local indium content as determined by EDX analysis averaged over InGaN layer thicknesses of 100–300 and 400–900 nm. b) Integral CL spectrum and frequency distribution of the local CL peak energy.

A second approach discussing fluctuations is to take the formation of microscopic indium droplets on the growth surface into consideration. Those droplets would lead to a lateral variation of the indium content but could also act as a drain for impinging indium atoms resulting in a variation of the mean indium content with layer thickness as described above. Johnson *et al.* first suggested to oppose droplet formation by modulating the indium flux during growth [3]. During GaN growth of a nominal InGaN/GaN superlattice with a period of about one or two monolayers, excess indium on the surface is supposed to be incorporated into the epitaxial film. In this paper this growth regime will be referred to as modulated growth. Results of two modulated grown InGaN layers differing in thickness (1.0 and 0.3 μm) and mean indium content (0.13 and 0.05 according to XRD measurements) are presented in Figure 2. Since no hints for the excistence of a superlattice were found by XRD or TEM measurements, a complete intermixing of InGaN and GaN probably occurs during growth. The mean composition of sample A is constant along growth direction as confirmed by EDX mappings, whereas this remains unclear for sample B as the low indium content makes appropriate measurements impossible. Although the indium distribution in Figure 2a still indicates the presence of lateral fluctuations, it appears to be less asymmetric than in the conventionally grown sample. The asymmetry for the last sample is a consequence of few extremely indium rich columns observed in the EDX mapping published in ref 8. Similar structures are not found in modulated grown samples. Moreover, EDX spot measurements carried out with long integration times at various points of the sample show the lateral variation of the indium content to be successfully reduced.

Figure 2b shows CL results of the modulated grown layers. In agreement with the distribution from Figure 2a, the asymmetry of the integral spectra as well as of the frequency distributions of the local peak energies is less pronounced compared to the conventionally grown sample. Moreover, the distinct multimodal character of the local peak energy distribution shown in Figure 1b can not be observed. However, considering sample A the local CL peak energy varies to the same extent as for the conventionally grown sample, resulting in an integral peak with a similar FWHM of 0.34 eV. In contrast, the value of the same FWHM for sample B amounts to only 0.19 eV and the lateral homogeneity is obviously improved as indicated by the very narrow frequency distribution of the local

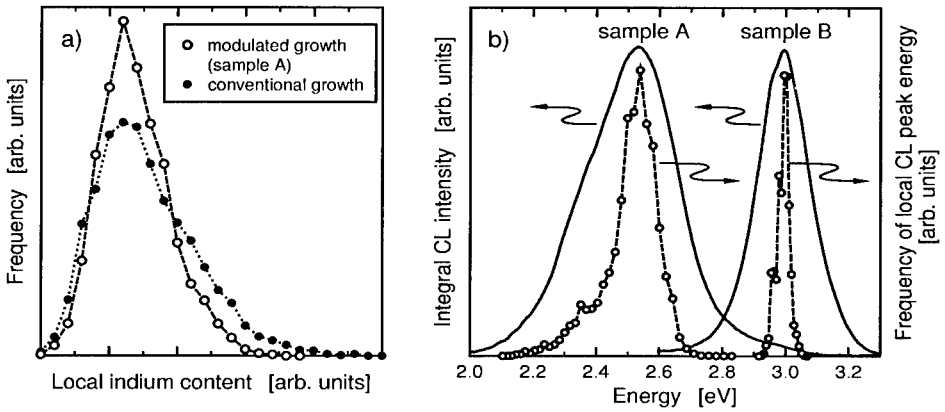


Figure 2: Modulated grown $In_xGa_{1-x}N$. Sample A (x = 0.13): 940 × (0.7 nm InGaN / 0.3 nm GaN) on 200 nm GaN. Sample B (x = 0.05): 300 × (0.5 nm InGaN / 0.5 nm GaN) on 30 nm GaN. a) Frequency distribution of the local indium content as determined by EDX analysis for sample A and the reference sample of Figure 1 averaged over InGaN layer thicknesses of 400–900 nm. b) Integral CL spectra and frequency distributions of the local CL peak energy for samples A and B.

CL peak energies. This has to be a consequence of the lower mean indium content and/or the smaller InGaN layer thickness of sample B.

Based on further CL experiments the extent of fluctuations in unstrained conventionally grown samples does not significantly change when the layer thickness is increased from 0.3 to 1 µm. Moreover, conventionally grown samples with mean indium contents comparably low as that of sample B show an integral luminescence peak which is broader by a factor of two and red-shifted by about 0.2 eV. This suggests that the improved homogeneity of sample B is a result of combining both the modulated growth technique and the low mean indium content. For higher indium contents as for sample A the concept of modulated growth fails. Due to the high indium fluxes required in this case the amount of indium on the surface is probably too high to be incorporated into the layer during the short period of nominal GaN growth. However, thermodynamically driven demixing as expected by the phase diagram of InGaN for higher indium contents could be an explanation as well.

A parameter worth to discuss in terms of fluctuations in InGaN is the strain state of the material. Karpov calculated phase diagrams for relaxed and strained InGaN, indicating the miscibility gap to extend into regions of relevant MBE growth temperatures and interesting indium contents up to 0.2 only in the case of relaxed material [2]. Thus one may expect significantly lower lateral fluctuations for fully strained InGaN layers as in InGaN/GaN quantum wells. Figure 3 summarizes the results for a multiquantum well (MQW) structure with conventionally grown InGaN wells containing roughly 10 % indium. High resolution TEM images confirm that the wells are fully strained. The mapping in Figure 3a generated by DALI clearly shows a lateral variation of the local lattice parameter within the wells. The fluctuations are irregular but marked by pronounced dot-like structures with diameters of 5 nm or less which are not correlated to extended defects. Similar structures were already reported by others [7]. Figure 3b shows the broad frequency distribution of the local indium content in the uppermost quantum well marked by several maxima. Despite the relatively small number of lattice points analysed for Figure 3b, the presented distribution is representative because analogous distributions for other wells look similar.

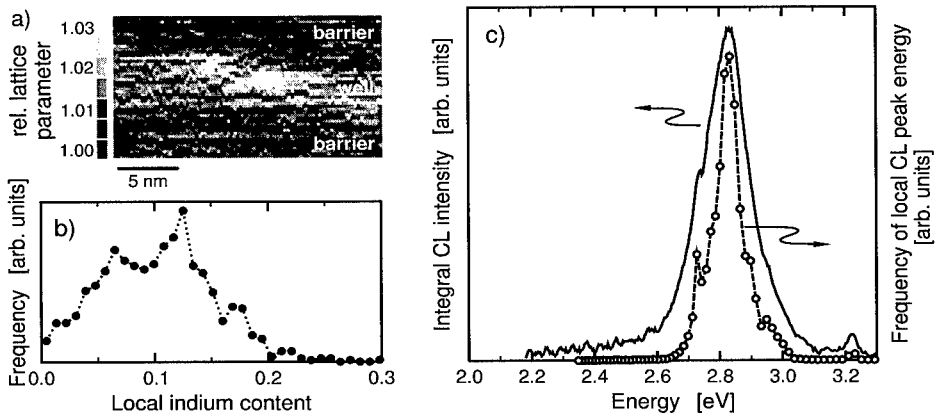


Figure 3: GaN/InGaN MQW: GaN (200 nm) / 5 × (5 nm InGaN / 10 nm GaN) / GaN (300 nm) / sapphire. a) Mapping of the local lattice parameter as determined by DALI. b) Frequency distribution of the local indium content in a single well. c) Integral CL spectrum and frequency distribution of the local CL peak energy.

Due to a different lateral extension of the EDX and DALI mappings the distribution in Figure 3b can not be simply compared to those in Figure 1a and 2a. However, Figure 3a prooves that variations of the indium content were not completly be avoided even in strained InGaN. Consequently these short-range fluctuations are rather related to the growth kinetics than to thermodynamical reasons. Also, it can not be excluded that fluctuations are caused by diffusion during growth of the final GaN capping layer carried out at higher temperatures compared to the well region.

Luminescence characteristics of the MQW are shown in Figure 3c. Due to the large well width they can be discussed without considering quantization effects. The FWHM of 0.18 eV for the integral CL peak is smaller than that extracted from Figure 1 corresponding to a thick layer grown under a similar indium flux. The frequency distribution of the local peak energy is narrower and less asymmetric as well. Thus the uniformity on a lateral scale accessible by CL is improved by the growth of strained quantum wells. However, mappings of the peak energy for this sample look similar to those of bulk-like samples published in ref. 6. They clearly show fluctuations on a scale of a few hundred nanometer roughly corresponding to the grain size of GaN. The point is how to reconcile this to the discussed dot-like structures on a nanometer scale. Excited carriers will relax into local potential minima due to diffusion resulting in a nearly constant recombination energy within their diffusion length as observed in CL mappings. It is not clear whether the dot-like structures observed by DALI form the dominant potential minima acting as preferred recombination centers. Assuming this case, the frequency distribution of mean dot composition obviously has to vary from grain to grain to be not inconsistent with the CL mappings. Furthermore, similar dot-like structures should occur in bulk-like samples as well. The difference between CL spectra in Figure 1b and 3c could arise from the undoubtedly different defect structures in these layers leading to a different impact of the dots on the recombination process.

Comparing the integral spectra of the MQW and the modulated grown sample B, similar values for the FWHM are surprisingly found although sample B is more homgeneous in the sense that its local peaks are broad but located at the same spectral position. Considering the higher density of extended defects in sample B compared to the MQW structure the broadening of the local spectra for

sample B is believed to result from short-range fluctuations of the composition and/or of the defect distribution which are not resolved by CL due to its limited resolution.

Conclusions

Strong compositional fluctuations in MBE grown InGaN bulk-like layers can be reduced by a modulated growth technique in case the indium content is sufficiently low. This fact is in agreement with the model of droplet formation on the growth surface assumed to be one possible source of inhomogeneities in the material. For higher indium concentrations the strain relaxation seems not to be the dominant factor for fluctuations because even strained quantum wells show fluctuations on the scale of the well width as well as of the GaN grain size. To understand these fluctuations quantum wells containing different amounts of indium and grown with different growth techniques have to be compared. Moreover, defects or dot-like structures should be identified as dominant recombination centers for which the growth on GaN with a significantly reduced dislocation density is a worthwhile approach.

Acknowledgment

This work was supported by the Volkswagen-Stiftung, contract no. I/74 452.

References

[1] I-hsiu Ho and G. B. Stringfellow, J. Cryst. Growth **178**, 1 (1997).
[2] S. Yu. Karpov, Internet J. Nitride Semicond. Res. **3**, 16 (1998).
[3] M. A. L. Johnson, W. C. Highes, W. H. Rowland, Jr., J. F. Schetzina, M. Leonard, H. S. Kong, J. A. D. Edmond and J. Zavada, J. Cryst. Growth **175/6**, 72 (1997).
[4] B. Jahnen, M. Albrecht, W. Dorsch, S. Christiansen, H. Strunk, D. Hanser and Robert F. Davis, MRS Internet J. Nitride Semicond. Res. **3**, 39 (1998).
[5] K. Hiramatsu, Y. Kawaguchi, M. Shimizu, N. Sawaki, T. Zheleva, Robert F. Davis, H. Tsuda, W. Taki, N. Kuwano and K. Oki, MRS Internet J. Nitride Semicond. Res. **2**, 6 (1997).
[6] H. Selke, P. L. Ryder, T. Böttcher, S. Einfeldt, V. Kirchner, D. Hommel, F. Bertram, T. Riemann and J. Christen, submitted to J. Cryst. Growth.
[7] Y. Narakuwa, Y. Kawakami, M. Funato, S. Fujita, S. Fujita and S. Nakamura, Appl. Phys. Lett. **70**, 981 (1997).
[8] H. Selke, M. Amirsawadkouhi, P. L. Ryder, T. Böttcher, S. Einfeldt, D. Hommel, F. Bertram, J. Christen, to be published in Mat. Sci. Eng. B.
[9] A. Rosenauer, S. Kaiser, T. Reisinger, J. Zweck, W. Gebhardt and D. Gerthsen, Optik **102**, 63 (1996).
[10] T. Böttcher, S. Einfeldt, V. Kirchner, S. Figge, H. Heinke, D. Hommel, H. Selke and P. L. Ryder, Appl. Phys. Lett. **73**, 3232 (1998).

RANGES OF DEPOSITION TEMPERATURES APPLICABLE FOR METALORGANIC VAPOR PHASE EPITAXY OF GAN FILMS VIA THE TECHNIQUE OF PENDEO-EPITAXY

D. B. Thomson, T. Gehrke, K. J. Linthicum, P. Rajagopal, and R. F. Davis

Department of Materials Science and Engineering, North Carolina State University, Box 7907, Raleigh, NC 27695-7907

Cite this article as: MRS Internet J. Nitride Semicond. Res. 4S1, G3.37 (1999)

ABSTRACT

Pendeo-epitaxy is a type of selective growth of thin films from the sidewalls of etched forms. The resulting films are suspended from the sidewalls and do not interface with the substrate. This process route has advantages over conventional lateral epitaxial overgrowth (LEO) techniques. In this research, pendeo-epitaxial growth of GaN films has been achieved on elongated GaN seed columns. The seed columns were etched from GaN grown on 6H-SiC (0001) substrates via metalorganic vapor phase epitaxy (MOVPE). Silicon nitride mask layers atop the GaN seed columns forced growth from the sidewalls. Pendeo-epitaxial growth of GaN was investigated using several growth temperatures. Higher growth temperatures resulted in improved coalescence due to greater lateral to vertical growth ratios.

INTRODUCTION

The III-Nitride community has shown considerable interest in the technique of lateral epitaxial overgrowth (LEO) of GaN and related materials. This interest was boosted by the report of Nakamura et al [1] of a projected laser diode lifetime of 10,000 hours in GaN-based devices fabricated using LEO. In conventional lateral epitaxy, GaN initially grows vertically within the openings of a patterned mask layer. Lateral growth of this material from these openings and over the masked areas results when the proper process parameters are employed. Transmission electron microscopy has shown that the masked areas stop the propagation of threading dislocations which arise from lattice mismatch at the GaN/AlN and AlN/6H-SiC interfaces. As such, the overgrown GaN regions contain four-to-six orders of magnitude lower density of dislocations relative to the unmasked regions [2].

Conventional single layer LEO films consist of alternating lateral regions of high and low defect density GaN. Device placement requires careful alignment with respect to the underlying mask stripes to take advantage of the superior quality material. Device size is limited to the width of the mask stripes. It is therefore desirable to have a continuous layer of low defect material over the entire GaN surface such that devices can be fabricated anywhere on the wafer without confinement to particular small areas.

Nam et al [3] have obtained the desired layer via repetition of the process route used to produce the first LEO GaN layer. In this case the second set of mask stripes were placed directly over the openings of the first LEO mask. This double LEO process requires two lithography steps and two depositions of GaN films beyond the growth of the initial seed layer. The process

Mat. Res. Soc. Symp. Proc. Vol. 537 © 1999 Materials Research Society

of pendeo-epitaxy (PE) is anticipated to yield the same result--a continuous layer of low defect density GaN--with only one lithography step and a single growth of GaN beyond the seed layer. As its name implies, pendeo-epitaxy is the epitaxial growth of crystalline material that hangs from freestanding forms and is suspended above the substrate. In the particular PE approach used in this research, etched columnar GaN forms are capped with a silicon nitride mask layer. As such, pendeo-epitaxial growth of the GaN films originates only from the sidewalls of these columns. The material grows laterally and vertically until it coalesces between and over the silicon nitride masks located atop the columns in the manner employed in the conventional LEO approach. A continuous layer of low defect density GaN is thus created. This process route is capable of producing continuous layers over large areas; it is limited only by the size of the substrate.

EXPERIMENTAL PROCEDURE

Pendeo-epitaxial growth of GaN films was performed in the manner shown schematically in Figure 1.

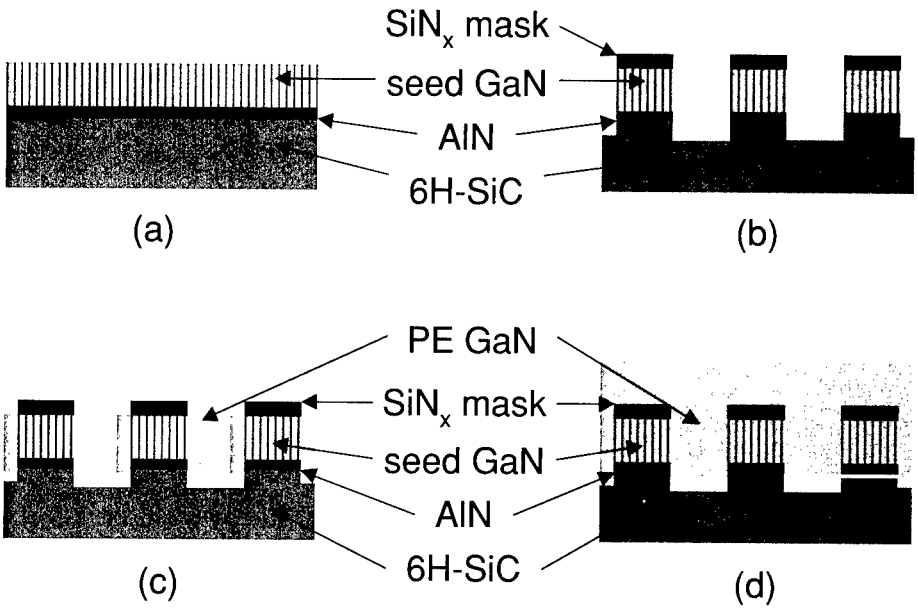


Figure 1. Schematic diagram showing the process steps for growth of pendeo-epitaxial GaN: (a) GaN seed layer, (b) etched GaN columns prior to PE growth, (c) partial growth of PE GaN showing growth only from the sidewalls, (d) coalesced growth of PE GaN.

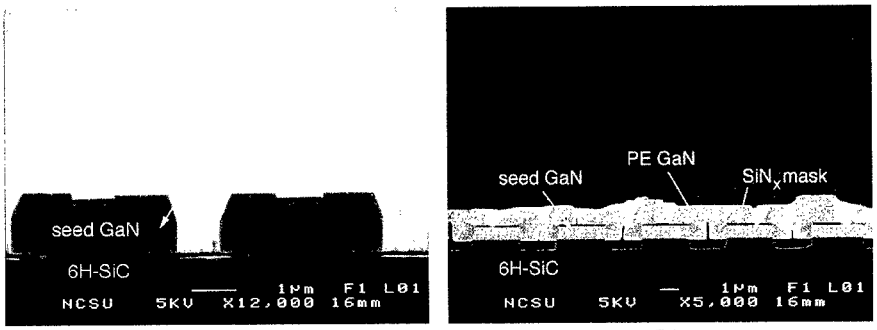
Each substrate was prepared via growth of a 1 μm thick GaN seed layer at 1000°C on an AlN buffer layer previously grown at 1100°C on a 6H-SiC(0001) substrate in a cold-wall, vertical, pancake-style, RF inductively heated metalorganic vapor phase epitaxy (MOVPE) system. Additional details of the growth experiments have been previously reported [4]. The consecutive deposition of a growth mask layer of silicon nitride (SiN_x) and an etch mask layer of nickel were achieved on the GaN seed layer using plasma enhanced chemical vapor deposition

(PECVD) and e-beam evaporation, respectively. The latter mask layer was patterned using standard photolithography techniques in parallel 2 μm wide stripes spaced 3 μm edge-to-edge and oriented along the $[1\bar{1}00]$ direction of the GaN film. Long columns containing the GaN seed material were produced via inductively coupled plasma (ICP) etching through the SiN_x, GaN and AlN layers and into the 6H-SiC substrate. Detailed procedures for the ICP etching have been previously reported [5]. The nickel etch mask was removed by dipping in HNO_3 for approximately five minutes. The samples were subsequently cleaned by consecutive dips in trichloroethylene, acetone, methanol, and HCl for five minutes each and blown dry with nitrogen.

Pendeo-epitaxial growth of GaN from the $(11\bar{2}0)$ sidewalls of the columns was performed at 45 torr and temperatures ranging from 1000°C to 1100°C via MOVPE. Reactants consisting of 26 μmol/min triethylgallium (TEG) and 1500 sccm ammonia were delivered into the growth chamber and entrained in 3000 sccm of hydrogen diluent. The morphological microstructure of the PE GaN layers was characterized using scanning electron microscopy (SEM-JEOL 6400 FE) in cross-section and plan view. Surface roughness was characterized by atomic force microscopy (AFM-Digital Instruments, Inc. Dimension 3000). Additional modes of PE growth of GaN and $Al_xGa_{1-x}N$ films and details regarding the procedures employed have been reported externally [6,7] and within this volume [8,9].

RESULTS AND DISCUSSION

Partially grown GaN pendeo-epitaxy after 30 minutes of growth at 1000°C is shown in Figure 2(a).



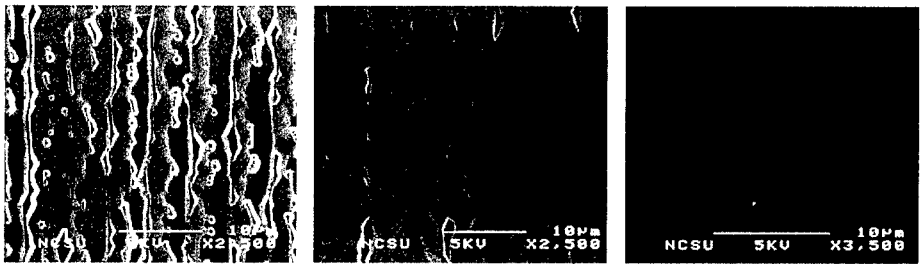
(a) **(b)**

Figure 2 Cross-sectional SEM micrographs of PE GaN grown at 1000°C for (a) 30 minutes, and (b) 80 minutes.

No nucleation of the GaN was observed on the surfaces of the etched SiC trenches. The SiN_x mask forced the GaN to grow only from the sidewalls of the etched GaN columns. Growth of the GaN could therefore begin only in the lateral directions. As the lateral growth progressed, the GaN began to grow vertically once (0001) top surfaces were created. As the vertical growth reached the top of the mask, lateral growth over the mask commenced. The high lateral to vertical growth ratio (approximately three to one) caused the GaN to wrap around the mask layers.

The results of allowing growth to continue for a total of 80 minutes at 1000°C are shown in Figure 2(b). Note the presence of the ~60° inclined $\{1\bar{1}01\}$ planes, which are the most stable and slowest growing planes in the GaN wurtzite crystal structure [3]. Gaps between the approaching growth fronts were also observed. These gaps suggest that the growth rates of the laterally growing faces decrease as they come into close proximity. The high vertical growth rates coupled with the continually decreasing space between converging growth fronts results in less GaN source material reaching these areas either by surface diffusion or by way of gaseous reactants.

The micrographs shown in Figure 3 demonstrate the effect of growth temperature on pendeo-epitaxial growth. Figure 3(a) is a plan view of the same film shown in Figure 2(b), which was grown for 80 minutes at 1000°C.

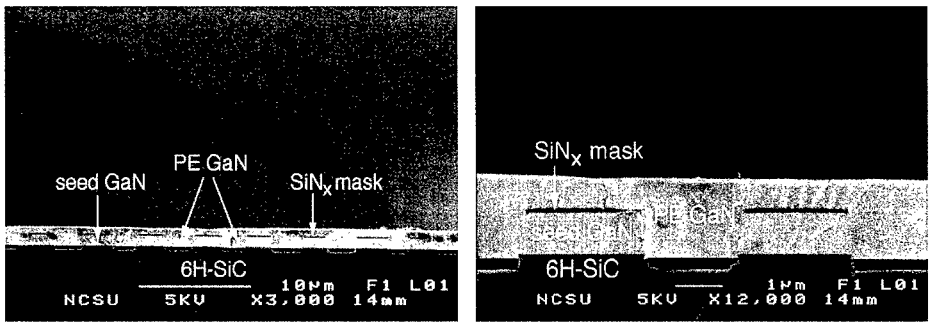


(a) (b) (c)

Figure 3 Plan view SEM micrographs of PE GaN grown for 80 minutes at temperatures of: (a) 1000°C, (b) 1050°C, and (c) 1080°C.

Coalescence of the GaN is observed in only a few regions. Figure 3(b) is a plan view of PE GaN grown for 80 minutes at 1050°C. The increase in temperature promoted the lateral growth such that the GaN coalesced over much of the surface. Growth for 80 minutes at a temperature of 1080°C resulted in a completely coalesced GaN surface shown in Figure 3(c). A faint periodicity consistent with the SiN_x stripe spacing is observed. Characterization of this surface using AFM revealed a RMS roughness of 1.32 nm. As the emphasis of the present study focused primarily on determination of parameters necessary for achieving coalescence, optimization of growth parameters subsequent to coalescence is expected to result in smoother PE GaN surfaces suitable for growing device structures.

A cross sectional view of coalesced PE GaN films grown for 80 minutes at 1080°C between and over several columns and masks, respectively, is shown in Figure 4(a). The origins of the darker areas have not yet been determined. Figure 4(b) is a higher magnification of coalesced PE GaN.



(a) (b)

Figure 4 Cross-sectional SEM micrographs of PE GaN grown at 1080°C for 80 minutes showing features at (a) low magnification and (b) high magnification.

The higher growth temperature promotes swift lateral growth until coalescence is achieved between the columns. As in the LEO approach, the GaN is observed to grow vertically over the edges of the SiN_x mask stripes and laterally across the top until it coalesces with the material growing laterally from the other side of the stripe.

CONCLUSIONS

Uniform layers of GaN anticipated to have very low dislocation densities over the entire GaN surface have been grown via the technique of pendeo-epitaxy. This process route is an improvement over conventional LEO and is a more efficient method of producing the same results as multiple layers of LEO. Growth temperature was observed to have a significant effect on the morphology of the PE GaN films. Coalescence improved with increasing growth temperatures due to greater lateral to vertical growth ratios. It is expected that pendeo-epitaxy will prove itself useful for improving device quality in optoelectronic and microelectronic applications.

ACKNOWLEDGMENTS

The authors acknowledge Cree Research, Inc. for the SiC wafers. This work was supported by the Office of Naval Research under contracts # N00014-96-1-0765 (Colin Wood, monitor) and N00014-98-1-0654 (John Zolper, monitor).

REFERENCES

1. S. Nakamura, The 2nd Intl. Conf. Nitride Semiconductors, Tokushima, Japan, October 25-31, (1997).
2. T. Zheleva, O.H. Nam, J.D. Griffin, M.D. Bremser and R.F. Davis, Mat. Res. Soc. Symp. Proc. **482**, 393 (1998).
3. O.H. Nam, T.S. Zheleva, M.D. Bremser, D.B. Thomson and R.F. Davis, Mat. Res. Soc. Symp. Proc. **482**, 301 (1998).
4. T.W. Weeks Jr., M.D. Bremser, K.S. Ailey, E.P. Carlson, W.G. Perry and R.F. Davis, Jpn. J. Appl. Phys. Lett., **67**, 401 (1995).
5. S.A. Smith, C.A. Wolden, M.D. Bremser, A.D. Hanser, R.F. Davis, and W.V. Lampert, Appl. Phys. Lett. **71**, 3631 (1998).
6. T.S. Zheleva, S.A. Smith, D.B. Thomson, K.J. Linthicum and R.F. Davis, J. Electr. Mat., submitted Nov. 1998.
7. K.J. Linthicum, T. Gehrke, D.B. Thomson, E.P. Carlson, P. Rajagopal, S. Smith and R.F. Davis, Appl. Phys. Lett., submitted Nov. 1998.
8. T. Gehrke, K.J. Linthicum, D.B. Thomson, P. Rajagopal, A.D. Batchelor and R.F. Davis, Mat. Res. Soc. Symp., this volume.
9. K.J. Linthicum, T. Gehrke, D.B. Thomson, K.M. Tracy, E.P. Carlson, S. Smith, T.S. Zheleva and R.F. Davis, Mat. Res. Soc. Symp., this volume.

PENDEO-EPITAXY - A NEW APPROACH FOR LATERAL GROWTH OF GALLIUM NITRIDE STRUCTURES

Tsvetanka S. Zheleva*, Scott A. Smith, Darren B. Thomson, Thomas Gehrke, Kevin J. Linthicum, Pradeep Rajagopal, Eric Carlson, Waeil M. Ashmawi, and Robert F. Davis
Department of Materials Science and Engineering,
North Carolina State University, Box 7907, Raleigh, NC 27695-7907
*Also with: Army Research Lab, 2800 Powder Mill Road, Adelphi, MD 20783
Corresponding Author (E-mail: Tsvetanka_Zheleva@ncsu.edu)

Cite this article as: MRS Internet J. Nitride Semicond. Res. 4S1, G3.38 (1999)

ABSTRACT

A new process route for lateral growth of nearly defect free *GaN* structures via Pendeo-epitaxy is discussed. Lateral growth of GaN films suspended from $\{11\bar{2}0\}$ side walls of [0001] oriented GaN columns into and over adjacent etched wells has been achieved via MOVPE technique without the use of, or contact with, a supporting mask or substrate. *Pendeo-epitaxy* is proposed as the descriptive term for this growth technique. Selective growth was achieved using process parameters that promote lateral growth of the $\{11\bar{2}0\}$ planes of GaN and disallow nucleation of this phase on the exposed SiC substrate. Thus, the selectivity is provided by tailoring the shape of the underlying GaN layer itself consisting of a sequence of alternating trenches and columns, instead of selective growth through openings in SiO_2 or SiN_x mask, as in the conventional lateral epitaxial overgrowth (LEO).

Two modes of initiation of the pendeo-epitaxial GaN growth via MOVPE were observed: Mode A - promoting the lateral growth of the $\{11\bar{2}0\}$ side facets into the wells faster than the vertical growth of the (0001) top facets; and Mode B - enabling the top (0001) faces to grow initially faster followed by the pendeo-epitaxial growth over the wells from the newly formed $\{11\bar{2}0\}$ side facets. Four-to-five order decrease in the dislocation density was observed via transmission electron microscopy (TEM) in the pendeo-epitaxial GaN relative to that in the GaN columns. TEM observations revealed that in pendeo-epitaxial GaN films the dislocations do not propagate laterally from the GaN columns when the structure grows laterally from the sidewalls into and over the trenches. Scanning electron microscopy (SEM) studies revealed that the coalesced regions are either defect-free or sometimes exhibit voids. Above these voids the PE-GaN layer is usually defect free.

INTRODUCTION

Recent studies on selected area growth (SAG) and lateral epitaxial overgrowth (LEO) of GaN structures on 6H-SiC [1-6] and Sapphire [7-10] have shown that the laterally overgrown regions have four-to-five orders of magnitude lower densities of dislocations compared to the regions of vertical growth. During the selective growth the GaN structure grows vertically and laterally at the same time, but the vertical growth dominates during the growth from the windows

Mat. Res. Soc. Symp. Proc. Vol. 537 © 1999 Materials Research Society

in SiO_2 (i.e. the growth rate of (0001) planes of GaN is higher than the growth rate of the GaN side facets), while the lateral growth dominates during the GaN growth over the SiO_2 (i.e. the growth rate of the GaN side facets is higher than the growth rate of the (0001) planes). Thus, the reduction in the defect density is associated with the change in the growth direction from vertical during the initial stages of growth from the openings in the SiO_2, to lateral over the SiO_2 in the subsequent stages of the lateral epitaxial overgrowth. Our previous studies on the development of the side facets morphology of the LEO-GaN as a function of the growth time [5,6], pointed that while the *crystallographic template* for the conventional vertical growth are the (0001) GaN faces, the crystallographic template for the lateral overgrowth are either the vertical $\{11\bar{2}0\}$ side facets if the SiO_2 stripes are oriented along $<1\bar{1}00>$ direction, or the 62° inclined $\{1\bar{1}01\}$ facets when the stripe edges are oriented along $<11\bar{2}0>$ direction, see the schematics in Fig.1. However, ***if the crystallographic template for the lateral overgrowth are the side GaN facets, then lateral growth would be possible even without a SiO_2 mask***. Then, a question rises: how to eliminate the SiO_2 mask and still to preserve the crystallographic templates for the vertical growth (the (0001) planes) as well as the crystallographic templates for the lateral growth - the side facets, $\{11\bar{2}0\}$ or the $\{1\bar{1}01\}$ planes, depending on the stripe orientation? The new approach for lateral growth of nearly defect free GaN structures, namely pendeo -epitaxy is an answer to the above question [11].

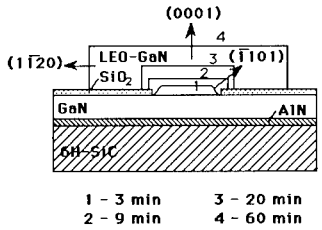


Figure 1. A schematic of the development of the side facet morphology of LEO-GaN structure as a function of the growth time in $[1\bar{1}00]$ orientation of the SiO_2 stripes. The vertical $\{11\bar{2}0\}$ side facets are the crystallographic templates for the lateral growth.

EXPERIMENT

The new technique, namely, pendeo-epitaxy has been developed and employed for the lateral growth of GaN films from the side walls of sequential and parallel GaN columns [11]. An alternative approach employed in the present research to achieve lateral and vertical epitaxy of GaN is comprised of the deposition of this material upon an aligned series of $<1\bar{1}00>$ oriented columns or wells of GaN having the vertical $\{11\bar{2}0\}$ side facets, as shown schematically in Fig.2.

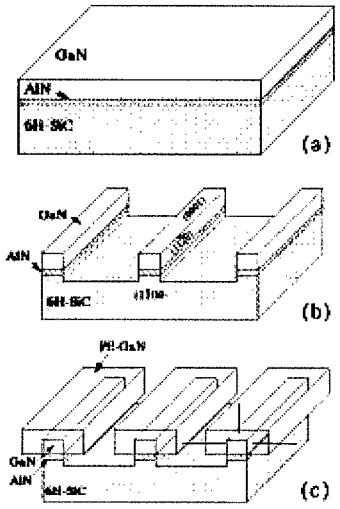


Figure 2. A schematic of the new process route for the pendeo-epitaxial growth of GaN layered structures. The PE-GaN growth includes the following major steps: (a) growth of a GaN layer on a AlN/6H-SiC substrate, (b) selective etching to form the side walls in the alternating GaN/AlN/substrate columns and trenches (wells), and (c) growth of the pendeo-epitaxial GaN layer before the coalescence.

The pendeo-epitaxial approach involves three major process steps: (i) growth of the underlying (seed) GaN layer on a suitable substrate, (ii) selective etching through a Ni mask [12] to form alternating GaN/AlN/substrate columns and trenches in the substrate, and (iii) growth of the pendeo-epitaxial GaN layer. No amorphous mask over the GaN seed layer is employed to support the laterally grown material and to separate it from a crystallographic surface. Thus, the lateral component of the GaN film grows free standing from the side walls of the columns into and over the etched trenches, as shown in Fig. 2(c). This laterally grown material does not make contact with the bottom surfaces of the trenches. As such, the term ***pendeo-*** (from the Latin "hangs on" or "suspends from") epitaxy was proposed to describe this process route [11]. Thus pendeo-epitaxy (PE), or the lateral growth from sidewalls of GaN posts into and over trenches provides an alternative process route to the conventional LEO technique, for growth of defect free GaN layers.

The side faces - crystallographic templates for the PE-GaN are prepared via etching of trenches (wells) or columns (posts), which include multiple sidewalls in the u-GaN/AlN/6H-SiC substrate-heterostructure. To form the columns and the trenches a dry etching technique with Cl_2 and Ar as process gasses, and Ni mask in inductively coupled plasma (ICP) system were utilized. Details of the dry plasma etching parameters of GaN related with the etch rates and selectivities as a function of the ICP power, dc bias, the gases pressure and flow rates, as well as gases percentages have been previously investigated [12]. The PE-GaN growth was performed via metalorganic vapor phase epitaxy (MOVPE) using triethylgallium (TEG) and ammonia

(NH_3) precursors, at 1080°C and 45 Torr. The TEG at 26 μmol/min and NH3 at 1500 sccm were used in combination with 3000 sccm H2 diluent. The morphology and microstructure of the pendeo-epitaxial GaN films was studied with scanning electron microscopy (SEM-JEOL 6400-FE); and transmission electron microscopy (TEM-TOPCON 002B).

RESULTS AND DISCUSSION

Two modes of initiation of the pendeo-epitaxial GaN growth via MOVPE were observed, as shown schematically in Fig. 3, and pictorially in Fig. 4 (a-d): Mode A - promoting the lateral growth of the $\{11\bar{2}0\}$ side facets into the wells faster than the vertical growth of the (0001) top facets; and Mode B - enabling the top (0001) faces to grow initially faster followed by the pendeo-epitaxial growth over the wells from the newly formed $\{11\bar{2}0\}$ side facets. SEM studies revealed that the coalesced regions are either defect-free or sometimes exhibit voids. Above these voids the PE-GaN material is usually defect free. Preliminary SEM and TEM studies reveal four-to-five times larger lateral growth rates of the PE-GaN compared to the growth rates for the LEO-GaN for a similar geometry. Studies with AFM revealed atomically flat top and side surfaces for the PE-GaN material.A four-to-five order decrease in the dislocation density in the pendeo-epitaxial GaN relative to that in the GaN columns (dislocation density ~$10^9 cm^{-2}$) was observed via TEM. TEM observations revealed that in pendeo-epitaxial GaN films the dislocations do not propagate laterally from the GaN columns when the structure grows laterally from the side walls into and over the trenches. The regions of coalescence of the pendeo-epitaxial GaN structures are usually defect free above the voids.

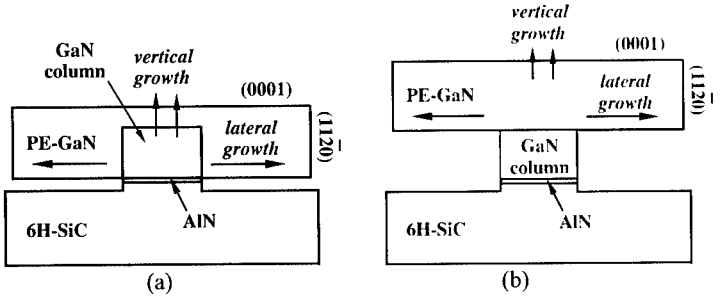


Figure 3. A schematic of the pendeo-epitaxial GaN growth in (a) Mode A and (b) Mode B.

Occasionally both growth modes are observed in a same column, i.e. on one side of the column - Mode A, and on the other side of the same column - Mode B. Our experiments revealed that slightly higher growth temperatures enhance the pendeo-epitaxial lateral growth from the side faces - Mode A. Thus differences in the morphology of the PE-GaN which appear as two different growth modes at same growth conditions are attributed to the fluctuations in the growth parameters as temperature and TEG flow rate, thus changing the diffusion characteristics. This suggests that there is a very narrow energy threshold associated with the parameters of the

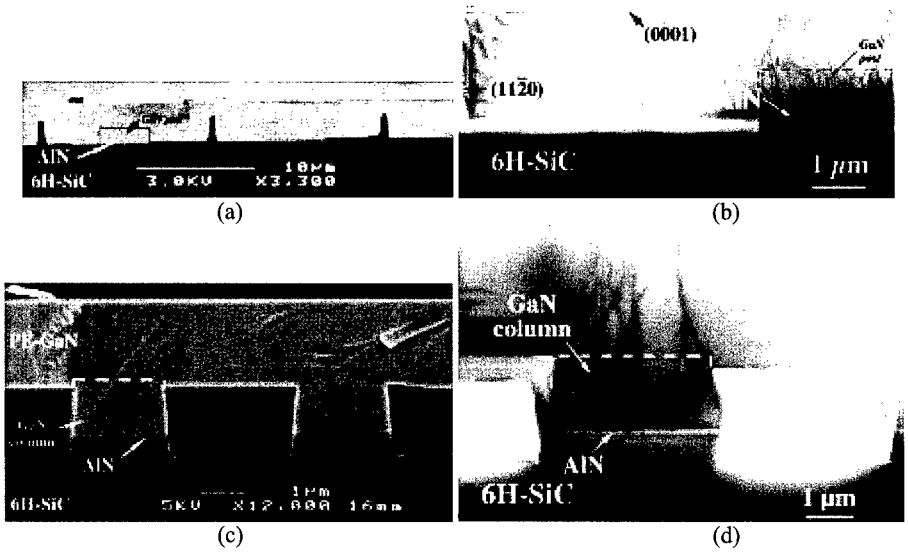


Figure 4. SEM (a) and TEM (b) micrographs of PE-GaN growth in Mode A; SEM (c) and TEM (d) of PE-GaN growth in Mode B.

growth kinetics as mean free path and average life times until adsorption and incorporation of the adatoms, which enhances the growth either along [11$\bar{2}$0] (Mode A), or along [0001] Mode B. Preliminary studies of the accommodation of the thermal stress in the PE-GaN structures reveal five-to-ten times reduction in the thermal stress compared to similar geometries of LEO-GaN structures.

Application of the pendeo-epitaxial growth technique in combination with a silicon nitride mask layer capping the seed GaN columns before the PE-GaN growth helps to achieve a continuous GaN layer of very low defects density within a single lithography step (see K. Linthicum et all., D. Thomson et all., and T. Gehrke et all., this volume).

SUMMARY

A new technique - ***pendeo-epitaxy*** has been developed and employed for the lateral growth of GaN films from the side walls of sequential and parallel GaN columns. The new approach for the pendeo-epitaxial growth of GaN layered structures involves the following major stages: (a) growth of a GaN layer on a suitable substrate; (b) selective etching through a mask to form alternating GaN/AlN/substrate columns and trenches in the substrate, and (c) growth of the pendeo-epitaxial GaN layer. The pendeo-epitaxial GaN growth revealed two modes of growth at similar growth conditions: Mode A: PE-GaN growth from the side {11$\bar{2}$0} walls of the GaN/AlN/substrate column into and over the wells, and Mode B: PE-GaN growth initiated from the (0001) planes followed by the lateral growth over the wells. Differences in the morphology

of the PE-GaN layers are attributed to the fluctuations in the growth parameters as temperature and TEG flow rate, thus changing the diffusion characteristics. TEM studies revealed that the laterally grown regions exhibit four-to-five times lower dislocation density, compared to the regions within the GaN column and these defects do not propagate laterally into the PE-GaN regions. SEM and TEM studies revealed four-to-five times larger lateral growth rates of the PE-GaN compared to the growth rates for the LEO-GaN for a similar geometry.

ACKNOWLEDGMENTS

The authors acknowledge Cree research , Inc. for the SiC wafers. This work was supported by the Office of Naval Research under contracts # N00014-96-1-0765 (Colin Wood, monitor) and N00014-98-1-0654 (John Zolper, monitor). T. Zheleva acknowledges the National Research Council and National Academy of Sciences, and Dr. Kenneth A. Jones from the Army Research Lab, Adelphi, MD for the personal support.

REFERENCES

1. O.H. Nam, M.D. Bremser, B. Ward, R. J. Nemanich, and R.F. Davis, Jpn. J. Appl. Phys, **36**, Part 2, No. 5A, L532 (1997)
2. T.S. Zheleva, O.H. Nam, M.D. Bremser, and R.F. Davis, Appl. Phys. Lett., **71**, (17) 2472 (1997).
3. O.H. Nam, T.S. Zheleva, M.D. Bremser, and R.F. Davis, Appl. Phys. Lett., **71,** (18), 2638 (1997).
4. T.S. Zheleva, O.H. Nam, J.D. Griffin, M.D. Bremser, and R.F. Davis, MRS Symp. Proc., **482,** 393 (1997).
5. O.H. Nam, T.S. Zheleva, M.D. Bremser, and R.F. Davis, J. Electr. Mater., **27**, No.4, 233 (1998).
6. T. Zheleva, O.H. Nam, W.M. Ashmawi, J.D. Griffin, R.F. Davis (submitted to J. Vac. Sci. & Technol).
7. A.Usui, H. Sunakawa, A. Sakai, A.A. Jamaguchi, Jpn. J. Appl. Phys. **36**, L899 (1997).
8. A.Sakai, H. Sunakawa, A. Usui, Appl. Phys. Lett. **71**, 2259 (1997).
9. H. Marchand, J.P. Ibbetson, P.T. Fini, P. Kosodoy, S. Keller, S. denBaars, J.S. Speck, U.K. Mishra, Materials Internet Journal - Nitride Semiconductor Research, **3**, 3 (1998).
10. Zhong H.Y., M.A.L. Johnson, T. McNulty, J.D. Brown, J.W. Cook Jr., J.F. Schezina, Materials Internet Journal -Nitride Semiconductor Research, **3**, 6 (1998).
11. T. Zheleva, S. Smith, D. Thomson, K. Linthicum, and R.F. Davis (submitted to J. Electr. Mater.)
12. S.A. Smith, C. Wolden, M.D. Bremser, A.D. Hanser, R.F. Davis , W.V. Lampert, Appl. Phys. Lett., **71** (25), 3631 (1997).

EFFECTS OF SURFACE PREPARATION ON EPITAXIAL GAN ON 6H-SIC DEPOSITED VIA MOCVD

Z. Y. Xie*, C. H. Wei*, L. Y. Li*, J. H. Edgar*, J. Chaudhuri**, and C. Ignatiev**

*Department of Chemical Engineering, Kansas State University, Manhattan, KS 66506
**Department of Mechanical Engineering, Wichita State University, Wichita, KS 67208

Cite this article as: MRS Internet J. Nitride Semicond. Res. 4S1, G3.39(1999)

ABSTRACT

A comparison was made of 6H-SiC surfaces etched with H_2, C_2H_4/H_2, and HCl/H_2, and the resulting crystal quality of epitaxial GaN films deposited on these substrates. To remove the many fine scratches and to smooth the rough surfaces typical of commercial SiC substrates, the Si-face 6H-SiC substrates were etched in H_2, C_2H_4/H_2, and HCl/H_2 at 1450 °C. GaN was subsequently deposited on these etched surfaces after first depositing a low temperature GaN buffer layer via metalorganic chemical vapor deposition (MOCVD). The surface morphologies after etching and after GaN deposition were characterized by atomic force microscopy and Normaski differential interference contrast microscopy, while the crystal quality of the GaN films was assessed by double crystal x-ray rocking curves and x-ray topography. 6H-SiC substrate surfaces were improved in terms of the removal of scratches and the reduction of surface roughness, and both surface morphology and crystal quality of the subsequently deposited GaN films were enhanced. However, the dislocation density was not decreased by the surface etching. The best GaN film was produced by etching the substrate in pure H_2 for 40 minutes before growth. Recommendations for the optimum substrate treatment are made.

INTRODUCTION

GaN has long been a promising material for optoelectronic devices operating in the blue to ultra-violet region [1-2], but the lack of GaN bulk crystals hinders the improvement of GaN epitaxial film quality. Sapphire is the most common substrate for GaN epitaxy, but because of large differences in lattice constants(13.8%) and thermal expansion coefficients(25.4%), the threading dislocation density is typically high in the GaN film. In contrast, 6H-SiC has a smaller lattice mismatch (3.5%) with GaN, making it a better candidate for GaN growth [3].

High quality GaN was successfully deposited on 6H-SiC substrates via MOCVD by several groups [4-6], but no detailed investigation of the effects of the 6H-SiC substrate surface treatment prior to GaN growth has been reported. Compared to sapphire, the surface quality of commercial 6H-SiC substrates is poor, containing various defects that may deteriorate the quality of epitaxial layer. Some defects, such as dislocations, and micropipes (holes approximately a micrometer in diameter) originate in the bulk of the substrate, while other defects such as ridges and scratches result from the lapping and polishing process. The later defects can be almost fully removed by etching the surface with hydrogen, with or without propane or HCl [7-8]. In the case of SiC epitaxy, defects in the film propagating from the substrate are minimized by in situ etching of substrates [7-8]. Furthermore, to avoid the formation of double position boundaries(DPB), 6H-SiC (off-axis) are etched and annealed to produce surface step heights corresponding to an integral multiple of the 6H-SiC unit cell (15 Å) [9-10]. The effect of the substrate is expected to be similar for GaN, hence, much attention should be given both to growth conditions and surface preparation of 6H-SiC for GaN epitaxial growth.

Mat. Res. Soc. Symp. Proc. Vol. 537 © 1999 Materials Research Society

In this letter, we studied the etching of 6H-SiC substrates using H_2, C_2H/H_2, and HCl/H_2 to remove scratches and pits. The quality of the substrtate surfaces thus produced were characterized, then GaN films were epitaxially deposited on these substrates. Finally, GaN films were examined, and a correlation between the surface treatment and film quality, both bulk structure and surface features, was developed.

EXPERIMENT

Substrate etching was performed in a cold-wall horizontal quartz reactor with an inside diameter of 50 mm operated at atmospheric pressure. The substrates were heated by a boron nitride coated graphite susceptor, and their temperature was measured both with an optical pyrometer and an R-type thermocouple, which were calibrated by the melting point of Si. The substrates were n-type, on-axis Si-face 6H-SiC (0001) wafers. Prior to etching, the substrates were ultrasonically degreased in organic solvents, dipped in 10% HF acid, and rinsed in deionized water. The etching temperature was fixed at 1450 °C for all experiments, and the other experimental conditions were summarized in Table I.

Table I. Summary of on-axis Si-face 6H-SiC (0001) substrate etching conditions.

Sample	Etching	Time (mins)	FWHM of DCX (arcsec)
1	no treatment	N/A	423
2	H_2 etching	10	395
3	H_2 etching	40	378
4	100 ppm C_2H_4/H_2 etching	40	398
5	0.5% HCl/H_2 etching	10	418

The subsequent growth of GaN was performed in a vertical-type MOVPE reactor operated at low pressure (76 Torr). Before loading into the reactor, the etched substrates were also degreased and dipped in HF acid. Trimethylgallium (TMG) and ammonia (NH_3) were the Ga and N sources, and Pd-cell purified H_2 was used as the carrier gas. The substrates in table I were loaded into the reactor simultaneously for one run, and preheated at 1100 °C for 10 minutes in H_2 for surface cleaning using a rf induction heater. To compare the effects of substrate etching on the subsequent GaN growth, the experimental conditions were the same for each run, and all deposits had a GaN buffer layer deposited at 550 °C.

The resulting etched 6H-SiC surfaces and the final GaN films were characterized by Nomarski differential interference contrast microscopy (NDIC) and atomic force microscopy (AFM). The quality of the GaN films was assessed by X-ray double crystal rocking curves and X-ray double crystal topography.

RESULTS AND DISCUSSION

The AFM image of an as-received on-axis Si-face 6H-SiC substrate shows randomly oriented scratches, varying in depth and width (Fig. 1a). Some extreme scratches were broad (~200 nm) and deep (10 nm), and disturbed the nucleation and surface morphology of the GaN film. Other defects such as micropipes and epitaxial pits were also observed (not shown). However, after etching 10 minutes in H_2, the scratches began to disappear, and a periodic texture

in one direction ([1-100]) of roughly parallel ridges formed as seen in Fig. 1b. The large shallow trench caused by a nonuniform etching rate on the (0001) surface at an early stage of etching. After etching for 40 minutes, the surface became smoother, and the scratches were completely removed (Fig. 1c). The terrace pattern was clear with a wider terrace (approximately 0.5 μm) than that (0.2 μm) in Fig. 1b. The etching behavior of C_2H_4/H_2 mixture was similar to the H_2 with a slightly slower etch rate. The width and smoothness of the terraces from C_2H_4/H_2 etching were narrower and rougher than those for H_2 etching due to the low etching rate. Fig. 1d shows the surface after etching in 0.5% HCl/H_2 for 10 minutes. Although the etch rate was higher, the residual scratches interrupted by terraces were still observed because of a short etching time. In terms of surface root mean square (RMS) values, the surface roughness was reduced from approximately 1.85 nm to below 1.0 nm for all etched 6H-SiC surfaces with a best surface morphology for H_2 etching for 40 minutes.

Our 6H-SiC etching results were largely consistent with other groups [8, 11] with the exception that no well-defined straight step structure was observed, which we contributed to the low etching temperature. Nevertheless, most scratches were removed using the above etching method, and the improved surfaces were obtained.

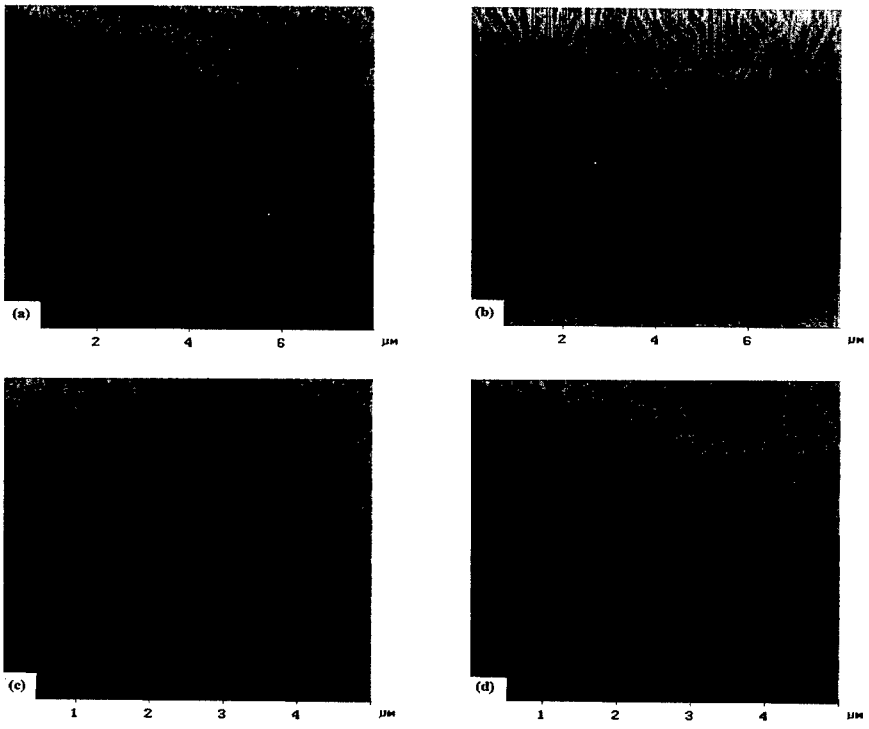


Figure 1. AFM images of 6H-SiC substrates, (a) as-received, no treatment, (b) after H_2 etching for 10 mins, (c) after H_2 etching for 40 mins, (d) after 0.5 % HCl/ H_2 etching for 10 mins.

The resulting GaN films had mirror-like surfaces as observed by the naked eye. However, some interesting features were illuminated by Normaski differential interference contrast microscopy. Fig 2a is the surface of the GaN film deposited on the untreated 6H-SiC substrate. There is a high density of cracks, caused by the residual stress for the heteroepitaxial growth [12-13], between which very smooth GaN surfaces dominate. A relatively high density ($1.6x10^3/cm^2$) of pits or pinholes (nominally 5μm in diameter) was mostly distributed along the cracks or at crack intersections. When GaN was deposited on the substrate etched by H_2 for 40 minutes, the resulting GaN surface was similar to that in Fig. 2a, except that the density of pits decreased by a factor of four ($4.0x10^2/cm^2$), and the pit diameter also decreased to 3 μm. Regardless of which etch was used, the density of pinholes was decreased compared to that of the untreated substrate surface.

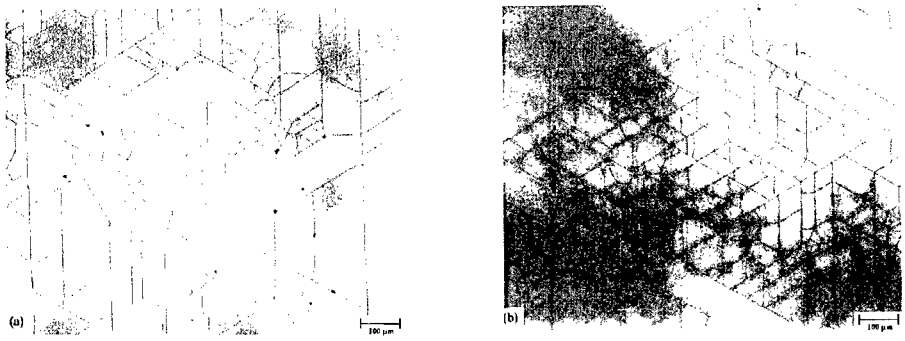


Figure 2. NDIC images of GaN films grown on 6H-SiC substrates, (a) as-received, no treatment, (b) after H_2 etching for 40 mins. Magnification: 200X

What caused these pits? To answer this question, we compared our GaN surface morphologies with those obtained by other groups. Weeks *et al.* [5] deposited GaN thin films on vicinal and on-axis 6H-SiC (0001) substrates using high temperature AlN buffer layers. Many small pits (nominally 30 nm in diameter) were observed, and the pit density was decreased by increasing the AlN deposition temperature. Random pinholes were also seen on the resulting GaN surfaces, and the density was decreased by increasing the GaN growth temperature. This phenomena was attributed to the possibly incomplete coalescence of GaN. Our observations were consistent with their results; however, the density of the pits increased when the 6H-SiC substrate surface quality was poor. The density and size of pits were increased greatly ($5.3x10^3/cm^2$ and 7.5 μm in diameter respectively) when a high density of etch pits was intentionally introduced on the substrate surface after the etching of the 6H-SiC substrate in 2% HCl/H_2 for 30 minutes at 1450 °C. Therefore, the incomplete coalescence of GaN was attributed to the micropipes or deep pits originating on the 6H-SiC substrate surface. GaN nucleation on these defects is difficult; if nucleation does occur, the GaN can not fill the defects, and leaves the GaN can not completely coalesce on these defects. Not only circular defects (pits or holes), but also wide and deep scratches can cause the incomplete coalescence of GaN films. Fig. 3a shows GaN surfaces separated by several deep and large scratches. The rough GaN surface was due to the unoptimized growth condition. The side walls of scratches on the 6H-SiC substrates have different orientations, which results in low growth rate or growth direction not parallel to c-axis, compared to the growth on the basal plane of (0001). Sometimes, even shallow scratches

disturbed the nucleation and growth of GaN. As shown in Fig. 3b, the GaN growth pattern was disturbed by the scratches with concentrated steps grown along the scratches. The reason of the resulting pinholes on GaN films will be further studied and presented in another paper.

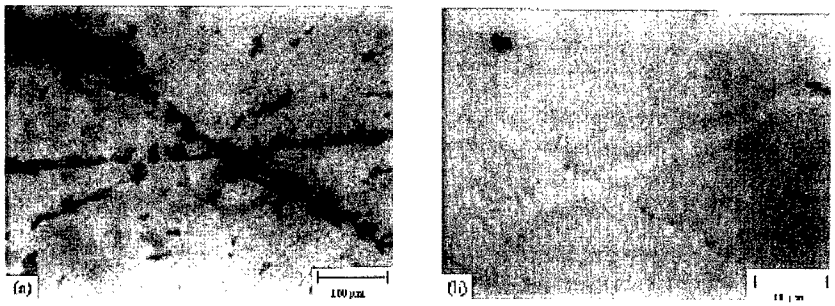


Figure 3. NDIC images of GaN film surfaces, (a) incomplete coalescence of GaN film separated by the substrate scratches, (b) the GaN film surface was disturbed by the scratches. Magnification: 400X.

Table I. displays the FWHM of the resulting GaN films deposited on the substrates etched at different conditions. The results are consistent with surface quality as evaluated by AFM. The FWHM of the GaN film grown on as-received substrate (sample1) had highest value, and thus the poorest crystal quality. The FWHM decreased with the increasing of H_2 etching time (sample 2 and 3). The crystal quality of the GaN film deposited on sample 4 was between sample 2 and 3 due to the slower etching rate with the adding of C_2H_4. The last sample (sample 5) had a FWHM value close to sample 1, since the residual surface scratches were not completely removed. Although the FWHM has high values caused by unoptimized growth conditions, these values are comparable to each other because they were deposited in the same run. As a result, the GaN deposited on the 40 minute H_2 etched substrate has the best quality, which is consistent with the AFM results.

An x-ray double crystal topograph was performed on sample 3. The reflection direction was [00.2]. The low angle grain boundaries were clearly identified to be repeated in the film. Linear defects were screw and mixed dislocations, which are common both in SiC substrates and GaN films. There is no evident difference between GaN samples deposited on untreated or etched 6H-SiC substrates. Dislocation defects presents in the substrates would propagate into epitaxial film, and can not been removed by the etching method.

CONCLUSIONS

In summary, the as-received commercial 6H-SiC substrates were etched using H_2, C_2H_4/H_2, and HCl/H_2 with a best surface improvement for the etching in H_2 for 40 minutes. The surface morphologies of those samples deposited on the etched substrates improved in terms of the decreasing of the pinhole density. These pinholes and other defects were attributed to the scratches, micropipes, and pits originating on the as-received 6H-SiC substrates. The crystal quality was increased as measured by DCX. However, the density of dislocation was not

decreased by the substrate surface etching. The optimized etching condition is a 40-minute H_2 etching at 1450 °C which was verified by the resulting GaN film surface morphology, and narrowing of FWHM of DCX. The improvement of GaN films in surface morphology and crystal quality is a direct result of the improved substrate surfaces. Therefore, the surface etching of 6H-SiC is an effective way to improve the quality of GaN epitaxial films until the surface defects of as-received 6H-SiC substrates are reduced.

ACKNOWLEDGMENTS

The authors gratefully acknowledge financial support by National Science Foundation (NSF) grant number DMR-9627333.

REFERENCE

1. G. Jacob, M. Boulou, and D. Bios, J. Lumin. **17**, 263 (1978).
2. H. Amano, N. Sawaki, I. Akasaki, and Y. Toyoda, Appl. Phys. Lett. **48**, 353 (1986).
3. M. E. Lin, B.Sverdlov, G. L. Zhou, and H. Morkoc, Appl. Phys. Lett. **62**, 3479 (1993).
4. S. Tanaka, S. Iwai, and Y. Aoyagi, J. Cryst. Growth **170**, 329 (1997).
5. T. W. Weeks Jr., M. D. Bremser, K. S. Ailey, E. Carlson, W. G. Perry, E. L. Piner, N. A. El-Masry, and R. F. Davis, J. Mater. Res. **11 (4)**, 1011 (1996).
6. C. F. Lin, H. C. Cheng, G. C. Chi, M. S. Feng, J. D. Guo, J. M. Hong, and C. Y. Chen, J. Appl. Phys. **82 (5)**, 2378 (1997).
7. J. A. Powell, D. J. Larkin, and P. B. Abel, J. Electron. Mater. **24**, 295 (1995).
8. C. Hallin, F. Owman, P. Mårtensson, A. Ellison, A. Konstantinov, O. Kordina, and E. Janzén, J. Cryst. Growth, **181** 241 (1997).
9. F. Owman, C. Hallin, P. Mårtensson, and E. Janzén, J. Cryst. Growth **167**, 391 (1996).
10. D. J. Smith, S.-C. Y. Tsen, B. N. Sverdlov, G. Martin, and H. Morkoc, Solid-State Elec. **41 (2)**, 349 (1997).
11. S. Karisson, and N. Nordell, Mater. Sci. Forum **264-268**, 363 (1998).
12. K. Hiramatsu, T. Detchprohm, and I. Akasaki, Jpn. J. Appl. Phys. **32**, 1528 (1993).
13. S. Nakamura, J. Cryst. Growth **170**, 11 (1997).

High Quality Hydrothermal ZnO Crystals

M. Suscavage, M. Harris, D. Bliss, P. Yip, S.-Q. Wang, D. Schwall, L. Bouthillette, J. Bailey,* M. Callahan,* D. C. Look,** D. C. Reynolds,** R. L. Jones,*** and C. W. Litton***

Air Force Research Laboratory, Sensors Directorate, Hanscom AFB, MA 01731, U.S.A.
*Solid State Scientific Corporation, Hollis, NH 03049, U.S.A.
**University Research Center, Wright State University, Dayton OH 45435, U.S.A.
***Air Force Research Laboratory, Materials and Manufacturing Directorate, Wright-Patterson AFB, OH 45433, U.S.A.

MRS Internet J. Nitride Semicond. Res. 4S1, G3.40(1999)

ABSTRACT

Zinc Oxide crystals have historically been grown in hydrothermal autoclaves with a basic mineralizer; however, doubts have been raised about the quality of such crystals because they have often exhibited large x-ray rocking curve widths and low photoluminescence (PL) yield with large linewidths. Several ZnO crystals were grown hydrothermally and sliced parallel to the c-plane. This resulted in opposite surfaces (the C^+ and C^-) exhibiting pronounced chemical and mechanical differences. Different surface treatments were investigated and compared by PL both at room temperature and liquid helium temperatures, and by double axis X-ray rocking curve measurements. The high quality of hydrothermally-grown ZnO is substantiated by the narrow rocking curve widths and sharp PL peaks obtained. A critical factor in obtaining these results was found to be surface preparation.

INTRODUCTION

Zinc oxide is a wide band-gap semiconductor (3.37eV) [1] with potential for applications as emitter devices in the blue to ultraviolet region and as a substrate material for GaN based devices. Because of its high vapor pressure, growth of ZnO from the melt is difficult, and growth by vapor deposition is difficult to control. Hydrothermally grown ZnO has been used previously[2] for surface acoustic wave devices, which do not need the high quality surface that optical or semiconductor device applications require. Therefore, we have performed an initial study of surface preparation and subsequent characterization on hydrothermally grown ZnO in order to produce surfaces suitable for epitaxy.

EXPERIMENTAL

Hydrothermal autoclaves made of high strength steel were used for crystal growth. Because of the high normality of the mineralizing solution, a sealed platinum liner (see reference 2 for an example) was used to isolate the crystal growth environment from the walls of the autoclave.[2] The mineralizer solution was a mixture of Li_2CO_3 , 4 N KOH, and 4 N NaOH, with the fill quantity at 80%. The nutrient was prepared from 99.99% ZnO (Alfa Aesar) powder having particle size < 3μm, which was sintered for 4 hrs in air at 1350°C in a platinum crucible. The seeds were (0001) plates of ZnO from previous hydrothermal growth runs. During growth, the nutrient zone was at 355°C with a temperature gradient of 10°C declining towards the seed zone. Growth rates in the [0001] directions on the basal seed plates averaged 10 mils per day for the 30

Mat. Res. Soc. Symp. Proc. Vol. 537 © 1999 Materials Research Society

day runs, but growth was anisotropic: the ratio of growth rates between the fast (C^+) and slow (C^-) growth directions was 3 to 1.

Wafers were sliced and the C^+ and C^- planes were identified by etching in nitric acid, following the method developed by Mariano and Hanneman.[3] Surface properties were analyzed by : double axis x-ray rocking curve with a high resolution four circle x-ray diffractometer; room temperature PL with a 0.25m grating monochrometer, ccd detector, and a 275nm, 5ns pulsed variable wavelength laser source; PL at 4 K with a 1.26m grating spectrometer and at 2.1 K with a high resolution 4.0m grating spectrometer, both equipped with an RCA C31034A photomultiplier and employing a HeCd laser.

For this study, two different surface conditions or surface treatments were studied: a mechanical polish provided by a commercial service, and a chemomechanical polish performed by Eagle-Picher Corporation. We also compared our hydrothermal ZnO (grown at AFRL/Hanscom) to vapor-phase grown ZnO provided by Eagle-Picher. For this comparison, low temperature PL was used to evaluate the presence or absence of excitonic peaks.

RESULTS AND DISCUSSION

The crystal growth characteristics of hydrothermal ZnO are dictated by anisotropy between the two opposite surfaces of the basal plane. The opposite sides of a basal plane wafer have different atomic arrangements at their surfaces due to this anisotropy. That is, the C^+ side comprises a Zn-rich layer, and the C^- side comprises an O-rich layer. The resulting electronic charge distribution is illustrated in Fig. 1, adapted from the work of Mariano and Hanneman.[3]

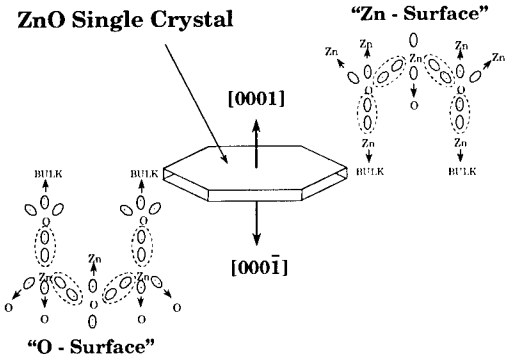


Figure 1. Electronic Charge Distribution of Zinc Oxide.

Typically, seeds were slices cut parallel to the basal plane to maximize the yield of (0001) wafers. The growth habit of hydrothermal ZnO crystals grown on basal plane seeds is shown in Fig. 2.[4] For crystal growth in the [0001] direction or C^+ sector, the growth rate was faster and the crystal color is clear to light yellow-green. For the [000$\bar{1}$] direction or C^- sector, the growth rate was about 1/3 as fast and the color is typically dark green. Slices were cut as shown from the light green and dark green sectors to distinguish between their chemical and electronic properties. Because of the different growth rates, we speculate that the different colors are due to a difference in impurity incorporation between the two sectors.

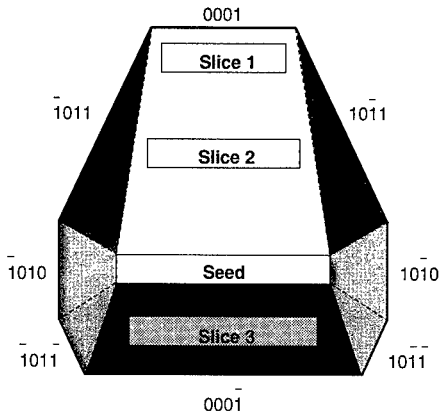


Figure 2. Growth habit of hydrothermal Zinc Oxide.

Trace analysis by glow discharge mass spectrometry (GDMS) revealed a slight difference in impurity concentration between the two sectors. The dark sector contains 3-5 ppm of iron, about twice as much as the light sector. This result is similar to other reports on ZnO.[4] The light sector contains 5-6 ppm each of aluminum and silicon, twice as much as the dark sector. Analysis of the free electron concentration by temperature dependent Hall effect revealed further differences. The dark green sector had a low resistivity, with a free carrier concentration of $3x10^{18}$ cm^{-3} at room temperature. The light green sector showed high resistivity, with room temperature electron concentration of $2x10^{12}$ cm^{-3} and mobility of ~ 175 cm^2/V-sec. From a fit of n vs.1/T, it was determined that the dominant donor in this sector is 0.34 eV below the conduction band, and that donor and acceptor concentrations were about $7x10^{15}$ and $1x10^{15}$ cm^{-3}, respectively. Thus, the purity in this sector is quite high.

One possible explanation accounting for the chemical and electrical data could entail growth-rate dependent incorporation of impurities or native defects. Differential segregation of impurities may contribute to the chemical and electronic differences between the two sectors, but there is no evidence that dopants like silicon or aluminum could be responsible for the deep level defect. Nor is there any evidence that iron could account for the shallow donor in the dark sector. Another possible explanation is that stoichiometric defects, complexed with impurities, act as compensation centers in the light sector, reducing the free-carrier optical absorption.

Each slice cut parallel to the C-plane has both a Zn-side and an O-side. Both sides of the wafers were polished in the same manner to determine the mechanical and optical properties of the two surfaces. The two surfaces have different chemical reactivities and mechanical properties as a result of surface anisotropy, so that given the same surface treatment, each side shows different results. This is illustrated in Table I which shows the rocking curve half-widths and PL intensities for two different polishing methods. The x-ray rocking curve measures strain in the sub-surface region, where Cu Kα radiation at 1.54 Å has a penetration depth of about 2 microns. A dramatic reduction by a factor of two is seen in the rocking curve width after the combined chemical-mechanical polish. A similar result is seen in the PL intensity at room temperature. At the excitation wavelength of 275 nm the absorption coefficient of ZnO is very high, and therefore the probe depth is on the order of a few nanometers. Thus PL is a very good indicator of surface quality. A comparison of PL intensities indicates the surface is much less damaged by chemical polishing than by mechanical polishing.

Table I. Effect of different surface treatments on hydrothermal ZnO

Surface Preparation Description	**Mechanical polish**		**Eagle Picher polish**	
Crystal faces	C^+	C^-	C^+	C^-
X-ray rocking curve FWHM (arc-sec)	108	104	43	37
3.28 eV PL relative intensity at room temp	0.04	0.5	1.1	1.5

Photoluminescence measurements at room temperature are useful for comparing the quality of ZnO samples. Because of the large exciton binding energy of 60 meV, exitonic emission will survive well above room temperature.[1] Thus, the measurement is an indicator for possible stimulated emission and lasing from ZnO at room temperature. Under pulsed excitation at 275 nm, the emission peak position is close to the expected energy of the free exciton. The bandgap of ZnO at room temperature is 3.37 eV,[1] and the observed PL emission peak is at 3.28eV. A comparison of the PL emission spectra for the same ZnO wafer after the two different surface treatments is shown in Figure 3.

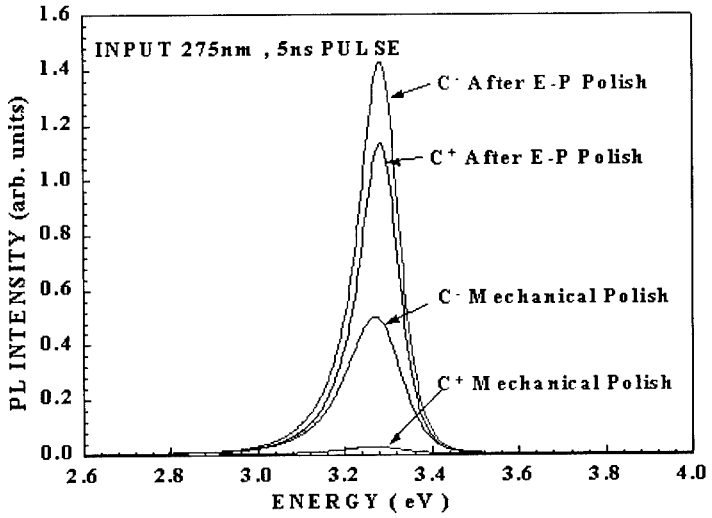


Figure 3. Room Temperature PL comparing different polishes.

Low temperature PL measurements give additional information on the fine structure of the emission. Photoluminescence (at 2.1 K) is clearly observed in the intrinsic spectral region from hydrothermally grown ZnO samples. Emission from both the ground state and excited states of the free exciton is shown in Fig. 4. The ground state emission is shown in both the absence (solid line) and presence (dashed line) of an applied magnetic field. The ground state consists of a Γ_5 allowed exciton (3.3758eV), and a Γ_6 forbidden exciton (3.3740eV) which is allowed in the presence of an applied magnetic field. Observation of both the Γ_5 and Γ_6 excitons is characteristic of good quality material.

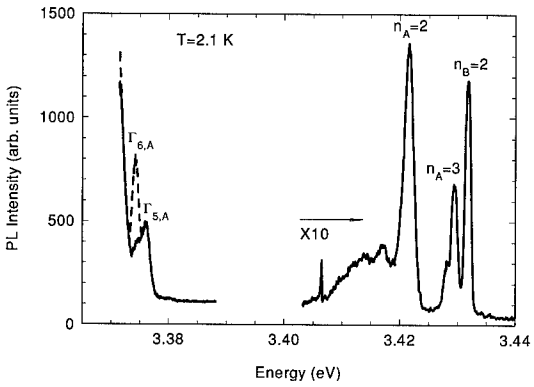


Figure 4. PL Emission of hydrothermal zinc oxide sample.

The observation of excited states of the ground state excitons is even more indicative of high quality material. The n= 2 states of the Γ_5 and Γ_6 excitons associated with a valence band are not resolved, and occur at 3.4214eV. The n= 3 states of these excitons are resolved and occur at 3.4295eV for the Γ_5 exciton and at 3.4280eV for the Γ_6 exciton. The selection rules are relaxed for the excited state transitions. From the emission spectra, the exciton binding energies can be obtained assuming the excited states are hydrogenic. The n= 2 state of the exciton associated with the B-valence band is observed at 3.4318eV. The ground state B-exciton (not shown) occurs at 3.3885eV. These data demonstrate that high quality ZnO can be grown by the hydrothermal technique.

The PL spectra in Fig. 5 compare hydrothermal ZnO grown at AFRL Hanscom with vapor-phase grown ZnO provided by Eagle-Picher.

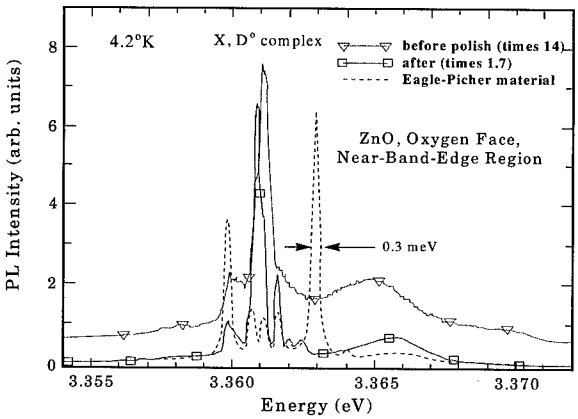


Figure 5. Photoluminescence (at 4.2 K) comparing hydrothermal ZnO and vapor-phase grown ZnO.

Photoluminescence of both Hanscom's hydrothermal and Eagle-Picher's (E-P) vapor-transport grown ZnO crystals (at 4.2 K) is most intense in the near-band-edge energy region, as shown in Figure 5. Spectra have been slightly shifted in energy to

facilitate direct comparisons. This figure is for the PL from oxygen face. All the sharp transitions are emissions from the decay of an exciton bound to a complex of a neutral donor and some unknown impurity or defect (X, D° complex). A comparison of the FWHM and intensity for the two samples with the same surface preparation (E-P polish) but different growth methods shows nearly identical material quality . A comparison of PL spectra for the same Hanscom crystal before and after E-P polish demonstrates the importance of surface preparation. PL from this sample after E-P polish (square markers) is sharper and eight times stronger than before E-P polish (triangle markers). The energy positions of lines this sharp are subject to strain and other point-to-point variations.

The high quality of both Hanscom's hydrothermal and E-P's vapor-transport ZnO crystals is again indicated by the sharp PL (not shown) from the zinc face of the two samples (at 4.2 K) which have received E-P's polish. For the zinc face, the comparison of PL spectra from the same Hanscom sample before and after E-P polish is even more striking than from the oxygen face: PL from the hydrothermal sample before the E-P polish was much broader and three orders of magnitude less intense.

CONCLUSIONS:

High quality, bulk ZnO was grown hydrothermally. The high quality of the crystals in this study was demostrated by narrow x-ray rocking curves and sharp PL peaks. The crystal color is non-uniform because of its anisotropic crystal growth habit in which the growth rate of each sector depends on orientation. Slices cut from the lighter region are semi-insulating, whereas those from the dark sector are n-type conducting. Anisotropy is also seen in surface quality of polished slices. For slices cut and polished on both sides of the basal plane, the oxygen face yields sharper and more intense room temperature PL peaks, and a narrower x-ray rocking curve. Improved polishing methods result in significantly improved surface quality as measured by the PL and rocking curve widths. When properly polished, hydrothermal ZnO exhibits optical properties similar to vapor phase grown ZnO. Therefore, proper surface preparation is necessary to evaluate the quality of ZnO substrates. For epitaxy, e.g. of GaN, special care is required to insure that ZnO surfaces are of high quality.

ACKNOWLEDGEMENTS

This work was funded in part by Air Force Office of Scientific Research.

REFERENCES

(1) D. M. Bagnall, Y. F. Chen, Z. Zhu, T. Yao, M. Y. Shen, and T. Goto, Appl. Phys. Lett. 73 (1998) 1038.

(2) R. R. Monchamp, "Growth of Zinc Oxide Crystals – Interim Engineering Progress Report," Airtron Division of Litton Industries, Morris Plains, New Jersey, ASD project Nr.-7-988, Contract No. AF33(657)-8795, November, 1964.

(3) A. N. Mariano and R. E. Hanneman, J. Appl. Phys. 34 (1963) 384.

(4) D. F. Croxall and R. Ward, J. Cryst. Growth, 22 (1974) 117.

DISORDERING OF InGaN/GaN SUPERLATTICES AFTER HIGH-PRESSURE ANNEALING

M.D. McCluskey*, L.T. Romano**, B.S. Krusor**, D. Hofstetter**, D.P. Bour**, M. Kneissl**, N.M. Johnson**, T. Suski***, J. Jun***

*Department of Physics, Washington State University, Pullman, WA 99164-2814
**Xerox PARC, 3333 Coyote Hill Rd., Palo Alto, CA 94304
*** Unipress, Ul. Sokolowska 29, 01-142 Warsaw, Poland

Cite this article as: MRS Internet J. Nitride Semicond. Res. 4S1, G3.42 (1999)

ABSTRACT

Interdiffusion of In and Ga is observed in InGaN multiple-quantum-well superlattices for annealing temperatures of 1250 to 1400°C. Hydrostatic pressures of up to 15 kbar were applied during the annealing treatments to prevent decomposition of the InGaN and GaN. In as-grown material, x-ray diffraction spectra show InGaN superlattice peaks up to the fourth order. After annealing at 1400°C for 15 min, only the zero-order InGaN peak is observed, a result of compositional disordering of the superlattice. Composition profiles from secondary ion mass spectrometry indicate significant diffusion of Mg from the *p*-type GaN layer into the quantum well region. This Mg diffusion may lead to an enhancement of superlattice disordering. For annealing temperatures between 1250 and 1300°C, a blue shift of the InGaN spontaneous emission peak is observed, consistent with interdiffusion of In and Ga in the quantum-well region.

INTRODUCTION

The development of blue light-emitting diodes (LEDs) [1] and laser diodes (LDs) [2] has focused a great deal of research activity on GaN-based III-V nitrides. The band gaps of $In_xGa_{1-x}N$ alloys cover a wide spectral range, from red (InN) to UV (GaN), making this alloy system ideal for optoelectronic applications [3]. The diffusion characteristics of host and impurity atoms in $In_xGa_{1-x}N$ alloys are of considerable interest [4]. In this paper, results from structural and optical studies of In-Ga interdiffusion in InGaN/GaN multiple quantum wells (MQWs) are presented.

While compositional disordering of superlattices within the InAlGaAs materials system has been extensively studied [5,6], superlattice disordering in III-nitrides has only recently been observed [4]. The interdiffusion of In and Ga in $In_xGa_{1-x}N$ alloys is complicated by the immiscibility of InN and GaN [7], which can result in phase separation in thick InGaN layers [8] and MQW structures [9]. In this study, we have investigated the diffusion of In and Ga in annealed $In_{0.18}Ga_{0.82}N$/GaN MQW structures. We observe quantum-well superlattice disordering, with no phase separation, for annealing temperatures from 1250 to 1400°C.

Mat. Res. Soc. Symp. Proc. Vol. 537 © 1999 Materials Research Society

EXPERIMENTAL DETAILS

The MQW structures were grown by metalorganic chemical vapor deposition (MOCVD). The structures consist of a 1 μm GaN:Mg layer, a 20 period superlattice of 16 Å $In_{0.18}Ga_{0.82}N$ well / 64 Å GaN barrier, and a 4 μm GaN:Si layer on a sapphire substrate. The thickness of the well plus barrier was determined by the spacing between satellite peaks in the x-ray diffraction (XRD) spectrum. A barrier-to-well thickness ratio of approximately 4:1 was measured with transmission electron microscopy (TEM). The In concentration in the InGaN quantum wells was determined by Rutherford backscattering spectrometry (RBS), by assuming the absence of In within the GaN barriers. Since the In concentration in the barriers is nonzero, however, the estimated In concentration of $x = 0.18$ should be regarded as an upper bound.

The samples were annealed at temperatures ranging from 1200 to 1400°C in a high-pressure furnace [10]. Pressures of up to 15 kbar were applied, with purified N_2 as a pressure-transmitting medium, in order to prevent decomposition of the GaN and InGaN. Pieces of Mg were placed in the high-pressure furnace near the sample to provide a Mg overpressure during annealing. To ensure the quasi-equilibrium conditions for the high-pressure annealing, GaN powder was placed in the crucible. The temperature was increased from room temperature, at a rate of 1800°C/h, until it reached a point ~100°C below the annealing temperature. At that point, the rate was reduced to 1000°C/h until the annealing temperature was reached. After annealing for 15 min, the temperature was decreased at a rate of 3000°C/h.

To enable optical pumping studies, the top GaN:Mg layer was etched to a thickness of 150 nm by chemically-assisted ion beam etching (CAIBE) after the high-pressure anneal. Optical pumping was performed with a pulsed 337-nm N_2 laser with a peak power of 250 kW. The laser light was focused to a 100 μm wide by 4-mm long stripe. The pump beam was attenuated by inserting a variable number of 1-mm thick glass slides between the lenses and the sample. The output of the InGaN/GaN MQW sample was collected by a 30 × microscope objective, focused onto a quartz fiber, and fed into an Oriel spectrometer with a resolution of 1 nm and a grating with 1200 lines/mm. The light was detected by a photodetector array with 1024 elements at the output slit. Intensity versus wavelength data was acquired by collecting light for up to 300 s in order to maximize the signal-to-noise ratio.

RESULTS

X-ray diffraction

The XRD spectra for the as-grown and annealed material are shown in Fig. 1. In the as-grown spectrum, InGaN (0006) satellite diffraction peaks were observed up to the 4th order. The satellite peaks arise from the periodicity of the quantum-well superlattice. The XRD spectrum for material that was annealed at 1200°C for 15 min (not shown) is identical to the as-grown spectrum. After annealing at a temperature of 1250°C for 15 min, the intensities of the 1st, 2nd, and 3rd order peaks were reduced, and the 4th order peak was not detected. The reduction in satellite peak intensity is consistent with interdiffusion of In and Ga in the MQW region, resulting in a broadening of the quantum well profiles. Previous results from XRD and transmission electron microscopy indicated that after annealing at 1400°C for 15 min, the quantum well region was replaced by a relatively uniform InGaN layer [4].

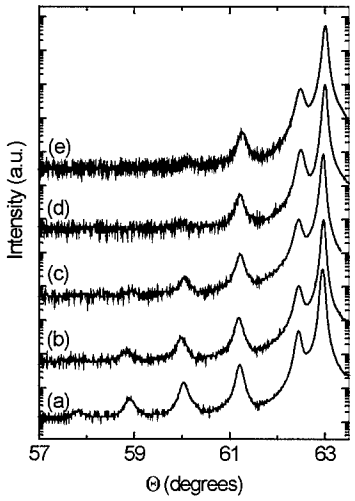


Figure 1. X-ray diffraction spectra for (0006) reflections of InGaN/GaN MQWs: (a) as-grown, and annealed for 15 min at (b) 1225°C, (c) 1250°C, (d) 1275°C, and (e) 1300°C.

Secondary Ion Mass Spectrometry

The In and Mg concentrations were measured as a function of depth with secondary ion mass spectrometry (SIMS). The depth resolution was limited to ~500 Å, due to surface roughness, so that the individual quantum wells were not resolved. Before annealing, the Mg concentration is constant to a depth of 1 μm, after which point it sharply decreases to a level below the detection limit (~10^{16} cm^{-3}). Compared to Mg, however, In does not show significant diffusion under these annealing conditions [4].

The In-Ga interdiffusion in the MQW region is correlated with the diffusion of Mg. It is possible that the diffusion of Mg enhances the interdiffusion of In and Ga in InGaN/GaN MQWs. Impurity induced disordering was first observed in Zn-diffused AlAs/GaAs superlattices [11]. In the case of $In_xGa_{1-x}As$/GaAs MQW's with $x = 0.15$, significant interdiffusion has been observed at temperatures less than 700°C [12]. The fact that no interdiffusion is observed in $In_xGa_{1-x}N$/GaN MQW's for temperatures below 1300°C is a result of the comparatively low rates of diffusion in the III-V nitrides. Although our results are suggestive of impurity induced disordering, further studies will be required to determine the effect of impurities on the interdiffusion of In and Ga in InGaN.

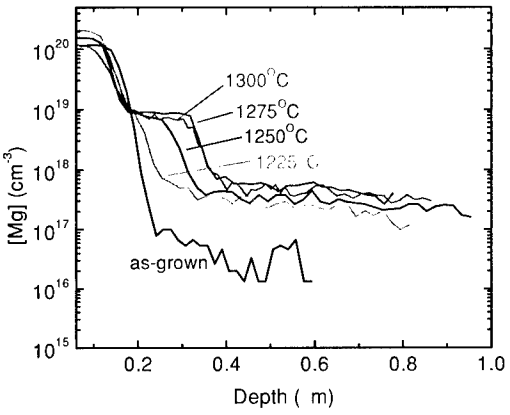


Figure 2. SIMS profiles of Mg in InGaN MQWs, for as-grown and annealed material.

Spontaneous Emission

Spontaneous emission peaks for as-grown and annealed samples are shown in Fig. 3. The decrease in peak wavelength is consistent with In-Ga interdiffusion, which increases the band gap of the InGaN quantum wells [13]. The peak intensities of the annealed samples were reduced by a factor of ~50 with respect to the as-grown samples. To obtain comparable signals, larger pump intensities were used for the annealed material than for the as-grown material. While the as-grown material exhibited lasing for sufficiently high pump intensities, lasing was not observed for the annealed samples. The shift of the spontaneous emission peak is plotted in Fig. 4 for several annealing temperatures.

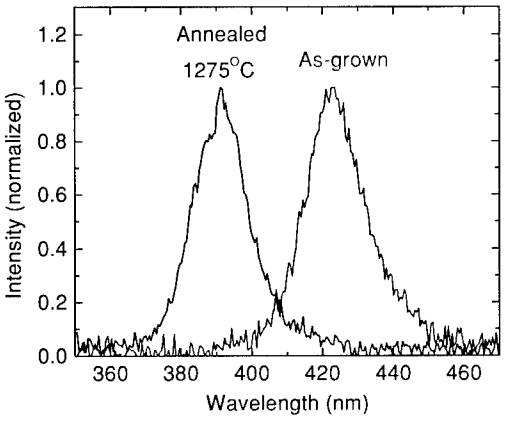


Figure 3. Emission spectra of InGaN MQWs before and after annealing.

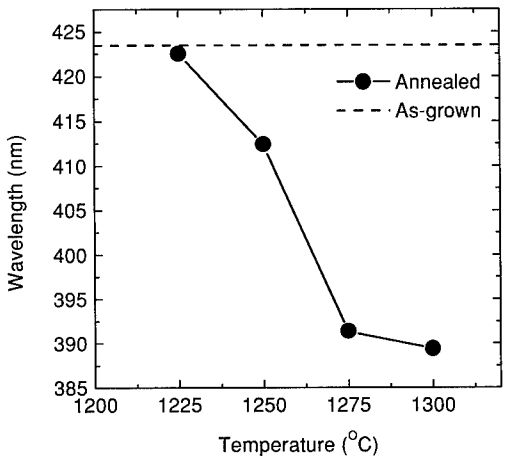


Figure 4. Spontaneous emission peak wavelengths for as-grown and annealed InGaN MQWs.

CONCLUSIONS

In conclusion, compositional disordering has been observed in $In_xGa_{1-x}N$/GaN MQW's with $x = 0.18$. This disordering results in a blue shift of the spontaneous emission peak. Similar to the case of Zn-diffusion in AlGaAs, it is conceivable that Mg-diffusion enhances In-Ga interdiffusion in InGaN.

ACKNOWLEDGMENTS

The authors are pleased to thank P. Floyd for helpful discussions. The work at Xerox was supported by DARPA MDA972-96-3-0014. The work at Unipress was supported by KBN 7T08A 007 13.

REFERENCES

1. S. Nakamura, M. Senoh, N. Iwasa, and S. Nagahama, Jpn. J. Appl. Phys. **34**, L797 (1995).
2. S. Nakamura, M. Senoh, S. Nagahama, N. Iwasa, T. Yamada, T. Matsushita, H. Kiyoko, and Y. Sugimoto, Jpn. J. Appl. Phys. **35**, L74 (1996).
3. See, for example, F.A. Ponce and D.P. Bour, Nature **386**, 351 (1997).
4. M.D. McCluskey, L.T. Romano, B.S. Krusor, N.M. Johnson, T. Suski, and J. Jun, Appl. Phys. Lett. **73**, 1281 (1998).

5. L.L. Chang and A. Koma, Appl. Phys. Lett. **29**, 138 (1976).
6. D. Hofstetter, B. Maisenhölder, and H.P. Zappe, IEEE Journal of Selected Topics in Quantum Electronics **4**, 794 (1998).
7. I-hsiu Ho and G.B. Stringfellow, Appl. Phys. Lett. **69**, 2701 (1996).
8. R. Singh, D. Doppalapudi, T.D. Moustakas, and L.T. Romano, Appl. Phys. Lett. **70**, 1089 (1997).
9. M.D. McCluskey, L.T. Romano, B.S. Krusor, D.P. Bour, N.M. Johnson, and S. Brennan, Appl. Phys. Lett. **72**, 1730 (1998).
10. T. Suski, J. Jun, M. Leszczyński, H. Teisseyre, S. Strite, A. Rockett, A. Pelzmann, M. Kamp, and K.J. Ebeling, J. Appl. Phys. **84**, 1155 (1998).
11. W.D. Laidig, N. Holonyak, Jr., M.D. Camras, K. Hess, J.J. Coleman, P.D. Dapkus, and J. Bardeen, Appl. Phys. Lett. **38**, 776 (1981).
12. W.D. Laidig, J.W. Lee, P.K. Chiang, L.W. Simpson, and S.M. Bedair, J. Appl. Phys. **54**, 6382 (1983).
13. K.S. Chan, E.H. Li, and M.C.Y. Chan, IEEE J. Quantum Electron. **34**, 157 (1998).

SYNTHESIS OF NITROGEN-RICH GaNAs SEMICONDUCTOR ALLOYS AND ARSENIC-DOPED GaN BY METALORGANIC CHEMICAL VAPOR DEPOSITION

M. Gherasimova, B. Gaffey, P. Mitev, and L. J. Guido
Department of Electrical Engineering, Yale University, Box 208284, New Haven, CT 06520

K. L. Chang and K. C. Hsieh
Department of Electrical and Computer Engineering, University of Illinois, 1406 W. Green St., Urbana, IL 61801

S. Mitha
Charles Evans & Associates, 301 Chesapeake Dr., Redwood City, CA 94063

J. Spear
Philips Electronic Instruments, 125 West Gemini Dr., Tempe, AZ 85283

Cite this article as: MRS Internet J. Nitride Semicond. Res. 4S1, G3.44(1999)

ABSTRACT

Arsenic-doped GaN films and GaNAs films have been synthesized by MOCVD. Samples were grown on sapphire, GaN-coated sapphire, and GaAs substrates. Composition, structure, and phase distribution were characterized by EPMA, SIMS, XRD, and TEM. The arsenic content increases demonstrably as the growth temperature descreases from 1030 to 700 °C. In the high temperature limit, high quality arsenic-doped GaN forms on GaN-coated sapphire. In the low temperature regime, nitrogen-rich GaNAs forms under some growth conditions, with a maximum arsenic mole fraction of 3%, and phase segregation in the form of GaAs precipitates occurs with an increase in arsine pressure. Preferential formation of the nitrogen-rich phase on GaN-coated sapphire suggests the presence of substrate-induced "composition pulling".

I. INTRODUCTION

Group III nitride semiconductor alloys with mixing on the anion sublattice are of considerable interest because of their potential application to a wide range of optoelectronic devices. The large difference in bond lengths between group III nitrides and arsenides results in an enormous miscibility gap in the pseudo-binary phase diagram, making it difficult to synthesize alloys in the intermediate composition range. While arsenic-rich alloys have been studied by a number of research groups, there are only a few reports on the synthesis of nitrogen-rich compounds.[1-3] In the present work, nitrogen-rich GaNAs alloys and arsenic-doped GaN have been synthesized by metalorganic chemical vapor deposition (MOCVD). Emphasis was placed on determining the influence of growth parameters, and the choice of substrate material, on the composition, phase distribution, and structural properties of these materials.

II. EXPERIMENTAL PROCEDURE

All of the samples described herein were grown in a conventional, horizontal-flow MOCVD reactor held at a pressure of 100 torr. Palladium-purified hydrogen was used as the carrier gas with a total flow rate of 8 slm. Trimethylgallium, ammonia, and arsine precursors were employed during growth, with the ammonia and trimethylgallium flows kept constant at 4 slm and 50 μmol/min, for all samples, while the arsine flow was varied between 4 and 400 sccm. Growths were performed on bare sapphire and GaAs substrates, as well as on GaN pseudo-substrates,[4] for the purpose of studying the relationship between gas phase chemistry and arsenic incorporation in the solid. In addition, a two-step growth method was employed in some cases to optimize electronic properties.[5] Film composition was determined using quantitative electron probe microanalysis (EPMA), by measuring the nitrogen Kα line and gallium and arsenic Lα line intensities, with the electron beam energy ranging from 6 to 13 keV. Substrate and surface contamination effects were eliminated as sources of error by performing variable-energy measurements. The arsenic mole fraction (x) and III-V stoichiometry ratio (s) were derived as follows

$$x = \frac{[\text{As atomic \%}]}{[\text{As atomic \%}] + [\text{N atomic \%}]} \quad ; \quad s = \frac{[\text{Ga atomic \%}]}{[\text{As atomic \%}] + [\text{N atomic \%}]}$$

Mat. Res. Soc. Symp. Proc. Vol. 537 © 1999 Materials Research Society

Secondary ion mass spectroscopy (SIMS) analysis was also performed for quantification purposes, with the CsM^+ molecular ion technique used for GaNAs alloys,[6] and an arsenic implant standard employed to calibrate arsenic doping. Transmission electron microscopy (TEM) and x-ray diffraction (XRD) measurements were performed to evaluate the structural properties of these materials.

III. RESULTS

A. Effects of Growth Temperature on Arsenic Incorporation

The general trend observed in all experiments is that an increase in growth temperature leads to a decrease in arsenic incorporation. Table I summarizes our observations for samples grown with an arsine flow of 4 sccm. These films were deposited on GaN pseudo-substrates, except for the 1030 °C sample which was grown using the two-step method. At 950 and 1030 °C the arsenic content is below the EPMA detection level so SIMS analysis was used for quantification.

Table I. Arsenic incorporation dependence on growth temperature.

Temperature (°C)	Composition (%)	Measurement	Stoichiometry (s)
700	3.2 ± 0.3	EPMA	0.98 ± 0.02
800	0.19 ± 0.02	EPMA	0.96 ± 0.02
900	0.10 ± 0.04	EPMA	0.98 ± 0.02
950	0.02	SIMS	0.99 ± 0.01
1030	2×10^{16} cm^{-3}	SIMS	0.97 ± 0.02

B. Effects of Substrate Material on Phase Separation

The phase distribution of GaNAs films grown at 700 °C exhibits a strong dependence on the choice of substrate. Phase segregation was observed in some samples, Table II, with multi-faceted GaAs particles (average size ≈ 10–30 μm) precipitating on top of specular GaNAs films. For cases were more than one phase is present, EPMA measurements were conducted on all visually distinct features. The influence of substrate in the present work is consistent with the well-documented composition pulling phenomenon[7] (e. g., the trend for samples grown with 4 sccm of arsine).

C. High Temperature Growth of Arsenic-Doped Gallium Nitride

Previously we demonstrated that arsenic doping significantly improves the electronic properties of GaN epitaxial layers.[8] The present work confirms our original findings, and provides additional data on the chemical and structural properties of these materials. At a growth temperature of 1030 °C, the arsenic doping level increases from 2×10^{16} to 2×10^{17} cm^{-3} in

Table II. Phase distribution dependence on substrate and arsine flow.

AsH_3 flow → Substrate↓	4 sccm	40 sccm	400 sccm
GaN	GaNAs	GaNAs + GaAs	GaAs
Al_2O_3	GaNAs + GaAs	GaAs	GaAs
GaAs	GaAs	GaAs	NA

response to a change in arsine pressure from 0.03 to 3.23 torr. In addition, no appreciable difference in arsenic concentration is found for samples deposited on GaN pseudo-substrates as compared to those prepared using the two-step growth method. Figure 1 shows that the residual impurity content does not change significantly as arsine is added to the growth chemistry. In particular, the oxygen concentration does not increase with arsenic incorporation – which supports the claim that the arsine cylinder was the source of oxygen contamination in our original experiment.

High-resolution x-ray diffraction measurements were performed to determine the influence of arsine on macroscopic film structure. In particular, diffraction space maps were obtained for the symmetric (004) and asymmetric (101) reflections – the omega scan component of these maps provides a measure of epitaxial layer tilt and column twist. Table III gives the full-width at half-maximum values derived from these measurements for both a conventional high-quality GaN layer and an arsenic-doped film with [As] = 2 x 10^{17} cm^{-3}. Lateral coherence length measurements were also made using the (104) reflection to estimate the average grain size.

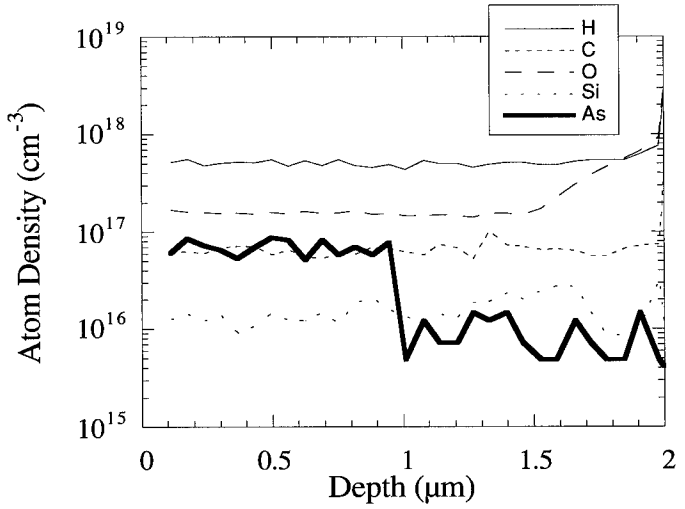


Figure 1. SIMS depth profile for 1 μm GaN:As film grown on GaN pseudo-substrate. Arsine pressure during the growth of the doped layer = 0.33 torr.

Table III. Summary of XRD measurements on high-temperature films.

Physical Property	Undoped GaN	Arsenic-doped GaN
Layer Tilt (degrees)	0.101	0.101
Column Twist (degrees)	0.129	0.273
Coherence Length (Å)	7750 ± 150	8200 ± 200

D. Low Temperature Growth of Nitrogen-Rich GaNAs Alloys

A series of samples has been grown on GaN pseudo-substrate at 700°C, with the arsine flow varying from 0 to 400 sccm. The GaN control sample has a rough surface, while the introduction of 4 sccm arsine yields a specular film containing approximately 3% of arsenic. A further increase in arsine flow to 40 sccm leads to the formation of multi-faceted GaAs precipitates; however, EPMA analysis shows that the composition of the GaNAs region saturates at 3%.

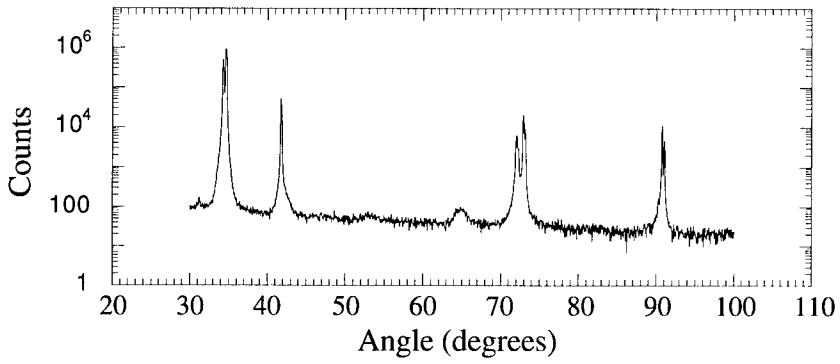


Figure 2. X-ray powder diffraction scan for GaNAs sample grown at 700°C.

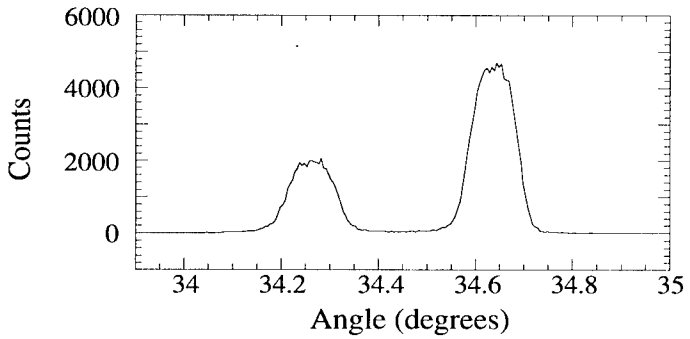


Figure 3. High resolution x-ray rocking curve showing (002) GaN and GaNAs peaks.

Finally, at 400 sccm of arsine, a rough but continuous GaAs film is synthesized with the nitrogen content reduced to below the SIMS detection limit. Figure 2 shows an x-ray powder diffraction scan for a sample prepared using 4 sccm of arsine. The strong peak at 34.6° is caused by the diffraction from the (002) planes of the GaN pseudo-substrate.

A high resolution x-ray rocking curve about the (002) GaN peak is shown in Figure 3. The second peak at smaller diffraction angle (34.2°) is attributed to GaNAs with approximately 4% arsenic mole fraction, assuming that the GaNAs layer is pseudomorphic with GaN. If instead the GaNAs is presumed to be fully relaxed the diffraction peak separation suggests an arsenic content of almost 8%.

TEM measurements were also performed to examine the microstructure of these GaNAs films. The cross-sectional image shown in Figure 4 is representative of films grown at 700°C with 4 and 40 sccm of arsine. There are two particularly important features to notice. First, the landscape is separated into vertical columns that are roughly 250 Å wide. These same features are observed in a control sample (without arsenic) that consists of a 700°C GaN layer deposited on a GaN pseudo-substrate. The origin of these columns is most likely the three-dimensional mode of growth by which GaN islands nucleate on the substrate surface. As the growth proceeds, these islands grow in size and eventually coalesce to form a contiguous film. Such columns with a large vertical-to-horizontal aspect ratio are expected to form if the vertical growth rate is much greater than its lateral counterpart. The initial areal density of nuclei decreases exponentially with an increase in growth temperature, and, as a consequence, the final width of the column just before coalescence is much larger in samples grown at higher temperature. This viewpoint is consistent with the absence of column boundaries in the GaN pseudo-substrate region of Figure 4, since their average width is expected to be larger than the length scale of the image. Second, there are many distinct changes in contrast along the length of each column, some of which may be caused by phase separation into nitrogen- and

arsenic-rich regions, and others which are indicative of the presence of stacking faults. By comparison, the 700°C GaN control sample exhibits considerably fewer contrast fringes along the length of each column.

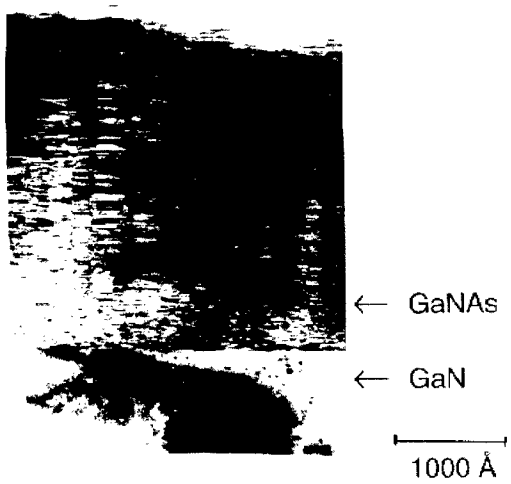


Figure 4. Cross-sectional TEM image : GaNAs film grown at 700°C on GaN pseudo-substrate.

IV. SUMMARY & CONCLUSIONS

Arsenic-doped GaN and nitrogen-rich GaNAs films have been synthesized using a conventional MOCVD reactor with trimethylgallium, ammonia, and arsine precursors. Direct deposition of GaN on sapphire at 1030°C in the presence of arsine causes a significant reduction in growth rate. The growth rate of undoped GaN is 2.4 μm/h, which is similar to that if GaN deposited via the two-step method, but it decreases to 1.7 μm/h at an arsine pressure of 0.33 torr. Complete growth inhibition occurs at an arsine partial pressure of 3.23 torr. This observation suggests that arsenic may have a strong surfactant effect. The nitrogen content is below the SIMS detection limit for films deposited directly on GaAs substrates, which suggests the presence of strong composition pulling. All arsenic-containing films deposited on GaN-coated sapphire at 4 sccm of arsine are continuous and specular – with the notable exception of the sample grown at 900°C, which is very rough relative to those grown at both higher and lower temperatures. This may be indicative of a change in the mode of growth or crystal structure (zincblende vs. wurtzite). At the high-temperature limit (1030°C), arsenic-doped GaN is formed with significantly better structural and electronic properties than otherwise identical samples without arsenic. At the low-temperature limit (700°C), non-homogeneous films are formed with GaNAs alloy regions containing stacking faults surrounded by GaAs (or perhaps arsenic-rich alloy inclusions).

VI. ACKNOWLEDGMENTS

Funding for ongoing research at the Yale University Optoelectronic Materials and Devices Laboratory has been provided by the National Science Foundation (ECS-92537600). M. Gherasimova and B. Gaffey are grateful for individual financial support provided by an NEC Graduate Student Fellowship and the Fannie and John Hertz Foundation, respectively. Authors gratefully acknowledge the assistance with the EPMA measurements provided by Dr. J. Eckert at the Yale University Geology Department.

VII. REFERENCES

[1] K. Iwata, H. Asahi, K. Asami, R. Kuroiwa, and S. Gonda, Jpn. J. Appl. Phys. **37**, 1436 (1998).

[2] R. Kuroiwa, H. Asahi, K. Asami, S.-J. Kim, K. Iwata, and S. Gonda, Appl. Phys. Lett. **73**, 2630 (1998).

[3] Y. Zhao, 1998 Electronic Materials Conference, Charlottesville, June, 1998.

[4] Sapphire substrate coated with a high-quality, 1 μm thick GaN epitaxial layer.

[5] 300 Å of GaN deposited on sapphire at 550 °C, followed by an arsenic-bearing test layer.

[6] The basic method is described in J. Appl. Phys. **64**, 3760 (1988). In the present case, the arsenic mole fraction was obtained by dividing the $(CsAs)^+$ ion counts by the sum of the $(CsAs)^+$ and $(CsN)^+$ signals.

[7] K. Hiramatsu, Y. Kawaguchi, M. Shimizu, N. Sawaki, T. Zheleva, R. F. Davis, H. Tsuda, W. Taki, N. Kuwano, and K. Oki, MRS Internet J. Nitride Semicond. Res., Vol. 2, Article 6.

[8] L. J. Guido, P. Mitev, M. Gherasimova, and B. Gaffey, Appl. Phys. Lett. **72**, 2005 (1998).

Si DELTA DOPED GaN GROWN BY LOW-PRESSURE METALORGANIC CHEMICAL VAPOR DEPOSITION

Jong-Hee Kim, Gye Mo Yang, Sung Chul Choi, Ji Youn Choi,
Hyun Kyung Cho, Kee Young Lim, Hyung Jae Lee

Semiconductor Physics Research Center and
Department of Semiconductor Science and Technology,
Chonbuk National University, Chonju 561-756, Korea

Cite this article as: MRS Internet J. Nitride Semicon. Res. 4S1, G3.49(1999)

ABSTRACT

Si delta-doping in the GaN layer has been successfully demonstrated by low-pressure metalorganic chemical vapor deposition at a growth temperature of 1040 °C. Si delta-doping concentration increases and then decreases with an increase in delta-doping time. This indicates that delta-doping concentration is limited by the desorption process owing to much higher thermal decomposition efficiency of silane at high growth temperatures of GaN. In addition, it was observed that the use of a post-purge step in the ammonia ambient reduces Si delta-doping concentration. From capacitance-voltage measurement, a sharp carrier concentration profile with a full-width at half maximum of 4.1 nm has been achieved with a high peak concentration of 9.8 x 10^{18} cm^{-3}.

INTRODUCTION

In the past decade, though many inherent problems originating from the heteroepitaxial growth in wide-bandgap III-V nitride materials exist, there have been considerable developments that have led to the remarkable demonstrations of high-brightness blue light emitting diodes [1,2], laser diodes [3], and high-frequency field-effect transistors (FETs) [4,5]. In particular, high-frequency FETs using GaN/AlGaN heterostructures have been realized using uniformly Si doped layers. In III-V compound semiconductors such as GaAs, FETs with characteristics superior to those of conventionally doped transistors have been fabricated using the delta-doping technique [6], which can achieve very narrow doping distribution along the epitaxial growth direction and up to now has been studied in a variety of materials and devices [7-9]. It was recently demonstrated that the inclusion of delta doping could improve laser stability in the face of temperature variations, in comparison with conventional quantum well lasers [10].

Even though the growth temperature of GaN in metalorganic chemical vapor deposition (MOCVD) is much higher than that of conventional III-V compound semiconductors, it is considered to be important to investigate delta-doping in III-V nitride materials for high-performance device applications. To our knowledge, up to now there are no reports about the application of delta-doping on III-V nitrides. In this letter, we demonstrate Si delta doping in GaN grown by low-pressure MOCVD and investigate the effects of delta-doping time and post-delta-doping purge step on carrier concentration.

Mat. Res. Soc. Symp. Proc. Vol. 537 © 1999 Materials Research Society

EXPERIMENTAL

The samples used in this study were grown in a vertical rotating MOCVD reactor operating at 200 Torr. Trimethylgallium (TMG), ammonia (NH_3), and 100 ppm silane (SiH_4) in hydrogen were used as Ga, N, and Si delta-dopant precursors, respectively. Substrates used in this experiment were c-plane sapphires, which were degreased in an organic solvent and then slightly etched in a hot solution of $3H_2SO_4$: H_3PO_4 for 10 min. After the thermal cleaning in H_2 environment at 1070 °C for 10 min, a 20-nm-thick GaN buffer layer was deposited at 520 °C. Finally, the substrate temperature was raised to 1040 °C to grow the GaN overlayer. The V/III ratio for the GaN overlayer was 1560. Under these conditions, background doping was 8 x 10^{16} cm^{-3} n-type. The growth procedure for Si delta-doped GaN was as follows. First, an undoped GaN layer (1.7 μm) was grown, after which TMG supply was stopped for 10 s on top of the GaN layer, while at that time ammonia was kept flowing. At this pre-delta-doping purge step, the surface became N-rich. This was followed by Si deposition for several tens of seconds under a Ga-free condition. The SiH_4 flow rate was 2~4 nmol/min. Then, we deposited an undoped GaN cap layer by two different methods: (1) post-delta-doping purge step for 10 s with flowing ammonia followed by the growth of a cap layer; and (2) direct growth of a cap layer without the post-delta-doping purge step. After the structure growth, a Schottky barrier was fabricated by thermal evaporation of gold through a shadow mask containing 620 μm dots. Aluminum was

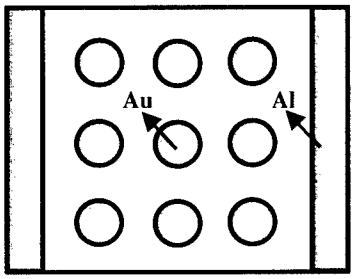


Fig. 1. Schematic diagram of fabricated devices for Si delta-doped GaN.

deposited over a large area on the perimeter of the crystal face to serve as an ohmic contact as shown in Fig. 1. The carrier concentration was obtained by capacitance-voltage (C-V) measurement, which was performed with a 1 MHz capacitance meter (Boonton 72-4B) at room temperature.

RESULTS AND DISCUSSION

The C-V profiles of Si delta-doped GaN layers depending on the delta-doping time are shown in Fig. 2. Silane flow rate was 4 nmol/min, and the pre- and post-purge times on both sides of delta doping were the same, i.e., 10 s. Figure 2 demonstrates that Si delta-doped GaN can be successfully grown using MOCVD. The maximum C-V concentration of Si delta-doped GaN does not increase with the increase in delta-doping time, in contrast to a strong linear dependence

for Si delta-doped GaAs [11]. This shows that the Si delta-doping process might be dominated by the desorption of Si dopant from the nongrowing surface. The growth temperature of GaAs is lower than that of GaN. Therefore, as a result of low thermal decomposition efficiency of Si doping precursors, Si delta-doping concentration in GaAs is mainly determined by the adsorption process [11]. However, due to the high growth temperature of GaN, the thermal decomposition efficiency of Si doping precursors will be much higher than that in the case of GaAs. This means that the adsorption/desorption process can quickly approach equilibrium. Si delta-doping concentration is therefore determined by the equilibrium between the adsorption and desorption processes with the desorption step limiting. This eventually leads to the above-mentioned relationship between the electron density and the delta-doping time.

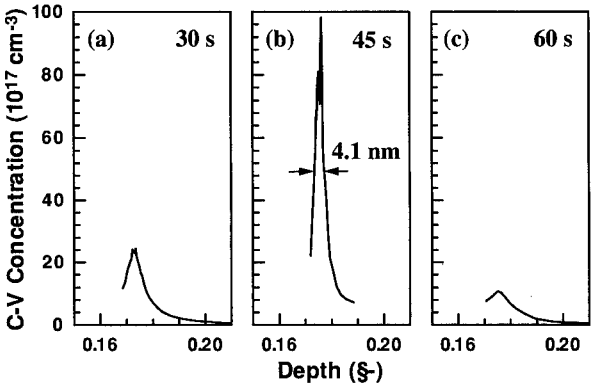


Fig. 2. C-V profiles of Si delta-doped GaN grown under different delta-doping times of (a) 30 s, (b) 45s, and (c) 60 s.

On the other hand, silicon dopants ideally should be confined to a single atomic monolayer by the growth interruption technique. However, the doping profile will be broadened by dopant diffusion and segregation processes. Usually, the broadening of the doping profile is estimated from the full width at half-maximum (FWHM) of the C-V profile. In the case of GaN, the diffusion process may significantly affect the broadening of the doping profile because the growth temperature of GaN is much higher than that of conventional III-V compound semiconductors. As can be seen in Fig. 2(b), however, the FWHM of the C-V profile in Si delta-doped GaN is as narrow as 4.1 nm. This sharp distribution profile is comparable with the values for Si delta-doped GaAs [12]. It indicates that the diffusion effect is small for Si delta doping in GaN by low-pressure MOCVD. Using optimized growth condition, the delta-doping technique in GaN has the feasibility of the fabrication of high performance electronic and opto-electronic devices.

The basic delta-doping procedure includes pre-purge, delta-doping, and post-purge steps. The function of pre-purge step is to completely suspend growth of the host material for minimized memory effect of growing species on subsequent delta-doping. The post-purge step minimizes the dopant memory effect, after which growth of the host material is resumed. However, in the case of delta-doped GaAs the use of the pre-purge and post-purge step in the group V containing ambient reduces Si delta-doping concentration [13]. Figure 3 shows the room-temperature C-V profiles of Si delta-doped GaN layers grown under different post-delta-doping conditions. The pre-purge time before delta doping was 10 s. During the delta-doping step on the nongrowing GaN surface, silane flow rate was 2 nmol/min and delta doping time was 60 s. The C- V profile

corresponding to the Si delta-doped structure with a post-purge time of 10 s is shown in Fig. 3(a). It shows a FWHM of 11.6 nm and a maximum C-V concentration of 2.8 x 10^{18} cm^{-3}. On the other hand, Si delta-doped GaN without the post-delta-doping purge step shown in Fig. 3(b) has a much higher peak concentration of 7 x 10^{18} cm^{-3} than the structure obtained with the post-purge step. In addition, it indicates a sharp profile with a FWHM of 5.2 nm. Obviously, when a post-purge step is included in the delta-doping sequence of GaN, Si evaporation will make it extremely difficult to achieve a higher Si delta-doping concentration. This phenomenon is similar to the reported result for Si delta-doped GaAs grown by MOCVD [13]. The above results confirm that the optimized delta-doping time and the delta-doping sequence without the post-purge step should be considered in order to maximize the delta-doping concentration.

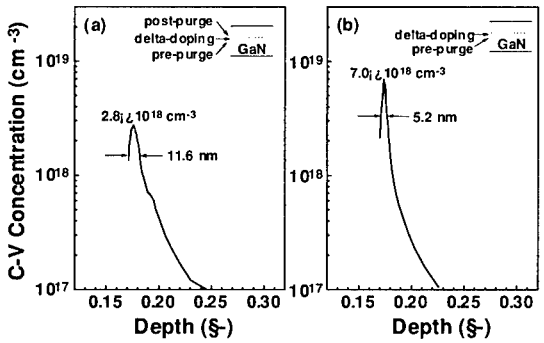


Fig. 3. Effect of post-delta-doping purge step on room-temperature C-V profiles of Si delta-doped GaN. (a) Ammonia post-purge (10 s) step after delta-doping. (b) Direct growth of GaN host material without post-purge step.

CONCLUSION

Si delta-doped GaN layers have been successfully grown by low-pressure MOCVD. From C-V measurement, we found that the delta-doping of Si in GaN has a dependence on delta-doping time that differs from that of Si delta-doping in GaAs and that it may be dominated by the desorption process of Si. Additionally, to obtain a higher Si delta-doping concentration, it is essential to utilize the delta-doping sequence that does not have a post-delta-doping purge step.

ACKNOWLEDGMENTS

This work was partially supported by MSTK and by KOSEF through the Semiconductor Physics Research Center at Chonbuk National University, and by the Ministry of Education of Korea.

REFERENCES

1. P. Kozodoy, A. Abare, R. K. Sink, M. Mack, S. Keller, S. P. DenBaars, U. K. Mishra and D. Steigerwald: Mat. Res. Soc. Symp. Proc. **468**, 481 (1997).
2. S. Nakamura, M. Senoh, N. Isawa, S. Nagahama, T. Yamada and T. Mukai: Jpn. J. Appl. Phys. **34**, L1332 (1995).
3. S. Nakamura, M. Senoh, S. Nagahama, N. Isawa, T. Yamada, T. Matsushita, H. Kiyoku, Y. Sugimoto, T. Kozaki, H. Umemoto, M. Sano and K. Chocho: Jpn. J. Appl. Phys. **37**, L309 (1998).
4. J. Burm, W. J. Schaff, L. F. Eastman, H. Amano and I. Akasaki: Appl. Phys. Lett. **68**, 2849 (1996).
5. Q. Chen, M. A. Khan, J. W. Yang, C. J. Sun, M. S. Shur and H. Park: J. Appl. Phys. **69**, 794 (1996).
6. S. Nakajima, K. Otobe and N. Shiga: IEEE Trans. Electron. Devices **39**, 771 (1992).
7. E. F. Schubert: J. Vac. Sci. Technol. **A 8**, 2980 (1990).
8. G. Li and C. Jagadish: Solid State Electron. **41** (1997) 1207.
9. J.-H. Kim, D. H. Lim, G. M. Yang, Y. G. Shin, K. Y. Lim and H. J. Lee: Appl. Phys. Lett. **69**, 1870 (1996).
10. O. Buchinsky, M. Blumin and D. Fekete: Appl. Phys. Lett. **72**, 1484 (1998).
11. H. M. Shieh, W. C. Hsu and C. L. Wu: Appl. Phys. Lett. **63**, 509 (1993).
12. E. F. Schubert, J. B. Stark, B. Ullrich and J. E. Cunningham: Appl. Phys. Lett. **52**, 1508 (1988).
13. G. Li and C. Jagadish: Mater. Sci. Eng. B **33**, 182 (1995).

INFLUENCE OF THE FIRST PREPARATION STEPS ON THE PROPERTIES OF GAN LAYERS GROWN ON 6H-SIC BY MBE

R. Lantier[*], A. Rizzi[*,**], D. Guggi[*], H. Lüth[*], B. Neubauer[***], D. Gerthsen[***], S. Frabboni[**], G. Colì[****], and R. Cingolani[****].

[*]*Institut für Schicht- und Ionentechnik (ISI), Forschungszentrum Jülich, D-52425 Jülich, Germany*

[**]*Istituto Nazionale di Fisica della Materia - Dipartimento di Fisica, Università di Modena, I-41100 Modena, Italy*

[***]*Laboratorium für Elektronenmikroskopie, Universität Karlsruhe, D-76128 Karlsruhe, Germany*

[****]*Istituto Nazionale Fisica della Materia, Dipartimento Scienza dei Materiali, Università di Lecce, I-73100 Lecce, Italy*

Cite this article as: MRS Internet J. Nitride Semicond. Res. 4S1, G3.50(1999)

ABSTRACT

The Gan heteroepitaxy on 6H-SiC is affected by the bad morphology of the substrate surface. We performed a hydrogen etching at 1550°C on the 6H-SiC(0001) substrates to obtain atomically flat terraces. An improvement of the structural properties of GaN grown by MBE on such substrates after deposition of a LT-AlN buffer layer is observed. A value of less than 220 arcsec of the FWHM of the XRD rocking curve, showing a reduced screw dislocations density, is comparable with the best results reported until now for thick GaN samples. Photoluminescence showed a structured near band edge emission spectrum with evidence of the A, B and C free exciton recombinations.

INTRODUCTION

GaN heteroepitaxy calls for a standing improvement in structural material properties to the aim of device application [1]. The best reported laser diodes up to now are based on the epitaxial lateral overgrowth (ELOG) of GaN thick layers on a strip-shaped SiO_2 structured $GaN/Al_2O_3(0001)$ substrate [2]. ELOG is used to reduce the number of threading dislocations originating at the interface with the substrate. SiC is a promising substrate because of the closer lattice match (3.5% mismatch) and thermal expansion coefficent among the commonly available substrates for GaN heteroepitaxy. Despite these positive properties, the quality of GaN grown on SiC is not that extremely better than that of the same material grown on sapphire [3,4], apart from the XRD results reported in Ref. [5]. One possible reason might be the poor surface morphology of the substrate, with defects that might propagate into the epitaxial structure, degrading its quality. Exposing the silicon carbide surface to hydrogen flow at high temperatures is already reported to give rise to large atomically flat terraces and to lead to the disappearance of scratches [6,7]. We decided to perform this treatment on the 6H-SiC wafers, that have been used as substrates for the MBE growth of GaN. For comparison the same growth process was

Mat. Res. Soc. Symp. Proc. Vol. 537 © 1999 Materials Research Society

considered on SiC substrates wet chemically etched by common procedures. The main interest was then to analyze the influence of this substrate preparation of the use of different buffer layers as well, on the structural and optical properties of GaN.

EXPERIMENT

The deposition of nitride layers on 6H-SiC(0001) Si-terminated substrates (CREE Research Inc.) was carried out in a small VG MBE system, where the active nitrogen was provided by an SVTA RF source operating at 13.56 MHz, 350 W. After thermal annealing up to 800°C in UHV the GaN epitaxy always was performed at 770°C in nearly stochiometric conditions, slightly Ga-rich, after the deposition of a low temperature (LT)-buffer layer (T=550°C -600°C). Prior to insertion into the UHV system some SiC substrates (H*-6H-SiC in the following) were heated up to 1550°C in He flux in a quartz reactor, then a mixture of He:H_2 (7:1) was let flowing for 10 minutes (2 l/min, 1 atm). Surface morphology of these substrates was checked before and after the etching by means of a Digital Instrument AFM in Tapping Mode. Before the introduction in the MBE chamber the as-received substrates were cleaned in a standard way [8], whereas the H_2 etched 6H-SiC substrates were just dipped in a 10% HF solution.
The GaN epitaxial layers were then analyzed by means of XRD, TEM and PL. High resolution and reciprocal space mapping were performed in a Philips XPD1 diffractometer with Cu $K_{\alpha 1}$ and a wavelength resolution $\Delta\lambda/\lambda \sim 10^{-5}$. The TEM analyses were carried out with electron microscopes of the types Philips CM 200 FEG/ST and CM 30 TEM/ST. Plan-view specimens and cross-section samples along the $<1\bar{1}00>$- and $<11\bar{2}0>$-projections were prepared by dimple-grinding and Ar+-ion milling on a liquid-nitrogen cooled sample holder. Two-beam diffraction conditions were applied to identify edge and screw dislocations with the $\vec{g}\cdot\vec{b}=0$ criterion. The dislocation densities were determined by measuring the specimen volume, which is obtained from the extinction contours and the known extinction lengths for the applied diffraction vectors and the dislocation lengths.
Photoluminescence spectra were measured at 10K using an He-Cd laser for excitation at 325 nm with a power of approximately 10 mW on the sample.

RESULTS AND DISCUSSION

First the SiC surface morphology was analyzed by AFM. The as polished, solvent cleaned 6H-SiC (0001) substrates showed a high density of scratches of different depth (maximum 7 - 8 nm), as is seen in Fig.1a. These features remained unchanged also after the usual chemical etching [8] followed by thermal annealing in UHV. Hydrogen etching of such a surface produces wide atomically flat terraces (Fig. 1b), separated by 15 Å high steps, corresponding to one 6H-SiC unit cell, in good agreement with other results reported in the literature [6,7]. The steps form a regular array and are all seen to lie along the $<1\bar{1}00>$ directions; in contrast with what is stated in Ref. [7] we were not able to see two different set of steps.
Three types of samples have been considered for the present study (Tab. I) and the properties of the GaN epilayers have been compared.

Tab. I – MBE epitaxial structures.

	A	*B*	*c*
Substrate	6H-SiC	6H-SiC	H*-6H-SiC
LT-buffer (thickness)	GaN (10 nm)	AlN (26 nm)	AlN (26 nm)
Epi-layer (~1 μm of thickness)	GaN	GaN	GaN

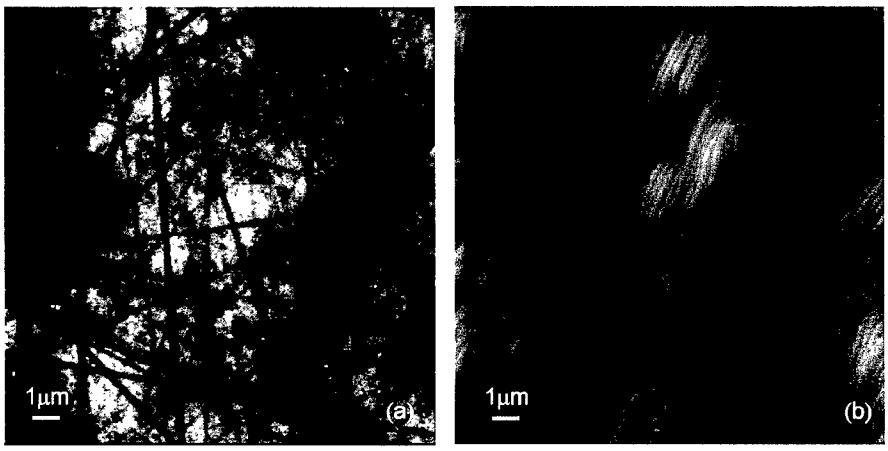


Fig.1 - AFM images of an as-received (a) and of a hydrogen etched (b) 6H-SiC (0001) surface. sample.

The FWHM of x-ray rocking curve of the GaN (0002) reflection (acquired with open detector) decreases from 618 arcsec for the material grown on the GaN buffer to 378 arcsec using the AlN buffer layer instead. A further clear improvement leading to a FWHM of 228 arcsec was obtained by deposition of the AlN buffer/GaN layers on a hydrogen etched substrate.

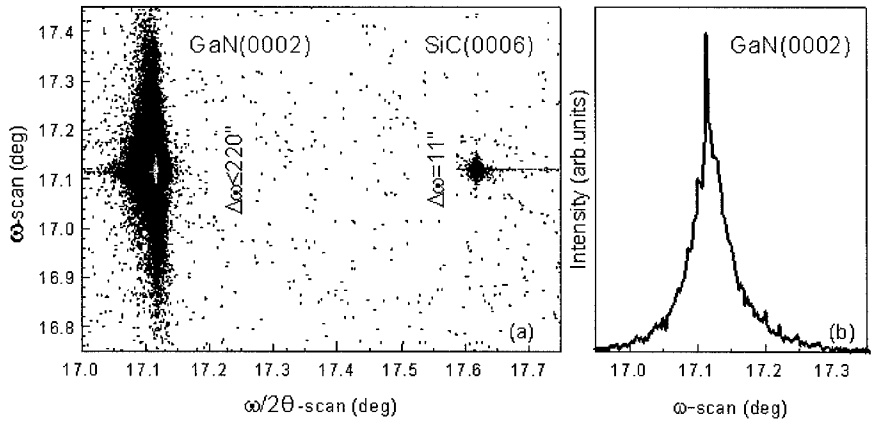


Fig. 2 - (a) Reciprocal space map of the sample *c* in the region of the GaN (0002) and SiC(0006) reflections. (b) ω-scan rocking curve of the GaN (0002) reflection.

For this last sample we performed also measurements in the triple axis diffraction mode. A series of ω-2θ scans taken for different offset values of ω gives the reciprocal space map reported in Fig. 2a. Small lattice constant variations are observed, as shown by the FWHM of 35 arcsec in a direction parallel to the diffraction vector. In the perpendicular direction the reciprocal lattice point of GaN shows a broadening with a FWHM of less than 220 arcsec. This is due to microscopic tilts of the layer and is an indication of a low number of screw and mixed dislocations, that are the ones distorting the (0002) planes, as pointed out in Ref. [9]. The ω-scan line shape gives evidence of a peak with a FWHM of around 90 arcsec, superimposed on a broader one (Fig. 2b). This might be due to a well aligned and extended grain probably in the upper part of the epi-layer, where the dislocation denstity decreases.

The TEM analysis yielded a screw dislocation density N_{screw} of 4.4×10^{9} cm^{-2} and an edge and mixed dislocation density N_{edge} of 9×10^{9} cm^{-2} for the GaN on the hydrogen-etched substrate. Slightly higher values of $N_{screw} = 7.5\times10^{9}$ cm^{-2} and $N_{edge} = 1.5\times10^{10}$ cm^{-2} were obtained for the sample *b*. However, error margins of ± 50 % can occur due to the uncertainties of the specimen volume determination. HR-TEM measurement on sample *c* revealed an atomically abrupt interface between the SiC substrate and the AlN buffer layer, which also corresponds to a flat GaN surface (RMS ~ 5 nm), as proved by AFM results, not reported here. Furthermore a flat GaN surface morphology is of obvious relevance for the growth of complex heterostructures.

PL measurements were performed on the three samples in Tab. I and the results are shown in Fig.3. The spectra of the samples grown on the AlN buffer (*b* and *c*) layer show predominantly near band edge (NBE) emission. In the spectrum of sample *a*, grown on a GaN buffer, the most intense emission is centered at 3.389 eV, to be assigned to the first LO-phonon replica of the free exciton, estimated at 3.458 eV. Higher phonon replicas are also observed. As can be seen in the

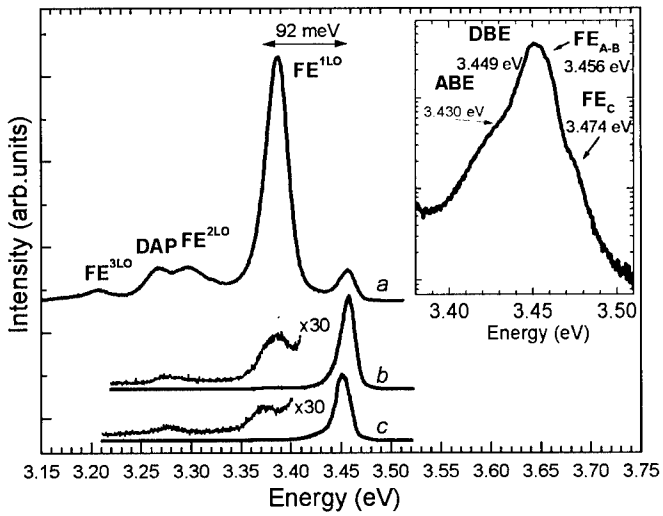


Fig. 3 - Photoluminescence spectra at 10K for the three GaN samples. In the inset just the NBE region is reported for the sample *c* using a logarithmic scale for the intensity.

inset the NBE peak for the sample *c* consists of the superposition of a dominant donor bound exciton at 3.449 eV and A and B excitons at 3.456 eV. A shoulder at higher energies is attributed to the C exciton, whereas on the low energy side some contribution from an acceptor BE is identified. The same features are also measured on sample *b* slightly shifted to higher energies due to a different state of strain. These emissions persist up to room temperature. For the relaxed GaN "bulk" material several values are reported for the position of the free exciton, ranging from 3.469 eV [10] to 3.499 eV [11]. Whatever energy location we choose as reference for relaxed GaN, the emissions of our samples are downshifted, indicating the presence of biaxial tensile stress. This is commonly interpreted in terms of the difference in the thermal expansion coefficients of GaN and SiC.

If compared to analogous spectra (GaN on SiC) by Monemar *et al.* [12], in our case the FE_{A-B} emissions shift to lower energies. This is assigned to a higher state of strain in our GaN epi-layers. From the HR-XRD analysis of sample *c* we could extract, for the strain perpendicular to the basal plane, a value close to – 0.11%, the one predictable if one takes into account the difference in the thermal expansion coefficients of GaN and SiC. Monemar reported an axial strain of - 0.07% which was determined in GaN layers grown by MOVPE on 6H-SiC without a buffer layer. This difference must be assigned to a different defect structure, which influences the release of the strain.

Worth noting is that the two samples grown with the same buffer layer on differently treated SiC showed similar spectra, though the different density of screw dislocations, that could be inferred from the XRD measurements. In fact, the only effect to be expected is a reduction of the optical efficiency. Screw and mixed dislocations are predicted to have deep defect states in the gap [13] and indeed some CL studies related them to non-radiative recombination centers [14]. We did not register a big difference in the optical efficiency of the two samples.

Concerning the phonon replicas we note that samples grown on different buffer layers exhibit a substantial variation of the phonon-replica intensity: Actually it is well known that in polar materials the strong exciton-phonon coupling leads to important polaron corrections to the polariton wavefunctions. The recombination rate of the dressed polariton (zero-phonon line) or of its phonon replicas depends on the actual density of scattering centers available in the crystal, resulting in a sample-dependent intensity ratio of the luminescence lines. This might be related to existence of grains of high crystalline quality in the sample *a*, whereas the dominant no phonon excitonic emission in the two samples *c* and *b* let us suppose the presence of other defects, acting as scattering centers, connected to the different growth mechanism on the LT-AlN or to the diffusion of impurities from the buffer. The density of threading dislocations, does not seem to play such a big role in the scattering of the exciton polaritons promoting the no-phonon line.

CONCLUSIONS

We proved that the growth of GaN on SiC substrates results in better structural quality when using a LT- AlN buffer instead of a LT GaN-buffer, at least for the growth conditions we used. The FWHM of the XRD ω-scan becomes lower. A big difference is also seen in the PL properties: a LO-phonon replica dominates the spectrum of the sample grown on the GaN LT-buffer whereas the NBE emissions become dominant by using an AlN buffer. A further clear improvement in the structure of GaN has been achieved by using a hydrogen etched substrate with atomically flat terraces. The ω-scan FWHM of 220 arcsec we obtained for this GaN layer is comparable with the best value for MBE GaN reported so far [4]. However it must be noticed that in that case the epilayer was nucleated on a thick HVPE GaN on SiC. The narrow broadening of the symmetrical reflections in the rocking curve is usually associated with a low number of screw and mixed dislocations. Taking into account that those defects are probably

non-radiative recombination centers and also considering the role of TDs in generating V-defects in QWs structures, the reduction of the density of screw dislocations can be considered a promising result. Preliminary AFM results showing a reduced surface roughness are also encouraging.

ACKNOWLEDGMENTS

The authors like to thank A. Fattah and prof. H. Wenzl for the high temperature hydrogen etching, R. Schmidt for taking part at some of the experiments and K. Wambach and F. Ringelmann for the technical support. The financial support of the Deutsche Forschungsgemeinschaft is kindly ackowledged.

REFERENCES

[1] For recent reviews, see: F. A. Ponce and D. P. Bour, Nature **386**, 351 (1997); J. W. Orton and C. T. Foxon, Rep. Prog. Phys. **61**, 1 (1998)
[2] S. Nakamura, M. Senoh, A. Nagahama, N. Iwasa, T. Yamada, T. Matsushita, H. Kiyoku, Y. Sugimoto, T. Kozaki, H. Umemoto, M. Sano and K. Chocho, Jpn. J. Appl. Phys. **37**, L309 (1998)
[3] C. F. Lin, H. C. Cheng, G. C. Chi, M. S. Feng, J. D. Guo, J. Minghuang Hong and C. Y. Chen, J. Appl. Phys. **82**, 2378 (1997)
[4] M. A. Johnson, Shizuo Fuijta, W. H. Rowland JR, K.A. Bowers, W. C. Hughes, Y. W. He, N. A. WEl Masry, J. W. Cook JR, J. F. Schetzina, J. Ren and J. A. Edmond, Solid- State El. **41**, 213 (1997)
[5] W. Li and W. Ni, Appl. Phys. Lett. **68**, 2705 (1996)
[6] F. Owen, C. Hallin, P. Mårtensson and E. Janzén, J. Cryst. Growth **167**, 391 (1996)
[7] V. Ramachandran, M. F. Brady, A. R. Smith, R. M. Feenstra and D. W. Greve, J. Electron. Mater. **27**, 308 (1998)
[8] M. E. Lin, S. Strite, A. Agarwal, A. Salvador, G.L. Zhou, N. Teraguchi, A. Rockett and H. Morkoc, Appl. Phys. Lett. **62**, 702 (1993)
[9] B. Heyng, X. H. Wu, S. Keller, Y. Li, D. Kapolnek, B. P. Keller, S. P. DenBaars and J. S. Speck, Appl. Phiys. Lett. **69**, 643 (1995)
[10] B. J. Skromme, Mat. Science and Eng. B **B50,** 117 (1997)
[11] C. Merz, M. Kunzer, U. Kaufmann, I. Akasaki. and H. Amano, Solid State Commun. **95** 597 (1995)
[12] B. Monemar, J. P. Bergman, I. A. Buyanova, W. Li, H. Amano and I. Akasaki., MRS Internet J:Nitride Semicond. Res. **1**,2 (1996)
[13] J. Elsner, R. Jones, P. K. Sitch, V. D. Porezag, M. Elnster, Th. Frauenheim, M. I. Heggie, S. Oberg, and P. R. Briddon, Phys. Rev. lett. **79,** 3672 (1997)
[14] S. J. Rosner, E. C. Carr, M. J. Ludowise, G. Girolami, and H. I. Erikson, Appl. Phys. Lett. **70**, 420 (1997)

EFFECTS OF SUSCEPTOR GEOMETRY ON GAN GROWTH ON SI(111) WITH A NEW MOCVD REACTOR

Yungeng Gao,* Daniel A. Gulino,* and Ryan Higgins**

* Department of Chemical Engineering and Condensed Matter and Surface Science Program, Ohio University, Athens, OH 45701

** Condensed Matter and Surface Science Program, Ohio University, Athens, OH 45701

Cite this article as: MRS Internet J. Nitride Semicon. Res. 4S1, G3.53(1999)

ABSTRACT: High quality GaN films on AlN buffer layers were grown on Si(111) with a new, commercial, two-injector vertical rotating disk MOCVD reactor (CVD, Inc.). It was found that the geometry of the susceptor greatly affected the structural quality of the epilayers on Si. For the original susceptor geometry, though single crystal GaN films could be obtained, the films were dark gray in appearance with a rough morphology, and the best x-ray rocking curve FWHM was 2.33°. After modifying the susceptor geometry, transparent, mirror-like single crystal GaN films were obtained with the best x-ray rocking curve FWHM being 0.24°. Photoluminescence (PL) and infrared reflectance (IR) spectra of the grown films were compared. The film growth rate was found to increase with decrease of the growth pressure. A 2-D simulation of the flow, heat transfer, and chemical species transport in the reactor showed a more symmetric flow, larger velocity gradient, and lower upward velocity with the modified susceptor, which may be the main reason for the improvement of the structural quality of the films.

I. INTRODUCTION

GaN has attracted much research interest due to its potential application in optical, high temperature, and high power devices. Although high quality GaN films have been achieved by MOCVD growth, the mechanism is still not fully understood. Factors found to affect MOCVD growth of GaN include substrate properties,[1] any buffer layer and its growth conditions,[2] epilayer growth temperature and pressure,[3] V/III molar flow ratio,[4] inlet flow rate and reactor configuration,[5] among others, but a careful control of these factors does not guarantee a high quality film. The growth of GaN on silicon is very difficult due to their large difference in lattice constant, crystal structure, and thermal expansion coefficient,[6] yet silicon is a very attractive material since it offers the possibility of incorporating GaN devices in silicon devices. In this work, a new, commercial, two-injector, vertical rotating disk MOCVD reactor (CVD Equipment Corporation) was used to grow GaN on Si(111). After experiencing difficulties with film growth using the standard geometry, we modified it and found that the susceptor geometry greatly affected the structural quality of the films.

II. EXPERIMENT

A new, commercial MOCVD system (CVD, Inc.) was used for GaN growth. It consists of a gas delivery system, pumping system, and reaction chamber. The reaction chamber is

Mat. Res. Soc. Symp. Proc. Vol. 537 © 1999 Materials Research Society

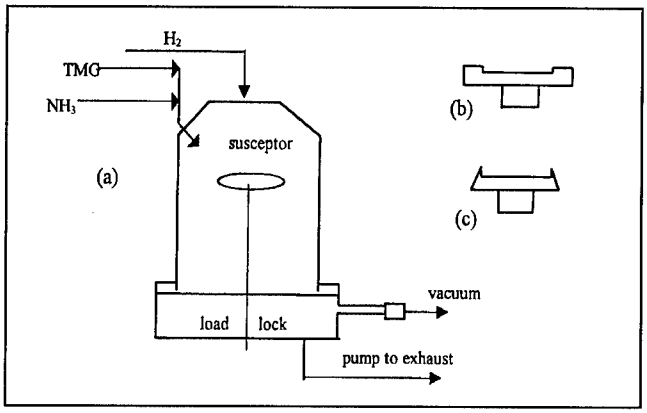


Figure 1. (a) schematic of the MOCVD reaction chamber. (b) original susceptor shape. (c) modified susceptor shape.

schematically illustrated in Figure 1a. It is a two-injector, vertical, cold-wall reactor with a rotating molybdenum susceptor inductively heated by RF. The susceptor is capable of processing one wafer with a diameter of 1 inch per run. A thermocouple is placed inside a quartz shaft underneath the susceptor to monitor the growth temperature. A closed loop vacuum pumping system enables the reactor to be operated over a pressure range of 10 to 760 torr with good stability. A high vacuum loadlock is interfaced to the reactor to isolate it from the ambient environment during wafer loading and unloading operations. Figures 1(b) and (c) show the original and modified susceptor, respectively. The original, manufacturer-supplied susceptor has a diameter of 37.5 mm, including a circular central part (which has a diameter of 25.5 mm) and an outer edge of 6 mm width. The central part of the modified susceptor was unchanged from the original, but the outer edge was cut and tapered. The diameter at the base of the modified susceptor was 31.5 mm.

The source gases were ammonia (NH_3), trimethylgallium (TMGa), and trimethylaluminum (TMA). Hydrogen was used as a carrier gas. Silicon (111) was used as the substrate, and it was cleaned in acetone, 2%HF, and UHP deionized water, then dried with N_2. Prior to growth, it was heated at 1050°C under a hydrogen flow of 2 slpm for 5 min. A total inlet gas flow rate of 1.0 slm was used. The inlet flow distribution was 0.4 slpm H_2, 0.3 slpm NH_3, and 0.3 slpm H_2 to push the TMA or TMG. The carrier gas flow rate through the TMA bubbler (28°C) or TMG bubbler (-10°C) was 1 sccm. The calculated V/III molar flow ratio was 4390. An AlN buffer layer with a thickness of around 100 nm was grown at 1050°C.[7] The GaN epilayer was grown at 1000°C for 45 minutes. Four samples were grown under the above conditions, but with differing susceptor geometry, growth pressure, or susceptor rotation rate as shown in Table I. Sample 1 was the best of the samples deposited using the original susceptor.

Table I. Sample growth conditions.

	sample 1	sample 2	sample 3	sample 4
susceptor shape	original	modified	modified	modified
pressure (torr)	76	10	10	76
spin rate (rpm)	60	150	60	150

X-ray diffraction (XRD), Photoluminescence (PL), and Infrared Reflectance (IR) were used to characterize the deposited films. XRD was performed with a Rigaku X-ray diffractometer with

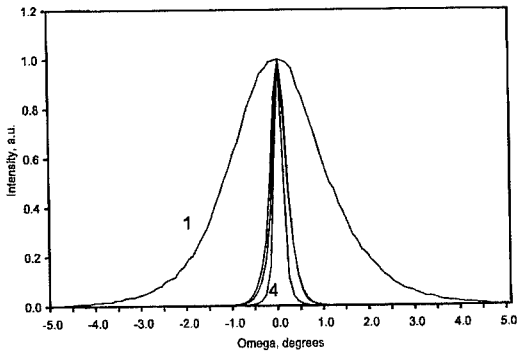


Figure 2. X-ray rocking curves on the GaN (0002) reflection. The curves for samples 1 and 4 are labeled.

a wide angle automated goniometer and computer-based data acquisition and analysis system. IR data was collected on a Perkin-Elmer Spectrum 2000 spectrometer using unpolarized light with a reflectance angle of 0° from the normal. A gold mirror was used as the reference. PL emission at 9.5K was measured. A He-Cd laser beam (325 nm, 9 mw) was used as the excitation source. The optical signal was detected by Princeton Instruments back-illuminated CCD camera model TEA-CCD-512 TK with a UV/AR coating and controlled by a computer. Commercial CFD software (FLUENT) was used to characterize the fluid dynamics in the reactor.

III. RESULTS

The appearance of sample 1 was rough and dark gray, while samples 2 through 4 appeared transparent and mirror-like.

3.1 XRD Results

Theta-2 theta scans of the samples showed that, in addition to Si reflections, only four other reflections were detectable, i.e. GaN (0002), AlN (0002), GaN (0004), and AlN (0004). This showed that the epilayers were single crystal and in the wurtzite phase. Figure 2 is the X-ray rocking curve on the GaN (0002) reflection. The FWHM of samples 1 to 4 were 2.33°, 0.36°, 0.40°, and 0.24°, respectively (shown in order 1, 3, 2, 4 in the figure with curves for samples 1 and 4 labeled), showing that the structural quality of the GaN films was much improved using the modified susceptor.

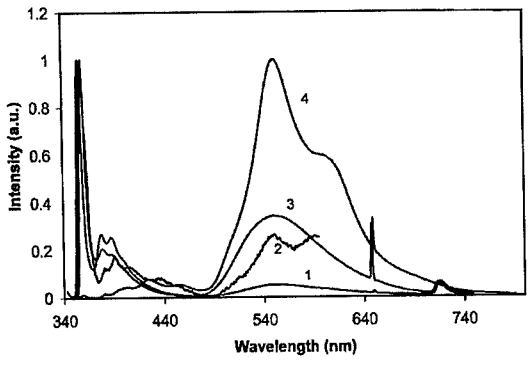


Figure 3. Photoluminescence spectra of the samples.

3.2 PL Results

Figure 3 shows the photoluminescence (PL) spectra of the samples. A very strong near band edge emission was observed at 358.5 nm on samples 1 and 2 and at 356.5 nm on sample 3. The FWHM of these peaks were 61, 62, and 59 meV, respectively. Two additional peaks at 378 nm and 388 nm were also observed on these

samples. Sample 4 showed a very weak near band edge emission but a very strong yellow luminescence, which is surprising considering that the X-ray rocking curve of this sample was the narrowest.

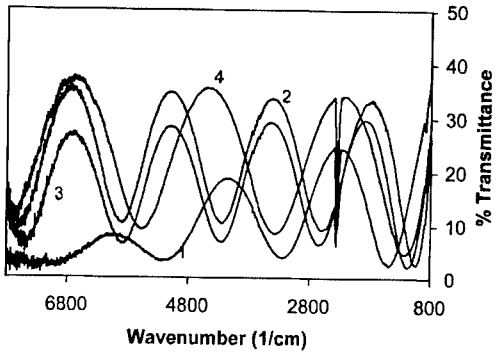


Figure 4. IR transmittance spectra.

3.3 IR Results

From the number of interference fringes that occurred between two frequencies of the IR transmittance spectra as seen in Figure 4, we calculated the thickness of the films,[8] which were 1.12, 1.27, 1.32, and 0.95 μm, respectively, for samples 1 to 4. It was interesting to note the thickness (growth rate) differences among samples 2 to 4. The growth rates under different susceptor spin rates (60 rpm vs. 150 rpm) were almost the same, while there was a significant difference among the growth rates under different growth pressures, and the growth rate decreased with increasing pressure. This result was also confirmed by the thickness of sample 1, which was thinner than samples 2 or 3. From Figure 4 we can also see that the interference fringes of sample 1 attenuate quickly at higher frequencies, which indicates the inferior quality of the film. Figure 5 shows the IR absorbance spectra of the films. A strong, sharp LO phonon mode in wurtzite GaN is observed at 735 cm^{-1} on sample 4, which further confirms both the high quality of the film and the x-ray rocking curve results. The LO phonon mode was also observed on sample 2 at 738 cm^{-1}. The phonon mode of sample 1 is shifted to a higher frequency of 743 cm^{-1}. The LO phonon mode of AlN was also observed at around 882 cm^{-1}. No GaN or AlN LO phonon mode was observed on sample 3; the reason for this is not clear.

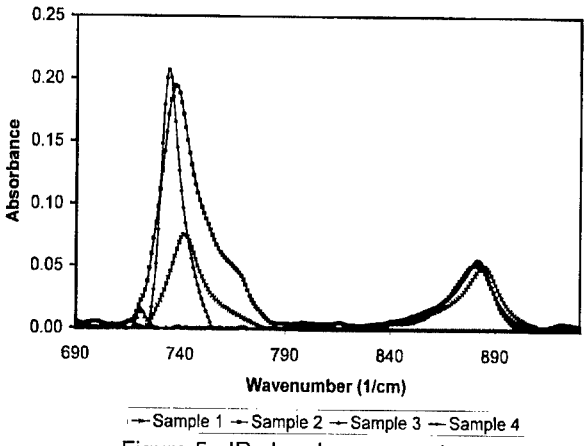


Figure 5. IR absorbance spectra.

3.4 Reactor Simulation Results

The fluid dynamics in the reactor with the two different susceptors was simulated using a 2-D model. The model consisted of a numerical solution of the Navier-Stokes equations coupled with heat transfer and mass transport of chemical species using FLUENT software. The effects of variable gas properties and buoyancy was included, but did not include the rotation of susceptor and chemical reactions. A detailed 3-D simulation with susceptor rotation is being conducted and the

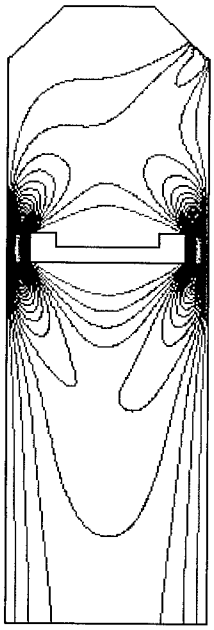


Figure 6. Vertical velocity contours for the original susceptor model.

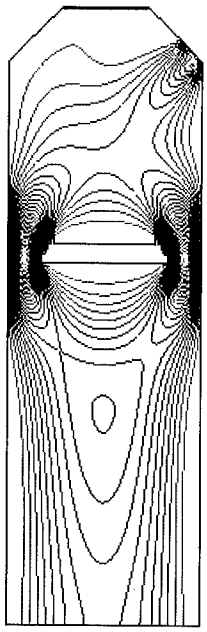


Figure 7. Vertical velocity contours for the modified susceptor model.

results will be reported later. Figures 6 and 7 show the vertical velocity contour in the reactor with the only difference being susceptor geometry. From the figures, the following differences are noted: (1) the velocity distribution above the modified susceptor is more symmetric, and (2) the velocity gradient is larger above the modified susceptor. The model also indicates that the upward velocity above the original susceptor is more than twice that of the modified susceptor. (This is not discernable from the Figures.) The more symmetric flow, larger velocity gradient, and lower upward velocity may be the primary reasons for the improvement of the structural quality of the films.

IV. CONCLUSIONS

The effect of susceptor geometry on the growth of GaN on silicon substrate using a new MOCVD system was studied. A modified susceptor was found to change the fluid dynamics in the reactor, resulting in a gas flow that is more symmetric, has a larger gradient, and has a weaker recirculation flow over the susceptor. The structural quality of films grown on the modified susceptor was much improved regardless of the susceptor rotation rate and growth pressure. Combining the PL and IR results, high structural and optical quality films could be obtained at 10 torr and 150 rpm with the modified susceptor.

ACKNOWLEDGMENTS

Partial support for this work under grant BMDO-DURISP N00014-96-0782 is gratefully acknowledged. The authors wish to thank T. Lin, W. Jadwisienczak, H. Richardson, and B. Mehta at Ohio University for their help with both film and flow characterization.

REFERENCES

1. H. Morkoc, S. Strite, G. B. Gao, M. E. Lin, B. Sverdlov, and M. Burns, J. Appl. Phys. 76, 1363 (1994).
2. J. N. Kuznia, M. A. Khan, D. T. Olson, R. Kaplan, and J. Freitas, J. Appl. Phys. 73, 4700 (1993)

3. T. Sasaki, and T. Matsuoka, J. Appl. Phys. 77, 193 (1995).
4. M. Tchounkeu, O. Briot, B. Gil, J. P. Alexis, and R. L. Aulombard, J. Appl. Phys. 80, 352 (1996).
5. S. Nakamura, Y. Harada, and M. Seno, Appl. Phys. Lett.58, 2021 (1991)
6. G. A. Martin, B. N. Sverdlov, A. Botchkarev, H. Morkoc, D. J. Smith, S.-C. Y. Tsen, W. H. Thompson, M. H. Nayfeh, Mat. Res. Soc. Symp. Proc. 67, vol. 395 (1996).
7. A. Watanabe, T. Takcuchi, K. Hirosawa, H. Amano, K. Hiramatsu, and I. Akasaki, J. Crystal Growth 128, 391 (1993).
8. N. J. Harrick, Appl. Opt. 10, 2344 (1971).

STRUCTURE OF AlN ON Si (111) DEPOSITED WITH METAL ORGANIC VAPOR PHASE EPITAXY

Eric Rehder,[*] M. Zhou,[**] L. Zhang,[***] N. R. Perkins,[*] S. E. Babcock,[*,**] and T. F. Kuech[*,***]
[*]Materials Science Program, [**]Dept. of Materials Science, and [***]Dept. of Chemical Engineering
University of Wisconsin – Madison, Madison, WI 53706.

Cite this article as: MRS Internet J. Nitride Semicond. Res. 4S1, G3.56 (1999)
Revised Jan. 18. 1999

ABSTRACT

The surface morphology and structure of AlN deposited by metal organic vapor phase epitaxy (MOVPE) on Si (111) at growth temperatures ranging from 825 to 1175 °C was investigated. Transmission electron microscopy (TEM), reflection high energy electron diffraction (RHEED), atomic force microscopy (AFM), and secondary ion mass spectrometry (SIMS) techniques were used to study the resulting film structure. Growth at high temperatures but less than ~1100 °C, resulted in a wire texture with some degree of in-plane alignment with $(0001)_{AlN}$ // $(111)_{Si}$, $<10\bar{1}0>_{AlN}$ // $<\bar{2}11>_{Si}$, and $<11\bar{2}0>_{AlN}$ // $<\bar{1}10>_{Si}$. Deposition at temperatures greater than 1100°C results in single crystal films consisting of domains 60 nm across with an aspect ratio near unity. Growth below 1100°C leads to degraded crystal quality with the grains developing random rotational misalignments around the AlN [0001] axis. Growth at lower temperatures produces islands elongated along the $[11\bar{2}0]$ direction. At the growth temperature of 825°C, the aspect ratio of the islands increased to 3 and a width of 25 nm. Cross-sectional TEM reveals that these islands are faceted due to slow growth on the $\{1\bar{1}01\}$ planes.

INTRODUCTION

Nitride-based III-V materials have been receiving attention due to their ability to lase in the green and blue spectral regions. However, these materials are difficult to fabricate. The strong bonding of N_2 and low nitrogen solubility in molten Ga results in very high nitrogen overpressures during crystallization of a nitride crystal from the melt. These difficulties have prevented the production of useful GaN bulk crystals. Lack of a single-crystal nitride substrate requires devices to be made through heteroepitaxial growth. GaN and AlN also have a coefficient of thermal expansion, lattice constant and crystal structure different from other III-V semiconductors. Nitrides therefore need to be grown on a substrate different from those normally used for compound semiconductor growth, such as GaAs or InP.

The highest quality materials have used either silicon carbide or sapphire substrates [1,2]. These materials can be expensive and limited in size. Additionally, the lattice mismatch to these substrates is quite large and even the highest quality materials contain a high concentration of lattice mismatch related structural defects. Silicon substrates have been successfully used for nitride growth. A Si (111) substrate will have the required hexagonal surface symmetry. The low cost and availability of this substrate makes it an attractive alternative to silicon carbide and sapphire substrates.

Previous work using Si substrates centered upon growth of AlN and GaN. Much of this work was done in ultra-high vacuum (UHV) using molecular beam epitaxy (MBE) or sputtering to produce the layers [3,4]. Single crystal films could be grown under optimized conditions. As with most nitride heteropitaxial growth, the films contained a dense network of structural defects.

Direct growth of GaN on Si (111) is difficult due to poor film nucleation, however single crystal AlN buffer layers have been grown directly on Si (111) [5]. The optimization of AlN

Mat. Res. Soc. Symp. Proc. Vol. 537 © 1999 Materials Research Society

growth on Si (111) was carried out using metal organic vapor phase epitaxy (MOVPE). In MOVPE growth, the metal organic precursor, trimethyl aluminum, and ammonia are carried to the growth surface in a hydrogen carrier gas. The precursors undergo a series of chemical reactions, which can take place both in the gas stream and on the substrate. These reactions result in a growth surface possessing a distribution of organic compounds and deposited film species. On the other hand, the UHV-based techniques only deliver the specific inorganic film species. MOVPE films could therefore have different material properties due to the modified surface kinetics.

A possible limitation in the MOVPE process is the purity of the gas sources. Impurities may be present in the reactor from a variety of sources. Contaminants in the source materials, reaction by-products and real as well as 'virtual' leaks can all lead to unwanted chemical impurities in the growing film. Virtual leaks are the slow release of impurities, such as water, absorbed on internal reactor and gas line surfaces. The virtual leaks are largely due to air exposure during installation or sample exchange. These impurity sources contain notably different contaminants. Most of the air is quickly removed, but the surface adsorbed water tends to persist in the system for extended periods. The gas source-based impurities are metal alkoxides and reaction byproducts from the decomposition of the metalorganic specie. These contaminants are complex metalorganic molecules that may decompose and yield C impurities in the growing film.

During MOVPE growth of most III-V materials, the requirements on the oxygen or water content in the reactor are relaxed because of the volatility of III-V oxides within a H_2 ambient at high temperatures. Alternatively, Si readily forms surface oxides in the presence of trace amounts of oxygen or water, a process that was studied by Ghidini and Smith [6]. Higher temperatures were found to promote oxide desorption. At the high temperature of 1000°C, the partial pressure of water within the reactor must be less than 10^{-4} Torr to have an oxide-free Si surface. This constraint is a significant practical limitation to growth upon Si substrates.

AlN growth was studied here at growth temperatures between 825 and 1175°C. Under these conditions, the maximum allowable water vapor pressure in the reactor tolerated before surface silicon oxides will form range from $5x10^{-7}$ to $5x10^{-2}$ Torr. The Si substrates initially received a brief dilute HF dip prior to sample loading. A 2.5 minute anneal at 1175 °C in hydrogen was performed to initiate each sample with hopefully identical oxide-free Si surfaces. Growth was carried out for 30 min. with a V/III ratio of 10000 at a reactor pressure of 76 Torr, which resulted in films 200 to 300 nm in thickness. To probe the influence of reactor chemistry, an additional sample was grown at 1125°C with the ammonia flow rate doubled.

The samples were analyzed for chemical, structural, and surface defects, using *ex situ* reflection high energy electron diffraction (RHEED), transmission electron microscopy (TEM), surface ion mass spectrometry (SIMS), and atomic force microscopy (AFM).

RESULTS AND DISCUSSION

AFM analysis was performed in both contact and tapping modes. The samples were populated by a dense network of small islands as shown in Figure 1. The island size is comparable to the size of a standard AFM probe, requiring detailed measurements to confidently image these features. The surface morphology contains small islands as shown in Figure 1. Samples grown above 1100°C have rounded features. At lower growth temperatures, the islands become elongated with widths decreasing from 60 to 25 nm. The variations in the island aspect ratio and relative orientation was determined and are given in Figure 2. The island lateral growth rate varies with in plane crystal direction. At high temperature s, the islands have an aspect ratio near 1 resulting in a flat angular orientation. Below 1100 °C the islands extend preferentially in the $[11\bar{2}0]$ directions.

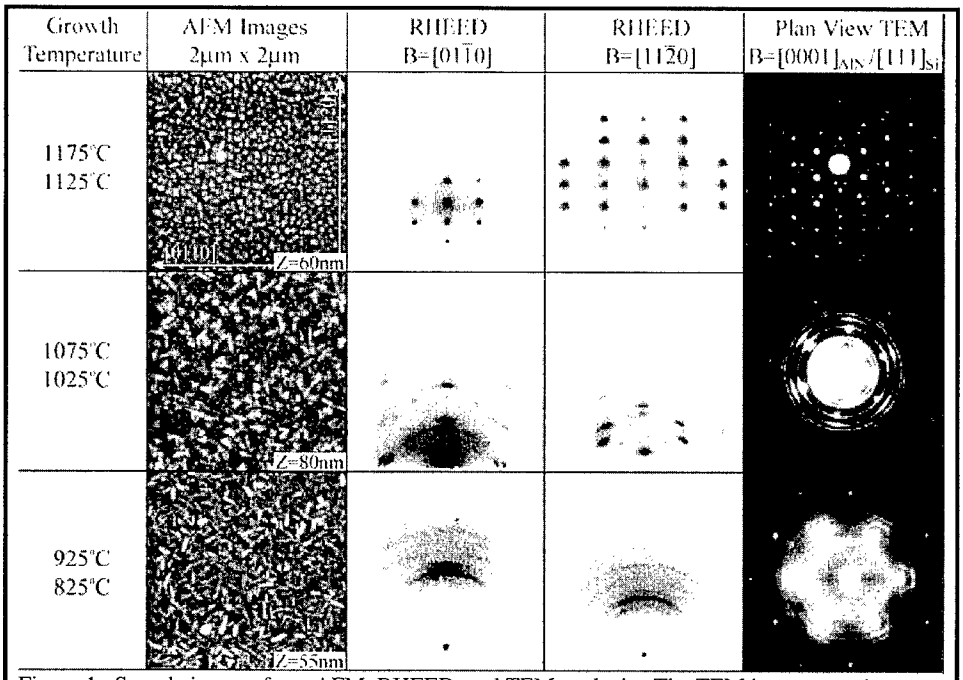


Figure 1. Sample images from AFM, RHEED, and TEM analysis. The TEM image contains diffraction from both Si and AlN. The diffraction patterns were obtained by TEM-selected area diffraction and obtained on the 1125, 1025, and 925 °C samples.

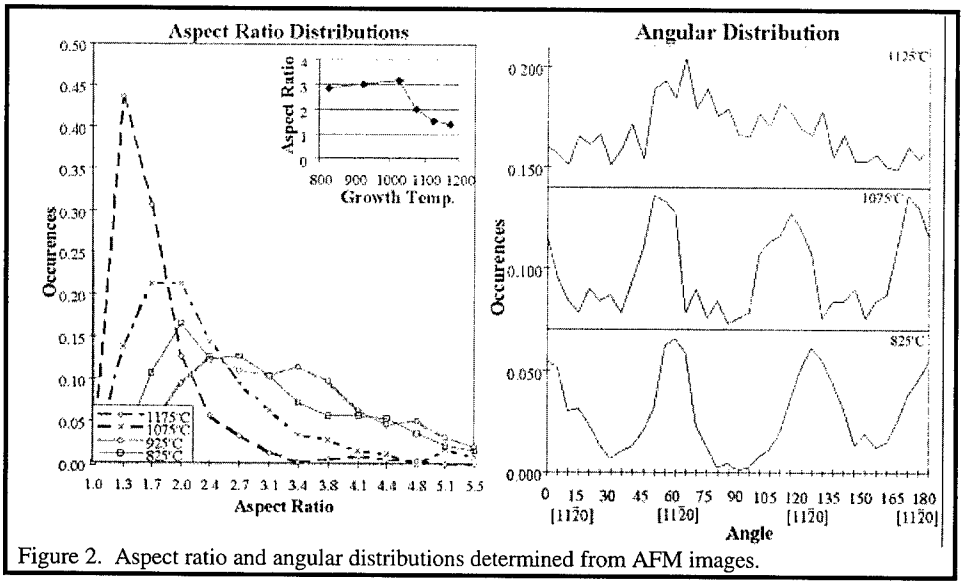


Figure 2. Aspect ratio and angular distributions determined from AFM images.

Figure 3 presents cross sectional images of the islands obtained from TEM and AFM. The island sidewalls are inclined nearly 60 degrees from the $[01\bar{1}0]$ direction, which identifies the sidewall facet as a $\{1\bar{1}01\}$ plane. The extension of the sidewall indicates this to be a slow growth crystal face. This same preferential faceting and growth rate variation has been observed during epitaxial lateral overgrowth of GaN [7,8].

Both RHEED and TEM were used to examine the microstructure of the samples. The diffraction patterns in Figure 1 exhibit a clear transition in structure at 1100 °C. For growth temperatures greater than 1100°C, the following in plane film orientations were determined: $(0001)_{AlN}$ // $(111)_{Si}$, $<10\bar{1}0>_{AlN}$ // $<\bar{2}11>_{Si}$, and $<11\bar{2}0>_{AlN}$ // $<\bar{1}10>_{Si}$. At temperatures below 1100°C, the diffraction patterns indicate a textured, polycrystalline structure. The absence of the (0002) ring in these diffraction patterns indicates that very few if any of the grains have their [0002] axis inclined from the Si [111] axis. Identical behavior at 1100°C has been noted in work by Watanabe et al. and Weeks et al [5,2]. Plan view TEM dark-field micrographs indicate that the average grain sizes in these textured samples are 50, 36, and 35 nm for growth temperatures of 1175, 1075, and 925°C respectively.

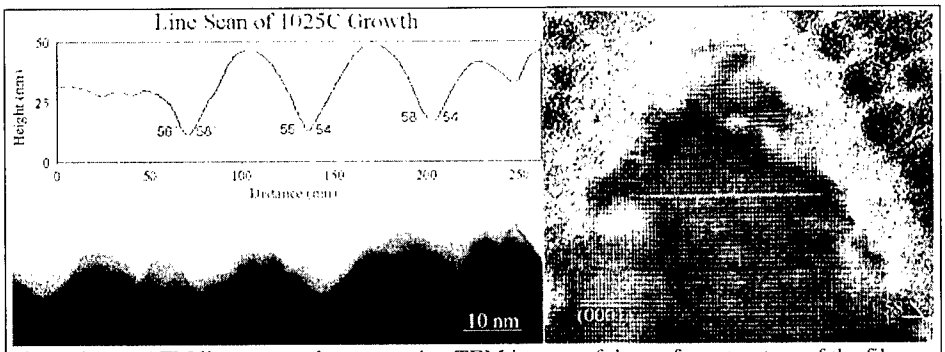


Figure 3. An AFM line scan and cross section TEM images of the surface structure of the films detailing the faceted $\{1\bar{1}01\}$ planes. There is good correspondence between the TEM and AFM determined surface roughness.

Doubling the ammonia flow rate during growth at 1125°C was found to greatly deteriorate the sample quality. The RHEED image of this sample appeared very similar to the sample grown at 825°C. Additionally, the island distribution was also comparable to the samples grown at low temperature. This observation indicates that increasing the ammonia flow rate has similar effects on sample structure as lowering the growth temperature. The ammonia is known to have a high water concentration, which would lead to increased oxygen incorporation at high ammonia flow rates.

Impurity incorporation during AlN growth was determined through SIMS measurements of the samples grown at 1125 and 1075°C. Both samples exhibit significant amounts of carbon at the substrate interface. These SIMS measurements are complicated by the surface roughness, however the carbon and oxygen found at the surface do extend deep into the AlN layer. The bulk of the films were found to contain oxygen with the sample grown at 1075°C having three times more oxygen than the sample grown at 1125°C.

The microstructure of all the films is characterized by small grains whose interiors are largely free of defects as determined from TEM. Growth above 1100°C results in films with grains aligned to the Si substrate. Below a growth temperature of 1100°C the grain structure loses this

epitaxial relationship but retains an overall texture. The angular variation increases with decreasing growth temperatures. The loss of epitaxy at lower growth temperatures was initially thought to be caused by the oxidation of the Si surface prior to growth. The trimethyl aluminum source can also contain low levels of oxygen contaminants, which could lead to the high oxygen content of these films. A high oxygen content would obscure any oxygen signal which might be originating from SiO_2 at the interface. Surface roughness also complicates and degrades the depth resolution in the SIMS measurement.

Surface kinetics can also play a role in determining epitaxy and physical structure. Surface transport is dependent on the growth temperature, surface adsorbed species and existing surface structure. Independent of contamination issues on the Si surface, such factors can play a fundamental role in the determination of the microstructure. The observed grain size and wire texture are attributed to surface transport during film nucleation. At higher temperatures the increased surface diffusion results in the formation of few large, stable nuclei. Furthermore, the high temperatures allow the nuclei to homogeneously orient themselves with the Si substrate in a low energy configuration. This conclusion accounts for the results obtained with UHV deposition, where a reduction in growth temperature below a critical value produced an identical degradation of crystal structure to wire texture [3]. However, this temperature occurred at 700°C under UHV sputtering instead of the 1100°C found for the MOVPE deposition reported here and also by Watanabe et al [5]. The chemical species present during MOVPE growth, may limit surface diffusion similar to a reduction in temperature. Thus to surmount the limited surface diffusion, the temperature must be increased from 700 to 1100°C during MOVPE growth.

CONCLUSIONS

The physical structure of MOVPE-grown AlN on Si (111) is sensitive to both the temperature and V/III ratio. The films are characterized by granular structures. Single crystal films are observed above 1100°C at a V/III ratio of 10000. Below 1100°C, the AlN grains are not epitaxial but exhibit a preferred texture. The surface contains a network of faceted islands exhibiting slow growth on $\{1\bar{1}01\}$ planes. The differential growth rate of the island facets yields nominally round islands at a growth temperature of 1175°C and islands with an aspect ratio near 3 at 825°C.

ACKNOWLEDGEMENTS

The work in this paper was supported by the ONR MURI (C. Wood) on compliant substrates. The authors are grateful to Ho-Yin Mok for assistance with sample analysis. Facilities support of the NSF supported UW MRSEC on Nanostructured Materials and Interfaces is gratefully acknowledged.

REFERENCES:

1. M. Fatemi, A. E. Wickenden, D. D. Koleske, M. E. Twigg, J. A. Freitas, Jr., R. L. Henry, and R. J. Gorman, Appl. Phys. Lett., **73**, 608-610(1998).
2. T. W. Weeks, Jr., M. D. Bremser, K. S. Ailey, E. Carlson, W. G. Perry, and R. F. Davis, Appl. Phys. Lett., **67**, 401-403 (1995).
3. W. J. Meng, J. Heremans, and Y.T. Cheng, Appl. Phys. Lett., **59**, 2097-2099 (1991).
4. M.A. Sanchez-Garcia, E. Calleja, E. Monroy, F. J. Sanchez, F. Calle, E. Munoz, R. Beresford, J. of Crystal Growth **183**, 23 (1998).

5. A. Watanabe, T. Takeuchi, K. Hirosawa, H. Amano, K. Hiramatsu, and I. Akasaki, J. Crystal Growth **128**, 391 (1993).
6. G. Ghidini and F.W. Smith, J. Electrochem. Soc. **131**, 2924 (1984).
7. D. Kapolnek, S. Keller, R. Vetury, R. D. Underwood, P. Kozodoy, S. P. Den Baars, and U. K. Mishra, Appl. Phys. Lett, **71**, 1204-1206 (1997).
8. J. Park, P. A. Grudowski, C. J. Eiting, and R. D . Dupuis, Appl. Phys. Lett., **73**, 333-335 (1998).

INFLUENCE OF DOPING ON THE LATTICE DYNAMICS OF GALLIUM NITRIDE

A. Kaschner, H. Siegle*, A. Hoffmann, C. Thomsen

Institut für Festkörperphysik, Technische Universität Berlin, Hardenbergstraße 36, 10623 Berlin, Germany

*Present address: Lawrence Berkeley National Laboratory, Berkeley, California 94720, USA

U. Birkle, S. Einfeldt, D. Hommel

Institut für Festkörperphysik, FB 1, Univ. Bremen, Kufsteiner Str. NW 1, 28359 Bremen, Germany

Cite this article as: MRS Internet J. Nitride Semicond. Res. 4S1, G3.57 (1999)

Abstract

We present results of Raman-scattering experiments on GaN doped with Si, C, and Mg, respectively, grown by molecular beam epitaxy (MBE). The influence of the different dopants on strain and free-carrier concentration was investigated. Furthermore, we report on several local vibrational modes (LVM) around 2200 cm^{-1} in Raman spectra of highly Mg-doped GaN. A possible explanation of these high-energy modes in terms of hydrogen-related vibrations is given. We also found a variety of new structures in the range of the GaN host lattice phonons. Secondary ion mass spectroscopy (SIMS) was applied to determine the concentration of magnesium and unintentionally incorporated hydrogen.

Introduction

Much attention has been paid to the wide-bandgap material GaN due to its high potential for optoelectronic and high-power electronic applications [1]. Controlled p- and n-doping is a major issue for the fabrication of electronic devices based on group III-Nitrides. The growth of doped GaN epilayers and heterostructures by molecular beam epitaxy offers the advantage of lower unintentional dopant concentration in the material. Among the optical properties of doped GaN the influence of doping on the lattice dynamics is of special interest. Raman-spectroscopy is a powerful tool to investigate the correlation between doping, strain [2], and free-carrier concentration [3].
Moreover, dopant atoms can give rise to local vibrational modes (LVM) due to their different masses compared with those of the substituted elements [4]. High-energy modes are reported for Mg-doped GaN [5, 6] which were assumed to be related to hydrogen complexes. This is of special interest, because hydrogen is known as a compensating center for magnesium acceptors. To our knowledge, no LVM for Si-, C-, or Mg-doped GaN in the range of the host lattice phonons have been reported in literature so far.

Experiment

The Raman-scattering experiments were carried out in backscattering geometry with a triple-grating spectrometer equipped with a cooled charge-coupled device detector. The 488 nm line of an Ar^+/Kr^+ mixed-gas laser was used for excitation. The Raman shifts were determined with an accuracy better than 1 cm^{-1}. Microscope optics allowed spatially-resolved measurements with a resolution of about 0.7 μm.

Mat. Res. Soc. Symp. Proc. Vol. 537 © 1999 Materials Research Society

The samples under study were Si-, C-, and Mg-doped GaN films of about 1 µm thickness grown on sapphire (0001) substrates by MBE; the details are given elsewhere [7]. The Mg-doped samples A and B were p-conductive with a hole concentration at room temperature of $3.7 \cdot 10^{17}$ cm^{-3} and $1.4 \cdot 10^{17}$ cm^{-3}, respectively, whereas the other two samples were compensated but n-conductive. Secondary ion mass spectroscopy was applied to determine the concentration of magnesium and hydrogen. The measured concentrations are accurate to within 20% deviation. The dopant concentration of the Si- and C-doped GaN films were estimated in terms of growth conditions. The free-electron concentration in the Si-doped samples varied from $8.1 \cdot 10^{15}$ cm^{-3} to $1.3 \cdot 10^{20}$ cm^{-3} as determined by Hall measurements.

Results

1. Local vibrational modes in doped GaN

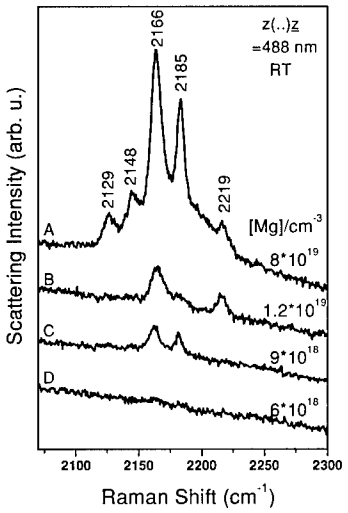


Figure 1: *Room-temperature Raman spectra of GaN with different magnesium content in the high-energy range.*

Figure 1 shows Raman spectra of samples with the respective magnesium concentrations of $8 \cdot 10^{19}$ cm^{-3} (A), $1.2 \cdot 10^{19}$ cm^{-3} (B), $9 \cdot 10^{18}$ cm^{-3} (C) and $6 \cdot 10^{18}$ cm^{-3} (D) in the high-energy region. In the spectrum of sample A with the highest magnesium concentration a new mode appears at 2129 cm^{-1} in addition to the four LVM described in Ref. 5. Apparently, the intensity of the modes correlates with the magnesium content. A Mg-concentration of around $1 \cdot 10^{19}$ cm^{-3} is necessary for some of the high-energy modes to appear well-resolved in the spectra. The hydrogen concentration for all the samples investigated is about $1 \cdot 10^{19}$ cm^{-3} as determined by secondary ion mass spectroscopy. Since hydrogen was not intentionally supplied during growth its incorporation possibly arises from the residual water vapor pressure in the growth chamber.

Yi et al. [8] observed a similar structure of five modes around 2800 cm^{-1} in Mg-doped GaN grown by metalorganic vapor phase epitaxy (MOVPE). These modes were attributed to symmetric and asymmetric C-H_n (n=1, 2, 3) vibrations due to carbon incorporation caused by the decomposition of the magnesium precursor during growth. Remarkably, the frequency ratio for all the five modes is between 1.33 and 1.34. This is close to $\sqrt{2}$, a value expected for similar vibrations with carbon (m_C=12.01 u) replaced by magnesium (m_{Mg}=24.31 u). This implies that magnesium is built into the lattice on a nitrogen site with force constants similar to those of carbon, an interpretation which seems doubtful. Furthermore, there are experimental and theoretical articles that determined the frequency of the Mg-H vibration above 3000 cm^{-1} [5, 9].

Alternatively, hydrogen-decorated native defects or hydrogen at extended defects such as dislocations can give rise to high-energetic vibrations. When the Fermi level reaches a value below 2.1 eV the formation of V_{Ga}-H_n complexes with n=1, 2, 3 is likely to occur with a predicted frequency of 3100 cm^{-1} for a V_{Ga}-H complex [10]. This is much higher than the frequencies we observe, even if anharmonic terms may lower the frequency considerably [10].

However, we rather believe that the magnesium incorporation causes the high-energy modes indirectly by creating defects or by lowering the Fermi level and therefore making the the hydrogen complex formation likely [11].

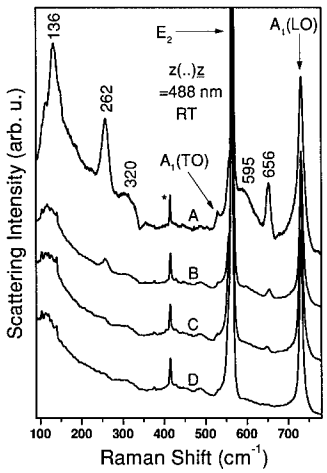


Figure 2: Room-temperature Raman spectra (normalized to E_2 intensity) of GaN with different magnesium content in the low-energy range. Apart from the host lattice phonons five additional modes are observed. The peak marked by an asterisk is a phonon from the sapphire substrate.

Apart from the five high-energy modes the highly Mg-doped samples exhibit new vibrational modes in the region of the acoustic and optical GaN phonons. We found structures at 136 cm^{-1}, 262 cm^{-1}, 320 cm^{-1}, 595 cm^{-1} and 656 cm^{-1}. Figure 2 displays the low-energy part of the Raman spectra of the four samples in the same sequence as in Figure 1. The broad structures centered around 320 cm^{-1} and 595 cm^{-1} may result from disorder-activated scattering, in which built-in defects yield a relaxation of the q=0 selection rule for first-order Raman scattering. This interpretation is supported by the fact that from sample D to A the forbidden A_1(TO) mode at 533 cm^{-1} increases considerably in intensity. Limmer et al. [12] reported on a disorder-activated Raman-mode around 300 cm^{-1} in ion-implanted GaN which is close to our 320 cm^{-1} mode. Furthermore, the cut-off at 340 cm^{-1} fits well with calculated phonon dispersion curves [13, 14]. On the other hand, the modes at 136 cm^{-1}, 262 cm^{-1} and 656 cm^{-1} probably do not originate from disorder-activated scattering since the phonon density of states (PDOS) does not exhibit marked structures in this frequency range [14]. Recently, a mode at 656 cm^{-1} was observed in GaN after annealing at 1000°C and related to a damaged-sapphire substrate [15]. The mode we observed at 656 cm^{-1} is of different origin since it does not scale with the intensity of the sapphire mode at 418 cm^{-1} nor with other modes of the damaged-sapphire at e.g. 770 cm^{-1} but rather with the Mg-concentration.

We thus believe these structures in the low-energy range to be correlated with magnesium. Equation (1) gives us a rough estimate of the magnesium local vibrational mode frequency from the effective masses of the GaN and LVM vibrations.

$$\frac{\omega_{GaN}}{\omega_{LVM}} \approx \sqrt{\frac{\mu_{LVM}}{\mu_{GaN}}} \qquad (1)$$

Assuming that magnesium occupies a gallium site we obtain a value of about 640 cm^{-1} for N-Mg vibrations using $\omega_{GaN} = \omega(E_1(TO)) = 560\ cm^{-1}$.

Though the 656 cm^{-1} mode lies in the range of the optical phonons its observation may be possible because the PDOS is relatively low in the region from 640 cm^{-1} to 675 cm^{-1} as confirmed by second-order Raman-scattering [13] and time-of-flight neutron spectroscopy [14]. We hence assign the 656 cm^{-1} mode to a local vibrational mode of magnesium in GaN. The Mg-concentration in the 10^{19} cm^{-3} range is apparently sufficient to observe the LVM without resonant excitation.

The nature of the 136 cm^{-1} and 262 cm^{-1} mode remains unclear. Since the density of states is also relatively low in the energy range of the two modes in question it is conceivable that they are also LVM.

We did not observe any LVM for the Si- and C-doped GaN samples in low-energy range nor in the high-energy range.

2. Biaxial Stress due to incorporation of dopants

Due to its nonpolar character the E_2 phonon frequency is a good measure for biaxial stress in GaN layers. Biaxial compressive stress increases the phonon frequency. Values of 4.2 cm^{-1}/GPa [2], 6.2 cm^{-1}/GPa [16] and 7.7 cm^{-1}/GPa [17] have been reported. Figure 3 shows the dependence of the E_2 frequency on the dopant concentration. While the E_2 values remain nearly constant between 567 cm^{-1} and 568 cm^{-1} over the whole doping range in case of the silicon doping series, we see a strong hardening in the magnesium series for Mg-concentrations exceeding $1 \cdot 10^{19}$ cm^{-3}. This

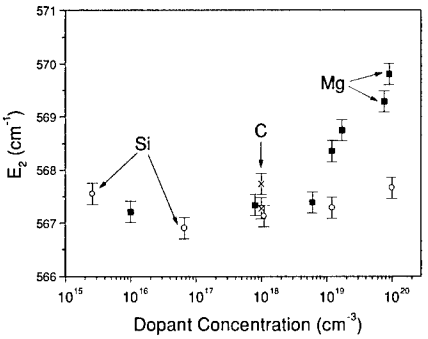


Figure 3: *Position of the E_2 mode for different doped GaN samples.*

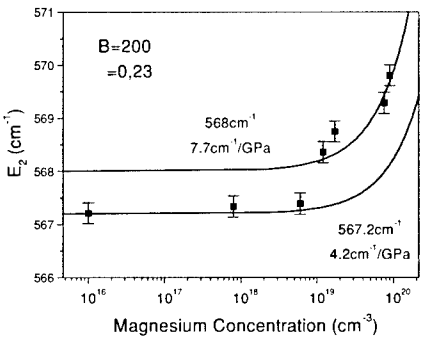


Figure 4: *E_2 position vs. Mg-concentration. The lines show the predicted behavior using eq. (2) and (3) with different values for the bulk E_2 frequency and the E_2 shift. The values for B and ν are taken from Ref. 2.*

behavior can be explained by the different size of the dopant atom (r_{Mg}=0.14 nm) and the replaced host atom (r_{Ga}=0.126 nm). Using equation (2) one can calculate the influence of this effect on the strain [2].

$$\varepsilon = \frac{c - c_0}{c_0} = \frac{\left[1 - \left(\frac{r_{Mg}}{r_{Ga}}\right)^3\right] \cdot C}{3N} \qquad (2)$$

Here, N is the number of lattice sites of the host matrix, C the dopant concentration, c and c_0 the strained and unstrained lattice constant, respectively. Equation (3), where B is the bulk modulus and ν is the Poisson ratio, correlates the strain with the biaxial stress.

$$\sigma = \varepsilon \cdot \frac{B}{\nu} \qquad (3)$$

Figure 4 shows the experimental data of the Mg-doped samples and calculated curves with different values for the strain-free E_2 frequency and $\Delta\omega(E_2)/\Delta\sigma$. It is obvious that the observed behavior can be explained by a size effect qualitatively, but the uncertainty for the basic GaN material parameters renders exact calculations difficult.

When substituting gallium by silicon one would expect the same effect but with opposite sign since the atomic radius of silicon is smaller than that of gallium. Surprisingly, we did not observe any significant shift for the E_2 frequency up to a silicon concentration of $1 \cdot 10^{20}$ cm^{-3}. The highly Si-doped samples do also exhibit a large free-carrier concentration (see next chapter). Therefore we

believe, that the size effect is compensated by the change of the lattice constant due to free electrons [17]. Following Ref. 18 a free-carrier concentration of $5 \cdot 10^{19}$ cm^{-3} should increase the lattice constant by 0.01% which equals the absolute value of the size effect caused by the same silicon concentration.
The carbon concentration of the samples in our study is too low to observe a significant E_2 shift.

3. Determination of the free-carrier concentration

The interaction of free charge carriers with longitudinal optical phonons leads to the observation of longitudinal phonon plasmon modes (LPP) [3]. If damping can be neglected the frequency of the LPP modes is given by equation (4).

$$\left(\omega_{LPP}^{\pm}\right)^2 = 0.5 \cdot \left\{\omega_L^2 + \omega_P^2 \pm \left[\left(\omega_L^2 + \omega_P^2\right)^2 - 4\omega_P^2\omega_T^2\right]^{\frac{1}{2}}\right\} \qquad (4)$$

Here, ω_L and ω_T are the frequencies of the LO and TO phonons, respectively. The plasmon frequency is correlated with the free-carrier concentration.

$$\omega_P^2 = \frac{ne^2}{m^* \varepsilon_\infty \varepsilon_0} \qquad (5)$$

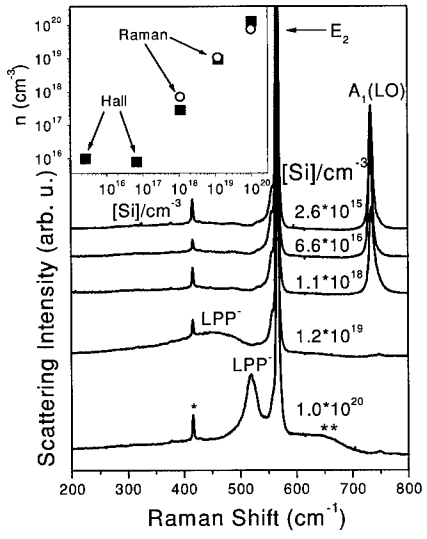


Figure 5: Room-temperature Raman spectra of different Si-doped samples. The inset shows the carrier concentration determined by Hall and Raman measurements vs. Si-content.

In equation (5) n and m* are the concentration and effective mass of the charge carriers, ε_∞ the high-frequency dielectric constant.
In Figure 5 the spectra of five samples with silicon concentrations between $2.6 \cdot 10^{15}$ cm^{-3} (top) and $1.0 \cdot 10^{20}$ cm^{-3} (bottom) are plotted. The two highest doped samples exhibit LPP$^-$ modes at 450 cm^{-1} and 520 cm^{-1}. The A_1(LO) mode already vanished and therefore the LPP$^+$ mode appears at 2580 cm^{-1} and 1070 cm^{-1} (not shown). From equations (4) and (5) we calculated the corresponding carrier concentration to be $7.4 \cdot 10^{19}$ cm^{-3} and $1.0 \cdot 10^{19}$ cm^{-3}, respectively. Notice that in both spectra a structure at around 650 cm^{-1} (**) appears which is only known from highly doped GaN [19]. The A_1(LO) mode of the sample with a silicon concentration of about $1.1 \cdot 10^{18}$ cm^{-3} appears slightly asymmetric typical for carrier concentrations between $5 \cdot 10^{17}$ cm^{-3} and $1 \cdot 10^{18}$ cm^{-3}. For the remaining two samples the free-carrier concentration is too low to cause any shift or broadening of the A_1(LO) mode and cannot be determined by this method. The inset of Figure 5 compares the free-carrier concentration determined by Hall measurements and by Raman spectroscopy as a function of the silicon concentration. Both data sets agree well. Raman spectroscopy offers the advantage that the free-carrier concentration can be determined with a spatial resolution better than 1 µm without contacting the samples.

Conclusions

In this work we have shown that a variety of information about doped GaN crystals can be obtained by Raman spectroscopy. We found LVM of magnesium in the region of the host lattice phonons as well as in the high-energy range which now may serve as an indicator for the incorporation of magnesium. No LVM were observed for our Si- and C-doped GaN samples. Doping with atoms of a different size than the substituted host atom causes internal stress which can be obtained via the shift of the nonpolar E_2 mode. For Mg-doped samples we found that the biaxial stress increases with dopant concentration while in case of silicon the size effect is roughly compensated by the increasing free-carrier concentration. The free carrier concentration of doped GaN can be determined by the frequency of the LPP modes.

Acknowledgment

We thank W. Kriegseis (University of Gießen) and M. Straßburg (TU Berlin) for carrying out the SIMS measurements. A.K. acknowledges the support of an Ernst von Siemens scholarship and H.S. a DAAD fellowship.

References

[1] See for example, S. N. Mohammad, A. Salvador, and H. Morkoç, Proc. of the IEEE **83**, 1306 (1995).

[2] C. Kisielowski, J. Krüger, S. Ruvimov, T. Suski, J. W. Ager III, E. Jones, Z. Lilienthal- Weber, M. Rubin, E. R. Weber, M. D. Bremser, and R. F. Davis, Phys. Rev. B 54, 17745 (1996).

[3] P. Perlin, J. Camassel, W. Knap, T. Taliercio, J. C. Chervin, T. Suski, I. Grzegory, S. Porowski, Appl. Phys. Lett. 67, 2524 (1995).

[4] A. S. Barker, Jr. and A. J. Sievers, Rev. Mod. Phys. **47**, Suppl. 2, S1 (1975).

[5] M. S. Brandt, J. W. Ager III, W. Götz, N. M. Johnson, J. S. Harris, R. J. Molnar, and T. D. Moustakas, Phys. Rev. B **49**, R14758, (1994).

[6] W. Götz, N. M. Johnson, D. P. Bour, M. D. McCluskey, and E. E. Haller, Appl. Phys. Lett. **69**, 3725 (1996).

[7] S. Einfeldt, U. Birkle, C. Thomas, M. Fehrer, H. Heinke, and D. Hommel, Mat. Sci. Eng. B **50**, 12 (1997).

[8] G.-C. Yi and B. W. Wessels, Appl. Phys. Lett. **70**, 357 (1997).

[9] J. Neugebauer and C. G. van de Walle, Phys. Rev. Lett. **75**, 4452 (1995).

[10] C. G. van de Walle, Phys. Rev. B **56**, R10020 (1997).

[11] A. Kaschner, H. Siegle, M. Straßburg, A. Hoffmann, C. Thomsen, U. Birkle, S. Einfeldt, and D. Hommel: "Low-energy lattice vibrations in Mg-doped GaN grown by MBE", submitted to Appl. Phys. Lett.

[12] W. Limmer, W. Ritter, R. Sauer, B. Mensching, C. Liu, and B. Rauschenbach, Appl. Phys. Lett. **72**, 2589 (1998).

[13] H. Siegle, G. Kaczmarczyk, L. Filippidis, A. P. Litvinchuk, A. Hoffmann, and C. Thomsen, Phys. Rev. B **55**, 7000 (1997).

[14] J. C. Nipko, C.-K. Loong, C. M. Balkas and R. F. Davis, Appl. Phys. Lett. **73**, 34 (1998).

[15] M. Kuball, F. Demangeot, J. Frandon, M. A. Renucci, J. Massies, N. Grandjean, R. L. Aulombard, and O. Briot, Appl. Phys. Lett. **73**, 960 (1998).

[16] T. Kozawa, T. Kachi, H. Kano, H. Nagase, N. Koide, and K. Manabe, J. Appl. Phys. **77**, 4389 (1995).

[17] I.-H. Lee, I.-H. Choi, C.-R. Lee, E.-J. Shin, D. Kim, S. K. Noh, S.-J. Son, K. Y. Lim, and H. J. Lee, J. Appl. Phys. **83**, 5787 (1998).

[18] M. Leszczynski, H. Teisseyre, T. Suski, I. Grzegory, M. Bockowski, J. Jun, S. Porowski, K. Pakula, J. M. Baranowski, C. T. Foxon, T. S. Cheng, Appl. Phys. Lett. **69**, 73 (1996).

[19] F. Demangeot, J. Frandon, M. A. Renucci, C. Meny, O. Briot, and R. L. Aloumbard, J. Appl. Phys. 82, 1305 (1997).

MOLECULAR BEAM EPITAXY OF HIGH QUALITY InGaN ALLOYS USING AMMONIA: OPTICAL AND STRUCTURAL PROPERTIES.

Nicolas Grandjean*, Jean Massies*, Mathieu Leroux*, Marguerite Laügt*, Philippe Vennéguès*, Stéphane Dalmasso*, Pierre Ruterana**, Lionel Hirsch***, Serge Barrière***

* CRHEA-CNRS, Rue Bernard Grégory, Sophia Antipolis, 06560 Valbonne, France
** LERMAT-CNRS, 6 Bd Maréchal Juin, 14050 Caen Cedex, France
*** IXL, ENSERB-CNRS, 351 cours de la libération, 33405 Talence, France

Cite this article as: MRS Internet J. Nitride Semicond. Res. 4S1.G3.59 (1999)

ABSTRACT

The growth of InGaN layers was carried out by molecular beam epitaxy (MBE). The nitrogen precursor was ammonia. The optical and structural properties of the InGaN layers have been investigated by transmission electron microscopy (TEM), x-ray diffraction (XRD) and photoluminescence (PL). For optimized growth conditions, the PL spectrum of InGaN (x=0.1) alloy is narrow (FWHM ≤ 50 meV) and the Stokes shift measured by PL excitation is weak (<50 meV), i.e. near band edge transitions are observed. Under these conditions, flat surfaces can be obtained, and InGaN/GaN quantum wells (QWs) with sharp interfaces can be grown. On the other hand, when growth conditions depart from a narrow optimum window, the structural quality of the samples strongly degrade, whereas the luminescence spectra are dominated by deep levels, exhibiting a strong Stokes shift. MBE grown light emitting diodes (LEDs) using InGaN/GaN QWs have been fabricated. Their electroluminescence (EL) peaks at 440 nm at 300K.

INTRODUCTION

The ternary alloy InGaN has a direct band gap ranging from 1.9 eV (InN) to 3.4 eV (GaN) and has now shown its potentiality for light emitters in the visible range of the electromagnetic spectrum. [1]. Most of the nitride based structures and devices are currently fabricated using metal-organic chemical vapor deposition (MOCVD), which has proven its ability for the growth of high quality nitrides [1]. MBE is however emerging as an alternative growth technique. It allows the use of high efficiency *in situ* characterization tools (reflection high energy electron diffraction (RHEED), mass spectroscopy...) and high quality GaN can be grown in the two versions of the MBE of nitrides, *i.e.* using NH_3 or an N_2 plasma source [2,3]. Presently, apart MOCVD, InGaN/GaN QW based LEDs have been reported only by plasma-assisted MBE growth [4]. We show in this paper that NH_3 is also well suited for achieving InGaN/GaN QWs with sharp interfaces. LEDs have been processed from that material and exhibit room temperature EL at 440 nm.

EXPERIMENTS

The growth of GaN and InGaN was carried out in a Riber 32 P MBE system equipped with RHEED and laser reflectivity facilities. Ga and In were provided by double-filament effusion

Mat. Res. Soc. Symp. Proc. Vol. 537 © 1999 Materials Research Society

cells. A flow of 50 sccm of purified NH_3 was used for the growth of both GaN and InGaN. Before growing the InGaN alloys or QW structures, 2 µm-thick GaN epilayer were deposited on (0001) sapphire substrates following the procedure described in ref. [3]. The substrate temperature was decreased around 600°C to grow InGaN. The growth rate is 0.2 µm/h and the thicknesses ranging from 70 to 200 nm. Concerning the In composition, it has been checked by XRD, Rutherford back scattering, and RHEED intensity oscillations. The two first techniques give roughly the same In composition while RHEED leads to larger values. Actually, RHEED intensity oscillations are observed only at the beginning of the growth. Therefore, a growth transient which can be provoked in particular by In surface segregation could affect the measurements. The structural properties of the layers were assessed by TEM and XRD. The optical properties were studied by PL using a 10 mW HeCd laser as excitation source.

RESULTS AND DISCUSSIONS

The specificity of InGaN MBE growth with NH_3, compared to plasma sources, is the cracking of this nitrogen precursor on the growing surface which depends on the substrate temperature. This implies that the amount of nitrogen active species is a function of the substrate temperature. For instance, it has been reported that the decomposition of NH_3 below 450°C is insignificant [5]. When increasing the substrate temperature, the NH_3 efficiency increases too but remains rather low (4 % at 700°C). Therefore, with the aim of growing GaInN alloy, we have to take care of the high dissociation rate of InN, the high In volatility and the NH_3 cracking efficiency pattern. We have determined that the best InGaN properties are obtained for temperatures ranging between 570 and 620°C.

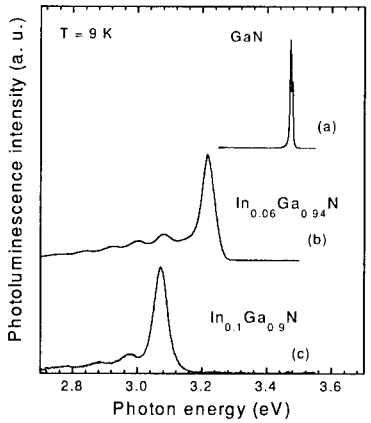


Figure 1: 9 K PL spectra of InGaN layers

Fig. 1 displays two low temperature (9 K) PL spectra of InGaN layers grown at ~600°C with a growth rate of 0.2 µm/h (the GaN spectrum is given in Fig. 1(a) as reference). The indium compositions are 6% and 10% in Figs. 1(b) and 1(c), respectively. A sharp PL peak (full width at half maximum (FWHM) of ~50 meV) is observed for the two In compositions. The transition

energies are 3.22 eV and 3.07 eV. The PL spectra of InGaN layers exhibits also deep luminescence on the low energy side of the main PL peak. Unfortunately, interference makes difficult to ascribe this luminescence to standard shallow donor acceptor pair recombinations or to deep-levels, or other origins (In rich and/or strain relaxed areas). When growth conditions depart from an optimum window, this deep-level PL dominates the spectra. Fig. 2 shows a cross section TEM image of a thin $In_{0.06}Ga_{0.94}N$ layer (160nm) deposited at 570°C and 0.18 µm/h on GaN template. One can see that no further defects are introduced in the InGaN layer. Only the preexistent dislocations propagate into the InGaN layer resulting in pits at the surface as for the case of MOCVD growth [6].

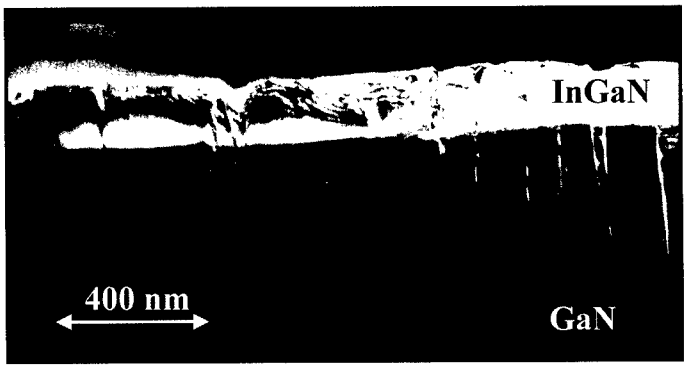


Figure 2: TEM image in cross section of an $In_{0.6}Ga_{0.94}N$ layer grown at 570°C and 0.18 µm/h

The strain state of the $In_{0.06}Ga_{0.94}N$ layer has been checked by XRD reciprocal space mapping of the [-105] and [105] reflections. Fig. 3 shows that the 160nm-thick InGaN layer is almost perfectly pseudomorphically strained onto the GaN template.

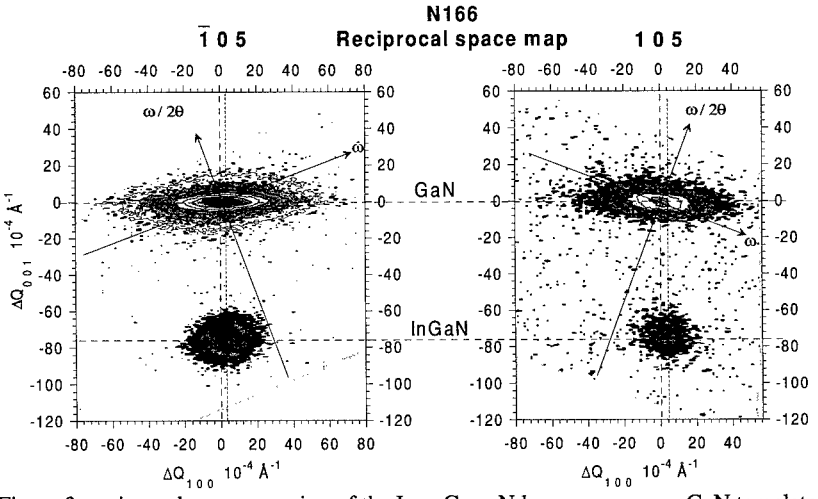


Figure 3: reciprocal space mapping of the $In_{0.06}Ga_{0.94}N$ layer grown on a GaN template

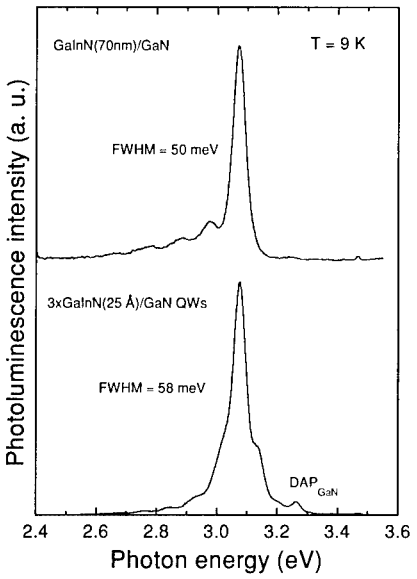


Figure 4: 9 K PL spectra of a GaInN layer (70nm) and of a 3xInGaN(25Å)/GaN(35Å) QWs

The InGaN alloys, previously characterized, have been used to grow InGaN/GaN QWs. Fig. 4 displays the 9 K PL spectrum of 3 GaInN/GaN QWs of width 25 Å. The In composition is about 10 %. For comparison, the upper spectrum in Fig. 4 corresponds to a bulk GaInN of similar composition. The peak energy of the QW sample is only slightly blue shifted (3.08 eV) relative to that of the bulk (3.07 eV). Actually, it is known that the energy of nitride QWs is determined by the interplay between quantum confinement and polarization field [7,8].
LEDs with a 5 InGaN(25Å)/GaN(35Å) active region have been grown on sapphire by MBE and characterized by TEM. Fig. 5 and 6 show low magnification and high resolution TEM image of the structure, respectively. One can clearly distinguish the wells. It should be remarked that the first well is thinner that the other ones (Fig. 7). The In surface segregation effect is likely responsible for such a feature.



Figure 5: dark field TEM image of the 5 GaInN(25Å)/GaN(35Å) QWs (LED active region)

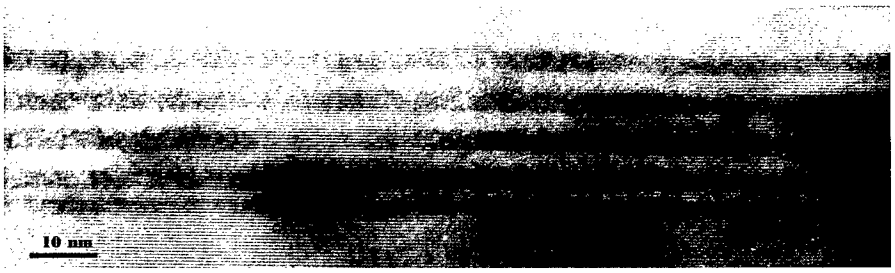


Figure 6: high resolution TEM image of LED active region

The room temperature electroluminescence spectrum of the LED of Figs. 5 and 6 is reported in Fig. 7. The EL emission is in the blue region of the visible electromagnetic spectrum with EL maxima at 440 nm for injection currents of 20 mA. The linewidth of the EL spectrum is 40 nm. A maximum output power of 10 μW at 20 mA has been measured using a calibrated Si diode. This is still low compared to the current MOCVD state of the art. Nevertheless, the demonstration of LEDs based on InGaN/GaN MQW structures grown entirely by MBE is encouraging in view of the fabrication of more sophisticated devices. Actually, epitaxial lateral overgrowth (ELOG) substrates will certainly boost the MBE based nitride device development in the near future.

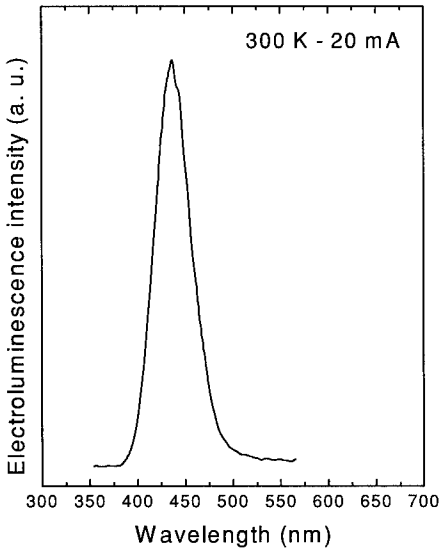


Figure 7: room temperature EL of a LED with a 5 GaInN(25Å)/GaN(35Å) QW active region

CONCLUSIONS

InGaN layers have been grown by MBE using ammonia as nitrogen precursor. The PL spectrum of InGaN ($x \leq 0.1$) alloy is narrow (FWHM $\leq$ 50 meV) and TEM reveals InGaN layers of reasonable quality. They are pseudomorphically strained on the GaN template as demonstrated by XRD reciprocal space mapping. InGaN/GaN quantum wells with sharp interfaces have been grown and inserted in the active region of LEDs. Their room temperature electroluminescence yields blue emission at 440 nm with a FWHM of 40 nm.

ACKNOWLEDGMENTS

This work is supported in part by BRITE EURAM EC contract N° BRPR-CT96-0334 " ANISET ".

REFERENCES

[1] S. Nakamura and G. Fasol, *The Blue Laser Diode*, (Springer, Berlin (1997))

[2] G.Popovici, H.Morkoç and S.Mohammad, in *Group III Nitride Semiconductor Compounds*, edited by B.Gil (Clarendon Press, Oxford (1998)) *and references therein.*

[3] N. Grandjean, J. Massies, P. Vennéguès, M. Leroux, F. Demangeot, M. Renucci, and J. Frandon, J. Appl. Phys. **83**, 1379 (1998)

[4] H. Tews, R. Averbeck, A. Graber and H. Riechert: Electron. Lett. **32**, 2004 (1996)

[5] M. Mesrine, N. Grandjean and J. Massies: Appl. Phys. Lett. **72,** 350 (1998)

[6] Y. Kawaguchi, M. Shimizu, M. Yamaguchi, K. Hiramatsu, N. Sawaki, W. Taki, H. Tsuda, N. Kuwano, K. Oki, T. Zheleva, R.F. Davis, J. Cryst. Growth **189/190**, 24 (1998)

[7] T.Takeuchi, S.Sota, H.Sakai, H.Amanoa, I.Akasaki, Y.Kaneko, S.Nakagawa, Y.Yamaoka, N.Yamada, J. Cryst. Growth. **189/190**, 616 (1998)

[8] S.F. Chichibu, A.C. Abare, M.S. Minsky, S. Keller, S.B. Leisher, J.E. Bowers, E. Hu, U.K. Mishra, L.A. Coldren, S.P. DenBaars, and T. Sota, Appl. Phys. Lett. **73**, 2006 (1998)

PROPERTIES OF EPITAXIAL ZnO THIN FILMS FOR GaN AND RELATED APPLICATIONS

H. Shen*, M. Wraback*, J. Pamulapati*, S. Liang**, C. Gorla**, and Y. Lu**

*U.S. Army Research Laboratory, Sensors and Electron Devices Directorate,
AMSRL-SE-EM, 2800 Powder Mill Rd., Adelphi, MD 20783-1197
pshen@arl.mil
**Dept. of Electrical and Computer Engineering, Rutgers University,
Piscataway, NJ 08855-0909

Cite this article as: MRS Internet Nitride Semicond. Res. 4S1, G3.60 (1999)

ABSTRACT

In this paper, we present a detailed study of high quality (110) ZnO films, epitaxially grown on R-plane sapphire substrates by metal-organic chemical vapor deposition (MOCVD). The epitaxial relationships are $(11\bar{2}0)$ ZnO//$(01\bar{1}2)$ Al_2O_3 and $[0001]$ ZnO//$[0\bar{1}11]$ Al_2O_3 as confirmed by X-ray diffraction (θ-2θ, and ϕ-scan) and high-resolution cross-sectional transmission electron microscopy (HR-TEM). Low temperature photoluminescence (PL) indicates the ZnO thin films are almost strain free. Optical absorption and reflection measurements with linearly polarized light indicate a strong optical anisotropy. The polarization rotation towards the C-axis associated with the optical anisotropy is utilized to demonstrate an optically addressed ultra-fast, ultraviolet light modulator.

INTRODUCTION

High quality zinc oxide (ZnO) films are useful for many applications. One of the more recent applications is the use of ZnO as a substrate for growth of GaN based materials[1-3] since the lattice mismatch between GaN and ZnO is relatively small. Due to a lack of low cost ZnO substrates, high-quality ZnO buffer layers on other substrates are of particular interest. In addition, it is also possible to develop UV lasers and modulators from these ZnO films.[4,5]

The most common technologies used for depositing ZnO films are laser ablation and sputtering.[6] Improvements have been made through triode sputtering and other new deposition techniques. Despite these advancements, there are still some problems associated with sputtering. Metal-organic chemical vapor deposition (MOCVD)[7,8] is an alternative technique for growth that has advantages such as chemical and thermodynamic dependent growth, control at the atomic level, large area deposition, and the possibility of different *in situ* doping processes. While most research has focused on ZnO films grown on (0001) oriented sapphire substrates (i.e. C-plane Al_2O_3), less research has been done on ZnO grown on other planes. In this paper we report a detailed study of the properties of ZnO grown on $(01\bar{1}2)$ oriented sapphire (R-plane).

Mat. Res. Soc. Symp. Proc. Vol. 537 © 1999 Materials Research Society

SAMPLE GROWTH

The samples used in this study were grown by MOCVD. R-plane sapphire was used as the substrate. The precursors used were DiEthyl Zinc (DEZn – $(C_2H_5)_2Zn$) and O_2. Typical growth conditions are as follows: chamber pressure of 20 to 50 torr; a growth temperature of 250 to 600 °C; and a total carrier gas flow from the top of 5000 to 15000 sccm. The thickness of the sample is 1 μm[9].

STRUCTURAL PROPERTIES

Figure 1 shows the x-ray θ-2θ scans from the sample. From the scan we found that ZnO film has a $(11\bar{2}0)$ orientation. The insert of Figure 2 shows the ϕ-scan from the $\{21\bar{3}0\}$ family of reflections for ZnO. We found that the angular separation is 180°, the same as predicted by theory for a single crystal. Also shown is the ϕ-scan from the $\{12\bar{3}5\}$ family of planes from sapphire. The position of the $\{21\bar{3}0\}$ peaks from ZnO and the $\{12\bar{3}5\}$ peaks from Al_2O_3 coincide in the ϕ-scans. From this we found that the epitaxial relationship for ZnO films grown on R-plane sapphire is:

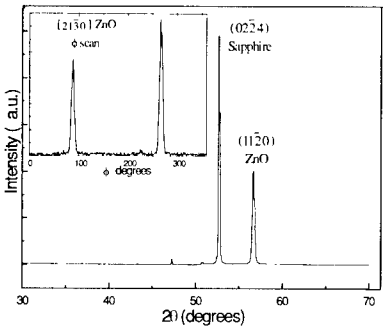


Figure 1: X-ray 2θ scan, insert: ϕ-scans of the $\{21\bar{3}0\}$ family of planes.

$(11\bar{2}0)$ ZnO//$(01\bar{1}2)$ Al_2O_3 and $[0001]$ ZnO//$[0\bar{1}11]$ Al_2O_3.

Figure 2 shows a cross-sectional TEM lattice image of the interface between ZnO and R-sapphire. The interface is observed to be atomically sharp and semi-coherent. The 18.3% misfit along the $[1\bar{1}00]$ direction of ZnO is relieved by extra half planes on the sapphire side of the interface. On average, there is one dislocation for every five $(1\bar{1}00)$ planes. The misfit between the two lattices is completely accommodated by misfit dislocations.

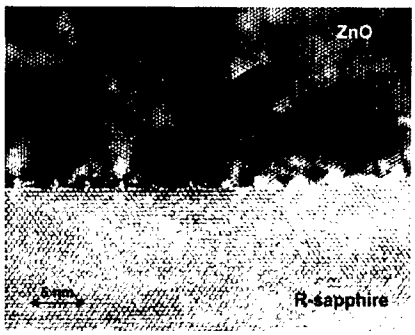


Figure 2: TEM image of the interface between ZnO and R-sapphire. The view is along the c-axis of ZnO .

OPTICAL PROPERTIES

Figure 3(a) shows the room temperature PL spectrum. The feature at 3.28eV is due to band-edge recombination. The broad feature at 2.35eV (green emission) is the recombination of free electrons with holes via interstitial zinc, or via defects at the grain boundaries[10,11]. From Fig. 3(a), the ratio of the integrated intensities of the band-edge emission to the deep level emission (broad band green emission) at room temperature is approximately 3:1. Similar results were observed form ZnO grown by molecular beam epitaxy (MBE)[1].

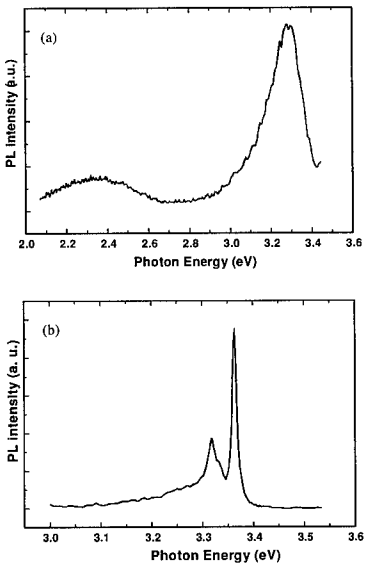


Figure 3: Photoluminescence from ZnO/R-sapphire; (a) room temperature, (b) 10k.

Figure 3(b) shows the low-temperature PL spectrum collected at 11K. The peak at 3.363eV is from donor-bound exciton (D^oX) transition, while the feature at 3.320eV is from the acceptor-bound exciton transition. Note that the position of the D^oX is in good agreement with 4K PL results from bulk ZnO[2] indicating that the thin film is almost strain free. The full width at half maximum of this feature is about 6 meV, compared to 3 meV (4.2K) from bulk ZnO and 8.9 meV (4.2K) from ZnO grown on GaN/SiC by MBE, indicating a film of high quality.

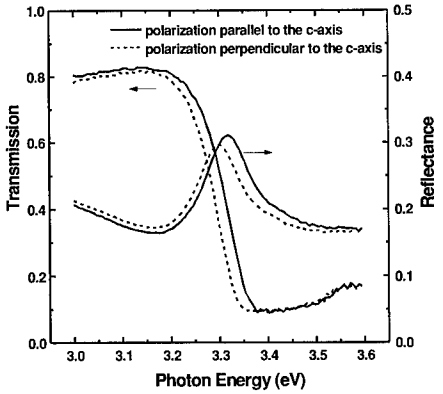


Figure 4: Transmission and Reflectivity of ZnO on R-plane sapphire as a function of photon energy for light polarized parallel (solid lines) and perpendicular (dashed lines) to the c-axis of the ZnO.

We have observed strong optical anisotropy from the ZnO film. Figure 4 shows the transmission T and reflectivity R of the ZnO film measured as a function of photon energy for light polarized parallel and perpendicular to the c-axis of ZnO. Although the shape of the transmission and reflectivity curves are similar for the two polarizations, the curves for $p//c$ are shifted to higher energy by ~20 meV with respect to those for $p\perp c$. This phenomenon is primarily related to the anisotropy in absorption associated with the polarization selection rules[12], combined with the separation in energy of the C band from A and B bands. The energy separation of A and B bands is unresolved at room temperature. From a linear fit to the square root singularity, we found that the

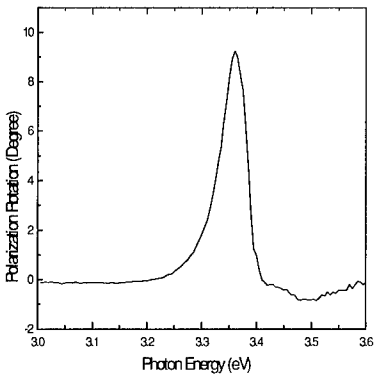


Figure 5: Polarization rotation as a function of photon energy for normal incident light linearly polarized at 45° with respect to the c-axis.

separation between the A(B) and C bands is about 21 meV, which is significantly smaller than the 40 meV separation measure in bulk ZnO at low temperature (1.6K to 4K). The reason for this is still unclear.

For normal incident light linearly polarized at 45° with respect to the c-axis, we have observed a large polarization rotation toward the c-axis (Figure 5). This rotation is related to the anisotropic absorption with[13]

$$\theta = \mathrm{Tan}^{-1}\left[(T_{//} / T_{\perp})^{1/2}\right] - 45°$$

where $T_{//}$ and $T_{\perp}$ are the transmission for $p//c$ and $p\perp c$, respectively. A maximum rotation of 10° occurs at 3.335 eV. This rotation was used to demonstrate a high-contrast, high-speed ultraviolet light modulator.

OPTICAL MODULATOR

We use ultraviolet pulses with a center wavelength corresponding to the static rotation maximum to test the modulator. The polarization of the prove pulse was oriented at 45° with respect to the c-axis of the ZnO modulator. Another ultraviolet pulse (pump pulse) is used to control the intensity of the transmitted probe pulse. The transmission of the probe at the photon energy corresponding to the maximum static rotation was monitored as a function of the delay time between the pump and probe pulses. A phase compensator and polarizer placed after the modulator were oriented for minimum transmission of the probe in the absence of the pump[14].

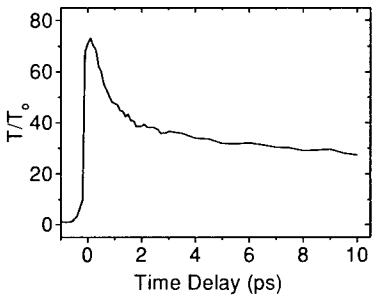


Figure 6: Normalized probe transmission as a function of time delay between the pump and probe pulses.

Figure 6 shows the normalized probe transmission T/T_o through the crossed polarizer as a function of time delay. T_o is the transmission in the absence of the pump. At negative time delays, for which the probe precedes the pump, $T/T_o=1$, as expected. As the pump and probe pulses become temporally coincident in the modulator, a sharp, pulse-width limited rise in probe transmission is observed at time delay $\tau=0^+$ which reaches a maximum more than 70 times greater than its value for negative time delays. This peak value in the normalized transmission is defined as the contrast ratio for the device. The pump-induced transmission possesses an initial decay time of 0.75 ps, followed by a slower decay to a quasi-equilibrium value within 100 ps

(not shown). Subsequent return to equilibrium occurs on a nanosecond time scale. The full width at half maximum of the modulation curve is less than 3 ps.

CONCLUSION

We have studied the structure and optical properties of high quality epitaxial $(1\bar{1}20)$ ZnO films on $(01\bar{1}2)$ sapphire substrates. The epitaxial relationship has been determined. TEM results indicate that the interface is semi-coherent. A sharp, excitonic, band-edge PL peak obtained at 11K indicates a strain free film that exhibits excellent quality. We have also observed a strong optical anisotropy that is utilized in a normal incidence, high-contrast, ultraviolet light modulator.

REFEREENCES

1. M. A. L. Johnson, S. Fujita, W. H. Rowland, Jr., W. C. Huges, J. W. Cook, Jr., and J. F. Schetzina, Journal of Electronic Materials, **25**, 855 (1996).
2. F. Hamdani, A. Botchkarev, W. Kim, H. Moorkoc, M. Yeadon, J. M. Gibson, S.-C. Y. Tsen, D. J. Smith, D. C. Reynolds, D. C. Look, K. Evans, C. W. Mitchel and P. Hemenger, Appl. Phys. Lett., **70**, 467 (1997).
3. F. Hamdani, M. Yeadon, D. J. Smith, H. Tang, W. Kim, A. Salvador, A. E. Botchkarev, J. M. Gibsor, A. Y. Polyakov, M. Skowronski, and H. Morkoc, J. Appl. Phys. **83**, 983 (1998).
4. P. Zu, Z. K. Tang, G. K. L. Wong, M. Kawasaki, A. Ohtomo, H. Koinuma, and Y. Segawa, Solid State Commun., **103**, 459 (1997).
5. D. M. Bagnall, Y. F. Chen, Z. Zhu, T. Yao, S. Koyama, M. Y. Shen, and T. Goto, Appl. Phys. Lett, **70**, 2230 (1997).
6. V. Srikant, V. Sergo, and D.R. Clarke, J. Am. Cer. Soc. **78**, 1931 (1995).
7. P. Roth, and D. F. Williams, J. Appl. Phys. **52**, 6685 (1981)
8. B. Cockayne, and P. J. Wright, J. Crystal Growth, **68**, 223 (1984).
9. C. R. Gorla, N. W. Emanetoglu, S. Liang, W. E. Mayo, Y. Lu, M. Wraback, and H. Shen, to be published in J. Applied Physics
10. S. Takata, T. Minami and H. Nanto, Jpn. J. Appl. Phys. **20**, 1759 (1981).
11. S. Tanaka, K. Takahashi, T. Sekiguchi, K. Sumino, and J. Tanaka, J. Appl. Phys. **77**, 4021 (1995).
12. W.Y. Liang and A.D. Yoffe, Physical Review Letters, **20**, 59 (1968).
13. H. Shen, M. Wraback, J. Pamulapati, M. Dutta, P.G. Newman, A. Ballato, and Y. Lu, Appl. Phys. Letts. 62, 2908 (1993).
14. M. Wraback, H. Shen, S. Liang, C.R. Gorla, and Y. Lu, to be published in Appl. Phys. Letts.

Comparative Growth of AlN on Singular and Off-Axis 6H and 4H-SiC by MOCVD

S. Wilson, C. S. Dickens, J. Griffin, M. G. Spencer

Materials Science Research Center of Excellence, School of Engineering, Howard University, Washington, DC 20059

Cite this article as: MRS Internet J. Nitride Semicond. Res. 4S1, G3.61 (1999)

Abstract

A comparison study of the growth of aluminum nitride (AlN) single crystal epitaxy on 6H-SiC and 4H-SiC substrates has been performed. The material has been characterized using atomic force microscopy (AFM) and reflective high energy electron diffraction (RHEED). AlN crystals were deposited on the following 6H-SiC substrates: singular with and without an initial SiC epilayer, and 3.5° off-axis with and without an initial SiC epilayer. AlN crystals were deposited on 8.0° off-axis 4H-SiC with and without initial SiC epilayers. AFM shows that the deposition of AlN on 6H-SiC and 4H-SiC with an initial SiC epilayer displays high quality quasi-two dimensional growth as atomically flat or step flow epitaxy.

Introduction

AlN is a wide band-gap (Eg = 6.2ev at RT) semiconductor material that is suitable for acoustic and visible to deep ultraviolet opto-electronic semiconductor devices [1][2]. One of the biggest drawbacks for growing nitride materials is the availability of suitable substrates [3] [2]. At this time there are no commercial nitride substrates, but researchers have learned to grow heteroepitaxially on semiconductors such as silicon carbide (SiC) and sapphire (Al_2O_3) to produce quality single crystal AlN material [4][5][3].

In this paper, the surface morphology of single crystal AlN deposited on 6H-SiC and 4H-SiC substrates with and without initial SiC epilayers are compared to determine which substrates promote superior growth.

Experimental Procedure

The AlN experiments were performed in a low pressure MOCVD reactor. This reactor possesses a vertical pancake configuration and is heated resistively. The AlN

Mat. Res. Soc. Proc. Vol. 537 © 1999 Materials Research Society

depositions were performed between 1160°C and 1190°C at 10torr with a total H_2 carrier flow of 5L. The precursors used were trimethylaluminum (TMA) and 5% ammonia (NH_4) balanced in hydrogen (H_2).

The substrate materials for the experiment were 6H and 4H single crystal SiC. All of the substrates were supplied by Cree Research with bulk dopings on the order of $10^{18}cm^{-3}$. The epilayers were grown on the SiC substrates by vapor phase or liqiud phase epitaxy. All the epilayers were approximately 4μm with dopings ranging from the high $10^{16}cm^{-3}$ to low $10^{17}cm^{-3}$. In total, there were 7 different silicon-faced substrates. The substrates were as follows:

Table 1. SiC Substrate Material

Poly Type	Orientation	Epilayer*
6H	singular	n-type
6H	3.5° off-axis	p-type
6H	3.5° off-axis	p+-type
6H	singular	none
6H	3.5° off-axis	none
4H	8° off-axis	p-type
4H	8° off-axis	none

* On-axis by LPE and off-axis by VPE

Several surface cleaning experiments were performed to determine the best method for sample preparation before growth. Three different cleaning procedures were performed for both 6H and 4H-SiC substrates without epilayers. After being cleaned, the growth surfaces were compared using RHEED.

For the first cleaning procedure, two substrates, one 6H and one 4H, were prepared by a thorough cleaning using standard solvents, trichloroethylene (TCE), acetone, and methanol. The two samples were then placed in the reactor, ramped up to 1200°C in H_2, and allowed to sit for 10 minutes. The second cleaning procedure was exactly the same as the first except the two samples were ramped up to 1200°C in vaccum. As for the last procedure, two substrates , one 6H and one 4H, were prepared

by a thorough cleaning using standard solvents, trichloroethylene (TCE), acetone, and methanol. The samples were then cleaned in a standard RCA sequence as follows: HNO_3 heated to 70°C for 15 minutes; followed by a 1:1:5 mixture of $NH_4OH:H_2O_2:H_2O$ heated to 70°C for 15 minutes; followed by a 1:1:5 mixture of $HCl:H_2O_2:H_2O$ heated to 70°C for 15 minutes; 50:1 H_20:HF for 1 minute. After the acid etches, the substrates were rinsed in deionized water and blown dry with filtered nitrogen

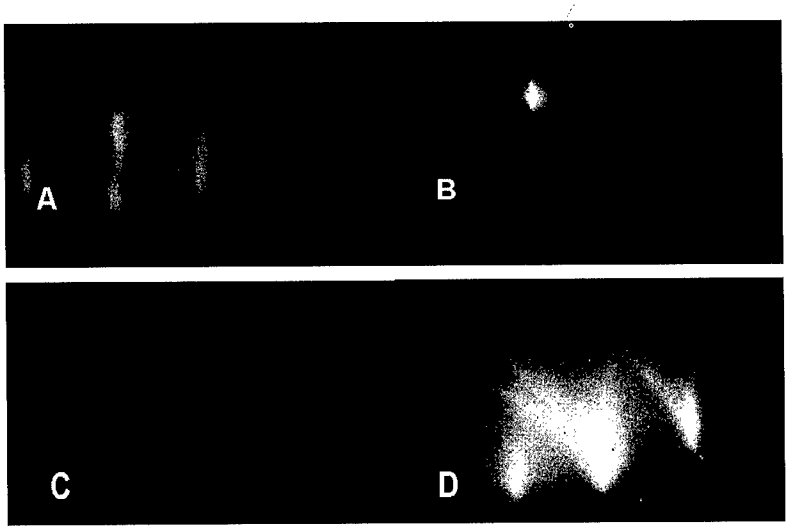


Figure 1. RHEED patterns of (A) 6H-SiC annealed at 1200°C in H_2 for 10 min (B) 6H-SiC prepared with RCA (C) 4H-SiC annealed at 1200°C in H_2 for 10 min. and (D) 4H-SiC prepared with RCA. RHEED for samples annealed in vacuum resemble the RHEED for the sample annealed in H_2.

The cleaning procedure which included the RCA clean produced the "best" RHEED (Figs. 1B and 1D). Therefore, all of the 6H-SiC and 4H-SiC substrates were prepared by a thorough cleaning using standard solvents and then cleaned using the RCA sequence. We noted that whatever the cleaning procedure the oxidation removal from the 6H-SiC was more complete than on 4H-SiC.

Directly after cleaning, AlN was deposited using various growth parameters optimized for the type of substrate in relation to crystallinity. Following each deposition,

RHEED was performed to determine the degree of crystallinity (Figure 2). If a sample displayed poor crystallinity, the growth was re-optimized in relation to the temperature or V/III ratio and repeated. After growth, the surfaces of the AlN epitaxy were analyzed using AFM to determine quality and type of growth .

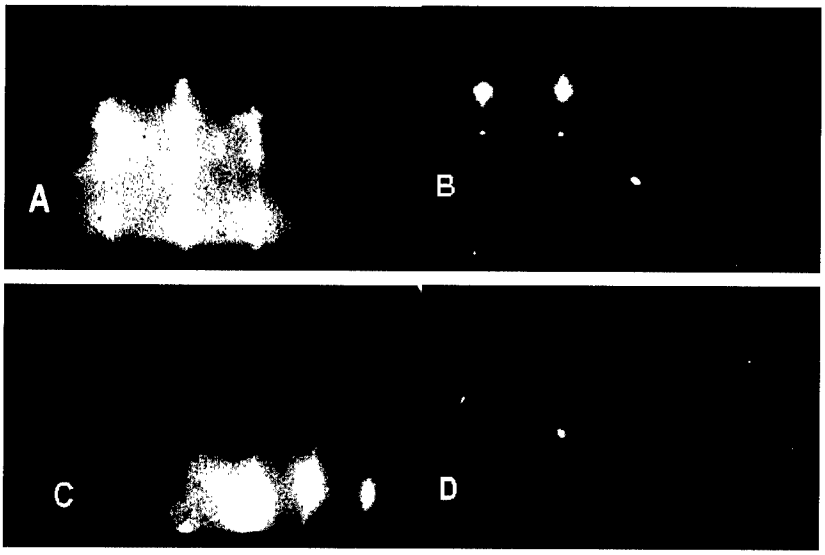


Figure 2. Typical RHEED patterns of (A) AlN/6H-SiC smooth surface (B) AlN/6H-SiC rough surface (C) AlN/4H-SiC smooth surface and (D) AlN/4H-SiC rough surface.

Results and Discussion

The morphology of AlN deposited on 6H-SiC with a intermediate SiC epitaxial is shown in Figures 3-5. In all cases a quasi 2-D step flow growth is observed. We note that these are not atomic steps, but are at least 40 angstroms in height and probably represent step bunching. The average measurement of roughness of the surfaces was 17 to 25 nm. When AlN is deposited on 6H-SiC without epitaxial growth, we have seldom observed step flow like growth. Figure 6 and 7 show morphology that is typical of growth directly on 6H-SiC substrates. This growth is randomly nucleated. This type of growth is characteristic of nitride material on a substrate without a buffer layer [6][7].

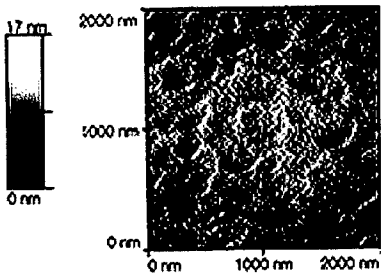


Fig. 3. AlN/n-type epi./6H-SiC singular

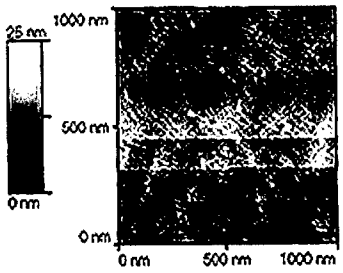


Fig. 4. AlN/p-type epi/6H-SiC off-Axis

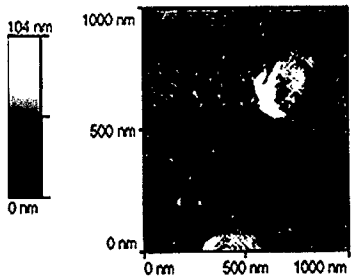


Fig. 5. AlN/p+-type epi/6H-SiC off-Axis

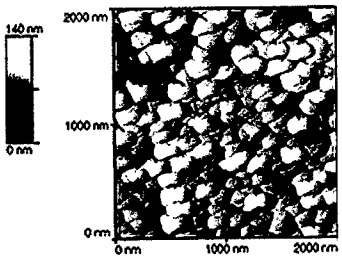


Fig. 6. AlN/6H-SiC Singular

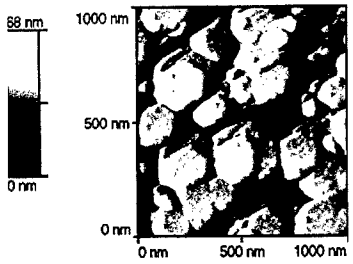


Fig. 7. AlN/6H-SiC off-Axis

When growth of AlN was performed on 4H-SiC substrates the quality of the material was not as reproducible as that on 6H-SiC. Despite the overall quality of the

growths on SiC, we were able to obtain step flow growth when the starting contained an initial epitaxial layer. Like the 6H-SiC , the 4H-SiC with initial SiC epilayers (Figure 8) displayed either a smooth surface or a step flow growth. In relation to figure 8, the AlN on 4H-SiC sample with an initial p-type epilayer displays high quality step flow growth with a surface step to step height of approximately 14nm.

Again like the 6H-SiC, the 4H-SiC samples (Figs. 9 and 10) without an initial epilayer displayed 3-D random nucleated growth. The islands formed in relation to the nucleation are small, approximately 30nm above the coalesced surface, and independent.

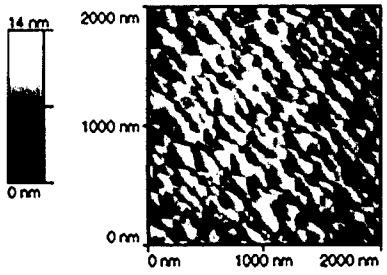


Figure 8. AlN/p-type epi/4H-SiC off-axis

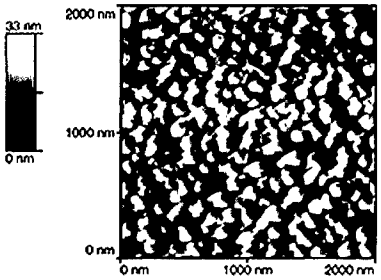


Figure 9. AlN/4H-SiC off-axis

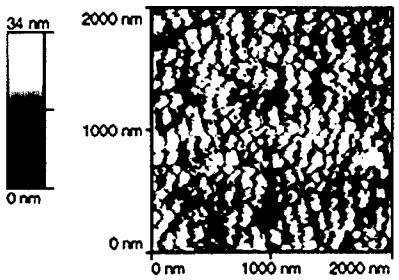


Figure 10. AlN/4H-SiC off axis

Conclusion

AlN was deposited on off-axis and singular 6H and 4H-SiC substrates with and without initial SiC epilayers. All of the AlN deposited on the SiC with initial epitaxial layers displayed relatively flat surface or step flow growth. The AlN deposited on the singular 6H-SiC with the n-type initial SiC epilayer and on the off-axis 6H-SiC with the p-type initial SiC epilayer achieved atomically smooth morphology. The other samples, AlN deposited on off-axis 6H-SiC with an initial n-type SiC epilayer and AlN deposited on singular 4H-SiC with an initial p-type SiC epilayer, achieved high quality 2-D step flow growth.

Acknowledgements

The authors acknowledge the support of the Office of Naval Research, contract monitor Dr. Colin Wood.

References

1. J.K Liu, K. M. Lakin, and K. L. Wang, J. Appl. Phys. 46, 3703 (1975).
2. K. Wongchotigul, N. Chen, D. P. Zhang, X. Tang, and M. Spencer, Mat. Lett. 26, 223 (1996).
3. K. Kawabe, R. Tredgold, and y. Inuishi, Elect. Eng. Japan 87, 62 (1967).
4. B. Fulde and T. Niemyski, Elec. Tech. 3, 3, (1970).
5. S. Strite and H. Morkoc, J. Vac. Sci. Tech. B 10, 1237 (1992).
6. H. Amano, N. Sawaki, ans I. Akasaki, Appl. Phys. Lett. 48, 353 (1986)
7. T. Sasaki and T. Matsuoka, J. Appl. Phys. 77, 192 (1995).

GALLIUM NITRIDE GROWTH USING DIETHYLGALLIUM CHLORIDE AS AN ALTERNATIVE GALLIUM SOURCE

Ling Zhang,[*] Rong Zhang,[*] Marek P. Boleslawski,[**] T.F. Kuech [*]
[*]Department of Chemical Engineering, University of Wisconsin, Madison, WI 53706.
[**]Aldrich Chemical, Milwaukee, WI.

Cite this article as: MRS Internet J. Nitriden Semicond. Res. 4S1, G3.62 (1999)

ABSTRACT

Metal organic vapor phase epitaxy (MOVPE) of GaN has been carried out using diethyl gallium chloride (DEGaCl) and ammonia. The growth rate and efficiency of the DEGaCl-based growth decreases with increasing temperature when compared to trimethyl gallium (TMG)-based growth under similar conditions. Both low temperature buffer and the high temperature GaN layers were grown using the DEGaCl-NH_3 precursor combination on the basal plane of sapphire and compared to similar structures grown using TMG and NH_3. DEGaCl-based growth reveals an improved growth behavior under identical growth conditions to the conventional TMGa and ammonia growth. X-ray, Hall, and atomic force microscopy (AFM) measurements have been carried out on these samples providing a direct comparison of materials properties associated with these growth precursors. For the DEGaCl-based growth, the x-ray rocking curve line width, using the (0002) reflection, is as low as 300 arcsec on a 2.5-micron thick film. A RMS surface roughness of ~0.5nm measured over a 10x10 micron area.

INTRODUCTION

GaN and related materials have been extensively investigated due to their potential applications in short wavelength optoelectronics and high temperature, high power, high frequency electronics[1]. Metalorganic vapor phase epitaxy (MOVPE) and hydride vapor phase epitaxy (HVPE) have been widely used and have generated materials with electrical and optical properties suitable for some device applications[2]. The growth conditions and hence the resulting materials properties in these two systems are different due to the different gallium precursors, operating conditions and reactor structure. MOVPE commonly uses trimethyl gallium or triethyl gallium, which can have complicated gas phase chemistry including the formation of adducts with NH_3. HVPE utilizes GaCl generated *in situ* through the reaction of liquid Ga with HCl. The gas phase chemistry is potentially simpler than that in MOVPE system. Slow gas phase switching times and the general difficulties in growing Al-based materials hamper the use of the HVPE technique to applications involving heterojunctions. GaN produced by the HVPE technique does result in a greatly reduced intensity of the defect-based luminescence referred to as the yellow band (YL) when compared to the TMG-based materials. This has been attributed to the lack of carbon in the HVPE growth system but is present in the growth sources used in MOVPE-growth systems. Intentional introduction of carbon into HVPE materials can result in the appearance of YL[3]. If a controlled amount of GaCl can be introduced into a cold wall MOVPE reactor, a low carbon source could be combined with the advantages of the MOVPE reactor environment.

Diethyl gallium chloride (DEGaCl) is used here as a Ga source in GaN growth. DEGaCl will decompose to GaCl through the β-elimination reaction in the gas phase allowing the *in situ* formation of GaCl at relatively low gas phase temperatures:

Mat. Res. Soc. Proc. Vol. 537 © 1999 Materials Research Society

$$(C_2H_5)_2GaCl \rightarrow GaCl + 2C_2H_4 + H_2$$

This source was successfully used in GaAs growth that resulted in high uniformity, low carbon content GaAs film[4,5]. GaAs selective area growth, with a complete selectivity of GaAs growth with respect to SiO_2, Si_3N_4, and Al_2O_3 masking materials, has been demonstrated over a wide range of process window[6,7,8]. The temperature range for GaAs using this source was 400-800°C and the higher temperature range of 1000-1150°C, required for conventional GaN growth, has not been investigated. We report here on the use of diethyl gallium chloride (DEGaCl) for the large area growth of GaN within a MOVPE system. The present work demonstrates the utility of the DEGaCl source in GaN epitaxial growth.

EXPERIMENTAL PROCEDURE:

The GaN growth was carried out in a horizontal MOCVD reactor operated at a pressure of 76 Torr. RF induction was used to heat the graphite susceptor. Trimethyl gallium (TMGa), diethyl gallium chloride (DEGaCl) and NH_3 were used as precursors in a hydrogen carrier gas. The DEGaCl bubbler was kept at 60 °C which requires a heated source line to the reactor. Sapphire c-plane substrates were initially etched in H_3PO_4:H_2SO_4=1:3 solution at 70°C for 15 minutes, loaded into the reactor and then heated in a flowing H_2 ambient to 1100°C for 10 minutes prior to the growth. Three comparison sample structures were used in this study. Samples A and C consists of an all DEGaCl or all TMGa-based growth respectively, allowing comparison of the growth chemistry under identical growth process conditions. Sample B is a structure comprised of an initial GaN layer that is identical to Sample C with an additional homoepitaxial GaN layer grown using DEGaCl. Samples A and B have a similar final thickness allowing a comparison of the impact of the initial nucleation of the GaN buffer layer on materials properties. These structures are summarized in Table 1.

All buffer layers were deposited at a temperature of 525°C and heated at a rate of 25°C per minute to 1050°C, then annealed at 1050°C for 10 minutes. The subsequent GaN epilayers in all samples were grown at a temperature of 1000 to 1150°C for 1 hour. The additional GaN layer grown in Sample B using the DEGaCl source was initiated by heating the sample structure (Sample C) to the growth temperature under a high NH_3 partial pressure and directly starting the subsequent growth. The typical gas flows employed were 65μmol/min for Ga, 4.9 slm for NH_3 and an additional 4 slm for H_2 carrier gas.

Crystalline quality was measured by double crystal x-ray rocking curve at (002) and (104) Bragg peaks. Surface morphology was determined using an atomic force microscope (AFM). Room temperature Hall and C-V measurements were also obtained.

RESULT AND DISCUSSION:

Figure 1 shows the growth efficiency, which is related to the growth rate, as a function of growth temperature using DEGaCl and TMGa. The growth efficiency (GE) is defined as the thickness of epitaxial film GaN (μm/min) deposited per Ga source flux (μmole/min) in the reactor feed. This calculation considers TMGa source to be monomeric in the gas phase while DEGaCl gas phase consists of both dimeric and monomeric species. DEGaCl gas phase at 60°C has a dimer mole fraction of 0.75[9]. The GE for both TMGa and DEGaCl increases with increasing temperature over the range 1000 to 1050 °C. At higher temperature, the GE of TMGa source was nearly temperature independent over the range of 1050 °C to 1150 °C, typical of a mass-transport-limited growth. The GE of DEGaCl source, however, decreased with increasing temperature from 1050 °C to 1150 °C. This behavior, we believe, can be attributed to

thermodynamic factors. In the case of GaAs growth from DEGaCl, the growth rate is mass transport limited from 550-850 °C, which was the upper limit of the investigated temperature range[4]. The simplest set of chemical reactions important at the GaN growth front in the case of DEGaCl are summarized as:

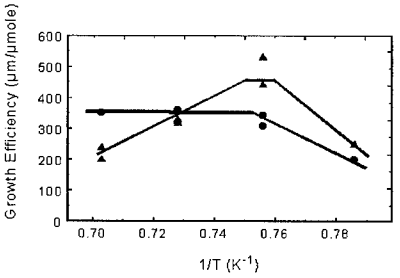


Figure 1: The GaN growth efficiency, which is the ratio of the GaN film growth rate (µm/min) to Ga molar feed (mol/min) into the reactor as a function of temperature for both DEGaCl (-▲-) and TMGa (-●-)sources.

$$(C_2H_5)_2GaCl \rightarrow GaCl + 2C_2H_4 + H_2$$

$$GaCl + NH_3 \rightarrow GaN + HCl + H_2$$

$$GaN + HCl \Leftrightarrow GaCl + \frac{1}{2}N_2 + \frac{1}{2}H_2$$

The last reaction implies equilibrium between the steady state concentrations of HCl and GaCl at the growth front. The MOVPE growth front has often been considered to be near thermodynamic equilibrium in many cases[10]. If this is the case for the high temperature growth of GaN, the supersaturation at the growth front will decrease with increasing temperature due the reversible reaction associated with the HCl reacting at the GaN surface.

The growth rate of GaN at a temperature of 1050°C as function of the carrier gas flow rate into the bubbler, for both DEGaCl and TMGa, is presented in Figure 2. The Ga flux, n_{Ga} in moles/min, is calculated as:

$$n_{Ga}(Q_{H_2}) = \frac{aQ_{H_2}P_{GaSource}}{22400(P_T - P_{GaSource})},$$

where Q_{H_2} is the flow rate of H_2 carrier gas through the bubbler, $P_{Ga\ source}$ is the vapor pressure of DEGaCl at the bubbler temperature, P_T is the total pressure within the bubbler, and α is factor describing the degree of associating of the Ga source and assumes a value greater than unity, i.e. a=1 for a monomeric source, 2 for a dimeric source, and so on. The DEGaCl source has a much lower vapor pressure (0.5 Torr at 60°C) than TMGa source (30 Torr at –10°C), requiring a larger flow rate of the carrier gas H_2 in order to carry out the same amount of Ga precursor. The GaN growth rate of using TMGa is linearly dependent on Ga flux into the reactor, which is linear with H_2 carrier gas flow rate through the bubbler. The GaN growth rate from DEGaCl may have an indication of saturation at high carrier gas flow rates. This saturation is most probably due to source supply limitations at high carrier gas rates due to the low vapor pressure of the DEGaCl.

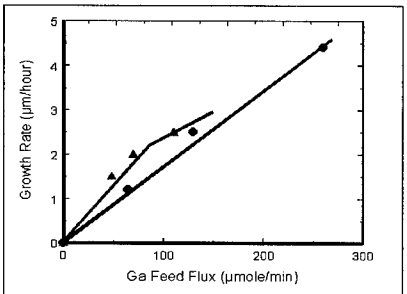


Figure 2. The growth rate of GaN is a function of the calculated Ga flux from the bubbler feed into the reactor for both DEGaCl (-▲-) and TMGa (-●-) sources.

Typical AFM images of the GaN surface morphology for sample structures A, B, and C are given in Figure 3. The surface of both Samples A

and B were obtained using DEGaCl source. The GaN surface morphology of these samples is quite smooth with sharp faceted step edges being readily apparent in the micrographs. The Sample C, grown using only the TMGa source for both buffer and high temperature layers, has a morphology typical of MOVPE GaN layers with a smooth surface and meandering steps. The average RMS roughness of Sample A was ~ 0.5nm measured by AFM over a 10x10-micron area. The all-TMGa sample, Sample C, was slightly rougher with a RMS roughness value of ~1.1nm. The difference in surface morphology can be attributed to the presence of the GaCl source at the growth front. Vapor phase epitaxy or VPE, utilizing inorganic halogen-based sources, can often lead to more faceted growth than MOVPE. The local thermal-equilibrium at the growth front implies the possibility of an etching or back-reaction reaction as indicated in the chemical reaction scheme outlined above. Surface asperities and defects would be active sites for the removal of GaN from the surface, through these back reactions, resulting in a reduction in surface roughness and the promotion of specific crystal facets. Additionally many chemical impurities form volatile chloride species enabling the possibility of higher purity films at these elevated temperatures.

The measured thin film properties for these structures, grown at 1050°C, are given in Table 1. The x-ray rocking curve line width, using the (0002) reflection, was as low as 300 arcsec on a 2.5-micron thick film for Sample A, utilizing an all- DEGaCl chemistry. The carrier concentration was measured to be as low as 1×10^{16} cm^{-3} by high frequency C-V measurement. Hall data yielded a much higher value for the carrier concentration than C-V data. The carrier concentration in our samples is very high near the initial growth interface due to the highly defected region at the GaN/sapphire interface. The Hall measurement data of Samples B and C can be analyzed by a simple two-layer Hall effect model allows the bulk electrical parameters to be extracted[11]. We can use the measured properties on Sample C as input into such an analysis, allowing the electrical properties of the subsequently grown DEGaCl-based layer to be estimated. The calculated results indicate that the top DEGaCl-based GaN film in Sample B had a mobility of 600 $cm^2/V\cdot sec$ and a carrier concentration of $2x10^{16}$ cm^{-3}, which agrees well with the C-V data on this sample.

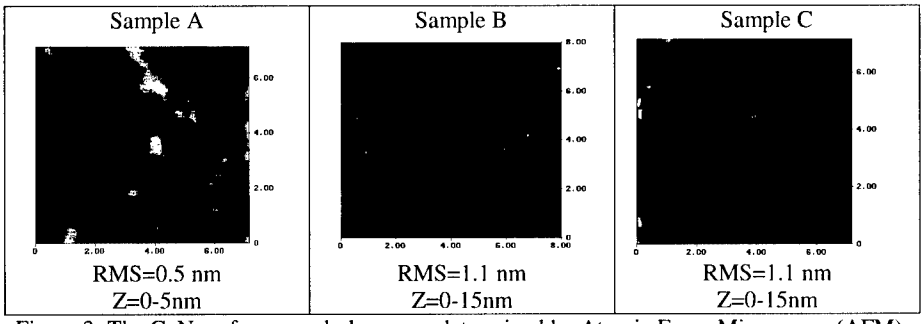


Figure 3: The GaN surface morphology was determined by Atomic Force Microscopy (AFM) for samples grown using DEGaCl or TMGa source. The sample images are obtained over a 10x10 micron area. The full range of height (Z) is indicated. The sample structure and related film properties are given in Table 1.

Additional DEGaCl-based GaN film properties as a function of temperature and V/III ratio are given in Figure 4. The carrier concentration was measured by C-V technique and the X-ray diffraction rocking curve was measured at both (002) and (104) Bragg reflections. The GaN crystal quality increased with increasing growth temperature over 1000°C to 1100°C. V/III ratio has an optimized value of ~ 3500 at a temperature of 1050°C in our reactor.

Table 1. GaN film properties for sample structures A, B, C grown at 1050°C

Sample Structure	**Sample A**	**Sample B**	**Sample C**
Properties	DEGaCl buffer and high temperature layer	DEGaCl high temperature layer on Sample C	TMGa buffer and high temperature layer
X-ray FWHM (arcsec) at (0002)	300"	550"	700"
RMS Roughness (nm) over 10x10μm area	0.51	1.14	1.18
Hall Concentration (cm^{-3})	1×10^{18}	3×10^{18}	2.5×10^{18}
Hall Mobility ($cm^2/V\cdot sec$)	80	80	62
CV Concentration (cm^{-3})	1×10^{16}	2×10^{16}	2×10^{16}
Thickness (μm)	2.5	0.7+1.5=2.2	1.5

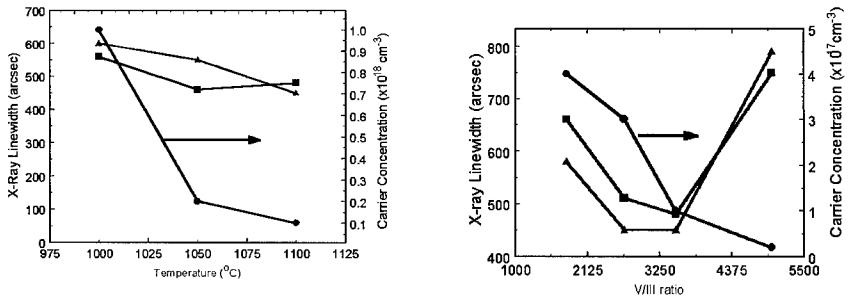


Figure 4: The change in GaN materials properties with growth temperature (Fig. 4a) and inlet V/III ratio (Fig. 4b) were obtained for films grown using the DEGaCl source. The structural quality were measured by x-ray rocking curves about the (002) and (104) Bragg reflections, symbols -▲- and -●- respectively. The carrier concentration (-●-) was obtained by C-V measurement.

SUMMARY:

The diethyl gallium chloride (DEGaCl) source was first studied for GaN growth in a MOVPE reactor. This Cl-based precursor exhibits a difference in growth rate and efficiency from the conventional TMGa-based growth. The DEGaCl-based growth efficiency decreases with increasing temperature indicating that the growth front may be close to local thermodynamic equilibrium. The presence HCl-related reactions at the growth front can influence the surface morphology and chemical purity by providing reaction pathways for the removal of surface structural and chemical defects and impurities. The DEGaCl source provides a reduced carbon growth chemistry within a MOVPE-based reactor.

ACKNOWLEDGMENTS

The authors would like to thank Aldrich for providing the DEGaCl source. The research funding from the ONR MURI on Compliant Substrates (C. Wood) and facilities support from the NSF UW-Materials Research Science and Engineering Center is gratefully acknowledged.

REFERENCE:

[1] H. Morkoc, S. Strite, G. B. Gao, M. F. Lin, B. Sverdlov, and M. Burns, *J. Appl. Phys.* 76, 1363 (1994)
[2] S. Nakamura, G. Fasol, *The blue Laser Diode-GaN light Emitters and lasers (spring-Velag, Heidelberg,* (1997).
[3] R. Zhang and T.F. Kuech, Appl. Phys. Lett. 72, 1611-1613 (1997).
[4] T. F.Kuech, R.Potemski and F. Cardone *J. Cryst. Growth* V124, 318-325 (1992)
[5] A. Narmann, M.L.Yu *Surface Science* V270, 1041-1047 (1992)
[6] T.F.Kuech *J. Cryst. Growth* V115, 52-60 (1991)
[7] Ko-ichi Yamaguchi, K. Okamoto, *Jpn. J. Appl. Phys.* V32 4885-4888, (1993)
[8] Y. Shiraishi, N. Furuhata, A. Okamoto, *J. Cryst. Growth* V182, 255-265 (1997)
[9] N. I. Buchan, R. M. Potemski, and T. F. Kuech, *J. Chem. Engi. Data*, V36, No. 4 (1991)
[10] G.B. Stringfellow, *Organometallic Vapor Phase Epitaxy,* (Academic Press, San Diego, 1989) Chap. 3.
[11] D.C Look, R.J.Molnar, *Appl. Phys. Lett.* 70, 23 (1997).

PIEZOELECTRIC LEVEL SPLITTING IN

GaInN/GaN QUANTUM WELLS

C. Wetzel, T. Takeuchi, H. Amano, and I. Akasaki

High Tech Research Center and Department of Electrical and Electronic Engineering,
Meijo University, 1-501 Shiogamaguchi, Tempaku-ku, Nagoya 468-8502, Japan

Cite this article as: MRS Internet J. Nitride Semicond. Res. 4S1, G3.66(1999)

ABSTRACT

Identification of the electronic band structure in AlInGaN heterostructures is the key issue in high performance light emitter and switching devices. In device-typical GaInN/GaN multiple quantum well samples in a large set of variable composition a clear correspondence of transitions in photo- and electroreflection, as well as photoluminescence is found. The effective band offset across the GaN/GaInN/GaN piezoelectric heterointerface is identified and electric fields from 0.23 - 0.90 MV/cm are directly derived. In the bias voltage dependence a level splitting within the well is observed accompanied by the quantum confined Stark effect. We furthermore find direct correspondence of luminescence bands with reflectance features. This indicates the dominating role of piezoelectric fields in the bandstructure of such typical strained layers.

INTRODUCTION

Heterostructures of GaInAlN alloys cover a wide range of electronic band gap energies and in combination with their physical stability provide an ideal wide bandgap system that in contrast to the family of SiC allows for advanced bandgap engineering over a wide energy range. Along with this advantage comes the challenge of a large lattice mismatch between the binary constituents and large biaxial stress in heteroepitaxy is the immediate consequence. Yet, owing to a great mechanical stability, mismatch of up to 2 or 3 % is readily supported in GaInN films of 40 nm thickness [1,2]. As we have shown in x-ray k-space mapping of both lattice constants a, within the growth plane, and c, along the growth direction, pseudomorphic growth can be achieved in $Al_yGa_{1-y}N$ for $y < 0.25$ (thickness 500 nm) and $Ga_{1-x}In_xN$ $x < 0.2$ (thickness 40 nm) [1].

Biaxial strain in wurtzite with partly ionic bonding directly lead to large piezoelectric effects. This is evidenced directly by strong Franz-Keldysh oscillations (FKOs) in strained GaInN films [3,4,5] and by a quantum confined Stark effect in the luminescence shift of GaInN/GaN quantum wells [6]. Similar results have been observed in AlGaN/GaN quantum wells [7]. While early piezoresistive measurements indicate very large piezoelectric coefficients [8] summarized in the quasi-cubic coefficient e_{14} = 0.56 C/m^2 and even higher values are predicted in first principles calculations e_{14} = 0.79 C/m^2 [9] we derive more modest values of e_{14} = 0.1 C/m^2 from the interpretation of FKOs [5]. These smaller values are also in line with a trend of other compounds versus their ionicity [10]. The immediate question is the role these effects play in the unexpected properties of GaInN/GaN heterostructures and devices. To this end we here perform a photoreflection (PR), electroreflection (ER) and photoluminescence (PL) analysis of a series of device-typical $Ga_{1-x}In_xN$/GaN multiple quantum well structures.

Mat. Res. Soc. Proc. Vol. 537 © 1999 Materials Research Society

EXPERIMENTAL

Pseudomorphic $Ga_{1-x}In_xN$/GaN heterostructures were grown along the *c*-axis by metal organic vapor phase epitaxy (MOVPE) on sapphire using low temperature deposited AlN buffer layers [6]. Samples consist of 5 sequences of nominally undoped L_z=3 nm $Ga_{1-x}In_xN$ wells embedded in 6 nm GaN barriers. The maximum composition is estimated to be $x = 0.2$. At this barrier width coupling of states between the wells is strongly suppressed. The set is grown either directly on 2 μm GaN or embedded in a GaN *pn*-junction with the *p*-side and a transparent contact on top. For reflection measurements we used a Xe white light source and a 325 nm 40mW HeCd laser for modulation (PR). The same laser was used for PL. In ER a sinusoidal voltage of 0.2 V_{pp} at 2 kHz and a variable offset was applied to modulate reflection in the *pn*-diode sample. All experiments were performed at room temperature.

PHOTOREFLECTION AND LUMINESCENCE IN GaInN/GaN MQW

PL and PR on nine samples with different well composition are presented in Fig. 1 in the sequence of the PL peak energy. A series of narrow oscillations arbitrarily labeled C_0 ... C_4 appears in the range of 3.2 – 3.7 eV range. Even sharper modulation appears near 3.42 eV (for the present purpose labeled N_0). A series of weaker but broad PR contributions N_1 – N_3 appears at lower energy the lowest of which has its maximum very close to the PL peak energy of the respective sample. This finding is in contrast to results by Chichibu *et al.* [11] where PR signal can be identified only at higher energies. Those levels would possibly correspond to levels N_1 or N_2 in our samples. A different signal amplitude may have contributed in this discrepancy. From the clear signature of N_3, both in PL and PR, we propose that this PL originates in a well defined electronic level rather than a logarithmic edge of a randomly distributed property such as proposed in earlier work.

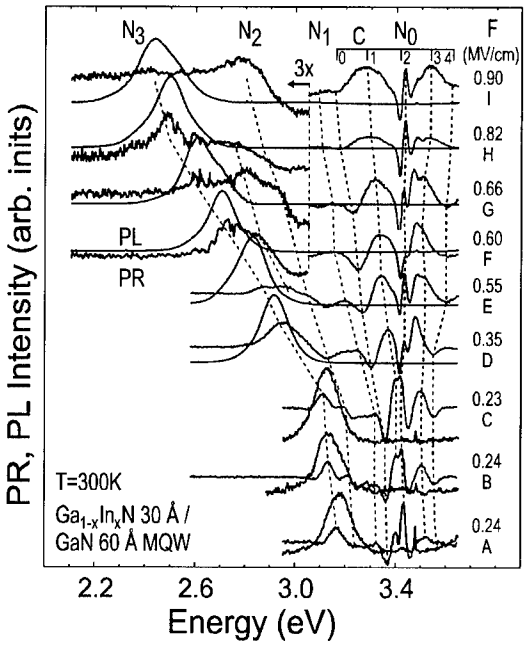


Figure 1 *Photoreflection and photoluminescence of strained 3 nm GaInN/6nm GaN MQWs for 9 different compositions. Associated features are connected by dashed lines and grouped in features C_0 ... C_4 and N_0 ... N_3. In all samples a PR contribution appears close to the PL maximum. Interpreted electric field values are indicated on the right.*

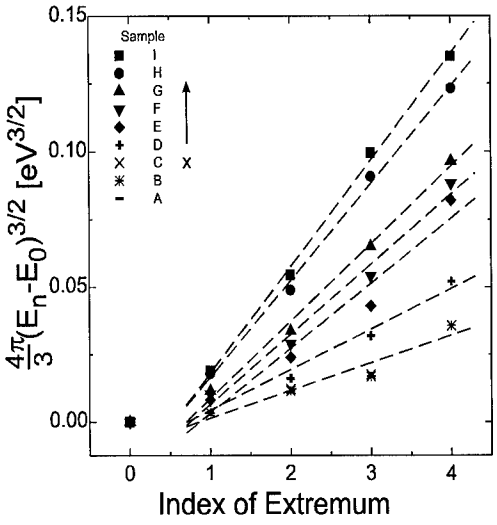


Figure 2 *Interpreation of PR extremas C_i close to the GaN barrier bandgap. A good linear approximation indicates the nature of Franz-Keldysh oscillations and electric fields values are derived.*

The sharp oscillation in N_0 is attributed to excitons in the GaN barriers or the GaN epilayer underneath the MQW. The splitting in the order of 30 meV into the different excitons is below the current interest of our interpretation. Oscillations in the vicinity of N_0, namely C_0 ... C_4 strongly resemble FKOs above a critical point in the joint density of states (DOS) in the presence of a large electric field F. One minimum is close to N_0 and a distortion of both signals must be expected within some range around N_0. The coexistence of excitonic features of GaN in N_0 and such FKOs indicate that the electric field is limited to the range of the GaInN quantum wells.

In other systems it has been demonstrated that the interpretation of PR data may involve a large number of parameters to accurately describe the observations. Especially surface termination and layers of native oxide in general could affect the assignment of reflection data to the properties of the volume material. For this purpose we have studied solvent cleaned surfaces of GaN layers in angular resolved photoelectron spectroscopy [12]. Even without any thermal treatment we found that films are merely covered by one or two monolayers of oxygen only. Furthermore a perfectly hexagonal crystal structure of GaN is found up to the top-most atomic layers. This indicates, that reflectivity properties should not be affected by such layers in GaN. FKOs appear in reflectivity in the vicinity of an interband transition between states of carriers that are free to move along an electric field, e.g., near a three dimensional critical point in the joint DOS with fields applied along the normal of the layers. This is typically the case in bulk material or in low dimensional structures at energies above the quantum well. In the approximation proposed by Aspnes [13] the separation of oscillation extrema in $E_i = E(C_i)$ corresponds to the electro-optical energy $\hbar\Theta$ and to the electric field. Fig. 2 plots $4/(3\pi)\ (E_i\text{-}E_0)^{3/2}$ versus the extremum index i. Within each set points can be well approximated by straight lines. Note that according to the approximation scheme C_0 should be the origin of the linear interpolation. In this experiment the value of C_0, however is not better known than any other point in the linear approximation and C_0 can not act as the origin of the interpolation. The slope of the interpolation corresponds to $(\hbar\Theta)^{3/2}$ and to the electric field $F = (\hbar\Theta)^{3/2}\ (2\mu)^{1/2} / (e\hbar)$. Herein μ = 0.2 m_0 is the joint effective DOS mass assumed to be constant at the GaN value. The derived field values are indicated as labels in Fig. 1. Fields span a large range from $F = 0.23$ to 0.90 MV/cm and should directly reflect the piezoelectric field within the quantum wells. According to the interpretation of FKOs the three dimensional critical point would be associated closely to C_0 somewhere between the minimum and the maximum below in N_1. This level $E_{3d} = (E(C_0) + E(N_1))/2$ has an apparent binding energy $E_{loc}=E(N_0)\text{-}E_{3d}$ with respect to the excitonic bandgap in the GaN barrier N_0. This value also increases with x and is plotted in Fig. 3 versus the derived

electric field values. We indeed observe a clear linear correlation and an inverse slope parameter of $E_{loc}/F \approx \Delta E_{loc}/\Delta F = 3.1\text{x}10^{-9}$ eV m/V which defines an effective dipole. The value very closely matches the dipole of an elementary charge e in the piezoelectric field F across the well with $L_z = 3$ nm. We consequently propose that E_{loc} corresponds to the effective band offset across the heterointerface of each quantum well GaN/GaInN/GaN. This direct correspondence can be used to accurately determine either electric fields, well width or strain [14]. At lower energy the PR signal reveals two signatures labeled N_2 and N_3 that for increasing x split into two clearly separated levels. PL is found to follow the lower one in energy N_3. At present parameters of the quantum well system are not sufficiently established as to make sufficient accurate predictions on the levels of the individual quantized states.

ELECTROREFLECTION IN A MQW *pn*-JUNCTION

In order to reveal more details on this splitting we performed electroreflectance spectroscopy of a MQW structure embedded in an *pn*-junction. Fig. 4. presents the results obtained under variable DC bias voltages. Due to the field induced by the *pn*-junction, the condition of a +2.5 V bias roughly corresponds to the case of the MQW wells studied above. Again several transitions are identified that lie close to levels previously labeled N_0, N_1 and N_2. Upon driving the *pn*-junction into the blocking regime and increasing the reverse bias level N_0 shifts to lower energy while levels N_2 and N_3 appear to merge.

The shift of N_0 can be interpreted as the electric field induced effective bandgap shrinkage caused by the Franz-Keldysh effect. Assignment of the origin of the observed signal from within the structure is not very clear. Besides the layers of the barriers also the adjacent doped contact regions may contribute in this signal. Due to high impurity concentrations doped layers, however, are less likely to produce a clear feature at the band edge. Assuming an origin right within the barriers of the MQW structure an effective field of 0.43 MV/cm can be estimated for the highest reverse voltages. Levels N_2 and N_3 must be associated with the quantized states within the QW. The merging of those levels clearly shows to be controlled by the applied electric field. Takeuchi *et al.* [6] have demonstrated in a similar structure that the PL peak energy also shows a strong dependence on the bias voltage. In that work a successive blue shift was observed for the PL under increasing reverse voltage and attributed to the quantum confined Stark effect (QCSE). Assuming a simple Stark splitting of levels N_2 and N_3 a field of 0.42 MV/cm corresponds to +2V bias in very good agreement with the shift of N_0. Comparing with the PL results in Fig. 1 this level should be associated with N_3 and the effective splitting with respect to N_2 could be described within the picture of this QCSE. At this point the proper nature of N_2 and its different field dependence is not obvious.

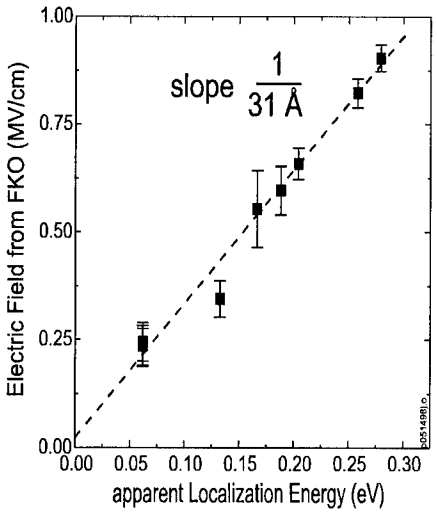


Figure 3 *Correlation of derived electric field and apparent localization energy or effective band offset across the GaN/GaInN/GaN heterointerface.*

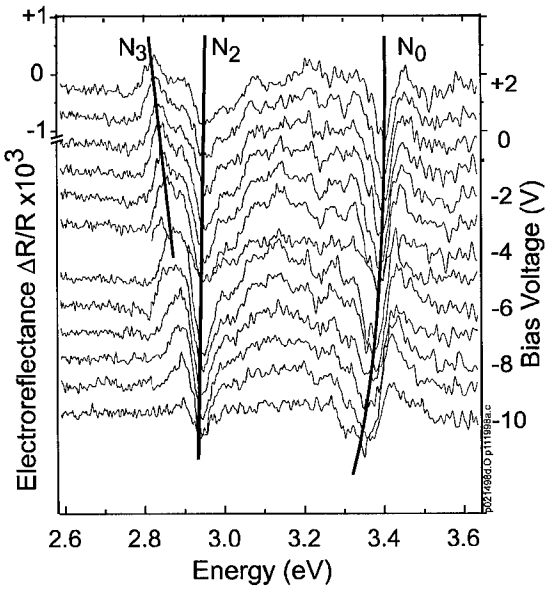


Figure 4 *Electroreflection in MQW pn-diode under variable (reverse) bias. Extrema closely corresponding to levels N_0, N_2, and N_3 in PR are identified. N_0 shifts in the increasing electric field while N_2 and N_3 merge indicating their field controlled splitting and a finite piezoelectric field for open terminal conditions.*

Fact, however, is, that we here observe an electric field controlled splitting of levels within the quantum well [15]. The merging of N_2 and N_3 than corresponds to an effectively vanishing field inside the well in agreement with findings by Takeuchi *et al.* [6]. This point of merging is achieved at finite reverse bias of $\approx$ -8 V and this is clear evidence of a finite electric field for open terminal conditions. Beyond the fields induced by doping in the *pn*-junction this is proof of finite piezoelectric field acting in the strained well. From the polarity of the diffusion field and the applied voltages we confirm the assignment of the direction of the piezo field to point from growth surface to the substrate for this biaxially compressed GaInN/GaN structure.

This result also suggests that splitting of N_2 and N_3 in Fig. 1 without applied bias voltages is also controlled by the piezoelectric field. In Fig. 1, where spectra are plotted in the sequence of PL energy or attributed x, all levels N_0, N_1, N_2 and N_3 appear to originate in one point. In the ER experiment, however, levels clearly approach different points. This is well understood, when considering, that in the ER experiment, only the electric field is varied, while in the PR series, the entire sample structure is changed inducing the combined effects of well depth, quantization energies, and piezoelectric fields associated with the variable strain. As shown in the interpretation of the osciallations C_i, splitting of N_0 and N_1 is controlled by the electric field. In the result of the ER level splitting of N_2 and N_3 are also controlled by the electric field [15]. This strongly suggests, that the electric field plays an important role in the entire sequence of levels N_0, N_1, N_2, and N_3 as seen in the PR. Work on the details of the full interpretation are currently underway.

SUMMARY

A detailed analysis of the electronic bandstructure in GaInN/GaN multiple quantum wells was performed by photoreflection and electroreflection spectroscopy. Franz-Keldysh-like oscillations are observed near the GaN band edge corresponding to large electric fields of 0.23 -- 0.90 MV/cm. The field increases with decreasing PL energy in correlation with the InN-fraction in the wells. A critical point in the joint DOS appears well below the barrier bandgap energy. This localization correlates with the electric field and appears to follow the well width. We therefore propose that this level indicates the effective heterostructure band offset across the strained GaInN layers. In electroreflection we confirm that levels in the well are controlled by electric fields. We confirm

results of the quantum confined Stark effect in PL and observe a field dependent splitting of two levels in the well. A similar splitting arises as a function of composition. For the highest composition case, where the largest fields are identified, we observe four evenly separated levels in PR. Comparing PR and PL we find a direct correspondence of the levels, most notably a close correspondence of PR signal close to the PL evidencing the existence of a discrete level at the energy of luminescence.

ACKNOWLEDGMENT

This work was partly supported by the Ministry of Education, Science, Sports and Culture of Japan (contract nos. 09450133 and 09875083, and High-Tech Research Center Project) and JSPS Research for the Future Program in the Area of Atomic Scale Surface and Interface Dynamics under the project of Dynamic Process and Control of Buffer Layer at the Interface in Highly-Mismatched Systems.

REFERENCES

1 T. Takeuchi, H. Takeuchi, S. Sota, H. Sakai, H. Amano, and I. Akasaki, Jpn. J. Appl. Phys. **36**, L177 (1997).
2 I. Akasaki and H. Amano, Jpn. J. Appl. Phys. **36**, 5393 (1997).
3 C. Wetzel, H. Amano, I. Akasaki, T. Suski, J.W. Ager, E.R. Weber, E.E. Haller, and B.K. Meyer, Nitride Semiconductors, Proc. Mater. Res. Soc. **482**, 489 (1998).
4 C. Wetzel, T. Takeuchi, S. Yamaguchi, H. Katoh, H. Amano, and I. Akasaki, Appl. Phys. Lett. **73**, 1994 (1998).
5 C. Wetzel, S. Nitta, T. Takeuchi, S. Yamaguchi, H. Amano, and I. Akasaki, MRS Internet J. Nitride Semicond. Res. **3**, 31 (1998). No warranty! http://nsr.mij.mrs.org/3/31/Default.html
6 T. Takeuchi, C. Wetzel, S. Yamaguchi, H. Sakai, H. Amano, I. Akasaki, Y. Kaneko, S. Nakagawa, Y. Yamaoka, and N. Yamada, Appl. Phys. Lett. **73**, 1691 (1998).
7 A. Hangleiter, J.S. Im, H. Kollmer, S. Heppel, J. Off, F. Scholz, MRS Internet J. Nitride Semicond. Res. **3**, 15 (1998).
8 A.D. Bykhovski, V.V. Kaminski, S. Shur, Q.C. Chen, and M.A. Khan, Appl. Phys. Lett. **68**, 818 (1996).
9 F. Bernardini, V. Fiorentini, and D. Vanderbilt, Phys. Rev. Lett. **79**, 3958 (1997).
10 S. Shur in Compound Semiconductors Spring I (1998) p.12
11 S. Chichibua, T. Azuhata, T. Sota, and S. Nakamura, Appl. Phys. Lett. **69**, 4188 (1996).
12 R. Denecke, J. Morais, C. Wetzel, J. Liesegang, E.E. Haller, C.S. Fadley, Proc. Mater. Res. Soc. **468**, 263 (1997).
13 D.E. Aspnes, Phys. Rev. B **10**, 4228 (1974); Phys. Rev. **153**, 972 (1967).
14 C. Wetzel, T. Takeuchi, S. Yamaguchi, H. Katoh, H. Amano, and I. Akasaki, Proc. 2nd Int. Symp. Blue Laser & Light Emitting Diodes, Kisarazu, Chiba, Japan, 1998. p.646-9.
15 C. Wetzel, T. Takeuchi, H. Kato, H. Amano, and I. Akasaki, Proc. 24th Int. Conf. on the Physics of Semiconductors, Jerusalem, Israel, August 2-8, 1998. *in print.*

PHOTOLUMINESCENCE EXCITATION SPECTROSCOPY OF CARBON-DOPED GALLIUM NITRIDE

E. E. Reuter*, R. Zhang**, T. F. Kuech**, S. G. Bishop*

*University of Illinois Microelectronics Lab, 208 N. Wright St., Urbana, IL 61801

**Department of Chemical Engineering, University of Wisconsin, Madison, Wisconsin 53706

Cite this article as: MRS Internet J. Nitride Semicond. Res. 4S1, G3.67 (1999)

ABSTRACT

We have done a comparative study of carbon-doped GaN and undoped GaN utilizing photoluminescence (PL) and photoluminescence excitation (PLE) spectroscopies in order to investigate deep levels involved in yellow luminescence (YL) and red luminescence (RL). When the GaN was excited by above-bandgap light, red luminescence (RL) centered at 1.82 eV was the dominant below-gap PL from undoped GaN, but carbon-doped GaN below-gap PL was dominated by yellow luminescence (YL) centered at 2.2 eV. When exciting PL below the band-gap with 2.4 eV light, undoped GaN had a RL peak centered at 1.5 eV and carbon-doped GaN had a RL peak centered at 1.65 eV. PLE spectra of carbon-doped GaN, detecting at 1.56 eV, exhibited a strong, broad excitation band extending from about 2.1 to 2.8 eV with an unusual shape that may be due to two or more overlapping excitation bands. This RL PLE band was not observed in undoped GaN. We also demonstrate that PL spectra excited by below gap light in GaN films on sapphire substrates are readily contaminated by 1.6-1.8 eV and 2.1-2.5 eV chromium-related emission from the substrate. A complete characterization of the Cr emission and excitation bands for sapphire substrates enables the determination of the excitation and detection wavelengths required to obtain GaN PL and PLE spectra that are free of contributions from substrate emission.

INTRODUCTION

The most common deep, below-gap luminescence that has been observed in GaN is the yellow luminescence (YL), a broad band centered at about 2.2 eV which appears in most published photoluminescence (PL) spectra of GaN [1-5]. The cause of the YL has been attributed to intrinsic crystal defects [3] and to impurities such as carbon [1,2], to a Ga-site vacancy and related complexes [6,7], or to a combination of several mechanisms [5]. It has also been found that the YL is far less intense in GaN grown by hydride vapor phase epitaxy (HVPE) than in GaN grown by metal organic chemical vapor deposition (MOCVD), and it should be noted that HVPE growth of GaN does not involve carbon containing source materials [8]. Another deep, below-gap PL band has been observed in GaN grown by HVPE and is centered at about 1.8 eV [9,10]. This weak red luminescence (RL) band is difficult to observe in GaN that has strong YL which may explain why RL is usually reported only from GaN grown by HVPE.

Two mechanisms have commonly been suggested to explain the YL in GaN. The mechanism with the widest acceptance involves a radiative transition from a shallow donor level to a deep acceptor level with a depth of 860 meV or to a deep double donor or V_{Ga} and related complexes. [2,3,6,7]. A second proposed mechanism is a transition from a deep double donor to a shallow acceptor [4]. Recent experiments have suggested that there may be more than one recombination channel responsible for the YL [5], with the specific channels present depending on the measurement temperature and how the GaN was grown. While many shallow and deep defect- and impurity-related levels have been reported for GaN [2, 10, 12, 13, 14, 16],

Mat. Res. Soc. Symp. Proc. Vol. © 1999 Materials Research Society

specific associations of these levels with proposed models for the YL have not been definitively proven.

It is important to note that the sapphire substrates often used for growing GaN usually contain Cr^{3+} impurities which contribute to a broad PL emission from the substrate in the same spectral region as the YL from GaN. Sapphire containing Cr^{3+} also exhibits a sharp line emission at 1.79 eV when pumped in the broad Cr^{3+} absorption bands centered at 2.2 eV and 3.0 eV [15]. When luminescence is excited by photons with energy below the bandgap of GaN from samples consisting of thin (several micron thick) GaN epilayers grown on thick sapphire substrates containing Cr^{3+}, the luminescence observed can be a mixture of emission from the substrate and the GaN and in some cases may be primarily from the substrate.

Ideally PL and photoluminescence excitation (PLE) spectroscopy excited with photon energies below the GaN bandgap would be performed on free-standing GaN epilayers removed from their substrates. However, the substrate removal is difficult and PL and PLE measurements are routinely performed on thin films still mounted on their substrates[3,17]. Some workers have pointed out that even when PL is pumped with photon energies above the GaN bandgap, it is possible for intense GaN PL in the blue spectral range to excite Cr^{3+} luminescence from the sapphire substrate [15]. Although the excitation of substrate emission is even more probable for direct optical pumping below the GaN bandgap, several PLE investigations of GaN in the below-gap spectral range have been reported in which 3-5 micron thick epitaxial layers of GaN on sapphire substrates were employed [3,17]. These publications make no mention of precautions to avoid distortion of the PLE spectra by substrate emission which complicates the interpretation of their reported PLE lineshapes and low energy thresholds.

The present work demonstrates the effectiveness of PLE spectroscopy in the investigation of optical absorption and emission below the bandgap of GaN. PLE spectroscopy involves detecting luminescence intensity at a selected wavelength within a luminescence band as a function of the wavelength of the exciting light, thus isolating one luminescence band and providing information about the absorption energies required to excite that luminescence band. Above-gap excitation of GaN typically produces broad, featureless, mid-gap PL spectra comprising multiple, overlapping YL and RL bands from deep defect or impurity levels [2, 9, 11]. PLE spectroscopy in the below-gap spectral range can detect extrinsic absorption bands which selectively and separately excite these overlapping PL bands. In the work presented here, the selective excitation isolates a broad RL band associated with C-doping, enabling its PL and PLE spectra to be obtained without interference from overlapping emission bands. In addition, we characterize the PL and PLE of the sapphire substrate in order to obtain a complete understanding of the potential influence of sapphire substrate emission on GaN PL and PLE.

EXPERIMENT

GaN samples were grown on (0001) sapphire substrates using NH_3, Ga, and HCl, and some samples were doped with carbon by introducing C_3H_8 into the reactor, as described in detail elsewhere [5]. These samples were 30 μm to 50 μm thick. Hall measurements showed that both the undoped and the C-doped samples were n-type with a concentration of 4×10^{18} cm^{-3}. The undoped samples were analyzed by secondary ion mass spectroscopy (SIMS) and found to have a carbon concentration of less than 2×10^{16} cm^{-3}, while the samples grown with C_3H_8 had a carbon concentration of about 5×10^{18} cm^{-3}. To serve as a standard for comparison, we also examined a sample of bare (0001) sapphire crystal of the same grade as usually used as a substrate for GaN growth.

Luminescence measurements were carried out with the samples mounted in a liquid helium cryostat. The tunable light source for PLE spectroscopy was provided by a xenon lamp dispersed through a 0.25 m focal length double monochromator. The source for PL spectra was

either the xenon lamp/monochromator or the 325 nm line of a He-Cd laser, and the luminescence was analyzed by a 1 m focal length single grating monochromator and detected by a GaAs photomultiplier tube. The PL and PLE of a bare sapphire sample were measured under the same conditions as the GaN samples to determine whether the substrate could be responsible for some or all of the PLE signals measured from the GaN on sapphire samples.

RESULTS

A comparison of the low temperature PL spectra of the undoped GaN and C-doped GaN samples, excited above the bandgap at 3.81 eV, is shown in Fig. 1. The undoped GaN has weak YL, with peak intensity at 2.2 eV about 1000 times less than that of the exciton intensity at 3.47 eV. Also, the RL peak intensity, at 1.82 eV, is higher than that of the 2.2 eV YL in the undoped GaN. In contrast, the PL spectrum of the C-doped sample is dominated by YL, about 100 times weaker than the exciton intensity, while the RL of the C-doped GaN is just visible as a low energy tail on the YL peak.

As seen in Fig. 2 which shows PLE spectra detected at 2.2 eV, the bare sapphire, undoped GaN, and C-doped GaN all have similar, weak PLE in the 2.4 to 2.8 eV region. In the GaN sample, this suggests that the PLE in this range results from exciting light that passes through the GaN layer to excite 2.2 eV luminescence from the sapphire substrate. At exciting energies above 2.8 eV, the C-doped sample appears to have a PLE onset that cannot be attributed solely to the substrate, and possibly a second onset near 3.2 eV. The undoped GaN, which has much weaker YL than the C-doped GaN, does not exhibit a clear PLE onset above 2.8 eV, but rather exhibits a PLE spectrum remarkably similar to bare sapphire over the entire range of 2.3 to 3.3 eV. It is clear that extraction of the GaN PLE from the mixture of GaN and sapphire PLE is only possible for GaN with relatively strong YL and even then the GaN PLE can only be clearly distinguished in selected portions of the spectrum.

Fig. 3 shows PLE spectra of a bare sapphire substrate when detected at 2.43 eV, 2.19 eV, and 1.56 eV. When detected at the higher two energies, the sapphire exhibits a PLE

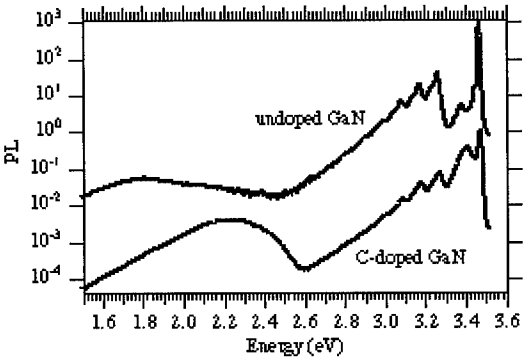


Figure 1. 5 K PL excited by He-Cd laser at 3.81 eV, comparing C-doped GaN and undoped GaN. Intensity has been scaled to 1 at the near-gap peak, and the curves have been offset vertically for viewing. The vertical axis is log-scaled.

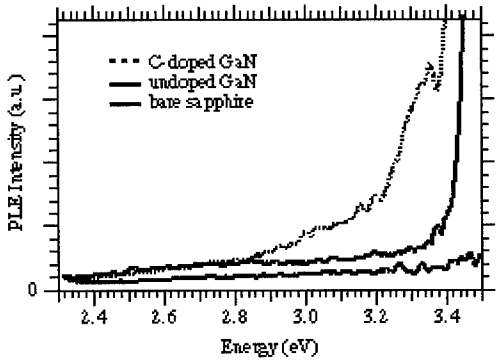


Figure 2. 5 K PLE spectra, detected at 2.2 eV, of C-doped GaN (top spectrum), undoped GaN (middle), and bare sapphire (bottom), each spectrum taken under identical conditions and corrected for the intensity spectrum of exciting light.

intensity which increases with increasing exciting light energy from 2.4 to 3.4 eV; however, when detecting at 1.56 eV the PLE intensity of the sapphire is significantly lower over the same spectral range. While the spectral shape and intensity of the sapphire PLE at the higher detecting energies in Fig. 3 is unfortunately quite similar to that which may be expected from GaN PLE spectra, the sapphire PLE detected at 1.56 eV is weaker which indicates that the substrate should contribute less to the GaN/substrate PLE mixture when detecting at 1.56 eV. These spectra and additional sapphire PL and PLE spectra have indicated that there is strong sapphire luminescence only in the range 1.6–1.8 eV and above 2.1 eV, so that PLE of RL from GaN on a sapphire substrate may be detected at or below 1.6 eV with little substrate contamination.

Fig. 4 compares PL spectra excited below the bandgap of GaN with 2.95 eV light for a sample of undoped GaN on a sapphire substrate and for a sample of bare sapphire. The sapphire has significant PL in the 2.1 to 2.5 eV range in addition to the characteristic sharp-line chromium emission between 1.65 and 1.8 eV. The YL from the GaN/sapphire sample has a PL spectrum which is almost identical to that of the sapphire. In particular, note that the PL intensity of the GaN/sapphire sample at 2.2 eV is less than double that of the bare sapphire sample, which clearly indicates that for GaN layers on sapphire, the PLE excited near 2.95 eV at best will be due to a mixture of luminescence from the substrate and the GaN layer, and at worst will be due almost entirely to the sapphire.

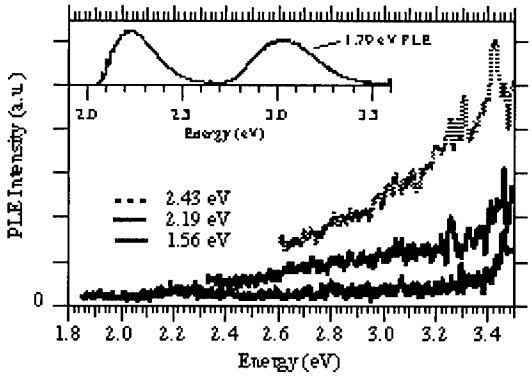


Figure 3. Comparison of the 5 K PLE of a bare piece of sapphire substrate when detecting at 2.43 eV, 2.19 eV, and 1.56 eV. The inset shows the sapphire PLE detected at 1.79 eV, which is a sharp Cr-related line. PLE spectra have been corrected for the intensity spectrum of the exciting light.

RL band PLE spectra of undoped GaN and C-doped GaN detected at 1.56 eV are shown in Fig. 5, as well as a PLE spectrum of bare sapphire for comparison. A broad RL excitation band extends from 2.1 to 2.8 eV for the C-doped sample and is virtually non-existent in the undoped GaN and the bare sapphire. A second C-doped sample which was grown with a different propane flow rate exhibits a nearly identical PLE band (not shown) to that of the C-doped GaN shown in Fig. 5. In contrast to the PLE of the YL, which was contaminated by substrate luminescence, the PLE of the RL from the C-doped GaN exhibits a clearly distinguishable excitation band which is nearly as strong as the band-edge PLE intensity. Any concerns that this PLE band could be substrate-

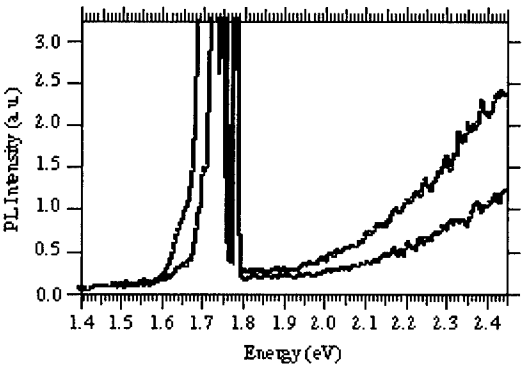


Figure 4. 5 K PL of bare sapphire and undoped GaN on a sapphire substrate, excited by 2.95 eV light. It is clear that the bare sapphire sample has luminescence in the 2.1 to 2.5 eV range. The chromium emission from the sapphire is visible in both spectra between 1.6 and 1.8 eV.

related are removed by noting that the chromium/sapphire PLE band which peaks at 3.0 eV is weak or non-existent in the PLE spectrum of the C-doped GaN. The unusual shape of the C-related excitation band suggests that it may result from two or more overlapping excitation bands. Two broad excitation peaks may be identified in the C-doped GaN PLE (Fig. 5), with peak energies near 2.3 eV and 2.6 eV, but the actual excitation mechanism could easily involve more than two overlapping processes which cannot all be distinguished in this PLE spectrum.

Since RL from the C-doped GaN was barely discernible on the tail of the YL in the above-gap-pumped PL spectrum (Fig. 1), we present for comparison a PL spectrum (Fig. 6) excited with 2.4 eV light, below the GaN band gap in the broad C-excitation-band. A RL band is clearly visible in the C-doped GaN when excited at this energy; however, the peak intensity occurs at 1.64 eV when pumped at 2.4 eV, as compared to a peak intensity at 1.82 eV in the undoped GaN when pumped above the gap. When PL is excited from the undoped GaN by 2.4 eV light another RL band appears, this one weak and broad with a peak at about 1.5 eV. RL luminescence would appear to be due to several different processes which result in emission in the 1.4 to 2.0 eV range, an assertion that is corroborated by the RL PLE spectrum (Fig. 5) which has an excitation band which appears to be a combination of two or more overlapping peaks.

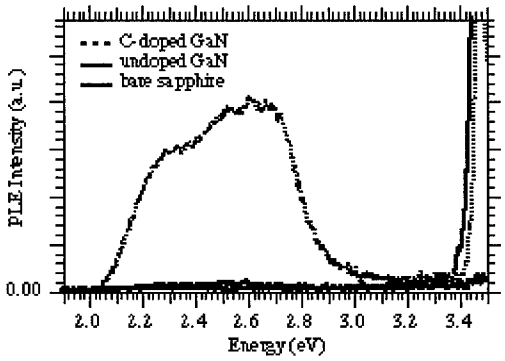


Figure 5. 5 K PLE of C-doped GaN, undoped GaN, and bare sapphire, detecting luminescence at 1.56 eV. Note the strong, multi-peaked excitation band of the C-doped GaN between 2.1 and 2.8 and the absence of this band in the undoped GaN and the bare sapphire. Spectra have been corrected for the intensity spectrum of the exciting light.

Although no RL-related zero phonon line (ZPL) was observed from these GaN samples, it is worthwhile to estimate where the ZPL might occur if the RL emission and absorption bands are indeed strongly phonon-assisted, as may be expected for transitions involving energy levels deep within the bandgap. Comparing Fig. 5 and Fig. 6, we may estimate that the zero phonon line (ZPL) for RL emission and absorption could be near the midpoint between the onset of the emission and absorption bands which results in an estimate of 2.0 +/- 0.2 eV for RL ZPL.

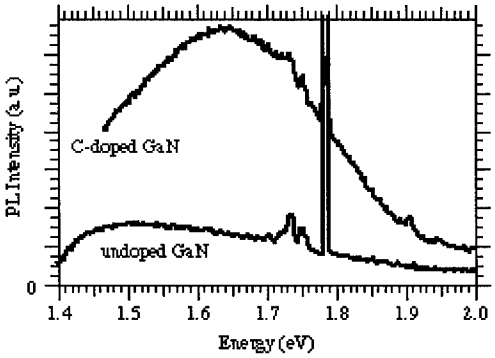


Figure 6. 5 K PL of C-doped GaN and undoped GaN, excited at 2.4 eV. The RL is now easily observed in the C-doped sample. There is also chromium emission from the sapphire substrate in the 1.7 eV to 1.8 eV range.

CONCLUSIONS

The interpretation of YL PLE spectra of GaN on sapphire substrates can be complicated by contamination of the GaN PLE with chromium-related luminescence from the sapphire substrate. As a result, YL PLE spectra of GaN on sapphire should be re-examined, preferably on samples which have had

the substrate removed from the GaN epilayer. In contrast, the PLE of RL, which is observed in some HVPE grown GaN samples on sapphire substrates, is not significantly affected by the chromium substrate luminescence when detected at 1.6 eV and below and therefore may be studied with fewer complications than the PLE of YL in GaN on sapphire.

A strong, broad PLE band of C-doped GaN, detecting at 1.56 eV, has been observed for the first time. This RL band only appears clearly in the C-doped GaN when it is pumped in the broad band between 2.1 and 2.8 eV. If the RL is strongly phonon-assisted, it could have a ZPL with energy of 2.0 +/– 0.2 eV. PL and PLE data suggested that RL may be excited by two or more overlapping PLE bands and RL emission may result from several overlapping luminescence bands including PL bands with peak energies near 1.5 eV, 1.64 eV, and 1.82 eV.

ACKNOWLEDGEMENT

This work was supported by NSF under the Engineering Research Centers Program (ECD 89-43166), DARPA (MDA 972-94-1-004), and the JSEP (0014-90-J-1270).

REFERENCES

1. J. I. Pankove and J. A. Hutchby, J. Appl. Phys. **47**, 5387 (1976).
2. T. Ogino and M. Aoki, Jpn. J. Appl. Phys. **19**, 2395 (1980).
3. D. M. Hofmann, D. Kovalev, G. Steude, B. K. Meyer, A. Hoffmann, L. Eckey, R. Heitz, T. Detchprom, H. Amano, and I. Akasaki, Phys. Rev. B **52**, 16702 (1995).
4. E. R. Glaser, T. A. Kennedy, K. Doverspike, L. B. Rowland, D. K. Gaskill, J. A. Freitas, Jr., M. Asif Khan, D. T. Olson, J. N. Kuznia, and D. K. Wickenden, Phys. Rev. B **51**, 13326 (1995).
5. R. Zhang and T. F. Kuech, Appl. Phys. Lett. **72**, 1611 (1998).
6. E. Calleja, F. J. Sanchez, D. Basak, M. A. Sanchez-Garcia, E. Munoz, I. Izpura, F. Calle, J. M. G. Tijero, and J. L. Sanchez-Rojas, Phys. Rev. B **55**, 4689 (1997).
7. J. Neugebauer, and C. G. Van de Walle, Appl. Phys. Lett. **69**, 503 (1996).
8. R. J. Molnar, K. B. Nichols, P. Maki, E. R. Brown, and I. Melngailis, Mater. Res. Soc. Symp. Proc., **378**, 479 (1995).
9. W. Götz, L.T. Romano, B.S. Krusor, N.M. Johnson, and R.J. Molnar, Appl. Phys. Lett. **69**, 242 (1996).
10. S. J. Rhee, S. Kim, E. E. Reuter, S. G. Bishop, and R. J. Molnar, Appl. Phys. Lett. **73**, 2636 (1998).
11. R. Zhang and T. F. Kuech in *Nitride Semiconductors*, edited by F. A. Ponce, S. P. DenBaars, B. K. Meyer, S. Nakamura, and S. Strite (Mat. Res. Soc. Proc. **482**, Pittsburgh, PA, 1998) p. 709.
12. U. Kaufmann, M. Kunzer, C. Merz, I. Akasaki, and H. Amano in *Gallium Nitride and Related Materials*, edited by F. A. Ponce, R. D. Dupuis, S. Nakamura, and J. A. Edmond (Mat. Res. Soc. Proc. **395**, Pittsburgh, PA, 1996) p. 633.
13. S. Fischer, C. Wetzel, E. E. Haller, and B. K. Meyer, Appl. Phys. Lett. **67**, 1298 (1995).
14. M. Ilegems, R. Dingle, and R.A. Logan, J. Appl. Phys. **43**, 3797 (1972).
15. K. Maier, J. Schneider, I. Akasaki, and H. Amano, Jpn. J. Appl. Phys. **32**, 846 (1993).
16. U. Kaufmann, M. Kunzer, M. Maier, H. Obloh, A. Ramakrishnan, B. Santic, and P. Schlotter, Appl. Phys. Lett. **72**, 1326 (1998).
17. M. Banas, G. Liu, J. Ramer, K. Zheng, S. Hersee, K. Malloy in *Gallium Nitride and Related Materials*, edited by F. A. Ponce, R. D. Dupuis, S. Nakamura, and J. A. Edmond (Mat. Res. Soc. Proc. **395**, Pittsburgh, PA, 1996) p. 583.

GaN CVD Reactions: Hydrogen and Ammonia Decomposition and the Desorption of Gallium

Michael. E. Bartram and J. Randall Creighton

Sandia National Laboratories, Albuquerque, NM, USA, 87185-0601

Cite this article as: MRS Internet J. Nitride Semicond. Res. 4S1, G3.68 (1999)

Abstract

Isotopic labeling experiments have revealed correlations between hydrogen reactions, Ga desorption, and ammonia decomposition in GaN CVD. Low energy electron diffraction (LEED) and temperature programmed desorption (TPD) were used to demonstrate that hydrogen atoms are available on the surface for reaction after exposing GaN(0001) to deuterium at elevated temperatures. Hydrogen reactions also lowered the temperature for Ga desorption significantly. Ammonia did not decompose on the surface before hydrogen exposure. However, after hydrogen reactions altered the surface, $N^{15}H_3$ did undergo both reversible and irreversible decomposition. This also resulted in the desorption of N_2 of mixed isotopes below the onset of GaN sublimation. This suggests that the driving force of the high nitrogen-nitrogen bond strength (226 kcal/mol) can lead to the removal of nitrogen from the substrate when the surface is nitrogen rich. Overall, these findings indicate that hydrogen can influence GaN CVD significantly, being a common factor in the reactivity of the surface, the desorption of Ga, and the decomposition of ammonia.

Introduction

For a model of GaN CVD processes to be applicable over a wide range of conditions, the chemistry model must utilize accurate rate constants. However, this first requires identification of the reactions and the reaction products formed on the deposition surface and in the gas phase. This study has revealed relationships between reactions of the hydrogen carrier gas, Ga desorption, and ammonia decomposition on GaN. Shown in equation 1, this was achieved using

(1) $Ga(CH_3)_{3\,g} + N^{15}H_{3\,g} + D_{2\,g} + GaN^{14} \rightarrow GaN +$ reaction products

isotopic labeling to distinguish nitrogen in ammonia from that in the substrate and the carrier hydrogen from that originating in ammonia.

Experimental

D_2 reactions were performed in a small cold-wall batch reactor connected directly to a UHV (ultra-high vacuum) surface analysis chamber via isolation seals. $N^{15}H_3$ reactions were conducted in UHV and consisted of $1x10^{-7}$ Torr exposures lasting in duration from 30 to 300s. The UHV chamber was equipped with x-ray photoelectron spectroscopy (XPS), low energy electron diffraction (LEED), and mass spectroscopy for temperature programmed desorption (TPD). The mass spectrometer was enclosed in a liquid nitrogen cooled shroud with an opening of only 1.5mm approximately 5mm in line of sight of the GaN(0001) surface. The GaN(0001) surface used in this study had a hexagonal LEED pattern with sharp spots [1] and a high contrast to background (figure 1). Although the symmetry and orientation of this excellent diffraction pattern remained unchanged over the entire surface ($1cm^2$), XRD and TEM have been used to show that this substrate was polycrystalline, as found for other GaN films.

Mat. Res. Soc. Proc. Vol. 537 © 1999 Materials Research Society

Hydrogen Reactions and Ga Desorption

TPD experiments revealed that ammonia adsorbed only reversibly on this surface in UHV. However, deuterium exposures at 2 Torr and 1200K for 120s in a chamber adjoining the UHV chamber altered both the LEED pattern and the surface reactivity. The resulting LEED spots were diffuse and had fine structure consistent with the presence of steps in multiple domains [2] as shown in figure 1. In addition, this new surface did adsorb ammonia *irreversibly* as well as reversibly, as discussed in the next section. Dramatic effects of hydrogen on GaN morphology and growth have been observed previously. [3]

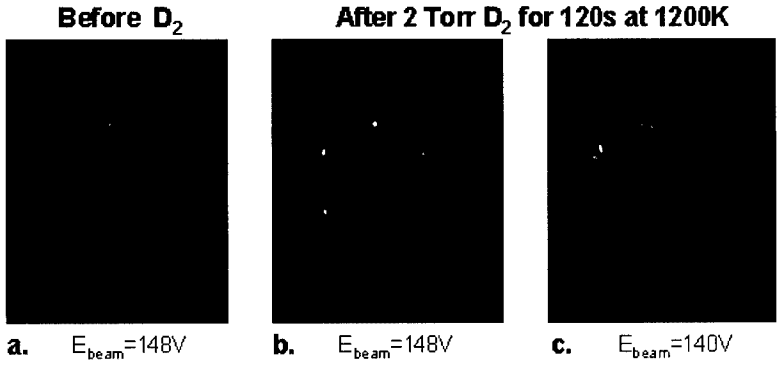


Figure 1. LEED photos before and after D_2 reactions. The surface did not decompose ammonia irreversibly in UHV until after reaction with D_2.

After stopping the reaction, evacuating at 1200K, and then cooling the substrate to room

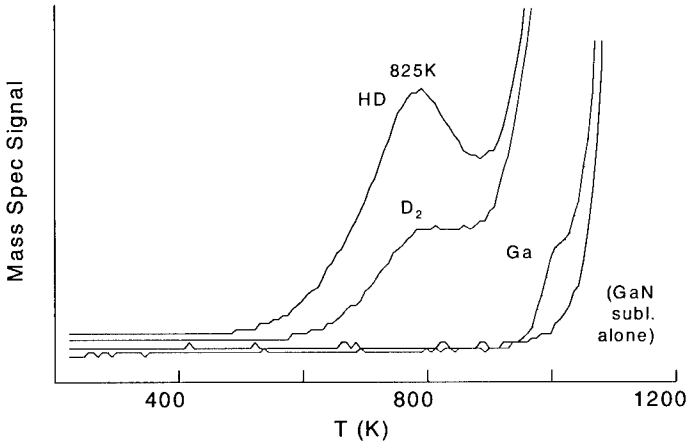


Figure 2. TPD spectra after D_2 reaction and evacuation at 1200K.

temperature, TPD detected only D_2, HD, and Ga, (figure 2) above the normal desorption of Ga and N_2. [4] HD likely results from the reaction of D with H left in the bulk from the CVD process. The desorption state at 825K before the onset of the much greater hydrogen desorption is suggestive of dihydrogen being formed from hydrogen atoms adsorbed on the surface (adatoms) followed by diffusion of hydrogen from the GaN solid (equation 2). The 825K desorption is 200

(2) $GaN(D_n\ H_{n\ surface/bulk}) \leftrightarrow D_{2\,g} + HD_g + GaN$

deg.C higher than reported on GaN(0001) previously. [5] However, that surface was not pretreated with hydrogen at elevated temperatures and was less reactive consequently. In another case, the desorption of hydrogen from polycrystalline GaN at slightly lower than 800K was reported. [6]

The spectra in figure 2 demonstrate that the rate of hydrogen diffusion from GaN is relatively slow, since the desorption of D_2 and HD is clear evidence that not all of the hydrogen was removed during the 1200K evacuation *prior* to TPD. Consistent with the need for post-growth annealing thought to remove hydrogen from GaN for the activation of Mg acceptors, this implies equation 2 may be reversible at CVD pressures. Nevertheless, this alone does not prove conclusively that hydrogen adatoms can be formed from hydrogen coming from the GaN solid or from the gas-phase.

The appearance of Ga at a temperature below the onset for GaN congruent sublimation [4] in figure 2 (equation 3) demonstrates that hydrogen exposures can lower the temperature

(3) $2GaN \rightarrow 2Ga_g + N_{2\,g}$

for Ga desorption. This also implies that hydrogen can react with the surface (equation 4),

(4) $3D_a/GaN + GaN \leftrightarrow ND_{3\,g} + Ga_g + GaN$

removing surface nitrogen. One might assume this occurs via ammonia formation. However, sampling the chamber gas-phase during deuterium reactions with a mass spectrometer as well as attempts to condense reaction products on a liquid nitrogen cooled trap could not verify this.

In lieu of direct evidence of ammonia formation, it should be noted that a necessary prerequisite for the formation of ammonia is the dissociation of hydrogen (equation 5) and more

(5) $D_{2\,g}$ (or $D_{n\,bulk}$)+ $GaN \rightarrow 2D_a/GaN$

importantly, the *availability* of hydrogen adatoms for reaction on the surface. In principle, an isotopic exchange experiment exposing GaN to both H_2 and D_2 to observe HD in the reactor at a level above that evolved from the solid would be sufficient proof of hydrogen dissociation. Unfortunately, reaction on the heater alone produced HD at too high of a rate to be sensitive to only the GaN chemistry.

As an alternative, evidence of hydrogen adatom availability on GaN was obtained by performing a two-step experiment utilizing (1) hydrogen (D_2) within the GaN substrate in conjunction with (2) ammonia adsorbed on the GaN surface. First, a reservoir of hydrogen was loaded in GaN by reacting with deuterium at 2 Torr and 1200K for 120s. The surface was then exposed to $N^{15}H_3$ at room temperature. The resulting TPD spectra are shown in figure 3. Although the signal was very low, the detection of mass 19 ($N^{15}H_2D$) as evidence of isotopic exchange between D atoms and $N^{15}H_3$ (equation 6) [5,6] demonstrates that hydrogen adatoms

(6) $2D_a/GaN + 2N^{15}H_{3\,g} \rightarrow [\ 2D\text{---}N^{15}H_{3\,a}/GaN\ ] \rightarrow H_{2\,g} + 2N^{15}H_2D_g + GaN$

resulting from hydrogen exposures are indeed available for reaction on the surface. In the absence of deuterium pre-reactions, additional experiments designed to test for artifacts showed that $N^{15}H_3$ exposure alone does not produce a mass 19 desorption peak (figure 3). Also, consideration of mass spec fragmentation patterns associated with N^{15} ammonia as well as the

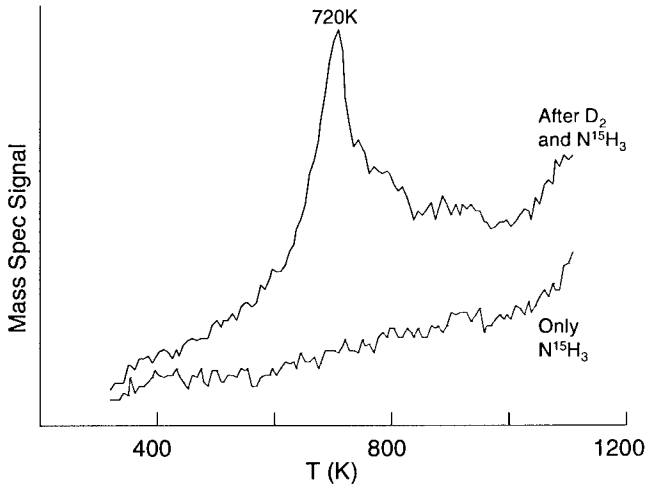


Figure 3. The desorption of $N^{15}H_2D$ (mass 19) as evidence of D adatom availability on the surface for isotopic exchange with $N^{15}H_3$ after D_2 dissociation.

possible presence of N^{14} ammonia or water impurities shows that these species can yield a mass of 19amu *only* if they contain deuterium.

Ammonia Reactions

As noted in the previous section, ammonia is adsorbed both reversibly and irreversibly on GaN(0001) after hydrogen exposure at high temperature. The reversible reaction results in the desorption of ammonia above 850 K. This rather high temperature suggests ammonia first dissociates at room temperature or above as in equations 7 and 8. It is important to point out that $N^{14}H_3$ was not detected under any condition.

(7) $N^{15}H_{3\,g} + GaN^{14} \leftrightarrow N^{15}H_{2\,a}/GaN^{14} + H_a/GaN^{14}$

(8) $N^{15}H_{2\,a}/GaN^{14} + \rightarrow N^{15}H_a/GaN^{14} + H_a/GaN^{14}$

(9) $N^{15}H_a/GaN^{14} + \rightarrow N^{15}{}_a/GaN^{14} + H_a/GaN^{14}$

(10) $2H_a/GaN^{14} + \rightarrow H_{2\,g} + GaN^{14}$

(11) $2N^{15}{}_a/GaN^{14} + \rightarrow N^{15}N^{14}{}_g + GaN^{15}$

Lack of significant ammonia reformation until high temperatures allows hydrogen-hydrogen reactions to compete on GaN, resulting in the desorption of dihydrogen above 850K (equation 10). This is coupled with irreversible ammonia adsorption and as shown in figure 4, nitrogen-nitrogen reactions also become competitive on the surface at a temperature below the onset for GaN sublimation. The desorption of $N^{15}{}_2$, $N^{15}N^{14}$, and $N^{14}{}_2$ suggests displacement of nitrogen from the GaN^{14} substrate can occur when the surface is nitrogen rich as in equation 11. With the desorption of ammonia and hydrogen taking place at much higher temperatures, each of these results are quite different from those reported previously. [5] Also, the desorption of dinitrogen was not detected previously, [5] which is consistent with the minimal reactivity observed in the absence of hydrogen pretreatment.

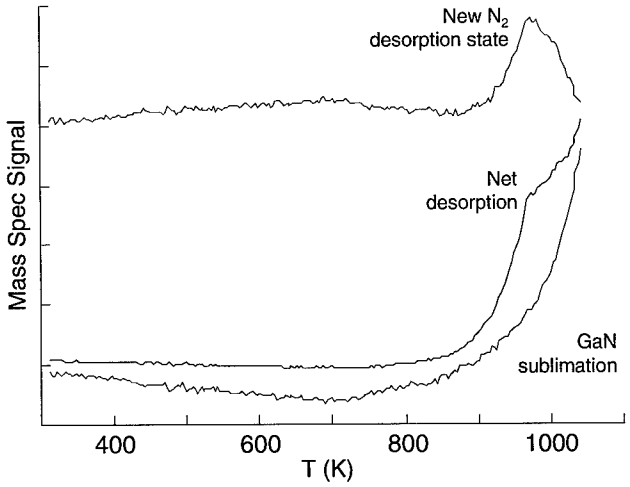


Figure 4. The desorption state for $N^{14}{}_2$ after exposing GaN^{14}(0001) to $N^{15}H_3$ and subtracting the GaN^{14} sublimation background. $N^{15}N^{14}$ and $N^{14}{}_2$ desorptions were similar to that shown for $N^{14}{}_2$.

These reaction pathways are not entirely surprising when the well-known Haber-Bosch process [7,8] for ammonia synthesis is considered (equation 12). Although the reaction is

(12) $N_2 + 3H_2 \leftrightarrow 2NH_3$

facilitated with a K-promoted Fe/Al2O3 catalyst, high nitrogen and hydrogen pressures are required to maintain the equilibrium in favor of ammonia. This is partly a consequence of the tremendous stability of N_2, having a nitrogen-nitrogen bond strength of 226 kcal/mol. The results presented here show that this same driving force could be a factor in reversing the deposition of GaN; if growth conditions do not incorporate nitrogen adatoms and/or surface nitrogen fully, those in close proximity will have a propensity to form N_2. Obviously, this points out the need to have precursor flow rates well matched to achieve a desired deposition-to-etch rate ratio in GaN CVD.

The formation of $N^{14}{}_2$ reveals that N^{14} is certainly available for reaction and yet the desorption of $N^{14}H_3$ was not detected. Therefore, it is unlikely that equation 9 is reversed under the transient conditions inherent in a TPD experiment. However, this does not rule out the possibility of hydrogen adatoms removing surface nitrogen via equation 5 in conjunction with equation 4, given sustained hydrogen exposures as in CVD processes or the experiments described above.

Summary Conclusion

The numerous chemical equations considered in this study can be summarized quite simply as shown in figure 5. Without the reaction of hydrogen to form steps (defects) on the surface, ammonia does not decompose in UHV. However, once ammonia decomposition takes place, yielding surface hydrogen in a sequence of reactions (proceeding from left to right), this reaction becomes chemically linked with hydrogen adatoms from carrier decomposition at every step in the sequence (pushing the reaction back to the left). Therefore, while conclusive proof of ammonia formation from the reaction of hydrogen carrier adatoms was not obtained in this study, fundamental chemical concepts (Le Chatelier's principle) would suggest that hydrogen adatoms could be a significant factor in decreasing the rate of ammonia decomposition. Certainly in the extreme case, nitrogen may well be removed from the surface as ammonia via reaction with hydrogen adatoms from the carrier (reaction from right to left), lowering the Ga desorption temperature. Conversely, when the surface is rich in nitrogen, the driving force to make dinitrogen will offer an entirely different route for irreversible removal of nitrogen from the surface (reaction from left to right). Seemingly complicated, these interwoven reactions leading to contrasting sets of both deposition and etching reactions may also be viewed as part of the key to manipulating materials properties and qualities via careful selection of growth conditions.

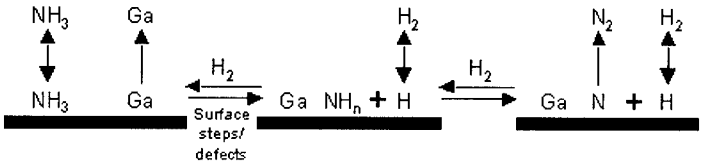


Figure 5. Schematic illustration of the relationship between hydrogen reactions, Ga desorption, and ammonia decomposition in GaN CVD.

Acknowledgments

Technical discussions with Jung Han are noted with appreciation. This work was performed at Sandia National Labs under DOE contract DE-AC04-94AL85000.

References

[1] V.M. Bermudez, D.D. Koleske, A.E. Wickenden, *Appl. Surf. Sci.* ***126***, 69 (1998).
[2] K.D. Gronwald, M. Henzler, *Surf. Sci. 117*, 180 (1982).
[3] M. Hashimoto, H. Amano, N. Sawaki, I. Akasaki, *J. Cryst. Gr. 68*, 163 (1984).
[4] O. Ambacher, M.S. Brandt, R. Dimitrov, T. Metzger, M. Stutzmann, R.A. Fischer, A. Miehr, A. Bergmaier, G. Dollinger, *J. Vac. Sci. Technol. B 14(6)*, 3532 (1996).
[5] R. Shekhar, K.F. Jensen, *Surf. Sci. 381*, L581 (1997).
[6] C.-M. Chiang, S.M. Gates, A. Bensaoula, J.A. Schultz, *Chem. Phys. Let. 246*, 275 (1995).
[7] F. Bottomley, R.C. Burns, Eds., *Treatise on Dinitrogen Fixation*, Wiley, 1979.
[8] G. Ertl, D. Prigge, *J Catal. 79*, 359 (1983).

QUANTUM-CONFINED STARK EFFECT AND RECOMBINATION DYNAMICS OF SPATIALLY INDIRECT EXCITONS IN MBE-GROWN GaN-AlGaN QUANTUM WELLS

Pierre Lefebvre*, Bernard Gil*, Jacques Allègre*, Henry Mathieu*, Nicolas Grandjean**, Mathieu Leroux**, Jean Massies**, Pierre Bigenwald ***

* Groupe d'Etude des Semiconducteurs - CNRS - Université Montpellier II.
Case Courrier 074. 34095 Montpellier Cedex 5, France.
**Centre de Recherche sur l' Hétéro-Epitaxie et ses Applications - CNRS
Rue B. Grégory. F-06560 Valbonne, France.
***LPM - Université d'Avignon - 33, rue Pasteur. 84000 Avignon, France.

Cite this article as: MRS Internet J. Nitride Semicond. Res. 4S1, G3.69 (1999)

ABSTRACT

We analyze the low-temperature photoluminescence decay times, for a series of MBE-grown samples embedding GaN-AlGaN quantum wells. We investigate a variety of configurations in terms of well widths, barrier widths and overall strain states. We find that not only the wells but also the barriers are submitted to large built-in electric fields. In the case of narrow barriers (5 nm), these fields favor the nonradiative escape of carriers from narrow wells into wider wells. When all wells have the same width, the field in such narrow barriers allow us to observe the recombination of long-lived "inter-well" excitons at energies close to those of the short-lived "intra-well" excitons. Our results also prove that the energies and the dynamics of excitonic recombinations depend on the parameters of the heterostructures in a complicated way, due to the interplay of piezoelectric and spontaneous polarizations.

INTRODUCTION

Nitride semiconductor quantum wells (QWs) are emerging as promising systems for the realization of blue-UV light emitters and detectors [1,2]. Their importance is such that it is crucial to obtain a better comprehension of mechanisms that rule optical processes in these heterostructures, especially from the dynamical viewpoint. In particular, it has been recently shown [3-8] that some original behaviors are due to the presence, along the growth axis of the QWs, of built-in electric fields of several hundred kV/cm. Considering the large lattice-mismatch between the constituents, these fields have been assigned [5-8] to the piezoelectric effect, due to very large piezoelectric coefficients. In fact, theoretical investigations [9,10] have established that two mechanisms, essentially similar in nature, should be considered to explain the large electric fields reported thus far. According to these studies, the values of the fields in the wells and in the barriers depend on the *difference* of piezoelectric polarizations between the two materials and on the *difference* of their so-called spontaneous (or equilibrium) polarizations.

The latter polarizations are essentially provoked by the nonideal c/a ratio of lattice parameters in the hexagonal elementary cells. The magnitudes of these spontaneous polarizations have been found to be particularly large in group-III nitride semiconductors; in fact, they are the largest of all III-V compounds [9], with values comparable to those for ZnO or BeO. However, Bernardini and Fiorentini have also calculated that the spontaneous polarizations of GaN and InN are not

Mat. Res. Soc. Proc. Vol. 537 © 1999 Materials Research Society

very different. Thus, for ideal (disorder-free) InGaN-GaN QWs, the main effect which induces built-in electric fields is the difference of piezoelectric polarizations. On the other hand, this is not the case for the GaN-AlGaN pair, because the spontaneous polarizations of the two compounds are really different. Both spontaneous and piezoelectric contributions have to be considered for GaN-AlGaN QW systems. For ideal infinite GaN/GaAlN superlattices, with well and barrier widths L_W and L_B, the electric fields in the wells and in the barriers are given respectively by [10,11]:

$$E_W = L_B \,.\, (|P^{sp}{}_W| - |P^{sp}{}_B| - |P^{pz}{}_W| - |P^{pz}{}_B|) / (\varepsilon_B L_W + \varepsilon_W L_B) \qquad (1),$$

$$E_B = L_W \,.\, (|P^{sp}{}_B| + |P^{pz}{}_W| + |P^{pz}{}_B| - |P^{sp}{}_W|) / (\varepsilon_B L_W + \varepsilon_W L_B) \qquad (2),$$

where ε_W and ε_B are the dielectric constants for the GaN wells (W) and the AlGaN barriers (B). $P^{sp}{}_W$ and $P^{sp}{}_B$ are the spontaneous polarizations which have the same sign in both materials. On the other hand, $P^{pz}{}_W$ and $P^{pz}{}_B$ (the piezoelectric polarizations) have opposite signs, at least for QW systems which are pseudomorphically grown (i.e. lattice-matched) on GaN buffer layers, themselves grown on sapphire substrates (this is the case of our samples). Indeed, GaN layers undergo a small biaxial compression, while AlGaN layers are under biaxial tension. A first interesting result expressed by these equations is that the field inside the GaN QWs is **not** directly given only by the piezoelectric effect in the GaN layer. The second interesting result is that this field inside the QWs is a growing function of the **barrier** width.

In this paper, we present time-resolved photoluminescence (TRPL) experiments which support the above theoretical predictions, in particular in terms of the role played by the barriers in GaN - AlGaN QW systems.

EXPERIMENTS

The samples were grown by molecular beam epitaxy on sapphire substrates, followed by a 2 μm thick GaN buffer layer, grown at 800°C. Next, GaN/GaAlN multiple- or single- QWs have been deposited, all samples being terminated by 30 nm thick GaAlN layers, with the same Al composition as the barriers. These barriers have thicknesses of 5 nm for the two multiple QWs presented and of 30 nm for the single QW. All samples have been grown in the same setup, under identical growth conditions. Thus, there is no reason to expect important differences between them, in terms of bulk or interface nonradiative processes, for instance.

Sample 1 is a single GaN / $Ga_{0.91}Al_{0.09}N$ QW with nominal thickness of 17 MLs (1 ML = 2.59 Å). Sample 2 is made of ten GaN / $Ga_{0.89}Al_{0.11}N$ QWs having all the same nominal thickness of 6 MLs. Sample 3 contains four GaN / $Ga_{0.89}Al_{0.11}N$ QWs with respective thicknesses: 3, 7, 11 and 15 MLs, nominally, from the surface towards the GaN buffer layer.

Detailed results of continuous-wave spectroscopy, at T = 2K, are available elsewhere [12-14]. In summary, Sample 1 shows a single PL peak at 3389.3 meV, well below the excitonic gap of GaN, due to a strong electric field. The latter induces a very small oscillator strength for the fundamental transition, which explains that no reflectivity feature corresponds to the PL line. Sample 2 exhibits a single intense PL line at 3583.2 meV, Stokes-shifted by ~30 meV from the corresponding strong reflectivity structure. The PL lines of the 15, 11, 7 and 3 ML-wide QWs in Sample 1 peak respectively at 3462.0, 3513.3, 3569.0 and 3671.9 meV. All PL lines are Stokes-shifted from their reflectance structure by ~40-50 meV. This is assigned [15] to the localization of excitons on areas where the QWs exceed their nominal thicknesses by 2 MLs. Thus, we have considered such "enlarged" well thicknesses in our envelope function calculations of transition energies. These calculations include excitonic effects and the material parameters have been

taken from Refs. [16-18]. The magnitude of the electric field in the QWs is a fitting parameter: a very good agreement is found between calculated and measured energies provided that we include fields of 600 kV/cm for Sample 1 and of 450 kV/cm for Samples 2 and 3 [13].

Such a difference of internal fields does not result from different strain states. This is proved by the energies of the A, B and C excitons in the GaN buffers, measured by reflectivity. It is well-known that these energies have a direct correlation [16] with the amount of residual in-plane compressive strain in GaN layers grown on sapphire. These energies are respectively, of 3480.0, 3486.5 and 3503.0 meV, for Sample 1, 3478.8, 3484.7 and 3502.0 meV, for Sample 2, and 3482.2, 3488.8 and 3506.4 meV, for Sample 3.

We see that the strain in GaN layers is almost the same for all samples: it is slightly smaller for Sample 2 than for Sample 1, and slightly smaller for Sample 1 than for Sample 3. From these results and assuming that AlGaN layers are lattice-matched onto the GaN buffers, we find that the **differences** of piezoelectric polarizations of wells and barriers are almost identical for the three samples. This is a first evidence that the magnitudes of internal fields are not a simple function of the compressive strain in the GaN layers. Instead, the larger electric field in Sample 1 can be explained by the thicker barriers, according to Eq. (1). Consistently, the "opposite" field in the barriers should be 4-5 times weaker for Sample 1 than for the other samples [see Eq. (2)].

For TRPL experiments, the excitation is provided by laser pulses with λ = 270 nm and with typical temporal width of 2 ps, at a repetition frequency of 82 MHz. A helium closed-cycle cryostat is used for cooling the samples down to a minimum of 8 K. The PL is analyzed through a spectrometer and detected by a streak camera. The overall time-resolution of the setup is ~5 ps. Figure 1(a) shows the temporal evolution of the PL spectrum of Sample 1. We find that the decay is multi-exponential in all regions of this spectrum. We get a satisfactory fitting only when including at least three exponential decays. We also notice a red-shift of the line of ~6 meV for increasing times, which suggests some band filling effects and the partial screening of the internal field by photocarriers, at short times.

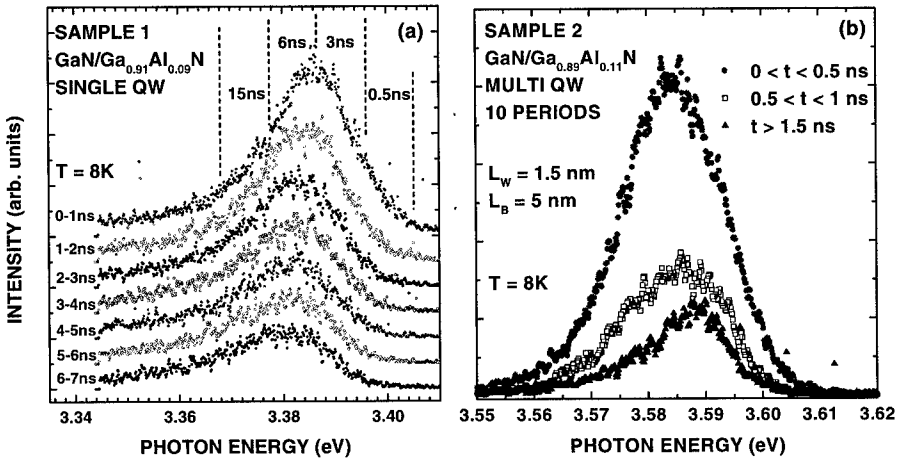


Figure 1: Evolution with time of the PL of Samples 1 (a) and 2 (b), shown by the spectra recorded on various time intervals. Indicative decay times are shown for various spectral ranges.

The overall decay time is of more than 10 ns, especially in the low-energy range, where it reaches the upper limits of our time detection. Such decay times are fairly comparable with the estimations of ~35 ns for the radiative lifetime of such localized excitons, that we made via variational envelope-function calculations of the excitonic oscillator strength [19,20], including a

field of 600 kV/cm. On the other hand, the PL decay times, displayed in Fig. 2, for the QWs of Sample 3 are much shorter than the radiative lifetimes, estimated for a field of 450 kV/cm.

These radiative lifetimes are again of several nanoseconds, and increase almost exponentially with the well width. The experimental decay times rather show a linear increase and are of the order of several tens of picoseconds. Moreover, we have measured here clear mono-exponential decays. We interpret these decays as arising from the competition between radiative recombinations and the nonradiative transfer of carriers across the barriers, from each well into its wider neighbor and, eventually, into the GaN buffer. This interpretation is supported by the linear increase of the times for reaching maximum PL intensity, when going from the narrowest QW (arbitrarily assigned to zero-delay) to the widest QW (see open circles in Fig. 2). Indeed, the latter result strongly suggests a kind of recycling of the carriers that are lost by a well, which cross the barrier and feed the neighboring wider well. This kind of transfer is made possible by the quantum coupling of the different QWs across the thin (5 nm) barriers. Each electron subband corresponds to a wave function delocalized over the entire multi-QW system. An electron in an excited state, which is mainly localized in a given well, can either recombine radiatively with a hole within this well, or thermalize, by phonon emission, towards a lower-lying state of the entire structure, which happens to be mainly localized on another well. The efficiency of this process is a growing function of the probability of leakage of the envelope function in the adjacent well, which is small in the present case (for the electron state centered on the 3 ML QW, the probability in this well is ~180 times larger than in the 7 ML QW). If the QWs were strongly coupled, the carriers would thermalize even more efficiently towards their ground state: the recombinations from narrow wells would have even shorter lifetimes. By enhancing the leakage probablility, the strong built-in electric fields in the barriers slightly favor such carrier transfers.

We can only propose a qualitative picture of the electric fields in all layers, because many material parameters are still poorly known. Theoretical calculations indicate that the general band profiles in our samples should resemble those sketched in Fig. 3, but these are only valid for ideal insulators, *i.e.* band curvatures are likely to occur due to free carriers, in real samples.

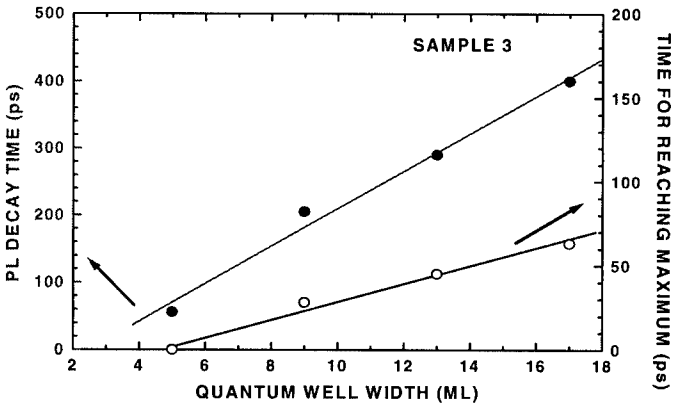
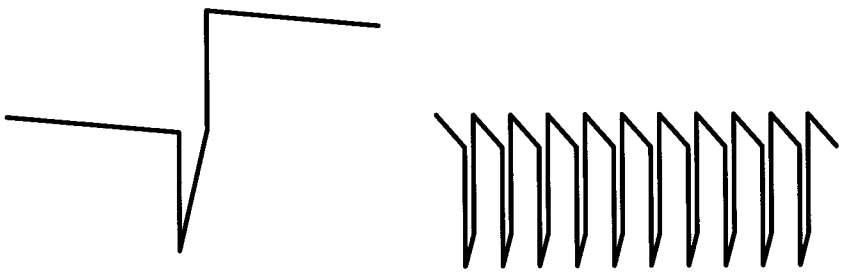


Figure 2: PL decay times (solid circles) versus QW width (nominal widths increased by two units have been used). Open circles show the change of the time for reaching maximum PL intensity.



SAMPLE 1 SAMPLE 2

Figure 3: Sketch of conduction band minima in Samples 1 and 2 as deduced from Eqs (1) and (2), in the case of GaN/GaAlN QWs without any free carriers. Reasonable values of fields, widths, and potential discontinuities have been used, and both figures have the same scale.

The case of Sample 3, not shown, should be like the case of Sample 2, except for the varying well widths. We remark that we have assumed, for multi-QWs, an overall "flat" band profile. We have an indication of this lineup by analyzing TRPL results obtained on Sample 2 (see below).

Figure 1(b) shows the change of the PL spectrum of Sample 2 versus time. Contrary to the case of the single QW, we observe a clear **blue-shift** of 5 meV of the PL maximum between small and large delays. This totally unusual behavior, and the somewhat irregular shape of the spectrum, suggest that this PL line is made of several contributions, due to a variety of configurations in terms of local well and barrier widths. This is confirmed by the multi-exponential decay in all regions of the spectrum. Dominant fast components (typical decay times of 200 ps) are present for the entire line, whereas much slower decays (typically 2.5 ns) are rather present in the high-energy part of the line. We interpret these slow decays as arising from spatially indirect, inter-well exciton recombinations, whereas fast decays rather correspond to excitons recombining within a given well.

Inter-well transitions are favored, here, by the electric fields which push electrons towards the left-hand side of the QW (see Fig. 3), while holes in its left-hand next neighbor are pushed to the right. Nervertheless, intra-well and inter-well recombinations cannot be observed simultaneously without an essential mechanism, namely the strong in-plane localization of electrons and holes [12-15,20,21], with trapping energies of several tens of meV, and localization radii smaller than the Bohr radius [21]. Then, there are statistically some occurences for which the in-plane distance of the localization sites of the electron and the hole is large (compared *e.g.* to the barrier width). In such cases, an inter-well recombination is more probable than its intra-well counterpart.

Variational calculations of transition energies and oscillator strengths allow us to get a satisfactory description of experimental results: we have performed a series of calculations assuming variations and permutations of well and barrier widths near their nominal values (e.g. between 6 and 9 MLs, for QWs), for a model-system made of three QWs. We find a "band" of short-lived "intra-well" excitons covering the range between 3585 and 3625 meV and two "bands" of inter-well excitons at 3595-3605 meV and 3615-3620 meV. Inter-well excitons lie at larger energies than intra-well excitons mainly because of a smaller binding energy. But it is crucial to note that the energies of the two types of transitions would be completely different if the general band profile was not "globally flat", as shown in Fig. 3.

CONCLUSION

We have shown the key role played by the complex interplay of piezoelectric and spontaneous polarizations in GaN-GaAlN QWs, by analyzing time-resolved PL experiments on such samples. This interplay induces a complex dependence of built-in electric fields on layer thicknesses and biaxial strains. Consequently, each sample should be considered individually (a single QW cannot be regarded as a multiple QW) and original behaviors appear, in terms of excitonic energies and lifetimes and of carrier transfer mechanisms. These particularities pave the way for versatile applications of such QWs, which are undoubtedly promised to a bright future.

REFERENCES

[1] S. Nakamura and G. Fasol, "The Blue Laser Diode" - Springer Verlag Berlin, 1997.
[2] *See, for instance* "Group III Nitride Semiconductor Compounds", Edited by B. Gil, The Clarendon Press -1998, ISBN 0-19-850159-5.
[3] J. S. Im, J. Off, A. Sohmer, F. Scholtz and A. Hangleiter, Materials Science Forum, **264-268**, 1299 (1998).
[4] N. Grandjean and J. Massies, Appl. Phys. Lett. **73**, 1260 (1998).
[5] J. S. Im, H. Kollmer, J. Off, A. Sohmer, F. Scholz and A. Hangleiter, Mat. Res. Soc. Symp. Proc. **482**, 513 (1998).
[6] H. Amano, T. Takeushi, S. Sota, H. Sakai and I. Akasaki, Mat. Res. Soc. Symp. Proc. **449**, 1143 (1997).
[7] K. P. O'Donnell, T. Breitkopf, H. Kalt, W. Van der Stricht, I. Moerman, P. Demeester and P. G. Middleton, Appl. Phys. Lett. **70**, 1843 (1997).
[8] J. S. Im, H. Kollmer, J. Off, A. Sohmer, F. Scholz, and A. Hangleiter, Phys. Rev. B **57**, R9435 (1998).
[9] F. Bernardini, V. Fiorentini and D. Vanderbilt, Phys. Rev. B **56**, R10024 (1997).
[10] F. Bernardini and V. Fiorentini, Phys. Rev. B **57**, R9427 (1998).
[11] F. Bernardini and V. Fiorentini, to be published.
[12] P. Lefebvre, B. Gil, J. Allègre H. Mathieu, N. Grandjean, M. Leroux, J. Massies, P. Bigenwald and P. Christol, 24th International Conference on the Physics of Semiconductors, Jerusalem (july 1998). To be published.
[13] M. Leroux, N. Grandjean, M. Laügt, J. Massies, B. Gil, P. Lefebvre and P. Bigenwald, Phys. Rev. B **58**, 13371R (1998).
[14] P. Lefebvre, J. Allègre, B. Gil, H. Mathieu, P. Bigenwald, N. Grandjean, M. Leroux and J. Massies, Phys. Rev. B, *to be published.*
[15] G. Bastard, C. Delalande, M. H. Meynadier, P. M. Frijlink and M. Voos, Phys. Rev. B. **29**, 7042 (1984); C. Delalande, M. H. Meynadier and M. Voos, Phys. Rev. B **31**, 2497 (1985).
[16] M. Tchounkeu, O. Briot, B. Gil, J. P. Alexis, and R.-L. Aulombard, J. Appl. Phys. **80**, 5352 (1996).
[17] M. Suzuki, T. Uenoyama and A Yanase, Phys. Rev. B **52**, 8132 (1995).
[18] S.L. Chuang and C.S. Chang, Phys. Rev. B **54**, 2491 (1996)
[19] B. Gil and P. Bigenwald, Solid Stat. Commun. **94**, 883,(1995), P. Bigenwald and B. Gil, Phys. Rev. B **51**, 9780, (1995).
[20] A. V. Kavokin, Phys. Rev. B **50**, 8000 (1994); E. L. Ivchenko, A. V. Kavokin, Sov. Phys. Semicond. **25**, 1070 (1991).
[21] P. Lefebvre, J. Allègre, B. Gil, A. Kavokin, H. Mathieu, W. Kim, A.Salvador, H. Morkoç and A. Botchkarev, Phys. Rev. B **57**, 9447R (1998).

ENHANCED GaN DECOMPOSITION AT MOVPE PRESSURES

D.D. KOLESKE, A.E. WICKENDEN, R.L. HENRY, M.E. TWIGG, J.C. CULBERTSON, AND R.J. GORMAN, Code 6800, Electronic Science and Technology Division, Naval Research Laboratory, Washington, D.C. 20375

Cite this article as: MRS Internet J. Nitride Semicond. Res. 4S1, G3.70 (1999)

ABSTRACT

GaN decomposition was studied above 800 °C in flowing H_2 and N_2 for pressures ranging from 10 to 700 torr. From careful weighings of the GaN film on sapphire before and after annealing, the rates for GaN decomposition, Ga surface accumulation, and Ga desorption were obtained. An enhancement in the GaN decomposition rate was observed in H_2 pressures greater than 100 torr. Even with this enhanced GaN decomposition, the Ga desorption rate is nearly constant at higher pressures. As a result, Ga droplets accumulate on the surface. For N_2 pressures ranging from 76 to 400 torr no net enhancement in the GaN decomposition rate is observed and the GaN decomposition rate is reduced compared to identical annealing conditions in H_2. This suggests that H_2 is acting chemically to reduce the barrier for GaN decomposition. This may occur through a surface mediated dissociation of H_2 followed by the formation of more mobile and volatile hydrogenated N and Ga species. The significance of this study for GaN growth is that by increasing the GaN decomposition, the Ga atoms diffuse farther and subsequently re-incorporate into the growing lattice, increasing the GaN crystal quality. Connections between the enhanced GaN decomposition rate and the coalescing of nucleation layer during the ramp to high temperature and the consequences for the high temperature growth are discussed.

INTRODUCTION

GaN is of current interest for the fabrication of blue light emitting diodes [1], lasers [2] and for high power electronic devices [3]. It has been shown that the GaN quality plays a strong role in the device performance [1-3]. Typically, GaN is grown at high temperature (> 1000 °C) using MOVPE with N to Ga ratios larger than 1000 on sapphire or SiC substrates using a thin buffer layer. The high temperature is necessary for efficient catalytic dissociation of NH_3 and the large V/III ratio is needed to offset the N loss from the growing film [4]. The growth temperature is larger (i.e. 100-500 °C) than the threshold temperature for GaN decomposition, and it is not currently understood to what extent GaN decomposes during growth at MOVPE pressures.

Previously, we suggested that decomposition of the GaN film during growth enhances GaN ordering, by eliminating more weakly incorporated Ga and N atoms [4]. At equilibrium the growth rate is zero. For a positive growth rate close to equilibrium, the incorporation rate of atoms into the growing lattice is slightly larger than the decomposition rate [4-6]. Recently, we showed how the GaN decomposition rate is enhanced in flowing H_2 for pressures greater than 100 torr [7]. This result was explained by assuming chemical dissociation of H_2 on the GaN surface which then increases Ga surface mobility and enhances N_2 desorption. This paper reports a more detailed study of GaN decomposition in both H_2 and N_2 as a function of pressure and temperature, where the role of H_2 on the enhanced GaN decomposition rate is clarified.

EXPERIMENTAL DETAILS

Details of the GaN growth are discussed elsewhere [8]. The GaN films were grown at 76 torr using a close-spaced showerhead reactor design. This same reactor was also used to study the GaN decomposition. The growth process resulted in specular GaN growth over the 2" sapphire wafer, with excellent thickness uniformity. Temperature reproducibility of the susceptor was a major concern for the decomposition study. The temperature was calibrated by observing the melting point of 0.005" diameter Au wire and correlating it to a thermocouple in close

Mat. Res. Soc. Proc. Vol. 537 © 1999 Materials Research Society

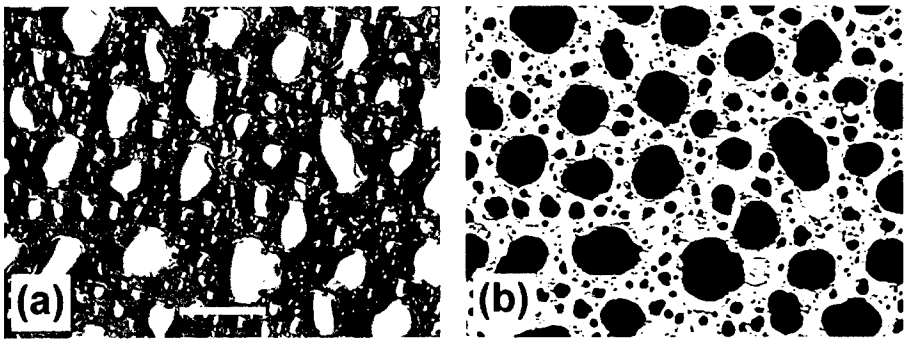


Figure 1. (a) Phase contrast and (b) transmission Normarski images of GaN surface heated for 20 minutes in H_2 at a pressure of 150 torr at a temperature of 811 °C. The bar on image (a) indicates a length of 20 μm.

proximity to with the backside of the susceptor. Temperature measurement in the reactor was found to be reproducible to within 5 °C after 8 months of use.

For the decomposition study, pieces of the GaN on sapphire were cleaved and weighed to within 0.1 mg using an analytical balance [7]. Repeated weighing of the GaN on sapphire pieces were reproducible to within 0.1 mg. The pieces were reintroduced into the reactor and heated under varying conditions using either 6 SLM flow of H_2 or 3 SLM of N_2. Each piece was ramped at 25 °C per minute to the annealing temperature, which ranged from 800 to 1130 °C. After annealing for a set time and cooling, each piece was re-weighed in air to determine the mass loss. If Ga droplets were observed, they were removed by etching in dilute HNO_3 and rinsing with DI water. (On some samples which were not etched, the Ga droplets were found to be very stable in air even up to several months, suggesting minimal oxidation of the liquid Ga droplets.) Each piece was then weighed again to determine the weight of liquid Ga. Finally, the piece was annealed at 1080 °C until the remaining GaN was decomposed, leaving only the initial bare sapphire surface. The bare sapphire weight was used to calculate the sapphire area in order to convert the measured weights to kinetic rates (atoms/cm^2) [7].

RESULTS

After annealing GaN in the absence of NH_3, the most notable change in the GaN surface morphology is the appearance of Ga droplets as shown in Fig. 1. For Fig. 1, the GaN surface was annealed at a temperature of 811 °C for 20 minutes in H_2 at a pressure of 150 torr. The Ga droplets are observable as the lighter regions in the phase contrast image (Fig. 1(a)) and as the darker regions in the transmission image (Fig 1(b)). Because the GaN decomposition rate is larger than the Ga desorption rate, the liquid Ga droplets accumulate on the surface and coalesce into larger droplets, similar to the liquid droplet growth mechanism developed by Family and Meakin [9]. In flowing H_2 Ga droplets were observed for pressures greater than 22 torr [7] for anneals at 992 °C. Compared to the Ga droplets in flowing H_2, the Ga droplets in flowing N_2 were barely discernable even at the highest magnification of 1000x. The droplet size increased as both the anneal temperature and the pressure were increased in H_2 and in N_2 for temperature greater than 1000 °C.

For temperatures ranging from 800 - 1000 °C, the H_2 pressure had a strong influence on both the quantity of Ga and the Ga droplet size. This is shown in Fig. 2, where the kinetic rates for Ga accumulation (i.e. liquid Ga on the surface), GaN decomposition, and Ga desorption are plotted as a function of pressure. Figs. 2(a) through 2(c) show the rates at anneal temperatures of 992 °C, 902 °C, and 811 °C, respectively. It is clear from Fig. 2(a) that the GaN decomposition rate (filled circles) and the surface Ga accumulation rate (open squares) increase as the pressure is increased. The Ga desorption rate (filled diamonds) changes slightly as a function of pressure, peaking near 76 torr in Fig. 2(a), 100 torr in Fig. 2(b), and 120 torr in Fig. 2(c). The increase in the Ga desorption rate at these pressures is due to a maximum in the Ga surface area to volume

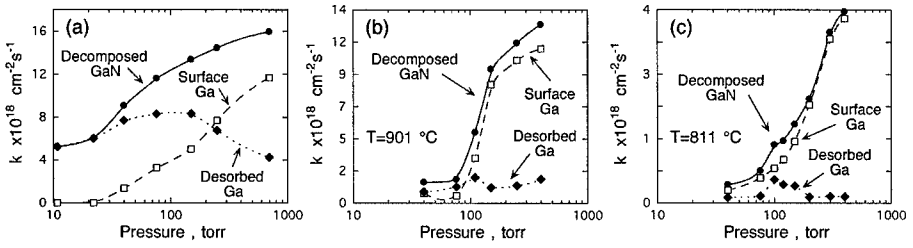


Figure 2. Plot of the GaN decomposition rate in H_2 (solid circles) at various pressures at (a) 992 °C, (b) 902 °C, and (c) 811 °C. The Ga desorption rate (solid diamonds) and the rate of Ga accumulation (open squares) on the surface during the anneal are also plotted.

ratio which then decreases as the droplets coalesce. Clearly, as shown in Fig 2(b) and 2(c), the buildup of Ga on the surface directly coincides with the increase in the GaN decomposition rate.

Arrhenius plots of the GaN decomposition and Ga desorption rates in both H_2 and N_2 are plotted in Figs. 3 and 4, respectively. Because the GaN decomposition rates depend strongly on the H_2 pressure, the decomposition rates in H_2 (solid circles, solid line) are plotted only for 76 torr. From this data, the fit yields a pre-exponential of $(6.3\pm0.4)\times10^{30}$ $cm^{-2}s^{-1}$ and an activation energy, E_A, of 2.96 ± 0.06 eV. This is in close agreement with previous measurements of GaN decomposition in vacuum, where pre-exponentials of 4×10^{29} $cm^{-2}s^{-1}$ [10] and 5×10^{28} $cm^{-2}s^{-1}$ [11] and an E_A of 3.1 eV [10, 11] were measured. For comparison, values of the pre-exponentials and E_A for the GaN decomposition and Ga desorption kinetics are listed in Table 1. Arrhenius plots of the GaN decomposition at higher H_2 pressures gave slopes that were smaller than the slope measured at 76 torr, giving significantly smaller E_A at higher pressures. These values for E_A were not explicitly calculated because it is not clear if the GaN decomposition at these higher pressures is governed by a single, simple chemical mechanism. The GaN decomposition rates were also measured in N_2 at pressures of 76 (open diamonds) and 150 torr (open squares). At fixed temperature in N_2, the GaN decomposition rate was approximately constant for pressures up to 400 torr. In N_2, an exponential fit gives a larger pre-exponential of $(1.2\pm0.1)\times10^{32}$ $cm^{-2}s^{-1}$ and an substantially larger E_A of 3.62 ± 0.04 eV compared to the kinetic parameters measured in

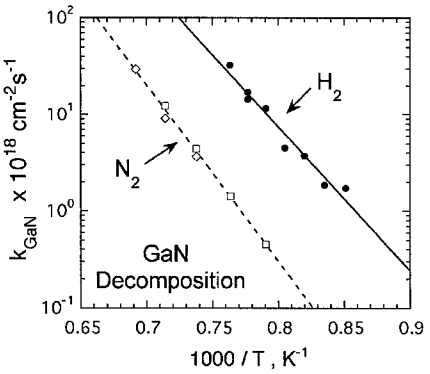


Figure 3. Arrhenius plot of the GaN decomposition rate vs. the reciprocal temperature under H_2 (filled circles, solid line) and N_2 (open diamonds and squares, dashed line). The pre-exponent and activation energy from the fit are listed in Table 1.

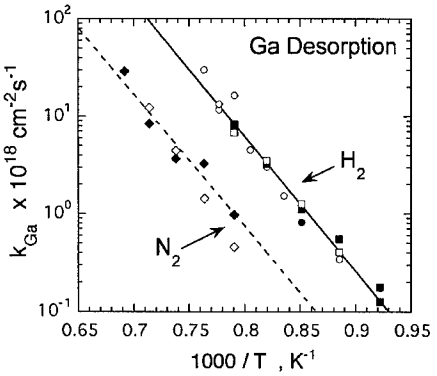


Figure 4. Arrhenius plot of the Ga desorption rate vs. the reciprocal temperature under H_2 (filled and open circles and squares, solid line) and N_2 (filled and open diamonds, dashed line). The pre-exponent and activation energy from the fit are listed in Table 1.

TABLE I. Values for the kinetic parameters for GaN decomposition and Ga desorption. The first column lists the event, either GaN decomposition or Ga desorption and a brief description of the conditions for the study. The second column lists the measured pre-exponential and the third column lists the measured activation energy, E_A. The reference for the work listed in the table is shown in the fourth column.

Event	pre-exponent	E_A (eV)	Ref.
GaN Decomposition			
Thermogravimetry	$4x10^{29}$ $cm^{-2}s^{-1}$	3.1	10
Mass Spectroscopy	$5x10^{28}$ $cm^{-2}s^{-1}$	3.1	11
Mass Spectroscopy	$1.2x10^{31}$ $cm^{-2}s^{-1}$	3.93	12
H_2 at 76 torr	$(6.3\pm0.4)x10^{30}$ $cm^{-2}s^{-1}$	2.96±0.06	this work
N_2 at 76 and 150 torr	$(1.2\pm0.1)x10^{32}$ $cm^{-2}s^{-1}$	3.62±0.04	this work
Ga Desorption			
desorption from liquid Ga	-	2.8	14
RHEED study	$1.0x10^{28}$ $cm^{-2}s^{-1}$	2.69	15
H_2 at 40, 76, 150, 250 torr	$(6.6\pm0.5)x10^{29}$ $cm^{-2}s^{-1}$	2.74±0.06	this work
N_2 at 76 and 150 torr	$(5.3\pm0.4)x10^{28}$ $cm^{-2}s^{-1}$	2.69±0.08	this work

H_2. The GaN decomposition kinetic parameters measured in N_2 are closer to the mass spectroscopy work of Ambacher and coworkers [12] as shown in Table I.

GaN decomposition was also studied as a function of time at a fixed pressure of 150 torr and temperature of 811 °C. Images of the surface after (a) 3, (b) 10, (c) 20, and (d) 80 minutes are shown in Fig. 5. As shown in Fig. 5, the average Ga droplet size increases as the surface is annealed as described by the model of Family and Meakin [9]. After an initial incubation time, the GaN decomposition rate, Ga surface accumulation rate, and the Ga desorption rate were relatively constant in time suggesting zeroth order kinetics. Also, for one experiment the GaN surface was predosed with trimethylgallium for 10 minutes at 600 °C prior to the high temperature anneal in H_2. In agreement with the work of Pisch and Schmid-Fetzer who observed enhanced GaN decomposition on Ga predosed surfaces [13], a 34% increase in the GaN decomposition rate was observed on the Ga predosed surface. While the increase in the GaN decomposition rate by Ga predosing the surface is significant, it is not as large as the increase observed in Fig. 2 when the H_2 pressure is increased from low (< 76 torr) to high pressure (> 150 torr). From this work it is apparent that the GaN decomposition rates depend strongly on the ambient gas (i.e. H_2 or N_2), the pressure, and the condition of the initial surface.

Contrary to the large range in the measured kinetic parameters for GaN decomposition, the measured E_A for Ga desorption were found to be both independent of pressure and ambient gas composition. The data shown in Fig. 4 for H_2 were measured at 40 (solid circles), 76 (open circles), 150 (solid squares), and 250 (open squares) torr. From a fit to all the data a pre-exponential of $(6.6\pm0.5)x10^{29}$ $cm^{-2}s^{-1}$ and an E_A of 2.74±0.06 eV were measured [7]. In N_2, the desorption rates were measured at 76 (solid diamonds) and 150 (open diamonds) torr, yielding a pre-exponential of $(5.3\pm0.4)x10^{28}$ $cm^{-2}s^{-1}$ and an E_A of 2.69±0.08 eV. Both measurements of the

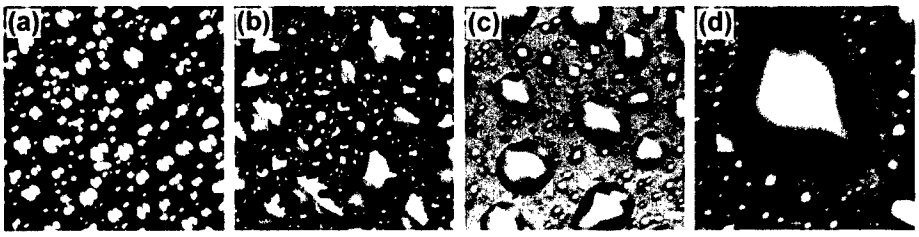


Figure 5: The growth in the Ga droplet size is shown for GaN surfaces anneal at 811 °C for (a) 3, (b) 10, (c) 20, and (d) 80 minutes in H_2 at a pressure of 150 torr.

Ga desorption E_A are in excellent agreement with the value of 2.8 eV for Ga desorption from liquid Ga [14], and 2.69 eV for Ga desorption from GaN in vacuum [15]. The pre-exponential measured in H_2 is 12.5 larger than in N_2, which is close to the mass ratio of N_2 to H_2 of 14. The mechanism for Ga desorption suppression in N_2 and implications for GaN growth will be discussed in the next section.

DISCUSSION AND CONCLUSIONS

GaN thermal decomposition has been extensively studied in vacuum [10-12, 16-19]. From these previous studies activation energies, E_A, of 3.1 eV [10, 11] and 3.93 eV [12] were measured as listed in Table 1. In this study, we have shown how the measured kinetic parameters vary depending on the pressure and ambient gas. For example, in N_2 a larger E_A (3.62 eV) is measured compared to a lower E_A (2.96 eV) measured in H_2 at 76 torr. The E_A are even lower in H_2 when the pressure is increased above 100 torr. These differences in the E_A reflect a change in the GaN decomposition mechanism when GaN is heated in H_2 vs. heating in N_2.

The decomposition rate enhancement at high pressure coincides with an increase in liquid Ga coverage. Recently, Pisch and Schmid-Fetzer showed that liquid Ga can catalyze GaN decomposition for temperatures as low as 720 °C [13]. Although Ga droplet formation coincides with an increase in the GaN decomposition rate, it is not known if the liquid Ga accumulation is the cause or a result of the increased GaN decomposition rate. In Fig. 2, we show that the GaN decomposition rate is enhanced at higher pressure in H_2. However, no enhancement is observed in N_2. This implies that the GaN surface is chemically altered in H_2 and that N is preferentially removed from the lattice while the Ga desorption rate remains relatively constant.

To preferentially remove N from the lattice, the H_2 must first dissociate and adsorb on the surface. Ga metal is known to dissociate H_2 at high temperatures to form Ga hydrides [20]. The hydrogenated N and Ga species have the potential to be both more mobile and also more volatile. More mobile hydrogenated Ga species have been proposed to explain the increase in the Ga diffusion length when H_2 or atomic H is used in the MBE growth of GaAs [21]. In addition, Okamoto and coworkers have recently showed a suppression of 3D growth morphology when atomic H is used during MBE growth of GaN [22], implying an increase in the surface mobility for the hydrogenated Ga atoms. Increasing the Ga diffusion length would more rapidly uncover new areas of the GaN surface for N_2 desorption, which is $10\text{-}10^4$ times faster than the Ga desorption rate for the temperature range of 800-1100 °C [4, 15]. Furthermore, the surface H can form more volatile NH_x species. Both an increased rate of NH_x desorption and an increased GaH mobility, will lead to the formation and growth of Ga droplets as shown in Figs. 1 and 5. When N_2 is substituted for H_2, the E_A for decomposition is larger because the chemical pathways for forming hydrogenated N and Ga species are absent. In N_2, the kinetic barrier to GaN decomposition is larger and may be limited by the formation and desorption rate of N_2.

Compared to the GaN decomposition kinetics, Ga desorption is simpler. The E_A listed in Table 1 all are in the range 2.69-2.8 eV, implying that the Ga desorption mechanism is similar under varying pressures and ambient gas flows. The agreement in the E_A for Ga desorption from liquid Ga [14] and the similarity of the measured E_A values in Table 1, suggest that the Ga atoms desorb from a Ga rich surface. As shown in Fig. 4, the measured pre-exponential factor in H_2 is 12.5 times the measured pre-exponential factor in N_2, which is close to the mass difference of 14 between N_2 and H_2. With the N_2 and H_2 molecules initially near room temperature (21 °C), their impact with the hot surface (near 800-1050 °C) would likely result in a general heat removal from the surface. The heat transfer between the N_2 and the hot surface is more efficient than between H_2 and the surface, because of its larger mass (more impulsive collision) and slower speed (mean speed of N_2 is 3.7 times slower than H_2) its collision time with the surface is longer. As a result of the increased collision time, heat transfer from the hotter surface Ga atoms to the cooler N_2 molecules is more efficient, resulting in a reduced population density of the Ga surface vibrations which lead to Ga desorption. The net effect of this is a reduction in attempt frequency (i.e. pre-exponential factor) for Ga desorption in N_2 compared to H_2.

This study of GaN decomposition has several consequences for the growth of GaN. We have found that the material quality is substantially improved when GaN growth is conducted above 100 torr. When the GaN epitaxial layer is grown above 100 torr, we find a near doubling of the electronic mobility (μ > 500 cm^2/Vs for intentionally Si doped films with n = $2\text{-}3x10^{17}$ cm^{-3}) compared to films growth at 76 torr [7]. For films grown above 100 torr, the GaN grain size

increased from < 1 μm to 2-5 μm, which may be directly responsible for the increased mobility [23]. Other groups using close-spaced or high speed rotating disk reactors have also reported improved electric properties when the pressure of the GaN growth is greater than 100 torr [24, 25]. Larger grains and narrower x-ray rocking curve widths have been reported for the growth of unnucleated GaN on sapphire in H_2 compared to N_2 [26], suggesting that the enhanced decomposition in H_2 aids in the breakup of smaller grains. Changes in the nucleation layer evolution during the ramp from low to high temperature have also been observed as a function of H_2 pressure [25, 27]. Enhanced GaN decomposition in H_2 may also increase the size and aid in the coalescence of the low temperature nucleation layers as shown by Han et al. [25]. If insufficient NH_3 is supplied, the GaN nucleation layer may be entirely decomposed [28], especially if the nucleation layer is annealed under higher H_2 pressure.

This study illustrates the significant differences between reduced and atmospheric pressure MOVPE GaN growth and the influence of carrier gas chemistry. We have demonstrated the direct influence of H_2 pressure on the GaN decomposition rate. A more thorough understanding of the GaN decomposition mechanism at the higher growth pressures currently used by many groups may serve to clarify the mechanisms contributing to GaN growth.

ACKNOWLEDGEMENTS

We thank JA Freitas, Jr. and W.J. Moore for characterization of films. This work is supported by the Office of Naval Research and the ONR Power Electronic Building Block Program (PEBB) monitored by George Campisi.

REFERENCES

[1] S. Nakamura, M. Senoh, and T. Mukai, Appl. Phys. Lett. 64,1687 (1994).
[2] S. Nakamura, M. Senoh, S. Nagahama, N, Iwasa, T. Yamada, T. Matsushita, H, Kiyoku, Y. Sugimoto, Jpn. J. Appl. Phys. 35, L74 (1996).
[3] S.N. Mohammad, A.A. Salvador, and H. Morkoc, Proc. IEEE 83, 1306 (1995); S. Strite and H. Morkoc, J. Vac. Sci. Technol. B 10, 1237 (1992); R.F. Davis, Proc. IEEE 79, 702 (1991).
[4] D.D. Koleske, A.E. Wickenden, R.L. Henry, W.J. DeSisto, and R.J. Gorman, J. Appl. Phys. 84, 1998 (1998).
[5] S.Yu. Karpov and M.A. Maiorov, Surf. Sci. 393, 108 (1997).
[6] R. Heckingbottom in *Molecular Beam Epitaxy and Heterostructures*, eds. L.L. Chang and K. Ploog, (Martinus Nijhoff, Dordrecht, 1985). p. 71.
[7] D.D. Koleske, A.E. Wickenden, R.L. Henry, M.E. Twigg, J.C. Culbertson, and R.J. Gorman, Appl. Phys. Lett. 73, 2018 (1998).
[8]. M. Fatemi, A.E. Wickenden, D.D. Koleske, M.E. Twigg, J.A. Freitas, Jr., R.L. Henry, and R.J. Gorman, Appl. Phys. Lett. 73, 608 (1998).
[9]. F. Family and P. Meakin, Phys. Rev. Lett. 61, 428 (1988).
[10]. Z.A. Munir and A.W. Searcy, J. Chem. Phys. 42, 4223 (1965).
[11]. R. Groh, G. Gerey, L. Bartha, and J.I. Pankove, Phys. Stat. Sol. A 26, 353 (1974).
[12] O. Ambacher, M.S. Brandt, R. Dimitrov, T. Metzger, M. Stutzmann, R.A. Fischer, A. Miehr, A. Bergmaier, and G. Dollinger, J. Vac. Sci. Technol. B 14, 3532 (1996).
[13] A. Pisch and R. Schmid-Fetzer, J. Cryst. Growth 187, 329 (1998).
[14]. R.E. Honig and D.A. Kramer, RCA Rev. 30 , 285 (1969).
[15] O. Brandt, H. Yang, and K.H. Ploog, Phys. Rev. B 54, 4432 (1996).
[16] W.C. Johnson, J.B. Parsons, and M.C. Crew, J. Phys. Chem. 36, 2651 (1932).
[17] R.J. Sime and J.L. Margrave, J. Phys. Chem. 60, 810 (1956).
[18] R.C. Schoonmaker, A. Buhl, and J. Lemley, J. Phys. Chem. 69, 3455 (1965).
[19] A.S. Bolgar, S.P. Gordienko, E.A. Ryklis, and V.V. Fesenko, in: Chemistry and Physics of the Nitrides (ed. by G.V. Samsonov) [in Russian], (Naukova, Dumka, Kiev 1968), p. 151; also see I.G. Pichugin and D.A. Yas'kov, Izvestiya Akademii Nauk SSSR, Neorganicheskie Materialy 6, 1973 (1970).
[20] H. Remy, *Treatise on Inorganic Chemistry*, (Elsevier, New York, 1960), p. 18; W.R.S. Garton, Proc. Phys. Soc. A 64, 509 (1951).
[21] Y. Morishita, Y. Nomura, S. Goto, and Y. Katayama, Appl. Phys. Lett. 67, 2500 (1995).
[22] Y. Okamoto, S. Hashiguchi, Y. Okada, and M. Kawabe, Jpn. J. Appl. Phys. 37, L1109 (1998).
[23]. S.D. Hersee, J.C. Ramer, and K.J. Malloy, MRS Bulletin 22, 45 (1997).

[24] B.T. McDermott, R. Pittman, E.R. Gertner, J. Krueger, C. Kisielowski, Z. Lilienthal-Weber, and E. Weber, Talk D2.2 at Fall Material Research Society Meeting, Boston, 1997.
[25] J. Han, and T.-B. Ng, R.M. Biefeld, M.H. Crawford, D.M. Follstaedt, Appl. Phys. Lett. 71, 3114 (1997).
[26] T.J. Kistenmacher, D.K. Wickenden, M.E. Hawley, and R.P. Leavitt, Mat. Res. Soc. Symp. Proc. 395, 261 (1996).
[27] J.C. Ramer, K. Zheng, C.F. Kranenberg, M. Banas, and S.D. Hersee, Mat. Res. Soc. Symp. Proc. 395, 225 (1996).
[28] Y. Kobayashi, T. Akasaka, and N. Kobayashi, Jpn. J. Appl. Phys. 37, L1208 (1998).

DEFECT STATES IN SiC/GaN- AND SiC/AlGaN/GaN- HETEROSTRUCTURES CHARACTERIZED BY ADMITTANCE AND PHOTOCURRENT SPECTROSCOPY

H.WITTE*, A.KRTSCHIL*, M.LISKER*, J.CHRISTEN*, F.SCHOLZ**, J.OFF**

* Institute of Experimental Physics, University of Magdeburg, PO Box 4120, 39016 Magdeburg, Germany

** 4th Institute of Physics, University of Stuttgart, D- 70550 Stuttgart, Germany

Cite this article as: MRS Internet J. Nitride Semicond. Res. 4S1, G3.71 (1999)

ABSTRACT

Deep defect levels in n-type GaN/AlN/6H-SiC- and GaN/AlGaN/6H-SiC- heterostructures grown by Metallorganic Vapor Phase Epitaxy were analyzed by Thermal and Optical Admittance and Photocurrent Spectroscopy. The various thermal and optical transitions in the spectra originating from both the Schottky contact as well as the GaN/SiC- and AlGaN/GaN-heterojunctions were separated. This was achieved by variation of the modulation frequency, the use of different contact arrangements and by comparison with reference spectra from GaN/Sapphir samples and SiC substrates. In the GaN/AlGaN/SiC structures a bias voltage dependent peak shift was found which is correlated to an interface related defect distribution. In additionally to, SiC related defects, defect-band-transitions involving defects with transition energies at 2.2eV, 1.85eV, E_G-(470±40) meV and E_G-(65-95) meV were found for the GaN layer.

INTRODUCTION

Besides their optoelectronic potential, GaN and their related compounds are very important for high-frequency, high-power and high- temperature electronic devices /1/. Especially, heterostructures based on GaN and AlGaN on SiC- substrate are main parts of some novel devices such as MESFET´s, MODFET´s, bipolar transistors /1/, UV-detectors /2/, LED`s and laser diodes /1/. Defects states in the layers and in the interface regions influence both optical /3/ and electrical /4/ properties. For example, in GaN / p-type SiC -structures the photoluminescence and electroluminescence spectra show defect related transitions /3/ which cause tunneling-assisted currents described in /4/. Furthermore, in GaN / p-type SiC heterojunctions, indications on interface defect states were found by C-V-characteristics /5/ and by admittance spectroscopy /6/.

In GaN/AlGaN pin-structures on SiC-substrates, Mg-related recombination centers were found with temperature dependent dark current measurements and with current-DLTS having activation energies of 0.191eV and 0.207eV, respectively /7/.

The aim of this paper is to present evidences for defects and localize these traps in the layers and interfaces using Thermal and Optical Admittance Spectroscopy. We show, that defect spectra of heterostructures can be led back to those of the corresponding single layers on sapphire. We were able to separate the different heterojunctions by variation of the modulation frequency and the contact arrangement of the samples.

These investigations provide the for the determination of the capacitance and conduction values of the individual parts of the heterostructure. Only with these knowledge an calculation of the concentrations of the different traps would be possible. The quantitative analysis will be the aim of future work.

Mat. Res. Soc. Proc. Vol. 537 © 1999 Materials Research Society

EXPERIMENTAL

The first group of samples consist of a n-type 6H-SiC- substrate (carrier concentration of about $1.5*10^{18}cm^{-3}$), a 17nm thick AlN nucleation layer followed by a 1µm thick, nominally undoped, n-type GaN layer. The second kind of heterostructures is based on the same SiC substrate followed by a 500nm thick AlGaN buffer layer ([Al] 43-47%). The undoped GaN top layer is 500nm thick. All layers were grown by Metallorganic Vapor Phase Epitaxy (MOVPE) at a growth temperature of 1000°C. For reference measurements we investigated various undoped GaN layers deposited with the same MOVPE equipment on sapphire substrates as well as the SiC substrate itself.

The samples were cleaned with organic solutions and etched in HF (SiC) and ammonium hydroxyd (GaN) solution. Ohmic contacts were formed by sputtering of Ni on SiC- substrate and by evaporation of Al- layer on GaN followed by an annealing process at 700°C for 10 min. in an inert gas atmosphere. The Schottky contacts were realized by sputtering of a 100nm thick Pt-layer having a diameter of 1mm. Sandwich arrangement with the ohmic contact on the SiC substrate and the Schottky contact on the GaN side as well as coplanar arrangement consisting of both contacts on the GaN layer were used. All GaN on sapphire samples are contacted in coplanar arrangement. For further reference measurements, contacts on the SiC sample were deposited in sandwich arrangement using a Pt Schottky contact. All Schottky contacts show rectifying behavior up to a frequency range of about 100kHz - 500kHz.

Thermal Admittance Spectroscopy (TAS) measurements were carried out in the temperature region between 78K and 450K using a high precision LCR-meter (HP 4284A) at modulation frequencies between 20Hz and 1MHz under zero bias conditions. The experimental set up and the evaluation method is described in detail in /8/. For the Optical Admittance Spectroscopy (OAS) an optical-electrical cryostat was used for measurements at temperatures between 78 and 295K. A monochromator illumination system yielded monochromatic light with wave length between 300nm and 3000nm (see also /9/).

RESULTS AND DISCUSSION

In TAS spectra of all heterostructures with sandwich contacts a peak is observed at a temperature of about T_{max}=85K at 1MHz. A peak with identical T_{max} is also found in the reference spectrum of the n-type SiC sample (thermal activation energy (61±5)meV, see Table 1). Thus, we conclude that these peaks are caused by the same defect level. The origin of this electron trap is probably the N-donor in 6H-SiC /10/. This behavior corresponds very well with TAS investigations of n-type GaN layers grown by LPCVD on n-type 6H-SiC- substrates described in /6/.

In contrary, three electron traps with activation energies between 130 meV and 320meV were found in the reference samples consisting of GaN/AlN/Sapphire layers using TAS (see also Table I). These defects are well known from the literature, for example in /6/,/13/ and /14/ detected by DLTS and TAS in MOVPE and MBE grown material. The discrepancy between the detection of defects in the heterostructures and the reference samples shows, that the high doping concentration in the SiC substrate dominates the TAS signals of the heterostructures strongly.

In GaN/AlGaN/SiC-heterostructures a bias voltage dependent shifting peak at frequencies between 0.5 and $2.5*10^5$ 1/s is observed by AS in reverse direction, as shown in Fig.1. The peak height remains constant at about (2-3) nF. Because of the conductance of the SiC-substrate we used the Kramers-Kronig transformation of the admittance data to eliminate the series resistance/11/. A bias dependent shift of an AS peak position is well known from Si/SiO_2- interface defect distributions (for example see /12/). We conclude, that this peak is caused either by an intermediate layer in one of the heterojunctions, gradients of defect states in the interface re-

gions, or interface defect state distributions. A similar behavior is also observed in n-type GaN (LPCVD grown) /p-type SiC heterostructures (for more details see /6/).

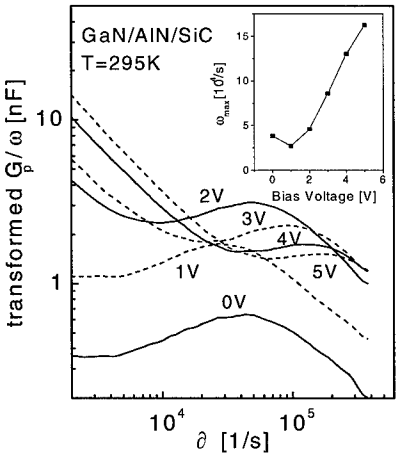


Fig. 1 : Transformed Conductance /11/ as a function of frequency of the GaN/AlGaN/SiC heterostructure for different reverse bias voltages. The insert shows the shift of the peak maximum with increasing bias voltage.

The TAS and AS results clearly show, that all components of the heterostructures, i.e. the SiC substrate, the AlGaN and GaN layers, the corresponding heterojunctions as well as the Schottky contact on the GaN top layers contribute to the measured signals.

In order to separate these different parts of the heterostructures we compare OAS spectrum of the GaN/AlN/SiC structure with OAS spectra of the SiC-substrate and of GaN layers on sapphire (Fig. 2). The spectrum of the heterostructures in coplanar contact arrangement shows the same structure as the spectra of GaN on sapphire. However, in sandwich arrangement the heterostructures show the SiC-spectrum, leading to the conclusion that the GaN/SiC-spectrum with sandwich contacts is influenced by the SiC-side of the heterojunction and the coplanar arrangement is dominated by the Schottky contact on the GaN layer, respectively. All defect-band transitions in the OAS spectra are summarized in Table 1 together with TAS results.

Another method to separate the various parts of the structures is based on the variation of the modulation frequency, visualized in Fig. 3. In the GaN/AlGaN/SiC heterostructures the near band gap region (NBG) of AlGaN and GaN below 3.4eV occurs. With increasing frequency the Schottky contact on the GaN layer breaks down, the NBG peaks vanish and the SiC-side of the heterojunction (peak at 2.65eV) dominates the OAS spectrum.

Using coplanar contact arrangement and low frequencies OAS spectra of the heterostructures which dominated by defects of the GaN layer were measured. The defect-to-band transitions found are shown in Table I.

In the OAS spectra of the GaN/Al/SiC we have to distinguish between the near band gap region involving defects-to-(opposite) band transitions, the blue band originating from transitions from deep defects to the opposite band, the yellow band which is comparable to the yellow luminescence band and the deep defect at 1.85eV. All, these defects were also found in MBE grown GaN (seen /6/ and /9/) as well as in MOVPE grown GaN layers on sapphire (see /13/ and /14/) .

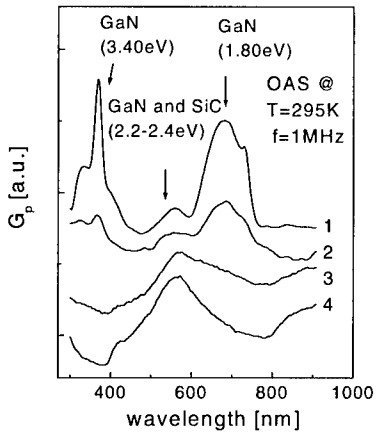


Fig. 2 : Optical Admittance Spectra of different GaN structures. 1- GaN on sapphire; 2- GaN/AlN/SiC with coplanar contacts; 3- GaN/AlN/SiC with sandwich contacts; 4- 6H-SiC.

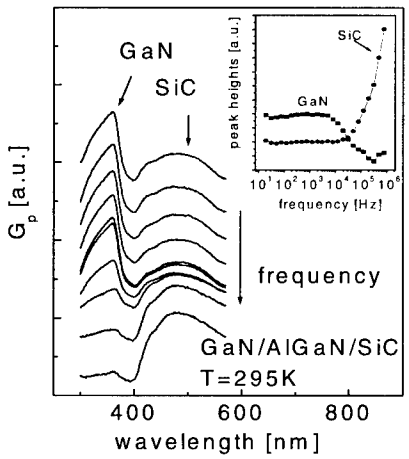


Fig. 3 : Optical Admittance Spectra of an GaN/$Al_{0.43}Ga_{0.57}N$/SiC heterostructure for different modulation frequencies. The peak heights of the both peaks at 3.4eV (GaN) and 2.56eV (SiC) are plotted as a function of the frequency in the insert.

Differences between the OAS spectra of the GaN/AlN/Sapphire sample and the GaN/AlN/SiC heterostructures show up in the near band region. For the GaN/AlN/SiC-heterostructures shallower transitions (E_G-18meV) were observed in comparison of the GaN/AlN/Sapphire reference samples (E_G-(65-95)meV). One reason may be a dominance of shallower defects, for example the Si level, in the GaN layer on SiC.

The similarities in the OAS spectra between the GaN/AlN/SiC heterostructure and the reference samples on Sapphire show that the substrate material influences not the occurrence of these defects qualitative. Otherwise, the quantitative analysis of these defects will be make in the future.

Table I : Summary of observed thermal activation energies and peak maximum temperatures of GaN/AlN/Sapphire-layers and in heterostructures measured with TAS and with OAS detected defect-band-transition energies of various layer structures. A band gap energy of E_G= 3.44eV at 295K was used according to /15/. The meaning of the abbreviations is : NBG near band gap region; BB blue band region, YB yellow band region and SiC-peak ; DT deep defect-band transition.

method	GaN/AlN/Sapphire	GaN/AlN/SiC	GaN/AlGaN / SiC	n-type SiC
TAS	(130-170) meV (276±28) meV (320±24) meV	peak at 85K	peak at 85K	peak at 85K (61±5)meV
OAS /NBG	(65-95)meV below gap	18meV below gap	3.42eV	-
OAS / BB	290; 370 , 460 and 760meV below gap	(450-510) meV below gap	-	
OAS / YB+SiC	2.2eV	2.22-2.26 eV	-	2.25eV
OAS / DT	1.82eV	1.87eV	-	-

In the OAS spectra of the GaN/AlGaN/SiC structures only the near band gap (NBG) peak consisting of the GaN (360nm) and the AlGaN (290nm) layers occurs. Other defect-band transitions were not observed. A corresponding PC spectrum on the reference sample AlGaN/AlN/Sapphire shows only the near band gap peak similar to the spectra of the heterostructures. We assume this behavior in the OAS spectra is caused by the high resistivity of the AlGaN layer within the heterostructures.

In summary, n-type GaN/AlN/6H-SiC- and n-type GaN/AlGaN/6H-SiC-heterostructures were characterized for defect levels in the GaN-layers using thermal and optical admittance spectroscopy. Different contact arrangements, variation of modulation frequency and comparison with spectra of GaN/Sapphire and SiC samples enables us to assign the signals to the individual junctions. A defect distribution correlated with the interface between GaN and SiC is found by admittance spectroscopy. Using OAS some deep defect- band-transition in the GaN layer of the GaN/Al/SiC heterostructure were detected.

ACKNOWLEDGMENT

This work was financially supported by the Deutsche Forschungsgemeinschaft under contract number WI 1619/1-1 and by the Kultusministerium Sachsen-Anhalt contract number 002KD1997.

REFERENCES

/1/ S.N.Mohammad, H.Morkoc : Progr. Quant. Electr. 20, 361-525 (1996)
/2/ A.Osinsky, S.Gangopadhya, B.W.Lim, M.Z.Anwar, M.A.Khan, D.V.Kuksenkov, H.Temkin : Appl. Phys. Lett. 72, 742 (1998)
/3/ J.T.Torvik, C.Qiu, M.Leksono, J.I.Pankove : Appl. Phys. Lett. 72, 1371 (1998)
/4/ J.T.Torvik, M.Leksono, J.I.Pankove, B.VanZeghbroeck, H.M.Ng, T.D. Moustakas : Appl. Phys. Lett. 72, 945 (1998)

/5/ N.I.Kusnetzov, A.E.Gubenco, A.E.Nicolaev, Yu.V.Melnik, M.N.Blashenkov, I.P.Nikita, V.A.Dmitriev : Mater. Sci. Engin. B46, 74 (1997)
/6/ A.Krtschil, H.Witte, M.Lisker, J.Christen, U.Birkle, S.Einfeldt, D.Hommel, M.Topf, B.K.Meyer : Mater. Res. Soc. Symp. Proc. 482, 887 (1997)
/7/ V.A.Dmitriev : MIJ-NSR 1 (1997) Art. 29
/8/ J.Barbolla, S.Duenas, L.Bailon : Sol. State Electron. 35, 285 (1992)
/9/ A.Krtschil, M.Lisker, H.Witte, J.Christen, U.Birle, S.Einfeldt, D.Hommel ; Accepted for Mater. Science and Engineering B
/10/ G.Pensl, T.Troffer : Sol. State Phenomena 47-48, 115 (1996)
/11/ C.Leon, M.Martin, J.Santamaria, J.Skarp, G.Gonzalez-Diaz, F.Sanchez-Queseda : J. Appl. Phys. 79, 7830 (1996)
/12/ E.H.Nicolian, J.R.Brews : MOS Physics and Technology, John Wiley & Sons, New York, 1982
/13/ P.Hacke, H.Okushi : Appl. Phys. Lett. 71, 524 (1997)
/14/ W.Götz. N.M.Johnson, D.P.Bour, C.Chen, H.Liu, C.Kuo, W.Imler : Mater. Res. Soc. Symp. Proc. 395, 443 (1996)
/15/ B.Monemar : Phys. Rev. B 10, 676 (1974)

MICROSTRUCTURE OF GaN GROWN ON (111) Si BY MOCVD

D. M. Follstaedt, J. Han, P. Provencio and J. G. Fleming

Sandia National Laboratories, Albuquerque, NM 87185-1056

Cite this article as: MRS Internet J. Nitride Semicond. Res. 4S1, G3.72 (1999)

ABSTRACT

Gallium nitride was grown on (111) Si by MOCVD by depositing an AlN buffer at 1080°C followed by GaN at 1060°C. The 2.2 μm layer cracked along {1-100} planes upon cooling to room temperature, but remained adherent. We were nonetheless able to examine the material between cracks with TEM. The character and arrangement of dislocations are much like those of GaN grown on Al_2O_3: ~2/3 pure edge and ~1/3 mixed (edge + screw), arranged in boundaries around domains of GaN that are slightly misoriented with respect to neighboring material. The 30 nm AlN buffer is continuous, indicating that AlN wets the Si, in contrast to GaN on Al_2O_3.

INTRODUCTION

Hexagonal GaN is being widely studied because of its large, direct bandgap and high thermal stability. Applications are envisioned in technologies involving short wavelength (green, blue and UV) optoelectronics and high-temperature or high-power electronics. A key issue for growth of GaN has been the lack of an ideal substrate, since GaN substrates are not readily available and other semiconductors have large lattice mismatches. Most GaN has been grown on sapphire (Al_2O_3); vapor-phase growth usually begins with deposition of a low temperature GaN buffer followed by the complete layer at near 1000°C. Applications with sapphire are limited by its lack of electrical conductivity and high cost.

We have investigated growth of GaN on Si with the intent of integrating short-wavelength devices into Si-based microelectronics, as well as providing an alternative substrate. We have grown GaN by metal-organic chemical vapor deposition (MOCVD) on (111) Si and obtained microstructures much like those for sapphire, but cracking during cooling to room temperature limits use of our current materials. Here we use transmission electron microscopy (TEM) to examine dislocations in the GaN and the structure of the AlN buffer layer grown at the interface with the Si, and compare them to corresponding microstructures of GaN grown on Al_2O_3. An introduction to this work and our related approaches to growth on Si is given elsewhere [1].

GROWTH OF GaN

A 1000 rpm rotating disk reactor with 4.75" quartz chamber was used to grow AlN and GaN with trimethylgallium, trimethylaluminum, and ammonia precursors at 30 Torr [1]. Several investigations indicate that growing an AlN buffer first on Si avoids the formation of amorphous Si_3N_4 since N reacts more exothermically with Al than Si; this is important for attaining good epitaxial growth of GaN [2,3]. Our methods follow those of Watanabe et al [2] who found that AlN buffer growth at >1000°C leads to good epitaxy, in spite of the 17% lattice mismatch of GaN with Si. We grew a 30 nm AlN buffer at 1080°C, followed by 2.2 μm of GaN at 1060°C.

In situ reflectivity indicated that the GaN surface was smooth immediately after growth at 1060°C. However, upon cooling to room temperature, a dense set of cracks with separations

Mat. Res. Soc. Symp. Proc. Vol. 537 © 1999 Materials Research Society

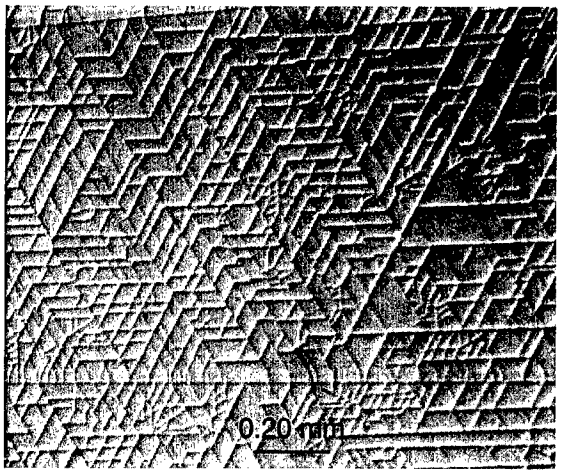


Figure 1. Nomarski optical micrograph showing cracking of GaN on (111) Si along {1-100} planes.

from 20 to 100 μm was found along {1-100} planes, as seen in Figure 1. The layer is expected to have relaxed fully at the growth temperature, as found for GaN grown on Al_2O_3 using in situ stress monitoring techniques [4]. The greater thermal expansion coefficient of GaN as compared to that of Si ($5.6x10^{-6}$/K vs. $2.6x10^{-6}$/K, respectively) then explains cracking since the GaN layer would be put into tension upon cooling. In spite of cracking, the GaN layer adhered to the substrate. X-ray diffraction of such layers gives (0002) GaN reflections with FWHM of 900 arcsec, similar to those found previously [2].

TEM CHARACTERIZATION OF DEFECTS IN GaN

Cross-section TEM specimens were successfully prepared by usual metallographic polishing and ion milling methods for both [110] and [1-12] Si orientations in spite of the cracking. Cracks were found passing directly across the layer and into the Si substrate. The cracks were open with no indication of subsequent deposition, consistent with their forming after growth [1]. No evidence of de-adhesion of the layer from the substrate was seen where the cracks cross the interface into the Si. The GaN layer was found to be single phase and with no 30°-misoriented grains as seen in other material grown by molecular beam epitaxy (MBE) [5]. Selected-area diffraction demonstrated the epitaxial orientation seen previously for GaN on (111) Si [2,3,5]:

(0001) ‖ (111)	interface plane
[1-100] ‖ [11-2]	direction in plane
[11-20] ‖ [1-10]	"

Dislocations thread from the buffer layer to the surface of the GaN layer along the c-axis, growth direction. Examination in cross-section with different diffracting beams can be used to determine the Burger's vectors of individual dislocations, which for hexagonal close-packed lattices are [6]: **a** (or 1/3<11-20>, in the basal lattice plane), **c** (<0001>, along the hexagonal axis), or **a+c** (1/3<11-23>, mixed character). In Figure 2, image (a) uses the (0004) reflection to illuminate the cores of dislocations with Burger's vectors having a c-axis component. Image (b) uses (1-100) to image those with a basal plane component. Detailed examinations with several reflections indicate that almost all dislocations are detected in Figure 2b) and have a basal-plane component. Those with a c-axis component seen in Fig. 2a (~1/3 of the total) are almost all of mixed character. The additional ones in Fig. 2b (~2/3 of the total) have purely basal-plane Burger's vectors, **b** = **a**; since the dislocation lines are fairly straight along the c-axis, these are edge dislocations. Very few dislocations have **b** = **c** corresponding to pure screw character. This distribution of Burger's vectors is like that found by us [7] and others [8] in GaN on sapphire.

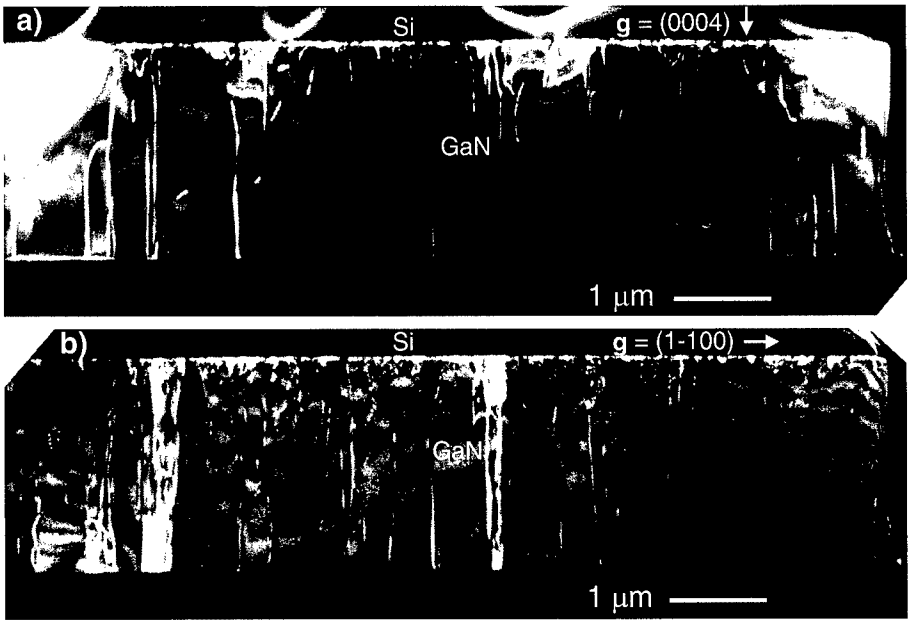


Figure 2. Weak-beam TEM images obtained near [11-20] orientation. a) **g** = (0004), with cores of dislocations having **b** = **a** + **c** illuminated. b) g = (1-100), with cores of all dislocations illuminated. A crack running through the layer and into the Si substrate is seen at far right.

Plan-view TEM gives additional insight into the dislocation arrangement. A specimen was prepared by placing thinned epoxy on the specimen surface to penetrate into cracks, removing excess epoxy from the surface, and carefully backthinning with the specimen attached to a grid for structural support. The thinned area is at the surface of the GaN layer and allows defects threading to it to be detected. In Figure 3, the dislocations are viewed nearly end-on and appear as short black-white segments. They often lie along continuous curves that form boundaries between domains of material with slightly differing orientations. A similar arrangement is found for threading dislocations in GaN grown on sapphire [9]. Plan-view images allow more surface area to be examined than in cross-section and give the most accurate determination of dislocation density at the surface: $8x10^9$ disl/cm^2 for this specimen. This density is like that found for GaN grown on sapphire [7], although lower values have been achieved [8].

By examining this greater surface area, an additional defect with a low density is found. Two void-like defects were identified in Figure 3 (small white spots, arrowed) by examining their contrast with changes in TEM objective lens focus. Such defects have been termed "nanotubes" if they have extended length into the GaN, or "pinholes" if they are pits located at surface [10]. Since we do not have depth information, we cannot determine which of the two classifications apply. Other images taken under high resolution conditions show that the {1-100} lattice planes form facets around the voids. Their areal density is ~$1x10^8$/cm^2, again comparable to that found in GaN grown on sapphire [10].

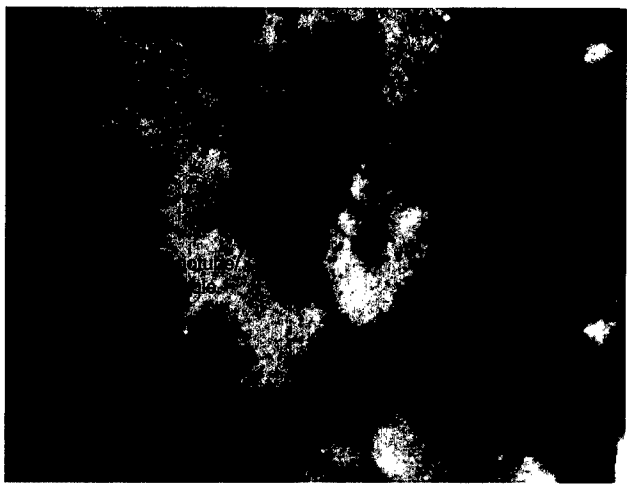


Figure 3. Plan-view TEM image of the surface of the GaN layer, obtained near [0001] orientation using g = (1-100) two-beam conditions in bright-field. Dislocations appear as short black-white lines, and often form continuous curves at boundaries between domains of material with slightly differing orientations; two are noted with nearby dashed lines. Two void-like defects (nanotubes or pinholes) are also noted with arrows.

EXAMINATION OF AlN BUFFER LAYERS

The buffer layer was found to be continuous over extended distances in cross-section images. It's thickness varies somewhat as seen in Figure 4a, but it is readily identified from the GaN overlayer. By tilting the specimen slightly to vary the contrast in bright field, or by weak-beam examinations like Figure 4b, the layer is seen to be composed of grains that are 20-40 nm across and slightly misoriented with respect to each other.

Dislocations in the GaN just above the buffer interact with each other, as seen in Figure 4. The dislocations extend into the AlN buffer at near-normal incidence. In some cases, they appear to coincide with grain boundaries in the buffer; two instances are arrowed in Figure 4b. This suggests that the misorientations between AlN buffer grains may directly produce some of the dislocations threading through the GaN. Perhaps if a buffer layer with larger grains were formed, the GaN would have fewer defects.

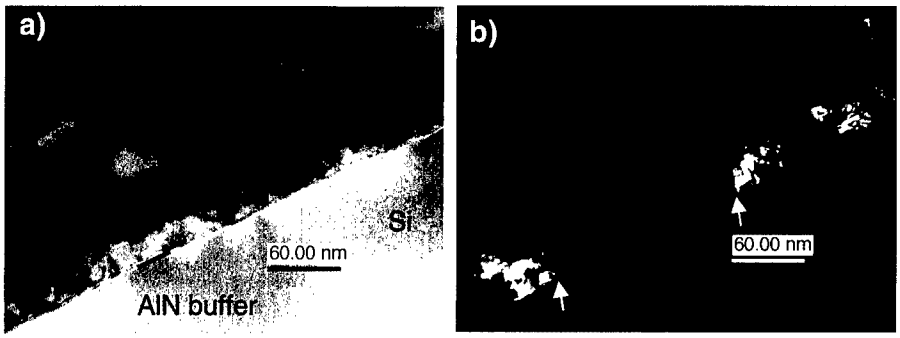


Figure 4. a) Bright-field, (3-300) two-beam image of AlN buffer on Si near [11-20] cross-section orientation with dislocations extending into GaN layer. b) Corresponding weak-beam image showing 20-40 nm grains in the buffer with contrast between them indicating slight orientation differences. Two dislocations appear to originate at grain boundaries in the buffer (arrowed).

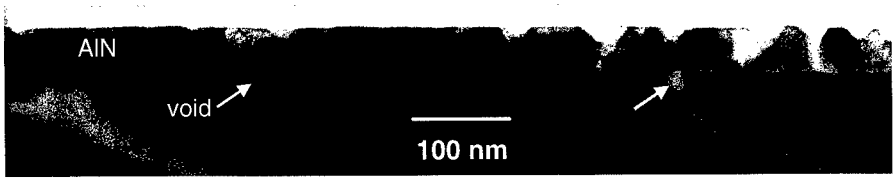


Figure 5. Cross-section TEM image of 40 nm AlN buffer grown on (111) Si, seen in [11-20] orientation with g = (0002) two-beam conditions. Grains in the AlN buffer are faceted at the top surface, and two voids (arrowed) can be seen just below the interface in the Si.

Having a continuous 30 nm-thick AlN layer on Si implies that the AlN "wets" the Si under our conditions, indicating that the AlN/Si interface has lower energy than the AlN/vacuum surface. A continuous AlN layer was also found for an even thinner (8 nm) buffer grown on Si by MBE [3]. Such continuous layers differ greatly from those observed for GaN grown by MOCVD on Al_2O_3 using a low-temperature buffer layer followed by high-temperature growth. For GaN/Al_2O_3 the layer must be 0.4 μm thick before it is continuous [10]. The wetting may indicate that more favorable bonding is occuring between nitrides and the Si. Such good bonding is suggested by the adhesion of the layer to the substrate as evidenced by the cracks propagating across the interface instead of along it. Thus Si appears to be the preferred substrate for initiating growth of nitrides when used with an AlN buffer.

A cross-section TEM specimen was also made of a 40 nm-thick AlN buffer layer grown alone on (111) Si at 1100°C. The layer was again found to be continuous with slight misorientations between grains, as seen in Figure 5. Our examinations indicated two other features of this layer. First the individual grains composing the buffer exhibit faceting on the growth surface; the facets appear to be {1-101} lattice planes. Secondly, a few voids were found in the Si immediately beneath the interface, which suggests that Si may be diffusing into the AlN.

DISCUSSION

Microstructural features of GaN grown on Si are compared with those for growth on sapphire in Table I. Cracking clearly remains a problem for the Si substrate that must be overcome before devices can be made. The microstructures of threading dislocations are very similar in GaN grown on the two substrates; in both cases the threading dislocations appear due to small local misorientations between adjacent materials. It may be possible to influence the dislocation density with Si by varying the growth conditions of the AlN buffer.

The buffer layers are very different, with AlN wetting Si but GaN not wetting Al_2O_3 even after subsequent high-temperature growth. This difference this may reflect a change in bonding across the interface, although differing deposition temperatures and differences between AlN and GaN need to be considered. Since Si is covalent whereas Al_2O_3 is ionic, the change may be due to covalent bonding of the AlN to the Si. The faulting seen [8] in nucleation layers for GaN on Al_2O_3 is associated with the low-temperatures needed to induce growth of GaN, which then occurs in both its fcc and hcp phases; we have not detected faulting in our high-temperature AlN buffer layers.

Table I. Comparison of Microstructures: GaN/Al_2O_3 versus GaN/Si

		GaN/Al_2O_3	GaN/Si (this work)
Cracking:		no	yes, {1-100} planes
Dislocations:	density	$10^8 - 10^{10}$ /cm^2 [7-9]	$8x10^9$ /cm^2
	character	1/3 mixed, 2/3 edge [8]	1/3 mixed, 2/3 edge
	arrangement	boundaries [9]	domain walls
	nanotubes, pinholes	$10^6 - 10^8$ /cm^2 [10]	~10^8 /cm^2
Buffer:	type (temperature)	GaN (550°C) [7]	AlN (1080°C)
	wetting	no	yes
	thickness for continuity	~0.4 μm [11]	~ 30 nm
	microstructure	faulted (hcp/fcc) [8]	hcp grains (20-40 nm)

ACKNOWLEDGEMENTS

The authors would like to thank S. Hearne and J. Floro for discussions about stress in GaN layers during growth, and S. R. Lee for discussions about cracking in GaN layers on Si. This work at Sandia National Laboratories supported by the United States Department of Energy under Contract DE-AC04-94Al85000. Sandia is a multiprogram laboratory operated by Sandia Corporation, a Lockheed Martin Company for the United States Department of Energy.

REFERENCES

1. J. Han, J. G. Flemming and D. M. Follstaedt, Mat. Res. Soc. Symp. Proc. 512, 53 (1998).
2. A. Watanabe, T. Takuchi, K. Hirosawa, H. Amano, K. Hiramatsu and I. Akasaki, J. Crystal Growth, 128, 391-396 (1993).
3. S. Guha and N. A. Bojarczuk, Appl. Phys. Lett. 72, 415 (1998).
4. S. Hearne, J. A. Floro and I. Tsong, private communication (in situ stress measurements).
5. S. N. Basu, T. Lei and T. D. Moustakas, J. Mater. Res. 9, 2370 (1994).
6. J. P. Hirth and J. Lothe, *Theory of Dislocations*, 2nd ed. (Krieger Publishing Co., Malabar, FL, 1992) p. 270.
7. Dislocations were analyzed as described herein; the growth of our GaN on sapphire is discussed by T.-B. Ng, J. Han, R. M. Biefeld and M. V. Weckwerth, J. Electron. Mat. 27, 190 (1998).
8. X. H. Wu, L. M. Brown, D. Kapolnek, S. Keller, B. Keller, S. P. DenBaars and J. S. Speck, J. Appl. Phys. 80, 3228 (1996).
9. X. J. Ning, F. R. Chien, P. Pirouz, J. W. Yang and M. A. Khan, J. Mater. Res. 11, 580 (1996).
10. Z. Liliental-Weber, Y. Chen, S. Ruvimov and J. Washburn, Phys. Rev. Lett. 79, 2835 (1997).
11. X.H. Wu, P. Fini, S. Keller, E.J. Tarsa, B. Heying, U.K Mishra, S.P. DenBaars and J.S. Speck, Jpn. J. Appl. Phys. Pt.2, 35 L1648 (1996).

ION CHANNELING ANALYSIS OF GALLIUM NITRIDE IMPLANTED WITH DEUTERIUM

W. R. Wampler and S. M. Myers
Sandia National Laboratories, Albuquerque, NM 87185-1056, wrwampl@sandia.gov

Cite this article as MRS Internet J. Nitride Semicond. Res., 4S1, G3.73 (1999)

ABSTRACT

Ion channeling and transmission electron microscopy were used to examine the microstructure of GaN implanted with deuterium (D) at high (>1 at. %) and low (< 0.1 at. %) D concentrations. At high concentrations, bubbles and basal-plane stacking faults were observed. Ion channeling showed the D was disordered relative to the GaN lattice, consistent with precipitation of D_2 into bubbles. At low D concentrations, bubbles and stacking faults are absent and ion channeling shows that a large fraction of the D occupies sites near the center of the c-axis channel.

INTRODUCTION

Hydrogen is incorporated into GaN during growth by MOCVD and also during subsequent processing [1]. This hydrogen strongly affects the electrical properties by passivation of dopants and lattice defects. Release of hydrogen from GaN films requires annealing at temperatures above 800°C [2]. However, large reductions in resistivity of Mg doped GaN can be achieved by annealing at lower temperatures where H is not released from the material [3,4]. This indicates that the atomic configuration of H within the GaN lattice significantly affects its influence on electrical properties.

Here we use ion channeling to examine the lattice location of deuterium implanted into wurtzite GaN. Results from the channeling measurements are compared with first-principles calculations of the lattice configuration of hydrogen in GaN [5,6]. In addition, we use ion channeling and TEM to examine lattice defects produced by the implantation of deuterium.

EXPERIMENTAL PROCEDURES

Wurtzite GaN films with (0001) orientation and thickness in the range of 1.4 - 2.3 μm were grown epitaxially by MOCVD on 420 μm thick c-oriented sapphire substrates as described elsewhere [7]. The GaN was n-type with a carrier density of ~ $10^{17}/cm^3$ as determined by conductivity and Hall-effect measurements. The samples were implanted at room temperature with deuterium (D) at 50 keV to fluences of $10^{15}/cm^2$ and $10^{17}/cm^2$. This gives D concentration profiles peaking 0.4 μm beneath the surface at concentrations of about 0.05 and 5 atomic % for these two fluences [8].

Ion channeling measurements were done with the samples mounted on a 3 axis goniometer. D was analyzed by counting protons from the $D(^3He,p)\alpha$ nuclear reaction with an incident beam of 0.85 MeV $^3He^+$ ions. With this energy D at depths up to about 1 μm will be detected and the peak in the nuclear reaction cross section [8] at 0.6 MeV occurs at the depth of the D. Analysis beams of 2 MeV ^4He were used to examine lattice damage caused by the D implantation. Energy spectra of ^4He backscattered at 155 degrees were recorded for angles of incidence near the c-axis. The analysis beam size was typically 1 mm square and the angular divergence was 0.05 degree.

Mat. Res. Soc. Symp. Proc. Vol. 537 © 1999 Materials Research Society

EXPERIMENTAL RESULTS AND INTERPRETATION

Lattice defects due to D implantation

Transmission electron microscopy, both plan view and cross section, shows that GaN implanted with 50 keV H to fluences of $2x10^{16}/cm^2$ and $10^{17}/cm^2$ and then vacuum annealed at 886°C for one hour, contains cavities with a typical size of 10 nm at the H implant depth [8]. These cavities are believed to result from precipitation of H_2 gas. Such samples also contain planar defects typically ~50 nm in diameter, which are shown by high resolution imaging [8] to be (0001) basal plane stacking faults containing one extra Ga-N bilayer bounded by a partial edge dislocation loop with a Burgers vector c/2[0001]. The atomic configuration of such faults has been discussed elsewhere [9]. TEM showed these cavities and stacking faults were not present in GaN implanted with H to a lower fluence of $10^{15}/cm^2$ and annealed at 886°C. The cavities and stacking faults can be seen in the micrographs shown in figure 1.

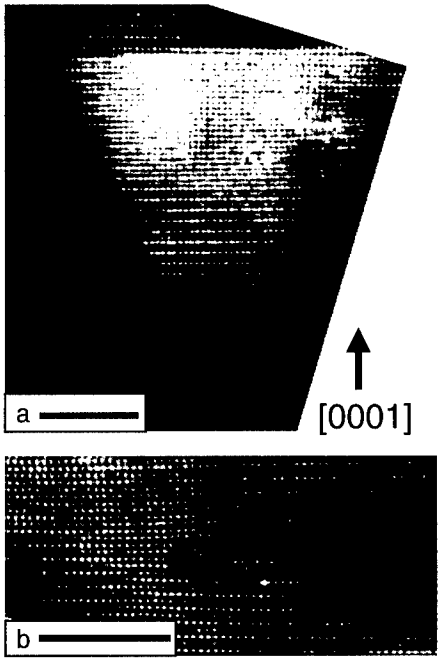


Fig. 1. Cross-section TEM of a bubble (a) and a stacking fault (b) in GaN implanted with $2x10^{16}$ H/cm^2 and then vacuum annealed at 886°C for one hour. The bars indicate 5 nm.

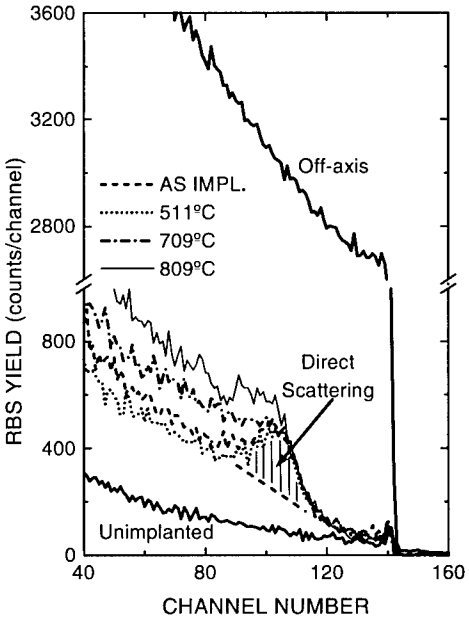


Fig. 2. Energy spectra for channeled 2 MeV ^{4}He backscattered from GaN. Yield from the implanted region appears at channels in the range from 90-120, while the surface corresponds approximately to channel 140.

Figure 2 shows channeled backscattering spectra for 2 MeV ^{4}He incident along the [0001] axis for GaN implanted at room temperature with 10^{17} D/cm^2. Also shown for comparison is a spectrum for an off-axis unchanneled or random direction obtained by averaging spectra taken at several off-axis orientations, and a channeled spectrum taken on a sample as-grown, i.e. not implanted with D. The channeled spectrum for a low-dose ($10^{15}/cm^2$) implanted sample (not shown) was the same as those for unimplanted samples. The low backscattering yield for axial

channeling in the unimplanted GaN of ~ 2% of random yield near the surface and 3.2% of random yield at the depth of D implantation, is consistent with a film which has few lattice defects.

Room-temperature implantation of 10^{17} D/cm^2 at 50 keV creates a direct scattering peak, which is shaded in the figure, at an energy corresponding to He scattered from Ga at the depth of the implanted D, and increases the yield at lower energies due to dechanneling. Subsequent one hour vacuum anneals in the temperature range 511-709°C removes the direct scattering peak and increases the dechanneling step. The direct scattering peak shows that prior to annealing, Ga atoms are displaced from lattice sites into the open [0001] channel, thereby enhancing the backscattering yield of channeled ^{4}He ions. We refer to these displaced Ga atoms generically as Ga interstitials without implying a specific lattice location. The disappearance of this direct scattering peak with annealing indicates a return to lattice sites. The associated increase in dechanneling is consistent with the formation of extended defects with large strain fields, eg. dislocations, which dechannel the ^{4}He with little direct scattering. Reference 10 gives more detailed discussion of defect analysis by ion channeling.

The area under the direct scattering peak can be used to calculate the areal density of Ga interstitials. The number of counts in the peak is given by

$$Y = N_{He}\, \sigma_R\, \Omega\, N_i\, f\,, \qquad (1)$$

where N_{He} is the number of incident ^{4}He ions, σ_R is the Rutherford differential cross section for scattering of ^{4}He from Ga, Ω is the solid angle subtended by the detector, N_i is the areal density of interstitial Ga and f is the flux enhancement due to channeling at the location of the interstitial Ga. With Y = 3500 from the channeled spectrum before annealing (fig. 2) and f = 2 from computer simulations (discussed later) of ^{4}He channeling in GaN assuming all Ga interstitials are near the center of the [0001] channel, we obtain $N_i = 3.0\text{x}10^{16}$/cm^2. This number is smaller by two orders of magnitude than the areal density of collisional displacements caused by the D implantation, which is estimated to be ~40 displacements per incident ion or $4\text{x}10^{18}$ displacements/cm^2. However, the areal density of Ga interstitials estimated from the direct scattering peak is close to the areal density 3.5 x 10^{16}/cm^2 of Ga atoms displaced by the bubbles [8]. This result suggests the following model for bubble formation: the vacancies and interstitials produced by atomic displacements mostly recombine, however a small fraction of the vacancies agglomerate and combine with H to form high pressure H_2 bubbles, leaving a corresponding number of interstitials in the neighboring lattice. At temperatures in the range from 500 to 700°C most of these interstitials annihilate, possibly by diffusing to the surface while some agglomerate into the stacking faults seen by TEM.

If it is assumed that the dechanneling step is due to strain fields from the dislocation loops bounding the stacking faults, then the number of these defects and the areal density of interstitial atoms enveloped by them can be estimated from the height of the dechanneling step. In general the areal density of a defect is related to dechanneling by the equation [10]

$$N_D = \sigma_d^{-1} \ln[(1-\chi_v)/(1-\chi_D)]\,, \qquad (2)$$

were χ_D is the channeled backscattering yield above the step divided by the random or unchanneled yield, and χ_v is the corresponding quantity in the absence of defects. The cross section for dechanneling by the strain field of a dislocation is given by [10]

$$\sigma_d = K\,(a_{TF}\, b)^{1/2}\,/\psi_1 \qquad (3)$$

where a_{TF} is the Thomas-Fermi screening distance, b is the length of the Burgers vector, ψ_1 is a critical angle for dechanneling. Using a value K=1.2, derived elsewhere for axial channeling perpendicular to an edge dislocation [11], we obtain $\sigma_d = 5.3 \times 10^{-7}$ cm^2/cm. With $\chi_v = 0.032$ and $\chi_D = 0.19$ from the channeled spectrum after annealing at 809°C, eq. 2 yields $N_D = 3.4 \times 10^{-5}$ cm/cm^2. Assuming the stacking faults are circular with a diameter of 50 nm estimated from TEM, this value of N_D implies that the associated areal density of extra Ga and N atoms is 1.0×10^{15}/cm^2. This number is smaller by a factor of 70 than the areal density of Ga and N atoms calculated to be displaced by bubble formation.

We also conclude that the bubbles themselves do not contribute significantly to direct scattering and dechanneling. The combined basal plane area of the bubbles per unit sample area is estimated to be ~3 cm^2/cm^2 [8]. If the He ions re-enter the lattice at random locations after traversing a bubble, the direct scattering and dechanneling from the bubbles should be about three times that of the external surface, which is small compared to the observed direct scattering and dechanneling as can be seen in figure 2.

Location of D in the GaN lattice

The location of foreign atoms relative to the host lattice can be determined by ion channeling [10]. Here we use the D(^{3}He,p)α nuclear reaction to study the lattice location of D implanted into GaN. The yield is proportional to the local flux of ^{3}He at the location of the D. For angles of incidence far from major axes or planes the flux of ^{3}He is nearly the same at all locations in the lattice. However, when the analysis beam is aligned along the c-axis, channeling reduces the flux near the rows of host atoms and increases the flux near the center of the open channels relative to fluxes with off-axis alignment. This will give rise to a dip in the NRA yield if the D is near the host atom rows, for example at a substitutional site, or conversely, to a peak in the NRA yield if the D is near the center of the channel. The absence of a peak or dip would indicate that the D is randomly located relative to the lattice.

Figure 3 shows the measured NRA yield normalized to the off-axis or random yield versus the angle between the analysis beam direction and the c-axis. For GaN implanted to the low dose of 10^{15} D/cm^2 there is a narrow peak ~40% above the random yield, whereas for GaN implanted with 10^{17} D/cm^2 there is no peak. The absence of a peak for the high dose implanted sample is consistent with the idea that at high concentrations most of the D precipitates as gas into cavities which would give random location for the D relative to the GaN lattice sites. The peak for the low dose sample shows that a large fraction of the D is in the open channels. The height of this peak was observed to be a function of the analysis beam dose. Figure 4 shows the peak height as a function of off-axis ^{3}He analysis beam dose to the sample. The increase in peak height with beam dose shows that the analysis beam is causing the D to change its location in the lattice. The increase saturates after a few microcoulombs. The data shown in figure 3 were all taken after this beam induced increase had saturated. Measurements of the NRA yield after one

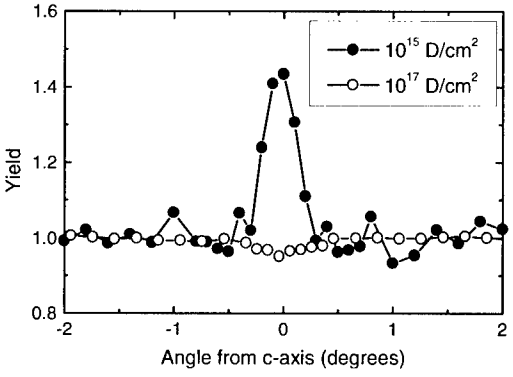


Fig. 3. NRA yield versus angle from the c axis.

hour vacuum anneals showed the peak remained unchanged up to 411°C, decreased with increasing temperature above 511°C, and became poorly resolved by 809°C.

We have carried out computer simulations of the yield versus angle for various D locations in the GaN lattice. These simulations were done using a statistical equilibrium continuum (SEC) model [12] modified for the case of channeling along the c-axis in wurtzite GaN. The SEC model has previously been used to determine the lattice location of D implanted into silicon [12]. Our calculations use Doyle Turner potentials [13] for the GaN lattice with 24 rows. The model includes dechanneling due to thermal vibration of the host atoms. RMS vibrational amplitudes of 0.00735 nm for Ga and 0.00806 nm for N were used [14]. The SEC model gave good agreement with the observed channeling dip for 2 MeV ^{4}He backscattered from the host lattice as shown in figure 5, providing an important validation of the model. The NRA yield curves were calculated using a vibrational amplitude of 0.010 nm for the D. The D vibrational amplitude was estimated assuming a harmonic oscillator model with a vibrational frequency of ~ 2300 cm^{-1} for the D-N stretch mode determined from infrared absorption measurements [15] and from first principles calculations [9]. Except for the S site, changes in D vibrational amplitude by factors of 2 do not significantly change the calculated yield curves. The yields calculated by the SEC model correspond to values averaged over all azimuthal angles. In order to compare with the SEC model, the data shown in figures 3 (NRA) and 4 (RBS) are averages of measurements at many azimuthal angles.

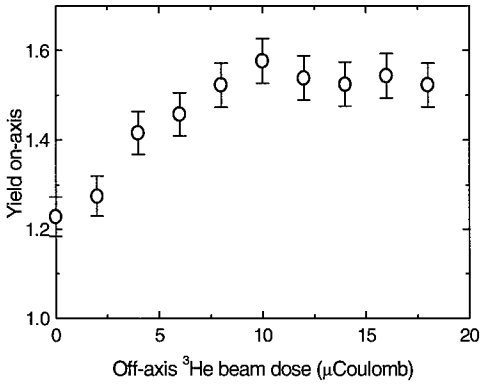


Fig. 4. NRA yield at axial alignment verses off-axis beam dose for GaN implanted with 10^{15}D/cm^2.

Figure 5 shows the yield predicted by the SEC model for various locations of D in the channel as indicated in the inset diagram. Curve C is for D at the channel center, curve S is for D in line with the host atom rows which includes substitutional sites. Also shown is the yield for D at a bond-center site midway between the Ga and N atoms at the channel edge. Another site which has been proposed for hydrogen in GaN is the nitrogen antibonding site which is along the tetrahedral bond direction

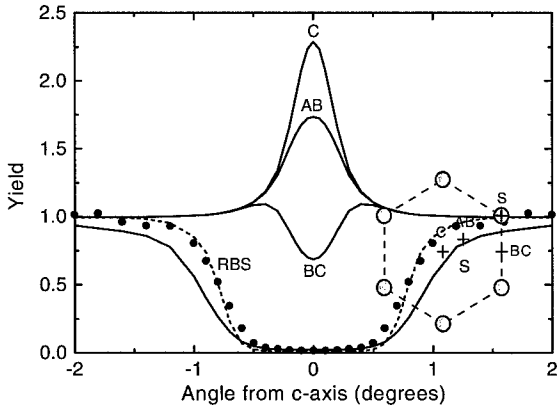


Fig. 5. Solid curves show the NRA yield versus angle calculated by the SEC model for D at the various indicated locations in the c-axis channel. The calculated backscattered yield (dashed curve) agrees well with measured azimuthally averaged yield (dots) of backscattered 2 MeV ^{4}He

~0.10 nm from the N atoms but opposite the neighboring Ga atoms [6]. The channeling yield curves for the one quarter of nitrogen antibonding and bond center sites in-line with the host atom rows, are the same as for the S site. The yield curves for the remaining three quarters of these sites, at locations indicated in the inset diagram as BC and AB in the inset diagram, are shown in figure 5. In the wurtzite structure the two types of AB and BC sites are not equivalent and need not be equally occupied by D. The peak we observe in the measured NRA yield shows that a large fraction, of order 50% or more, of the D occupies sites near the channel center such as the C or AB sites in the sample implanted with 10^{15} D/cm^2.

The increase in NRA channeling yield with analysis beam dose which we observe, and the fact the D depth distribution does not broaden during thermal release, suggest that the D is bound at lattice defects. First-principles calculations have been reported for H bound to vacancies in GaN [6]. These calculations predict that H in a N vacancy will be located near the center of the vacancy. Accordingly, D trapped at N vacancies is expected to be located substitutionally at the N lattice site which would correspond to the S site shown in figure 5. Our NRA channeling data excludes significant occupation of D at this site.

D in a Ga vacancy should form a strong covalent bond with one of the N neighbors [6]. This would place the D about 0.10 nm from an N atom along the tetrahedral bond direction. Since the GaN bond length is 0.20 nm the predicted position for D in a Ga vacancy is therefore very close to the bond center location, in the absence of relaxation of the lattice around the vacancy. Therefore, the yield curves for D in a Ga vacancy for the N whose bond is along the c direction, should be similar to the curve for the S site. For D bound to the other three N, the yield curve should be similar to that of the BC site shown in figure 5. Both of these sites for D at a Ga vacancy give a dip in the channeling yield as shown in figure 5. In a recent study, IR absorption bands were observed due to H-N and D-N stretch mode vibrations in GaN implanted with H and D [15]. These absorption bands were tentatively assigned to H or D bound to N at Ga vacancies. Our channeling results show that most of the implanted D is not at such sites since this would give a dip in the NRA channeling yield in contrast to the peak we observe. It therefore seems appropriate to consider other defect-related sites, including interstitials or solution sites adjacent to defects as possible binding sites for D.

ACKNOWLEDGMENTS

The authors thank Jung Han for supplying the GaN and Alan Wright for insightful discussions of energy and structure calculations for hydrogen in GaN. This work was supported by the U.S. Department of Energy under contract DE-AC04-94AL8500, in part under auspices of the Office of Basic Energy Sciences. Sandia National Laboratories is a multi-program laboratory operated by Sandia Corporation, a Lockheed Martin Company, for the U.S. Department of Energy.

REFERENCES

1. S. J. Pearton, in GaN and related materials, edited by S. J. Pearton (Gordon and Breach, London, 1997) chapter 14.
2. J. M. Zavada, R. G. Wilson, C. R. Abernathy and S. J. Pearton, Appl. Phys Lett. **64,** 2724 (1994).
3. M. Miyachi, T. Tanaka, Y. Kimura, H. Ota, Appl. Phys. Lett. **72,** 1101 (1998).
4. S. J. Pearton, J. W. Lee, and C. Yuan, Appl. Phys. Lett. **68,** 2690 (1996).
5. J. Neugebauer, and C. G. Van de Walle, Phys. Rev. Lett. **75,** 4452 (1995).
6. C. G. Van de Walle, Phys. Rev. **B56,** 10020 (1997).

7. J. Han, T. B. Ng, R. M. Biefeld, M. H. Crawford, and D. M. Follstaedt. Appl. Phys Lett. **71,** 3114 (1997).
8. S. M. Myers, T. J. Headley, C. R. Hills, J. Han, G. A. Petersen, C. H. Seager and W. R. Wampler, MRS Internet J. Nitride Semicond. Res. 4S1,G5.8 (1999).
9. Z. Liliental-Weber, C. Kisielowski, S. Ruvimov, Y. Chen, J. Washburn, I Grzegory, M. Bockowski, J. Jun and S. Porowski, J. Electron. Mater. **25**, 1545 (1996).
10. L. C. Feldman, J. W. Mayer and S. T. Picraux, *Materials Analysis by Ion Channeling*, (Academic, New York, 1982), pp. 88-135.
11. Y. Quéré, Phys. Stat. Sol. **30,** 713 (1968).
12. B. Bech-Nielsen, Phys. Rev. **B37**, 6353 (1988).
13. P. A. Doyle and P. S. Turner, Acta Crystalogr. Sect.A **24**, 390 (1968).
14. A. Yoshiasa, K. Koto, H. Maeda and T. Ishii, Jpn. J. Appl. Phys. **36**, 781 (1997).
15. M. G. Weinstein, C. Y. Song, M. Stavola, S. J. Pearton, R. G. Wilson, R. J. Shul, K. P. Killeen and M. J. Ludowise, Appl. Phys Lett. **72**, 1703 (1998).

OPTICAL PROPERTIES OF Si-DOPED $Al_xGa_{1-x}N/Al_yGa_{1-y}N$ (x=0.24-0.53, y=0.11) MULTI-QUANTUM-WELL STRUCTURES

H. HIRAYAMA and Y. AOYAGI

The Institute of Physical and Chemical Research (RIKEN)
2-1 Hirosawa, Wako-shi, Saitama, 351-0198, Japan, hirayama@postman.riken.go.jp

Cite this article as: MRS Internet J. Nitride Semicond. Res. 4S1, G3.74(1999)

ABSTRACT

We demonstrate strong ultraviolet (UV) (280-330nm) photoluminescence (PL) emission from multi-quantum-well (MQW) structures consisting of AlGaN active layers fabricated by metal-organic chemical-vapor-deposition (MOCVD). Si-doping is shown to be very effective in order to enhance the PL emission of AlGaN QWs. We found that the optimum values of well thickness and Si-doping concentration of $Al_xGa_{1-x}N/Al_yGa_{1-y}N$ (x=0.24-0.53, y=0.11) MQW structure for efficient emission were approximately 3nm and $2\times10^{19}cm^{-3}$, respectively. In addition, the PL intensities of AlGaN, GaN and InGaN quantum well structures are compared. We have found that the PL emission at 77K from a $Al_{0.53}Ga_{0.47}N/Al_{0.11}Ga_{0.89}N$ MQW is as strong as that of InGaN QWs.

INTRODUCTION

GaN and related nitrides are currently of great interest for the application to optical devices operating in the visible and ultraviolet (UV) energy range. Blue laser diodes (LDs) and blue-green light-emitting diodes (LEDs) have been developed in recent years [1-3]. High-power, long-lifetime InGaN multi-quantum well (MQW) lasers have been demonstrated [1].

The AlGaN alloy is a useful material for optical devices operating in the UV, because direct transition emission can be adjusted between 3.4eV (GaN) and 6.2eV (AlN). The wide transition range of AlGaN covers the entire lasing wavelength range covered by UV gas and solid state lasers, for example, XeCl(308nm) and KrF(248nm) excimer lasers or N_2(337nm), He-Cd(325nm), SHG-Ar(257nm) lasers. UV semiconductor lasers are attractive in comparison with gas lasers because of small size, long lifetime, high efficiency and continuous-wave (CW) operation. CW-UV lasers using AlGaN materials are believed to replace UV gas lasers in the near future. For the realization of UV semiconductor lasers, several technical problems such as current injection through high Al content AlGaN crystals or efficient UV emission from AlGaN QW structures must be solved. Especially, the realization of high optical gain from AlGaN in UV emission range is most important for the use as the active region of UV lasers.

Many research groups have obtained a strong emission of InGaN QWs when the In content is 10-20%. However the emission efficiency of binary GaN is much weaker than that of InGaN and actually not useful for active region in a semiconductor laser. The mechanism of the efficient emission in InGaN alloy in comparison with GaN has been investigated using Nichia's samples [4,5]. It was reported that the quantum efficiency of InGaN-based quantum well lasers is enhanced by the effect of localized excitons in nano-scale In segregated (In-rich) regions of the quantum well [5]. The efficient emission of InGaN is observed even when the In incorporation is only a few percent.

On the other hand, AlGaN QW structure with respect to strong UV emission has not yet been well investigated and its optical property is still unknown even though it is very important

Mat. Res. Soc. Symp. Proc. Vol. 537 © 1999 Materials Research Society

material in order to realize UV (especially for wavelength shorter than 360nm) optical devices. Recently, we fabricated AlGaN QW and quantum dot (QD) structures for the purpose of intense UV emission [6].

In this work, we report on the $Al_xGa_{1-x}N/Al_yGa_{1-y}N$ (x=0.24-0.53, y=0.11) MQW structures fabricated by metal-organic chemical-vapor-deposition (MOCVD) and demonstrate an intense UV (280-330nm) photoluminescence (PL). We also compare the PL intensity between AlGaN, GaN and InGaN QW structures.

EXPERIMENTS AND DISCUSSIONS

The structures were grown at 76 torr on the Si-face of an on-axis 6H-SiC(0001) substrate, by a conventional horizontal-type MOCVD system. As precursors ammonia (NH_3), trimethylaluminum (TMAl), trimethylgallium (TMGa), and tetraethylsilane (TESi) were used with H_2 as carrier gas. N_2 gas was independently supplied by a separate line and mixed with the H_2 just before the substrate susceptor. Typical gas flows were 2 standard liters per minute (SLM), 2 SLM, and 0.5 SLM for NH_3, H_2, and N_2, respectively. The molar fluxes of TMGa and TMAl for the growth of $Al_xGa_{1-x}N$ (x=0.11-0.53) were 38μmol/min and 2.6-45μmol/min, respectively. At this condition, the growth rate was approximately 2.5μm/h. The substrate temperature measured with a thermocouple located at the substrate susceptor during the growth was 1140°C for all layer.

At first, we investigated the growth condition of high Al content AlGaN alloy. Figure 1 shows the 77K PL spectra of AlGaN films grown directory on very thin (~10nm) AlN buffer layer. The thickness of all the AlGaN film was approximately 400nm. As seen in Fig. 1, single peak emission was obtained for Al contents of 0.11-0.53. The phonon-replica peaks, seen at the low energy side of each spectra, confirms the good crystal quality of the AlGaN. The typical value of full width at half maximum (FWHM) of the spectrum was 20meV for $Al_xGa_{1-x}N$ (x=0.10-0.12) and 65meV for $Al_xGa_{1-x}N$ (x=0.30-0.60) at 77K. For an Al content of 0.6, an additional emission peak around the wavelength of 290nm probably originating from defects was observed besides the 264nm peak. Therefore, the highest Al content we used in this experiment was 0.53.

Figure 2 shows schematic layer structure of the fabricated (a) $Al_{0.53}Ga_{0.47}N/Al_{0.11}Ga_{0.89}N$ and (b) $Al_{0.24}Ga_{0.76}N/Al_{0.11}Ga_{0.89}N$ MQW sample. In order to achieve a flat surface suitable for the growth of AlGaN quantum well, an approximately 400nm thick $Al_{0.53}Ga_{0.47}N$ buffer layer for sample (a), and 100nm-thick $Al_{0.24}Ga_{0.76}N$ followed by an 300nm-thick $Al_{0.35}Ga_{0.65}N$ buffer layer for sample (b) were deposited. The buffer layer was found to provide a step-flow grown surface as confirmed by atomic force microscopy (AFM). After that, for sample (a), 5-layer MQW structure consisting of 2.7-6.7nm-thick $Al_{0.11}Ga_{0.89}N$ wells and 8nm-thick undoped $Al_{0.53}Ga_{0.47}N$ barrier layers, and 20nm-thick $Al_{0.53}Ga_{0.47}N$ capping layer were grown. Also, for sample (b), 6-layer MQW structure consisting of 2-5nm-thick Si-doped (undoped) $Al_{0.11}Ga_{0.89}N$ wells and 6nm-thick undoped $Al_{0.24}Ga_{0.76}N$ barrier layers, and 10nm-thick $Al_{0.24}Ga_{0.76}N$ capping layer were grown. The well and barrier thickness is estimated simply from the growth rate of bulk.

Figure 3 shows PL spectra measured at 77K of the undoped $Al_{0.53}Ga_{0.47}N/Al_{0.11}Ga_{0.89}N$ 5-layer MQW structures excited with an Ar-SHG laser (257nm) for various well thickness. The spectra of the $Al_{0.53}Ga_{0.47}N$ bulk without $Al_{0.11}Ga_{0.89}N$ well is also shown for comparison of emission intensity. As seen in Fig. 3, the peak wavelength of QW emission shifts from 344nm to 271nm as the well thickness decreases from 6.7nm to 2.7nm. We attribute these shift to the increased quantization energy in the QWs. We cannot see the emission from barrier or capping layers for each MQW spectrum, which indicates that the emission from the quantum well is efficient. The well emission intensity is strongest for a well thickness of 3.3nm. The emission peak wavelength of 400nm-thick $Al_{0.53}Ga_{0.47}N$ buffer layer from the sample without QW is slightly longer than

that of 2.7nm-thick MQW structures. This may be because that the barrier bandgap is extended due to the strain compensation between barrier and well. The rapid reduction of the PL intensity with the increase of the well thickness may be caused by a reduction of the radiative recombination probability due to a separation of electron and hole wave-functions in the large piezoelectric field of the well [7]. The reduction of the emission intensity for the thin well may be mainly due to the increase of nonradiative recombination on the hetero-interfaces between well and barrier.

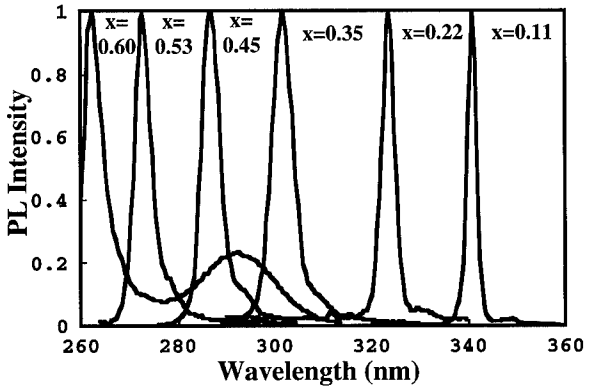


Fig. 1. 77K PL spectra of $Al_xGa_{1-x}N$ (x=0.11-0.60) films grown on the 6H-SiC substrates.

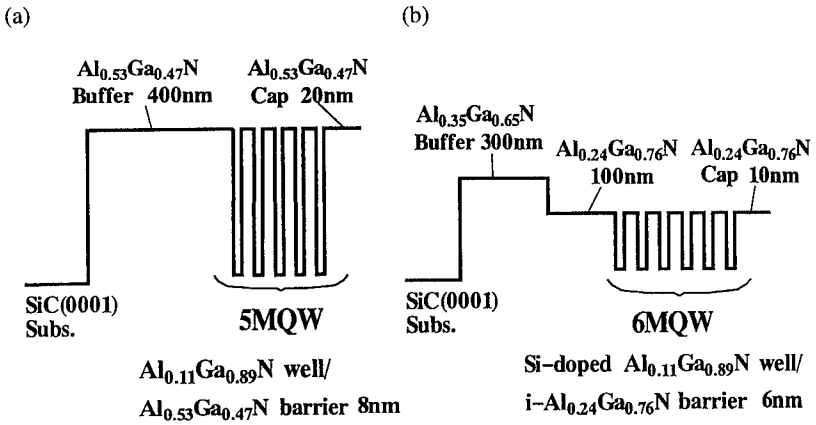


Fig. 2. Schematic layer structure of (a) $Al_{0.53}Ga_{0.47}N/Al_{0.11}Ga_{0.89}N$ and (b) $Al_{0.24}Ga_{0.76}N/Al_{0.11}Ga_{0.89}N$ MQW sample.

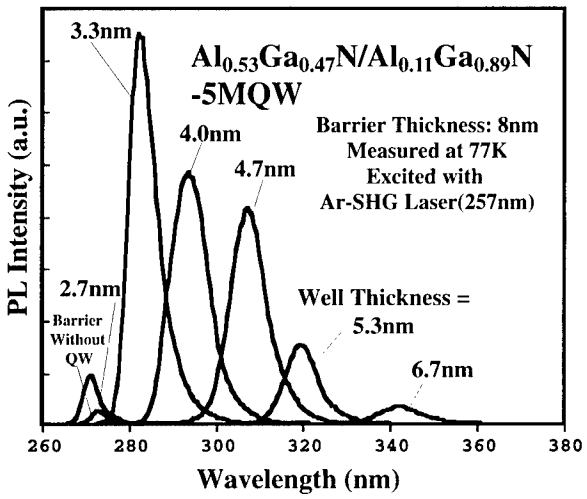


Fig. 3. PL spectra measured at 77K of the undoped $Al_{0.53}Ga_{0.47}N/Al_{0.11}Ga_{0.89}N$ 5-layer MQW structures excited with Ar-SHG laser (257nm) for various well thickness.

Figure 4 shows the room temperature PL spectra of the undoped $Al_{0.24}Ga_{0.76}N/Al_{0.11}Ga_{0.89}N$ 6-layer MQW structures excited with a XeCl excimer laser for various well thickness. The peak wavelength of QW emission shifts from 344nm to 323nm as the well thickness decreases from 5nm to 2nm. The 321nm weak emission originates from $Al_{0.24}Ga_{0.76}N$ barrier layers. The dependence of the PL intensity on the QW thickness was similar to that obtained for $Al_{0.53}Ga_{0.47}N/Al_{0.11}Ga_{0.89}N$ MQWs. The optimized well thickness was also around 3nm.

Figure 5 shows PL spectra measured at 77K from 3nm thick Si-doped and undoped $Al_{0.24}Ga_{0.76}N$ /$Al_{0.11}Ga_{0.89}N$ 6-layer MQWs excited with a He-Cd laser. Si-doping was used only in the QW layers. The doping concentration was changed from 8×10^{18} to $5\times10^{19}cm^{-3}$. The emission intensity increases drastically by Si-doping. The PL intensity is enhanced by 2-3 times with a Si-doping concentration of $2\times10^{19}cm^{-3}$, as seen in Fig 5. We can see phonon replica peaks on the low energy side of main peaks for a doping concentration below $2\times10^{19}cm^{-3}$. We assume that the screening of piezoelectric field with doping is causing the PL intensity enhancement, as reported in the case of InGaN QWs[8].

Finally, we will compare the emission intensity of AlGaN, GaN and InGaN QWs. Figure 6 shows the PL emission spectra measured at 77K of $Al_{0.53}Ga_{0.47}N/Al_{0.11}Ga_{0.89}N$ 5-layer MQW, $Al_{0.24}Ga_{0.76}N/Al_{0.11}Ga_{0.89}N$ 6-layer MQW, $Al_{0.12}Ga_{0.88}N/GaN$ 5-layer MQW and $In_{0.02}Ga_{0.98}N/In_{0.20}Ga_{0.80}N$ single-QW structures. All samples are undoped with optimized well thickness. All samples were excited with Ar-SHG laser with the same excitation condition. As can be seen in Fig. 6, the 280nm emission of the $Al_{0.53}Ga_{0.47}N/Al_{0.11}Ga_{0.89}N$ MQW is as strong as that of the $In_{0.02}Ga_{0.98}N/In_{0.20}Ga_{0.80}N$ QW and much stronger than those of the $Al_{0.24}Ga_{0.76}N/Al_{0.11}Ga_{0.89}N$ or $Al_{0.12}Ga_{0.88}N/GaN$ MQWs at 77K. However, the temperature dependence of PL intensity was strongest for $Al_{0.53}Ga_{0.47}N/Al_{0.11}Ga_{0.89}N$ MQW and the emission intensity was much reduced at room temperature. We believe that the emission mechanism of AlGaN QWs is much different from that of InGaN QWs. We suggest that the strong UV

emission from AlGaN QWs originates in the confinement states which is stable only at low temperature, though, at this moment we don't know the exact mechanism.

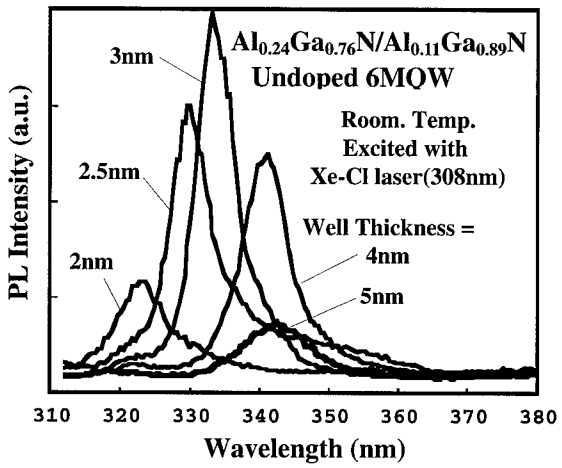


Fig. 4. Room temperature PL spectra for various well thickness from the undoped $Al_{0.24}Ga_{0.76}N/Al_{0.11}Ga_{0.89}N$ 6-layer MQW structures excited with a XeCl excimer laser.

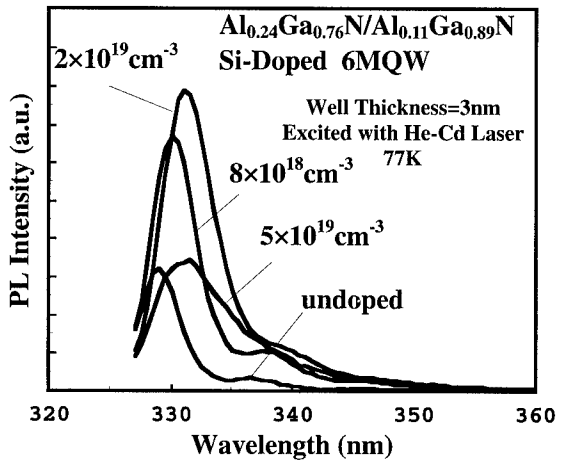


Fig. 5. PL spectra measured at 77K from 3nm thick Si-doped and undoped $Al_{0.24}Ga_{0.76}N$ /$Al_{0.11}Ga_{0.89}N$ 6-layer MQWs excited with a He-Cd laser.

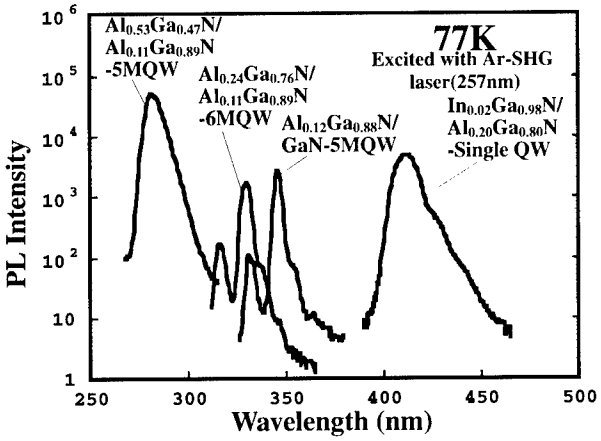


Fig. 6. PL emission spectra of $Al_{0.53}Ga_{0.47}N/Al_{0.11}Ga_{0.89}N$, $Al_{0.24}Ga_{0.76}N/Al_{0.11}Ga_{0.89}N$, $Al_{0.12}Ga_{0.88}N$/GaN MQW and $In_{0.02}Ga_{0.98}N/In_{0.20}Ga_{0.80}N$ single-QW structures.

CONCLUSION

We have demonstrated strong UV (280-330nm) PL emission from AlGaN MQW structures fabricated by MOCVD. Si-doping was shown to be very effective in order to enhance the emission of AlGaN QWs. We investigated systematically the optimized well thickness and the Si-doping concentration of $Al_xGa_{1-x}N/Al_yGa_{1-y}N$ (x=0.24-0.53, y=0.11) MQW structure with respect to efficient emission and found that the optimum values were approximately 3nm and $2\times10^{19}cm^{-3}$, respectively. The, PL intensities of AlGaN, GaN and InGaN quantum well structures were compared. We found that the emission at 77K from a $Al_{0.53}Ga_{0.47}N/Al_{0.11}Ga_{0.89}N$ MQW was as strong as that from the InGaN QWs.

REFERENCES

1. S.Nakamura, M.Senoh, S.Nagahama, N.Iwasa, T.Yamada, T.Matsushita, Y.Sugimoto, and H.Kiyoku, Jpn. J. Appl. Phys., **36**, L1059 (1997).
2. S.Nakamura, T.Mukai, and M.Senoh, Appl. Phys. Lett., **64**, 1687 (1994).
3. S.Nakamura, M.Senoh, S.Nagahama, N.Iwasa, T.Yamada, T.Matsushita, Y.Sugimoto, and H.Kiyoku, Appl. Phys. Lett., **69**, 3034(1996).
4. S.Chichibu, T. Azuhata, T Sota, and S. Nakamura, Appl. Phys. Lett. 70, 2822(1997).
5. Y.Narukawa et al, Appl. Phys. Lett., **70**, 891(1997).
6. H.Hirayama and Y.Aoyagi, 2nd International Symposium on Blue Laser and Light Emitting Diodes, Tu-P42 Chiba (1998).
7. M. Buonglorno Nardelli, K. Rapcewicz, and J. Bernholc, Appl. Phys. Lett., **71**, 3135(1997).
8. S.Chichibu, D.Cohen, M.Mack, A.Abare, P.Kozodoy, M.Minsky, S.Fleischer, S.Keller, J.Bowers, U.Mishra, L.Coldren, D.Clarke, and S.DenBaars, Appl. Phys. Lett., **73**, 496(1997).

EPITAXIAL GROWTH OF III-NITRIDE LAYERS ON ALUMINUM NITRIDE SUBSTRATES

L.J. Schowalter,[*,†] Y. Shusterman,[*] R. Wang,[*] I. Bhat,[*] G. Arunmozhi,[*] and G.A. Slack[*,†]

[*]Physics, Appl. Physics, & Astronomy Dept., Rensselaer Polytechnic Inst.,
Troy, NY 12180, schowl@rpi.edu
[†]Crystal IS, Inc., Latham, NY 12110

Cite this article as: MRS Internet J. Nitride Semicond. Res. 4S1, G3.76

ABSTRACT

High quality, epitaxial growth of AlN and $Al_xGa_{1-x}N$ by OMVPE has been demonstrated on single-crystal AlN substrates. Here we report characterization of epitaxial layers on an a-face AlN substrate using Rutherford Backscattering/ion channeling, atomic force microscopy (AFM), x-ray rocking curves, and preliminary electrical characterization. Ion channeling along the $[10\bar{1}0]$ axis gives a channeling minimum yield of 1.5% indicating a very high quality epitaxial layer.

INTRODUCTION

While III-nitride epitaxy offers great potential for optoelectronic, high temperature and high power devices, the common use of sapphire has many disadvantages. The use of single crystal III-nitride substrates should allow improved epitaxial growth, improved thermal and chemical compatibility, as well as improved thermal conductivity.

We have succeeded in growing single crystals of AlN exceeding 1 cm in length and 0.5 cm in diameter using the technique of sublimation and recondensation [1]. Substrates of AlN have been cut from these single crystals boules with either the $(11\bar{2}0)$ (a-face) or the (0001) (c-face) orientation. Here we report preliminary results from the growth of AlN and $Al_xGa_{1-x}N$ layers on the a-face substrates.

GROWTH PROCEDURES

All growths were carried out in an rf-heated, hot-wall, horizontal reactor [2]. The growth temperature was 1100 °C, while the growth pressure was 100 torr. Trimethylaluminum (TMA), trimethylgallium (TMG) and ammonia (NH_3) were used as the source materials, and the carrier gas was hydrogen. An AlN substrate and a c-plane sapphire substrate were placed side by side to compare epitaxial quality and calibrate the growth rate. After a chemical clean and prior to the epitaxial growth, the substrates were thermally treated at 1100 °C under 2 slm of hydrogen flow for 5 min and under a mixed stream of 1slm ammonia and 2 slm hydrogen for 10 min. After this treatment, the flow rates of H_2 and NH_3 were adjusted to 3 slm and 2 slm respectively, and then TMA (for AlN growth) or a combination of TMA and TMG (for alloy growth) was switched into reactor. In all cases, the flow rate of TMA was 30 sccm.

Under these conditions, the AlN growth rate was about 0.5 μm/hour (for the sapphire substrate) as determined by FTIR measurements. Typical growth times were about 1.5 hours. The 50% alloy discussed below was achieved with 3sccm and 30sccm flow rates of TMG and TMA, respectively. Doping was accomplished by using 11.1 ppm silane in a hydrogen carrier gas.

Mat. Res. Soc. Symp. Proc. Vol. 537 © 1999 Materials Research Society

CHARACTERIZATION AND ANALYSIS

In Fig. 1, an AFM image of an AlN substrate is shown prior to epitaxial growth. This particular substrate was cut so as to expose the $(11\bar{2}0)$ plane of atoms (the a-face) and was misoriented by less than 1°. It can be seen that substrate surface is nearly atomically flat. Examination of the substrate over a wider area indicates that all evidence of mechanical damage (scratches, etc.) has been removed unlike prior work [3] where micro scratches were observed on the substrate surface after just a mechanical polish. We do observe pit-like defects which may be associated with dislocations intersecting the surface but their origin has not been convincingly determined at this time. Their density is approximately 3×10^3 cm^{-2}.

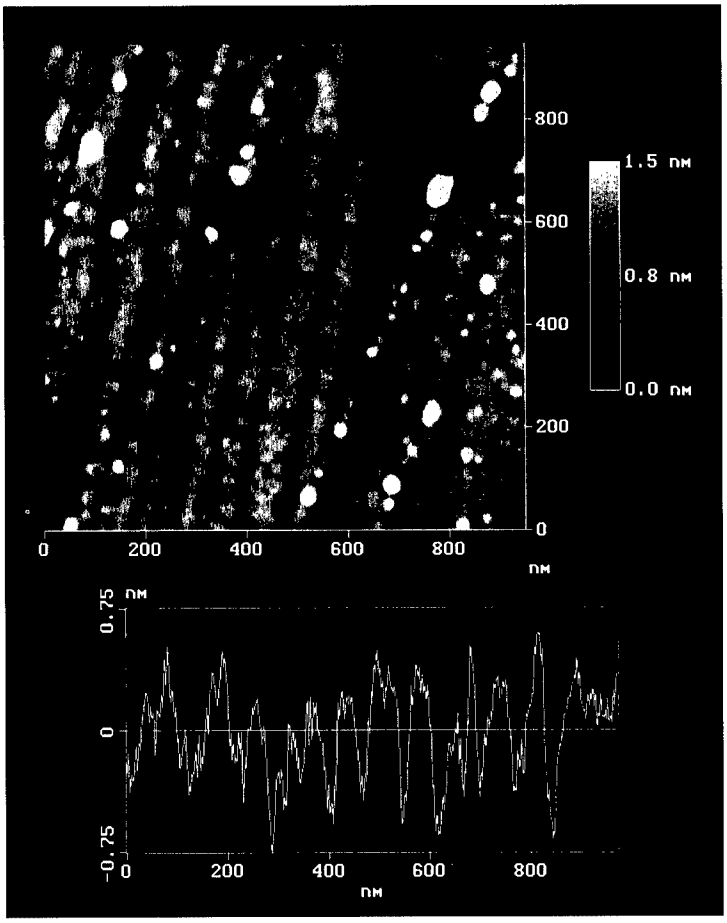


Fig. 1: An AFM image of the bare AlN substrate prior to growth.

In Fig. 2, an AFM image of a 0.7-μm-thick AlN epitaxial layer, grown on a slightly vicinal AlN substrate, is shown. Atomic steps seem to have organized into semi-regular arrays during

growth giving rise to a grating effect across the surface. The height of the step bunches is approximately 4 nm. The density of defects across the surface, observed with AFM, increased by approximately 1 order of magnitude from the clean substrate. This increase includes the appearance of short line-like defects that were not observed on the original substrate. The origin of these defects is still being investigated.

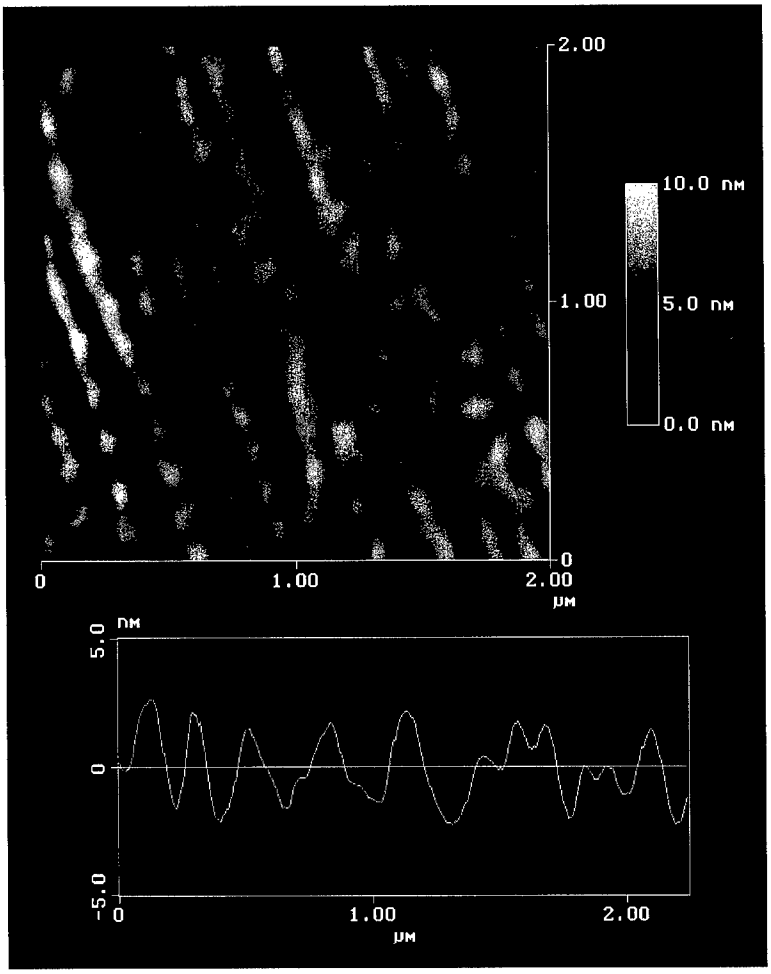


Fig. 2: An AFM image of a 0.7-μm-thick epitaxial AlN layer grown on the a-face of an AlN substrate.

We have also performed AFM characterization of the surface of a 1-μm-thick epitaxial film of $Al_{.5}Ga_{.5}N$. This film showed a much rougher surface morphology even though the epitaxial quality as determined by x-ray diffraction and ion channeling was very good as discussed below. The surface was found to have many mounds on the surface with approximately 30° facet angles.

Of course, it should also be noted that the growth process has not yet been optimized for growth of $Al_xGa_{1-x}N$ alloy layers.

Rutherford backscattering/ion channeling measurements were used to determine the crystal quality of the original substrate, the epitaxial AlN layer and the epitaxial $Al_{.5}Ga_{.5}N$ layer. The results from the later two layers are shown in Figs. 3 and 4. These measurements were performed at the SUNY-Albany Dynamatron accelerator with 2 MeV He^4 ions. The minimum yield was measured along the $[10\bar{1}0]$ axis, which is perpendicular to the $(11\bar{2}0)$ surface plane of this substrate. We obtained a channeling minimum yield χ_{min} of 1.5% for both the AlN substrate and for the AlN epitaxial layer. The χ_{min} is the ratio of the backscattering yield along the crystallographic axis compared to the scattering yield along a random direction and a value of 1.5% indicates excellent crystal quality (see, for example, ref. 4 where a χ_{min} of 2.1% was measured on a high quality, 3-μm-thick GaN layer grown under optimal conditions on sapphire). The χ_{min} measured for the 1-μm-thick $Al_{.5}Ga_{.5}N$ layer was 2.2%, which is still excellent even though the growth parameters were not optimized as pointed out above.

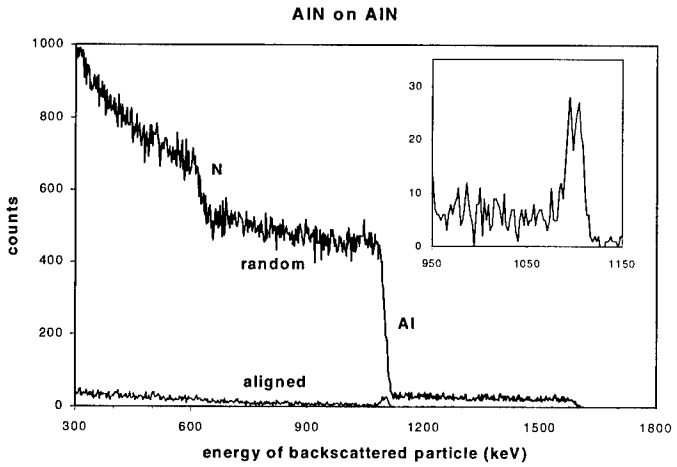


Fig. 3: RBS spectra measured for a random direction and along the $[10\bar{1}0]$ axis for a 0.7-μm-thick AlN layer grown on the a-face of an AlN substrate. The inset shows a blow-up of the Al surface peak.

Note also in Fig. 3 that some Ga contamination is seen in the epitaxial film. The Ga concentration is approximately 1% and helps to serve as a marker for the epitaxial AlN film. The ion channeling minimum yield on the AlN/sapphire layer grown under identical conditions was 40%.

The insets in Figs. 3 and 4 show the onset of the Al and the Ga peaks, respectively. In Fig. 3, the surface peak is due to the scattering of the He ions by Al ions on the surface prior to the He ions starting to channel in the crystal. In Fig. 4, it is interesting to note that the Ga surface peak is nearly missing in spite of the fact that the alloy was grown under constant TMA and TMG flux. This suggests that the surface layer is depleted of Ga and suggests that some surface reconstruction may have occurred which preferentially put Al on the surface. Another possibility is that the epitaxial layer preferentially lost Ga during the cool down phase after growth.

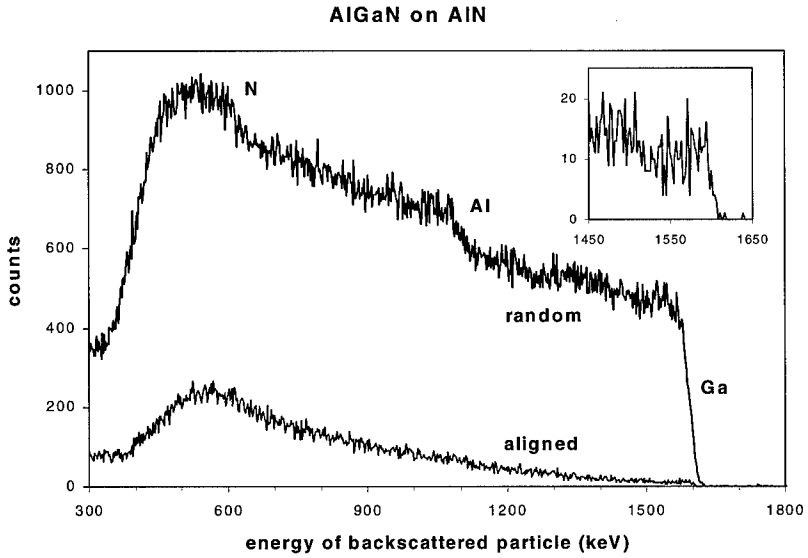


Fig. 4: RBS spectra measured for a random direction and along the $[10\bar{1}0]$ axis for a 1-μm-thick $Al_{.5}Ga_{.5}N$ layer grown on the a-face of an AlN substrate. The inset shows a blow-up of the nearly absent, Ga surface peak.

Double crystal, x-ray diffraction (Bede diffractometer, Cu K_α) radiation was also used to characterize the quality of the epitaxial layers. A GaSb (004) reflection was used to monochromatize the x-rays and the $(11\bar{2}0)$ reflection was scanned. The epitaxial AlN/AlN substrate was shown to consist of several crystal grains, with small angles (of the order of 50-100 arcsecs) between them. The relative peak amplitudes could be varied by moving the x-ray beam across the surface. This observation coincided with optical observations that indicated possible grain boundaries across the substrate surface. The largest grain was approximately 3mm × 5mm. A rocking curve, FWHM of the epitaxial AlN layer was approximately 250 arc sec. when all the crystal grains were considered simultaneously. However, the FWHM of individual grains appeared to be less than 100 arc sec.

The $Al_{.5}Ga_{.5}N$ alloy was doped with Si as described above using a silane/hydrogen flow rate of 3 sccm. The 1-μm-thick film exhibited a resistivity of approximately 20 Ω-cm. Hall measurements were made using In dots that allowed good Ohmic contacts to be made to the epitaxial layer. The concentration of carriers was approximately 10^{17} cm^{-3} with a mobility of ~10 cm^2/V-s. Generally groups have found that doping of $Al_xGa_{1-x}N$ alloys is difficult at high Al fraction [5,6] probably due to the inferior material quality. Our results here are in good agreement with Bemser et al. [7] for high concentration Al alloys grown on 6H-SiC(0001) substrates.

CONCLUSION

We have demonstrated that a-face AlN substrates can be prepared for excellent homoepitaxial growth of AlN. In addition, we have demonstrated high quality alloy growth of $Al_{.5}Ga_{.5}N$ on these substrates that showed excellent electrical conductivity even though the

growth conditions were not optimized. The AlN substrates offer an excellent opportunity to achieve high quality epitaxial growth of AlGaN alloys on a high thermal conductivity, electrically insulating substrate with minimal thermal expansion mismatch.

ACKNOWLEDGEMENTS

The contributions of Jonathan Ward in substrate preparation are hereby gratefully acknowledged. This work was partially supported by the Ballistic Missile Defense Organization (BMDO) and ONR. The support and advice of Dr. C.E.C. Wood at ONR was greatly appreciated. In addition, Crystal IS received support from BMDO and was managed by the Materials Directorate of the Air Force Research Laboratory, USAF, Wright-Patterson AFB.

REFERENCES

1. The growth procedure is described in: G.A. Slack and T. McNelly, J. Cryst. Growth 34, 263 (1976) and 42 560 (1977).
2. H. Lu and I. Bhat, Gallium Nitride and Related Materials, MRS Proc. Vol. 395, ed. F.A. Ponce, R. D. Dupuis, S. Nakamura, and J.A. Edmond (Pittsburgh, Mat. Res. Soc., 1996) p. 497.
3. H. Lu, I. Bhat, B.-C. Lee, G. Slack, and L. Schowalter, Nitride Semiconductors, MRS Proc. Vol. 482, ed. R.A. Ponce, S.P. DenBaars, B.K. Meyer, S. Nakamura, and S.Strite (Pittsburgh, Mat. Res. Soc., 1998) p. 277.
4. H. Kobayashi and W.M. Gibson, Appl. Phys. Lett. **73**, 1406 (1998).
5. X. Zhang, P. Kung, A. Saxler, D. Walker, T. C. Wang, and M. Razeghi, Appl. Phys. Lett. **67,** 1745 (1995).
6. J. M. Redwing, J. S. Flynn, M. A. Tischler, W. Mitchel, and A. Saxler, Gallium Nitride and Related Materials, MRS Proc. Vol. 395, ed. F.A. Ponce, R. D. Dupuis, S. Nakamura, and J.A. Edmond (Pittsburgh, Mat. Res. Soc., 1996) p. 201.
7. M.D. Bremser, W.G. Perry, O.H. Nam, D.P. Griffis, R. Losing, D.A. Ricks, and R.F. Davis, J. Electronic Materials, **27**, 229 (1998).

EFFECT OF BUFFER LAYER AND III/V RATIO ON THE SURFACE MORPHOLOGY OF GAN GROWN BY MBE

E. C. Piquette, P. M. Bridger, R. A. Beach, and T. C. McGill

Thomas J. Watson, Sr. Laboratory of Applied Physics
California Institute of Technology, Pasadena, CA 91125

Cite this article as: MRS Internet J. Nitride Semicond. Res. 4S1, G3.77(1999)

ABSTRACT

The surface morphology of GaN is observed by atomic force microscopy for growth on GaN and AlN buffer layers and as a function of III/V flux ratio. Films are grown on sapphire substrates by molecular beam epitaxy using a radio frequency nitrogen plasma source. Growth using GaN buffer layers leads to N-polar films, with surfaces strongly dependent on the flux conditions used. Flat surfaces can be obtained by growing as Ga-rich as possible, although Ga droplets tend to form. Ga-polar films can be grown on AlN buffer layers, with the surface morphology determined by the conditions of buffer layer deposition as well as the III/V ratio for growth of the GaN layer. Near-stoichiometric buffer layer growth conditions appear to support the flattest surfaces in this case. Three defect types are typically observed in GaN films on AlN buffers, including large and small pits and "loop" defects. It is possible to produce surfaces free from large pit defects by growing thicker films under more Ga-rich conditions. In such cases the surface roughness can be reduced to less than 1 nm RMS.

INTRODUCTION

In recent years the group III-nitride materials system has shown promise and suitability for a wide variety of device applications. Large efforts and advances have been made in the growth of device quality films by the techniques of MOCVD and HVPE, particularly for optoelectronics and HFET applications, while the growth of GaN by molecular beam epitaxy (MBE) has received relatively less attention. However, because of the ability to produce quality films of both crystal polarities (Ga-polar and N-polar) [1] MBE has gained renewed interest for fabrication of polarity dependent devices, such as piezo-electronics. For these, and the majority of device applications, it is desirable to prepare films with flat surfaces. An example is the GaN/AlGaN HEMT structure, where the mobility and density of the 2-D electron gas improves as the interface becomes flatter [1]. In this work, we present an atomic force microscopy (AFM) study of GaN surfaces prepared under a variety of conditions by MBE, and describe the growth parameters employed to produce both rough and relatively flat surfaces of both wurtzite crystal polarities.

EXPERIMENT

Gallium nitride layers were grown on c-plane sapphire substrates using a radio frequency plasma source for active nitrogen. The source gas was high purity N_2, regulated and filtered, and introduced into the plasma source via a precision leak valve. The typical system pressure during

Mat. Res. Soc. Symp. Proc. Vol. 537 © 1999 Materials Research Society

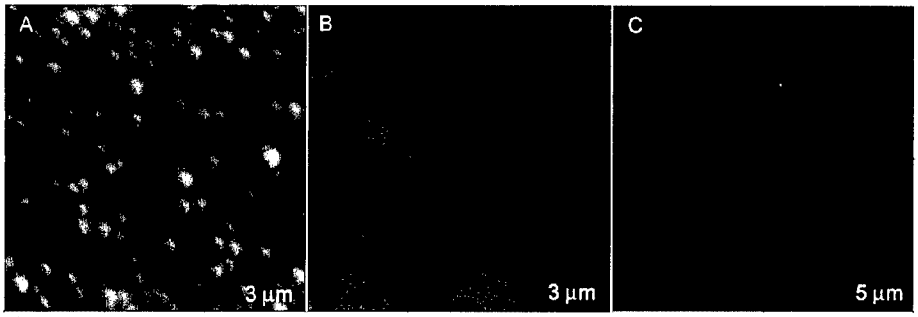


Figure 1: AFM micrographs of GaN grown on sapphire using GaN buffer layers. For nitrogen rich growth of the main layer (A) a rough surface and fine-grained microstructure results, while growth under slightly (B) and more heavily Ga-rich (C) conditions leads to larger grain size and flatter surfaces. The surface pictured in (C) is quite flat, with pit defects lying at the coalesced island boundaries. The vertical scale is 100 nm in these images.

growth was 8×10^{-5} torr. Effusion cells were used as sources of Ga, Al, and Si. The substrates were backside coated with Ti to assist in radiative heating, and were loaded into the vacuum system without chemical treatment.

For each growth, the substrate was first heated to 800 °C and exposed to the nitrogen beam for 30 minutes at 450W RF power and at reduced nitrogen flow. Reflection high-energy electron diffraction (RHEED) patterns were bright streaks after the nitridation stage, indicating the formation of an AlN layer at the surface. A thin GaN or AlN buffer layer was then deposited at a nominal growth rate of 0.15 microns per hour at a plasma source power of 350W. For growth of GaN buffer layers, the III/V ratio was set close to unity, while for growth of AlN buffer layers the Al cell temperature was variably set to 1100 °C, 1120 °C, or 1130 °C representing N-rich, near stoichiometric, and Al-rich growth conditions, respectively. The growth time for the buffer layers was 2-3 minutes. After buffer layer deposition, the samples were soaked under the nitrogen beam for 8 minutes. The main GaN layer was then deposited at a rate of approximately 0.4 microns per hour.

A series of samples was grown utilizing GaN buffer layers, wherein subsequent growth of the main layer was carried out under N-rich, slightly Ga-rich, or heavily Ga-rich conditions. For GaN layers grown on AlN buffer layers, flux conditions were slightly Ga-rich and constant. The total thickness of these layers was about 1 micron. Additionally, one sample was grown to a thickness of 2 microns using an AlN buffer layer. All films were doped with Si to approximately 10^{17} cm^{-3}. The surface morphology of these layers was studied by atomic force microscopy in Tapping Mode using a Bioscope AFM with a Digital Instruments Nanoscope IIIa controller.

RESULTS

GaN buffer layers

The surface morphology of GaN films is seen to depend strongly on the III/V ratio employed during RF plasma MBE growth. As has been previously observed [2-4], the RHEED image abruptly changes from spotty to streaky as flux conditions move from nitrogen-rich to gallium-rich. The surface morphology of films grown on GaN buffer layers and under various

flux conditions is shown in Figure 1. For growth under N-rich conditions (Fig. 1A) the RHEED image is spotty and the surface is rough. This is presumably because the suface mobility of atoms is low on the nitrogen terminated GaN surface, so step-flow growth is hindered and statistical roughening proceeds. For growth under slightly Ga-rich conditions (Fig. 1B), the grain size is improved and the surface is dominated by flat topped regions separated by shallow canyons. The surface roughness is approximately 10 nm RMS in this case. Shown in Fig. 1C is a sample grown under more highly Ga-rich conditions. These conditions are within the Ga condensation range, as evidenced by the formation of droplets that sparsely covered the surface of this sample. However, the film surface between droplets is seen to be very flat, with RMS roughness of 2-3 nm. Pits are observed at the grain boundaries.

AlN buffer layers

Samples grown using GaN buffer layers on sapphire were found to be N-polar [1] based on etch tests using molten KOH [5, 6], while films grown using AlN buffer layers were Ga-polar. We observe that both polarities seem to behave similarly in the effects of III/V ratio on surface morphology and growth mode [7,8]. Additionally, for films grown on AlN buffers, the exact conditions of buffer layer deposition are seen to be highly important. Shown in Figure 2 are AFM scans of GaN films grown under identical conditions except for the Al/N flux ratio during growth of the buffer layer. If the AlN buffer is deposited under Al-rich conditions (Fig. 2A), the RHEED pattern dims and ultimately disappears as aluminum builds up on the surface. The fine-grained microstructure observed is likely formed by nitridation of condensed Al during and after buffer deposition. Figure 2B shows the GaN film surface using an AlN buffer layer grown near effective 1-to-1 flux stoichiometry. In this case, the buffer layer RHEED pattern remained very streaky and displayed a faint 2-fold reconstruction upon nitrogen soak. The surface appears quite flat but with V-shaped hexagonal pits approximately 200 nm in size. For the case of nitrogen-rich AlN buffer layer deposition, the resulting GaN film surface is shown in Figure 2C. Flat regions exist, yet the surface remains rough on the 500 nm lateral scale. Although streaky RHEED patterns were observed during GaN growth for all these samples, only

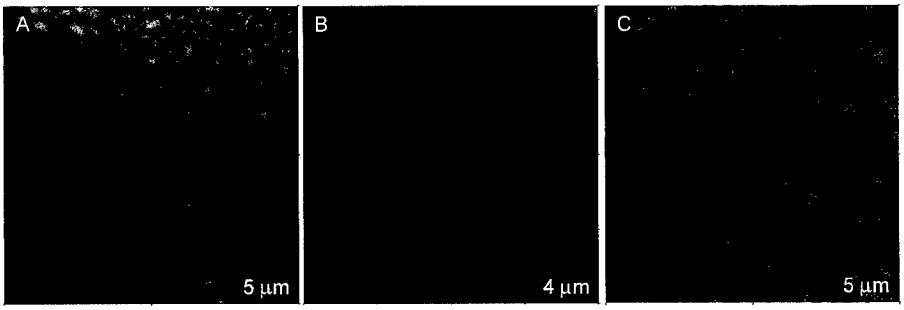


Figure 2: AFM micrographs of GaN grown on sapphire using an AlN buffer layer. The aluminum cell temperature was set to (A) 1130 °C, (B) 1120 °C, and (C) 1100 °C during growth of the buffer layers, corresponding to Al-rich, near-stoichiometric, and N-rich conditions, respectively. The GaN layer was grown under the same slightly Ga-rich conditions in all cases. The vertical scale is 100 nm.

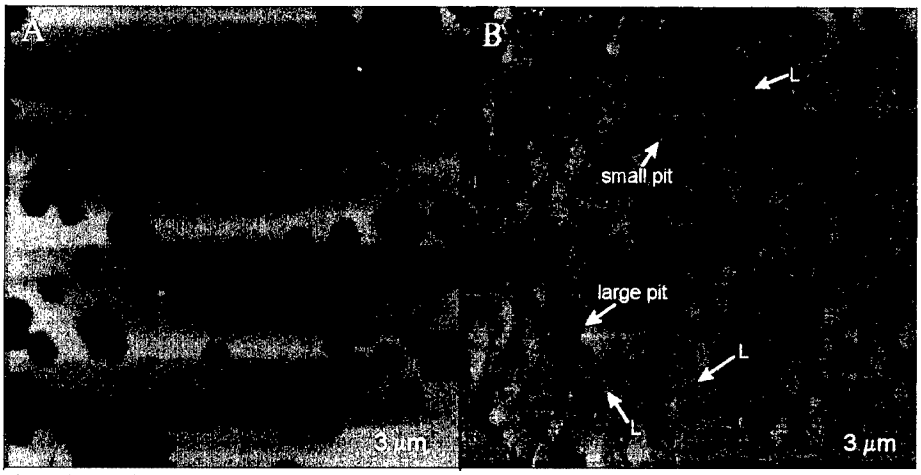


Figure 3: Tapping Mode AFM height (A) and phase (B) data taken from the center region of the 2 micron thick GaN sample. Three categories of defects are observed: large hexagonal pits, small pits, and "loop-like" defects (L). The height scale is 100 nm and 25 degrees in A and B respectively.

the AlN buffer layers grown under stoichiometric flux conditions showed a streaky RHEED image. We believe that the film-buffer interface is smoothest in this case, and that this is the most relevant condition for the subsequent growth of flat GaN surfaces.

AFM images of a 2 micron thick GaN layer grown on a "stoichiometric" AlN buffer layer are shown in Figures 3 and 4. We see in Figure 3 the same general morphology as in Figure 2B. In the AFM Tapping Mode phase image (Fig. 3B), three types of structures are present on these surfaces which we refer to as large pits, small pits, and "loop" defects. While a detailed study of these defects has not yet been done, we may tentatively associate the small pit defects to the intersection of threading dislocations with the surface [9], while the larger hexagonal pits may be remnants of island coalescence. The nature of the "loop" structures is at this point uncertain. As is shown in Figure 4, the large pit defects are not present near the edge of the wafer for this sample. This is due to a degree of temperature nonuniformity across the 2 inch substrate. The substrate temperature is slightly lower toward the edge of the wafer, where the Ga re-evaporation rate is correspondingly reduced. Often, for Ga-rich growth conditions, we have observed the formation of droplets near the substrate perimeter but see none near the center of the wafer. AFM scans near the edges of samples also tend to display flatter morphology. This morphological nonuniformity is believed to result from the coupled effects of relatively higher substrate temperature and lower effective III/V ratio near the center of the substrate as compared to the edge. The surfaces away from the wafer center, shown in Figure 4, are very flat, with RMS roughness less than 1 nm. It is in these flat regions near the substrate edge that the best HEMT performance has been observed by other groups [1, 10].

CONSLUSION

The surface morphology of GaN was studied by AFM for a variety of growth conditions. For growth on GaN buffer layers, the films were observed to be N-polar and strongly dependent

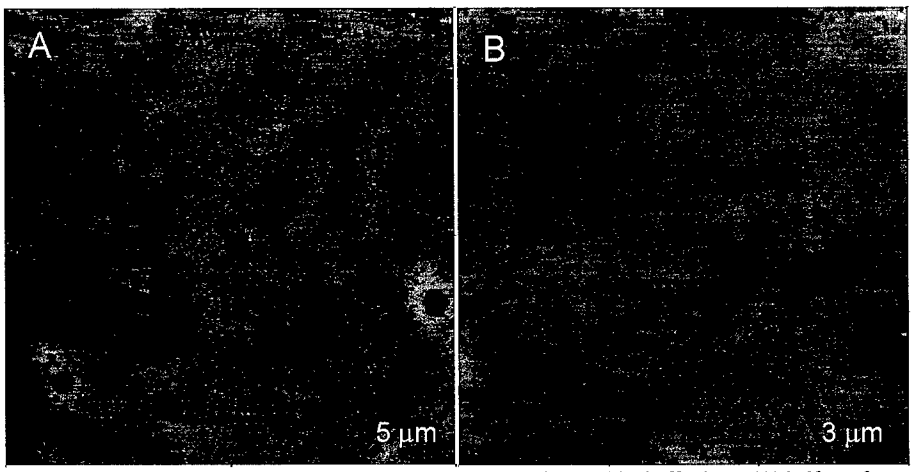


Figure 4: AFM scans of two micron thick GaN layer grown using an AlN buffer layer (A) halfway from center to edge, and (B) near the edge of the 2 in. sapphire wafer. The more Ga-rich conditions toward the edge of the substrate serve to reduce (A) and ultimately eliminate (B) the large pit defects, but the small pits and "loop" defects remain. The height scale is 30 nm.

on III/V flux ratio. The flattest surfaces were obtained by growing as Ga-rich as possible, although Ga droplets tend to form if the III/V ratio is too high. Films grown on AlN buffer layers were observed to be Ga-polar, with the surface morphology strongly dependent on the conditions of buffer layer deposition. Near-stoichiometric buffer growth conditions appear to support the flattest surfaces in this case, likely because these conditions result in the smoothest buffer layer interfaces. Three defect types are typically observed in GaN films on AlN buffers, including large and small pits and "loop" defects. It is possible to produce surfaces free from large pit defects by growing thicker films under more Ga-rich conditions. In such cases the surface roughness can be reduced to less than 1 nm.

ACKNOWLEDGEMENTS

This work was supported by the Defense Advanced Research Projects Agency and the Electric Power Research Institute under contract number MDA972-98-1-0005.

REFERENCES

[1] M. J. Murphy, T. J. Eustis, H. Wu, W. Yeo, W. J. Schaff, O. Ambacher, J. Smart, J. R. Shealy, and L. F. Eastman, presented at the 17th North American MBE Conference, Penn State, **G.5** (1998).

[2] S. L. Buczkowski, Z. Yu, M. Richards-Babb, N. C. Giles, L. T. Romano, and T. H. Myers, Mater. Res. Soc. Symp. Proc. **449**, 197 (1997).

[3] T. D. Moustakas, T. Lei, and R. J. Molnar, Pysica B **185**, 36 (1993).

[4] H. Riechert, R. Averbeck, A. Graber, M. Schienle, U. Strauss, and H. Tews, Mater. Res. Soc. Symp. Proc. **449**, 149 (1997).

[5] M. Seelmann-Eggebert, J. L. Weyher, H. Obloh, H. Zimmermann, A. Rar, and S. Porowski, Appl. Phys. Lett. **71**, 2635 (1997).

[6] J. M. Van Hove, M. F. Rosamond, R. Hickman II, J. J. Klaassen, C. Polley, A. Wowchak, and P. P. Chow, presented at the 17th North American MBE Conference, Penn State, **G.3** (1998).

[7] L. T. Romano and T. H. Myers, Appl. Phys. Lett **71**, 3486 (1997).

[8] E. J. Tarsa, B. Heying, X. H. Wu, P. Fini, S. P. DenBaars, and J. S. Speck, J. Appl. Phys. **82**, 5472 (1997).

[9] P. M. Bridger, Z. Z. Bandic, E. C. Piquette, and T. C. McGill, Appl. Phys. Lett **73**(23) in press (1998).

[10] M. J. Murphy, private communication.

RELAXATION PHENOMENA IN GaN/ AlN/ 6H-SiC HETEROSTRUCTURES

N.V. Edwards,*¤ A.D. Batchelor,† I.A. Buyanova,* L.D. Madsen,* M.D. Bremser,‡# R.F. Davis,‡
D.E. Aspnes,‡ and B. Monemar*

*Linköping universitet, Materiefysik, Linköping, Sverige, S-58183
¤ginger@ifm.liu.se
†Analytical Instrumentation Facility, Box 7531, N.C. State University, Raleigh, NC, USA 27695
†North Carolina State University, Raleigh, NC, USA 27695
#Now at Aixtron Inc., 1569 Barclay Blvd., Buffalo Grove, IL, USA 60089

Cite this article as: MRS Internet J. Nitride Semicond. Res. 4S1, G3.78 (1999)

ABSTRACT

We have developed a method to modulate the strain state (normally > 4 kbar, tensile) of moderately thick (~2 μm) GaN based structures grown on 6H-SiC to a range 0 to -2 kbar of compressive stresses by introducing a strain-mediating layer (SML) above the standard high-temperature AlN buffer layer. The strain characteristics of subsequently deposited nitride layers can be modulated by changing the growth parameters of the SML layer. This is achieved by *in-situ* techiniques during crystal growth without degrading the optical and structural properties of the deposited layers.

INTRODUCTION

By conventional wisdom, simple structures grown on Al_2O_3 are in compression,[1-4] while those grown on 6H-SiC are in tension.[1,5,6,7] It is usually assumed for growth on 6H-SiC that compressive lattice-mismatch stresses[3,4] are relieved after a few nanometers of growth[8] and tensile thermal mismatch stresses[3,4] persist thereafter. Optical data in the literature also give the impression that compressive stress is the inevitable result of growth on Al_2O_3 substrates,[9,10] while the relative scarcity of data for GaN on 6H-SiC has reinforced the impression that only tensile material can be grown on this substrate.[5,11,12]

However, for GaN film/ AlN buffer/ 6H-SiC substrate heterostructures, we have observed a greater versatility in achievable residual stresses than predicted by conventional wisdom or observed thus far for films on Al_2O_3 substrates.[13] Here GaN films are mostly compressive for films less than about 0.7μm thick, are tensile up to about 2μm, then abruptly become less tensile with stress values near 1 kbar thereafter. Despite this increased flexibility, the thickness dependence means that a given combination of growth and material parameters nonetheless dictates a unique value of stress in the overlying film. However, the inclusion of a negligibly thin (~375-750Å) strain mediating layer (SML) of GaN or AlGaN between the AlN buffer layer and overlying GaN film can potentially circumvent these trends for moderately thick (~2μm) GaN layers (normally >4kbar, tensile), yielding a range of stresses between 0 and -2kbar, compressive. Thus the SML, when used in conjunction with current buffer layer technology, provides even greater flexibility than the AlN/ SiC combination alone. In fact, it enables otherwise unachievable combinations of growth temperatures, film thicknesses and residual stresses.

Such capability is potentially of interest for nitride valence band engineering and device processing applications. But these applications require that residual stress be controlled in device active regions without sacrificing material quality or violating device design parameters. To demonstrate the suitability of the SML approach for potential device applications, we report the interfacial properties, surface morphology, crystalline quality, and optical properties of GaN films grown with SMLs relative to those grown without them. We find that the SML has the capacity to alter the growth rate and stress state of the GaN film but does not appreciably degrade its optical, structural or surface properties.

Mat. Res. Soc. Symp. Proc. Vol. 537 © 1999 Materials Research Society

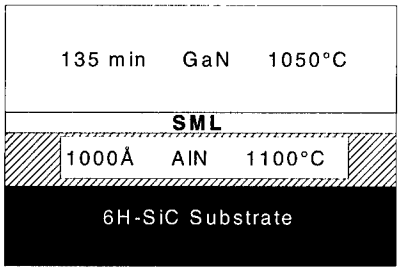


Fig. 1. Structure, compositions, layer thicknesses, and growth parameters common to all SML samples.

EXPERIMENTAL DETAILS

In-plane residual stresses (σ_{xx}) were determined from the energies E_A, E_B, and E_C of the A, B, and C excitons observed in optical data obtained with a single-beam low-temperature reflectometer as described previously.[12] The samples were imaged in cross-section with a JEOL 6400FE field emission scanning electron microscope (SEM). Photoluminescence (PL) was excited by the UV line (334.5 nm) of an Ar^+ ion laser and dispersed using a 0.5 m Jobin-Yvon monochromator with a GaAs photomultiplier tube. Sample surfaces were characterized by a Digital Instruments (DI) Dimension 3000 Scanned Probe Microscope (SPM) operated in tapping mode®. X-ray diffraction (XRD) was carried out with a Philips MRD system using the high resolution optics (triple axis mode).

Four SML samples were examined in the context of twenty-five other GaN films[13] grown by metal organic chemical vapor deposition (MOCVD)[14] with the same V-III ratio and no doping. The structures were all grown on 6H-SiC substrates. All included a 1000 Å AlN buffer layer grown at 1100°C and were subjected to the same rate of post-growth cooling. The structure of the four SML-containing samples is shown in Fig. 1; SML growth parameters are given in Table I. Except for the presence of the SML these samples are nominally identical to Sample 5, which does not have a SML.

RESULTS & CONCLUSIONS

The effect of the SML is apparent in Fig. 2. Here film thickness vs. E_A and σ_{xx} is plotted for samples with and without SMLs, represented by the numbered X's and filled circles, respectively. General stress trends for simple GaN/ AlN/ 6H-SiC heterostructures, as described previously,[13] are apparent in the main sequence of filled circles.

Table I. Properties of SMLs and associated GaN films. Note that the SML *d* is projected from known growth rates* while the GaN film *d* was measured by cross-section SEM.

	SML Properties				Properties of Associated GaN Film			
	Material	time at T(°C)	~*d* (Å)	*d* (μm)	σ_{xx} (kbar)	PL Linewidth (meV)	XRD FWHM (arcsec)	AFM Rms Roughness (Å)
1	GaN	2 min 1000	375	0.9	0.26	3.56	53	3.95
2	GaN	6 min 1120	450	2.1	-1.02	3.27	56	4.49
3	GaN	4 min 1000	750	2.2	-0.44	4.26	59	6.85
4	$Al_{0.13}Ga_{0.87}N$	2 min 1000	375	1.2	-1.98	4.35	59	2.72
5	------	------	---	1.9	4.63	8.13	52	2.61

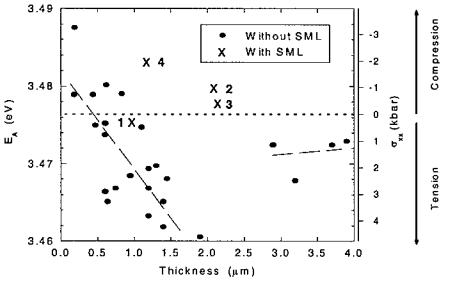
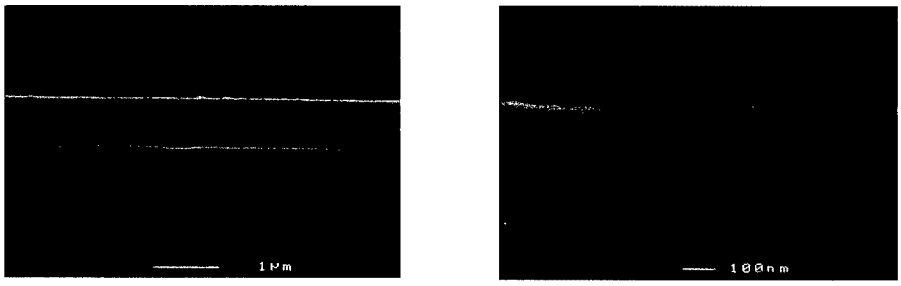


Fig. 2. E_A and σ_{XX} vs. thickness d for GaN films on 6H-SiC. Points [•] represent samples without strain mediating layers (SML); X's represent samples with SMLs.

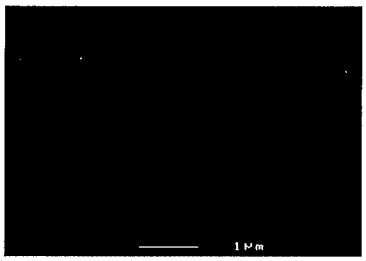
Sample 1 has a GaN SML that was grown for 2 minutes at 1000°C, corresponding to a projected layer thickness of ~375Å.[14] The SML/ film interface was not resolvable with the SEM (Figs. 3a and b). But instead we found a heavily striated region above the 1000Å AlN buffer layer—suggesting the possibility of strain anisotropy in the (0001) direction—that is divided by a crack extending fully across the sample. Not surprisingly, this sample is nearly relaxed.[15] Here σ_{xx} = 0.26 kbar instead of the 4.63 kbar tensile observed for Sample 5. A cracked sample is not ostensibly useful for device purposes, but it is reported because of relevance for the recognized device processing problem of lifting nitride epilayers from their substrates.

Similar layered regions of differing contrast are observed in Sample 2 for a GaN SML ~450Å thick, grown for 6 minutes at 1120°C. These regions are seen in low and high magnification in Figs. 4a and b, respectively. However, instead of cracking, the film has a division into two light and dark bands on the low magnification scale, in addition to the striations seen at high magnification. This film is slightly compressive, with σ_{xx} = -1.02 kbar. Surprisingly, SML parameters like these may prove to be useful if they can indeed create strain anisotropies in the (0001) direction without cracking the overlying GaN film. The introduction of strain anisotropies perpendicular to the direction of growth is currently thought to be the best option for optimizing nitride valence band configurations for minimal laser threshold currents.[16]

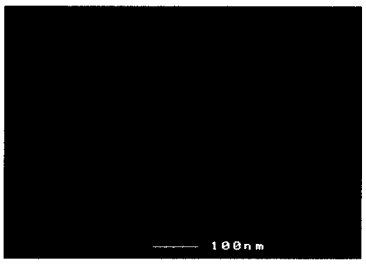
A simple change in SML growth parameters eliminates this c-plane anisotropy. If the SML of Sample 1 is grown for 4 min at 1000°C instead of 2 min, the resulting film (Sample 3; Fig. 4c) is without resolvable cracks or c-plane anisotropy at either high or low magnification and becomes slightly compressive. If the SML growth parameters of Sample 1 are reproduced with $Al_{0.13}Ga_{0.87}N$ instead of GaN, the resulting film (Sample 4; Fig. 4d) is also free from cracks and c-plane anisotropy. But the σ_{xx}=-1.98 kbar achieved here is comparable to compressive stresses obtained on Al_2O_3 substrates.[15] These can be contrasted to the interfacial properties of Sample 5, shown in Fig. 4e. Without the SML to "getter" the residual stress, the film is not only the most tensile in the set, but it also suffers from cracks distributed throughout the film, which precludes any useful removal of the epilayer from the substrate.



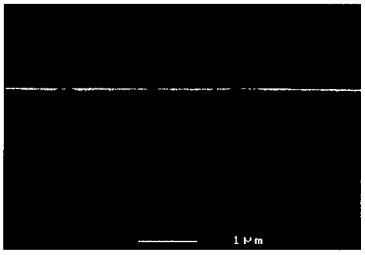
Figs. 3a and b. Lower magnification SEM micrograph of Sample 1, left. Right shows high magnification view of the buffer layer/ SML/ overlying GaN film interfaces for the same sample.



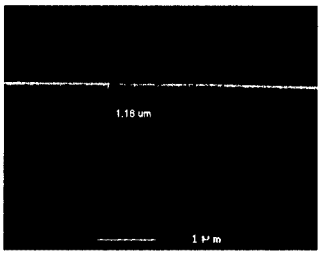
a)



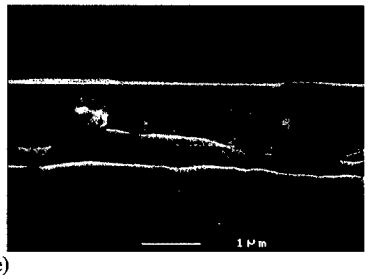
b)



c)



d)



e)

Fig. 4. **(a)** Low magnification view of Sample 2 (with SML); **(b)** Buffer layer/ film interface at high magnification of the Sample 2; **(c)** Low magnification view of Sample 3 (with SML); **(d)** Low magnification view of Sample 4 (with SML); **(e)** Low magnification view of Sample 5 (without SML).

We also find that growth of the overlying GaN film for 135 minutes at 1050°C does not always result in the expected[14] 2µm thickness for this layer if an SML is used. Sample 1 has a total thickness of only 0.97µm, while Sample 4 is only 1.2µm thick. Both samples have SMLs with projected thicknesses <400Å. Samples 2 and 3 are by contrast the expected thickness, and their SMLs are >400Å. To explain this behavior we must consider the anticipated morphology of the SML. Initial investigations of GaN growth on the high-temperature AlN buffer layer determined that growth was layer-by-layer only after an initial coalescence of two-dimensional, flat-topped islands that occurs *after ~400Å of growth.*[14] It is plausible that the samples with reduced growth rates had SMLs that were not fully planarized and that growth was in fact occurring on non-(0001) planes. Growth on such planes occurs at significantly reduced rates, due in theory to reduced Ga incorporation relative to that for the (0001) direction.[17] The degree of reduction of growth rate would then depend on the degree of coalescence of the thin SML.

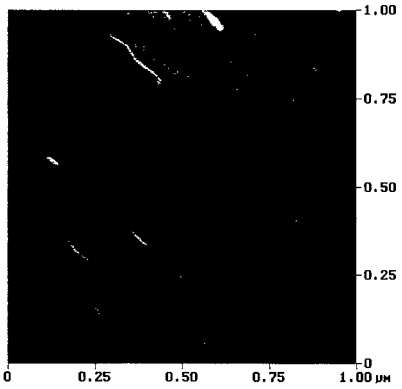


Fig. 5. SPM micrograph of the surface of Sample 4 (with SML). Image rms roughness was 2.7Å; rms roughness in boxed region is 0.15Å.

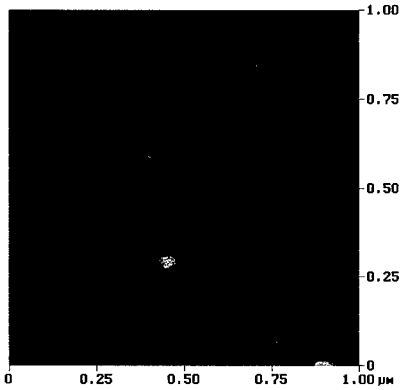


Fig. 6. SPM micrograph of the surface of Sample 5 (without SML). Image rms roughness was 2.61Å; rms roughness in boxed region is 1.48Å.

By contrast how the SML modifies the sample stress is not straightforward since the relaxation phenomena in GaN/ AlN/ 6H-SiC heterostructures are not well-understood.[13] Neglecting microstructural explanations, the "stress-trend" behavior of Fig. 2 for samples without SMLs is consistent with a gradual relaxation of pseudomorphic growth and predominance of tensile stresses upon cooling with increasing film thickness described in Ref. 13. We have hypothesized that the specific thicknesses at which these processes occur vary with substrate orientation and growth temperature, but it remains unclear whether the SML merely modifies the thickness at which these relaxation processes occur or circumvents them altogether. Nonetheless—and despite such marked differences in the interfacial character of the films—our film characterizations indicate that there is very little variation in the optical quality, surface morphology and structure of GaN films grown on SMLs. SPM measurements yielded root mean square (rms) roughnesses on the order of 3 to 7 Å, comparable to any of the smoothest films in Fig. 2.[18] Fig. 5 shows the morphology of a representative SML-containing sample (Sample 4), and it is remarkably similar to the morphology of Sample 5, shown in Fig. 6. Representative broadband PL spectrum of typical

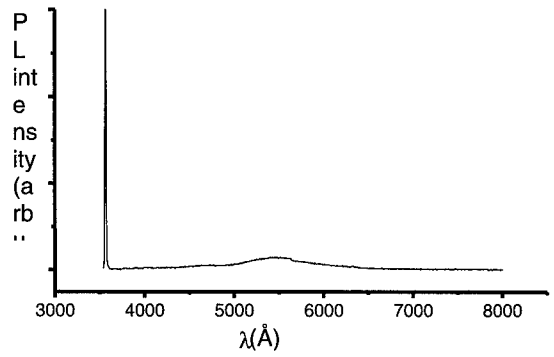


Fig. 7. Representative broadband PL spectrum of SML containing samples. (Sample 4)

quality is shown in Fig. 7; we see that the spectra are dominated by (predominantly bound) excitonic emission with relatively weak yellow-band emission, typical of good-quality, strained MOCVD-grown films. The linewidth of the excitonic emission ranged from 3 to 5 meV, also indicative of good material quality. Linewidth variations occurred as expected with residual stress. XRD θ-2θ full width at half-maximum (FWHM) intensity values were in the 53-59 arcsec range, and, like the PL linewidths, are not significantly different from the FWHM obtained for Sample 5 (accounting for variations in residual stress). Thus the SML has the capacity to alter the growth rate and stress state of a GaN film, but *does not appreciably degrade its optical, structural or surface properties.*

ACKNOWLEGEMENTS

It is a pleasure to acknowledge the financial support of the Office of Naval Research (ONR) under contract number N-00014-93-1-0255.

REFERENCES

[1]H. Amano, K. Hiramatsu, and I. Akasaki, Jpn. J. Appl. Phys. **27**, Part1 L1384 (1988).
[2]T. Detchprohm, K. Hiramatsu, K. Itoh, and I. Akasaki, Jpn. J. Appl. Phys. **31**, Part 10B L1454 (1992).
[3]Landolt-Börnstein, Vol. 17, edited by O. Madelung (Springer, New York, 1982).
[4]*Properties of Group III Nitrides*, edited by J.H. Edgar (INSPEC, IEEE, London, 1994).
[5]I.A. Buyanova, J.P. Bergman, B. Monemar, H. Amano, I. Akasaki, Appl. Phys. Lett. **68**, 1255 (1996).
[6]W. Shan, R.J. Hauenstein, A.J. Fischer, J.J. Song, W.G. Perry, M.D. Bremser, R.F. Davis and B. Goldenberg, Phys. Rev. B **54**, 13 460 (1996).
[7]D. Volm, K. Oettinger, T. Streibl, D. Kovalev, M. Benchorin, J. Diener, B.K. Meyer, J. Majewski, L. Eckey, A. Hoffman, H. Amano, I. Akasaki, K. Hiramatsu, and T. Detchprohm, Phys. Rev. B **53**, 16 543 (1996).
[8]K. Hiramatsu, T. Detchprohm, and I. Akasaki, Jpn. J. Appl. Phys. **32**, 1528 (1993).
[9]R. Dingle, D.D. Sell, S.E. Stokowski, and M. Ilegems, Phys. Rev. B **4**, 1211 (1971).
[10]W. Shan, T.J. Schmidt, X.H. Yang, S.J. Hwang, J.J. Song, and B. Goldenberg, Appl. Phys. Lett. **66**, 985 (1995).
[11]B.J. Skromme, H. Zhao, B. Goldenberg, H.S. Kong, M.T. Leonard, G.E. Bulman, C.R. Abernathy, S.J. Pearton, Proc. Mat. Res. Soc. **449**, Boston, Ma., 1996.
[12]N.V. Edwards, S.D. Yoo, M.D. Bremser, T.W. Weeks, Jr., O.H. Nam, H. Liu, R.A. Stall, M.N. Horton, N.R. Perkins, T.F. Kuech, R.F. Davis, and D.E. Aspnes, Appl. Phys. Lett. **70**, 2001 (1996).
[13]N.V. Edwards, M.D. Bremser, R.F. Davis, S.D. Yoo, C. Karan, and D.E. Aspnes, Appl. Phys. Lett., accepted for publication September 14, 1998.
[14]T.W. Weeks, Jr., M.D. Bremser, K.S. Ailey, E. Carlson, W.G. Perry, and R.F. Davis, Appl. Phys. Lett. **67**, 401 (1995).
[15]N.V. Edwards, S.D. Yoo, M.D. Bremser, Ts. Zheleva, M.N. Horton, N.R. Perkins, T.W. Weeks, Jr., H. Liu, R.A. Stall, N.R. Perkins, T.F. Kuech, and D.E. Aspnes, Mat. Sci. And Eng. B **50**, 134 (1997).
[16]K. Domen, K. Horino, A. Kuramata, and T. Tanahasi, Appl. Phys. Lett. **70**, 987 (1997).
[17]X.H. Wu, C.R. Elsass, A. Abare, M. Mack, S. Keller, P.M. Petroff, S.P. DenBaars, and J.S. Speck, Appl. Phys. Lett. **72**, 692 (1998).
[18]NV. Edwards, M.D. Bremser, R.F. Davis, A.D. Batchelor, and D.E. Aspnes, unpublished.

GROWTH AND CHARACTERIZATION OF $B_xGa_{1-x}N$ ON 6H-SiC (0001) BY MOVPE

C. H. Wei*, Z. Y. Xie*, J. H. Edgar*, K. C. Zeng**, J. Y. Lin**, H. X. Jiang**, C. Ignatiev***, J. Chaudhuri*** and D. N. Braski****

*Department of Chemical Engineering, Kansas State University, Manhattan, KS 66506
**Department of Physics, Kansas State University, Manhattan, KS 66506
***Department of Mechanical Engineering, Wichita State University, Wichita, KS 67260
****High Temperature Material Laboratory, Oak Ridge National Laboratory, Oak Ridge, TN 37831

Cite this article as: MRS Internet J. Nitride Semicond. Res. 4S1, G3.79(1999)

ABSTRACT

Boron was incorporated into GaN in order to determine its limits of solubility, its ability of reducing the lattice constant mismatch with 6H-SiC, as well as its effects on the structural and optical properties of GaN epilayers. $B_xGa_{1-x}N$ films were deposited on 6H-SiC (0001) substrates at 950 °C by low pressure MOVPE using diborane, trimethylgallium, and ammonia as precursors. A single phase alloy with x=0.015 was successfully produced at a gas reactant B/Ga ratio of 0.005. Phase separation into pure GaN and $B_xGa_{1-x}N$ alloy with x=0.30 was deposited for a B/Ga reactant ratio of 0.01. This is the highest B fraction of the wurtzite structure alloy ever reported. For B/Ga ratio $\geq$ 0.02, no $B_xGa_{1-x}N$ was formed, and the solid solution contained two phases: wurtzite GaN and BN based on the results of Auger and x-ray diffraction. The band edge emission of $B_xGa_{1-x}N$ varied from 3.451 eV for x=0 with FWHM of 39.2 meV to 3.465 eV for x=0.015 with FWHM of 35.1 meV. The narrower FWHM indicated that the quality of GaN epilayer was improved with small amount of boron incorporation.

INTRODUCTION

One of the most limiting aspects of GaN is its relatively poor crystal quality, due to the necessity of heteroepitaxy. Sapphire (0001) and 6H-SiC (0001) are the most common substrates for GaN epitaxy, but both suffer from large lattice constant mismatches, 16% and 3.5% respectively. It may be possible to reduce or eliminate the lattice constant mismatch by adding boron to GaN, thereby forming a $B_xGa_{1-x}N$ alloy. However, the solubility of boron in GaN under typical growth conditions (by either MOVPE or MBE) may be limited, since hexagonal BN (similar in structure to graphite) is the stable structure at low pressure. The wurtzite structure, the most stable structure for GaN, is only a metastable structure for BN; it is normally produced by shock-compression. This disparity of crystal structures between GaN and BN probably results in a very low mutual solubility.

Several groups attempted to form epitaxial $B_xGa_{1-x}N$ alloys using sapphire as the substrate. A.Y. Polyakov *et al* reported that the highest solubility of boron in GaN was 1% at 1000 °C by MOVPE [1]. Vezin *et al* produced a single phase of $B_xGa_{1-x}N$ with x up to 4.56% by MBE [2]. In the present work, 6H-SiC (0001) was used as a substrate, since less boron incorporation (x=0.17) would be necessary to eliminate the lattice constant mismatch. The smaller lattice constant mismatch may be important in enhancing the boron solubility via epitaxial stabilization;

Mat. Res. Soc. Symp. Proc. Vol. 537 © 1999 Materials Research Society

the minimization of the overall free energy by maintaining an epitaxial structure by incorporating an element (boron in this case) at a concentration which exceeds the solubility limit [3].

Another motivation for developing $B_xGa_{1-x}N$ alloys is the possibility of fabricating BGaN-based semiconductor devices operating in the UV region. For this application, it is important to know how the energy band gap of $B_xGa_{1-x}N$ changes with B content. Honda *et al* predicted the bandgap energy of $B_xGa_{1-x}N$ increased with boron composition based on Harrison's theory assuming wurtzite BN in GaN [4].

In this paper, $B_xGa_{1-x}N$ films were successfully grown on 6H-SiC substrates by MOVPE. The effects of the gas phase B/Ga ratio on the solid film's growth rate, surface morphology, and structural were studied. Also, the bandgap energy of $B_xGa_{1-x}N$ was determined from photoluminescence measurements.

EXPERIMENT

$B_xGa_{1-x}N$ films were deposited on the Si face of on-axis 6H-SiC (0001) substrates in a vertical reactor by MOVPE at 76 Torr. The 6H-SiC substrates were ultrasonically degreased in sequential baths of trichloroethylene, acetone and methanol, rinsed in deionized water, then dipped into a 10 % HF solution to remove the native oxide layer. Prior to growth, the 6H-SiC substrates were annealed in hydrogen at 1000 °C for 10 minutes. Trimethylgallium (TMG) and ammonia (NH_3) were Ga and N source gases, and hydrogen was the carrier gas. The boron precursor was 0.01% diborane (B_2H_6) diluted in H_2. Diborane and ammonia have been commonly used to produce BN [5]. The B_2H_6 and NH_3 were separately introduced into the reactor and mixed just above the susceptor to avoid their parasitic gas phase reaction at room temperature [6]. A GaN buffer layer with 20-30 nm thickness was grown at 565 °C and ramped to 950 °C for crystallization. This buffer layer was essential for wetting the 6H-SiC substrates for later continuous film growth. The growth temperature was increased to 950 °C for the growth of $B_xGa_{1-x}N$. The TMG and NH_3 were fixed at 18 μmol/min and 1.5 slm, respectively. The B/Ga ratio in the gas phase was varied from 0 to 0.2.

The $B_xGa_{1-x}N$ composition was determined using a PHI 660 scanning Auger microprobe (SAM) after bombarding the surface with argon ions for several seconds to remove surface contamination. The crystal structure of $B_xGa_{1-x}N$ was examined by X-ray diffraction (XRD) and its quality was obtained from the full width at half maximum (FWHM) of x-ray rocking curves.

The surface morphology of the samples was investigated by scanning electron microscopy (SEM) and atomic force microscopy (AFM). The thickness of films was measured by cross-sectional SEM, but for very thin layers, the growth rate was estimated from the argon-ion sputtering rate during Auger measurements. Photoluminescence (PL) measurements were performed at 10 K to study the optical properties of the films and determine the band edge emission of the samples.

RESULTS AND DISCUSSION

The influence of the B/Ga ratio in the gas phase on the $B_xGa_{1-x}N$ growth rate is plotted in Fig. 1. The growth rate sharply decreased from 1.8 to 0.4 μm/hr as the B/Ga was increased from 0.01 to 0.02; otherwise, the growth rate was fairly constant for B/Ga ratios in the 0-0.1 and 0.02-0.1 ranges. For B/Ga ratio higher than 0.2, the growth rate of $B_xGa_{1-x}N$ dropped to zero and only BN layer was produced. Apparently, higher concentration of diborane in the gas phase prevented

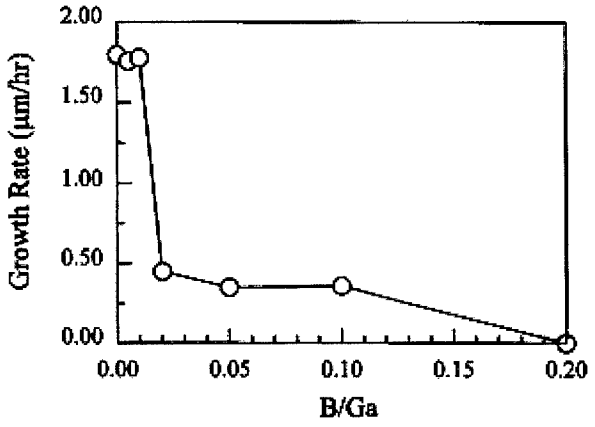


Figure 1. $B_xGa_{1-x}N$ growth rate versus B/Ga ratio.

the formation of $B_xGa_{1-x}N$, but favored pure BN growth. The drop-off in the growth rate is attributed to the growth of different structure in the deposited films; highly-faceted big crystals were produced at B/Ga ≤ 0.01, while tiny irregular shape particles with very smooth surface were observed as B/Ga ratio was higher than 0.02.

Figures 2(a) and 2(b) show SEM images of $B_xGa_{1-x}N$ with B/Ga ratio of 0.005 and 0.01, respectively. Well-faceted crystals are seen in both samples. However, the crystal size and size distribution in Fig. 2(a) are much smaller than in Fig 2(b). As shown in Fig. 2(b), the surface of the film contained the matrix film and two distinct shapes: well (0001) oriented epicrystals and agglomerated crystals on top of the surface. Some of the agglomerated crystals also showed a hexagonal structure, but the [0001] growth direction was roughly parallel to the substrate surface. These features strongly suggest that phase separation occurred in the film deposited at B/Ga=0.01, while single crystals of $B_xGa_{1-x}N$ were formed at B/Ga=0.005.

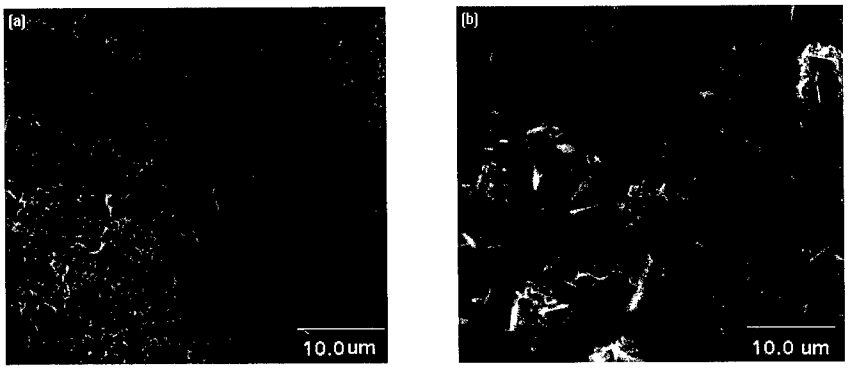


Figure 2. SEM images of $B_xGa_{1-x}N$ films deposited at different B/Ga ratios. (a) B/Ga=0.005; (b) B/Ga=0.01.

The Auger spectra of $B_xGa_{1-x}N$ grown at different B/Ga ratios are shown in Figs. 3 and 4. The spectra shown in Fig. 3 is the film deposited at B/Ga=0.01. As described in the SEM section, this film was composed of hexagonal crystals, agglomerated crystals, and matrix material. The relative atomic concentrations of the three element- B, Ga, and N- are shown above each spectrum, which were calculated using the sensitivity factor of 0.11, 0.22 and 0.17 for B, Ga, and N, respectively. The main gallium, nitrogen, and boron peaks occur at 1067, 384 and 179 eV, respectively. The matrix material was a B-rich phase with relatively high concentration of boron (Fig. 3(a)). The agglomerated crystals were $B_xGa_{1-x}N$ alloy (Fig. 3(b)) and the well-orientated hexagonal crystals just pure GaN (Fig. 3(c)). These results confirmed that the phase separation occurred in the film grown at B/Ga=0.01. The oxygen and carbon peaks were detected in all samples but decreased with the depth away from the surface. Figure 4 displays the Auger spectra of the films deposited at higher B/Ga ratio. The boron concentration in the samples increased with increasing B/Ga ratio. However, the Ga peak disappeared and only BN was produced at B/Ga=0.2.

Figure 5 shows θ-2θ XRD spectra of films with B/Ga of 0.005, 0.01 and 0.05. The $B_xGa_{1-x}N$ alloys were detected and the (0002) peak shifted toward the SiC (0006) reflection in Figs. 5(a) and 5(b), which indicated the c lattice parameter was reduced with the increase of boron in GaN. The concentration of boron was 0.015 and 0.30 in Fig. 5(a) and Fig. 5(b), respectively, which was determined by the relative shift of the $B_xGa_{1-x}N$ peak with respect to the GaN (0002) peak

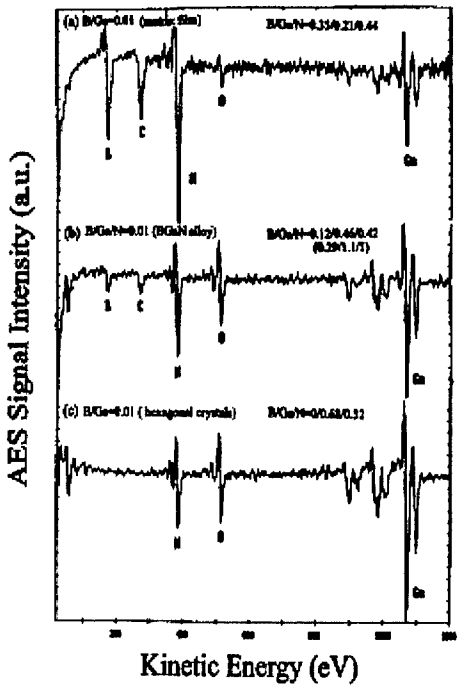


Figure 3. Auger spectra of $B_xGa_{1-x}N$ grown at B/Ga=0.01.

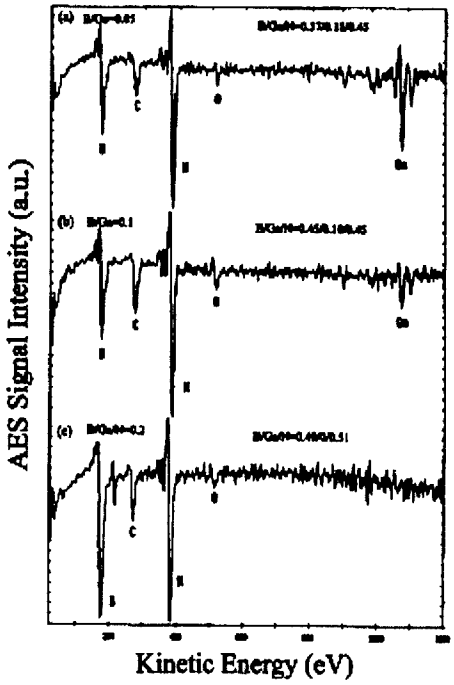


Figure 4. Auger spectra of the samples grown at B/Ga ratio of (a) 0.05; (b) 0.1; (c) 0.2.

applying Vegard's law. The sample grown at B/Ga=0.005 was a single crystal alloy of $B_{0.015}Ga_{0.985}N$ with wurtzite structure. However, the sample produced at B/Ga=0.01 showed a phase separation of GaN and $B_{0.3}Ga_{0.7}N$. When the B/Ga ratio was increased to 0.05, no $B_xGa_{1-x}N$ peak was detected and only a broad and low intensity of GaN (0002) peak was observed. The decrease in x-ray peak density and increase in peak width shown in Fig. 5c indicate that the quality of film became poor at high B/Ga ratio.

The PL spectra measured at 10 K for the films with B/Ga ratios of 0, 0.005, 0.05 and 0.1 are given in Fig. 6. The band edge emission of pure GaN shown in Fig. 6(a) was 3.451 eV with FWHM of 39.2 meV, which was ascribed to the neutral donor bound exciton recombination labeled I_2. The I_2 line increased to 3.465 eV with FWHM of 35.1 meV when the B/Ga ratio was equal to 0.005. Two weak peak transitions at 3.267 and 3.178 eV shown in Fig. 6(b) were attributed to donor-acceptor (D-A pair) recombination. The narrower FWHM of $B_xGa_{1-x}N$ at B/Ga ratio of 0.005 (x=0.015) compared with B/Ga=0 (pure GaN epilayer) suggests that the quality of GaN epilayer was improved with small amount of boron incorporation. It seems that the band edge transition of $B_xGa_{1-x}N$ shifted to high energy with increasing B/Ga ratio. However, when the B/Ga ratio was increased to 0.05, two peaks appeared at 3.358 eV and 3.323 eV as shown in Fig. 6(c). The emission peaks at 3.358 eV and 3.323 eV were possibly due to band edge transitions and impurity related transitions, respectively. As the B/Ga ratio increased to 0.1, the PL spectrum shows a much broader emission band, indicating poor crystalline quality at high B/Ga ratio.

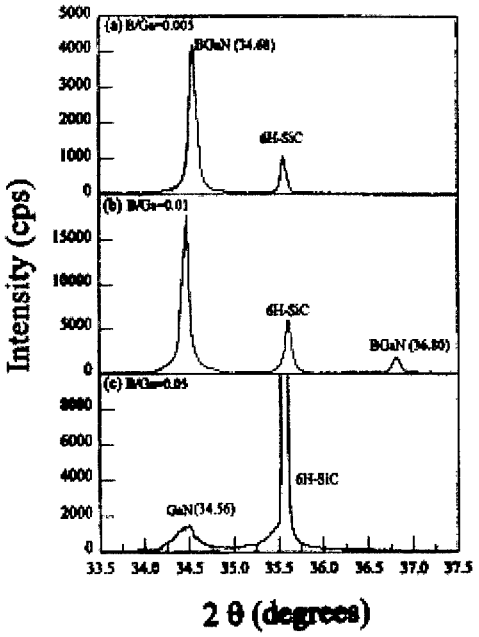


Figure 5. XRD θ-2θ scans of films deposited at different B/Ga ratios. (a) B/Ga=0.005; (b) B/Ga=0.01; (c) B/Ga=0.05.

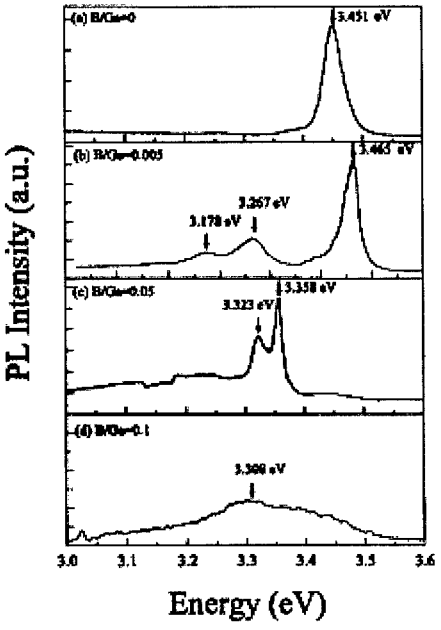


Figure 6. PL spectra of films measured at 10 K at different B/Ga ratios. (a) B/Ga=0; (b) B/Ga=0.005; (c) B/Ga=0.05; (d) B/Ga=0.1.

CONCLUSIONS

We have grown $B_xGa_{1-x}N$ films on 6H-SiC (0001) substrates at 950 °C by MOVPE. These studies show that single phase, single crystal of $B_xGa_{1-x}N$ can be produced at B/Ga ratio of 0.005. Phase separation occurred in the films when the B/Ga ratio was above 0.01. The boron concentration in the solid phase was as high as 30% reported for the first time. The quality of the GaN epilayer can be improved with small amount of boron addition.

ACKNOWLEDGEMENTS

This work was supported by the Army Research Office, grant number DAAH04-96-1-0320, and the National Science Foundation, grant number DMR-9627333.

REFERENCES

1. A. Y. Polyakov, M. Shin, M. Skowronski, D. W. Greve, R. G. Wilson, A. V. Govorkov, and R. M. Desrosiers, J. Electron Mater. **26**, 237 (1997).
2. Vincent Vezin, Satoshi Yatagai, Hiroyuki Shiraki and Satoshi Uda, Jpn. J. Appl. Phys. **36**, 1483 (1997).
3. Alex Zunger, in *Handbook of Crystal Growth*, D. T. J. Hurle, ed., Vol. 3. (Elsevier, Amsterdam, 1994), p.999.
4. T. Honda, M. Tsubamoto, Y. Kuga and H. Kawanishi, Mat. Res. Soc. Symp. Proc. Vol. **482**, 1125 (1998).
5. C. Gómez-Aleixandre, A. Essafti, M. Fernández, J. L. G. Fierro, and J. M. Albella, J. Phys. Chem. **100**, 2148 (1996).
6. T. Matsuda, N. Uno, H. Nakae, and T. Hirai, J. Mater. Sci. **21**, 649 (1986).

OPTICAL AND STRUCTURAL PROPERTIES OF Er^{3+}-DOPED GaN GROWN BY MBE

R. H. Birkhahn, R. Hudgins, D. S. Lee, B.K. Lee and A. J. Steckl*
A. Saleh**, R. G. Wilson**, J. M. Zavada***

*University of Cincinnati, Nanoelectronics Lab, Cincinnati, OH 45221-0030
**Charles Evans & Associates, Sunnyvale, CA 94086
***USARO, Research Triangle Park, NC 27709

Cite this article as: MRS Internet J. Nitride Semicond. Res. 4S1, G3.80(1999)

ABSTRACT

We report the morphological and compositional characteristics of Er-doped GaN grown by MBE on Si(111) substrates and their effect on optical properties. The GaN was grown by molecular beam epitaxy using solid sources (for Ga and Er) and a plasma gas source for N_2. The films emit by photoexcitation in the visible and near infrared wavelengths from the Er atomic levels. The morphology of the GaN:Er films was examined by AFM. Composition was determined by SIMS depth profiling that revealed a large Er concentration at 4.5×10^{21} atoms/cm^3 accompanied by a high oxygen impurity concentration.

INTRODUCTION

Interest in GaN for optoelectronic devices has taken center stage recently since the fabrication of blue lasers by several research groups. These and other optical nitride devices are based on varying Al, In, and Ga composition in heterostructures to achieve wavelength-specific emission. Rare earth (RE) elements are also known to sharply emit light at specific wavelengths independent of the host, which is due to atomic transitions. As a result, devices based on RE materials should be easier to fabricate and require less materials or device design manipulation.

Rare earth elements have found wide use in a variety of light-emitting applications, from RE-doped fibers for infrared transmission to upconversion lasers to the phosphors found in CRT tubes. In most cases, the RE emits light at wavelengths specific to the atomic transitions between its 4f energy levels. For years, study of REs incorporated into a semiconductor matrix proceeded because of the possibility that carrier injection from the host could provide the energy necessary to stimulate emission. In addition, semiconductors can be easily integrated into existing electronics. Er is a rare earth well known[1] for its near-infrared (IR) emission (1.5 μm) which corresponds to the optical fiber loss minimum. Although other Er atomic levels exist, transitions with photonic emission from these states are normally observed only in glass hosts. Typically, the IR transitions seen from RE elements represent the lowest energy transition possible between 4f levels. Er incorporated into Si[2,3,4,5] or GaAs[6,7,8,9] has been the most commonly studied system, with its characteristic emission only well documented at infrared wavelengths.

Recently, we have reported[10,11,12,13] the successful in-situ incorporation of Er into GaN by molecular beam epitaxy (MBE) on both sapphire and silicon, which produces room temperature visible and IR emission by both photoluminescence (PL) and electroluminescence (EL). We also have reported[14] on Pr-doped GaN grown on Si (111) substrates and the resulting novel visible red emission at 650 nm by EL and PL, not previously observed outside of glass hosts.

Mat. res. Soc. Symp. Proc. Vol. 537 © 1999 Materials Research Society

Spectroscopically, these specific RE atomic levels in the visible region for Pr^{3+} ($^3P_0$) and Er^{3+} ($^2H_{11/2}$, $^4S_{3/2}$) are both known to have high likelihood of transition[15] but, for reasons not yet clear, they are not observed when doped into other semiconductor hosts. The only previously reported system[16,17,18,19] in which RE-doped semiconductors emit in the visible is ZnSe:Er.

EXPERIMENTAL

We have grown in situ-doped GaN:Er on a variety of substrates (Al_2O_3, Si, 6H-SiC, HVPE GaN) by solid source and RF-assisted molecular beam epitaxy (MBE). The Riber MBE32 system used for growth has been described previously[10,11]. The samples were pretreated by cleaning in acetone, methanol and deionized water before insertion into the loadlock. They were subsequently outgassed at ~950°C before growth. During growth, the Ga cell temperature was kept constant for a beam equivalent pressure of ~8.2×10^{-7} Torr. The rf-plasma source was kept constant at 400W with a N_2 flow rate of 1.5 sccm, corresponding to a chamber pressure of mid-10^{-5} Torr. The growth temperature was varied from 750-950°C and the Er cell temperature was maintained at 1100°C.

For this paper, we have studied and characterized the GaN:Er films grown on Si (111) for their optical and compositional properties. The optical properties were characterized by photoluminescence (from UV to IR) at room temperature using a HeCd laser (325 nm). Structural properties were examined based on morphology and composition. Standard surface techniques were utilized for morphology and composition was determined by secondary ion mass spectrometry (SIMS).

RESULTS AND DISCUSSION

Optical

All the samples emit, regardless of substrate, at visible (green) and IR wavelengths corresponding to Er inner shell transitions. The green emission shown in Fig. 1 at 537 and 558 nm from the $^2H_{11/2}$ and the $^4S_{3/2}$ levels, respectively, is quite intense at room temperature. In addition to the Er^{3+} spectral lines, the scans also contained traces of GaN band edge emission near 370 nm and a broad background peaking near ~460 nm. The general trend of the visible and IR emission lines vs. substrate growth temperature is shown in Fig. 2. The visible 537 and 558 nm lines increase with growth temperature up to a certain cutoff after which emission is quenched. The open symbols represent one growth experiment in which the buffer layer was altered in an attempt to optimize conditions. Generally, the IR and the $^4S_{3/2}$ lines have opposite trends. This could be explained by visualizing[10] the Er^{3+} energy level diagram. Carriers transferred from the GaN to the Er atoms cascade non-radiatively until they reach the $^2H_{11/2}$ and

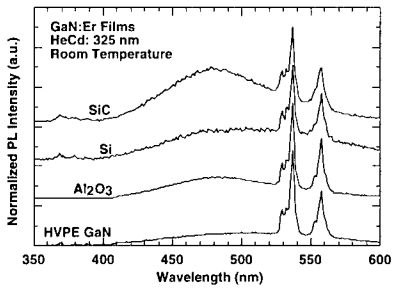


Figure 1: Visible PL spectrum of Er-doped GaN films. The PL is performed at room temperature with the He-Cd laser line at 325 nm.

$^4S_{3/2}$ states. At this point, two competitive processes occur: (a) de-excitation directly to the $^4I_{15/2}$ ground state or (b) cascading to the lowest excited state ($^4I_{13/2}$) followed by a radiative (at 1.54 μm) drop to the ground state. Carriers that radiate from the higher energy states decrease the number available for the $^4I_{13/2}$ state. This trend can also be seen in the buffer layer comparison at 750°C growth temperature: the increase in visible line intensity is accompanied by a decrease in IR emission.

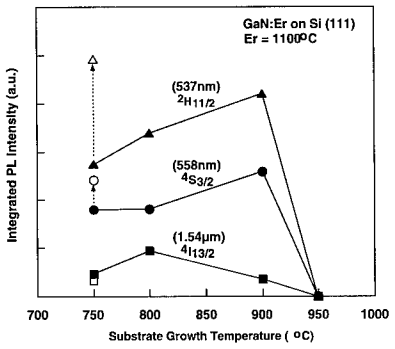


Figure 2: Integrated PL intensity of Er emission from samples grown on Si as a function of growth temperature. The open symbols represent a different buffer layer.

Surface

Surface images of the GaN films were taken by scanning electron microscopy (SEM) and atomic force

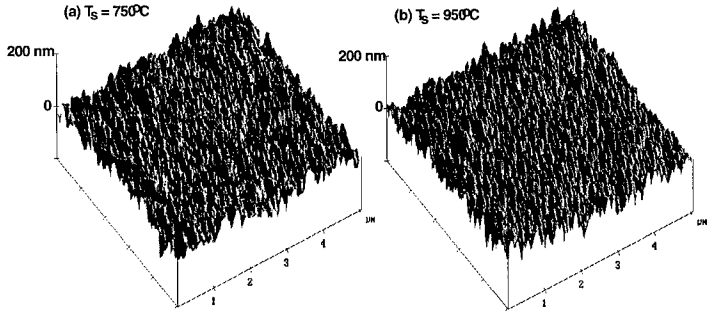


Figure 3: AFM images of the GaN:Er films on Si (111). Growth temperature was (a) 750°C and (b) 950°C. Er cell temperature was 1100°C.

microscopy (AFM). The SEM images were reported previously[11]. AFM surface images of two GaN:Er films grown at 750°C and 950°C are shown in Fig. 3. The average roughness (R_a) of film surfaces for GaN grown at various temperatures is shown in Fig. 4. All scans were taken at random points from the center of the 2-inch wafers. The overall trend indicates that a growth temperature of 900°C leads to a maximum in surface roughness. GaN:Er films grown at 800°C or 1050°C exhibit an R_a one order of magnitude lower. Roughness appears to vary linearly with the Er concentration measured in GaN by SIMS (see Fig. 7). This corresponds well with our findings on sapphire[20].

Composition

A representative SIMS depth profile of the Er concentration of a GaN:Er film on Si is shown in Fig. 5. At this substrate temperature of 750°C, the Er incorporation profile is very uniform at a concentration of ~6×10^{20} atoms/cm^3, corresponding to ~0.7 at.% throughout the film. For this set of experiments, the maximum Er concentration achieved was 5 at.% at a growth temperature of 900°C. The unintentional impurity concentrations of Si and O are shown in Fig. 6. The amount of Si observed in the GaN film is typically at the background limit of the measurement. However, there is evidence that the Si is diffusing into the GaN from the substrate. The maximum such diffusion measured is 1.2 μm into the film. The level of oxygen incorporated into the film is relatively high. The profile is also not uniform, which indicates a buildup of oxygen in the chamber during growth. The concentration of oxygen tracks the amount of Er as seen in Fig. 7.

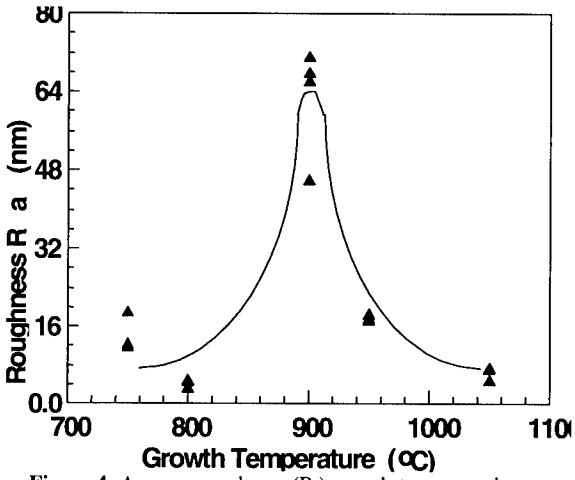


Figure 4: Average roughness (R_a) vs. substrate growth temperature by AFM of GaN:Er films on Si (111).

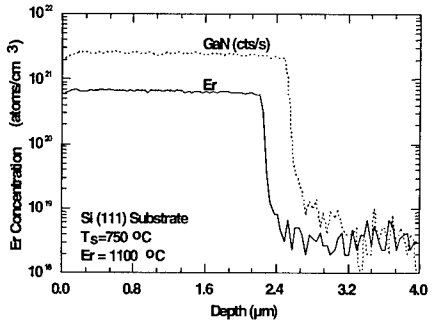


Figure 5: SIMS depth profile of Er concentration from film grown on Si. Er cell = 1100°C.

At higher growth temperatures (>900°C), the amount of Er drops even though the cell temperature remained constant at 1100°C. This indicates that oxygen can incorporate more readily at higher temperatures and that some thermal or surface kinetic process freezes out Er atoms. The solid source Er material is 99.9% pure and does contain trace amounts of oxygen and other impurities. This requires further investigation since oxygen has a known role in enhanced IR emission[21,22,23,24] from Er in other semiconductors.

SUMMARY

In summary, we have reported the optical, morphological, and compositional characteristics of Er-doped GaN grown by MBE on Si (111) substrates. We observed novel

green emission from Er in GaN and demonstrated that the occurrence of this effect is independent of the substrate. Corresponding structural properties of the films on Si were examined by AFM. Composition data provided by SIMS demonstrated that we have incorporated a high concentration (5 at.%) of Er in GaN and revealed a relatively high level of unintentional oxygen doping. Since emission from these films is already visible under ambient light, we expect that the intensity can be further optimized by choice of substrate, growth temperature, and Er flux.

This work was supported by a BMDO/ARO contract (L. Lome and J. Zavada) and a ARO AASERT grant. Equipment support was provided by an ARO URI grant and the Ohio Materials Network.

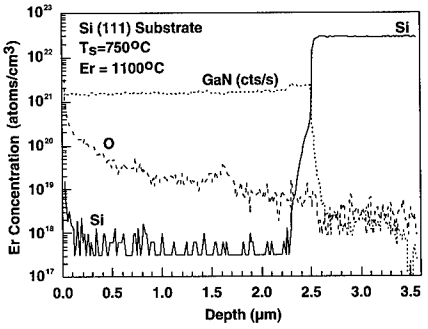


Figure 6: SIMS impurity depth profile for O and Si. Er cell = 1100°C.

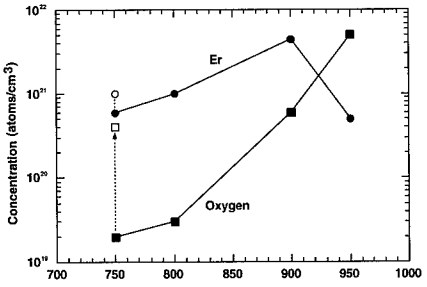


Figure 7: Concentration of Er and O as a function of growth temperature. The open symbols represent a different buffer layer. Er cell = 1100°C.

REFERENCES

[1] S. Coffa, G. Franzo, and F. Priolo, MRS Bulletin **23**, 25 (April 1998).

[2] F.Y.G. Ren, J. Michel, Q. Sun-Paduano, B. Zheng, H. Kitagawa, D.C. Jacobson, J.M. Poate and L.C. Kimerling, Mat. Res. Soc. Symp. Proc. **301**, 87 (1993).

[3] G. Franzo, F. Priolo, S. Coffa, A. Polman and A. Carnera, Appl. Phys. Lett. **64** (17), 2235 (1994).

[4] F. Priolo, G. Franzo, S. Coffa, A. Polman, V. Bellani, A. Carnera and C Spinella, Mat. Res. Soc. Symp. Proc. **316**, 397 (1994).

[5] I.A. Buyanova, W.M. Chen, G. Pozina, W.X. Ni, G.V. Hansson and B. Monemar, J. Vac. Sci. Tech. B **16** (3), 1732 (1998).

[6] R.S. Smith, H.D. Muller, H. Ennen, P. Wennekers and M. Maier, Appl. Phys. Lett. **50** (1), 49 (1987).

[7] S.J. Chang and K. Takahei, Appl. Phys. Lett. **65** (4), 433 (1994).

[8] D.W. Elsaesser, Y.K. Yeo, R.L. Hengehold, K.R. Evans and F.L. Pedrotti, J. of Appl. Phys. **77** (8), 3919 (1995).

[9] K. Takahei and A. Taguchi, J. of App. Phys. **77** (4), 1735 (1995).

[10] A.J. Steckl and R. Birkhahn, Appl. Phys. Lett. **73** (12), 1700 (1998).

[11] R. Birkhahn and A.J. Steckl, Appl. Phys. Lett. **73** (15), 2143 (1998).

[12] A. J. Steckl , M. Garter, R. Birkhahn and J. Scofield, Appl. Phys. Lett. **73** (17), 2450 (1998).

[13] M. Garter, J. Scofield, R. Birkhahn and A. J. Steckl, Appl. Phys. Lett. **74** (2), (1999).

[14] R. Birkhahn, M. Garter and A. J. Steckl. Appl. Phys. Lett. to be published.

[15] K. A. Gschneidner and L. Eyring, **Vol. 11-Two-Hundred-Year Impact of Rare Earths on Science**, in *Handbook on the Physics and Chemistry of Rare Earths* North Holland Physics Publishing, New York, 1988.

[16] J.D. Kingsley and M. Aven, Phys. Rev. **155** (2), 235 (1967).

[17] M.R. Brown, A.F.J. Cox, W.A. Shand and J.M. Williams, J. Physics C: Solid State Physics **4**, 1049 (1971).

[18] H. Kobayashi, S. Tanaka and H. Sasakura, Jpn. J. Appl. Phys. **12** (10), 1637 (1973).

[19] I. Szczurek, H.J. Lozykowski and T. Szczurek, J. Luminescence **23**, 315 (1981).

[20] R. Birkhahn, R. Hudgins, D. Lee, A. J. Steckl, R. J. Molnar and J. M. Zavada, J. Vac. Sci. and Tech. B, to be published.

[21] J. E. Colon, D. W. Elsaesser, Y. K. Yeo, R. L. Hengehold and G. S. Pomrenke, Appl. Phys. Lett. **62** (2), 216 (1993).

[22] P. N. Favennec, H. L'Haridon, D. Moutonnet, M. Salvi and M. Gauneau, Jpn. J. Appl. Phys. **29** (4), L524 (1990).

[23] P.N. Favennec, H. L'Haridon, D. Moutonnet, M. Salvi and M. Gauneau, Mat. Res. Soc. Symp. Proc. **301**, 181 (1993).

[24] J. Michel, J. L. Benton, R. F. Ferrante, D. C. Jacobson, D. J. Eaglesham, E. A. Fitzgerald, Y. H. Xie, J. M. Poate and L. C. Kimerling, J. Appl. Phys. **70** (5), 2672 (1991).

Part IV

Epitaxial Lateral Overgrowth and Selective Growth

SELECTIVE AREA GROWTH (SAG) AND EPITAXIAL LATERAL OVERGROWTH (ELO) OF GaN USING TUNGSTEN MASK

Yasutoshi Kawaguchi[1], Shingo Nambu[1], Hiroki Sone[1],
Masahito Yamaguchi[1], Hideto Miyake[2], Kazumasa Hiramatsu[2],
Nobuhiko Sawaki[1], Yasushi Iyechika[3] and Takayoshi Maeda[3]

[1]Department of Electronics, School of Engineering, Nagoya University,
Furo-cho, Chikusa-ku, Nagoya, 464-8603, Japan
[2]Department of Electrical and Electronic Engineering, Faculty of Engineering, Mie University,
1515 Kamihama-cho, Tsu, Mie, 514-8507, Japan
[3]Tsukuba Research Laboratory, Sumitomo Chemical Co., Ltd,
6 Kitahara, Tsukuba, Ibaraki, 300-3294, Japan

Cite this article as: MRS Internet J. Nitride Semicond. Res. 4S1, G4.1 (1999)

ABSTRACT

Selective area growth (SAG) and epitaxial lateral overgrowth (ELO) of GaN using tungsten (W) mask by metalorganic vapor phase epitaxy (MOVPE) and hydride vapor phase epitaxy (HVPE) have been studied. The selectivity of the GaN growth on the W mask as well as the SiO_2 mask is excellent for both MOVPE and HVPE. The ELO-GaN layers are successfully obtained by HVPE on the stripe patterns along the $<1\bar{1}00>$ crystal axis with the W mask as well as the SiO_2 mask. There are no voids between the SiO_2 mask and the overgrown GaN layer, while there are triangular voids between the W mask and the overgrown layer. The surface of the ELO-GaN layer is quite uniform for both mask materials. In the case of MOVPE, the structures of ELO layers on the W mask are the same as those on the SiO_2 mask for the $<11\bar{2}0>$ and $<1\bar{1}00>$ stripe patterns. No voids are observed between the W or SiO_2 mask and the overgrown GaN layer by using MOVPE.

INTRODUCTION

Wide band gap GaN and related nitrides have shown potential use in light emitting diodes (LEDs) and laser diodes (LDs) in green to blue light regions [1,2]. These materials have also shown usefulness in electronic devices as an AlGaN/GaN heterostructure field effect transistors (HFETs) [3,4]. The HFET structures have received interest because of the high performance with a high output power in microwave frequencies. The static induction transistors (SITs) also have a possibility for the power device at microwaves and have been expected to show ultimate performance at high temperatures because of no saturation of the drain current and the negative temperature coefficient of the leakage current [5]. For the past decades, various efforts have been done to realize power devices at high frequencies. One of the main difficulties have been on the formation of high quality metal-semiconductor contact with an embedded structure.

Selective area growth (SAG) and epitaxial lateral overgrowth (ELO) of GaN has attracted much attention in the fabrication of optical and electrical devices with high performance [6,7]. Nishinaga *et al.* developed the idea of the SAG/ELO technique further and named this technique micro-channel epitaxy (MCE), that the lateral overgrown region on the mask will be free from dislocations which might be originated at the hetero-interface [8]. Recently, Sakai *et al.*[9], Matsushima *et al.*[10] and Nam *et al.*[11] demonstrated that the SAG/ELO technique of GaN gives us an embedded structure of amorphous SiO_2 stripes in a high crystalline quality epitaxial layer. This technique will provide us embedded metal electrodes in an epitaxial GaN layer. If we could realize an embedded metal gate electrode in the epitaxial

Mat. Res. Soc. Symp. Proc. Vol. 537 © 1999 Materials Research Society

GaN layer, we might realize SITs made from GaN, which will show high performance at high temperature, high frequency and high power operations.

In a previous study, we attempted the SAG of GaN using tungsten (W) masks by metalorganic vapor phase epitaxy (MOVPE) for the first time [12]. In this study, we compare the SAG of GaN using W mask to that of SiO_2 mask by MOVPE by means of scanning electron microscope (SEM) and cathodoluminescence (CL) measurements. Furthermore, the SAG/ELO of GaN using W masks by hydride vapor phase epitaxy (HVPE) are demonstrated for the first time.

EXPERIMENTAL METHODS

The SAG of GaN using W masks was performed by atmospheric HVPE and MOVPE system on 3.0-4.5 μm thick (0001) GaN layer grown on a (0001) sapphire substrate with an low temperature (LT) buffer layer by MOVPE. A 120-nm-thick W film was deposited on the GaN surface by RF sputtering at R.T. Stripe windows of 10 μm wide with a periodicity of 20 μm was developed on the W film with conventional photolithography and wet chemical etching. The etching of W was performed with H_2O_2 at R.T. In the case of HVPE, GaCl and NH_3 were used as the source gases, and N_2 was used as the carrier gas. The flow rates of HCl and NH_3 were 10 cc/min and 0.5 *l*/min, respectively. The growth temperature was 1090°C. In the case of MOVPE, TMG and NH_3 were used as the source gases, and H_2 was used as the carrier gas. The flow rates of TMG and NH_3 were 18.7 μmol/min and 2.5 *l*/min, respectively. The growth temperature was 1060°C. More details of the preparation and growth processes by MOVPE were described in Ref. [12].

RESULTS AND DISCUSSION

The advantage of HVPE is at the high growth rate, which allows us to get a thick homogeneous layer and to obtain the GaN layer with good crystalline quality. According to previous results of the SAG/ELO using SiO_2 mask by HVPE, the selectivity of the GaN growth on window regions was excellent and the thick ELO GaN layers had good crystalline quality [9,13,14]. Figures 1(a)-1(c) show typical SEM images of the SAG-GaN by HVPE using $<1\bar{1}00>$ stripe W masks. At the growth time of 3 min (Fig. 1(a)), the growth of GaN only within the window region indicates good selectivity with the W mask as well as the SiO_2 mask. We obtained trapezoidal shapes in cross-section with the smooth (0001) surface on the top. The sidewalls formed rough surfaces. At 30 min (Fig. 1(b)), the ELO of GaN occurred. The ELO-GaN layer did not contact to the W mask and ELO-GaN layer over the W mask had the reverse-mesa shapes. At the overgrown GaN region, the top (0001) surfaces vanish and it has triangular cross-sectional shape with rough sidewalls. As a result, the structure of the SAG is characterized by combination of the reverse-mesa and the ordinary-mesa shaped planes. By increasing the growth time, the overgrown GaN region became wider and finally coalesced. After the growth time of 60 min (Fig. 1(c)), the ELO-GaN region coalesced one another and formed continuous, flat and specular surface. We could see triangular voids formed on the W mask owing to the reverse-mesa formation during the initial overgrowth stage. On the other hand, by using the SiO_2 mask, there were no voids on the SiO_2 mask.

In the previous work, we succeeded in the SAG of GaN using W masks by MOVPE for the first time [12]. In this work, we compare the W mask and the SiO_2 mask in terms of shape and crystalline quality of the SAG-GaN. Figures 2(a)-2(d) show the typical SEM images of the

SAG-GaN at the growth time of 120 min. No GaN polycrystals are observed on the W and SiO_2 mask regions. Triangular voids were not observed on the W mask in comparison with ELO-GaN grown by HVPE (Figs. 1(b) and 1(c)). It is not clear at present why these differences occurs. There are several differences in growth conditions between MOVPE and HVPE such as growth atmosphere (H_2 or N_2), and source gases (TMG or Ga and HCl), which might cause the formation of voids on the W mask. The ELO of GaN is seen in the lateral direction. In the stripe

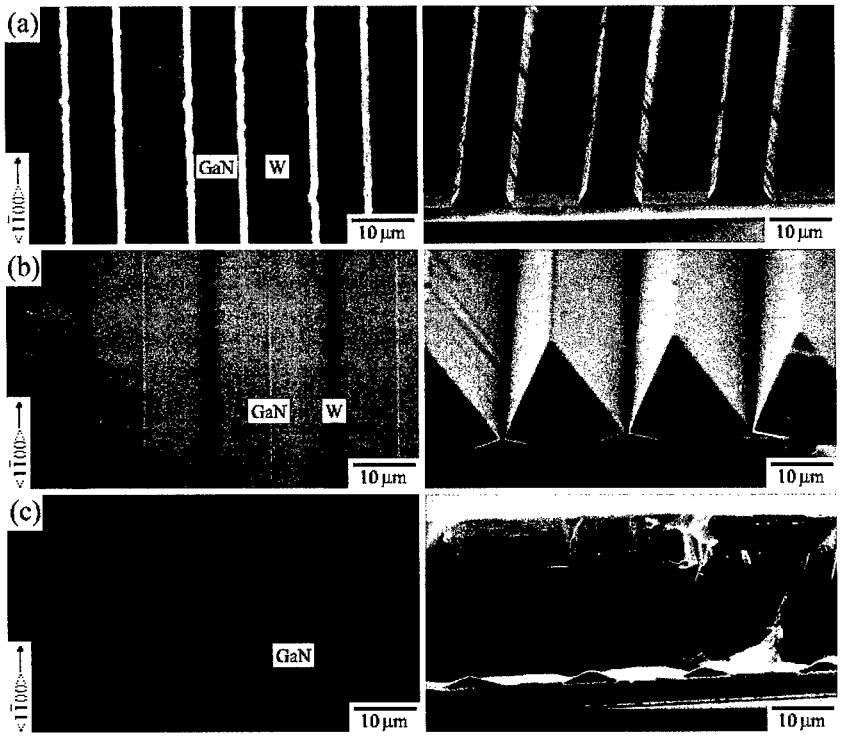


Fig. 1 SEM images of the SAG-GaN by HVPE using the W mask along the $<1\bar{1}00>$ crystal axis. The growth time of the SAG is (a) 3 min, (b) 30 min and (c) 60 min.

pattern along the $<11\bar{2}0>$ crystal axis of GaN on the (0001) surface (Figs. 2(a) and 2(c)), we obtained triangular shapes in cross-section, which comprised $\{1\bar{1}01\}$ facets at both sides. The cross-sectional shapes were the same for both mask materials. In the $<1\bar{1}00>$ stripe pattern (Figs. 2(b) and 2(d)), we obtained trapezoidal cross-sectional shapes with a smooth (0001) surface on the top and rough surfaces on both sides. The lateral overgrowth width on the SiO_2 mask have 3.5 μm, which is larger than 2.6 μm on the W mask. The difference in lateral overgrowth rates by the W and SiO_2 mask materials might be in relation to the difference in the shapes of the sidewalls, the surface migration of source materials on the masks or the interface energy between the ELO-GaN layer and masks.

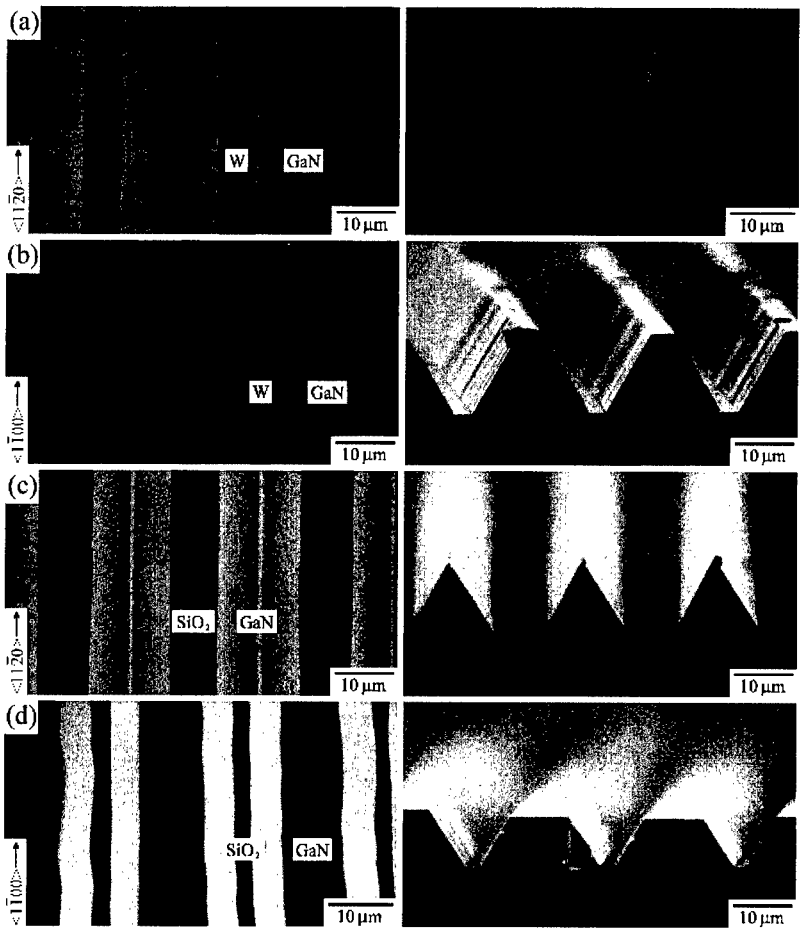


Fig. 2 SEM images of the SAG-GaN by MOVPE with the growth time of 120 min. The SAG was carried out using the W mask along (a) the $<11\bar{2}0>$ axis and (b) the $<1\bar{1}00>$ axis, and using the SiO_2 mask along (c) the $<11\bar{2}0>$ axis and (d) the $<1\bar{1}00>$ axis.

To compare crystalline qualities of the SAG-GaN grown by MOVPE with the growth time of 120 min, we measured CL spectra at 133 K for the area of 10 μm × 10 μm on the surface, which schematically shows in Fig. 3. Figure 4 shows the CL spectra by the SAG-GaN using the W mask along (a) the $<11\bar{2}0>$ axis and (b) the $<1\bar{1}00>$ axis, and using the SiO_2 mask along (c) the $<11\bar{2}0>$ axis and (d) the $<1\bar{1}00>$ axis, and (e) high quality GaN underlying layer for the SAG. Near-band-edge emission peak is observed in every SAG-GaN sample, however, which shows red-shift about 25 meV as compared to the result shown in a GaN thin layer. The GaN layer grown on the sapphire substrate is given a compressive strain, while the SAG-GaN is relaxed this strain and then the peak energy shifted low energy side. It is still to be studied how the strain is effective SAG-GaN. Full-width at half-maximum on CL spectra by SAG-GaN are about 60 meV and these value are equal to that obtained in the GaN layer. This suggests that the crystalline qualities of GaN obtained by the SAG is excellent.

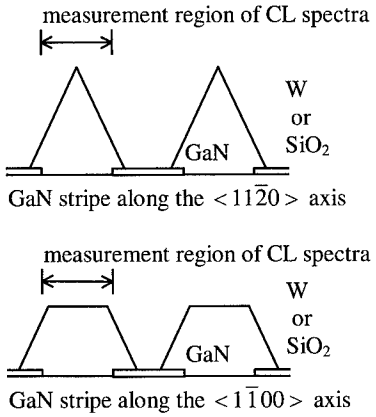


Fig. 3 Schematic diagrams of CL measurements. CL spectra measured from the GaN stripe region of 10 μm × 10 μm on the surface.

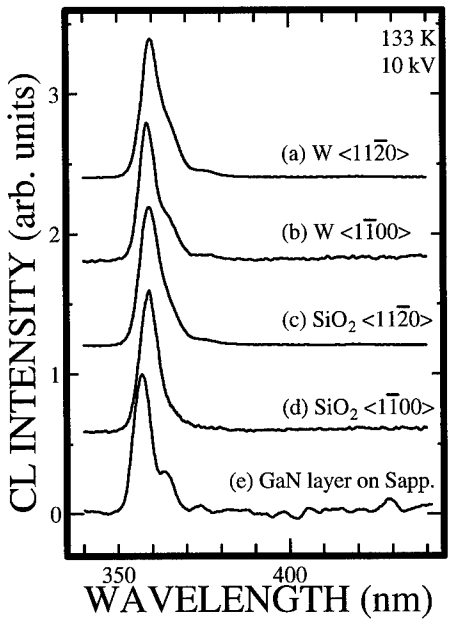


Fig. 4 CL spectra at 133 K from the GaN stripe obtained by the MOVPE-SAG using the W mask along (a) the <11$\bar{2}$0> axis and (b) the <1$\bar{1}$00> axis, and using the SiO_2 mask along (c) the <11$\bar{2}$0> axis and (d) the <1$\bar{1}$00> axis, and (e) high quality GaN underlying layer for the SAG.

CONCLUSIONS

The SAG/ELO of GaN using W mask by MOVPE and HVPE was studied. In both growth methods, GaN polycrystals were observed neither on the W mask region nor on the SiO_2 mask region. In the case of HVPE, the overgrown GaN region became wider, coalesced and finally formed continuous, flat and specular surface. Triangular voids were formed on the W masks due to reverse-mesa formation during the initial overgrowth stage. In the case of MOVPE, we obtained triangular cross-sectional shapes with {1$\bar{1}$01} facets at both sides for the W and SiO_2 masks along the <11$\bar{2}$0> crystal axis, while the trapezoidal cross-sectional shapes with smooth (0001) surface on the top and rough surfaces on both sides along the <1$\bar{1}$00> crystal axis. The lateral overgrown rate on the W mask was higher than that on the SiO_2 mask There were no voids between the W or SiO_2 mask and the overgrown GaN layer by using MOVPE.

ACKNOWLEDGMENTS

This work was partly supported by the Proposed-Based R&D Program of NEDO (97S02-015) and JSPS Research for the Future Program of Atomic Scale Surface and Interface Dynamics.

REFERENCES

[1] H. Amano, M. Kito, K. Hiramatsu and I. Akasaki: Jpn. J. Appl. Phys. **28** (1989) L2112.
[2] S. Nakamura and G. Fasol: The blue laser diode (Splinger-Verlag Berlin Heidelberg, 1997)
[3] Y. -F. Wu, B. P. Keller, S. Keller, N. X. Nguyen, M. Le, C. Nguyen, T. J. Jenkins, L. T. Kehias, S. P. DenBaars and U. K. Mishra: IEEE Electron Device Lett. **18** (1997) 438.
[4] Y. -F. Wu, B. P. Keller, P. Fini, S. Keller, T. J. Jenkins, L. T. Kehias, S. P. DenBaars and U. K. Mishra: IEEE Electron Device Lett. **19** (1998) 50.
[5] C. O. Bozler and G. D. Alley: IEEE Trans. Electron Devices **ED-27** (1980) 1128.
[6] Y. Ujiie and T. Nishinaga: Jpn. J. Appl. Phys. **28** (1989) L377.
[7] S. Nakamura, M. Senoh, S. Nagahama, N. Iwasa, T. Yamada, T. Matsushita, H. Kiyoku, Y. Sugimoto, T. Kozaki, H. Umemoto, M. Sano and K. Chocho: Appl. Phys. Lett. **72** (1998) 211.
[8] R. Vetury, H. Marchand, J. P. Ibbetson, P. T. Fini, S. Keller, J. Speck, S. P. DenBaars and U. K. Mishra: *Extended Abstracts of 25th International Symposium on Compound Semiconductors*, Nara (1998) S-2
[9] A. Sakai, H. Sunakawa and A. Usui: Appl. Phys. Lett. **71** (1997) 2259.
[10] H. Matsushima, M. Yamaguchi, K. Hiramatsu and N. Sawaki: J. Cryst. Growth **189/190** (1998) 78.
[11] O. -H. Nam, M. D. Bremser, T. S. Zheleva and R. F. Davis: Appl. Phys. Lett. **71** (1997) 2638
[12] Y. Kawaguchi, S. Nambu, H. Sone, T. Shibata, H. Matsushima, M. Yamaguchi, H. Miyake, K. Hiramatsu and N. Sawaki: Jpn. J. Appl. Phys. **37** (1998) L845.
[13] T. Shibata, H. Sone, K. Yahashi, M. Yamaguchi, K. Hiramatsu, N. Sawaki and N. Itoh: J. Cryst. Growth **189/190** (1998) 67.
[14] A. Usui, H. Sunakawa, A. Sakai and A. A. Yamaguchi: Jpn. J. Appl. Phys. **36** (1997) L899.

EPITAXIAL LATERAL OVERGROWTH OF GaN ON SiC AND SAPPHIRE SUBSTRATES

ZHONGHAI YU[*], M.A.L. JOHNSON[*], J.D. BROWN[*], N.A. EL-MASRY[**], J. F. MUTH[*], J.W. COOK, JR.[*], J.F. SCHETZINA[*], K.W. HABERERN[***], H.S. KONG[***], AND J.A. EDMOND[***]

[*] Department of Physics, North Carolina State University, Raleigh NC 27695, jan_schetzina@ncsu.edu

[**] Department of Materials Science and Engineering, North Carolina State University, Raleigh NC 27695

[***] Cree Research Inc, 4600 Silicon Drive, Durham NC 27703

Cite this article as: MRS Internet J. Nitride Semicond. Res. 4S1, G4.3 (1999)

ABSTRACT

The epitaxial lateral overgrowth (ELO) process for GaN has been studied using SiC and sapphire substrates. Both MBE and MOVPE growth processes were employed in the study. The use of SiO_2 versus SiN_x insulator stripes was investigated using window/stripe widths ranging from 2 μm/4 μm to 3 μm/15 μm. GaN film depositions were completed at temperatures ranging from 800 °C to 1120 °C. Characterization experiments included RHEED, TEM, SEM and cathodolumenescence studies. The MBE growth experiments produced polycrystalline GaN over the insulator stripes even at deposition temperatures as high as 990 °C. In contrast, MOVPE growth produced single-crystal GaN stripes with no observable threading dislocations.

INTRODUCTION

Growth of GaN and other III-V nitrides on mismatched substrates such as sapphire or SiC produces a columnar material consisting of many small hexagonal grains [1]. The individual grains have a distribution of tilt and rotation within the GaN film that gives rise to very large dislocation densities and broad x-ray rocking curves (300-400 arc sec). In spite of this high degree of disorder, there have been demonstrations of very bright blue and green LEDs and blue/violet laser diodes at Nichia Chemical [2-5] and elsewhere [6-9]. These light-emitting devices, all prepared by MOVPE, exhibit dislocation densities of 10^9-10^{10} per cm^2 but function as very bright light emitters as though these internal disruptions to periodicity are virtually absent – perhaps due to some unknown passivation process associated with the MOVPE growth process itself.

Recently, however, there have been demonstrations of defect reduction in GaN layers grown on sapphire [10-16] and SiC [17-19] using an epitaxial lateral overgrowth (ELO) technique. The ELO technique is illustrated schematically in Fig. 2. First, a high quality 1-2 μm thick layer of GaN is grown by MOVPE. Next, standard deposition and photolithographic techniques are employed to prepare a set of parallel SiO_2 stripes oriented along a $[1\bar{1}00]$ GaN crystal direction separated by window areas which expose the underlying GaN. A second deposition of GaN onto this patterned substrate is then initiated. During the initial GaN growth, the SiO_2 stripes function as non-wettable surfaces and no GaN deposition occurs on them. However, once the GaN film growth from the window stripes reaches the tops of the SiO_2 stripes, epitaxial lateral overgrowth of GaN commences. The ELO process produces stripes of GaN (5–10 μm wide) over the original SiO_2 stripes which display a remarkable reduction in dislocation density to $\leq 10^6$ per cm^2. It is on these low-dislocation-density single-crystal GaN stripes that Nichia Chemical has

Mat. Res. Soc. Symp. Proc. Vol. 537 © 1999 Materials Research Society

produced laser diodes having very long CW lifetimes (10,000 hrs) [20]. In this paper, the results of a systematic study of GaN/ELO on sapphire and SiC substrates are reported in which both MBE and MOVPE growth processes were employed.

EXPERIMENTAL DETAILS

MBE growth experiments were performed in an EPI 930 system using elemental Ga and active nitrogen generated within RF plasma sources. The system is equipped with three RF plasma sources which permit growth of GaN at temperatures up to ~1000 °C. The MOVPE growth experiments were carried out in a low pressure, vertical-flow, cold-wall reactor featuring high-speed substrate rotation. Both systems are equipped with optical pyrometers for substrate temperature measurements.

Pre-nucleated GaN/sapphire and GaN/SiC wafers prepared by MOVPE were used for all of the ELO experiments. These wafers were coated with ~100nm of either SiO_2 or SiN_x using a low temperature plasma process. Next, a mask set was employed to define a series of parallel insulator stripes along a GaN [$1\bar{1}00$] crystal direction separated by VIAs (windows) using standard photolithographic techniques. RIE was then used to remove the insulator (SiO_2 or SiN_x) from the window areas and expose the underlying parallel GaN stripes. Window/stripe widths ranging from 2 μm/4μm up to 3μm/15μm were employed in the present study. The patterned wafers were then returned to the growth chambers where ELO growth of GaN was initiated. All GaN ELO layers were intentionally doped with Si (~$1x10^{18}$ electrons/cm^3).

The GaN ELO samples were characterized using a JEOL JSM-6400 scanning electron microscope (SEM) equipped with a model SP13064-6400 digital scan generator (DSG). Digital electron microscope images are acquired by the DSG with the aid of a computer which takes control of the instrument's horizontal and vertical scan coils, acquires a video signal at each pixel, and forms a digital image. Image pixel densities of up to 2560 x 1920 pixels are then stored on computer as a high-resolution digital image. The SEM is also equipped with an Oxford Instruments Mono-CL cathodoluminescence (CL) accessory. With this unit it is possible to obtain spectral CL scans from 180 nm to 900 nm. In addition, monochromatic CL images of samples under investigation can be obtained at any selected wavelength in this wavelength range. In the present study, digital CL images at 560 nm (deep level emission) and at 364 nm (band edge emission) were obtained for selected GaN ELO samples.

Vertical-cross-section transmission electron micrographs were also obtained for selected samples using a Topcon model 002B transmission electron microscope operating at 200 kV. The TEM micrographs were taken under two-beam conditions using the c-axis as the operating vector [g = (0002)].

RESULTS AND DISCUSSION

MBE Growth Experiments

MBE growth of GaN was completed at temperatures ranging from 800 °C up to 990 °C using multiple nitrogen plasma sources. All of these experiments produced similar results, as is illustrated schematically in Figure 1. It is seen from the SEM micrograph shown in the figure that the GaN film growth onto the insulator areas consists of small randomly oriented columnar structures. RHEED patterns consisted of a concentric ring pattern from the overgrowth regions superposed on a spotty pattern from the window areas. This behavior was observed for samples prepared over the entire range of temperatures investigated. These results indicate that MBE cannot be used to prepare low dislocation density GaN by the ELO technique. This is so, most

likely, because of the limited range of temperatures available for MBE growth of GaN at present. The upper temperature for MBE film growth is limited by the availability of active nitrogen present in the process. Even by employing three active nitrogen plasma sources, the highest growth temperature that we were able to employ was about 990 °C.

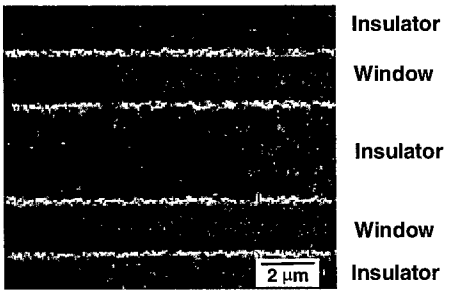
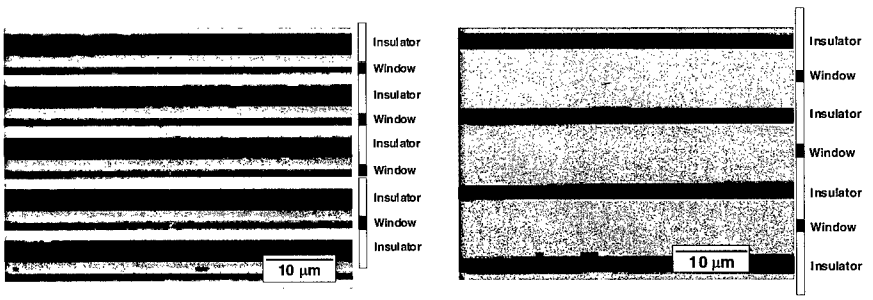


Figure 1. SEM micrograph of MBE-grown GaN surface. RHEED studies imply polycrystalline growth over insulator areas for all MBE-grown samples.

MOVPE Growth Experiments

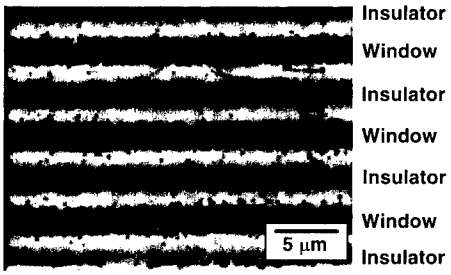
The MOVPE GaN/ELO growth experiments were performed at substrate temperatures ranging from 1050 °C up to 1120 °C. During the initial GaN/ELO growth sequence by MOVPE, the insulator stripes function as non-wettable surfaces and no GaN deposition occurs on them. However, once the GaN film growth from the window stripes reaches the tops of the insulator stripes, epitaxial lateral overgrowth of GaN commences. All of the MOVPE experiments produced GaN single-crystal stripes over the insulator areas that showed a large reduction in threading dislocations. In many of the samples, no threading dislocations were observed in TEM vertical-cross-section studies. As the substrate temperature was increased, the growth morphology changed from ELO having inclined lateral sidewalls ($\{1\bar{1}01\}$ planes) that spread rapidly towards the centers of the periodic insulator stripes to an epitaxial lateral growth featuring vertical sidewalls corresponding to $\{11\bar{2}0\}$ planes. This is illustrated by the SEM micrographs shown below in Figure 2 This type of morphology change with increasing growth temperature was observed when either SiO_2 or SiN_x insulator stripes were employed.



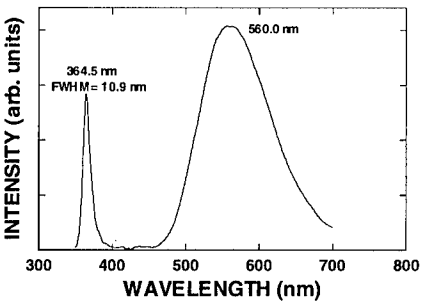
(a) (b)

Figure 2. SEM photos showing GaN/ELO with (a) inclined lateral side-walls at low growth temperatures (~1050 °C) and (b) vertical sidewalls at high growth temperatures (~1120 °C)

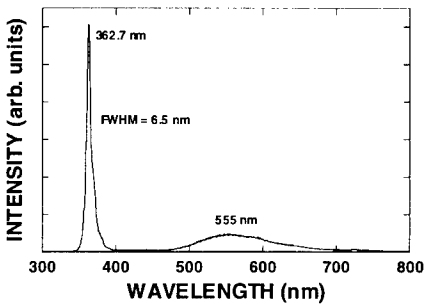
Cathodoluminescence studies revealed a marked difference in the CL originating from the GaN growing in the window areas compared with that from the GaN/ELO. This is shown in Figure 3 where CL images and spectra are displayed. Figure 3(a) shows a panchromatic image



(a)



(b)



(c)

Figure 3. (a) Panchromatic CL image of a GaN/ELO surface. Light emission is more intense over insulator areas. Window CL is dominated by deep-level emission (b) whereas, near the center of the ELO stripes, the CL is primarily near bandedge emission (c).

of a GaN/ELO surface. It is seen that the window regions emit very little CL and this is largely deep level emission as shown in Figure 3(b). In contrast, the CL from the ELO regions is very bright and consists mainly of near bandedge emission as shown in Figure 3(c).

Figure 4 shows a vertical cross-section TEM image of a GaN/ELO sample. It is seen that the region beneath the insulator strip contains many threading dislocations (about 10^{10} per cm^2). In contrast, the ELO above the insulator stripe contains no visible threading dislocations. Directly above the insulator stripe some misfit dislocations running parallel to the insulator surface are visible, but these diminish in density as the ELO process progresses. Threading dislocations continue to propagate upwards through the window regions as shown. For the growth parameters employed in this study, a lateral-to-vertical growth rate (LTVGR), as defined by Park et al. [15], of about 2.0 was obtained for all of the ELO growth experiments using both sapphire and SiC substrates.

The growth temperature employed for the ELO process had a profound effect on the ELO sidewalls as discussed above, and also on the void geometry that occurs near the centers of the insulator stripes where two adjacent GaN/ELO single crystal stripes coalesce. This is illustrated in Figure 5 where TEM micrographs obtained for ELO samples grown at 1080 °C and 1120 °C,

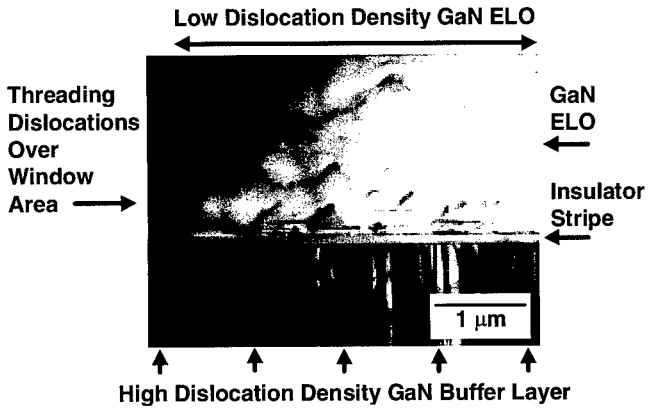
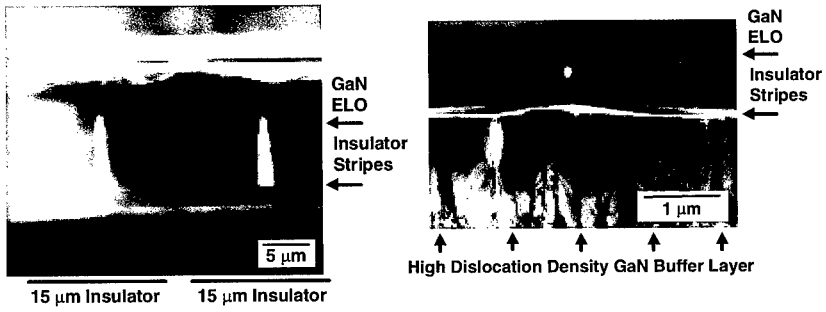


Figure 4. TEM vertical cross-section micrograph of GaN/ELO sample.



(a) (b)

Figure 5. (a) GaN/ELO with vertical sidewalls ($\{1\bar{1}20\}$ planes); (b) GaN/ELO with inclined sidewalls ($\{1\bar{1}01\}$ planes)

respectively. In the case of ELO growth at 1120 °C, which proceeds with vertical sidewalls, there are large voids formed at the centers of the insulator stripes (white triangles in Figure 5(a). This is similar to the void structure reported by Nakamura [20]. In contrast, the void structure for ELO growth at 1080 °C consist of only a small (~100 nm diameter) circular hole immediately above the insulator stripe as shown in Figure 5(b). It should be emphasized that both types of depositions produce ELO have little or no threading dislocations.

Note also in Figure 5(b) that the insulator stripe (SiO_2 in this case) appears to be buckled near the center of the micrograph and no longer makes intimate contact with the GaN buffer layer below the stripe. This phenomenon was seen in several ELO samples using SiO_2 stripes and becomes more problematic for high temperature ELO growth. The use of SiN_x stripes eliminated this problem as is illustrated in Figure 4 and Figure 5(a).

Double-layer ELO samples were also prepared by rotating the substrate by 60 degrees, such that a second set of insulator stripes were fabricated along another equivalent $[1\bar{1}00]$ direction. This resulted in additional dislocation reduction within the areas of the windows of the first ELO

layer. This dislocation reduction is illustrated in Figure 6, where monochromatic images of the near bandedge CL emission at 364 nm is shown for each ELO layer.

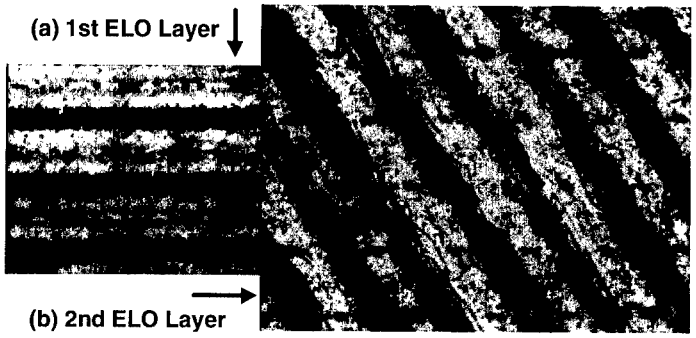


Figure 6. Monochromatic CL emission at 364 nm for double-layer ELO sample.

REFERENCES

1. F. A. Ponce, MRS Bulletin **22** (1997) 51.
2. S. Nakamura, T. Mukai, M. Senoh, Appl. Phys. Lett. **64** (1994) 1687.
3. S. Nakamura, M. Senoh, N. Iwasa, S. Nagahama, App. Phys. Lett. **67** (1995) 1868.
4. S. Nakamura, M. Senoh, S. Nagahama, N. Iwasa, T. Yamada, T. Matsushita, Y. Sugimoto, H. Kiyoku, Appl. Phys. Lett. **70** (1995) 1417.
5. S. Nakamura and G. Fasol, *The Blue Laser Diode* (Springer-Verlag: Heidelberg) (1997).
6. J. Edmond, H.S. Kong, M. Leonard, G. Bulman, G. Negley, Inst. of Phys. Conf. Series **142**, (1996).
7. I. Akasaki, S. Sota, H. Sakai, T. Tanaka, M. Koike, H. Amano, Electronics Lett. **32**(12), (1996) 1105.
8. G.E. Bulman, K. Doverspike, S.T. Sheppard, T.W. Weeks, H.S. Kong, H.M. Dieringer, J.A. Edmond, J.D. Brown, J.T. Swindell, J.F. Schetzina, Electron. Lett. **33** (1997) 1556.
9. M.P. Mack, A. Abare, M. Aizcorbe, P. Kosokoy, S. Keller, U.K. Mishra, L. Coldren, S. DenBaars, MRS Internet J. Nitride Semicond. Res. **2** (1997) 41.
10. T. Detchprohm, T. Kuroda, K. Hiramatsu, N. Sawaki, H. Goto, Inst. of Phys. Conf. Series **142** (1996) 859.
11. A. Usui, H Sunakawa, A. Sakai, A.A. Yamaguchi, Jpn. J. Appl. Phys. **36** (1997) L899.
12. D. Kapolnek, S. Keller, R. Vetury, R.D. Underwood, P. Kozodoy, S.P. DenBaars, U.K. Mishra, Appl. Phys. Lett. **71** (1997) 1204.
13. A Sakai, H Sunakawa, A Usui, Appl. Phys. Lett. **71** (1997) 2259.
14. Zhonghai Yu, M.A.L. Johnson, T. McNulty, J.D. Brown, J.W. Cook, Jr. and J.F. Schetzina, MRS Internet J. Nitride Semicond. Res. **3** (1998) 6.
15. J. Park, P.A. Grudowski, C.J. Eiting, and R.D. Dupuis, Appl. Phys. Lett. **73**, 333 (1998).
16. X. Li,m S.G. Bishop, and J.J. Coleman, Appl. Phys. Lett. **73**. 1179 (1998).
17. O Nam, M.D. Bremser, B.L. Ward, R.J. Nemanich, R.F. Davis, Jpn. J. Appl. Phys. **36** (1997) L532.
18. Tsvetanka S. Zheleva, Ok-Hyun Nam, Micheal D. Bremser, Robert F. Davis, Appl. Phys. Lett. **71** (1997) 2472.
19. O-H Nam, MD Bremser, TS Zheleva, RF Davis, Appl. Phys. Lett. **71** (1997) 2638.
20. S. Nakamura, M. Senoh, S. Nagahama, N. Iwasa, T. Yamada, T. Matsushita, H. Kiyoku, Y. Sugimoto, T. Kozaki, H. Umemoto, M. Sano, K. Chocho, Appl. Phys. Lett. **72** (1998) 211.

FAST LATERAL EPITAXIAL OVERGROWTH OF GALLIUM NITRIDE BY METALORGANIC CHEMICAL VAPOR DEPOSITION USING A TWO-STEP PROCESS

H. Marchand,* J.P. Ibbetson,* P.T. Fini,** X.H. Wu,** S. Keller,*
S.P. DenBaars,** J.S. Speck,** U.K. Mishra*

*ECE Dept., University of California, Santa Barbara, CA 93106
**Materials Department, University of California, Santa Barbara, CA 93106

Cite this article as: MRS Internet J. Nitride Semicond. Res. 4S1, G4.5 (1999)

ABSTRACT

We demonstrate a two-step process wherein the lateral epitaxial growth (LEO) of GaN from <$10\bar{1}0$>-oriented stripes is initiated at a low V/III ratio to produce smooth, vertical $\{11\bar{2}0\}$ sidewalls, and where the V/III ratio is subsequently raised in order to increase the lateral growth rate. We find that the formation of the $\{1\bar{1}01\}$ facets is inhibited using this two-step process, and that it is possible to maintain the $\{11\bar{2}0\}$ sidewalls while achieving a large lateral growth rate. The ratio of lateral to vertical growth rate has been increased by up to factor of 2.6 using this approach relative to identical growth conditions without the initiation at low V/III ratio. The effect of lateral growth rate on the structural properties of the stripes is discussed.

INTRODUCTION

Lateral epitaxial overgrowth (LEO) is an attractive method to produce GaN films with a low density of extended defects, which is beneficial both to studies of the fundamental properties of the GaInAlN materials system and to GaN-based device technology. Recent studies have confirmed that the density of threading dislocations (TDs) is reduced by 3-4 orders of magnitude in the LEO material grown on 6H-SiC[1], Al_2O_3[2,3,4], and Si(111)[5] substrates, and the mechanisms of threading dislocations evolution with respect to the facet configuration of the LEO stripes have been investigated.[1,4,6,7] Optical studies of LEO GaN[8,9,10] and InGaN quantum wells[9] have been reported. Finally, the use of LEO GaN has resulted in marked improvements in the lifetime of laser diodes,[11] while GaN p-n junctions,[12] InGaN single[13] and multiple[14] quantum well light emitting diodes, and GaN/AlGaN heterojunction field-effect transistors[15] fabricated on LEO GaN exhibit a ~3 orders of magnitude reduction of the leakage current compared to identical devices based on bulk GaN.

LEO GaN is obtained by performing a regrowth on a conventional GaN layer (e.g. GaN/Al_2O_3) that is partially masked by an amorphous layer such as SiO_2 or Si_3N_4. The process is anisotropic and can be characterized by two extreme crystalline orientations when using stripes as mask openings.[16] Stripes aligned along the <$11\bar{2}0$> orientation are bound by smooth $\{10\bar{1}1\}$ facets under a wide range of growth conditions[17] and tend to exhibit slow lateral overgrowth.[16] On the other hand, <$10\bar{1}0$>-oriented stripes exhibit a wider variety of sidewall facets and lateral growth rates. We have recently reported[18] that the morphology of such stripes depends on the growth temperature and fill factor,[19] and proposed that these effects result from variations of the V/III ratio with temperature (due to incomplete decomposition of NH_3) and pattern geometry (related to differential enhancement of Ga and N species supply from the mask regions), in relation to the configuration of the dangling bonds on the various facets. This interpretation appears to be confirmed by a systematic study of the effect of the input V/III ratio.[20] At low V/III ratio, the sidewalls consist of inclined $\{11\bar{2}2\}$ facets and the lateral growth rate is small. As the V/III ratio is increased, smooth vertical $\{11\bar{2}0\}$ facets appear; in this regime the lateral growth

Mat. Res. Soc. Symp. Proc. Vol. 537 © 1999 Materials Research Society

rate varies approximately linearly with the V/III ratio, up to the point where $\{10\bar{1}1\}$ facets are formed, which results in a jagged morphology and a drop of the lateral growth rate.

For device applications it is desirable to maximize the lateral growth rate while avoiding the formation of jagged sidewalls. In this paper we report on a two-step process that results in a reduction of the growth time necessary to achieve full coalescence of adjacent LEO stripes. The overgrowth is initiated in conditions that lead to smooth sidewalls, after which the growth parameters are changed to increase the lateral growth rate. We show that the stripe morphology is essentially determined by the growth conditions of the first overgrowth step, which greatly extends the range of conditions to achieve smooth LEO stripes.

EXPERIMENT

The LEO GaN was grown on 2 μm-thick GaN prepared by MOCVD on 2-inch diameter sapphire wafers using a conventional two-step process.[21] Samples were coated with 200-nm-thick SiO_2 using plasma-enhanced chemical vapor deposition, and 5 μm-wide openings oriented in the $<10\bar{1}0>$ direction[16] were patterned using standard UV photolithography and wet chemical etching. The mask width was varied to give fill factors[19] of 0.01 to 0.5, corresponding to mask widths of 495 to 5 μm. The LEO growth was performed at 76 Torr and 1060°C using hydrogen as the carrier gas. No dopants were intentionally introduced during growth.

In this paper we discuss the properties of six samples whose growth parameters are listed in Table I. Uncoated samples were characterized by scanning electron microscopy (SEM) using a JEOL 6300F field emission microscope operating at 15 kV. Specimens for transmission electron microscopy (TEM) were prepared by wedge polishing followed by standard Ar^+ ion milling. Images were recorded on a JEOL 2000FX microscope operated at 200 kV. The room-temperature photoluminescence was excited using a HeCd laser (325 nm, ~20 mW/cm^2) and detected using a 1/8 m grating monochromator and a photomultiplier tube.

RESULTS

Figure 1(a,b) shows SEM micrographs of sample A, overgrown in a single 15-minute step using 3.6 slm of NH_3, which results in jagged sidewalls ($\{10\bar{1}1\}$ facets). Figure 1(c,d) shows micrographs of sample B, grown under the same conditions except that the overgrowth was initiated under half the NH_3 flow for the first 3 minutes. Sample B shows smooth vertical sidewalls ($\{11\bar{2}0\}$) and a slightly larger lateral growth rate. Although the samples shown in Fig. 1 were grown consecutively using the same GaN/Al_2O_3 substrate and patterning run, the elimination of the $\{10\bar{1}1\}$ facets following the overgrowth initiation at low V/III ratio is reproducible and appears to be insensitive to process parameters such as threading dislocation density of GaN/Al_2O_3 substrate, fill factor, and growth parameters of the second step.

Table I Precursor flow and step durations

Sample	Step 1 Duration (s)	Step 1 TMGa (μmol/min)	Step 1 NH_3 (slm)	Step 2 Duration (s)	Step 2 TMGa (μmol/min)	Step 2 NH_3 (slm)
A	900	100	3.6	---	---	---
A2	3600	100	3.6	---	---	---
B	90	100	1.8	810	100	3.6
B2	900	100	1.8	900	100	3.6
C	90	100	1.8	1710	50	1.8
D	90	100	1.8	1710	50	3.6

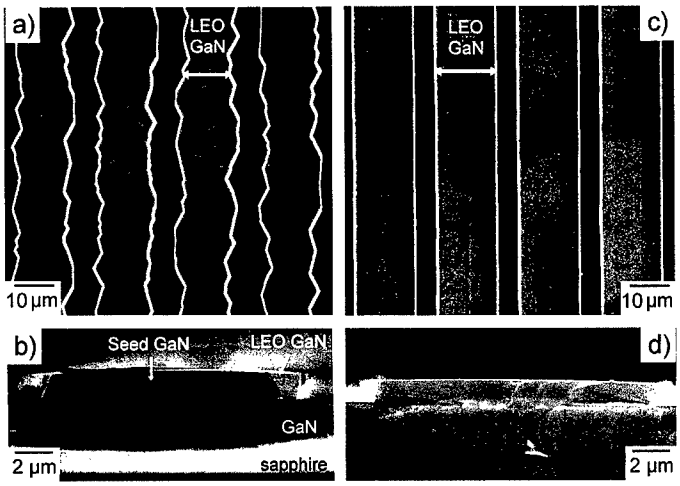


Figure 1 SEM micrographs of sample A (a: plan view, b: cross-section) and Sample B (c: plan view, d: cross-section) for a fill factor of 0.25. The edges of the mask are indicated by dark markers in (d).

Figure 2 illustrates the effect of TMGa and NH_3 flow rates on the ratio r of lateral to vertical growth rate. In Refs 18 and 20 we have shown that an increase in fill factor (i.e. reduction of the mask spacing) has a similar effect as an increase in the input V/III ratio; thus the horizontal axis can be understood both as a geometrical factor and as an indirect V/III scale. The curve for sample A shows that r rolls off as the $\{10\bar{1}1\}$ facets appear at high fill factors for the one-step process. On the other hand, r increases monotonically with fill factor for the samples grown in two steps (B, C, and D). Comparing samples A and B at the high-fill factor end of their respective curves provides a conservative estimate of ~30% for the increase in r associated with

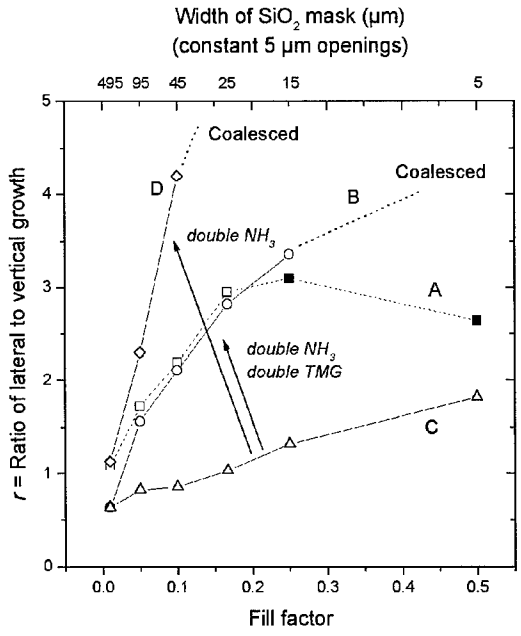


Figure 2 Ratio of lateral to vertical growth as a function of fill factor for samples A-D. The lateral growth is defined as the width of the GaN growth above the mask opening. The data points for a given curve are results from a single growth on a sample patterned with the various fill factors. The solid symbols indicate jagged sidewalls ($\{10\bar{1}1\}$ facets).

the two-step process (the actual gain was limited by the rapid coalescence of sample B). A typical sample grown in one step in the conditions for sample D at a fill factor of 0.1 would exhibit jagged sidewalls and $r \approx 1.6$ (not shown); the two-step process (sample D) results in smooth sidewalls and $r = 4.2$, a factor of 2.6 larger.

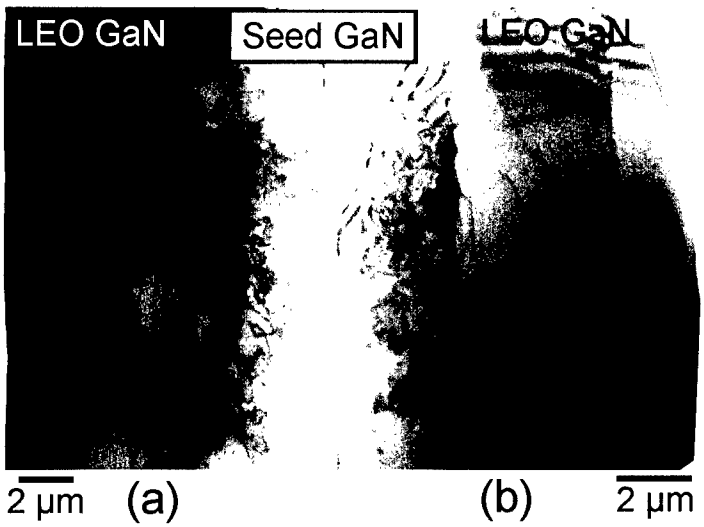


Figure 3 Plan view TEM micrographs of (a) Sample A2 and (b) Sample B2 (bright field, g=2$\bar{1}$10).

Figure 3 shows plan-view TEM micrographs of samples A2 and B2, which are similar to samples A and B except for the growth duration. For both samples the LEO region is free of threading dislocations. The LEO region of sample A2 (Fig. 3a) contains a large number of dislocations with line direction along the <10$\bar{1}$0> direction (parallel to the stripe direction); a significant fraction of those dislocations bends towards the <11$\bar{2}$0> direction perpendicular to the stripe. Sample B2 (Fig. 3b) also exhibits dislocations with line direction parallel to the stripe direction, however their density is much smaller than for sample A2. Although additional microstructural studies are required to fully understand dislocation evolution during LEO, Fig. 3 clearly indicates that the LEO stripe overgrown in two steps contains much fewer extended defects than the stripes grown with the one-step process. This can be

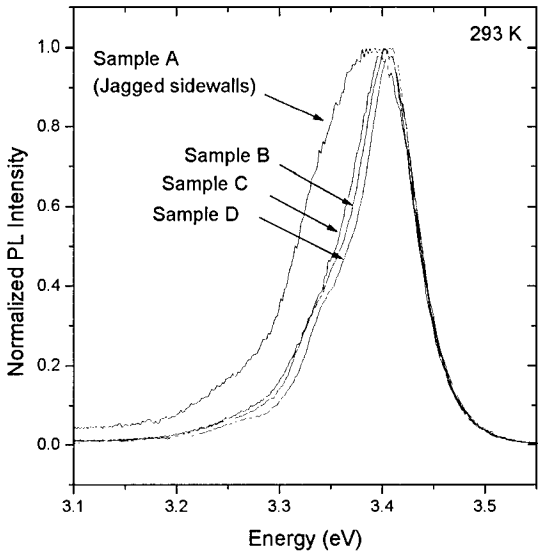


Figure 4 Room-temperature PL of samples A-D.

related to the facet configuration of the two samples: at the onset of the overgrowth only sample A2 has inclined facets that tend to favor the lateral spreading of dislocations (see e.g. Refs. 1 and 2).

Figure 4 shows the room-temperature PL spectra of samples A-D around the band edge of GaN. In this experiment the light emission from both the LEO and the seed regions was collected.[22] Sample A shows a fairly broad peak (FWHM ~120 meV) centered at 3.390 eV while samples B, C, and D have a narrower peak (FWHM ~75 meV) centered at ~3.405 eV. Although a detailed study of the optical properties is necessary to clarify the issue, the difference between the two sets of samples is most likely related to the residual strain in the LEO stripes, that is, samples B, C, and D are under slightly larger compressive stress than sample A.[8,9,10] The possibility that the incorporation of impurities depend on the stripe morphology cannot be excluded and could also explain some of the differences between the two sets of samples.

DISCUSSION

Figure 2 illustrates the effect of varying the TMG and NH_3 flow rates over a wide range of conditions while exposing only the $\{11\bar{2}0\}$ facets, which brings additional insight into the mechanisms of lateral growth. Comparing samples C and D indicates that the lateral growth rate increases with increasing NH_3 flow rate (or V/III ratio); on the other hand, comparing samples B and C indicates that the lateral growth rate increases when the partial pressure of both reactants is increased while keeping the input V/III ratio constant. Thus the NH_3 partial pressure appears to be more important in determining the lateral growth rate. The reasons for this are unclear but could be related to the difference in diffusivity in the gas phase or residence time on the various surfaces between the nitrogen and gallium species, such that the effective variation of partial pressures at the growing surface is significantly different than that of the input flow.

Our results indicate that the two-step process is suitable for increasing the lateral growth rate, which is a potential technological advantage. However, although samples B, C, and D exhibit a smooth morphology and a relatively low density of extended defects, their microstructure appears to be slightly inferior to that of typical samples grown with a slower lateral growth rate. Preliminary x-ray diffraction measurements indicate that the crystallographic tilt[4,7] between the seed region and the LEO region scales with the ratio r.[23] This tilt correlates with the density of edge dislocations observed above the edge of the mask opening and, correspondingly, at the merging front of two adjacent stripes. Therefore, the residual density of dislocations in a fully-coalesced LEO film is likely to be higher for a larger lateral growth rate. It is not clear, however, that this will be a limiting factor for the fabrication of devices based on LEO GaN.

Finally, we note that it is possible to extend the two-step scheme to variations of other growth parameters, such as growth temperature, carrier gas, total pressure, and doping level. Our preliminary results indicate that, in all cases, process variations that would normally be unfavorable to the $\{11\bar{2}0\}$ facets had little effect on the stripe morphology over a wide range of conditions provided that the overgrowth was initiated with smooth sidewalls. However we have observed that the $\{10\bar{1}1\}$ and $\{11\bar{2}2\}$ facets can reappear at very high fill factor and very low temperature, respectively. This suggests that the stripe morphology tends towards the equilibrium shape dictated by the driving forces (as set by the growth conditions[18]), but that the use of a seed to establish the initial morphology results in a kinetically-limited morphological evolution.

CONCLUSIONS

We have demonstrated a two-step process that results in a significant increase (up to a factor of 2.6) of the lateral growth rate while preserving smooth $\{11\bar{2}0\}$ sidewalls during the LEO of GaN stripes aligned in the $<10\bar{1}0>$ directions. The microstructure of the LEO stripes

grown with the two-step process is comparable to that of stripes grown using a conventional one-step process. The two-step process allows one to extend the range of growth conditions for LEO with $\{11\bar{2}0\}$ sidewalls to higher NH_3 partial pressure and higher V/III ratios, which should allow greater flexibility in the design of device structures based on LEO GaN.

ACKNOWLEDGEMENTS

This work was supported by ONR (C. Wood) and AFOSR (G. Witt), and made use of the MRL Central Facilities supported by the NSF under award DMR-9123048. HM acknowledges financial support from the NSERC (Canada) and a Raychem Fellowship. PF ackowledges financial support from a NDSE Graduate Fellowship provided by ONR.

REFERENCES

1. T.S. Zheleva, O.-H. Nam, M.D. Bremser, and R.F. Davis, Appl. Phys. Lett. 71, 2472 (1997).
2. A. Sakai, H. Sunakawa, and A. Usui, Appl. Phys. Lett. 71, 2259 (1997).
3. H. Marchand, J.P. Ibbetson, P.T. Fini, P. Kozodoy, S. Keller, J.S. Speck, S.P. DenBaars, and U.K. Mishra, MRS Internet J. Nitride Semicond. Res. 3, 3 (1998).
4. H. Marchand, X.-H. Wu, J.P. Ibbetson, P.T. Fini, P. Kozodoy, S. Keller, J.S. Speck, S.P. DenBaars, and U.K. Mishra, Appl. Phys. Lett. 73, 747 (1998).
5. H. Marchand, N Zhang, L. Zhao, Y Golan, P T Fini, J P Ibbetson, S. Keller, S P DenBaars, J S Speck, and U K Mishra, 25th Int. Symp. on Compound Semicond., Nara, Japan, 12-16 Oct. 1998.
6. O.-H. Nam, M.D. Bremser, T.S. Zheleva, and R.F. Davis, Appl. Phys. Lett. 71, 2638 (1997).
7. A. Sakai, U. Sunakawa, and A. Usui, Appl. Phys. Lett. 73, 481 (1998); A. Usui, H. Sunakawa, N. Kurado, A. Kimura, A. Sakai, and A.A. Yamaguchi, 2nd Int. Conf. on Blue Laser and Light Emitting Diodes, Chiba, Japan, Sept. 29 – Oct. 2, 1998.
8. J.A. Freitas, Jr., O.-H. Nam, R.F. Davis, G.V. Saparin, and S.K. Obyden, Appl. Phys. Lett. 72, 2990 (1998).
9 S. Chichibu, H. Marchand, S. Keller, P. Fini, J.P. Ibbetson, M. Minsky, S. Fleischer, J.S. Speck, J. Bowers, E. Hu, U.K. Mishra, S.P. DenBaars, T. Deguchi, T. Sota, and S. Nakamura, 2nd Int. Conf. on Blue Laser and Light Emitting Diodes, Chiba, Japan, Sept. 29 – Oct. 2, 1998.
10. X. Li, S.G. Bishop, and J.J Coleman, Appl. Phys. Lett. 73, 1179 (1998).
11. S. Nakamura, M. Senoh, S. Nagahama, N. Isawa, T. Yamada, T. Matsushita, H. Kiyoku, Y. Sugimoto, T. Kozaki, H. Umemoto, M. Sano, M. Chocho, Appl. Phys. Lett. 72, 211 (1998).
12. P. Kozodoy, J.P. Ibbetson, H. Marchand, P.T. Fini, S. Keller, S.P. DenBaars, J.S. Speck, U.K. Mishra, Appl. Phys. Lett. 73 975 (1998).
13. T. Mukai, K. Takekawa, S. Nakamura, Jpn. J. Appl. Phys. 37 L839 (1998).
14. C. Sasaoka, H. Sumakawa, A. Kimura, M. Nido, A. Usui, and A. Sakai, J. Cryst. Growth 189, 61 (1998).
15. R. Vetury, H. Marchand, J.P. Ibbetson, P.T. Fini, S. Keller, J.S. Speck, S.P. Denbaars, and U.K. Mishra, 25th Int. Symp. on Compound Semicond., Nara, Japan, Oct 12-16, 1998
16. D. Kapolnek, S. Keller, R. Vetury, R.D. Underwood, P. Kozodoy, S.P. DenBaars, and U.K. Mishra, Appl. Phys. Lett. 71 (1997) 1204.
17. Y. Kato, S. Kitamura, K. Hiramatsu, and N. Sawaki, J. Cryst. Growth 144, 133 (1994).
18. H. Marchand, J.P. Ibbetson, P.T. Fini, S. Keller, S.P. DenBaars, J.S. Speck, and U.K. Mishra, J. Cryst. Growth (in press).
19. The fill factor (FF) is defined as the ratio of the stripe opening width to the pattern period, such that an infinitely wide mask corresponds to FF=0 and a planar GaN film corresponds to FF=1.
20. J.P. Ibbetson, H. Marchand, P.T. Fini, X.H. Wu, S. Keller, S.P. DenBaars, J.S. Speck, and U.K. Mishra, 40th Electronic Materials Conference, Charlottesville, VA, 24-26 June 1998; H. Marchand, J.P. Ibbetson, P.T. Fini, S. Chichibu, S.J. Rosner, S. Keller, S.P. DenBaars, J.S. Speck, and U.K. Mishra, 25th Int. Symp. on Compound Semicond., Nara, Japan, Oct 12-16, 1998.
21. B.P. Keller, S. Keller, D. Kapolnek, W.N. Jiang, Y.-F. Wu, H. Masui, X.H. Wu, B. Heying, J.S. Speck, U.K. Mishra, and S.P. DenBaars, J. Electr. Mater. 24 (1992) 1707.
22. Selective-area PL measurements on LEO GaN and InGaN are reported in Ref. 9.
23. P.T. Fini, unpublished results.

TEM STUDY OF DEFECTS IN LATERALLY OVERGROWN GaN LAYERS

Z. Liliental-Weber, M. Benamara, W. Swider, J. Washburn, J. Park,* P. A. Grudowski,* C. J. Eiting,* and R. D. Dupuis*

Materials Science Division, Lawrence Berkeley National Laboratory, Berkeley CA 94720, 62/203
* Microelectronics Research Center, The University of Texas at Austin, Austin TX 78712-1100

Cite this article as: MRS Internet J. Nitride Semiconductor. Res. 4S1, G4.6 (1999)

ABSTRACT

Transmission electron microscopy was applied to study defects in laterally overgrown GaN layers, with initial growth on Al_2O_3 substrates followed by further growth over SiO_2 masks. Dislocations found in the overgrown areas show changes in line direction. Most dislocations propagate along c-planes. In the overgrown material planar defects (faulted loops) are present on c-planes and their presence is most probably related to segregation of excess point defects and impurities present in this material. They appear to be initiated by the fast lateral growth. Some dislocations with screw orientation become helical resulting from climb motion.

Formation of voids and also a high dislocation density was observed at the boundaries where two overgrowing fronts meet. Tilt and twist components were observed for these boundaries that were different for different overgrown strips grown in the same crystallographic direction suggesting that the GaN subgrain orientations on the two sides of a SiO_2 mask are responsible for the final tilt and twist value.

INTRODUCTION

Lack of good lattice match for epitaxial growth of GaN on Al_2O_3 or SiC results in high dislocation density. The lateral epitaxial overgrowth (LEO) technique is a promising method to reduce dislocation density in heteroepitaxial systems. It has recently been utilized in the deposition of GaN by metal organic chemical vapor deposition (MOCVD) [1-5]. The LEO approach consists of masking parts of the defective epilayer (GaN grown on Al_2O_3 or SiC) with thin strips of an amorphous layer so that the dislocations under the mask are prevented from propagating into the overgrown parts of the layer during subsequent growth. Several recent reports [1-7] for this type of growth show substantial reduction of threading dislocation density.

EXPERIMENTAL AND DISCUSSION

The III-N epitaxial films for this work were grown by low-pressure MOCVD in an EMCORE D125 reactor system at a pressure ~100 Torr and at temperatures in the range 1030¡C ² Tg ² 1100¡C. Hydrogen was used as the main process gas and also as the carrier gas for the metal alkyl sources. Trimethylgallium (TMGa), and trimethylaluminium (TMAl) were used as Column III precursors. High-purity ammonia was used as the N source. Typical molar flow rates were [TMGa] ~ $2x10^{-4}$ mole/min and [NH3] ~0.57 mole/min, resulting in V/III ratios ~2,800.

Mat. Res. Soc. Symp. Proc. Vol. 537 © 1999 Materials Research Society

First, (0001) GaN heteroepitaxial "substrates" were prepared by growing ~2 μm of doped or undoped GaN on (0001) sapphire at Tg ~1050¡C. Silicon dioxide (SiO_2) 100 nm thick was then used as a mask material to produce selective-area growth. These masks were then patterned exposing parallel or concentric strips. Overgrown strips oriented along the [1$\bar{1}$00] and [11$\bar{2}$0] directions have been studied.

Transmission electron microscopy was applied to study the structure of GaN films grown on these patterned substrates. Cross-section and plan-view thin films were prepared. Two types of overgrown areas were studied, those where overgrown areas were separated from each other and cases where overgrown areas were allowed to meet .

Different shapes of the overgrown strips for the separated overgrowths were observed (Fig. 1). A majority of the strips grown along [1$\bar{1}$00] direction had rectangular or trapezoidal shapes with flat surfaces on (0001). The walls of the rectangular strips were along (11$\bar{2}$0) planes, but in the trapezoidal strips the inclined walls were on (1$\bar{1}$01) planes. However, the strips grown along [11$\bar{2}$0] direction were triangular, with inclined walls along {1$\bar{1}$01} planes. Occasionally more complicated wall shapes were also observed. It appears that the shape or faceting is also influenced by impurity presence. Fig. 2 shows that the overgrowth started with a rectangular shape, but the shape changed presumably when impurities started to accumulate on the facet walls.

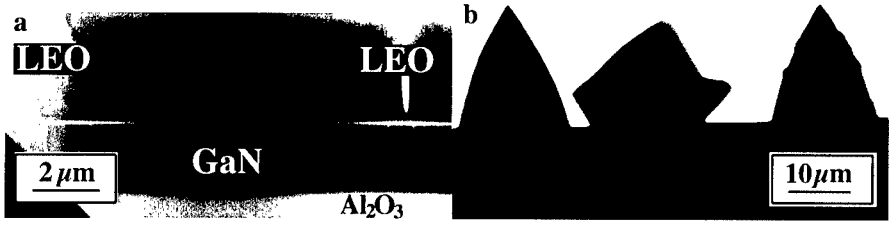


Fig. 1. Cross-section micrographs obtained for the GaN strips grown: (a) along [1$\bar{1}$00] and (b) [11$\bar{2}$0] directions.

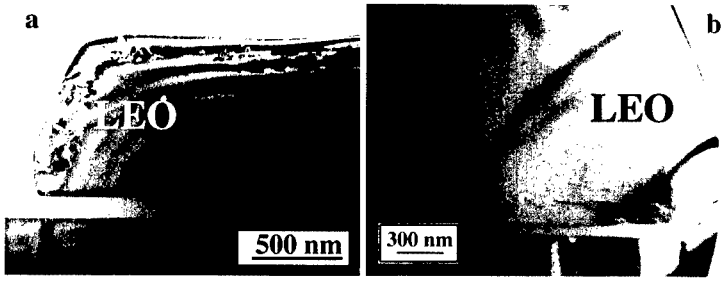


Fig. 2. (a) Cross-section TEM micrograph showing the shape of the overgrown strip near the SiO_2 mask edge. Note change of shape from rectangular to the inclined on (1$\bar{1}$01); (b) Micrograph showing bending of dislocations close to the SiO_2 mask.

Different types and different densities of defects were observed for the open areas between masks (homoepitaxial growth) and in the areas above the SiO_2 masks (lateral overgrowth). In the homoepitaxial parts threading dislocations were present with the dislocation density in the range of $7x10^8$ cm^{-2}. However, in the overgrown areas defect densities and their

type varied depending on the lateral growth rate, strip shape and depending on whether two strips came into contact with each other or if the strips remained separated. In the separated strips defect density was much lower.

Schematically the distribution of dislocations is shown in Fig. 3. In the free standing triangular strips all dislocations present in the homoepitaxial parts ("open mask") bend toward the side walls. At some particular hight of the triangle each threading dislocation will become close to a side wall. The image force will then cause dislocation bending toward the free surface in order to decrease the length of dislocation line. This phenomenon was previously observed in GaN for dislocations bending toward pinhole walls [8-9]. In this case only the triangular tip will be free of threading dislocations, as was also observed in the pyramids grown on SiC through circular openings [2].

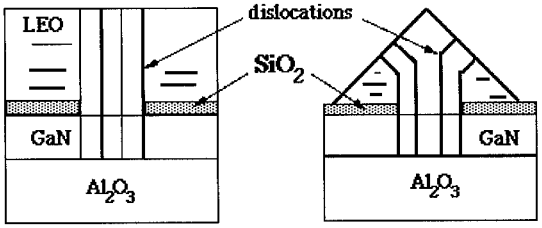


Fig. 3. Schematic showing bending of dislocations: (a) in the rectangular and (b) in the triangular shape strips.

In the case of the rectangular strips, depending on the lateral growth rate only a few of the dislocations located close to the SiO_2 mask edge will be at a close enough distance from the strip wall, that the image force can cause their bending toward the free surface. If the lateral growth rate is fast enough then bent dislocations should be found only close to the SiO_2 mask and further vertical growth over the mask should be threading dislocation free. This was observed experimentally (Fig. 2b). For areas above the SiO_2 mask no vertical threading dislocations along the c axis were observed.

Plan-view micrographs show a very specific distribution of dislocations. In the homoepitaxial parts defect density remains practically unchanged compared to traditional growth of GaN on sapphire. They are often distributed as small angle grain boundaries. At the border where lateral growth starts, dislocations elongated along the strip were observed (Fig. 4a). Some of them bend toward the side walls of the strips. Dislocation density in the overgrown areas is much smaller, and even when they are present their line direction is almost parallel to the sample surface. They do not propagate to the top layers. However, much higher density of dislocations (about 10^{12} cm-2) was observed where two strips meet (Fig. 4b). These dislocations will propagate to the layers grown on top. Different contrast on the two sides of such a border is observed showing the misorientation.

However, other typical defects are present in the overgrown areas. Planar defects such as faulted prismatic dislocation loops were observed. They are all formed on the c planes (Fig. 5a) and their density is in the range of 10^9-10^{10} cm^{-2}. These defects are similar to the defects observed in bulk GaN platelets grown from a Ga melt under a high hydrostatic pressure of nitrogen [10]. Because of the high growth rate in the lateral direction a growth mistake due to accumulation of point defects or impurities can lead to the formation of stacking faults on the c planes and therefore, to the formation of prismatic dislocation loops on these planes.

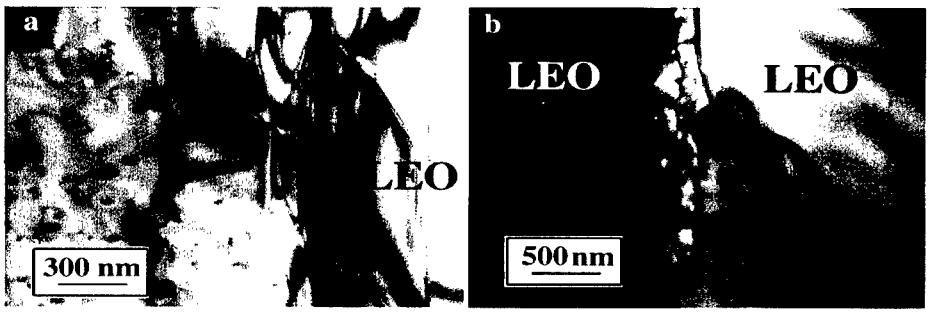


Fig. 4. Plan-view micrograph showing: (a) the interface between the homoepitaxial GaN with dislocations at grain boundaries and the area where the overgrowth starts with dislocation lines along the strip length; (b) meeting fronts of two strips showing high dislocation density.

This high growth rate in the lateral direction prevents formation of straight threading dislocations and the formation of pinholes and nanotubes. However, both these defects, pinholes and nanotubes were observed near the boundary where two overgrown fronts meet. At each such meeting front a large void was formed extending approximately about 10 nm above the oxide mask. In most cases such a void is like a pinhole with facets on $(1\bar{1}01)$ planes (Fig. 6). It is believed that formation of these voids is related to impurity accumulation at the meeting fronts (similarly as for formation of pinholes [8,9]). Only when the local impurity level decreases (at a greater distance from the SiO_2 mask) can such voids be overgrown.

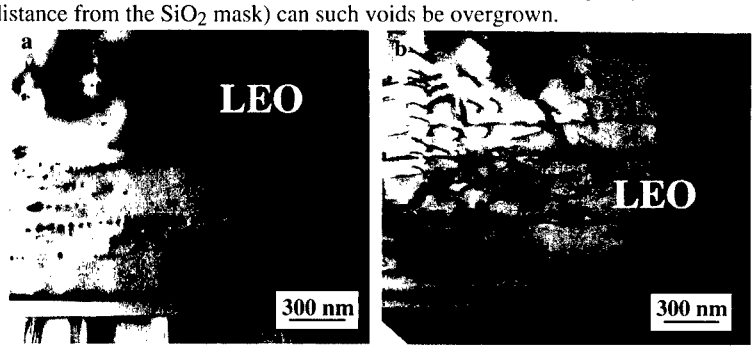


Fig. 5. Defects formed in the overgrown areas: (a) dislocation loops, (b) helical dislocations.

Misorientation between the two meeting growth fronts was also observed resulting in grain boundaries with much larger tilt and twist component than those normally observed in GaN grown on sapphire. Misorientation reveled by diffraction patterns taken on the two sides of the meeting fronts were different from strip to strip suggesting that this misorientation is determined by the particular subgrains from which the overgrowth starts. A very high dislocation density can be produced at the meeting points of two growing fronts. Mostly mixed and edge types of dislocations were formed in these areas. This high dislocation density is primarily a result of the misorientation between the two meeting growth fronts.

Beside planar defects on the c planes, helical dislocations were also observed in some overgrown areas suggesting a supersaturation of point defects. Accumulation of point defects could induce climb of straight dislocations having a screw orientation to form helical dislocations (Fig. 5b). Since these samples were not annealed after growth, it is believed that

excess point defects are formed during growth and that they subsequently condense on dislocations during cooling from the growth temperature.

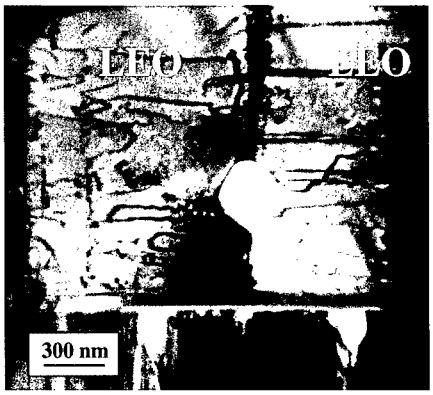


Fig. 6. Cross-section micrograph showing a void and dislocations at the meeting front of two overgrown strips

These results show that LEO samples contain three different areas with different types of defects and different defect densities. The homoepitaxial parts contain threading dislocations and other defects similar to traditionally grown samples. The laterally overgrown areas have planar defects (faulted dislocation loops), some bent threading dislocations and occasionally helical dislocations. Areas where two growth fronts meet, have voids and a high dislocation density at the boundary. It is logical to assume that by introducing a second SiO_2 mask over homoepitaxial areas and carrying out a second overgrowth it should be possible to practically eliminate threading dislocations in the sample. However, in order to do this an increased number of masks would be required, e.g. masks need to be placed over the homoepitaxial parts of the layers and also over the meeting fronts of the first overgrown areas.

CONCLUSIONS

These observations show that by lateral overgrowth one can decrease the density of threading dislocations intersecting the growth surface. These are the most deleterious defects for device structures, since they continue to propagate into the next layer grown on top of the GaN layer. Planar defects are still formed in the overgrown areas and their density can reach the same value as the density of threading dislocations in GaN grown directly on sapphire. However, planar defects formed on c-planes do not propagate into any layer grown on top and so might be much less damaging for device structures. Also the density of these defects may be related to the impurity level in the sample. Different types of masks (without oxygen) might lead to a lower density of planar defects. The faceting of overgrown stripes was influenced by the crystallographic orientation and probably by the presence of impurities (since growth along $[11\bar{2}0]$ direction immediately leads to facet formation on energetically favorable slow growth $(1\bar{1}01)$ planes inclined 62_i to the c-plane).

Two types of defects were observed in the overgrown areas: dislocations (which change their line direction from vertical toward horizontal (parallel to the c-plane) and planar defects-

mostly faulted dislocation loops that lie in the c plane. Occasionally helical dislocations were formed by interaction between screw dislocation segments and excess point defects.

At the boundaries where two growth fronts meet a much higher tilt and twist component was observed than that for subgrain boundaries in traditionally grown GaN. This misorientation was shown by diffraction patterns taken on the two sides of such boundaries. In addition, voids are also formed at these "meeting boundaries" which are most probably related to the presence of impurities, e.g. oxygen from the SiO_2 masks.

Lateral overgrowth does appear to be a promising technique to achieve lower defect density, especially if impurity levels can be further reduced.

ACKNOWLEDGMENT

TEM work was supported by the Director, Office of Basic Science, Materials Science Division, U.S. Department of Energy, under the Contract No. DE-AC03-76SF00098. The use of the facility at the National Center for Electron Microscopy at Lawrence Berkeley National Laboratory is greatly appreciated. Crystal growth was supported by the National Science Foundation under Grant No. DMR-93-12947, the NSF Science and Technology Center Program under Grant No. CHE-89-20120 and partially by ONR under contract N00014-95-1-1302, monitored by J. C. Zolper.

REFERENCES:

1. T.S. Zheleva, O.H. Nam, M.D. Bremser, and R.F. Davis, Appl. Phys. Lett. **71**, 2472 (1997).
2. T.S. Zheleva, O.H. Nam, J.D. Griffin, M.D. Bremser, and R.F. Davis, Mat. Res. Soc. Symp. **484**, 393 (1998).
3. D. Kaplonek, S. Keller, R. Ventury, R.D. Underwood, P. Kozodoy, S.P. DenBaars, and U.K. Mishra, Appl. Phys. Lett. **71**, 1204 (1997).
4. O.H. Nam, M.D. Bremser,T.S. Zheleva,and R.F. Davis, Appl. Phys. Lett. **71**, 2638 (1997).
5. H. Marchand, J.P. Ibbetson, P.T. Fini, P. Kozodoy, S. Keller, J.S. Speck, S.P. DenBaars, and U.K. Mishra, MRS Internet J. Nitride Semicond. Res. **3**, 3 (1998).
6. J. Park, P.A. Grudowski, C.J. Eiting, and R.D. Dupuis, Appl. Phys. Lett. **73**, 333 (1998).
7. R.D. Dupuis, J. Park, P.A. Grudowski, C.J. Eiting, and Z. Liliental-Weber, J. Cryst. Growth in print.
8. Z. Liliental-Weber, Y. Chen, S. Ruvimov, and J. Washburn, "Formation Mechanism of Nanotubes in GaN" Phys. Rev. Lett. **79**, 2835 (1997).
9. Z. Liliental-Weber, S. Ruvimov, W. Swider, Y. Kim, J. Washburn, S. Nakamura, R.S. Kern, Y. Chen, and J.W. Yang, MRS Proc. vol. **482**, 375 (1998).
10. Z. Liliental-Weber, C. Kisielowski, S. Ruvimov, Y. Chen, J. Washburn, I. Grzegory, M. Bockowski, J. Jun, and S. Porowski, J. Electr. Mat. vol. **25** #9, 1545-50.

EPITAXIAL LATERAL OVERGROWTH OF GaN WITH CHLORIDE-BASED GROWTH CHEMISTRIES IN BOTH HYDRIDE AND METALORGANIC VAPOR PHASE EPITAXY

R. Zhang[a,b], L. Zhang[a], D.M. Hansen[a], Marek P. Boleslawski[c], K.L. Chen[b], D.Q. Lu[b], B. Shen[b] Y.D. Zheng[b], and T.F. Kuech[a]

[a] Department of Chemical Engineering, University of Wisconsin, Madison, WI 53706
[b] Department of Physics, Nanjing University, Nanjing 210093, China
[c]Aldrich Chemical, Milwaukee, WI

Cite this article as: MRS Internet J. Nitride Semicond. Res. 4S1, G4.7 (1999)

ABSTRACT

Epitaxial lateral overgrowth (ELO) of GaN on SiO_2-masked (0001) GaN substrates has been investigated by using chloride-based growth chemistries via hydride vapor phase epitaxy (HVPE) and metal organic vapor phase epitaxy (MOVPE). Diethyl gallium chloride, $(C_2H_5)_2GaCl$, was used in as the MOVPE Ga precursor. The lateral and vertical growth rates as well as the overgrowth morphology of ELO GaN structures are dependent on growth temperature, V/III ratio and the in-plane orientation of the mask opening. A high growth temperature and low V/III ratio increase the lateral growth rate and produce ELO structures with a planar surface to the GaN prisms. High-quality coalesced and planar ELO GaN has been fabricated by both growth chemistries. The use of the diethyl gallium chloride source allows for the benefits of HVPE growth to be realized within the MOVPE growth environment.

INTRODUCTION

GaN and related compounds are being developed for short wavelength light-emitting devices, such as laser (LD) and light-emitting diodes (LED), in addition to high temperature and high power electronics. GaN-based LEDs and LDs have been successfully developed and are being commercialized. Several factors impede the further development of GaN devices. A principal difficulty is the high density of dislocations within the GaN epilayers, which can be as high as 10^8-$10^{10}/cm^2$ [1]. Recently, epitaxial lateral overgrowth (ELO) has been demonstrated to effectively reduce the dislocation density in the GaN epilayers within the lateral overgrown regions [2]. Long-lifetime GaN LDs fabricated on ELO-grown materials has been reported [3]. Most reports on GaN ELO have used the metalorganic vapor phase epitaxy (MOVPE) growth technique [4,5]. Hydride vapor phase epitaxy (HVPE) is also a very attractive technique for GaN ELO. HVPE utilizes GaCl generated *in situ* through the reaction of liquid Ga with HCl. HVPE offers a high growth rate and high material quality for GaN growth [6,7]. The typical growth rate can be as high as 100-200 μm/hr. The halide process has been shown to offer a higher lateral-to-vertical growth rate ratio [8] than MOVPE materials, which is critical for ELO. GaN produced by the HVPE technique does result in a greatly reduced intensity of the defect-based luminescence referred to as the yellow band (YL) when compared to the TMG-based MOVPE materials. This has been attributed to the lack of carbon in the HVPE growth system but is

Mat. Res. Soc. Symp. Proc. Vol. © 1999 Materials Research Society

present in the growth sources used in MOVPE-growth systems. Intentional carbon introduction into HVPE materials can result in the appearance of YL [9]. If a controlled amount of GaCl can be introduced into a cold wall MOVPE reactor, a low carbon source could be combined with the advantages of the MOVPE reactor environment. Diethyl gallium chloride (DEGaCl) is used here as a Ga source in GaN ELO growth. DEGaCl will decompose to GaCl through the β-elimination reaction in the gas phase allowing the *in situ* formation of GaCl at relatively low gas phase temperatures:

$$(C_2H_5)_2GaCl \rightarrow GaCl + 2C_2H_4 + H_2 \qquad (1).$$

The decomposition of the DEGaCl to GaCl near the growth front makes it possible to realize a high quality growth of GaN through a HVPE chemistry at high V/III ratio. This source was successfully used in GaAs growth that resulted in high uniformity, low carbon content GaAs film [10, 11]. GaAs selective area growth, with a complete selectivity of GaAs growth with respect to SiO_2, Si_3N_4, and Al_2O_3 masking materials, has been demonstrated over a wide range of process window [12,13,14]. The present work demonstrates the utility of the DEGaCl source in GaN ELO. In this paper, we systematically investigate the GaN ELO by using both HVPE and MOVPE with DEGaCl as the Ga source. It has been found that both the growth rate and the geometric shape of the GaN prisms are dependent on the growth condition and the orientation of the window opening. High growth temperatures and a low V/III ratio are helpful in enhancing the lateral overgrowth. Under optimized growth conditions, high quality ELO GaN films are produced with a planar surfaces and free of observable voids at the coalescence interface.

EXPERIMENTS AND RESULTS

The initial GaN 'substrate' is a 1μm thick GaN film grown by MOVPE on a (0001) sapphire substrate. The masking material a ~100nm thick patterned CVD SiO_2 layer. There are two kinds of pattern used in this study. The first pattern is a radial pattern consisting of many ~5 μm wide stripe openings in the masking materials with a 0.74° angle separation. An additional pattern consisted of 2-4μm wide parallel stripe openings on a 12μm pitch oriented along the $<1\bar{1}00>$ orientation. The substrates were used in a subsequent ELO GaN growth step in both HVPE and MOVPE systems, with DEGaCl as the Ga source in the latter case. In the HVPE process, the growth temperature is varied over the range of 1030-1100°C. The input V/III ratio, calculated as the ratio of the input NH_3 to input HCl flow rates, is controlled between 33 to 83 corresponding to a NH_3 mole fraction, $[NH_3]$, of 0.076-0.12. Nitrogen was used as the carrier gas. In the MOVPE process, the growth temperature is varied over the range of 1000-1100°C, while the input V/III ratio is varied over the range of 1800-3400. The hydrogen is used as the carrier gas in this case.

The extent and properties of the GaN ELO on SiO_2-masked substrates were determined. Both the growth rate and the morphology of ELO regions depend on the growth conditions and stripe or opening orientation. Figure 1 presents the typical growth morphology, obtained through scanning electron microscopy (SEM) on a HVPE GaN ELO sample on a radial patterned substrate using the growth conditions of T_g=1050°C, input mole fraction $[NH_3]$=0.12 and HCl input mole fraction of [HCl]=0.0022. In the Figure 1(a) is an image of an ELO GaN prism obtained within an opening oriented along the $<11\bar{2}0>$ direction while Figure 1(c) is an image of a $<1\bar{1}00>$-oriented prism. The prism shown in Figure 1(b) was formed in a direction

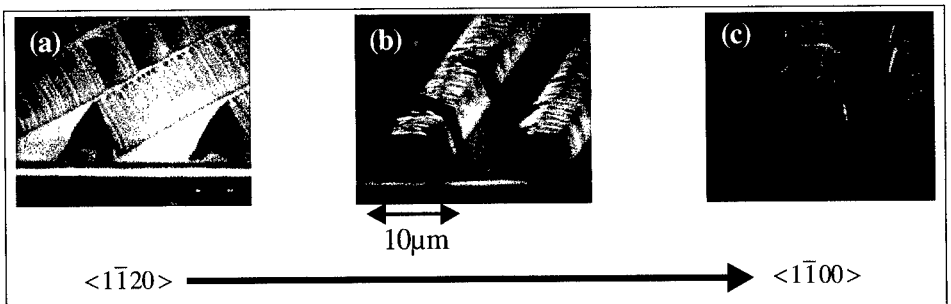


Figure 1: The orientation dependence of GaN ELO prisms grown by HVPE. The stripe opening was varied from the $<11\bar{2}0>$ to $<1\bar{1}00>$ in-plane directions.

intermediate to the $<11\bar{2}0>$ and $<1\bar{1}00>$ directions. The prism cross-section changes with the different stripe orientations. The cross-section of the $<11\bar{2}0>$ prisms is a triangle with a base angle of ~62°, which indicates that these prism sidewalls are $(1\bar{1}01)$ planes. The cross-sectional shape of the $<1\bar{1}00>$-oriented prism is a trapezoid. It is worthwhile to point out that the $<11\bar{2}0>$-oriented prism has the smoothest sidewalls, while the $<1\bar{1}00>$-oriented prism has much rougher sidewalls. This may indicate that the $(1\bar{1}01)$ planes are the more stable growth facets under these growth conditions. Both the lateral and vertical growth rates are dependent on the stripe opening orientation. From Figure 1, we find that the $<11\bar{2}0>$-oriented prism has the lowest lateral growth rate but the highest vertical growth rate. The $<1\bar{1}00>$-oriented prism has the highest lateral growth rate and the lowest vertical growth rate.

The SEM observations also reveal a strong dependence of the geometric prism shape on the specific growth conditions. Figure 2 shows two SEM micrographs of the cross-sections of GaN HVPE ELO prisms oriented along the $<11\bar{2}0>$ and $<1\bar{1}00>$ directions, respectively. The growth conditions employed for these samples were T_g=1100°C, $[NH_3]$=0.076 and [HCl]=0.023. The conversion efficiency of the HCl to GaCl is approximately 60-70%. As the growth

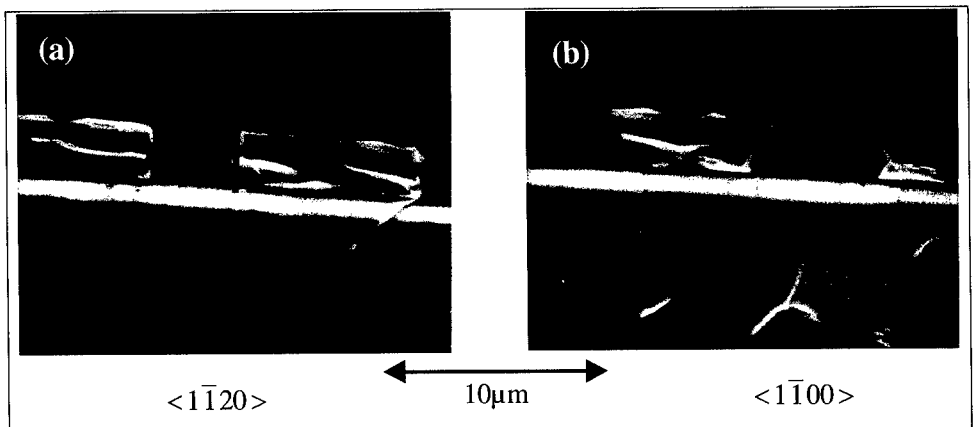


Figure 2: The orientation dependence of cross-sections of prisms grown under high temperature and low V/III ratio. The heavy lines indicate the bounding surfaces of the ELO regions.

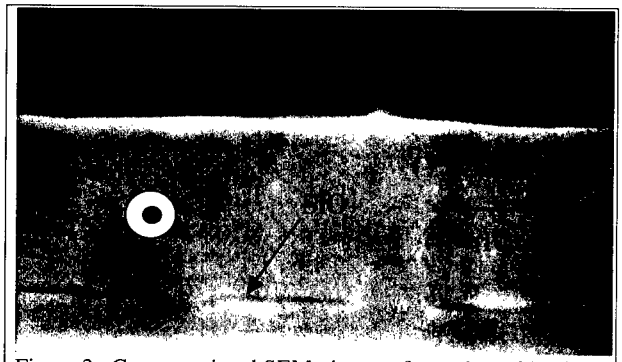


Figure 3: Cross-sectional SEM picture of a coalesced ELO GaN sample grown by HVPE. There is no void observed at the coalescence interface.

temperature is elevated and the V/III ratio decreased, the cross-sectional shape of the ELO prisms change. The $<11\bar{2}0>$ prism cross-section changes from a triangle to a rectangle, and that of the $<1\bar{1}00>$ prism changes from a trapezoid to a reverse-trapezoidal structure. The latter result has not been previously reported in the GaN ELO literature.

Under optimized growth conditions, high-quality coalesced ELO GaN films on parallel patterned substrates, having planar surfaces, have been fabricated by the HVPE technique. A cross-sectional SEM image of the coalesced film is shown in Figure 3. The growth temperature is 1100°C and $[NH_3]$=0.076, [HCl]=0.023 for this sample. No observable void was found at the coalescence interface under these conditions.

MOVPE GaN ELO, when using DEGaCl, exhibit similar trends to the HVPE samples. As shown in Figure 4, the MOVPE ELO GaN samples grown in $<1\bar{1}00>$-oriented parallel stripes under the same V/III ratio of 3500, have a changing morphology with growth temperature. The cross-section of ELO GaN prisms is strongly dependent on growth temperature over the range 1100°C to 1000°C. The cross-section of ELO GaN prisms grown at 1100°C is close to rectangular, while those of ELO GaN prisms grown at lower than 1050°C are triangular. The lateral growth rate of ELO GaN increases with increasing growth temperature while the growth temperature at this V/III ratio only weakly influences the vertical growth rate.

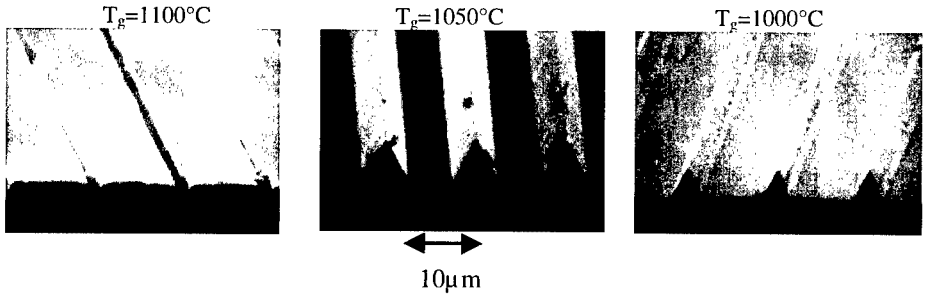


Figure 4: The growth temperature dependence of MOVPE ELO GaN by using DEGaCl on the $<1\bar{1}00>$ - oriented parallel stripes with a constant V/III ratio of 3500.

The dependence of MOVPE GaN ELO, using DEGaCl, on the V/III ratio during growth has been investigated and is shown in Figure 5. These GaN ELO samples were grown at the growth temperature of 1100°C over the V/III ratio range of 3500-1800. The cross-section of ELO GaN prisms grown with V/III ratio of 1800 is rectangular, while those of ELO GaN prisms grown with higher V/III ratio are trapezoidal, with sloping facets becoming evident. The lateral and vertical growth rates are somewhat dependent on the V/III ratio at this temperature with a lower V/III ratio leading to a higher vertical growth rate.

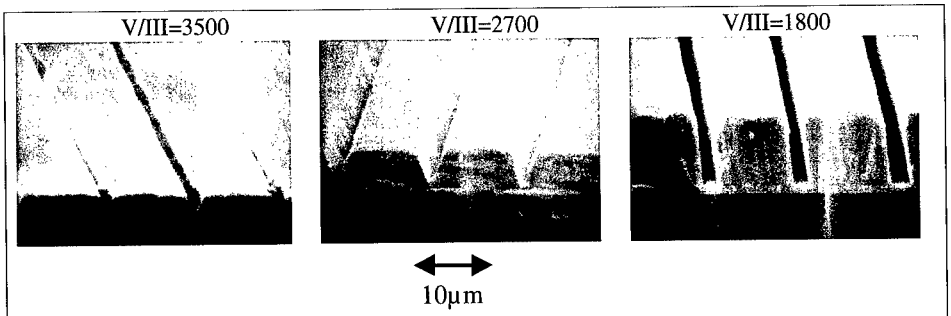


Figure 4: The dependence of MOVPE ELO GaN by using DEGaCl with the $<1\bar{1}00>$-oriented parallel stripes pattern at the constant growth temperature of 1100°C.

DISCUSSION

The resulting structure during the ELO process is known to be dependent on the gas phase transport of reactants to the growth front, which is dependent on the growth conditions and mask geometry. The difference in growth behavior between the inorganic, GaCl-based growth, and conventional MOVPE ELO using trimethyl gallium, also indicates that the growth chemistry plays an important role in the local growth rates and facet formation [8]. The chemical and physical properties of mask and substrate materials affect the surface diffusion [15], nucleation and kinetics. The lateral and vertical growth rates of ELO GaN are thus determined by the interplay of these various influences at the growth front. The local growth environments near a mask opening will differ from those in large-scale deposition and the optimization of the material properties and growth habit of the localized regions may be quite different from that found on non-masked regions. Under the conventional conditions for HVPE deposition, it has been suggested from the observed large surface roughness of HVPE-grown large scale GaN films that the (0001) plane is not the most stable growth facet [6]. Under such conditions, the most stable growth front is thought to be the $(1\bar{1}01)$ planes. Higher growth temperatures and lower V/III ratios decrease the supersaturation (driving force) [8]. The resulting lower growth rate would enhance the surface diffusion rate of reactants over the (0001) plane to adjacent, more favored growth facets and result in a higher lateral growth rate and a variety of prismatic structures. The use of a chloride-containing Ga source in both these systems allows for the addition of several chemical reactions to the growth front chemistry. The simplest set of chemical reactions important at the GaN growth front in the case of chloride-based growth is:

$$GaCl + NH_3 \rightarrow GaN + HCl + H_2 \qquad (2)$$

$$GaN + HCl \Leftrightarrow GaCl + \frac{1}{2}N_2 + \frac{1}{2}H_2 \qquad (3)$$

where in the DEGaCl case, the GaCl is generated through the intramolecular decomposition of the growth source as presented in Equation 1. Reaction 3 implies equilibrium between the steady state concentrations of HCl and GaCl at the growth front. The MOVPE growth front has often been considered to be near thermodynamic equilibrium [16]. If this is the case for the high temperature growth of GaN, the supersaturation at the growth front will decrease with increasing temperature due the reversible reaction associated with the HCl reacting at the GaN surface. A similarity between the growth habits and behavior between the HVPE and MOVPE-DEGaCl systems is therefore expected.

The presence of chlorine in the growth system can modify the growth habit from the trimethyl gallium based growth. Experimentally, the chloride-based systems lead to both higher lateral-to-vertical growth and desirable growth facets, such as vertical sidewalls over a broader

range of growth conditions. The near surface concentration of GaCl in the HVPE system is higher than in the DEGaCl systems. If adsorbed chlorine or GaCl species can stabilize certain facets, the higher concentration of GaCl within the HVPE would more readily promote the formation of specific facets, such as the $\{1\bar{1}00\}$ planes, over the DEGaCl-based MOVPE growth. Regardless of the specific chemical mechanism, the use of GaCl within either of these systems leads to improved ELO characteristics over conventional MOVPE growth using simple metal alkyls.

CONCLUSIONS

ELO of GaN has been systematically investigated by using chloride-based growth chemistry in both HVPE and MOVPE, through the use of DEGaCl, systems. The lateral and vertical growth rates as well as the morphology of the ELO regions depend on the growth condition and orientations of opening stripes. The high growth temperatures and a low V/III ratio enhance the lateral overgrowth. The reverse trapezoid prism has been fabricated in $[1\bar{1}00]$ stripes under the growth temperature of 1100°C and the V/III ratio of 33. Under the optimized ELO conditions, high quality flat-topped and coalesced GaN ELO films have been successfully fabricated and no observable voids found at the coalescence interface.

ACKNOWLEDGEMENTS

R. Z., K.L. Chen, D.Q. Lu, B. Shen and Y.D. Zheng thank the financial support of the China "863" national high-tech development program. The authors would like to acknowledge the financial support of the ONR MURI on Compliant Substrates, and the facilities support of the NSF Materials Research Science and Engineering Center on Nanostructured Materials and Interfaces, USA.

REFERENCES

1 F.A. Ponce and D.P. Bour, Nature, **386**, 351(1997).
2 A. Sakai, H. Sunakawa and A. Usui, Appl. Phys. Lett., **71**, 2259(1997).
3 S. Nakamura, M. Senoh, S. Nagahama, N. Iwase, T. Yamada, T. Matsushita, H. Kiyoku, Y. Sugimoto, T. Kozaki, H. Umemoto, M. Sano and K. Chocho, Appl. Phys. Lett., **72**, 211(1998).
4 O-H. Nam, M.D. Bremser, T.S. Zheleva and R.F. Davis, Appl. Phys. Lett., 71, 2638(1997)
5 H. Matsushima, M. Yamaguchi, K. Hiramatsu and Sawaki, Proc. 2nd Int. Conf. Nitride Semiconductors, Tokushima, Japan, 1997, p492.
6 N.R. Perkins, M.N. Horton, Z.Z. Bandic, T.C. McGill and T.F. Kuech, Mat. Res. Sci. Symp. Proc. **395**, 243 (1996).
7 R.J. Molnar, K.B. Nichols, P. Maki, E.R. Brown and I. Melngailis, Mater. Res. Soc. Symp. Proc., **378**, 479 (1995).
8 J-O Carlsson, Solid State & Mater. Sci., **16**, 161(1990).
9 R. Zhang and T.F. Kuech, Appl. Phys. Lett. 72, 1611-1613 (1997).
10 T. F. Kuech, R. Potemski and F. Cardone *J. Cryst. Growth* V124, 318-325 (1992).
11 A. Narmann, M.L.Yu *Surface Science* V270, 1041-1047 (1992).
12 T.F. Kuech, *J. Cryst. Growth* V115, 52-60 (1991).
13 Ko-ichi Yamaguchi, K. Okamoto, *Jpn. J. Appl. Phys.* V32 4885-4888, (1993).
14 Y. Shiraishi, N. Furuhata, A. Okamoto, *J. Cryst. Growth* V182, 255-265 (1997).
15 A. Usui and T. Nishinaga, Jpn. J. Appl. Phys., **36**, L899(1997).
16 G.B. Stringfellow, *Organometallic Vapor Phase Epitaxy*, (Academic Press, San Diego, 1989) Chap. 3.

GAN: FROM SELECTIVE AREA TO EPITAXIAL LATERAL OVERGROWTH

X. Li, S. G. Bishop and J. J. Coleman

University of Illinois, Urbana, IL 61801

Cite this article as: MRS Internet J. Nitride Semicond. Res. 4S1, G4.8 (1999)

ABSTRACT

The evolution of the topography of GaN stripes as a function of stripe width (2 – 120 μm), fill factor and substrate smoothness has been explored. The spatially resolved optical properties of these structures have been characterized by cathodoluminescence imaging and line scans. Implications from the optical study have been discussed.

INTRODUCTION

Epitaxial lateral overgrowth (ELO) of GaN on patterned substrates has been widely studied since the realization of a long lifetime GaN-based laser diode (LD) using this technique.[1] It is believed that ELO reduces dislocation density by blocking the dislocation propagation from the under layer using the oxide mask. Using ELO to reduce dislocation density on mismatched heteroepitaxial semiconductor layers can be dated back to the extensive study of ELO by liquid phase epitaxy (LPE) by Nishinaga *et al.*[2] It has been demonstrated by many groups that the application of this technique leads to the growth of extremely low dislocation density materials including GaAs, InP, Ge_xSi_{1-x} on Si substrates and InGaAs on a GaAs substrate. In addition, the ELO technique is useful to relieve stress caused by both the lattice mismatch and the difference in thermal expansion coefficient.[3]

An ELO process starts from a basic selective area epitaxial (SAE) substrate which is usually patterned lithographically with a dielectric material such SiO_2 or SiN_x as the mask. In the ideal SAE case, deposition can only take place within the openings but not on the mask. However, lateral growth on top of the mask beyond the opening is possible. Illustrated in Figure 1 (cross-section view) are three possible types of sidewall growth topographies for stripe patterns. In the case of Figure 1(a), there is zero tendency for lateral growth and a rectangular cross section with the same width as the mask opening is obtained. GaN rectangular shaped waveguides and GaN hexagonal microprisms with smooth vertical facets have been fabricated.[4,5] In the case of a nonzero ratio of lateral-to-vertical growth rate, which depends on the mask pattern and the growth conditions, growth beyond the opening can be obtained (Figure 1(b)). Kapolnek *et al.* have reported anisotropy in GaN epitaxial lateral growth.[6] Prolonged growth leads to the coalescence of adjacent selectively grown stripes and a flat surface across the entire substrate, as demonstrated by Nam *et al.* for GaN growth using SiC substrates.[7] Figure 1(c) shows another type of topography where the vertical growth planes face out as growth proceeds and a triangular cross section is developed. For GaN selective growth on a 10 μm wide stripe, Kato *et al.* identified the side facets of the triangle as (1101).[8] Prolonged growth in this case also leads to the coalescence of the selectively grown stripes by growing on the side facets of the triangle, and eventually the top surface will level off. Usui *et al.* have recently demonstrated the growth of a continuous thick GaN film with low dislocation density by hydride vapor face epitaxy (HVPE) from the coalescence of (1101) facets on the oxide mask.[9] We have previously reported the selective growth of GaN by atmospheric pressure MOCVD, with focus on the topography and optical properties of the wide stripes (50 - 125 μm).[10] Recently, we have also demonstrated the ELO of GaN from narrow stripes (2 – 6 μm) with triangular cross sections and

Mat. Res. Soc. Symp. Proc. Vol. 537 © 1999 Materials Research Society

explored the spatially resolved optical properties at each ELO stage.[11] In this paper, we explore the evolution of topography of GaN structures grown by SAE and subsequent ELO as a function of pattern geometry and growth parameters. We also discuss the origin of different emission bands of GaN through spatially resolved cathodoluminescence study.

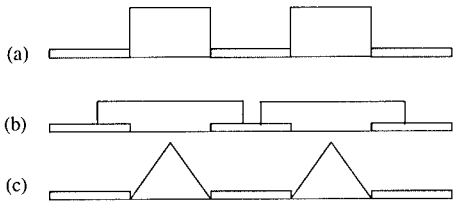


Figure 1 A schematic of three types of growth topography (cross section) for stripe patterns (a) SAE with vertical sidewalls. (b) ELO with vertical sidewalls (c) SAE with triangular cross section.

EXPERIMENTAL

The GaN growth was carried out in a vertical configuration atmospheric pressure MOCVD reactor. TMGa and NH_3 were used as Ga and N precursors, respectively. H_2 was used as a carrier gas. A buffer layer grown at ~ 550°C was deposited on (0001) sapphire substrate before the growth of GaN epi-layer. Lithographically defined patterns were formed either on a 3 μm thick GaN epilayer or directly on a GaN buffer layer. Patterns studied include stripes (50 – 120 μm) spaced by 350 μm, arrays of narrow stripes (2- 6 μm wide) spaced by 2 – 10 μm between stripes and by 350 μm between stripe arrays. A cross structure (25 x 80 μm) is also studied in this report. The stripes were oriented either perpendicular or parallel to the sapphire $(11\bar{2}0)$ flat. Under our typical growth condition, the lateral growth rate for these two directions differ by a factor of 1.5. The patterned samples were then heated under NH_3 in the MOCVD chamber to ~1020°C for the growth of the GaN overlayer. A Zeiss SEM equipped with Oxford MonoCL setup was used for morphology and optical characterization. All cathodoluminescence (CL) spectra and images were taken at room temperature. A DI nanoscope III AFM was used for topography measurements. Details of the growth condition and the CL setup have been described previously.[10,12]

RESULTS AND DISCUSSION

1. Topography Evolution

1.1 Topography Evolution with stripe width

We have grown GaN wide stripes (25 – 120 μm) spaced by 350 μm on a 3 μm thick GaN epilayer. Figure 2 shows an AFM image of a 75 μm wide stripe. Growth rate enhancement is a common phenomenon in selective area epitaxy, due to the lateral diffusion of source materials from the masked to the open area. The nominal growth thickness in this case is 0.2 μm. The enhancement factor is in the range of 5 – 10 from the stripe center to the edge. Under the specified experimental condition, 5 μm-wide plateaus are observed at the edges. As previously reported, the width of the terraces do not appear to change with stripe width and presumably is limited by the surface diffusion length of the Ga species.[10] Note that wide stripes grown directly on a low-temperature-grown buffer layer do not form wide plateaus, probably because of the smaller diffusion length due to rough surface.

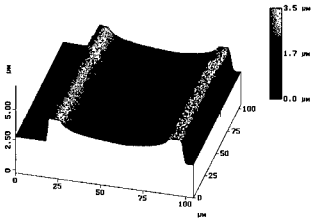


Figure 2 AFM image of a 75 μm GaN stripe grown on a 3 μm GaN epilayer.

Figure 3 shows a SEM image of a cross structure and an AFM image of part of the cross. As in the case of stripes, plateaus are observed at the edges of the cross. The plateau shape is different because the concentration gradient of the source materials, which drives the lateral diffusion, depends on the geometry of the pattern. For stripes, diffusion comes from both sides of the stripe equally. For a cross structure of this width, the lateral diffusion of source materials between the two arms goes to both arms, while the middle of the convex edge of the cross gets enhancement similar to the stripe case. In fact, the width of the plateau at the middle point of the convex edge is about 5 um, as is the case for the stripes. Note that the rough morphology of the edges in this structure can be improved by increasing the NH_3 flow, as described in the previous paper for the stripes.[10]

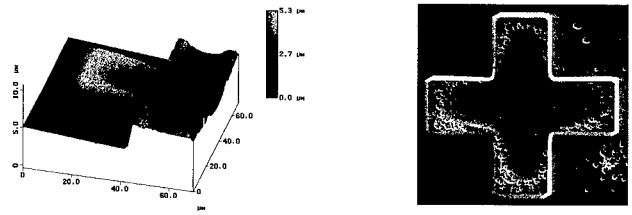


Figure 3 Right: SEM image of a 25 μm cross structure. Left: AFM image of the same structure, partial. The arm width of the cross is 25 μm and the length is 80 μm.

Based on the nature of the plateau, one can speculate that as the stripe width decreases, the stripe should continue having the two plateaus on both sides but the concave profile in the middle should be reduced with stripe width. Furthermore, for stripes narrower than the plateau width (5 μm in this case), the top should be leveled. Figure 4 shows an AFM image of an array of 3.5 μm wide stripes and its cross section. Indeed, these stripes show flat tops and vertical sidewalls. This is the case illustrated in Figure 1(a).

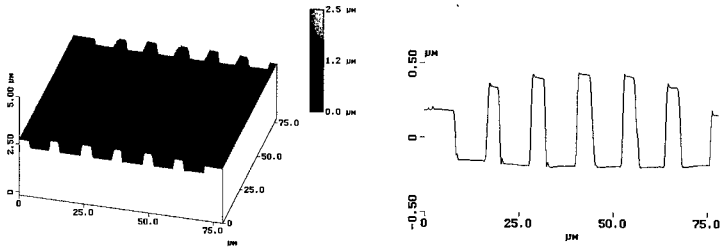


Figure 4 an AFM image of an array of 3.5 μm wide stripes (left) and its cross section (right).

1.2 Topography evolution with growth condition

However, stripes with triangle cross sections, case (c) in Figure 1, can be formed easily. Shown in Figure 5 is an array of 5 μm wide stripes with triangular cross sections. It has been reported that the topography of the stripes depends on pattern orientation and growth parameters such as growth temperature, flow rates and V/III ratios.[13-15] We report here that two other factors also play a role: fill factor (ratio of open to masked area) and surface roughness. (1) Fill factor effect: a small fill factor (e. g. narrow stripes near a large masked area) favors the formation of triangular cross sections. Smaller fill factor give rise to larger effective flow rate of Ga species due to lateral enhancement from the masked region, and thus smaller surface diffusion length on the (0001) surface. (2) Surface roughness effect: SAE directly on a low-temperature-grown buffer layer (rough) yields triangular stripes while SAE on a high quality GaN epilayer yields rectangular stripes. Rough surface also results in smaller surface diffusion length. The above observation and analysis are consistent with the following picture: the small diffusion length on the (0001) plane makes it a fast and thus invisible growth plane because the adsorbed Ga species do not diffuse to the side walls. Our hypothesis is consistent with that proposed by Nam *et al.* in their study of the effect of Ga flow rate on the stripe morphology.[14]

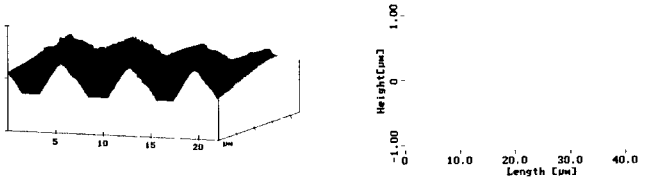


Figure 5 an AFM image of an array of 5 μm wide stripes and its cross section.

Similar to the rectangular shaped stripes, prolonged growth over these triangular stripes also lead to lateral overgrowth on the masked area. [9,11]

2. Spatially resolved optical characterization

2.1 Reverse contrast between yellow and band-edge emission

It has been proposed that yellow emission originates from threading dislocations and threading dislocations quench band-edge luminescence.[16,17] Figure 6 and 7 show two cases where precise reverse contrast between the band-edge and yellow emission has been observed in CL imaging.

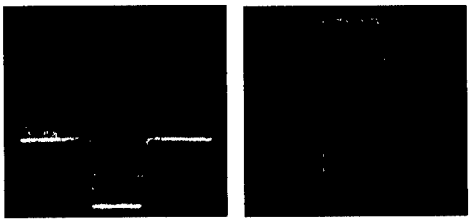


Figure 6 CL images of the cross taken at 360 nm (left) and 560 nm (right). See Figure 3 for the corresponding SEM image.

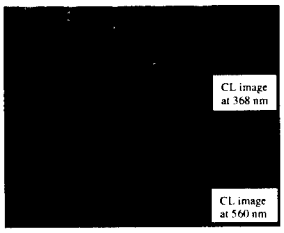


Figure 7 CL images of an array of triangular stripes with 3.7 μm opening and 5 μm spacing taken at 368 nm (upper) and 560 nm (lower).

It is important to note that precise reverse contrast is not observed in all of our samples. Locations with stronger band-edge emission sometimes also show strong yellow band. Figure 4 in reference 11 is an example of the non-reversed contrast between yellow and band-edge emission. TEM analysis of samples with reverse and identical contrast in CL imaging of band-edge and yellow emission is underway to investigate whether threading dislocations are the source of yellow band.

2.2 Donor-acceptor pair (DAP) recombination

Shown in Figure 8 are the CL images taken at 385 nm (DAP recombination)[10] for the cross structure and a 50 μm stripe. For the 50 μm stripe, the first group of bright lines appears at the boundaries between the plateaus and the concave profiles. They are oriented along the stripe direction. The second group appears at the boundary between the steep walls of the concave profile and its largely flat middle part (see Figure 2 for profile). For the cross, strong DAP emission appears at the boundary between plateaus and the concave profile. This implies that DAP recombination is associated with stress created by high aspect ratio in topography.

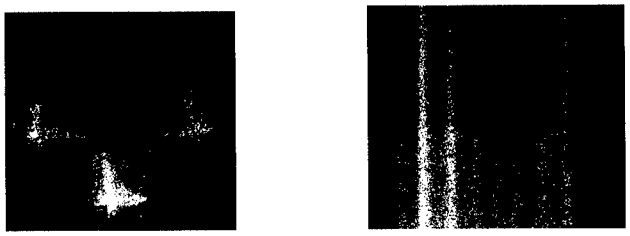


Figure 8 CL images taken at 385 nm for the cross structure (left, see Figure 3 for its SEM image) and a 50 μm stripe (topography is similar to the 75 μm stripe shown in Figure 2).

2.3 ELO of GaN: improvement of optical properties

Shown in Figure 9 are the CL images (top) and line scans (bottom) taken at 368 nm (left) and 560 nm (right) for an array of stripes with triangular cross sections, at the ELO stage before coalescence. These stripes were grown on a GaN buffer layer. Topography is similar to the one shown in Figure 5. The original stripe opening defined by lithography patterning is 5 μm and the spacing is 7 μm. For the CL distribution in the opening region, see Figure 7 and related text for discussion. It is apparent, especially from the CL line scan, that the ELO part of GaN show stronger band-edge emission (dip in the line scan is due to the gap between stripes) and weaker yellow emission than the GaN grown in the stripe opening. Similar optical characterization showing the improvement of band-edge and yellow emission through the ELO of GaN stripes with rectagular cross sections has been reported.[18,19] In addition, we have observed the appearance of the free exciton peak in the ELO region.[11]

Assuming the ELO region has low dislocation density as reported by other groups,[7] the weak yellow band in the ELO region may indicate that yellow band emission is associated with dislocations. However, it could also be a result of reduced strain in the ELO material. Furthermore, point defects and impurity level in the ELO region and the vertical grown region may also be different, which could contribute to the reduction of the yellow band.

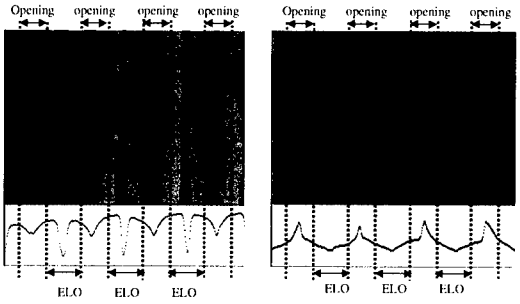


Figure 9 CL images and line scans taken at 368 nm (left) and 560 nm (right) for an array of stripes at the ELO stage before coalescence with triangular cross section.

SUMMARY

We have reported the topography evolution of GaN stripes as a function of pattern geometry, growth parameters and substrate. Wide stripes with the plateaus on both sides evolve with stripe width into flat top stripes with vertical sidewalls. Small fill factor and rough substrate favor the formation of triangular stripes. These GaN structures have been characterized by CL and implications of the spatial correlation of optical properties have been discussed.

ACKNOWLEDGEMENT

The authors wish to thank D. S. Roh and A. M. Jones for technical assistance and X. Li would like to acknowledge the support of a NSF Grant (DMR-9714289).

REFERENCES

[1] S. Nakamura, M. Senoh, S. Nagahama et al. *Appl. Phys. Lett.* **72**, 211 (1998).
[2] T. Nishinaga, T. Nakano and S. Zhang, *Jpn. J. Appl. Phys.* **27**, L964 (1988).
[3] S. Naritsuka and T. Nishinaga, *J. Cryst. Growth* **174**, 622 (1997).
[4] T. Tanaka, K. Uchida, A. Watanabe, and S. Minagawa, *Appl. Phys. Lett.* **68**, 976 (1996).
[5] T. Akasaka, Y. Kobayashi, S. Ando, and N. Kabayashi, *Appl. Phys. Lett.* **71**, 2196 (1997).
[6] D. Kapolnek, S. Keller, R. Vetury, R. D. Underwood, P. Kozodoy, S. P. Den Baars, and U. K. Mishra, *Appl. Phys. Lett.* **71**, 1204 (1997).
[7] O. Nam, M. D. Bremser, T. S. Zheleva, and R. F. Davis, *Appl. Phys. Lett.* **71**, 2472 (1997) and T. S. Zheleva, O. Nam, M. D. Bremser, and R. F. Davis, *Appl. Phys. Lett.* **71**, 2638 (1997).
[8] Y. Kato, S. Kitamura, K. Hiramatsu, N. Sawaki, *J. Cryst. Growth* **144**, 133 (1994).
[9] A. Usui, H. Sunakawa, A. Sakai and A. A. Yamaguchi, *Jpn. J. Appl. Phys.* **36**, L899 (1997).
[10] X. Li, A. M. Jones, S. D. Roh, D. A. Turnbull, S. G. Bishop, and J. J. Coleman, *J. Electron. Mater.* **26**, 306 (1997). X. Li, A. M. Jones, S. D. Roh, D. A. Turnbull, E. E. Reuter, S. Q. Gu, S. G. Bishop, and J. J. Coleman, *Mater. Res. Soc. Sym. Proc.* **395**, 943 (1996).
[11] X. Li, S. G. Bishop and J. J. Coleman, *Appl. Phys. Lett.* **73**, 1179 (1998).
[12] X. Li and J. J. Coleman, *Appl. Phys. Lett.* **70**, 438 (1997).
[13] J. Park, P. A. Grudowski, C. J. Eiting, and R. D. Dupuis, *Appl. Phys. Lett.* **73(3)**, 333 (1998).
[14] O. Nam, T. S. Zheleva, M. D. Bremser, and R. F. Davis, *J. Electron. Mater.* **27**, 233 (1998).
[15] H. Marchand, preprints.
[16] S. J. Rosner, E. C. Carr, M. J. Ludowise, G. Girolami, H. I. Erikson, *Appl. Phys. Lett.* **70**, 420 (1997).
[17] F. A. Ponce, D. P. Bour, W. Gotz , P. J. Wright, *Appl. Phys. Lett.* **68**, 57 (1996).
[18] J. A. Freitas, Jr., O. Nam, R. F. Davis, G. V. Saparin, and S. K. Obyden, *Appl. Phys. Lett.* **72**, 2990 (1998).
[19] Z. Yu , M.A.L. Johnson, T. Mcnulty, J.D. Brown, J.W. Cook,Jr, J.F. Schetzina, *MRS Internet J. Nitride Semicond. Res.* **3**, 6(1998).

PROCESS ROUTES FOR LOW DEFECT-DENSITY GAN ON VARIOUS SUBSTRATES EMPLOYING PENDEO-EPITAXIAL GROWTH TECHNIQUES

K.J. Linthicum*, T. Gehrke*, D.B. Thomson*, K.M.Tracy*, E.P. Carlson*, T. P. Smith*, T.S. Zheleva**, C.A. Zorman***, M. Mehregany***, and R.F. Davis*

*Department of Materials Science and Engineering, North Carolina State University, Raleigh, NC 27965, Kevin_Linthicum @NCSU.EDU

**U.S. Army Research Laboratory, AMSRL-SE-EM, Adelphi, MD 20783

***Department of Electrical, Systems and Computer Engineering and Science, Case Western Reserve University, Cleveland, OH 44106

Cite this article as: MRS Internet J. Nitride Semicond. Res. 4S1, G4.9(1999)

ABSTRACT

GaN films have been grown on 6H-SiC substrates employing a new form of selective lateral epitaxy, namely pendeo-epitaxy. This technique forces regrowth to start exclusively on sidewalls of GaN seed structures. Both discrete pendeo-epitaxial microstructures and coalesced single crystal layers of GaN have been achieved. SEM and TEM analysis are used to evaluate the morphology of the resulting GaN films. Process routes leading to GaN pendeo-epitaxial growth using silicon substrates have also been achieved and the preliminary results are discussed.

INTRODUCTION

The III-nitride scientific community has been forced to grow thin films of GaN and related nitride materials using heteroepitaxial growth routes and techniques because of the dearth of bulk substrates of these materials. The resultant 10^8 – 10^{10} cm^{-2} density of threading dislocations limits the properties of the resulting films and the devices fabricated in these materials. As such, there has been substantial research regarding selective area growth (SAG) and lateral epitaxial overgrowth (LEO) techniques for GaN deposition [1-9], fueled in part by the recent announcement by Nakamura, et al. [10] of the dramatic increase in projected lifetime of their GaN-based blue light-emitting laser diodes fabricated on LEO material. Using these approaches, researchers have been able to grow GaN films containing dislocation densities of ≈ 10^5 cm^{-2} in the areas of overgrowth. However, to benefit from this reduction in defects, the placement of devices incorporating LEO technology is limited and confined to regions on the final GaN device layer that are located on the overgrown regions.

In this paper, we report the achievement of a new approach to selective epitaxy of GaN, namely, pendeo- (from the Latin: to *hang* or be *suspended*) epitaxy (PE) as a promising new process route leading to a continuous, large area layer or discrete platforms of this material. An initial form of GaN pendeo-epitaxy without the use of a seed-mask was first reported by Zheleva et.al. [11]. The current approach incorporates mechanisms of growth exploited by the conventional LEO process by using an amorphous mask to prevent vertical propagation of threading dislocations; however, it extends beyond the conventional LEO approach to employ the substrate itself as a *pseudo-mask* as discussed by Linthicum et.al. [12]. This unconventional approach differs from LEO in that growth does not initiate through open windows on the (0001) surface of the GaN seed layer, instead it is forced to selectively begin on the side walls of a

Mat. Res. Soc. Symp. Proc. Vol. 537 © 1999 Materials Research Society

tailored microstructure comprised of forms previously etched into the seed layer. Continuation of the pendeo-epitaxial growth until coalescence over and between these forms results in a complete layer of low defect-density GaN. This is accomplished in one regrowth step, and the need to align devices or masks for the growth of a second layer over particular areas of overgrowth on the final GaN layer is eliminated. This approach may be more widely applicable than just GaN, as indicated by Gehrke et.al. [15]. Additionally, we report for the first time the ability to grow GaN pendeo-epitaxial films on silicon substrates. The achievement of GaN layers with surface areas limited only by the size of the available silicon substrates is now conceivable.

The following sections describe the experimental parameters necessary to achieve GaN films via PE, describe and discuss the microstructural evidence obtained for the resulting films and provide a summary of this research.

EXPERIMENTAL PROCEDURES

Each pendeo-epitaxial GaN film and the underlying GaN seed layer and the AlN buffer layer were grown in a cold-wall, vertical pancake style RF inductively heated metallorganic vapor phase epitaxy (MOVPE) system. Two distinct process routes were explored for growth on (i) on-axis (0001)6H-SiC substrates and (ii) on-axis (111)Si substrates. In the former, each seed layer consisted of a 1 μm thick GaN film grown on a 100 nm thick AlN buffer layer previously deposited on a (0001) 6H-SiC substrate. Details of the experimental parameters used for the growth of these two layers are given in Ref. 13. In the growth on the Si substrates, a 1 μm (111)3C-SiC film was initially grown on a very thin (111)3C-SiC layer produced by conversion of the (111)Si surface via reaction with C_3H_8 entrained in H_2. Both the conversion step and SiC film deposition were achieved using a cold-wall, vertical geometry, RF inductively heated atmospheric pressure chemical vapor deposition (APCVD) reactor. Details of the experimental parameters used for the conversion step and the growth of the 3C-SiC layer are given in Ref. 14. A 100 nm thick AlN buffer layer and a 1 μm GaN seed layer were subsequently deposited in the manner used for the 6H-SiC substrates and noted above.

A 100 nm silicon nitride growth mask was deposited on the seed layers via plasma enhanced CVD. A 150 nm nickel etch mask was subsequently deposited using e-beam evaporation. Patterning of the nickel mask layer was achieved using standard photolithography techniques followed by dipping in HNO_3 for approximately five minutes. The samples were subsequently cleaned by consecutive dips in trichloroethylene, acetone, methanol, and HCl for five minutes each and blown dry with nitrogen. The final, tailored, microstructure consisting of seed forms was fabricated via removal of portions of the nickel etch mask via sputtering and by inductively coupled plasma (ICP) etching of portions of the silicon nitride growth mask, the GaN seed layer and the AlN buffer layer. Critical to the success of the pendeo-epitaxial growth, the etching of the seed-forms was continued completely through the exposed GaN and AlN layers and into either the 6H-SiC substrate or the 3C-SiC layer, thereby removing all III- nitride material from the areas between the side walls of the forms. The seed-forms used in this study were raised rectangular stripes oriented along the <1-100> direction, thereby providing a plurality of GaN sidewalls (nominally (11-20) faces). Seed form widths of 2 and 3 μms coupled with separation distances of 3 and 7 μms, respectively, were employed. The remaining nickel mask protecting the seed structures during the ICP etching process was removed using HNO_3. Immediately prior to pendeo-epitaxial growth, the patterned samples were dipped in a 50% HCl solution to remove the surface oxide from the walls of the underlying GaN seed structures.

A schematic of the pendeo-epitaxial growth of GaN is illustrated in Figure 1. There are three primary stages associated with the pendeo-epitaxial formation of this material: (i) initiation of lateral homoepitaxy from the sidewalls of the GaN seed, (ii) vertical growth and (iii) lateral growth over the silicon nitride mask covering the seed structure. Pendeo-epitaxial growth of GaN was achieved within the temperature range of 1050-1100°C and a total pressure of 45 Torr. The precursors (flow rates) of triethylgallium (26.1 μmol/min) and NH_3 (1500 sccm) were used in combination with a H_2 diluent (3000 sccm). Additional experimental details regarding the pendeo-epitaxial growth of GaN and $Al_xGa_{1-x}N$ layers employing 6H-SiC substrates are given in Refs. 15 ,16, and 17. The morphology and defect microstructures were investigated using scanning electron microscopy (SEM) (JEOL 6400 FE) and transmission electron microscopy (TEM) (TOPCON 0002B, 200 KV).

RESULTS AND DISCUSSION

The pendeo-epitaxial phenomenon is made possible by taking advantage of growth mechanisms identified by Zheleva et.al.[7] in the conventional LEO technique, and by using two additional key steps, namely, the initiation of growth from a GaN face other than the (0001) and the use of the substrate (in this case SiC) as a mask. By capping the seed-forms with a growth mask, the GaN was forced to grow initially and selectively only on the GaN sidewalls. Common to conventional LEO, no growth occurred on the silicon nitride mask covering the seed forms. Deposition also did not occur on the exposed SiC surface areas at the higher growth temperatures employed to enhance lateral growth. The Ga- and N-containing species more likely either diffused along the surface or evaporated (rather than having sufficient time to form GaN nuclei) from both the silicon nitride mask and the silicon carbide substrate. The pronounced effect of this is shown in Figure 2 wherein the newly deposited GaN has grown truly suspended (*pendeo-*) from the sidewalls of the GaN seed structure. During the second PE event (ii), vertical growth of GaN occurred from the advancing (0001) face of the laterally growing GaN. Once the vertical growth became extended to a height greater than the silicon nitride mask, the third PE event (iii) occurred, namely, conventional LEO-type growth and eventual coalescence over the seed structure, as shown in Fig. 3. A cross-sectional TEM micrograph showing a typical pendeo-epitaxial growth structure is shown in Fig. 4. Threading dislocations extending into the GaN seed structure, originating from the GaN/AlN and AlN/SiC interfaces, are clearly visible.

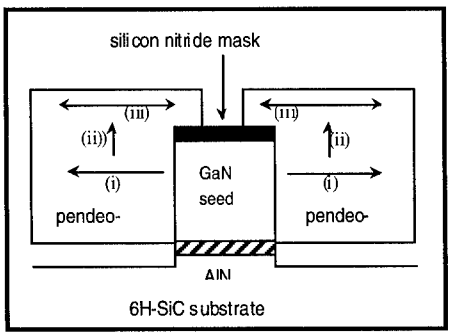


Figure 1. Schematic ofGaN pendeo-epitaxial growth process steps.

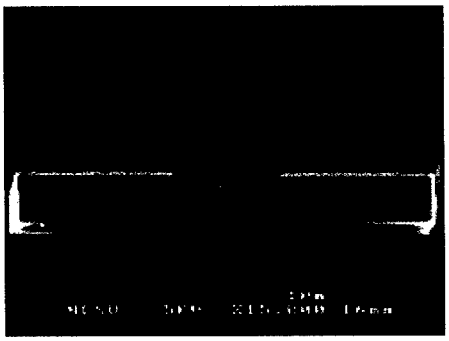


Figure 2. Cross-sectional SEM of a GaN pendeo-epitaxial growth structure with limited vertical growth from the seed sidewalls and no growth on the seed mask.

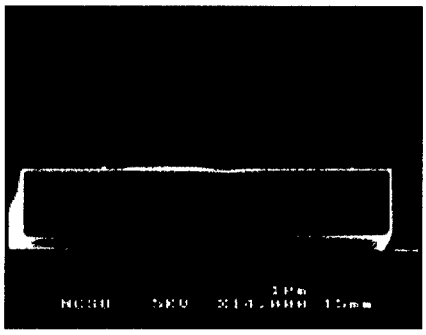


Figure 3. Cross-sectional SEM of a GaN/AlGaN pendeo-epitaxial growth structure showing coalescence over the seed mask.

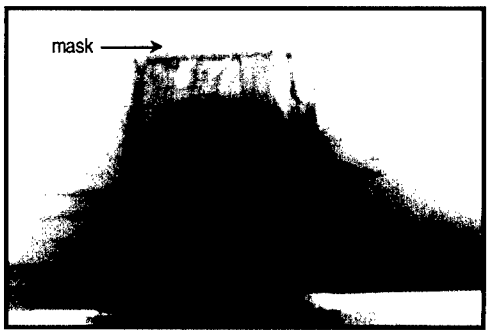
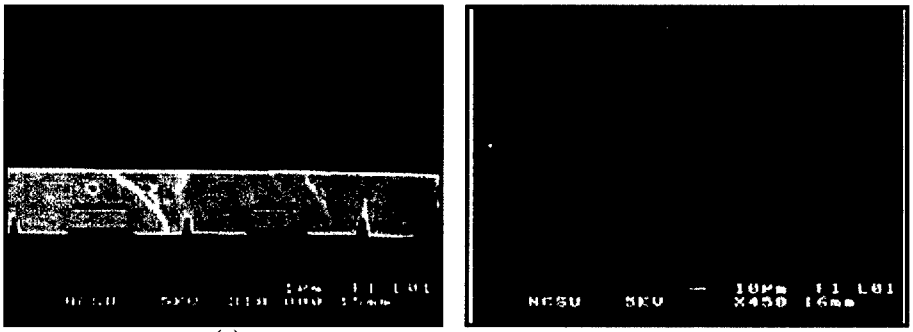


Figure 4. Cross-sectional TEM of a GaN pendeo-epitaxial growth structure showing confinement of threading dislocation under the seed mask, and a drastic reduction of defects in the regrown areas.

The silicon nitride mask acted as a barrier to the further vertical propagation of these defects into the laterally overgrown pendeo-epitaxial film. Since the newly deposited GaN is suspended above the SiC substrate, there are no defects associated with the mismatches in lattice parameters between GaN and AlN and between AlN and SiC. Preliminary analysis of the GaN seed/GaN pendeo-epitaxy interface revealed evidence of threading dislocations or stacking faults within the (0001) planes. This indicates evidence of the lateral propagation of the defects, however, there is yet no evidence that the defects reach the (0001) surface where device layers will be grown. As in the case LEO, there is a significant reduction in the defect density in the regrown areas.



(a) (b)

Figure 5. Pendeo-epitaxial growth with coalescence over and between the seed forms resulting in a single GaN layer. 5(a) Cross-section SEM. 5(b) Plane-view SEM

The continuation of the pendeo-epitaxial growth results in coalescence with adjacent growth fronts and the formation of a continuous layer of GaN, as observed in Figure 5. This also results in the practical elimination of all dislocations stemming from the heteroepitaxial growth of GaN/AlN on SiC. Clearly visible in Fig. 5(a) are the voids that form when adjacent growth

fronts coalesce. Optimization of the pendeo-epitaxial growth technique should eliminate these undesirable defects.

The maximum diameter of commercially available 6H- and 4H-SiC substrates is currently limited to approximately two inches. As such, the development of a process route for achieving the pendeo-epitaxial growth of (0001)GaN on (111)Si was undertaken. Unlike silicon carbide and sapphire substrates, the development of process routes leading to the growth of GaN films on silicon substrates have lagged behind. The slow progress has been due in part to the difficulty in the nucleation and two dimensional growth of GaN caused by a combination of significant mismatches in lattice parameters and coefficients of thermal expansion and the chemical stability of the phases in the growth environment. To address these concerns, a 3C-SiC transition layer was employed between the Si wafer and the AlN buffer layer for three reasons. Firstly, an on-axis (111)Si substrate was used which allowed for deposition of the (111)3C-SiC polytype. The SiC layer is preferred for the growth of the 2H-AlN buffer layer of sufficient quality for the subsequent growth of the single crystal GaN seed layer. Secondly, as described above, PE growth of GaN is obtained on SiC because under the growth conditions used for this growth, Ga and N atoms will not bond to the SiC surface in numbers and in time sufficient to cause gallium nitride nuclei to form. Thirdly, the 3C-SiC layer is needed as a diffusion barrier to prevent the interaction of Si atoms with the Ga and N species found in the growth environment. If there is either no diffusion barrier or a diffusion barrier of insufficient thickness, the Si atoms from the substrate have sufficient energy at the temperatures used for PE growth to diffuse to the surface of the AlN buffer layer and react with the gallium nitride layer. This results in the formation of large voids in the underlying Si substrate, the "poisoning" of the GaN film, and the formation of polycrystalline GaN-containing material.

The results of an SEM analysis of PE-grown GaN on a (111)Si substrate is shown in Fig. 6. The rough surface morphologies of the (111)3C-SiC and the AlN buffer layer as well as the relatively poor quality of the GaN seed layer are clearly visible. In contrast, the pendeo-epitaxially grown GaN is of relatively superior quality in terms of surface roughness. Analysis via TEM of the PE GaN layer and optimization of the process routes to improve the PE technique using 3C-SiC are the subjects of ongoing research. Finally, Figure 7 shows a SEM image of coalesced pendeo-epitaxially grown GaN on a silicon substrate.



Figure 6. Cross-sectional SEM of pendeo-epitaxial GaN grown on a (111)Si substrate. Clearly visable is the rough surface morphology of the AlN buffer layer and 3C-SiC transition layer.

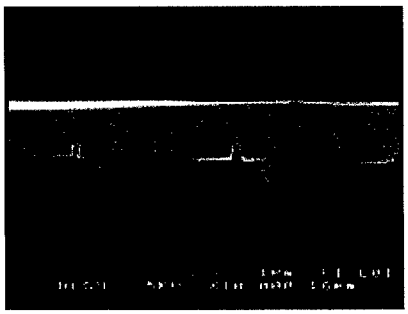


Figure 7. Low magnification cross-sectional SEM of pendeo-epitaxial GaN on a (111)Si substrate and a 3C-SiC transition layer showing coalescence over and between GaN seed forms.

CONCLUSION

We have reported on the development of pendeo-epitaxial process routes as a potential way of growing uniformly low-defect density thin films over the entire surface of a substrate. In particular, we have achieved a method to grow GaN using pendeo-epitaxy on 6H-SiC substrates. We have demonstrated both discrete pendeo-epitaxial structures and coalesced layers of GaN. In addition, we report our preliminary results regarding the ability to grow pendeo-epitaxial GaN on silicon substrates. This latest development provides a possible pathway for the fabrication of device quality GaN thin films grown on large area silicon wafers.

ACKNOWLEDGEMENTS

The authors acknowledge Cree Research, Inc. and Motorola for the SiC and the silicon wafers respectively. This work was supported by the Office of Naval Research under contracts N00014-96-1-0765 (Colin Wood, monitor) and N00014-98-1-0654 (John Zolper, monitor).

REFERENCES

1. R. Underwood, D. Kapolnek, B. Keller, S. Keller, S. Denbaars, and U. Mishra, Topical Workshop on Nitrides, Nagoya, Japan, September, 1995.
2. Y. Kato, S. Kitamura, K. Hiramatsu, and N. Sawaki, J. Cryst. Growth, **144**, 133 (1994).
3. O. Nam, M. Bremser, B. Ward, R. Nemanich, and R. Davis, Mat.Res. Soc. Symp. Proc., **449**, 107 (1997).
4. O. Nam, M. Bremser, B. Ward, R. Nemanich, and R. Davis, Jpn.J. Appl. Phys., Part 1 **36**, L532 (1997).
5. A. Sakai, H. Sunakawa, and A. Usui, Appl. Phys. Lett., **73**, 481 (1998).
6. H. Marchand, X. Wu, J. Ibbetson, P. Fini, P. Kozodoy, S. Keller, J. Speck, S. Denbaars, and U. Mishra, Appl. Phys. Lett., **73**, 747 (1998).
7. T. Zheleva, O. Nam, M. Bremser, and R. Davis, Appl. Phys. Lett., **71**, 2472 (1997).
8. O. Nam, T. Zheleva, M. Bremser, and R. Davis, Appl. Phys. Lett., **71**, 2638 (1997).
9. H. Zhong, M. Johnson, T. McNulty, J. Brown, J. Cook Jr., J. Schezina, Materials Internet Journal, Nitride Semiconductor Research, **3**, 6, (1998).
10. S. Nakamura, M.Senoh, S. Nagahama, N. Iwasa, T. Yamanda, T. Matsushita, H. Kiyoku, Y. Sugimoto, T. Kozaki, H. Umemoto, M. Sano, and K. Chocho, Proc. of the 2nd Int. Conf. On Nitride Semicond., Tokushima, Japan, October, 1997
11. T. Zheleva, S. Smith, D. Thomson, K. Linthicum, T. Gerhke, P. Rajagopal, R.Davis, (submitted to the Journal of Electronic Materials).
12. K. Linthicum, T. Gehrke, D.Thomson, E. Carlson, P. Rajagopal, T.Smith, R. Davis, (submitted to Applied Physics Letters).
13. T. Weeks, M. Bremser, K. Ailey, E. Carlson, W. Perry, and R. Davis, Appl. Phys. Lett., **67**, 401 (1995).
14. C. Zorman, A. Fleischman, A. Dewa, M. Mehregany, C. Jacob, S. Nishino, and P. Pirouz, J. Appl. Phys., **78**, 5136 (1995)
15. T. Gehrke, K. Linthicum, D. Thomson, P. Rajagopal, A. Batchelor, R. Davis, Mat. Res. Soc. Symp., this volume.
16. D. Thomson, T. Gehrke, K. Linthicum, P. Rajagopal, T. Zheleva, R. Davis, Mat. Res. Soc. Symp., this volume.
17. T. Zheleva, et.al., Mat. Res. Soc. Symp., this volume.

HOMO- AND HETERO-EPITAXIAL GALLIUM NITRIDE GROWN BY MOLECULAR BEAM EPITAXY

C.T. Foxon[1], T.S. Cheng[1], D. Korakakis[1,4], S.V. Novikov[1,5], R.P. Campion[1], I. Grzegory[2], S. Porowski[2], M. Albrecht[3], H.P. Strunk[3]

[1]School of Physics and Astronomy, University of Nottingham, University Park, Nottingham NG7 2RD, England
[2]High Pressure Research Center Polish Academy of Sciences, Sokolowska 29/37, 01-142 Warsaw, Poland
[3]Institute of Materials Science VII, University of Erlangen-Nurnberg, Cauerstrasse 6, 91058 Erlangen, Germany
[4]School of Electrical and Electronic Engineering, University of Nottingham, University Park, Nottingham NG7 2RD, England
[5]Ioffe Physical-Technical Institute, St. Petersburg, 194021, Russia

Cite this article as: MRS Internet J. Nitride Semicond. Res. 4S1, G4.11 (1999)

Abstract

Various methods have been used to initiate growth by Molecular Beam Epitaxy (MBE) of GaN on sapphire, or other substrates, but there is always a problem with morphology and with a high defect density which results in the formation of a sub-grain boundary structure. We show that by using, homo-epitaxial growth on properly prepared bulk GaN substrates, combined with high temperature growth, we obtain a significant improvement in surface morphology. Growth at sufficiently high temperature leads to a rapid smoothing of the surface and to almost atomically flat surfaces over relatively large areas. Multi-Quantum Well structures grown on such GaN epitaxial films are dislocation free with abrupt interfaces.

Introduction

The Group III-Nitrides are an important class of semiconductors now being used for light emitting diodes (LEDs), short wavelength blue/ultra-violet (UV) laser diodes (LDs) and high temperature electronic devices. LEDs are already commercially available from a number of suppliers [1,2]. Recently, blue/UV laser diodes have been demonstrated with room temperature cw operational lifetimes in excess of 3000 hours [3]. Projected lifetimes of >10000 hours have been announced at a number of recent international conferences. Other device structures based on the group III-Nitride system, grown both by Metal Organic Vapour Phase Epitaxy (MOVPE) and Molecular Beam Epitaxy (MBE), including high-power high-frequency FETs [4] and solar blind UV photo-detectors [5] have also been reported.

During the growth of GaN layers, either by MOVPE or MBE, one would ideally grow under stoichiometric conditions. However, for films grown by MBE, it is difficult to achieve growth under exact stoichiometric conditions and films are usually grown slightly Ga or N-rich. Films grown under N-rich conditions show a columnar structure [6] and they are not suitable for device purposes. Films grown under Ga-rich conditions at low temperatures show large hexagonal features of wurtzite GaN, in a polycrystalline background and with additional Ga droplets. It is common practise, therefore, to use a slightly Ga-rich growth mode at high temperature, the excess Ga being desorbed.

Mat. Res. Soc. Symp. Proc. Vol. 537 © 1999 Materials Research Society

Amongst the various growth methods for group III-nitrides, MBE has provided most insight into the growth kinetics, because of the in-situ analytical measurements such as reflection high energy electron diffraction (RHEED). A variety of GaN RHEED patterns have been seen and reported in the literature, during or after MBE growth, these include (1 × 1), (2 × 1), (2 × 2), (2 × 3), (3 × 2), (3 × 3), (4 × 6) and (5 × 5). The un-reconstructed (1 × 1) pattern has been shown to correspond to a monolayer of Ga, which is tightly bound to the GaN [7,8]. On top of this relatively stable Ga adlayer, there are mobile Ga adatoms which give rise to the surface reconstruction.

One of the most severe problems hindering both MBE and MOVPE progress in this field is the lack of a suitable substrate material on which lattice-matched group III-nitrides films can be grown. So far the best device results have been obtained on insulating sapphire or SiC substrates. For most optoelectronic devices a vertical configuration is normal; however, growth on dielectric substrates such as sapphire, requires a planar device configuration, which is a disadvantage for many of the present GaN-based devices. Growth on sapphire and SiC substrates leads to a large lattice mismatch and a significant difference in thermal expansion coefficient, which in turn leads to high defect density in the epitaxial wafers. Unlike the other III-V compounds in which defects such as dislocations are detrimental to device performance, the nitride films are relatively unaffected. For example, the presence of a high density of dislocations does not appear to limit the efficiency of LEDs [9], but more recent evidence suggests that this is because of the low diffusion rate for carriers in GaN [10]. There is also evidence that dislocation motion in nitride semiconductors is much lower than in other III-V compounds [11]. However, it has been suggested that the electron mobility in GaN depends strongly on the dislocation density [12]. Therefore, bulk GaN substrates would be the ideal choice for a number of reasons; there would be zero lattice and thermal mismatch, a conducting or insulating substrate would be available, the dislocation density in epitaxial films would be low, the thermal conductivity would be high and the cleavage planes would be perpendicular to the (0001) surface.

The purpose of this paper is to demonstrate that by using high quality bulk GaN substrates and appropriate MBE growth conditions, dislocation free atomically flat GaN epitaxial films and Multi-Quantum Well (MQW) structures can be obtained. By contrast films grown under equivalent conditions on sapphire have subgrain boundaries and inferior properties.

Experimental Details

The high quality bulk GaN substrates used in this study were grown from the Ga solutions at nitrogen pressures of 12-15 kbar and at temperatures of 1500-1600°C. They were hexagonal platelets 6-8 mm in size, highly conductive if grown from the solutions in Ga or semi-insulating if doped with Mg during growth. Due to the absence of inversion symmetry, the GaN substrate has two distinctly different crystal orientations - (0001) and $(000\bar{1})$ corresponding to the Ga and N polarity respectively. The $(000\bar{1})$ hexagonal face corresponding to the N-polarity is chemically active and therefore it could be prepared for epitaxy by mechano-chemical polishing [13], which gives atomically flat surfaces without subsurface damage. All the studies reported in our paper were obtained on this polarity.

The MBE growth was performed in two different systems, a commercial Varian Modular GEN-II system equipped with a high density RF source (HD25) from Oxford Applied Research (OAR) and a purpose built mini-MBE system equipped with a CARS25 RF source also from OAR. The GEN-II system has elemental Al, Ga, In, Si and Mg sources and the mini-MBE system an elemental Ga source in addition to the nitrogen source. Growth rates in the two systems are typically 0.8 and 0.3 μm/hour respectively under stoichiometric conditions. More details of the growth procedures are reported elsewhere [14]. The substrates were mounted on molybdenum holders with indium, with gallium-tin alloy [15], or on a special designed metal-free holder. RHEED patterns prior to, during and after growth were monitored using a reflection high energy electron diffraction

equipment. In the GEN-II system a video camera is linked to a high quality Super VCR system and in the mini-system a video capture card is used to store images on a PC system.

The Atomic Force Microscope (AFM) images of the grown layers and structures were obtained using a Topometrix Explorer 2000 system non-contact mode.

Results and Discussions

Typically for both MBE and MOCVD, GaN growth on sapphire is implemented as a three step process [16]. For MBE, the substrate is first exposed to a nitrogen plasma [17] to change the surface to AlN [18]. Next a GaN or AlN buffer layer is grown either at low temperature, 550°C [17], or at higher temperatures, 750°C [19]. Finally epitaxial layers are grown at about, 750-850°C. The aim of this three step process is first to wet the sapphire surface with GaN or AlN and to minimise the effect of the large lattice mismatch between substrate and epilayer. Nevertheless, the region close to the interface is structurally poor, with a very high dislocation density.

In our experience, GaN films grown by MBE on sapphire, even under optimum conditions, show rather poor RHEED patterns compared with other III-V compounds. Growth at a low substrate temperature, 600°C, produces a high density of small, oriented sub-grains. Growth at higher temperature, about 750-850°C, results in a similar structure, but on a much larger scale, as illustrated in Figure 1. In this case, the individual sub-grains are typically 0.3 to 0.5 μm diameter and a detailed AFM study of one of the individual islands shows that they are nearly atomically flat with a root mean squared (rms) roughness of 0.1 nm in the best cases. Such films are continuous with typical electron mobilities of 180-200 $cm^2V^{-1}s^{-1}$ at a carrier density of around $5x10^{17}$ cm^{-3}.

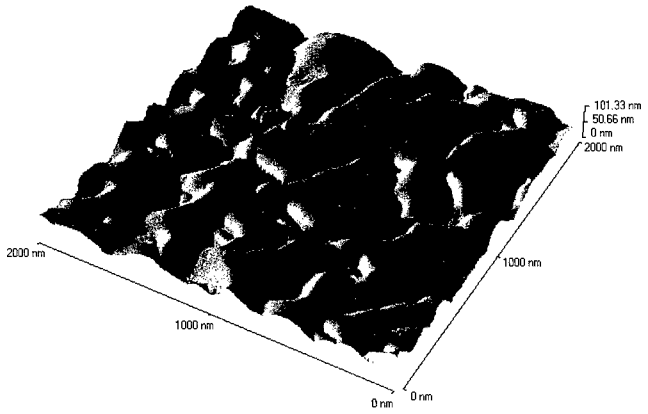


Figure 1. 3D AFM image of GaN layer on sapphire substrate.

For example, (InGa)N/GaN MQWs grown on such GaN on sapphire substrates using this MBE method, show very poor structural and optical properties. Transmission Electron Microscopy (TEM) studies of such MQW structures demonstrate that we have non-planar QWs, which follow the non-planar heterointerface between the GaN epitaxial layer and the QWs. The optical properties of the MQWs, show rather weak broad emission with no band-edge related features.

By contrast, growth on bulk GaN substrates show completely different behaviour. We have grown GaN layers on the bulk GaN crystals at temperatures >750°C, under slightly Ga-rich conditions.

During growth, we usually observe a streaky (1 × 1) RHEED pattern, which becomes stronger after the first minutes of epitaxy. Sometimes, during growth we can see a (2 × 2) RHEED pattern. Strong Kikuchi features are observed and the intensity of the specular spot is much stronger than in films grown on sapphire. On cooling the GaN layers grown under slightly Ga rich conditions, a clear (2 × 2) reconstruction is always observed below ~300°C.

There are two different configurations for Ga on the surface which can possibly give rise to a (2 × 2) reconstruction. The first arises from additional Ga on top of the first complete Ga monolayer, this (2 × 2) reconstruction is formed on cooling to low temperature via an order/disorder transition from excess Ga on the surface. The second (2 × 2) configuration can potentially arise from vacancies in the first layer of Ga, which terminates the surface, this (2 × 2) reconstruction is formed by evaporation of a finite number of Ga atoms from the Ga terminating layer. It is entirely reasonable that increasing the temperature will increase the probability of desorption for Ga and that, therefore, a vacancy induced (2 × 2) reconstruction is entirely possible especially during growth at high temperatures. Further studies are in progress to clarify this situation.

In contrast to growth on sapphire, AFM studies of GaN surfaces grown by home-epitaxy, show remarkably flat surfaces over large areas as shown in Figure 2. Line scans in the non-contact mode show atomically flat surfaces over large area with overall rms roughness for a typical 2x2 μm^2 surface of <0.1 nm over the whole area. It is important to note that there is about two orders of magnitude difference between the scales in Figure 1 and Figure 2. We can conclude therefore that the growth proceeds in the 2D mode where the lateral growth rate is very much larger than the growth rate normal to the direction of growth. TEM studies of the GaN films grown under such conditions show no additional dislocations in the epitaxial layer, whereas similar studies on GaN films grown on sapphire show dislocation densities of $>10^9$ cm^{-2}, even under optimum conditions. In addition, the high optical quality of the homo-epitaxy of GaN has already been demonstrated [20,21].

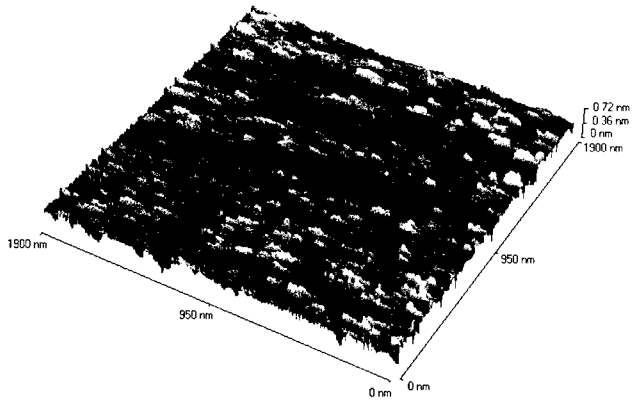


Figure 2. 3D AFM image of GaN layer on bulk GaN substrate

We have also grown (AlGa)N/GaN MQWs on top of our homo-epitaxial GaN layers. The growth rates were similar to those used for the GaN and the growth temperature was unchanged. TEM studies of such structures show that, in contrast to MQWs grown on sapphire substrates, high quality dislocation free structures are observed for large areas (>250nm), as shown in Figure 3. In other

regions we see some evidence for wavy interfaces, but the origin of the perturbation is not yet established. In this figure almost atomically abrupt interfaces are observed between the QW and barrier regions. The above films have also been characterised using X-ray diffraction. Powder diffractometer studies show additional satellite peaks from the MQW periodicity and the experimental data follows closely the theoretical model for the ideal structure.

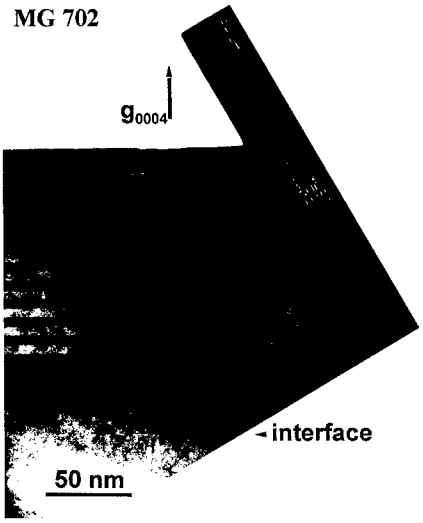


Figure 3. TEM image of an AlGaN/GaN MQWs grown on bulk GaN substrate.

Conclusions

Whilst various techniques for the initiation of growth on sapphire, or other substrates with a large mismatch, can improve the quality of films grown by MBE, there remains a fundamental problem with morphology. The high density of dislocations results in the formation of a sub-grain boundary structure. By contrast, homo-epitaxial growth under appropriate conditions on properly prepared bulk GaN substrates results in greatly improved morphology and RHEED patterns. Growth at sufficiently high temperature leads to rapid smoothing of the surface and to atomically flat surfaces over relatively large areas. Multi-Quantum Well structures grown on such GaN epitaxial films are dislocation free with very abrupt interfaces.

Acknowledgement

Pressure crystallisation of GaN and surface preparation studies have been supported by the Polish Grant No 7 7834 95/C2399. The work on MBE growth was supported by grants from LAQUANI (ESPRIT 20968), EPSRC (GR/L77157 and GR/L35423), Royal Society, INTAS, NATO (HTECH.LG971309).

References

[1] S. Nakamura, T. Mukai and M. Senoh, Appl. Phys. Lett. **64**, 1687 (1994).
[2] S. Nakamura, M. Senoh, N. Iwasa, S.I. Nagahama, T. Yamada and T. Mukai, Jpn. J. Appl. Phys. **34**, L1332 (1995).
[3] S. Nakamura, M. Senoh, N. Iwasa, S.I. Nagahama, N. Iwasa, T. Yamada, T. Matsushita, Y. Sugimto and H. Kiyoku, Appl. Phys. Lett. **70**, 1417 (1997).
[4] Z. Fan, S. N. Mohhammad, O. Aktas, A. E. Botchkarev, A. Salvador and H. Morkoç, Appl. Phys. Lett., **69**, 1229 (1996).
[5] K. S. Stevens, M. Kinniburgh and R. Beresford, Appl. Phys. Lett. **66**, 3518 (1995).
[6] M. A. Sanchez-Garcia, E. Calleja, E. Monroy, F. J. Sanchez, F. Calle, E. Munoz and R. Beresford, J. Cryst. Growth **183**, 23 (1998).
[7] A. R. Smith, R. M. Feenstra, D. W. Greve, M. S. Shin, M. Skowronski, J. Neugebauer and J. E. Northrup, Appl. Phys. Lett., **72**, 2114 (1998).
[8] A. R. Smith, R. M. Feenstra, D. W. Greve, J. Neugebauer and J. E. Northrup, Phys. Rev. Lett., **79**, 3934 (1997).
[9] S. D. Lester, F. A. Ponce, M. G. Craford, D. A. Steigerwald, Appl. Phys. Lett. **66**, 1249 (1995).
[10] T. Sugahara, H. Sato, M. Hao, Y. Naoi, S. Kurai, S. Tottori, K. Yamashita, K. Nishino, L. T. Romano and S. Sakai, Jpn. J. Appl. Phys. **37**, L398 (1998).
[11] L. Sugiura, J. Appl. Phys. **81**, 1633, (1997).
[12] H. M. Ng, D. Doppalapudi, T. D. Moustakas, N. G. Weimann and L. F. Eastman, Appl. Phys. Lett. **73**, 821 (1998).
[13] J. L. Weyher, S. Muller, I. Grzegory, and S. Porowski, J. Cryst. Growth, **182**, 17 (1997).
[14] S. E. Hooper, C. T. Foxon, T. S. Cheng, L. C. Jenkins, D. E. Lacklison, J. W. Orton, T. Benswick, A. Kean, M. Dawson, G. Duggan, J. Cryst. Growth **155**, 157 (1995).
[15] R. Held, S. M. Seutter, B. E. Ishaug, A. Parkhomovsky, A. M. Dabiran, P. I. Cohen, G. Nowak, I. Grzegory, and S. Porowski, to be published.
[16] T. Matsuoka, N. Yoshimoto, T. Sasaki, and A. Katsui, J. Electron. Mater. **21**, 157 (1992).
[17] T. D. Moustakas, T. Lei, and R. J. Molnar, Physica B **185**, 36 (1993).
[18] N. Grandjean, J. Massies, M. Leroux, Appl. Phys. Lett. **69**, 2071 (1996).
[19] H. Tews, R. Averbeck, A. Graber, and H. Riechert, Electron Lett. **32**, 2004 (1996).
[20] G. Teisseyre, G. Nowak, M. Leszczynski, I. Grzegory, M. Bockowski, S. Krukowski, S. Porowski, M. Mayer, A. Pelzmann, M. Kamp, K.J. Ebeling, G. Karczewski, MRS Internet J. Nitride Semicond. Res. **1**, 13 (1996).
[21] M. Mayer, A. Pelzmann, M. Kamp, K.J. Ebeling, H. Teisseyre, G. Nowak, M. Leszczynski, I. Grzegory, M. Bockowski, S. Krukowski, B. Lucznik, S. Porowski, G. Karczewski, Jpn. J. Appl. Phys. **36**, L1634 (1997).

Part V

Theory, Defects, Transport, Bandstructure

COMPUTATIONAL MATERIALS SCIENCE, AN INCREASINGLY RELIABLE ENGINEERING TOOL: ANOMALOUS NITRIDE BAND STRUCTURES AND DEVICE CONSEQUENCES

A. Sher,* M. van Schilfgaarde,** M. A. Berding,* S. Krishnamurthy,* and A.-B. Chen***

*SRI International, 333 Ravenswood Avenue, Menlo Park, CA 94025
**Sandia National Laboratories, Livermore, CA 94551
***Auburn University, Physics Department, Auburn, AL 36849

Cite this article as: MRS Internet J. Nitride Semicond. Res. 4S1, G5.1 (1999)

ABSTRACT

Computational materials science has evolved in recent years into a reliable theory capable of predicting not only idealized materials and device performance properties, but also those that apply to practical engineering developments. The codes run on workstations and even now are fast enough to be useful design tools. A review will be presented of the current status of this rapidly advancing field. Examples of the accuracy of the codes are displayed by comparing the predicted atomic volumes, and cohesive and excess energies of several materials with experiment. As a further demonstration of the methods, the band structures of AlN, GaN, and InN in wurtzite and zinc blende structures will be presented. There are anomalies in the conduction and valence bands of these materials. Some consequences on light emitting and power devices made from these materials will be examined.

1. INTRODUCTION

General reviews, with extensive references, have been published on the properties of compound semiconductors and their pseudobinary alloys [1,2]. This review focuses on fundamental properties of the compounds and their pseudobinary alloys that can be calculated from an *ab initio* theoretical, or computational standpoint [for details see Ref. 2]. Its purpose is twofold: first to summarize much of what electronic structure theory has contributed recently to the understanding of some aspects of the III-nitride alloys; and, second, to provide some foundation for modern techniques, to provide the nonspecialist with a basis to assess the validity and limitations of the techniques employed in the literature.

Section 2 introduces the virtues and limitations of the local-density approximation (LDA) [3] and two higher order corrections, gradient corrections [4] and screened exchange [5]. The discussions will be couched in terms of a self-consistent, all-electron theory that employs full potentials between the electrons and ions and a linear muffin-tin orbital (LMTO) [6] basis [2,7]. This procedure takes proper account of the *d* states, which is essential to obtaining accurate results in materials like GaInN alloys. Section 3 summarizes some recent results on fundamental properties of nitride alloys [2,8]. Section 4 is devoted to concluding remarks.

2. GENERAL THEORY

An exact, or nearly exact, theory of the ground state in condensed matter is immensely complicated by the correlated behavior of the electrons. For materials with wide-band or itinerant electronic motion, a one-electron picture is adequate, meaning that to a good approximation the electrons (or quasiparticles) may be treated as independent particles moving in an effective

Mat. Res. Soc. Symp. Proc. Vol. 537 © Materials Research Society

external field. The effective field consists of the coulombic interaction of electrons+nuclei, plus an additional effective potential that originates in the correlated electronic motion. This potential must be calculated self-consistently, such that the effective one-electron potential created from the electron density generates through the eigenvectors of the corresponding one-electron Hamiltonian, the same charge density.

2.1 The Local-Density Approximation

The LDA approximates the formally exact (but unknown) energy functional as one that consists of the coulomb energy, plus a functional of the density, dubbed the "exchange-correlation" energy density. This ansatz leads, as in the Hartree-Fock [9] case, to an equation of motion for electrons moving independently in an effective field, except that in LDA the potential is strictly local. The local form of this potential vastly simplifies the computational effort. Unlike in Hartree-Fock theory, there is no formal justification for associating the eigenvalues of the LDA Hamiltonian with energy bands. However, in one sense, the LDA is an approximation to Hartree-Fock theory where there is a formal justification for this interpretation. Thus, it is expected that the LDA eigenvalues bear a close resemblance to energy bands, and they are widely so interpreted. We mention in passing that the LDA is not merely an approximate Hartree-Fock theory, but determines the exchange energy from a theory of the homogeneous electron gas (jellium). Thus, unlike Hartree-Fock theory, the LDA generates the correct total energy and bands for that problem. On the whole, the LDA predicts with good accuracy ground state properties (such as structural properties and elastic constants) in itinerant materials. Figure 1 illustrates the accuracy of the LDA for s-p bonded systems. In this figure the predicted volume per particle of all the common semiconductors is compared with experiment. The difference is less than 5% in the worst case. If the bond lengths were compared instead of the volumes, the percentage errors decrease by a factor of 3. Most errors are less than 1%. Errors in predicted elastic constants of these same compounds are typically less that 10% and the largest are 15% [1]. In fact, there has been very little progress in improving on the LDA for ground-state properties of solids.

2.2 Gradient Correction Approximation

One of the largest errors in the LDA is the heat of formation of the crystal from the separated elements. It is widely accepted that most of the error can be attributed to errors in the free atom; thus, errors in the heats of reaction among different solid phases tend to be much smaller (typically 1/5 as large). Gradient corrections [4] (generalizing the functional to the local plus a term essentially proportional to the Laplacian of the density) largely undoes the large error in the heat of formation from the separated elements. We show in Figure 2 some results from a recently developed generalized gradient approximation (GGA) of Perdew, Burke, and Enzerhof, the so-called "PBE" functional [4]. The percentage errors between the measured and predicted cohesive energies (the energy difference per unit cell between the assembled solid and its separated atoms), are seen to decrease appreciably when GCAs are applied. The excess energies, the difference per unit cell between the cohesive energies of the solid and the best-bound constituent compounds, are also shown in Figure 2. The excess energies are not improved by the addition of GCA.

2.3 Screened Exchange

While for the most part the LDA does a pretty reasonable job in the prediction of optical properties, it tends to underestimate the energy bandgaps (roughly by a constant). Gradient corrections do not improve on the LDA gaps; they do not redress the fundamental problem with the LDA, which errs in the gaps for a reason closely related to the errors in the Hartree-Fock approximation. The exact nonlocal exchange operator of Hartree-Fock has a long-range part which is overestimated in a solid because it neglects the ability of the host to screen this term. In the LDA, the exchange operator is replaced by a local exchange and correlation potential, which thus misses entirely the long-range nature of exchange. In semiconductors, the long-ranged part of this interaction should be present but reduced (screened) by the high-frequency dielectric

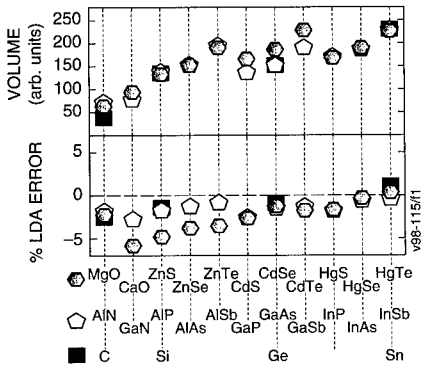


Figure 1. The experimental volume per unit cell and the percent difference between the theoretical and experimental values for several II-VI, III-V, and group IV compounds. The percent differences would be reduced by a factor of three if the bond lengths were treated instead of the volumes.

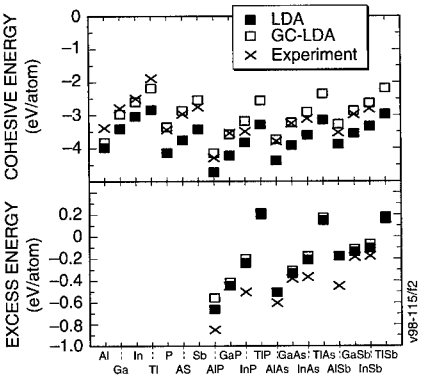


Figure 2. The cohesive energies and excess energies of several group III and V metals, and III-V compounds. Theory numbers are presented for LDA and GC-LDA along with the corresponding experimental values for comparison. Note the GC-LDA values fit experiment better than the LDA predictions, but the excess energies predictions are not improved as much.

constant ε. Since this dielectric constant is large compared with unity, the LDA does better by ignoring the nonlocal interaction all together than does Hartree-Fock theory by putting it in unscreened.

Harrison's model of the gap underestimate provides us with a clear physical picture of the missing ingredient in the LDA and semiquantitative estimate for the correction [10]. The LDA uses a fixed one-electron potential for all the energy bands; that is, the effective one-electron potential is unchanged for an electron excited across the gap. Thus, it neglects the electrostatic energy U cost associated with the separation of electron and hole for such an excitation. This Harrison modeled by noting a coulombic repulsion between the local excess charge and the excited electron. U is screened by the surrounding medium so that an estimate for the additional energy cost, and therefore a rigid shift for the entire conduction band including a correction to the bandgap is U/ε. This simple model produces a correction of the right order of magnitude, although formal theories that incorporate this correction show more complex behavior.

The GW approximation [11] has been the only way to correct errors in the optical properties that are inherent in the LDA. Formally, the GW approximation is the first term in the series expansion of the self-energy in the screened coulomb interaction W. However, the series is not necessarily convergent, and in any case such a viewpoint offers little insight. It is more useful to think of the GW approximation as being like Hartree-Fock theory, but with a frequency-dependent, nonlocal screened interaction W replacing the bare coulomb interaction.

There have been several attempts to introduce approximations to the GW theory. Very recently, Rücker introduced a generalization of the LDA functional to account for excitations [5]. His approach, which he calls the "screened exchange" (SX) theory, differs from the usual GW approach in that the latter does not use the LDA at all except to generate trial wave functions needed to make the quantities such as G, ε^{-1}, and W. His scheme was implemented in the LMTO-atomic spheres approximation (LMTO-ASA) [6], and promises to be extremely efficient for the calculation of excited-state properties, with accuracy approaching that of the GW theory. The screened exchange formalism is described in Ref. [2], and the reader is referred to that paper for further detail.

Although it is not essential to the theory, Rücker's implementation uses only the static response function, so that the one-electron equations have the Hartree-Fock form. The theory is formulated in terms of a generalization of the LDA functional, so that the N-particle LDA ground state is exactly reproduced, and also N+1-particle ground state is generated with a corresponding accuracy, provided interaction of the additional electron and the N particle ground state are correctly depicted. In some sense, Rücker's approach is a formal and more rigorous embodiment of Harrison's model. Results of the band gap predictions of the LDA and SX are presented in Figure 3. The improvement of the SX predictions from the consistently underestimated gaps predicted by the LDA is obvious. With the addition of SX to the structural property predictions of LDA, *ab initio* theory can now reliably generate all the numbers needed for insertion into statistical theories to accurately simulate performance and processing of semiconductor devices. The next section provides examples of this capability.

3. EQUILIBRIUM THERMODYNAMIC PROPERTIES

3.1 Bulk Compounds

The two most common phases reported for the III-nitrides are the hexagonal wurtzite structure and the cubic zinc blende structure, the wurtzite structure being the ground state for each case; transformation to a third polymorph, the rock salt structure, is observed under pressure [12,13]. Calculated and experimental lattice constants of AlN, GaN, and InN in the zinc blende and wurtzite structures are summarized in Reference [14]. The agreement between theory and available experiment is quite good; as a general rule, the LDA accurately predicts structural properties in compounds where the electrons are itinerant. Because wurtzite is the lowest energy state of the III-nitrides, there is far less experiment information on their properties in the zinc blende phase, although the latter phase is of interest because of the possibility of alloying the nitrides with other cubic III-V compounds.

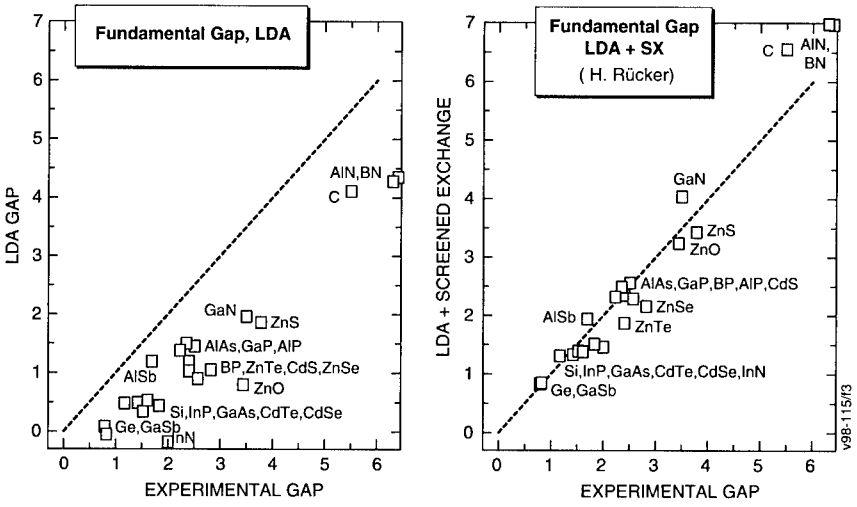


Figure 3. The LDA and LDA+SX predicted energy gaps, versus the experimental values for all the common semiconductor materials. Screened exchange obviously corrects the major errors in the LDA predictions.

3.2 Nitride-Based Alloys

Cation-substituted alloys are attractive candidates for optoelectronic, high-temperature, and high-power device applications because of the flexibility they offer to tune both the lattice constant and band gap. While alloys can be formed by mixing constituents on the cation and/or sublattice, most attention has been focused on alloys where the substitution is on the cation sublattice—for example, GaInN and AlGaN which form the basis for blue and green LEDs and laser diodes [15]. The mixed group V alloys have been the subject of fewer experimental investigations, owing to the enormous size difference between nitrogen and the other group V elements, and the resulting large miscibility gap.

3.3 Electronic Properties

The band structure of the nitride-based compounds and alloys is fundamental to the determination of electronic and optical properties exploited in device design. In this section the band structures of nitride compounds in both the zinc blende and wurtzite structures are discussed. The properties of the alloys are also discussed. Finally, some unusual features of the GaN band structure, and the impact that it has on the hot-electron properties are examined.

Compound Band Structures. In the past several years, there have been several band calculations using the local-density [13,2,16-18], the GW [11,19-20], and the screened exchange (LDA+SX) [2] approximations. The agreement between the PWPP and FP-MLTO bands, both calculated within the LDA, is relatively good; a notable difference in the two calculations is in their predictions of the position of the deep *s*-like bands, which the PWPP cannot expect to reproduce since it lacks hybridization with the deep *d* levels.

There are two principal errors in band structures calculated using the LDA. The first is that the deep cation *d* levels in GaN and InN are too high [2,21]. The second principal error, and the most technologically important, is the tendency of the LDA (as discussed in Section 2) to underestimate the band gap [22]; indeed, the LDA gap comes out slightly negative in InN.

The band structures for zinc blende and wurtzite structures of GaN, calculated with the LDA+SX, are shown in Figure 4. The minimum energy gaps are also summarized in Table I, where the LDA, GW, and experimental gaps are also shown for comparison. With the exception of AlN in the zinc blende structures, all of the nitride compounds have direct band gaps.

The GW and LDA+SX theory both produce significant improvement to the LDA bands, although there are some discrepancies. In the current implementation, the LDA+SX is more approximate than the GW theory because LDA+SX includes only the long-ranged part of nonlocal screened exchange potential. The deep *d* orbitals essentially require an on-site, orbital-dependent Hartree-Fock-like exchange, which the current LDA+SX theory lacks. Existing GW calculations pseudize out the deep d orbitals, but presumably an all-electron GW calculation would rectify this error, as it does in ZnSe [27]. The LDA+SX theory does, however, widen the upper valence bands by the same amount as do GW calculations (compare the full and dotted lines in Figure 4). Furthermore, because a limited basis set consisting of one principal quantum number per *l*-channel was used in the LDA+SX calculations, the high-lying conduction bands are not very reliable. The InN direct gap is rather badly underestimated. It is not clear at this stage what the origin of the error is. Possibly the deep In *d* orbitals are inadequately treated; it may be connected with the fact that the starting LDA gap is negative. For further comparisons of the various calculated eigenvalues at some high symmetry points in the Brillouin zone, see Ref. [2]. There are some differences in the present SX calculations and those in Ref. [2], mainly that *f* orbitals and the nonspherical corrections to the ASA potential are added here to render the LDA bands almost identical to full-potential ones.

Alloy Band Structures. Calculating the properties of random alloys is, in general, a far more difficult task than calculating the properties of the compounds, and several calculational approaches are generally applied to the problem. In the virtual crystal approximation (VCA), the alloy is modeled by replacing the varying potential due to the alloy disorder by an average potential, approximated by a compositional-weighted average of the potentials of the constituents. Such a crude approximation can be expected to produce poor results in predicting the properties of the nitride alloys, particularly those of the anion-substituted alloys for which

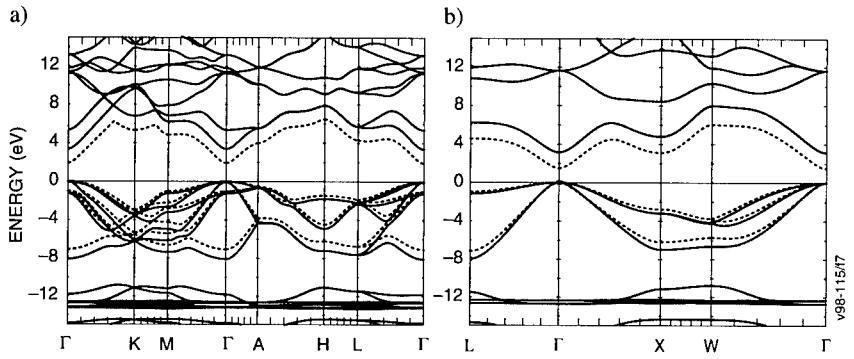


Figure 4. Energy bands of (a) wurtzite and (b) zinc blende GaN calculated in the LDA+SX. Dotted lines show several of the LDA bands.

Table I: Band gaps of AlN, GaN, and InN from various calculations and from experiment. GW energies were taken from Ref. [11]. LDA were taken from Ref. [2] and LDA+SX were taken from Ref. [2] and this work.

	Wurzite			Zinc blende					
	E_g^Γ(eV)			E_g^Γ(eV)			E_g^χ(eV)		
	AlN	GaN	InN	AlN	GaN	InN	AlN	GaN	InN
LDA	4.3	1.9	−0.3	4.1	1.9	−0.4	3.2	6.4	2.8
LDA+SX	6.4	3.4	0.8	6.3	3.1	0.7	5.1	4.8	4.1
GW	5.8	3.5		6.0	3.1		4.9	4.7	
exp	6.28[a]	3.5[b]	1.9[c]		3.4[d]				

v98-115/f11

[a]From Perry and Rutz [23].
[b]From Monemar [24].
[c]From Tansley and Foley [25].
[d]From Hong et al. [26].

there are large chemical and bond length differences. Strong scattering theories such as the coherent potential approximation (CPA) build upon the VCA by including a complex self-energy to describe the alloy inhomogeneities (see Ref. [1] and references therein). The CPA theory can include both on-site disorder arising from differences in diagonal terms in the potential, and off-site or off-diagonal disorder arising from differences in bond lengths. Wei et al. developed a method particularly well suited to the entrenched supercell method of the *ab initio* methods in which relatively small supercells, or special quasi-random structures (SQS), are specified to reproduce the expected atom-atom correlation function in a fully random structure [28]. Finally, averaging over samplings of random configurations can also be used to predict the composition-dependent properties of alloys.

In many cases, the band gap of the alloy $A_{1-x}B_xC$ is fit to the function form

$$E_g(x) = (1-x)\,E_g^{AC} + x\,E_g^{BC} - bx(1-x) \quad , \tag{1}$$

where b is the bowing parameter. Several theoretical calculations have been directed at the properties of the technologically important cation-substituted nitride alloys [29-31]. From 32-atom supercells in the wurtzite (zinc blende) structure, van Schilfgaarde calculated the

bowing parameter in the cation-substituted nitrides [2] and found $b = 0.3(0.6)$ for AlGaN, $b = 3.6(3.5)$ for AlInN, and $b = 1.7(1.3)$ for GaInN. Two values for the experimental bowing parameters for AlGaN have been reported: ~0 eV [30,31] and ~1 eV [32,33].

More dramatic changes in the energy bands are observed in the anion-substituted nitride alloys. Analogous behavior is not observed in the cation-substituted nitride-based alloys discussed above. Several authors noted that there is a strong localization of the band edge wave functions in GaAsN [34,35] and AlAsN [34] owing to large chemical and size differences between nitrogen and arsenic. The localization is extremely sensitive to the alloy concentration, the detailed configuration of the impurities, and the lattice relaxation around the impurities. Bellaiche et al. [36] used empirical pseudopotentials with large, fully relaxed, randomly occupied supercells to examine the properties of the anion-substituted alloys GaPN and GaAsN, and found substantial compositional-dependent downward bowing of the band gap, comparable to experiment. In the dilute alloy, impuritylike levels in the band gap associated with the minority constituents, were predicted at ~0.6 eV for phosphorus in GaN and at ~0.75 eV for arsenic in GaN. LDA calculations of a single impurity in large supercells of 216 atoms reveal similar localized levels, though they tend to appear to be resonances in the valence band and near the valence-band maximum, rather than localized states within the gap [37], as Bellaiche and Zunger found.

High-Field Transport. Transport calculations have been reported for several nitride alloys in both zinc blende and wurtzite structures [38-41]. Because the calculation of the hot electron transport is sensitive to details of the band structures employed, results reported in these works differ substantially. In the work by Krishnamurthy et al. [38], a hybride empirical tight-binding pseudopotential Hamiltonian was fit to the nitride band structures calculated using the LDA+SX discussed above. For GaN in both the zinc blende and wurtzite crystal structures, LDA+SX predicts that the central valley inflection points in both structures lies below the energy separation between the central valley minimum and the bottom of the first satellite valley. This character is illustrated in Figure 5a for the zinc blende phase and Figure 5b for the wurtzite phase of GaN; aside from the nitrides, this has not been found in any other group IV, III-V compound, or II-VI compound seminconductor. Also, the empirically derived nitride band structures used in other transport studies of the nitrides apparently did not possess this property [39-41]. As a consequence of the inflection point lying below the minimum of the first satellite valley, an anomalous drift velocity-field characteristic is predicted, shown in Figures 6a and 6b. While these velocity-field curves superficially resemble that of other materials, the mechanism responsible for the peak is quite different in GaN. Although the peak group velocity occurs at the inflection point (Figure 5), the electron effective mass goes to infinity at the reflection point, and becomes negative above it, where electrons are then *decelerated* by the applied field. This deceleration by the field results in the peak in the drift velocity being reached before electrons have sufficient energy to transfer to the satellite valley. The anomalous negative differential resistance velocity-field curves are supported by examination of the electron distribution. Tracking the electrons in various valleys indicates that all of the electrons remain in the Γ valley for fields well above that at which the peak in the drift velocity occurs, indicating that the negative differential resistance is caused by band structure features in the Γ valley, rather than by scattering into a satellite valley. Electron populations at 300 K as a function of energy for different field strengths applied in the (100) direction in the zinc blende structure are plotted in Figure 7, where drifted distributions are found. The peak drift velocity predicted for GaN is quite high, and is comparable to that of the best found in other materials [1], and the breakdown fields for GaN will probably be enormous.

Hot electron device designs will have to take account of the reported anomalous behavior. For example, GaN-based devices that require high peak drift velocity-field products will work well, but those like the Gunn oscillator, whose speed depends on the drift velocity that occurs after the valley in the velocity-field curve, are not likely to fare well. Also, devices that depend on avalanche breakdown may not function well. A more complete examination of these questions needs to be undertaken.

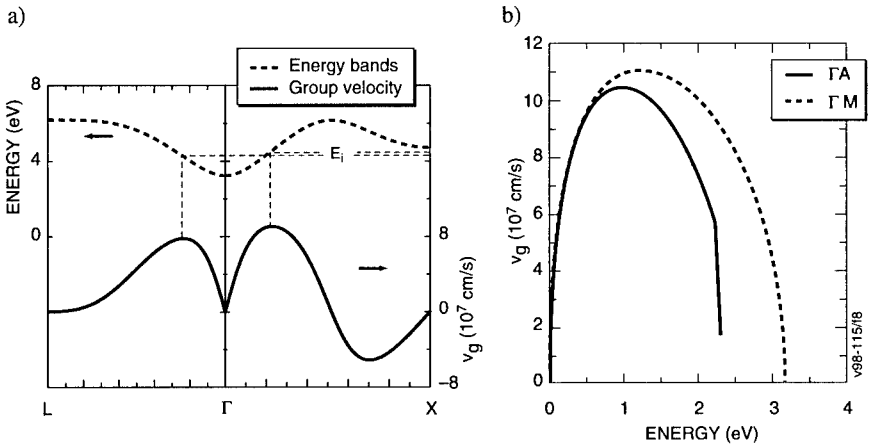


Figure 5. The conduction band structure and group velocity in (a) zinc blende and (b) wurtzite GaN. The inflection point corresponds to a maximum in the group velocity.

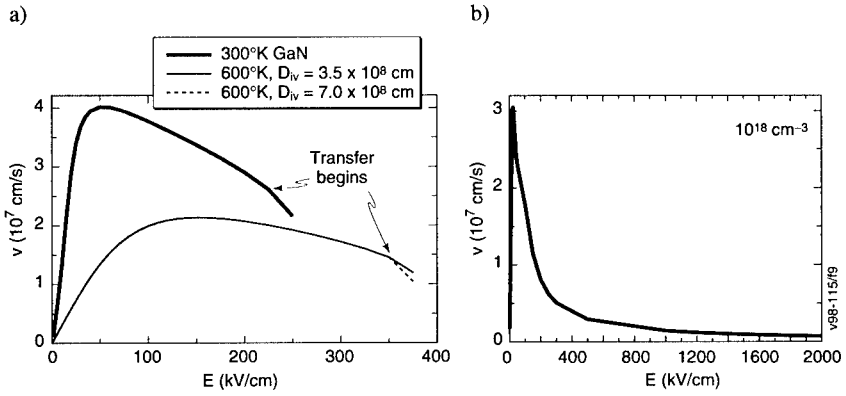


Figure 6. Velocity-field characteristics (a) at 300°K and 600°K for zinc blende GaN and (b) at 300°K for wurtzite GaN with carrier concentrations of 10^{18} cm^{-3}. Arrows indicate the fields at which the intervalley scattering begins to be important.

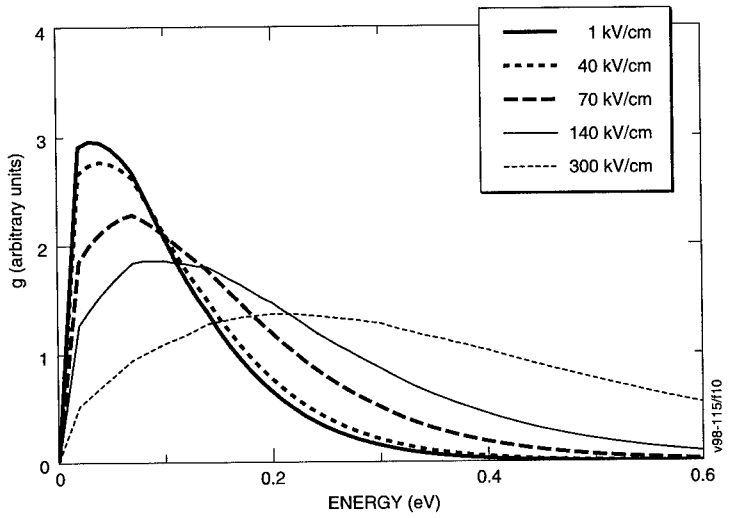


Figure 7. Electron distribution at 300°K along the (100) direction for several applied electric fields. For fields below 225 kV/cm, nearly all of them remain in the central Γ-valley.

4. SUMMARY

Theoretical predictions of the structural properties of the nitride-based compounds have been shown to be in good agreement with experiment. For AlInN, GaInN, and the mixed group V alloys, large miscibility gaps are predicted due mostly to the large size mismatch among the constituents.

Both LDA+SX band structures for the nitride compounds have been presented and predict band gaps that are in good agreement with experiment. Based on a fit to the LDA+SX bands, the velocity-field characteristics of the nitrides have been examined and have been found to show some anomalies due to the inflection point lying below any higher-lying minima. This anomaly must be taken into account in designing hot-electron devices.

ACKNOWLEDGMENTS

This work was supported by the Defense Advanced Research Projects Agency and the Electric Power Research Institute through a subcontract with the University of Florida, Contract No. UF-EIS-9809001-SRI.

REFERENCES

1. A.-B. Chen and A. Sher, Semiconductor Alloys, (Plenum, New York, 1995).
2. M. van Schilfgaarde, A. Sher, and A.-B. Chen, J. Cryst. Growth **178**, 8 (1997).
3. P. Hohenberg and W. Kohn, Phys. Rev. **136**, B864 (1964).
   W. Kohn and L. J. Sham, Phys. Rev. **140**, 1133 (1965).
4. J. P. Perdew, K. Burke and M. Enzerhof, Phys. Rev. Lett. **77**, 3865 (1996).
5. H. R Rücker (unpublished).
6. O. K. Andersen, Phys. Rev. B **12**, 3060 (1975).
7. M. Methfessel, Phys. Rev. B **38**, 1537 (1988).
8. M. A. Berding, M. van Schilfgaarde, and A. Sher, *Thermodynamics and Electronic Properties of GaN and Related Alloys* (unpublished).
9. R. Pandey, J. E. Jaffe, and N. M. Harrison, J. Mater. Res. **8**, 1922 (1993).
10. W. A. Harrison, Phys. Rev. B **31**, 2121 (1985).
11. Rubio, J. L. Corkill, M. L. Cohen, E. L. Shirley, and S. G. Louie, Phys. Rev. B **48**, 11810 (1993).
12. D. Elwell and M. M. Elwell, Prog. Cryst. Growth Charact. **17**, 53 (1988).
13. N. E. Christensen and I. Gorczyca, Phys. Rev. B **50**, 4397 (1994); *Ibid.*, **47**, 4307 (1993).
14. W. G. Bi and C. W. Tu, J. Appl. Phys. **80**, 1934 (1996).
15. S. Nakamura, Chapter xxx, this volume, 1998.
16. V. Fiorentini, M. Methfessel, and M. Scheffler, Phys. Rev. B **47**, 13353 (1993).
17. W. R. L. Lambrecht, B. Segall, J. Rife, W. R. Hunter, and D. K. Wickenden, Phys. Rev. B **51**, 13516 (1995).
18. K. Miwa and A. Fukumoto, Phys. Rev. B **48**, 7897 (1993).
19. M. Palummo, L. Reining, R. W. Godby, C. M. Bertoni, and N. Börnsen, Europhysics Lett. **26**, 607 (1994).
20. M. Palummo, R. Del Sole, L. Reining, F. Bechstedt, and G. Cappellini, Solid State Commun. **95**, 393 (1995).
21. W. R. L. Lambrecht, B. Segall, S. Strite, G. Martin, A. Agarwal, H. Morkoa, and A. Rockett, Phys. Rev. B **50**, 14155 (1994).
22. For a general overview of the density functional theory and its applications, see the review by R. O. Jones and O. Gunnarsson, Rev. Mod. Physics, **61**, 688 (1989).
23. P. B. Perry and R. F. Rutz, Apply. Phys. Lett. **33**, 319 (1978)
24. Monemar, Phys. Rev. B **10**, 676 (1974).
25. T. L. Tansley and C. P. Foley, J. Appl. Phys., **59** 3241 (1986).
26. H. Hong, D. Pavlidis, S. W. Brown, and S. C. Rand, J. Appl. Phys. **77**, 1705 (1995).
27. F. Aryasetiawan and O. Gunnarsson, Phys. Rev. B **54**, 17564 (1996).
28. S.-H. Wei, L. G. Ferreira, J. E. Bernard, and A. Zunger, Phys. Rev. B **42**, 9622 (1990).
29. K. Kim, S. Limpigumnong, W. R. L. Lambrecht, and B. Segall, MRS. Proc. **449**, 929 (1997).
30. L. Bellaiche, S. H. Wei, and A. Zunger, Phys. Rev. B **21**, 13872 (1997).

31. A. F. Wright and J. S. Nelson, Appl.. Phys. Let. **66**, 3465 (1995); *ibid.* Appl. Phys. Let **66**, 3051 (1995).

32. M. A. Khan, R. A. Skogman, R. G. Schulze, and M. Gershenzon, Appl. Phys. Lett. **43**, 492 (1983).

33. D. K. Wickenden, C. B. Bargeron, W. A. Bryden, J. Miragliotta, and T. J. Kistenmacher, Appl. Phys. Lett. **65**, 2024 (1994).

34. M. R. H. Khan, Y. Koide, H. Itoh, N. Sawaki, and I. Akasaki, Solid State Comm. **60**, 509 (1986).

35. Koide, H. Itoh, M. R. H. Khan, K. Hiramatu, N. Sawaki, and I. Akasaki, J. Appl. Phys. **61**, 4540 (1987).

36. Rubio and M. L. Cohen, Phys. Rev. B, **51** 4343 (1995).

37. J. Neugebauer and C. G. Van de Walle, Phys. Rev. B **51**, 10568 (1995).

38. L. Bellaiche, S.-H. Wei, and A. Zunger, Appl. Phys. Lett. **70**, 3558 (1997).

39. M. van Schilfgaarde (unpublished).

40. S. Krishnamurthy, M. van Schilfgaarde, A. Sher, A.-B. Chen, Appl. Phys. Lett. **71**, 1 (1997).

41. Gelmont, K. Kim, and M. Shur, J. Appl. Phys. **74**, 1818 (1993).

42. N. S. Mansour, K. W. Kim, and M. A. Littlejohn, J. Appl. Phys. **77**, 2834 (1995).

43. J. Kolnik, I. H. Oguzman, K. Brennan, R. Wang, P. Ruden, Y. Wang, J. Appl. Phys. **78**, 1033 (1995).

ABSORPTION COEFFICIENT AND REFRACTIVE INDEX OF GaN, AlN AND AlGaN ALLOYS

J. F. MUTH[**], J. D. BROWN[*], M. A. L. JOHNSON[*], ZHONGHAI YU[*], R. M. KOLBAS[**], J. W. COOK, JR[*]. and J. F. SCHETZINA[*]

* Department of Physics, North Carolina State University, Raleigh NC 27695
** Department of Electrical and Computer Engineering, North Carolina State University, Raleigh NC 27695

Cite this article as : MRS Internet J. Nitride Semicond. Res. 4S1, G5.2 (1999)

ABSTRACT

The design of optoelectronic devices fabricated from III-nitride materials is aided by knowledge of the refractive index and absorption coefficient of these materials. The optical properties of GaN, AlN and AlGaN grown by MOVPE on sapphire substrates were investigated by means of transmittance and reflectance measurements. Thin (less than 0.5 μm) single crystal films were employed to insure that transmission measurements could be obtained well above the optical band gap. The influence of alloy broadening on the absorption edge was investigated by using a series of AlGaN alloy samples with a range of Al compositions. The optical absorption coefficient above the band gap was obtained for AlGaN having up to 38% Al composition. The refractive index below the band gap was determined for the same series of samples. These properties provide information critical to the optimal design of solar blind detectors or other optoelectronic devices.

INTRODUCTION

The III-nitrides, including GaN, InN, and AlN, have proven to be robust materials for the development of blue/green LEDs and violet lasers lasers [1]. The AlGaN alloys also hold great promise for developing ultraviolet photodetectors [2]. In photodetector applications, the wide band gap of the nitrides aids to minimize the dark current, thereby increasing the detector sensitivity. The transparency to visible light will reduce the need for the extensive external filters that are required when detectors sensitive to the visible portion of the spectrum are employed. Multilayered Bragg mirrors and filters fabricated from these materials also have applications for lasers and photodetectors. Currently there has been only a limited amount of information reported [3,4] about the fundamental optical properties of AlGaN alloys which makes design of these devices difficult. The relative immaturity of this materials system also means that there may be some variance in the properties of the materials produced by different workers. In this paper, we report the refractive index and absorption coefficient for AlGaN thin film compositions of up to 38 % obtained by means of reflectance/transmittance spectroscopy.

For light below the band gap of the semiconductor, the interference within the thin film modulates both the reflection and transmission spectrum. Above the band gap, the high absorption coefficient causes the film to absorb any multiple reflections of the light. For these materials, unless the film is less than ~ 1 μm thick, there is seldom enough signal for commercial spectrophotometers to obtain an accurate ratio measurement. Due to the short penetration depth of the light above the band gap, reflection measurements become more dependent on the surface

Mat. Res. Soc. Symp. Proc. Vol. 537 © 1999 Materials Research Society

condition of the semiconductor, but have been used with great success to gather information about band structure.

In the spectral region around the band gap the situation is complicated, for in addition to going from a transparent to an absorbing Fabry-Perot cavity, the excitonic structure becomes important. This is especially true in the case of nitride materials, where the binding energy of the exciton is strong (> ~20 meV). The three closely spaced valence bands lead to three strong absorption features, the A, B, and C exciton. The selection rules also make the transmission and reflection polarization dependent. The birefringence of the hexagonal material and the scattering from the columnar grain structure found in most nitride materials further complicates matters. In semiconductor alloys, fluctuations in composition broaden the exciton making the absorption features less distinct. However, the continuum absorption of the exciton still influences the absorption spectra, even when the excitonic features are no longer clearly visible. In general, all nitride epitaxial films are also highly strained, with strain being dependent on substrate material and on buffer layer.

In general, the traditional incident plane wave approach to thin film transmission and reflection problems assumes that the films are of uniform thickness and have a flat surface morphology. In practice, this is a challenge especially when the crystal grower would like to have a reasonable growth rate and also has to dope the film for electrical properties.

In the case of thin films that have surface roughness, some of the light is scattered and misses the detector. This lowers the experimental values of transmittance and reflectance with the effect being more pronounced at shorter wavelengths. Even a small error in the experimental values can lead to large errors in the determining the index of refraction [5]. The scattering also disrupts the phase of the plane wave leading to a loss of coherence in the thin film and a dampening of the modulation of the transmission and reflection spectra. Swanepoel [6,7], Szcxyrbowski [8], and Nowak [9] have considered the effects of surface roughness and thickness variations on the optical spectrum of thin films and their models were incorporated into the present model.

Another factor to consider in these thin film models is that the solution contains an index-thickness product (nd). Thus, the index of refraction and the thin film thickness are intimately related. In very thin films such as those used in this study, although the order number of the interference peaks is known, only a few data points can be obtained for the Swanepoel procedure for determining the thickness. With the film thickness known experimentally to ~ 7% from SEM measurements, the index of refraction of the films was determined using the same method as Ambacher [3]. The absorption coefficient was found using the reflectance data and the incoherent multilayer model by Wemple [10].

The exciton theory of Elliott [11] was used to fit the absorption coefficient data to find the optical band gap. Even with the exciton dissociated, it has a strong influence upon the absorption spectra that non-excitonic models can not fit [12,13]. Since the individual excitons could not be observed for alloy compositions above 5 % due to alloy broadening, for practicality the three excitons were grouped into one parameter and assigned a single binding energy.

EXPERIMENTAL DETAILS

The GaN, AlGaN, and AlN epitaxial films measured in this work were prepared in a low pressure, vertical flow, cold walled, high speed substrate rotation MOVPE reactor. This system was designed and built at NCSU and is integrated into a multi-chamber nitride growth cluster tool. The substrates for deposition were 2-inch diameter double-side-polished sapphire wafers. Sample preparation was as previously described [14]. Epitaxial films were deposited in a typical two step process, with a low temperature buffer layer to nucleate growth [15]. The low

temperature buffer layer was GaN for GaN growth, and AlN for AlGaN and AlN growth in order to minimize the effects of the buffer layer optical properties on the measurements of the epitaxial films. The epilayer growths of AlGaN and AlN films were performed at chamber pressures ranging from 20 to 76 Torr with the trimethylaluminum injected separately from the trimethylgallium source using hydrogen carrier gasses in both cases. Separate metallorganic injection and reduced pressures allow for the independent control of composition and velocity of the metallorganic species in order to limit parasitic reaction of the group III precursors [16]. With this technique, precise control of epilayer composition, uniformity, growth rate (0.5 – 1.5 μm/hr), and crystal quality was achieved.

The aluminum composition of the samples was estimated from the cathodoluminescence (CL) spectra. The CL was measured using a JEOL JSM-6400 SEM with an Oxford instruments mono-CL accessory. With this unit it is possible to obtain spectral CL scans from 180 nm to 900 nm, or to obtain monochromatic images within the available wavelength range. For these samples, an accelerating voltage of 5-10 kV was used with a beam current of 10 nA. The CL emission is from an interaction volume which extends through the sample into the substrate, including the lower quality buffer layer material.

The surface quality of the films was evaluated using differential interference contrast optical microscopy in order to anticipate any difficulties with light scattering from the surface.

Optical transmission intensity measurements were made from 200-3300 nm using a Cary 5E spectrophotometer. The reflectance measurements were taken from 250-900 nm with a Perkin-Elmer Lambda 9 spectrophotometer with a normal incidence reflectance accessory and calibrated uv-enhanced mirrors for use as references. The spectrophotometers were used in a double beam mode, where the optical energy passing through the samples is ratioed with the optical energy of a reference beam. No apertures were used in the reference and sample beams. This was very beneficial for making measurements above the band gap since it is experimentally difficult to obtain truly identical apertures and balance the instrument at very high absorbance. The spectrophotometer slit width was kept constant in the visible and UV portion of the spectrum to keep the spectral bandwidth constant. The spectral bandwidth was 0.1 nm to allow for observation of sharp excitonic features or closely spaced interference fringes. The double-side-polished substrates served to minimize scattering of the light.

RESULTS

The properties of the $Al_xGa_{1-x}N$ films analyzed in this study are summarized in Table 1.

Table 1: Thin $Al_xGa_{1-x}N$ films on double-polished sapphire.

Sample	1	2	3	4	5	6
CL Peak (eV)	3.40	3.76	3.96	4.11	4.24	5.88
x	0	0.18	0.27	0.34	0.38	1
Thickness (μm)	0.37	0.39	0.37	0.39	0.42	0.4
Optical Band Gap (eV)	3.43	3.80	4.00	4.18	4.36	6.20

Figure 1 shows the CL of the samples which was used to assign the alloy composition of the material using a bowing parameter of 1 eV [17]. The thin nature of the films and the relatively low accelerating voltage minimized the effect of self absorption upon the true peak position [18] although the peak position was still red shifted in relation to the optical band gap

found by fitting the absorption data. The CL indicated that the material was of high quality, although some deep level luminescence was observed.

The transmission data obtained for the sequence of thin samples is shown in Figure 2. The AlN layer demonstrates the influence of surface morphology upon transmission measurements. Due to scattering, the amplitude of the modulations is suppressed and the transmission steadily decreases with shorter wavelengths. The transmission results for the AlGaN nitride films ranging in aluminum composition from 0.18 to 0.38 (films 2-5) show that little scattering occurs and that the films are of uniform thickness. The thin GaN layer grown on a GaN buffer layer shows some unusual behavior. In addition to the excitonic band edge which produced a distinct room temperature excitonic feature indicative of high material quality, another absorption slope just below the excitonic edge was visible. This was distinct from the Urbach tail which normally occurs from phonon broadening of the exciton. Examination of the film by differential interference contrast optical microscopy revealed the presence non-uniform regions within the film. This increased the light scattering in the film and also influenced the effective refractive index.

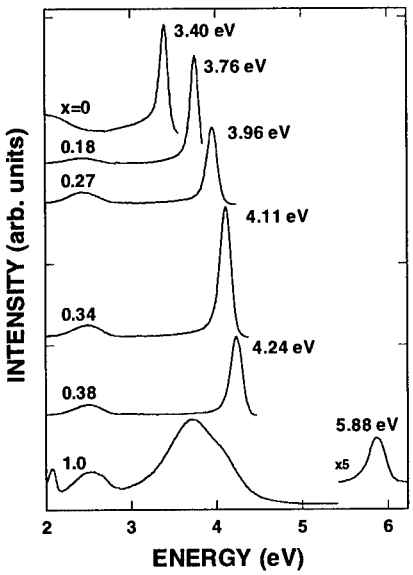


Figure 1. Cathodoluminescence for $Al_xGa_{1-x}N$ Samples

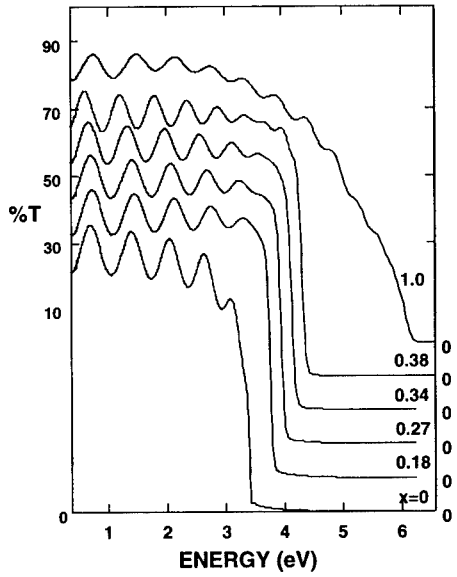


Figure 2. Transmission data for $Al_xGa_{1-x}N$ Sample

The index of refraction, shown in Figure 3, was computed by fitting the transmission data as described in the introduction. The values obtained were about 3 percent lower than those obtained by Ambacher [3]. This is perhaps due to the influence of the buffer layer on the effective index of the film.

The calculated absorption coefficients are plotted in Figure 4. The thin nature of the films and smooth surface morphologies permitted extraction of the absorption coefficient well

above the band gap. In the binary compound, the GaN exciton is clearly visible, and just below the excitonic band edge an absorption tail attributed to the buffer layer is visible. In the alloy films, x=0.27, 0.34, and 0.38, the exciton is suppressed by alloy broadening. The clearly recognizable AlN band edge is shown, but due to the excessive scattering it was not possible to obtain accurate values for the absorption coefficient above 1.5 x 10^5 cm-1.

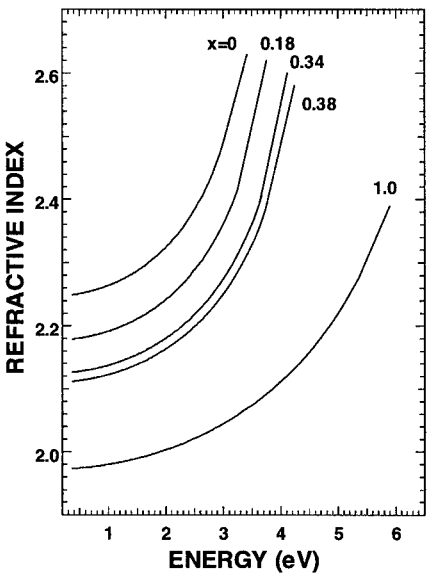


Figure 3. Below band gap refractive index for $Al_xGa_{1-x}N$

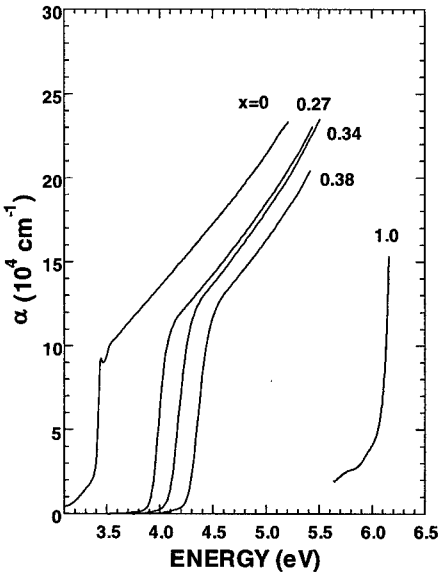


Figure 4. Absorption coefficient determined from transmission measurements

CONCLUSIONS

We have investigated the optical properties of GaN, AlGaN alloys and AlN using scanning electron microscopy cathodoluminescence along with reflectance and transmission spectroscopy. The films used were less than 0.5 μm in thickness which permits direct calculation of the absorption coefficient well above the band gap. The index of refraction below the band gap was obtained by fitting the transmission spectra, and the optical band gap was obtained by fitting the transmission data with Elliott's theory of absorption. The absorption coefficient and index of refraction show reasonable agreement with those determined by other workers. These results provide further information of importance toward the design optimization of optoelectronic devices employing the III-nitrides.

REFERENCES

1. S. Nakamura, M.Senoh, S. Nagahama, N. Iwasa, T. Yamada, T. Matsushita, H. Kiyyoku and Y. Sugimoto, Jpn. J. Appl. Phys. **35,** L74 (1996)
2. S. N. Mohammad, A. Salavador, and H. Morkoc, Proc. IEEE 1306 (1995); S. N. Mohammad and H. Morkoc, "Progress and Prospects of Group III-V Nitride Semiconductors," *Progress in Quantum Electronics*, 1996 Vol. 20, Numbers 5 and 6, pp. 361-525
3. O. Ambacher, M. Arzberger, D. Brunner, H. Angerer, F. Freudenberg, N. Esser, T. Wethkamp, K. Wilmers, W. Richter and M. Stutzmann, MIJ-NIR **2**, Art. 22 (1997)
4. G. Yu, H. Ishikawa, M. Umeno, T. Egawa, J. Watanabe, T.Jimbo and T. Soga, Appl. Phys. Lett **72**, 2204 (1998)
5. F. Abeles and M L Theye, Surf. Sci. **5**, 325 (1966)
6. R. Swanepoel, J. Phys. E **16,** 1214 (1983)
7. R.Swanepoel, J. Phys. E **17**, 896 (1984)
8. J. Szczyrbowski, J. Phys. D **11**, 583 (1978)
9. M. Nowak, Thin Solid Films **254**, 200 (1995)
10. S.H. Wemple and J.A. Seman, App. Opt. **12**, 2947 (1973)
11. R.J. Elliott, Phys Rev **108**, 1384, 1957
12. C. Tanguy, IEEE J. Quantum Electron **32**, 1746, (1998)
13. M.D. Sturge, Phys Rev **127**, 768, (1962)
14. Zhonghai Yu, M.A.L. Johnson, J.D. Brown, N.A. El-Masry, J.W. Cook, Jr., and J.F. Schetzina. Proc. of IX Int. Conf. on MOVPE, LaJolla, CA (May 1998). (To be published in J. Cryst. Growth)
15. S. Nakamura and G. Fasol, *The Blue Laser Diode* Springer-Verlag, New York, 1996.
16. Y. Koide, H. Itoh, N. Sawaki, M Hashimoto, and I Akasaki. *J. Electrochem. Soc.* **133,** 1956 (1986)
17. Y. Koide, H. Itoh, M.R.H. Khan, K. Hiramatsu, N. Sawaki, and I. Akasaki, J. Appl. Phys. **61**, 4540 (1987)
18. K. Knobloch, P. Perlin, J. Krueger, E.R. Weber, C. Kisielowski, MIJ-NSR **3**, Art. 45 (1998)

DEFECT COMPLEXES AND NON-EQUILIBRIUM PROCESSES UNDERLYING THE P-TYPE DOPING OF GaN

Fernando A. Reboredo[1] and Sokrates T. Pantelides[1,2]
[1]Department of Physics and Astronomy, Vanderbilt University, Nashville, TN 37235
[2]Solid State Division, Oak Ridge National Laboratory, Oak Ridge, TN 37831
pantelides@vanderbilt.edu
Cite this article as: MRS Inter J. Nitride Semicond. Res. 4S1, G5.3 (1999)

ABSTRACT

It is well known that hydrogen plays a key role in p-type doping of GaN. It is believed that H passivates substitutional Mg during growth by forming a Mg_s-N-H_i complex; in subsequent annealing, H is removed, resulting in p-type doping. Several open questions have remained, however, such as experimental evidence for other complexes involving Mg and H and difficulties in accounting for the relatively high-temperature anneal needed to remove H. We present first principles calculations in terms of which we show that the doping process is in fact significantly more complex. In particular, interstitial Mg plays a major role in limiting p-type doping. Overall, several substitutional/interstitial complexes form and can bind H, with vibrational frequencies that account for hitherto unidentified observed lines. We predict that these defects, which limit doping efficiency, can be eliminated by annealing in an atmosphere of H and N prior to the final anneal that removes H.

INTRODUCTION

GaN is the most promising wide-gap material for blue-green optoelectronics, but further improvements are needed to enhance performance and reliability for commercial applications. A major issue is to increase p-type conductivity. It has been established that H enhances the incorporation of dopants such as Mg, but it must be removed by post-growth annealing to activate the dopants.[1,2] In general, only a relatively small fraction of the total Mg is activated.[3,4]

Theory has offered a simple account of the process[5,6]: In the absence of H, Mg shallow acceptors are compensated by N vacancies (V_N^+) and Ga interstitials (Ga_i^{+++}), both of which are donors and have low formation energies in p-type material.[7] When H is present, it passivates substitutional Mg (Mg_{Ga}^-) by forming a Mg_{Ga}-N-H complex.[5] The Fermi level rises to the mid-gap region and the formation of V_N^+ and Ga_i^{+++} is suppressed. Subsequent annealing removes H and activates Mg_{Ga}^-. Theory predicted[5] the vibrational frequency of the Mg_{Ga}-N-H complex at 3360 cm^{-1} and, experiments[4] have since found a line at 3125 cm^{-1} whose intensity decreases during annealing. Nevertheless, there are unambiguous indications that the doping process is more complex. The temperature needed to remove H (~700°C) is much higher than expected from the calculated energy to break the Mg_{Ga}-N-H bond (~1.5 eV).[5] Photoluminescence, infrared, and Raman data show clearly that other Mg-related defects are present.[1,3,4] In particular, in material grown by molecular beam epitaxy (MBE), where typically only 10% of Mg is electrically active, infrared and Raman lines in the 2000-cm^{-1} range have been attributed to direct Mg-H bonds.[3] Theory so far has not offered any potential candidates for these complexes.

Here, we report first-principles calculations of key defect reactions and show that p-type doping is in fact a significantly more complex process. In particular, we show that, in addition to Mg_{Ga}-N-H, interstitial Mg (Mg_i) and its complexes play a major role in controlling the process. In Ga-rich growth conditions, compensation of Mg_{Ga}^- occurs mainly though the formation of Mg substitutional-interstitial pairs with a configuration $(Mg_{Ga}\text{-N-Mg})^+$ analogous to Mg_{Ga}-N-H (Fig. 1a). Other defects that play a role are V_N^+, Mg_i^{++}, Ga_i^{+++}, $(Mg_{Ga}\text{-N-}Ga_+)^{++}$, and Mg_{Ga}-V_N. *This plethora of substitutional/interstitial (SI) Mg-related complexes accounts for the high degree of*

Mat. Res. Soc. Symp. Proc. Vol. 537 © 1999 Materials Research Society

Mg incorporation in electrically inactive forms. When H is present, all these complexes are passivated, forming direct Ga-H and Mg-H bonds. The calculated vibrational frequencies of these bonds are in the 2000-cm^{-1} range and provide an identification for infrared and Raman lines that have remained unexplained.[3] Finally, our analysis yields a testable prediction: For samples that show the vibrational signatures of hydrogenated SI complexes, a pre-anneal in an atmosphere of N and H followed by annealing in a N atmosphere would significantly enhance Mg activation.

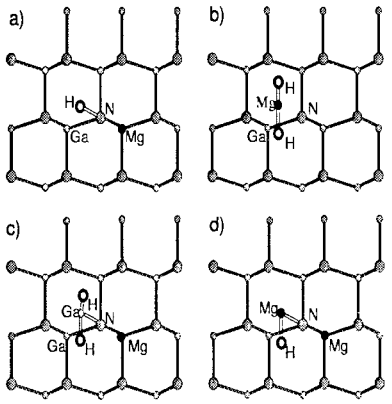


Fig. 1 Schematic representation of some complexes studied in this work: a) Mg_{Ga}-N-H complex; b) Mg_iH_2; c) Mg_{Ga}-N-Ga_i-H_2; and d) Mg_{Ga}-N-Mg_i-H.

METHOD

The calculations were performed in the framework of density functional theory and the local density approximation for exchange and correlation, using ultrasoft pseudopotentials and a plane-wave basis set[8] The Ga 3d electrons and the Mg 2p electrons were treated as valence electrons. Additional details for the pseudopotentials can be found in Ref. 9. The energy cutoff for the basis set was chosen at 25 Ry after studies showed convergent results. Supercells of 32 atoms where used in general but some key results were tested in a 64 cubic cell to ensure convergence with supercell size. Such supercells were also found to be well converged in similar cases by earlier investigators.[9,10]

We used three special **k** points corresponding to the hexagonal symmetry[11] in the wurtzite phase and the {.5,.5,.5} special **k** point in the cubic structure. Results for cubic and wurtzite GaN are generally the same (within 0.1 eV) except in some cases where topology matters. Those cases will be discussed explicitly. All atoms in the supercell were relaxed until the force on each atom was less than 0.15 eV/A. The calculation of the H-related normal modes involved a partial dynamical matrix that included the H atoms and their neighbors. The normal modes were calculated in the harmonic approximation. In a second step, the anharmonic corrections for the transition from the ground to the first excited state of the stretch modes were calculated in a standard way[12] using the coefficients of the polynomial that fits the energy as a function of the amplitude along the normal mode trajectory.

RESULTS

Much of the theoretical literature on defects and impurities in GaN has so far focused on formation energies. However, in a compound semiconductor the formation energies of point defects are functions of the chemical potential of one of the host atoms and the Fermi energy. In the

presence of impurities, formation energies of defect complexes are also functions of the impurity chemical potentials. To avoid much of this complexity, we carried out our analysis by examining key *sequences of defect reactions* that can be studied by using the same supercell containing identical atomic species and excess charges. The resulting reaction energies are more accurate than absolute formation energies of individual defects, especially charged ones. Values for the latter are available in the literature.[5-7,9,10] We will use these values in our analysis, especially the more accurate calculations that treat the Ga d electrons as valence electrons.

We start with the doping process in the absence of H. For p-type material and Ga-rich conditions, V_N^+ and Ga_i^{+++} have low formation energies and comparable concentrations.[7] These native defects are deep donors and their electrons recombine with holes so that p-type doping is thwarted. We have taken the next step and investigated the possible reactions of V_N^+ and Ga_i^{+++} with Mg_{Ga}^-. We found the following:

a) Mg_{Ga}-V_N pairs form with a *small gain in energy* (0.4 eV) with respect to the isolated point defects.

b) $(Mg_{Ga}\text{-N-}Ga_i)^{++}$ complexes form with a large gain in energy (1.6 eV). These complexes have a structure very similar to that of the Mg_{Ga}-N-H (Fig.1a) complexes that have been studied extensively by Van de Walle and Neugebauer. In particular, the Ga_i occupies the antibonding site on the N side of a Mg_{Ga}-N bond. Once the complex $(Mg_{Ga}\text{-N-}Ga_i)^{++}$ forms, additional energy is gained by an exchange between the Mg_{Ga}^- and Ga_i^{+++} to yield interstitial Mg (Mg_i^{++}). The additional energy gain is 1.7 eV, for a net gain of 3.3 eV.

Once Mg_i^{++} are available, they pair up with isolated Mg_{Ga}^- to form $(Mg_{Ga}\text{-N-}Mg_i)^+$ complexes. This pairing yields an extra energy gain of 0.7 eV, for a *large net energy gain of 4.0 eV.* (Table I).

Table I

Relative formation energies of different defects in p-type GaN in Ga-rich conditions. A doped crystal with a concentration of sustitutional Mg_{Ga}^- and a Ga_i^{+++} or V_{N+} are the zero energy references as indicated.

Complex	Energy (eV)	Complex	Energy (eV)
$[Mg_{Ga}^-]$; Ga_i^{+++}	0 (reference)	$[Mg_{Ga}^-]$; V_N^+	0 (reference)
$(Mg_{Ga}\text{-N-}Ga_i)^{++}$	-1.6	Mg_{Ga}-V_N	-0.3
Mg_i^{++}	-3.3		
$(Mg_{Ga}\text{-N-}Mg_i)$+	-4.0		

We emphasize that the results of Table 1 are obtained with identical supercells (same atoms, same charge states) in each case so that the relative energies listed are very accurate. For an absolute comparison of the energies of interstitial- and vacancy-related complexes one needs the absolute formation energies of Ga_i^{+++} and V_N^+, which represent a major challenge. Boguslawski et al. have reported the most accurate calculations that current capabilities allow and found the two energies to be comparable.[7] Note, however, that, even if the formation energy of Ga_i^{+++} were to be larger than that of V_N^+ by as much as 2.5 eV,[5] the SI complexes just described would have to be taken into account to properly describe the physics of p-type doping.

The clear conclusion then is that the entire family of SI defects play a role in controlling doping. Under equilibrium Ga-rich conditions in the absence of other impurities, $(Mg_{Ga}\text{-N-}Mg_i)^+$ is the dominant defect responsible for thwarting p-type doping, followed by Mg_i^{++}, and $(Mg_{Ga}\text{-N-}Ga)^{++}$. In p-type material under equilibrium N-rich conditions, Ga_i are suppressed in favor of other native defects[5,7] that do not exchange with Mg_{Ga}. On the other hand, if thermodynamic

equilibration does not occur during low-temperature growth, the formation of defects is governed by kinetics so that any or all stable defects may form irrespective of their formation energies.

We turn now to the case when H is present. First, we confirmed the known result that Mg_{Ga} binds an H atom in a Mg_{Ga}-N-H configuration. In addition, the SI complexes bind one or two H atoms, depending on their formal charge, and Ga_i^{+++} binds up to three H atoms. In particular, we carried out detailed calculations on the following complexes $(Mg_{Ga}\text{-}N\text{-}Ga_i\text{-}H)^+$, $Mg_{Ga}\text{-}N\text{-}Ga_i\text{-}H_2$, $(Mg_iH)^+$, Mg_iH_2, and $Mg_{Ga}\text{-}N\text{-}Mg_i\text{-}H$. In this context we note that the distinction between cubic and hexagonal GaN is important: the geometries of some of the hydrogenated SI complexes are quite different in the two isomorphs (we will discuss the geometries later in the paper). From here on we will confine our discussion to hexagonal GaN, which is the material that is most commonly used for experiments and device fabrication.

There is a substantive difference between Mg_{Ga}-N-H and the hydrogenated SI (SI-H) complexes: In Mg_{Ga}-N-H, H acts as a donor constituent, whereas in the SI-H complexes H acts as an acceptor constituent. The latter have occupied energy levels in the gap which is consistent with higher formation energies (Table II). Nevertheless, as we shall see below, the SI-H complexes play a key role in the non-equilibrium processing that is needed to achieve p-type doping.

Table II

Relative formation energies of H-compensated defects (in eV). The H chemical potential is chosen to be the formation energy of H_2 in an interstitial site.

Complex	Ga-rich; H-rich	N-rich; H-rich
Mg_{Ga}-N-H	0 (reference)	-3.6
Mg_iH_2	3.9	3.9
Mg_{Ga}-N-Ga-H_2	4.2	4.1
Mg_{Ga}-N-Mg-H	4.1	0.5

Infrared and Raman spectra[3] have found several lines in the vicinity of 2150 cm^{-1} that were initially attributed to Mg_{Ga}-H stretch modes because they where absent in control samples without Mg.[3] Subsequent theory, however, found that H does not bind directly to Mg_{Ga} , but rather forms the Mg_{Ga}-N-H complex whose calculated vibrational frequency is 3360 cm^{-1}.[5] In recent experiments, Gotz et al.[4] detected the 3125-cm^{-1} infrared line that corresponds to Mg_{Ga}-N-H and observed it decrease as a function of annealing that activates Mg acceptors. They did not report measurements in the 2000-cm^{-1} range. Earlier work had proposed that V_N^+ may be the dominant compensating defect. Upon hydrogenation, V_N^+ traps an H atom but their calculated frequency is less than 600 cm^{-1}.[6] Accordingly, the identification of the vibrational lines in the vicinity of 2150-cm^{-1} has remained an important open problem.

We calculated the vibrational frequencies of several SI-H complexes and indeed found Mg-H and Ga-H in the vicinity of 2000-cm^{-1}. The uncertainty in the calculations is ~200 cm^{-1} so that identification of the observed defects cannot be made by simply comparing theoretical and experimental vibrational frequencies. Symmetry and other considerations, however, help narrow the choices. We discuss here the strongest candidates to account for the experimental data.

Mg_iH_2 is a stable complex with the Mg_i near the hexagonal (O) interstitial site[7] (see Fig. 1b) and the two H's are along the c direction. The point symmetry is C_{3v}. There is no reflection symmetry along the c direction and the two Mg-H bond lengths are different, namely 1.55 A and 1.78 A . The two "spring constants" are also different and, as a result, the two H's oscillate almost independently of each other. The short Mg-H bond has a stretch mode at 2001 cm^{-1}. The long Mg-H bond has a stretch mode at 1570 cm^{-1}. The wag-mode frequencies are 1370 cm^{-1} and 1200 cm^{-1} respectively. The entire ``molecule" oscillates with frequencies lower than 500 cm^{-1}.

Turning back to the short-bond stretch mode, we note that the movement of the atoms is in the c direction, making it difficult to detect by infrared absorption if the wave vector of the incident light is oriented in the c direction. These considerations and the calculated frequencies make the short-bond stretch mode of the Mg_iH_2 complex an excellent candidate for the Raman lines[3] at 2151 cm^{-1} and 2185 cm^{-1} that are not seen by infrared experiments. The long-bond stretch mode frequency is too small to explain the second peak of the pair in the experimental data. The second peak in the pair might be due to an anharmonic coupling between the stretch mode and the vibration of the whole molecule. The frequencies of these "molecular" modes are low enough for their first excited states to be populated at room temperature. If this is the case, the relative amplitude of these peaks should be a function of the temperature.

We now consider the complex Mg_{Ga}-N-Ga_i-H_2. In this defect, the H's (see Fig. 1c) are again located on either side of Ga_i (see Fig. 1b). Again we found a short Ga-H bond (1.50 A) and a long Ga-H bond (1.82 A). The symmetry of the defect is no longer C_{3v} because of the presence of Mg_{Ga}. Consequently the Ga_i-H bonds are not oriented exactly in the c direction so that the stretch modes are accessible to infrared spectroscopy when the wave vector of the light is in the c direction. We obtained a frequency of 2270 cm^{-1} for the short-bond stretch mode and 1500 cm^{-1} for the long-bond stretch mode. The high-frequency mode is a strong candidate to explain the second pair of peaks observed experimentally at 2168 cm^{-1} and 2219 cm^{-1}. Here again the pair of excitations might be due to the influence of anharmonic couplings.

Finally, in Fig. 1d we show schematically the structure of Mg_{Ga}-N-Mg_i-H. The stretch mode frequency of this complex is calculated to be 1320 cm^{-1}. We are not aware of experimental data in this range of frequencies. Measurements in the range 1000-2000 cm^{-1} would be highly desirable to test the theoretical predictions.

We now discuss the implications of the above results on understanding the doping process during growth by MBE or chemical vapor deposition (CVD). During growth by MBE, the temperatures are relatively low (~800°C) and H is present unintentionally.[3] Experiments have shown that p-type doping is achieved with about 10% of the Mg in the sample being active. In material with very high Mg content (10^{20} cm^{-3}), moderate H content and low doping efficiency, distinct infrared and Raman lines have been observed in the vicinity of 2200 cm^{-1},[3] which we have now identified as due to SI-H complexes. We note that our analysis, having identified these SI complexes as limiting doping efficiency, also suggests a process to eliminate the undesirable SI-H complexes and increase doping efficiency: Annealing in a *H-rich atmosphere* or, better yet, in an atmosphere rich in both H and N, will lead to the conversion of the SI-H complexes to Mg_{Ga}-N-H complexes. This result follows naturally from the fact the SI-H complexes have larger formation energies (Table 2). The N atmosphere helps by suppressing formation of Ga_i and V_N, both of which are detrimental to p-type doping,[5,7] and favors formation of V_{Ga} *whose presence helps convert* Mg_i to Mg_{Ga}. A subsequent anneal in a N-rich atmosphere would activate Mg as in the case of the CVD-grown films[1] (see also below).

During CVD growth of GaN, H is introduced in ample quantities at relatively high temperatures (~1000 °C). If the material were fully equilibrated, the dominant hydrogenated defect would indeed be Mg_{Ga}-N-H as suggested by earlier theory[5] and confirmed by Table 2. There are strong indications, however, that the material is generally not fully equilibrated.

In their pioneering and extensive studies of CVD GaN, Nakamura et al.[1] found photoluminescence peaks which they attributed to Mg-H complexes. These experiments determine the energy levels of the underlying defects but provide no structural information. Theoretical results on energy levels are not reliable for identification purposes. It would be highly desirable to correlate the luminescence data with infrared and/or Raman data to facilitate identification.

It is possible that, by empirical means, suppression of SI-H defects is currently achieved in the growth of high-quality GaN. Nevertheless, systematic infrared and Raman data in both the

2000-cm^{-1} and 3000-cm^{-1} range would help unravel further the complexity of p-type doping. For example, SI-H defects are a natural candidate to account for the fact that annealing CVD material to remove H requires higher temperatures than theory can account for in terms of breaking the H bonds in the Mg_{Ga}-N-H complexes.[5] The rate-limiting step for Mg activation may very well be determined by the conversion of SI-H complexes to Mg_{Ga}-N-H. We, therefore, propose the following: CVD samples should be checked for the presence of SI-H complexes via their infrared signatures in the 2000-cm^{-1} range. If present, a pre-anneal in a H and N atmosphere followed by annealing in an N atmosphere would again produce optimum activation.

CONCLUSIONS

We have shown that complexes involving self-interstitials and interstitial impurities play a major role in the p-type doping process. The theoretical prediction of these defects provides an identification of the infrared and Raman lines observed in MBE-grown material. The combined experimental and theoretical information suggests that the control of these defects is the ultimate key in achieving higher p-type conductivity. Systematic experimental studies, especially using infrared and Raman spectroscopies, guided by the present theoretical results, would offer the promise of achieving higher p-type conductivity. The most important conclusion of the present work is that an annealing stage in H-rich atmosphere followed by annealing in a N-rich atmosphere would generally improve p-type doping efficiency. We anticipate that similar defect complexes may also form in the case of other dopants such as Be and possibly in the case of n-type dopants as well as in other wide-gap semiconductors.

ACKNOWLEDGEMENTS

The authors would like to thank V. Fiorentini and A. Filippetti for providing us the ultrasoft pseudopotentials and M. Ferconi for related discussions. This work was supported in part by the National Science Foundation Grant DMR9803768 and by the William A. and Nancy F. McMinn Endowment at Vanderbilt University.

REFERENCES

1. S. Nakamura, T. Mukai, and M. Senoh, Appl. Phys Lett. 64, 1687 (1994); S. Nakamura et al., Jpn. J. Appl. Phys. 35, L74 (1996).
2. J. A.Van Vechten, J. D. Zook, R. D. Horning and B. Goldenberg, Jpn. J. Appl. Phys. 31, 3662 (1992); M. Johnson and D. P. Bour, Appl. Phys. Lett. 68, 3470 (1996).
3. M.S. Brandt et al., Appl. Phys Lett. 64, 2264 (1994); M. S. Brandt et al., Phys. Rev. B 49, 14758 (1994) and references therein.
4. W. Goetz, N. M. Johnson, J. Walker, D. P. Bour, and R. A. Street, Appl. Phys. Lett. 68, 667 (1996); W. Goetz, N. M. Johnson, D. P. Bour, M. D. McCluskey, and E. E. Haller, Appl. Phys. Lett. 69, 3725 (1996); W. Goetz, N
5. J. Neugebauer and C. G. Van de Walle, Phys. Rev. B 50, 8067 (1994); Phys. Rev. Lett. 75, 4452 (1995); *ibid.*, Appl. Phys. Lett. 68, 1829 (1996).
6. C. G. Van de Walle, Phys Rev. B 56, R10020 (1997).
7. P. Boguslawski, E. L. Briggs, and J. Bernholc, Phys. Rev. B 51, 17255 (1995).
8. M. C. Payne, M. P. Teter, D. C. Allan, T. A. Arias and J. D. Joannopoulos, Rev. Mod. Phys. 64, 1045 (1992).
9. F. Bernardini, V. Fiorentini, and A. Bosin, Appl. Phys. Lett. 70, 2990 (1997).
10. C. H. Park and D. J. Chadi, Phys. Rev. B 55, 12995 (1997).
11. D. J. Chadi, and M. L. Cohen, Phys. Rev. B 8, 5747 (1973).
12. L. D. Landau and E. M. Lifshitz, *Quantum Mechanics,* (Pergamon, Oxford, 1997).

ROLE OF THE SUBSTITUTIONAL OXYGEN DONOR IN THE RESIDUAL N-TYPE CONDUCTIVITY IN GaN

W.M. Chen,[*] I.A. Buyanova,[*] Mt. Wagner, [*] B. Monemar, [*] J.L. Lindström, [**] H. Amano [***], I. Akasaki [***]

[*] Department of Physics and Measurement Technology, Linköping University, S-581 83 Linköping, SWEDEN, wmc@ifm.liu.se
[**] Swedish Defense Research Establishment, Box 1165, S-581 11 Linköping, SWEDEN
[***] Department of Electrical and Electronic Engineering, Meijo University, 1-501 Shiogamaguchi, Tempaku-ku, Nagoya 468, JAPAN

Cite this article as: MRS Internet J. Nitride Semicond. Res. 4S1, G5.4(1999)

ABSTRACT

A detailed photoluminescence (PL) study reveals a striking similarity in local vibrational properties of a defect center in GaN as compared to that for the substitutional O_P donor in GaP. This observation could be interpreted as if the center is in fact related to the substitutional oxygen donor in GaN. The deep-level nature experimentally determined for the defect center calls for caution of a commonly referred model that the substitutional oxygen donor is responsible for the residual n-type conductivity in GaN.

INTRODUCTION

Oxygen is one of the most common impurities which is frequently present during growth and processing steps as a contaminant, and can be unintentionally incorporated into many semiconductors including III-nitrides. This uncontrolled introduction of the oxygen impurity may affect and sometimes degrade the performance of semiconductor devices. The understanding of the role of oxygen in altering the material properties, and eventually a control of its introduction, are therefore of crucial importance for a reliable device operation. The substitutional oxygen donor has recently been suggested to be responsible for a long-standing materials problem - the residual n-type conductivity in oxygen-containing GaN. This conclusion was based both on theoretical calculations of the formation energy and the electronic structure of the oxygen donor in GaN [1,2] and on experimental observation of a strong correlation between the oxygen content in the material and the free electron concentration [3]. Though there is so far no direct experimental evidence available as to the exact form of the oxygen center and its geometric structure, the suggestion seemed to be reasonable and consistent until recently, when a new photoluminescence emission (denoted as the 0.88-eV PL below) of a deep center has provided microscopic information on local vibrations of the defect.

In this paper, we shall demonstrate that these local vibrations resemble those reported earlier for the substitutional O_P donor in GaP. This striking similarity, together with the electronic structure revealed from a detailed PL study of the deep center, has led us to suggest that the substitutional O_N donor in GaN could be a deep donor, and thus to call for caution in assessing its role in the n-type conductivity of the material.

Mat. Res. Soc. Proc. Vol. 537 © 1999 Materials Research Society

EXPERIMENTAL

The samples studied in this work were a variety of wurtzite GaN layers, typically 1- 200 μm thick, grown by hydride vapor phase epitaxy (HVPE) or metal organic chemical vapor deposition (MOCVD) on (0001) sapphire or 6H SiC substrates. The conductivity of the samples before electron irradiation varies over a wide range from highly n-type ([n] ~ higher 10^{18} cm^{-3}), highly compensated ([n] ~ 10^{16} - lower 10^{17} cm^{-3}) to highly p-type ([p] ~ higher 10^{17} cm^{-3}). These samples were irradiated by 2.5-MeV electrons at room temperature with a dose of $1x10^{17}$ - $4x10^{18}$ cm^{-2}, to enhance the 0.88-eV PL intensity.

In PL experiments, the samples were excited by the 334 or 351 nm UV lines of an Argon ion laser. The resulting PL was spectrally dispersed by a 0.85-m double grating monochromator, and monitored by a cooled Ge detector. In temperature dependent PL studies, the sample temperature was varied between 1.5 K and room temperature. A magnetic field up to 14 T was applied in Zeeman studies of the PL spectra, with the aid of a superconducting magnet.

RESULTS AND DISCUSSION

Defect Models

A typical low-temperature 0.88-eV PL spectrum in GaN is shown as the upper curve in Fig.1. The observation of this PL emission in electron irradiated GaN was first reported by Linde et al [4]. It can be observed in all the GaN epilayers studied, indicating that it is related to either a native defect or a common contaminant. This 0.88-eV PL is characterized by a relatively sharp no phonon (NP) line near 0.88 eV, accompanied by a rich structure of phonon replicas on the lower energy side. A detailed inspection of the phonon replicas reveals many local phonon modes, apart from the known lattice phonons. This in fact represents a rare case in GaN when so many local phonons have been well resolved. What is more unusual and

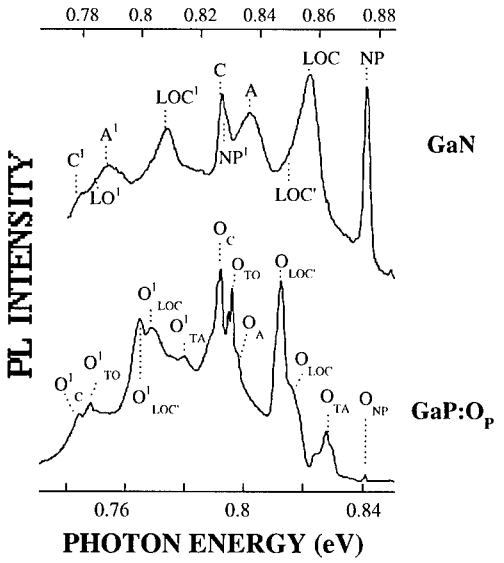


Fig. 1 The 0.88-eV PL in GaN (the upper curve) and the 0.841-eV in GaP (the lower curve) taken at 1.6 K. The horizontal scales for the photon energy are shifted relatively to line up the NP lines of the two spectra, for easy comparison. The definitions of the notations follow mostly those commonly used in the literature [5]. NP for no-phonon, TA for transverse acoustic phonon of the host lattice, TO for transverse optical phonon of the host lattice, LO for longitudinal optical phonon of the host lattice, LOC, LOC', A and C for local phonons. Superscript 1 denotes the involvement of an additional phonon $\hbar w_0$.

Table I. A summary of the local phonon energies from the 0.841-eV PL in GaP and the 0.88-eV PL in GaN. The definitions of the notations for local phonons, i.e. LOC, LOC', A and C, follow mostly those commonly used in the literature [5]. Superscript 1 denotes the involvement of an additional phonon $\hbar w_0$.

Local Phonon Modes	Energy Shifts (meV)	
	0.841-eV PL in GaP	0.88-eV PL in GaN
LOC	24.7	19.1
LOC'	28.4	26.2
A	43.0	39.6
C	48.7	49.1
LOC^1	24.7+47.5	19.1+48
LOC'^1	28.4+47.5	26.2+48
A^1	43.0+47.5	39.6+48
C^1	48.7+47.5	49.1+48

surprising is that a striking similarity has been found between these local phonons in GaN and those observed in the O_P related 0.841-eV PL emission in GaP. To illustrate that, the 0.841-eV PL in GaP is also shown in Fig.1 (the lower curve), but shifted in energy to line up the NP lines of the two PL emissions. The local phonon modes involved in the two cases are listed in Table I for an easy comparison. It is rather obvious that nearly all the local phonons are indeed similar in energy for these two semiconductors, excluding the lattice phonons which are different between them. This fact can either be interpreted as a pure coincidence or it can indicate that a similar defect is involved. Since this seems to be the only case, to our knowledge, that such a striking similarity in nearly all local phonon modes was found between two defect systems in semiconductors, a pure coincidence seems to be rather unlikely. If this is the case, the knowledge on physical properties of the 0.841-eV PL center in GaP can be inferred to the 0.88-eV PL center in GaN.

Fortunately, the 0.841-eV PL in GaP was the subject of intensive investigations during the seventies and eighties, and a great deal of its properties have been established. The origin of the 0.841-eV PL has unambiguously been associated with the radiative transition between the valley-orbit states $1s(E) \rightarrow 1s(A_1)$ of the isolated, substitutional O_P donor in its neutral charge state [5], as the final step of the electron capture to the positively charged O_P donor. The phonon sideband on the low energy side of the 0.841-eV PL (Fig.1 and Table I) has in fact been regarded as characteristic for the O_P donor in GaP. From the observed isotope shifts ($O^{16} \rightarrow O^{18}$) in the energy of O_{LOC} and $O_{LOC'}$, for example, they are believed to be primarily dominated by the motion of the O atom [5]. To possess similar local vibrations in GaN, the corresponding defect should have similar local surroundings and bonding as the O_P donor in GaP, i.e. one oxygen and four gallium atoms, at least within the nearest neighbor shell. The only candidate is then the substitutional O_N donor in GaN, either an isolated donor or a complex involving O_N, as the defect responsible for the 0.88-eV PL. Due to the striking similarity between the local phonons observed in the 0.88-eV PL in GaN and the 0.841-eV PL in GaP, the other constituent(s) of the complex defect should reside beyond the nearest neighbor shell.

It is interesting to note that the energies of many other localized phonons (such as O_A, O_C and hw_0), not fully understood so far for the O_P donor in GaP, are also remarkably similar between the O_P donor in GaP and the O_N donor in GaN (Table I).

The role of post-growth electron irradiation in enhancing the 0.88-eV PL intensity in GaN is not yet fully understood and requires further studies. A change in the Fermi level position by the electron irradiation might be one of the explanations, which has been shown to be important for

the observation of the 0.841-eV PL emission in the case of the O_P donor in GaP. Other possibilities include an irradiation induced formation or activation of the corresponding PL center.

Recombination Models

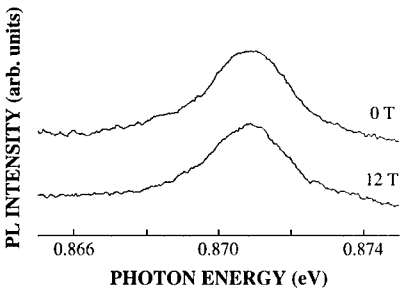


Fig.2 The 0.88-eV PL spectra in GaN taken at 2 K in the vicinity of the NP line, at magnetic fields of 0 and 12 T.

The recombination mechanism of the 0.88-eV PL in GaN could thus be explained in terms of an electronic transition related to the substitutional O_N center, either an isolated donor or a complex involving O_N.

Within the first model of an isolated, substitutional O_N donor, two possible mechanisms responsible for the 0.88-eV PL can be a transition between an excited state and the ground state of the O_N donor in its neutral charged state (in the same fashion as the 0.841-eV PL in GaP), or in its negatively charged state. In the latter case, the capture of the second electron to the O_N donor is assumed not to cause a large lattice relaxation of the defect due to a severe softening of the Ga-O bonds so that the local phonon modes are reasonably well preserved. This is not the case for the O_P donor in GaP, of which a large lattice relaxation was observed upon the capture of the second electron [5]. The situation may be quite different in GaN in the presence of a lower-symmetry wurtzite crystal field and a more rigid and compact crystal lattice.

To determine whether the 0.88-eV PL originates from an electronic transition within the neutral or negatively charged state of the isolated O_N donor, a detailed magnetooptical (Zeeman) study was carried out. This was based on the expectations that a different behavior between the two charge states should be observed upon application of an external magnetic field. In the neutral charge state, only one electron is bound to the O_N donor. Both the 1s ground state and the excited states are at least spin degenerate and are expected to split in the magnetic field. In the case of the negatively charged state two electrons are bound to the donor. The ground state is then expected to be a non-degenerate singlet, where the spins of the two electrons are paired off. The excited states can, however, be either degenerate or non-degenerate. In Fig.2, PL spectra in a close vicinity of the NP line are shown with or without applying a magnetic field. As it is clear from the figure, no noticeable splitting can be detected when the magnetic field was along the c-axis or was tilted by an angle with respect to the c-axis. It should be noted that the size of the expected Zeeman splitting, assuming a common value of g close to 2 in GaN, is comparable to the PL linewidth and is expected to be observed in the experiments. Therefore the absence of any splitting or broadening can be taken as a piece of strong evidence that the recombination occurs between the singlets. In other words, both the excited and ground state are non-degenerate. This experimental fact excludes the possibility of the neutral charge state of the O_N donor as responsible for the 0.88-eV PL, leaving the negatively charged state as a possible model.

In the second model that an internal electronic transition at a complex defect involving the O_N donor is responsible for the 0.88-eV PL, both the ground and excited state should be singlets to agree with the Zeeman results.

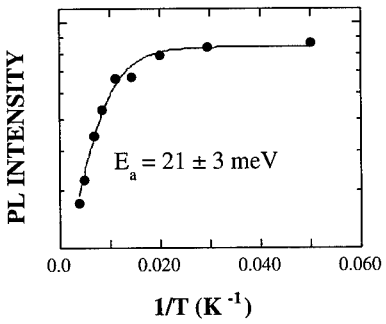


Fig.3 An Arrhenius plot of the integrated intensity of the 0.88-eV PL emission. The activation energy E_a for the thermal quenching can be estimated.

Binding Energy

In order to assess the role of the O_N donor in GaN in the residual n-type conductivity, the knowledge on the binding energy of the O_N donor in GaN is essential. From the PL transition energy, the energy separation between the ground and excited state can be determined to be around 0.88 eV. The determination of the binding energy thus requires the knowledge of the ionization energy from the excited state to the bottom of the conduction band. This can be done by temperature dependent studies of the PL intensity, where the thermal quenching of the PL is a direct result of the thermal ionization process. In Fig.3 such a thermal quenching spectrum of the 0.88-eV PL is shown. The activation energy of the thermal quenching, i.e. the energy separation between the excited state to the bottom of the conduction band, was estimated to be about 21 meV. It should be pointed out that this value is fairly close to the binding energy expected for the effective-mass donor electron in GaN. Adding the value of 0.88 eV between the ground and excited state, it totals a value of approximately 0.9 eV for the binding energy of the electron for the 0.88-eV PL center.

In the model of the isolated, negatively charged O_N donor, this corresponds to the binding energy of the second electron at the donor. Or equivalently, the (-/0) level of the O_N donor in GaN is located at ~ E_c - 0.9 eV. Disregarding the possibility of a negative-U effect, granted by the assumption of the absence of a large lattice distortion discussed above, the binding energy of the first electron at the O_N donor in GaN should be larger than 0.9 eV. Within this model, the isolated, substitutional O_N donor is too deep to be ionized at room temperature to account for the residual n-type conductivity in GaN. Other origins must therefore be sought in this case. From a strong correlation between the oxygen content and the free electron concentration [3], however, it seems reasonable to assume that the shallow donor(s) responsible for the residual n-type conductivity in O-containing GaN should somehow be related to oxygen. It can be an O-related defect, other than the isolated substitutional O_N donor, such as an oxygen interstitial or a complex involving substitutional or interstitial oxygen.

Within the second model of a complex involving the O_N donor, the binding energy of the isolated O_N donor can not be deduced in a similar way. The value of 0.9 eV determined for the ionization energy from the ground state of the complex can be largely contributed by the potential of the O_N donor. A quantitative analysis is, however, hardly possible. Based on the experimental observation that the electronic transition is strongly coupled to the local vibrations, a major part of the defect wavefunction should be localized near the O_N donor. This implies that the O_N donor is most likely a deep donor, and can thus not be responsible for the residual n-type conductivity in GaN.

SUMMARY

A striking similarity in the local vibrational properties between the 0.88-eV PL in various wurtzite GaN samples and the 0.841-eV PL in GaP has been revealed from a detailed photoluminescence study. This similarity, together with the earlier unambiguous identification of these local vibrations originating from the isolated, substitutional O_P donor in GaP, suggests that the 0.88-eV PL in GaN is due to an electronic transition related to the substitutional O_N donor. Though the exact geometric structure of the center can not be determined at present, possible models have been discussed in terms of the isolated O_N donor or a complex defect involving the O_N donor. Within the model of the isolated O_N donor, the 0.88-eV PL could originate from the capture of the first or second electron to the O_N donor. The Zeeman studies of the electronic structure of the defect states involved in the recombination seem to rule out the possibility that the first electron capture could be responsible. In combination with the temperature dependent studies of the 0.88-eV PL, the isolated O_N donor is concluded to be a deep donor with a large binding energy large than 0.9 eV. It is thus too deep to be responsible for the high residual n-type conductivity in GaN. Within the second model (i.e. an O_N-related complex defect giving rise to the 0.88-eV PL), the other constituent(s) of the complex defect should reside beyond the nearest neighbor shell to account for the similarity in the local vibrations between O_N in GaN and O_P in GaP. A strong coupling of the electronic transition with the local vibrations also seems to indicate that the O_N donor in GaN is a deep donor. This work therefore calls for caution with the commonly referred model, where the O_N donor is suggested to be responsible for the residual n-type conductivity in O-rich GaN.

REFERENCES

1. J. Neugebauer, C. G. Van de Walle, "Atomic geometry and electronic structure of native defects in GaN", Phys. Rev. B 50 (11), 8067 (1994).

2. Jörg Neugebauer and Chris G. Van de Walle, "Gallium vacancies and the yellow luminescence in GaN", Appl. Phys. Lett. 69 (4), 503 (1996).

3. G. Wetzel, T. Suski, J. W. Ager, E. R. Weber, E. E. Haller, S. Fischer, B. K. Meyer, R. J. Molnar, P. Perlin, " Pressure induced deep gap state of oxygen in GaN", Phys. Rev. Lett. 78 (20), 3923 (1997).

4. M. Linde, S. F. Uftring, G. D. Watkins, V. Härle and F. Scholz, "Optical detection of magnetic resonance in electron-irradiated GaN", Phys. Rev. B55, R10177 (1997).

5. For a review, see e.g. P.J. Dean " Oxygen in GaP" in "Deep Centers in Semiconductors" ed. S.T. Pantelides (Gordon and Breach Science Pub. New York, 1986) p.185; P.J. Dean and C.H. Henry, Phys. Rev. 176, 928 (1968).

INTERFACE EFFECTS ON THE PERSISTENT PHOTOCONDUCTIVITY IN THIN GaN AND AlGaN FILMS

O. P. Seifert *, O. Kirfel *, M. Munzel *, M. T. Hirsch *, J. Parisi *
M. Kelly **, O. Ambacher **, and M. Stutzmann **

* University of Oldenburg, FB8/EHF, D-26129 Oldenburg
** Technical University of Munich, Walter Schottky Institute, D-85748 Garching

Cite this article as: MRS Internet J. Nitride Semicond. Res. 4S1, G5.5 (1999)

Abstract

Thin films of GaN and its alloy AlGaN are investigated with respect to their properties of the persistent photoconductivity (PPC). In this work, we show that the film-substrate interface plays an important role for the metastable electrical effect. Strongly absorbed bandgap light causes an increase of photoconductivity which is about one order of magnitude higher when the sample is illuminated from the substrate side near the interface than from the growth side. To access the interface properties at the substrate, we use temperature-dependent Hall effect measurements. The smallest PPC effect was observed for the GaN film with the best interface properties grown on SiC.

I. Introduction

GaN and its alloys with In and Al have become the most favorite candidates for blue light emitting diodes, laser diodes, and high-temperature, high-power electronic devices [1,2]. It has been shown very early that intrinsic defects play an important role in the electrical behavior of these materials [3,4]. Extensive studies on defect-related behavior like, e.g., the "yellow band luminescence" or the consequences of additional defect-rich layers for Hall measurements [5,6] have been performed. Also the persistent photoconductivity (PPC) observed by several groups [7,8], is discussed as a result of native defects in GaN. However, since the PPC seems to be present independent of the doping, alloying and growth method, other sources for the long-time constants connected with the metastability have to be considered. In this work, we investigate the influence of the interfacial and defect-rich layer on the PPC and Hall effect measurements.

II. Experiment

The samples were grown by metal-organic chemical vapor deposition (MOCVD) as well as by molecular beam epitaxy (MBE). As substrate material, both sapphire and SiC were used. For some samples, a 50nm thick GaN low-temperature buffer layer was also grown. Ohmic contacts were prepared in a coplanar van der Pauw geometry by electron beam evaporation of 20nm Ti and 100nm Al and subsequent annealing in N_2 atmosphere at 900°C for around 60s. For the light-dependent PPC measurements, an Oxford cryostat CF1204 was used in combination with a Xenon lamp and a Bentham M300 monochromator. In this setup, it is possible to mount the sample for front- and backside illumination. Temperature-dependent Hall effect measurements were carried out in a Janis ST300 cryostat and Bruker B-E 10 magnet system. In Table I, the samples under investigation are summarized.

Mat. Res. Soc. Proc. Vol. 537 © 1999 Materials Research Society

Table I: Samples used in this work for PPC and Hall effect measurements
* the grower did not provide any details about the buffer

Sample	Alloy	Growth	Buffer	Substrate	dopant	n_{eff} [cm^{-3}]
SM3	GaN	MBE	none	sapphire	unint. n-type	$3,0x10^{17}$
SM5	$Al_{0.15}Ga_{0.85}N$	MBE	none	sapphire	Si, n-type	$2,1x10^{18}$
SI3	GaN	MOCVD	yes*	sapphire	Si, n-type	$7,5x10^{18}$
SM1	GaN	MOCVD	50nm GaN	sapphire	unint. n-type	$5,5x10^{17}$
SI6	GaN	MOCVD	yes*	SiC	Si, n-type	$1,7x10^{18}$

III. Results of photoconductivity measurements

The buildup transients for the PPC have been measured for different values of the excitation wavelength. PPC was observed in all samples. However, the PPC magnitude under similar illumination conditions varied significantly for GaN and AlGaN and also showed differences with respect to samples with different interface regions.
For the $Al_{0.15}Ga_{0.85}N$ sample, the magnitude of the PPC, i.e., the excess conductivity due to illumination compared to the dark conductivity value, is in the order of 250%, whereas for all GaN samples grown on *sapphire* it is between 10% and 60%. However, for the GaN sample grown on *SiC*, the PPC magnitude is only around 1%. One main difference between these GaN samples is given by the substrate. Therefore, a simple but significant test for the influence of the interface between the substrate and the GaN film on the PPC behavior is to use strongly absorbed bandgap light for excitation and observe the PPC buildup transients under frontside illumination (i.e., from the growth side) and backside illumination (i.e., sample is illuminated through the substrate). In Fig. 1, the *excess* conductivity transients for a GaN sample grown on sapphire is shown. For illumination from the substrate side with strongly absorbed bandgap light of λ=300nm (4.1eV), the increase in conductivity is about one order of magnitude higher than in the case of illumination from the growth side.

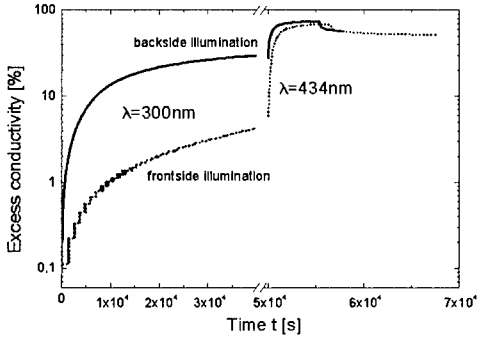


Fig. 1: Comparison of excess conductivity transients under different illumination conditions for a GaN sample grown on sapphire. The dotted line results from illumination from the frontside, the solid line from illumination from the substrate side (backside). At t=0s, the first illumination cycle with strongly absorbed bandgap light (λ=300nm) is started. The second cycle of illumination with subbandgap light of λ=434nm starts at ~$5x10^4$s. For the subbandgap light illumination, both transients exhibit about the same value at the end of illumination. But for illumination with strongly absorbed bandgap light, the excess conductivity is by a factor of ten higher when illuminated through the substrate (i.e., light absorption takes place near the substrate-GaN interface) than illuminated from the growth side.

Comparing this difference with the behavior of the sample under illumination with subbandgap light of λ=434nm (2.9eV), the change in conductivity is the same independent of the illumination direction. For a more detailed understanding of the influence of the interfacial layer between the substrate and the GaN film on the PPC effect, an analysis of the photoconductivity *buildup* transients can be very helpful.

The buildup transient measurements were performed as follows: the samples were kept in the dark at 340K for 2h to reach equilibrium dark conditions and afterwards cooled down to 100K. The conductivity increase due to illumination at each wavelength was then measured for 4h. Then the samples were heated again up to 340K for several hours in the dark. This cycle was repeated for all measurement wavelengths between 400nm and 1000nm. The photon flux for all measurements was kept constant at ~ $2x10^{14}$ $s^{-1}cm^{-2}$. The widely used stretched exponential fit shows good agreement for each transient on a linear time scale. However, the fit was not satisfying on a logarithmic time scale. Therefore, we use a different approach and characterize the conductivity transients in analogy to Ref. [9] by plotting the value of the conductivity after 14400s (4h) of illumination versus the photon energy used for the excitation, as shown in Fig 2. We use a linear fit of the data, to estimate a threshold energy E_{th} for the optical excitation.

In Fig. 2(a), we compare the PPC excitation behavior of MBE grown GaN and AlGaN samples without a buffer layer. The threshold energy for the GaN sample (SM3) is at 1.1eV, whereas for the $Al_{0.15}Ga_{0.85}N$ sample (SM5) we find a threshold energy at 1.6eV. The bandgap of the GaN and the $Al_{0.15}Ga_{0.85}N$ sample are 3.4eV and 3.8eV, respectively. Therefore, we conclude that the optical excitation for both samples occurs from defects located in the bandgap at energies ranging from 2.2eV to 2.3eV. These values correlate well with the energy of the maximum of the yellow luminescence in photoluminescence (PL) measurements [9-13]. A recently published work on depth profiling of the yellow luminescence [14] also shows a strong increase in the ratio of yellow emission to near-band-edge emission near the interface. All these results strengthen the idea that the interface is important for the PPC.

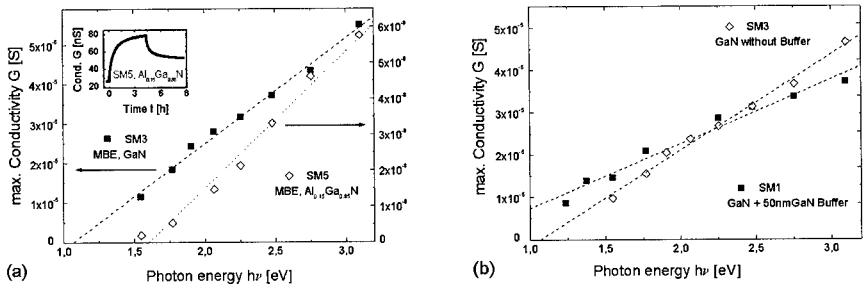


Fig. 2. Conductivity after 14400s of illumination versus the photon energy used for excitation. The dashed and dotted lines are linear fits to the data. The intersection with the energy axis yields an estimation for the lower threshold energy limit E_{th} for optical excitation.

(a) We find a difference in threshold energy for GaN (E_{th}=1.1eV) and $Al_{0.15}Ga_{0.85}N$ (E_{th}=1.6eV) which compares well with the differences of their bandgap energies. The inset shows a typical conductivity transient: illumination with λ=434nm starts at t=0 and ends at t=14400s.

(b) A comparison between two samples with and without buffer yields a threshold energy of E_{th}=0.5eV for the sample with 50nm GaN buffer and E_{th}=1.1eV for the sample without buffer.

Therefore, we compare samples with different interfaces, i.e., SiC as substrate material or an additional GaN buffer layer. The PPC in these samples is, in general, smaller compared to the PPC in films grown directly on sapphire, e.g., the PPC observed in sample SI6, grown on SiC, evaluates to only 1% of total change of conductivity. This change was correlated to a bad signal to noise ratio and, therefore, unfortunately did not allow for a meaningful analysis of the buildup tranients. In Fig. 2(b) a comparison of a sample containing a 50nm GaN buffer (SM1) with a sample without buffer (SM3) is shown. There is a significant difference in the threshold energy for the optical excitation observable. For the sample SM1, grown on sapphire with an additional buffer layer, this energy shifts down to a lower energy of 0.5eV. At this point of our investigations on the buildup transients of the conductivity, it is obvious that the interfacial layer near the substrate plays an important role in the PPC behavior.

IV. Results of van der Pauw and Hall effect experiments

The influence of a defect-rich layer close to the interface can be accessed by Hall effect measurements [5,6]. Therefore, we performed temperature-dependent Hall effect measurements to compare the results of the PPC with the results of the Hall-measurements. The samples were kept in the dark at 350K for around 2h. Afterwards they were cooled down to 10K. Starting from this temperature, the measurements were performed up to 340K. Figure 3 shows the results for the sample SI3 (sapphire substrate), SM1 (50nm GaN buffer), and SI6 (SiC substrate). For each sample the *effective* Hall-carrier concentration n_{eff} exhibits a minimum with respect to temperature. A similar behavior of n_{eff} was observed in GaN grown by hydride vapor phase epitaxy (HVPE) [5,6] and explained with a two-layer model of a GaN and a defective interface region or a continuous increasing defect concentration towards the substrate.
For our samples, the temperature position of these minima clearly depends on the substrate and buffer layer. For the sample SI3 (sapphire substrate), the n_{eff} minimum is very broad and located at 170K. The sample SM1 (50nm GaN-buffer layer) exhibits a sharper minimum located at 150K. For the sample SI6 (SiC substrate), the n_{eff} minimum is very sharp and shifted down to 60K.

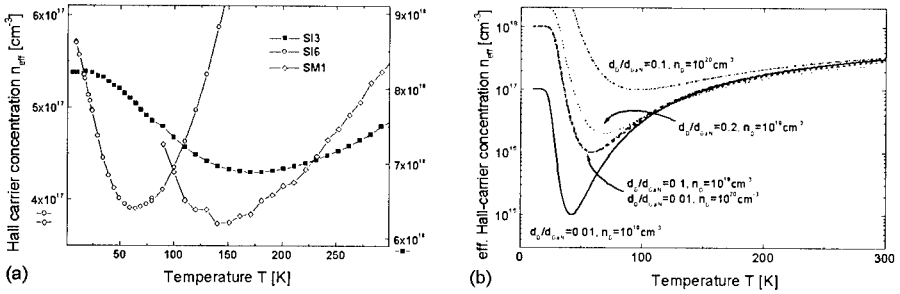


Fig. 3(a) Effective Hall-carrier concentration n_H versus temperature T measured for sample SI3 (GaN/sapphire), SM1 (GaN/GaN-Buffer/sapphire), and SI6 (GaN/SiC). The left vertical axis is for the open symbols, the right vertical axis belongs to the filled symbols.
Fig. 3(b) Simulation of the effective Hall-carrier concentration n_{eff} with varied defect layer thickness d_D at two defect densities n_D of $10^{19}cm^{-3}$ and $10^{20}cm^{-3}$, respectively. For the simulations, the mobility μ_D=1cm²/Vs in the defect layer and μ_{GaN}=400cm²/Vs in the GaN film were kept constant. The carrier concentration in the GaN film was assumed to behave according to $n_{GaN}=10^{18}cm^{-3}*\exp(-30meV/kT)$

The position and the shape of the minimum contain information about the thickness and the electrical properties (i.e. the mobility μ_D and the carrier concentration n_D) of the defect-rich layer near the substrate. The minimum gets broader and shifts to higher temperatures with increasing thickness or higher carrier concentration n_D of the defect-rich layer, respectively. Figure 3(b) shows the effective Hall-carrier concentration n_{eff} calculated according to equation (4) in [5], assuming a thermally activated carrier concentration ($N_c=10^{18}cm^{-3}$, $\Delta E=30meV$) and a moderate mobility ($\mu_{GaN}=400cm^2/Vs$) of the GaN film and a nearly degenerate interface layer ($n_D=10^{19}cm^{-3}$) with low mobility ($\mu_D=1cm^2/Vs$).
The experimental and theoretical results can be explained by differences in the interface quality correlated to the different lattice constants of sapphire and SiC. For the GaN/sapphire system, the lattice mismatch is 16% [15], whereas for the GaN/SiC system it is only 3.4% [15]. The sample SI3 shows the broadest minimum at the highest temperature (170K), i.e., the interface layer dominates the electrical properties of the sample up to room temperature. The sharper minimum at lower temperature (150K) of the sample SM1 is the result of a thinner or less defective interface layer. These better interface properties can be correlated to the buffer layer of this sample. For the sample SI6 on SiC substrate, the sharp minimum at low temperature (60K) indicates the best interface properties. It is this sample which shows the smallest PPC effect as well.
From all the presented results, we conclude that it is either the inhomogenity at the interface itself which causes the PPC effect or that the defects involved in PPC must have an increased concetration in the defective interface region. Enhancement of the quality at this interface may be a way to reduce or fully suppress the PPC.

V. Summary

We have shown that the defect layer at the GaN/substrate interface is important for the PPC effect in GaN and related alloys. Photoconductivity excited with bandgap light from the substrate side is about one order of magnitude larger than in the case the sample is illuminated from the growth side. We used temperature-dependent Hall effect measurements to access the interface properties of the GaN/substrate interface. The GaN film on SiC with the best interface properties according to the Hall effect measurements shows the lowest PPC under subbandgap illumination. From the results of this work it would be interesting to study whether GaN films grown on other substrates like $LiGaO_2$ or $LiAlO_2$ [16] with a lattice mismatch of only ~0.4% to GaN or by the new epitaxial lateral overgrowth technology ELOG [17] will not only improve the growth behavior, but could also eliminate the unwanted metastability of PPC.

References:

1. S. Nakamura, T. Mukai, M. Senoh, Appl. Pyhs. Lett. **84** 1687 (1994)
2. M. Asif Khan, J. N. Kuznia, et. al, Appl. Phys. Lett. **62** 1786 (1993)
3. D. M. Hofmann, D. Kovalev, G. Steude , B. K. Meyer, A. Hoffmann, L. Eckey, R. Heitz, T. Detchprom, H. Amano, I. Akasaki, Phys. Rev. B **52** 16702 (1995)
4. M.S. Feng, H.N. Chen, Y.F. Chen, M.C. Leé, J. Appl. Phys. **82** 899 (1997)
5. D.C. Look, R.J. Molnar, Appl. Phys. Lett. **70** 3377 (1997)
6. W. Götz, L.T. Romano, J. Walker, N.M. Johnson, R.J. Molnar, Appl. Phys. Lett. **72** 1214 (1998)
7. M.T. Hirsch, J. A. Wolk, W. Walukiewicz, E. E. Haller, Appl. Phys. Lett. **71** 1098 (1997)

8. G. Beadie, W. S. Rabinovich, A. E. Wickenden, D. D. Koleske, S. C. Binari, J. A. Freitas , Jr., Appl. Phys. Lett. **71** 1092 (1997)
9. C. V. Reddy, K. Balakrishnan, H. Okumura, S. Yoshida, Appl. Phys. Lett. **73** 244 (1998)
10. E. Calleja, F. J. Sanchez, D. Basak, M. A. Sanchez-Garcia, E. Munoz, I. Izpura, F. Calle, J. M. G. Tijero, J. L. Sánchez-Rojas , B. Beaumont, P. Lorenzini, P. Gibart, Phys. Rev. B **55** 4689 (1997)
11. H. M. Chen, Y. F. Chen, M. C. Lee, M. S. Feng, Phys. Rev. B **56** 6942 (1997)
12. D. Brunner, Diploma Thesis (Technical Univ. of Munich, 1997)
13. W.G. Perry, M.B. Bremser, R.F Davis, J. Appl. Phys. **83** 469 (1998)
14. L.W. Tu, Y.C. Lee, S.J. Chen, I. Lo, D. Stocker, E.F. Schubert, Appl. Phys. Lett. **73** 2801 (1998)
15. M. Lescyczynski, H, Teisseyre, T. Suski, I. Grzegory, M. Bockowski, J. Jun, K. Pakula, J.M. Baranowski, C.T. Foxon, T.S. Cheng, Appl. Phys. Lett. **69** 73 (1996)
16. J.D. MacKenzie, S.M. Donovan, C.R. Abrnathy, S.J. Pearton, P.H. Holloway, R. Linares, J. Zavada, B. Chai, J. Electrochem. Soc. **145** 2581 (1998)
17. S. Nakamura, M. Senoh, S.-I. Nagahama, N. Iwasa, T. Yamada, T. Matsushita, H. Kiyoku, Y. Sugimoto, T. Kozaki, H. Umemoto, M. Sano, K. Chocho, Appl. Phys. Lett. **72** 211 (1998)

STUDIES ON CARBON AS ALTERNATIVE P-TYPE DOPANT FOR GALLIUM NITRIDE

U. Birkle, M. Fehrer, V. Kirchner, S. Einfeldt, D. Hommel

S. Strauf, P. Michler, J. Gutowski

University of Bremen, Inst. of Solid State Physics, Kufsteiner Str., 28359 Bremen, Germany

Cite this article as: MRS Internet J. Nitride Semicond. Res. 4S1, G5.6(1999)

Abstract

GaN layers were grown by molecular beam epitaxy and doped with carbon of nominal concentrations ranging from 10^{16} cm^{-3} to 10^{20} cm^{-3}. The incorporation of carbon leads to a reduction of the background electron concentration by one order of magnitude but the material remains n-type. For high carbon concentrations a re-increase of the carrier concentration is observed which is related to selfcompensation. Investigations of the donor-acceptor-pair luminescence show that doping with carbon is accompanied by the generation of a new donor exhibiting a thermal activation energy of about 55 meV. Layers grown by atomic layer epitaxy are marked by an increased intensity of the donor-acceptor-pair band luminescence which is attributed to the enforced incorporation of carbon onto the nitrogen sublattice. The yellow luminescence is found to be a typical feature of all carbon doped layers in contrast to nominally undoped samples.

Introduction

The realization of electronic and optoelectronic devices such as heterojunction bipolar transistors and laser diodes, requires the control of dopant profiles as well as a high p-type conductivity. P-type doping of GaN and of other wide-bandgap semiconductors is in general difficult to achieve and not yet well understood. A compensation mechanism likely induced by a high energy gain caused by an electron transfer from a donor state to an acceptor state with gain values close to the bandgap value is discussed as one of the most important reasons [1].

Today, magnesium is widely used for p-type doping of GaN due to its relatively low thermal activation energy of approx. 170 meV compared to other group II dopants such as Zn, Hg and Cd. Hole concentrations of up to 10^{18} cm^{-3} at room-temperature (RT) are attainable. However, magnesium features several disadvantages like its limited solubility in GaN, its high vapour pressure and low sticking coefficient, its tendency for segregation and diffusion and a low ionization ratio of about one percent at RT. As a result of the latter high magnesium concentrations are necessary in the layers which consequently leads to low mobilities and hence conductivity's. In hydrogen containing growth environments magnesium acceptors are passivated due to the formation of neutral Mg-H complexes. As a result, an additional post-growth treatment like thermal annealing or low energy electron beam irradiation is required to achieve p-type conductivity. Passivation by hydrogen is reported for the dopants calcium [2] and carbon [3] as well.

Alternative group II dopants have recently been investigated. P-type GaN was achieved by implantation of Ca and its ionization energy was determined to 169 meV [2]. Beryllium received some interest and p-type conductivity was obtained in cubic GaN when it is was codoped with

Mat. Res. Soc. Proc. Vol. 537 © 1999 Materials Research Society

oxygen [4, 5]. Theoretical calculations confirm the advantage of the codoping method and predict an ionization energy of 60 meV for the beryllium acceptor in wurtzite GaN [6].

Group IV elements can form acceptors or donors in GaN depending on whether they are located on the nitrogen or gallium sublattice, respectively [7]. As it is known from GaAs, this amphoteric behaviour critically depends on the growth conditions [8]. Especially carbon has received a considerable interest as a possible p-type dopant in GaN. It should preferentially occupy nitrogen sites due to its similarity to nitrogen in terms of atomic radius and electronegativity. Moreover, it has proved to be a highly efficient acceptor in GaAs featuring a shallow acceptor level and high solubility as well as a low diffusion coefficient in this material. P-type conductivity of carbon doped GaN was observed for cubic material [9] whereas little is known for this dopant in wurtzite GaN. Theoretical considerations predict an excellent solubility of this element in GaN [1, 10] and no segregation was found in layers grown by molecular beam epitaxy (MBE) doped with a concentration of 2×10^{20} cm^{-3} [11]. Furthermore, the lack of d-electrons in carbon are assumed to result in a shallower acceptor level compared to magnesium [12]. In this paper, a study on the behaviour of carbon in wurtzite GaN is presented with the intention to check if this element can be an alternative p-type dopant to magnesium.

Experiment

GaN films were synthesized in an EPI 930 MBE system equipped with an EPI Unibulb radio frequency (rf) nitrogen plasma source. All layers were grown with a V/III flux ratio close to unity. Layers with thickness of about 1 μm were deposited on sapphire (0001) after a nitridation step and the growth of 40 nm undoped GaN which should guarantee similar nucleation conditions for all layers under investigation. The growth rate and growth temperature were 640 nm/h and 750°C, respectively. Hydrogen passivation of acceptors is not expected to occur since annealing experiments of magnesium doped samples did not change the electrical properties of these films. Carbon doping was realized by use of a resistively heated graphite filament. The density of the incorporated carbon in GaN was calculated via the growth and C doping of GaAs layers, assuming a carbon sticking coefficient of unity for both materials and an acceptor ionization ratio of unity at RT for GaAs. This results in maximum nominal carbon concentrations of about 2×10^{20} cm^{-3} in the GaN samples under investigation, limited by the maximum heating power of approx. 550 W for the carbon filament. In the following, an unintended background carbon concentration in nominally undoped GaN layers is neglected. Free carrier concentrations as well as mobility's were measured by Hall-effect in van der Pauw geometry assuming a Hall factor of unity. Photoluminescence (PL) investigations were carried out by using a HeCd laser at a wavelength of 325 nm.

Results and discussion

Undoped GaN layers grown under optimized growth conditions exhibit background electron concentrations of about 2×10^{17} cm^{-3} at RT. The ionization energy of the corresponding donor is determined to 30 meV by Hall-effect measurements. The influence of the carbon doping level on the carrier concentration is shown in Figure 1. The error bars represent the standard deviation of samples grown under identical conditions. The carrier concentration decreases with increasing nominal carbon doping levels of up to approx. 2×10^{19} cm^{-3} resulting in a compensation of about one order of magnitude. For even heavier doped layers the carrier concentration raises again. As a result, all layers under investigation remain n-type. Figure 1 also

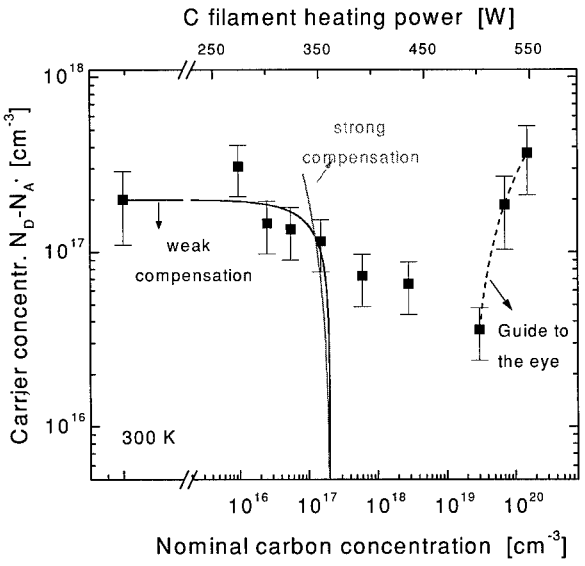


Figure 1: Room-temperature carrier concentration vs. nominal carbon concentration in GaN:C. The dashed curves correspond to the expected compensation behavior as described in the text.

contains theoretical curves for the expected dependency of the carrier concentration on the carbon doping level in compensated material, assuming that the concentration and ionization energy of the background donor remain constant with values of 2 x 10^{17} cm^{-3} and 30 meV, respectively, and that every carbon atom forms a single acceptor. The two curves correspond to the standard approximation of weak and strong compensation in a non-degenerated semiconductor and can be found elsewhere [13]. Obviously, the experimental data do not follow this simple compensation mechanism. It can be explained by assuming that only a part of the carbon atoms forms an acceptor in GaN. Referring to theoretical calculations of Boguslawski *et al.* [1, 7] and Neugebauer *et al.* [10] carbon should be preferably incorporated on a nitrogen site where it forms an acceptor. However, there is also a tendency that carbon atoms will be incorporated on Ga sites where they act as donors. Especially the formation of selfcompensating C_{Ga}-C_N pairs may occur due to the large energy gain close to the value of the band gap originating from an electron transfer from C_{Ga} to C_N. Moreover, there is a gain by the large binding energy of about 1 eV of nearest neighbor C^+-C^- pairs. As a result, this should produce a high solubility of carbon in GaN. The increase of the carrier concentration in Figure 1 can therefore be explained by the entire selfcompensation of carbon acceptors. This is also known from carbon doping of GaAs where carbon likely forms atomic clusters at high doping levels [14].

The lack of a complete carrier compensation close to the value of 2 x 10^{17} cm^{-3} and the missing of a carrier type inversion for higher carbon doping levels in Figure 1 can be explained by an accompanying generation of donors in addition to the background donors. This is supported by PL experiments indicating the formation of a deeper donor correlated to carbon. Figure 2 shows the temperature dependence of the DAP zero-phonon line intensity for two different GaN:C samples. The value of approx. 55 meV determined for the thermal activation energy is significantly higher compared to the value of the background donor. A lineshape analysis of the DAP band using this activation energy leads to an binding energy of the carbon correlated acceptor of approx. 230 meV which is about 15 meV lower than the value found for the magnesium acceptor in our GaN:Mg samples. A detailed review of the DAP analysis is given in Ref. [15].

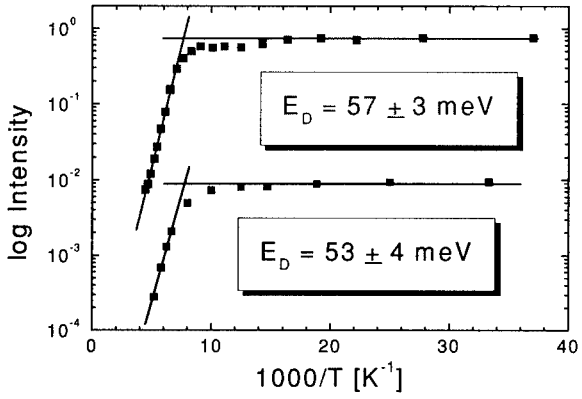


Figure 2: Arrhenius plots of the intensity of the zero phonon replica of the donor-acceptor-pair (DAP) band for two different GaN:C samples.

Room-temperature Hall mobility's of the samples from Figure 1 are shown in Figure 3. For low carbon densities a rather small effect on the mobility is expected. The decrease for carbon concentrations above 5 x 10^{16} cm^{-3} may be interpreted as scattering at ionized carbon atoms and / or at extended defects induced by the carbon doping. For doping levels above 2 x 10^{19} cm^{-3} the mobility's seem to saturate. This may be explained by a transition from isolated Coulomb scattering into dipole scattering which is theoretically predicted in Ref. [16] and experimentally verified in Ref. [17] for the method of reactive codoping where donor-acceptor complexes form the dipole similar to the predicted C^--C^+ pairs for GaN:C .In summary, the results suggest that carbon forms both a donor and an acceptor which is in good agreement with Ref. [1, 7].

To achieve p-type conductivity in GaN:C despite of the amphoteric behavior of carbon, the growth of GaN:C by atomic layer epitaxy was investigated. By subsequently supplying Ga, C and N to the growth surface by closing and opening the corresponding shutters in this sequence, the probability of carbon to incorporate on the nitrogen sublattice is hopefully increased. At the same time the formation of C^+-C^- pairs may be reduced. The PL spectrum of a sample grown by ALE is shown in Figure 4. A clear DAP band starting at 3.261 eV can be identified as well as an impurity bound exciton at 3.466 eV which is approx. 5 meV lower compared to the donor bound excition of nominal undoped samples. It is yet not clarified whether the peak at 3.455 eV is still the donor bound exciton or a superposition of both, acceptor- and donor bound exciton.

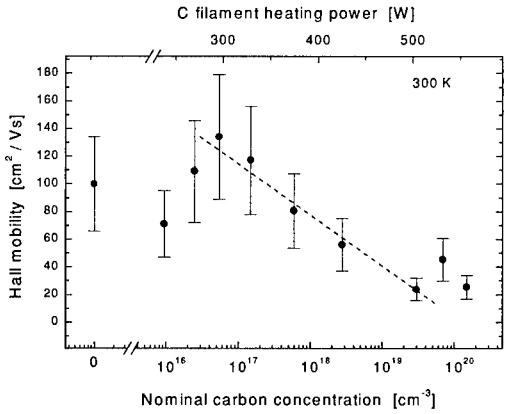


Figure 3: Room-temperature Hall mobility's vs. nominal carbon concentration of the samples from Figure 1. The line is a guide to the eye.

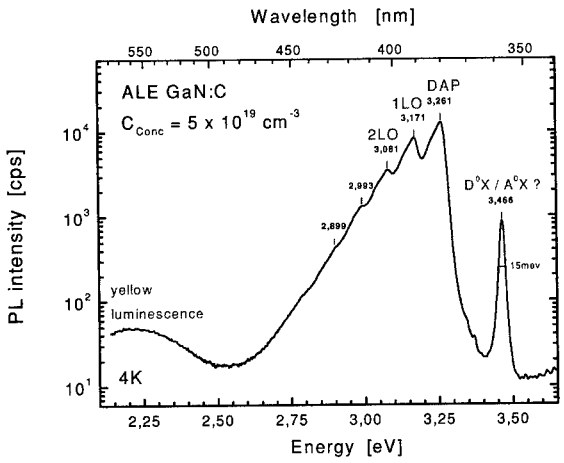


Figure 4: PL spectrum taken at 4 K of a GaN:C sample grown by ALE as described in the text. The nominal carbon concentration was 3 x 10^{19} cm^{-3}. The DAP zero-phonon-line is centered at 3.261 eV followed by its LO-phonon replicas.

The DAP recombination of this sample is more pronounced in terms of intensity and clear occurrence of the phonon replicas compared to those of conventionally carbon doped GaN layers discussed before. Electrical measurements characterize the layer to be highly resistive and the type of conduction could not be determined. This suggests that carbon can be more effectively incorporated on nitrogen sites to form an acceptor if the material is grown by ALE.

The appearance of the yellow luminescence at around 2.2 eV can be seen in Figure 4 as well. The yellow luminescence is a common feature of all grown carbon doped samples. For very high carbon doping levels the PL is sometimes even dominated by this emission. In comparison, nominally undoped as well as silicon and magnesium doped films grown in our system show a neglectabe weak yellow luminescence. Ogino and Aoki found a strong indication that the yellow luminescence is correlated to the carbon and that its intensity increases with the carbon doping level [18]. They assumed that the emission is generated by the transition between a shallow donor and a deep acceptor. They further assigned this deep level to a complex, namely C_N-V_{Ga}. In contrast, Glaser *et al.* suggested a transition between a deep donor and a shallow acceptor which they assumed to be carbon on the nitrogen site [19].

Conclusions

In summary, it was found that only a part of carbon forms an acceptor in n-type GaN resulting in a partial compensation of the background electron concentration. For doping levels above 3 x 10^{19} cm^{-3} a re-increase of the electron concentration is observed which can be explained by the formation of selfcompensating C_{Ga}-C_N pairs which is in good agreement with theoretical predictions. PL investigations of carbon doped GaN show both, the generation of a deeper donor than in undoped samples and the appearance of the yellow emission.

Up to now, carbon has not stated to be a superior dopant compared to Mg. One possible approach to achieve p-type conductivity by carbon doping is the use of alternative growth techniques like ALE to enforce carbon on the nitrogen site and to prevent selfcompensating nearest neighbor pairs. This has to be further investigated.

References

[1] P. Boguslawski, E. L. Briggs, J. Bernholc, Appl. Phys. Lett. **69**, 232 (1996)
[2] J. W. Lee, S. J. Pearton, J. C. Zolper, R. A. Stall, Appl. Phys. Lett. **68** (15), 2102 (1996)
[3] M. Sato, Appl. Phys. Lett. **68**, 935 (1996)
[4] O. Brandt, H. Yang, H. Kostial, K. H. Ploog, Appl. Phys. Lett. **69**, 2707 (1996)
[5] H. Asahi, K. Iwata, H. Tampo, R. Kuroiwa, K. Asami, S. Nakamura, S. Gonda, 10th Intern. Conf. on MBE, Cannes, France (1998), to be published in J. Cryst. Growth
[6] F. Bernardini, V. Fiorentini, A. Bosin, Appl. Phys. Lett. **70**, 2990 (1997)
[7] P. Boguslawski, J. Bernholc, Phys. Rev. B **56**, 9496 (1997)
[8] H. Ito, T. Ishibashi, Jpn. J. Appl. Phys. **30**, 944 (1991)
[9] C. R. Abernathy, J. D: MacKenzie, S. J. Pearton, W. S. Hobson, Appl. Phys. Lett. **66**, 1969 (1995)
[10] J. Neugebauer, C. G. Van de Walle, *Festkoerperprobleme* Vol. **35**, ed. by R. Helbig (Vieweg, Braunschweig/Wiesbaden), p. 25 (1997)
[11] B. Ya Ber, Yu. A. Kudriavtsev, A. V. Merkulov, S. V. Novikov, D. E. Lacklison, J. W. Orton, T. S. Cheng, C. T. Foxon, Semicond. Sci. Technol. **13**, 71 (1998)
[12] S. Strite, Jpn. J. Appl. Phys. Vol. **33**, L699 (1994)
[13] S. M. Sze, *Physics of Semicondutor Devices* (Wiley, New York, 1981), p. 38
[14] *Application Note* of the EPI Carbon Filament Source (CFS)
[15] S. Strauf, P. Michler, J. Gutowski, U. Birkle, S. Einfeldt, V. Kirchner, H. Heinke, D. Hommel, Proc. 2nd Int. Symp. Blue Lasers and Light Emitting Diodes, ed. by K. Onabe *et al.*, Ohmsha Ltd. (Tokyo), p. 574 (1998)
[16] T. Yamamoto, H. Katayama-Yoshida, Proc. of the MRS Spring Meeting Symp. D (1998)
[17] O. Brandt, H. Yang, H. Kostial, K. H. Ploog, Appl. Phys. Lett. **69**, 2707 (1996)
[18] T. Ogino, M. Aoki, Jpn. J. Appl. Phys. **19**, 2395 (1980)
[19] B. R. Glaser, T. A. Kennedy, K. Doverspike, L. B. Rowland, D. K. Gaskill, J. A. Freites, M. Asif Khan, D. T. Olson, J. N. Kuznia, D. K. Wickenden, Phys. Rev. B

THE BEHAVIOR OF ION-IMPLANTED HYDROGEN IN GALLIUM NITRIDE

S. M. Myers, T.J. Headley, C.R. Hills, J. Han, G.A. Petersen, C.H. Seager, W.R. Wampler

Sandia National Laboratories, Albuquerque, NM 87185-1056, smmyers@sandia.gov

Cite this article as: MRS Internet J. Nitride Semicond. Res. 4S1, G5.8 (1999)

ABSTRACT

Hydrogen was ion-implanted into wurtzite-phase GaN, and its transport, bound states, and microstructural effects during annealing up to 980°C were investigated by nuclear-reaction profiling, ion-channeling analysis, transmission electron microscopy, and infrared (IR) vibrational spectroscopy. At implanted concentrations $\vee$1 at.%, faceted H_2 bubbles formed, enabling identification of energetically preferred surfaces, examination of passivating N-H states on these surfaces, and determination of the diffusivity-solubility product of the H. Additionally, the formation and evolution of point and extended defects arising from implantation and bubble formation were characterized. At implanted H concentrations $\wedge$0.1 at.%, bubble formation was not observed, and ion-channeling analysis indicated a defect-related H site located within the [0001] channel.

INTRODUCTION

We investigated the transport, bound states, and microstructural effects of ion-implanted H in GaN. This work was undertaken for two reasons: first, the behavior of the implanted system provides information on a range of fundamental atomic processes involving H and defects; in addition, H implantation may ultimately be used in device processing for purposes such as electrical isolation and controlled separation of layers. This work builds upon several prior studies of implanted H in GaN [1-3].

Our experiments examined nominally undoped, wurtzite-phase GaN grown on sapphire by metal-organic chemical vapor deposition (MOCVD). The implanted concentrations of H ranged from hundredths of an atomic percent to several at.% and spanned two regimes of behavior distinguished by the absence or presence of H_2 bubbles. Atomic processes and microstructural evolution were investigated at temperatures up to 980°C using nuclear-reaction profiling of the H, ion-channeling analysis of defects and H lattice location, transmission electron microscopy (TEM), and infrared (IR) spectroscopy of the local vibrational modes of the H. More thorough descriptions of the ion-channeling analyses and IR spectroscopy appear elsewhere [4,5].

EXPERIMENTAL PROCEDURE

The MOCVD GaN films were grown with (0001) orientation and thicknesses in the range 1.4-2.3 μm as discussed elsewhere [6]. The nominally undoped material was of n-type with a free-carrier density of ~10^{17} cm^{-3} as determined by conductivity and Hall-effect measurements. Hydrogen was ion-implanted into these films at room temperature in a turbomolecular-pumped vacuum of ~10^{-7} Torr. Subsequent vacuum annealing was carried out in a quartz furnace tube that was continuously ion-pumped to a pressure of ~10^{-7} Torr.

Mat. Res. Soc. Proc. Vol. 537 © 1999 Materials Research Society

Experiments involving nuclear-reaction analysis (NRA) of H employed the deuterium isotope (^{2}H), which was detected by counting protons from the ^{3}He-induced reaction ^{2}H(^{3}He,p)^{4}He using a Si surface-barrier detector. As a result of the energy dependence of the reaction cross section [7] and the continuous slowing of the ^{3}He particles within the target, the proton yield was affected by the depth distribution of the ^{2}H as well as by its quantity, and ^{2}H concentration versus depth could be obtained by measuring proton yield versus incident ^{3}He energy and performing a deconvolution [8]. Ion-channeling analysis of ^{2}H lattice location was carried out using the same nuclear reaction with the specimen manipulated in a 3-axis goniometer. The thickness of the GaN films was monitored by Rutherford backscattering spectrometry (RBS) with 1.7-MeV ^{1}H to determine when annealing produced significant loss of material. Ion-channeling analysis of defects was performed using RBS with 2-MeV ^{4}He. All of the channeling analyses were axial, with rotational averaging about the axis to avoid planar channeling.

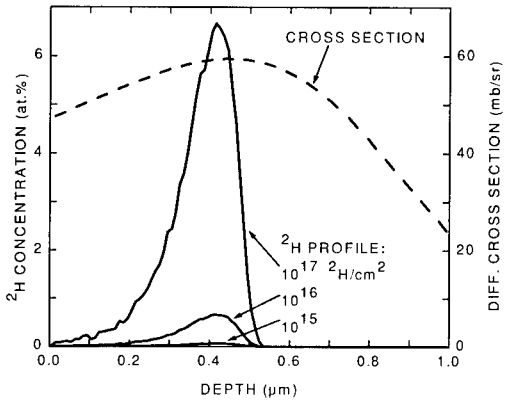


Fig. 1. Calculated depth profiles of implanted ^{2}H and the differential nuclear cross section for 0.85-MeV ^{3}He with a scattering angle of 135°.

Infrared vibrational spectroscopy was carried out using the ^{1}H and ^{2}H isotopes with multiple implanted layers being introduced to increase signal strength. These measurements were made at room temperature with a resolution of 4 cm^{-1}. Samples for TEM were prepared by ion-thinning and were observed at an electron energy of 300 keV.

RESULTS AND INTERPRETATION

Hydrogen Release During Isochronal Annealing

The retention of implanted ^{2}H within GaN was monitored by NRA during a sequence of 1-hour vacuum anneals at temperatures incremented by ~100°C. These experiments were carried out on specimens that had been implanted with 10^{15}, 10^{16} or 10^{17} ^{2}H/cm^2 at room temperature and 50 keV to produce the calculated [9] depth profiles shown in Fig. 1. The NRA was performed with an incident ^{3}He energy of 0.85 MeV, which, using published results for the nuclear cross section [7] and He stopping powers [10], is calculated to result in the depth-dependent differential cross section shown in Fig. 1. The nuclear-reaction yield under these conditions provides a quantitative measure of the amount of ^{2}H remaining within the implanted region.

Results from these experiments are presented in Fig. 2, where the retained fraction of ^{2}H is plotted versus temperature. The anneal at the highest temperature, 980°C, produced significant loss of material from the GaN film as observed by RBS, so that the corresponding datum does not provide a quantitative measure of ^{2}H release by diffusion. In the case of the lowest implantation dose, effects of the analysis beam on the release were observed, so each measurement was made at a new location on the specimen.

For all three doses, the ^2H remained localized in the implanted region during the release rather than assuming a diffusion-broadened profile. This is seen from the representative concentration-versus-depth profile in Fig. 3, which was measured in the sample implanted with 10^{17} $^2H/cm^2$ after the anneal sequence had reached 886°C and about 2/3 of the ^2H had been lost. This profile was obtained by measuring the proton yield from the nuclear reaction as a function of incident ^3He energy and performing a deconvolution [8], giving a distribution represented by contiguous straight-line segments. The depth resolution of this method is about 0.2 μm for GaN, which suffices to exhibit the property of interest.

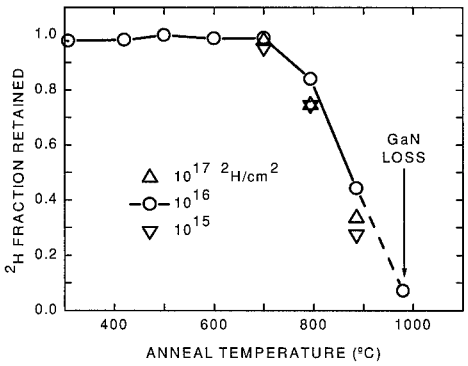


Fig. 2. Release of ion-implanted ^2H from GaN during isochronal annealing.

The release of ^2H is seen from Fig. 2 to occur in approximately the same temperature range for implanted concentration from hundredths of an atomic percent to several at.%, notwithstanding fundamental differences in the state of the ^2H at the lower and higher concentrations that are discussed below. For the lowest dose, the temperature range of release is consistent with earlier work where H was implanted to comparable concentrations in undoped material [1,3]. The absence of diffusion broadening of the implanted peak during the release indicates that the H exists predominantly in bound states rather than being in mobile solution. The nature of these states is addressed in the remainder of this paper.

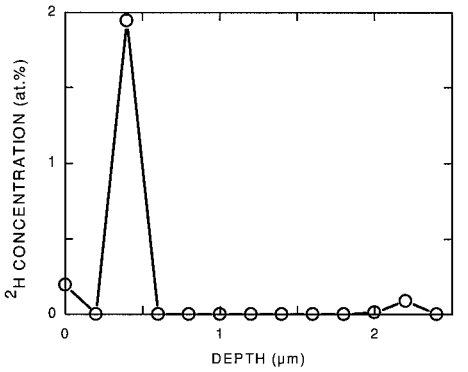


Fig. 3. Depth profile of ion-implanted ^2H in GaN after implantation of 10^{17} $^2H/cm^2$ at 50 keV and isochronal annealing extending to 886°C.

H_2 Bubble Formation with Wall Chemisorption of H at Implanted Concentrations ∨1 at.%

When the implanted concentration of H was ∨1 at.%, H_2 bubbles formed within the GaN. After annealing in the temperature range of H release, TEM showed most of these bubbles to be polyhedra with a single (0001) facet and 6 $\{10\bar{1}1\}$ facets, a shape which reduces to a 6-sided pyramid when the hexagonal basal-plane facet is equilateral. Representative high-resolution images in plan view and cross section are shown in Fig. 4. With no noted exceptions, the base of the polyhedral bubbles was toward the surface of the sample and the apex toward the sapphire substrate. Such an absence of inversion symmetry along [0001] indicates that the facets have a preferred polarity. The identification of this polarity requires determination of the polarity of the epitaxial film. Although this is challenging, several groups have concluded on the basis of convergent-beam electron diffraction and other measurements that smooth MOCVD GaN on

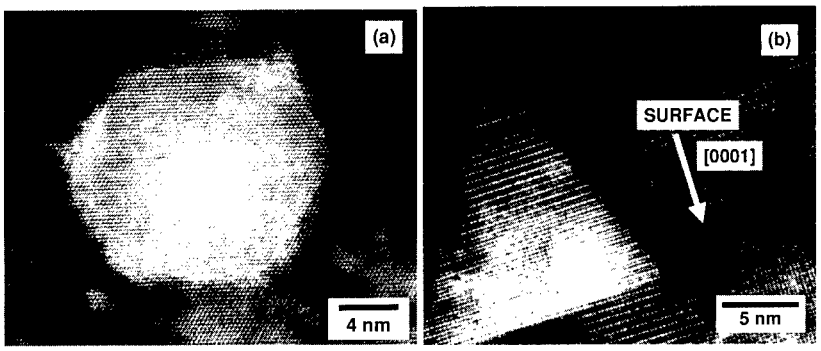


Fig. 4. High-resolution TEM images of bubbles in GaN: (a) plan-view in [0001] orientation and (b) cross-section in [11$\bar{2}$0] orientation. The implanted layer was injected with 2×10^{16} ^{1}H/cm^2 at room temperature, and the specimen was then annealed at 886°C for 1 hour.

sapphire has N atoms above Ga atoms along [0001]-oriented bonds, or, equivalently, that the unreconstructed top surface of the film is terminated by Ga atoms [11-14]. This implies that the (0001) and {10$\bar{1}$1} internal surfaces of the observed bubbles, both comprising close-packed Ga-N bilayers, have N-terminated polarity. Since the bubbles formed after growth, we conclude that these surfaces were energetically preferred.

In view of the relatively high reactivity of N and the transfer of electronic charge from Ga to N in GaN, a preference for N-terminated surfaces is surprising unless these surface are H-passivated. We obtained evidence for such passivation from IR vibrational spectroscopy, as discussed more fully elsewhere [5]. Under conditions of implantation where bubbles formed, but not otherwise, we observed new IR absorption peaks at 3182 and 3216 cm^{-1} for ^{1}H, as shown in Fig. 5, and at 2364 and 2386 cm^{-1} for ^{2}H. These absorptions are ascribed to N-H centers, based both on comparisons with materials known to contain N-H and on the size of the departure of the isotope shift from $\sqrt{2}$. The frequencies lie above those reported when the concentration of implanted H is $\wedge$0.1 at.% [2], a regime where we did not observe bubble formation and the H is believed bound to defects. Moreover, the integrated strength of the absorptions in Fig. 5 corresponds to about 4 % of the implanted H being in the IR-active state, and this is consistent with estimates of the number of chemisorption sites on the bubble walls. We consider these findings strongly indicative of H passivation of the bubble walls.

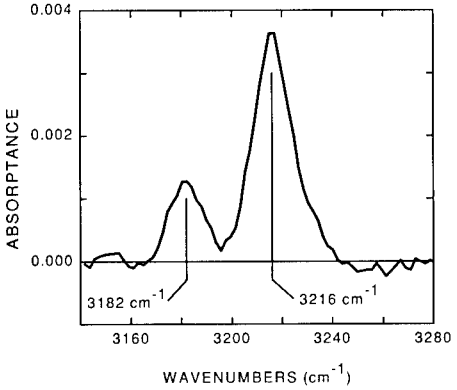


Fig. 5. Infrared absorption peaks ascribed to ^{1}H chemisorbed on bubble walls. The specimen was implanted with 2×10^{16} ^{1}H/cm^2 in each of 5 layers and then annealed at 600°C for 1 hour.

During isochronal annealing sequences similar to those of Fig. 2, the strength of the IR absorptions shown in Fig. 5 decreased before the total amount of ^2H measured by NRA. This is seen in Fig. 6, where both quantities are plotted versus anneal temperature. We infer that the chemisorbed state is less stable than the molecular gas under the conditions of these experiments.

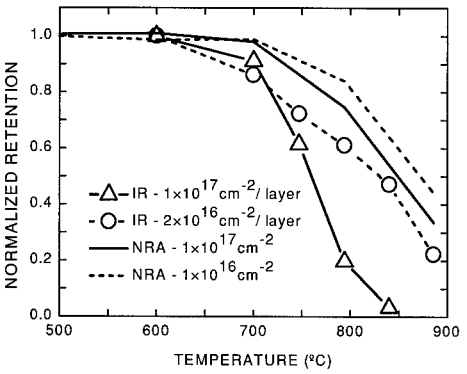


Fig. 6. Decrease of H-related IR absorptions during isochronal annealing, compared with the loss of total H measured by NRA.

Isothermal Release from Bubbles and the Diffusivity-Solubility Product of H

In order to characterize further the thermal release of H from H_2 bubbles, we used NRA to measure the amount remaining during isothermal vacuum annealing at 794 and 886°C. The specimens were implanted with 1×10^{17} $^2H/cm^2$ at 50 keV, and the areal density of ^2H within the implanted layer was monitored using a ^3He energy of 0.85 MeV, replicating conditions depicted in Fig. 1. The results obtained at 886°C are presented in Fig. 7. Depth profiling at selected points in the sequence, using procedures described for Fig. 3, showed that the retained ^2H was always localized in the implanted layer rather than developing a diffusion-broadened distribution.

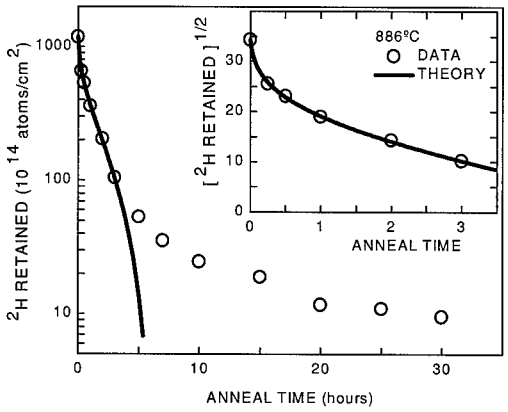


Fig. 7. Release of ion-implanted ^2H from GaN during isothermal annealing at 886°C.

From the TEM observations discussed above, we conclude that the release shown in Fig. 7 was predominantly from H_2 gas within bubbles. Furthermore, we assume, in accord with theoretical predictions [15], that the transport of the H through the matrix occurred by dissociation of the molecule followed by atomic diffusion. Then, using the approximation of steady-state diffusion, the variation with time of the retained areal density of H atoms, Λ, is given by

$$(d/dt)\Lambda = -D\, N_{H0}\, (P^*/P_0)^{1/2} / X \qquad (1)$$

where D is the effective diffusion coefficient, N_{H0} is the solubility of mobile H in local equilibrium with the H_2 gas at some reference pressure P_0 small enough for the gas to behave ideally, P^* is the fugacity of the H_2 gas in the bubbles, and X is the diffusion distance to the

surface, taken to be single-valued for simplicity. The fugacity can be defined in terms of the chemical potential and related through it to the equation of state:

$$\ln(P^*/P_0) \equiv (\mu-\mu_0)/kT = (kT)^{-1} \int_{P_0}^{P} V(P')\, dP' \qquad (2)$$

where μ_0 is the chemical potential at the reference pressure and V(P) is the volume per H_2 molecule at pressure P as given by the equation of state. At lower pressures where the ideal-gas equation of state is applicable, $P^* \rightarrow P$. In order to complete the description of the system, a relationship must be specified between P and Λ. This is accomplished by noting that

$$V(P) = 2V_b/\Lambda \qquad (3)$$

where the function V(P) is given by the equation of state and V_b is the combined bubble volume per unit sample area. Solution of Eqs. (1)-(3) shows that that $\Lambda^{1/2}$ decreases linearly with time at lower pressures where V(P) follows the ideal equation of state, while a more rapid initial transient is predicted if the starting pressure is high enough for the gas to behave non-ideally. Such behavior is evident in the inset of Fig. 7, where the initial part of the measured isotherm is plotted as $\Lambda^{1/2}$ versus t. The curve through the data represents a solution of Eqs. (1)-(3) in which the amplitude of the initial transient was fitted by adjusting V_b or, equivalently, the initial bubble pressure P_1, and the variation at longer times was fitted by adjusting the diffusivity-solubility product $D\times N_{H0}$ for P_0 = 1 bar. In this way we obtained P_1 = 6 GPa and $D\times N_{H0}$ = 2.2×10^6 atoms cm^{-1} s^{-1} for T = 886°C; the analogous experiment at 794°C yielded P_1 = 9 GPa and $D\times N_{H0}$ = 2.0×10^5 atoms cm^{-1} s^{-1}.

It is apparent from the semilog plot in Fig. 7 that a small fraction of the implanted H, ~5 %, was released much more slowly than predicted by Eqs. (1)-(3). We consider two possible explanations for this. First, the residual H might conceivably exist in some bound state more stable than H_2 gas within the bubbles. A difficulty, however, is that we did not find IR absorptions associated with the H retained to long times, nor did this H exhibit the channeling effects in NRA that would be expected for a unique atomic position relative to the host lattice; hence, the bound state in question apparently does not involve N-H or Ga-H bonding. If, alternatively, the strongly retained H is imagined to exist as H_2 molecules, there is the problem of identifying a location where the molecules are more stably bound than the open volumes of the bubbles.

A second interpretation, and one which we currently consider more viable, is that the release takes place from H_2 bubbles over the entire anneal sequence, but the diffusivity-solubility product $D\times N_{H0}$ decreases with time due to a shift in the Fermi level as the H concentration in solution decreases. Theoretical calculations reported for the cubic, zincblende variant of GaN [15] and a recent treatment of the hexagonal, wurtzite phase [16] both indicate that dissociated H in solution exists predominantly as H^+ or H^-, depending upon the position of the Fermi level, with the neutral atom always being less stable. Additionally, the positive ion is predicted to be much more mobile than the negative ion. Our tentative interpretation of the release isotherm is then that, during ~95% of the release, the solution concentrations of H^+ and H^- exceed the concentrations of other electrically active species, and as a result the Fermi level is stabilized at a position such that $[H^+] \sim [H^-]$, with $D\times N_{H0}$ being nearly constant as a result. In the last stages of the release, however, the H_2 pressure in the bubbles, and hence the H chemical potential, decreases until the H concentration in the lattice is less than that of donors unrelated to H; at this point, the Fermi level rises, reducing the fraction of mobile H^+ and increasing that of the less-mobile H^-.

Bubble-Related Defect Microstructure and Its Evolution with Temperature

By using ion-channeling analysis in conjunction with TEM to characterize implantation-related defects, we elucidated the atomic processes associated with bubble formation and defect annealing. Figure 8 shows channeling results for a specimen that was implanted with 10^{17} $^2H/cm^2$ at 50 keV and room temperature and then subjected to a series of 1-hour vacuum anneals at increasing temperature. The exhibited RBS spectra were produced by 2-MeV ^4He incident along the [0001] axis with the sample at room temperature, and an unchanneled, or random, spectrum is included for reference. Backscattering yield from the implanted region appears at channels in the range 90-120, while the surface corresponds approximately to channel 140.

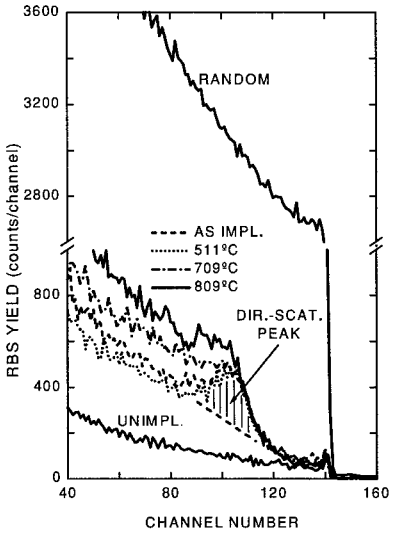


Fig. 8. Channeled RBS spectra from GaN before and after ^2H implantation and annealing, obtained using 2-MeV ^4He.

A direct-scattering peak appears in the channeled spectrum after implantation and before annealing, as indicated in the figure. As discussed more fully elsewhere [4], the presence of this peak means that Ga atoms are removed from substitutional lattice sites into the open [0001] channel. Analysis of the area under the peak indicates that the areal density of Ga interstitials is 3.0×10^{16} cm^{-2} [4]; this is equal within experimental uncertainty to the areal density of Ga atoms displaced by bubble formation, which we calculate from the known H areal density and H_2 gas pressure to be 3.4×10^{16} cm^{-2}. This finding is consistent with the following model of bubble formation: the equally numerous vacancies and interstitials produced by collisional atomic displacements mostly undergo annihilation by recombination; however, a small fraction of the vacancies agglomerate and collect H to form high-pressure H_2 bubbles, thereby constraining the recombination and leaving a corresponding number of interstitials within the lattice.

Annealing in the temperatures range 511-709°C is seen in Fig. 8 to remove the direct-scattering peak and introduce a dechanneling step. This indicates a return of Ga atoms to substitutionality, accompanied by the formation of extended defects with large strain fields to produce the observed dechanneling with relatively little direct scattering. Transmission electron microscopy after this evolution showed the predominant extended defect to be a (0001) stacking fault containing one extra Ga-N bilayer and bounded by a partial dislocation, a configuration discussed in detail elsewhere [17]. A part of one such stacking fault is seen in the high-resolution cross-section TEM image of Fig. 9. Analysis of the amplitude of the dechanneling step gives the density of the stacking faults. The result indicates that only a small fraction of the Ga interstitials present before annealing, about 3%, agglomerate in this way [4]; the remainder undergo annihilation, presumably by migrating to the surface of the film.

Hydrogen Behavior in the Absence of Bubbles at Concentrations ∧0.1 at.%

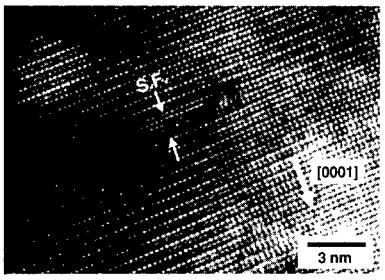


Fig. 9. High-resolution cross-section TEM image showing a part of one stacking fault in H-implanted GaN after annealing at 886°C.

When GaN was implanted with 50-keV ^{2}H at room temperature to a dose of 10^{15} cm^{-2}, ion-channeling analysis revealed that a large fraction of the ^{2}H occupied a well-defined location relative to the host lattice. Figure 10 shows the nuclear-reaction yield from the ^{2}H as a function of angle from the [0001] direction, with the elastic backscattering yield from Ga superimposed for comparison; these yields were produced by 0.85-MeV ^{3}He and 2-MeV ^{4}He, respectively. The detected H site is believed to be defect related, since the amplitude of the channeling peak rises markedly during initial impingement of the ^{3}He analysis beam, and rises more rapidly when that beam is tilted from the channeling orientation so that more atomic displacements are produced. Numerical simulations of the channeling indicate that the narrow peak in the nuclear-reaction yield can be produced only by ^{2}H that is displaced into the central region of the open [0001] channel [4]. During a succession of 1-hour anneals at increasing temperature, this peak remained essentially unchanged after 411°C, but decreased in amplitude with increasing temperature from 511°C upward, becoming poorly resolved by 809°C.

Previously, ^{1}H implanted to similar concentrations in GaN was found by IR spectroscopy to have local vibrational modes in the frequency range 2983-3150 cm^{-1} [2]. These modes were assigned with confidence to N-H centers, which were plausibly hypothesized to be located in the Ga vacancy. The absorption spectrum evolved with increasing anneal temperature and disappeared at about 700°C. The similarity with our experiments raises the possibility that the same H state was probed by the two techniques; this is not necessarily so, however, since the fraction of the implanted H contributing to the observed IR peaks may have been as small as 10% [18]. In any case, the Ga vacancy does not appear viable for the trap observed by channeling, since H tetrahedrally bonded to a neighboring N would not protrude into the [0001] channel. It therefore seems appropriate to consider other defects, including those of interstitial type, as possible binding sites.

Since the H state or states probed by the ion channeling and IR spectroscopy disappear after annealing at temperatures ∧800°C, these are apparently not the states from which the final release near 900°C occurs. The last state of the H is also believed not to involve bubbles or extended defects, since, in cross-section TEM of GaN implanted with 10^{15} ^{2}H/cm^2 at 50 keV and then annealed at 886°C for 1 hour, we did not observe such microstructural features produced by the implantation. Conceivably, H_2 forms within vacancy-type defects at the most elevated temperatures.

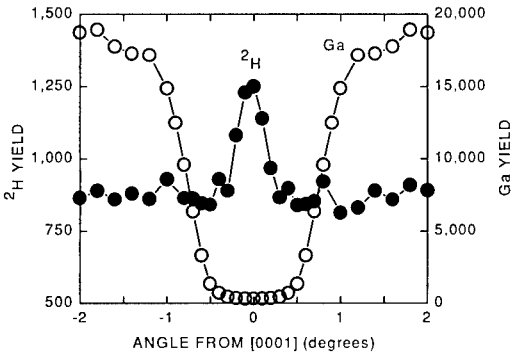


Fig. 10. Channeling scans after implanting 10^{15} ^{2}H/cm^2 into GaN at room temperature.

SUMMARY

We investigated the behavior of ion-implanted H in MOCVD GaN on sapphire at concentrations ranging from hundredths of an atomic percent to several at.%. The results of these experiments were interpreted in terms of underlying physical processes, providing new information on fundamental aspects of H and defect behavior.

At implanted concentrations $\vee$1 at.%, faceted H_2 bubbles formed with (0001) and $\{10\bar{1}1\}$ faces of N-terminated polarity, indicating that such surfaces were energetically preferred. Infrared spectroscopy showed localized vibrational modes attributable to N-H on the bubble walls at a coverage of ~1 monolayer. From this we concluded that the otherwise highly reactive N-terminated surfaces were passivated by H, and that the attendant large reduction in surface energy probably affected the observed selection of surfaces. During isochronal annealing, the N-H state detected by IR spectroscopy diminished at somewhat lower temperatures than the total quantity of H measured by NRA, indicating that the chemisorbed state was less stable than the H_2 gas.

Hydrogen was strongly retained within the bubbles, undergoing release only at temperatures $\vee$800°C. By analyzing retention-versus-time isotherms, the pressure within the bubbles and the diffusivity-solubility product of the H were evaluated. We provisionally hypothesized that most of the release occurred with the Fermi level stabilized by ionized H atoms in solution in such a way that $[H^+] \sim [H^-]$.

Our examination of defects arising from the higher-dose implantations and attendant bubble formation led to several mechanistic inferences. The added volume of the bubbles is believed to be accommodated by the agglomeration of implantation-generated vacancies, and this leaves a corresponding number of host-atom interstitials within the lattice. These interstitial defects undergo substantial evolution in the approximate temperature range 500-700°C; most are annihilated, presumably at the surface, with a small residual being incorporated into basal-plane stacking faults bounded by partial dislocations.

At implanted concentrations $\wedge$0.1 at.%, bubble formation was not observed, and the H was concluded from channeling analysis to occupy a defect-related interstitial site in the [0001] channel. Prior to thermal release from the specimen, the H apparently moves to a more stable state that is not characterized by a unique lattice sites and is not IR-active, conceivably H_2 within vacancy defects.

ACKNOWLEDGEMENTS

The authors benefited greatly from interactions with D. M. Follstaedt, S. J. Pearton, M. J. Stavola, and A. F. Wright. The work was supported by the Office of Basic Energy Sciences, U. S. Dept. of Energy, under Contract DE-AC04-94AL85000. Sandia National Laboratories is a multiprogram laboratory operated by Sandia Corp., a Lockheed Martin Company, for the U. S. Dept. of Energy.

REFERENCES

1. J.M. Zavada, R.G. Wilson, C.R. Abernathy, and S.J. Pearton, Appl. Phys. Lett. **64**, 2724 (1994).
2. M.G. Weinstein, C.Y. Song, M. Stavola, S.J. Pearton, R.G. Wilson, R.J. Shul, K.P. Killeen, and M.J. Ludowise, Appl. Phys. Lett. **72**, 1703 (1998).
3. S.J. Pearton, R.G. Wilson, J.M. Zavada, J. Han, and R.J. Shul, Appl. Phys. Lett. **73**, 1877 (1998).

4. W.R. Wampler and S.M. Myers, MRS Internet J. Nitride Semicond. Res. **4S1**, G3.73(1999).
5. C.H. Seager, S.M. Myers, G.A. Petersen, J. Han, and T.J. Headley, J. Appl. Phys., in press.
6. T.-B. Ng, J. Han, R.M. Biefeld, and M.V. Weckwerth, J. Electron. Mater. **27**, 190 (1998).
7. W. Möller and F. Besenbacher, Nucl. Instrum. Meth. **168**, 111 (1980).
8. S. M. Myers, G. R. Caskey, Jr., D. E. Rawl, Jr., and R. D. Sisson, Jr., Metall. Trans. A **14**, 2261 (1983).
9. Ion ranges were calculated using the TRIM-90 Monte-Carlo code described by J. F. Ziegler, J. P. Biersack, and U. Littmark, *The Stopping and Range of Ions in Solids* (Pergamon, New York, 1985), and by J. F. Ziegler, 1990, unpublished.
10. J. F. Ziegler, *Helium Stopping Powers and Ranges in All Elements* (Pergamon, New York, 1977).
11. F. A. Ponce, D. P. Bour, W. T. Young, M. Saunders, and J. W. Steeds, Appl. Phys. Lett. **69,** 337 (1996).
12. B. Daudin, J. L. Rouvière, and M. Arlery, Appl. Phys. Lett. **69**, 2480 (1996).
13. M. Seelmann-Eggebert, J. L. Weyher, H. Obloh, H. Zimmermann, A. Rar, and S. Porowski, Appl. Phys. Lett. **71**, 2635 (1997).
14. Z. Liliental-Weber, O. Richter, J. Washburn, K. Pakula, J. Baranowski, I. Grzegory, S. Porowski, and J. Y. Yang, reported at the 1998 Spring Meeting of the Materials Research Society.
15. J. Neugebauer and C. G. Van de Walle, Phys. Rev. Lett. **75**, 4452 (1995).
16. A.F Wright, to be published.
17. Z. Liliental-Weber, C. Kisielowski, S. Ruvimov, Y. Chen, J. Washburn, I. Grzegory, M. Bockowski, J. Jun, and S. Porowski, J. Electron. Mater. **25**, 1545 (1996).
18. M.J. Stavola, private communication.

SPECTROSCOPY OF PROTON IMPLANTED GaN

M.G. Weinstein,* M. Stavola,* C.Y. Song,* C. Bozdog,* H. Przbylinska,* G.D. Watkins,*
S.J. Pearton,** and R.G Wilson,+

*Dept. of Physics, Lehigh University, Bethlehem, Pennsylvania 18015
**University of Florida, Dept. of Materials Science, Gainesville, Florida 32611
+Consultant, Stevenson Ranch, California 92065

Cite this article as: MRS Internet J. Nitride Semicond. Res. 4S1, G5.9 (1999)

Abstract

Vibrational spectroscopy, photoluminescence, and optically detected electron paramagnetic resonance (ODEPR) have been used to characterize the defects produced in undoped and Si-doped GaN by the implantation of hydrogen. Several new vibrational bands were found near 3100 cm^{-1} in GaN that had been implanted with protons. These frequencies are close to those predicted for V_{Ga}-H_n complexes, leading to the tentative assignment of the new lines to V_{Ga} defects decorated with different numbers of H atoms. The proton implantation also produces an infrared PL band centered at 0.95 eV and the ODEPR spectrum labeled LE1, both of which were seen previously for electron-irradiated GaN.

Introduction

The III-V nitrides have eclipsed alternative wide bandgap semiconductors for optoelectronic device applications in the near UV and visible and show promise for high temperature/power electronics.[1-3] These successes have depended, in part, on an improved understanding and control of defect processes such as the hydrogen passivation of acceptors in the nitrides.[4-7] Of particular interest here are recent studies of the interaction of hydrogen with native defects[8] and experimental results for the defects introduced in GaN by high-energy electron irradiation.[9,10] In this paper we report results for the defects introduced by the implantation of hydrogen into GaN. The defects created by the implantation that are decorated by H have been studied by vibrational spectroscopy. PL and ODEPR spectra have been measured for the same H-implanted samples and compared with recent results obtained for GaN irradiated with 2.5 MeV electrons.[9,10]

Experimental

The 2.5μm thick GaN samples used in our experiments were grown by metalorganic chemical vapor deposition (MOCVD) on sapphire substrates at 1040°C using trimethylgallium and ammonia. Nominally undoped layers had n-type background concentrations of ~ $5x10^{16}$ cm^{-3}. A Si-doped sample contained an n-type carrier concentration of ~5 x 10^{18} cm^{-3}. Protons (and/or deuterons) were implanted at five different energies between 25 and 300 keV in order to create hydrogen profiles with concentrations in the mid-10^{19} cm^{-3} range to a depth of ~2.1μm. Annealing was performed in flowing N_2 at temperatures between 300°C and 700°C. Absorption measurements were made at both normal incidence and by multiple internal reflection so that light polarizations both parallel and perpendicular to the c-axis of the epilayer could be studied. Infrared absorption spectra were measured for the range 1800-4000 cm^{-1} with a Bomem DA.3 Fourier transform spectrometer equipped with an InSb detector. The measurements were made near 4.2K with a resolution of 2 cm^{-1}. Luminescence was excited with the 351 nm line of an Ar-ion laser. PL in the infrared was detected with a North Coast Ge detector and PL in the visible

Mat. Res. Soc. Proc. Vol. 537 © 1999 Materials Research Society

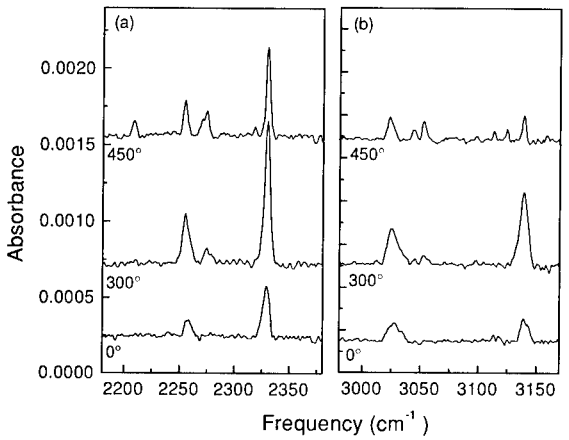


Fig 1. Vibrational spectra measured near 4.2K for (a) deuterium-implanted GaN and (b) hydrogen-implanted GaN samples which were subsequently annealed at the temperatures indicated.

was detected with a UV-extended Si detector. ODEPR spectra were recorded with a 35 GHz spectrometer at 1.7K.

Vibrational Spectroscopy

Spectra are shown in Fig. 1(a) for an undoped GaN sample that had been implanted with deuterium and then annealed at successively higher temperatures. In as-implanted samples, two new vibrational bands were found at 2254.7 cm^{-1} and 2329.7 cm^{-1}. In the samples implanted with hydrogen [Fig. 1(b)], two corresponding lines were found at 3139.5 cm^{-1} and 3023 cm^{-1}. Upon annealing, several weaker bands emerge in both the H- and D-implanted samples. The frequency ratios of the two sets of vibrational lines are near 1.344, i.e., close to $\sqrt{(m_D/m_H)}$, confirming that these are hydrogen vibrations. The H and D modes of corresponding defects were identified and are listed together in Table I. (Two weak D modes were not well resolved and are not listed.) Spectra were also measured for Si-doped samples (N_D=5 x 10^{18} cm^{-3}) that had been implanted with H or D. The same vibrational bands were seen in these samples, but

Table I. Frequencies of vibrational bands observed in GaN that was implanted with H or D. The bands are divided into three groups, each of which shows similar behavior upon annealing. The frequency ratio $r \equiv \omega_H/\omega_D$ and the annealing temperatures where the band intensities are reduced to ~50% of their maximum value are given.

Group	ω_H (cm^{-1})	ω_D (cm^{-1})	*r*	*T* (°C)
III	2982.8	2208.4	1.351	675
I	3023.1	2254.7	1.341	450
II	3043.5	2270.5	1.340	550
II	3052.0	2274.5	1.342	550
II	3112.8	2318.0	1.343	550
II	3124.3	--------	-------	550
I	3139.5	2329.7	1.348	450
II	3150.5	-------	-------	550

were shifted by ~2 cm^{-1}, presumably due to different amounts of strain in the layers. Thus the centers shown in Fig. 1 do not involve Si impurities that might have been introduced unintentionally in the undoped GaN samples.

Spectra were also measured for an undoped sample which had been implanted with overlapping profiles of both H and D to probe whether any of these vibrational bands might be due to defects which contain more than one hydrogen atom. (Additional vibrational lines can appear for multi-H centers when complexes are formed that contain both H and D).[11] No additional lines were observed in the spectra for these samples.

Fig. 2 shows the annealing behavior of several of the vibrational bands. Comparing Fig. 2(a) to 2(b), one can see that the bands we have assigned to H and D modes of corresponding defects, show similar annealing behavior, supporting the associations we have made. Furthermore, the bands can be divided into three groups as indicated in Table I. Group I vibrational bands are strong in the as-implanted samples and reduced to 50% of their maximum by an anneal at 450°C. The group II bands begin to grow in at ~ 300°C, and then decay to 50% of their maximum intensity near 550°C. There is a single band labeled group III that grows in near 450°C and then decays to half its maximum intensity near 675°C. (In the D-implanted sample, the intensity of this lowest frequency band at 2208.4 cm^{-1} was easy to follow for the different annealing temperatures. However, in the H implanted samples, the band at 2982.8 cm^{-1}, though seen consistently in samples annealed at 450° and above, was relatively weak and its intensity could not be characterized quantitatively.)

Vibrational frequencies have been calculated by Van de Walle for V_N-H and V_{Ga}-H_n complexes in GaN.[8] The predicted frequencies are 3100 cm^{-1} for V_{Ga}-H and 3470 cm^{-1} for V_{Ga}-H_4 and are close to the vibrational frequencies we have measured. Van de Walle also predicted a frequency of 600 cm^{-1} for the V_N-H complex,[8] much lower than the vibrational frequencies we have seen. Therefore, comparison with theory leads us to suggest that the lines we have observed correspond to nitrogen-dangling-bond defects that are decorated by hydrogen. The vibrational frequencies we have measured are also close to the frequency observed previously for the passivated Mg acceptor in GaN (3125 cm^{-1}),[5] where the H is believed to be bonded to one of the Mg atom's neighbor N atoms.[5-7] Additional evidence that an N-H stretching mode is being observed comes from the isotopic frequency ratio $r \equiv \omega_H/\omega_D$ which is sensitive to the atom to which the hydrogen is attached. For the vibrational lines observed in H- and D- implanted GaN,

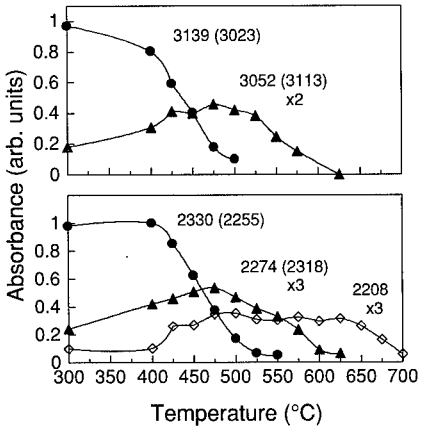


Fig 2. The intensities of selected absorption lines vs. annealing temperature for GaN samples that were implanted with hydrogen (a) and deuterium (b). The frequency of the band for each set of data is shown. The frequencies given in parentheses are for bands with annealing behavior very similar to the ones shown. (Curves are shown to guide the eye.)

r = 1.344 (the average of the values reported in Table I) which is very close to the ratio previously reported for the Mg-H complex in GaN, r = 1.346,[5] where the H is believed to bonded to N. Further, these ratios are smaller than those reported previously for Ga-H bonds in H-implanted GaAs where r ≈ 1.39,[12] further confirming that the new lines observed near 3100 cm^{-1} in GaN can be associated with N-H bonds.

The annealing behavior of the defects we have observed in H-implanted GaN is similar to that of defects seen previously in H-containing InP. In as-grown[13-15] and H-implanted[16] InP there is a strong band at 2316 cm^{-1} that has been assigned to a P-H stretching mode of a V_{In}-H_4 complex.[14,15,17] A lower frequency band at 2201 cm^{-1} has also been assigned to a P-H stretching mode of V_{In}-H.[14,17,18] Additional weak lines have been seen between these frequencies.[14,16] Ewels *et al*[17] have calculated the frequencies of the V_{In}-H_n complexes and have proposed that the partial dissociation of the V_{In}-H_4 complex upon annealing leads to the formation of V_{In}-H_n centers with fewer H atoms, and thus lower frequencies, to explain the presence of several H-stretching bands. Similarly, in our GaN studies, we suggest that the N-H stretching modes we observe belong to a family of V_{Ga}-H_n complexes. We therefore tentatively assign the highest frequency band at 3139.5 cm^{-1} to a V_{Ga}-H_4 complex. The evolution of the spectrum upon annealing would therefore be due to the successive, partial dissociation of the V_{Ga}-H_n centers and thus the weaker lines at lower frequency are due to V_{Ga}-H_n complexes with fewer than four H atoms. Further support for such a scheme comes from the calculations of Van de Walle who found that the binding energy of H decreases for the V_{Ga}-H_n complexes as n increases.[8]

This assignment of the hydrogen-stretching bands and their annealing behavior appears not to be supported by our results for the GaN samples that had been co-implanted with H and D because additional lines due to centers that may contain both hydrogen isotopes were not observed. Results for V_{In}-H_n complexes in InP provide further guidance here. In a previous study of H and D implanted InP, similar results were obtained and no line splittings were observed,[16] even though the line observed at 2316 cm^{-1} has been assigned to a V_{In}-H_4 complex.[14,15,17] It was found later that in samples where H and D had been introduced during growth (which gives rise to much sharper lines), the 2316 cm^{-1} band was split into a triplet by the presence of both H and D, but with a line splitting of only ~ 0.5 cm^{-1}, too small to have been observed in the implanted samples.[15] The line widths in our proton implanted GaN samples are ~ 5 cm^{-1} which would also prevent the observation of such small line splittings. Thus, if the situation in GaN is similar to that proposed previously for InP,[15] the lack of line splittings upon

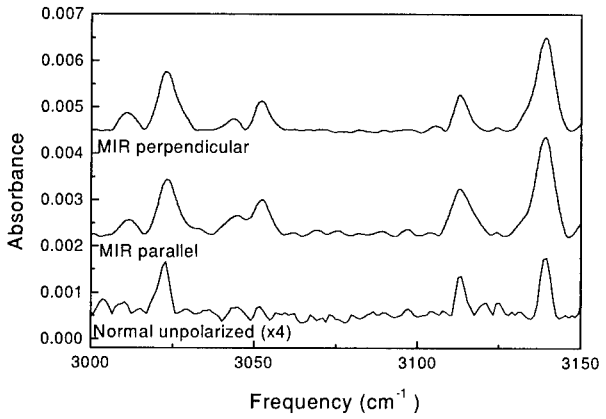


Fig. 3. Vibrational spectra measured by multiple internal reflection for the polarization parallel to the plane of the sample or the perpendicular polarization with a component normal to the epitaxial layer. Also shown for comparison is a spectrum measured with the light beam (unpolarized) at normal incidence to the epitaxial layer.

the coimplantation of H and D in our experiments on GaN does not rule out the assignments for the H-stretching bands we have suggested above.

The infrared measurements described up to this point were measured with the probing light normal to the sample where the polarization of the light must be in the plane of the epitaxial layer (i.e., the a-b plane of the wurtzite GaN). Therefore, vibrational modes that might have their transition-dipole moments perpendicular to the layer (i.e., along the c-axis for GaN) cannot be excited. To investigate the possibility that there might be a preferential alignment of the hydrogen-implantation-related defects in the wurtzite lattice, the ends of the sapphire substrate were beveled at 45° to fabricate a multiple-internal-reflection (MIR) prism. Spectra measured for normal incidence and by MIR with in- and out-of- plane polarizations are compared in Fig. 3. Although the MIR geometry increased the signal to noise ratio of the measurements, no significant difference was observed between the different polarizations. This result suggests that none of the defects introduced by the proton implantation that we observe by vibrational spectroscopy are preferentially aligned along the c-axis of the wurtzite GaN or that any possible line splittings for different defect orientations are too small to be resolved in our experiments. Similarly, Clerjaud *et al.* have reported that for Mg-H complexes in p-type GaN, there was no difference observed for spectra measured by MIR for different polarizations of the exciting light.[7]

Photoluminescence and ODEPR

Nominally undoped GaN samples have been examined by PL and ODEPR before and after the implantation of hydrogen. The as-grown samples show the strong 2.2 eV yellow-luminescence band and the ODEPR spectra previously attributed to the dominant donor and a deep defect that are seen in GaN [Fig. 4(a)].[19] The implantation of hydrogen into our samples greatly reduced the intensity of the yellow luminescence. The implantation also produced a near infrared luminescence band centered at ~0.95 eV, very similar to a band reported previously that is produced by high-energy electron irradiation.[9,10,20] The near-infrared PL spectra seen for electron-irradiated and proton-implanted samples are compared in Fig. 5.

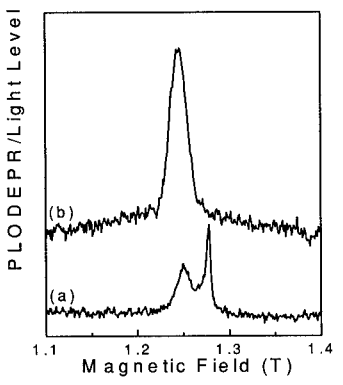


Fig 4. PLODEPR spectra in (a) as-grown, undoped GaN, observed in the 2.2 eV PL band and (b) following H-implantation observed in the IR PL band

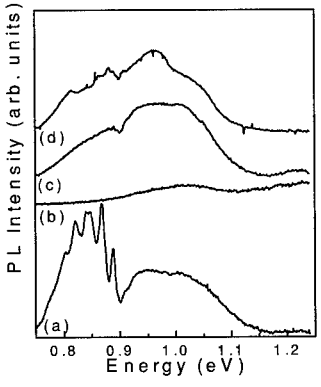


Fig. 5. PL in the IR for (a) an electron-irradiated GaN sample (2.5 MeV, 1.5×10^{18} e/cm^2); an undoped GaN sample (b) before and (c) after H-implantation; and (d) an additional H-implanted sample.

In the previous results for electron-irradiated samples [Fig. 5(a)], a broad, structureless band ranging from ~0.75 to 1.1 eV with its peak at 0.95 eV was observed. A sharply structured band to the low energy side of this broad band was also produced. Proton implantation also produced the broad 0.95 eV band (spectra b-d). In one proton-implanted sample (spectrum d), the sharply structured band was seen, but only weakly; in other samples this band was not observed.

Electron-irradiated GaN shows several new ODEPR spectra labeled LE1-LE4 associated with the near-IR luminescence.[9,10] Our proton implanted samples show only the S = ½ spectrum LE1 [Fig 4(b)]. Spectrum LE2, associated with the more sharply structured luminescence band, and the two ODEPR spectra attributed to displaced Ga atoms were not seen in our proton-implanted samples. At present, the defects responsible for the near-IR photoluminescence and associated ODEPR spectra have not been identified. Nonetheless, the defects created by proton implantation give similar spectroscopic signatures, making the electron-irradiation results an interesting baseline with which to compare the defects that result from ion implantation.

The work at LU was supported by ONR Grant No. N00014-94-1-0117. The work at UF was partially supported by NSF Grant No. DMR 9421109.

1. F.A. Ponce and D.P. Bour, Nature **386**, 351 (1997).
2. *GaN and Related Materials*, edited by S.J. Pearton (Gordon and Breach, Amsterdam, 1997).
3. *Gallium Nitride (GaN)*, edited by J. Pankove and T.D. Moustakas (Academic, Boston, 1997).
4. S. Nakamura, N. Iwasa, M. Senoh, and T. Mukai, Jpn. J. Appl. Phys. **31**, 1258 (1992).
5. W. Götz, N.M. Johnson, D.P. Bour, M.D. McCluskey, and E.E. Haller, Appl. Phys. Lett. **69**, 3725 (1996).
6. J. Neugebauer and C.G. Van de Walle, Phys. Rev. Lett. **75**, 4452 (1995).
7. B. Clerjaud, D. Côte, and A. Lebkiri, Proceedings 8th International Conference on Shallow-Level Centers in Semiconductors, Phys. Stat. Sol. (b) **210**, (1998), to be published.
8. C.G. Van de Walle, Phys. Rev. B **56**, R10020 (1997).
9. M. Linde, S.J. Uftring, G.D. Watkins, V. Härle and F. Scholz, Phys. Rev. B **55**, 10177 (1997).
10. G.D. Watkins, M. Linde, P.W. Mason, H. Przybylinska, C. Bozdog, S.J. Uftring, V. Härle, F. Scholz, W.J. Choyke and G.A. Slack, *Defects in Semiconductors, ICDS-19*, edited by G. Davies and M.H. Nazaré (Trans Tech, Switzerland, 1997), p. 1087.
11. M. Stavola, *Identification of Defects in Semiconductors*, edited by M. Stavola (Academic, Boston, 1999), vol. 51B, p. 153.
12. B. Pajot, J. Chevallier, A. Chaumont, and R. Azoulay, *Defects in Electronic Materials*, edited by M. Stavola, S.J. Pearton, and G. Davies (Mat. Res. Soc., Pittsburgh, 1988), p. 345.
13. R.C. Newman, Semicond. Sci. Technol. **5**, 911 (1990).
14. R. Darwich, B. Pajot, B. Rose, D. Robein, B. Theys, R. Rahbi, C. Porte, and F. Gendron, Phys. Rev. B **48**, 17776 (1993).
15. F.X. Zach, E.E. Haller, D. Gabbe, G. Iseler, G.G. Bryant, and D.F. Bliss, J. Electron. Mat. **25**, 331 (1996).
16. D.W. Fischer, M.O. Manasreh, and G. Matous, J. Appl. Phys. **71**, 4805 (1992).
17. C.P. Ewels, S. Öberg, R. Jones, B. Pajot, and P.R. Briddon, Semicond. Sci. Technol. **11**, 502 (1996).
18. B. Clerjaud, D. Côte, and C. Naud, Phys. Rev. Lett. **58**, 1755 (1987).
19. E.R. Glaser, T.A. Kennedy, K. Doverspike, L.B. Rowland, D.K. Gaskill, J.A. Freitas, M. Asaaf-Khan, D.T. Olson, J.N. Kuznia, W.K. Wickenden, Phys. Rev. B **51**, 13326 (1995).
20. I.A. Buyanova, Mt. Wagner, W.M. Chen, B. Monemar, J.L.. Lindström, H. Amano, and I. Akasaki, Appl. Phys. Lett. **73**, 2968 (1998).

A CRITICAL COMPARISON BETWEEN MOVPE AND MBE GROWTH OF III-V NITRIDE SEMICONDUCTOR MATERIALS FOR OPTO-ELECTRONIC DEVICE APPLICATIONS

M.A.L. JOHNSON[*,**], ZHONGHAI YU[*], J.D. BROWN[*], F.A. KOECK[*], N.A. EL-MASRY[**], H.S. KONG[***], J.A. EDMOND[***], J.W. COOK, JR.[*], AND J.F. SCHETZINA[*]
*Department of Physics, North Carolina State University, Raleigh, NC 27603
jan_schetzina@ncsu.edu
**Department of Material Science and Engineering, North Carolina State University, Raleigh, NC 27603
***Cree Research, Inc., Durham, NC

Cite this article as: MRS Internet J. Nitride Semicond. Res. 4S1, G5.10 (1999)

ABSTRACT

A systematic study of the growth and doping of GaN, AlGaN, and InGaN by both molecular beam epitaxy (MBE) and metal-organic vapor phase epitaxy (MOVPE) has been performed. Critical differences between the resulting epitaxy are observed in the p-type doping using magnesium as the acceptor species. MBE growth, using rf-plasma sources to generate the active nitrogen species for growth, has been used for III-Nitride compounds doped either n-type with silicon or p-type with magnesium. Blue and violet light emitting diode (LED) test structures were fabricated. These vertical devices required a relatively high forward current and exhibited high leakage currents. This behavior was attributed to parallel shorting mechanisms along the dislocations in MBE grown layers. For comparison, similar devices were fabricated using a single wafer vertical flow MOVPE reactor and ammonia as the active nitrogen species. MOVPE grown blue LEDs exhibited excellent forward device characteristics and a high reverse breakdown voltage. We feel that the excess hydrogen, which is present on the GaN surface due to the dissociation of ammonia in MOVPE, acts to passivate the dislocations and eliminate parallel shorting for vertical device structures. These findings support the widespread acceptance of MOVPE, rather than MBE, as the epitaxial growth technique of choice for III-V nitride materials used in vertical transport bipolar devices for optoelectronic applications.

INTRODUCTION

The recent development of III-V Nitride semiconductor devices for optoelectronic applications has been driven by improvements in the epitaxial growth of these semiconductor materials. Heterostructures have been fabricated across a range of AlN-GaN-InN compositions with bandgaps ranging from 6.2 eV (ultraviolet) to 1.9 eV (red) for LED, laser diode, and photodetector applications [1,2]. Heterostructure epitaxy has traditionally been performed using either MBE or MOVPE in many semiconductor material systems [3,4]; however, most of the recent device application demonstrations for III-V nitrides have used MOVPE, particularly in the commercially driven work at Nichia Chemical and Cree Research [5,6]. MBE growth for optoelectronic device applications has lagged behind. Initially, this was attributed to the unavailability of an appropriate source of active nitrogen species for MBE [1]. Through the development of nitrogen rf plasma sources for MBE, the quality of the resulting epitaxial layers has improved [7,8,9,10]. Despite these advances, demonstration of high quality vertical devices such as laser diodes or high brightness LEDs grown by MBE has not occurred [8,11].

In this work, we compare the growth of III-V nitride materials by MBE and MOVPE in order to examine the fundamental differences in the epitaxial growth and the influence on

Mat. Res. Soc. Proc. Vol. 537 © 1999 Materials Research Society

resulting devices. We have studied three areas of critical importance for light emitting devices. First is the difference in the epilayer growth morphology; second is the doping of GaN with magnesium for p-type conductivity; and finally, the deposition of InGaN quantum wells with compositions in the visible emission range. This comparison provides a twofold benefit of identifying critical areas for further exploration in crystal growth and deepening the understanding of the underlying physical processes at work in successful epitaxial deposition.

EXPERIMENTAL PROCEDURE

MOVPE growth was performed in a vertical flow rotating wafer (up to 2000 rpm) system designed and built at NCSU. A radiatively heated substrate mount, of original high reliability design, can achieve temperatures up to 1200°C, as measured by an optical pyrometer. 50-mm diameter sapphire wafers were used as the base substrate with a typical low temperature GaN nucleation layer. Trimethylgallium (TMGa), trimethylaluminum (TMAl), trimethylindium (TMI) and ammonia were used as precursors with nitrogen and hydrogen carrier gases at a reactor pressure of 76 Torr. Silane and bis(cyclopentadienyl) magnesium were used as dopant sources. Growth temperatures for GaN ranged from 1060°C to 1130°C. The conditions resulted in 2D epitaxial growth at rates of 1-2 μm/hr. InGaN growth was conducted in a manner similar to Yoshimoto at temperatures from 725°C to 800°C [12].

MBE growth was performed in an EPI Model 930 system using elemental group III and dopant sources. Rf plasma sources were used to generate the active nitrogen species. Pre-nucleated GaN/SiC substrates were used for the MBE deposition. Growth temperatures ranged from 750°C to 900°C for GaN and 670°C to 700°C for InGaN resulting in growth rates of 0.4-2 μm/hr. A modulated beam technique was used to grow InGaN as previously described [11].

The MOVPE and MBE were connected as a multichamber UHV cluster tool. This allows for the growth of sophisticated heterostructures with specific layers grown in either the MBE or MOVPE system where applicable. Characterization of epitaxial layers included: scanning electron microscopy using a JEOL JSM6400 SEM, photoluminescence (PL) using a 12 mW He-Cd laser source, and Nomarski microscopy using an Olympus BX60 microscope and image capture system. Vertical cross section samples were studied in a Topcon 002B Transmission Electron Microscope (TEM) with g=$(1\bar{1}00)$ at 200 kV.

LED samples were prepared following standard lithography techniques and using Ni/Au and Ti/Al as p-type and n-type contact metals, respectively.

RESULTS AND DISCUSSION

Epitaxial Layer Surface Morphology and Magnesium Doping

The surface morphology of epitaxially grown GaN exhibits an obvious difference between MOVPE and MBE deposited material. As shown in the SEM micrograph in Figure 1a, undoped or n-type doped MBE grown GaN exhibits a "wormy" structure. This surface structure has been previously reported and the degree of texture can be minimized, although not eliminated, through changes in the nitrogen plasma source operating conditions [8,9,10,13,14]. The MOCVD grown undoped material is smooth and uniform as shown in Figure 1b.

Magnesium was used as a p-type dopant for both MBE and MOVPE grown of GaN. For MOVPE growth, the surface of p-type material is smooth and featureless. However, in MBE growth, there is a dramatic change in surface texture with the evolution of a faceted surface with increasing magnesium flux as shown in Figures 1c and 1d. Cross sectional TEM studies revealed the facet morphology to be related to the pre-existing dislocation structure [4].

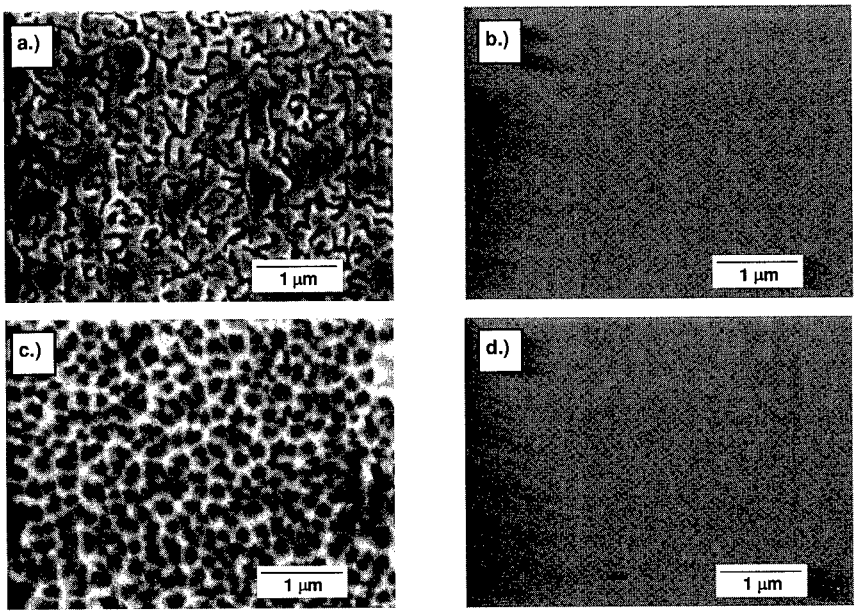


Figure 1: Scanning Electron Micrographs of as Grown Surfaces: a.) Undoped GaN by MBE; b.) Undoped GaN by MOVPE; c.) Magnesium Doped GaN by MBE; and d.) Magnesium Doped GaN by MOVPE.

The spacing of the contrast features in the plan view SEM image of this surface is consistent with a dislocation density of 10^8-10^{10}cm^{-2}. We feel that this segregation is related to the nature of doping in the MBE environment from a source that is at a lower temperature (300°C) than the substrate (750°C). Based on normalized flux measurements, we estimate the sticking coefficient of magnesium to be almost two orders of magnitude less than that of the gallium. As previously reported, a further increase in the magnesium flux beyond a maximum level results in a reduction in magnesium incorporation, a transformation in the growth morphology observed by RHEED to 2D, and n-type conductivity behavior [16].

Hydrogen plays an important role in the p-type doping of GaN grown by MOVPE. The formation of a Mg-H complex, with a characteristic blue PL, during subsequent activation annealing is thought to be the acceptor species responsible for p-type doping [15]. Ammonia and carrier gasses are the source of hydrogen to the MOVPE process in a viscous flow pressure regime. Although the presence of hydrogen in the molecular flow pressure regime of MBE may have some influence on the surface morphology of undoped GaN layers, addition of hydrogen to the nitrogen plasma does not provide a similar effect in the magnesium doping MBE grown GaN [16, 17]. A conversion in the PL spectrum to the characteristic blue has not been observed following post-growth annealing of MBE deposited magnesium doped material.

Though these phenomenon are still not well understood, there is a clear difference between both the incorporation and activation of magnesium doped GaN grown by MOVPE as compared with MBE. Magnesium doping by MBE results in a featured surface which would have a negative impact on optoelectronic devices grown by this technique.

InGaN Growth

The growth of InGaN layer, which have a high equilibrium vapor pressure of nitrogen, points to another significant difference between MBE and MOVPE growth. In MBE, the active species of nitrogen participating in epitaxial growth are atomic nitrogen and excited molecules, which are generated and injected from a plasma source. As a result, the dissociation pathways for nitrogen from the InGaN alloy can play a dominant role and special techniques of modulated beam growth have been employed to stabilize the growing surface and limit the precipitation of metal droplets [11]. This method results in a layered InGaN/GaN structure as shown in the TEM image of Figure 2. The defect structure replicates the defects that are present in the underlying substrate, with dislocations bridging the InGaN layered structure. This InGaN multiple quantum well test structure was grown to a 50% indium composition, and emits the green PL spectrum shown in Figure 2b. To our knowledge, this is the highest reported mole fraction of optical quality InGaN grown by MBE.

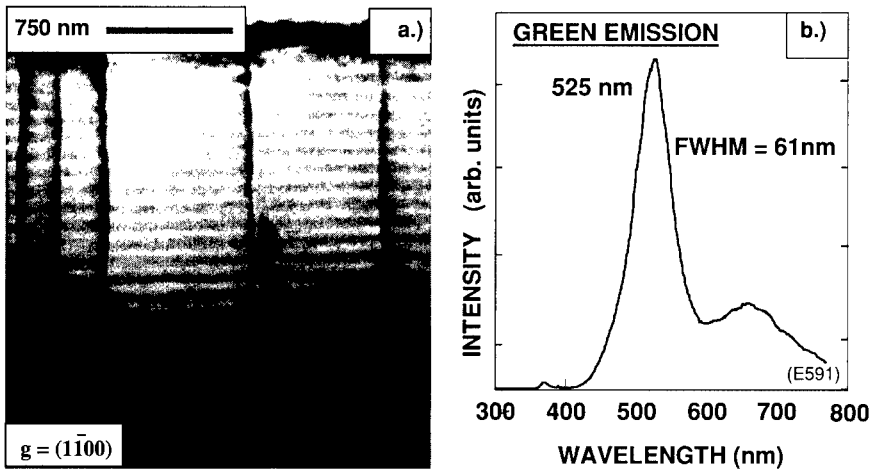


Figure 2: MBE Grown InGaN MQW Structure a.) Cross Sectional TEM Image (200 kV) and b.) Room Temperature PL Spectrum

In MOVPE, ammonia is thermally dissociated during growth and is the source of active nitrogen. While a ratio of TMI to TMGa of 10 is necessary to achieve the desired InGaN alloy compositions, it is possible to directly deposit high quality InGaN by MOVPE [12]. Using these methods, blue and green LED's have been commercially produced by MOVPE [5].

The use of ammonia as the source for active nitrogen plays another important role by providing hydrogen to the MOVPE process. Hydrogen appears to passivate the threading dislocations during MOVPE growth and render them electrically neutral. Adding hydrogen to the nitrogen plasma does not appear to produce a similar beneficial effect in MBE [16].

InGaN Quantum Well Light Emitting Diodes

LED test structures were fabricated from MOVPE and MBE grown material. Test structures were single quantum well devices with similar doping levels and compositions. As shown in Figure 3a and 3b, InGaN alloys that emit light in the blue and violet region of the spectrum have been grown. Note the two orders of magnitude difference in forward current for

luminescence to be the clearly visible in room light, from 50mA for the MBE grown structure down to only 0.5 mA for the MOVPE grown material. Higher current is consistent with the presence of parallel conduction pathways shorting across the MBE grown LED structure.

Another significant difference between MBE and MOVPE grown LEDs is the typical current-voltage (I-V) characteristics shown in Figures 3c and 3d. MBE grown diodes exhibit a rather low reverse breakdown voltage. The IV characteristics for the MBE grown diode are as would be expected for a diode with shorting pathways parallel to the diode junction. We feel this to be the critical difference limiting MBE grown vertical device structures. While high quality InGaN can be deposited by MBE, the pre-existing dislocations, ranging in density of 10^8-10^{10}cm^{-2}, are replicated and act as parallel shorting pathways in MBE grown device structures. This is exactly the behavior expected in a traditional semiconductor, such as GaAs, possessing a high dislocation density. Fortunately, in the MOVPE growth environment, dislocations are rendered electrically neutral, perhaps due to the presence of hydrogen from the dissociated ammonia. As a result, diode structures which are free of parallel conduction pathways can be grown by MOVPE and the fabrication of vertical device structures is possible, even with dislocation densities as high as 10^8-10^{10} cm^{-2}.

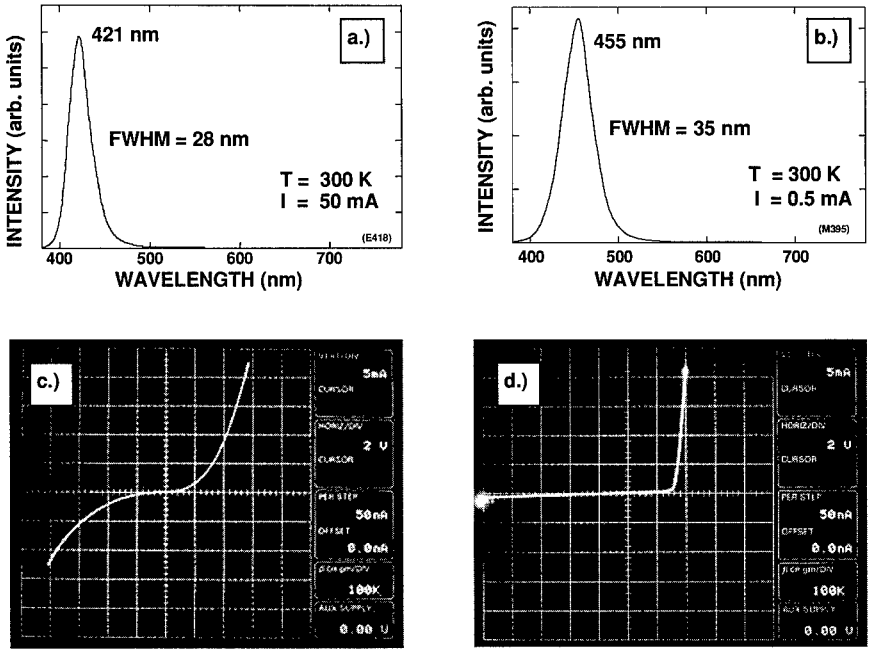


Figure 3: Spectrum for InGaN quantum well LEDs grown by a.) MBE and b.) MOVPE. I-V curve trace for LEDs grown by c.) MBE and d.) MOVPE. Note the substantially lower forward current and reduced breakdown voltage for the MOVPE grown LEDs.

CONCLUSIONS

We have compared the growth of III-V nitride materials by MBE and MOVPE. Critical differences exist in the p-type doped GaN material. A textured surface evolves for MBE grown GaN:Mg, which may be related to the pre-existing dislocation density of the material coupled with difficulties in depositing magnesium with its high vapor pressure at this growth temperature. Although InGaN can be grown by either method with a bandgap tailored to emit light in the visible range of interest for devices, the presence of a high density of shorting dislocations across the diodes limits InGaN QW LEDs grown by MBE. This is the significant factor limiting MBE growth and allowing the successful implementation of MOVPE for III-V nitride optoelectronic applications.

ACKNOWLEDGEMENTS

Thanks to J. Matthews for his assistance with epitaxial equipment maintenance, sample preparation, and device processing. Financial support provided by DARPA and Cree Research.

REFERENCES

1. Strite and H. Morkoç, J. Vac. Sci. Technol. B **10**, 1237 (1992).
2. S. Pearton, *GaN and Related Materials*, Gordon and Breach Science Publishers, Netherlands, 1997.
3. G.B. Stringfellow, *Organometallic Vapor Phase Epitaxy Theory and Practice*, Academic Press, New York, 1989.
4. M.A. Herman and H. Sitter *Molecular Beam Epitaxy Fundamentals and Current Status*, Springer-Verlag, New York, 1996.
5. S. Nakamura and G. Fasol, *The Blue Laser Diode* Springer-Verlag, New York, 1996.
6. K. Doverspike, G.E. Bulman, S.T. Sheppard, H.S. Kong, M. Leonard, H. Dieringer, T.W. Weeks, Jr., J. Edmond, J.D. Brown, J.T. Swindell, J.F. Schetzina, Y.K Song, M. Kuball, and A. Nurmikko, Mater. Res. Soc. Symp. Proc. **482**, 1169 (1998).
7. W.C. Hughes, W. Rowland, Jr., M.A.L. Johnson, S. Fujita, J.W. Cook, Jr., J.F. Schetzina, J. Ren, and J.A. Edmond, J. Vac. Sci. Technol. B **13**, 1571 (1995).
8. M.A.L. Johnson, Zhonghai Yu, C. Boney, W.H. Rowland, Jr., W.C. Hughes, J.W. Cook, Jr., and J.F. Schetzina Mater. Res. Soc. Symp. Proc. **449**, 271 (1997).
9. H. Riechert, Mater. Res. Soc. Symp. Proc. **449**, 149 (1997).
10. J. M. Van Hove, G.J. Cosimini, E. Nelson, A.M. Wowchak, and P.P. Chow, J. Cryst. Growth **150**, 908 (1995).
11. M.A.L. Johnson, J.D. Brown, N.A. El-Masry, J.W. Cook, Jr., J.F. Schetzina, H.S. Kong, and J.A. Edmond J. Vac. Sci. Technol. B **16**,1282 (1998).
12. N. Yoshimoto, T. Matsuoka, T. Sasaki, and A. Katsui, Appl. Phys. Lett. **59**, 2251 (1991).
13. O. Zsebok, J.V. Thordson, T.G. Anderson, MRS Internet J. Nitride Semicond. Res., **3** 14 (1998).
14. R.J. Molnar and T.D. Moustakis, J. Appl. Phys **76** 4587 (1994).
15. J. Neugebauer and C.G. Van de Walle, Mater. Res. Soc. Symp. Proc. **395**, 645 (1996).
16. M.A.L. Johnson, Zhonghai Yu, C. Boney, W.H. Rowland, Jr., W.C. Hughes, J.W. Cook, Jr., and J.F. Schetzina Mater. Res. Soc. Symp. Proc. **449**, 215 (1997).
17. S.L. Buczkowski, Zhonhai Yu, M. Richards-Babb, N.C. Giles, L.T. Romano and T.H. Myers **449**, 197 (1997).

Part VI

Surfaces, Theory, Processing, Devices

Characteristic Temperature Estimation for GaN-Based Lasers

T. Honda*, H. Kawanishi*, T. Sakaguchi**, F. Koyama** and K. Iga**

*Department of Electronic Engineering, Kohgakuin University,

2665-1 Nakano-machi, Hachiohji-shi, Tokyo 192-0015, Japan

e-mail: ct11761@ns.kogakuin.ac.jp

TEL:+81-426-22-9291 ext. 3440 FAX: +81-426-25-8982

**Precision and Intelligence Laboratory, Tokyo Institute of Technology

4259 Nagatsuta, Midori-ku, Yokohama 226-8503, Japan

Cite this article as: MRS Internet J. Nitride Semicond. Res. 4S1, G6.2 (1999)

Abstract

We have estimated the characteristic temperature T_0 of GaN-based vertical-cavity surface-emitting lasers. The density matrix theory including intraband relaxation broadening has been taken into account. The estimated T_0 is about 300 K, which suggests a good temperature characteristic in GaN-based lasers.

Introduction

Gallium nitride (GaN) and related compounds have large bandgap energies and are attractive for light-emitting devices operating in blue to ultraviolet spectral regions [1,2]. Recently, room temperature pulsed operation of GaN-based laser diodes (LDs) has been reported [3]. In these reports, it was shown that the introduction of a quantum well (QW) structure as an active layer is very effective for realizing the GaN-based laser. The characteristic temperature of lasers is one of the important parameters for applications such as to optical memories, from the viewpoint of high-temperature operation. A less sensitive temperature is preferable for wide-ranging applications. In this paper, we report the estimation of temperature sensitivity for a GaN-based laser with a quantum well structure as the active layer.

The internal quantum efficiency of GaN QW layers is one of the important issues in terms of low power consumption and operation reliability. In the first step, carrier confinement in a GaN QW layer is estimated.

Mat. Res. Soc. Symp. Proc. Vol. 537 © 1999 Materials Research Society

Carrier Confinement Ratio

We have assumed the equilibrium condition in a single QW structure and defined the confinement ratio as a function of the density of states, as shown in the following equation.

$$R_{conf} = \frac{N_{2D}}{N_{2D} + N_{3D}} \tag{1}$$

Where, R_{conf}, $N_{2D}$and N_{3D} are the confinement ratio, number of carrier in a QW layer and barrier layers, respectively. In this estimation, we have assumed a quantum well with a finite offset. The density of states in the single QW layer (2-dimensional), $g_{2D}(E)$ and the barrier layer (3-dimensional), $g_{3D}(E)$ can respectively be written as [4]

$$g_{2D}(E)_i = \frac{1}{2\pi^2}\left(\frac{2m}{\hbar^2}\right)^{\frac{3}{2}}\sqrt{E_i} \tag{2}$$

$$g_{3D}(E) = \frac{(2m)^{\frac{3}{2}}}{2\pi^2\hbar^3}\left(\sqrt{E} - \sqrt{\Delta E}\right). \tag{3}$$

The total carrier concentration, N_{tot} in the QW and barriers is expressed as

$$N_{tot} = \int \left\{g_{2D}(E) + g_{3D}(E)\right\} f(E, E_f) dE \,. \tag{4}$$

Where, $f(E,E_f)$ is Fermi distribution function. From eqs. (1) - (4), we can derive the equation of the carrier confinement ratio.

The confinement ratio of the GaN/AlGaN QW structure as a function of the injected carrier density is shown in Fig. 1. We also show that of the GaAs/AlGaAs QW for comparison. We assumed that the band offset ratios of $\Delta Ec/\Delta Ev$ are 0.71/0.29 [5,6] for GaN/AlGaN QWs and 0.65/0.35 [7] for GaAs/AlGaAs QWs. In the case of GaN-based VCSELs, an injected carrier density higher than 5 x 10^{18} cm^{-3} is roughly required for laser operation. A high confinement ratio is required at high carrier densities for laser device application. If we adopt an AlGaN layer with an aluminum composition higher than 10% as the barrier layer, the confinement ratio is almost unity, which means that all injected carriers are confined to the QW layer. In this case, we can regard the QW layer as an infinite potential well.

Optical Gain

The optical gain of GaN QW layers is an important parameter in the estimation of the threshold current density. The estimation of the linear gain for GaN QWs is carried out using the density-matrix theory with intraband relaxation broadening [8-10]. This model is already established for GaAs-based and InP-based semiconductor lasers, and the calculated results show good agreements with those of experiments. We assumed the square of the dipole moment, $\langle R_{ch}^2 \rangle$ to be a function of bandgap energy and GaN quantum wells to have an infinite potential barrier. The parameters used in this estimation are summarized in Table I. The linear gain is given by [9]

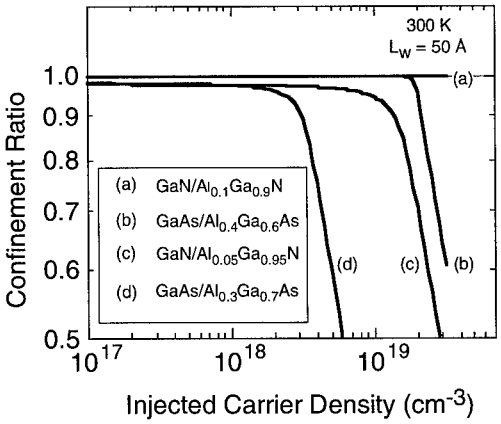


Fig. 1 Confinement ratio as a function of injected carrier density.

$$\alpha(\omega) = \omega\sqrt{\frac{\mu}{\varepsilon}}\left\{\frac{1}{\pi\hbar d}\left(\frac{m_c m_v}{m_c + m_v}\right)\right\}\sum_{n=0}^{M-1}\int_{E_{cn}+E_{vn}+E_g}^{\infty}\langle R_{ch}^2\rangle(f_c - f_v)L(E_{cv} - \hbar\omega)dE_{cv} \quad , \tag{5}$$

where

$$L(E_{cv} - \hbar\omega) = \frac{\hbar/\tau_{in}}{(E_{cv} - \hbar\omega)^2 + (\hbar/\tau_{in})^2} \tag{6}$$

$$\langle R_{ch}^2\rangle = \frac{3}{2}\left(\frac{1 + \frac{E_{cn}}{\varepsilon_{cn}}}{2}\right)\left(e \cdot \frac{4.4}{E_g[eV]}\right) \quad (C^2 \cdot Å^2) \tag{7}$$

ω denotes the angular frequency, μ is the magnetic permeability, ε is the dielectric constant, n is the refractive index of the active layer. The Fermi-Dirac distribution in the conduction band $f_c(E)$ and valence band $f_v(E)$ are assumed, and τ_{in} is the intraband relaxation time. E_{cn} and ε_{cn} denote sub-band energy and total energy of electron in quantized level, respectively

Characteristic Temperature

The maximum gain is plotted as a function of the injected carrier density in Fig. 2. At present, the intraband relaxation time of a GaN system has not yet been reported. Therefore, we assumed that the relaxation time τ_{in} is 0.1 ps, which is normally used in the case of estimation for GaAs-based laser [8]. In InGaN QWs Lasers, it is reported that τ_{in} is 0.05 ps [10]. Now, we assumed τ_{in} is independent on temperature, its affection for the temperature dependence of threshold current is negligible. We also assumed that the bandgap energy of GaN and the change of the optical cavity length have a negligible dependence on temperature, taking into consideration the small change

Table I Material parameters used in the estimation.

Materials	Bandgap energy	Effective mass, m_c	Effective mass, m_v	Reflective index
GaN	3.4 eV	$0.2m_0$	$0.8m_0$	2.8
$Al_{0.1}Ga_{0.9}N$	3.7 eV	-	-	-

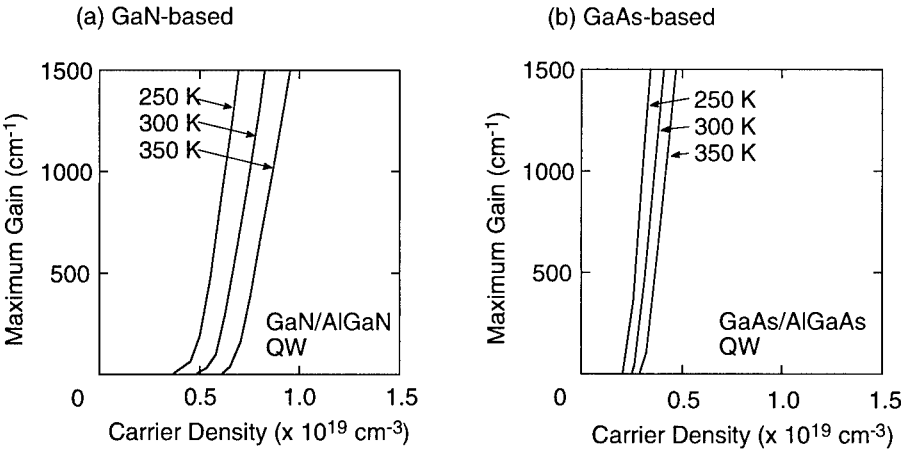


Fig. 2 Maximum gain dependence on injected carrier density. Active layers of (a) and (b) are GaN and GaAs, respectively.

of temperature near 300 K is considered. The blue/ultraviolet vertical-cavity surface-emitting lasers (VCSELs) are candidates for use in optical imaging systems such as high-density optical memories and photolithography because these lasers have advantages in the fabrication of two-dimensional array structures, as well as low power consumption [11]. The structure shown in Fig. 3 is considered for our estimation of the threshold current density. We did not consider a change of the optical cavity length to be a function of the temperature, which indicates that the threshold current density of GaN is higher than that of GaAs. However, the temperature sensitivity of a transparent carrier density on GaN QWs is almost the same as in the case of GaAs QWs. Although the required threshold current density is still high, the characteristic temperature T_0 of GaN-based VCSELs is expected to be ~ 300 K as shown in Fig. 4. It has been reported that the temperature sensitivities of stripe-type InGaN QW lasers are about 170 [12] and 320 K [13]. The ideal characteristic temperature of GaN QWs is comparable to that of GaAs QWs. The estimation shows that the GaN-based VCSEL has good operation reliability for application to systems.

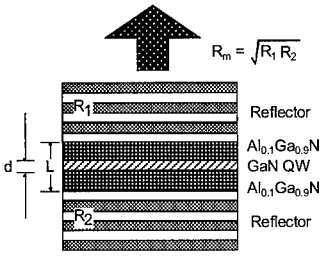


Fig. 3 VCSEL Structure used in this study.

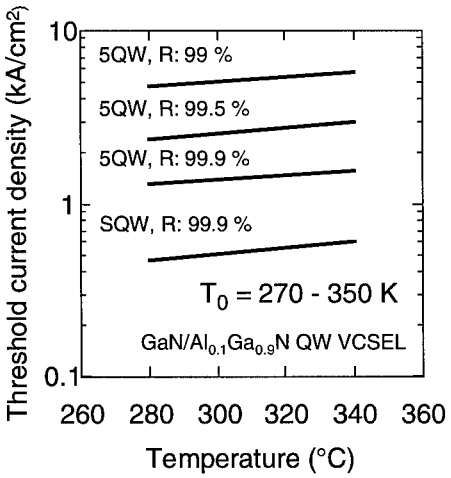


Fig. 4 Threshold current density dependence on temperature.

It has been reported that the ideal characteristic temperature of GaAs QWs is about 330 K [14], which is compatible with our estimation using the same method as that for GaN QWs. On the other hand, the experimental characteristic temperature of GaAs is lower than the estimated one. The estimated high T_0 in GaN LDs might be due to the suppress a carrier leakage over heterobarriers [14], or the automatic introduction of a low dimensional structure like as a localized state in an active layer [13].

Summary

In summary, we have estimated the threshold current density of GaN-based VCSELs using QW layers as an active layer and the characteristic temperature T_0 of GaN-based lasers. However, a high-injected carrier density is required for the laser operation to achieve the estimated sensitivity of about 300 K, which suggests the possibility of a high-temperature operation of GaN-based VCSELs.

Acknowledgment

The authors would like to thank Professor Emeritus Y. Suematsu of Tokyo Institute of Technology for his encouragement. This work is supported by High-Tech Research Center Project and GRANT-IN-Aid for Encouragement of Young Scientists (No. 09750012) from the Ministry of Education, Science, Sports and Culture. This work was carried out as a part of the JSPS Research for the Future Program (JSPS-RFTF96R16201).

References

1. H. P. Maruska and J. J. Tietjen: Appl. Phys. Lett. **15**, 327 (1969).
2. I. Akasaki, H. Amano, S. Sota, H. Sakai, T. Tanaka and M. Koike: Jpn. J. Appl. Phys. **34**, L1517 (1995).
3. S. Nakamura, M. Senoh, S. Nagahama, N. Iwasa, T. Yamada, T. Matsushita, H. Kiyoku and Y. Sugimoto: Jpn. J. Appl. Phys. **35**, L74 (1996).
4. M. W. Praire and R. M. Kolbas: Superlattice and Microstructures **7**, 269 (1990).
5. S. H. Wei and A. Zunger: Appl. Phys, Lett. **69**, 2719 (1996).
6. G. Martin, S, Strite, A. Botchkarev, A. Agarwal, A. Rockett, H. Morkoç, W. R. L. Lambrecht and B. Segall: Appl. Phys. Lett. **65**, 610 (1994).
7. H. Kroemer: Surf. Sci. **174**, 299 (1985).
8. M. Asada and Y. Suematsu: IEEE J. Quantum Electron. **21**, 434 (1985).
9. M. Asada, A. Kameyama and Y. Suematsu: IEEE J. Quantum Electron. **20**, 745 (1984).
10. S. Nakamura, M. Senoh, S. Nagahama, N. Iwasa, T. Yamada, T. Matsushita, Y. Sugimoto and H. Kiyoku: Appl. Phys. Lett. **69**, 1568 (1996).
11. T. Honda, A. Katsube, T. Sakaguchi, F. Koyama and K. Iga: Jpn. J. Appl. Phys. **34**, 3527 (1995).
12. S. Nakamura, M. Senoh, S. Nagahama, N. Iwasa, T. Yamada, T. Matsushita, Y. Sugimoto and H. Kiyoku: Jpn. J. Appl. Phys. **36**, L1059 (1997).
13. S. Nakamura, M. Senoh, S. Nagahama, N. Iwasa, T. Yamada, T. Matsushita, H. Kiyoku and Y. Sugimoto: 43rd Spring Meet. Jpn. Soc. Appl. Phys. & Related Soc., 29aZB-14, Asaka (1996).
14. N. K. Dutta: J. Appl. Phys. **53**, 7211 (1982).
15. T.-H. Chong and K. Kishino: IEEE J. Quantum Electron. **27**, 1501 (1991).

GAN NANOTUBES

Seung Mi Lee,[a] Young Hee Lee,[a,b] Yong Gyoo Hwang,[c] J. Elsner, [d] Dirk Porezag,[e] and Thomas Frauenheim[d]

[a]Department of Semiconductor Science and Technology, Jeonbuk National University, Jeonju 561-756, Korea
[b]Dept. of Physics and Semiconductor Physics Research Center, Jeonbuk National University, Jeonju 561-756, leeyh@sprc2.chonbuk.ac.kr*
[c]Dept. of Physics, Wonkwang University, Iksan 570-749, Korea
[d]Universitaet-GH Paderborn, Fachbereich Physik, Theoretische Physik, 33095 Paderborn, Germany
[e]Code 6690, Complex Systems Theory Branch, Naval Research Laboratory, Washington, D.C. 20375-5320, USA

Cite this article as: MRS Internet J. Nitride Semicond. Res. 4S1, G6.3 (1999)

ABSTRACT

We perform parametrized density-functional calculations to predict the stability and formation mechanism of GaN nanotubes. Strain energies of GaN nanotubes are comparable to those of carbon nanotubes, suggesting the possibility for the formation of GaN nanotubes. We note that an intermediate phase with [4,6,10] polygons exist at armchair tube edge, which may play as a nucleation seed of further tube growth.

INTRODUCTION

Carbon nanotubes (C-nTs) have been synthesized during the formation of fullerenes using arc discharge of graphite rods [1]. Recently single-wall carbon nanotubes have been produced with high yields by the laser vaporization of graphite powders mixed with small amount of transition metals [2-4]. Since then, researchers on carbon nanotubes have been activated. The physical properties of carbon nanotubes as denoted *(n,m)* are correlated with their diverse phases. Armchair *(n,n)* carbon nanotubes are metallic [5,6], while zigzag *(n,0)* C-nTs are semiconductors with a finite band gap except the case of $n - m = 3k$ (k: integer) which is a small band gap semiconductor [7]. Band gap can be controlled by varying the diameter, thus allowing band gap engineering [5, 8]. Strong electron field emission from C-nTs have been observed, suggesting the applicability to flat panel displays [9, 10]. Despite such efforts, applications of C-nTs to memory devices and quantum transport devices are still challenging.

With an advent of epitaxial growth techniques for GaN, efficient blue light-emitting diodes have been realized, promising its application to full color display [11]. Although $In_xGa_{1-x}N$ has been tried for band gap engineering by varying In composition, it is still difficult to grow and control high In composition due to the strain between InGaN and substrate [12]. Therefore, a new form of GaN structure is always desirable if possible.

In this report, we propose a new phase of GaN, a nanotube (nT), using parametrized density functional (DF) calculations. We will show that GaN nTs are as stable as carbon nTs and can be synthesized under some extreme conditions. Pure boron-nitride and boron-carbon-nitride nTs have been successfully produced by arc discharge [13, 14]. The existence of BN-nTs suggests the possibility of other nitride nT synthesis such as CN and GaN. The present calculations show that the strain energies, the energy costs to wrap up graphitic GaN sheets into nTs, are comparable with those of carbon nTs, ensuring again the possibility of GaN nT formation. Yet,

Mat. Res. Soc. Proc. Vol. 537 © 1999 Materials Research Society

the initial nucleation seeds for GaN nT formation will play a crucial role for growth. We find that an intermediate phase which is composed of [4,6,10] polygons may play as a nucleation seed during the growth.

THEORETICAL APPROACHES

We adopt in this work self-consistent charge density-functional-based tight-binding (SCC-DFTB) approach. The SCC-DFTB method uses a basis of numerically obtained *s*, *p*, and *d* atomic orbitals. Hamiltonian overlap matrix elements are evaluated by two-center approach. Charge transfer is taken into account through the incorporation of a self-consistency scheme for Mulliken charges based on the second-order expansion of the Kohn-Sham energy in terms of charge density fluctuations. The diagonal elements of the Hamiltonian matrix employed are then modified by the charge-dependent contributions in order to describe the change in the atomic potentials due to the charge transfer. The off-diagonal elements have additional charge-dependent terms due to the Coulomb potential of ions. They decay as 1/r and thus account for the Madelung energy of the system. Further details of the SCC-DFTB method have been published elsewhere [15].

RESULTS AND DISCUSSION

Various GaN crystal phases exist under different experimental growth conditions [12]. The Wurtzite phase is the thermodynamically stable structure at ambient conditions, whereas the zincblende (ZB) phase can be stabilized on various cubic substrates [16, 17]. We first calculate the total binding energies of ZB and graphitic phases of GaN using SCC-DFTB method in order to study the relative stabilities. We choose a cubic supercell of 216 atoms for ZB GaN and 200 atoms for the graphitic sheet. Periodic boundary conditions are applied along the *x*-, *y*-, and *z*-directions. For the graphitic phase, a large vacuum region between graphitic sheets is included. Figure 1 shows total binding-energy curves obtained by the SCC-DFTB calculations. The binding energy of the ZB GaN is -5.91 eV/atom with the nearest neighbor distance of 1.950 Å, or equivalently the cubic lattice constant of 4.503 Å. The calculated bulk modulus is 195 GPa, in good agreement with the reported local-density-approximation results [18]. A considerable amount of electron charge (0.56 e) is transferred from Ga atom to N atom, resulting in an ionic bonding nature. The binding energy of the graphitic GaN is -5.55 eV/atom with the nearest neighbor distance of 1.775 Å, smaller than that of the ZB GaN. This difference in the binding energy suggests the graphitic GaN to be energetically unfavorable over the ZB or the wurtzite GaN. Yet this small magnitude of the energy difference opens the possibility of forming graphitic sheets as a metastable phase.

We next calculate the strain energy per atom required in order to wrap up a graphitic sheet into a tube. Periodic boundary conditions are applied with vacuum regions (10 Å) between tubes. Strain energies decrease with increasing the tube diameter as expected (Fig. 2). We note that strain energies of GaN nanotubes are relatively insensitive to the detailed structures, in good contrast with the fact that armchair carbon nTs are more stable than zigzag carbon nTs [8]. The transferred charges are localized in p_z orbitals of N sites [19]. The circumferential N-N distances in GaN armchair and zigzag nTs are 2.66 and 3.07 Å, respectively, much larger than the C-C distances in C-nTs (1.42 and 1.23 Å). This gives relatively less rehybridization and less bond-bending, making the strain energies in GaN nTs insensitive to the detailed structures of tubes. Both C-nTs and GaN nTs follow classical elasticity theory stating that the strain energy is proportional to the inverse square of the tube diameter. The fact that the strain energies of GaN nTs are comparable to those of C-nTs ensures a possibility for the synthesis of GaN nTs.

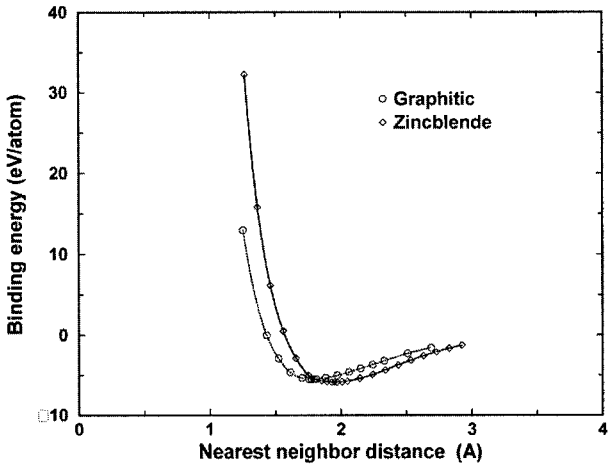


Figure 1. Total energy curves of cubic and graphitic GaNs as a function of nearest neighbor distance, calculated by SCC-DFTB method. The equilibrium distance is 1.95 Å for zincblende and 1.775 Å in graphitic sheet. The curves are fitted by the cubic-spline method.

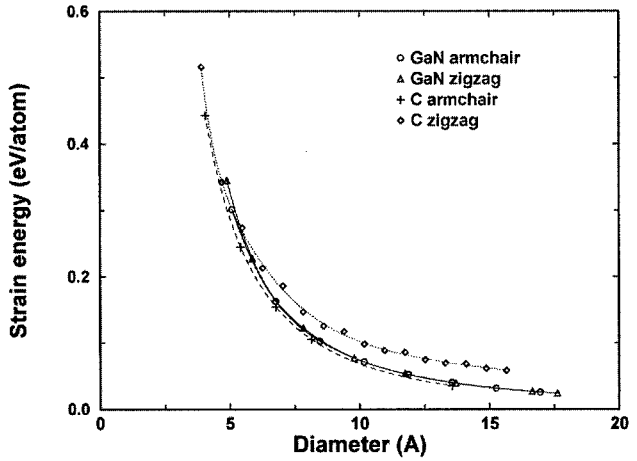


Figure 2. Strain energies as a function of diameter for armchair and zigzag GaN nanotubes. The strain energies of carbon nanotubes are also shown for comparison [8]. The curves are fitted by the least-square method.

The stability and long tube formation strongly depend on the edge structures. For armchair tubes, the Ga-N pairs are formed, as shown in Fig. 3(a). For the edge energy calculations we choose (5,5) nanotube with a vacuum region of 10 Å. Both open edges with three more layers from the edges are fully relaxed by the steepest decent relaxation scheme. The edge Ga-N pairs are stabilized by forming asymmetric dimers with a dimer bond length of 1.58 Å, shorter than the surface bond length of 1.78 Å, and an asymmetry of 0.23 Å. The N atoms where charges are accumulated, form up-atoms and occupied states. This buckling is similar to that of asymmetric dimerizations on Si(100) surfaces [20]. For zigzag tubes we choose (9,0) nanotube which has similar diameter to (5,5) nanotubes. Zigzag edge has either Ga-terminated or N-terminated edges. The Ga-terminated and the N-terminated edges on both sides of the edges are chosen in order to keep the stoicheometry in the calculations. The edges are then fully relaxed similarly to the armchair tubes. The Ga-terminated surface states are degenerate at Fermi level. Full relaxation of this edge results in symmetry-breaking and two Ga-N pairs are formed, as shown in Fig. 3(b). The N-terminated edges are stable with shorter bond lengths of 1.69 Å, compared with a surface bond of 1.78 Å (Fig. 3(c)). The edge energy of armchair and zigzag tube is 2.82 and 4.32 eV/Ga-N pair, respectively, suggesting that the armchair edge is more stable than the zigzag edge.

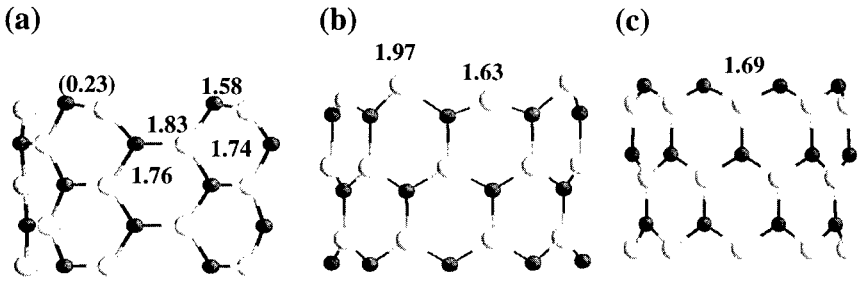


Figure 3. Atomic geometries of GaN nanotube edges for (a) armchair edge, (b) Ga-terminated zigzag edge and (c) N-terminated zigzag edges. Lighter and darker atoms represent Ga and N respectively. The values in parenthesis is the asymmetry. All units are in Å.

We find an intermediate phase of armchair edges which is formed during the molecular dynamics simulations at high temperature [19], as shown in Fig. 4. Instead of forming buckling at armchair edge, the edges form [4,6,10] polygons where the Ga-N bonds at edges are 1.69 and 1.88 Å at hexagon and square edges, respectively. Weak bonds are formed with bond lengths of 1.99 Å between the edge atoms and the second layer atoms. These weak bonds play an important role in the fragmentation process [19]. The energy difference from fully relaxed (5,5) nanotube is 0.37 eV per GaN edge pair. This intermediate phase is in fact similar to that of BN nanotube edges [21]. Depositing Ga-N pair to the square at edge will generate a complete hexagon, suggesting that [4,6,10] polygons may play as a nucleation seed during the growth of the GaN nanotubes.

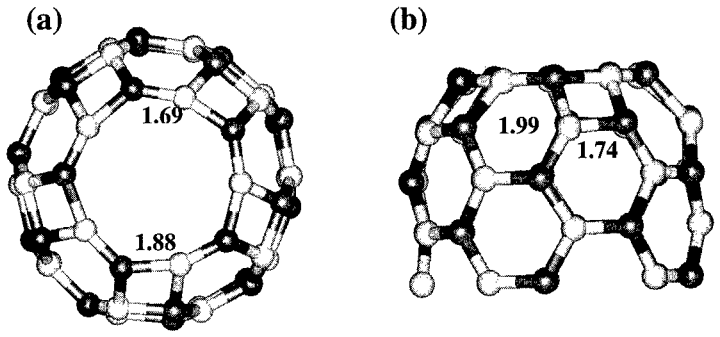


Figure 4. (a) Top and (b) side views of an intermediate phase of (5,5) GaN nanotube. Brighter and darker atoms represent Ga and N atoms, respectively. All units are in Å.

Stability of the edge can also be examined by the frustration energy, *i.e.*, the energy required to have a bond-switching at the edge. With a single bond-switching at armchair tube edge, one N-N and one Ga-Ga bonds are generated, as shown in Fig. 5. The N-N bond is stable with a bond length of 1.45 Å, whereas the Ga-Ga bond is repulsive. This is understandable due to the charge transfers from Ga atom to N atom, resulting in less screening for Ga ion-ion repulsive interactions. The energy increased by 1.58 eV. The frustration at Ga-terminated edge creates one N-N bond and two Ga-Ga bonds, requiring an extra energy cost of 3.22 eV. On the other hand, the frustration at N-terminated edge generates two N-N bonds and one Ga-Ga bond. This requires only 0.02 eV. This small energy cost originates from the energy gain by forming two N-N bonds. This suggests that frustration effect may dominate the front growing edges in case of N-terminated edge of zigzag nanotubes and tubes may not grow further. Catalytic growth similar to the single-wall carbon nanotubes [2, 14] may be necessary to have a long tube growth at zigzag GaN nanotubes.

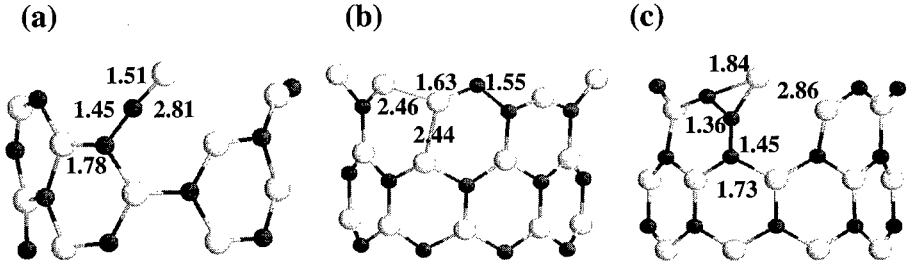


Figure 5. Frustrated edge structures of (a) (5,5) armchair edge, (b) Ga-terminated zigzag edge and (c) N-terminated zigzag edge. Brighter and darker atoms represent Ga and N atoms, respectively. All units are in Å.

CONCLUSION

In summary, we have performed density-functional based tight-binding total energy calculations to search for the stability and formation mechanism of GaN nTs. The calculations for the strain energy reveal that GaN nTs are as stable as C-nTs and can be formed at some extreme conditions. The armchair edge is stable and an intermediate phase with [4,6,10] polygons may play as a nucleation seed for a long tube growth.

ACKNOWLEDGMENTS

This work was supported by the KOSEF through the SPRC at Jeonbuk National University and by the Deutsche Forschungsgemeinschaft.

REFERENCES

* To whom correspondence should be addressed.

[1] S. Iijima and T. Ichihashi, Nature **363**, 603 (1993).

[2] A. Thess *et al.*, Science **273**, 483 (1996).

[3] T. Guo *et al.*, Chem. Phys. Lett. **243**, 49 (1995).

[4] M. Terrones *et al.*, Nature 388, **52** (1997).

[5] N. Hamada *et al.*, Phys. Rev. Lett. **68**, 1579 (1992).

[6] J. W. Mintmire *et al.*, Phys. Rev. Lett. **68**, 631 (1992).

[7] We follow the notation by M. S. Dresselhaus *et al.*, in *Science of Fullerenes and Carbon Nanotubes*, (Academic Press, 1996) Chapter 19.

[8] D.-H. Oh and Y. H. Lee, Phys. Rev. B **58**, 7407 (1998).

[9] W. A. de Herr *et al.*, Science **270**, 1179 (1995).

[10] A. G. Rinzler *et al.*, Science **269** (1995).

[11] S. Nakamura *et al.*, Appl. Phys. Lett. **64**, 1687 (1994).

[12] For a general review, see, for instance, *Semiconductors and Semimetals*, vol. **50**, Eds. J. I. Pankove and T. Moutakas, (Academic Press, New York, 1998).

[13] A. Loiseau *et al.*, Phys. Rev. Lett. **76**, 4737 (1996).

[14] K. Suenaga *et al.*, Science **278**, 653 (1997).

[15] M. Elstner *et al.*, Phys. Rev. B **58**, 7260 (1998).

[16] T. Lei *et al.*, J. Appl. Phys. **71**, 4933 (1992); R. C. Powell *et al.*, J. Appl. Phys. **73**, 189 (1993).

[17] S. Strite *et al.*, J. Vac. Sci. Technol. B **9**, 192 (1991).

[18] K. Miwa and A. Fukumoto, Phys. Rev. B **48**, 7897 (1993).

[19] S. M. Lee and Y. H. Lee, unpublished.

[20] S. M. Lee and Y. H. Lee, Surf. Sci. **347**, 329 (1996); D.-H. Oh and Y. H. Lee J. Kor. Phys. Soc. **28**, S167 (1996); J. E. Northrup, Phys. Rev. B **47**, 10032 (1993).

[21] X. Blase et al., Phys. Rev. Lett. **80**, 1667 (1998).

[22] Y. H. Lee, S. G. Kim, and D. Tomanek, Phys. Rev. Lett. **78**, 2393 (1997).

CHARACTERIZATION OF HOT-ELECTRON EFFECTS ON FLICKER NOISE IN III-V NITRIDE BASED HETEROJUNCTIONS

W.Y. Ho[a)], W.K. Fong[a)], Charles Surya[a,1)], K.Y. Tong[a)], L.W. Lu[b,2)], and W.K. Ge[b)]

[a)] Department of Electronic Engineering, The Hong Kong Polytechnic University, Hong Kong.
[b)] Department of Physics, The Hong Kong University of Science and Technology, Hong Kong.
[1)] e-mail address: ensurya@polyu.edu.hk
[2)] Permanent address: Laboratory of Semiconductor Materials Sciences, Institute of Semiconductors, Chinese Academy of Sciences, P.O. Box 912, Beijing 100083, P.R. China.

Cite this article as: MRS Internet J. Nitride Semicond. Res. 4S1, G6.4 (1999)

ABSTRACT

We report experiments on hot-electron stressing in commercial III-V nitride based heterojunction light-emitting diodes. Stressing currents ranging from 100 mA to 200 mA were used. Degradations in the device properties were investigated through detailed studies of the I-V characteristics, electroluminescence, Deep-Level Transient Fourier Spectroscopy and flicker noise. Our experimental data demonstrated significant distortions in the I-V characteristics. The room temperature electroluminescence of the devices exhibited 25% decrement in the peak emission intensity. Concentration of the deep-levels was examined by measuring the Deep-Level Transient Fourier Spectroscopy, which indicated an increase in the density of deep-traps from 2.7×10^{13} cm^{-3} to 4.21×10^{13} cm^{-3} at $E_1 = E_C - 1.1$eV. The result is consistent with our study of *1/f* noise, which exhibited up to three orders of magnitude increase in the voltage noise power spectra. Our experiments show large increase in both the interface traps and deep-levels resulted from hot-carrier stressing.

INTRODUCTION

The III-V nitrides family, AlN, GaN, InN, and their ternary alloys are all wide direct bandgap semiconductors. They have significant applications in optoelectronics, particularly in the blue to UV range [1-4]. Since there are no native substrates for epitaxial growth of nitride films, (0001) sapphire is the most widely used substrate because of its hexagonal structure and high temperature stability. The large stress due to lattice mismatch between nitride film and sapphire substrate leads to defective film growth, such as microtwins, (0001) stacking faults and deep-level defects. Moreover, interface traps in the heterostructure may significantly affect the performance of the devices. In this paper, we report degradations of the optical and electrical properties in III-V nitride heterojunctions due to high current stressing and its effects on deep-levels and low-frequency excess noise.

Deep-levels at the bulk regions of the devices are examined by Deep-Level Transient Fourier Spectroscopy (DLTFS). The technique was first described by Weiss and Kassing [5], which is a DLTS utilizing Fourier analysis of the capacitance transient collected as a function of temperature. It has significant advantages over both rate window and lock-in amplifier type systems in terms of sensitivity and energy resolution.

Flicker noise in semiconductor devices is highly sensitive to the presence of crystalline defects [6-10], however, it has not yet received the necessary attention in III-V nitride based

Mat. Res. Soc. Proc. Vol. 537 © 1999 Materials Research Society

devices. Experiments by the author on Random Telegraph Noise in GaAs/AlGaAs double barrier heterostructures showed that the low-frequency noise arise from the thermal activation of carriers to traps located at the heterointerface [8]. Flicker noise measurement can, therefore, be utilized as a sensitive tool for characterizing defect states in semiconductors [9,10]. The variation of the noise on high current stressing will, therefore, reflect the changes of the heterointerface traps resulting from hot-electron degradation. These traps are located at the barrier layers and usually at energy levels beyond the range that can be detected by conventional techniques such as DLTS. By detailed examination of both the DLTFS and *1/f* noise of the devices we provide a more complete picture on hot-electron degradation of the devices.

EXPERIMENT

Systematic study on hot-electron degradation in AlGaN/InGaN heterojunctions was conducted on commercial blue Light Emitting Diodes (LEDs) manufactured by Nichia Chemical Industries Ltd. by means of high current stressing with a dc current of 200 mA for 40 minutes. Detailed measurement of I-V characteristics over a wide temperature range, room temperature electroluminescence (EL), DLTFS and flicker noise were carried out before and after the current stress to examine the degradations of the optoelectronic properties of the LEDs.

DLTFS measurements were conducted from 77 K to 500 K using Bio-Rad DL8000, a high sensitivity, $10^{-7}(N_D - N_A) < N_{DL} < 10^{-5}(N_D - N_A)$, system equipped with a 1 MHz Boonton bridge. To obtain the DLTFS, the devices were periodically pulsed to 1 V for trap filling followed by the application of a -5.0 V reverse bias, V_R, to the device. A transient recorder was used to sample data points from the capacitance transient, $C(t)$, resulting from discharging the deep-levels. Discrete Fourier coefficients of $C(t)$ were computed, providing the basis for direct evaluation of the time constant and the amplitude for each transient. Analysis by Weiss and Kassing [5] showed that the time constant τ_{DL} is related to the Fourier coefficient given by $\tau_{DL} = T_w b_n / 2\pi n a_n$, where a_n and b_n are the n^{th} order cosine and sine coefficients of the capacitance transience, $C(t)$, and T_w is the period.

The low-frequency noise of the devices, which were biased with a passive current source at 0.7 mA, was characterized from room temperature down to about 120 K. Detailed experimental set-up was described in previous publications [6,8]. The current noise power spectral density is shown to be

$$S_I(f) = 4(\Delta I_o)^2 \iiint N_T(E) \frac{\tau}{1 + 4\pi^2 f^2 \tau^2} dx dy dz dE, \qquad (1)$$

in which $N_T(E)$ is the interface trap density, ΔI_0 is the current fluctuation due to the capture of one single carrier and τ is the fluctuation time constant. Low-frequency noise in GaAs/A1GaAs based semiconductor heterostructures was shown to originate from trapping and detrapping of carriers by localized states. The capture of charged carriers may arise either from a tunneling or thermally activated process. For flicker noise originating from the thermal activation of carriers to localized states in the energy barrier, the fluctuation time constant, τ, is a thermally activated parameter given by $\tau = \tau_0 \exp(E/k_B T)$, where τ_0 is typically taken to be the inverse phonon frequency of the order 10^{-14} second, and E is the activation energy. This stipulates a strong temperature dependence for τ. The Lorentzian, $\tau/(1 + \omega^2\tau^2)$, in Eq. 1 is a sharply peaked function of the activation energy at $E_p = -k_B T \ln(\tau_0 \omega)$. Thus, the properties of flicker noise are highly sensitive to the concentration and energy distribution of the traps at around E_p.

RESULTS

Typical I-V curve for the pre-stressed device is shown in curve A of Fig. 1. The data shows that the I-V characteristics of the device are well behaved with very low leakage current. However, there was a significant increase in the leakage current of the same device as a result of hot-electron stressing, as shown in curve B of Fig. 1. Previous study of Random Telegraph Noise in GaAs/A1GaAs based heterojunctions by the author clearly showed that localized states in the tunneling barrier are responsible for both the *1/f* noise and trap assisted tunneling. Therefore such large increase in the leakage current indicates a corresponding large increase in the trap concentration in the barrier region of the heterojunction.

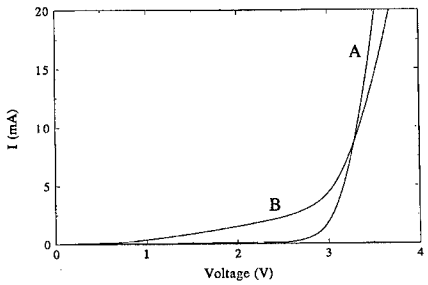


Fig. 1: Typical room temperature I-V characteristics of the LED before hot-electron stressing (curve A) and after 40 minutes of hot-electron stressing at 100 mA (curve B).

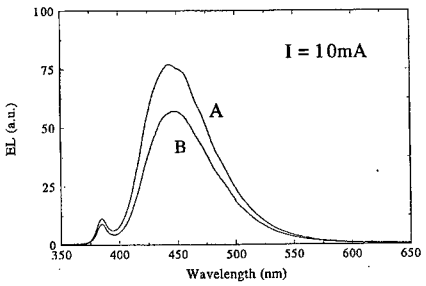


Fig. 2: Typical room temperature electroluminescence of the device before hot-electron stressing (curve A) and after 40 minutes of hot-electron stressing at 100 mA (curve B).

Typical room temperature EL characteristics are shown in curve A of Fig. 2, which indicates a dominant peak at about 450 nm and a much smaller peak at about 380 nm. After hot-electron stressing we observe significant deviations of the EL from its pre-stressed values, which demonstrated approximately 25% decrease in intensity at its peak emission wavelength at approximately 450 nm. The lowering in EL suggests that hot-electron stressing led to substantial increase in non-radiative recombination centers in the heterostructures. It is noteworthy that we do not observe any new peaks in the EL due to the stressing experiment.

The DLTFS results, as shown in Fig. 3, show a significant increase in the magnitude after current stressing which is attributed to the increase in the concentration of deep levels. The results on the optoelectronic properties of the devices are compared to the experimental data from DLTFS measurements. The first sine coefficient, b_1, of $C(t)$ is shown to be comparable to the conventional DLTS signal with a time constant of about 64 ms [5]. Using a reverse bias of V_R = –5.0 V, the experimental data exhibited a deep-level trap at $E_1 = E_C - 1.1$ eV with a concentration of 2.70×10^{13} cm^{-3} and a capture cross section of 5×10^{-14} cm^2. We also observed a shift towards lower temperature for the DLTFS signal peak using a, bias voltage V_R = –6 V. This is indicative of field-enhanced electron emission showing that the deep-levels were electron states. Hot-electron stressing led to increase in the concentration of deep-levels. The DLTFS signal is shown in curve B of Fig. 3. From the data we found that $E_1 = E_C - 1.1$ eV with a concentration of 4.21×10^{13} cm^{-3} and a capture cross section of 5×10^{-14} cm^2. It is interesting to note that the DLTFS signal in Fig. 3 shows that a second deep-trap may exist at a shallower energy level. However, due to limited temperature range that can be accomplished by our

system, we did not observe its peak in the DLTFS signal and therefore unable to evaluate this level accurately.

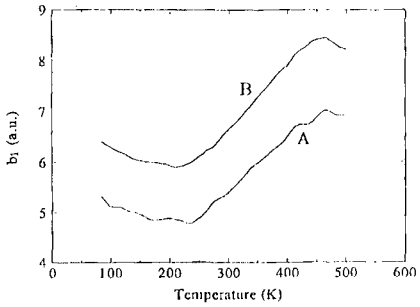


Fig. 3: DLTFS signal for the pre-stressed device (curve A) and the stressed device (curve B).

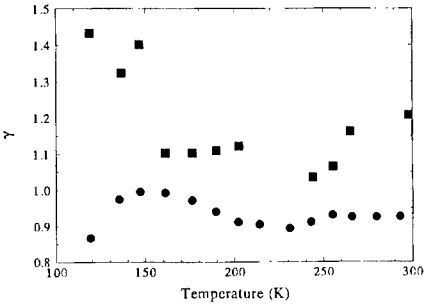


Fig. 4: The frequency exponent, γ, of $S_V(f)$ versus device temperature before current stressing (solid circles) and after stressing (solid squares).

The noise power spectral densities were found to be proportional to $1/f^{\gamma}$ where γ varied between 0.85 to 1 as the device temperature was lowered from room temperature to 120 K. The results are indicated by solid circles in Fig. 4. After hot-electron stressing, we observe a dramatic change in the frequency exponent, γ. This is sufficient proof that the observed *1/f* noise originated from a thermally activated process. There is no alternative model that can adequately explain the systematic temperature dependence of γ.

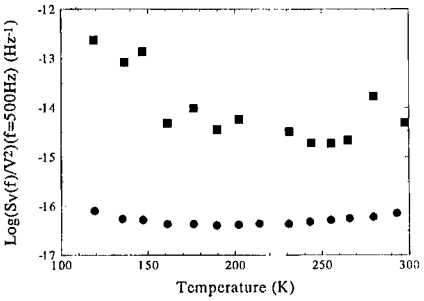


Fig. 5: The normalized voltage noise power spectra, $S_V(f)/V^2$, at f = 500 Hz versus device temperature before stressing (solid circles) and after stressing (solid squares).

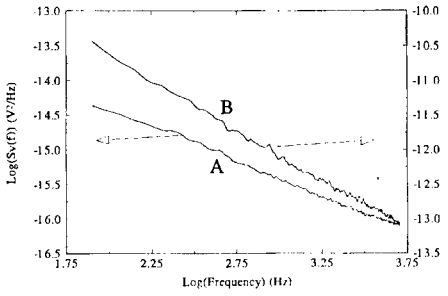


Fig. 6: Typical voltage noise power spectra, Sv(f), for the pre-stressed device (curve A) and the stressed device (curve B) measured with a biasing current of 0.7 mA.

The voltage noise power spectra were found to be sensitive to temperature change as well. Typical results for the normalized noise power spectra, $S_V(f)/V^2$, at f =500 Hz, are represented by solid circles in Fig. 5. It is found that $S_V(f)/V^2$ decreased from 7×10^{-17} Hz^{-1} to about 4×10^{-17} Hz^{-1} at 200 K. Further lowering in the device temperature led to an increase in $S_V(f)/V^2$ to about 8×10^{-17} Hz^{-1} at 120 K. An increase by as much as 3 orders of magnitude in the noise power spectra is observed over the temperature range in which the experiment was conducted.

Typical voltage noise power spectra before and after the hot-electron stressing experiment are shown in curves A and B of Fig. 6 respectively. The voltage noise power spectra, were measured at T = 147 K with the biasing current set at 0.7 mA. Such drastic increase in the noise magnitude subsequent to hot-electron injection stipulates that the noise capture and emission of carriers by traps at the heterojunctions. Unfortunately, without detailed information of the device calculation of the exact values of the trap density would be impossible.

CONCLUSION

In conclusion, we have conducted systematic characterizations of hot-electron stressing on the properties of III-V nitride LEDs. The stressing experiment is seen to cause significant degradations in both the I-V and electroluminescence of the devices. Our experimental data demonstrate that high dc current stressing leads to significant increase in the concentration of deep states at $E_I = E_C - 1.1$ eV. Within the range of our experimental conditions we do not observe the generation of new deep states at different energy levels. Flicker noise from the devices was studied in detail from room temperature to 120 K. The results showed that the noise originated from the thermal activation of carriers to localized states in the junction, leading to the modulation of the device conductance. Hot-electron stressing result in significant generation of heterointerface traps in the heterostructures leading to three orders of magnitude increase in the voltage noise power spectra. Both the deep-levels and the hetcrointerface traps are believed to play significant roles in the degradation of the optoelectronic properties of the devices.

ACKNOWLEDGEMENT

The work is supported by a Hong Kong Polytechnic University research grant and an RGC grant number POLYU107/96E.

REFERENCES

1. S.N. Mohammad and H. Morkoc, Progress in Quantum Electronics **20** (5-6), 361-525 (1996).
2. J.S. Foresi, and T.D. Moustakas, Appl. Phys. Lett. **62** (22), 2859-2861 (1993).
3. M. Koike, S. Ye,ma,saki, S. Naga,i, N. Koide, a,nd S. Asami, Appl. Phys. Lett. **68** (10), 1403 – 1405 (1996).
4. Shuji Nakamura, Takashi Mukai, and Masayuki Senoh, Appl. Phys. Lett. **64** (13), 1687-1689 (1994).
5. S. Weiss, R. Kassing, Solid-State Electron. **31**, 1733 (1989).
6. C. Surya a,nd T. Y. Hsiang, Phys. Rev. B **35**, 6343–6347 (1987).
7. F.N. Hooge, IEEE Trans. Electron Devices **41** (11), 1926–1935 (1994).
8. C. Surya, S. H. Ng, E. R. Brown, and P. A. Maki, IEEE Trans. Electron Devices **41** (11), 2016–2022 (1994).
9. Z. Celik-Butler and T. Y. Hsiang, IEEE Trans. Electron Devices **35**, 1651–1655 (1988).
10. L.K.J. Vandamme, IEEE Trans. Electron Devices **41** (11), 2176-2187 (1994).

CHARACTERIZATION OF FLICKER NOISE IN GaN BASED MODFETs AT LOW DRAIN BIAS

W.Y. Ho[1], W.K. Fong[1], C. Surya[1,a], K.Y. Tong[1], W. Kim[2], A. Botcharev[2], and H. Morkoc[2,b]

[1] Department of Electronic Engineering, The Hong Kong Polytechnic University, Hong Kong.
[2] Department of Electrical and Computer Engineering and Coordinated Science Laboratory, University of Illinois, U.S.A.
[a] email: ensurya@polyu.edu.hk
[b] Present address: Virginia Commonwealth University, Richmond, VA 23284.

Cite this article as: MRS Internet J. Nitride Semicond. Res. 4S1, G6.5(1999)

ABSTRACT

We report systematic characterizations of flicker noise in GaN based MODFETs. Flicker noise was measured across the channel of the devices from room temperature to 130 K. The voltage noise power spectra, $S_V(f)$ were found to be proportional to $1/f^{\gamma}$, where γ depends on the device temperature as well as the gate bias. Study of $S_V(f)$ as a function of the biasing condition was conducted in detail and was found to vary as $V_D^2/(V_G-V_T)^{\beta}$ where β changes with temperature from about 2.1 at room temperature to about 0.9 at 130K. Analyses of the data showed that the noise originated from thermal activation of carriers to localized states in the channel area. The data suggested that the trapping and detrapping of carriers did not lead to fluctuations in the carrier concentration as postulated in the McWhorter's model. However, more work is needed to determine if surface mobility fluctuations played key role in the $1/f$ noise.

INTRODUCTION

In the past several years, an intensive effort in the development of III-V nitride based devices has been expended [1]. The high electron saturation velocity, large breakdown field, high thermal conductivity, and superb mechanical stability of GaN are among its properties that make it an excellent candidate for high-temperature and high-power applications at high frequencies [2]. The accomplishments made over the past couple years clearly demonstrate the rapid pace in which III-V nitride based FETs are being developed. However, the investigation of noise properties, particularly low-frequency noise has not yet gotten the necessary attention.

Flicker noise is an important figure-of-merit for semiconductor devices. It represents the lower limit of the signal that can be processed by the device. Previous studies of the phenomenon had shown that flicker noise in electron devices often arises from material defects which manifest themselves as the trapping and detrapping of carriers by localized states and grain boundary motion [3-5]. The objective of our work is to identify the underlying physical noise processes to pave the way for improving the noise properties of the device. To accomplish this, we studied the voltage noise power spectral density, $S_V(f)$, over a wide range of temperatures and biases to investigate the role of localized states in the fluctuation process.

EXPERIMENT

Gallium nitride based MODFETs were fabricated with reactive MBE on (0001) sapphire substrates. An 800Å AlN buffer layer was first grown at 800°C followed by the deposition of a

Mat. Res. Soc. Proc. Vol. 537 © 1999 Materials Research Society

1.2μm thick undoped GaN layer. The two-dimensional electron gas was formed at the heterointerface between the i-GaN layer and a 30Å i-AlGaN spacer layer which serves to separate the 2-dimensional electron gas from the ionized dopants to increase the mobility of the carriers. The electron donor layer consists of a 120Å-thick Si doped AlGaN layer of concentration 5×10^{18} cm^{-3}. Ti/Al/Ti/Au (200Å/1700Å/450Å/550Å) multilayers were deposited to form ohmic contacts to the drain and source regions. The gate length and gate width are 2μm and 40μm, respectively.

The low-frequency noise of the device was characterized from room temperature down to 130 K, with the gate biased at a fixed voltage and the conduction channel was current biased with a passive current source. The detailed experimental set-up was described in previous publication [6].

RESULTS AND DISCUSSIONS

The experimental values for $S_V(f)$ at 500Hz at $V_G = 0.8V$ and $V_D = 0.2V$ were found to be relatively insensitive to temperature change and were about 4×10^{-12} V^2Hz^{-1} over the entire temperature range as shown in Fig. 1. However, $S_V(f)$ exhibited strong dependencies on both the gate and drain voltages.

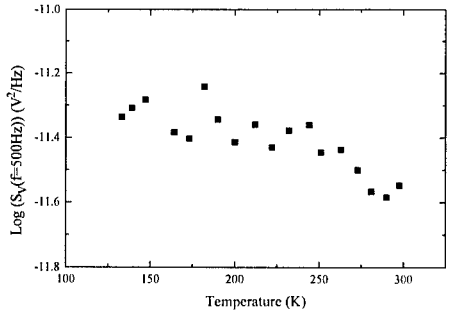


Fig. 1: The voltage noise power spectral density, $S_V(f=500Hz)$, over the conduction channel as a function of device temperature.

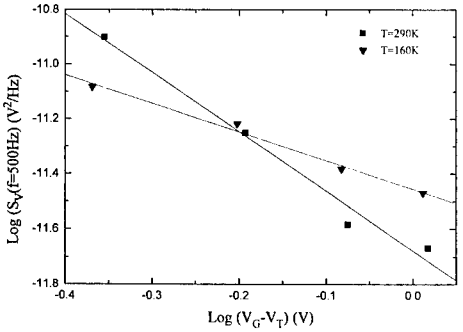


Fig. 2: Log[$S_V(f=500Hz)$] is plotted versus Log($V_G - V_T$) at T = 290 K and T = 160K.

The experimental results showed that $S_V(f) \propto V_D^2/(V_G - V_T)^\beta$ where β varied between 2.1 at room temperature to about 0.9 at T = 130K. Typical results of Log $S_V(f)$ versus Log $(V_G - V_T)$ at T = 290K and 160K are shown in Fig. 2, which clearly indicates changes in β. Typical plot of Log $S_V(f)$ versus Log V_D at 263K is shown in Fig. 3 for f=500Hz. The slope of the best fit is 2.05, which demonstrates a quadratic relationship with V_D.

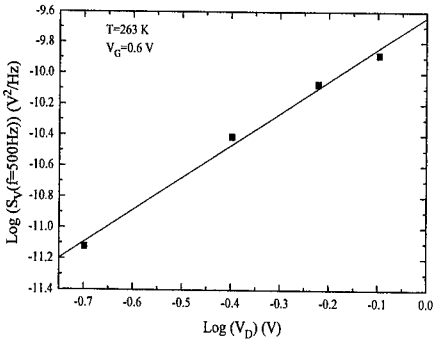


Fig. 3: Log[$S_V(f$=500Hz)] is plotted versus Log(V_D) at V_G = 0.6 V and T = 263K.

Flicker noise in semiconductor devices has been a subject of interest for many years [6,7]. Of the various models presented in the past, the thermal activation model proposed by Dutta and Horn [7] stands out in its success in explaining the temperature dependence of the noise. Application of the model in field-effect transistors was investigated by Surya and Hsiang [6] who suggested that $1/f$ noise arises from thermal activation of carriers to traps at different energy levels. In this case the voltage noise power spectral density is

$$S_V(f) = C\int dE \frac{N_T(E)\tau}{1+4\pi^2 f^2 \tau^2}, \qquad (1)$$

where C is a proportionality constant and E is the activation energy. It is shown that the Lorentzian peaks sharply at $E_p = -k_B T \ln(2\pi\tau_0)$. Consequently $1/f$ noise is highly sensitive to trap distribution at E_p. It can be shown that $\gamma = 1$ if $N_T(E)|_{E\approx Ep}$ is independent of E; $\gamma > 1$ if $N_T(E)|_{E\approx Ep}$ increases with E; and $\gamma < 1$ if $N_T(E)|_{E\approx Ep}$ decreases with E. Since E_p varies linearly with temperature, traps at energy level will be responsible for the observed noise as the device temperature is varied. Then γ will vary according to the relationship as discussed above if $\frac{\partial N_T(E)}{\partial E}$ changes with energy.

The observation of a systematic variation of γ as a function of T in our experimental data is indicative of a thermally activated process that underlies the noise. The experimental values of γ versus T for V_C = 0.8 V and V_D = 0.2 V are indicated in Fig. 4 in which γ decreased from 1.03 to about 0.85 when T varied from room temperature to 250K. Further decrease in the device temperature led to a gradual increase of γ to 0.98 at 220K. Below 220K, γ slowly decreased to about 0.9 as the device temperature was lowered to 130K.

Both traps at the GaAlN/GaN interface or along the line defects within the two-dimensional electron gas are viable candidates for the observed $1/f$ noise. Given the high

concentration of line defects in GaN, the latter mechanism is highly probable for our devices. To further investigate the physical origin of the noise we study the variations of γ as a function of V_G. It is observed that γ exhibited a systematic dependence in the applied gate bias. Typical results are shown in Fig. 5, for V_D = 0.2V at T = 250K where γ decreased initially from 0.9 to about 0.85 as V_G varied from 0.4V to 0.6V. Subsequent increase in V_G led to increase in γ to 0.96 at V_G = 1V. This can be explained by the change in band bending in the AlGaN layer with the application of a voltage bias resulting in a change in the trap energy levels with respect to the Fermi level in the device. Depending on the actual distribution of $N_T(E)$ it may lead to a change in γ. Base on these results it appears that the noise arises from trapping and detrapping at GaN/AlGaN interface.

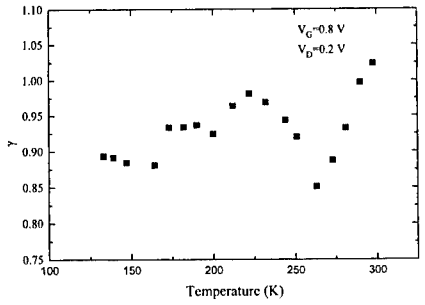


Fig. 4: The temperature dependence of the frequency exponent, γ.

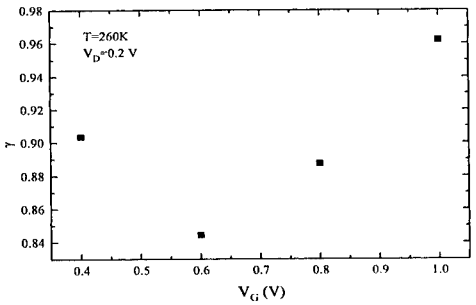


Fig. 5: Gate bias dependence of the frequency exponent, γ, at T = 260K and V_D = 0.2V.

McWhorter postulated that the capture of an electron by a trap causes the local modulation of the Fermi Level leading to fluctuations in the local carrier concentration. However, it was shown that the process may also lead to fluctuations in the carrier mobility due to Coulombic scattering. Studies on low-frequency noise in field-effect transistors showed that $S_V(f) \propto (V_D/(V_G - V_T))^2$ for noise dominated by number fluctuations. On the other hand, for $1/f^{\gamma}$ noise dominated by surface mobility fluctuations, the dependence of $S_V(f)$ on V_G arises from the screening effect by the two-dimensional electron gas which generally demonstrate a different V_G dependence from number fluctuations and would exhibit stronger dependencies on temperature due to the variations of the screening parameter with T. The experimental results in Fig. 2 clearly deviated from the quadratic relationship as stipulated by numbers fluctuation model. However, a more definitive study that involves the characterization of random telegraph noise, which allows exact measurements of the fluctuations in the channel resistance resulting from

single-electron events, is needed to conclusively prove the underlying fluctuating quantity of the noise. Such a phenomenon is typically seen in sub-micrometer size devices.

CONCLUSION

We have conducted systematic characterizations of $1/f^{\gamma}$ noise in GaN MODFETs. Detailed analyses of the magnitudes and γ of the voltage noise power spectra showed that the noise originated from the thermal activation of carriers to localized states either at the AlGaN/GaN heterointerface or line defects within the two-dimensional electron gas. Our experimental data suggest that trapping and detrapping at the heterointerface dominated the observed flicker noise. In addition, it was found that $S_V(f) \propto V_D^2/(V_G - V_T)^{\beta}$ where β varied from about 2.1 at room temperature to about 0.9 at 130K. This suggests that the capture and emission of carriers by interface traps did not result in number fluctuations. A more detailed study of random telegraph noise is needed to confirm if surface mobility fluctuations due to Coulombic scattering played a major part in the observed noise.

Acknowledgement

The research conducted at the Hong Kong Polytechnic University is supported by an RGC grant number POLYU 107/96E. The research at the University of Illinois was funded by grants from AFOSR and ONR under the program management of Drs. G.L. Witt, C.E.C. Wood, Y.S. Park, and M. Yoder.

References

[1] S.N. Mohammad and H. Morkoc, Progress in Quantum Electronics **20** (5-6), 361-525 (1996).

[2] H. Morkoc, S. Strite, G.B. Gao, M.E. Lin, B. Sverdlov, and M. Burns, J. Appl. Phys. **76** (3), 1363-1398 (1994).

[3] C. Surya, S.H. Ng, E.R. Brown, and P.A. Maki, IEEE Trans. Electron Devices **41** (11), 2016-2022 (1994).

[4] C. Surya, W. Wang, W.K. Fong, C.H. Chan, and P.T. Lai, Solid-State Electron. **39** (11), 1577-1580 (1996).

[5] W.Y. Ho and C. Surya, Solid-State Electron. **41** (9), 1247-1249 (1997).

[6] C.H. Cheng and C. Surya, Solid-State Electron. **36** (3), 475-479 (1993).

[7] P. Dutta and P.M. Horn, Rev. Modern Phys. **53** (3), 497-516 (1981).

MONTE CARLO SIMULATION OF HALL EFFECT IN n-TYPE GaN

J.D. Albrecht[†], P.P. Ruden[†], E. Bellotti[‡], and K.F. Brennan[‡]

[†]ECE Department, University of Minnesota, Minneapolis, MN 55455
[‡]School of ECE, Georgia Institute of Technology, Atlanta, GA 30332

Cite this article as: MRS Internet J. Nitride Semicond. Res. 4S1, G6.6 (1999)

ABSTRACT

Results of Monte Carlo simulations of electron transport for wurtzite phase GaN in crossed, weak electric and magnetic fields are presented. It is found that the Hall factor, $r_H = \mu_{Hall}/\mu_{drift}$, decreases monotonically as the temperature increases from 77K to 400K. The low temperature value of the Hall factor increases significantly with increasing doping concentration. The Monte Carlo simulations take into account the electron-lattice interaction through polar optical phonon scattering, deformation potential acoustic phonon scattering (treated as an inelastic process), and piezoelectric acoustic phonon scattering. Impurity scattering due to ionized and neutral donors is also included, with the latter found to be important at low temperature due to the relatively large donor binding energy which implies considerable carrier freeze-out already at liquid nitrogen temperature. The temperature dependences of the electron concentration, drift mobility, and Hall factor are calculated for donor concentrations equal to 5×10^{16} cm^{-3}, 10^{17} cm^{-3}, and 5×10^{17} cm^{-3}. The Monte Carlo simulations are compared to classical analytical results obtained using the relaxation-time approximation, which is found to be adequate at low temperatures and sufficiently low carrier concentrations so that inelastic scattering effects due to optical phonons and degeneracy effects are negligible. The influence of dislocations on the Hall factor is discussed briefly.

INTRODUCTION

Electronic characterization of epitaxially grown GaN relies on temperature dependent Hall measurements to accurately determine carrier concentration and mobility. Analysis of measured Hall data has already led to the examination of several effects unique to GaN Hall measurements. Specifically, the variation of the electron Hall mobility in the presence of a highly conducting layer at the interface between the substrate and the epitaxial GaN crystal has been resolved[1], and the dependence of the Hall measurement on the orientation of the current with respect to threading dislocations has recently been explained[2]. Also, the low temperature behavior of measured electron mobilities in heavily doped GaN has been found to be consistent with transport associated with band-tailing and impurity-band states[3]. Exceptions aside, interpretations of GaN Hall data often make the assumption that $\mu_{Hall} = \mu_{drift}$, independent of temperature[4,5]. One consequence of assuming a unity Hall factor is that total donor concentrations and donor activation energies extracted from electrical measurements are difficult to analyze with confidence.

Mat. Res. Soc. Symp. Proc. Vol. 537 © 1999 Materials Research Society

We present new calculations of the Hall factor, r_H, for n-type wurtzite GaN that predict a monotonic decrease with increasing temperature for fixed donor concentrations. The presentation of calculated electron concentration, Hall factor, and drift mobility is followed by a comparison to relaxation-time approximation results and by a discussion of the Hall factor for dislocation dominated scattering.

HALL SIMULATION

Due to thermal fluctuations in the calculated drift velocity components, calculations of electron drift velocity in crossed electric and magnetic fields using the Monte Carlo method were, until recently, limited to high electric and magnetic field conditions[6]. Advances in computation speed and in the transport simulation algorithm have enabled the application of the Monte Carlo method to weak field conditions. Hall simulations have been reported for a variety of semiconductor materials: Si and Ge[7], InSb and other highly polar semiconductors[8], and GaAs[9]. For GaN, electron drift velocities for both large and small static electric fields have been calculated in this manner and low field drift mobility expressions suitable for device modeling have been developed for temperatures above 300K[10].

The present Hall factor calculations use the same approximate GaN analytic band structure which has been published previously[10], although for the present study of low field transport only the parabolic part of the central conduction band valley is relevant. The electric field strengths are chosen small enough to ensure that ohmic conduction is modeled, and the magnetic field is held in the low field regime such that $\mu_{drift}|B| = 1.5 \times 10^{-2}$. For instance, at liquid nitrogen temperature and $N_D = 10^{17}$ cm^{-3}, the electric field in the linear regime is taken to be less than 0.5 kV/cm which results in $\mu = 2490$ cm^2 V^{-1}sec^{-1} and, consequently, $|B| = 0.06$ Tesla. The free flight motion of the electrons in crossed electric and magnetic fields is carried out in the usual way for Monte Carlo simulations[6]. The scattering parameters are the same as those in reference 10 and references therein. We favor acoustic deformation potential scattering with energy dissipation over the elastic approximation. This treatment of the acoustic phonon scattering prevents the simulated electron distribution from artificially skewing towards higher energies as would otherwise occur when polar optical phonon scattering is negligible. In addition, neutral impurity scattering is included in our calculations. The effects of neutral impurities become important at low temperatures in material that is not dominated by dislocation scattering.

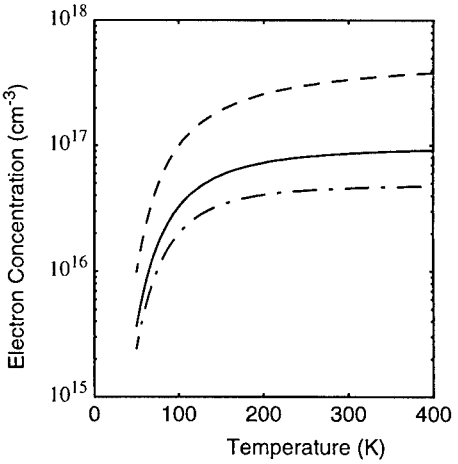


Figure 1: Electron concentration vs. temperature for GaN with donor doping densities of 5×10^{16} cm^{-3} (dash-dotted), 10^{17} cm^{-3} (solid), and 5×10^{17} cm^{-3} (dashed).

In Figure 1, the electron concentration is plotted as a function of temperature using

the screened shallow donor binding energy results of Wang, *et al* for different background electron concentrations[11]. The temperature effects on the carrier screening are taken into account for this calculation. The figure clearly shows that for uncompensated GaN at liquid nitrogen temperature there is a large fraction of neutral donor impurities present.

Scattering due to neutral donors is adapted for the Monte Carlo method from the relaxation-time result of Meyer and Bartoli[12]. An analytic expression for the total scattering rate which is valid over the entire energy range of electron energies can be derived from ref. 12. The neutral impurity scattering rate in terms of the total collision cross section, σ_c, is written as:

$$\left.\frac{1}{\tau_c}\right|_{\text{neut. imp.}} = N^x v \sigma_c \tag{1}$$

where

$$\sigma_c = \pi a_o^2 \left(\frac{11.2}{w}\right) \frac{(1+e^{-50w})(1+80.6w+23.7w^2)}{(1+41.3w+133w^2)} \left\{ \left(\frac{w}{6}\right) \frac{(12+18w+7w^2)}{(1+w)^3} \right\}, \tag{2}$$

N^x is the concentration of neutral donor scattering centers, v is the electron velocity, E_D is the donor binding energy, $w = (a_o k)^2 = E/E_D$, and $a_o = e^2/2\kappa_0 E_D$ which defines an effective Bohr radius. Since scattering of low energy electrons by neutral impurities is velocity randomizing, the collision cross section differs from the momentum-transfer cross section of Meyer and Bartoli[12] only for incident particles with energies much greater than the donor binding energy. The Born approximation is valid for fast electrons where the term in { } of equation (2) is dominant. The collisions are treated as elastic and exchange effects are neglected.

In the Monte Carlo simulation, the final scattering states are determined using the angular distribution derived from the Born scattering amplitude given by[13]

$$f_{Born}(\theta) = -\frac{2}{a_o q^2}\left[\left(1+\frac{a_o^2 q^2}{4}\right)^{-2} - 1\right] \qquad q = 2k\sin\frac{\theta}{2} \tag{3}$$

where θ is the angle between initial and final k-vectors. It is easily shown that the normalized probability distribution of scattering angles is

$$P(\cos\theta) = \frac{\int_{-1}^{\cos\theta} |f_{Born}(\theta)|^2 d\cos\theta}{\int_{-1}^{+1} |f_{Born}(\theta)|^2 d\cos\theta} = \frac{[4+w(1-\cos\theta)]^2}{[2+w(1-\cos\theta)]^4} \frac{6[1+w]^3}{[12+18w+7w^2]}. \tag{4}$$

A flat angular distribution results in the low energy ($w \to 0$) limit. This is consistent with the velocity randomizing behavior for low electron energy implicit in the phenomenological collision cross section of equation (2).

RESULTS AND DISCUSSION

Figures 1 and 2 display the calculated free carrier concentrations and electron drift mobilities for fixed doping concentrations. For uncompensated GaN, Figure 1 indicates that the ionized impurity concentration at 77K is a small fraction of that at 300K. In Figure 2, the temperature dependent drift mobility is plotted for ionized impurity concentrations corresponding to Figure 1. The dashed curves at low temperature indicate the analytical relaxation-time approximation[14] to the drift mobility including all of the scattering mechanisms except polar optical phonon scattering. The decrease in mobility at low temperature is caused in part by neutral impurity scattering. For the lowest doping concentration considered in this calculation, $N_D = 5 \times 10^{16}$ cm^{-3}, we find that the neutral impurity scattering plays a large role at low temperature because of the significant carrier freeze-out evident from Figure 1. At 77K, the relaxation-time approximation result for the mobility is 16% higher than that shown in Figure 2 without the inclusion of neutral impurity scattering effects. The low temperature mobility obtained by Monte Carlo simulation which includes energy dissipation in the acoustic deformation potential scattering is slightly larger than that obtain from the analytical relaxation-time model which uses an elastic approximation.

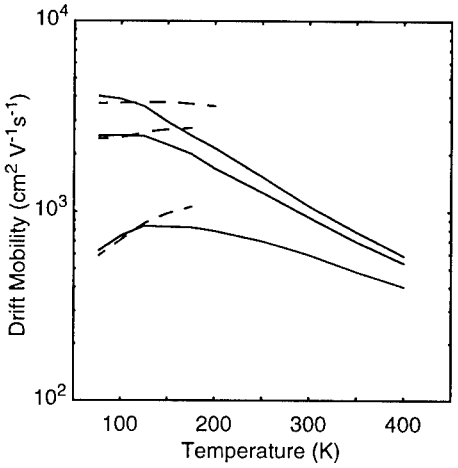


Figure 2: Electron drift mobility vs. temperature for GaN with donor doping densities of 5×10^{16} cm^{-3} (top line), 10^{17} cm^{-3} (middle), and 5×10^{17} cm^{-3} (lowest). The dashed lines indicate the relaxation-time approximation at low temperature.

If the mobility at 77K was dominated solely by ionized impurity scattering such that $\mu \sim T^{3/2}/n_I$, the decrease in mobility at low temperatures would not be as great or would completely vanish for uncompensated GaN. Conversely, a greater decrease in drift mobility is evident for heavily compensated GaN since the ionized impurity concentration remains substantial at low temperatures[15,16]. Our calculations indicate that having an acceptor concentration of 5×10^{16} cm^{-3} reduces the 77K mobility for GaN with 10^{17} cm^{-3} donors to approximately 800 cm^2 V^{-1}s^{-1}, or by 30%. Further reductions in mobility from dislocation scattering have been predicted and recently measured by Ng, *et al*[17] for lateral drift normal to charged dislocations in *n*-type GaN films.

The Hall factor determined from our Monte Carlo simulation is plotted in Figure 3 with the error bars indicating the maximum deviation from the average steady-state value. In this context, steady-state was established by simulating 10^7 collisions. The number of collisions was chosen sufficiently large such that the estimated electron drift velocity perpendicular to the applied electric field can be resolved above the thermal fluctuations. Fluctuations in the Monte Carlo drift velocity are inversely proportional to the square-root of the number of collisions simulated. In all three plots of Figure 3, r_H decreases with increasing temperature to a value approaching 1.2. A similar downward trend from 1.5 toward 1.2 at room temperature has been calculated using a variational technique[15]. The increase in r_H at low temperatures is due to dom-

inant impurity scattering. We also expect that r_H should exhibit a similar trend at low temperature for Hall measurements of mobility perpendicular to the growth direction in samples where scattering from threading dislocations is dominant.

When the mobility is limited solely by dislocation scattering and this process can be modeled by scattering from a line charge, r_H can be estimated by computing the average momentum relaxation time. It follows from the analytic expression given in reference 2 that,

$$r_H = \frac{\langle \tau_m^2 \rangle}{\langle \tau_m \rangle^2} = \frac{\pi}{8}\gamma \exp(-1/\gamma)[K_2(1/(2\gamma))]^{-2}[8 + 60\gamma + 210\gamma^2 + 315\gamma^3]; \ \gamma = \frac{8m^*\lambda^2 k_B T}{\hbar^2}. \quad (5)$$

Here, K_2 is the second order modified Bessel function and λ is the Debye screening length. In Figure 4, r_H as obtained from equation (5) is plotted for drift perpendicular to threading dislocations as a function of temperature. The free carrier density used to determine the screening length is that shown in Figure 1 for uncompensated GaN. The region of interest in Figure 4 is at low temperatures where dislocation scattering may be dominant[17]. Specifically, r_H is smaller than but close to 1.93 (the $\lambda \rightarrow \infty$ limit). From this estimate, it is reasonable to expect that when electron mobility is dominated by dislocation scattering, the Hall factor will tend to values larger than the room temperature value – perhaps to an extent greater than the Monte Carlo simulations for material without dislocations predict in Figure 3.

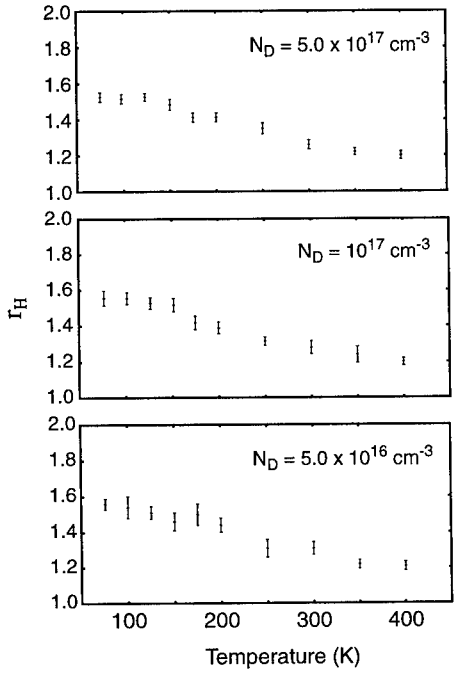


Figure 3: Hall factor vs. temperature for fixed doping concentrations from Monte Carlo simulations.

In summary, Monte Carlo simulations of electron transport in crossed electric and magnetic fields are used to compute mobility and Hall factor values at various temperatures and doping concentrations. This technique is particularly desirable for simulating Hall transport governed by polar optical phonon scattering and we show that r_H should be approximately 1.2 for temperatures above 300K. At lower temperatures r_H deviates farther from unity, and the values obtained by simulation are consistent with those obtained from classical analytical approximations. We have also addressed Hall measurements of lateral mobility, which can be dominated by scattering from threading dislocations when dislocation densities are high. In those cases, we predict that r_H will remain significantly larger than unity at low temperature, especially for low carrier concentrations where screening is weak.

ACKNOWLEDGEMENTS

This work benefited from useful discussions with J.R. Meyer. A grant from the Minnesota Supercomputer Institute is gratefully acknowledged. This work was supported in part by Hughes Research Laboratories and by NSF under grant number ECS-9811366. The work at Georgia Tech was sponsored in part by NORTEL through contract E21-5D7 and by ONR through contract E21-K19.

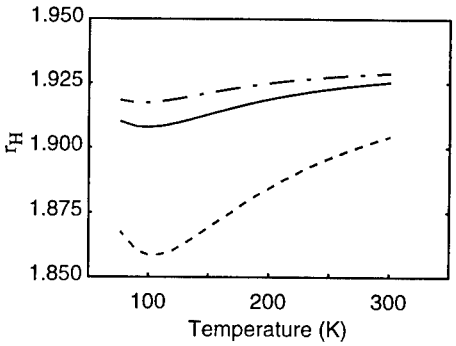


Figure 4: Hall factor resulting from dislocation scattering vs. temperature with constant donor doping densities of 5 x 10^{16} cm^{-3} (dash-dotted), 10^{17} cm^{-3} (solid), and 5 x 10^{17} cm^{-3} (dashed).

REFERENCES

[1]D.C. Look and R.J. Molnar, *Appl. Phys. Lett.*, **70**, 3377 (1997).
[2]N.G. Weimann, L.F. Eastman, D. Doppalapudi, H.M. Ng, and T.D. Moustakas, *J. Appl. Phys.*, **83**, 3656 (1998).
[3]R.J. Molnar, T. Lei, and T.D. Moustakas, *Appl. Phys. Lett.*, **62**, 72 (1993).
[4]W. Götz, L.T. Romano, J. Walker, N.M. Johnson, and R.J. Molnar, *Appl. Phys. Lett.*, **72**, 1214 (1998).
[5]W. Götz, N.M. Johnson, C. Chen, H. Liu, and W. Imler, *Appl. Phys. Lett.*, **68**, 3144 (1996).
[6]A.D. Boardman, W. Fawcett, and J.G. Ruch, *Phys. Stat. Sol.*, **4**, 133 (1971).
[7]J.E. Dijkstra and W. Th. Wenckebach, *Appl. Phys. Lett.*, **70**, 2428 (1997).
[8]P. Warmenbol, F.M. Peeters, and J.T. DeVreese, *Phys. Rev. B*, **33**, 1213 (1986).
[9]C.K. Williams, H.A. Littlejohn, T.H. Glisson, and J.R. Hauser, *Superlattices and Microstructures*, **2**, 201 (1986).
[10]J.D. Albrecht, R.P. Wang, P.P. Ruden, M. Farahmand, and K.F. Brennan, *J. Appl. Phys.*, **83**, 4777 (1998).
[11]R.P. Wang, P.P. Ruden, J. Kolnik, I. Oguzman, and K.F. Brennan, *Mat. Res. Soc. Symp. Proc.*, **445**, 935 (1997).
[12]J.R. Meyer and F.J. Bartoli, *Phys. Rev. B*, **24**, 2089 (1981).
[13]See, e.g., L. Schiff, *Quantum Mechanics*, McGraw-Hill, New York (1955).
[14]For a canonical list of analytical relaxation-time approximations see D.C. Look, *Electrical Characterization of GaAs Materials and Devices*, John Wiley & Sons, New York (1989).
[15]D.C. Look, J.R. Sizelove, S. Keller, Y.F. Wu, U.K. Mishra, and S.P. DenBaars, *Solid State Commun.*, **102**, 297 (1997).
[16]A.E. Wickenden, D.K. Gaskill, D.D. Koleske, K. Doverspike, D.S. Simons, and P.H. Chi, *Mat. Res. Soc. Symp. Proc.*, **395**, 679 (1996).
[17]H.M. Ng, D. Doppalapudi, T.D. Moustakas, N.G. Weimann, and L.F. Eastman, *Appl. Phys. Lett.*, **73**, 821 (1998).

BASE TRANSIT TIME IN ABRUPT GaN/InGaN/GaN and AlGaN/GaN/AlGaN HBTs

Shean-Yih Chiu, A. F. M. Anwar and Shangli Wu

Electrical and Systems Engineering Department, University of Connecticut, CT 06269
anwara@engr.uconn.edu

Cite this article as: MRS Internet J. Nitride Semicond. Res. 4S1, G6.7 (1999)

Abstract

Base transit time, τ_b, in abrupt npn GaN/InGaN/GaN and AlGaN/GaN/AlGaN double heterojunction bipolar transistors (DHBTs) is reported. Base transit time strongly depends not only on the quasi-neutral base width, but also on the low field electron mobility, μ_n, in the neutral base region and the effective electron velocity, S_c, at the edge of base-collector heterojunction. μ_n and S_c are temperature-dependent parameters. A unity gain cut-off frequency of 10.6 GHz is obtained in AlGaN/GaN/AlGaN DHBTs and 19.1 GHz in GaN/InGaN/GaN DHBTs for a neutral base width of 0.05um. It is also shown that non-stationary transport is not required to study τ_b for neutral base width in the range of 0.05um for GaN-based HBTs.

Introduction

Wide bandgap group III-nitride semiconductors are currently being pursued for possible high temperature and high power applications. Current gain as high as 10^5 is reported for GaN/SiC HBT [1]. In order to investigate high frequency performance the behavior of the base transit time, τ_b, needs to be investigated. Mohammad et al. [2] has reported the dependence of τ_b on base doping concentration in a graded GaN/InGaN HBT.

The double integral formulation of τ_b by Kroemer [3] for HBTs is based upon the assumption that excess minority carrier concentration at the edge of base-collector depletion layer is negligible. Roulston [4] emphasized upon the use of a finite carrier velocity (saturation velocity) at the edge of the base-collector depletion region, thereby, introducing the component of base transit time due to velocity saturation. A more general formulation for carrier velocity at b-c heterojunction was used by Hafizi et al. [5]. Jahan et al. [6], based upon a self-consistent calculation of thermionic and tunneling components of the total current, proposed a tunneling factor for the determination of carrier velocity at the b-c junction. In this paper, the method formulated by Jahan et al. [7] is used in the determination of the effective electron velocity at base-collector junction which affects the electrons transport across base-collector junction.

In this paper, τ_b in abrupt GaN/InGaN/GaN and AlGaN/GaN/AlGaN HBT is reported. The computation of τ_b includes the effects of bandgap narrowing, carrier saturation and partitioning of the total current into thermionic and tunneling components. Results obtained from an ensemble Monte Carlo simulation are used in the determination of low field mobility, μ_n.

Mat. Res. Soc. Proc. Vol. 537 © 1999 Materials Research Society

Theory

Base transit time, τ_b, can be expressed as a sum of $\tau_{b1} + \tau_{b2}$, where

$$\tau_{b1} = \int_0^{W_B} \frac{n_{ib}^2(x)}{N_{AB}(x)} \int_x^{W_B} \frac{1}{D_n(y)} \frac{N_{AB}(y)}{n_{ib}^2(y)} dy dx \quad (1)$$

and

$$\tau_{b2} = \frac{1}{S_c} \frac{N_{AB}(W_B)}{n_{ib}^2(W_B)} \int_0^{W_B} \frac{n_{ib}^2(x)}{N_{AB}(x)} dx$$

where $N_{AB}(x)$ is the base doping concentration, $n_{ib}^2(x) = n_{ic}^2 \exp(\Delta_g / kT)$ is the effective intrinsic carrier concentration in base region. The effective bandgap narrowing across the emitter-base heterojunction, $\Delta_g(In_xGa_{1-x}N) = x \cdot E_g(InN) + (1-x) \cdot E_g(GaN) - x \cdot (1-x) E_{gb}$ (E_{gb}=1.0 eV)[8] where x is the In-mole fraction in $In_xGa_{1-x}N$ and n_{ic} is the effective intrinsic carrier concentration in emitter region. τ_{b1} is the component of the base transit time due to diffusion in the neutral base region and τ_{b2} accounts for the finite base-collector junction velocity, S_c. The effective minority carrier velocity, S_c, characterizing electron transport across the space-charge region at the base-collector junction is formulated as $S_c = v_{th} \cdot \gamma \cdot \exp[(qv_{jp} - \Delta E_c)/kT]$ [9], where ΔE_c is the conduction band discontinuity, v_{jp} is the applied voltage drop at the collector, γ is the tunneling transmission factor, and v_{th} is the thermal velocity. The factor γ is determined by invoking the proper partitioning of the total current into tunneling and thermionic components [7]. WKB method is used to compute the transmission probability required in calculating the tunneling component of the total current.

Results and Discussions

5×4 μm^2 single finger npn GaN/$In_xGa_{1-x}N$ and $Al_{0.2}Ga_{0.8}N$ HBTs are investigated. The material parameters used in the simulation are as follows: m_e(GaN)=0.2m_0, m_h(GaN)=0.6m_0 [10], m_e(InN)=0.115m_0 [11], m_h(InN)=1.6m_0 [12], m_e(AlN)=0.314m_0, m_h(AlN)=0.71m_0 [13], $E_{gGaN}(T)$=3.503+5.08 $\times 10^{-4} \times T^2/(T-996)$ eV, $E_{gInN}(T)$=2.01-1.8 $\times 10^{-4} \times T$ eV, $E_{gAlN}(T)$=6.118-1.799 $\times 10^{-3} T^2/(T+1462)$ eV [14], ε_{GaN}=9.5 ε_0, ε_{InN}=19.6 ε_0 and ε_{AlN}=8.5 ε_0 [13] where ε is static dielectric constant, m_0 is electron rest mass, T is absolute temperature (K), and ε_0 is permittivity in vacuum. Emitter and collector doping concentrations equal 5×10^{17} cm^{-3}. The base is 0.05um wide and is doped uniformly 10^{19} cm^{-3}. The conduction band offset, ΔE_c, is assumed to be 75% of the difference in bandgaps of the constituting semiconductor alloys [15].

In Fig. 1(a) the low field mobility, μ_n, and the diffusion coefficient, D_n, are plotted as a function of temperature for $In_{0.2}Ga_{0.8}N$ and GaN at a doping concentration of 10^{19} cm^{-3}. The low field mobility data is obtained from an ensemble Monte Carlo simulation which accounts for piezoelectric, ionized impurity, alloy, intervalley, acoustic and polar optical phonon scattering [16]. The diffusion constant $D_n = kT/q \cdot \mu_n \cdot [F_{1/2}(\varsigma_n)/F_{-1/2}(\varsigma_n)]$ where $\varsigma_n = (E_{fn} - E_c)/kT$ is the reduced Fermi level for electrons and $F_{\pm 1/2}(\varsigma_n)$ is the Fermi-Dirac integral. D_n initially increases followed by gradual decrease beyond T=200K. In Fig. 1(b) the base-collector electron junction velocity, S_c, is plotted as a function of base-collector bias, V_{bc},

for varying In-mole fraction with temperature as a parameter. Due to a smaller band offset at the b-c junction S_c approaches thermal velocity at lower V_{bc} for x=0.1 as compared to that at x=0.2. The behavior of S_c for AlGaN/GaN/AlGaN is similar to that of GaN/InGaN/GaN.

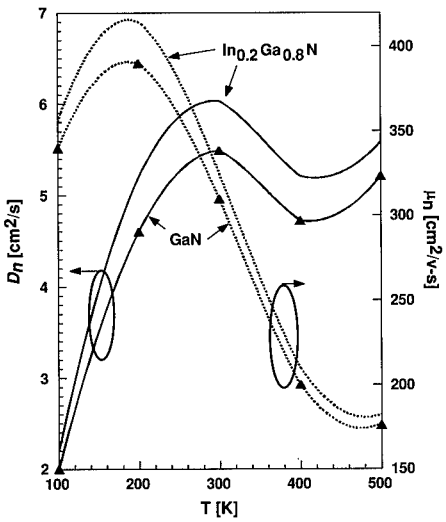


Fig. 1(a) Low field mobility μ_n and diffusion coefficient D_n for $In_{0.2}Ga_{0.8}N$ and GaN as a function of temperature at a doping concentration of 10^{19} cm^{-3}. Solid triangles represent D_n and μ_n for GaN.

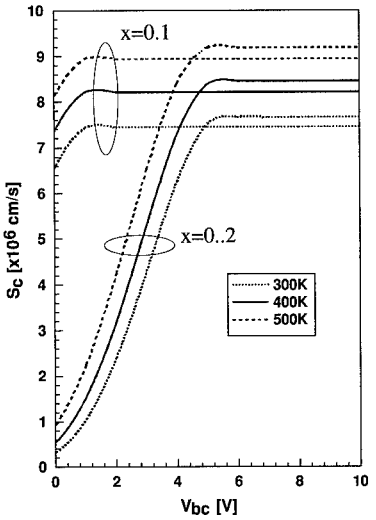


Fig. 1(b) The effective electron velocity at base-collector junction, S_c , versus V_{bc} for $In_xGa_{1-x}N$/GaN.

In Fig. 2(a) the base transit time τ_b is plotted as a function of V_{be} for V_{bc} =3.0 V. τ_b decreases with increasing In-mole fraction in GaN/$In_xGa_{1-x}N$/GaN HBTs, irrespective of temperature and this behavior can be explained with the aid of Fig. 1. A higher S_C at x=0.1 results in a lower τ_{b2} as compared to that at x=0.2 for V_{bc} = 3V. The magnitude of τ_{b1} at x=0.1 is slightly greater than that at x=0.2. This may be attributed to a slightly higher low field mobility at x=0.1 that results in a lower diffusion constant as compared to that at x=0.2. The relative magnitudes of τ_{b1} and τ_{b2} reflects the role of the transport processes namely drift-diffusion versus thermionic field emission. As seen from Fig 2(b), the diffusion controlled component of the base transit time τ_{b1} is always the dominating time constant at elevated temperatures. However, at higher D_n at 300K results in a lower τ_{b1} and a higher τ_{b2}. Or in other words, at 300K the contribution of thermionic field emission related component of the base transit time τ_{b2} becomes significant. τ_b for Al_2Ga_8N/GaN HBTs at V_{bc} =3.0 V is controlled by τ_{b2} and is due to the small electron effective velocity.

The dependence of τ_b upon base width for a base doping concentration of 10^{19} cm^{-3} at room temperature is shown in Fig.3. V_{be}=2V and V_{bc}=3V are assumed. As expected, τ_b increases with increasing base width. For extremely narrow base widths, the dominant component of τ_b is τ_{b2}. As compared to $In_xGa_{1-x}N$-based HBTs, GaN-based HBTs have higher τ_b due to lower low field mobility and lower effective electron velocity at base-collector junction. The above calculation is performed using stationary transport. The validity of the above

approximation is shown in Fig. 4, where the average velocity is plotted as a function of distance. As noted, the average velocity remains constant over a base width variation from 0.02μm to 0.8μm for both GaN and In_2Ga_8N in the presence of an applied field of 500KV/cm. For

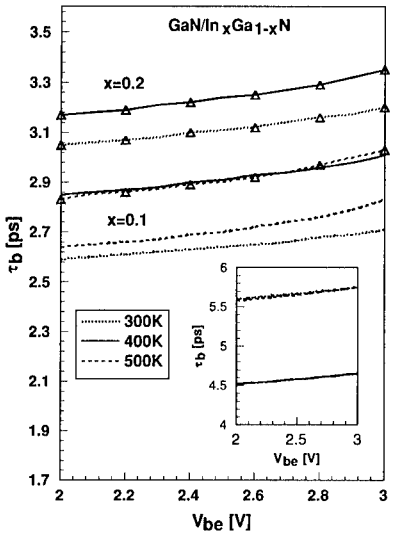


Fig. 2(a) τ_b is plotted as a function of V_{bc} at various temperature for $GaN/In_xGa_{1-x}N$ HBTs with base doping concentration of 10^{19} cm^{-3}, V_{bc}=3V. Base width equals 0.05um. The inset shows τ_b for $Al_{0.2}Ga_{0.8}N/GaN$ DHBT. Lines represent x=0.1 and lines with open triangles represent x=0.2.

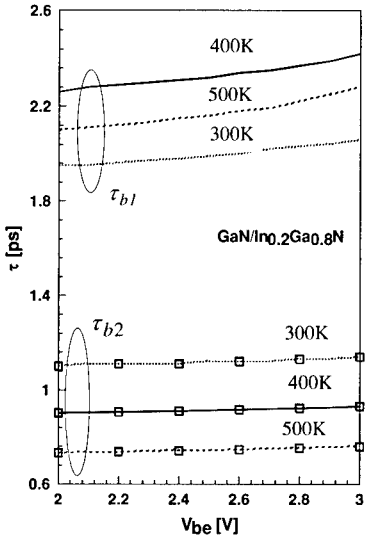


Fig. 2(b) Shows τ_{b1} and τ_{b2} for $GaN/In_{0.2}Ga_{0.8}N$ DHBT. Lines represent τ_{b1} and lines with open squares represent τ_{b2}.

comparison a similar plot for GaAs is also shown where the applied electric field is 10KV/cm. For GaAs the effect of non-stationary transport is clear and for base widths less than 1μm assuming stationary transport data becomes questionable.

In Fig. 5, the unity gain cutoff frequency $f_T = 1/(2 \cdot \pi \cdot \tau_{ec})$ is plotted as a function of collector current density, J_c, where $\tau_{ec} = \tau_e + \tau_b + \tau_c$ is the total transit time from emitter to the collector. τ_e is emitter charging time, expressed as $\tau_e = r_e \cdot C_{je}$ where r_e is the dynamic resistance and C_{je} is the base-emitter junction capacitance. $\tau_c = R_c \cdot C_{jc}$ is the collector charging time where R_c is the collector resistance and C_{jc} is the collector junction capacitance. For collector current densities below 100 A/cm^2 τ_c dominant time constant, however for current densities above 100 A/cm^2 τ_b dominates. An f_T of 19.1 GHz is obtained at 500K for $GaN/In_2Ga_8N/GaN$ DHBT. A higher low field mobility and b-c junction velocity in $Al_{0.2}Ga_{0.8}N/GaN$ DHBT produce a f_T of 10.6 GHz at 300K

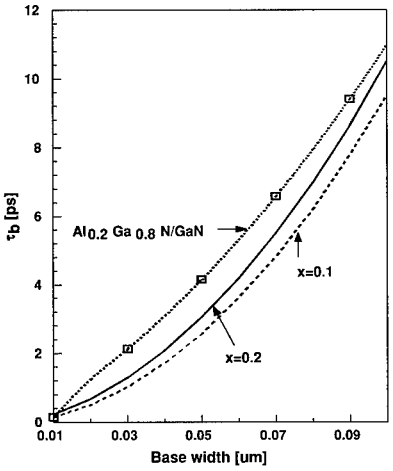


Fig. 3 τ_b is plotted as a function of base width with In-mole fraction as a parameter for GaN/$In_xGa_{1-x}N$ and $Al_{0.2}Ga_{0.8}N$/GaN HBTs (solid triangles). A base doping of 10^{19} cm^{-3}, T=300K, V_{be}=2.0V and V_{bc}=3.0V are considered.

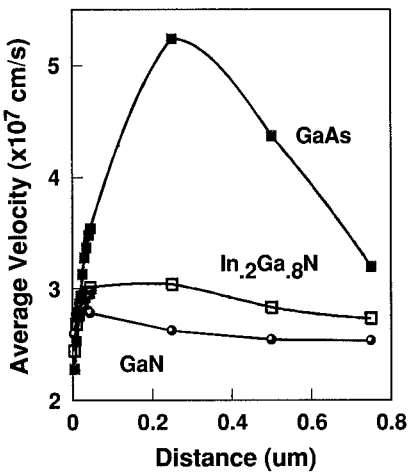


Fig.4 Average velocity is a function of distance at high electric field for GaAs, GaN, and $In_{0.2}Ga_{0.8}N$.

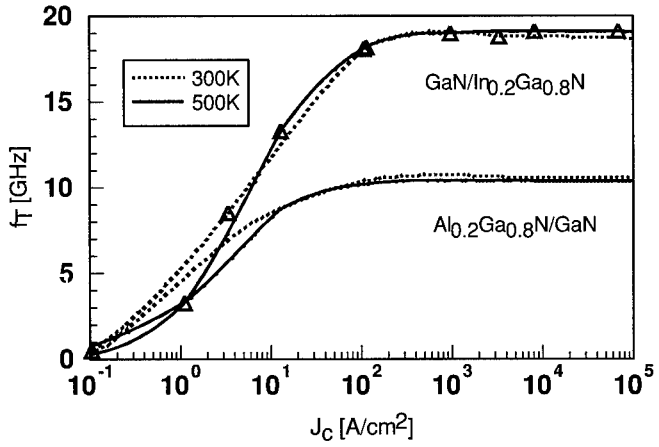


Fig. 5 f_T is shown as a function of collector current density at various temperatures for GaN/$In_{0.2}Ga_{0.8}N$ and $Al_{0.2}Ga_{0.8}N$/GaN HBTs. Base width equals 0.05um with $N_{AB}=10^{19}$ cm^{-3}. Solid lines represent T=500K and dashed lines represent T=300K

Conclusion

Base transit time in abrupt GaN/InGaN/GaN and AlGaN/GaN/AlGaN HBTs are determined by accounting for bandgap narrowing, carrier degeneracy and the proper low field mobility. A narrow base width with a consequently large base resistance is recommended along with a lower In-mole fraction to realize superior unity gain current cut-off frequency, f_T. f_T=10.6 GHz at T=500K for $Al_{0.2}Ga_{0.8}N$/GaN HBT and f_T= 19.1 GHz at T=300K for GaN/$In_{0.2}Ga_{0.8}N$ have been demonstrated.

References

[1] J. Pankove, S. S. Chang, H. C. Lee and R. J. Molnar, TEDM, 389 (1994)
[2] S. N. Mohammad and H. Morkoc, J. Appl. Phys., **78**, 4200 (1995)
[3] H. Kroemer, Solid-State Electron., **28**, 1101 (1985)
[4] D. J. Roulston, IEEE Electron Device Lett., **11**, 88 (1990)
[5] M. Hafizi, D. C. Streit, L. T. Tran, K. W. Kobayashi, D. K. Umemoto, A. K. Oki, and S. K. Wang, IEEE Electron Device Lett., **12**, 581 (1991)
[6] M. M. Jahan and A. F. M. Anwar, Solid-State Electron., **39**, 133 (1996)
[7] M. M. Jahan and A. F. M. Anwar, Solid-State Electron., **39**, 941 (1996)
[8] Y. Koida, H. Itoh, M. R. H. Khan, K. Hiramatsu, N. Sawaki, and I. Akasaki, J. Appl. Phys. **61**, 4540 (1987)
[9] C. D. Parikh and F. A. Lindholm, IEEE Trans. on Electron Devices, **39**, 1303 (1992)
[10] M. A. Khan, R. A. Skogman, J. M. Van Hove. S. Krishanakutty, and R. M. Kolbas, Appl. Phys. Lett. **56**, 1257 (1991)
[11] H. Morkoc, S. Strite, G. B. Gao, M. E. Lin, B. Sverdlov, and M. Burns, J. Appl. Phys. **76**, 1363 (1994)
[12] D. W. Jenkins and J. D. Dow, Phys. Rev. B**39**, 3317 (1992)
[13] M. S. Shur and M. A. Khan, MRS Bulletin. 44, 1997
[14] A. Dmitriev and A. Oruzheinikov, Internat. Symp. on Blue Lasser and Light Emitting Diodes, 360 (1996)
[15] Richard T. Webster and A. F. M. Anwar, MRS, Symp. Proc., **482**, 929, Boston, 1997
[16] S. Wu, Richard T. Webster and A. F. M. Anwar, Proc. 1997 International Semicond. Device Research Symp., 385, University of Virginia, 1997

THEORETICAL STUDIES OF ZnO AND RELATED $Mg_xZn_{1-x}O$ ALLOY BAND STRUCTURES

Walter R. L. Lambrecht, Sukit Limpijumnong, and B. Segall
Department of Physics, Case Western Reserve University, Cleveland, OH 44106-7079
Cite this article as: MRS Internet J. Nitride Semicond. Res. 4S1, G6.8 (1999)

ABSTRACT

First principles calculations are carried out for ZnO, MgO and $ZnMgO_2$ in various crystal structures. The nature of the valence band ordering in ZnO is shown to depend strongly on the Zn3d band position. MgO in the wurtzitic form is found to gave an unusual 5-fold coordiated structure. The band gap dependence in the alloy system is found to be in fair agreement with experimental data and the band-offset is predicted to be type I.

INTRODUCTION

Recently, ZnO has attracted attention not only as a suitable closely lattice-matched substrate for GaN but also as a potentially useful active optoelectronic material in its own right [1, 2, 3, 4, 5] This raises new questions not only about the basic properties of ZnO but also about those of related materials which can be combined with ZnO in heteroepitaxial device structures. In fact, one would need a material with a higher band gap to use as barrier in order to make ZnO quantum wells. Ohtomo et al. [6] showed that it is possible to grow $Mg_xZn_{1-x}O$ alloy films with the wurtzite structure over a certain range of concentrations. This possibility was far from obvious because MgO has the rocksalt rather than the wurtzite structure.

In this paper, we first re-examine the band structure of ZnO. Although this material has been studied extensively in the past, [7, 8, 9, 10] there are some remaining open questions about its band structure. Most notably, there has been a long-standing controversy over the nature of the valence band ordering. The question is: is it the usual Γ_9 above Γ_7 as proposed by Park et al. [13] or the inverse ordering as suggested by Thomas [12]. Recently, new results supporting Park et al.'s point of view has been obtained by Reynolds et al. [14]. We show that this ordering depends crucially on the position of the Zn3d bands, which is not correctly obtained in the local density approximation (LDA). We also present results of our total energy results for ZnO in both wurtzite and zincblende structure.

Next, we present results of first-principles calculations of the relative stability of the wurtzite, zincblende and rocksalt forms of MgO and obtain an estimate for the expected gap in wurtzitic MgO. We also present preliminary results for an ordered $ZnMgO_2$ structure, which allows us to obtain a first idea of the expected band gap dependence in this system. Using the dielectric midgap energy charge neutrality point model, [11] we obtain an estimate of the band-offset between ZnO and MgO.

METHOD OF CALCULATION

The computational method used in this work is the density functional theory in the local density approximation (LDA). The Kohn-Sham equations are solved using the full-potential linear muffin-tin orbital (LMTO) method developed by Methfessel [15]. Details of the computational procedure (sphere radii choice, angular momentum cut-off paramters, size of basis sets) are similar to those in recent work on GaN and related materials and were carefully checked for convergence [17].

For the study of the alloys, we used zincblende derived structures as a model system. The gaps in wurtzite are usually slightly larger than those in zincblende forms. The differences between the gaps in the two structures typically vary linearly across the alloy system as we found in previous

Mat. Res. Soc. Symp. Proc. Vol. 537 © 1999 Materials Research Society

Table I: Properties of ZnO

	wurtzite		zincblende
	expt	theory	theory
a (Å)	3.25	3.21	
c/a (Å)	1.602	1.608	
u	0.382	0.380	
a_{cubic}			4.49
volume per molecule (Å^3)	23.8	23.4	22.6
E_{coh} (eV/molecule)		8.9	8.9
bulk modulus B (GPa)		157	159

Table II: Selected eigenvalues (in eV) from the top of the valence band.

	present FP-LMTO	pseudopotential[a]	GW[b]	expt[c]
Γ^d_{5v}	-0.7	-0.85	-0.8	-0.85
Γ_{3v}	-3.8	-4.0	-5.0	-4.3
$A_{1,3}$	-2.1	-2.37	-2.48	-2.0
$A_{5,6}$	-0.4	-0.43	-0.43	-0.45
Zn 3d average	-5.1	-5.21	-6.4	-6.95

[a] Schröer et al. [9]
[b] Massida et al. [10]
[c] Girard et al. [8]
[d] Note that we use Rashba's [19] notation for the symmetrylabeling and thus our Γ_5 and Γ_6 are interchanged from those in Girard et al. [8]

work on $In_xGa_{1-x}N$ alloys [18]. As a model 50 % compound, we used the chalcopyrite structure. While this is usually a low energy modification and does not quite display the properties of a random alloy, it does nevertheless give some idea of the band-gap bowing. More extensive studies of the disorder effects on band gap bowing are required and are in progress.

The valence band ordering depends crucially on the nature of the spin-orbit coupling. We have studied these within the atomic sphere approximation [16] to the LMTO method. Prior checks show that the band-structure without spin-orbit coupling in this approximation is close to that obtained in the full-potential method.

RESULTS

ZnO total energy and band structure

Our calculated total energy and related parameters are summarized in Table I and are seen to be in good agreement with experimental data.

In Table II, we compare some of the band structure energies with photoemission data by Girard et al. [8]. One may see that the deeper eigenvalues are slightly too high in LDA (except for $A_{1,3}$) which is a result of the increasing self-energy corrections. In particular, one may notice the underestimate of the Zn 3d bands. The latter is of special importance because its hybridization with the O2p band strongly affects the details of the valence band maximum near the gap.

Table III gives our results for the eigenvalues near the band gap. These were obtained in the ASA because we only have spin-orbit coupling included in that version of our LMTO codes. However, the ASA band structure without spin-orbit coupling is in good agreement with that obtained from the FP-LMTO method, except for having a slightly larger band gap. Since the gap needs to be corrected anyway, this is not a serious problem.

We now discuss the effects of the Zn3d band position on the valence band maximum. Accord-

Table III: Band gaps and valence band splittings in ZnO.

	theory		Expt.[a]
	without Zn 3d shift	with	
minimum gap at Γ	1.4	1.8	3.437
$E_A - E_B$ (meV)	37	9.5	9.5
$E_B - E_c$ (meV)	80	34.0	39.7
Zn 3d band position (at Γ) (eV)	-5.05	-6.25	-6.95[b]

[a] Ref. [14]
[b] Ref. [8]

ing to the Hopfield model,[20] the $\Gamma_9 - \Gamma_7$ splittings are given by

$$E_{\Gamma_9} - E_{\Gamma_7} = \frac{\Delta_c + \Delta_s}{2} \pm \sqrt{(\Delta_c + \Delta_s)^2 - \frac{8}{3}\Delta_c\Delta_s} \quad (1)$$

The Δ_s denotes the spin-orbit splitting that would be obtained in the cubic zincblende structure and is 3 times the value of the $\Delta_2 = \Delta_3$ parameters of the Rashba-Shika-Pikus model Hamiltonian.[17]

The experimental values for the A-B, and B-C splittings, where the A, B, and C valence band states are given in order of decreasing energy, are given in the last column of Table III. Now, one can interpret these with A having Γ_9 and B and C having Γ_7 symmetry, in which case one obtains as crystal field and spin-orbit coupling parameters $\Delta_c = 42.0$ meV and $\Delta_s = 16.7$ meV, or with B having Γ_9 and A and C having Γ_7 character, in which case one obtains Δ_c=43.3 meV and $\Delta_s = -13.1$ meV. The possibility of a negative spin-orbit coupling arises from the hybridization with the Zn3d band. Indeed, a lower lying d band contributes a negative component to the spin-orbit splitting.[21, 22]

Without spin-orbit coupling and in a pure LDA calculation, we obtain a band gap of 1.3 eV and a crystal field splitting of the valence band maximum $\Gamma_6 - \Gamma_1$ of 95 meV. The results with spin-orbit included also indicate too large a spin-orbit and crystal field splitting. When we empirically shift the Zn3d band position in our Hamiltonian, we find that the gap, the crystal field splitting and the spin-orbit splitting depend sensitively on the Zn3d band position. However, if we shift the Zn 3d band all the way down to its experimental position [8] of -6.95 eV, we find that the crystal field splitting becomes as low as 16 meV. The best fit is obtained for a shift of about 1.2 eV and is included in Table III. In order to see whether this case corresponds to a negative or positive spin-orbit splitting, we perform an analogous calculation for zincblende ZnO. In that case, the spin-orbit coupling splits the Γ_{15} into a quadruplet Γ_8 and a doublet Γ_7 and we can unambigously determine the sign of the spin-orbit splitting without the need for a tedious inspection of the eigenvectors. When we shift the Zn3d band in zincblende to the same position as in wurtzite, we find a spin-orbit splitting of -12 meV. This is consistent with the value extracted from the wurtzite case using Hopfield's model. Hence, our present results seem to support a negative spin-orbit splitting. Our calculated values extracted from column 2 of Table III are $\Delta_s = -12.9$ meV and $\Delta_c = 37.4$ meV. However, we caution that the results are quite sensitive to the d-band position. A slightly larger d-band shift results in a positive spin-orbit splitting. However, we then would face the problem of how to explain the serious underestimate of Δ_c. We note that our LDA calculaton should tend to overestimate the Δ_c because the underestimate of the gap increases the repulsive coupling between the Γ_1 valence and Γ_1 conduction band states. Further work is required to fully interpret the data of Ref. [14].

The question now arises as to why the required shift of the Zn3d band appears to be less than that indicated by the photoemission data. This is a rather subtle question. The origins of the discrepancies between theory and experiment are the difference between Kohn-Sham eigenvalues

Table IV: Total energy results for MgO.

	theory				expt.[a]
	relaxed wurtzite	ideal wurzite	zinc-blende	rock-salt	rock-salt
a (Å)	3.413	3.199			
c/a	1.204	1.633			
u	0.5	0.375			
bond length (Å)	1.971 $\perp c$	1.959	1.959	2.071	2.1075
	2.055 $\parallel c$				
a_{cubic}		4.524		4.141	4.215
volume per molecule (Å^3)	20.7	17.8	17.8	17.8	18.7
Bulk modulus B (GPa)	148		129	178	153-162
E_{coh} (eV/molecule)	11.56	11.39	11.36	11.67	10.41

[a] From Ref. [25] and refs. therein.

of density functional theory and quasiparticle energies. Because of the energy dependence of the self-energy operator, it may be impossible to obtain both valence band maximum and Zn3d bands consistently from one energy independent Hamiltonian. Clearly, part of the shift must arise from a better treatment of exchange, one of the main errors of LDA being the incomplete cancellation of the self-interaction by the averaged exchange [23, 24]. This can be handled by an improved energy independent Hamiltonian, (here obtained empirically but in possibly justifiable by means of improved density functionals). However, there still remains an energy dependent part in the true quasiparticle shift, in particular for deep localized narrow bands such as Zn 3d bands.

MgO wurtzite/rocksalt stability

As a starting point for investigating the rocksalt versus wurtzite relative stability in the alloy system, we here examind the end compound MgO. In Table IV we give our total energy results for four structures of MgO, the equilibrium structure (rocksalt), the relaxed (and ideal) wurtzite structure, and the zincblende structure. The ideal wurtzite has bond lengths and cohesive energy very close to that of zincblende. When the structural parameters for MgO in a wurtzitic lattice (c/a and u) are relaxed, however, we find that $u = 1/2$. This implies that the Mg and O atoms lie in the same plane. In other words the buckled hexagonal rings of the wurtzitic basal plane become flat. It also means that the Mg is at equal distance from the O below and above it along the c-axis. The coordination is thus either 3-fold if one only counts the atoms in the plane or rather 5-fold when one includes the atoms above and below, for which the bond lengths are slightly larger than the in-plane ones. (See Table IV). The five-fold coordination is consistent with the tendency for ionic compounds to prefer a high coordination. The energy of this hypothetical structure is 0.10 eV/molecule above that of the rocksalt structure and lower than zincblende (or ideal wurtzite) by 0.2 eV/molecule. We found that a further continuous distortion can turn this "degenerate" wurtzitic structure into the rocksalt structure. Calculations with the structure confined to such a transformation path indicate that there is a barrier which would mean that the wurtzitic structure is indeed metastable. Details of this will be presented elsewhere. The c/a and u parameters of MgO are thus very different from those in ZnO, which are closer to ideal wurtzite and are given in the previous section.

Alloys

In view of the above noted complication of MgO and ZnO having very different types of c/a and u parameters, it is far from obvious what will happen to the structure at intermediate compositions. In order to bypass this problem, we decided to first investigate the alloy band gap bowing behavior in zinblende alloys first.

Table V: LDA band gaps.

	ZnO	MgO	$ZnMgO_2$
zincblende	0.75	3.76	2.115
wurtzite	1.27	3.69	
rocksalt		5.24	

Our LDA band gaps for zincblende ZnO, MgO and chalcopyrite $ZnMgO_2$ are given in Table V along with those of some of the other structural modifications. From the zincblende results we obtain a slight bowing toward lower gaps with bowing coefficient b of 0.56 eV, defined in the usual manner by

$$E_g(x) = (1-x)E_g(A) + xE_g(B) - bx(1-x), \tag{2}$$

where A=ZnO, B=MgO and x is the relative amount of MgO in the alloy.

The experimental gap of MgO in rocksalt is 7.8 eV, which requires a gap correction of 2.56 eV. With this correction applied to wurtzitic MgO, we obtain an estimated gap of 6.25 eV. This is consistent with the experimental results of Ohtomo et al. [6] who obtained $Mg_xZn_{1-x}O$ alloys up to $x = 0.4$. Beyond 0.3, MgO phase-separation started to occur. These results were obtained by a laser ablation growth technique. The band gaps obtained from the shift of the optical transmission measurements varied from 3.3 eV in ZnO to 4.1 eV at about $x = 0.36$. These are all room temperature gaps which differ from our theory estimates by about 0.1 eV. Using our estimated value of 6.25 for MgO and a gap of 3.4 eV for ZnO, and our bowing coefficient of 0.56 eV predict a gap of 4.2 eV at 33 % MgO, consistent with their results.

Band-offsets

Within the dielectric midgap energy model, the band-offsets are obtained by aligning a suitably defined midgap point which plays the role of a charge neutrality point. In other words, when this level is aligned, negligible charge transfer from one material to the other is assumed to occur. This defines the self-consistent line-up of the two band structures. So, one only needs to calculate where the valence band maximum lies with respect to this midgap point. Our midgap energy points for relaxed wurtzitic MgO and ZnO are 3.03 eV and 1.55 eV above their valence band maxima respectively. This would result in a valence band offset between pure MgO and ZnO of 1.48 eV. With the above estimated gap difference of 2.85 eV, this gives a conduction band offset of 1.37 eV. Taking into account the various uncertainties, the conduction band to valence band ratio is predicted to be about 1. The alignment is of type-I.

CONCLUSIONS

In summary, we have obtained total energy and band structure results for ZnO and MgO in various relevant crystal structures. Our results of LDA calculations for ZnO total energy properties and band structure are in good agreement with experimental data, except for the details of the valence band splitting at the meV scale and the usual LDA shortcomings regarding gaps and deep semicore like band positions. We showed that the latter play a crucial role in determining the sign of the spin-orbit coupling and while we could not definitively solve the controversy about the valence band ordering, our present results seem to support a negative spin-orbit splitting. We found that MgO confined to the wurtzite structure has an unusual behavior with a structure which is really 5-fold rather than 4-fold coordinated. We found a small gap bowing and an overall gap dependence consistent with the data by Ohtomo et al. [6]. We find that the gap of wurtzitic MgO is significantly lower than that of rocksalt MgO. We predict type-I band offsets between ZnO and $Mg_xZn_{1-x}O$ alloys with an approximately 1/1 valence band to conduction offset ratio.

Supported by the Office of Naval Research.

REFERENCES

1. D. C. Reynolds, D. C. Look, and B. Jogai, Solid State Communn. **99**, 873 (1996).
2. D. C. Reynolds, D. C. Look, B. Jogai, and H. Morkoç, Solid State Communn. **101**, 643 (1997).
3. D. C. Look, D. C. Reynolds, J. R. Sizelove, R. L. Jones, C. W. Litton, G. Cantwell, and W. C. Harsh, Solid State Communn. **105**, 399 (1998).
4. D. C. Reynolds, D. C. Look, B. Jogai, and T. C. Collins, Phys. Rev. B **56**, 13753 (1997)
5. D. C. Reynolds, D. C. Look, B. Jogai, C. W. Litton, T. C. Collins et al., Phys. Rev. B. **57**, 12151 (1998); Phys. Rev. B **58**, 13276 (1998).
6. A. Ohtomo, M. Kawasaki, T. Koida, K. Masubichi, H. Koinuma, Y. Sakurai, Y. Yoshida, T. Yasuda, and Y. Segawa, Appl. Phys. Lett. **72**, 2466 (1998).
7. U. Rössler, Phys. Rev. **184**, 733 (1969).
8. R. T. Girard, O. Tjernberg, G. Chiaia, S. Söderholm, U. O. Karsson, C. Wigren, H. Nylén, and I. Lindau, Surf. Sci. **373**, 409 (1997).
9. P. Schröer, P. Krüger, and J. Pllmann, Phys. Rev. B **47**, 6971 (1993).
10. S. Massida, R. resta, M. Posternak, and A. Baldereschi, Phys. Rev. B **52**, R16977 (1995).
11. M. Cardona and N. E. Christensen, Phys. Rev. B **35**, 6182 (1987).
12. D. G. Thomas, J. Phys. Chem. **15**, 86 (1960).
13. Y. S. Park, C. W. Litton, T. C. Collins,a nd D. C. Reynolds, Phys. Rev. **143**, 512 (1966).
14. D. C. Reynolds, D. C. Look, B. Jogai, C. W. Litton, G. catnwell, and W. C. Harsh, unpublished.
15. M. Methfessel, *Phys. Rev. B* **38**, 1537 (1988).
16. O. K. Andersen, O. Jepsen, and M. Šob, in *Electronic Band Structure and its Applications*, edited by M. Yussouff, (Springer, Heidelberg, 1987), p.1.
17. K. Kim, W. R. L. Lambrecht, B. Segall, M. van Schilfgaarde, Phys. Rev. B **56**, **56**, 7363-7375 (1997)
18. Kwiseon Kim, Ph. D. thesis 1998, Case Western Reserve University, unpublished.
19. E. I. Rashba, Sov. Phys. Solid State, **1**, 368 (1959).
20. J. J. Hopfield, J. Phys. Chem. Solids **15**, 97 (1960).
21. K. Shindo, A. Morita, and H. Kamimura, *J. Phys. Soc. Japan.* **20**, 2054 (1965)
22. M. Cardona, *Phys. Rev.* **129**, 69 (1963).
23. M. Städele, J. A. Majewski, P. Vogl, and A. Görling, Phys. Rev. Lett. **79**, 2089 (1997).
24. D. Vogel, P. Krüger, and J. Pollmann, Phys. Rev. B **52**, R14316 (1995); Phys. Rev. B **54**, 5495 (1996); Phys. Rev. B **55**, 12836 (1997).
25. G. Timmer and G. Borstel, Phys. Rev. B **43**, 5098 (1991).

TRANSPORT, GROWTH MECHANISMS, AND MATERIAL QUALITY IN GaN EPITAXIAL LATERAL OVERGROWTH

Michael E. Coltrin, Christine C. Willan, Michael E. Bartram, Jung Han,
Nancy Missert, Mary H. Crawford, Albert G. Baca

Sandia National Laboratories, Albuquerque, NM 87185

Cite this article as: MRS Internet J. Nitride Semicond. Res. 4S1, G6.9 (1999)

ABSTRACT

Growth kinetics, mechanisms, and material quality in GaN epitaxial lateral over-growth (ELO) were examined using a single mask of systematically varied patterns. A 2-D gas phase reaction/diffusion model describes how transport of the Ga precursor to the growth surface enhances the lateral rate in the early stages of growth. In agreement with SEM studies of truncated growth runs, the model also predicts the dramatic decrease in the lateral rate that occurs as GaN over-growth reduces the exposed area of the mask. At the point of convergence, a step-flow coalescence mechanism is observed to fill in the area between lateral growth-fronts. This alternative growth mode in which a secondary growth of GaN is nucleated along a single convergence line, may be responsible for producing smooth films observed to have uniform cathodoluminescence (CL) when using 1μm nucleation zones. Although emission is comprised of both UV (~365nm) and yellow (~550nm) components, the spectra suggest these films have reduced concentrations of threading dislocations normally associated with non-radiative recombination centers and defects known to accompany growth-front convergence lines.

INTRODUCTION

GaN grown on sapphire or SiC has a high defect density due to a significant lattice mismatch at the substrate-material interface. This high defect density (>10^9 per cm^2 [1]) contributes to the poor electrical and optical materials quality [2-4]. There have been many demonstrations that epitaxial lateral overgrowth (ELO) can reduce the dislocation density in GaN films grown by metal-organic chemical vapor deposition (MOCVD) [5-7]. This reduction is the key to fabricating optoelectronic and electronic devices with high performance and reliability.

It has been shown that ELO feature morphology is influenced by several factors that include temperature, V/III ratio, and the mask fill factor [8-11]. The manipulation of these factors results in the cross-section morphology changing systematically from triangles, to five-sided polygons, to rectangles. The manner in which these initial growth features converge and coalescence into continuous films has a direct effect on optical quality and uniformity of the resulting smooth film.

EXPERIMENT

A 2 μm thick GaN base layer was grown by MOCVD in a rotating disk reactor on 2-in diameter sapphire wafers using a low temperature buffer layer followed by high temperature planar growth. This was then covered with 1000 Å SiO_2 or Si_3N_4 and patterned using standard

Mat. Res. Soc. Proc. Vol. 537 © 1999 Materials Research Society

photolithography techniques. Sub-sets of dot and line patterns, varied systematically with respect to both nucleation and mask dimensions were included in a single pattern. The dimensions in each sub-set are denoted as w:m, where w is nucleation width (varied from 1μm to 8μm) and m is the masked width (varied from 1μm to 32μm). A fill factor θ is defined as w/(w+m). Line and dot patterns were oriented both in the preferential ELO <1-100> direction and in the <1-210> direction, which yields a smaller lateral to vertical growth ratio [5]. The ELO growth was performed at substrate temperatures of 1000°C, 1050°C, or 1090°C using H_2 as a carrier gas. The total pressure was 140 Torr with a TMG flow rate of 18 sccm and 44% NH_3. An in-situ optical growth monitor was used to measure the growth rate of a center control section with a 1 cm diameter that contained no patterning. Samples were characterized by scanning electron microscopy (SEM) and cathodoluminescence (CL).

MODEL OF ELO TRANSPORT LIMITATIONS

In ELO, growth does not occur on the dielectric masking material. Thus, the Ga precursor is not consumed (depleted) above the mask, creating an extra supply of reactants that can be transported via gas-phase diffusion to unmasked areas. This additional source of Ga species leads to growth rate enhancement on the unmasked regions, which will drop-off with distance from the mask. We have constructed a steady-state (time-independent) 2-D finite-difference model of the gas-phase diffusive transport and growth-rate enhancement of GaN during ELO.

The model solves the diffusion equation (Laplace's equation) for the Ga concentration, n, in 2-D,

$$\frac{\partial^2 n}{\partial x^2} + \frac{\partial^2 n}{\partial y^2} = 0 \qquad (1)$$

using a simple iteration scheme. The top boundary condition specifies that the concentration is a constant across the domain. Zero-flux boundary conditions are used at the left and right boundaries. At the surface, there is a zero-flux boundary condition on masked regions. For exposed regions, the boundary condition states that the diffusive flux of Ga species to the surface equals the rate of destruction due to deposition chemistry, i.e.,

$$D\frac{\partial n}{\partial y} = kn, \qquad (2)$$

where D is the diffusion constant (with units of cm^2/s), and k is the surface reaction rate constant (with units of cm/s).

The model calculates the **growth rate enhancement**, i.e., the growth rate in the unmasked region divided by the normal growth rate when masking (ELO) is not used. The only parameter needed in the model is the **ratio** D/k. The diffusion constant is estimated from previous work modeling GaAs growth [12] to be 28.1 cm^2/s at 1050 °C and 140 Torr. A surface reaction probability of one for the Ga species corresponds to a rate constant k of 24,700 cm/s [13], which yields a value of D/k of 11.4 μm. Using a unit reaction probability might seem unreasonable. However, since the system is transport limited, results of the model are insensitive to the value of the rate constant used. Figure 1 shows the calculated growth rate (normalized by the growth rate g_0 for the case of no masking) for patterns in the series x:(5-x), x:(9-x) and x:(18-x) plotted as a function of θ.

A very large growth-rate enhancement is seen at small θ, a factor of 6.6 for a 1:8 (θ = 0.111) pattern. The growth rate slows dramatically as the ratio of the exposed to unexposed areas increases, dropping to 3.75 at θ = 0.222, for example. For the range of feature dimensions that we studied, the growth-rate enhancement depended only on θ, and not on w and m. For example,

the calculated growth rate on a 1:8 feature matches that on a 2:16 feature to within 0.5%. The calculated growth rate g was empirically observed to have a power-law dependence on the fill-factor, i.e.,

$$g = g_o\theta^{-0.862}, \tag{3}$$

where g_0 is the growth rate where no masking is used. The solid curve in Figure 1 is the fit from Eq. (3), which describes the 2-D transport results almost exactly.

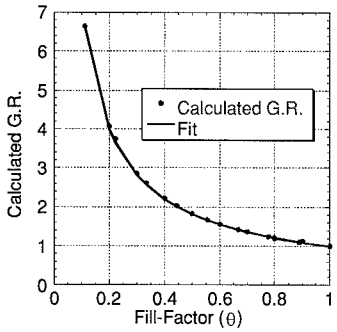


Figure 1. Growth rate g (normalized by the unenhanced growth rate g_0) calculated by the 2-D transport model as a function of fill-factor θ. Solid line shows the fit from Eq. (3).

One interesting feature of the model is that the total growth rate averaged over both the masked and unmasked regions is very weakly dependent on θ, and is very nearly g_o, the unenhanced value. It is easily seen that the average growth rate is

$$\overline{g} = g\theta = g_o\theta^{0.138}, \tag{4}$$

which is consistent with the weak θ dependence.

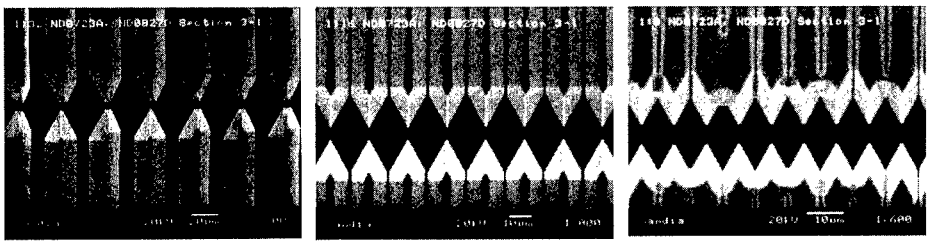
During the actual growth process the masked regions are overgrown, and the ratio of exposed GaN to dielectric material, i.e., θ, decreases continuously. These calculations show that the growth rate should drop dramatically and continuously as overgrowth proceeds. The growth rate enhancement due to the transport effects should follow Eq. (3) as θ drops throughout the fill-in process. The growth rate will drop to g_0 when the gap is completely filled.

This model is confirmed by the series of SEM photos in Figure 2, which shows the overgrowth from 1:32, 1:16, and 1:8 mask patterns from the same growth run. Analysis of the SEMs shows that the 1:32 area has overgrown the dielectric mask by d = 12 μm. The features from the 1:16 pattern have not begun to touch, and thus have growth less than d = 8 μm. The 1:8 features have touched, but are not yet coalesced into a smooth film, and thus the lateral growth distance is around d = 4 μm. Finally, GaN from a 1:4 pattern not shown coalesced into a smooth film, indicating that d > 2 μm. Thus, the extent of lateral growth has dropped precipitously with fill-factor. Note that the gap between the upper and lower set of features is simply due to a gap in the lithographically defined mask pattern.

Equation (3) is the model growth rate as a function of θ at any point in time. This simple differential equation can be integrated to give the growth front as a function of time

$$x(t) = \left[(a+1)g_o\left(L/2\right)^a t + x_o^{a+1}\right]^{1/(a+1)}, \tag{5}$$

where a=0.862, L is w+m (exposed plus masked distances), and x_0 is w/2. Differentiating Eq. (5) with respect to time yields g of Eq. (3), where $\theta = 2x/L$.



(a) (b) (c)

Figure 2. SEM micrographs showing the extent of lateral overgrowth from patterns of different masked dimensions (a) 1:32 (x600 magnification), (b) 1:16 (x1000), (c) 1:8 (x1600)

Figure 3 compares the lateral growth distance $d = x(t)-x_0$ for two sets of mask patterns, with the masked lines running along the 11(-2)0 and 1(-1)00 directions in Figure 3a and Figure 3b, respectively. All of the parameters in Eq. (5) are known except the unenhanced growth rate g_0, which is determined from the measured lateral growth distance from the 1:32 pattern, i.e., θ = 0.0303. Agreement between the model and experiment is quite good.

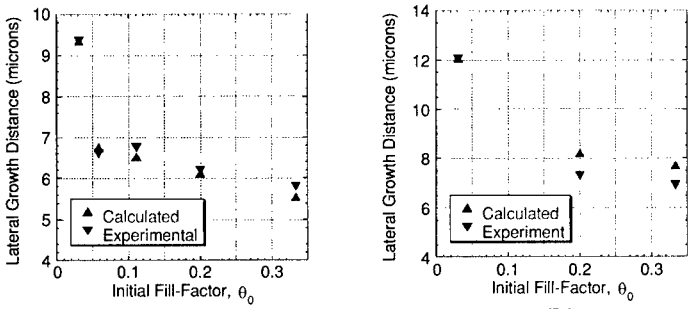


Figure 3. Comparison of lateral growth distance as a function of initial fill-factor measured from the SEM micrographs and calculated from Eq. (5).

AN ALTERNATIVE COALESCENCE MECHANISM

SEM "snap-shots" reveal that coalescence can also occur via a mechanism quite different from that observed in previous ELO studies. Typically, coalescence of adjacent features results from each growth front progressing laterally until the region in between is filled completely. [11] However as shown in Figure 4a, the adjacent lateral growth fronts have only just come to the point of convergence and yet the vertical height of the coalescence region has nearly reached the level of the upper-most surfaces. This apparent enhancement in the local growth rate is consistent with the decrease described by the ELO transport model. Since the lateral rate is reduced greatly by the time the convergence point is reached, the creation of a reaction site on the surface more favorable to growth will be conducive to a *relatively* greater rate. In this case, it is the point of convergence itself, where the lateral growth fronts first come in contact, which serves as the reaction site for initiating new growth. This observation of local growth rate

enhancement under conditions where lateral growth is limited by TMG gas-phase transport, also supports previous suggestions that competition by various crystal faces for nutrients diffusing on the surface has an important role in GaN growth [14].

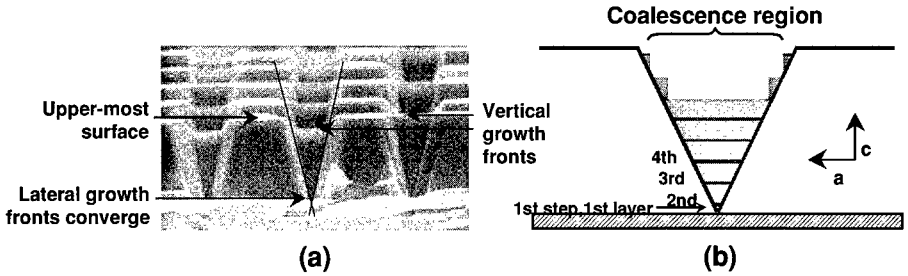


Figure 4. (a) SEM of a selective area growth dot pattern showing that adjacent lateral growth fronts have only just touched. (b) Diagram of the step-flow coalescence mechanism.

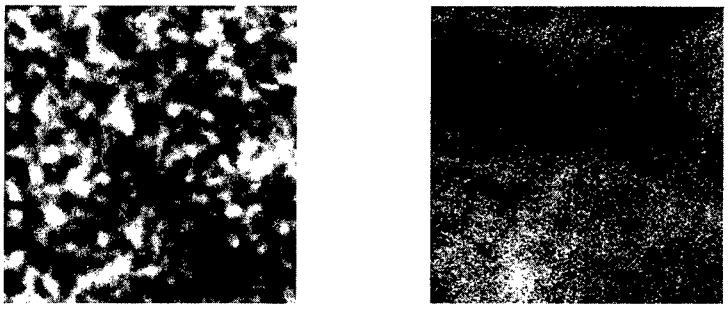
As proposed in Figure 4b, the first "step" and the first layer of GaN is initiated at the moment of contact between adjacent growth fronts. This new surface provides an avenue for rapid growth of one layer at a time since prior to convergence, the lateral progress of a single layer is inhibited by the inert mask. Each new surface then defines new steps along the initial growth fronts for the nucleation of each subsequent layer, as suggested by the slight upward curvature of the vertical growth front end-points in Figure 4a. Thus, a step-flow coalescence mechanism is responsible for the rapid lateral rate. This in turn drives the vertical rate, filling the coalescence region. Since crystal growth in the coalescence region begins at a single point or line, films having more uniform properties may result. The data in the next section support this.

CATHODOLUMINESCENCE

Cathodoluminescence (CL) with a sub-micron spatial resolution, is a useful method to characterize the optical quality of GaN films. The CL was measured from samples of both planar GaN and smooth coalesced films grown with the ELO technique. Using an SEM to excite luminescence (100pA beam current at 10 keV), [15] band-edge or deep-level defect band emission imaging was selected with filters.

Figure 5a shows band-edge emission at 363 nm for a 144 μm^2 area of non-ELO GaN. The mottled appearance is characteristic of GaN and has been attributed to threading dislocations in the material that appear as non-radiative recombination centers [16]. Figure 5b shows band-edge emission for a similar area of a fully coalesced ELO region grown using a 1:1 mask pattern on the same wafer. SEM reveals this region to have a smooth surface, and as shown in the figure, the luminescence intensity does not show a periodicity corresponding to the underlying mask. In addition, the luminescence intensity is much more uniform than for the planar GaN, suggesting a reduction of the threading dislocation density due to the ELO growth. The overall luminescence intensity of the ELO sample is approximately 25% less than the intensity of the non-ELO material. This suggests that other types of non-radiative point defects may be introduced that affect the overall optical quality of the material.

Additional CL tests on samples with varying fill factor show that as the amount of ELO material is increased relative to the nucleation area, the overall intensity of band-edge and deep level emission increased. Also, as the amount of ELO material is increased, the uniformity of the CL is decreased. This illustrates the important trade-off between luminescence uniformity and luminescence intensity in the development of a GaN base for the fabrication of devices.



(a) (b)

Figure 5. (a) CL image at 363 nm of non-ELO GaN (4 μm grown at 1050°C). (b) CL image of ELO GaN from a 1:1 pattern (4 μm grown at 1050°C).

ACKNOWLEDGMENTS

This work was performed at Sandia National Laboratories and supported by the U. S. Department of Energy under contract number DE-AC04-94AL85000. Technical support provided by Jeff Figiel, Mike Banas, and R. Guild Copeland is noted with appreciation.

REFERENCES

1. S. Nakamura, T. Mukai, M. Senoh, Appl. Phys. Lett. 64, 1687-1689 (1994).
2. S. Keller, B.P. Keller, Y.F. Wu, B. Heying, D. Kapolnek, J.S. Speck, U. K. Mishra, and S.P. DenBaars, Appl. Phys. Lett. 68, 15254 (1996).
3. S. Nakamura, M. Senoh, S. Nagahama, N. Iwasa, T. Yamada, T. Matsushita, H. Kiyoku, Y. Sugimoto, T. Kozaki, H. Jumemoto, M. Sano, and K. Chocho, Appl. Phys. Lett, 72, 211 (1998)
4. N. G. Weimann, L.F. Eastman, D. Dharanipal, H.M. Ng, and T.D. Moustakas, J. Appl. Phys. 83, 3656 (1998).
5. D. Kapolnek, S. Keller, R. Vetury, R.D. Underwood, P. Kazodoy, S.P. Denbaars, and U.K. Mishra, Appl. Phys. Lett. 71, 1204-1206 (1997).
6. T.S. Zheleva, O.-H. Nam, M.D. Bremser, and R.F. Davis, Appl. Phys. Lett. 71, 2472 (1997).
7. O.-H. Nam, M.D. Bremser, T.S. Zheleva, and R.F. Davis, Appl. Phys. Lett. 71, 2638 (1997).
8. O.-H. Nam, T.S. Zheleva, M.D. Bremser, and R.F. Davis, J. Elec. Mat. 27, 233-237 (1998)
9. H. Marchand, J.P. Ibbetson, P.T. Fini, S. Keller, S.P. DenBaars, J.S. Speck, and U.K. Mishra, Submitted to J. Crystal Growth, (1998).
10. A. Kimura, C. Sasaoka, A. Sakai, A. Usui, Mat. Res. Symp. Proc. 482, 119-124 (1998)
11. B. Beaumont, M. Vaille, G. Nataf, A. Bouille, J.-C. Guillaume, P. Vennegues, S. Haffouz, and Pierre Gibart, MRS Internet J. of Nitride Semiconductor Res. 3, Art. 20 (1998).
12. M. E. Coltrin and R. J. Kee, *Mater. Res. Soc. Symp. Proc.*, **145**, 119 (1989).
13. M. E. Coltrin, R. J. Kee, and F. M. Rupley, *Int. J. Chem. Kinet.*, **23**, 1111 (1991).
14. S. Kitamura, K. Hiramatsu, and N. Sawaki, *Jpn. J. Appl. Phys.*, **34**, L1184 (1995).
15. C. H. Seager, N. A. Missert, D. R. Tallant, and W. L. Warren, J. Appl. Phys. 83, 1153 (1998).
16. S. J. Rosner, E. C. Carr, M. J. Ludowise, G. Girolami and H. I. Erikson, Appl. Phys. Lett. 70, 420 (1997).

ELECTRONIC STRUCTURE AND OPTICAL PROPERTIES OF $ZnGeN_2$

Sukit Limpijumnong, Sergey N. Rashkeev and Walter R. L. Lambrecht
Department of Physics, Case Western Reserve University, Cleveland, OH 44106

Cite this article as: MRS Internet J. Nitride Semicond. Res. 4S1, G6.11 (1999)

ABSTRACT

The electronic band structure, structural and bonding, and some linear and nonlinear optical properties are calculated for a new ternary nitride compound $ZnGeN_2$ using first-principles methods. Good agreement is obtained with crystallographic data and with absorption data on the band gap. The prospects for use as nonlinear optical material are discussed.

INTRODUCTION

The most common way to achieve band-structure engineering of semiconductor compounds is to make alloys using cations or anions from the same column of the parent compound. For example, GaN can be modified by making $In_xGa_{1-x}N$ alloys, i.e. replacing Ga by another group III element In. On the other hand, one may also replace every other group-III element by a group II and a group IV element. This will lead to a new kind of ternary compounds II-IV-N_2, such as, e.g. $ZnGeN_2$. This kind of chemical substitution is well known in more traditional III-V compounds: e.g. GaP $\rightarrow$$ZnGeP_2$. Typically because the replacement of a group III by a group II and IV element leads to stringent conditions on local charge neutrality, this leads to a well defined cation-ordered crystal structure rather than a disordered alloy. This may avoid the disadvantages of alloy disorder scattering in the transport. In addition, most semiconductor alloys are in principle only metastable and some (like $In_xGa_{1-x}N$ alloys) suffer from rather severe phase segregation problems. In most III-V semiconductors the III$\rightarrow$(II,IV) replacement leads to a superstructure of the zincblende structure, known as the chalcopyrite structure. The ordering is also typically accompanied by a local structural distortion of the tetrahedral first nearest neighbor environment. In other words, the anion makes different bond lengths with each of the two cations and thus is displaced off-center from the cation tetrahedron surrounding it. The latter may in addition slightly distort from the regular tetrahedron shape. This leads to an overall c/a distortion of the tetragonal lattice. These anisotropies in the structure translate in anisotropies in the electronic and optical properties. Among others, this makes the chalcopyrites suitable for second order nonlinear optics: the anisotropy in index of refraction leads to the possibility of phase matching light beams of different frequencies that can be generated by second-order nonlinear optical susceptibilities because the structure is noncentrosymmetric. It also splits certain degeneracies in the band structure and thus plays a similar role as strain in strained superlattices which is well known to be an efficient way to tailor the band structure of semiconductors. The difference is that in II-IV-V_2 compounds, this can be done in the bulk semiconductor instead of only in thin films.

In the case of nitrides, a similar family of compounds may be conceived but because the natural stacking favored by nitrides is hexagonal (because of the higher ionicity), we now

Mat. Res. Soc. Symp. Proc. Vol. 537 © 1999 Materials Research Society

have to think of structures derived from wurtzite by cation ordering. It turns out that a well-defined ordering also exists and has been found in a number of II-IV-N_2 compounds.[1-4] The same cation ordering is also found in $LiGaO_2$ [5], which can be thought of as a I-III-VI_2 analog of ZnO. As a starting point for studying the properties of this family of materials we here present computational results for $ZnGeN_2$. $ZnGeN_2$ can be synthesized in bulk form by reacting Zn or Zn_3N_2 with Ge_3N_4 powders [1,2] or in polycrystalline thin film form by a $HCl+NH_3$ based process similar to the one used for GaN synthesis [6] and more recently has been grown epitaxially by MOCVD [7]. Its crystal structure was determined by neutron diffraction [8]. Here we present the first electronic structure study of this material to the best of our knowledge.

METHOD OF COMPUTATION

The density functional method is used in the local density approximation and solved using the full-potential linearized muffin-tin orbital method [9]. Care must be taken to treat the Zn 3d bands which are overlapping with the bottom of the N2p valence band. In order to also treat the higher lying 4d like atomic wave function character mixed in with the valence and conduction band states a so-called coupled panel calculations [10,11] is used. Because the interatomic spacings in the nitrides is unusually small, and the structure is open because of the tetrahedral bonding, fairly small Ge and Zn spheres have to be used. This means that it becomes advisable to treat even rather deep semicore levels such as Ge3d as bands, which was thus done here.

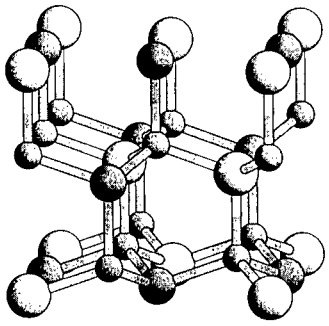


Figure 1: Crystal structure of $ZnGeN_2$: small spheres N, dark medium spheres Zn, light large spheres Ge.

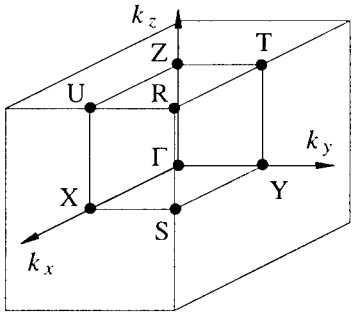


Figure 2: Brillouin zone of $ZnGeN_2$. X, Y, Z correspond to a, b, c with a horizontal, b normal to the page, and c vertical in Fig.1 .

As far as structures are concerned, we consider an idealized GaN wurtzite derived structure with the proper cation ordering but without bond relaxation, a structure in which the anion position is relaxed inside its nearest neighbor tetrahedron without cation sublattice distortions and finally, the actual experimental crystal structure. The latter is orthorombic with space group $Pna2_1$. Its relation to the wurtzite can be described as follows. The **a**-axis of the orthorhombic structure is along the [01-10] axis (or $\mathbf{a}_2$-$\mathbf{a}_3$) of wurtzite and the unit cell is double the lattice spacing of wurtzite in that direction, i.e.

approximately $a_{wz}\sqrt{3}$ with a_{wz} the wurtzite a-lattice constant, the **b**-axis is along the wurtzite [1000] direction (or $\mathbf{a}_1$) and also takes a doubled lattice spacing, and the **c**-axis is along **c** of wurtzite and takes the same lattice spacing as wurtzite. The actual lattice parameters are a=0.545 nm, b=0.6441 nm and c=0.5194 nm, which is close to a=0.5524 nm, b=0.6378 nm and c=0.5185 nm which one would obtain from GaN lattice constants in the above described way. The crystal structure is shown in Fig. 1 and the corresponding Brillouin zone is shown in Fig. 2.

For calculating the optical properties we use an atomic sphere approximation to the linear muffin-tin orbital method. The calculation of the imaginary part of the dielectric constant $\varepsilon_2(\omega)$ is done in the usual independent particle approximation without including local field effects. From it the index of refraction tensor and hence the birefringence is obtained in the usual manner by calculating first the real part of the dielectric function by Kramers-Kronig transformation and then taking the complex square root. The method for the second harmonic generation coefficient calculations is described elsewhere [12].

RESULTS

Structure and binding energy

The results of the total energy calculations are summarized in Table I. The bond lengths calculated in the model in which only the anion sublattice relaxes with respect to a fixed and undistorted cation lattice is relaxed are close to the average values obtained in the actual experimentally determined structure. This indicates that this is the most important factor in the relaxation. In fact, we find the cohesive energy calculated at the experimental lattice constant differs by less than 0.1 eV from it. The value for the bulk modulus is close to that of GaN. As usual for LDA, the volume per unit cell is slightly underestimated.

Table I: Structural and total energy properties of $ZnGeN_2$.

	Expt structure	Ideal structure	Anion relaxed Structure
Average Zn-N bond length (nm)	0.2019[a]	0.193	0.2014
Average Ge-N bond length (nm)	0.1885[b]	0.193	0.1857
Unit cell volume (nm^3)	0.182	0.177	0.178
Bulk modulus (Gpa)		187	189
Cohesive energy (eV/atom)	19.02	18.66	19.08
Formation enthalpy (kcal/mol)	-36		-36
LDA band gap (eV)	1.77	1.38	1.98
$a_g=dE_g/dlnV$ (eV)			-6.3

a. Actual bonds vary from 0.2005 to 0.2026 nm
b. Actual bonds vary from 0.1857 to 0.1898 nm

We also calculated the enthalpy of formation from the elements in their standard state, i.e. the reaction energy:

$$Zn(s)+Ge(s)+N_2(g)\rightarrow ZnGeN_2. \qquad (1)$$

In order to obtain adequate cancellation of the typical overbinding energies of LDA, the cohesive energies of Zn and Ge in their standard solid forms (hcp and diamond structure, respectively) were calculated at the same LDA level as the right hand side of the

equation. The LDA binding energy of the N_2 molecule was taken from Jones and Gunnarsson [13]. The negative number indicates that it is thermodynamically favorable to form the compound. Using the experimental enthalpy of Ge_3N_4, we can conclude that also the reaction

$$3Zn(s) + Ge_3N_4(s) + N_2 \rightarrow 3ZnGeN_2 \qquad (2)$$

is exothermic with enthalpy 30 kcal/mol.

Electronic properties

The band gaps are rather sensitive to the structure and are as usual severely underestimated by the LDA. One may expect a gap correction similar to that of GaN, i.e. about 1 eV. This would then lead to a predicted band gap of about 2.8 eV, in fair agreement with the value 2.7 eV obtained by optical absorption by Larson et al. [6]. This corresponds to the middle of the blue region of the spectrum.The band gap is found to be direct. The band structure is shown in Fig. 3 compared to that of GaN with the latter presented in the same Brillouin zone as $ZnGeN_2$ to facilitate the comparison.
The conduction band mass is found to be 0.23 along c, 0.25 along a and 0.26 along b, implying a slightly larger mass in-plane than perpendicular to the c-plane of the wurtzitic structure, similar to GaN [11].

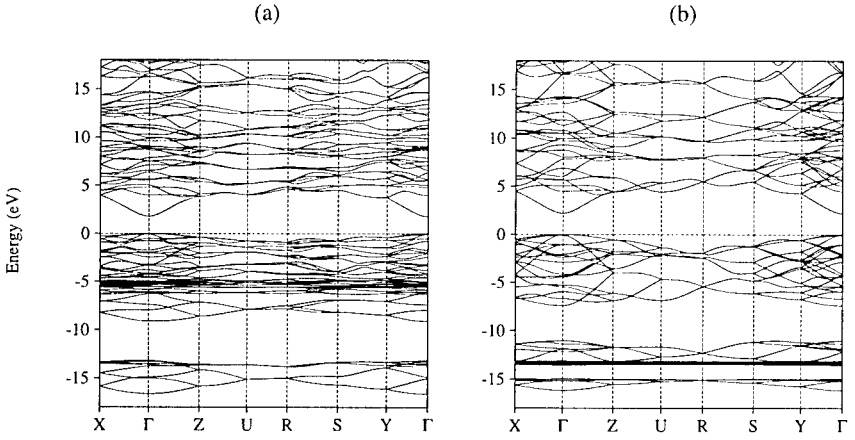


Figure 3: LDA band structures of $ZnGeN_2$ (a), and GaN (b) in the same Brillouin zone.

Optical properties

Fig. 4 shows the calculated imaginary parts of the dielectric function. Clearly, they exhibit anisotropy in all three directions. An analysis in terms of interband transitions will be presented elsewhere. Overall, the shape of the optical response is similar to that of GaN with a relatively flat region above the minimum direct band gap and an onset of the E1, E2 type transitions at about 6-7 eV. On the other hand, the indices of refraction shown in Fig. 5 derived from these show an almost uniaxial rather than biaxial behavior. The y and z components are quite close while the x component is different. The

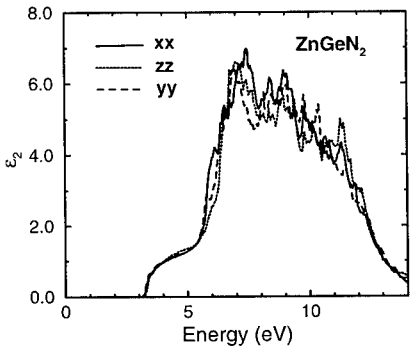


Figure 4: Imaginary part of the dielectric tensor of $ZnGeN_2$

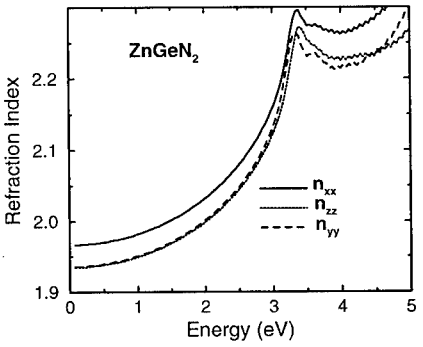


Figure 5: Indices of refraction of $ZnGeN_2$

birefringence is about 0.03 in the static limit (i.e. for low frequency compared to the gap but still only containing electronic contributions.) Viewed in this way as approximately uniaxial, it is a positive uniaxial crystal because the index of refraction along the axis which most differs from the other two is larger than the other two. Thus, it is possible to do type I (eeo) phasematching for second harmonic or sum frequency generation. It is of interest to compare this with GaN for which the birefringence is similar, also about 0.03 and also positive uniaxial, but now with the c-axis as the optical axis.[14] In GaN only type II (oeo) phase matching using the xzx component is possible because the xzz component of $\chi^{(2)}$ vanishes by symmetry. Note that in the usual notation the first component in xzx indicates the sum frequency or doubled frequency, while the last two indicate the fundamental. In the notation for phase matching however, it is the last index that indicates the sum frequency. In the oeo SHG phase matched process $[n_e(\omega)+n_o(\omega)]/2=n_o(2\omega)$, so only half the birefringence is effectively usable, meaning that the maximum frequency for which SHG is possible is smaller than for the eeo process. The calculated second harmonic generation coefficients of $ZnGeN_2$ in the static limit are given in Table II. The optimal coefficient that is phase matchable is the zxx component. Surprisingly, these SHG coeficients are smaller than in GaN by an order of magnitude [12]. The reason for this is not entirely clear but it appears to be a result of a large degree of cancellation between the so-called pure interband and mixed inter- and intraband contributions. This is illustrated in Fig. 6 for one of the components of the imaginary part of the SHG susceptibility.

Table II: SHG coefficients in $ZnGeN_2$ in the static limit (in pm/V)

zzz	zyy	zxx
-0.800	-0.293	-0.682

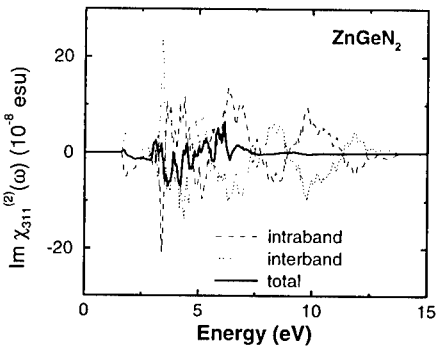


Figure 6: Imaginary part of $\chi_{zxx}^{(2)}(-2\omega,\omega,\omega)$ in $ZnGeN_2$ and its decomposition in intra- and interband components.

CONCLUSIONS

$ZnGeN_2$ is found to be a direct band gap semiconductor with a band gap corresponding to blue light and is a thermodynamically stable compound in contrast to $In_xGa_{1-x}N$ alloys. We found that the relaxations from the idealized wurtzite structure with ordered cations is dominated by a relative displacement of the anion versus the cation sublattice so as to accommodate the different bond lengths of Zn-N and Ge-N. A model which includes only this relaxation gives results for total energy, unit cell volume and average bond-lenghts of each type in good agreement with the experimentally determined structure.
Since this material has recently been grown in epitaxial thin film form, it would seem of interest to further study it for optoelectronic applications. Supported by Ballistic Missile Defense Organization Science and Technology through a STTR contract with NZ-Applied Technologies.

REFERENCES

1. M. Maunaye and J. Lang, Mater. Res. Bull. **5**, 793 (1970).
2. T. Endo, Y. Sato, H. Takizawa, and M. Shimida, J. Mater. Sci. Lett. **11**, 424 (1992).
3. P. Eckerlin, Z. anorg. allg. Chem. **5**, 225 (1967).
4. M. Wintenberger, F. Tcheou, J. David,and J. Lang, Z. Naturforsch. **35b**, 604 (1980).
5. S. Limpijumnong, W. R. L. Lambrecht, B. Segall, and K. Kim, in *III-V Nitrides*, ed. F. A. Ponce, T. D. Moustakas, I. Akasaki, and B. A. Monemar, Mat. Res. Soc. Symp. Proc. Vol. 449, (Mater. Res. Soc., Pittsburgh 1997), p. 905.
6. W. L. Larson, H. P. Maruska, and . A. Stevenson, J. Electrochem. Soc. **121**, 1674 (1974).
7. L. D. Zhu, P. H. Maruska, P. E. Norris, P. W. Yip, and L. Bouthilette, MRS Internet J. Nitride Semicond. Res. 4S1, G3.8 (1999).
8. M. Wintenberger, M. Maunaye, and Y. Laurent, Mat. Res. Bull. **8**, 1049 (1973).
9. M. Methfessel, Phys. Rev. B **38**, 1537 (1988).
10. D. J. Singh, Phys. Rev. B **43**, 6388 (1991).
11. K. Kim, W. R. L. Lambrecht, B. Segall, and M. van Schilfgaarde, Phys. Rev. B **56**, 7363 (1997).
12. S. N. Rashkeev, W. R. L. Lambrecht, and B. Segall, Phys. Rev. B **57**, 3905 (1998).
13. R. O. Jones and O. Gunnarsson, Rev. Mod. Phys. **61**, 689 (1989).
14. E. Ejder, Phys. Status Solidi (a) **6**, 442 (1971).

ELECTRICAL CHARACTERIZATION OF DEFECTS INTRODUCED IN n-GaN DURING HIGH ENERGY PROTON AND He-ION IRRADIATION

S. A. Goodman, F. D. Auret, F. K. Koschnick,* J.-M. Spaeth,* B. Beaumont** and P. Gibart**
Department of Physics, University of Pretoria, Pretoria 0002, South Africa
*Fachbereich Physik, Universität GH Paderborn, Paderborn, Germany
**CRHEA-CNRS, Valbonne, France.

Cite this article as: MRS Internet J. Nitride Semicond. Res. 4S1, G6.12 (1999)

ABSTRACT

We report on the electrical properties of defects as determined by deep level transient spectroscopy (DLTS) introduced in epitaxially grown n-GaN by 2.0 MeV protons and 5.4 MeV He-ions. After He-ion bombardment three electron traps ER3 (E_c - 0.196 eV), ER4 (E_c - 0.78 eV), and ER5 (E_c - 0.95 eV) were introduced uniformly in the region profiled by DLTS with introduction rates of 3270 ± 200, 1510 ± 300, and 3030 ± 500 cm^{-1} respectively. Capture cross section measurements revealed that the electron capture kinetics of ER5 is similar to that of a line defect. A defect with similar electronic properties as ER3 is observed after 2.0 MeV proton irradiation. The emission rate of ER3 depends on the electric field strength in the space-charge region. This emission rate is modelled according to the Poole-Frenkel distortion of a square well with a radius of 20 ± 2 Å or alternatively, a Gaussian well with a characteristic width of 6.0 ± 1 Å. Hence, we conclude that ER1 is a point defect which appears to have an acceptor like character. Two additional electron traps, ER1 (E_c - 0.13 eV) and ER2 (E_c - 0.16eV) with introduction rates of 30 ± 10 and 600 ± 100 cm^{-1} not thusfar observed after electron or He-ion bombardment were observed after proton irradiation.

INTRODUCTION

Gallium nitride has recieved a great deal of attention due to its unique properties and is fast becoming an established material for wide band gap optoelectronic devices. It continues to show potential as a suitable material for high temperature and power applications [1]. It has unique applications in blue, green and ultraviolet light emitting diodes, detectors and blue lasers [2]. The device performance of several device types, including fast switches [3] and detectors [4], has been improved by subjecting the devices to controlled doses of particle irradiation. For this, and any other form of defect engineering, it is essential that the electronic properties of the defects involved should be known so that their influence on materials properties and device behaviour can be calculated. Further, the structure and composition of the defects should be known so that they can be reproducibly introduced. In the case of GaN, the investigation of particle induced defects is still in its infancy and only a few papers have appeared concerning the electrical characterisation of radiation induced defects.

Regarding studies of defects induced in GaN by high energy (MeV) particles, Linde *et al* have firstly reported that 2.5 MeV electrons introduced two broad photoluminescence bands in a 1 μm thick GaN/Al_2O_3 layer [5]. Thereafter, Look *et al* used Hall measurements to detect and identify the nitrogen vacancy at 0.07 eV below the conduction band in GaN, introduced during irradiation with 0.7 - 1.0 MeV electrons. [6] Subsequently, Fang *et al* observed, using deep level transient spectroscopy, that electron irradiation introduced a defect, which they labelled *E*, with a level at 0.18 eV below the conduction band. [7]

In this paper we report the introduction rates and electronic properties of defects introduced in n-GaN by 5.4 MeV He-ion and 2.0 MeV proton irradiation. The dependence of

Mat. Res. Soc. Proc. Vol. 537 © 1999 Materials Research Society

the emission rate on electric field strength of defect ER3 is presented and discussed and we also present the true capture cross section of a deep lying defect, ER5.

EXPERIMENTAL PROCEDURE

For this study, 5 μm thick GaN epitaxial layers grown at 1080^{0}C on a 250 Å GaN buffer layer on sapphire by metal-organic vapor phase epitaxy (MOVPE) were either exposed to 5.4 MeV He-ions from a ^{241}Am radio-nuclide source or 2.0 MeV protons from a Van de Graaff accelerator. The nominally undoped GaN epitaxial layer had a free carrier concentration of approximately 2 - 3 x 10^{16} cm^{-3}. After boiling the samples in aqua-regia for ten minutes the samples were degreased [8]. Prior to ohmic contact fabrication the oxide layer was removed form the sample surface using a HCl : H_2O (1 : 1) solution for 10 seconds [9]. The composite ohmic contact layer [10] was Ti/Al/Ni/Au (150 Å/2200 Å/400 Å/500 Å). The contact fabrication was followed by a five minute anneal at 500 ^{0}C in an inert gas atmosphere. Gold Schottky barrier diodes (SBDs), 0.5 mm in diameter and 3000 Å thick were resistively deposited, these diodes had reverse leakage currents of the order of 10^{-10} A at 1 V and ideality factors between 1.05 and 1.10. The samples were exposed to 5.4 MeV He-ions by placing them on an ^{241}Am foil. The activity of the radionuclide being 192 μCi.cm^{-2} and the dose rate was 7.1 x 10^6 cm^{-2}.s^{-1}. Sampes exposed to 2.0 MeV protons in the Van de Graaff accelerator recieved a dose of (3 ± 1) x 10^{11} cm^{-2} at a dose rate of approximately 1 x 10^{10} cm^{-2}s^{-1}. A two-phase lock-in-amplifier-based (LIA) deep level transient spectroscopy (DLTS) system was used for the defect characterization in the as-grown material and the particle bombarded material. In order to simplify the determination of the emission kinetics of ER3 at different electrical field strengths in the space-charge region, isothermal DLTS was used.

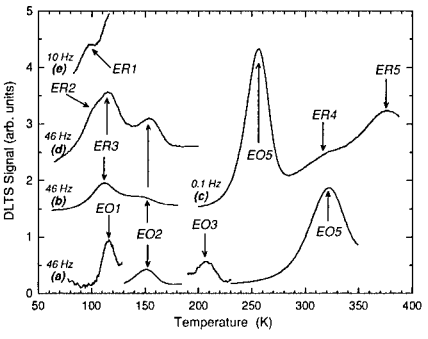


Figure 1: Curve (a): DLTS spectrum of as-grown MOVPE n-GaN. Curves (b) and (c): spectra recorded after 5.4 MeV He-ion irradiation. Curves (d) and (e): spectra recorded after 2.0 MeV proton irradiation. Curves (a) – (c) were recorded using a reverse bias (V_r) of 2.0 V and filling pulse amplitudes (V_p) of 2.2 V. For curves (d) and (e), V_r = 2.0 V and V_p = 0.5 V.

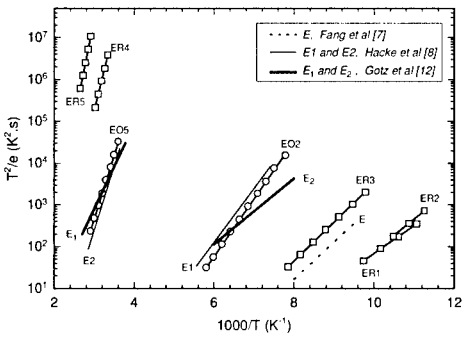


Figure 2: DLTS Arrhenius plots of defects in as grown n-GaN (open circles) and high ebergy He-ion and proton irradiation (open squares). Other lines are for defects detected in GaN by other authors.

RESULTS AND DISCUSSION

Fig. 1 depicts the DLTS spectra of control (curve (a)), 5.4 MeV He-ion irradiated (curves (b & c)) and 2.0 MeV proton irradiated (curves (d & e)) epitaxial n-GaN. Consider

ELECTRICAL CHARACTERIZATION OF DEFECTS INTRODUCED IN n-GaN DURING HIGH ENERGY PROTON AND He-ION IRRADIATION

S. A. Goodman, F. D. Auret, F. K. Koschnick,* J.-M. Spaeth,* B. Beaumont** and P. Gibart**
Department of Physics, University of Pretoria, Pretoria 0002, South Africa
*Fachbereich Physik, Universität GH Paderborn, Paderborn, Germany
**CRHEA-CNRS, Valbonne, France.

Cite this article as: MRS Internet J. Nitride Semicond. Res. 4S1, G6.12 (1999)

ABSTRACT

We report on the electrical properties of defects as determined by deep level transient spectroscopy (DLTS) introduced in epitaxially grown n-GaN by 2.0 MeV protons and 5.4 MeV He-ions. After He-ion bombardment three electron traps ER3 (E_c - 0.196 eV), ER4 (E_c - 0.78 eV), and ER5 (E_c - 0.95 eV) were introduced uniformly in the region profiled by DLTS with introduction rates of 3270 ± 200, 1510 ± 300, and 3030 ± 500 cm^{-1} respectively. Capture cross section measurements revealed that the electron capture kinetics of ER5 is similar to that of a line defect. A defect with similar electronic properties as ER3 is observed after 2.0 MeV proton irradiation. The emission rate of ER3 depends on the electric field strength in the space-charge region. This emission rate is modelled according to the Poole-Frenkel distortion of a square well with a radius of 20 ± 2 Å or alternatively, a Gaussian well with a characteristic width of 6.0 ± 1 Å. Hence, we conclude that ER1 is a point defect which appears to have an acceptor like character. Two additional electron traps, ER1 (E_c - 0.13 eV) and ER2 (E_c - 0.16eV) with introduction rates of 30 ± 10 and 600 ± 100 cm^{-1} not thusfar observed after electron or He-ion bombardment were observed after proton irradiation.

INTRODUCTION

Gallium nitride has recieved a great deal of attention due to its unique properties and is fast becoming an established material for wide band gap optoelectronic devices. It continues to show potential as a suitable material for high temperature and power applications [1]. It has unique applications in blue, green and ultraviolet light emitting diodes, detectors and blue lasers [2]. The device performance of several device types, including fast switches [3] and detectors [4], has been improved by subjecting the devices to controlled doses of particle irradiation. For this, and any other form of defect engineering, it is essential that the electronic properties of the defects involved should be known so that their influence on materials properties and device behaviour can be calculated. Further, the structure and composition of the defects should be known so that they can be reproducibly introduced. In the case of GaN, the investigation of particle induced defects is still in its infancy and only a few papers have appeared concerning the electrical characterisation of radiation induced defects.

Regarding studies of defects induced in GaN by high energy (MeV) particles, Linde *et al* have firstly reported that 2.5 MeV electrons introduced two broad photoluminescence bands in a 1 μm thick GaN/Al_2O_3 layer [5]. Thereafter, Look *et al* used Hall measurements to detect and identify the nitrogen vacancy at 0.07 eV below the conduction band in GaN, introduced during irradiation with 0.7 - 1.0 MeV electrons. [6] Subsequently, Fang *et al* observed, using deep level transient spectroscopy, that electron irradiation introduced a defect, which they labelled *E*, with a level at 0.18 eV below the conduction band. [7]

In this paper we report the introduction rates and electronic properties of defects introduced in n-GaN by 5.4 MeV He-ion and 2.0 MeV proton irradiation The dependence of

Mat. Res. Soc. Proc. Vol. 537 © 1999 Materials Research Society

the spectra for the as-grown material (curve (a)). In this defect labelling nomenclature, "E" implies electron trap and "O" that the material was grown by MOVPE. From the literature it appears that EO2 and EO5 are the same as the E1 and E2, respectively, observed by Hacke *et al* in n-GaN grown by hydride vapor-phase epitaxy [11]. These two defects also have similar sigantures as E_2 and E_1, respectively, detected by Götz *et al* in MOCVD grown GaN [12].
After exposing the GaN to 5.4 MeV He-ions, three prominent additional defects, ER3, ER4 and ER5, were observed (curves (b) and (c) in Fig. 1), defects, ER4 and ER5, were detected after recording DLTS spectra using a filling pulse frequency of 100 mHz, i.e. an emission rate of about 0.23 s^{-1}. The DLTS signatures of ER4 and ER5 were determined (Table I and Fig. 2) by using pulse frequencies of between 4.6 and 220 mHz. Note that under "typical" DLTS recording conditions (emission rates of 50 - 200 s^{-1}) the DLTS peaks of ER4 and ER5 would occur at (430 – 450 K) and (470 – 500 K) respectively, which is probably why they were not previously detected.

TABLE I. Electronic properties of defects introduced in epitaxial n-GaN by 5.4 MeV He-ion and 2.0 MeV proton irradiation.

Defect label	E_T (eV)	σ_{na} (cm^2)	T_{peak}[(a)] (K)	η (cm^{-1})	Similar defects
EO1	0.21	4×10^{-14}	114	grown in	
EO2	0.27	8×10^{-15}	156	grown in	E1[11]
EO3	0.45	7×10^{-13}	208	grown in	
EO5	0.61	1×10^{-14}	322	grown in	E2 [11]
2.0 MeV PROTON					
ER1	0.13	2×10^{-16}	98	30±10	
ER2	0.16	4×10^{-15}	103	400±150	
ER3	0.20	4×10^{-15}	121	600±100	E [7], $V_{Ga}N_i^{2-}$ [14]
5.4 MeV He-ION					
ER3	0.20	4×10^{-15}	121	3270±200	E [7], $V_{Ga}N_i^{2-}$ [14]
ER4	0.78	1×10^{-15}	323[(b)]	1510±300	—
ER5	0.95	3×10^{-14}	377[(b)]	3030±500	N_i [13], $V_{Ga}N_i^-$ [14]

[(a)] Peak temperature at a LIA frequency of 46 Hz, i.e. an emission rate of 108 s^{-1}. [(b)] Peak temperature at 0.1 Hz

The levels of ER4 (E_C - 0.78 eV) and ER5 (E_C - 0.95 eV) are the deepest radiation induced levels below the conduction band yet detected by DLTS. The only radiation induced defect related transitions with roughly the same energy as the ER4 and ER5 are those reported by Linde *et al* after a photoluminescence (PL) study of electron irradiated GaN [5]. These authors found that electron irradiation introduces two PL bands centred around 0.85 and 0.93 eV, respectively, and using optically detected magnetic resonance, they tentatively identified the latter as a Ga_I^{2+}-complex. Due to the fundamental differences in the origin of DLTS and PL spectra, no direct comparison between their PL and our DLTS spectra is possible.

However, since Ga interstitials are formed during irradiation, they, or complexes including them, are likely to yield deep levels which can be detected by DLTS. Alternative possibilities for structure of ER5 is the N-interstitial, which was predicted to result in levels near the center of the band gap [13], and the $V_{Ga}N_i^-$ and $V_{Ga}N_i^{2-}$ states with levels calculated to be in the upper half of the bandgap [14].

Curves (d) and (e) in Fig. 1, recorded using different filling pulse conditions, show that proton bombardment introduces the defects ER1 – ER3. Defect, ER1 could only be clearly detected when using pulse widths, t_p, of less than 2 μs. Using a filling pulse width of t_p = 400 ns, we have determined the activation energy of ER1 as 0.13±0.01 eV below the conduction band (Fig. 2). For pulse widths larger than 1 μs, the ER3 peak appears and seems to reach a maximum for a pulse width of about 1 ms at 121 K, indicating that ER3 has a small electron capture cross section.

As the ER3 amplitude grows with increasing pulse width, it obscures the detection of the much smaller ER1 peak. When increasing the pulse width to above 1 ms, the ER3 peak showed a broadening. The extraordinary large pulse widths required to detect ER2 indicate that its real electron capture cross section is even smaller that of ER3 (unlike their almost identical apparent capture cross-sections).

The signature of ER3 was determined using t_p = 50 μs. This pulse width yields a strong ER3 signal but it is too narrow for ER2 to capture a significant amount of carriers and thus to contribute to the DLTS signal at the temperatures where we studied ER3. The energy level thus determined, E_C - 0.20±0.01 eV, is similar to that of a defect, labelled *E*, with a level at E_C - 0.18 eV, observed by Fang *et al* [7] after electron irradiation of MOVPE (metal-organic vapor phase epitaxy) grown GaN. These authors pointed out that, should this defect have a temperature activated capture cross section, its actual position in the bandgap may be close to that of V_N (E_C - 0.07) [6], but no firm identification has yet been made. To extract the electronic properties of ER2, spectra which were recorded at different frequencies, using pulses just sufficient to saturate ER3, were subtracted from spectra recorded with a wide enough pulse to clearly show the ER2 signal. This procedure yielded an activation energy of 0.16±0.03 eV.

In Fig. 3 the experimentally measured emission rate of ER3 as a function of the square root of the electric field in the space charge region is shown. In order to establish the potential associated with this defect the experimental data was modelled making use of various simple defect potential models. It would appear that the square well and the gaussian well with their particular physical dimensions, both provide an adequate description of defect ER3. In an attempt to understand how both potentials describe the experimental results, a comparison of the distortion of these potentials at a reasonably high (2.5 x 10^5 V/cm) electric field strength was investigated. Figure 4 schematically represents the distortion of a square and a gaussian well. It is clear from this figure that using either a gaussian or a square well with the specified physical attributes can adequately describe the enhanced emission kinetics of ER3.

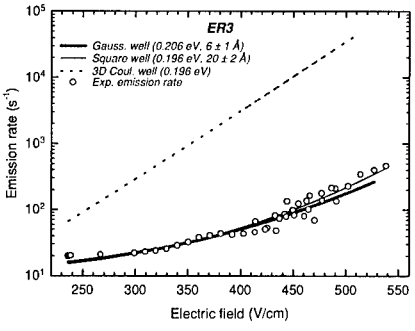


Figure 3: The experimental and modelled emission kinetics of defect ER3 as a function of electric field strength in the space charge region.

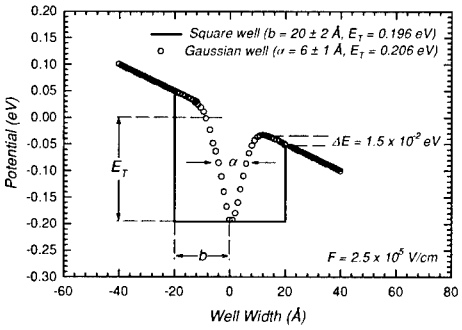


Figure 4: The reduction in potential for a gaussian and a square well, when the electric field strength in the space charge region is 2.5 x 10^5 V/cm.

Capture cross section (σ_n) measurements of ER5 were performed using pulse widths, t_p, of between 50 ns and 50 ms. As shown in Fig. 5, the DLTS signal of ER5 increased monotonically with t_p for the whole pulse width range investigated. Because the total concentration of radiation induced defects in the sample used for this measurement was much lower than the free carrier concentration, this incomplete filling of ER5 is not due to a competition for electrons between ER5 and the shallow donors. The presence of a straight line region in the plot of ΔC/C vs log(*t*) in Fig. 5 is similar to what has been observed for carrier capture by traps which are *not randomly* distributed, but which are arranged along lines [15].

In such a case the capture rate is limited by a Coulomb barrier which increases with increasing charge capture onto the extended defects. The data presented here strongly suggests that ER5 is a line defect, or an extended defect, where charge build-up governs the capture rate.

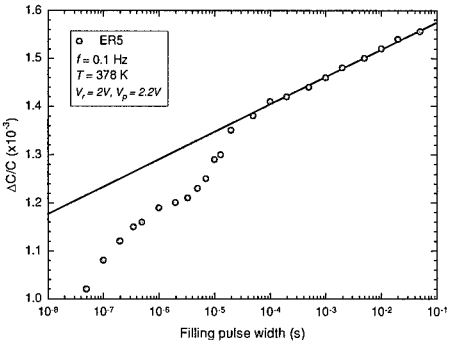


Figure 5: DLTS signal (S(t) = ΔC/C) as function of log(t) for ER5. The error in S(t) is about the same as the height of the symbol.

Regarding the formation mechanism for such a defect, it should be noted that 5.4 He-ions can transfer sufficient energy to the GaN lattice to cause defect spikes or extended regions of disorder.

CONCLUSIONS

In conclusion, we have determined the electronic properties of 4 electron defects (EO1 – EO3, EO5) present in as-grown MOVPE n-GaN. This material was then subjected to high energy He-ion or proton irradiation, wherupon additional electron defects were introduced. After the 5.4 MeV He-ion irradiation 3 additional defects (ER3 – ER5) were measured. The emission charateristics of defect ER3 does not exhibit the typical dependence on $F^{1/2}$ that is classicaly used to determine the electronic type of the defect. The temperature dependance of the capture cross-section of defect, ER5 suggests that it may be a line or an extended defect. After 2.0 MeV proton irradiation 3 defects (ER1 – ER3) were observed. Thusfar the major proton irradiation induced defect ER2 has not been observed in similar material exposed to high energy He-ions. Defect ER3 is similar to that observed after 5.4 MeV He-ion irradiation.

ACKNOWLEDGMENTS

We gratefully acknowledge financial assistance from the South African Foundation for Research Development. We also thank G. Myburg for ohmic contact metallisation and W.E. Meyer for assistance with the isothermal DLTS measurements.

REFERENCES

[1] K. Doverspike, A. E. Wickenden, S. C. Binarii, D. K. Gaskill and J. A. Freitas, Mat. Res. Soc. Symp. Proc. Vol. 395, p897 (1996).

[2] S. Nakamura and G. Fasol, in "The blue laser diode", (Springer Verlag, 1997).

[3] M. Lambsdorff, J. Kohl, J. Rosenzweig, A. Axmann and J. Schneider, Appl. Phys. Lett. 58, 1881 (1991).

[4] V. M. Rao, W-P Hong, C. Caneau, G-K. Chang, N. Papanicolaou, and H. B. Dietrich, J. Appl. Phys. 70, 3943 (1991).

[5] M. Linde, S.J. Uftring, G.D. Watkins, V. Harle and F. Scholz, Phys. Rev. B 55, R10177 (1997).

[6] D.C. Look, D.C. Reynolds, J.W. Hemsky, J.R. Sizelove, R.L. Jones and R.J. Molnar, Phys. Rev. Lett. 79, 2273 (1997).

[7] Z-Q. Fang, D. C. Look, W. Kim, Z. Fan, A. Botchkarev and H. Morkoc, Appl. Phys. Lett. 72, 2277 (1998).

[8] P. Hacke, T. Detchprohm, K. Hiramatsu, and N. Sawaki, Appl. Phys. Lett. 63, 2676 (1993).

[9] J.K. Sheu, Y.K. Su, G.C. Chi, W.C. Chen, C.Y. Chen, C.N. Huang, J.M. Hong, Y.C. Yu, C.W. Wang, and E.K. Lin, J. Appl. Phys. 83, 3172 (1998).
[10] S. Ruminov, Z. Liliental-Weber, J. Washburn, K.J. Duxstad, E.E. Haller, Z.-F. Fan, S.N. Mohammed, W. Kim, A.E. Botchkarev, and H. Morkoc, Appl. Phys. Lett. 69, 1556 (1996).
[11] P. Hacke, T. Detchprohm, K. Hiramatsu and N. Sawaki, Appl. Phys. Lett. 63, 2676, (1993).
[12] W. Götz, N. M. Johnson, H. Amano and I. Akasaki, Appl. Phys. Lett. 65, 463 (1994).
[13] J. Neugebauer and C.G. Van de Walle, Phys. Rev. B 50, 8067 (1994).
[14] T. Mattila, A.P. Seitsonen and R.M. Nieminen, Phys. Rev. B 54, 1474 (1996).
[15] T. Wosinski, J. Appl. Phys. 65, 1566 (1988).

ELECTRICAL CHARACTERIZATION OF SPUTTER DEPOSITION INDUCED DEFECTS IN n-GaN

F. D. Auret, S. A. Goodman, F. K. Koschnick,* J.-M. Spaeth,* B. Beaumont** and P. Gibart**

Department of Physics, University of Pretoria, Pretoria 0002, South Africa

*Fachbereich Physik, Universität GH Paderborn, Paderborn, Germany

**CRHEA-CNRS, Valbonne, France.

Cite this article as: MRS Internet J. Nitride Semicond. Res. 4S1, G6.13 (1999)

ABSTRACT

We have used current-voltage (*I-V*) measurements to assess and compare the electrical characteristics of resistively evaporated and sputter deposited Au Schottky contacts on epitaxially grown GaN. These *I-V* measurements revealed that resistively deposited Au contacts exhibited excellent rectification properties: high barrier height, low reverse current and good ideality factor ($n = 1.04$). In contrast, sputter deposited contacts had poor characteristics: low barrier height, high reverse current and non-linear forward *I-V* characteristics. The cause of this is thought to be defects introduced at and near the surface during sputter deposition. Deep level transient spectroscopy (DLTS) showed that at least four defects, with energy levels at 0.22±0.02 eV, 0.30±0.01 eV, 0.40±0.01 eV and 0.45±0.10 eV below the conduction band, were introduced in the GaN during sputter deposition. The first of these defects has similar electronic properties as a radiation induced defect in GaN, speculated to be the nitrogen vacancy, while the second appears to be the same as a defect in the as-grown material. The latter two defects have not previously been observed in as-grown or processed epitaxial GaN.

INTRODUCTION

Gallium nitride is a direct wide band-gap semiconductor which has unique applications in blue, green and ultraviolet light emitting diodes, detectors and blue lasers [1]. Because of its low thermal generation rates and high breakdown fields, an inherent property of wide bandgap semiconductors, it also has recently also shown to be important in the field of high temperature and power electronics [2]. The fabrication of these electronic devices requires, among others, metallisation for ohmic or Schottky contacts on the GaN. The metallisation method chosen for this purpose has to fulfil several requirements, including good adhesion of the metal to GaN. Sputter deposition is a metallisation method which is frequently employed because sputter deposited layers exhibit better adhesion compared to layers deposited by other methods [3]. In addition, sputter deposition facilitates the stoichiometric deposition of compounds and controllable deposition of high melting point metals, and yields high deposition rates. However, due to the energetic particles involved, sputter deposition is damaging on an atomic scale and causes lattice disorder at and below to the semiconductor surface [4].

It has been reported that the barrier heights of sputter-deposited Schottky contacts on n-type Si [5] and n-type GaAs [6] are lower than those of similar contacts deposited by other less damaging processes (e.g. resistive evaporation), while for p-type Si [7] and p-type GaAs [8] the

Mat. Res. Soc. Proc. Vol. 537 © 1999 Materials Research Society

opposite was found. Using deep level transient spectroscopy (DLTS) [9], it was shown that this barrier height alteration was accompanied by the introduction of sputter deposition induced defects at and below the semiconductor surface, thought to be the cause of the barrier alteration [4]. No studies have yet been reported for GaN where the contact quality and metallization induced defects are investigated as function of the metallization process.

In this paper we report the current-voltage (*I-V*) characteristics of resistively evaporated and sputter deposited Au Schottky contacts on epitaxially grown GaN. We also report the properties of the defects, determined by DLTS, present in epitaxially grown GaN before and after sputter deposition of Au Schottky contacts thereon. We show that sputter deposition introduces at least four electron traps, two of which have not previously been observed in as-grown or in processed epitaxial GaN.

EXPERIMENTAL PROCEDURE

For this study we used epitaxial GaN with a free carrier density of $(2–3)\times10^{16}$ cm^{-3}, grown by organo-metallic vapor phase epitaxy (OMVPE). Before contact fabrication, the samples were cleaned [10] by first boiling them in aqua-regia and rinsing in de-ionised water, and then degreasing them by boiling in trichloroethylene followed by rinsing in boiling isopropanol and thereafter in de-ionised water. Finally, the samples were dipped in HCl:H_2O (1:1) for 10 seconds. After this cleaning, Ti/Al/Ni/Au (150 Å/2200 Å/400 Å/500 Å) ohmic contacts [11] were fabricated on the GaN and annealed at 500 °C for 5 minutes in Ar. Prior to Schottky barrier diode (SBD) fabrication, the samples were again degreased and dipped in an HCl:H_2O (1:1) solution. Following this, circular Au Schottky contacts, 0.6 mm in diameter and 1 μm thick, were sputter-deposited on the GaN through a metal contact mask, as close as possible to the ohmic contact to minimise the diode series resistance. Sputter deposition was performed in DC mode at a power of 0.141 kW in an Ar pressure of $4.8\text{x}10^{-3}$ mbar at a rate of 4.5 nm s^{-1}. For control purposes, Au SBDs were resistively deposited next to the sputter deposited SBDs.

Room temperature current-voltage (*I-V*) measurements were used to assess the quality of the Schottky contacts. The sputter deposition induced defects were characterised by DLTS using a Stanford Research lock-in amplifier (model SR830), which facilitates transient analysis at pulse frequencies of as low as 1 mHz. The energy level, E_T, in the bandgap and apparent capture cross section, σ_a, of a defect, the combination of which is referred to as its DLTS "signature", were determined from Arrhenius plots of T^2/e vs $1/T$, where e is the emission rate at a temperature T.

RESULTS AND DISCUSSION

I-V Measurements

I-V measurements showed that resistively deposited Au SBDs exhibited excellent rectification properties (Fig. 1). The forward *I-V* curves of these diodes are linear for at least seven decades of current and the ideality factor calculated, assuming thermionic emission, was 1.04. The barier height of these diodes is (0.96±0.02) eV and the current at a 1 V reverse bias, I_R, is $< 10^{-11}$ A. In contrast, Fig. 1 shows that the sputter deposited contacts exhibit poor rectification characteristics: non-linear forward *I-V* characteristics and high reverse currents ($\bullet\ 2\times10^{-4}$ A). Because the forward log(*I*) vs *V* characteristics of the sputter deposited diodes were non-linear, no ideality factor was calculated. The barrier height estimated from the reverse *I-V* characteristics

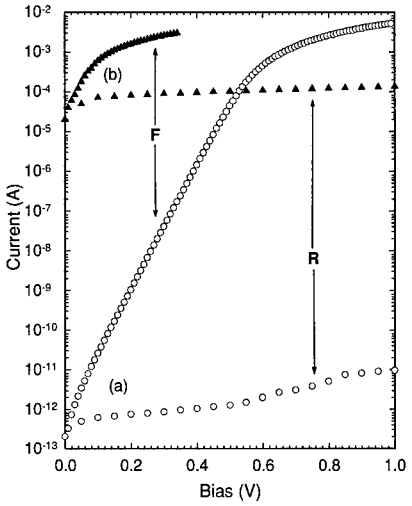


Figure 1: Room temperature forward (F) and reverse (R) *I-V* curves of Au contacts deposited on n-GaN by: (a) resistive evaporation (circles); (b) sputter deposition (triangles).

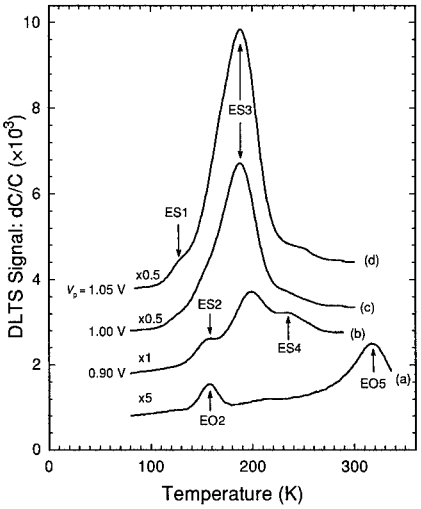


Figure 2: Curve (a): DLTS spectrum of resistively deposited SBD on epitaxial *n*-GaN. Curves (b) - (d) are for a sputter deposited SBD using a lock-in frequency of 46 Hz, a filling pulse width of 0.2 ms, a reverse bias of 1 V and filling pulse amplitudes, V_p, as indicated.

(assuming thermionic emission) of these diodes was (0.47±0.03) eV, which is significantly lower than the barrier height of resistively deposited contacts. These *I-V* measure-ments confirm that, as for Si [5] and GaAs [6], sputter deposition of Schottky contacts on n–GaN yields diodes with a drastically reduced barrier height and inferior rectification characteristics. It should be pointed out, however, that sputter-deposited Au contacts adhered much better to the GaN than resistively evaporated Au contacts.

DLTS Measurements

Fig. 2 depicts the DLTS spectra of control (resistively deposited) and sputter-deposited diodes. Curve (a) shows that the control sample contained two defects, labelled EO2 and EO5, with energy levels at 0.27±0.01 eV and 0.61±0.02 eV below the conduction band, respectively. In this defect labelling nomenclature, "E" implies electron trap and "O" that the material was grown by OMVPE. From the literature it appears that EO2 and EO5 are the same as the E1 and E2, respectively, observed by Hacke *et al* in n-GaN grown by hydride vapor-phase epitaxy [12]. These two defects also have similar sigantures as E_2 and E_1, respectively, detected by Götz *et al* in MOCVD grown GaN [13]. Curves (b) - (d) in Fig. 2 show that after sputter deposition, defects labelled ES1, ES2/EO2, ES3 and ES4 are detected. These curves also show that the peak heights of the sputter induced defects increase strongly with increasing filling pulse height, indicating an increase of the concentration of the sputter induced defects towards the Au/GaN interface. This

trend was also previously observed for defects introduced by sputter deposition of Schottky contacts on Si [5] and GaAs [6]. Note that EO5 is absent in the spectra of sputter deposited SBDs. The reason for this is that the energy level of EO5 is 0.61 eV below the conduction band whereas the barrier height of the sputter deposited SBDs is only 0.47 eV. Therefore, during the quiescent DLTS bias the EO5 level remains below the Fermi level [14] and, consequently, it does not emit carriers.

For determining the defect signatures, the overlapping peaks in Fig. 2 had to be separated. To achieve this, we followed two strategies. Firstly, we recorded spectra at fixed values of the quiescent bias, V_r, and filling pulse amplitude, V_p, but at different filling pulse durations, t_p, in the range 20 ns < t_p < 100 μs. Secondly, we kept V_r and t_p constant and recorded spectra while increasing V_p in steps of 0.05 V up to the flatband condition. Some of these spectra are depicted in Fig. 3. The ES2/EO2 peak was found to be well defined for 50 ns < t_p < 5 μs (curve (b)), whereas the ES4 peak is best defined for 500 ns < t_p < 5 μs (curve (c)). The ES3 peak only appears for t_p • 10 μs (curve (d)). Spectra recorded at different V_p, while V_r and t_p were kept constant, revealed the presence of another defect, ES1, for V_p • 1.25 V (curve (f) in Fig. 3).

The separation between the ES1 and ES2/EO2 peak positions was more clearly observed at low pulse frequencies and therefore the signature of ES1 was determined using frequencies of below 10 Hz. The defect signatures of ES2/EO2, ES3 and ES4, were determined using pulse widths where their peak shapes were optimised as described above and frequencies of 1 - 220 Hz. From Fig. 3, where we compare the signatures of the sputter induced defects to those of radiation-induced defects and defects in as-grown OMVPE GaN, it seems that two of the defects observed after sputter deposition may be the same as other defects previously reported in GaN.

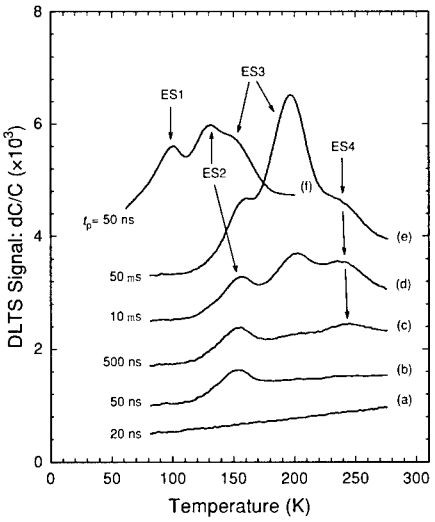


Figure 3. DLTS spectra of a sputter deposited Au Schottky contact on epitaxial GaN recorded using V_r = 1 V and different pulse widths, as indicated in the figure. Spectra (a) - (e) and (f) were recorded at V_p = 1.1 and 1.2 V, respectively, and lock-in amplifier frequencies of 46 Hz and 1 Hz, respectively.

Firstly, the signature of ES1, with a level at E_C - 0.22±0.02 eV, is similar to that of the ER3 defect with a level at E_C - 0.20±0.01 eV, which was observed after 5.4 MeV He-ion irradiation and 2 MeV proton irradiation of the same epitaxial GaN [15]. ER3, in turn, is thought to be the same as a defect, labelled *E*, with a level at E_C - 0.18 eV, observed by Fang *et al* [16] after electron irradiation of MBE-grown GaN. These authors pointed out that, should the capture cross section of this defect be temperature activated, then its actual position in the bandgap may be close to that of V_N (E_C - 0.07) [16], but no firm identification has yet been made. Secondly, ES2, with a level at E_C - 0.30±0.01 eV, has almost the same DLTS "signature" as EO2, with a level at E_C - 0.27±0.01 eV, which is

present in as-grown GaN. If these defects are the same, then it implies that sputter deposition resulted in an increase of the EO2 (ES2) concentration towards the GaN surface.

The ES3 and ES4 defects, with levels at E_C - 0.40±0.01 eV and E_C - 0.45±0.10 eV, have not been observed before in irradiated or in as-grown epitaxial n-GaN. Their signatures also do not correspond to those of defects introduced by nitrogen implantation of GaN, where it was suggested that one of the defects thus introduced may be a N interstitial [17]. These observations suggest that ES3 and ES4 are not related to the simple radiation induced point defects detected up to now. This can be explained by the fact that sputter deposition introduced several defects, other than the point defects introduced by high-energy irradiation. The formation of such complex type defects is the result of energetic particles, like Ar ions, entering the GaN during sputter deposition and losing energy at a high enough rate to create defects in close proximity of each other which can combine or interact.

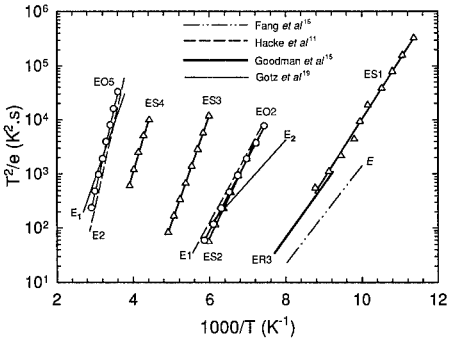


Figure 4: DLTS Arrhenius plots of defects in as-grown and particle-processed epitaxial GaN. Open circles and triangles are for defects present before and after sputter deposition, respectively, detected in the present study.

The peak shape and electronic properties of ES4 were found to be strongly dependent on the pulse height. Increasing the pulse height resulted in a broadening of the peak and a shift to lower temperatures. The same behaviour could not be induced when maintaining a fixed pulse level, and increasing the reverse bias, ruling out the possibility of this behaviour being due to electric field assisted emission. This behaviour of ES4 is similar to that of defects introduced during low energy Ar ion bombardment of GaAs where it was shown that those defects are located close to the surface and have a band-like energy distribution [18].

CONCLUSIONS

We have shown that sputter deposition of Au Schottky contacts on n-GaN results in SBDs with poor rectification properties and introduces electron traps, labelled ES1 - ES4. ES1, is located at E_C - 0.22±0.02 eV and has a similar DLTS signature as the E and ER3 defects, introduced in epitaxial GaN by high energy electron and He-ion irradiation, respectively. ES2 seems to be the same as the EO2 defect in as-grown GaN. The concentrations of ES1 - ES4 increase strongly towards the interface, indicating that this is the region where most of the sputter-induced damage resides. The ES3 and ES4, with energy levels at E_C - 0.40±0.01 eV and E_C - 0.45±0.10 eV, respectively, have not previously been observed in as-grown or particle bombarded GaN. Finally, it should be stressed that the sputter-deposited Au contacts adhered considerably better to GaN than resistively evaporated Au contacts.

ACKNOWLEDGMENTS

We gratefully acknowledge financial assistance from the South African Foundation for Research Development and the Forschungszentrum Jülich, International Bureau. We also thank G. Myburg for ohmic contact metallisation and C. du Toit for sputter deposition.

REFERENCES

[1] S. Nakamura and G. Fasol, in "The blue laser diode", (Springer Verlag, 1997).

[2] K. Doverspike, A. E. Wickenden, S. C. Binarii, D. K. Gaskill and J. A. Freitas, Mat. Res. Soc. Symp. Proc. Vol. 395, p897 (1996).

[3] L. I. Maissel: in "Handbook of thin film technology", (ed. L. I. Maissel and R. Glan), 1-4; 1970, New York, McGraw-Hill.

[4] F. H. Mullins and A. Brunnschweiler, Solid State Electron. **19**, 47 (1976).

[5] E. Grussell, S. Berg and L. P. Andersson, J. Electrochem. Soc. **127**, 1573 (1980).

[6] D. A. Vanderbroucke, R. L. van Mierhaegte, W. H. Lafrere and F. Cardon, Semicond. Sci. Technol. **2**, 293 (1987).

[7] S. J. Fonash, S. Ashok and R. Singh, Appl. Phys. Lett. **39**, 423 (1981).

[8] F. D. Auret, S. A. Goodman, Y. Leclerc, G. Myburg and C. Schutte, Materials Science and Technology **13**, 945 (1997).

[9] D. V. Lang, J. Appl. Phys. **45**, 3023 (1974).

[10] P. Hacke, T. Detchprohm, K. Hiramatsu and N. Sawaki, Appl. Phys. Lett. **63**, 2676, (1993).

[11] S. Ruvimov, Z. Liliental-Weber, J. Washburn, K. J. Duxstad, E. E. Haller, Z.-F. Fan, S. N. Mohammed, W. Kim, A. E. Botchkarev and H. Morkoc, Appl. Phys. Lett. **69**, 1556, (1996).

[12] P. Hacke, T. Detchprohm, K. Hiramatsu, N. Sawaki, K. Tadatomo and K. Miyake, J. Appl. Phys. **76**, 304 (1994).

[13] W. Götz, N. M. Johnson, H. Amano and I. Akasaki, Appl. Phys. Lett. **65**, 463 (1994).

[14] Q. Y. Ma, M. T. Schmidt, X. Wu, H. L. Evans and E. S. Yang, J. Appl. Phys. **64**, 2469 (1988).

[15] F. D. Auret, S. A. Goodman, F. K. Koschnick, J.-M. Spaeth, B. Beaumont and P. Gibart, Appl. Phys. Lett. (L98-6265), January18, 1999.

[16] Z-Q. Fang, D. C. Look, W. Kim, Z. Fan, A. Botchkarev and H. Morkoc, Appl. Phys. Lett. **72**, 2277 (1998).

[17] D. Haase, M. Schmid, W. Kürner, A. Dörnen, V. Härle, F. Scholtz, M. Burkard and H. Schweitzer, Appl. Phys. Lett. **69**, 2525 (1996).

[18] F. D. Auret, G. Myburg, S. A. Goodman, L. J. Bredell and W. O. Barnard, Nucl. Instr. and Meth. in Phys. Res. B**67**, 411 (1992).

PHOTOLUMINESCENCE OF FS-GaN

TREATED IN ALCOHOLIC SULFIDE SOLUTIONS

Y.V.Zhilyaev, M.E.Kompan, E.V.Konenkova*, S.D.Raevskii

A.F.Ioffe Physico-Technical Institute, Russian Academy of Sciences,
Politekhnicheskaya 26, St. Petersburg, 194021, Russia
* lena@triat.ioffe.rssi.ru

Cite this article as: MRS Internet J. Nitride Semicond. Res. 4S1, G6.14(1999)

Abstract

Results are presented on the photoluminescence of n-GaN (T=300 K) after surface treatment with sulfide (Na_2S and $(NH_4)_2S$) solutions in water or isopropyl alcohol.

It has been shown that the intensity of the n-GaN photoluminescence band is enhanced as a result of the surface treatment with alcoholic sulfide solutions, this enhancement being greater for a strongly basic Na_2S solution than for a weakly basic $(NH_4)_2S$ solution.

Introduction

The progress in UV semiconductor optoelectronics relies not only on the advance of fabrication methods of III-V nitrides but on the surface treatment methods as well. In the last years a number of studies [1-3] was published dealing with modification of the electronic properties of the GaN surface treated with liquid or gaseous agents. For chemical treatment in solutions, both acids and bases are used: HCl, HF, NH_4F, HNO_3, H_2SO_4, H_3PO_4, H_2O_2, NH_4OH, NaOH, KOH [3]. Studies of the electronic properties of III-V semiconductor surfaces aim first of all at reducing the surface recombination velocity, increasing the photoluminescence quantum yield and so on. To achieve modification of the surface electronic properties, aqueous [4] or alcoholic [5] solutions of sulfides (Na_2S and $(NH_4)_2S$) can be used.

In this study an attempt was undertaken to apply the technology of surface passivation employing alcoholic sulfide solutions in order to improve the electronic properties of GaN, in particular, the photoluminescence intensity.

Experiment

The specimens under study were n-GaN layers ($n=5\times10^{18}$ cm^{-3}) of a thickness 200-400 μm grown on sapphire substrates by chloride gas transport epitaxy [6]. After termination of the epitaxial growth process the layers were separated from the substrate (free-standing GaN).

Chemical treatment of the GaN surface was performed by dipping the semiconductor specimen at room temperature for 1 min into one of the following solutions: 10% aqueous

Mat. Res. Soc. Proc. Vol. 537 © 1999 Materials Research Society

solution of $(NH_4)_2S$, 1% solution of $(NH_4)_2S$ in isopropyl alcohol ($i\text{-}C_3H_7OH$), and saturated Na_2S solutions in water or isopropyl alcohol.

The room temperature photoluminescence was excited with a pulsed nitrogen laser (λ=337 nm, I=20 W). The experimental setup was similar to that of Ref. [7].

Results

The experimental results are as follows. The photoluminescence intensity of n-GaN increased as a result of the sulfide treatment of the surface in solutions of both sodium sulfide and ammonium sulfide (Fig.1). The most pronounced intensity increase (by a factor of 3.6) compared with the intensity of untreated n-GaN was observed for treatment with the saturated solution of Na_2S in isopropyl alcohol.

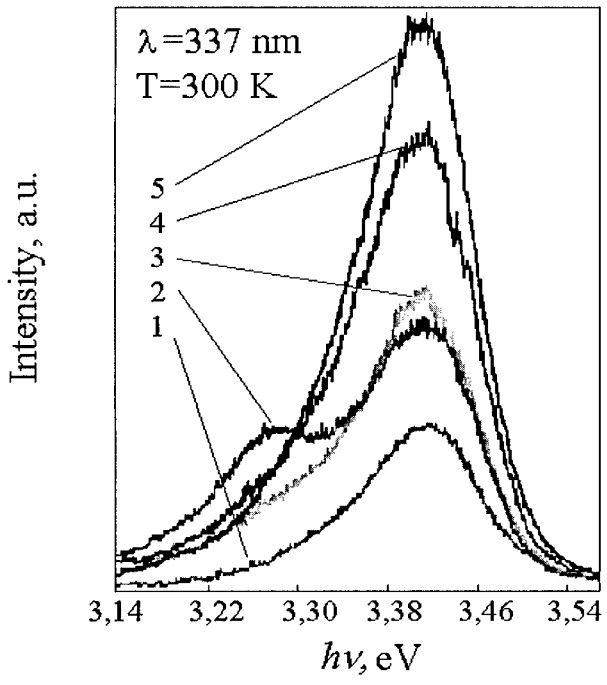


Fig.1. Photoluminescence spectra of the n-GaN surface after sulfidizing in one of the following four solutions: 10% aqueous solution of $(NH_4)_2S$ (2), 1% solution of $(NH_4)_2S$ in isopropyl alcohol ($i\text{-}C_3H_7OH$) (3), and saturated Na_2S solutions in water (4) or isopropyl alcohol (5). The photoluminescence peak intensity of untreated GaN (1) is assumed to be unity.

The increase in the GaN photoluminescence intensity following treatment with sulfide solutions in isopropyl alcohol can possibly be explained using mechanisms of the chemical processes taking place during sulfidizing of GaAs surface[8]. Sodium sulfide is known to be a salt of a strong base and a weak acid whereas ammonium sulfide is a salt of a weak base and a weak acid. It is therefore evident that in the case of treatment with alcoholic solutions of sodium sulfide the rate of chemical reaction with the GaN surface should be higher than for treatment in alcoholic solutions of ammonium sulfide. In the chemical treatment of III-V semiconductor surfaces (GaAs) the chemical reaction rate is the dominant factor affecting electronic properties of the surface [8], and it can be presumed that this should be true in the instance of III-V nitrides as well. Considering the fact that the chemical reaction rate for the aqueous sodium sulfide solutions is the lowest among the solutions used, it is no wonder that the effect of the chemical treatment of GaN surfaces in these solutions is practically unobservable (Table I).

As seen from a comparison of the photoluminescence intensity of GaN observed in this study and that of GaAs treated with strongly basic salts (Na_2S) and weakly basic salts ($(NH_4)_2S$) as measured in Ref.9, the photoluminescence intensity enhancement in both semiconductors is in good agreement with the adopted reaction mechanisms [8].

It should be note that similar increasing of photoluminescence intensity observed after the anneal of GaN at a temperature of 1000 °C or the sputtering with nitrogen ions [10].

Table I. The observed intensities of the photoluminescence peaks of GaN and GaAs [9] after various chemical treatments in sulfide solutions.

Treatment	*GaN* ($n=5\times10^{18}c\bullet^{-3}$)	*GaAs* ($n=1\times10^{18}c\bullet^{-3}$) *[9]*
	I, a.u.	I, a.u.
untreated	1,0	1,0
$(NH_4)_2S+H_2O$	1,7	1,5
$(NH_4)_2S+i\text{-}C_3H_7OH$	1,9	1,7
Na_2S+H_2O	2,9	1,5
$Na_2S+i\text{-}C_3H_7OH$	3,6	2,3

Conclusions

Thus, a new technique of GaN surface passivation - sulfidization in alcoholic solutions has been suggested. The chemical treatment of the n-GaN surface with sulfide solutions in isopropyl alcohol appears to reduce the surface states density. The degree of the photolumunecsence intensity increases reached with solutions of the sulfide of a strong base [Na_2S] is larger than that of weak-base sulfide [$(NH_4)_2S$].

Acknowledgement

The authors would like to thank V.N Bessolov for stimulating their interest in this study and V.M.Botnarjuk for his help with GaN epitaxial growth. This study was supported in part by a grant from the Russian Foundation for Basic Research (Grant 97-02-18088).

References

1. M.Onkubo, Jpn. J. Appl. Phys. **36**, L955 (1997).
2. J.R.Mileham, S.J.Pearson, C.R.Abernathy, Y.D.Mackenzie, R.J.Shul, S.R.Kilcoyne, Appl. Phys. Lett. **67**(8), 1119-1121 (1995).
3. S.W.King, J.P.Barnak, M.D.Bremser, K.M.Tracy, C.Ronning, R.F.Davis, R.J.Nermanich, J. Appl. Phys. **84**(9), 5248-5260 (1998).
4. C.J.Sandroff, R.N.Nottonburg, J.C.Bischoff, R.Shat, Appl. Phys. Lett. **51**(1), 33-35 (1987).
5. V.N.Bessolov, A.F.Ivankov, •.V.••nenkova, •.V.Lebedev, Techn. Phys. Lett. **21**(1), 20-21 (1995).
6. V.V.Bel'kov, V.M.Botnaryuk, L.M.Fedorov, I.N.Goncharuk, S.V.Novikov, V.P.Ulin, Y.V.Zhilyaev, T.S.Cheng, N.J.Jeffs, C.T.Foxon, N.I.Katsavets, I.Harrison, J. Crystal Growth **187**, 29 (1998).
7. M. E. Kompan, I. Yu. Shabanov, Phys. Solid State **39**(7), 1030-1034 (1997).
8. V.N.Bessolov, •.V..••nenkova, •.V.Lebedev, Phys. Solid State **39**(1), 54-57 (1997).
9. V.N.Bessolov, M.V.Lebedev, N.M.Binh, M.Friedrich, D.R.T.Zahn, Semicond. Sci. Technol. **13**(6), 611-614 (1998).
10. J.C.Zolper, M.H.Crawford, A.Howard, J.Rames, S.D.Hersee, Appl. Phys. Lett., **68**(2), 200-203 (1996).

EFFECT OF OXYGEN ION IMPLANTATION IN GALLIUM NITRIDE

W. Jiang*, W.J. Weber*, S. Thevuthasan*, G.J. Exarhos*, B.J. Bozlee**

*Pacific Northwest National Laboratory, Richland, WA 99352, weilin.jiang@pnl.gov
**University of Great Falls, Great Falls, MT 59405

Cite this article as: MRS Internet J. Nitride Semicond. Res. 4S1, G6.15 (1999)

ABSTRACT

Epitaxial single crystal GaN films (2.0 μm thick) were implanted 60° off the <0001> surface normal with 600 keV O^+ ions at 190 or 210 K over a range of ion fluences from 4.8×10^{17} to 5.0×10^{20} ions/m^2. The implantation damage, as determined by *in-situ* Rutherford Backscattering Spectrometry in a <0001> channeling geometry (RBS/C), ranged from dilute defects up to the formation of a disorder saturation state that was not fully amorphous. The relative disorder on the Ga sublattice exhibited a sigmoidal dependence on ion fluence. Results show that GaN crystals are extremely resistant to the ion implantation damage as compared to other ceramic materials like SiC. An asymmetric shape in the angular scan curve around the <0001> axis, which might be associated with the Ga lattice distortion in the crystal structure, was observed for the as-irradiated material to the highest ion fluence (5.0×10^{20} O^+/m^2) at 210 K. Comparisons of Ga disorder depth-profiles from the experiment and SRIM97 simulations suggest that the damage peaks shift to greater depths at the low irradiation temperature (210 K). Significant recovery of these defects was not observed in the isochronal annealing steps (20-min) up to 970 K.

INTRODUCTION

Gallium nitride (GaN) is being widely investigated as a material for ultraviolet emitting lasers [1] and high-power or high-temperature electronic devices [2]. A fundamental understanding of ion-implantation effects and damage recovery processes in GaN is important to effectively utilize ion-implantation techniques in electronic device fabrication. Much work to date has focused on n-type and p-type implantation doping [3-7] and the effects on electrical and structural properties [3-6]. Oxygen implantation is of interest as a possible alternative n-type dopant and its role as a background impurity in as-grown GaN [8]. Oxygen-implanted GaN has been shown to exhibit n-type character after 1320 K annealing, and no measurable change in the oxygen distribution is observed even after annealing to 1400 K [3]. In the present study, the effects of oxygen implantation on structure and subsequent annealing are investigated by *in-situ* Rutherford Backscattering Spectroscopy in a channeling geometry (RBS/C).

EXPERIMENTAL PROCEDURES

The n-type GaN single-crystal films (2.0 μm thick) used in the present investigation were obtained from Epitronics and were epitaxially grown by MOVPE on a sapphire substrate. The ion implantation and *in-situ* RBS/C measurements on these <0001>-oriented films were performed using a 3.4 MV tandem accelerator within the Environmental Molecular Sciences Laboratory (EMSL) at the Pacific Northwest National Laboratory. The 600 keV O^+ ions were implanted at an angle of 60° relative to the surface normal in order to produce shallow damage that could be readily measured by 2 MeV helium ion channeling. Specimens were implanted at low

Mat. Res. Soc. Proc. Vol. 537 © 1999 Materials Research Society

temperatures (190 K or 210 K) to various fluences ranging from 4.8×10^{17}-5.0×10^{20} O^+/m^2, equivalent to 0.026-26.7 displacements per atom (dpa) at the depth of ~0.2 μm (damage peak position), where a threshold displacement energy of 25 eV for both Ga and N sublattices have been assumed in the SRIM-97 (full cascade) simulations. The implanted areas (1.2×1.2 mm^2) had uniform ion distributions. Ion fluence integration was achieved by applying a positive voltage of 300 V to the target in order to prevent secondary electron emissions.

Subsequent post-irradiation and post-annealing *in-situ* axial-channeling analyses were performed along <0001> using 2.0 MeV He^+ beams at a scattering angle of 150°. During annealing, samples were heated by an electron beam from a negatively biased filament, and a steady flow of liquid nitrogen provided sample cooling. Specimen temperatures were maintained with an uncertainty of ±5°C by adjusting both the filament current and the bias voltage (up to a maximum of -500 V) between the filament and the grounded sample. Conventional chromel-alumel thermocouples were used to measure the temperatures on the sample front surfaces. Isochronal annealing at different temperature intervals for 20 minutes was used to follow the damage recovery processes over the temperature range from room temperature up to as high as 970 K. After each isochronal annealing step, a channeling measurement along the <0001> direction was performed *in-situ* at a temperature below the anneal temperature to insure the annealing process was quenched. For annealing steps above 300 K, spectra were taken after the sample cooled to room temperature. During the ion implantation and channeling measurements, the vacuum in the target chamber was typically in the range of 10^{-6} Pa, where carbon contamination on the sample surface was not found.

RESULTS AND DISCUSSION

A sequence of *in-situ* RBS/C spectra for GaN/Al_2O_3 irradiated at 210 K to various O^+ fluences is shown in Fig. 1, along with random-equivalent and virgin (unirradiated) spectra. The

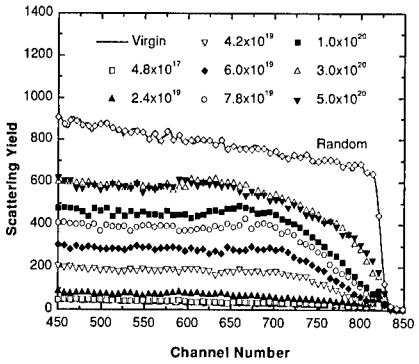


Fig. 1. A sequence of 2.0 MeV He^+ RBS/C spectra taken *in-situ* for a <0001> GaN (2 μm thick) on sapphire implanted (60° off surface normal) in different areas with 600 keV O^+ ions at 210 K (dose unit: O^+/m^2). Also included are a random spectrum and a channeling spectrum from a virgin area.

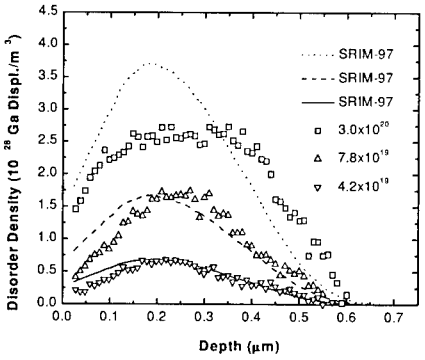


Fig. 2. Comparison of the experimentally determined disorder density profiles (from Fig. 1) for Ga sublattice with the normalized profile from SRIM-97 simulations, suggesting the damage peak shifts into the bulk at 210 K (dose unit: O^+/m^2).

backscattering yields are monotonically increasing with ion dose up to 3.0×10^{20} O^+/m^2 (or 16.0 dpa at the damage peak). At the highest dose (5.0×10^{20} O^+/m^2), the damage accumulation appears to have saturated. The result suggests that full amorphization cannot be achieved at this temperature under O^+ ion irradiation. In contrast, almost two orders of magnitude lower C^+ [9] or Si^+ [10] dose (in dpa) would have been sufficient to completely amorphize SiC over a large depth at similar temperatures. At lower irradiation temperatures with heavier ions, complete amorphization of GaN does occur. For example, complete amorphization in GaN at 77 K is reported after Si^+ ion fluences of 2.4×10^{20} ions/m^2 [4] and after Ar^+ and Ca^+ ion fluences of 6×10^{19} ions/m^2 [11].

The density profiles of Ga atomic disorder for ion doses of 3.0×10^{20}, 7.8×10^{19} and 4.2×10^{19} O^+/m^2 are extracted from the RBS/C spectra (Fig. 1) under the assumption of linear dechanneling approximation [9,12], and are shown in Fig. 2 as a function of depth. Also included in the figure are the normalized profiles from SRIM-97 simulations. Due to saturation of damage and apparent shift of the damage profile to greater depths, the measured damage profile induced by 3.0×10^{20} O^+/m^2 irradiation does not match the simulated damage profile for this ion fluence. However, at a lower ion fluence (4.2×10^{19} O^+/m^2), the peak position of the measured disorder profile is in reasonable agreement with the simulated profile predicted by SRIM-97. As the ion fluence increases, the damage distribution appears to shift to greater depths. Since the profiles do not become wider and no evidence of defect diffusion to surface is found, the defects are expected to be immobile at this low temperature (210 K). The effect of damage peak shifts may be partly attributed to the interaction of Ga sublattice with oxygen dopants, which were implanted into the depth region between 0.2 and 0.5 μm. Further investigations are planned to depth-profile the dopant in the irradiated sample. In a related study, Zolper and co-authors [3] have reported the SIMS profiles for implanted ^{18}O (5×10^{18} ions/m^2) in GaN and did not observe redistribution of the implanted species after annealing at 1400 K for 15 s.

The dependence of relative Ga atomic disorder (at the damage peak) on the O^+ ion dose (in dpa) is shown in Fig. 3. Full amorphization corresponds to 1.0 on the vertical scale. The 190 and 210 K irradiations performed at different times show no difference within the experimental error

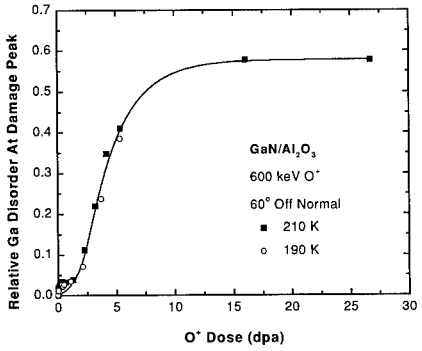


Fig. 3. Relative Ga disorder as a function of ion dose in displacements per atom (dpa) at the damage peak for 600 keV O^+ implanted GaN crystal on sapphire at 210 and 190 K. The solid line is a sigmoidal fit to the data.

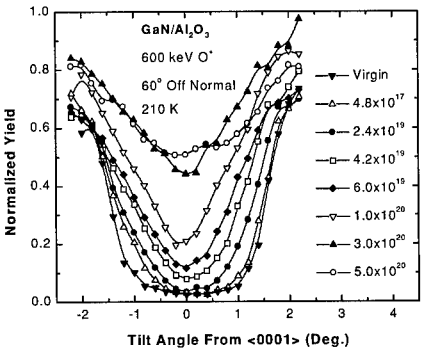


Fig. 4. Angular dependence of the normalized scattering yield of 2.0 MeV He^+ ions around <0001> axis in the GaN crystalline film (2.0 μm thick) on sapphire with various ion fluences (O^+/m^2) for the as-irradiated specimen at 210 K.

and give reproducible results. The maximum relative Ga disorder at saturation under the experimental conditions is ~60% at the damage peak. The solid line in Fig. 3 is a sigmoidal fit to the data. Similar sigmoidal dependence of disorder on dose is observed in ion-implanted SiC [9,10,12-14 and refs. therein] at comparable low temperatures; however, in the case of SiC, full amorphization (100 % disorder) is achieved at significantly lower doses. Since we have not yet established how much of the disorder in Fig. 3 is due to amorphization and how much is due to defects or chemical effects (reactions with oxygen), any interpretation of the sigmoidal dependence is premature.

Figure 4 shows the evolution of the angular scan curves around the <0001>-axial direction with ion fluence. The random level for amorphous GaN corresponds to unity of the normalized yield. Despite the independence of minimum yields on the scanning path, the shape of the angular curves could be influenced by planar channeling [15], particularly for high-quality crystalline samples. A specific scanning path leading to a broad dip curve was selected in this study with a half-angular width of ~1.7° for the virgin (unimplanted) crystal, which is considered to help observe the changes in the atomic displacements more clearly. The dip curves in Fig. 4 are rather symmetric and change slowly with increasing ion dose below 1.0×10^{20} O^+/m^2. However, the shape becomes asymmetric for the highest dose case (5.0×10^{20} O^+/m^2), which might be associated with the disturbance of the Ga sublattice in the crystal structure. Similar dip curves have also been observed for ion-implanted 6H-SiC materials [16].

The minimum yield χ_{min} and the half-angular width $\Psi_{1/2}$ are illustrated in Fig. 5 as a function of ion fluence. A χ_{min} of 1.0 indicates complete amorphization of the GaN material. The minimum yield, which reflects the level of the atomic disorder at surface, shows similar dependence on ion dose as in Fig. 3. However, the minimum yield has not yet saturated at 3.0×10^{20} O^+/m^2 due to the lower displacement dose at the surface (~7 dpa) relative to the displacement dose at the damage peak (~16 dpa) at this ion fluence. In fact, the minimum yield at the surface for this displacement dose is consistent with that at the damage peak (Fig. 3) for the same dose. This suggests that the surface is not significantly affecting the accumulation of damage at this dose level. The half-angular width ($\Psi_{1/2}$) in Fig. 5 decreases slowly at lower doses (below 1.0×10^{20} O^+/m^2, or ~2.3 dpa

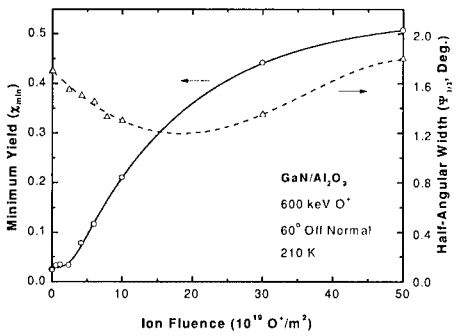


Fig. 5. Minimum yield (χ_{min}) and half-angular width ($\Psi_{1/2}$) obtained from O^+ ion implanted GaN crystal on sapphire at 210 K with various ion fluences. The solid (for χ_{min}) and dashed (for $\Psi_{1/2}$) lines are polynomial fits.

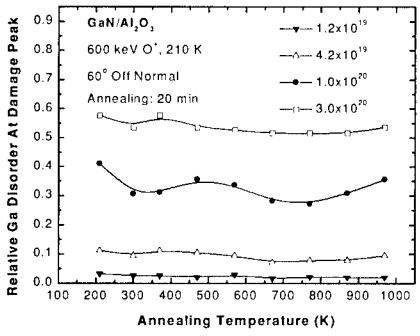


Fig. 6. Relative disorder on the Ga sublattice at damage peak as a function of annealing temperature for various ion fluences (O^+/m^2) at 210 K. Symbols indicate experimental data and the solid lines are polynomial fits.

at surface). Although the decrease in $\Psi_{1/2}$ could be contributed from dopants and localized lattice distortion [17], it might also arise partly from the increase of Ga atomic spacing along the ion track [16]. The lattice expansion in Ca^+- and Ar^+-implanted GaN was observed by XRD measurements [7]. According to the polynomial curve fit (dashed line) in Fig. 5, the width tends to increase at ion fluences above 2.0×10^{20} O^+/m^2, which might again be related to the crystalline structural distortion discussed above.

Studies of defect recovery in the ion-implanted GaN materials have not been performed until recently. It has been found experimentally that defects produced by Si^+ implantation do not undergo significant thermal recovery at annealing temperatures up to 1070 K [4] or 1370 K [5]. However, rapid thermal annealing (RTA) studies at 1420 K [18] show a considerable amount of reduction in the Ga atomic disorder produced by irradiation at liquid nitrogen temperature with Mg^+ and Ca^+ ions. In the present study, *in-situ* RBS/C method is employed and the isochronal thermal annealing data (20-min) are shown in Fig. 6, where four ion fluences have been chosen as examples. The Ga atomic disorder at the damage peak for the as-implanted specimens ranged from ~3% up to ~58% and only some fluctuations of the Ga atomic disorder were observed as a result of the annealing processes. In general, no significant annealing effects occurred up to 970 K in any of the irradiated samples, which covered the full range of atomic disorder in this study. This is in contrast to gradual reduction of Si atomic disorder in Si^+ [10], C^+ [9] and He^+ [13] implanted 6H-SiC in a comparable annealing temperature range. The thermal stability of the defects in GaN is not yet fully understood. It might be partly associated with the nature of the defects produced. Optical measurements on these samples, to be reported in a subsequent publication, indicate ingrowth of a color center near 440 nm produced by the ion implantation. Significant broadening in the band edge absorption line and an increase in refractive index also were determined from optical transmission and ellipsometry measurements. These effects are consistent with ion induced lattice disorder. Further work is planned to explore the nature of the defects formed and the attendant recovery mechanisms.

CONCLUSIONS

It has been shown that full amorphization of GaN may not be possible under 600 keV O^+ irradiation at temperatures down to ~200 K. The irradiation-induced damage profile shifts to greater depths with increasing dose, and damage saturates at a value of ~60 %. This may be due to a ballistic or chemical effect, since defects do not appear to be mobile at this temperature. The accumulation of damage on the Ga sublattice exhibits a sigmoidal dependence on dose. An observed asymmetric shape in the dip curve for an ion fluence of 5.0×10^{20} O^+/m^2 may be associated with a disturbance or perturbation on the Ga sublattice. No significant defect recovery is observed in GaN (irradiated at 210 K) as a result of 20-min isochronal anneals at temperatures up 970 K.

ACKNOWLEDGMENT

This work was supported by the Division of Materials Science, Office of Basic Energy Sciences, U.S. Department of Energy under Contract DE-AC06-76RLO 1830. Operational support for the EMSL accelerator laboratory was provided by the Office of Biological and Environmental Research, U.S. Department of Energy under Contract DE-AC06-76RLO 1830.

REFERENCES

[1] S. Nakamura, MRS Bulletin **23** (5), 37 (1998).

[2] M.S. Shur, in *Power Semiconductor Materials and Devices*, edited by S.J. Pearton, R.J. Shul, E. Wolfgang, F. Ren, and S. Tenconi (Mater. Res. Soc. Proc. **483**, Warrendale, PA, 1998) pp. 15-26.

[3] J.C. Zolper, R.G. Wilson, S.J. Pearton, R.A. Stall, Appl. Phys. Lett. **68**, 1945 (1996).

[4] H.H. Tan, J.S. Williams, J. Zou, D.J.H. Cockayne, S.J. Pearton, R.A. Stall, Appl. Phys. Lett. **69**, 2364 (1996).

[5] J.C. Zolper, M.H. Crawford, J.S. Williams, H.H. Tan, R.A. Stall, Nucl. Instrum. Methods in Phys. Res. B **127/128**, 467 (1997).

[6] B. Mensching, C. Liu, B. Rauschenbach, K. Kornitzer, W. Ritter, Mater. Sci. and Eng. B **50**, 105 (1997).

[7] C. Liu, B. Mensching, K. Volz, B. Rauschenbach, Appl. Phys. Lett. **71**, 2313 (1997).

[8] B.-C. Chung and M. Gershenzon, J. Appl. Phys. **72**, 651 (1992).

[9] W. Jiang, W.J. Weber, S. Thevuthasan, D.E. McCready, Surf. Interface Anal. (1998), in press.

[10] W. Jiang, W.J. Weber, S. Thevuthasan, D.E. McCready, Nucl. Instrum. Methods in Phys. Res. B **143**, 333 (1998).

[11] C. Liu, B. Mensching, M. Zeitler, K. Volz, B. Rauschenbach, Phys. Rev. B **57**, 2530 (1998).

[12] W. Jiang, W.J. Weber, S. Thevuthasan, D.E. McCready, Nucl. Instrum. Methods in Phys. Res. B, January, (1999), in press.

[13] W. Jiang, W.J. Weber, S. Thevuthasan, D.E. McCready, J. Nucl. Mater. **257**, 295 (1998).

[14] W.J. Weber, L.M. Wang, N. Yu, Nucl. Instrum. Methods in Phys. Res. B **116**, 322 (1996).

[15] M.L. Swanson, in *Handbook of Modern Ion Beam Analysis,* edited by J.R. Tesmer and M. Nastasi (Materials Research Society, Pittsburgh, PA, 1995) p. 258.

[16] W. Jiang, W.J. Weber, S. Thevuthasan, submitted to 1998 MRS Fall Meeting, Symposium N, (1998).

[17] W.K. Chu, J.W. Mayer, M.-A. Nicolet, *Backscattering Spectrometry* (Academic Press, 1978) pp. 269-271.

[18] C. Liu, A. Wenzel, K. Volz, B. Rauschenbach, Nucl. Instrum. Methods in Phys. Res. B, January, (1999), in press.

PIEZOELECTRIC FIELD EFFECT ON OPTICAL PROPERTIES OF GaN/GaInN/AlGaN QUANTUM WELLS

JIN SEO IM, H. KOLLMER, O. GFRÖRER, J. OFF, F. SCHOLZ, AND A. HANGLEITER

4. Physikalisches Institut, Universität Stuttgart, D-70550 Stuttgart, Germany
E-mail: j.s.im@physik.uni-stuttgart.de

Cite this article as: MRS Internet J. Nitride Semicond. Res. 4S1, G6.20 (1999)

ABSTRACT

We designed and studied two sample groups: first, GaInN/AlGaN/GaN quantum wells with asymmetric barrier structure and secondly, GaInN/GaN quantum wells with asymmetrically doped barriers. Time-resolved measurements on the asymmetric structure reveal an enhanced oscillator strength when the AlGaN barrier is on top of the GaInN quantum well, indicating a better carrier confinement in such a structure. The photoluminescence emission energy of the GaInN/GaN quantum well with doped GaN barriers shifts towards higher energy than that of undoped samples due to screening, but only when the GaN barrier layer below the quantum well is doped. In contrast, the sample where only a GaN cap layer above the quantum well is doped, shows no blue-shift. These results, showing asymmetries in GaInN/GaN quantum wells, provide confirming evidence of the piezoelectric field effect and allow us to determine the sign of the piezoelectric field, which points towards the substrate in a compressively strained quantum well. Furthermore, we performed model calculations of the global band bending and the screening effect, which consistently explain our experimental findings.

INTRODUCTION

GaInN/GaN/AlGaN-based quantum wells (QW's) have played a key role in the rapid development of short-wavelength light emitters [1]. But the recombination mechanism in the the quantum wells has been unclear and strongly controversial. For some time, the puzzling optical properties have been explained in terms of localized excitons at potential minima due to composition fluctuations or quantum-dot-like states due to phase separation [2,3,4,5]. On the other hand, a strain-induced piezoelectric field has casted a fresh light on the interpretation of the optical transitions in GaN/GaInN/AlGaN QW's [6,7,8,9]. Now, in this paper, we approach these discussions from a new view point: the piezoelectric field breaks the inversion symmetry of the quantum well. Testing the lack of the symmetry is, therefore, unambiguously related to testing the existence of the piezoelectric field. Samples designed on this purpose are classified by two groups: one with asymmetric barriers and the other one with asymmetrically doped barriers. Our results not only verified the piezoelectric field effect, but also revealed field screening due to doping and how to enhance carrier confinement related to the direction of the field.

EXPERIMENTAL

Our samples were grown on (0001)-oriented sapphire substrates using low-pressure metalorganic vapor phase epitaxy (LP-MOVPE) and employing an AlN nucleation layer. The GaInN layers were grown below temperatures of 800 °C with N_2 as a carrier gas. Reciprocal space mapping of X-ray diffraction intensity shows that GaInN grown on GaN buffers is coherently strained up to thicknesses of some 100 nm [10]. In this study, two groups of samples

Mat. Res. Soc. Symp. Proc. Vol. 537 © 1999 Materials Research Society

were designed and fabricated to introduce an asymmetry into quantum wells. First, a nominally undoped 7 nm GaInN QW was sandwiched between asymmetric barrier layers, which consist of a 300 nm GaN buffer, a 60 nm GaN cap layer, and an additional 20 nm AlGaN layer below or above the quantum well. The AlN and InN mole fraction of AlGaN and GaInN layers are estimated as 15 % and 6 %, respectively. The second sample group consists of 6 nm GaInN QW's sandwiched between doped or undoped GaN barrier layers: in one sample both the GaN buffer and the GaN cap layer are doped with Si, and in another one only the GaN cap but not the buffer layer is doped. The Si-doping level is estimated as $(1\text{-}2) \times 10^{18}\,cm^{-3}$. As reference samples, 6 nm and 3 nm GaInN QW's with nominally undoped GaN barrier layers were grown. Time-resolved photoluminescence (TRPL) spectroscopy with resonant excitation of the quantum wells was performed at 5 K using a setup already described elsewhere [7].

RESULTS AND DISCUSSION

Asymmetric barrier structure

This section focuses on GaInN/GaN QW's with an additional AlGaN barrier above or below the quantum well. Low-temperature photoluminescence spectra of these two quantum wells with asymmetric barrier structure are summarized in Fig. 1. To start with time-integrated spectra (doted curves), the sample with an AlGaN barrier below the quantum well has an emission maximum at 3.060 eV, and the other one, in contrast, exhibits a broad emission band with two maxima at 3.146 eV and 3.236 eV. A more detailed picture is given by time-resolved spectra (solid curves). At short delay times, both samples show an emission line near 3.245 eV, but their temporal behaviors are clearly different afterwards: in the sample with the AlGaN barrier on top of the quantum well, an additional lower-energy emission line emerges with increasing time and finally reaches 3.146 eV, i.e. 120 meV below the emission line at early times, but the other sample with the AlGaN-barrier below the quantum well shows a dramatic red-shift by about 220 meV, even 65 meV below the emission maximum of a simple GaInN/GaN QW (dot-dashed line).

Furthermore, we have a closer look at the emission lines which dominate at long delay times and measure the decay traces of each sample at the luminescence maxima in the late time

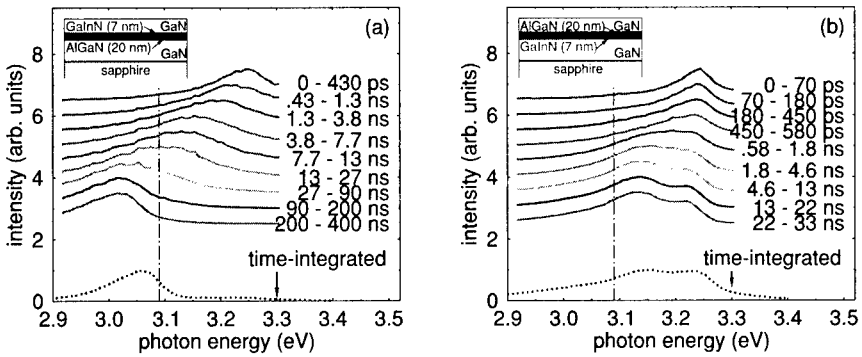


Figure 1: *Time-integrated (doted curves) and time-resolved (solid curves) low-temperature spectra of GaInN/GaN quantum wells with an additional AlGaN barrier below (a) or above (b) the quantum well. The dot-dashed lines indicate the emission energy of a simple GaInN/GaN quantum well. The insets show schematic pictures of the sample structures.*

interval. We find that the luminescence intensity of the sample with an AlGaN barrier above the quantum well decays much faster than that of the other one with an AlGaN barrier below the quantum well (see Fig. 2). At long delay times, we obtain a decay time of 77 ns for the former, which is about 500 times smaller than that of 34 μs for the latter.

The origin of these differences between samples can be well explained by a piezoelectric field in the quantum well: if there were no electric field in the quantum well, both samples would be identical in optical properties. The additional AlGaN barrier gives a rise to increased electron confinement and oscillator strength when it is placed where electrons are pushed by the electric field. Therefore, the shorter decay time of the sample with the AlGaN barrier on top of the quantum well indicates directly that the piezoelectric field points towards the substrate.

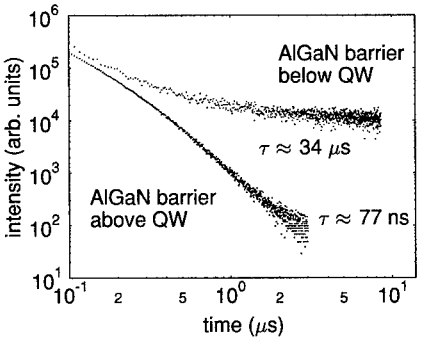


Figure 2: *Luminescence decay in asymmetric structures.*

Bearing in mind the direction of the field, we performed numerical calculations of the conduction bands to give a quantitative explanation. An electrostatic potential energy, induced by a spatially inhomogeneous electron distribution, is calculated using a solution of Poisson's equation and taken into account iteratively in solving the effective-mass Schrödinger equation. At first, we calculated the conduction band of a simple 7 nm GaInN/GaN quantum well with a piezoelectric field of 300 kV/cm. The GaN layers are assumed relaxed and have no piezoelectric field. A background carrier density of $5 \times 10^{16}\,cm^{-3}$, which is estimated in nominally undoped samples, is applied. The result of the self-consistent calculation, which is depicted in Fig.3 , reveals a strong global band bending. The band in the GaN buffer layer is bent upwards, and electrons are depleted. The positive space-charge in the GaN buffer layer and electrons accumulated in the quantum well and the GaN cap layer build a electrostatic field (F_{scr}) which points in an opposite direction to that of the piezoelectric field (F_{piezo}) and screens it. Therefore, the effective field (F_{eff}) in the quantum well is smaller than the strain-induced piezoelectric field, and this calculation results in F_{eff} of 240 kV/cm, which is reduced by about 20 % of F_{piezo}.

The calculated band structures with an additional AlGaN barrier are more complex (see Fig. 4). The AlGaN and GaInN layer are assumed to be in tension and compression, respectively. Strain-induced piezoelectric fields are estimated as 350 kV/cm for the former and 300 kV/cm for the latter with an opposite direction. To take a glance at the conduction bands, the enhanced electron confinement with an AlGaN barrier above the GaInN quantum well are clearly recognizable as expected previously. A further comparison between the band structures reveals that the potential energy drop over the quantum wells is not equal. In case with an AlGaN barrier above the quantum well, a depletion region is built in the GaN buffer and cap layer. The electrons accumulated in the quantum well screen the piezoelectric fields both in the quantum well and in the AlGaN barrier. With an AlGaN barrier below the quantum well, electrons are accumulated in the GaN buffer layer, and the depletion region in the GaN cap layer screens the piezoelectric field in the AlGaN barrier but reinforces that in the quantum well. The screening effect, therefore, depends on the placement of the AlGaN barrier: F_{eff} is calculated as 240 kV/cm and 330 kV/cm for the AlGaN barrier above and below the quantum well, respectively.

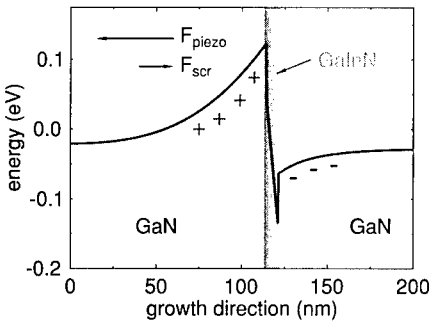


Figure 3: *Calculated conduction band structure of a GaInN/GaN single quantum well with a piezoelectric field.*

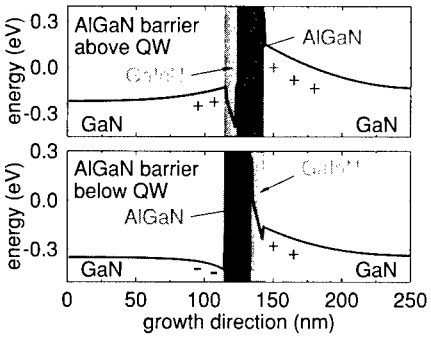


Figure 4: *Calculated conduction band structures of samples with an additional AlGaN barrier.*

At this point, the energetic position of the emission lines can be well understood. The emission line of the sample with the AlGaN barrier below the quantum well lies about 65 meV below the emission line of the simple quantum well without AlGaN barrier. The different effective field (F_{eff}) accounts for this emission energy difference (ΔE): $\Delta E = \Delta F_{eff} \times L_z$. The calculated effective field difference results in an energy shift of about 60 meV, which is well comparable with the experimental results if considering well unknown parameters, e.g. the electron concentration. On the other hand, the AlGaN barrier above the quantum well enhances the electron confinement, and therefore the increased confinement energy leads to an emission energy higher than that of the simple quantum well. The temporal red-shift of two the samples can be explained by the recovery of the piezoelectric field screened partially by carriers injected optically at early times.

Asymmetrically doped quantum well

To test in more detail the lack of the inversion symmetry due to the piezoelectric field and screening effects, we study GaInN/GaN quantum wells with varied doping in the GaN buffer and cap layer as described in the experimental section. The low-temperature photoluminescence spectra of these samples are shown in Fig. 5. The emission maximum of the 3 nm GaInN quantum well with nominally undoped GaN barrier layers lies at 2.875 eV and shifts toward 2.460 eV with increased well width of 6 nm. This energy difference allows us to estimate an effective field of about 1.4 MV/cm in the quantum well. The emission energy of the sample where only a GaN cap layer is doped is almost the same as that of the sample with undoped GaN barrier layers. In contrast, the sample doped in both the GaN buffer and cap layer shows a blue-shift of about 260 meV. We observed in addition that the stimulated emission of 6 nm quantum wells appears at almost the same energetic position, confirming that there is no significant variation of In content or well width among our samples [11].

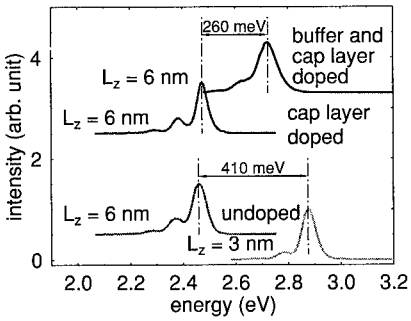


Figure 5: *Photoluminescence spectra of GaInN/GaN single QW's with and without Si-doping in the GaN barriers.*

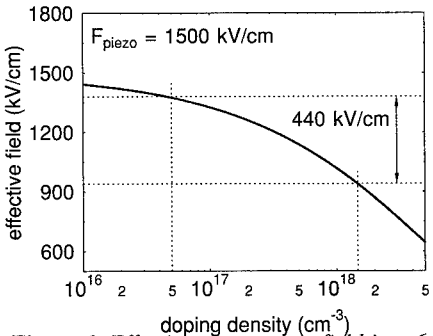


Figure 6: *Effective electrostatic field in a 6 nm quantum well versus doping density for a intrinsic piezoelectric field of 1500 kV/cm.*

These experimental results indicate that the piezoelectric field is screened only when the GaN buffer layer below the quantum well is doped. Considering the calculated band structure shown in Fig. 4, a space-charge region is built in the GaN buffer layer and induces an electrostatic field screening the piezoelectric field together with electrons accumulated in the hetero-interface between the quantum well and GaN cap layer due to the piezoelectric field. The doping level of the GaN buffer layer, therefore, has a dominant influence on the screening but not that of the GaN cap layer. It is interesting to note that this asymmetry confirms the direction of the piezoelectric field determined earlier: unless it were the case, the emission line of the sample where only the GaN cap layer is doped would shift toward lower energy.

To calculate the screening field analytically, we develop a simple model as follows. Under the abrupt approximation, the depletion-region width l below the quantum well can be expressed as $l = (2\varepsilon_0\varepsilon_r\Phi/eN_D)^{1/2}$ with a potential drop $\Phi = F_{eff} \times L_z$ over the quantum well. The doping density N_D is assumed as spatially homogeneous, and the electron concentration in the depletion region is neglected. Integrating over the depletion-region width gives the resultant electric screening field $F_{scr} = eN_D l/\varepsilon_0\varepsilon_r$. The effective field $F_{eff} = F_{piezo} - F_{scr}$ is therefore

$$F_{eff} = F_{piezo} + \frac{eN_D L_z}{\varepsilon_0 \varepsilon_r}\left\{1 - \sqrt{1 + \frac{2\varepsilon_0 \varepsilon_r F_{piezo}}{eN_D L_z}}\right\}, \qquad (1)$$

where ε_0 and ε_r are the permittivity of the vacuum and the dielectric constant of GaN, respectively. For a doping density of 5×10^{16} cm^{-3}, an intrinsic piezoelectric field of 300 kV/cm, and a well width of 7 nm, an effective field is given by this equation as 243 kV/cm in good agreement with the previous result of numerical calculation. The effective fields can be therefore well calculated by this simple analytical model in a good approximation.

Now, we apply this model to the experimental results. A doping level of $(1 - 2)\times10^{18}$$cm^{-3}$ results in a blue-shift of about 260 meV in a 6 nm quantum well, which means a reduction of the effective field by 440 kV/cm (≈ 260 meV/6 nm) to 940 kV/cm. Fig. 6 shows the values of F_{eff} as a function of the doping density with a piezoelectric field of 1500 kV/cm according to Eq.1. Both the difference of the effective field strength and the corresponding doping density can be very well explained by the model.

SUMMARY

The asymmetric behavior of GaInN/AlGaN/GaN quantum wells provide confirming evidence of the piezoelectric field effect and allow us to determine the direction of the field which points towards the substrate. With reference to the direction, an additional AlGaN barrier on top of the GaInN quantum well enhances the electron confinement leading to increased oscillator strength. The doping level of the GaN buffer layer below the quantum well has a crucial role in screening the piezoelectric field, but not that of the cap layer above the quantum well.

ACKNOWLEDGMENTS

Financial support of this work by the Deutsche Forschungsgemeinschaft (DFG) is gratefully acknowledged. J.S.I. acknowledges support by the Deutscher Akademischer Austauschdienst (DAAD).

Bibliography

1. S. Nakamura and G. Fasol, *The Blue Laser Diode* (Springer, Berlin, 1997).
2. S. Chichibu, T. Azuhata, T. Sota, and S. Nakamura, Appl. Phys. Lett. **69**, 4188 (1996).
3. Y. Narukawa, Y. Kawakami, S. Fujita, S. Fujita, and S. Nakamura, Phys. Rev. B **55**, R1938 (1997).
4. Y. Narukawa, Y. Kawakami, M. Funato, S. Fujita, S. Fujita, and S. Nakamura, Appl. Phys. Lett. **70**, 981 (1997).
5. S. Chichibu, T. Sota, K. Wada, and S. Nakamura, J. Vac. Sci. Technol. B **16**, 2204 (1998).
6. T. Takeuchi, S. Sota, M. Katsuragawa, M. Komori, H. Takeuchi, H. Amano, and I. Akasaki, Jpn. J. Appl. Phys. **36**, L382 (1997).
7. J. S. Im, H. Kollmer, J. Off, A. Sohmer, F. Scholz, and A. Hangleiter, Phys. Rev. B **57**, R9435 (1998).
8. A. Hangleiter, J. S. Im, H. Kollmer, S. Heppel, J. Off, and F. Scholz, MRS Internet J. Nitride Semicond. Res. **3**, 15 (1998).
9. T. Takeuchi, C. Wetzel, S. Yamaguchi, H. Sakai, H. Amano, and I. Akasaki, Appl. Phys. Lett. **73**, 1691 (1998).
10. F. Scholz, J. Off, A. Kniest, L. Görgens, and O. Ambacher, to be published in Mat. Sci. Eng. B.
11. S. Heppel, J. Off, F. Scholz, and A. Hangleiter, to be published.

CONTROL OF THE POLARITY AND SURFACE MORPHOLOGY OF GAN FILMS DEPOSITED ON C-PLANE SAPPHIRE

M. Sumiya, T. Ohnishi*, M. Tanaka, A. Ohtomo**, M. Kawasaki**, M. Yoshimoto*, H. Koinuma*, K. Ohtsuka*** and S. Fuke

Department of Electrical and Electronic Engineering, Shizuoka University, 3-5-1 Johoku Hamamatsu, 432-8561, Japan
*Materials and Structures Laboratory, **Department of Innovative and Engineering Materials, Tokyo Institute of Technology, 4259 Nagatsuta Yokohama, 226-8502, Japan
***Research and Development Division, Sanken Electric Co. Ltd., 3-6-3 Kitano Niiza, 352-8666, Japan

Cite this article as: MRS Internet J. Nitride Semicond. Res. G6.23 (1999)

Abstract

Control of the polarity of GaN films deposited by metalorganic chemical vapor deposition was achieved by substrate nitridation and subsequent annealing of a buffer layer. The surface morphology and optical properties of 1.2μm GaN films were influenced by the different growth mode due to the polar direction. Coaxial impact collision ion scattering spectroscopy revealed that the polarity composition of a buffer layer on nitrided sapphire varied by annealing in a H_2 atmosphere. It was considered that the systematic variation of the surface morphology was caused by the polarity composition of the buffer layer.

Introduction

GaN, InGaN and AlGaN which have been successfully used in blue light emitting devices [1] have a wrutzite crystal structure. Epitaxial films of these materials grow along the polar c-axis direction and consequently have a polarity as illustrated in Fig.1. The importance of the polarity for understanding the fundamental mechanism of spontaneous and stimulated light emission from the GaN/InGaN/GaN quantum well structure has been recognized. Although the polarity of GaN has been intensively studied, not all of the results are consistent [2]. In order to obtain a common view about the polarity of GaN film, not only the identification of polarity but also the mechanism determining the polar growth direction must be studied.

Mat. Res. Soc. Symp. Proc. Vol. 537 © 1999 Materials Research Society

Irrespective of such growth techniques as metalorganic chemical vapor deposition (MOCVD) and molecular beam epitaxy (MBE), GaN epitaxial films are typically deposited on c-plane sapphire with a buffer layer deposited at low temperature [3]. There are many switching steps during GaN growth. For example, sapphire substrates are cleaned in a H_2 atmosphere at high temperature, the substrate temperature is ramped up after depositing the buffer layer, and the gas flow ratio (N_2, H_2, NH_3) in each step is changed to obtain high quality GaN films. Furthermore, the substrate is occasionally nitrided [4][5]. Each step involves the chemical reactions, which make the polarity issue complicated.

The polarity structure should be determined at the initial stage of the growth, i.e., at the interface since the rest of the film growth can be considered as a kind of homoepitaxy. The insert of a buffer layer forms another interface and substrate nitridation moderates the surface state [6]. We have investigated the influence of a buffer layer and substrate nitridation on GaN film growth from the point of view of these interfaces [7]. As a result of this study, it was possible to control the polarity of GaN films on c-plane sapphire [8].

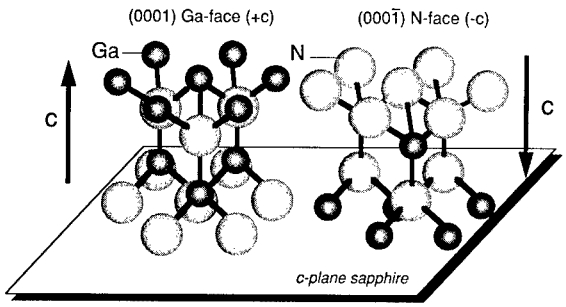


Fig.1 Schematic illustration of wrutzite GaN structure oriented along c-axis. Left side is (0001) Ga-face which is defined +c. Right side is (0001) N-face which is defined which is defined -c.

In this paper, GaN films with the different polarity were deposited under the same conditions except for the annealing time of the buffer layer. The systematic variation in the surface morphology will be presented. The influence of thickness and annealing time on the polarity of buffer layer was investigated in order to discuss the variation of surface morphology.

Experiment

GaN films with 1.2μm thickness were deposited on c-plane sapphire by a two-step atmospheric MOCVD method. Prior to deposition, the substrate was thermally cleaned in a H_2 gas flow at 1080°C for 10min. Substrate nitridation was carried out by heating at 1080°C in NH_3 for 5min. After deposition of a 160nm GaN buffer layer at 600°C, the buffer layer was annealed at 1040°C for up to 100min under a gaseous mixture of N_2, H_2 and NH_3. GaN films were deposited on the annealed buffer layer at 1040°C under the same conditions. The buffer layer as thick as 160nm was intentionally prepared for the purpose in this study. For comparison, high quality GaN films with 20nm buffer layer were also deposited on sapphire with and without nitridation. Identification of the polarity was carried out by coaxial impact collision ion scattering spectroscopy (CAICISS). The polarity of the GaN films was determined by comparison with CAICISS results for ZnO which not only has a wurtzite crystal structure but also lattice constants (a=0.3250nm, c=0.5207nm) close to those of GaN (a=0.3189nm, c=0.5185nm) [9].

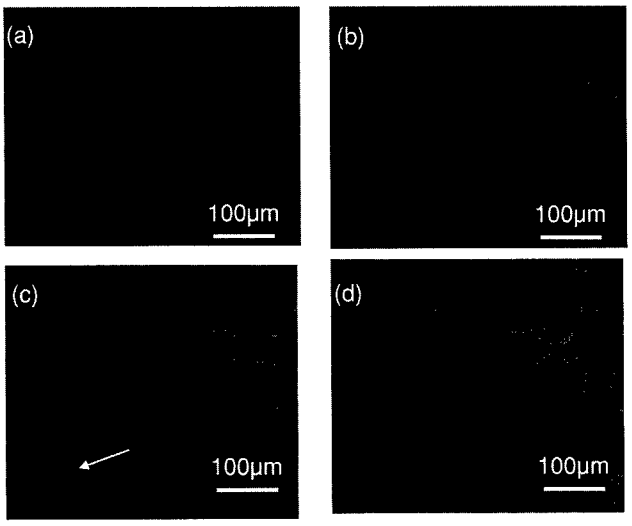


Fig.2 Surface morphology of GaN films deposited on the buffer layer whose polarity was controlled by the annealing time of (a) 30min, (b)40min, (c)60min and (d) 100min. GaN epilayers were deposited under the same conditions.

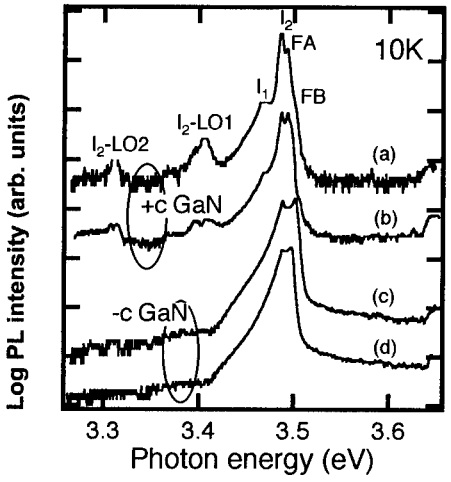


Fig. 3 PL spectra near band edge at 10K for +c and -c GaN films on (a) 20nm buffer layer, (b)160nm buffer layer annealed for 10min. (c) GaN on 20nm buffer and (d) 160nm buffer layer annealed for 60min. The substrate was nitrided in (b)-(d).

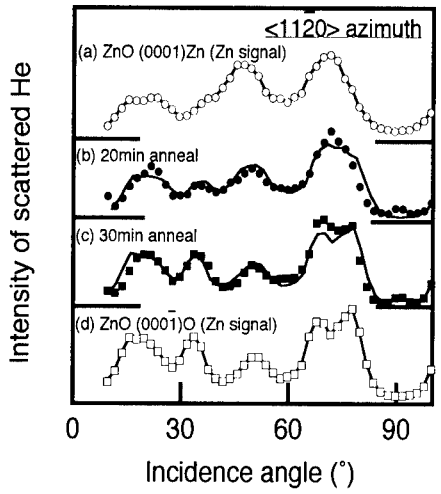


Fig. 4 CAICISS spectra of 160nm buffer layers on a nitrided sapphire for (b) 20min and (c) 30min. The lines in (b) and (c) are calculated line from the weight mean of the spectra of (a) +c and (d) -c ZnO (See the text).

Results and discussion

The surface morphology of GaN films on 160nm buffer layers annealed for 10min was featureless, i.e.,smooth while those on buffer layers annealed for more than 30min were hexagonal facet as shown in Fig.2. The polarity of GaN films with smooth and hexagonal facet surface were determined Ga- (0001) (+c polarity) and N-face (0001) (-c polarity), respectively, which was consistent with our previous results [10]. The "house-shaped" hexagonal structures are observed to form hexagonal "columns" as indicated by the arrow in Fig. 2(c). The ratio of "house-shaped" structure with {1101} and (0001) planes to the hexagonal column with {1100} and (0001) will be discussed later. The size of the hexagonal facet could be systematically controlled up to 60μm by variation of the annealing time of the buffer layer. It is important that the polarity and surface morphology of GaN films deposited even under the same conditions varied systematically with the annealing conditions of buffer layer.

The photoluminescence (PL) spectra for +c and -c GaN films are shown in Fig. 3. As can be clearly seen, the PL spectra varies significantly with the polarity. Although the peaks of +c GaN films can be identified, those of -$\bar{c}$ GaN films can not. PL properties should originate from the bulk GaN, or in other words, are never influenced by the polarity. Since the crystal structures of -c GaN are comparable to those of +c GaN films (See Fig.6), the difference in PL must be due to the different growth mode of the polar direction. It is possible that the amount of impurities depends on the polarity. Theoretical and experimental research about the incorporation of impurities is presently under way.

In order to consider the variations in surface morphology, the interfaces at the substrate or buffer layers were investigated. The nitrided substrate was investigated by reflection of high electron energy diffraction (RHEED) and X-ray photoelectron spectroscopy (XPS). A spotty RHEED pattern, which could be assigned as wurtzite AlN (1120), was observed in the azimuth [1100] of sapphire. The binding energy of nitrogen from the nitrided sapphire was observed at 403eV between nitrogen of AlN (397eV) [11] and nitrogen (408eV). The nitrogen was incorporated into the substrate about one unit (1.2nm) from the surface. CAICISS analysis by Shimizu et.al. revealed that AlN formed by the nitridation had -c polarity (N-face) terminated with Al atoms [12]. Figure 4 (b) and 4(c) shows the CAICISS spectra for the buffer layer annealed for 20 and 30min, respectively. The lines in Fig.4 (b) and 4(c) are calculated form the weight mean of +c and -c ZnO spectra of Fig.4 (a) and 4(d). The ratio of +c to -c domains on the surface (+c:-c) was evaluated as 50:50 and 20:80 for Fig.4 (b) and 4(c), respectively. It was verified that the polarity ratio at the buffer-layer surface varied with annealing time.

The above results leads us to hypothesize that the buffer layer on a nitrided sapphire should have both +c and -c domains due to imperfect nitridation. Since H_2 cleaning removes oxygen, the non-nitrided surface should be covered with Al atoms. At the very initial stage of GaN buffer growth, nitrogen atoms are bound to Al atoms regardless of a nitridation. Nitrogen atoms are bonded to three Al atoms and have one bond pointing upwards normal to the surface on the nitrided sapphire, reflecting -c polarity of AlN formed by a substrate nitridation. In contrast, nitrogen atoms are bonded to one Al atom, and Ga atoms are bounded to three nitrogen

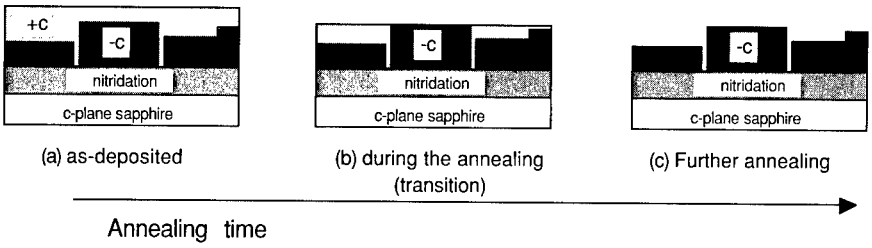


Fig. 5 Schematic illustration of the variation of buffer layer on a nitrided sapphire by the annealing. The annealing should enhanced the etching. (a) as-deposited buffer layer covered with +c changed to the buffer layer with (c) -c polarity through the transition (b).

atoms in the direction away from the surface on a non-nitrided sapphire. Both +c and -c nucleation due to imperfect nitridation should take place during the initial growth on nitrided sapphire. Taking the higher growth rate [13] and re-evaporation of the +c domain into account [7], we hypothesized that +c domains could cover -c domains at 600°C and that the selective evaporation of +c domains by subsequent temperature ramping (a type of an annealing) would leave -c domains in the buffer layer on the nitrided sapphire as illustrated in Fig.5.

In fact, the observed polarity of as-deposited 20nm buffer layer on nitrided sapphire was predominantly +c polarity and it turned to -c polarity after the annealing. The buffer layer was too thin to detect the transition from +c to -c polarity. It is expected that the polarity variation for the 160nm buffer layer should be an characteristic of the buffer layers on nitrided sapphire. Since the absorbance at 3.6eV from the 160nm buffer layer decreased with increasing annealing time, the reduction in the average thickness of the buffer layer was due to evaporation of +c domains as illustrated in Fig.5. Consequently, the ratio of +c to -c domains at the surface varied with the annealing time as shown in Fig.4. If it is accepted that the house-shaped and column hexagonal structure represent +c and -c polarity, respectively [13], the surface morphology of MOCVD-GaN films could represent the polarity composition at the buffer-layer surface acting as an indicator. Figure 6 shows that the column hexagonal facet of GaN films becomes dominant with

increased annealing time. The difference in the ratio between the buffer layer annealed for 30min and the GaN film on it will be pointed out. The transition in this case probably takes place critically during 20-30min annealing giving rise to large experimental errors, e.g., the variation with different batches, is considered to be one of the factors causing the difference. The polarity of a buffer layer should determine the polarity and surface morphology of the GaN films.

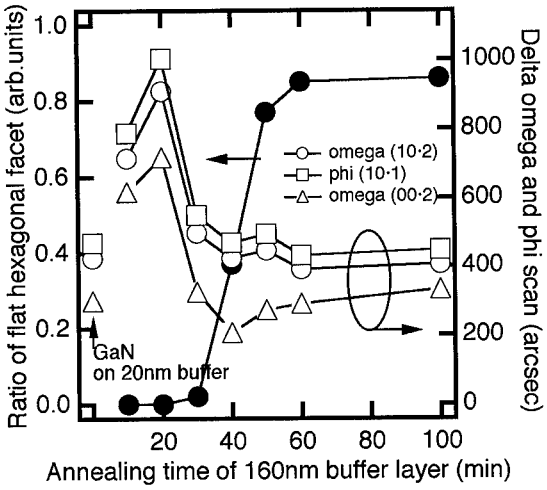


Fig. 6 Ratio of flat hexagonal fact of GaN films deposited on 160nm buffer layer annealed for up to 100min. The sapphire was nitrided. The values of crystal structure for those films and GaN film on 20nm buffer layer as a reference are also plotted.

Based on the results in this study, the -c polarity in MBE-GaN films [14] should be ascribed to substrate nitridation which is typical for this deposition process, since radical nitrogen used in MBE method should be more reactive with the surface of sapphire. However, not all of the nitridation results in -c polarity of MOCVD-GaN films. The fact that MOCVD-GaN films with smooth surface (+c polarity) were obtained in spite of substrate nitridation [5,7] was explained by insufficient evaporation of +c domains in the buffer layer. It is reasonable to conclude that the polar direction of GaN film growth on c-plane sapphire is determined by the mechanism as reported in this study.

Conclusion

Control of the polarity of MOCVD-GaN was achieved by annealing of thicker buffer layers on nitrided sapphire. The properties of 1.2μm GaN was influenced by the different growth mode of the polarity. The mechanism determining the polar direction of GaN films was investigated from the view point of the substrate nitridation and the buffer layer. The nitrogen atom to Al atom bonding configurations at the interface of substrate were found to be modified

by substrate nitridation. Substrate nitridation, thickness of the buffer layer and annealing (gas ratio, temperature ramp time etc.) after deposition of the buffer layer play a dominant role in determining the polarity and surface morphology of MOCVD-GaN films. The systematic variation of the surface morphology was caused by the polarity composition of the buffer layer.

References

[1]S. Nakamura, M. Senoh, S. Nagahama, N. Iwasa, T. Yamada, T. Matsushita, H. Kiyoku and Y. Sugimoto, Appl. Phys. Lett. **68**, 2105 (1996)

[2] E.S. Hellman; MRS Internet J. Nitride Semicond. Res.**3**, 11 (1998)

[3] I. Akasaki, H. Amano, Y. Koide, K. Hiramatsu and N. Sawaki, J. Crys. Growth **98**, 209 (1989)

[4]S. Keller, B. P. Keller, Y.-F. Wu, B. Heying, D.Kapolnek, J. S. Speck, U. K. Mishra and S. P. DenBaars; Appl. Phys. Lett. **68**, 1525 (1996)

[5] K. Uchida, A. Watanabe, F. Yano, M. Kouguchi, T. Tanaka and Minagawa; J. Appl. Phys. **79**, 3487 (1996)

[6] Y. Bolan, P. Fini, S. P. DenBaars and J. S. Speck; Jpn. J. Appl. Phys. 37, 4695 (1998)

[7]S. Fuke, H. Teshigawara, K. Kuwahara, Y. Takano, T. Ito M. Yanagihara and K. Ohtsuka; J. Appl. Phys. **83**, 764 (1998)

[8] M. Sumiya, T. Ohnishi, M. Tanaka, K. Ohtsuka I. Ohkubo, M. Kawasaki, M. Yoshimoto H. Koinuma and S. Fuke; Submitted to Appl. Phys. Lett.

[9] T. Ohnishi, A. Ohtomo, M. Kawasaki, K. Takahashi, M. Yoshimoto and H. Koinuma, Appl. Phys. Lett. **72**, 824 (1998)

[10] M. Sumiya, T. Ohnishi, H. Hesigawara, M. Tanaka, I. Ohkubo, M. Kawasaki, M. Yoshimoto, K. Ohtsuka, H. Koinuma and S. Fuke; Proc. of 2nd Intern. Symp. on Blue laser and Light Emitting Diodes, Chiba Japan, **339** (1998)

[11] A. Yamamoto, M. Tsujino, M. Ohkubo and A. Hashimoto; J. Crys. Growth **137**, 415 (1994)

[12] S. Shimizu and S. Sonoda; Private communication, 2nd Intern. Symp. on Blue laser and Light Emitting Diodes, Chiba Japan (1998)

[13] H. Yamane, M. Shimada, T. Endo and F. J. DiSalvo; Jpn. J. Appl. Phys. **37**, 3436(1998)

[14] S. Shimizu, Y. Suzuki, T. Nishihara, S. Hayashi and M. Shinohara; Jpn. J. Appl. Phys. **37**, L703 (1998)

THERMAL ANNEALING OF InGaN/GaN STRAINED-LAYER QUANTUM WELL

Michael C.Y. Chan,* Kwok-On Tsang,* E. Herbert Li,* and Steven P. Denbaars**

*Department of Electrical & Electronic Engineering, University of Hong Kong, Pokfulam, Hong Kong, ehli@eee.hku.hk

**Electrical and Computer Engineering and Materials Departments, University of California, Santa Barbara, CA 93106

Cite this article as : MRS Internet J. Nitride Semicond. Res. 4S1, G6.25 (1999)

ABSTRACT

Quantum well (QW) material engineering has attracted a considerable amount of interest from many people because of its ability to produce a number of optoelectronic devices. QW composition intermixing is a thermal induced interdiffusion of the constituent atoms through the hetero-interface. The intermixing process is an attractive way to achieve the modification of the QW band structure. It is known that the band structure is a fundamental determinant for such electronic and optical properties of materials as the optical gain, the refractive index and the absorption. During the process, the as-grown square-QW compositional profile is modified to a graded profile, thereby altering the confinement profile and the subband structure in the QW. The blue-shifting of the wavelength in the intermixed QW structure is found in this process.

In recent years, III-nitride semiconductors have attracted much attention. This is mainly due to their large bandgap range from 1.89eV (wurtzite InN) to 3.44eV (wurtzite GaN). InGaN/GaN quantum well structures have been used to achieve high lumens blue and green light emitting diodes. Such structures also facilitate the production of full colour LED displays by complementing the colour spectrum of available LEDs.

In this paper, the effects of thermal annealing on the strained-layer InGaN/GaN QW will be presented. The effects of intermixing on the confinement potential of InGaN/GaN QWs have been theoretically analysed, with sublattices interdiffusion as the basis. This process is described by Fick's law, with constant diffusion coefficients in both the well and the barrier layers. The diffusion coefficients depend on the annealing temperature, time and the activation energy of constituent atoms. The optical properties of intermixed InGaN/GaN QW structure of different interdiffusion rates have been theoretically analyzed for applications of novel optical devices. The photoluminescence studies and the intermixed QW modeling have been used to understand the effects of intermixing.

INTRODUCTION

Wide-bandgap semiconductors such as GaN, AlN, InN and their ternary compounds have been studied so as to realize the semiconductor blue-green laser. As a matter of fact, the demonstration of high-brightness blue-green light-emitting diodes from the wurtzite GaN semiconductor has stimulated a lot of research on the fabrication of blue-green laser diodes using nitride-based semiconductors [1-3]. InGaN/GaN single-quantum-well structures have been used to achieve high-power blue and green light-emitting diodes. Also, room temperature pulsed lasing of a strained InGaN/GaN multiquantum-well laser diode has recently been demonstrated.

The nature crystal structure of most of the group III nitrides is wurtzite. Strain is also present in most of the group III nitrides because of the lack of substrate materials with a matched

Mat. Res. Soc. Symp. Proc. Vol. 537 © 1999 Materials Research Society

lattice constant and a thermal expansion coefficient. Indeed, fundamental studies of the effects of strain on wurtzite band structure play an important role in understanding the electronic and optical properties of GaN-based optoelectronic materials and devices.

In order to tune the interesting wavelength, the concept of band-gap engineering is a useful tool to accept the particular devices operation [4]. Basically, intermixing process is one of easy way to achieve the modification of bandstructure. The intermixing process involves the interdiffusion of the constituent atoms of the heterostructure, the process temperature, and time. During the process the as-grown square-QW compositional profile is modified to a graded profile thereby altering the confinement profile and subband structure in the QW. The interdiffusion of InGaN/GaN QW system is more complex compared with AlGaAs/GaAs and InGaAs/GaAs because of the immiscibility of InN and GaN [5].

THEORETICAL MODEL

This paper presents a theoretical study of the effects of interdiffusion on a 25Å well/70Å barrier of an $In_{0.2}Ga_{0.8}N$/GaN MQW structure, whose properties leads to the shift in spontaneous emission rate. The effects of interdiffusion on the strains, the splitting of the heavy-hole (HH), the light-hole (LH), the crystal-field split-hole (CH) subbands, the conduction band (CB) and their dispersions, are calculated theoretically, based on the Hamiltonian derived using the multi-band k•p model by Chuang and Chang [6].

The QW composition intermixing refer to the thermal induced interdiffusion of the constituent atoms through the hetero-interface. In fact, the interdiffused QW (DFQW) structures created by both impurity induced and impurity-free vacancy promoted processes have recently attracted much attention [7-9]. The interdiffusion mechanism can be a single-phase diffusion for two constituent atoms or it can be a two-phase or multiple-phase one and/or for multiple species. In InGaN/GaN DFQW structures, only the interdiffusion of group-III atoms, i.e. In and Ga atoms, occurs as there is no N concentration gradient across the interface. The diffusion of group III atoms in the QW structure is usually described by the Fick's law with constant diffusion coefficients in both the well and the barrier layers. The composition profile after the interdiffusion is characterized by a diffusion length L_d defined as $L_d=\sqrt{(Dt)}$, where D is the diffusion coefficient and t is the annealing time of thermal processing. The In mole fraction across the InGaN/GaN DFQW structure after the interdiffusion is given by:

$$x_{In}(z)=\frac{x_0}{2}\left[erf(\frac{L_w+2z}{4L_d})+erf(\frac{L_w-2z}{4L_d})\right], \qquad (1)$$

where z denotes the co-ordinate along the crystal growth direction, L_w is the as-grown well width and x_0 is the as-grown In mole fraction.

To calculate the electron and hole wave functions in QW's, we use the multiband effective mass theory. It is a good approximation that the conduction and valence bands are decoupled. A parabolic band model and the Luttinger-Kohn Hamiltonian with strain components are used for the conduction and valence bands respectively. The envelope function scheme is adopted to describe the slowly varying part of the wavefunction. The effects of the quantum well confinement potential on the energies and envelope functions of the electron and hole subband edge at the zone centre of the Brillouin zone can be calculated separately, according to the Ben-Daniel and Duke model, using the one-dimensional Schrodinger-like equation that follows:

$$-\frac{\hbar^2}{2}\frac{d}{dz}\left[\frac{1}{m^*_{\perp r}(z)}\frac{d\psi_{rl}(z)}{dz}\right]+U_r(z)\cdot\psi_{rl}(z)=E_{rl}\psi_{rl}(z) \qquad (2)$$

where $\psi_{rl}(z)$ is the envelope function of the l^{th} subband for electrons(r=c) or holes (r=hh, lh for heavy hole and light holes respectively); $m_{\perp r}^*(z)$ is the corresponding carrier effective mass in the z direction; E_{rl} is the subband-edge energy. $U_r(z)$ is the confinement potential of the quantum well. Equation (2) is solved numerically using a finite difference method with the corresponding confinement profile. The strain of InGaN/GaN DFQW is compressive in nature, pushes the valence subbands downwards and further increases the bandgap.

The in-plane valence band dispersion of the wurtzite-InGaN/GaN QW is calculated using the parameters of GaN, InN as listed in Table I. Meanwhile, alloy properties of $In_xGa_{1-x}N$ are obtained by linear interpolation, except for the bandgap energy, in which a bowing parameter of b=1.8eV for InGaN/GaN is used [10]. The partition ratio for the band edge discontinuity at the heterojunction for the valence and conduction bands is assumed to be 33:67 for both QW systems.

Table I. Material Parameters used in calculating the band structure of InGaN/GaN QW.

Parameters	GaN	InN
a (Å)	3.190	3.544
E_g(eV) at 300K	3.44	1.89
$\Delta_1=\Delta_{cr}$ (meV)	10	27.8
$\Delta_2=\Delta_3$ (meV)	5.17	3.9
m_e^z (m_o)	0.2	0.11
m_e^t (m_o)	0.18	0.1
A_1	-6.56	-9.28
A_2	-0.91	-0.6
A_3	5.65	8.68
A_4	-2.83	-4.34
A_5	-3.13	-4.32
A_6	-4.86	-6.08
a_c (eV)	-11.8	-1.2
D_1 (eV)	0.7	0.35
D_2 (eV)	2.1	1.05
D_3 (eV)	1.4	1.32
D_4 (eV)	-0.7	-0.74
C_{13} (10^{11} dyn cm^{-2})	10	9.4
C_{33} (10^{11} dyn cm^{-2})	39.2	20

We assume that the injected carrier density is 1×10^{13} cm^{-2} in the InGaN-GaN DFQW. The spontaneous emission rate is calculated by integrating the emission rate over all the electrons and holes recombination processes. The spontaneous emission is given by the following equation:

$$r_{sp}(E)=\frac{q^2 n_r \omega}{\pi\hbar c^3 \varepsilon_0 m_0^2 L_w}\cdot\int dk\left|P_{pq}(k_{//})\right|^2\times f^e\left(E_p^e(k_{//})\right)\left[1-f^h\left(E_q^h(k_{//})\right)\right], \qquad (8)$$

where q is the electric charge, n_r is the refractive index, ε_0 is the dielectric constant of the vacuum, c is the speed of light, L_w is the width of the quantum well, E is the photon energy, P_{pq} is the optical matrix element, and f^e and f^h are the Fermi distribution functions for electrons in the conduction subband and holes in the valence subband respectively. To include the spectral broadening of each transition, the total spontaneous emission spectrum in a single DFQW structure is obtained using some spectral lineshape function over all transition energies E'. Such function is given by:

$$R_{sp}(E) = \int dE' \sum_{p,q} r_{pq}(E) \mathrm{L}(E - E'), \tag{9}$$

where L(E-E') is a Lorentzian line-broadening function given by

$$\mathrm{L}(E - E') = \frac{1}{\pi} \frac{\hbar/\tau_{in}}{(E'-E)^2 + (\hbar/\tau_{in})^2}, \tag{10}$$

where τ_{in} is the intraband relaxation time. Then, the spontaneous emission spectrum can be obtained.

The spontaneous emission spectrum of the InGaN/GaN DFQW is shown in Fig.1. The light emission can shift the photon energy from 2.96eV to 3.02eV within the range of L_d=0-4Å. The results show that a magnitude of spontaneous emission enhancement of more than 5%. The InGaN/GaN DFQW can be used in the blue LEDs, which can adjust the wavelength of the emitted photons according to the extent of intermixing.

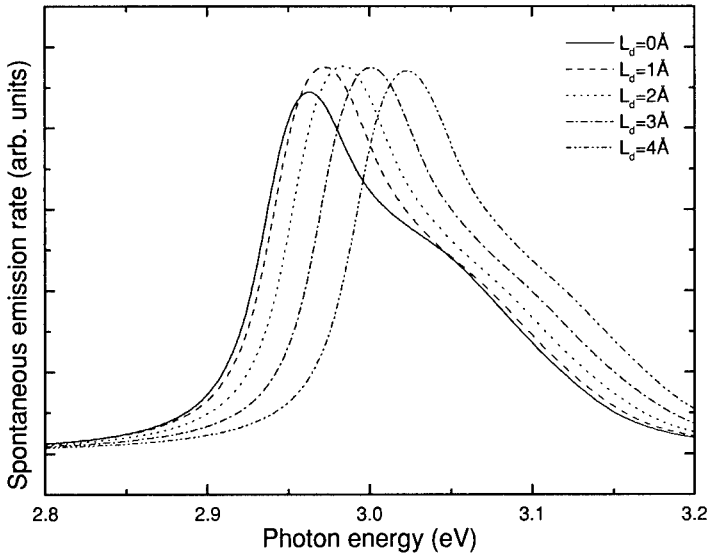


Fig.1 The spontaneous emission spectra of InGaN/GaN DFQW

EXPERIMENT

The InGaN/GaN MQW in this study were grown on c-plane sapphire substrates in an atmospheric pressure MOCVD reactor. The MQW structure consist of a 570Å GaN layer, a 10 period superlattice of 25Å $In_{0.2}Ga_{0.8}N$ well/70Å $In_{0.05}Ga_{0.95}N$ barrier, and a 2300nm GaN:Si layer on a sapphire substrate. The SiO_2 film was deposited on the sample surface using plasma enhanced chemical vapor deposition. Thermal annealing treatment was performed in a flowing N_2 ambient using the diffusion furnace at 1060°C for 60minutes. Photoluminescence spectra were taken with the 325nm line of a 15mW He-Cd laser at 10K. The PL spectra of the as-grown and intermixed MQW are shown in Fig. 2. The spectrum of the as-grown MQW is dominated by the intense localized exciton (2.950eV) related to the very strong blue luminescence. After the thermal annealing, there are six weak luminescence peaks in the region of 2.955-3.45eV. The transition line (at 2.955eV) for the InGaN/GaN MQW is due to the localized exciton transition from the InGaN well region and the first quantized level of exciton localization located at 3.197eV. Two emission peaks, at approximately 3.162 and 3.071eV, correspond to the LO phonon replicas (1 and 2LO) of the main emission line at 3.251eV from the GaN layer. The energy positions are separated by 90meV which is close to the longitudinal optical (LO) phonon energy of bulk InN (86meV) and GaN (91meV) [11]. Also, the GaN layer is observed at 3.45eV. The energy shift of localized excitons for the as-grown and the intermixed InGaN/GaN MQW is only observed to be 5meV. The effect of impurities enhanced intermixing is required to increase the rate of diffusion in the system.

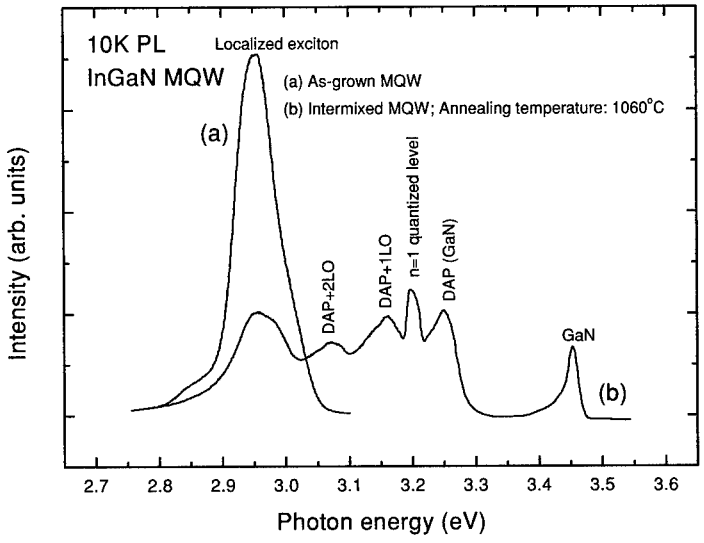


Fig.2 10K PL spectra of (a) the as-grown $In_{0.2}Ga_{0.8}N$ MQW and (b) the intermixed $In_{0.2}Ga_{0.8}N$ MQW at 1060°C for 60minutes

CONCLUSIONS

In this paper, the InGaN/GaN MQW intermixed structure is analyzed, and used to tune the operation wavelength of light emission in the device. Theoretically, the results show that the photon energy can be shifted from 2.96 to 3.02eV within the range of L_d = 0-4Å diffusion length, resulting in an enhancement of the spontaneous light emission. Experimentally, the PL of the intermixed MQW obtained the energy shifts from 2.95eV to 2.955eV (5meV blue-shift).

ACKNOWLEDGEMENTS

This work is supported by HKU-CRCG Grants. The authors would like to thank Dr. K.W. Cheah, Hong Kong Baptist University, for helping with the PL measurements, and Dr. C. Jagadish and Dr. H. H. Tan, Australian National University, for helping with the deposition of SiO_2 film.

REFERENCES

1. S. Nakamura, IEEE J. Selected Topics Quantum Electron. **3**, 712 (1997).
2. M. P. Mack, A. C. Abare, P. Kozodoy, M. Hanson, S. Keller, U. K Mishra, L. A. Coldren, S. P. Denbaars, institute of physics conference series, **156**, 367 (1998)
3. M. P. Mack, A. C. Abare, M. Hansen, P. Kozodoy, S. Keller, U. Mishra, L. A. Coldren, S. P. Denbaars, J. of crystal growth, **190**, 837 (1998)
4. E.H. Li, Editor, Quantum Well Mixing and Optoelectronic Device Applications, Milestone Series, vol. 145.
5. M. D. McCluskey, L. T. Romano, B. S. Krusor, N. M. Johnson, T.Suski, and J. Jun, Appl. Phys. Lett. **73**, 1281 (1998)
6. S. L. Chuang and C. S. Chang, Semicond. Sci. Technol. **12**, 252 (1997).
7. S. Yuan, Y. Kim, C. Jagadish, P. T. Burke, M. Gal, J. Zou, D. Q. Cai, D. J. H. Cockayne, and R. M. Cohen, Appl. Phys. Lett. **70**, 1269 (1997).
8. S. Burkner, M. Maier, E. C. Larkins, W. Rothemound, E. P. O'Reilly, and J. D. Ralston, J. Electronic Materials **24**, 805 (1995).
9. Gontijo, T. Krauss, J. H. Marsh, and R. M. De La Rue, IEEE J. Quantum Electron. **30**, 189 (1994).
10. Walter R. L. Lambrecht, Solid-State Electron. **41**, 195 (1997).
11. M. Smith, J. Y. Lin, H. X. Jiang, A. Khan, Q. Chen, A. Salvador, A. Botchkarev, W. Kim, and H. Morkoc, Appl. Phys. Lett. **70**, 2882 (1997)

XPS STUDY OF OXYGEN ADSORPTION ON (3X3) RECONSTRUCTED MBE GROWN GAN SURFACES

R. A. Beach, E. C. Piquette, and T. C. McGill
T. J. Watson, Sr. Laboratories of Applied Physics 128-95
California Institute of Technology, Pasadena, CA 91125

Cite this article as: MRS Internet J. Nitride Semicond. Res. 4S1, G6.26 (1999)

ABSTRACT

The incorporation of oxygen onto the (3x3) reconstructed surface of GaN(000$\underline{1}$) has been studied using X-ray Photoelectron Spectroscopy (XPS). It was found that the (3x3) reconstruction corresponds to a fractional Ga adlayer atop a Ga terminated GaN surface. Our measurements indicate a surface coverage of 1.15 ± 0.2 monolayers of relaxed Ga on the surface. The binding energy separation between the relaxed surface Ga3d core level and bulk Ga3d level was measured to be 1.1 ± 0.1 eV. A metallic component extending from the bulk GaN valence band maximum out to 0 eV was also present in the XPS spectrum. The separation between the bulk valence band maximum and the Fermi level of the metallic component was found to be 2.1 ± 0.1 eV. The relaxation of the surface Ga was found to decrease with oxygen exposure indicating Ga-O bonding, with oxygen adsorption terminating at 1.3 ± 0.2 monolayers. The O1s core level was found to have a FWHM of 2.0 ± 0.1 eV.

INTRODUCTION

Wide band gap semiconductors have attracted considerable attention for applications ranging from lasers to high power electronics. In the last few years, substantial improvement in the structural and electronic properties of GaN has been achieved. This has resulted in major advances in blue-green light-emitting diodes and lasers as well as HFET power devices. The performance of these devices, however, is still limited by a number of materials problems as well as difficulties in producing low resistance contacts. This is particularly true of p-type GaN where extremely high doping densities are required to produce p-type material. Reasonably good ohmic contacts to n-GaN have been found, and the interface chemistry of these contacts investigated. [1] The effects of adsorbates on Fermi-level pinning and Schottky barrier heights, however, is not well understood. A study of the (1x1) GaN surface has shown an increase in electron affinity of ~0.58 eV due to oxygen chemisorption. [2] These types of surface effects have strong implications for device fabrication. We report here a study of the (3x3) reconstructed surface of GaN(000$\underline{1}$) including effects due to oxidation.

EXPERIMENT

GaN was grown on sapphire (0001) substrates by RF assisted molecular beam epitaxy using a low temperature GaN buffer layer. The substrate temperature was held at 800°C during growth under slightly metal-rich conditions. The surface morphology and reconstruction were characterized by reflection high energy electron diffraction (RHEED). The RHEED pattern was streaky during growth, and showed a clear (3x3) reconstruction after cool down. The (3x3) reconstruction has been determined to correspond to N-polar GaN. [3] Nitrogen polarity

Mat. Res. Soc. Symp. Proc.Vol. 537 © 1999 Materials Research Society

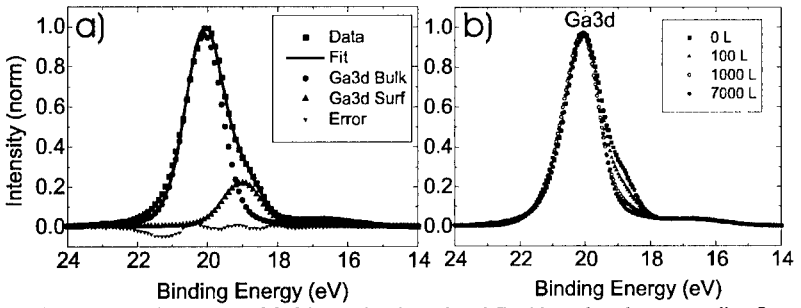


Figure 1: a) XPS spectrum of Ga3d area showing relaxed Ga side peak and corresponding fit. b) Spectra showing metallic Ga3d peak removal by oxygen exposure.

corresponds to a crystal structure in which the bond parallel to the c-axis is from a nitrogen to a gallium atom, and results in a Ga terminated surface having three dangling bonds. The polarity of our sample was confirmed after data acquisition *ex-situ* by etching in molten KOH. [7] After growth, the samples were moved under vacuum to an XPS chamber via a UHV transfer tube. Data was then taken over 4 regions of interest: the Ga3d core level, N1s core level, O1s core level, and the valence band region. Data acquisition was alternated with in-place exposure to O_2 at room temperature via a leak valve. The sample is in line of sight of a hot filament and the oxygen can therefore be considered excited. Oxygen exposure was measured by monitoring system pressure, and is given in Langmuirs (L), were $1L=10^{-6}$Torr s.

ANALYSIS

Several trends were detected in the XPS spectra during oxidation of the (3x3) surface. It was found that the (3x3) reconstruction of the GaN surface results in a second peak on the lower binding energy side of the bulk Ga3d peak in GaN (Fig.1a). The shift to lower binding energy is characteristic of metallic bonding between Ga atoms. This implies that the reconstruction corresponds to a fractional Ga adlayer atop a Ga terminated GaN surface. This is in agreement with a previous in-situ STM study of GaN reconstructions.[3] The Ga3d spectrum was fit to determine the relaxed Ga coverage of the surface. Figure 1a shows the results of a fit employing three peaks, one for each state of Ga, and one for the N2s state that lies at ~17 eV. Each Ga peak was fit by two identical spin-orbit split doublets consisting of the sum of a Lorentzian and Gaussian. The splitting was held at .46 eV and the branching ratio was set at .66. A Gaussian was used for the N2s peak. A good fit was obtained over most of the peak area with the largest error occurring on the high binding energy side of the Ga3d peak. This may be due to the asymmetric nature of photoemission from metallic core peaks, or possibly some residual inversion domains within the sample. Reference 2 found growth of a similarly positioned state with oxygen exposure on a (1x1) reconstructed surface of GaN. We, however, did not observe any growth of this state with oxygen exposure, and therefore are hesitant to ascribe it to O-Ga bonding. The effect of this error on determination of surface coverage should be minimal given the small area of the error. From this fit, the ratio of the bulk to metallic Ga3d peak areas was found to be 4.35±0.2. For calculating the surface coverage, we begin by assuming the measured intensity from a given core level of a single layer of atoms m monolayers below the surface (I_m) can be described by,

$$I_m = \sigma I e^{\frac{-m}{\lambda(E)\cos\alpha}} \quad (1)$$

where σ is the sensitivity factor for the given material and core level, [8] and I is an instrumental scale factor depending on primary beam current, detection efficiency, etc. The inelastic mean free path (IMFP) for electrons with energy E, is denoted by λ(E), and is expressed in atomic layers. The collection angle measured from the surface normal (α) was set at 45° for this study. We designate $I_o^{Ga3d}=\sigma_{Ga3d}I$ as the measured Ga3d peak intensity of a single monolayer of Ga on the surface. The measured intensities of the relaxed surface Ga3d and bulk Ga3d peaks can then be expressed by,

$$I_s^{Ga3d} = \chi I_o^{Ga3d} \quad (2)$$

$$I_B^{Ga3d} = I_o^{Ga3d}\left(\sum_m e^{\frac{-m}{\lambda(E)\cos\alpha}} - \chi\right) \quad (3)$$

Here, χ is the fractional surface coverage of relaxed Ga. By taking the ratio of these intensities, and solving for χ, an expression for the fraction of relaxed surface Ga can be obtained.

$$\chi = \frac{\beta}{(1+\beta)}\sum_m e^{\frac{-m}{\lambda(E)Cos\alpha}} \quad (4)$$

In eqn. 4, β is the ratio of surface to bulk peak intensities (1/4.35 in our measurements). Although the IMFP for GaN has not been measured, an estimate was obtained from a compilation of previous IMFP measurements. [4] We have used a value of 8.0 monolayers for the IMFP for 1467eV electrons from the Ga3d region, where one monolayer is the distance between Ga planes in the crystal. Using the above values for β, λ, and α, eqn. 4 results in 1.15±0.2 monolayers for the calculated surface coverage. This is larger than the expected fractional surface coverage assumed in the above model. Accounting for this excess surface coverage results in a value of 1.19±0.2 monolayers. Although there is some uncertainty introduced by the lack of a measured IMFP for GaN, it appears safe to conclude that the surface consists of ~1 monolayer of relaxed Ga. The (3x3) reconstruction has been found to consist of Ga adatoms positioned in three fold coordinated sites above a Ga termination layer. STM images show the Ga adatom positioned just above the valley between three Ga atoms in the termination layer.[3] Although Ga droplets can not be conclusively ruled out, our data indicates that the entire Ga termination layer is relaxed by the addition of this .11 monolayers of Ga adatoms.

The Ga3d metallic peak intensity decreases with oxygen adsorption indicating bonding between the Ga and oxygen. The valence band density of states (VBDOS) spectrum has the shape and position of the bulk GaN VBDOS

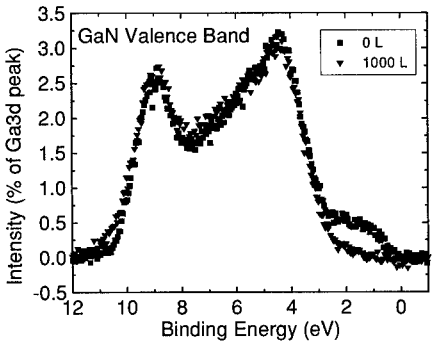


Figure 2: XPS spectrum of GaN valence band showing metallic ledge removal by oxidation.

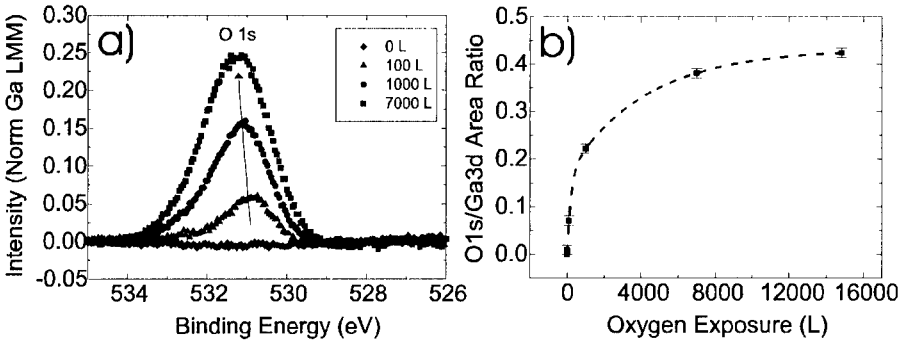


Figure 3: a) XPS spectrums showing oxygen 1s peak growth with oxygen exposure.
b) O1s to Ga3d peak area ratio as a function of exposure.

with an additional component extending to 0 eV (Fig.2). The VBDOS metallic component also decreases in intensity as the sample is exposed to O_2. This component is therefore associated with the metallic nature of the reconstructed surface. Using a linear extrapolation to estimate the position of the GaN valence band and the half height position of the metallic Fermi edge (E_F) results in E_F-VBM =2.1 ± 0.2eV. This is in agreement with an oxygen adsorption study of the (1x1) surface by Bermudez [2] in which they measured E_F-VBM = 2.4 ±0.2 eV. The O1s/Ga3d peak area ratio was measured as a function of oxygen exposure. The O1s peak position is seen to shift to higher binding energy relative to the GaLMM peak as oxygen exposure increases.(Fig.3a) This may indicate two states closely spaced in energy for oxygen adsorption. The two states may be due to the difference between binding to the Ga termination layer versus binding to the Ga adlayer. The oxidation was found to terminate with an O1s to Ga3d peak area ratio of 0.43 ± 0.1, corresponding to an oxygen surface coverage of 1.3 ±0.2 monolayers. This is much too high for simple adatom binding, therefore the Ga termination layer must participate in the oxidation. The saturation oxygen level suggests a single oxygen for each termination layer Ga atom, with additional coverage due to bonding with adatoms. The O1s peak was fit by a Gaussian and was found to have a FWHM of 2.0 ±0.1 eV before deconvolution of the instrumental broadening. This is significantly smaller than the 3.2 eV FWHM measured in [2] for the oxygen adsorption onto (1x1) GaN surfaces.

CONCLUSION

In summary, we have studied the (3x3) reconstruction of MBE grown GaN using X-ray photoelectron spectroscopy. We have characterized surface binding energy changes, and investigated the surface reaction with oxygen exposure. We have found a Ga3d surface binding energy change of 1.1 ± 0.1 eV and a metallic Ga adlayer Fermi-level to bulk valence band maximum separation of 2.1 ± 0.2 eV. We have observed the removal of surface relaxation by oxygen exposure and interpreted this as bonding of the surface Ga termination layer and adlayer with oxygen. The width of the O1s peak was found to be smaller for the (3x3) surface than that previously measured for the (1x1) surface.

ACKNOWLEDGEMENTS

This work was supported by DARPA and monitored by the ONR under Grant N00014-92-J-1845.

REFERENCES

[1] C.I. Wu and A. Kahn, J. Vac. Sci. Technol. B **16**(4) 2218 (1998)

[2] V.M. Bermudez, J. Appl. Phys. **80** (2) 1190 (1996)

[3] A.R. Smith, R.M. Feenstra, D.W. Greve, J. Neugebauer, and J.E. Northrup, Phys. Rev. Lett. **79** (20)3934 (1997)

[4] M.P. Seah and W.A. Dench, Surf. Int. Anal. **1**, 2 (1979)

[5] M.M. Sung, J. Ahn, V. Bykov, and J.W. Rabalais, Phys. Rev. B **54**(20) 14652 (1996)

[6] Y.N. Xu and W.Y. Ching, Phys. Rev. B **48**, 4335 (1993)

[7] M. Seelmann-Eggebert, J. L. Weyher, H. Obloh, H. Zimmermann, A. Rar, and S. Porowski, Appl. Phys. Lett. **71**, 2635 (1997).

[8] Physical Electronics, *Multipak Operator's Manual,* (1996)

THERMAL STABILITY OF GaN INVESTIGATED BY RAMAN SCATTERING

M. Kuball[(1)], F. Demangeot[(2)], J. Frandon[(2)], M.A. Renucci[(2)], N. Grandjean[(3)], and O. Briot[(4)]

[(1)] H.H. Wills Physics Laboratory, University of Bristol, Bristol BS8 1TL, UNITED KINGDOM
[(2)]Laboratoire de Physique des Solides de Toulouse, CNRS, Université Paul Sabatier,
F-31062 Toulouse Cedex, FRANCE
[(3)]CRHEA-CNRS, Rue Bernard Gregory, F-06560 Valbonne, FRANCE
[(4)]GES-CNRS, CC074 Université Montpellier II, Place E.Bataillon
F-34095 Montpellier Cedex 5, FRANCE

Cite this article as: MRS Internet J. Nitride Semicond. Res. 4S1, G6.28

ABSTRACT

We have investigated the thermal stability of GaN using Raman scattering. Noninvasive optical monitoring of the degradation of GaN during high-temperature processing has been demonstrated. GaN samples grown by molecular-beam epitaxy (MBE) and metalorganic vapor phase epitaxy (MOCVD) were studied. Characteristic features in the Raman spectrum identify three thermal stability regimes: (1) annealing below 900°C does not affect the GaN Raman spectrum; (2) annealing between 900°C and 1000°C results in the appearance of disorder-induced Raman scattering between the E_2 and A_1(LO) phonon; (3) annealing at temperatures higher than 1000°C gives rise to distinct Raman modes at 630 cm^{-1}, 656 cm^{-1} and 770 cm^{-1}. The evolution of the Raman spectrum of GaN with increasing annealing temperature is discussed in terms of disorder-induced Raman scattering. We find clear indications for an interfacial reaction between GaN and sapphire for annealing temperatures higher than 1000°C.

INTRODUCTION

The family of III-V nitrides (GaN, InGaN, AlGaN) has recently attracted much attention because of their wide spectrum of potential applications ranging from opto-electronic devices for the blue-ultraviolet spectral region to high temperature devices [1,2]. High-temperature processing of nitrides is an essential part of the nitride device fabrication, i.e., for the activation of Mg-acceptors to achieve p-doping of GaN or for the fabrication of ohmic contacts [3,4]. Monitoring the thermal stability of GaN during high-temperature annealing is therefore of great interest [5–7]. Since changes in the near-surface stoichiometry that deteriorate electrical properties occur at a temperature, which is about 100°C lower than the temperature where visible surface degradation occurs, it is essential to develop effective non-invasive *ex-situ* as well as *in-situ* monitoring techniques to assess changes in the quality of GaN and AlGaN layers at elevated temperatures. So far only time-consuming techniques like atomic force microscopy (AFM) and transmission electron microscopy (TEM) have been used to assess degradation effects [6,7].

In this report, we illustrate the potential applications of Raman scattering (complemented by photoluminescence experiments) to determine and monitor the degradation pathway of GaN during high-temperature annealing. The results of this study can be employed for the non-invasive optical monitoring of structural damage to GaN during high-temperature processing as well as for the non-invasive optical monitoring of passive and active nitride devices operating at elevated temperatures. Raman scattering provides information on vibrational states of GaN,

Mat. Res. Soc. Symp. Proc. Vol. 537 © 1999 Materials Research Society

which are sensitive to microscopic disorder. The crystalline quality can be judged from the peak shapes and the selection rules. GaN normally crystallize in the hexagonal wurtzite structure (space group C_{6v}^4) with four atoms in the unit cell. At **k=0** group theory predicts the following eight sets of phonon modes: $2A_1 + 2B_1 + 2E_1 + 2E_2$ of which only one A_1, one E_1 and two E_2 are Raman active. One set of A_1 and one set of E_1 corresponds to acoustic phonons, the B_1 modes are silent [8]. The activation of $\mathbf{q}\neq\mathbf{0}$ phonons of GaN by disorder allows us to probe and assess noninvasively changes in the crystalline quality of GaN. We find clear indications for a interfacial reaction between sapphire and GaN at elevated temperatures.

EXPERIMENT

Raman scattering and photoluminescence spectra were recorded from high-temperature annealed GaN layers. The samples were annealed in nitrogen ambient in a heating stage at temperatures from 100°C to 1100°C in 50–100°C steps, in a sequence of 20min anneals. A small amount of oxygen was present during the annealing. Raman spectra were collected after each annealing step on a Renishaw Raman microscope system 2000 using the 488nm line of an Ar^+-laser as excitation source. Photoluminescence spectra were recorded using a Renishaw ultraviolet (UV) Raman microscope system with the 244nm line of an intra-cavity frequency doubled Ar^+ laser as excitation source. The Raman measurements were performed in backscattering $\underline{Z}(Y,Y)\underline{Z}$ geometry, however, when necessary a full polarization analysis was performed. The studied GaN samples, 2 μm thick, were grown by molecular-beam epitaxy (MBE) and metalorganic vapor phase epitaxy (MOCVD) at growth temperatures of 980-1150°C on sapphire [0001] substrates, after a thin buffer layer of low temperature GaN had been deposited at 550-600°C. The MBE sample was doped with Mg, annealed in nitrogen ambient at 750°C for 30 min, with a free carrier concentration of about $3\times10^{17}cm^{-3}$ and a mobility of $8cm^2/Vs$. The MOCVD sample was unintentionally n-doped.

RESULTS

Raman scattering

Figure 1 shows Raman spectra of the MBE-grown GaN layer after various 20min anneals, recorded at room temperature in backscattering $\underline{ZY},Y)\underline{Z}$ geometry. The Raman spectrum shows before annealing (lowest spectrum) the allowed E_2(high) phonon at 567 cm^{-1} and the A_1(LO) phonon at 734 cm^{-1}. We observe at $534cm^{-1}$ the A_1(TO) mode which is usually not allowed in this configuration, however, might be related to a high defect density or the p-doping. The mode at 750 cm^{-1} is a reminiscent of the E_g sapphire mode. The shown spectra are normalized to the E_2 phonon intensity.

The Raman spectrum of the MBE-grown GaN layer remains unchanged for annealing temperatures up to 800–900°C. Heat treatments at temperatures between 900°C to 1000°C, however, result in a broad Raman peak, centered at $610cm^{-1}$, between the E_2 and A_1(LO) phonon lines. A polarization analysis reveals that this new feature in the Raman spectrum is present in parallel and in crossed polarizations [$\underline{Z}(Y,Y)\underline{Z}$, $Z(X,Y)\underline{Z}$]. The E_2 phonon shifts from $567cm^{-1}$ before annealing to $570cm^{-1}$ after annealing at 1000°C (inset of Fig. 1), whereas the A_1(LO) phonons remains unaffected within the experimental spectral resolution.

Annealing the sample at a temperature higher than 1000°C results in distinct Raman peaks at $630cm^{-1}$, $656cm^{-1}$ and $770cm^{-1}$. Their intensity increases in the subsequent annealing steps. The A_1(LO) phonon at $734cm^{-1}$ broadens and decreases in intensity. The E_1(TO) phonon

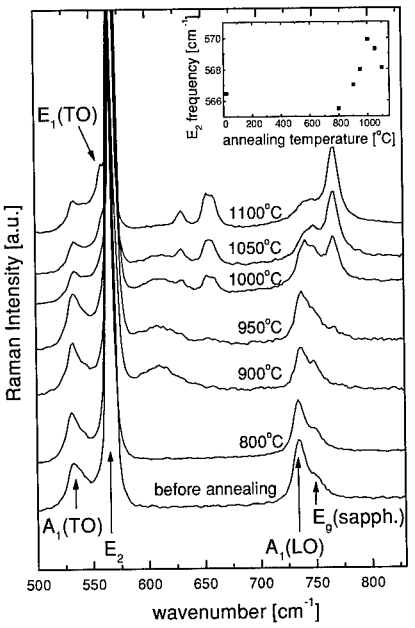


Figure 1: Raman spectra of the MBE-grown GaN sample after 20min anneals at various temperatures, recorded at room temperature in backscattering $Z(Y,Y)\underline{Z}$ geometry.

emerges at 559cm^{-1} on the low-energy side of the E_2 phonon (uppermost spectrum in Figure 1). We observe a tentative decrease in the E_2 phonon frequency for the 1100°C anneal (inset of Fig.1).

The Raman features induced by the 1000°C and 1100°C anneal are present in all polarization configurations with no evident polarization dependence. We note that the magnitude of the broad Raman peak at 610cm^{-1} after annealing at 1100°C is sample-to-sample dependent: it apparently decreases in Figure 1, whereas for other samples a further increase was observed during the high-temperature annealing. The dramatic changes in the Raman spectrum for anneals higher than 1000°C go along with modifications in the surface morphology. We observe a pitting of the surface, however, the surface remains visually mirror-like. Macroscopic disorder appears.

Additional Raman experiments were performed on the MOCVD-grown GaN sample. The observed characteristic changes in the Raman spectrum during the annealing sequence are similar to the results shown in Figure 1. The temperature regimes, however, appear to be somewhat different for the MBE- and MOCVD-grown sample. Figure 2 compares Raman spectra obtained from the MOCVD- and MBE-grown GaN sample (comparable layer thickness) in the spectral region of the A_1(LO) phonon, after annealing the sample at a temperature of 1050°C. The emerging distinct Raman peaks at 630cm^{-1}, 656cm^{-1} and 770cm^{-1}, illustrating the severe degradation of the sample, seem to be less pronounced for the MOCVD-grown GaN layer. The investigated MOCVD-grown GaN layer appears therefore to be thermally more stable than the investigated MBE-grown GaN layer.

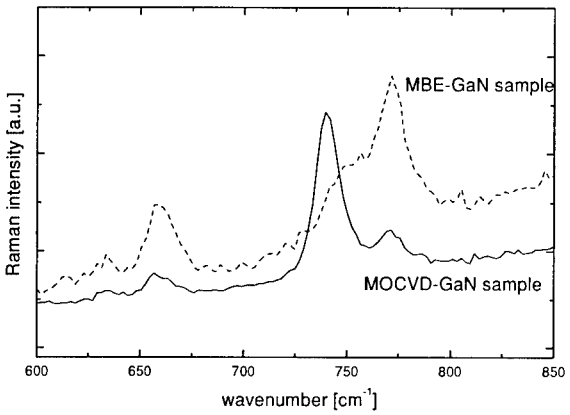


Figure 2: Raman spectra of MBE-grown GaN and MOCVD-grown GaN annealed at 1050°C.

Photoluminescence

Figure 3 and 4 show photoluminescence spectra of the MBE-grown GaN sample recorded in the spectral region of the well-known R-lines of sapphire and the GaN bandgap, respectively, after the various high-temperature anneals. Annealing at a temperature of 1000°C and 1100°C results in a strong photoluminescence signal around 1.75eV. Furthermore, we detect a shift and broadening of the sapphire R-lines. Figure 4 shows the photoluminescence spectrum of the MBE-grown GaN sample in the spectral region of the GaN bandgap. Before annealing we detect photoluminescence from the GaN bandgap at 3.4eV. Annealing at high temperature results in a decreasing bandgap photoluminescence intensity, a broadening of the photoluminescence signal, as well as a shift of the photoluminescence maximum towards higher photon energies.

DISCUSSION

The evolution of the GaN Raman spectrum shown in Figure 1 allows us to determine and monitor noninvasively the degradation pathway of GaN during the annealing sequence. Three thermal stability/degradation regimes can be identified: (1) annealing temperatures up to 800–900°C, (2) between 900° and 1000°C and (3) higher than 1000°C. Below 900°C no structural degradation of the GaN is evident from the Raman spectra. This is consistent with previous reports [7,8]. Such temperatures are well suited for high-temperature processing as well as active and passive high-temperature devices. Annealing temperatures higher than 900°C result in the degradation of the crystalline quality of the GaN layer, which is evident in the emerging broad Raman peak between the E_2 and A_1(LO) phonon (Figure 1). Microscopic defects created by the high-temperature annealing result in the breakdown of the translational symmetry and the activation of the phonon density of states in the Raman spectrum, i.e., the participation of $\mathbf{q}\neq\mathbf{0}$ phonons in the Raman scattering process (disorder-induced Raman scattering). The broad Raman peak at 610cm^{-1} is located in a spectral region with a high phonon density of states according to lattice dynamical calculations by Azuhata *et al.* [9]. It is present in all polarization configurations as expected for disorder-induced Raman scattering. Consistently, we observe a decreasing band edge photoluminescence signal during the annealing sequence as shown in Figure 4. Similar changes in the GaN photoluminescence spectrum were reported by Lin *et al.* [10] in

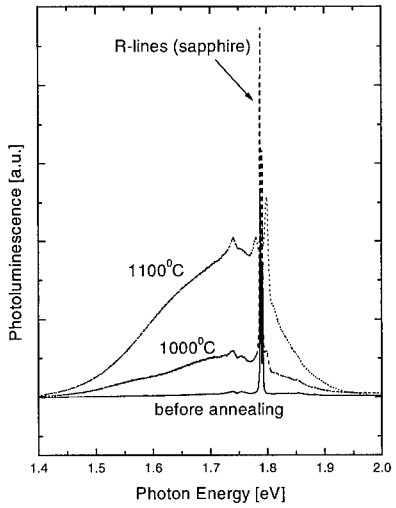


Figure 3: Photoluminescence spectrum of the MBE-grown GaN sample, after various 20min anneals.

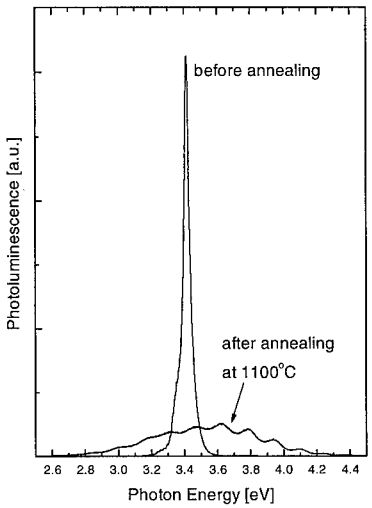


Figure 4: Photoluminescence spectrum of the MBE-grown GaN sample, after various 20min anneals.

low-temperature photoluminescence experiments on GaN samples, which were annealed at 900°C for 30min, i.e., pointing to non-radiative recombination centers. Note that no obvious modifications in the surface morphology are visible after the annealing. The observed frequency shift of the E_2 phonon by about $3cm^{-1}$ during the annealing sequence (inset of Figure 1) reflects the appearance of internal stress [11].

Forbidden sapphire modes were observed by Barker *et al.* [12] at $633cm^{-1}$, $652cm^{-1}$ and $770cm^{-1}$ on surface-damaged sapphire. The activation of the forbidden $770cm^{-1}$ sapphire mode for annealing temperatures higher than 1000°C (Figure 1) is therefore a clear indication for a degradation of the GaN/sapphire interface during the high-temperature annealing, i.e., a reaction between GaN and sapphire at the interface. No GaN modes or a high GaN phonon density of states is present around $770cm^{-1}$ and could contribute [9]. The observed photoluminescence signal at 1.75eV around the sapphire R-lines as well as the shift and broadening of the sapphire R-lines (Figure 4) consistently illustrate structural modifications at the GaN/sapphire interface (defects, stress) [13]. We note that no change in the Raman or the photoluminescence spectrum of sapphire was observed when a plain sapphire wafer was annealed under the same conditions. The assignment of the $630cm^{-1}$ and $656cm^{-1}$ Raman modes in Figure 1 is more difficult since both sapphire with its forbidden modes at $633cm^{-1}$ and $652cm^{-1}$ as well as GaN [9] contribute in this frequency range. Raman experiments on the side face of an annealed 6μm–thick MBE-grown GaN layer, however, indicate that the $630cm^{-1}$ and $656cm^{-1}$ Raman modes mainly arise from the GaN/sapphire interface region suggesting a larger contribution from the forbidden sapphire modes. The presence of the $E_1(TO)$ phonon at $559cm^{-1}$ after the 1100°C anneal (Figure 1) shows an evolving misorientation of the GaN layer during the high-temperature annealing.

CONCLUSIONS

We have demonstrated the great potential of Raman scattering to detect damage in GaN induced by high-temperature annealing. The results can be applied to monitor noninvasively damage in GaN during high-temperature processing as well as to monitor passive and active high-temperature nitride devices. Three distinct regimes of thermal damage where identified by characteristic Raman spectra. Raman scattering reveals thermal damage due to microscopic defects for anneals between 900°C and 1000°C based on the appearance of a disorder-induced Raman scattering signal between the E_2 and A_1(LO) phonon. The evolving Raman spectrum displays the GaN phonon density of states. Above 1000°C, Raman scattering probes an interfacial reaction between GaN and sapphire, illustrated by the activation of forbidden sapphire modes. The investigated MOCVD-grown GaN sample was found to be thermally more stable than the investigated MBE-grown GaN sample. Defect-related photoluminescence was found after the high-temperature annealing of GaN. The E_2 phonon frequency was analyzed to deduce information on internal stress. Annealing below 900°C has no effect on the GaN crystalline quality and is therefore well suitable for high-temperature applications of GaN.

ACKNOWLEDGEMENTS

We thank G.D. Pitt (Renishaw Transducers plc.) for financial support and supplying the heating stage, H. Sands and D.N. Batchelder (University of Leeds) for support for the ultraviolet photoluminescence experiments and B. Gil for helpful discussions and encouragement.

REFERENCES

[1] S. Nakamura, M. Senoh, S. Nagahama, N. Iwasa, T. Yamada, T. Matsushita, H. Kiyoku, Y. Sugimoto, T. Kozaki, H. Umemoto, M. Sano, K. Chocho, Appl. Phys. Lett. **72**, 211 (1998).

[2] Y.-K. Song, M. Kuball, A.V. Nurmikko, G.E. Bulman, K. Doverspike, S.T. Shappard, T.W. Weeks, M. Leonard, H.S. Kong, H. Dieringer, and J. Edmonds, Appl. Phys. Lett. **72**, 1418 (1998).

[3] S. Nakamura, T. Mukai, M. Senoh, and N. Iwasa, Jpn. J. Appl. Phys. **31**, L139 (1992).

[4] M.A. Khan, Q. Chen, R.A. Skogman, and J.N. Kuznia, Appl. Phys. Lett. **66**, 2046 (1995).

[5] M. Kuball, F. Demangeot, J. Frandon, M.A. Renucci, J. Massies, N. Grandjean, R.L. Aulombard, and O. Briot, Appl. Phys. Lett. **73**, 960 (1998).

[6] J.C. Zolper, M. Hagerott Crawford, A.J. Howard, J. Ramer, and S.D. Hersee, Appl. Phys. Lett. **68**, 200 (1996).

[7] J. Hong, J.W. Lee, J.D. MacKenzie, S.M. Donovan, C.R. Abernathy, S.J. Pearton, and J.C. Zolper, Semicond. Sci. Technol. 12, 1310 (1997).

[8] H. Siegle, G. Kaczmarczyk, L. Filippidis, A.P. Litvinchuk, A. Hoffmann, and C. Thomsen, Phys. Rev. B **55**, 7000 (1997).

[9] T. Azuhata, T. Matsunaga, K. Shimada, K. Yoshida, T. Sota, K. Suzuki, and S. Nakamura, Physica B **219&220**, 493 (1996).

[10] M.E. Lin, B.N. Sverdiov, and H. Morkoç, Appl. Phys. Lett. **63**, 3625 (1993).

[11] F. Demangeot, J. Frandon, M.A. Renucci, O. Briot, B. Gil, R.-L. Aulombard, MRS Internet J. Nitride Semicond. Res. **1**, 23 (1996).

[12] A. S. Barker, Jr., Phys. Rev. **132**, 1474 (1963).

[13] L. Grabner, J. Appl. Phys. **49**, 580 (1978).

Electroluminescence Properties of InGaN/AlGaN/GaN Light Emitting Diodes with Quantum Wells

A.E.Yunovich, V.E.Kudryashov, A..N.Turkin.

M.V.Lomonosov Moscow State University,Department of Physics,

A.N.Kovalev, F.I.Manyakhin.

Moscow Institute of Steel and Alloys,

Moscow, Russia.

E-mail: yunovich@scon175.phys.msu.su

Cite this article as : MRS Internet J. Nitride Semicond. Res. 4S1, G6.29 (1999)

Abstract

Electroluminescence spectra of light-emitting diodes based on InGaN/AlGaN/GaN heterostructures with single and multiple quantum wells (QWs) are analyzed by models of radiative recombination in 2D-structures with band tails. Equations of the model fit spectra quite good in a wide range of currents. Parameters of the fit are discussed and compared for single and multiple QWs. Tunnel effects play a sufficient role in blue LEDs with single QWs at low currents; they can be neglected in LEDs with multiple QWs. A new spectral band was detected at the high energy side of the spectra of green LEDs with multiple QWs; it is attributed with large scale inhomogenities of In distribution in InGaN QWs.*)

*) This work proceeds previous results of our group presented on EGW-3 [1].

Introduction

The problems of recombination mechanisms in InGaN/AlGaN/GaN heterostructures are not fully understood in spite of great progress in the development of GaN-based light-emitting diodes (LEDs). We have studied luminescence spectra of two groups of LED's based on structures with single InGaN quantum wells (SQWs, sent to Moscow University by Dr. S.Nakamura, Nichia Chemical Co.) and multiple quantum wells (MQWs, sent to Moscow University by Dr. M.Koike, Toyoda Gosei Co.) in a wide range of currents [2-6]. A model of radiative recombination in 2D-structures with band tails caused by potential fluctuations was successfully applied to describe the spectra [2-4]; tunnel radiative recombination was detected at

Mat. Res. Soc. Symp. Proc. Vol. 537 © 1999 Materials Research Society

low currents [5]. In this work spectra of blue and green LEDs with SQW and MQW active layers are compared and the model of recombination is analyzed. Changes of the parameters with current J and voltage V are discussed.

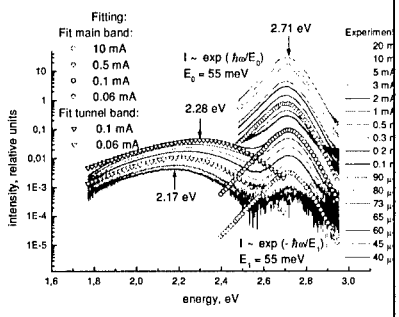


Figure 1a. Electroluminescence spectra of blue LED with SQW.

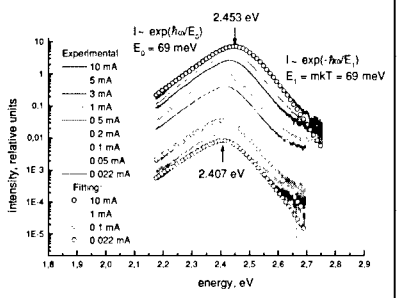


Figure 2a. Electroluminescence spectra of green LED with SQW.

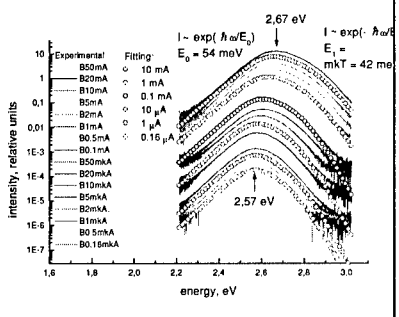


Figure 1b. Electroluminescence spectra of blue LED with MQW.

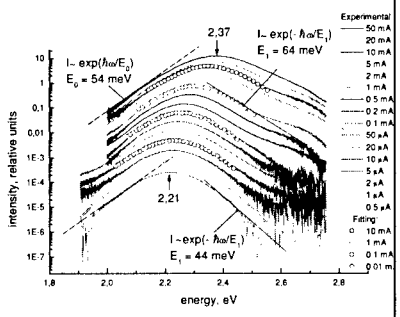


Figure 2b. Electroluminescence spectra of green LED with MQW.

Experimental results.

Both groups of LEDs were based on heterostructures grown on sapphire substrates by a MOCVD [2, 6]. A buffer layer was of GaN in Nichia samples [2] and of AlN in Toyoda samples [6]. The base layer was n-GaN:Si (4-5 mm).

The active layers of the structures were different: an SQW $In_xGa_{1-x}N$ (>3.5 nm) in Nichia LEDs and MQW $In_xGa_{1-x}N$/GaN (5 periods, a width of the period < 8 nm). Indium content (x in $In_xGa_{1-x}N$) varied in both cases (near x = 0.2 for green and near x = 0.4 for blue LEDs). Upper layers p-AlGaN:Mg and cap layers p-GaN:Mg have hole concentrations in the range $p = 5.10^{17}$-2.10^{18} cm^{-3}, higher for blue SQWs.

The spectra of blue and green LEDs with SQWs and MQWs are shown in a wide range of J (see Figs. 1, 2). The spectra of LEDs with SQWs could be measured down to 15 μA, that ones with MQWs to 0.15 μA. The cause of this difference is a tunnel component of nonradiative current most pronounced in blue LEDs with SQWs. Values of $\hbar\omega_{max}$ (≈2.65 eV) for blue SQWs LEDs do not depend on J.

There is another spectral band on the low energy side of the main blue line at low currents (see Fig. 1a). The maximum of this band is moving with the current J and voltage on the active layer U: $\hbar\omega_{max}$= eU+Δ (in the range = 2.1-2.3 eV). This band was described as a tunnel radiative recombination [4,5]. There is no tunnel band in blue LEDs with MQWs; in this case the blue line is moving with V.

Values of $\hbar\omega_{max}$ for green LEDs, both SQWs and MQWs, are moving with J and V, but in a wider range for MQWs: 2.2÷2.45 eV. A new band was detected at the high energy side (2.7÷2.8 eV) of the green line of MQWs (see Fig. 2b).

The main spectral lines have exponential tails: $I(\hbar\omega_{max}) \sim \exp(\hbar\omega_{max}/E_0)$ on the low energy side and $I(\hbar\omega_{max}) \sim \exp(-\hbar\omega_{max}/E_1)$ on the high energy side of the peaks. Values of E_0 = 50÷60 meV did not depend on the current and temperature T in a wide range of J. Values of E_1 were proportional to T: $E_1 = mkT$; $1 < m < 2$; m is almost equal to unity for SQWs and is in the range m = 1.5-1.7 for MQWs. E_1 was growing at higher direct currents, J >5 mA, due to heating of the LEDs.

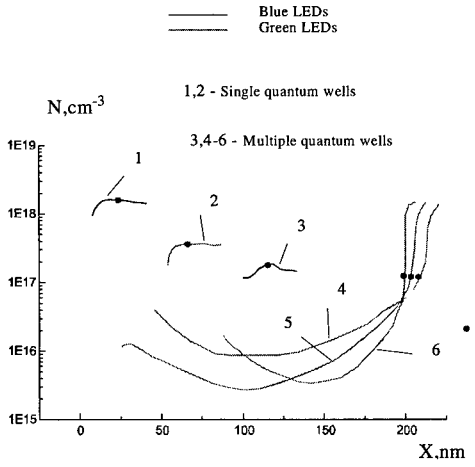


Figure 3. Distributions of charged centers in p-regions of p-n-heterojunctions; points - values of N_A^- at V = 0; begining of abscissa is at the n-interface. Blue (1,3) and green (2,4-6) LEDs with SQW (1,2) and MQW (3, 4-6).

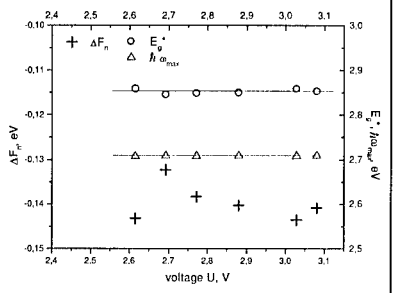


Figure 4a. Dependence of fitting parameters (ΔF_n, E_g^*, $\hbar\omega_{max}$) on the voltage for blue LED with SQW.

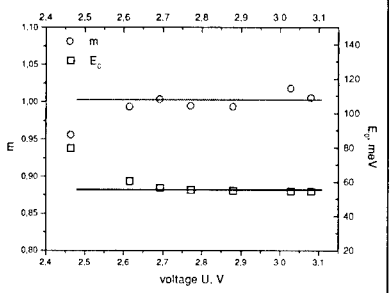


Figure 5a. Dependence of fitting parameters (m, E_0) on the voltage for blue LED with SQW.

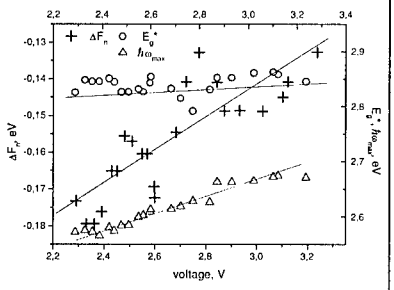


Figure 4b. Dependence of fitting parameters (ΔF_n, E_g^*, $\hbar\omega_{max}$) on the voltage for blue LED with MQW.

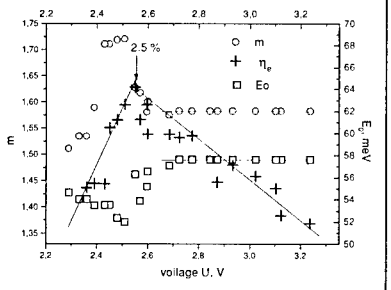


Figure 5b. Dependence of fitting parameters (m, E_0) and quantum efficiency η_e on the voltage for blue LED with MQW.

Current-voltage characteristics J(V) of blue and green LEDs had an exponential part at low currents, $J < 10^{-7}$ A at 300 K, a steep exponential growth in the range V = 2.3-2.7 V, a linear part at higher currents, J > 20 mA. Low currents could be understood as a tunnel component; tunnel currents in these LEDs play some role at J 3-4 orders of magnitude lower than that for SQW-based LEDs [2-5,7]; J(V) curves of SQW-based LEDs differed from MQW-based LEDs because of a wider active layer [1].

A good approximation of the J(V) curves for MQW LEDs was done when not only a series resistance R_s at the linear part at higher J was taken into account, but also the quadratic part: $J \sim (V\text{-}V_1)^2$. The fit of the curve J(V) at J > 0.1 mA by the equation:

$$V = \varphi_k + E_J \cdot [\ln(J/J_0) + (J/J_1)^{0.5}] + J \cdot R_s , \qquad (1)$$

A part $\sim(J/J_1)^{0.5}$ is sufficient between an exponential (injection) and a linear parts, in the range J=2÷30 mA, at usual working currents [1].

Distributions of charged centers in p- regions of InGaN/AlGaN/GaN p-n-heterostructures with MQWs and SQWs are shown, see Fig. 3 (see a method of measurements in [8]). The LEDs with MQWs have wider space charge width than ones with SQWs [2-5,7]; in both cases the width for green LEDs is wider than for blue ones. This fact corresponds to a low probability of tunnel effects in the LEDs with MQWs.

It seems that high Mg-doping of p- AlGaN and GaN- layers is more difficult for higher In concentration in InGaN active layers.

Discussion

We describe the main lines in spectra with a model previously applied for fitting the spectra of LEDs with SQW [1-3]. The model implies that an effective radiative recombination takes place when carriers of both singes are injected into the active layer at voltages on the layer U < V, U close to φ_k. Optical transitions $\hbar\omega$ are going between states $E_{(c)}$ and $E_{(v)}$ in tails of 2D-structure, caused by potential fluctuations. A model 2D- joint density of states is

$$N^{2D}(\hbar\omega - E_g^*) = [1 + \exp(-(\hbar\omega - E_g^*)/E_0)]^{-1} ; \qquad (2)$$

an effective energy gap $E_g^* = E_g(x,T)+\Delta E_{1c}+\Delta E_{1v}+\Delta E_p-E_{exc}-\Delta E_{D,A}$,
where $E_g(x,T)$ – the energy bandgap in the active layer - QW, ΔE_{1c},ΔE_{1v} – quantum size energy levels in conduction and valence bands, ΔE_p- lattice deformation shift, E_{exc}- energy of 2D-exciton, $\Delta E_{D,A}$- donor-aceptor potential shift of the effective bandgap. The values E_g^* received from this model are 2.98-3.05 eV for blue and 2.67-2.76 eV for green LED [3]. Spectral intensity $I(\hbar\omega)$ is proportional to Fermi-functions of electrons and holes with quasi-Fermi levels F_n, F_p as parameters (details in [2,3]):

$$I(\hbar\omega) \sim N^{2D}(\hbar\omega - E_g^*)\, f_c(\hbar\omega, m, kT, F_n)\,(1-f_v(\hbar\omega, 1-m, kT, F_p)); \quad (3)$$

Examples of the fit are shown in Figs. 2, 3. A change of $\hbar\omega_{max}$ in some range of J is caused mostly by changes of the parameter F_n; states in the tails are filled as V and J are growing (see Fig. 4). Parameters of the fit E_g^*, E_0, $E_1 = m \cdot kT$ can be seen in Figs. 4, 5 for blue MQWs and SQW. There is the evidence that a mechanism of recombination in the 2D-tail of states is not changed in some range. It is remarkable that when this mechanism begins the quantum efficiency η_e reaches a maximum (see Fig. 5b). When the states in the active layers are filled by current carriers at high J, the quantum efficiency η_e gradually falls.

There is a change of mechanism of recombination at lower currents; this can be concluded from Fig. 5b in spite of scattering of the points. Comparing spectra in the Figs. 1a and 1b we assume that this change is somewhat connected with tunneling.

A change of mechanism of recombination at higher currents in green LEDs, pronounced as a new band in Fig. 2b, can be connected with nonuniform distribution of Indium in the active layers InGaN more probable at higher In content.

Conclusions

Mechanism of radiative recombination in 2D- structures with band tails describe the main line in the spectra of both groups blue and green LEDs, with SQWs and MQWs, in a wide range of currents. The main difference in spectra of two groups is a role of tunnel effects at low currents in LEDs with SQWs. Moving of spectra with the voltage is more pronounced in green LEDs due to higher content of Indium and more pronounced density of states tails in the active InGaN layers.

Acknowledgments

Authors thank Dr. S.Nakamura (Nichia Chemical Co.) and Dr. M.Koike (Toyoda Goasei Co.) for sending LEDs to Moscow University; S.S.Mamakin and R.V.Grigoryev for help in measurements.

References

[1] Yunovich A.E., Kudryashov V.E., Turkin A.N., A.N.Kovalev, F.I.Manyachin The Emission Properties of Light Emitting Diodes utilising Multiple Quantum Wells InGaN/AlGaN/GaN. GaN MRS Intern. Journ.of Nitride Semic. Res., 3\44.

[2] Zolina K.G., Kudryashov V.E., Turkin A.N., Yunovich A.E., Nakamura S., Luminescense Spectra of Superbright Blue and Green InGaN/AlGaN/GaN Light-Emitting Diodes, *MRS Int. J. Of Nitride Semicond. Res.* **1** (1996) 11; *J. of the European Ceramic Society* **17** (1997) p.2033.

[3] Zolina K.G., Kudryashov V.E., Turkin A.N., Yunovich A.E., Luminescense spectra of blue and green InGaN/AlGaN/GaN light-emitting diodes, *Semiconductors.* **31** (9) (1997) p. 1055.

[4] A. Yunovich, A.Kovalev, F. Manyachin, V. Kudryashov, A.N.Turkin, K.G.Zolina. Mechanisms of electroluminescence in InGaN/AlGaN/GaN heterojunctions with quantum wells. Proc. of the Second Symposium on III-V Nitride Materials and Processes, Vol.98-02 Electrochem. Soc., Pennington, NJ, 1998, pp.83-102.

[5] Kudryashov V., Zolina K., Turkin A., Yunovich A., Kovalev A., Manyakhin F., Tunneling effects in light-emitting diodes based on InGaN/AlGaN/GaN heterostructures with quantum wells, *Semiconductors.* **31** (11) (1997) p. 1123.

[6] Koike M., Koide N., Asami S., Umezaki J., Nagai S., Yamasaki S., Shibata N., Amano H., Akasaki I., GaInN/GaN multiple quantum wells green LEDs, *Proc. of SPIE-Intern.Soc.Opt.Engin.* **3002** (1997).

[7] A.E.Yunovich, A.N.Kovalev, V.E.Kudryashov, F.I.Manyachin, A.N.Turkin, K.G.Zolina, "Tunnel Effects in Luminescence Spectra of InGaN/AlGaN/GaN Light-Emitting Diodes", MRS Symposium Proc., ***449***, 1167 (1997).

[8] F.I.Manyakhin, A.N.Kovalev, V.E.Kudryashov, A.N.Turkin, A.E.Yunovich, Semiconductors, ***33*** (1), (1999, to be published).

ELECTRICAL CHARACTERIZATION OF MOVPE-GROWN P-TYPE GaN:Mg AGAINST ANNEALING TEMPERATURE

Shizuo Fujita, Mitsuru Funato, Doo-Cheol Park, Yoshifumi Ikenaga, Shigeo Fujita

Department of Electronic Science and Engineering, Kyoto University, Kyoto 606-8501, Japan

Cite this article as: MRS Internet J. Nitride Semicond. Res. 4S1, G6.31(1999)

ABSTRACT

Hall effect measurements have been applied for the electrical characterization of p-type Mg-doped GaN grown by metalorganic vapor-phase epitaxy on sapphire substrates in terms of annealing temperature for dehydrogenation (N_2 annealing) and hydrogenation (H_2 annealing) of the acceptors. With the N_2 annealing temperature from 600 to 900 °C for dehydrogenation, both hole concentration and mobility increases, showing more activation of acceptors and less incorporation of unfavorable scattering centers probably originating from Mg-H bondings. The N_2 annealing at higher than the growth temperature results in reduced hole concentration, but the mobility gets higher. Some defects compensating acceptors may be induced at high temperature annealing, but they seem to be no scattering centers and be inactivated by successive hydrogenation and re-dehydrogenation at the optimum dehydrogenation temperature 900 °C. The electrical degradation of GaN due to thermal damage is not very destructive and can be well recovered by annealing treatments.

INTRODUCTION

It is now a common understanding that Mg acceptors doped in GaN by metalorganic vapor-phase epitaxy (MOVPE) are severely passivated with hydrogen in as-grown layers and can be activated to achieve p-type conductivity by post-growth thermal annealing in N_2 atmosphere resulting in dehydrogenation. With referring the earliest reports by Nakamura et al. [1], the thermal annealing has been considered to be effective at a temperature sufficiently lower than the growth temperature, e.g., at 600 °C or slightly higher. Although the doped Mg acceptors are expected to be activated almost completely at the present annealing conditions, there have not been a sufficient number of reports investigating the activation processes and the possible defects induced by thermal damage during the annealing.

Youn et al.[2] showed that there was an optimum annealing temperature resulting in the highest hole concentration, dependent on the existing defect structures in Mg-doped GaN (GaN:Mg) layers. The hole concentration decreased at higher annealing temperatures, different from the data in ref.[1] showing the constant hole concentration with annealing temperature above 650 °C, and this phenomenon was interpreted by generation of nitrogen vacancies compensating Mg at higher annealing temperatures. As is demonstrated in this work, the possibility of defect generation or other thermal effects may be an important factor to be taken into account in the discussion of the activation process of Mg acceptors.

In this study, aiming at detailed understanding of activation and degradation mechanism in GaN:Mg layers, characterization of electrical properties has done in terms of wide variety of the annealing temperature, including that higher than the growth temperature, for dehydrogenation in N_2 atmosphere. Effects of successive hydrogenation in H_2 atmosphere and re-dehydrogenation were also investigated.

Mat. Res. Soc. Symp. Proc. Vol. 537 © 1999 Materials Research Society

EXPERIMENTS

Mg-doped GaN layers of 1 μm in thickness were grown on sapphire substrates by MOVPE at around 1000 °C. The post-growth annealing was done either in N_2 or H_2 atmosphere at various temperatures between 600 and 1100 °C, being expected to result in dehydrogenation or (re)hydrogenation, respectively. The electrical characterization was done by temperature-variable Hall effect measurements with Van der Pauw samples, fabricated by evaporating Au/Ni electrodes. The AC-component of Hall voltage was detected under magnetic field modulation typically at 50mHz, which enabled the characterization of highly resistive samples as those with the resistivity of 10^8 Ω·cm. The simple one carrier analysis method has been applied for the calculation of hole concentration and hole Hall mobility from the Hall effect measurement data as a first approximation.

RESULTS AND DISCUSSION

Dehydrogenation

As-grown GaN:Mg samples have been subjected to thermal annealing in N_2 atmosphere for 20 min at different temperatures. The Hall effect measurements were conducted after fabricating the Au/Ni electrodes. Figure 1 shows the temperature dependence of hole concentration and hole Hall mobility with the annealing temperature as a parameter.

With the annealing from 600 to 900 °C the hole concentration slightly increases from 1 to 6×10^{17} cm^{-3} at room temperature (RT). The increase of hole concentration values at lower temperatures may be attributed to occurrence of impurity band conduction [3] which makes invalid to use the one carrier analysis method for calculating the actual hole concentrations. The Hall mobility at RT also increases with the annealing temperature. It is worth noticing that the mobility of 600 °C-annealed sample exhibits a plateau characteristics near RT, suggesting that

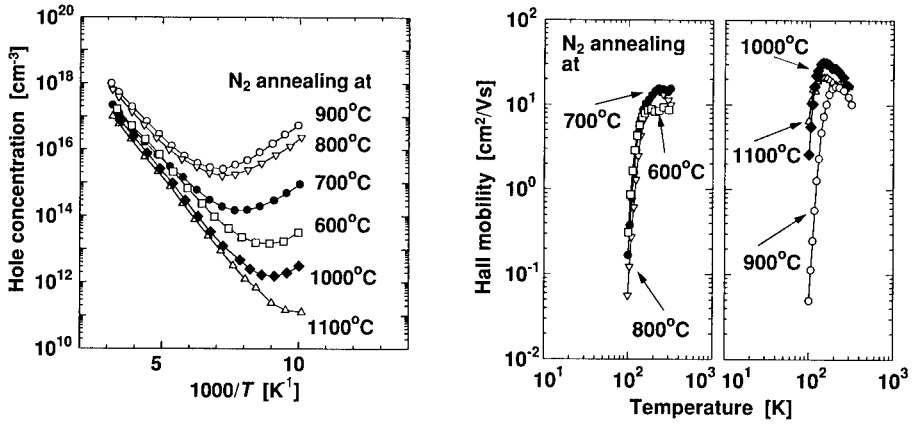


Fig. 1 Temperature dependence of hole concentration and hole Hall mobility of GaN:Mg samples subjected to different dehydrogenation (N_2 annealing) temperature.

the hole transport is severely suppressed by neutral impurity scattering. From these mobility data, it is speculated that the samples of insufficient acceptor activation (i.e., those annealed at lower temperatures) contain unfavorable scattering centers probably originating from Mg-H bondings.

On the other hand, for the samples annealed at 1000 or 1100 °C, which are higher than the growth temperature, the hole concentration decreases to mid-10^{16} cm^{-3}. However, one of the noticeable results is that the mobility becomes higher than those annealed at 700-900 °C and exhibits the more well-defined lattice scattering characteristics in Hall mobility data, i.e., that is proportional to $T^{-1.5}$ from 130 K to RT. The maximum mobility of the 1000 °C-annealed sample is 32 cm^2/Vs at 130K, which is the highest value among those observed in all samples examined here. If the decrease in hole concentration of those high-temperature annealed samples is due to generation of defects such as nitrogen vacancies, as has been suggested in ref.[2], the increased mobility and its lattice scattering characteristics cannot be explained.

From these investigations, it may be concluded that (i) with the higher annealing temperature up to the growth temperature more activation of acceptors proceeds and unfavorable scattering centers originating from Mg-H bondings decrease, and (ii) the annealing at the temperature higher than the growth temperature results in compensation but does not enhance the generation of scattering centers. In additions to those, it is seen that the mobility-temperature characteristics, where the mobility rapidly decreases below 200 K for all samples, are not different significantly irrespecive of different contribution of the impurity band conduction. This is probably because that the conduction at low temperatures is dominated by native crystallographic characteristics such as grain boundaries.

Figure 2 shows the low temperature (24 K) photoluminescence (PL) spectra of the annealed samples. The PL intensity decreases with the annealing temperature from 600 to 900 °C but in tern increases for 1000 °C, showing also no heavy degradation with generation of optical defects for the high temperature annealing. The change in the spectral shape may involve useful

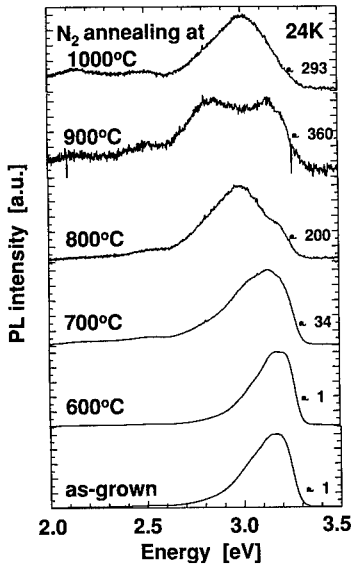


Fig. 2 24 K PL spectra of GaN:Mg samples subjected to different dehydrogenation (N_2 annealing temperature.

information on the phenomena occurred by the annealing, but the analysis has not been performed at present.

Rehydrogenation

Hydrogenation of active Mg acceptors in low resistive p-type GaN has been known to result in passivation of the acceptors and high resistivity [4-6]. In order to investigate the hydrogenation processes in more detail, which is also helpful for understanding the dehydrogenation processes, in this work the GaN:Mg samples subjected to dehydrogenation by annealing in N_2 atmosphere have been then annealed in H_2 atmosphere. The hydrogenation for each sample was done at 700 °C for 20 min.

Figure 3 summarizes the variation of hole concentration at RT against the dehydrogenation (previous N_2 annealing) temperature. The hydrogenation results in reduction of hole concentrations due to hydrogen passivation of acceptors. For the samples experienced the dehydrogenation by the N_2 annealing at 700-900 °C, as the N_2 annealing temperature is higher, more incomplete hydrogenation or passivation seems to result by the H_2 annealing. This phenomenon can easily be attributed to that more dehydrogenation has been proceeded in the sample subjected to N_2 annealing at higher temperatures. However, for the sample subjected to dehydrogenation at 1000 °C, only incomplete hydrogenation results compared to what we can expect from the behavior of those dehydrogenated at 700-900°C. The hole concentration of this sample was about 1×10^{17} cm^{-3}, which was similar to that dehydrogenated at 700 °C. After the hydrogenation, the hole concentration is still 4×10^{15} cm^{-3}, which is much higher that that of the latter, 3×10^{12} cm^{-3}. One of the possible interpretations for this phenomenon is that the hydrogen dominantly passivated the defects which had been generated by the thermal damage during the N_2 annealing at 1100 °C and compensated the Mg acceptors.

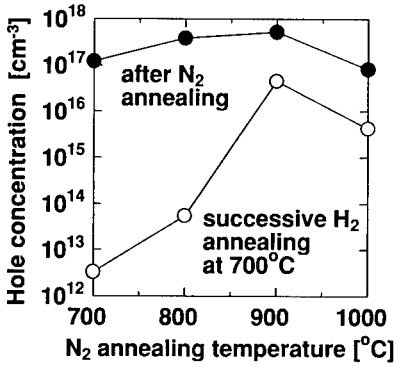


Fig. 3 Variation of hole concentration at RT after dehydrogenation (N_2 annealing) and successive hydrogenation (H_2 annealing) against the dehydrogenation temperature. The hydrogenation was done at the same condition, 700 °C and 20 min.

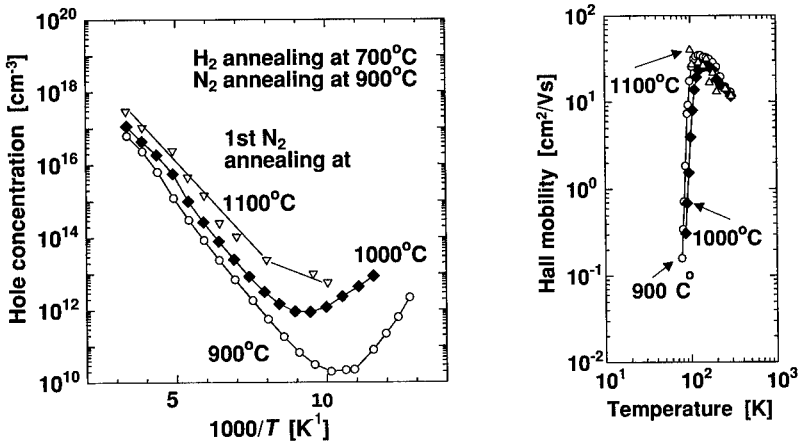


Fig. 4 Temperature dependence of hole concentration and hole Hall mobility of GaN:Mg samples experienced dehydrogenation, hydrogenation, and re-dehydrogenation, successively. The 1st dehydrogenation temperatures are shown as a parameter and the succesive hydrogenation and re-dehydrogenation were done at 700 °C and 900 °C, respectively.

Re-Dehydrogenation

For three samples which had been subjected to dehydrogenation at 900, 1000, and 1100 °C and then hydrogenation at 700 °C, the annealing was again done in N_2 atmosphere for re-dehydrogenation. In this experiment, the annealing temperature and time was fixed at 900 °C and 20 min, respectively, where from Fig. 1 the maximum dehydrogenation was expected.

The temperature dependence of the hole concentration and hole Hall mobility is shown in Fig. 4. This re-dehydrogenation process again activates Mg acceptors in GaN and results in p-type conductivity. It should be noted that the sample experienced the previous dehydrogenation (1st N_2 annealing) at 1100 °C showed the higher hole concentration and the higher Hall mobility compared to those at 900 or 1000 °C. The maximum mobility seems to be about 40 cm^2/Vs at 100K, which is even higher than all samples shown in Fig. 1. This again evidenced that any compensation centers generated in GaN:Mg with annealing in N_2 at 1100 °C do not seriously act as scattering or trapping centers and are almost inactivated by the successive thermal annealing treatments.

CONCLUSIONS

Successive dehydrogenation and hydrogenation of Mg acceptors in GaN have been done by N_2 and H_2 annealing, respectively, at different temperatures. For the dehydrogenation of as-grown GaN:Mg samples, the N_2 annealing at higher temperatures in the region below the growth temperature results in increase of both hole concentration and mobility, showing more activation of acceptors and reduction in unfavorable scattering centers associated with Mg-H bondings.

When the N_2 annealing is higher than the growth temperature, the hole concentration reduces. However, the remarkable result is that the mobility gets higher. The GaN:Mg layer may be subjected to thermal damage which induces some defects and these defects compensate the acceptors, showing reduction in the hole concentration. But these defects cannot be severe scattering centers and inactivated by successive hydrogenation. Even if the GaN experiences thermal damage by high temperature annealing, it is not destructive and can be well recovered by appropriate hydrogenation/dehydrogenation treatments afterwards. The phenomena that thermally-induced defects do not severely affect the electrical properties is an another "stable nature of defects" in GaN crystals, similarly to the optical properties against dislocations.

ACKNOWLEDGEMENTS

This work was supported in part by a Grant-in-Aid for Scientific Research from the Ministry of Education, Science, Sports and Culture. The Hall effect measurements were conducted with the facility at Kyoto University Venture Business Laboratory (KU-VBL).

REFERENCES

1. S. Nakamura, T. Mukai, M. Senoh and N. Iwasa, Jpn. J. Appl. Phys. **31**, L139 (1992).
2. D.H. Youn, M. Lachab, M. Hao, T. Sugahara, K. Yamashita, Y. Naoi and S. Sakai, *Extended Abst. 1998 Int. Conf. Solid State Devices and Materials, Hiroshima* (Business Center for Academic Societies, Tokyo, 1998), p.242.
3. W. Goetz, N.M. Johnson, J. Walker, D.P. Bour and R.A. Street, Appl. Phys. Lett. **68**, 667 (1996).
4. S. Nakamura, N. Iwasa, M. Senoh and T. Mukai, Jpn. J. Appl. Phys. **31**, 1258 (1992).
5. M.S. Brandt, N.M. Johnson, R.J. Molnar, R. Singh and T.D. Moustakas, Appl. Phys. Lett. **64**, 2264 (1994).
6. J.M. Zavada, R.G. Wilson, C.R. Abernathy and S.J. Pearton, Appl. Phys. Lett. **64**, 2724 (1994).

RAPID THERMAL PROCESSING OF IMPLANTED GaN UP TO 1500 °C

X. A. Cao,* S. J. Pearton,* R. K. Singh,* C. R. Abernathy,* J. Han,** R. J. Shul,** D. J. Rieger,** J. C. Zolper,*** R. G. Wilson,**** M. Fu,***** J. A. Sekhar,***** H. J. Guo ****** and S. J. Pennycook******

*Department of Materials Science and Engineering, University of Florida, Gainesville, FL 32611, USA

**Sandia National Laboratories, Albuquerque, NM 87185, USA

***Office of Naval Research, Arlington, VA 22217, USA

****Consultant, Stevenson Ranch, CA 91381, USA

*****Micropyretics Heaters International, Inc. Cincinnati, OH 45215, USA

******Oak Ridge National Laboratory, Solid State Division, Oak Ridge, TN 37831,USA

Cite this article as: MRS Internat J. Nitride Semicond. Res. 4S1, G6.33(1999)

ABSTRACT

GaN implanted with donor(Si, S, Se, Te) or acceptor (Be, Mg, C) species was annealed at 900-1500 °C using AlN encapsulation. No redistribution was measured by SIMS for any of the dopants and effective diffusion coefficients are $\leq 2\times10^{-13}$ $cm^2 \cdot s^{-1}$ at 1400 °C, except Be, which displays damage-enhanced diffusion at 900 °C and is immobile once the point defect concentration is removed. Activation efficiency of ~90% is obtained for Si at 1400 °C. TEM of the implanted material shows a strong reduction in lattice disorder at 1400-1500 °C compared to previous results at 1100 °C. There is minimal interaction of the sputtered AlN with GaN under our conditions, and it is readily removed selectively with KOH.

INTRODUCTION

The study of implanted species in GaN to this point has focused on activation of Si^+ or O^+ for n-type doping, Mg^+ or Ca^+ for p-type doping, or use of He^+, N^+ or H^+ for isolation[1-15]. For practical applications, the focus has been on the use of implantation for improving ohmic contact resistance on heterostructure field-effect transistors[16], and to producing p-n junctions for fabrication of junction field-effect transistors[12] and for light-emitting diodes[4]. At high implant doses ($\geq 5\times10^{14}$ cm^{-2}) it is clear that conventional rapid thermal annealing (RTA) at 1100-1200 °C can activate the dopants but not remove the ion-induced structural damage[14,15]. At higher annealing temperatures (≥1400 °C) it is difficult to provide a sufficiently high N_2 pressure to prevent dissociation of the GaN surface. Three different approaches have been reported - the first is use of an NH_3 ambient in a metal organic chemical vapor deposition (MOCVD) reactor[17], the second is use of a high N_2 overpressure (15 kbar) in a GaN bulk crystal growth apparatus[14], and the third is use of an AlN encapsulant to prevent nitrogen loss from the GaN[18]. The third approach is clearly the most convenient.

The amount of residual lattice damage in the implanted GaN after annealing is a function of ion dose - for the relatively high doses needed for source/drain doping, it has been shown previously that annealing temperatures of ≥1400 °C are desirable. We have found that Si, the most common n-type dopant, shows no detectable redistribution at 1400 °C, and that annealing

Mat. Res. Soc. Symp. Proc. Vol. 537 © 1999 Materials Research Society

at this temperature produces activation percentages of ≥90%[19,20]. Annealing at 1500 °C led to a reduction in both sheet electron concentration and electron mobility, which is consistent with self-compensation through site-switching of the Si. There is no available information on the other donor species, or on the possible acceptor dopants, in terms of their redistribution during ultra-high temperature annealing. In this paper we report on a Secondary Ion Mass Spectrometry (SIMS) study of GaN implanted with the group VI donors, S, Se and Te, and the acceptor species Mg, Be and C. Only Be is found to show redistribution during annealing, emphasizing the extremely good high temperature stability of dopants in GaN. We have also examined the activation kinetics of some of the implanted species.

EXPERIMENTAL

Layers of GaN 2-3 μm thick were grown at ~1040 °C on c-plane Al_2O_3 by atmospheric pressure Metal Organic Chemical Vapor Deposition(MOCVD), using triethylgallium and ammonia. From x-ray diffraction and photoluminescence measurements we know this material is typical of the current state-of-the-art heteroepitaxial GaN.

The samples were implanted at 25 °C with 150 keV $^{24}Mg^+$, 80 keV $^{9}Be^+$, 80 keV $^{12}C^+$, 200 keV $^{32}S^+$, 300 keV $^{80}Se^+$, or 600 keV $^{128}Te^+$ ions, at doses of 3-5×10^{14} cm^{-2}. This puts the projected range, R_p, of the implanted species at least 1500 Å into the GaN in all cases, avoiding effects due to near-surface point defect injection. The samples were capped with ~1000 Å of reactively sputtered AlN, and annealed at temperatures of 900-1450 °C under a N_2 ambient in the Zapper™ furnace described previously[14]. The dwell time at the peak temperature was ~10 secs. After annealing, the AlN was selectively etched in aqueous KOH at 80 °C[15]. The atomic distributions before and after annealing were measured by SIMS, and the data quantified using the as-implanted sample as a standard. The electrical properties were examined by Hall measurement, and the data was recorded at 25 °C in all cases.

RESULTS AND DISCUSSION

(a) Residual Damage

Figure 1 shows a plan view TEM and selected area electron diffraction pattern from a Si-implanted sample (150 keV, 5×10^{15} cm^{-2}) after annealing at 1100 °C for 10 secs. This is a high dose implant of the type used for making n^+ ohmic contact regions, and represents a worst-case scenario in terms of damage removal. The sample is still single-crystal as determined by the diffraction pattern, but contains a high density of extended defects (~10^{10} cm^{-2}). This is consistent with past reports of high backscattering yields in implanted GaN annealed at these conditions[14,15]. We ascribe these defects to the formation of dislocation loops in the incompletely repaired lattice.

By sharp contrast, annealing at 1400 °C for 10 secs brings a substantial reduction in the implant-induced defects, as shown in Figure 2. The sample is again single-crystal, but the only contrast in the TEM plan view is due to the lower density(~10^9 cm^{-2}) of threading dislocations arising from lattice-mismatch in the heteroepitaxy. This appears to correlate well with the fact that the highest electron mobility and carrier density in these samples was observed for 1400 °C annealing. Clearly the ultra-high temperature annealing is required to completely remove lattice damage in GaN implanted with high doses. However it may not be needed in lower dose material(≤5×10^{13} cm^{-2}) where the amount of damage created is correspondingly less.

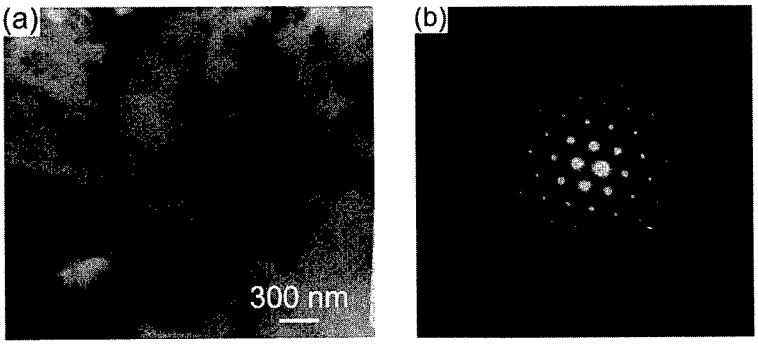


Fig. 1. (a) TEM plan view and (b) selected area diffraction pattern from Si^+ implanted GaN (5×10^{15} cm^{-2}, 150 keV) after 1100 °C, 10 sec annealing.

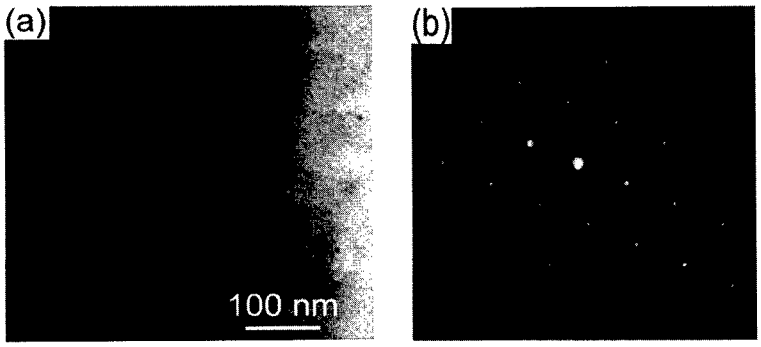


Fig. 2. (a) TEM plan view and (b) selected area diffraction pattern from Si^+ implanted GaN (5×10^{15} cm^{-2}, 150 keV) after 1400 °C, 10 sec annealing.

(b) Dopant Activation

(i) Donors

Figure 3(top) shows an Arrhenius plot of S^+ activation in GaN. The sheet carrier concentration measured at 25 °C shows an activation energy of 3.16 eV for the annealing temperature range between 1000-1200 °C and basically saturates thereafter. The maximum sheet electron density, ~7×10^{13} cm^{-2}, corresponds to a peak volume density of ~5×10^{18} cm^{-3}. This is well below that achieved with Si^+ implantation and annealing (>10^{20} cm^{-3})[17,20]. In the latter case the carrier density showed an activation energy of 5.2 eV. The physical origin of this activation energy contains several components – basically it is the energy required to move an implanted ion onto a substitutional lattice site and for it to show electrical activity. This latter

requirement means that compensating defects must also be annealed out. Even though implanted Si^+ at the same dose showed evidence of site-switching and self-compensation, it still produces a higher peak doping level than the non-amphoteric donor S, which is only slightly heavier (^{32}S vs. ^{28}Si). From temperature-dependant Hall measurements, we find a S^+ donor ionization level of 48±10 meV, so that the donors are fully ionized at room temperature.

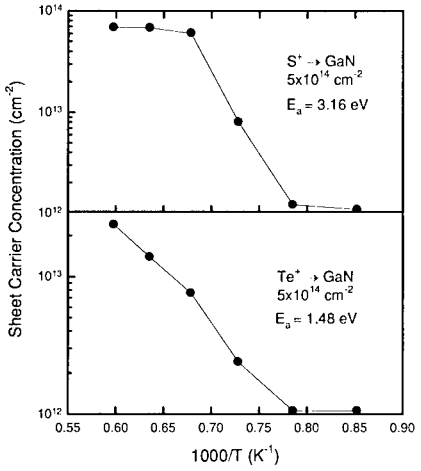


Fig. 3. Arrhenius plot of sheet electron density in S^+ (top) or Te^+ (bottom) implanted GaN versus annealing temperature.

Similar data is shown in Figure 3(bottom) for Te^+ implantation. The activation starts around the same temperature as for S, but much lower sheet electron densities are obtained, the activation energy is significantly lower (1.5 eV) and the carrier concentration does not saturate, even at 1400 °C. It is likely that because of the much greater atomic weight of ^{128}Te, even higher annealing temperatures would be required to remove all its associated lattice damage, and that the activation characteristics are still being dominated by this defect removal process. Residual lattice damage from the implantation is electrically active in all III-V semiconductors, producing either high resistance behaviors(GaAs) or residual n-type conductivity(InP, GaN). The only data available on group VI doping in epitaxial material is from Se-doped MOCVD material, where maximum electron concentrations of $2\times10^{18} - 6\times10^{19}$ cm^{-3} were achieved[21,22]. These are also below the values reported for Si-doping, and suggests the group VI donors do not have any advantage over Si for creation of n-type layers in GaN. From limited temperature-dependent Hall data, we estimate the Te ionization level to be 50±20 meV.

No redistribution of any of the donor species was observed during annealing up to 1500 °C, suggesting the diffusion coefficient is $\leq 2\times10^{-13}$ cm^2·s^{-1} for S, Se, Te and Si at this temperature.

(ii) Acceptors

The effects of post-implant annealing temperature on the sheet carrier concentrations in Mg^+ and C^+ implanted GaN are shown in Figure 4. There are two important features of the data: first,

we did not achieve p-type conductivity with carbon, and second only ~1% of the Mg produces a hole at 25 °C. Carbon has been predicted previously to have a strong self-compensation effect[23], and it has been found to produce p-type conductivity only in metal organic molecular beam epitaxy where its incorporation on a N-site is favorable[24]. Based on an ionization level of ~170 meV, the hole density in Mg-doped GaN would be calculated to be ~10% of the Mg acceptor concentration when measured at 25 °C. In our case we see an order of magnitude less holes than predicted. This should be related to the existing n-type carrier background in the material and perhaps to residual lattice damage which is also n-type in GaN, At the highest annealing temperature (1400 °C), the hole density falls, which could be due to Mg coming out of the solution or to the creation of further compensating defects in the GaN.

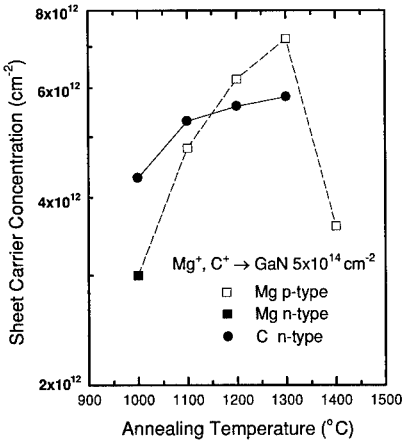


Fig. 4. Sheet carrier densities in Mg^+ or C^+ implanted GaN as a function of annealing temperature.

We did not observe any redistribution of either Mg or C for annealing up to 1450 °C, indicating a diffusivity of $\leq 2\times10^{-13}$ $cm^2 \cdot s^{-1}$ at this temperature. In the particular case of implanted Be, there was an initial broadening of the profile at 900 °C, corresponding to an effective diffusivity of $\sim 5\times10^{-13}$ $cm^2 \cdot sec^{-1}$ at this temperature. However there was no subsequent redistribution at temperatures up to 1200 °C. Implanted Be shows several types of anomalous diffusion in GaAs, including up-hill diffusion and movement in the tail of the profile, in addition to normal concentration-dependent diffusion, which also result from the non-equilibrium concentrations of point defects created by the nuclear stopping process of the implanted ions. It appears that in GaN, the interstitial Be undergoes a type of transient-enhanced diffusion until these excess point defects are removed by annealing, at which stage the Be is basically immobile.

SUMMARY AND CONCLUSIONS

Common acceptor and donor species have been implanted into GaN at room temperature, and subsequently annealed up to 1500 °C. With the exception of Be, which shows an apparent damage-assisted redistribution at 900 °C, none of the species show detectable motion under these conditions. This is promising for the fabrication of GaN-based power devices, which require creation of doped well or source/drain regions by implantation. The low diffusivities of implanted dopants in GaN means that junction placement should be quite precise and there will be less problems with lateral diffusion of the source/drain regions towards the gate. Finally, the results show the effectiveness of the AlN cap in protecting the GaN surface from dissociation, since if any of the surface was degraded during annealing, the implant profiles would no longer overlap.

ACKNOWLEDGEMENTS

The work of UF is partially supported by a DARPA/EPRI grant MDA 972-98-1-0006 (D. Radack/J. Melcher) and by an NSF grant DMR 9732865 (L. Hess). Sandia is a multiprogram laboratory operated by Sandia Corporation, a Lockheed-Martin company, for the US Department of Energy under contract No. DEAC04-94 AL 85000. The work of R. G. Wilson is partially supported by an ARO grant.

REFERENCES

1. J. C. Zolper, J. Cryst. Growth **178** 175 (1997).
2. J. C. Zolper, in GaN and Related Materials, Vol. **2** of Optoelectronic Properties of Semiconductors and Superlattices. (Gordon and Breach, NY 1997).
3. R. G. Wilson, Proc. Electrochem. Soc. Vol. **95-21** 152 (1995).
4. H. P. Maruska, M. Lioubtchenko, T. G. Tetreault, M. Osinski, S. J. Pearton, M. Schurman, R. Vaudo, S. Sakai, Q. Chen and R. J. Shul, Mat. Res. Soc. Symp. Proc. **483** 345 (1998).
5. J. C. Zolper, H. H. Tan, J. S. Williams, J. Zou, D. J. H. Cockayne, S. J. Pearton, M. H. Crawford and R. F. Karlicek Jr., Appl. Phys. Lett. **70** 2729 (1997).
6. S. C. Binari, H. B. Dietrich, G. Kelner, L. B. Rowland, K. Doverspike and D. K. Wickenden, J. Appl. Phys. **78** 3008 (1995).
7. C. Liu, B. Mensching, M. Zeitler, K. Volz, and B. Rauschenbach, Phys. Rev. B **57** 2530 (1998).
8. C. Ronning, N. Dalmer, M. Deicher, M. Restle, M. D. Bremser, R. F. Davis and H. Hofsass, Mat. Res. Soc. Symp. Proc. Vol. **468** 407 (1997).
9. H. Kobayashi, W. M. Gibson, Appl. Phys. Lett. **73** 1406 (1998).
10. T. Suski, J. Jun, M. Leszczynski, H. Teisseyre, I. Grzegory, S. Porowski, J. M. Baranowski, A. Rockett, S. Strite, A. Stanert, A. Turos, H. H. Tan, J. S. Williams and C. Jagadish, Mat. Res. Soc. Symp. Proc. Vol. **482** 703 (1998).
11. S. J. Pearton, C. R. Abernathy, C. B. Vartuli, J. C. Zolper, C. Yuan and R. A. Stall, Appl. Phys. Lett. **68** 2273 (1996).
12. J. C. Zolper, R. J. Shul, A. G. Baca, R. G. Wilson, S. J. Pearton and R. A. Stall, Appl. Phys. Lett. **68** 2273 (1996).
13. J. C. Zolper, R. G. Wilson, S. J. Pearton and R. A. Stall, Appl. Phys. Lett. **68** 1945 (1996).

14. J. C. Zolper, J. Han, S. B. Van Deusen, R. M. Biefeld, M. H. Crawford, J. Han, T. Suski, J. M. Baranowski and S. J. Pearton, Mat. Res. Soc. Symp. Proc. **482** 609 (1998).
15. H. H. Tan, J. S. Williams, J. Zou, D. J. H. Cockayne, S. J. Pearton and R. A. Stall, Appl. Phys. Lett. **69** 2364 (1996).
16. J. Burm, K. Chu, W. A. Davis, W. J. Schaff, L. F. Eastman and T. J. Eustis, Appl. Phys. Lett. **70** 464 (1997).
17. J. C. Zolper, J. Han, R. M. Biefeld, S. B. Van Deusen, W. R. Wampler, D. J. Reiger, S. J. Pearton, J. S. Williams, H. H. Tan and R. Stall, J. Electron. Mater. **27** 179 (1998).
18. J. C. Zolper, D. J. Reiger, A. G. Baca, S. J. Pearton, J. W. Lee and R. A. Stall, Appl. Phys. Lett. **69** 538 (1996).
19. M. Fu, V. Sarvepalli, R. K. Singh, C. R. Abernathy, X. A. Cao, S. J. Pearton and J. A. Sekhar, Mat. Res. Soc. Symp. Proc. **483** 345 (1998).
20. X. A. Cao, C. R. Abernathy, R. K. Singh, S. J. Pearton, M. Fu, V. Sarvepalli, J. A. Sekhar, J. C. Zolper, D. J. Rieger, J. Han, T. J. Drummond, R. J. Shul and R. G. Wilson, Appl. Phys. Lett. **73** 229 (1998).
21. M. S. Feng, J. D. Guo and G. C. Chi, Proc. Electrochem Soc. Vol. **95-21** 43 (1995).
22. C. C. Yi and B. W. Wessels, Appl. Phys. Lett. **69** 3026 (1996).
23. P. Bogulawski, E. L. Briggs and J. Bernholc, Phys. Rev. B **51** 17255 (1995).
24. C. R. Abernathy, J. D. MacKenzie, S. J. Pearton and W. S. Hobson, Appl. Phys. Lett. **66** 1969 (1995).

EXTRINSIC PERFORMANCE LIMITATIONS OF AlGaN/GaN HETEROSTRUCTURE FIELD EFFECT TRANSISTORS

P.P. Ruden[†], J.D. Albrecht[†], A. Sutandi[†], S.C. Binari[‡], K. Ikossi-Anastasiou[‡], M.G. Ancona[‡], R.L. Henry[‡], D.D. Koleske[‡], and A.E. Wickenden[‡]

[†]ECE Department, University of Minnesota, Minneapolis, MN 55455
[‡]Electronics Science and Technology Div., Naval Research Laboratory, Washington, DC 20375

Cite this article as: MRS Internet J. Nitride Semicond. Res. 4S1, G6.35 (1999)

ABSTRACT

Extrinsic effects on the DC output characteristics of AlGaN/GaN HFETs with 1μm gate lengths are examined. The devices investigated were fabricated on MOCVD-grown AlGaN/GaN heterostructures on sapphire substrates. An analytical model that takes into account parasitic resistances and thermal effects is constructed, and its results are compared with experimental data. With parameters determined from characterization experiments on the same wafer and from independent theoretical results, the agreement between the data and the model predictions is found to be very good. The model is then applied to performance predictions for devices with improved series resistances and heat sinking.

INTRODUCTION

The group III-nitride compound semiconductors have considerable potential for the fabrication of high frequency/high power electronic devices. Progress in the growth and process technology of these materials has recently led to the demonstration of very impressive results for the output current density, the gain cut-off frequency, and the output power density of AlGaN/GaN heterostructure field effect transistors (HFETs).[1,2,3] These encouraging results notwithstanding, the device design and the fabrication techniques are still far from optimized. For example, contact resistances are relatively large (compared to conventional III-V materials) and deleterious thermal effects are likely to limit the performance of the HFETs at high voltages and currents. This is particularly the case for devices fabricated on sapphire substrates, due to that material's relatively low thermal conductivity.

In this communication extrinsic effects that limit the performance of AlGaN/GaN HFETs are examined in the framework of an analytical model. The results are compared with experimental data from AlGaN/GaN HFETs. It is found that significant improvements in output current can be expected if the heat generated in the devices is removed effectively (for example by a flip-chip bonding technique, or by the use of a substrate with high thermal conductivity) and if the source and drain series resistances can be reduced.

DEVICE STRUCTURE

The III-nitrides used in this study were grown by MOCVD on sapphire substrates. The

Mat. Res. Soc. Symp. Proc. Vol. 537 © 1999 Materials Research Society

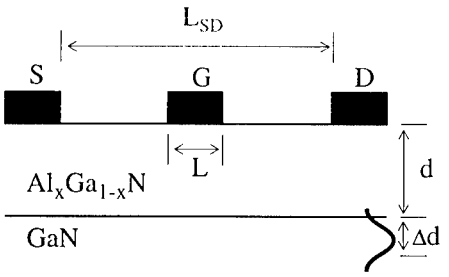


Figure 1: Schematic HFET diagram.

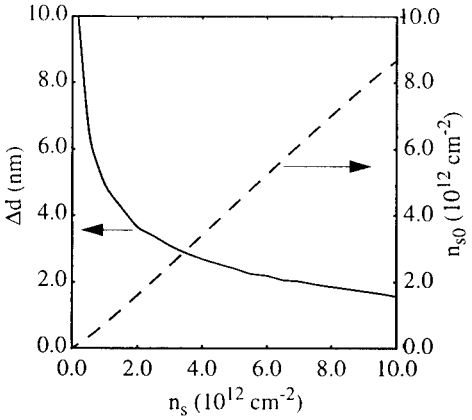


Figure 2: Calculated values of Δd and electron concentration in the lowest subband as a function of the total sheet carrier density.

material structure consisted of an AlN nucleation layer, followed by 3μm of undoped GaN and 200Å of nominally undoped $Al_{0.3}Ga_{0.7}N$. Ohmic contacts were formed using alloyed Ti/Al/Ni/Au, and the gate metallization was Pt/Au. Device isolation was accomplished through the use ECR dry etching. The source-to-drain spacing was 5μm and the gate length was 1μm. A schematic diagram of the HFETs is shown in Figure 1. The devices tested consist of two parallel gated channels of 75μm width, for a total gate width of 150μm.

DEVICE MODEL AND KEY PARAMETERS

The device model developed for this investigation is a charge-control/gradual-channel approximation model [4] that incorporates salient results of previous Monte Carlo electron transport simulations for GaN as a function of the ambient temperature.[5] A good approximation for the relationship between the channel carrier concentration, n_s, and the gate voltage is a critical prerequisite for an accurate charge-control model. Therefore, as an initial step, the capacitance vs. voltage characteristic (C-V) of the AlGaN/GaN layer structure is examined. A standard approximation that should be monitored closely is to evaluate the capacitance per unit area as $C = \varepsilon/(d + \Delta d)$ where d is the thickness of the barrier (AlGaN) layer and Δd is the effective thickness of the two-dimensional electron gas that forms the channel.[6] Clearly, the approximation of treating Δd as a constant, independent of the carrier concentration, is rather rough. This is seen immediately from a self-consistent solution of the coupled Schroedinger and Poisson equations.[7,8] By calculating the quasi-two-dimensional subband structure in this way and subsequently estimating the effective thickness as

$$\Delta d = \frac{1}{n_s}\int z n(z) dz \qquad (1)$$

the result shown in Figure 2 is obtained. Here n(z) is the total (three-dimensional) free electron density which is related to the (two-dimensional) channel carrier density by $n_s = \int n(z)dz$. The effective mass subband structure calculations are done using a self-consistent potential in the framework of the local density approximation. Also taken into account is the polarization charge at the interface that arises from the piezoelectric effect in the strained AlGaN barrier layer. At room temperature only the lowest three subbands are found to be significantly populated. The carrier density in the lowest subband which accounts for more than 80% of the

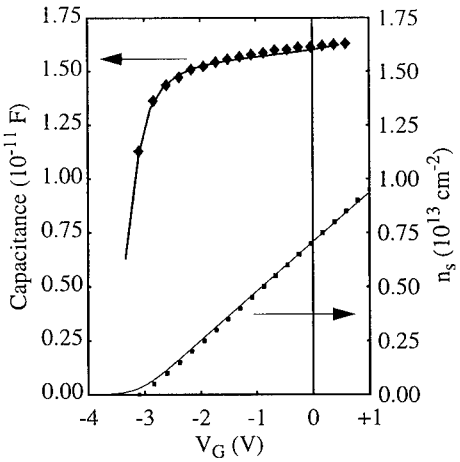


Figure 3: Comparison of the measured AlGaN/GaN heterostructure capacitance for a 75μm dot with calculated results. Also shown is the resulting n_s vs. V_g from the subband calculation (dots) and from equation (2).

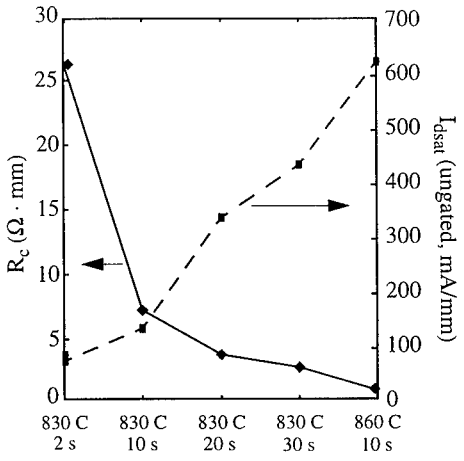


Figure 4: Measured (TLM) contact resistances and I_{dsat} for an ungated device for various anneal times and temperatures.

total is also shown in Figure 2. As is evident from the figure, Δd varies quite strongly with n_s.

From $dn_s/dV = C/q$ and $C(n_s) = \varepsilon/(d + \Delta d(n_s))$ the capacitance per unit area as a function of the gate voltage can be found by eliminating n_s. Comparing the calculated capacitance with experimental data for dot-shaped capacitors with 75μm diameter yields the agreement shown in Figure 3. While this result is very satisfactory from a point of view that focuses on the quantum confinement, it does not provide a convenient closed-form expression that can be used in a charge-control model. However, the following analytic relationship between the channel carrier concentration and the gate-to-channel voltage, V_g, accounts well for the integrated C-V data.

$$n_s(V_g, T) = MkT\log\left(\exp\left((V_g - V_t)\frac{1}{qMkT}\frac{\varepsilon}{(d+\Delta d)}\right)+1\right) \qquad (2)$$

Here M is an effective two-dimensional density of states, and the remaining symbols have their usual meanings. The good agreement between the simple expression (2) and the result of the self-consistent solution of the subband structure problem is shown in Figure 3.

For the analytic calculation of the drain current in the HFET, the relationship between the electron drift velocity, v, and the longitudinal electric field, E, is approximated as:

$$v(E, T) = \begin{cases} \dfrac{\mu(T)E}{1 + E/(E_1(T))} & E < E_c(T) \\ v_{sat}(T) & E \geq E_c(T) \end{cases} \qquad (3)$$

where μ(T) is the low field mobility and $E_1(T) = E_c/(\mu E_c/v_{sat} - 1)$.

The low field mobility, the saturation (peak) velocity, and the saturation (peak) field results of Monte Carlo simulations for electron transport in GaN have been parameterized as functions of temperature, doping concentration, and compensation.[5] These results are used in the present model, and the simple expression above is found to approximate the velocity vs. field curve quite well for $E \leq E_c$. The GaN channel is taken to be undoped, yielding [5] a low-field room temperature mobility of $1200 cm^2V^{-1}sec^{-1}$. This value is somewhat larger than measured Hall mobilities for the particular device structures for which we compare the model results to experimental data (typical values are $1100 cm^2V^{-1}sec^{-1}$ for $n_s = 9x10^{12}cm^{-2}$). Hence, the mobility is reduced by a small, temperature independent correction using Matthiessen's rule.

The analytic expressions for the drain current, I_d, as a function of the intrinsic gate and drain voltages, V_g and V_d, for the so-called linear and saturation regimes were presented in ref. [4]. The gate current is negligibly small for the operating conditions to be examined here.

In the present effort of accounting for the output DC characteristics of AlGaN/GaN HFETs, two extrinsic effects are included in the model. The first is the additional voltage drop across the source and drain series resistances, R_s and R_d, which leads to the following relations between the extrinsic (applied) voltages and the intrinsic voltages that actually control the channel.

$$V_{GS} = V_g + R_s I_d \tag{4}$$

$$V_{DS} = V_d + (R_s + R_d) I_d \tag{5}$$

R_s and R_d are comprised of the contact resistance and an access resistance associated with the rather large (2μm) spacing between the channel beneath the gate and the source and drain

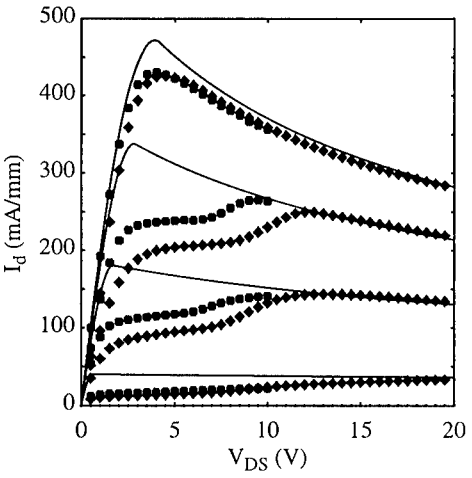


Figure 5: Comparison of the experimental (boxes 0 to 10V and diamonds 0 to 20V) and calculated (lines) drain current vs. drain-to-source bias in the absence of illumination. The gate voltages vary from 0 to -4V.

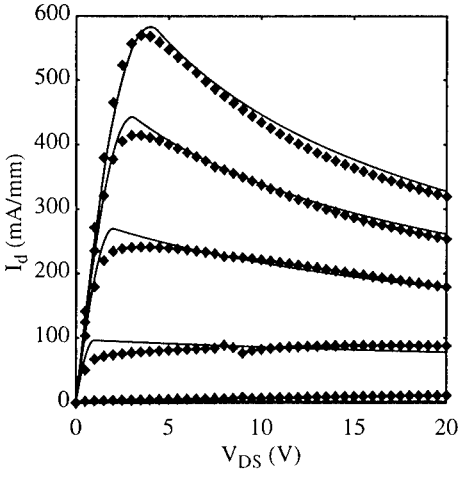


Figure 6: Comparison of the experimental (points) and calculated (lines) drain current vs. drain-to-source bias with device illumination. The gate voltages vary from 0 to -4V.

contacts, both of which are determined by separate TLM measurements. Representative values for the sheet resistivity and specific contact resistance obtained for the wafer examined here are ρ = 550...790Ω/□, depending on the location on the wafer, and R_c = 0.6Ω·mm. Series resistances may be reduced by lowering the contact resistance through improvements in the process and by lowering the access resistance through a reduction of the source-to-drain spacing. The former effect is clearly evident in Figure 4 where measured contact resistances for different alloying conditions are shown. The contact resistance can affect the current through a device as is shown in Figure 4. This data will be discussed in a forthcoming paper.

The second extrinsic effect is the self-heating of the device due to power dissipation. In order to obtain the ambient temperature of the channel which enters the electron velocity through eq. (3), the device temperature is determined from $T = T_0 + R_{th}I_dV_{DS}$. Here R_{th} is the thermal impedance and T_0 is the temperature of the heat sink at the backside of the substrate (T_0 = 300K). The specific thermal impedance of the device structure is determined independently by using a two-dimensional device simulator and is found to be well approximated by $24\cdot(1 + (T-T_0)\cdot10^{-3})$K·mm/W, where the temperature dependences of the thermal conductivities have been taken into account.

With its parameters determined either by independent calculations or direct measurements, the HFET model is run until self-consistent solutions for given V_{DS} and V_{GS} are reached.

RESULTS AND DISCUSSION

Figure 5 shows measured HFET output characteristics with the device in the dark. The data are taken sequentially, starting with V_{DS} sweeps from zero to V_{DSmax} for V_{GS} = 0, -1, -2, -3V. The calculated results are also displayed. All model parameters are consistent with TLM , C-V, and Hall data from this wafer. The thermal impedance is obtained from a separate simulation, as indicated above. Clearly the agreement between the data and the model results is quite good for large V_{DS}. In particular, the strong negative output conductance caused by the self-heating is well reproduced. For small and intermediate V_{DS} the model predicts larger currents than observed experimentally. We tentatively attribute the discrepancy to trapping of (primarily hot) electrons. Under high drain bias conditions the traps are either emptied or their electrostatic effect is reduced and the drain current approaches the model values.

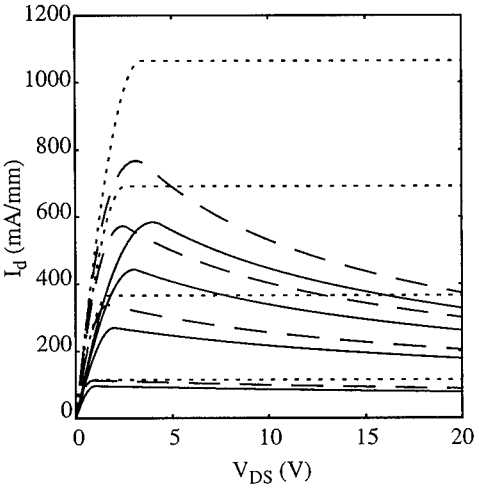


Figure 7: Comparison of expected HFET output characteristics of a device with decreased contact-to-channel spacing and reduced contact resistance (dashed curves) to the results of Figure 6 (solid curves). Also shown are the results expected for a perfectly heat sunk device (dotted curves).

A more detailed analysis of the low voltage characteristics shown in Figure 5 will be the subject of future work. However, to substantiate the trapping hypothesis, the output characteristics of the same device under illumination by a Hg pen lamp are examined in Figure 6 and compared to the model results. Due to the illumination, traps are unlikely to be occupied by electrons, the sheet resistivity decreases, and the output currents increase, particularly at low voltages. The agreement between the model and the data over the full drain-to-source voltage range under these conditions is very good. The maximum ambient temperature of the channel region is found to be approximately 500K.

Lastly, the limitations imposed on the device performance by the series resistances and by the thermal effects are examined in Figure 7. Here, the model results of Figure 6 are compared to the performance that would be expected from the same transistor structure, but with a contact resistance of 0.1 Ω·mm, a value that is typical of AlGaAs/GaAs HFETs [9], and gate-to-source and gate-to-drain contact spacings of 0.5μm (dashed curves). Also shown is the additional consequence of ideal heat sinking that completely eliminates the thermal effects (dotted curves). Clearly, even an improvement in series resistance alone can lead to larger ouput currents. A very significant improvement is predicted if the self-heating of the device can be suppressed.

The present comparison of results from a self-consistent model that includes parasitic resistances and self-heating effects indicates that considerable improvement in the output current densities of AlGaN/GaN HFETs can be expected even for relatively long channel devices. The model accounts well for experimentally observed DC output characteristics without resorting to the introduction of arbitrary parameters.

ACKNOWLEDGMENT

PPR acknowledges NRL's gracious hospitality during the spring of 1998. The work at the University of Minnesota was supported in part be Hughes Research Laboratories and by the National Science Foundation. The work at NRL was partially supported by the Office of Naval Research.

REFERENCES

1. N.X. Nguyen, C. Nguyen, and D.E. Grider, *Electronics Lett.*, **34**, 811 (1998).
2. G.J. Sullivan, J.A. Higgins, M.Y. Chen, J.W. Yang, Q. Chen, R.L. Pierson, and B.T. McDermott, Electronics Lett., **34**, 922 (1998).
3. S.T. Sheppard, K. Doverspike, W.L. Pribble, S.T. Allen, J.W. Palmour, L.T. Kehias, and T.J. Jenkins, Abstracts of 1998 Device Research Conference, Charlottesville, VA (1998).
4. P.P.Ruden, *IEEE Trans. Electron Devices*, **37**, 2267 (1990).
5. J.D. Albrecht, R.P. Wang, P.P. Ruden, M. Farahmand, and K.F. Brennan, *J. Appl. Phys.*, **83**, 4777 (1998).
6. M. Shur, *Physics of Semiconductor Devices*, Prentice-Hall, Inc., Englewood Cliffs, NJ (1990).
7. T. Ando, A.B. Fowler, F. Stern, *Rev. Mod. Phys.*, **54**, 437 (1982).
8. P.P. Ruden, M. Shur, A.I. Akinwande, J.C. Nohava, D.E. Grider, and J. Baek, *IEEE Trans. Electron Devices*, **37**, 2171 (1990).
9. K. Ikossi-Anastasiou, A. Ezis, and A.K. Rai, *IEEE Trans. Electron Devices*, **35**, 1786 (1988).

BEHAVIOR OF W AND WSi_x CONTACT METALLIZATION ON n- AND p- TYPE GaN

X. A. Cao,* F. Ren,** J. R. Lothian, *** S. J. Pearton,* C. R. Abernathy,* J. C. Zolper,**** M. W. Cole,***** A. Zeitouny,****** M. Eizenberg******* and R. J. Shul*******

*Department of Materials Science and Engineering, University of Florida, Gainesville, FL 32611, USA
**Department of Chemical Engineering, University of Florida, Gainesville, FL 32611, USA
***Multiplex Inc., South Plainfield, NJ 07080, USA
****Office of Naval Research, Arlington, VA 22217, USA
*****US Army Research Laboratory, WMRD, Aberdeen Proving Ground, MD 21105, USA
******Department of Materials Engineering, Technion - Israel Institute of Technology, Haifa 32000, Israel
*******Sandia National Laboratories, Albuquerque, NM 87185, USA

Cite this article as: MRS Internet J. Nitride Semicond. Res. 4S1, G6.39(1999)

ABSTRACT

Sputter-deposited W-based contacts on p-GaN (N_A~10^{18} cm^{-3}) display non-ohmic behavior independent of annealing temperature when measured at 25 °C. The transition to ohmic behavior occurs above ~250 °C as more of the acceptors become ionized. The optimum annealing temperature is ~700 °C under these conditions. These contacts are much more thermally stable than the conventional Ni/Au metallization, which shows a severely degraded morphology even at 700 °C. W-based contacts may be ohmic as-deposited on very heavily doped n-GaN, and the specific contact resistance improves with annealing up to ~900 °C.

INTRODUCTION

One of the limiting factors in GaN device technology are the relatively high ohmic contact resistances. In the search for improved contact characteristics, a wide variety of metallizations have been investigated on p-GaN besides the standard Ni/Au[1-7], including Ni[4,5,8], Au[4,7,9,10], Pd[4], Pd/Au[11,12], Pt/Au[6], Au/Mg/Au[9,13], Au/C/Ni[14], Ni/Cr/Au[12,15] and Pd/Pt/Au[6]. This area has been reviewed recently by Mohney and Lau[16], and by Liu and Lau[17]. Typically Ni, Pd or Pt is the metal in direct contact with the GaN, and the structure is annealed at 400 - 750 °C. This produces contact resistances in the 10^{-1} - 10^{-3} $\Omega \cdot cm^2$ range. For higher temperatures severe degradation in contact morphology is observed, usually resulting from the formation of the metal gallides[16].

For n-type ohmic contacts, the most popular metallization schemes have been those based on Al/Ti/n-GaN, often with overlayers of Au/Ni[16,17]. It is believed that diffusion of Al to the metal/GaN interface is a critical step in forming the lowest specific contact resistance, and that TiN formation produces a high concentration of nitrogen vacancies that lead to n^+ doping level and lower R_c values[17]. We have previously reported that both W and WSi_x on n^+ epi GaN layers (n ~ 10^{19} cm^{-3}) produce reasonable contacts (R_c ~ 8×10^{-5} $\Omega \cdot cm^2$), but extremely stable behavior[18,19] - annealing at 1000 °C led to a shallow reacted region of ≤ 100 Å, and in junction field-effect transistor structures these contacts can withstand implant activation anneals at 1100 °C[20].

In this paper we report on use of ion implantation to increase the doping level in GaN, which would be of particular interest for creating n^+ or p^+ regions in device structures, and also

Mat. Res. Soc. Symp. Proc. Vol. 537 © 1999 Materials Research Society

on the characteristics of W and WSi_x metal contacts on both n- and p-type GaN. The thermal stability of the refractory metal contacts is superior to that of the conventional Ni/Au scheme employed for p-GaN.

EXPERIMENTAL

P-type ($N_A = 10^{18}$ cm^{-3}), Mg-doped GaN layers 1 μm thick were grown on Al_2O_3 substrates by Molecular Beam Epitaxy using solid Ga and rf plasma-activated N_2[21]. Strong cathodoluminescence was observed at ~385 nm, with very little deep level emission. Undoped GaN layers ~3 μm thick were grown on Al_2O_3 by Metal Organic Chemical Vapor Deposition. These samples were implanted with 100 keV Si^+ ions at a dose of 5×10^{15} cm^{-2}, and annealed with AlN caps in place to 1400 °C for 10 secs[22]. This produced a peak n-type doping concentration of ~5×10^{20} cm^{-3}. W or $WSi_{0.45}$ layers ~ 1000 Å thick were deposited using an MRC501 sputtering system. The sample position was biased at 90 V with respect to the Ar discharge. Prior to sputtering, the native oxide was removed in a 20:1 H_2O:NH_4OH solution. Transmission line patterns were defined by dry etching the exposed metal with SF_6/Ar, and forming mesas around the contact pads using BCl_3/N_2 dry etching to confine the current flow. For comparison, on the p-GaN, Au(1000 Å)/Ni(500 Å) was deposited by e-beam evaporation, defined by lift-off and mesas formed by dry etching. Both n- and p-type samples were annealed for 60 secs (in some experiments this was varied from 30 - 300 secs) at 300 - 1000 °C under flowing N_2.

In addition, implantation of S, Se and Te for creation of n-type doping and of Mg, Be and C for p-type doping was examined in undoped MOCVD-grown GaN. Annealing was performed up to 1500 °C, using AlN cap layers for surface protection.

RESULTS AND DISCUSSION

(a) Implantation

Secondary Ion Mass Spectrometry(SIMS) did not detect any measurable redistribution for S, Se, Te, Mg or C at 1450 °C, implying effective diffusivities of $\leq 2\times10^{-13}$ $cm^2 \cdot sec^{-1}$ for each of these dopants at this temperature. The exception was Be, which displayed an apparent damage-assisted diffusion at 900 °C, but did not move at higher annealing temperatures. It appears that in GaN, the intersitial as-implanted Be undergoes a type of transient enhanced diffusion until excess point defects created by the nuclear stopping process of the implanted ions are removed by annealing, at which stage the Be is basically immobile.

While Si^+ implantation produced n-type doping levels up to 5×10^{20} cm^{-3}, the other donors were less effective. The maximum doping achieved with S^+ implantation was ~5×10^{18} cm^{-3}, while with Te^+ it was ~1.6×10^{18} cm^{-3}.

It is difficult to create p-type doping by implantation in GaN because of the large ionization levels of acceptor species and n-type character of residual lattice damage. We did not achieve p-type conductivity by implanting C^+, while a maximum doping level of 10^{17} cm^{-3} was obtained with Mg^+ under the same conditions.

(b) Contact Properties

(i) p-GaN

Figure 1 shows annealing temperature dependence of the I-V characteristics of the Ni/Au, W and WSi on p-GaN, with the measurements made at 25 °C in all cases. Note that for the optimum anneal temperatures (700 °C for Ni/Au and W, and 800 °C for WSi_x), the contacts are not ohmic, but are more accurately described as leaky Schottky diodes. In the case of W and WSi, we assume that annealing above the optimum temperature produces loss of N_2 and poorer contact properties.

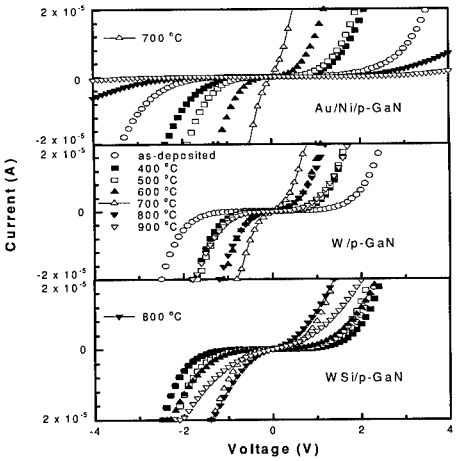


Fig. 1. Annealing temperature dependence of I-V characteristics of WSi, W and Ni/Au contacts on p-GaN(60 sec anneal times).

The contact morphology on the W and WSi metallization remained featureless to the highest temperature we investigated. This is in sharp contrast to the case of Ni/Au, as shown in Figure 2. For the latter metallization, islanding is quite severe after 700 °C annealing due to reaction of the Ni with the GaN[21-23].

Since the hole concentration in p-GaN will increase rapidly with temperature due to the higher ionization efficiency for the Mg acceptors, we would expect an improvement in contact properties at elevated temperatures. For example, from calculating the Fermi level position as a function of temperature, we find the ionization efficiency improves from ~10% at 25 °C to ~56% at 300 °C. Figure 3 shows the I-V characteristics for the 700 °C (Ni/Au and W) or 800 °C(WSi) annealed samples, as a function of the measurement temperature(25 - 300 °C). For the Ni/Au, the contacts become ohmic at ≥ 200 °C, while for W and WSi_x this occurs at 300 °C. The R_c values at 300 °C are 9.2×10^{-2} Ω·cm^2 (Ni/Au), 6.8×10^{-1} Ω·cm^2 (W) and 2.6×10^{-2} Ω·cm^2 (WSi). The TLM measurements showed that the substrate sheet resistance is reduced from 1.39×10^4 Ω/□ at 200 °C, to 8470 Ω/□ at 250 °C and 4600 Ω/□at 300 °C, indicating that the increased hole concentration plays a major role in decreasing R_c.

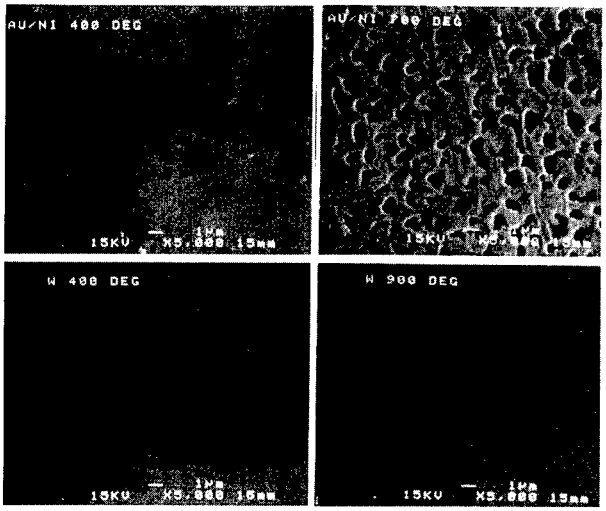


Fig. 2. SEM micrographs of Ni/Au contacts on p-GaN after 60 secs anneals at either 400 °C (top left) or 700 °C (top right), or W contacts after similar annealing at 400 °C (bottom left) or 900 °C (bottom right).

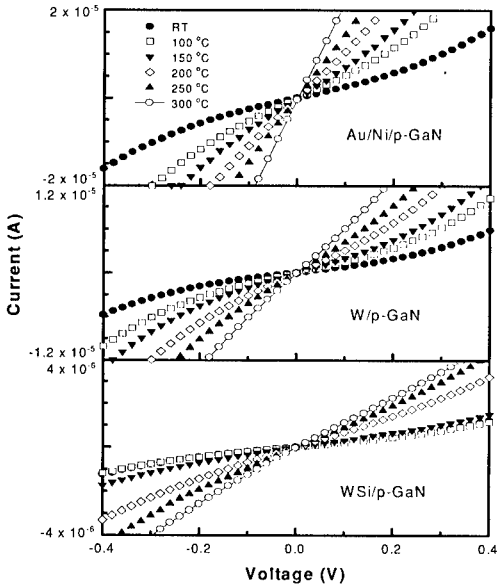


Fig. 3. Measurement temperature dependence of I-V characteristics of Ni/Au, W or WSi_x contacts on p-GaN.

(ii) n-GaN

Figure 4 shows the annealing temperature dependence of R_c for W contacts on Si-implanted GaN. The specific contact resistance improves with annealing up to ~950 °C, which appears to correspond to the region where the β-W_2N interfacial phase is formed. Cole et al[19]. reported that W and WSi contacts on GaN annealed in the range 750-850 °C showed the minimum degree of metal protrusion in the interfacial regions devoid of the β-W_2N phase, whereas at lower annealing temperatures the horizontal spatial extent of this phase was smaller and allowed more protrusions to develop. The excellent structural stability of the W on GaN was clear from both AES and SEM data on annealed samples.

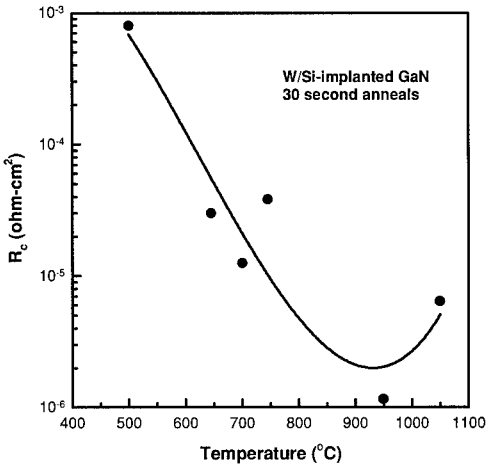


Fig. 4. Annealing temperature dependence of R_c for W contacts on Si-implanted GaN.

SUMMARY AND CONCLUSIONS

W and WSi ohmic contacts on both p- and n-type GaN have been annealed at temperatures from 300 - 1000 °C. There is minimal reaction (≤ 100 Å broadening of the metal/GaN interface) even at 1000 °C. Specific contact resistances in the 10^{-6} Ω·cm^2 range are obtained for W on Si-implanted GaN with a peak doping concentration of ~ 5×10^{20} cm^{-3}, after annealing at 950 °C. On p-GaN, leaky Schottky diode behavior is observed for W, WSi_x and Ni/Au contacts at room temperature, but true ohmic characteristics are obtained at 250 - 300 °C, where the specific contact resistances are typically in the 10^{-2} Ω·cm^2 range. The best contacts for W and WSi_x are obtained after 700 °C annealing for periods of 30 - 120 secs. The formation of β-W_2N interfacial phases appear to be important in determining the contact quality.

ACKNOWLEDGEMENTS

The work at UF is partially supported by a DARPA/EPRI grant (D. Radack/J. Melcher) and by an NSF grant (DMR-9732865) monitored by L. D. Hess. Sandia is a multiprogram laboratory operated by Sandia Corporation, a Lockheed-Martin company, for the US Department of Energy under contract No. DEAC04-94AL85000.

REFERENCES

1. S. Nakamura, in GaN and Related Materials II, ed. S. J. Pearton (Gordon and Breach, NY 1998).
2. S. Nakamura, T. Mukai and M. Senoh, Appl. Phys. Lett. **64,** 1687 (1994).
3. M. Schauler, C. Kirchner, M. Mayer, A. Pelzmann, F. Eberhard, M. Kamp , P. Unger and K. J. Ebeling, MRS Internet J. Nitride Semicond. Res. **2,** 44 (1997).
4. H. Ishikawa, S. Kobayashi, Y. Koide, S. Yamasaki, S. Nagai, J. Umezaki, M. Koike and M. Murakami, J. Appl. Phys. **81,** 1315 (1997).
5. K. V. Vassilevski, M. G. Rastegaeva, A. I. Babanin, I. P. Nikitina and V. A. Dmitriev, MRS Internet J. Nitride Semicond. Res. **1,** 38 (1996).
6. D. J. King, L. Zhang, J. C. Ramer, S. D. Hersee and L. F. Lester, Mat. Res. Soc. Symp. Proc. **468,** 421 (1997).
7. L. F. Lester, D. J. King, L. Zhang, J. C. Ramer, S. D. Hersee and J. C. Zolper, Mat. Res. Soc. Symp. Proc. **97-1,** 171 (1997).
8. I. Akasaki, H. Amano, S. Sota, H. Sakai, T. Tanaka and M. Koike, Jap. J. Appl. Phys. **34,** L1517 (1995).
9. L. L. Smith, R. F. Davis, M. J. Kim, R. W. Carpenter and Y. Huang, J. Mater. Res. **12,** 2249 (1997).
10. T. Mori, T. Kozawa, T. Ohwaki, Y. Taga, S. Nagai, S. Yamasaki, S. Asami, N. Shibata and M. Koike, Appl. Phys. Lett. **69,** 3537 (1996).
11. T. Kim, J. Khim, S. Chae and T. Kim, Mat. Res. Soc. Symp. Proc. **468,** 427 (1997).
12. J. T. Trexler, S. J. Pearton, P. H. Holloway, H. G. Mier, K. R. Evans and R. F. Karlicek, Mat. Res. Soc. Symp. Proc. **449,** 1091 (1997).
13. L. L. Smith, M. D. Bremser, E. P. Carlson, T. W. Weeks, Jr., Y. Huang, M. J. Kim, R. W. Carpenter and R. F. Davis, Mat. Res. Soc. Symp. Proc. **395,** 861 (1996).
14. J. T. Trexler, S. J. Miller, P. H. Holloway and M. A. Khan, Mat. Res. Soc. Symp. Proc. **395,** 819 (1996).
15. T. Kim, M. C. Yoo and T. Kim, Mat. Res. Soc. Symp. Proc. **449,** 1061 (1997).
16. S. E. Mohney and S. S. Lau, in GaN and Related Materials II, ed. S. J. Pearton (Gordon and Breach, NY 1998).
17. Q. Z. Liu and S. S. Lau, Solid -State Electron. **42,** 667 (1998).
18. M. W. Cole, F. Ren and S. J. Pearton, J. Electron. Soc. **144,** L275 (1997); Appl. Phys. Lett. **71,** 3004 (1997).
19. M. W. Cole, D. W. Eckart, W. Y. Han, R. L. Pfeffer, and T. Monahan, F. Ren, C. Yuan and R. A. Stall, S. J. Pearton, Y. Li and Y. Lu, J. App. Phys. **80,** 278 (1996).
20. J. C. Zolper and R. J. Shul, MRS Bulletin **22,** 36 (1997).
21. H. S. Venugopalan, S. E. Mohney, B. P. Luther, J. M. DeLucca, S. D. Wolter, J. M. Redwing and G. E. Bulman, Mat. Res. Soc. Symp. Proc. **468,** 431 (1997).
22. V. M. Bermudez, R. Kaplan, M. A. Khan and J. N. Kuznia, Phys. Rev. B **48,** 2436 (1993).
23. S. E. Mohney, B. P. Luther and T. N. Jackson, Mat. Res. Soc. Symp. Proc. **395,** 843 (1996).

PHOTOELECTROCHEMICAL ETCHING OF $In_xGa_{1-x}N$

Hyun Cho[1], S.M. Donovan[1], C.R. Abernathy[1], S.J. Pearton[1], F. Ren[2], J. Han[3] and R.J. Shul[3]

[1] Department of Materials Science and Engineering, University of Florida, Gainesville FL 32611
[2] Department of Chemical Engineering, University of Florida, Gainesville FL 32611
[3] Sandia National Laboratories, Albuquerque NM 87185

Cite this article as: MRS Internet J. Nitride Semicond. Res. 4S1, G6.40(1999)

Abstract

A comparison of KOH, NaOH and AZ400K solutions for UV photo-assisted etching of undoped and n^+ GaN is discussed. The etching is diffusion-limited ($E_a < 6kCal \cdot mol^{-1}$) under all conditions and is significantly faster with bias applied to the sample during light exposure. No etching of InN was observed, due to the very high n-type background doping ($> 10^{20}cm^{-3}$) in the material.

Introduction

To date relatively little success has been achieved with wet chemical etching of GaN with room temperature solutions [1]. Molten KOH and elevated temperature H_3PO_4 can produce etch pits on GaN [2,3]. Recently hot solutions (90-180°C) of KOH or NaOH in ethylene glycol and KOH or H_3PO_4 at similar temperatures have been used to produce well-defined crystallographic etching of wurtzite GaN after initial formation of mesas by dry etching [4]. If the GaN near-surface region has been damaged by processes such as dry etching or high temperature annealing, H_3PO_4, NaOH or KOH solutions have been found to remove the N_2-deficient material and stop at the underlying undamaged GaN [5]. Both AlN [6,7] and InN [8] can be etched in hot alkaline solutions of NaOH or KOH, but there has been little success with the alloy InGaN [9].

It has long been recognized that the dissolution rate of semiconductor materials may be enhanced in acid or base solutions by illumination with above bandgap light [10-14]. The basic mechanism for their photo-enhanced etching is oxidative dissociation of the semiconductor into its component elements (thereby consuming the photogenerated holes) and the subsequent reduction of the oxidizing agent in the solution by reaction with the photogenerated electrons. In most cases, n-type material is readily etched, in contrast to p-type samples where the inability to confine photogenerated holes at the semiconductor electrolyte interface prevents etching. The first photoenhanced wet etching of GaN at room temperature was reported using HCl/H_2O and KOH/H_2O solutions with He-Cd laser illumination [15]. Subsequently the Adesida group and others [16-24] employed broad-area Hg lamps and solutions of KOH, aqueous H_3PO_4 or tartaric acid/ethylene glycol to achieve maximum room-temperature etch rates typically in the range $1000\text{-}2000 Å \cdot min^{-1}$. In some cases the etched surfaces are smooth, but a more general result is the appearance of very rough microstructure. The etch mechanism appears to be creation of Ga_2O_3 on the GaN surface, and its subsequent dissolution by the acid or base solution.

In this paper we compare KOH, NaOH and AZ400K (a photoresist developer effective in etching AlN because it contains KOH) solutions for photoelectrochemical (PEC) etching of undoped and n^+ GaN either with or without biasing of the samples. We find in general that the etch rates increase sharply when the samples are biased during UV lamp exposure. We also

Mat. Res. Soc. Symp. Proc. Vol. 537 © 1999 Materials Research Society

examined PEC etching of thin film InN. Since this material is degenerately doped n-type (> $5\times10^{20}cm^{-3}$) due to the presence of residual shallow donors (possibly nitrogen vacancies), it appears that we are unable to create enough photogenerated carriers to enhance the oxidative dissociation of the InN and no etching was observed in any of our experiments.

Experimental

The GaN layers were ~ 2μm thick and were grown on Al_2O_3 substrates at 1040°C by Metal Organic Chemical Vapor Deposition. Both n^+ (n ~ $3\times10^{18}cm^{-3}$) and unintentionally doped (n ~ $3\times10^{16}cm^{-3}$) layers were used in these experiments. InN layers ~ 1μm thick were grown on Al_2O_3 at ~ 650°C by Metal Organic Molecular Beam Epitaxy. These films are degenerately n-type (~ $10^{20}cm^{-3}$) due to residual defects or impurities. Ti metal contacts were patterned by lift-off on the periphery of the samples, and etching performed in a standard electrochemical cell consisting of a teflon sample holder and a Pt wire cathode [2-6,9-14]. An unfiltered 450W Hg arc lamp ~ 15cm from the sample provided illumination of the samples, which were immersed in unstirred KOH, NaOH or H_2O/AZ400K solutions. Etch depths were measured by stylus profilometry, while the surface morphology was examined by both scanning electron microscopy (SEM) and tapping mode atomic force microscopy (AFM).

Results and discussion

Figure 1 shows the temperature dependence of GaN etch rate in KOH solutions either with or without bias and at two different molarities. From separate experiments we determined that molarity had little effect on etch rate in this range, and thus that biasing and doping level in the GaN were the key parameters. This is consistent with past data on SiC [10]. The n^+ GaN did not etch at all over a broad range of KOH concentrations (0.005-1M) when no Ti metal contact was present on the sample, probably due to the inability to separate e-h pairs under these conditions.

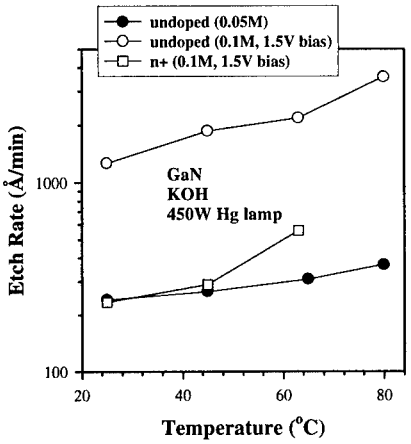


Figure 1. Temperature dependence of GaN PEC etch rate either with or without 1.5V bias in different molarity (0.05 or 0.1M) KOH solutions.

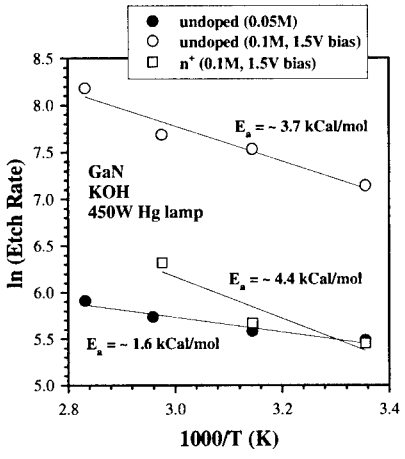


Figure 2. Arrhenius plot of GaN PEC etch rate either with or without 1.5V bias in different molarity (0.05 or 0.1M) KOH solutions.

The data is plotted in Arrhenius form in Figure 2. In all cases the activation energies are < 6kCal·mol^{-1}, consistent with diffusion-limited etching whose other characteristics are a square-root dependence of etch rate on time, relatively rough surfaces and a strong dependence of rate on solution agitation. This is consistent with the results of Youtsey et. al. [16-18, 20]

There was also a strong dependence of etched surface morphology on doping level and presence of bias, as shown in Figure 3. Note that in the case of biased undoped GaN, the etched surface morphology measured by AFM is fairly similar to that of the unetched material. The role of the biasing may be to provide more efficient separation of the photogenerated carriers with a resultant improvement in uniformity of the surface oxidation reactions.

Little work has been performed with NaOH as the electrolyte. Figure 4 shows the influence of solution molarity on the PEC etch rates of undoped and n^+ GaN at 25°C. The rates fall-off dramatically at high molarities (≥ 0.1M), most likely due to excessive oxidation of the surface. This effect is also seen with KOH solutions under the same conditions [21-23].

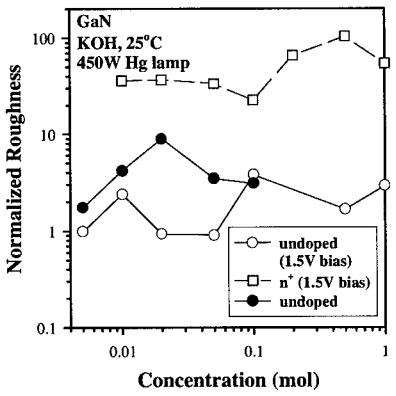


Figure 3. Normalized surface roughness (control has a value of 1) of PEC etched undoped or n^+ GaN in KOH solutions at 25°C as a function of solution molarity.

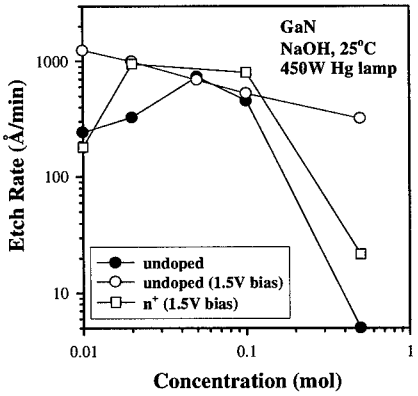


Figure 4. Etch rate of undoped or n^+ GaN either with or without 1.5V bias in NaOH solutions at 25°C as a function of solution molarity.

The temperature dependence of PEC etch rates in NaOH solutions is shown in Figure 5. The application of bias again strongly enhances the etch rates, but the temperature of the solution has little effect on n^+ material. Replotting this data in Arrhenius form (Figure 6) again shows the etching is diffusion-limited, as with KOH. Even the surface resulting from the etching is rough, quite anisotropic features can be transferred. Figure 7 shows a SEM micrograph of a sample where the entire GaN layer was etched.

The AZ400K developer solution is a particularly convenient one since it is so commonly used in lithography. We found that a $5H_2O$:1AZ400K mixture provided similar PEC etch rates to KOH or NaOH solutions with low (0.01-0.1M) molarities, as shown in Figure 8 for both undoped and n^+ GaN. There was no discernible difference between the surface morphologies with KOH, NaOH and AZ400K. The etching is again diffusion-limited with latter solution as shown in the Arrhenius data of Figure 9. Auger Electron Spectroscopy of etched surfaces generally showed that the average Ga-to-N ratio in the top 100Å of the surface remained similar to that of unetched control samples.

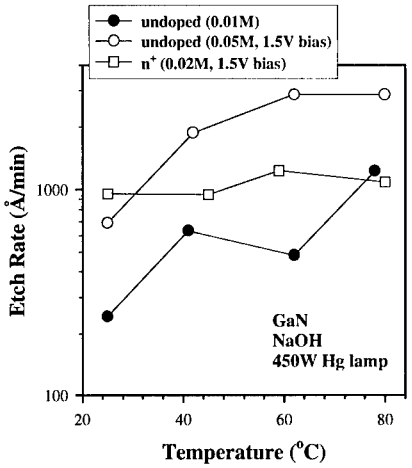


Figure 5. Temperature dependence of GaN PEC etch rate either with or without 1.5V bias in different molarity (0.05 or 0.1M) NaOH solutions.

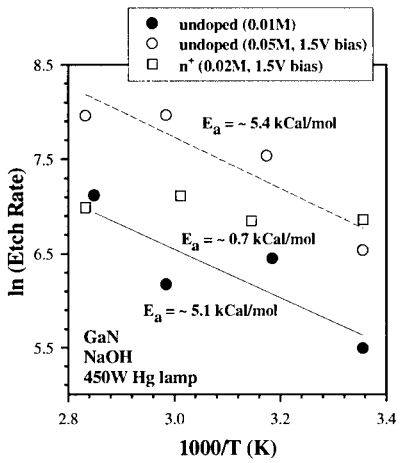


Figure 6. Arrhenius plot of GaN PEC etch rate either with or without 1.5V bias in different molarity (0.05 or 0.1M) KOH solutions.



Figure 7. SEM micrograph of features etched into GaN with 1.5V bias using a Ti mask and 0.02M NaOH solution.

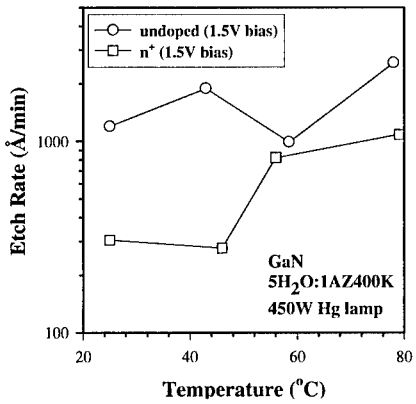


Figure 8. Temperature dependence of GaN PEC etch rate either with or without 1.5V bias in H_2O:AZ400K solutions.

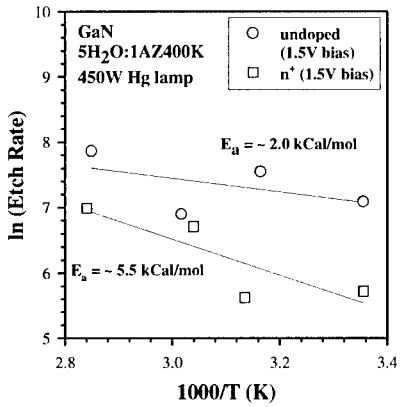


Figure 9. Arrhenius plot of GaN PEC etch rate either with or without 1.5V bias in H_2O:AZ400K solutions.

Summary and conclusions

The etch rate of GaN under UV-assisted photoelectrochemical conditions in KOH, NaOH and AZ400K solutions is found to be a strong function of solution molarity, sample bias and material doping level. At high illumination intensities, etch rates for unintentionally doped (n ~ $3\times10^{16}cm^{-3}$) GaN are $\geq$ 1000Å·min^{-1}. The etching is diffusion-limited under our conditions with an activation energy of < 6kCal·mol^{-1}. The etched surfaces are rough, but retain their stoichiometry. The dopant-selectivity capability may be particularly useful in applications such as base mesa etching in heterojunction bipolar transistors, where exposure of a thin p^+ base layer is necessary in order to make an ohmic contact.

Acknowledgements

The work at UF is partially supported by DARPA/EPRI contract (D. Radack / J. Melcher), No. MDA 972-98-1-0006. The work of H.C. is also partially supported by KOSEF. Sandia is a multiprogram laboratory operated by Sandia Corporation, a Lockheed-Martin company for the US Department of Energy under contract DEAC04-95 AL 85000.

References

1. see for example, C.B. Vartuli, S.J. Pearton, C.R. Abernathy, J.D. MacKenzie, F. Ren, J.C. Zolper and R.J. Shul, Solid State Electron. **41** 1947 (1997).
2. A. Shintani and S. Minagawa, J. Electrochem. Soc. **123** 707 (1996).
3. T. Kozawa, T. Kachi, T. Ohwaki, Y. Tager, N. Koide and M. Koike, J. Electrochem. Soc. **143** L17 (1996).
4. D.A. Stocker, E.F. Schubert and J.M. Redwing, Appl. Phys. Lett. **73** 2788 (1998).
5. B.J. Kim, J.W. Lee, H.S. Park, Y. Park and T.I. Kim, J. Electron. Mater. **27** L32 (1998).
6. J. R Mileham, S.J. Pearton, C.R. Abernathy, J.D. MacKenzie, R.J. Shul and S.P. Kilcoyne, Appl. Phys. Lett. **67** 1119 (1995).
7. J. R Mileham, S.J. Pearton, C.R. Abernathy, J.D. MacKenzie, R.J. Shul and S.P. Kilcoyne, J. Vac. Sci. Technol. A**14** 836 (1996).
8. Q.X. Guo, O. Kato and A. Adesida, J. Electrochem. Soc. **139** 2008 (1992).
9. C.B. Vartuli, S.J. Pearton, J.W. Lee, C.R. Abernathy, J.D. MacKenzie, J.C. Zolper , R.J. Shul and F. Ren, J. Electrochem. Soc. **143** 3681 (1996).
10. J.S. Shor and R.M. Osgood, Jr., J. Electrochem. Soc. **140** L123 (1993).
11. M.J. Grove, D.A. Hudson, P.S. Zory, R.J. Dalby, C.M. Harding and A. Rosenberg, J. Appl. Phys. **76** 587 (1994).
12. M.N. Ruberto, X. Zhang, R. Scarmozzino, A.E. Willner, D.V. Podlesnik, and R.M. Osgood, Jr., J. Electrochem. Soc. **138** 1174 (1991).
13. R. Khare and E.L. Hu, J. Electrochem. Soc. **138** 1516 (1991).
14. J. van de Ven and H.J.P. Nabben, J. Electrochem. Soc. **137** 1603 (1990).
15. M.S. Minsky, M. White and E.L. Hu, Appl. Phys. Lett. **68** 1531 (1996).
16. C. Youtsey, I. Adesida, L.T. Romano and G. Bulman, Appl. Phys. Lett. **72** 560 (1998).
17. C. Youtsey, G. Bulman and I. Adesida, J. Electron. Mater. **27** 282 (1998).
18. C. Youtsey, I. Adesida and G. Bulman, Appl. Phys. Lett. **71** 2151 (1997).
19. R.T. Leonard and S.M. Bedair, Appl. Phys. Lett. **68** 794 (1996).
20. C. Youtsey, I. Adesida and G. Bulman, Electron. Lett. **33** 245 (1997).
21. L.-H. Peng, C.-W. Chuang, Y.-C. Hsu, J.-K. Ho, C.-N. Huang and C.-Y. Chen, IEEE J. Selected Topics in Quantum Electronics **4** 564 (1998).
22. H. Lu, Z. Wu and I. Bhat, J. Electrochem. Soc. **144** L8 (1997).

23. L.-H. Peng, C.-W. Chuang, J.-K. Ho, C.N. Huang and C.-Y. Chen, Appl. Phys. Lett. **72** 939 (1998).
24. J. O, P.S. Zory and D.P. Bour, SPIE Proc. **3002** 117 (1997).

MODELING OF A GaN BASED STATIC INDUCTION TRANSISTOR

Gabriela E. Bunea,* S.T. Dunham** and T.D. Moustakas **

* Dept. of Physics, Boston University, Boston, MA, 02215, gbunea@bu.edu
** Dept. of Electrical and Computer Engineering, Boston University, Boston, MA, 02215

Cite this article as: MRS Internet J. Nitride Semicond. Res. 4S1, G6.41 (1999)

ABSTRACT

Static induction transistors (SITs) are short channel FET structures which are suitable for high power, high frequency and high temperature applications. GaN has particularly favorable properties for SIT operation. However, such a device has not yet been fabricated. In this paper we report simulation studies on GaN static induction transistors over a range of device structures and operating conditions. The transistor was modeled with coupled drift-diffusion and heat-flow equations. We found that the performance of the device depends sensitively on the thermal boundary conditions, as self-heating effects limit the maximum voltage swing.

INTRODUCTION

GaN is a wide-bandgap semiconductor (Eg=3.4 eV), and therefore has a high breakdown field [1] and low thermal generation rate. These properties combined with good thermal conductivity and stability make GaN an attractive material for high power/ high temperature and radiation harsh environment electronic devices. Monte Carlo simulations predict a peak electron velocity of 3.2×10^7 cm/s and a saturation electron velocity of 2.5×10^7 cm/s [2]. This makes possible high frequency operation of GaN devices.

SIT's are short channel FET structures in which the current, flowing vertically between source and drain, is controlled by the height of an electrostatically induced potential barrier under the source [3]. A cross-sectional diagram of the SIT is shown in Figure 1.

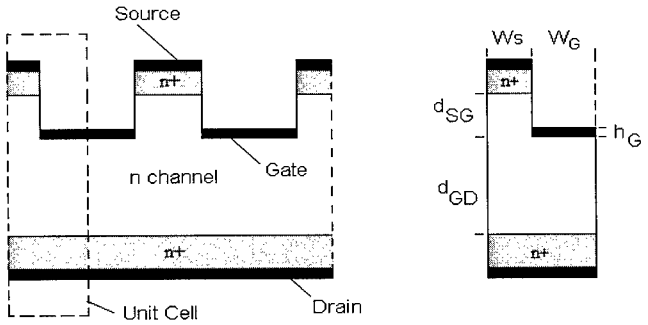


Figure 1. Cross-section of static induction transistor (SIT) structure considered in this work and the unit cell simulated with critical dimensions labeled.

Electrons are emitted from the source, which is at ground potential, and are accelerated to the drain, which is biased at positive potential, where they are collected [4]. A very thin heavily doped layer is deposited next to the drain and source contacts in order to form ohmic contacts. A grid structure is located in the space between the source and drain electrodes so the charged

Mat. Res. Soc. Symp. Proc. Vol. 537 © 1999 Materials Research Society

carriers can be externally modulated. The RF gain of the device is determined by the efficiency with which the modulation is affected. The grid structure is generally fabricated using pn or Schottky junctions.

A range of field effect transistors including MESFET, MISFET, inverted channel AlGaN/GaN and MODFET have been developed with potential applications for high power/ high temperature electronics [2,5-8]. To our knowledge, the highest cut-off frequency reported for GaN-based FET's is 52 GHz [9], and the maximum frequency of oscillations is over 97 GHz [10]. Significant results regarding the power output of GaN-based FET's have been reported by several groups [9, 11]. Wu reported an output power of 3 W/mm at 18 GHz, with a power added efficiency (PAE) of 19% for a 0.25 μm gate AlGaN/GaN MODFET [9]. In comparison, our SIT simulation results show a cut-off frequency f_T of 24.8 GHz, a maximum frequency of oscillations f_{max} of 75.2 GHz. Operated under class B, the output power decreases from 10.75 W/mm to 1.95 W/mm as the operating frequency changes from 2 GHz to 40 GHz. Correspondingly, the PAE changes from 73.8% to 9.1 %.

THEORY

Basic simulation equations and physical models

We employed a commercially available 2D device simulator (ATLAS [12]) which was modified appropriately for GaN, based on experimental observations and theoretical calculations. The transistor was modeled with coupled drift-diffusion and heat-flow equations. The effect of lattice temperature on the performance of the device was taken into account by including the thermoelectric factor in current density equations (1,2) and by adding the heat-flow equation (3).

$$J_n(x,y) = n(x,y)q\mu_n E(x,y) + qD_n\nabla n(x,y) - q\mu_n n(x,y)P_n(x,y)\nabla T(x,y) \tag{1}$$

$$J_p(x,y) = p(x,y)q\mu_p E(x,y) - qD_p\nabla p(x,y) - q\mu_p p(x,y)P_p(x,y)\nabla T(x,t) \tag{2}$$

$$C\frac{\partial T(x,y)}{\partial t} = \nabla(\kappa\nabla T(x,y)) + H(x,y) \tag{3}$$

where T is the lattice temperature, and P_n and P_p are thermoelectric power coefficients for electrons and holes, respectively, C is the heat capacitance per volume (1.97 J/K cm^3 [13]), κ is the thermal conductivity (1.3 W/cm K [14]) and H is the heat generation based on Joule effect.

The models used in the simulation are based on those from Si and GaAs, but have been modified to fit the available data for GaN. The temperature dependence of bandgap energy:

$$E_g(T) = E_g(0) - \frac{\alpha T^2}{T+\beta} \tag{4}$$

with $E_g(0)$=3.5 eV, α=9.39x10^{-4} eV/K, and β=772 K, based on optical absorption measurements [15]. The electron (hole) low-field mobility as a function of the impurity concentration (N) and temperature T is given by [12]:

$$\mu(N,T) = \mu_1 + \frac{\mu_2(\frac{T}{300})^{\beta} - \mu_1}{1+(\frac{T}{300})^{\gamma}(\frac{N}{N_{crit}})^{\delta}} \tag{5}$$

where μ_1, μ_2, β, γ, δ and N_{crit} were determined by fitting the values available from the literature for both electrons and holes [2,16-19]. For electrons: μ_1=15 cm^2/Vs, μ_2=1800 cm^2/Vs, β= -3.04,

γ= -2.55, δ= 0.66, N_{crit}= 8x10^{16} cm^{-3}. For holes: μ_1=0.14 cm^2/Vs, μ_2=880 cm^2/Vs, β= -1.5, γ=0, δ= 0.67, N_{crit}= 5.5x10^{14} cm^{-3}. A comparison between experimental and predicted values (from Monte Carlo simulation) of low field electron mobility versus doping level and the model used in our simulations is presented in Figure 2a. Figure 2b presents a similar comparison for the electron low field mobility versus temperature [19]. In our simulations, we employ a channel doping of 5x10^{16} cm^{-3}. The low field electron mobility reported for such a doping level is 900 cm^2/Vs [5,20]. However this mobility was measured laterally. There is evidence that the lateral mobility is reduced due to the scattering by charged dislocations, while the vertical mobility is significantly higher because the electrons are repelled from the dislocation lines by band bending due to the negative charge on the dislocations [21]. In our device, which is a vertical one, we employ a room temperature electron mobility of 1050 cm^2/Vs, which we believe is a reasonable value.

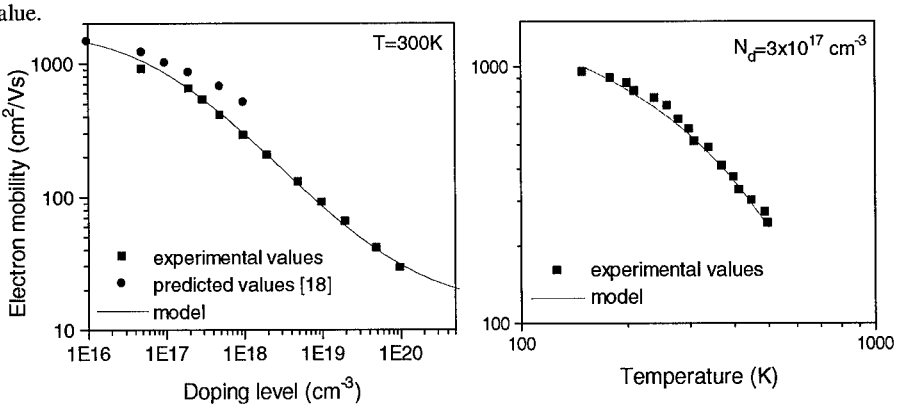


Figure 2. Electron mobility (a) versus doping level at T=300K [2, 16-19], and (b) versus temperature, for a doping level of 3x10^{17} cm^{-3} [19].

For high fields, we use a simple model for mobility versus electric field, which ignores the overshoot effect. This slightly underestimates the current, but the effect is minor for high power devices because they operate at high fields. In high electric fields, the saturation velocity is weakly dependent on temperature. The saturation velocity is modeled as a function of temperature by an empirical relation obtained by fitting the results from Monte Carlo simulation [18]:

$$v_{sat} = 2.87 \text{ x}10^7 - 9.8\text{x}10^3 \text{ x } T \text{ (cm/s)} \quad (6)$$

We assumed that optical recombination is given by:

$$R_{opt} = C_{opt}(np - n_i^2) \quad (7)$$

with C_{opt} =3x10^{-11}cm^3/s, from absorption experimental data and calculated electron energy band dispersion [15].

The generation rate of electron-hole pairs due to impact ionization is modeled according to Selberherr [22]:

$$G = \alpha_n \frac{|J_n|}{q} + \alpha_p \frac{|J_p|}{q} \quad (8)$$

To our knowledge, there are no experimental measurements of impact ionization rates on GaN. However, calculations of impact ionization rates using ensemble Monte Carlo simulation including the full details of all the relevant valence bands, based on pseudopotential approach, have been published recently [23]. We assume that the impact ionization rates (α_n and α_p) are dependent on the electric field and temperature for both electrons and holes according to the formula [12, 22]:

$$\alpha(E,T) = \alpha^{\infty} \exp[-(\frac{E^{crit}}{E})^{\beta}]\{1 + A[(\frac{T}{300})^{M} - 1]\} \tag{9}$$

The critical electric field also depends on T:

$$E^{crit}(T) = E_0^{crit}\{1 + B[(\frac{T}{300})^{M} - 1]\} \tag{10}$$

By fitting the results from [23], the parameters were found to be: for electrons (α^{∞} = 4.55 x 10^6 cm^{-1}, E_0^{crit}=1.19x10^7V/cm, β=1), for holes (α^{∞} = 1.48 x 10^6 cm^{-1}, E_0^{crit}=8.95x10^6 V/cm, β=1). Since there are no available results for T dependence of α, we use the values for silicon for both electrons and holes (A=0.588, B=0.248, M=1 [12]).

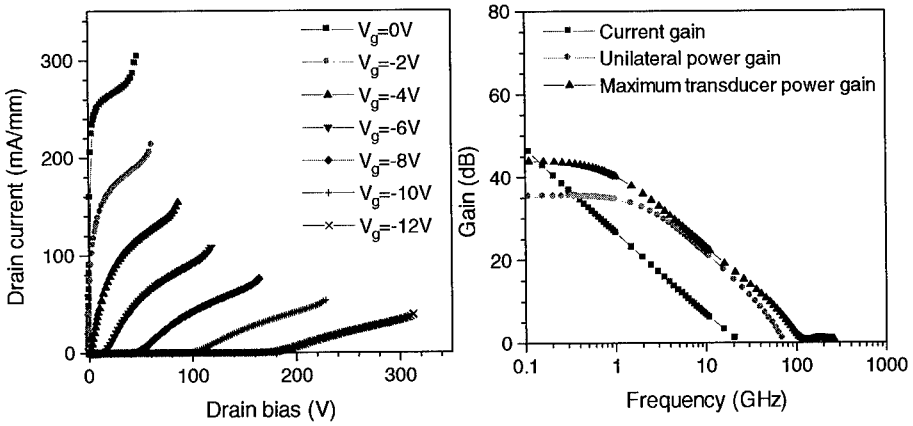
Device optimization

In order to optimize the SIT structure for operation at high power, high temperature and high frequency, DC, small signal and large signal analysis have been performed. Due to symmetry, we need to simulate only one unit cell of the transistor (Figure 1). In order to maximize the breakdown voltage as well as carrier mobility we want low doping in the channel, and 5x10^{16} cm^{-3} was chosen as a value that is achievable with current technology. As the distance between source and gate (d_{SG}) decreases, the voltage gain μ as well as transconductance, g_m increases. The value of d_{SG} is limited by the need to avoid the source to gate punch-through, when the depletion region from gate extends to that from the source. A large distance between gate and drain (d_{GD}) is desirable in order to have a large breakdown voltage. However as d_{GD} increases the series resistance also increases and this limits the frequency and current response of the device. The half-width of the source finger (W_S) determines the blocking voltage of the transistor, so it controls the voltage swing in power measurements. By balancing the above considerations we obtained the following values: the channel is 3 μm thick with a doping concentration of 5x10^{16} cm^{-3}; the n+ layers are 0.2 μm thick and have a doping concentration of 1x10^{19} cm^{-3}. The top of the device is modified in a comb configuration having the following dimensions: source half-width W_S=0.5 μm, gate half-width W_G=1.5 μm, gate height h_G=0.2 μm, d_{SG} =0.6 μm, d_{GD} =2.4 μm.

RESULTS

Our simulations indicate that the performance of the device is very sensitive to the thermal boundary conditions, as self-heating effects limit the voltage swing. In order to increase the power output we have assumed that the device is build on a SiC substrate. According to Binary [5] the SiC substrate allows about a 4x increase in power density due to the higher thermal conductivity of SiC compared to GaN or sapphire. For the same purpose, a layer of diamond paste is assumed to be present on the top of the device. We have calculated the equivalent thermal impedance of the SiC substrate and diamond layer, assuming that the length and height of the SIT is much smaller than the thickness and length of the SiC and diamond layers [12,24]. For one finger of the device, the calculations lead to a thermal impedance of 3300

W/cm^2 K for drain contact, 12000W/cm^2 K for source contact and 4050 W/cm^2 K for gate contact. Simulated drain I-V characteristics with the gate voltages varying from 0V to -12V are shown in Figure 3a. We notice that the breakdown voltage varies with the gate bias from about 50V at 0V gate bias to 320V at –12V gate bias. The simulations indicate that the breakdown is due to self-heating effects. Our results show that the performance of the device is not significantly affected by thermal generation as long as the maximum temperature in the device does not exceed 700K. The gains obtained by small signal ac simulations for a drain bias of V_d=100V and a gate bias of V_g=-6V are plotted as a function of frequency in Figure 3b. The cut off frequency is f_T=24.8 GHz and the maximum frequency of oscillations is f_{max}=75.2 GHz.



(a) (b)

Figure 3. Transistor characteristics: (a) drain I-V characteristics, and (b) gain versus frequency. The cut-off frequency is f_T=24.8 GHz and maximum frequency of oscillations f_{max}=76.5 GHz.

Large signal analysis was performed under class B, in order to obtain the output power and power added efficiency (PAE). In Figure 4 we present the output power and PAE as functions of frequency, with a DC drain bias of V_{DD}=180V, load resistance of 7.2x10^5 ohm and a gate bias voltage swing between 0 and –12 V. Under these conditions, the output power varies from 10.75 W/mm to 1.95 W/mm and PAE varies from 73.8 % to 9.1 % as we increase the operation frequency from 2 GHz to 40 GHz. The maximum theoretical PAE for operation under class B is 78.5 % [4]. Note that operation under class B requires two transistors and gate periphery of both transistors is included in output power calculations.

CONCLUSIONS

In conclusion, we modeled a static induction transistor based on GaN films. Our results show that with a SiC substrate and top side diamond paste as thermal sinks, the output power can be as high as 10.75 W/mm at 2 GHz operating frequency, with a PAE of 73.8 %. The cut-off frequency was found to be 24.8 GHz and the maximum frequency of oscillations was 75.2 GHz. These results demonstrate the excellent potential of GaN based static induction transistors for high power, high temperature and high frequency operation.

This work was supported in part by ONR through a subcontract by Raytheon.

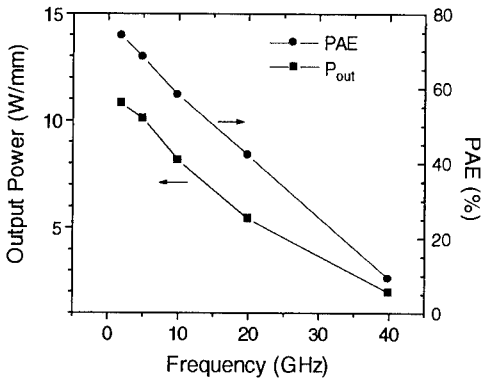


Figure 4. Output power and power added efficiency (PAE) versus frequency.

REFERENCES

[1] M.S. Shur, M.A. Khan, Mat. Res. Bull. **22** (2), 44 (1997).
[2] M.A. Khan, Q. Chen, M. Shur, B. Dermott, J. Higgins, J. Burm, W. Schaff, L. Eastman, Solid State Electron. **41**, 1555 (1997).
[3] R.R. Siergiej, R.C. Clarke, IEDM-95, 353 (1995).
[4] K. Moore, R.J. Trew, MRS Bulletin, March, 50 (1997).
[5] S. Binari, The 2nd Int. Conf. On III-V Nitrides, Tokushima, Japan (1997).
[6] R.J. Trew, M. Shin, W. Gatto, Solid State Electron. **41**, 1561 (1997).
[7] Y.F. Wu, B. Keller, S. Keller, D. Kapolnek, P. Kozodoy, S. Denbaars, U. Mishra, Solid State Electron. **41**, 1569 (1997).
[8] J. Burm, W. Schaff, G. Martin, L. Eastman, H. Amano, I. Akasaki, Solid State Electron. **41**, 247 (1997).
[9] Y.F. Wu, B. Keller, S. Keller, P. Fini, J. Pusl, M. Le, N. Nguyen, C. Nguyen, D. Widman, S. Keller, S. Denbaars, U. Mishra, Electron. Lett. **33**, 1742 (1997).
[10] M.A. Khan, Q. Chen, M. Shur, B. Dermott, J. Higgins, J. Burm, W. Schaff, L. Eastman, IEEE Electron Device Lett. **17**, 584 (1996).
[11] Y.F. Wu, B. Keller, S. Keller, N. Nguyen, IEEE Electron Device Lett. **18**, 438 (1997).
[12] Atlas User's Manual (Device simulation software), Silvaco Inc., Version 1.5.0. (1997).
[13] H. Anderson, *Physics Vade Mecum* (AIP, 1981).
[14] E.K. Sichel, J.I. Pankove, J. Phys. Chem. Solids **38**, 330 (1978).
[15] A.V. Dmitriev, A.L. Oruzheinikov, MRS Internet J. Nitride Semic. Res. **1**, 46 (1996).
[16] J.D. Albrech, MRS Nitride Symp. Proc., 423 (1996).
[17] M. Shur, J. Electron. Mat. **25**, 777 (1996).
[18] U. Bhapkar, M.S. Shur, J. Appl. Phys. **82** (4), 1649 (1997).
[19] W. Götz, N.M. Johnson, C. Chen, H. Liu, C. Kuo, W. Imler, Appl. Phys. Lett. **68** (22), 3144 (1996).
[20] S. Nakamura, T. Mukai, M. Senoh, Jpn. J. of Appl. Phys. **31**, 2883 (1997).
[21] N. Weimann, L. Eastman, D. Doppalapudi, H. Ng, T.D. Moustakas, J. Appl. Phys. **83**, 3656 (1998).
[22] S. Selberherr, *Analysis and simulation of semiconductor devices* (Wien-New York, 1984).
[23] I.H. Oguzman, E. Bellotti, K. Brennan, J. Kolnik, R. Wang, P. Ruden, J. Appl. Phys. **81** (12), 7827 (1997).
[24] E. Hahne, U. Grigull, Int. J. Heat Mass Transfer **18**, 751 (1975).

CONTACT RESISTANCE OF InGaN/GaN LIGHT EMITTING DIODES GROWN ON THE PRODUCTION MODEL MULTI-WAFER MOVPE REACTOR

R.W. Chuang, A.Q. Zou, and H.P. Lee
Dept. of Electrical and Computer Engineering, University of California, Irvine, CA 92697

Z.J. Dong, F.F. Xiong, and R. Shih
Alpha Photonics Inc., 2019 Saturn Street, Monterey Park, CA 91754

M. Bremser
AIXTRON Inc., 1670 Barclay Blvd., Buffalo Grove, IL, 60089 USA

H. Juergensen
AIXTRON AG, 15-17 Kackertstrasse, Aachen D-52072 Germany

Cite this article as: MRS Internet J. Nitride Semicond. Res. 4S1, G6.42(1999)

ABSTRACT

We report both the device fabrication and characterization of InGaN/GaN single quantum well LEDs grown on sapphire substrates using multi-wafer MOVPE reactor. To improve current spreading of the LEDs, a self-aligned process is developed to define LED mesa that is coated with a thin, semi-transparent Ni/Au (40 Å/40 Å) layer. A detailed study on the ohmic contact resistance of Ni/Cr/Au on *p*-GaN versus annealing temperatures is carried out on transmission line test structures. It was found that the annealing temperatures between 300 to 500 °C yield the lowest specific contact resistance r_c (0.016 Ω-cm^2 at a current density of 66.7 mA/cm). Based on the extracted r_c from the transmission line measurement, we estimate that the contact resistance of the *p*-type GaN accounts for ~ 88% of the total series resistance of the LED.

INTRODUCTION

The III-V nitride semiconductor materials system has become increasingly popular among the applications of UV/blue light emitting diodes (LEDs), laser diodes (LDs) and high-temperature electronic devices due to its large direct bandgap energy (3.4 eV for GaN at room temperature). Even though the potentials of III-V nitrides were well known for more than three decade, it was only until 1992 with the realization of Mg doped *p*-GaN film after the thermal annealing [1] could the realization of high brightness blue/green InGaN/GaN quantum well(s) LED [2] and the recent demonstrations of long-lifetime pulsed and CW blue LDs [3] be achieved. Despite the commercialization of LEDs, the low *p*-type doping concentration (and hence high *p*-type resistivity) in GaN still limits the device performance in two ways: first it reduces the current spreading in the LED. This causes most of the light to emit in the active region directly underneath the *p*-type contact, and is therefore blocked by the *p* contact. Secondly, low *p*-type doping results in a rather high and non-linear contact resistance. While the current spreading problem has been effectively resolved by depositing a thin semi-transparent metal layer on top of the *p*-GaN cap layer, high contact resistance is still a problem to be tackled. In the present work, we report the successful growth of single quantum well

Mat. Res. Soc. Symp. Proc. Vol. 537 © 1999 Materials Research Society

InGaN/GaN LEDs on multi-wafer MOVPE reactor with high thickness uniformity and the development of a self-aligned LED fabrication process that incorporates a thin current spreading layer. We also present detailed studies on the variation of contact resistance r_c of Ni/Cr/Au on *p*-doped GaN layer versus annealing temperature.

EXPERIMENT

The InGaN/GaN LED samples were first grown on the Aixtron production model multi-wafer MOVPE reactor. The structures consist of 1.5 μm *n*-GaN layer, a thin InGaN quantum well (4-8 nm), and a 0.5 μm *p*-GaN cap layer, all grown on 2-inch (0001) sapphire substrates. The growth uses standard precursors including TMGa and TMIn for Group III and NH_3 for Group V elements, and silane and $MgCp_2$ are used for n-type and p-type dopant sources, respectively. The un-intentionally doped GaN is *n*-type with carrier concentration ~ 1-3x10^{17}/cm^3. The *p*-type GaN with hole concentration of ~5x10^{17}/cm^3 are routinely achieved after post-growth annealing. The thickness uniformity across the diameter of a 2-inch wafer was evaluated using spectral reflectometry measurement in the range of 670 to 1100 nm.

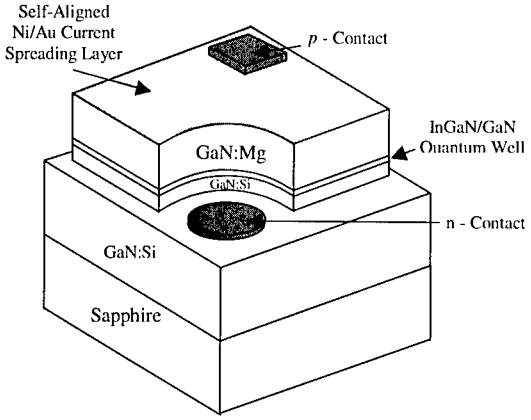


Fig. 1(a) The schematics of self-aligned InGaN/GaN LED structure. Note that a thin Ni/Au layer is deposited on top of the LED mesa to improve the current spreading.

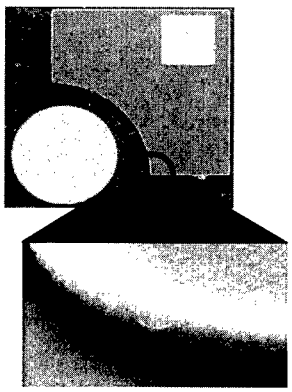


Fig. 1(b) SEM of a typical LED structure with a magnified view of the edges of mesa after RIE etching.

The process flow for fabricating a LED with a structure shown in **Fig. 1(a)**, is described as follows. First, a thin current spreading layer consists of Ni/Au (40 Å/40 Å) was deposited on the entire wafer using electron beam evaporation. The estimated optical absorption due to the current spreading layer is ~ 38% [4]. The sample is thermally annealed at 500°C under N_2 ambient for 100 seconds. The LED mesa is then defined by a photoresist pattern. This is followed by ion milling to remove all except the current spreading layer, and Reactive Ion Etching (RIE) in a mixture of Cl_2 and BCl_3 to remove the GaN all the way to the *n*-layer. In this way, the current spreading layer and the mesa are formed in a self-aligned way. **Figure 1(b)** shows the SEM micrographs of the RIE etched surface around the LED mesa. Both the

bottom and lateral surfaces of the etched mesa appear to be very smooth. Finally, Ni/Cr/Au (150 Å/150 Å/1200 Å) were e-beam evaporated to form both *n* and *p*-type contact pads. LEDs without current spreading layer are also fabricated for comparison. By varying the In composition and the thickness of the InGaN quantum well, LED emission from 420 to 490 nm were obtained.

To investigate the contact resistance to *p*-type GaN, a rectangular shaped, mesa isolated transmission line (TL) structure was fabricated. The width of the TL pattern is 300 μm while the spacing between adjacent Ni/Cr/Au contacts are varied from 5 to 50 μm at increments of 5 μm. The TL pattern is defined using RIE etching similar to the LED mesa etching. The wafer was then diced into several pieces each containing 4 TL patterns and was subsequently annealed at temperatures from 300°C to 600°C for 100 seconds. The TL structures are measured at constant current and the specific contact resistance r_c's were extracted using standard technique [5]. These experimental results will be discussed in the next section.

RESULTS AND DISCUSSIONS

Figure 2 shows a typical reflectance spectrum and the thickness nonuniformity across the diameter of a 2-inch LED sample. The thickness of *n*-GaN layer for this particular LED sample is ~ 3 μm. The epilayer thickness, d is calculated from $d = [\lambda^2/(2n\Delta\lambda)]$, where $\Delta\lambda$ is the wavelength separation between successive reflectance peak, and n is the refractive index of the GaN epilayer. The thickness shown in **Fig. 2** are averaged using $\Delta\lambda$ from 5 successive reflectance peaks. Thickness nonuniformity of less than < 1% is observed across the entire 2-inch wafer. The uniformity result we obtained on a typical LED device layer agrees reasonably well with Aixtron's own evaluation on 2-inch single-layer GaN wafer [6]. **Figure 3(a)** shows the current vs. voltage of the same LED wafer with and without the addition of the current spreading layer. It can be seen that the incorporation of current spreading layer has drastically reduced the spreading series resistance of the LED, which is caused by the high resistive *p*-GaN cap layer. With the current spreading layer, the operating voltage of the LED at 20 mA is reduced to 5 V or below. The use of self-alignment process for forming both the mesa and

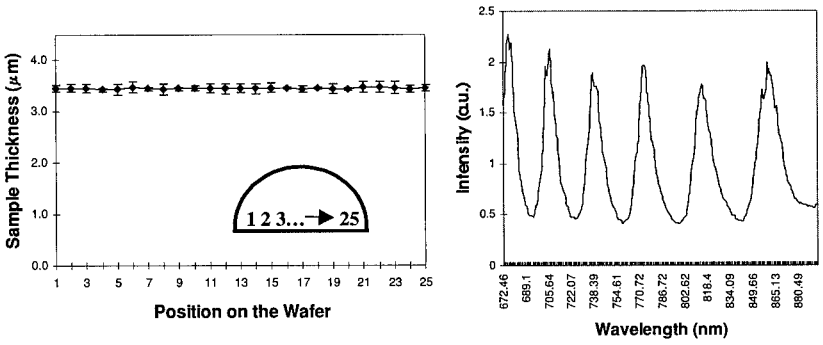


Fig. 2 Thickness uniformity across the diameter of a 2-inch LED wafer. A typical reflectance spectrum is also shown here.

current spreading layer ensures maximum current spreading of a LED. Microscope observation shows that uniform emission from the entire LED mesa except the *p*-contact pad is achieved. The measured series resistance of 9.19×10^4 μm^2 LED is ~26 Ω. **Figure 3(b)** shows the emission spectrum of a typical LED we fabricated. For this particular device, the emission peak is ~ 490 nm and the FWHM is ~ 50 nm.

Owing to the low carrier concentration of the *p*-type GaN and the relative large barrier height between the metal and *p*-GaN, the I-V characteristics of the TL are non-linear. That is, the contact resistance depends on the measurement current. **Figure 4** shows a typical resistance vs. contact separation at two current levels. **Figure 5** shows the extracted r_c for Ni/Cr/Au system at different measurement currents for samples annealed at different temperatures. In all cases, the value of r_c decreases monotonically with increasing current density (current/unit length) in the TL pattern and then approaches a saturation value. The specific contact resistance, r_c is seen to decrease monotonically with increasing current. The optimal annealing temperature is observed to be 300-500°C. Further increase in the annealing temperature at 600°C and above results in an increase of r_c. This phenomenon is likely caused by the formation of nitrogen vacancy that occurs when samples are subjected to high temperature treatments. The nitrogen vacancy in turn compensates the acceptor dopants at the metal/*p*-GaN interface. Several groups have already reported similar findings on these issues [7,8,9]. In addition, the presence of the high resistive Ni_3N and Ni_4N phases at the metal-semiconductor interface at the annealing temperature greater than 500 °C can also result in higher contact resistance [10]. The r_c measurement results are summarized in **Table I**. The lowest r_c we obtained is about 0.016 Ω–cm^2 (the resistivity of the TL sample extracted is on the average of 4.05 ± 0.15 Ω-cm). The values r_c we obtained are similar to previously reported data on Ni/*p*-GaN system [11,12]. The lowering of r_c due to thermal annealing below 600 °C is not clear at this stage. Earlier studies had suggested that thermal annealing of Ni/*p*-GaN helps to removes the contaminants at the

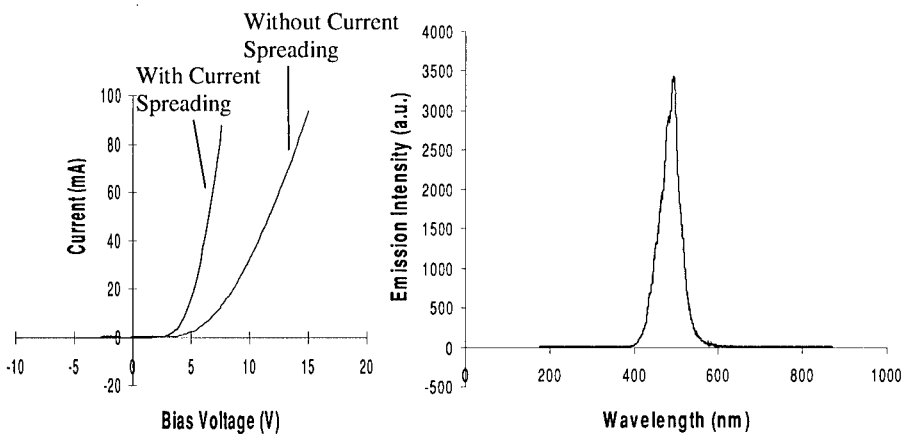


Fig 3 (a) The I-V of the LED with and without the current spreading layer; and (b) the emission spectrum of the LED.

interface resulting in lowering of r_c [12]. Recent results on the lowering of r_c by aqua regia etching of p-GaN has strongly suggested that surface oxide plays a paramount role on the specific contact resistance to p-type GaN [13].

From the LED I-V, the extracted series resistance is 26 Ω measured between 40 to 80 mA. The current density of the LED operating at 60 mA corresponds to an average current density of ~ 31.3 mA/cm for the TL measurement. From **Fig. 5**, the corresponding r_c extracted from the TL measurement is 0.021 Ω–cm^2. The estimated contact resistance of the LED is therefore ~ 22.9 Ω. Based on this estimate, over 88 % of the series resistance of the LED originates from the p-GaN contact resistance.

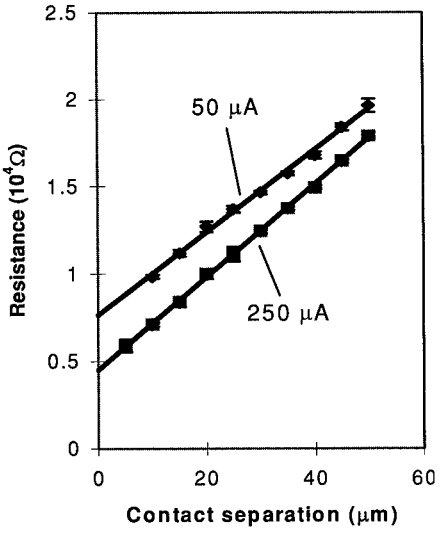


Fig. 4 The measured resistance versus spacing of the TL test pattern at two different measurement currents.

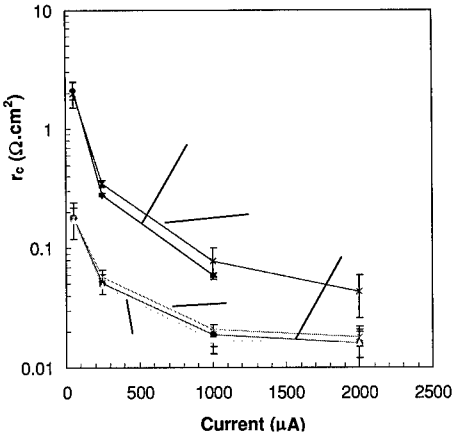


Fig. 5 The extracted r_c measured at different current levels and annealing temperatures. The width of the rectangular TL pattern is 300 μm.

	Specific Contact Resistance (Ω - Sqr. cm)									
Current (μA)	No Annealing	Std. Dev.	300 Deg. C	Std. Dev.	400 Deg. C	Std. Dev.	500 Deg. C	Std. Dev	600 Deg. C	Std. Dev
50	2.13	0.38	0.18	0.06	0.17	0.05	0.18	0.012	1.98	0.47
250	0.28	0.01	0.051	0.01	0.049	0.007	0.058	0.008	0.34	0.024
1000	0.06	0.002	0.019	0.004	0.017	0.004	0.021	0.002	0.078	0.023
2000			0.016	0.006	0.016	0.004	0.018	0.004	0.043	0.017

Table I The extracted average r_c and the corresponding standard deviations from the TL test pattern at different current levels for samples under different annealing temperatures.

CONCLUSION

We report highly uniform growth (thickness nonuniformity < 1%) of InGaN/GaN LED on 2-inch sapphire substrate using a multi-wafer MOVPE reactor. A self-aligned LED fabrication process is developed to incorporate a thin Ni/Au metal for improved current spreading of the LED device. It is also found that the annealing temperatures between 300-500 °C significantly reduce the contact resistance of as-deposited Ni/Cr/Au metals on *p*-type GaN. Specific contact resistance in the range of 0.016 to 0.021 Ω–cm^2 is achieved at annealing temperatures between 300°C to 500°C.

REFERENCE

1. S. Nakamura, N. Iwasa, M. Senoh, and T. Mukai, Jpn J. Appl. Phys., **31**, 1258, (1992).
2. S. Nakamura, T. Mukai, and M. Senoh, Appl. Phys. Lett., **64**, 1678, (1994).
3. S. Nakamura, M. Senoh, S. Nagahama, N. Naruhito, T. Yamada, T. Matsuchita, Y. Sugimoto, and H. Kiyoku, Appl. Phys. Lett., **69**, 1477, (1996).
4. Handbook on Optical Constants of Solids Vol. I, II, and III, edited by D. Palik, Academic Press, (1998).
5. H. Murrmann and D. Widmann, IEEE Tran. Electron Device., **16**, 1022-1024, (1969).
6. R. Beccard, O. Schoen, B. Schineller, D. Schmitz, M. Heuken, and H. Juergensen, Mat. Res. Soc. Symp. Proc., **Vol. 482**, 155, (1998).
7. L.F. Lester, J.M. Brown, J.C. Ramer, L. Zhang, S.D. Hersee, and J.C. Zolper, Appl. Phys Lett., **69**, 2737, (1996).
8. J.C. Zolper, D.J. Rieger, A.G. Baca, S.J. Pearton, J.W. Lee, and R.A. Stall, Appl. Phys. Lett., **69**, 538, (1996).
9. H.S. Venugopalan, S.E. Mohney, B.P. Luther, S.D. Wolter, and J.M. Redwing, J. Appl. Phys., **82(2)**, 15 July, 650, (1997).
10. J.K. Sheu, Y.K. Su, G.C. Chi, W.C. Chen, C.Y. Chen, C.N. Huang, J.M. Hong, Y.C. Yu, C.W. Wang, and E.K. Lin, J. Appl. Phys., **83(6)**, 15 March, 3172, (1998).
11. T. Mori, T. Kozawa, T. Ohwaki, Y. Taga, S. Nagai, S. Yamasaki, S. Asami, N. Shibata, and M. Koike, Appl. Phys. Lett. **69**, 3537, (1996).
12. H. Ishikawa, S. Kobayaxhi, Y. Kiode, S. Yamasaki, S. Nagai, J. Umesaki, and M. Koike, M. Murakami, J. Appl. Phys. **81**, 1315 (1997).
13. J.K. Kim, J.L. Lee, J.W. Lee, H.E. Shin, Y.J. Park, and T. Kim, Appl. Phys. Lett. **73**, 2953, (1998).

CRYSTAL STRUCTURE AND DEFECTS IN NITROGEN-DEFICIENT GaN

S. Oktyabrsky,* K. Dovidenko, A. K. Sharma, V. Joshkin** and J. Narayan

Center for Advanced Materials and Smart Structures, North Carolina State University, Raleigh, NC 27695,
* NYS Center for Advanced Technology, State University of New York at Albany, Albany, NY 12203,
** Department of Electrical and Computer Engineering, University of Wisconsin, Madison, WI, 53706

Cite this article as : MRS Internet J. Nitride Semicond. Res. 4S1, G6.43 (1999)

Abstract

We have studied crystal structure and associated defects in GaN films grown on sapphire under nitrogen-deficient conditions by metalorganic chemical vapor deposition (MOCVD) and pulsed laser deposition (PLD). The structural quality of the PLD films grown at 750 ^{0}C was comparable with those grown by MOCVD at 1050 ^{0}C having threading dislocations density of about 10^{10} cm^{-2} at a film thickness 150-200 nm. Microstructure of the PLD films grown at temperatures above 780^{0}C was found to be similar to that of nitrogen-deficient MOCVD films indicating the loss of nitrogen due to thermal decomposition of the nitride layers. Nitrogen-deficient MOCVD and PLD films exhibit polycrystalline structure with a mixture of cubic zinc-blende and wurtzite hexagonal GaN grains retaining tetragonal bonding across the boundaries and hence the epitaxial orientations and polarity. Renucleation of the wurtzite phase at different {111} planes of cubic GaN results in a rough and faceted surface of the film. Most of the stoichiometric films displayed (0001) Ga-face polarity, but the renucleated inclined wurtzite grains grew in the opposite N-face polarity. The major defects related to the cubic structural metastability are stacking faults and microtwins which being nuclei of the metastable cubic phase have an extremely low energy. We elucidate that the cubic phase is more stable under the nitrogen deficiency and, therefore, can exist without decomposition at higher nitrogen vacancy concentrations in the material.

Introduction

The influence of critical growth parameters such as V/III ratio and substrate temperature on the surface morphology, electrical and optical properties of GaN films has been studied extensively [1-6]. In many cases, however, the obtained results are specific for particular growth methods and do not provide the insight into general tendencies of the growth process. Therefore, it is important to compare the major characteristics of the films grown by different processing methods. In this paper, we will show the influence of nitrogen deficiency on the microstructure and typical defects in the films grown by atmospheric pressure metalorganic chemical vapor deposition (MOCVD) and pulsed laser deposition (PLD) techniques. Compared to MOCVD and MBE methods, the PLD is highly nonequilibrium method. It is known to deliver more energetic (10-100 times higher than MBE) species to the substrate. The stoichiometry of the deposited films is one of the important advantages of the PLD. Due to congruent ablation of the target and close proximity of the substrate, the PLD transfers the composition of the target to the substrate almost without change of the stoichiometry. In the case of PLD of group III-nitrides, the stoichiometry is affected by two major factors: firstly, a very big difference in partial pressures of the components: atomic nitrogen and metal, and secondly, formation of stable nitrogen

Mat. Res. Soc. Symp. Proc. Vol. 537 © 1999 Materials Research Society

molecules which reduces atomic nitrogen concentration. Therefore, special efforts should be made to increase nitrogen incorporation into the growing layer. In the conventional processing methods for III-N growth, MOCVD and MBE, the special means for atomic nitrogen generation are utilized, such as high-temperature pyrolisis of ammonia in MOCVD, or plasma nitrogen sources in MBE. In the case of laser ablation, it is in principle possible to transfer the composition from the stoichiometric target to the substrate. In general, raising the growth temperature is effective in improving the crystallinity and purity of epitaxial films unless it causes thermal decomposition of the crystal, which occur in GaN above 600 ^{0}C. Therefore, it is important to determine the growth temperature range in which thermal decomposition does not limit the properties of the nitrides. In this letter, we will focus on structural properties of GaN films grown by MOCVD and PLD under nitrogen-deficient conditions.

Experimental Details

To study the influence of the stoichiometry on the film microstructure we used GaN films grown by MOCVD or pulsed laser deposition (PLD). These methods have very different thermodynamic and kinetic parameters, and, therefore, comparison of the results is crucial for both studying growth-property correlations as well as understanding the mechanisms of defect formation under nonstoichiometric conditions. Atmospheric pressure vertical MOCVD reactor with a mixture of trimethylgallium, ammonia and nitrogen as a carrier gas was used to grow GaN films on α-Al_2O_3 (0001) substrates. The details of growth can be found elsewhere [7]. The growth process included nitridation, growth of a low-temperature AlN buffer layers and GaN films. The latter films were deposited at 950 ^{0}C with an average V/III mole ratio of 1000. We have also employed PLD to grow GaN on α-Al_2O_3 (0001). We used KrF excimer laser (wavelength - 248 nm, pulse frequency - 10-15 Hz, pulse duration 20 ns) to ablate a stoichiometric hot-pressed target. Target-substrate distance of 4.5 cm, energy density of 3-4 J/cm^2 were used to prepare 150-250 nm - thick films. The films were deposited at a substrate temperature of 720-800 ^{0}C in a vacuum chamber with a base pressure of $5x10^{-7}$ Torr on solvent cleaned substrates. The details of the target and substrate preparation, their characteristics and parameters of PLD are summarized elsewhere [8]. It should be emphasized that the PLD GaN films are much thinner (<0.3 μm) than MOCVD films (>0.5 μm).. The characterization of defects and interfaces in the films was carried out using transmission electron microscopy (TEM). A 200 keV Topcon 002B microscope with a point-to-point resolution of 1.8 Å was used for this study. The cross-sectional TEM samples were prepared by mechanical polishing followed by dimpling to a thickness of approximately 15-25 μm with final thinning using Ar-ion milling at 5 kV. Convergent beam electron diffraction (CBED) patterns were obtained using a focused probe of 10-15 nm with a convergence semiangle of 2 mrad.

Results

Fig. 1 shows cross-sectional micrographs of two GaN samples grown by MOCVD in the same run at the same substrate temperature of 950 ^{0}C. The sample shown in the Fig. 1(a) was placed close to the metalorganic jet in the MOCVD reactor and consequently was grown under ammonia- (or nitrogen-) deficient conditions. The film in the Fig. 1(b) was placed away from the metalorganic stream and grown under group III-deficient conditions. The film (b) was thinner than the film (a) indicating that the film (b) was also grown far from stoichiometric surface conditions, but in N-rich conditions. We have estimated the effective mole ratio of the components using growth rate vs. ratio calibration curves. The films in Figs. 1(a) and 1(b) have been grown at the V/III molar ratios of approximately 2000 and 500, respectively. The film

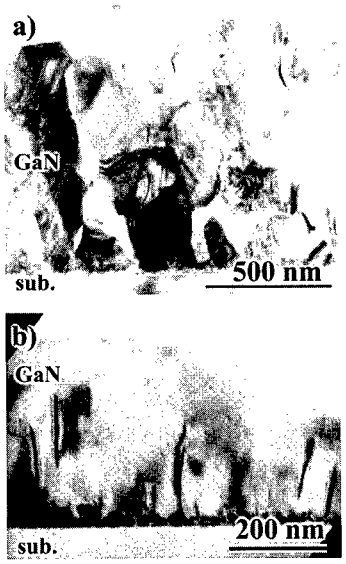


Fig. 1. TEM cross-sectional micrographs of the MOCVD-grown GaN at Ga-rich (a) and N-rich (b) conditions.

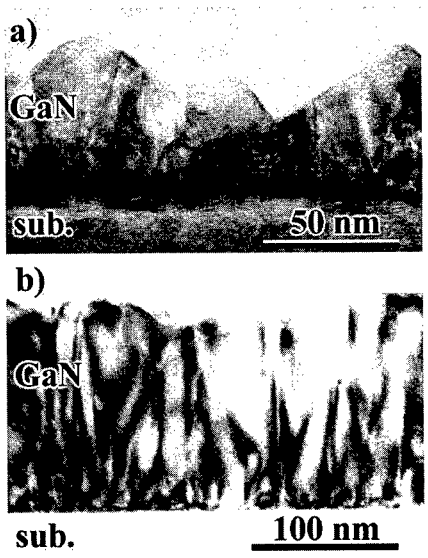


Fig. 2. TEM cross-sectional micrographs of the PLD-grown GaN films at 750 ^{0}C (a) and 780 ^{0}C (b).

grown under N-rich conditions has mirror-like surface and is very uniform, showing only tiny (~10 nm) pits at the dislocations and/or inversion domain boundaries, unlike the N-deficient film which looks hazy. The TEM image of this N-deficient film shows a very rough faceted surface with a hill-to-valley roughness of about 150 nm. This layer contains also misoriented grain and large pores between the grains.

Fig. 2 presents the images of GaN films grown by PLD. The major difference of these two films is the deposition temperature. The film in The Fig. 2(a) was grown at 780^{0}C while the one in The Fig.2(b) was grown at 750 ^{0}C. The film (a) exhibits very rough faceted surface with misoriented grains similar to the morphology presented in the Fig. 1(a). Note that the PLD films in the Fig. 2 are thinner than MOCVD films shown in the Fig. 1. The structural quality of the PLD film grown at 750 ^{0}C (Fig. 2b) is comparable to those grown by MOCVD in the temperature range 950-1050 ^{0}C. The PLD film at lower temperature (Fig. 2(b)) displays a typical columnar structure consisting of slightly misoriented subgrains bounded by threading dislocations with a density of about $2\cdot10^{10}$ cm^{-3} at a film thickness 150-200 nm as measured from plan-view TEM micrographs [9]. The threading dislocation density decreases with the thickness of the film, and it is quite close (factor 3-5 higher) to that for high-quality GaN films with a similar thickness. We show in the following that the PLD films grown at higher temperature are likely to be nitrogen-deficient.

The micrographs in Figs. 3(a) and 3(b) show the higher magnification cross-sectional images of GaN films grown by MOCVD with deficient ammonia flow and by PLD at 780^0 C, respectively. The major microstructural feature of the both films is the mixture of the wurtzite (hexagonal) and zinc-blende (cubic) phases. The presence of the grains of the cubic phase in the films is illustrated by selected area electron diffraction in the right inset of the Fig. 3(a) (MOCVD film), and the convergent beam electron diffraction (CBED) in the inset of the Fig. 3(b) (thin PLD film). The cubic structure has four equivalent families of close-packed {111}

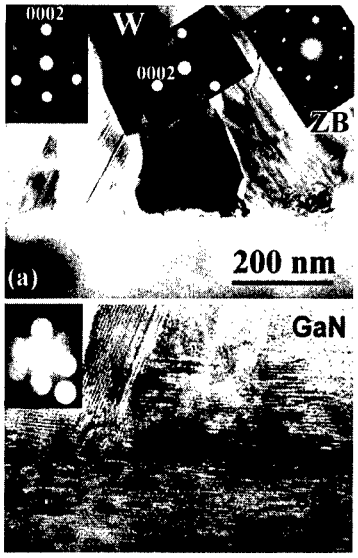


Fig.3. TEM images in [11$\bar{2}$0] projection of the GaN films: (a) N-deficient MOCVD showing both wurtzite (W) and zinc-blende (ZB) grains; the insets: ED patterns from a wurtzite grain oriented with c-axis normal to the surface (not shown in the image), from misoriented "W"-grain, and "ZB"-grain; (b) grown by PLD at 780^{0}C showing the mixture of wurtzite and zinc-blende GaN phases; the inset: micro-diffraction pattern of a small GaN grain with cubic symmetry in a (110) zone.

planes while the hexagonal structure has a single (0001) close-packed plane orientation. Two possible cubic orientations can nucleate on the (0001) hexagonal surface if the tetrahedral bonding is preserved across the interface. These orientations are schematically shown in Figs. 4(a) and (b). The tetrahedron of {111} planes is highlighted by the dashed lines for each orientation. Consequently, there are seven different orientations of the close-packed planes (one plane is common for both tetrahedra) in the cubic grains grown epitaxially on wurtzite structure. The growth of cubic zinc-blende phase can be stabilized during growth and large grains can be formed such as indicated by "ZB" in the Fig. 3(a). Otherwise, the wurtzite phase can renucleate with the basal plane parallel to on one of the seven {111} faces of the cubic grains with the crystallographic relationships (0001)//{111}, and <11$\bar{2}$0>//<1$\bar{1}$0>. Indeed, as clearly seen in the Figs. 3(a) and (b), the resultant microstructure of the film exhibits grains of cubic phase and large wurtzite grains misoriented by approximately 70^0 corresponding to the angle between {111} planes (70.5^0) of the cubic structure. Due to

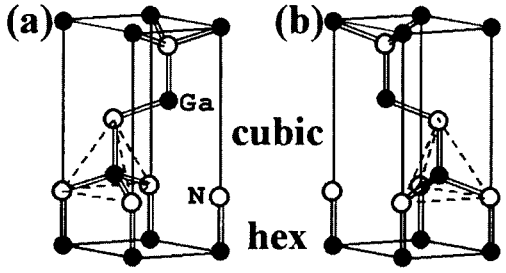


Fig. 4. Two possible orientations of zinc-blende cubic phase that can nucleate on the (0001) hexagonal wurtzite surface.

growth of these grains in different directions, the resulting film surface is very rough and faceted. The films, therefore, are polycrystalline but contain certain orientations of the phases. In addition, as deduced from the CBED patterns (Fig.3(a)-insets), the wurzite grains have different polarity depending on orientation (see below), that also provides the evidence for the epitaxial origin of wurtzite/zinc-blende interfaces.

Disscusion

The formation of the metastable zinc-blende GaN phase is most likely due to non-stoichiometry of the growth conditions. They result from the loss of nitrogen at a higher temperature in the PLD film or from nitrogen-deficient conditions in the MOCVD film. We envision that the cubic phase is more stable under the nitrogen deficiency and, therefore, can

exist without decomposition at much higher nitrogen vacancy concentrations in the material. It is worth comparing these results with the common procedures of cubic GaN growth. A well-established way to form the zinc-blende GaN is the growth on a substrate with cubic symmetry such as GaAs(001) [3-6]. The crystal structure of the GaN grown on GaAs can be controlled by changing V/III ratio in plasma-assisted MBE [4] or in low-pressure RF-plasma assisted MOCVD [5] techniques. The cubic GaN was formed under N-deficient conditions, and the hexagonal GaN was primarily grown under N-rich conditions. It was also shown [6] that the crystalline and optical quality of zinc-blende GaN film grown by conventional low-pressure MOCVD improved at low V/III ratios. These results also correlate with the enhanced stability of the cubic phase at lower V/III ratios.

The major defects related to the cubic structural metastability are stacking faults and microtwins which can be seen in the N-deficient films in the Figs. 1 through 3. These planar defects lie in the close-packed (0001) hexagonal and {111} cubic planes, and being nuclei of the metastable cubic phase these faults have an extremely low energy. A similar crystal structure of the GaN films was reported in a detailed study of the microstructure of the nucleation layer grown by MOCVD at 600 ^{0}C [10]. As-grown 20 nm thick layers exhibited cubic nature predominantly, and were converted into hexagonal upon exposure to 1080 ^{0}C annealing under ammonia flow. Formation of the cubic GaN at low temperature can also be the result of the nitrogen deficiency because of insufficient pyrolisis of ammonia at low substrate temperatures. However, another effect of low temperature growth, namely the increase of stacking disorder due to slower adatom mobility, cannot be ruled out. In any case, nonstoichiometric nitrogen-deficient surface promotes the shift of the equilibrium towards the cubic phase and (even if it is not the primary factor) stabilizes the growth of the cubic GaN.

As can be clearly seen from the Fig. 4, the hexagonal grains with c-axis normal to the substrate surface and those with the inclined c-axis would have opposite face polarity, if the latter grains are nucleated on the cubic phase faces and the polarity is preserved across the phase interface. We have used CBED to determine the polarity of the grains [11]. Due to dynamic electron beam scattering by the non-centrosymmetric specimen, the CBED pattern loses the inversion symmetry. Unlike a common method involving simulation of the CBED contarst for quite thick specimen regions [12,13], we have proposed a technique based on the study of the thinnest (< 150 Å) regions of the wurtzite grains [11]. The simulaton of the CBED as well as pendellössung curves (beam intensity vs. thickness) shows that the pattern from a very thin regions carries unambiguous information about polarity as can be seen in the inserts of the Fig. 3(a). In $[11\bar{2}0]$ orientation for the thinnest sections, the beams (0002), $(1\bar{1}0\bar{2})$ and $(\bar{1}10\bar{2})$ are stronger than $(000\bar{2})$, $(\bar{1}102)$ and $(1\bar{1}02)$, respectively, giving a fingerprint for the polarity determination. In this case, the [0002] direction aims from Ga to N in the wurtzite structure which corresponds to the Ga-polarity of the (0002) surface.

The smooth films grown under optimum or nitrogen-rich conditions by MOCVD and at optimum temperature by PLD have shown Ga-face (0001) polarity [11]. The same Ga-polarity has been found for the wurtzite grains with c-axis normal to the substrate surface as shown in the left inset of the Fig. 3(a). In the grains with the inclined c-planes, the outer surface correspond to N-face (right inset of the Fig. 3(a)) in agreement with the scheme in the Fig. 4.

The polarity of the growing film depends upon several factors including the parameters of nitridation step, recrystallization of low temperature buffer layer and the kinetics of growth of two polarities [14]. A detailed study of the surface morphology of the GaN films with the different polarities [15] has revealed that the Ga-face (0001) surface is much smoother than the surface with N-polarity $(000\bar{1})$. Therefore, films with Ga-polarity are preferable for applications. Most of the GaN films (both PLD and MOCVD grown) that we have investigated, had the Ga-polarity of the (0002) planes, some of them showed the presence of columnar inversion domains

[9]. Applying the present study to the initially polycrystalline low-temperature grown buffer layers, it should be noted, that the polarity of the primary orientation of the epitaxial GaN grains cannot be altered by the cubic phase formation (Fig. 4). However, the grains of the wurtzite phase with inclined c-axis will have the opposite polarity and under particular growth conditions can attain higher growth rates and become dominant. This mechanism will contribute to the roughness and defective microstructure of the GaN films.

Conclusions

In conclusion, we have shown that nitrogen-deficient growth of GaN results in formation of grains with cubic zinc-blende structure. Renucleation of the wurtzite phase at different {111} planes of cubic GaN leads to polycrystalline structure of the film with rough and faceted surface. Grains having cubic or hexagonal structure exhibit epitaxial relationships and preserve polarity of the Ga-N bonds across the interfaces. We elucidate that the cubic phase is more stable under the nitrogen deficiency and, therefore, can exist without decomposition at higher nitrogen vacancy concentrations in the material.

Acknowledgments

The work was supported by National Science Foundation through the Center for Advanced Materials and Smart Structures.

References

1. R. Held, D.E. Crawford, A.M. Johnston, A.M. Dabiran, and P.I.Cohen, J. Electronic Mat. **26**, 272 (1997).
2. O. Briot, J.P. Alexis, S. Sanchez, B. Gil, and R.L. Aulombard, Solid-State Electronics, **41**, 315 (1997).
3. D. Chandrasekhar, D.J.Smith, S. Strite, M.E. Lin, and H. Morcoç, J. Crystal Growth, **152**, 135 (1995).
4. O. Brandt, H. Yang, B. Jenichen, Y. Suzuki, L. Deritz, and K.H. Ploog, Phys. Rev., B **52**, R2253 (1995) .
5. M. Sato, J. Appl. Phys., **78**, 2123 (1995).
6. A. Nakadaira and H. Tanaka, J. Electronic Mat., **26**, 320 (1997).
7. V.A. Joshkin, J.C. Roberts, F.G. McIntosh, S.M. Bedair, E.L. Piner, and M.K. Behbehani, Appl. Phys. Lett., **71**, 234 (1997).
8. S. Oktyabrsky, K. Dovidenko, A.K. Sharma, J. Narayan, in *Advances of Laser Ablation of Materials*, edited by R. Singh, D. Lowndes, D. Chrisey, J. Narayan, T. Kawai, E. Fogarassy, (Mater. Res. Soc. Proc. **526**, San Francisco, 1988) pp.287-292.
9. K. Dovidenko, S. Oktyabrsky, J. Narayan, V. Joshkin, M. Razeghi, in *Nitride Semiconductors*, edited by F.A. Ponce, S.P. DenBaars, B.K. Meyer, S., Nakamura, S. Strite, (Mater. Res. Soc. Proc. **482**, Boston, 1997) pp. 411-416.
10. X.H.Wu, D. Kapolnek, E.J. Tarsa, B. Heying, S. Keller, B.P. Keller, U.K. Misra, S.P. DenBaars, and J.S. Speck, Appl. Phys. Lett., **68**, 1371 (1996).
11. K. Dovidenko, S. Oktyabrsky, J. Narayan, and M. Razeghi, MRS Internet J. Nitride Semicond. Res. *4S1*, G6.46 (1999).
12. Z. Liliental-Weber, C. Kisielowski, S. Ruvimov, Y. Chen, J. Washburn, I. Grzegory, M.Bockowski, J. Jun, and S. Porowski, J. Electron. Mat., 25, 1545 (1996).
13. F.A. Ponce, D.P.Bour, W.T. Young, M. Saunders, and J.W. Steeds, Appl. Phys. Lett., **69** 337 (1996).
14. J.L. Rouviere, M. Arlery, R. Niebuhr, K.H. Bachem, and O. Briot, Mat. Sci. Eng., **B43**, 161 (1997)
15. M. Seelmann-Eggebert, J.L Weyher, H. Obloh, H. Zimmermann, A. Rar, and S. Porowski, Appl. Phys. Lett., **71**, 2635 (1997).

INFLUENCE OF Si-DOPING ON CARRIER LOCALIZATION OF MOCVD-GROWN InGaN/GaN MULTIPLE QUANTUM WELLS

Yong-Hoon Cho*, T. J. Schmidt*, S. Bidnyk*, J. J. Song*,
S. Keller**, U. K. Mishra**, and S. P. DenBaars**

*Center for Laser and Photonics Research and Department of Physics
Oklahoma State University, Stillwater, OK 74078
**Electrical and Computer Engineering and Materials Departments
University of California, Santa Barbara, CA 93106

Cite this article as: MRS Internet J. Nitride Semicond. Res. 4S1, G6.44 (1999)

ABSTRACT

We have systematically studied the influence of Si doping on the optical characteristics of InGaN/GaN multiple quantum wells (MQWs) using photoluminescence (PL), PL excitation (PLE), and time-resolved PL spectroscopy combined with studies of optically pumped stimulated emission and structural properties from these materials. The MQWs were grown on 1.8-μm-thick GaN layers on c-plane sapphire films by metalorganic chemical vapor deposition. The structures consisted of 12 MQWs with 3-nm-thick InGaN wells, 4.5-nm-thick GaN barriers, and a 0.1-μm-thick $Al_{0.07}Ga_{0.93}N$ capping layer. The Si doping level in the GaN barriers was varied from 1 x 10^{17} to 3 x 10^{19} cm^{-3}. PL and PLE measurements show a decrease in the Stokes shift with increasing Si doping concentration. The 10 K radiative recombination lifetime was observed to decrease with increasing Si doping concentration (n), from ~ 30 ns (for $n < 1 \times 10^{17}$ cm^{-3}) to ~ 4 ns (for $n = 3 \times 10^{19}$ cm^{-3}). To elucidate whether non-radiative recombination processes affect the measured lifetime, the temperature-dependence of the measured lifetime was investigated. The reduced Stokes shift, the decrease in radiative recombination lifetime, and the increase in structural and interface quality with increasing Si doping indicate that the incorporation of Si in the GaN barriers results in a decrease in carrier localization at potential fluctuations in the InGaN active regions and the interfaces.

INTRODUCTION

Group III nitride semiconductors and their heterostructures have recently attracted much attention for their versatile applications as light emitting devices, solar-blind ultraviolet detectors, and high power/high temperature/high frequency devices [1-6]. Much interest has been focused on InGaN/GaN quantum wells (QWs) because of their applications as high brightness light emitting diodes and cw blue laser diodes [1,2]. Detailed knowledge of the effects of Si doping on the optical properties of these materials is crucial, especially for designing practical devices. Recently, the effects of Si doping on the optical properties of GaN epilayers [7,8], InGaN/GaN QWs [9-11], and GaN/AlGaN QWs [12,13] have been reported. However, the influence of Si doping on both optical properties and structural qualities in InGaN/GaN multiple quantum well (MQW) device structures is presently not well understood.

In this study, we present a comprehensive study of the optical properties of InGaN/GaN MQWs using photoluminescence (PL), PL excitation (PLE), and time-resolved PL (TRPL) spectroscopy, combined with studies of optically pumped stimulated emission (SE) and structural properties from these materials. In particular, the influence of Si doping in the GaN barriers on the characteristics of the MQWs is investigated. PL and PLE results show that

Mat. Res. Soc. Symp. Proc. Vol. 537 © 1999 Materials Research Society

increasing the Si doping concentration (n) reduces the Stokes shift of the InGaN emission. TRPL experiments show the 10 K recombination lifetime decreases with increasing n, from ~ 30 ns (for $n < 1 \times 10^{17}$ cm^{-3}) to ~ 4 ns (for $n = 3 \times 10^{19}$ cm^{-3}). In addition, it is shown that Si doping improves the structural and interface properties of the InGaN/GaN MQW samples from atomic force microscopy (AFM) images. From the results, we demonstrate that Si doping in the GaN barriers affects the interface quality of the InGaN/GaN MQW systems, and influences the optical properties.

EXPERIMENT

The InGaN/GaN MQWs used in this study were grown on c-plane sapphire films by metalorganic chemical vapor deposition, following the deposition of a 1.8-μm-thick GaN buffer layer. The structures consisted of 12 MQWs with 3-nm-thick $In_{0.2}Ga_{0.8}N$ wells and 4.5-nm-thick GaN barriers, and a 100-nm-thick $Al_{0.07}Ga_{0.93}N$ capping layer. Trimethylgallium (TMGa), trimethylindium (TMIn), trimethylaluminum, and ammonia were used as the precursors and disilane was used as the n-type dopant. The growth temperatures of the GaN base layer, the superlattice (SL) region, and the AlGaN capping layer were 1050, 790, and 1040°C, respectively. The TMGa and TMIn fluxes during the SL growth were 5 and 14 μmol/min, respectively, while the ammonia flow was held constant at 0.35 mol/min. In order to study the influence of Si doping in the GaN barriers, the disilane doping precursor flux was systematically varied from 0 to 4 nmol/min during GaN barrier growth. Accordingly, a doping concentration in the range of < 1×10^{17} to 3×10^{19} cm^{-3} was achieved for the different samples, which was determined by secondary ion mass spectroscopy and Hall measurements. To investigate the effect of Si doping on the GaN surface morphology, three reference 7-nm-thick GaN epilayers were also grown at 800 °C, which have different disilane flux rates of 0, 0.2, and 2 nmol/min during growth. The surface morphology of the reference samples were investigated using a Digital Instruments Nanoscope III AFM operated in tapping mode and the root-mean-square surface roughness was estimated by the AFM software. Details of the growth procedure and the other structural properties are given elsewhere [10,14]. PL and PLE spectra were measured using the 325 nm line of a 20 mW cw He-Cd laser and the quasi-monochromatic light from a xenon lamp dispersed by a 1/2 m monochromator, respectively. TRPL measurements were carried out using a picosecond pulsed laser system consisting of a cavity-dumped dye laser for sample excitation and a streak camera for detection. The output laser pulses from the dye laser had a duration of less than 5 ps and were frequency doubled into the UV spectral region by a nonlinear crystal. The overall time resolution of the system is better than 15 ps. The temperature of the sample in the experiments described above was varied from 10 to 300 K.

RESULTS AND DISCUSSIONS

Figure 1 shows 10 K PL (solid lines) and PLE (dashed lines) spectra of the main InGaN-related PL emission peak with the decay time plotted as a function of emission energy (open circles). The near-band-edge emission from the AlGaN cladding layer and the GaN barriers are also clearly seen at 3.60 and 3.48 eV, respectively. The PLE detection energy is set at the main PL peak energy. The contributions from the GaN barriers and the AlGaN capping layer are clearly distinguishable, and the band-edge PLE positions are coincident with the PL peak positions. A large Stokes shift of the PL emission from the InGaN wells with respect to the band-edge measured by PLE is clearly observed, which is attributed to crystal imperfections such as In alloy fluctuations and interface roughness. We observed that as the Si doping concentration increases, the Stokes shift decreases. The Stokes shift for the sample with $n = 3 \times 10^{19}$ cm^{-3} is ~

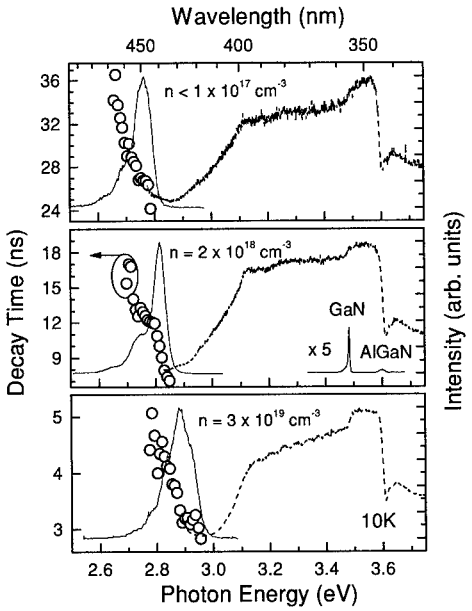


Figure 1. 10 K PL (solid lines), PLE (dashed lines), and TRPL data (open circles) of 12-period InGaN/GaN MQWs with Si doping concentrations ranging from $< 1 \times 10^{17}$ to 3×10^{19} cm^{-3} in the GaN barriers. The Stokes shift between the PL emission peak and the absorption band-edge observed from PLE spectra decreases significantly as the Si doping concentration increases. Luminescence decay times measured by TRPL are shown as a function of emission energy. With increasing Si doping concentration, the 10 K lifetimes decrease from ~ 30 ns (for $n < 1 \times 10^{17}$ cm^{-3}) to ~ 4 ns (for $n = 3 \times 10^{19}$ cm^{-3}).

120 meV smaller than that of the nominally undoped sample (see Table I). The effect of Si doping on the decay time of the MQWs was also explored using TRPL measurements. Figure 1 (open circles) shows the 10 K decay time (τ_d) monitored at different emission energies. The measured lifetime becomes longer with decreasing emission energy, and hence, the peak energy of the emission shifts to the low energy side as time proceeds. This behavior is characteristic of localized states, which in this case are most likely due to alloy fluctuations and/or interface irregularities in the MQWs [15]. A decrease in τ_d with increasing Si doping, from ~ 30 ns (for $n < 1 \times 10^{17}$ cm^{-3}) to ~ 4 ns (for $n = 3 \times 10^{19}$ cm^{-3}), is clearly seen, which can be attributed to a decrease in the potential fluctuations leading to recombination.

One should be very careful interpreting the low temperature lifetime results because the non-radiative recombination processes (which can be caused by poor sample quality) may affect the measured lifetime. To clarify this point, we investigated the temperature dependence of the lifetime as shown in Fig. 2. For the nominally undoped sample with $n < 1 \times 10^{17}$ cm^{-3} (open symbols), we observed an increase of τ_d with temperature (up to around 40 ns for the higher energy side emission) at temperatures below 70 K, in qualitative agreement with the temperature dependence of radiative recombination. As the temperature is further increased beyond a certain crossover temperature, T_c, which is determined by the radiative and non-radiative recombination rates, the lifetime starts to decrease, since non-radiative processes predominantly influence the emission. Further evidence of this is given by the fact that the lifetimes become independent of emission energy at higher temperatures. We note that T_c gradually increases as n increases: T_c ~ 70 K for $n < 1 \times 10^{17}$ cm^{-3}, T_c ~ 100 K for $n = 2 \times 10^{18}$ cm^{-3} (not shown here), and T_c ~ 140 K for $n = 3 \times 10^{19}$ cm^{-3}. This indicates that the decrease in lifetime is due to a decrease of the radiative recombination lifetime itself rather than an increased influence of non-radiative recombination

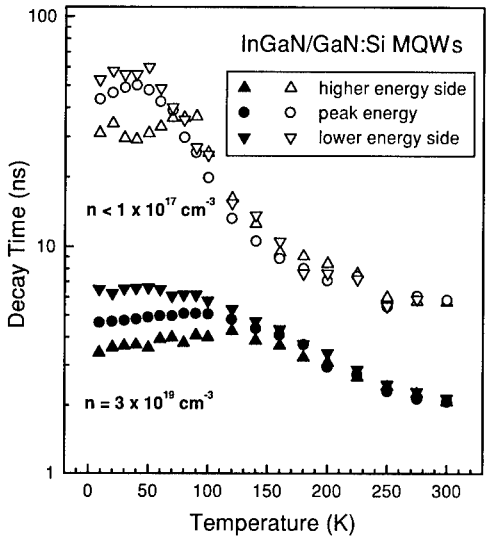


Figure 2. Temperature dependence of decay times monitored above (up triangles), below (down triangles), and at (circles) the emission peak for the InGaN/GaN MQWs with $n < 1 \times 10^{17}$ cm^{-3} (open symbols) and $n = 3 \times 10^{19}$ cm^{-3} (closed symbols) in the GaN barriers. The characteristic crossover temperature, T_c, (which is determined by the radiative and non-radiative recombination rates) gradually increases as n increases: $T_c \sim 70$ K for $n < 1 \times 10^{17}$ cm^{-3}, $T_c \sim 100$ K for $n = 2 \times 10^{18}$ cm^{-3} (not shown), and $T_c \sim 140$ K for $n = 3 \times 10^{19}$ cm^{-3}.

processes. Therefore, we conclude that the decrease in lifetime with increasing n is mainly due to a decrease in potential localization, and hence, a decrease in the carrier migration time into the lower tail states in the MQW active regions.

To further study the influence of Si doping on the structural properties, AFM measurements were carried out. Figure 3 shows 2 μm x 2 μm AFM images of three reference 7-nm-thick GaN films with different disilane flow rates during growth. The root-mean-square surface roughness estimated from AFM images was 0.49, 0.42, and 0.22 nm for GaN epilayers with disilane flow rates of (a) 0, (b) 0.2, and (c) 2 nmol/min during growth, respectively. Thus, smoother GaN surfaces with more homogeneous terrace length were achieved at higher Si doping levels. In addition, the recent high-resolution x-ray diffraction (HRXRD) study showed that as n increases, the full width at half maximum (FWHM) of the higher-order SL satellite peaks narrows: the FWHM of the second order SL peaks was observed to be 589, 335, and 234 arcsec for $n < 1 \times 10^{17}$, $n = 2 \times 10^{18}$, and $n = 3 \times 10^{19}$ cm^{-3}, respectively (see Table I) [14].

Table I. Observed Stokes shift, measured lifetime, T_c, HRXRD FWHM, and SE threshold density for InGaN/GaN MQW samples with different Si doping concentration n by adjusting disilane flow rate F_{Si}.

n (cm^{-3})	F_{Si} (nmol /min)	Stokes shift at 10K (meV)	Measured lifetime (nsec)		T_c (K)	HRXRD FWHM (arcsec) [a]			SE threshold density at 300 K (kW/cm^2) [b]
			10 K	300 K		SL-2	SL-1	SL0	
$< 1 \times 10^{17}$	0	~ 355	24 – 36	6	~ 70	589	312	219	58
2×10^{18}	0.26	~ 305	7 – 18	5	~ 100	335	276	229	55
3×10^{19}	4	~ 235	3 – 5	2	~ 140	234	212	227	165

[a] see Ref. [14]
[b] see Ref. [11]

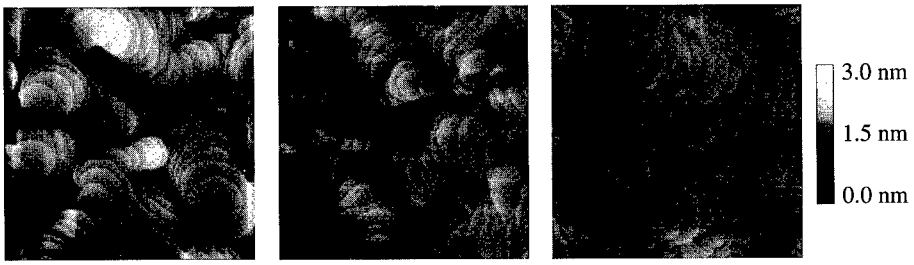


Figure 3. 2 μm x 2 μm AFM images of three 7-nm-thick GaN films with different disilane flow rates during growth. The root-mean-square surface roughness estimated from AFM images was 0.49, 0.42, and 0.22 nm for GaN epilayers with the disilane flow rate of (a) 0, (b) 0.2, and (c) 2 nmol/min, respectively. A higher quality GaN surface morphology and a larger average terrace length were achieved by increasing Si incorporation.

Accordingly, we conclude that Si doping in the GaN barriers significantly improves the structural and interface quality of the InGaN/GaN MQWs. Since the incorporation of Si atoms can change the quality and/or surface free energy of the GaN barriers, it may affect the growth condition (or mode) of the subsequent InGaN wells and the interfaces [7,16,17]. The observed experimental results such as (i) a decrease in Stokes shift and (ii) a decrease in radiative recombination lifetime with increasing Si doping can be explained in terms of a decrease in potential fluctuations and enhancement of the interfacial structural qualities with incorporation of Si in the GaN layers.

Finally, we note that the influence of Si doping on the emission efficiency and the SE threshold pump density was also investigated for the InGaN/GaN MQWs with different Si doping concentration in the GaN barriers [11]. For all the samples, power dependent PL studies show a strong blueshift of the spontaneous emission with increasing excitation density mainly due to band filling of the energy tail states. The blueshift is observed to cease shortly before the onset of SE [18]. The SE spectrum for the MQW sample with $n = 2 \times 10^{18}$ cm^{-3} was composed of many narrow peaks of less than 1 Å FWHM and there was no noticeable broadening of the SE peaks when the temperature was tuned from 175 to 575 K. Interestingly, only moderately Si doped MQW samples exhibited enhanced luminescence efficiency and a reduction of the SE threshold (see Table I). That is, the maximum emission intensity and the lowest SE threshold (55 kW/cm^2) were achieved for the sample with $n = 2 \times 10^{18}$ cm^{-3}, while a SE threshold of 165 kW/cm^2 was obtained for the sample with $n = 3 \times 10^{19}$ cm^{-3}. This fact, combined with the results presented in this paper, indicates that although Si doping improves the interface properties, it does not necessarily enhance the SE properties, reflecting the fact that localized carriers at potential fluctuations may play an important role in the emission from the InGaN/GaN MQW structures used for current state-of-art laser diodes.

CONCLUSIONS

We have investigated the optical properties of InGaN/GaN MQW structures as a function of Si doping concentration in the GaN barriers. As the Si doping of the GaN barriers increases, the Stokes shift of the PL emission peak with respect to the PLE band-edge was found to decrease. In addition, the radiative recombination lifetime measured at 10 K was observed to decrease significantly from ~ 30 ns for $n < 1 \times 10^{17}$ cm^{-3} to ~ 4 ns for $n = 3 \times 10^{19}$ cm^{-3} with increasing n. The results presented here, combined with the observed structural properties, are well explained

by a decrease in carrier localization at potential fluctuations with increasing Si doping of the GaN barriers. These potential fluctuations are most likely a result of In alloy fluctuations and/or thickness variations of the InGaN well regions. The influence of Si doping on the emission efficiency and stimulated emission threshold was also discussed.

ACKNOWLEDGMENTS

This work was supported by AFOSR, ARO, ONR, DARPA, and KOSEF.

REFERENCES

1. S. Nakamura, M. Senoh, N. Iwasa, S. Nagahama, T. Yamada, and T. Mukai, Jpn. J. Appl. Phys. Part 2 **34**, L1332 (1995).
2. S. Nakamura, M. Senoh, S. Nagahama, N. Iwasa, T. Yamada, T. Matsushita, Y. Sugimoto, and H. Kiyoku, Appl. Phys. Lett. **69**, 4056 (1996).
3. B. W. Lim, Q. C. Chen, J. Y. Yang, and M. A. Khan, Appl. Phys. Lett. **68**, 3761 (1996).
4. Y. F. Wu, B. P. Keller, S. Keller, D. Kapolnek, P. Kozodoy, S. P. DenBaars, and U. K. Mishra, Appl. Phys. Lett. **69**, 1438 (1996).
5. X. H. Yang, T. J. Schmidt, W. Shan, J. J. Song, and B. Goldenberg, Appl. Phys. Lett. **66**, 1 (1995).
6. H. Morkoç, S. Strite, G. B. Gao, M. E. Lin, B. Sverdlov, and M. Burns, J. Appl. Phys. 76, 1363 (1994).
7. S. Ruvimov, Z. Liliental-Weber, T. Suski, J. W. Ager III, J. Washburn, J. Krueger, C. Kisielowski, E. R. Weber, H. Amano, and I. Akasaki, Appl. Phys. Lett. **69**, 990 (1996).
8. E. F. Schubert, I. D. Goepfert, W. Grieshaber, and J. M. Redwing, Appl. Phys. Lett. **71**, 921 (1997).
9. P. A. Grudowski, C. J. Eiting, J. Park, B. S. Shelton, D. J. H. Lambert, and R. D. Dupuis, Appl. Phys. Lett. **71**, 1537 (1997).
10. S. Keller, A. C. Abare, M. S. Minsky, X. H. Wu, M. P. Mack, J. S. Speck, E. Hu, L. A. Coldren, U. K. Mishra, and S. P. DenBaars, Materials Science Forum **264 - 268**, 1157 (1998).
11. S. Bidnyk, T. J. Schmidt, Y. H. Cho, G. H. Gainer, J. J. Song, S. Keller, U. K. Mishra, and S. P. DenBaars, Appl. Phys. Lett. **72**, 1623 (1998).
12. A. Salvador, G. Liu, W. Kim, O. Aktas, A. Botchkarev, and H. Morkoç, Appl. Phys. Lett. **67**, 3322 (1995).
13. K. C. Zeng, J. Y. Lin, H. X. Jiang, A. Salvador, G. Popovici, H. Tang, W. Kim, and H. Morkoç, Appl. Phys. Lett. **71**, 1368 (1997).
14. Y. H. Cho, F. Fedler, R. J. Hauenstein, G. H. Park, J. J. Song, S. Keller, U. K. Mishra, and S. P. DenBaars, J. Appl. Phys. (to be published).
15. Y. H. Cho, G. H. Gainer, A. J. Fischer, J. J. Song, S. Keller, U. K. Mishra, and S. P. DenBaars, Appl. Phys. Lett. **73**, 1370 (1998).
16. H. J. Osten, J. Klatt, G. Lippert, B. Dietrich, and E. Bugiel, Phys. Rev. Lett. **69**, 450 (1992).
17. D. J. Eaglesham, F. C. Unterwald, and D. C. Jacobson, Phys. Rev. Lett. **70**, 966 (1993).
18. T. J. Schmidt, Y. H. Cho, G. H. Gainer, J. J. Song, S. Keller, U. K. Mishra, and S. P. DenBaars, Appl. Phys. Lett. **73**, 560 (1998); *ibid.* **73**, 1892 (1998).

THEORY OF THE GAIN CHARACTERISTICS OF InGaN/AlGaN QD LASERS

A.D. Andreev * and E.P. O'Reilly **

* A.F. Ioffe Physico-Technical Institute of Russian Academy of Sciences, Polytechnicheskaya 26, St.-Petersburg 194021, Russia; E-mail: A.Andreev@surrey.ac.uk
** Department of Physics, University of Surrey, Guildford GU2 5XH, UK

Cite this article as: MRS Internet J. Nitride Semicond. Res. 4S1, G6.45 (1999)

ABSTRACT

We present a theoretical analysis of the gain characteristics of InGaN/AlGaN quantum dot (QD) lasers. We calculate the elastic strain distribution caused by the lattice mismatch between the QD and the barrier using an original method which takes into account the hexagonal symmetry of the structure's elastic properties. The method is based on an analytical derivation of the Fourier transform of the strain tensor. The proposed approach is combined with a plane-wave expansion method to calculate the carrier spectrum and wave functions. The many-body gain of a laser containing a periodic array of QDs is calculated using the Padé approximation. We show that band gap reduction and the Coulomb enhancement of the interband transition probability can significantly modify the gain spectrum in InGaN/AlGaN QD lasers.

INTRODUCTION

Wide-band gap semiconductors are attracting considerable attention because of their potential as visible light emitting diodes [1]. At the same time, advances in growth technology has stimulated active investigations in the field of zero dimensional quantum dot (QD) structures. The first GaN-based structures with self-organized QDs have been fabricated recently [2-4]. Lasers based on self-organized QDs have potential advantages over conventional quantum well lasers because of their atomic-like density of states. For wide-band gap heterostructures additional benefits may arise from using QD structures instead of quantum well ones. Firstly, strain relaxation in QD structures is easier and therefore defect-free fabrication of strongly lattice-mismatched heterostructures may be possible. Secondly, because of the carrier localization, the role of many-body effects may increase, resulting in a stronger gain enhancement due to Coulomb interactions. Moreover, recent publications [5,6] demonstrate that light emission from InGaN quantum well lasers may originate from dot-like localized states formed because of indium composition fluctuations. It is therefore timely to undertake a theoretical investigation of the gain characteristics of GaN-based QD structures.

We present here a theoretical study of the elastic strain distribution, carrier spectrum and many-body gain in structures consisting of a periodic array of InGaN QDs embedded in an AlGaN matrix. Employing the Green's function and Fourier transform techniques we find the 3D strain distribution in the QDs. To calculate the carrier spectrum and wave functions we use the plane-wave expansion method. This method allows us to take account of the strain-induced modification of the band structure using analytical expressions for the Fourier transform of the strain tensor. We thus avoid explicit calculation of the strain distribution. The calculated carrier spectrum and wave functions are used as input for gain calculations including many-body effects. We demonstrate that band gap reduction and Coulomb enhancement of the interband transition probability significantly modify the gain spectrum.

For ease of calculation we use a model structure which assumes that the QDs all have the same shape and size, and form a periodic structure with periods $d_{\parallel}$ and d_z in the lateral and growth directions respectively.

Mat. Res. Soc. Symp. Proc. Vol. 537 © 1999 Materials Research Society

CALCULATION OF STRAIN DISTRIBUTION AND CARRIER SPECTRUM

The calculation of the spatial strain distribution in a QD structure requires solving a 3D problem in elasticity theory for a generally non-trivial quantum dot shape. This is often achieved by using finite-difference methods or atomistic techniques [7,8]. These methods require considerable computational effort. A simple method to calculate the strain field in semiconductor structures with QDs of arbitrary shape was presented in Ref. [9] for the case when the elastic properties are assumed to be isotropic and the elastic constants of the QD and matrix materials are equal. The effects of anisotropic elastic constants on the strain distribution were included later in [10] for cubic crystals. We briefly describe here the generalization of this approach for hexagonal crystals (details are given in [11]).

Consider a QD of arbitrary shape formed by embedding one kind of elastic material into a second elastic material with hexagonal symmetry. The displacement vector due to the lattice mismatch between the QD and matrix is expressed through the Green's tensor $G_{in}(\mathbf{r},\mathbf{r}')$ of the elastic equation:

$$u_i = u_i^{(0)} + \int_{\Omega'} G_{in}(r,r')\lambda_{nkpr}^{QD} e_{pr}^{(0)} dS_k' . \tag{1}$$

Here we use the usual rule for summation over 1,2,3 (i.e. x,y,z) for repeating indices; λ_{nkpr}^{QD} is the elastic tensor of the QD material, $u_i^{(0)}$ is the initial displacement associated with the strain tensor $e_{pr}^{(0)} = \varepsilon_a \delta_{pr} + (\varepsilon_a - \varepsilon_c)\delta_{p3}\delta_{r3}$, where $\varepsilon_a = (a^M - a^{QD})/a^{QD}$ and $\varepsilon_c = (c^M - c^{QD})/c^{QD}$ is the lattice mismatch. Integration in (1) is carried out over the QD surface. The Green's tensor is the solution of the equation:

$$\frac{\partial}{\partial x_k}\lambda_{iklm}(r)\frac{\partial}{\partial x_m}G_{in}(r,r') = -\delta(r-r')\delta_{in} . \tag{2}$$

Using a Fourier transform technique we solve Eq. (2) and find the Fourier transform of the strain tensor e_{ij} which corresponds to the displacement u_i in the structure with a single QD. When the elastic constants of the QD and matrix materials are equal, the solution of eq. (2) has the form [11]:

$$\tilde{e}_{ij}^{s}(\xi) = \tilde{\chi}_{QD}(\xi)\left\{ e_{pr}^{(0)} + \frac{(RP-SI)\xi_i\xi_j + (-RQ+SF)\xi_3(\xi_i\delta_{j3}+\xi_i\delta_{j3})/2}{IQ-FP} \right\}, \tag{3}$$

where

$$Q = (C_{13}+2C_{44}-C_{11})\xi^2 + (C_{33}-2C_{13}-4C_{44}+C_{11})\xi_3^2; \qquad I = (C_{13}+C_{44})\xi_3^2;$$
$$P = (C_{33}-2C_{44}-C_{13})\xi_3^2 + C_{44}\xi^2; \qquad R = (C_{11}+C_{12}+C_{13})\varepsilon_a + C_{13}(\varepsilon_c-\varepsilon_a);$$
$$F = C_{11}\xi^2 + (C_{13}+2C_{44}-C_{11})\xi_3^2; \qquad S = (C_{33}+C_{13}-C_{12}-C_{11})\varepsilon_a + (C_{33}-C_{13})(\varepsilon_c-\varepsilon_a).$$

Here C_{ij} denotes the elastic constants, ξ_i are the components of the vector in the inverse space. In Eq. (3) $\tilde{\chi}_{QD}$ denotes the Fourier transform of the QD characteristic function $\chi_{QD}(\mathbf{r})$, which is equal to unity inside the QD and zero outside. The strain tensor of the periodic array of QDs is then expressed through the Fourier series:

$$e_{ij}(\mathbf{r}) = \frac{(2\pi)^3}{d_1 d_2 d_3}\sum_{\mathbf{n}} \tilde{e}_{ij}^{s}(\xi_{\mathbf{n}})\exp(i\mathbf{k}_{\mathbf{n}}.\mathbf{r}), \tag{4}$$

where $\xi_n = 2\pi(n_1/d_1,\ n_2/d_2,\ n_3/d_3)$, d_i is the period in the i-th direction; and the summation is carried out over all values of n_i except the case when $n_1=n_2=n_3=0$ [10].

Equations (3) and (4) give an analytical expression for the strain tensor in a periodic array of QDs of arbitrary shape. It is worth noting that the QD shape enters the expressions only through the form of the Fourier transform of the characteristic function $\chi_{QD}(\mathbf{r})$, which can be found analytically for most dot shapes considered to date [10].

Figures 1 and 2 show the variation of $e_{ij}(\mathbf{r})$ through a cylindrical QD and a pyramidal QD respectively. The pyramid has sharp edges along the (001) and (111) directions; therefore near the QD boundary the strain tensor components vary rather steeply.

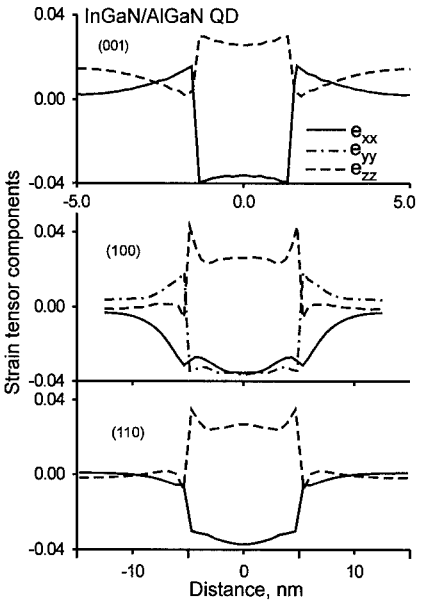


Fig.1 Strain tensor dependence on space position for a cylindrical $In_{0.5}Ga_{0.5}N/Al_{0.1}Ga_{0.9}N$ QD. The QD diameter is 10nm, height is 3nm, lateral period is 25nm, and period along z is 10 nm. Material parameters are from Refs.[12,13].

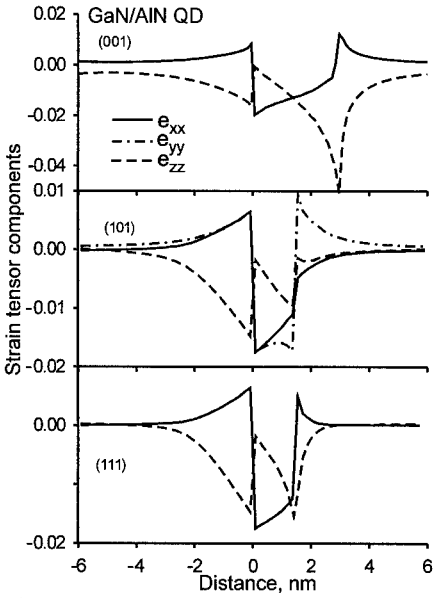


Fig.2 Strain tensor dependence on space position along three different directions for a GaN/AlN pyramidal QD. The QD base is 6x6nm, the height is 3nm, lateral period $d_{//}$ =18nm, and period along z, d_z =12nm. Material parameters are from Refs.[12,13].

The multiband envelope function approximation is commonly used to calculate the carrier spectrum in semiconductor quantum structures. This approach has proved to be a convenient and reliable tool to describe quantum size effects in quantum wells (QWs) as well as in QD structures. The coupling between the conduction and valence bands in wide-band gap GaN-based structures is relatively small over the energy range of interest. Therefore we used a simple one-band model with parabolic dispersion for the conduction band; the strain-induced shift of the band-edge is given by $a_c e_{ii}(r)$. To describe the valence band states we used a 6x6 Hamiltonian including strain-related deformation potentials [14,15], but ignoring the strain-induced piezoelectric fields. These fields are larger here than in III-V zinc-blende crystals, but can still be omitted because of the small dot sizes considered below. Because the spin-orbit constants in both GaN and InN are only of order a few meV, we set the spin-orbit interactions to zero, so that the 6x6 Hamiltonian is then decomposed into two independent 3x3 matrices. In contrast to GaAs/InAs-based QD structures, the effect of strain on the valence band edge potential profile is several times smaller in GaN-based QDs. Figure 3 shows the variation of the HH, LH and CH valence band edges along the z and x axes of the cylindrical dot, including the strain-induced splittings. In spite of the relatively large strain (around 4%), the splitting between the (H,L)H and CH bands is only around 150 meV, compared to several hundreds of meV for similar GaAs/InAs-based structures. The HH and LH practically do not split inside the QD, although a small splitting is found outside. Thus the

strain in a cylindrical QD does not split the degeneracy of the HH and LH bands, although it does separate off the CH band, because of its z-like character.

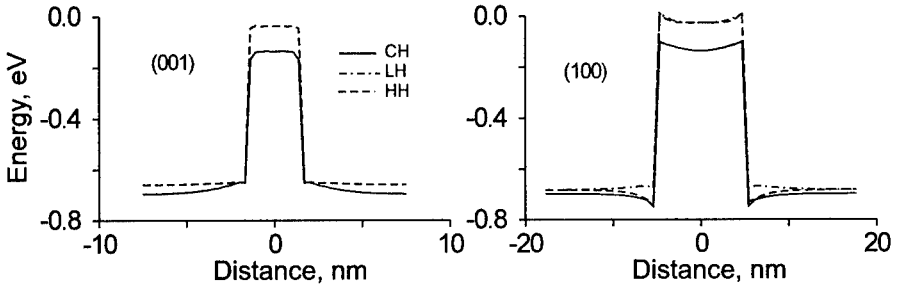


Figure 3. Spatial variation of the valence band edges, including strain-induced splittings. The structure parameters are the same as in Fig.1; the deformation potentials are assumed equal in the QD and matrix, with D_1 = 0.7 eV, D_2 = 2.1 eV, D_5 = -0.7 eV; the barrier height ratio (without strain) is taken as E_v/E_c =7/3 [16].

To calculate the carrier spectrum and wave functions we use a plane-wave expansion method. The idea of this method is to describe the carrier states as a linear combination of a suitably chosen set of bulk states associated with a periodic array of bulk wave vectors. The effective Hamiltonian is represented in the form

$$\hat{\mathbf{H}} = \hat{\mathbf{H}}_0 + \hat{\mathbf{V}} \tag{5}$$

where the 'perturbation' $\hat{\mathbf{V}}$ describes the difference between the potential in a unit cell of the periodic dot array, and the potential in the bulk Hamiltonian $\hat{\mathbf{H}}_0$ used to generate the basis states $|\mathbf{k}, \alpha\rangle$, where $\mathbf{k}$ is the momentum and α denote the type of the bulk carrier state, i.e. HH, LH or CH. The operator matrix $\hat{\mathbf{V}}$ in Eq.(5) should be obtained from the bulk-like Hamiltonian by making the substitution $k_i \rightarrow -i\partial / \partial_i$, to take account of the spatial dependence of the band parameters. Details of the interface boundary conditions are included by an appropriate application of the differential operators at each interface. The solution of the initial Schroedinger equation is found by expanding in a series with respect to the plane waves $|\mathbf{k}, \alpha\rangle \propto \exp(i\mathbf{k}.\mathbf{r})$. The coefficients of this series and the energies of the carrier states in an array of QDs are found numerically as the eigenvectors and eigenvalues of a matrix $\mathbf{A}$, involving matrix elements $V_{k\alpha,k'\alpha'}=\langle \mathbf{k}'\alpha'|\hat{\mathbf{V}}|\mathbf{k}, \alpha\rangle$, which are the Fourier transforms of the matrix $\hat{\mathbf{V}}$. The matrix elements $V_{k\alpha,k'\alpha'}$ depend linearly on the strain components. Therefore the Fourier transform of $\hat{\mathbf{V}}$ is expressed through the Fourier transform of the strain tensor and the QD characteristic function $\chi_{QD}(\mathbf{r})$. This means that using a plane-wave expansion method in conjunction with the Green's function approach for strain calculations, there is no need to calculate the full spatial strain distribution, unlike in other techniques. This simple trick considerably reduces the computation time to set up calculations and makes the plane-wave method very effective for the further study of QD optical properties and modeling of QD devices. We also note that the number of bulk states ("plane waves") which must be included to obtain a given level of accuracy is reduced in periodic structures with partly coupled QDs.

Figure 4 shows the calculated electron and hole energy levels for InGaN/AlGaN QDs. As the In content increases, the barrier heights become larger both for electrons and holes in the QD, with the energy levels then also shifting further away from the barrier band edges.

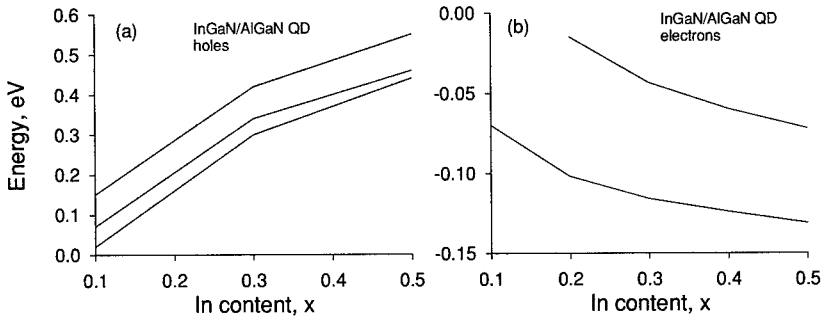


Figure 4. Dependence of the hole and electron energy levels on In content in an $In_xGa_{1-x}N/Al_{0.1}G_{0.9}N$ QD array. The energy is measured form the barrier valence (a) or conduction (b) band edge. The QD is cylindrical with a diameter of 5nm and height of 2nm; the periods are $d_{||}$=10nm and d_z=5nm. Valence band parameters are from [17], electron effective masses from [18], and the band offset ratio for unstrained materials is taken as E_v/E_c=7/3 [16].

GAIN MODELING

Many-body effects [19,20] such as Coulomb enhancement of the interband transition probability and band gap renormalization are important for gain modeling especially for wide band-gap semiconductors [21], because of the high exciton binding energies in these materials. We have used the Padé approximation to model the gain associated with a periodic array of QDs. We considered a structure where the dots are relatively close (the characteristic distance between the dots is comparable to the QD size), so that the dots are partially coupled and form a 3D QD superlattice [22]. We assumed therefore that the Coulomb interaction between the carriers is 3D-like and used the unscreened Coulomb potential, with $V(q)=4\pi e^2/(\varepsilon_0 q^2)$. We use a Lorentzian line-shape function to take account of broadening effects. This gives a reasonable description of the higher energy side of the gain spectra and of the peak gain value, but is less reliable on the lower energy side.

Figure 5 shows the calculated gain spectra for an InGaN/AlGaN QD laser. For comparison, the gain spectra calculated without Coulomb enhancement are also shown. We see from Fig.5 that the Coulomb enhancement strongly affects the peak gain value. In particular, at $N_e = 8 \times 10^{18}$

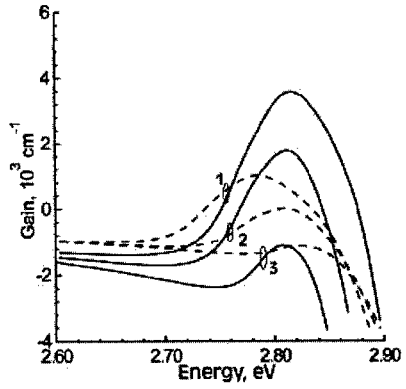


Figure 5. Calculated gain spectra for an $In_{0.5}Ga_{0.5}N/Al_{0.1}Ga_{0.9}N$ QD structure at T=300 K. Curves 3, 2 and 1 correspond to carrier densities (cm^{-3}) of $4x10^{18}$, $6x10^{18}$ and $8x10^{18}$, respectively. Dashed curves are results without Coulomb enhancement. The QDs are disk-like; the diameter and height are 5nm and 2 nm respectively. The QD array periods are $d_{||}$=7.5nm and d_z=4nm.

cm^{-3} the peak gain increases by a factor of 3.5 when the Coulomb enhancement is taken into account (see Fig.5). Thus we demonstrate that including many-body effects strongly modifies the gain spectrum of a laser based on a periodic array of InGaN QDs.

CONCLUSIONS

In conclusion, we have presented a simple technique to calculate the strain distribution due to a quantum dot embedded in a host crystal with hexagonal symmetry. We have used the technique to calculate the strain distribution associated with cylindrical and pyramidal (In)GaN quantum dots embedded in an AlGaN matrix. Our results for the cylindrical dot were then used as input to calculate the electron and hole confined state energies in a periodic array of cylindrical $In_{0.5}Ga_{0.5}N$ quantum dots embedded in a $Al_{0.1}Ga_{0.9}N$ matrix, and these were used to determine the material gain as a function of carrier density, both including and ignoring Coulomb interaction effects. We show that the Coulomb interaction considerably enhances the peak gain at a fixed carrier density, and conclude that InGaN quantum dots should provide a viable gain medium to achieve laser emission in the visible and near-UV spectral regions.

ACKNOWLEDGEMENT

This work was partially supported by the European Union BRITE-EURAM "RAINBOW" project.

REFERENCES

1. S. Nakamura, G. Fasol, *The Blue Laser Diode: GaN Based Light Emitters and Lasers* (Springer-Verlag, Berlin, 1997)
2. F. Widmann, B. Daudin, G. Feuillet, *et.al.,* J. of Appl. Phys, , **83**, 7618 (1998)
3. B. Daudin, F. Widmann, G. Feuillet, *et.al.,* Phys. Rev. B, **56**, R7069 (1997)
4. H. Hirayama, S. Tanaka, P. Ramvall, Y. Aoyagi, Appl. Phys. Lett., **72**, 1736 (1998)
5. J.S. Im, S. Heppel, H. Kollmer, *et.al.*, J. of Grystal Growth, **190**, 597 (1998)
6. Y. Narukawa, Y. Kawakami, M. Funato, *et.al.,* Appl. Phys. Lett., 70, 981 (1997)
7. M. Grundman, O. Stier, D. Bimberg, Phys. Rev. B, **52**, 11969 (1995)
8. A. Cusack, P. R. Briddon, M. Jaros, Phys. Rev. B, **54**, R2300 (1996)
9. J.R. Downes, D.A. Faux, E.P. O'Reilly, J. Appl. Phys., **81**, (10), 6700 (1997)
10. A.D. Andreev, J.R. Downes, D.A. Faux, E.P.O'Reilly, subm. to J. Appl.Phys.
11. A.D Andreev, E.P.O'Reilly, to be subm. to Phys.Rev. B.
12. A.F. Wright, J. Appl. Phys., **82**, 2833 (1997)
13. T.L. Tansley, E.M. Goldys, H. Godlevski, et.al., in *GaN and Related Materials*, edited by S.J. Pearton (Gordon and Breach Science Publish., New York, 1997), p.268
14. G.L. Bir, G.E. Pikus, *Symmetry and Strain-Induced Effects in Semiconductors* (Wiley, New York, 1972)
15. S.L. Chuang, C.S. Chang, Phys. Rev. B, **54**, 2491 (1996)
16. G. Martin, A. Botchkarev, A. Rockett, H. Morcos, Appl. Phys. Lett., **68**, 2541 (1996)
17. T.C. Yeo, T.C. Chong, M.F. Li, J. Appl.Phys., **83**, 1429 (1998)
18. T.C. Chong, Y.C. Yeo, M.F. Li, W.J. Fan, MRS Proc. vol. 482 (1997)
19. H. Haug, S.W. Koch, Phys. Rev. A, **39**, 1887 (1989)
20. W.W. Chow, S.T. Koch, M. Sargent III, IEEE J. of Quantum Electronics, **26**, 1052 (1990)
21. P.Rees, C. Cooper, P.Blood, *et.al.*, Electron. Lett., **31**, 1149 (1995)
22. A.D. Andreev, in *In-plane Semiconductor Lasers: from Ultraviolet to Mid-infrared*, SPIE Proc., **3284**, 151 (1998)

STUDY OF THIN FILMS POLARITY OF GROUP III NITRIDES

K. Dovidenko,* S. Oktyabrsky,** J. Narayan,* M. Razeghi***

*Center for Advanced Materials and Smart Structures, Dept. of Mat. Sci. & Eng., North Carolina State University, Raleigh, NC 27695, kddovide@eos.ncsu.edu
**NYS Center for Advanced Thin Film Technology, State University of New York, Albany, NY 12203
***Center for Quantum Devices, Northwestern University, Evanston, Illinois 60208.

Cite this article as: MRS Internet J. Nitride Semicond. Res. 4S1, G6.46 (1999)

Abstract

Thin films of GaN grown by MOCVD on (0001) sapphire were studied by transmission electron microscopy in order to correlate the observed extended defects with crystal polarity of the films. We propose relatively simple and unambiguous method of polarity determination for wurtzite group III nitrides based on the dependence of the intensity of diffracted beams upon thickness of the specimen. Due to the dynamic scattering by polar structure, the convergent beam electron diffraction patterns lose inversion symmetry and become in fact fingerprints of the structure carrying information about crystal polarity. In this study, we have used the thinnest regions of the specimens (< 15 nm) and multiple diffraction spots in high-symmetry orientation for polarity determination. The films were found to have Ga-polar surfaces, either being unipolar, or containing thin (10-30 nm in diameter) columnar inversion domains (IDs) of N-polarity. The occurrence of IDs was correlated with specific types of dislocation distribution in the films.

Introduction

In recent years the Group III nitride materials have generated tremendous interest due to their potential applications in high-efficiency LEDs (light-emitting diodes) and blue lasers. For device structures, high quality GaN and relative ternary alloy films and heterostructures are needed. The group III nitrides are materials with non-centrosymmetrical crystal structure, therefore, Ga- (Al-) polar or N-polar layers can be grown. Polarity of III-V nitride thin films is known to be an important factor in determining the surface roughness and properties of the as-grown material. Results of efforts of many groups on the polarity study are well reviewed by Hellman [1]. The primary focus of our investigations was the absolute polarity determination and correlations between the polarity and extended defects present in the GaN films grown on sapphire. The polarity of the layers was traditionally determined by convergent beam electron diffraction (CBED) [2-4] and multiple dark field transmission electron microscopy (TEM) techniques [5-6]. However, CBED method can only be applied for perfect crystals of considerable volume, while the GaN films often contain thin (of the order of 10 nm in diameter) pipe-like domains. The multiple dark field TEM imaging [5] allows to determine relative, not absolute polarity of such domains. Here we used a new method of polarity determination based on the different dependency of intensity vs. thickness for the specific diffracted beams revealing the non-centrosymmetric nature of the crystal. This allows the study of polarity for very thin,

Mat. Res. Soc. Symp. Proc. Vol. 537 © 1999 Materials Research Society

nanometer sized domains in GaN and other wurtzite structures as well as unambiguous absolute determination of film polarity.

Experimental

The GaN films in our study were grown on (0001) sapphire by metalorganic chemical vapor deposition (MOCVD) technique at temperatures around 1000^0 C. The details of the growth are reported elsewhere [7]. The films were found to be device-quality single-crystal and showed only excitonic bands in our photoluminescence studies [8]. Typical epitaxial relationships of $(0001)_{GaN} \| (0001)_{sap}$, and $[\bar{1}010]_{GaN} \| [\bar{1}\,\bar{1}20]_{sap}$ were observed for this system.

Multiple dark field technique was used to establish the inversion character of thin pipe-like domains observed in some samples. However, we were primarily interested in determining the absolute polarity of the layers and the inversion domains (IDs). For non-centrosymmetric crystal structures the opposite diffracted beams (those reflections of the diffraction pattern which reveal the non-centrosymmetry of the crystal structure) can have an order of magnitude difference in intensity due to dynamic (multiple) diffraction effects. Since the intensity of diffracted beams is also a function of a sample thickness, there is a unique distribution of intensity vs. thickness for each diffracted beam. The procedure to determine the absolute polarity of the films was to first calculate the intensities of different diffracted beams as a function of crystal thickness by multislice calculations. Experimental CBED patterns of different regions of GaN films in $[1\bar{2}10]$ orientation were obtained using small (about 2-4 nm) probe size. To determine the absolute polarity, we had to estimate the thickness of the crystal for the region of the CBED patterns to make sure that the thickness was below the critical for unambiguous results value. For that, the high resolution TEM (HRTEM) images were taken along with CBEDs and then compared with the simulated high resolution images obtained for wurtzite GaN. The multislice calculations for wurtzite GaN crystal structure in $[1\bar{2}10]_{GaN}$ zone were done using MacTempas© software. We also introduced into the calculations small (up to 1 mrad) tilts of the entire unit cell about the $[1\bar{2}10]_{GaN}$ direction. This corresponds to the tilt observed in most of the experimentally obtained TEM images of group III nitride films. The details of the image simulations in conjunction with polarity determination of wurtzite structures are reported elsewhere [9]. Experimental high-resolution TEM images and convergent beam diffraction patterns of GaN layers were obtained using Topcon 002B (200 kV) electron microscope with standard LaB_6 filament. The microscope has point-to-point resolution of 1.8 Å and nano-probe size beam capabilities.

Results and Discussion

According to our previous results [8, 10] two types of microstructure were found to be characteristic of MOCVD grown GaN films. Density of about 10^9 cm^{-2} was found to be typical for all extended defects (inversion domain boundaries, pure edge, mixed and screw dislocations) present in the films of the first type (A). The films of the second type (B) were found to be free from inversion domains and with low (down to 10^7 cm^{-2}) density of screw and mixed type dislocations. Here low-angle tilt sub-grain boundaries and associated with them threading edge dislocations (density ~ 10^{10} cm^{-2}) were found to be the main defects.

Fig. 1 (a) shows the typical cross-sectional TEM image of an A-type GaN film grown on basal plane of sapphire. The image was taken under $\vec{g}$=0002 weak beam dark field conditions near the $[1\bar{2}10]_{GaN}$ zone. It clearly shows the ~ 10 nm size columnar domain (marked by an arrow). From the cross-sectional TEM micrographs, the density of these pipe-type domains was

calculated to be about 10^9 cm^{-2}. We carried out multiple dark field TEM studies of these domains [10]. They showed inversion of the contrast in the images formed under the 0002_{matrix} and $000\bar{2}_{matrix}$ reflections (near the $[1\bar{2}10]_{GaN}$ zone) which established them to be domains of the opposite with respect to the matrix polarity. To determine the absolute polarity of the ID and the matrix material, we carried out calculations of intensities of different diffraction beams for the $[1\bar{2}10]$ zone of GaN wurtzite crystal structure as a function of specimen thickness. In our calculations, we assumed that the positive [0001] direction of the structure corresponds to the

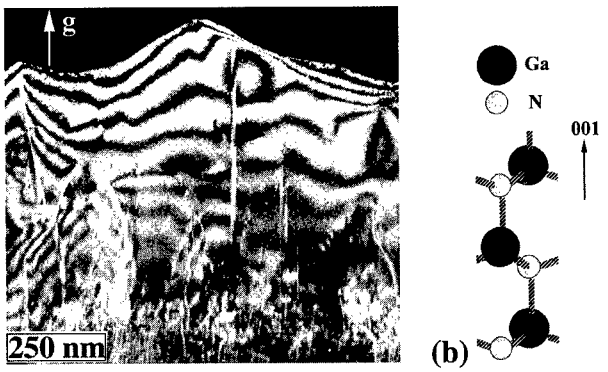


Fig. 1
(a) Weak beam dark field cross-sectional TEM image of a GaN film grown on sapphire. The arrow indicates the inversion domain. The image is taken near the $[11\bar{2}0]_{GaN}$ zone.

(b) Schematic representation of a GaN crystal structure viewed in $[11\bar{2}0]$ direction.

Ga-N bond as it is shown in the schematic representation of the GaN crystal structure in the Fig. 1 (b). The plots in Fig. 2 (a, b) show the calculated intensity vs. crystal thickness for 0002 and $10\bar{1}1$ GaN beams, respectively. The calculations were done for the reflections belonging to the $[1\bar{2}10]$ zone of GaN, no tilt was introduced into the calculations. The intensity of 0002 reflection for sample thickness in the range of 100 Å is about an order of magnitude higher than that of the opposite $000\bar{2}$ beam (Fig 2 a). For the other reflection (Fig. 2 (b)), there is again an order of magnitude difference in intensity between $[10\bar{1}\,\bar{1}]$ and $[10\bar{1}1]$ beams, the former being stronger in regions about 100 Å thick, the latter being stronger for about 200 Å sample thickness. Similar plots were calculated for different diffracted beams of the GaN $[1\bar{2}10]$ zone with and with out introduction of ≤1 mrad tilt. Hence, for the thinnest (below 140 Å) regions of GaN we expect to obtain higher intensity of 0002 CBED disc as compared to the opposite $000\bar{2}$.

We studied the polarity of many device-quality films grown by MOCVD and it was found that the layers had Ga-polarity (according to schematic representation shown in the Fig. 1 (b)). In each case, we took the HRTEM images along with the CBEDs in order to determine the thickness of the sample and made sure that it was below the thickness (~ 140 Å) where dynamic diffraction could give confusing results. As we have previously found, the samples containing IDs have Ga-face polarity. The CBED patterns and HRTEM images were obtained for adjacent areas inside and outside of the pipe-like domains. The results of our study are presented in Fig. 3. The small probe (about 3 nm in diameter) was used to obtain CBEDs outside (Fig. 3, a) and inside (Fig. 3, b) of the inversion domain shown in Fig. 3 (c). The intensity of one <0002> type

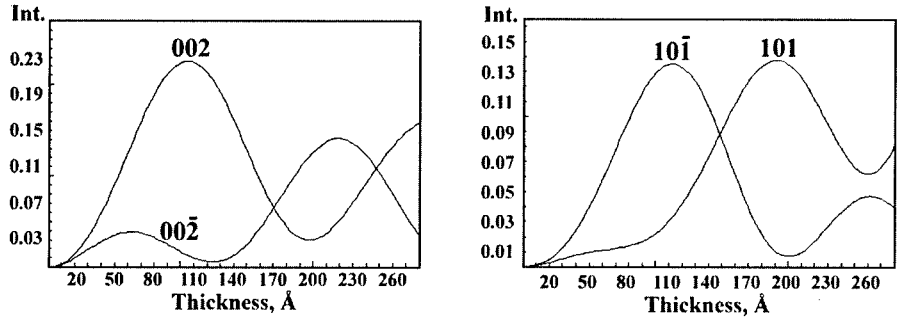


Fig. 2. Calculated intensities (arbitrary units) of <0002> and <10$\bar{1}$1> beams vs. sample thickness (Å) for [1$\bar{2}$10] zone of wurtzite GaN crystal structure.

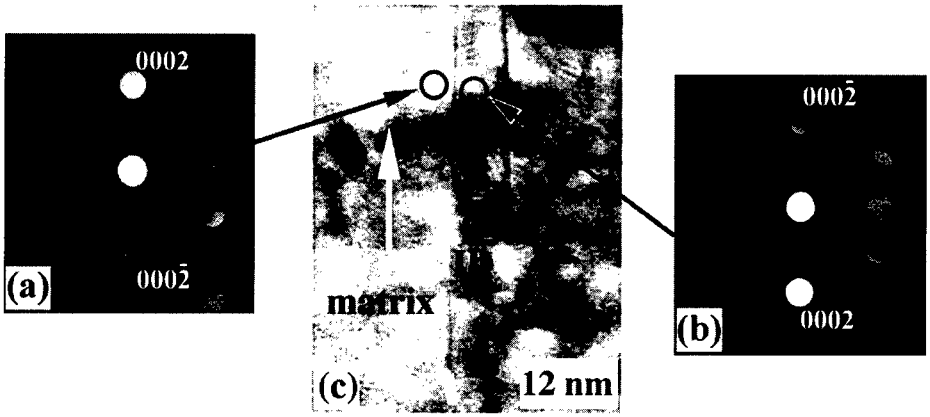


Fig. 3. CBED patterns obtained from (a) the GaN matrix; and (b) the inversion domain ID. The TEM image of the corresponding area of the cross-sectional GaN sample is shown in (c). Positions of the electron beam for taking the CBEDs are shown by circles. White arrow indicates the direction of film growth.

CBED disk in matrix diffraction pattern is much higher than that of the opposite disk. The comparison of the experimental HRTEM images taken in this particular place of the sample with results of our simulations [9] allowed us to estimate the thickness of the GaN layer to be about 70-90 Å. From the graph in Fig. 2 (a) for this thickness region, we can see that the intensity of 0002 beam is much stronger than that of 000$\bar{2}$. The intensity of 10$\bar{1}\,\bar{1}$ beam from Fig. 2 (b) is much higher then the intensity of 10$\bar{1}$1 beam. The distribution of intensities of CBED discs in Fig. 3 (a) confirms that the positive $[0002]_{matrix}$ direction of GaN matrix is directed along the growth axis of the film (indicated by a white arrow in Fig. 3 (c)). The CBED pattern taken inside the ID shows that the positive $[0002]_{ID}$ direction is opposite to the axis of growth. The simulated CBED pattern with indexed reflections calculated for the GaN thickness of 80 Å is shown in Fig. 4, which is in a good agreement with the experimental result (Fig. 3 (a)). It should be noted, that

the effect of small tilt (within 1 mrad) can produce slight variation in distribution of intensities of CBED disks. Nevertheless, general tendencies in the intensity vs. thickness curves remain the same. The study was repeated on many IDs found in several GaN films.

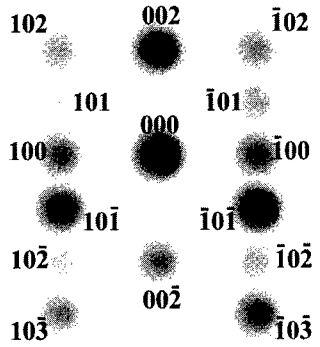


Fig. 4. Simulated convergent beam electron diffraction pattern obtained for 80 Å thickness of the $[1\bar{2}10]$ zone of GaN wurtzite structure. The reflections are indexed.

In accordance with our previous studies [8, 10] in unipolar (Ga-polar) films the major defects were found to be edge dislocations with the Burgers vector $\vec{b}=1/3[11\bar{2}0]$ primarily associated with low angle tilt sub-boundaries. No inversion domains were observed in these layers. The different type of microstructure is correlated with the presence of inversion domains of N-polarity. These films were found [10] to have approximately same density (about 10^9 cm^{-2}) of all extended defects present in the layers such as: screw, mixed and edge dislocations, IDs and basal stacking faults. We have also studied the influence of the layer polarity on surface roughness and to establish the relative rates of growth for different polarities. There are observations of flat and rough (grainy) surfaces in the case of Ga-polar GaN films containing no IDs, and pyramidal-type surfaces for N-polar GaN films [11]. Based on the experimental observations, the N-polar GaN surface was suggested to grow slower than the Ga-polar one [11]. This could also explain the observation of nanotubes in III-V materials as N-polar domains grow slower than the surrounding Ga-polar matrix and after certain thickness leaves empty tubes [4, 12, 13]. However, in our study, films were observed to be of Ga-polarity containing N-polar IDs. The surface of these ID-containing films was observed to be either rough with gaps and hillocks up to 200 nm or smooth within 2 nm range depending upon the growth conditions [10]. Rough GaN films mostly showed the presence of N-polar inversion domain just in the middle of a hillock. In the smooth ID- containing films, the IDs were threading through the whole layer thickness ending at the top surface. Thus, from our observations we can conclude that the dependence of the growth rate vs. surface polarity of GaN can itself be a function of growth conditions such as growth temperature and III/V flux ratio.

Conclusions

We have established the predominance of the Ga-polarity studying device-quality MOCVD films. The films are either unipolar, or contain thin N-polar pipe-like domains with the diameter of 10 - 30 nm. The polarity of thin areas of the III-V nitride samples has been determined by studying the distribution of intensities of the diffraction in high-symmetry CBED patterns. The CBED patterns lose inversion symmetry due to dynamic scattering and become in fact fingerprints of the structure carrying information about crystal polarity. The thickness of the

sample can be estimated by comparing the experimental HRTEM images taken at the same places as CBEDs with results of multislice image simulations. The polarity of the layers was correlated with the surface roughness. The Ga-face polar films containing IDs showed high (about 10^9 cm^{-2}) density of edge as well as screw dislocations randomly distributed throughout the layer, while the unipolar (Ga-polar) films had predominantly b=1/3[11$\bar{2}$0] dislocations (of about 10^{10} cm^{-2} density) associated with low-angle tilt sub-grain boundaries. Finally, from our observations of Ga-polar films with inclusions of IDs having both smooth (± 2 nm) and rough (± 200 nm) surfaces, we envisage that the ratio of growth rates of different polarities in Group III nitride films depends upon the growth conditions determining the overall film growth velocity.

References

1. E.S. Hellman, MRS Internet J. Nitride Semicond. Res. **3**, Article 11 (1998)
2. F. A. Ponce, C.G. Van de Walle, J.E. Northrup, Phys. Rev. B **53**, 7473 (1996).
3. J.L. Rouvierè, M. Arlery, A. Bourret, R. Niebuhr and K. Bachem in *Gallium Nitride and Related Materials I*, edited by F.A. Ponce, R.D. Dupuis, S. Nakamura, J.A. Edmond (Mater. Res. Soc. Symp. Proc. **395**, Pittsburgh, PA, 1996), pp. 393-398.
4. Z. Liliental-Weber, S. Ruvimov, Ch. Kisielowski, Y. Chen, W. Swider, J. Washburn, N. Newman, A. Gassamann, X. Liu, L. Schloss, E.R. Weber, I. Grzegory, M. Bockowski, J. Jun, T. Suski, K. Pakula, J. Baranowski, S. Porowski, H. Amano, I. Akasaki in *Gallium Nitride and Related Materials I*, edited by F.A. Ponce, R.D. Dupuis, S. Nakamura, J.A. Edmond (Mater. Res. Soc. Symp. Proc. **395**, Pittsburgh, PA, 1996), pp. 351-356.
5. R. Serneels, M. Snykers, P. Delavignette, R. Gevers, S. Amelinckx, Phys. Stat. Solidi B, **58**, 277 (1973).
6. L.T. Romano, J.E. Northrup, M.A. O'Keefe, Appl. Phys. Lett. **69**, 2394 (1996).
7. P. Kung, A. Saxler, D. Walker, X. Zhang, R. Lavado, K.S. Kim, M. Razeghi in *III-V Nitrides*, edited by F.A. Ponce, T.D. Moustakas, I. Akasaki, B.A. Monemar (Mater. Res. Soc. Symp. Proc. **449,** Pittsburgh, PA, 1997), pp. 79-84.
8. K. Dovidenko, S. Oktyabrsky, J. Narayan, V. Joshkin, M. Razeghi, Mater. Res. Soc. Symp. Proc. **482**, 411 (1998).
9. K. Dovidenko, S. Oktyabrsky, J. Narayan, M. Razeghi, J. Mater. Res., to be published.
10. K. Dovidenko, S. Oktyabrsky, J. Narayan, J. Mater. Res. (1998).
11. J.L. Rouviere, M. Arlery, R. Niebuhr, K.H. Bachem, O. Briot, MRS Internet J. Nitride Semicond. Res. **1**, article 33 (1996).
12. S. Ruvimov, Z. Liliental-Weber, C. Dieker, J. Washburn, M. Koike, H. Amano, I. Akasaki in *Gallium Nitride and Related Materials II*, edited by C.R. Abernathy, H. Amano, J.C. Zolper (Mater. Res. Soc. Symp. Proc. **468**, Pittsburgh, PA, 1997), pp. 287-293.
13. W. Quian, G.S. Rohrer, M. Skowronski, K. Doverspike, L.B. Rowland, D.K. Gaskill, Appl. Phys. Lett., **67**, 2284 (1995).

TEMPERATURE DEPENDENCE OF BOUND EXCITON EMISSIONS IN GaN

D. G. Chtchekine,[a] G. D. Gilliland,[a] Z. C. Feng,[b],† S. J. Chua,[b] D. J. Wolford,[c]

S. E. Ralph,[d],‡ M. J. Schurman,[e] and I. Ferguson[e]

[a]Physics Department, Emory University, Atlanta, GA 30322
[b]Institute of Material Research and Engineering, Singapore, 119260
[c]Physics Department and Microelectronics Research Center, Iowa State University, Ames, IA 50011
[d]School of Electrical and Computer Engineering, Georgia Institute of Technology, Atlanta, GA 30332
[e]Emcore Corporation, Somerset, NJ 08873
† Work initiated when ZCF was with Emcore Corp.
‡ Work initiated when SER was with Emory University

Cite this article as: MRS J. Nitride Semicond. Res. 4S1, G6.47 (1999)

ABSTRACT

The dissociation channels of two prominent bound exciton complexes in wurtzite GaN thin films are determined via an extensive temperature dependent photoluminescence study. The shallow donor bound exciton dissociation at low temperatures ($T \leq 50$ K) is found to be dominated by the release of a free exciton with thermal activation energy consistent with the exciton localization energy. At higher temperatures a second dissociation channel with activation energy $E_A = 28 \pm 2$ meV is observed. The dissociation of a bound exciton complex with exciton localization energy $E^X_{loc} = 11.7$ meV is also dominated by the release of a free exciton. In contrast to previous studies evidence is presented against the hypothesis of this emission being due to the exciton bound to an ionized donor. We find that it originates most likely from an exciton bound to a neutral acceptor.

INTRODUCTION

Recent progress in the epitaxial growth of high quality GaN materials has permitted the observation of new photoluminescence (PL) emissions. Although some of these new transitions have been positively identified,[1,2] broad PL linewidths preclude the definitive identification of other emissions. A bound exciton emission located ~12 meV below the free exciton is an example of such emission. This emission has been identified as a neutral acceptor-bound exciton (A^0,X)[3,4] or a neutral donor-bound exciton (D^0,X)[5] and more recently was assigned to an ionized donor-bound exciton (D^+,X).[6,7] The identification of the various emissions in GaN is essential to understanding and improving device performance via better dopants and more efficient luminescence.

The temperature dependence of the PL intensity of a bound exciton complex can be used to identify the kinetics of its thermal dissociation, and thus to provide a valuable insight into the origin of this complex. The main channel of thermal decay is the one with the least activation energy, E_A. In the case of a neutral donor-bound exciton complex in GaN the exciton delocalization from the neutral donor (E^X_{loc} ~ 6 meV) is likely to be the minimum-energy dissociation channel of that complex. Temperature dependent photoluminescence studies have been employed previously to investigate neutral donor-bound exciton emissions in

Mat. Res. Soc. Symp. Proc. Vol. 537 © 1999 Materials Research Society

GaN and other materials.[8-10] However, there exists some discrepancy in the reported values for the delocalization energy of the exciton bound to a neutral donor. The PL temperature study can be also used to clarify the origin of the bound exciton emission with E^X_{loc} = 11.7 meV, which we call I_X emission. If this emission is due to the ionized donor-bound exciton complex the minimum-energy dissociation is expected to proceed through the break-off of a loosely bound hole, and thus the thermal activation energy equals the binding energy of the hole. On the other hand, if the I_X emission originates from a neutral-impurity-center, the exciton delocalization is expected to be the lowest energy channel for thermal dissociation.

EXPERIMENT

We report on two lightly Si-doped GaN samples, each grown on (0001) sapphire with ~20 nm -thick GaN buffer by metalorganic chemical vapor deposition (MOCVD). Sample A has a GaN layer thickness of 3.3 μm and was highly resistive. Sample B has an epilayer thickness of 2 μm and a room temperature (RT) carrier concentration of $n \cong 6.3\times10^{16}$ cm^{-3}, as determined by Hall measurements.

PL spectra were obtained using the 325 nm line (3.815 eV) of a cw He-Cd laser focused to ~300 μm diameter resulting in ~0.5 W/cm^2 excitation power density. Samples were cooled to liquid-helium temperatures in a variable temperature (1.5 – 300 K) liquid-helium optical cryostat. The PL signal was dispersed by a 0.85-m double spectrometer providing accuracy of 0.01 nm, and detected by a cooled S-20 photomultiplier tube operating in photon-counting mode.

RESULTS AND DISCUSSION

Figure 1 shows the low temperature PL emissions from both samples. Free exciton (FE,X) emissions are identified by their PL intensity being insensitive to the temperature compared to the bound exciton emissions (D^0,X) and I_X (see Figure 2). (D^0,X) emission is identified by its well known spectral position ~6 meV below the A-band free exciton (FE_A,X).

Sample B shows a (FE_A,X) emission and a dominant (D^0,X) emission originating from neutral Si donors. Sample A also exhibits these two emissions. However their absolute position is blue-shifted by ~2.5 meV in comparison with Sample B. This is likely due to the difference in the degree of the residual stress. Sample A also exhibits two additional emissions: a B-band free exciton (FE_B,X) (very weak in Sample B) and a strong emission line labeled I_X at 3.4735 eV, which is located at 11.7 meV below the A-band free exciton line (FE_A,X). The I_X emission is marked by a strong LO-phonon replica at 3.382 eV, indicating a strong electron-phonon coupling. We determine an LO-phonon energy of $\hbar\omega_{LO}$ = 91.5 meV, consistent with the literature.[11] In Sample A the first excited state (2*S* state) of the A-band exciton is observed at 3.5035 eV, as also shown on Figure 1. The positive identification of this emission was confirmed by a magneto-spectroscopy study which will be published elsewhere. From the energy separation between 1*S* and 2*S* states we can determine the free exciton binding energy in the Coulomb potential approximation: $E^X_b = 4/3\times(E_{2S} - E_{1S}) = 24.4 \pm 0.5$ meV, consistent with other reports.[2]

To assess the temperature variation of the integrated intensity of the (D^0,X) and I_X emissions all strong near-bandedge lines have been fitted with Gaussian lineshapes (see Figure 1). The low-energy tails of the (D^0,X) and I_X emissions were disregarded during fitting;

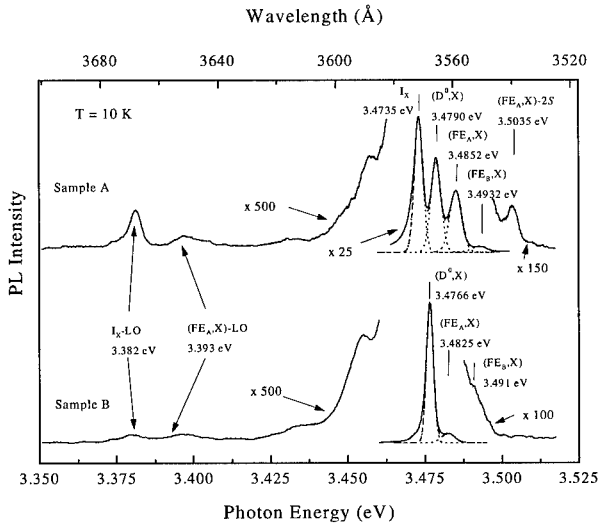


Figure 1. Low-temperature PL spectra of Samples A and B. Sample A is marked by a strong emission I_X at 3.473 eV. Dashed lines represent the fit with gaussian lineshapes (dotted lines). Strong LO-phonon replica of the I_X emission is observed at 3.382 eV. Transition at 3.5035 eV is due to the first excited state of the A-band free exciton.

importantly this does not change the character of their temperature dependence. A two-channel dissociation Arrhenius model was used to fit the temperature dependence of the PL integrated intensity of the (D^0,X) emission in Sample B:

$$\frac{I(T)}{I(0)} = \frac{1}{1 + C_1 \times \exp(-\frac{E_{1A}}{kT}) + C_2 \times \exp(-\frac{E_{2A}}{kT})} \qquad (1)$$

where I(T) and I(0) are the integrated intensities of the (D^0,X) emission at temperature T and 0 K, respectively, E_{1A} and E_{2A} are activation energies and C_1, C_2 are constants.

The temperature dependence of I_X emission was analyzed using a single-channel dissociation Arrhenius model:

$$\frac{I(T)}{I(0)} = \frac{1}{1 + C \times \exp(-\frac{E_A}{kT})} \qquad (2)$$

Figure 2 shows the temperature dependence of the integrated intensity of the (FE_A,X), (D^0,X) and I_X emissions, together with the results of the fitting. As shown, the temperature dependence of the (D^0,X) emission in Sample B is well described with the two-channel dissociation model of Eq. (1). We obtain activation energies E_{1A} = 5.9 ± 0.2 meV and E_{2A} = 28 ± 2 meV. The activation energy E_{1A} is in excellent agreement with the energy of exciton

localization on a shallow donor E^X_{loc} = 6.2 ± 0.4 meV (see Figure 1). The temperature dependence of the (D^0,X) emission in Sample A (fitted with a single-channel dissociation model due to a limited temperature range) exhibits thermal activation energy E_A = 5.6 ± 0.3 meV, which is also in a very good agreement with the exciton localization energy and the value of E_{1A} in Sample B. Therefore, we conclude that the dominant channel of thermal dissociation for the (D^0,X) complex at low temperatures (T ≤ 50 K) is the release of a free exciton.

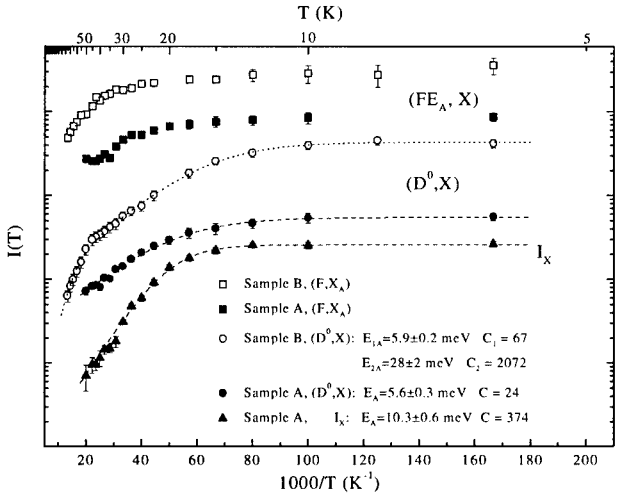


Figure 2. Temperature dependence of the integrated PL intensity of (FE_A,,X) emission (Samples A and B), (D^0,X) emission (Samples A and B), and I_X emission (Sample A). The plots are vertically displaced for the convenience of viewing. Dotted and dashed lines represent fits with Eq. (1) and Eq (2), respectively.

At higher temperatures another thermal dissociation channel with activation energy E_{2A} ≅ 28 meV is clearly observed (see Figure 2). The second dissociation channel may be due to the decay of the (D^0,X) complex via simultaneous exciton delocalization and exciton dissociation with activation energy $E_{2A} \cong E^X_b + E^X_{loc} \cong 30$ meV.[12] Alternatively, a neutral donor ionization process, with activation energy $E_{2A} = E_D \cong 29$ meV,[13] may also affect the PL intensity of the (D^0,X) emission, since it reduces the number of the neutral-donor centers to which photo-excited excitons can bind to form the (D^0,X) complexes.[8] A detailed study of exciton kinetics is required to determine which of these two channels governs the temperature dependence of the (D^0,X) emission at higher temperatures.

The temperature dependence of the I_X emission is well fit by Eq. (2) in the experimental temperature range, resulting in E_A = 10.7 ± 0.6 meV. This activation energy is very close to the exciton localization energy of the I_X complex: E^X_{loc} = 11.7 meV. This indicates that the I_X bound exciton complex dissociates by releasing a free exciton, similar to the (D^0,X) complex.

It has been suggested that the I_X emission is due to the exciton bound to the ionized donor.[6,7] The (D^+,X) complex is more stable in systems with a smaller ratio of the electron and

hole effective mass $\sigma = m_e/m_h$.[14] Maintaining the hole bound to the donor is the weak link in the stability of the (D^+,X) complex. A somewhat similar situation was reported in GaP[15] where the thermal release of the hole was favored over the exciton delocalization for isoelectronic traps.

We can estimate the binding energy of the hole in the current system by evaluating the electron-hole mass ratio, σ. From the value of the free exciton binding energy the exciton reduced mass can be estimated to be $\mu^* = (m^p_e \cdot m^p_h)/(m^p_e + m^p_h) = 0.162$. Here all masses are taken to be polaron masses due to the strong electron-phonon interaction in GaN. Taking the electron polaron mass $m^p_e = 0.22$[16], we find the hole polaron mass $m^p_h = 0.61$ and $\sigma^p = 0.36$. Since the value of σ^p is smaller than $\sigma_{crit.} = 0.43$,[14] the (D^+,X) complex is theoretically allowed in GaN. The hole binding energy can be now estimated in the approximation of the Coulomb potential using the Figure 1 of Skettrup *et al.*.[14] To find an upper limit for the hole binding energy we take a value of the electron-hole mass ratio: $\sigma = 0.3$, which is more favorable for the existence of the (D^+,X) complex. Let's denote a neutral donor energy level E_D (E_D = 29 meV[13]) and ionized donor-bound exciton energy level $E_{(D^+,X)}$. Then from the Figure 1 of Skettrup we obtain $(E_{(D^+,X)} - E_D)/E_D \cong 1\%$ which yields a hole binding energy of $E_h = E_{(D^+,X)} - E_D \cong 0.3$ meV. Since the distance between hole and donor can be estimated[14] at ~120 Å for σ = 0.3 and the sum of the polaron radii for electron and hole is ~20 Å in GaN, the electron-phonon interaction is not expected to affect the hole binding energy significantly. We may, therefore, conclude that the thermal dissociation of the (D^+,X) complex in GaN proceeds via the release of a free hole, with very small activation energy $E_A \leq 1$ meV, which should make the observation of this complex possible only at very low temperatures.

The results of Figure 2 for the I_X emission do not exhibit $E_A \cong 1$ meV; indeed we determine E_A = 10.7 meV. It is therefore very unlikely that I_X emission originates from a (D^+,X) complex. Since $E_A \cong E^X_{loc} = 11.7$ meV the main channel of dissociation for the I_X emission should be release of a free exciton, which is consistent with the neutral impurity-bound exciton model. Since the I_X emission indicates a strong coupling to LO-phonons, contrasting the (D^0,X) emission in our samples, we believe that it originates from a neutral acceptor-bound exciton. This hypothesis is also consistent with the fact that strong I_X emission is observed only in highly compensated samples. We can estimate the binding energy of this acceptor using Haynes' rule which has been shown to be valid for acceptors in GaN[17]: $E_b = E^X_{loc}/0.1 = 120$ meV. Therefore the free-to-bound (e, A^0) transition involving this shallow acceptor can be, in principle, observed around 3.390 eV. Unfortunately the observation of (e, A^0) emission is likely to be masked by the strong LO-phonon replica of the (FE_A,X) emission at 3.393 eV. The existence of such a shallow acceptor (E_b = 120 meV) in GaN would be significant since it would provide a more effective *p*-type dopant.

CONCLUSIONS

In summary, our temperature study of the shallow bound exciton emissions in GaN shows that the activation energy of thermal dissociation of the (D^0,X) complex at low temperatures ($T \leq 50$ K) is in good agreement with the exciton localization energy, thereby proving that at low temperatures the main dissociation channel of shallow bound exciton complexes in GaN is the release of a free exciton. At higher temperatures a second dissociation channel is clearly observed, which may be due to the process of simultaneous exciton delocalization and dissociation and/or neutral donor ionization. An analysis of the thermal stability of the ionized donor-bound exciton leads to the conclusion that the least-energy thermal decay of this complex should proceed via the release of a free hole, with a very small

activation energy $E_A \leq 1$ meV. This contradicts the results of our temperature study for the bound exciton emission with $E^X_{loc} = 11.7$ meV, for which we find the thermal activation energy $E_A = 10.7$ meV. Therefore, the assumption of this emission being due to the exciton bound to an ionized donor is not valid. Since the thermal activation energy and localization energy are in good agreement for this emission, similarly to the case of the (D^0,X) emission, we conclude that it originates from an exciton bound to a neutral impurity – most likely a neutral acceptor.

REFERENCES

1 B. J. Skromme, H. Zhao, B. Goldenberg, H. S. Kong, M. T. Leonard, G. E. Bulman, C. R. Abernathy, and S. J. Pearton, in *III-V Nitrides*, edited by F. A. Ponce, T. D. Moustakas, I. Akasaki, and B. A. Monemar (Mater. Res. Soc. Symp. Proc. **449**, Pittsburgh, 1997) p. 713.

2 D. Volm, K. Oettinger, T. Streibl, D. Kovalev, M. Ben-Chorin, J. Diener, B. K. Meyer, J. Majewski, L. Eckey, A. Hoffmann, H. Amano, I. Akasaki, K. Hiramatsu, and T. Detchprohm, Phys. Rev B **53,** 16543 (1996).

3 Y. Kawakami, Z. G. Peng, Y. Narukawa, S. Fujita, S. Fujita, and S. Nakamura, Appl. Phys. Lett. **69,** 1414 (1996).

4 K. Pakula, A. Wysmolek, K. P. Korona, J. M. Baranowski, R. Stepniewski, I. Grzegory, M. Bockowski, J. Jun, S. Krukowski, M. Wroblewski, and S. Porowski, Solid State Commun. **97,** 919 (1996).

5 S. Fischer, D. Volm, D. Kovalev, B. Averboukh, A. Graber, H. C. Alt, and B. K. Meyer, Mater. Sci. Eng. B **43,** 192 (1997).

6 D. C. Reynolds, D. C. Look, B. Jogai, V. M. Phanse, and R. P. Vaudo, Solid State Commun. **103,** 533 (1997).

7 B. Santic, C. Merz, U. Kaufmann, R. Niebuhr, H. Obloh, and K. Bachem, Appl. Phys. Lett. **71,** 1837 (1997).

8 B. K. Meyer, in *III-V Nitrides*, edited by F. A. Ponce, T. D. Moustakas, I. Akasaki, and B. A. Monemar (Mater. Res. Soc. Symp. Proc. **449**, Pittsburgh, 1997) p. 497.

9 G. D. Chen, M. Smith, J. Y. Lin, H. X. Jiang, M. A. Khan, and C. J. Sun, Appl. Phys. Lett. **67,** 1653 (1995).

10 G. D. Gilliland, Mater. Sci. Eng. R **18,** 141 (1997).

11 T. Kozawa, T. Kachi, H. Kano, Y. Taga, M. Hashimoto, N. Koide, and K. Manabe, J. Appl. Phys. **75,** 1098 (1994).

12 P. J. Dean, Phys. Rev. **157,** 655 (1967).

13 Y. J. Wang, R. Kaplan, H. K. Ng, K. Doverspike, D. K. Gaskill, T. Ikedo, I. Akasaki, and H. Amano, J. Appl. Phys. **79,** 8007 (1996).

14 T. Skettrup, M. Suffczynski, and W. Gorzkowski, Phys. Rev. B **4,** 512 (1971).

15 M. D. Sturge, E. Cohen, and K. F. Rodgers, Phys. Rev. B **15,** 3169 (1977).

16 H. C. Alt, B. K. Meyer, D. Volm, A. Graber, M. Drechsler, D. M. Hofmann, T. Detchprohm, A. Amano, and I. Akasaki, Mater. Sci. Forum **196,** 17 (1995).

17 C. Merz, M. Kunzer, U. Kaufmann, I. Akasaki, and H. Amano, Semicond. Sci. Technol. **11,** 712 (1996).

ROOM TEMPERATURE LASER ACTION IN LATERALLY OVERGROWN GaN PYRAMIDS ON (111) SILICON

S. Bidnyk,* B. D. Little,* Y. H. Cho,* J. Krasinski,* J. J. Song,*
W. Yang,** and S. A. McPherson**

*Center for Laser and Photonics Research and Department of Physics,
Oklahoma State University, Stillwater, Oklahoma 74078
**Honeywell Technology Center, Plymouth, Minnesota 55441

Cite this article as: MRS Internet J. Nitride Semicond. Res. 4S1, G6.48 (1999)

ABSTRACT

Single and multi-mode room temperature laser action was observed in GaN pyramids under strong optical pumping. The 5- and 15-micron-wide hexagonal-based pyramids were laterally overgrown on a patterned GaN/AlN seeding layer grown on a (111) silicon substrate by metal-organic chemical vapor deposition. The pyramids were individually pumped, imaged, and spectrally analyzed through a high magnification optical system using a high density pulsed excitation source. We suggest that the cavity formed in a pyramid is of a ring type, formed by total internal reflections of light off the pyramids' surfaces. The mode spacing of the laser emission was found to be correlated to the size of pyramids. The effects of pyramid geometry and pulse excitation on the nature of laser oscillations inside of the pyramids is discussed. Practical applications of the results for the development of light-emitting pixels and laser arrays are suggested.

INTRODUCTION

GaN and GaN-based heterostructures have been extensively studied due to their potential applications in the UV-blue spectral region[1] in a wide temperature range.[2-4] The success in fabrication of long lifetime cw edge-emitting laser diodes (LDs) was largely due to a significant reduction in defects attained by using laterally grown GaN on sapphire substrates.[5] The selective growth of wide bandgap semiconductors is believed to be one of the most important methods to realize high performance LDs in the short wavelength region.[6,7] However, because of the large physical dimensions of their resonator cavities (several hundred microns), traditional edge-emitting lasers may only be used for constructing one-dimensional arrays. On the other hand, surface-emitting lasers or microstructure-based lasers[8] (with a typical cavity of a few microns) could potentially be used for the development of two-dimensional laser arrays. In this work we demonstrate single-mode and multi-mode room temperature (RT) laser action in two-dimensional arrays of hexagonal GaN pyramids grown on (111) Si by the selective lateral overgrowth technique. We show that the geometry of each pyramid allows the formation of a high-finesse cavity through the utilization of total internal reflection inside of the pyramids.

EXPERIMENT

Samples used in this study were grown by low-pressure metal-organic chemical vapor deposition (MOCVD). First, a 0.10-μm-thick AlN buffer layer was deposited on the Si wafer and the GaN layer was subsequently grown resulting in a thickness of about 0.15 μm. To prepare samples for selective growth, a 0.1-μm-thick Si_3N_4 masking layer was deposited on the wafer by plasma-enhanced chemical vapor deposition. Arrays of openings were created by

Mat. Res. Soc. Symp. Proc. Vol. 537 © 1999 Materials Research Society

photolithography and reactive ion etching. The openings were arranged in a hexagonal pattern with a 20 μm spacing and the average diameter of the openings ranged from 2 to 5 μm depending on the size of pyramids to be grown. GaN growth was then performed in the MOCVD reactor with the ammonia flow set at 1.8 slm and the triethylgallium (TEG) flow varying 1.9 to 5.3 μmol/min over the course of 3 hours at a temperature of 1050 °C. The smaller TEG flow for the initial growth was used to avoid nucleation on the mask. The growth conditions are described elsewhere[9] in more detail. The result of the selective lateral overgrowth was a two-dimensional array of GaN pyramids. A scanning microscope image (SEM) image of one of the samples is shown in Fig. 1. The base diameter of the pyramids was estimated to be about 5 and 15 μm for the two different arrays of pyramids, which is considerably larger than corresponding 2 and 5 μm openings in the mask, indicating substantial lateral growth of the pyramids. Transmission electron microscope pictures revealed a drastic reduction in defect densities.

The samples were mounted on a translation stage that allowed 3-D positioning of the sample with ~1 micron resolution. The third harmonic of an injection-seeded Nd:YAG laser was used as the pumping source. The pulse width of the laser was varied from 5 to 25 ns by changing the Q-switch delay. The laser beam was focused to a diameter of 4 μm through a microscope objective. The laser light intensity was attenuated continuously using a variable neutral density filter. This study was performed in a surface emitting geometry where emission from the sample was collected through the same microscope objective in the direction normal to the sample surface.

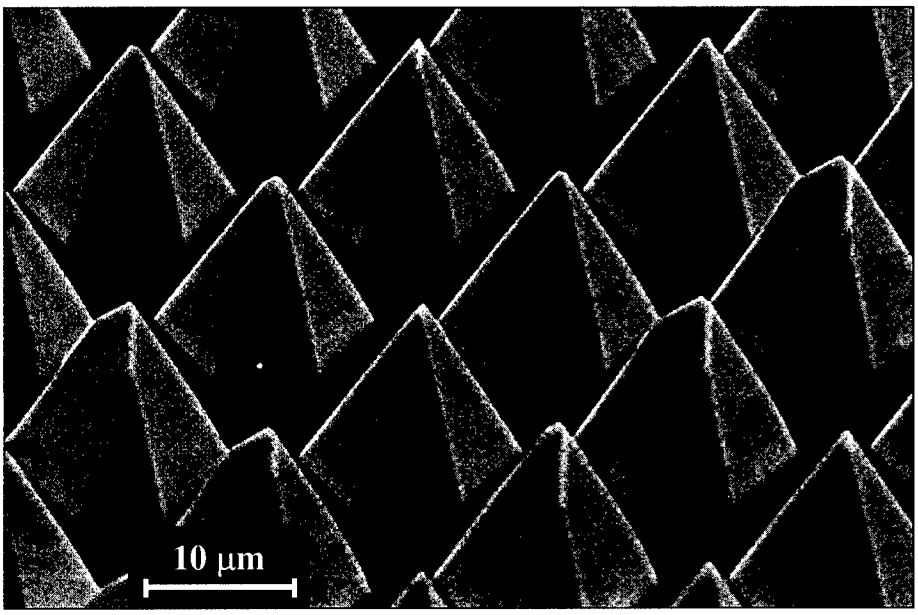


FIG. 1. SEM image of GaN pyramids with a 15 μm wide hexagonal base, grown on a (111) Si substrate by selective lateral overgrowth.

The details of the experimental configuration are described elsewhere.[10] This allowed us to pump, image, and spectrally analyze emission from separate pyramids.

RESULTS AND DISCUSSION

The RT emission spectra at different pump densities (~20-ns-pulses) near the lasing threshold for the 15-μm-wide pyramids are shown in Fig. 2. At excitation densities below the lasing threshold, only a spontaneous emission peak with a full width at half maximum (FWHM) of approximately 14 nm is present. The energy position as well as the spectral width of the peak are very similar to that observed from high-quality single-crystal GaN epilayers.[11] As the pump density is increased to values slightly above the lasing threshold, a very narrow peak with a FWHM of less than 0.3 nm appears on the low energy side of the spontaneous emission peak. Note that the FWHM of the stimulated emission peak in high-quality GaN epilayers is typically 2 nm at RT. The intensity of the peak shown in Fig. 2 increases superlinearly with excitation power. Both drastic narrowing of the spectra and the superlinear increase of intensity suggest that we observe single-mode laser action in the pyramids. The lasing threshold corresponds to

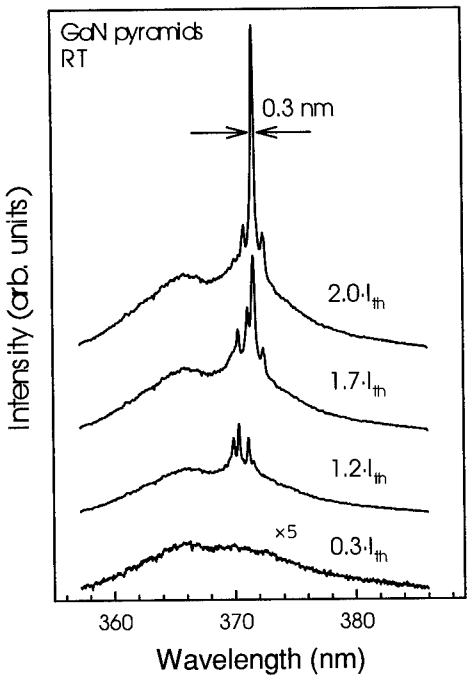


FIG. 2. Emission spectra of a pyramid under different levels of optical pumping above and below the lasing threshold at RT. At pump densities below the lasing threshold only a 14-nm-wide spontaneous emission peak is present whereas at excitation levels above the lasing threshold a narrow single-mode laser peak of less than 0.3 nm FWHM is observed.

an incident pump density of several MW/cm^2. However, most of the pump beam scatters off the pyramid surface. In order to estimate the coupling coefficient of the pump beam one has to consider the surface roughness and geometry of each specific pyramid.

For short excitation pulses it was also possible to observe multi-mode laser action in GaN pyramids, as shown in Fig. 3. In the case of the 15-μm wide pyramids (Fig. 3a) the average mode spacing was estimated to be 0.89 nm which corresponds to the perimeter of 58 μm for either a ring or standing-wave cavity (we assume $n_e = n - \lambda \cdot dn/d\lambda = 2.65$ for the effective refractive index of GaN at 370 nm, taken from Ref.[12]). For 5-μm wide pyramids (Fig. 3b) the mode spacing increased to approximately 2.2 nm which corresponds to a 23 μm in cavity perimeter. In both cases the perimeter of the cavity appears to be several times larger than the diameter of the pyramid base. This result suggests that the photon flux propagating in the cavity undergoes several ($N \geq 4$) reflections inside of the pyramid prior to completing one round trip. The difference in mode spacing for the two pyramids could be explained by the difference in their physical dimensions.

To understand the geometry of the cavity formed inside of a pyramid we have to consider the limited penetration depth of the pump. We expect that the gain region can only lie in the vicinity of the surface rather than deep in the body of the pyramid. The existence of a highly

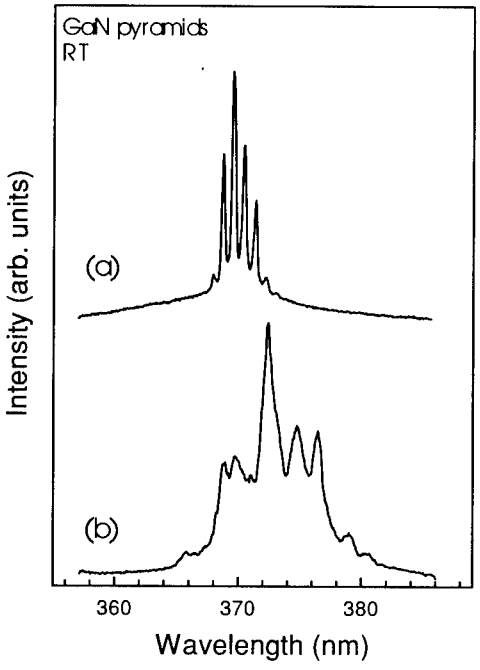


FIG. 3. Multi-mode laser action in (a) 15-μm-wide and (b) 5-μm-wide pyramids. The mode spacing corresponds to a cavity perimeter of 58 and 23 μm, respectively.

modulated lasing spectrum shown in Fig. 3a with such a short gain region suggests there are very small losses associated with cavity mirror reflectivity and absorption at the lasing wavelength. For multiple reflections, only highly reflective mirrors could provide a reasonable optical feedback. Under normal incidence, a GaN-air interface reflects back approximately $R = 0.2$ of the incident signal. Having N near-normal reflections will result only in $R^N < 10^{-3}$ (for $N \geq 4$) of the transmitted signal after one round trip in the cavity, which would require unrealistically high gain in a standing wave cavity with normally oriented end mirrors. Therefore, the cavity inside of the pyramid is most likely of a ring type formed by total internal reflections off the pyramid surfaces. This cavity could potentially lead to a large build-up of the electric field in the pyramid. The collected emission from the sample is believed to be only a scattered fraction of this field, as in the case of scattered stimulated emission observed in GaN epilayers.[13]

We further note that the pyramids used in this work are of much smaller size than conventional edge-emitting LD cavities. Even though efficient carrier injection and coupling of the emission have yet to be developed, these GaN microstructures could potentially be used as pixel elements and as high density two-dimensional laser arrays.[14,15] The Si substrate used to grow the pyramids might facilitate the integration of GaN microstructures into Si-based electronics.

CONCLUSION

We observed single-mode and multi-mode laser action in GaN pyramids under strong optical pumping at room temperature. The pyramids were individually pumped, imaged, and spectrally analyzed through a high magnification optical system using a high density pulsed excitation source. We suggest that the cavity formed in a pyramid is of a ring type, formed by total internal reflections of light off the pyramids' surfaces. The mode spacing of the laser emission was found to be correlated to the size of pyramids. This study suggests that GaN microstructures could potentially be used as pixel elements and high density two-dimensional laser arrays.

ACKNOLEDGEMENT

The authors would like to thank ONR, BMDO, NSF, and DARPA for the financial support.

REFERENCES

[1]See, for example, J. J. Song and W. Shan, in *Physics and Applications of Group III Nitrides Semiconductor Compounds,* edited by B. Gil (Oxford University Press, London, 1998).

[2]S. Bidnyk, T. J. Schmidt, Y. H. Cho, G. H. Gainer, J. J. Song, S. Keller, U. K. Mishra, and S. P. DenBaars, Appl. Phys. Lett. **72**, 1623 (1998).

[3]S. Bidnyk, B. D. Little, T. J. Schmidt, J. Krasinski, and J. J. Song, Proc. SPIE **3419**, pp. 35-43 (1998).

[4]S. Bidnyk, B. D. Little, T. J. Schmidt, Y. H. Cho, J. Krasinski, J. J. Song, B. Goldenberg, W. G. Perry, M. D. Bremser, and R. F. Davis, to be published in J. Appl. Phys.

[5]S. Nakamura, M Senoh, S Nagahama, N Iwasa, T Yamada, T Matsushita, H Kiyoku, Y

Sugimoto, T Kozaki, H Umemoto, M. Sano, K Chocho, Jpn. J. Appl. Phys. **37**, L309 (1998).

[6]Y. Kato, S. Kitamura, K. Hiramatsu, and N. Sawaki, J. Crystal Growth **144**, 133 (1994).

[7]S. Kitamura, K. Hiramatsu, and N. Sawaki, Jpn. J. Appl. Phys. **34**, L1184 (1995).

[8]J. J. Song, A. J. Fischer, T. J. Schmidt, S. Bidnyk, and W. Shan, Nonlinear Optics Vol. **18** (2-4), 269 (1997).

[9]W. Yang, S. A. McPherson, Z. Mao, S. McKernan, and C. B. Carter, (unpublished); T. S. Zheleva, O.-H. Nam, M. D. Bremser, and R. F. Davis, Appl. Phys. Lett. **71**, 2472 (1997).

[10]S. Bidnyk, B. D. Little, Y. H. Cho, J. Krasinski, J. J. Song, W. Yang, and S. A. McPherson, Appl. Phys. Lett. **73**, 2242 (1998).

[11]X. H. Yang, T. J. Schmidt, W. Shan, J. J. Song, and B. Goldenberg, Appl Phys. Lett. **66**, 1 (1995).

[12]E. Ejder, Phys. Status Solidi A **6**, 445 (1971).

[13]S. Bidnyk, T. J. Schmidt, G. H. Park, and J. J. Song, Appl. Phys. Lett. **71**, 729 (1997).

[14]K. Iga, S. Kinoshita, and F. Koyama, Electron. Lett. **23**, 134 (1987).

[15]F. Koyama, K. Tomomatsu, and K. Iga, Appl. Phys. Lett. **52**, 528 (1988).

NIIN AS AN OHMIC CONTACT TO P-GAN

D. B. Ingerly*, Y. A. Chang* and Y. Chen**
*Department of Materials Science and Engineering, University of Wisconsin, Madison, Wisconsin 53706-1595
**Hewlett-Packard Company, 3500 Deer Creek Road, Palo Alto, California 94304-1392

Cite this article as: MRS Internet J. Nitride Semicond. Res. 4S1, G6.49(1999)

ABSTRACT

Based on the criteria for the solid state exchange reaction with p-GaN, we have investigated the intermetallic compound NiIn as a possible ohmic contact. The contacts were fabricated by depositing NiIn on p-GaN films ($p \sim 2 \times 10^{17}$ cm^{-3}) using RF sputtering from a compound target. The as-deposited, NiIn contacts were found to be rectifying and using I-V characterization a Schottky barrier height of 0.82 eV was measured. Rapid thermal annealing of the contacts was shown to significantly decrease their resistance, with contacts annealed at 800 °C for 1 min yielding the lowest resistance. When annealed at 800 °C for 1 min NiIn contacts exhibited a specific contact resistance of 8-9 x 10^{-3} $\Omega\,cm^2$, as measured by the circular transmission line model. To allow a more universal comparison the more traditional Ni/Au contacts, processed under the same conditions, were used as a standard. Their measured specific contact resistance (ρ_c = 1.2 - 2.1 x 10^{-2} $\Omega\,cm^2$) was significantly higher than that of the NiIn contacts. Demonstrating that NiIn has promise as an ohmic contact to p-GaN and should be studied in greater detail.

INTRODUCTION

It has long been realized that the III-V nitrides have tremendous potential for optoelectronic devices operating in the blue and UV wavelengths as well as for use in high power-high temperature semiconductor devices. The III-V nitrides form a continuous alloy system whose direct band gap ranges from 6.2 eV (AlN) to 3.4 eV (GaN) to 1.9 eV (InN) at room temperature.[1] This potentially allows the fabrication of high efficiency optical devices, such as Light Emitting Diodes (LEDs), which can operate from orange to the UV region. The extension into the green and blue wavelengths completes the visible spectrum allowing semiconductor technology to be used for applications such as large full color displays and traffic lights.[2,3]

Early research into the nitrides outlined several problem areas, which hindered efforts to produce devices based on III-V nitride technology. Particularly the lack of p-GaN made the fabrication of efficient optical devices based on p-n junctions impossible, though some LEDs based on metal-insulator-semiconductors were fabricated.[1,3] Only recently due to advances in p-type doping has GaN started to realize its potential and there are now nitride based devices available. However, the metal contact to p-GaN is an important concern since high contact resistance will substantially reduce the performance of GaN based devices. In fact, the high resistance of the metal/p-GaN contact is one of the most significant issues limiting laser diode performance.

Most of the current work on finding low resistance metallizations to p-GaN has focused on high work function elemental metals deposited in multilayer structures.[4-11] This strategy is based on the Schottky model, which predicts that higher work function metals will result in lower Schottky barriers to p-type semiconductors. The limited experimental evidence available

Mat. Res. Soc. Symp. Proc. Vol. 537 © 1999 Materials Research Society

on metal/p-GaN contacts suggests that the Schottky model is at least partially applicable.[4] Of the several contact schemes to p-GaN that have been studied Au/Ni contacts have received the most attention. Despite being used in devices, the Au/Ni contacts typically exhibit a specific contact resistance (ρ_c) in the range of 10^{-3} and 10^{-2} Ω cm^2 range[7,8,12] and show poor thermal stability.[13] However, it is known that the specific contact resistance of p-GaN depends on many factors such as the quality of the bulk substrate and its surface preparation and processing conditions. Accordingly, it is difficult to judge the absolute resistance values reported.

In an attempt to find new metallizations that can be used to form ohmic contacts to p-GaN the solid-state exchange reaction was utilized. This reaction has been shown to be a systematic approach for tailoring metal/semiconductor contact properties.[14-17] The complete thermodynamic and kinetic model for the exchange mechanism has been comprehensively set forth by Swenson et al.[18] Based on the exchange mechanism criteria, the intermetallic compound NiIn was selected as possible ohmic contact to p-GaN.

The thermodynamically stable phase of NiIn (50:50 at % ratio) has a CoSn (B35) crystal structure, however, the metastable B2 phase often forms and is the structure of the NiIn films used in this study. This B2 phase is thermodynamically stable at high temperature in Ni-In alloys that have 51 to 58 % In.[19]

EXPERIMENTAL PROCEDURE

The GaN substrates used in this study are 1.2 μm thin films of single crystal GaN grown by metalorganic vapor phase epitaxy (MOVPE) on sapphire (0001). The GaN epilayer is Mg doped and was annealed to activate the dopants. A p-type carrier concentration of 2 x 10^{17} cm^{-3} with a mobility of 8 cm/V s was measured by Hall probe at room temperature. Prior to lithography, the substrates were ultrasonically degreased with Acetone and Methanol for 10 min each. These degreased substrates were then etched in HCl:H_2O (1:2) for 4 min and then rinsed in flowing H_2O for 10 min.

Using standard photolithography techniques the substrates were patterned with a circular transmission line model (TLM) pattern similar to the one detailed by Marlow.[20] Schottky barrier heights were measured by Current-Voltage (I-V) characteristics using the 140 μm diameter pad as the diode and the large area metallization as the ohmic contact. The specific contact resistance (ρ_c) measurements were conducted at 5 volts using the circular TLM pattern which consists of 7 different contact pads with gap spacing ranging from 4 to 25 μm. Once patterned, the substrates were then placed in a HCl:H_2O (1:4) solution for 20 seconds, blown dry with Nitrogen gas and immediately loaded into a vacuum chamber with the background pressure less than 2 x 10^{-7} torr.

The NiIn (50:50 at % ratio) was deposited by sputtering from a compound target to a nominal 80 nm thickness. The annealed NiIn films were found by X-ray diffraction to be in the metastable B2 crystal structure when deposited by RF sputtering under the conditions used. As a control standard, Ni/Au contacts were also fabricated. These films were deposited by e-beam evaporation, with Ni and Au film thickness of 20 and 100 nm, respectively.

After deposition, the photoresist was lifted off in an acetone bath leaving the patterned metal on the wafers. Following liftoff, the contacts were annealed in an AG Associated MiniPulse rapid thermal annealing (RTA) system with flowing high purity Nitrogen gas. The electrical properties of the contacts were measured with a Keithley Model 236 electrometer employed as a current source and voltage meter.

ELECTRICAL RESULTS

As discussed in the introduction, the intermetallic compound NiIn has been selected for study as an ohmic contact to p-GaN. However, it is difficult to compare the specific contact resistance for different metallizations reported by different researchers due to the wide variability in p-GaN substrates because these substrate differences can play an important role in the measured properties of the contacts. Therefore, in order to allow a more universal comparison of the NiIn metallization evaluated in this study we have used Ni/Au contacts as a standard.

All of the as-deposited contacts exhibited highly rectifying behavior; and it was decided that the Schottky barrier height is a more appropriate measure of these contacts' electrical behavior than the ρ_c at a given voltage. By evaluating the I-V behavior at small voltages the Schottky barrier and ideality factor can be determined by fitting the data to the following equation:

$$I = A^* S T^2 e^{(-q\phi_b/kT)}(e^{qV/nkT} - 1) \qquad (1)$$

where A^* is the Richardson constant, S is the diode area, T is the temperature, q is the electron charge, ϕ_b is the Schottky barrier height, k is the Boltzman constant, V is the applied voltage and n is the ideality factor.[21] Schottky barrier heights determined for the contacts in the as-deposited state are listed in Table 1. To the best of our knowledge, a value for NiIn on p-GaN has not been previously reported. However, the 0.77 eV value of the Schottky barrier height of Ni/p-GaN determined in this study is significantly higher than the 0.5 eV value reported by Mori, et al.[4] While the reason for such a discrepancy is not known, Ishikawa, et al[22] reported about the difficulty in measuring the barrier height of metals on p-GaN. Additionally the ideality factors for all of the contacts measured were significantly greater than 1; showing that the carrier transport mechanism is not entirely due to thermionic emission and suggesting that the interface is not uniform.[23] For the Schottky barrier measurement an ohmic contact is required in addition to the Schottky diode. In this study, the ohmic contact was approximated using a large area contact of the same metallization and while this contact is many times larger than the diode, it is not a true ohmic contact. Given the difficulties of measuring the barrier height of metals on p-GaN and the large ideality factors, the absolute value of barrier heights reported in this study should be interpreted accordingly.

Table 1. Ideality factors and Schottky barrier height for as-deposited contacts

Metallization	Ideality Factor (n)	Schottky Barrier Height
NiIn	1.22	0.82 eV
Ni/Au	1.16	0.77 eV

With increased annealing temperature the resistance of the NiIn/p-GaN contacts decreased. The lowest contact resistance occurs after annealing at 800 °C for 1 min, contacts subjected to a higher annealing temperature, 850 °C for 1 min or increased annealing time, 800 °C for 5 min showed a higher resistance than the samples annealed at 800 °C for 1 min. Table 2 gives the specific contact resistance on NiIn/p-GaN contacts at three different annealing conditions. One possibility for the increased resistances at more severe annealing conditions is oxidation of the NiIn layer. Scanning Auger Microscopy showed that significant oxidation occurred from the surface into over half of the NiIn film for contacts annealed at 800 °C for 1 min. It is possible that once a significant level of oxidation is reached at the metal/semiconductor interface the contact resistance will increase.

Table 2. Specific Contact Resistance for NiIn contacts

Annealing Conditions	Specific Contact Resistance
750 °C for 1 min	6.2 x 10^{-2} Ω cm^2
800 °C for 1 min	9.5 x 10^{-3} Ω cm^2
800 °C for 5 min	7.4 x 10^{-2} Ω cm^2

Due to the wide variability in p-GaN films and the direct role the films have in the measured specific contact resistance we have used Ni/Au contacts to p-GaN as a standard. Table 3 shows a comparison of NiIn contacts annealed at 800 °C for 1 min to Ni/Au annealed at 750 °C for 1 min. These contacts were subject to the same processing conditions and the annealing conditions used represent the optimum conditions found in this study for the two different metallizations. For both p-GaN substrates used, the NiIn contacts had a lower measured specific contact resistance than the Ni/Au contacts. Figures 1(a) and 1(b) show the I-V behavior of the annealed NiIn and Ni/Au contacts, respectively. These curves were measured on back-to-back 140 μm in diameter contacts. Figures 1(a) and 1(b) clearly show that these contacts do not exhibit true ohmic behavior.

Table 3. A comparison of specific contact resistance NiIn Vs. Ni/Au

Substrate	NiIn (800 °C for 1 min)	Ni/Au (750 °C for 1 min)
1	8.0 x 10^{-3} Ω cm^2	1.2 x 10^{-2} Ω cm^2
2	9.5 x 10^{-3} Ω cm^2	2.1 x 10^{-2} Ω cm^2

These electrical results show that NiIn has potential as an ohmic contact to p-GaN. However to understand the NiIn/p-GaN contacts, particularly its large resistance change upon annealing, will require careful interfacial characterization. At this time it is not clear what mechanism is responsible for the change in contact resistance due to annealing and the role oxidation may play in the measured resistance is equally unknown. It is this type of information, which is required not only to increase our understanding but also aid in the optimization of the NiIn contacts.

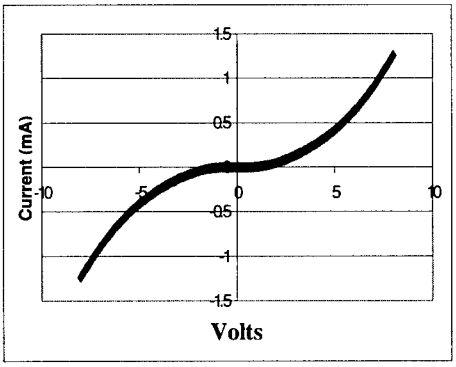


Figure 1(a) I-V behavior of NiIn/p-GaN contacts annealed at 800 °C for 1 min.

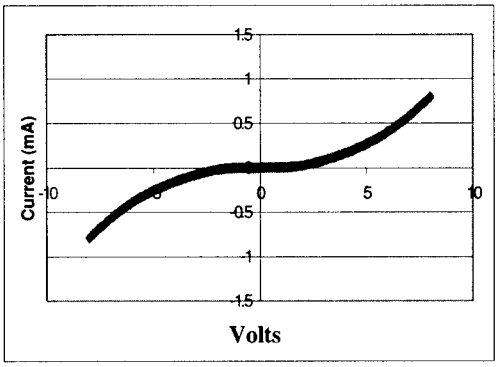


Figure 1(b) I-V behavior of NiIn/p-GaN contacts annealed at 750 °C for 1 min.

CONCLUSIONS

The intermetallic compound NiIn (50:50 at % ratio) was selected based on the criteria for the exchange mechanism as possible ohmic contacts to p-GaN. Contacts were fabricated on p-GaN films using RF sputtering from a compound target. In the as-deposited state these contacts were found to be rectifying and using I-V characterization a Schottky barrier height 0.82 eV was determined for the contact. Rapid thermal annealing of the NiIn contacts was shown to decrease their resistance with increasing annealing temperature. Contacts annealed at 800 °C for 1 min had the lowest resistance of the annealing conditions examined in this study. At this annealing condition the specific contact resistance of the NiIn contacts was measured to be 8 - 9 x 10^{-3} $\Omega\,cm^2$ using the circular TLM method. Annealing at higher temperatures or longer times resulted in an increase in specific contact resistance. It is speculated based upon Auger depth profiling that oxidation maybe responsible for this resistance increase at annealing conditions more severe than 800 °C for 1 min. The measured electrical properties of NiIn are promising since the specific contact resistance of NiIn is lower than the more traditionally used Ni/Au contact (ρ_c = 1.2 - 2.1 x 10^{-2} $\Omega\,cm^2$) processed under the same conditions.

ACKNOWLEDGEMENTS

The authors would like to thank Rick Schneider at the Hewlett-Packard Company for providing the p-GaN films used in this study and the National Science Foundation for its support of this project through grant number NSF-DMR-94-24478.

REFERENCES

1. H. Morkoc, S. Strite, G. B. Gao, M. E. Lin, B. Sverdlov, and M. Burns, J. Appl. Phys. **76**(3), 1363 (1994).
2. H. Morkoc and S. N. Mohammad, Science **267**, 51 (1995).
3. S. J. Pearton and C. Kuo, MRS Bulletin **22**, 17 (1997).
4. T. Mori, T. Kozawa, T. Ohwaki, Y. Taga, S. Nagai, S. Yamasaki, S. Asami, N. Shibata and M. Koike, Appl. Phys. Lett. **69**(23), 3537 (1996).
5. S. Nakamura, M. Senoh, N. Iwasa and S. Nagahama, Jpn. J. Appl. Phys. **34**, L797 (1995).
6. J. T. Trexler, S, J Miller, P. H. Holloway and M. A. Khan, Mater. Res. Soc. Sympo. Proc. **395**, 819 (1996).
7. T. Kim, M. C. Yoo, and T. Kim, Mater. Res. Soc. Symp. Proc. **449**, 1061 (1997).
8. D. J. King, L. Zhang, J. C. Ramer, S. D. Hersee, L. F. Lester, Mater. Res. Soc. Symp. Proc. **468**, 421 (1997).
9. L. L. Smith, R. F. Davis, M. J. Kim, R. W. Carpenter and Y. Huang, J. Mater. Res. **12**, 2249 (1997).
10. J. T. Trexler, S. J. Pearton, P. H. Holloway, M. G. Mier, K. R. Evans, and R. F. Karlicek, Mater. Res. Soc. Symp. Proc. **449**, 1091 (1997).
11. J. -S. Soon, H. –G. Kim, K. –H. Park, C. –S. Um, I. -L. Han, S. -H. Kim, H. –K. Jang, S. –J. Park, Mater. Res. Soc. Symp. Proc. **482**, 1053 (1998).
12. S. Nakamura, Mater. Res. Soc. Symp. Proc. **482**, 1145 (1998).
13. H.S. Venugopalan, S.E. Mohney, B. P. Luther, J. M. DeLucca, S. D. Wolter, J. M. Redwing, and G. E. Bulman, Mater. Res. Soc. Symp. Proc. **468**, 431 (1997).
14. C.-F. Lin, Y. A. Chang, N. Pan, J.-W. Huang, and T.-F. Kuech, Appl. Phys. Lett. **67**, 3587 (1995).

15. D. Y. Chen, Y. A. Chang and D. Swenson, Appl. Phys. Lett. **68**, 96 (1996).
16. D.Y.Chen, Y. A. Chang and D. Swenson, J. Appl. Phys. **81**, 297 (1997).
17. D. Y. Chen, Ph. D. Thesis, University of Wisconsin, Madison, WI (1997).
18. D. Swenson, C. –H. Jan, Y. A. Chang, J. Appl. Phys. **84**, (1998).
19. H. Okamoto, in T. B. Massalski (ed.), *Binary Alloy Phase Diagrams*, ASM International, Materials Park, OH, 2276 (1990) 2nd edn.
20. G. S. Marlow and M. B. Das, Solid-State Electronics **25**, 91 (1982)
21. D. K. Schroder, *Semiconductor Material and Device Characterization,* John Wiley and Sons, Inc, New York, NY, 151 (1990)
22. H. Ishikawa, S. Kobayashi, Y. Koide, S. Yamasaki, S. Nagai, J. Umezaki, M. Koike, and M. Murakami, J. Appl. Phys. **8**1(3), 1315 (1997).
23. R.T. Tung, J. Vac. Sci. Technol. B **11**(4), 1546 (1993).

GaN P-N STRUCTURES FABRICATED BY Mg ION IMPLANTATION

E.V. Kalinina, V.A. Solov'ev, A.S. Zubrilov, V.A. Dmitriev*,

PhysTech-WBG Research Group, Ioffe Institute, St. Petersburg, Russia

* MSRCE, Howard University, Washington, D.C., USA; TDI, Inc., Gaitherburg, MD, USA.

A.P.Kovarsky

Mekhanobr Analyt Institute, St.Petersburg, Russia;

Cite this article as: MRS Internet J. Nitride Semicond. Res. 4S1, G6.53 (1999)

Abstract

In this paper we report on the first GaN p-n diodes fabricated by Mg ion implantation doping of n-type GaN epitaxial layers. Ion implantation was performed at room temperature. Implantation dose ranged from 10^{13} to $2x10^{16}$ cm^{-2}. After implantation samples were annealed for 10-15 s at a wide temperature interval from 600°C to 1200°C in flowing N_2 to form p-type layers. Secondary ion mass spectroscopy, scanning electron microscopy with electron beam induced current and back scattered electron modes as well as current-voltage and capacitance-voltage measurements were used to study structural and electrical characteristics of the Mg implanted p-n structures.

Introduction

Gallium nitride is an attractive wide bandgap semiconductor material for high-temperature/high-power electronics and UV/visible optoelectronics. Recently significant progress has been made in fabrication of III-V-nitride-based laser diodes and blue/UV LEDs [1-4]. This progress was mainly based on the achievement of controlled GaN p-doping during MOCVD epitaxial growth followed by dehydrogenation annealing to activate the Mg-acceptors [5].

It is well known that ion implantation can be used to make devices based on the wide bandgap semiconductors such as silicon carbide [6]. This method allows to form selective doped regions with different and exactly controlled profiles of impurities and the concentration of these impurities is not limited by their solubility. This fact is especially important for creation of the high p-type conductivity in wide bandgap semiconductors that is connected with the relatively deep ionization levels for acceptor impurities in such materials [7]. For GaN, the problem of the high p-type conductivity is also complicated by high background shallow donor concentration due to native defects and the acceptor impurities passivation by hydrogen incorporating from the growth

Mat. Res. Soc. Symp. Proc. Vol. 537 © 1999 Materials Research Society

ambient [8, 9]. To date there has been a little work in the area of the device applications of ion implantation in GaN, and generally ion implantation has been used to introduce impurities in GaN for study of their optical properties as well as the damage and passivation processes in GaN [10]. Recently, both n- and p-type GaN, as well as semi-insulating (sheet resistance of $\geq 5 \times 10^9$ W/□) GaN have been demonstrated by using Si, Mg/P and N ion implantation, respectively, to MOCVD grown GaN with subsequent annealing at 1000-1100°C for 10 s [11]. In this report, the sheet p-type doping of 9.4×10^{11} cm^{-2} has been achieved at 1100°C annealing with a Mg activation percentage of ~62%, since only 1.53×10^{12} cm^{-2} of the 5×10^{14} cm^{-2} implanted acceptors were ionized assuming an energy level of 150 meV for Mg. For Si implantation, the achieved sheet n-type doping of 4.25×10^{13} cm^{-2} with ~93% activation percentage at 1050-1100°C annealing has been reported [12]. In addition, high-resistivity layers for increasing the Schottky barrier height were created by implantation Mg, Mg/P and Ca into n-GaN with subsequent activation annealing [13]. The only GaN device fabricated with ion implantation doping up to now is JFET with n-channel and p-gate formed by Si (100 keV, 2×10^{14} cm^{-2}) and Ca (40 keV, 5×10^{14} cm^{-2}) ion implantation, respectively, and a subsequent 1150°C 15 s rapid annealing to activate the implanted dopants [14]. Unfortunately, no detailed information on obtained gate junction properties was presented in that work.

In the present work an attempt was undertaken to apply ion implantation of Mg into n-GaN with subsequent activation annealing to form the p-n structures.

Experimental Procedure

Epitaxial n-GaN layers were grown by MOCVD on 6H-SiC (0001) substrates with concentration Nd-Na = 3×10^{18} cm^{-3}. The concentration of the uncompensated donors, Nd-Na, in the GaN layers was $(2\text{-}3) \times 10^{16}$ cm^{-3} according to evaluation from Raman measurements like to [15]. Into these n-GaN layers Mg was implanted at energy of 100 keV and at doses in the range from 10^{13} to 2×10^{16} cm^{-2}. Samples were annealed for 10-15 s in flowing N_2-gas at a temperatures in the range from 600 to 1200°C. The Ohmic contacts to n-SiC and Mg-implanted GaN were produced by vacuum thermal evaporation of Cr/Ni and Pd/Ni, respectively. Ni in the contacts was imployed as a mask during the preparation of 300 μm mesas in diameter by reactive ion plasma etching [16].

The thickness of the epilayers, the position of p-n junction inside the structure as well as the absence of the buffer layer at the GaN/SiC boundary were monitored by scanning electron

microscopy (SEM). The electron beam induced current (EBIC) and back scattered electron (BSE) techniques were used. Magnesium distribution profiles across the n-GaN layer after ion implantation and annealing were measured using secondary ion mass-spectroscopy (SIMS). The activation process of the Mg acceptors by post-implantation annealing was indicated with a hot point probe method. The current-voltage (I-V) characteristics under dc conditions at current densities up to 7 A. cm^{-2} and capacitance-voltage (C-V) characteristics at a frequency of 1 kHz were measured for resulting mesa structures at 300 K.

Results and Discussion

According to hot point probe data, the stable p-type conductivity was obtained for the samples with Mg implantation doses more than $1x10^{15}$ cm^{-2} and annealing temperature in the range 1000-1200°C. Mg implanted at doses less than $1x10^{15}$ cm^{-2} and annealed at temperatures lower than 1000°C did not produce a sharp n- to -p conversion in conductivity. The highest p-type conductivity was fixed at a dose $2x10^{16}$ cm^{-2} and annealing temperature 1100°C during 15 s.

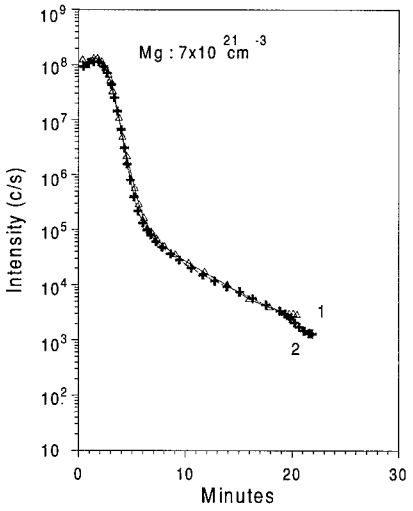


Figure 1. Mg depth profiles in the n-GaN epitaxial layer after ion implantation (curve 1) and after annealing (curve 2).

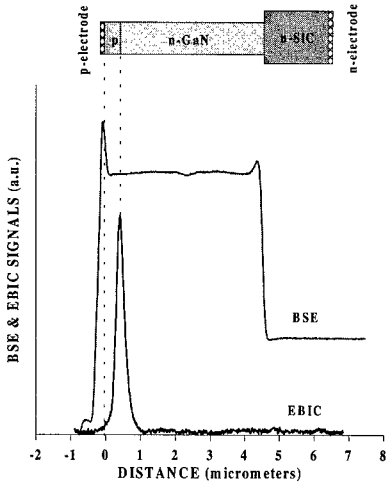


Figure 2. Cross-section of the Mg doped GaN p-n junction (top) and BSE/EBIC signal profiles across the p-n junction (bottom).

Figure 1 shows SIMS Mg profiles as-implanted in n-GaN epilayer at a dose of $2x10^{16}$ cm^{-2} and energy of 100 keV (curve 1) and after annealing at 1100°C during 15 s (curve 2). As seen such annealing keeps all as-implanted Mg in samples with maximum Mg concentration of $7x10^{21}$ cm^{-3}.

Figure 2 shows cross-section of the GaN p-n structure formed under such ion implantation and annealing conditions (top). BSE/EBIC signal profiles across GaN/SiC structure with p-n junction are shown in Figure 2 (bottom). According to the EBIC and BSE data no buffer was found at the GaN/SiC boundary. The thickness of epitaxial n-GaN layer obtained to be 4.5 μm. The p-n junction position was about 0.4 μm. The correct choice of the optimum parameters of measurements in SEM provided of the high precision in a determination of the position of p-n junction. Accelerating voltage was 10 keV and electron beam current was ~ $5x10^{-11}$ A.

Figure 3 shows (C-V) characteristic for 300 μm p-n mesa-structures in diameter formed by Mg ion implantation at a dose of $2x10^{16}$ cm^{-2} at energy of 100 keV followed by annealing at

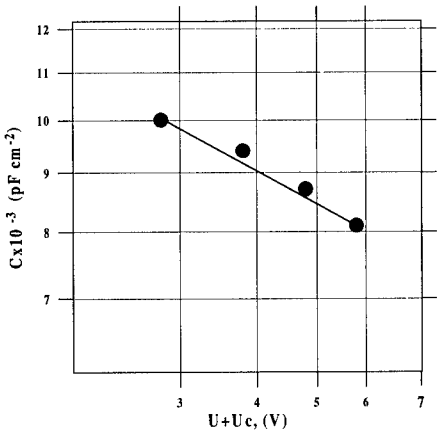


Figure 3. Capacitance-voltage characteristic for the GaN p-n junction fabricated by Mg ion implantation.

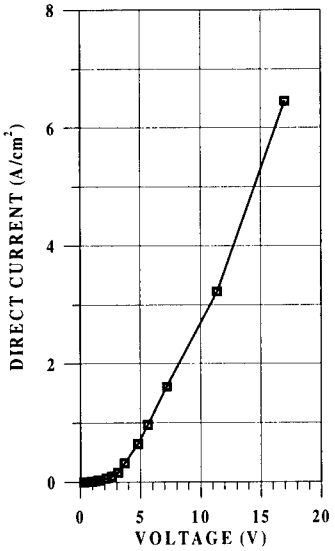


Figure 4. I-V characteristic of the Mg doped GaN p-n junction.

1100°C during 15 s. As follows from the analysis of (C-V) characteristics, the capacitance is proportional to the quantity $(U+U_c)^{-1/n}$, where n is a constant for a given sample characterizing the stepness of (C-V) characteristic, U - the applied reverse voltage to p-n junction, U_c - the contact potentials difference. Measured value of n=3 indicates that Mg ion-doped GaN p-n junctions are nearer to linearly-graded ones. The C-V characteristics in $V-C^{-3}$ co-ordinates were straight lines with cut-off voltage about 2.8 V.

Current-voltage characteristic under dc conditions for such p-n mesa-structures is showed in Figure 4. The breakdown voltage estimated as the value of the reverse voltage corresponding to the current value of 10^{-6} A and was equal to 15 V. The p-n junction diodes had good rectifying properties: a rectification factor was no less than 10^5 at a voltage of 3V.

Conclusion

Conditions for ion implantation with Mg to n-GaN and subsequent annealing have been established yielding stable p-type conductivity layers. It has been shown that by ion implantation with Mg to n-GaN, p-n junctions can be obtained at a specified depth and with reproducible electrical characteristics. Rectification factor no less than 10^5 has been obtained for such p-n junctions. These results evidence the opportunity of investigating the fundamentals of ion implantation into III-V nitrides and develop a new technological method for device formation.

Acknowledgements

The authors thank Prof. G.F. Kholujanov for helpful consultations, M.P. Vatnik for carrying out of ion implantation and V.Yu. Davydov for Raman measurements.

This work was supported in part by the Arizona State University.

References

[1] S. Nakamura, J. of Crystal Growth 170, 11 (1997).

[2] A. Nakamura, M. Senoch, N. Iwasa, and S. Nagahama, Jap. J. Appl.Phys., 34, part 2, No 7a, L 797 (1995).

[3] M. Asif Khan, Q. Chen, R.A. Skogman, J.N. Kuznia, Appl. Phys. Lett. 66 (16), 2046 (1995).

[4] R. J. Molnar, R. Singh, and T.D. Moustakas, Appl. Phys. Lett. 66 (3), 268 (1995).

[5] H. Amano, M. Kito, K. Hiramatsu, and I. Akasaki, Jpn. J. Appl. Phys. 28, L 2112 (1989).

[6] E.V. Kalinina, and G.F. Kholujanov, Inst. Phys. Conf. Ser. No 137: Chapter 6, 675 (1993).

[7] I. Akasaki, H. Amano, N. Koide, M. Kotaki, and K. Manate, Physica C 185, 428 (1993).

[8] P. Perlin, I. Gorczyca, N.E. Christensen, I. Grzegory, H. Teisseyne, and T Suski, Phys. Rev. B45, 13307 (1992).

[9] R.F. Davis, Physica B 185, 1 (1993).

[10] H.H. Tan, J.S. Williams, J. Zou, D.J.H. Cockayne, S.J. Pearton, and R.A. Stall, Appl. Phys. Lett. 69 (16), 2364 (1996).

[11] S.J. Pearton, C.B. Vartuli, J.C. Zolper, C. Yuan, and R.A. Stall, Appl. Phys. Lett. 67, 1435 (1995).

[12] S.C. Binari, H.B. Dietrich, G. Keiner, L.B. Rowland, K. Doverspike, and D.K. Wickenden, J. Appl. Phys. 78, 3008 (1995).

[13] K. Matocha, T.P. Chow, H. Lu, and I. Bhat, Abstracts ICSC111-N'97, WeP-60, 461, Sweden (1997).

[14] J.C. Zolper, R.J. Shul, A.G. Baca, R.G. Wilson, S.J. Pearton, and R.A. Stall, Appl. Phys. Lett. 68 (16), 2273 (1996).

[15] H. Harima, H. Sakashita, T. Inoue, S. Nakashima, Abstracts ICNS'97, P1-27, 86, Japan (1997).

[16] K.V. Vassilevski, V.E. Sizov, A.I. Babanin, Yu. Melnik, A.S. Zubrilov, Inst. Phys. Cong. Ser. 142, 1027 (1996).

AMPLIFICATION PATH LENGTH DEPENDENCE STUDIES OF STIMULATED EMISSION FROM OPTICALLY PUMPED InGaN/GaN MULTIPLE QUANTUM WELLS

T.J. Schmidt,* S. Bidnyk,* Yong-Hoon Cho,* A.J. Fischer,* J.J. Song,* S. Keller,**
U.K. Mishra,** and S.P. DenBaars**

*Center for Laser and Photonics Research and Dept. of Physics
Oklahoma State University, Stillwater, OK 74078
**Electrical and Computer Engineering and Materials Depts.
University of California, Santa Barbara, CA 93106

Cite this article as: MRS Internet J. Nitride Semicond. Res. 4S1, G6.54 (1999)

ABSTRACT

Optically pumped stimulated emission (SE) from InGaN/GaN multiple quantum wells (MQWs) grown by metalorganic chemical vapor deposition has been systematically studied as a function of excitation length (L_{exc}). Two distinct SE peaks were observed from these structures: one that originates at 425 nm at 10 K (430 nm at 300 K) and another that originates at 434 nm at 10 K (438 nm at 300 K). The SE threshold for the high energy peak was observed to always be lower than that of the low energy peak, but the difference was found to decrease greatly with increasing L_{exc}. A detailed study of the emission intensity of these two SE peaks as a function of excitation density shows that the two peaks compete for gain in the MQW active region.

INTRODUCTION

GaN-based semiconductors and related heterostructures are attracting an ever-increasing amount of attention due to their large direct band gaps, which make them promising materials for UV-blue-green light emitting devices,[1,2] solar-blind UV detectors,[3] and high power and high temperature devices.[4,5] In particular, the realization of high brightness blue and green light emitting diodes[1] and cw blue laser diodes[2] based on InGaN/GaN multiple quantum wells (MQWs) has focused the efforts of many research groups on these structures. Although a considerable amount of research has been conducted on the optical properties of these materials, there is still much left unknown about the optical processes associated with stimulated emission (SE) and lasing. To aid in a fundamental understanding of the processes leading to optical gain in these structures, excitation length dependent studies of optically pumped SE have been performed and illustrate dramatically different SE behavior for changes in the experimental conditions that would typically be insignificant in other semiconductor materials.

Recently, a considerable amount of attention has been given to the potential role of strongly localized band tail states on the SE and lasing processes in InGaN MQWs.[6-11] Although there exists a sizable amount of data to support localized carrier recombination as the mechanism leading to spontaneous emission in these materials,[8,9,12,13] the results for SE behavior in the literature are varied and often contradictory. This has led some research groups to assign the spontaneous emission peak to recombination of localized carriers, and the SE peak to a more traditional recombination mechanism: that of an electron-hole plasma originating from free carriers,[14] while others claim that strongly localized carriers are the origin of both spontaneous and SE.[9-11] With the recent observation of two different SE peaks from InGaN/GaN MQWs

Mat. Res. Soc. Symp. Proc. Vol. 537 © 1999 Materials Research Society

grown by Nichia Chemical Industries[11] we see the possibility that some of the varied results reported in the literature may stem from slightly different experimental conditions, which are shown here to result in significant changes in the SE behavior. We report the results of a detailed study of the SE behavior of these two SE peaks as a function of excitation length (L_{exc}) and excitation density (I_{exc}) and illustrate dramatically different SE behavior in InGaN MQWs for relatively small changes in the experimental conditions. The observation of these two distinct SE peaks from InGaN/GaN MQWs grown under different conditions by separate research groups suggests this SE behavior is a general property of present state-of-the-art InGaN based blue laser diodes. As such, a better understanding of the SE and lasing behavior of these structures is important for the development and optimization of future laser diode structures.

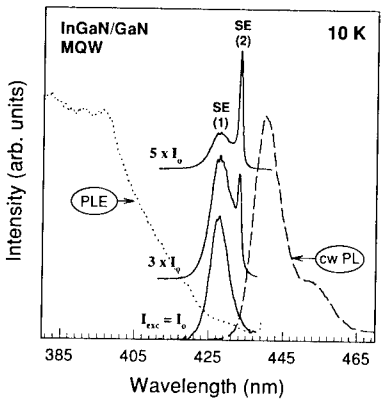


Figure 1: 10 K stimulated emission spectra (solid lines) from an InGaN/GaN MQW subjected to several excitation densities, where I_0 = 100 kW/cm^2. The low power PL (dashed line) and PLE (dotted line) spectra are also shown for comparison. The SE spectra have been normalized and displaced vertically for clarity.

EXPERIMENT

The InGaN/GaN MQWs used in this study were grown by metalorganic chemical vapor deposition (MOCVD) on 1.8 μm thick GaN buffer layers grown on (0001) oriented sapphire substrates. The active regions were made up of 12 quantum wells consisting of 3 nm thick $In_{0.2}Ga_{0.8}N$ wells and 4.5 nm thick GaN barriers. The structures were capped by 0.1 μm thick $Al_{0.07}Ga_{0.93}N$ layers. A detailed description of the growth conditions is given elsewhere.[15] The InGaN MQWs were optically pumped by the third harmonic of an injection seeded Nd:YAG laser (355 nm, 30 Hz, ~ 6 ns pulse width). The excitation beam was focused to a line on the sample using a cylindrical lens and the excitation length was varied using a mask connected to a computer controlled stepper motor. The emission was collected from one edge of the sample, coupled into a 1-meter spectrometer, and spectrally analyzed using an optical multi-channel analyzer.

RESULTS

Typical power dependent emission spectra at 10 K are shown in Fig. 1 for L_{exc} = 1300 μm. At low I_{exc}, we observe a broad spontaneous emission peak centered at ~ 441 nm, consistent with low power cw photoluminescence (PL) spectra. As I_{exc} is increased, a new peak emerges at ~ 428 nm [designated here as SE peak (1)] and grows superlinearly with increasing I_{exc}. If we continue to increase I_{exc}, we observe another new peak at ~ 433 nm [designated here as SE peak (2)] which also grows superlinearly with increasing I_{exc}. SE peak (1) is observed to be the statistical distribution of a multitude of narrow (< 0.1 nm) emission lines. No significant broadening of these emission lines was observed as the temperature was tuned from 10 K to over 500 K. This is illustrated in Fig. 2. SE peak (2) is observed to always be considerably narrower than SE peak (1). Both SE peaks are seen to originate on the high energy side of the low power spontaneous emission peak (given by the dashed line in Fig. 1) and are seen to be redshifted by more than 30

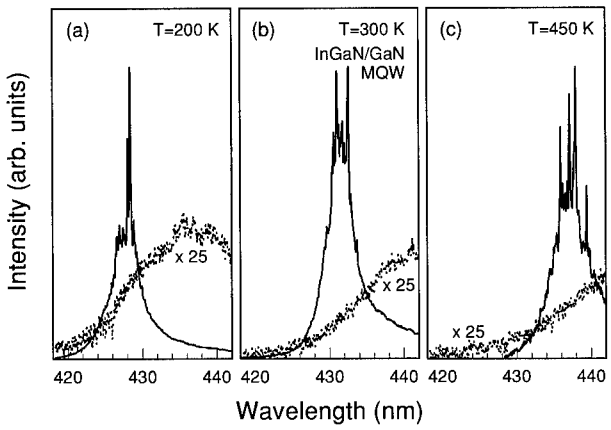


Figure 2: Stimulated emission spectra of SE peak (1) at (a) 200 K, (b) 300 K, and (c) 450 K illustrating SE peak (1) is composed of a multitude of narrow (< 0.1 nm) stimulated emission peaks that do not noticeably broaden with increasing temperature. The SE spectra shown were collected for excitation densities twice the SE threshold for the respective temperatures. The spontaneous emission spectra (dotted lines) are also shown for excitation densities half that of the SE threshold at each temperature. The SE spectra have been normalized for clarity.

nm below the start of the "soft" absorption edge. Both SE peaks were found to be highly TE polarized, with a TE to TM ratio of ~ 200. SE peak (2) has been the subject of previous experiments performed by the authors and has been attributed to stimulated recombination of localized states through the use of energy selective optically pumped SE studies showing "mobility edge" type behavior in the SE spectra as the excitation photon energy is varied,[16] and through nanosecond nondegenerate optical pump-probe experiments showing the onset of SE has a direct impact on the bleaching dynamics of the band tail states in these samples.[17]

Figure 3(a) shows the SE thresholds (I_{th}) of SE peaks (1) and (2) as a function of L_{exc}. We note that I_{th} for peak (2) is larger than that of peak (1) for all excitation lengths employed, but approaches that of peak (1) with increasing L_{exc}. The high SE threshold of peak (2) with respect to peak (1) and its increased presence for longer L_{exc} suggest that it results from a lower gain process than that of peak (1). Fig. 3(b) shows the peak positions of SE peak (1) and SE peak (2) as a function of L_{exc} at 10 K. For L_{exc} less than ~ 500 μm, only SE peak (1) is observed. It has a peak emission wavelength of ~ 425 nm (430 nm) and a SE threshold of ~ 100 kW/cm^2 (475 kW/cm^2) at 10 K (300 K). As I_{exc} is increased and/or L_{exc} is increased, a new SE peak [SE peak (2)] at 434 nm (438 nm at RT) emerges. The peak positions were measured for I_{exc} fixed relative to the SE thresholds of the respective peaks; *i.e.* $I_{exc} = 2 \times I_{th}$. As L_{exc} is increased, SE peak (1) shifts to longer wavelengths (due to a re-absorption process), while the peak position of SE peak (2) is observed to be weakly dependent on L_{exc}. The apparent blueshift of SE peak (2) with increasing L_{exc} seen in Fig. 3(b) is a result of the experimental conditions. Since the SE threshold of SE peak (2) is a strong function of L_{exc}, the peak positions shown for small L_{exc} are for I_{exc} considerably higher than for large L_{exc}. The slight redshift of SE peak (2) with increasing I_{exc} due to many-body effects and lattice heating then manifests itself as the apparent blueshift seen in Fig. 3(b). The same phenomenon is observed at room temperature, as shown in the inset of Fig. 3(b). The redshift of SE peak (1) with increasing L_{exc} can be explained by gain and absorption competition in the "soft" absorption edge of the InGaN active regions, where gain saturation with longer L_{exc} combined with the background absorption tail leads to the observed redshift. The fact

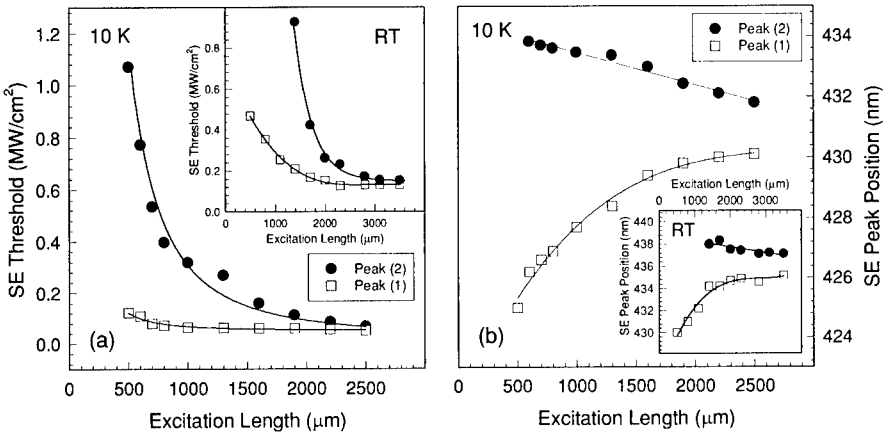


Figure 3: (a) Stimulated emission threshold as a function of excitation length for SE peaks (1) and (2) at 10 K. (b) Peak position of SE peaks (1) and (2) as a function of excitation length at 10 K. The insets show the behavior observed at room temperature. The solid lines are given only as guides for the eye.

that SE peak (2) does not experience a re-absorption induced redshift with increasing L_{exc} is explained by the significant reduction of the absorption tail in this spectral region (see Fig. 1).

The gain saturation behavior of SE peak (1) is consistent with the observation of Kuball *et al.*[18] of a high gain mechanism in the band tail region of MQWs with similar active regions. The large spectral range exhibiting gain is explained by compositional fluctuations inside the active region. The redshift of SE peak (1) with increasing L_{exc} is consistent with observations of a redshift in the optical gain spectrum with increasing L_{exc} reported by Mohs *et al.*[19] It is also consistent with the observation by Nakamura[20] that the external quantum efficiency of his cw blue laser diodes *decreases* with *increasing* cavity length. These similarities, combined with the relatively low SE threshold of SE peak (1) with respect to SE peak (2) and its similar spectral position with laser emission from diodes of similar structure,[21] suggests that lasing in current state-of-the-art cw blue laser diodes originates from the gain mechanism responsible for SE peak (1). The microscopic origin of this gain is the subject of continuing research, but is shown here to be different than the localized state recombination responsible for SE peak (2). Its origin may lie in an entirely different degree of carrier localization. Further experiments are needed to clarify this issue.

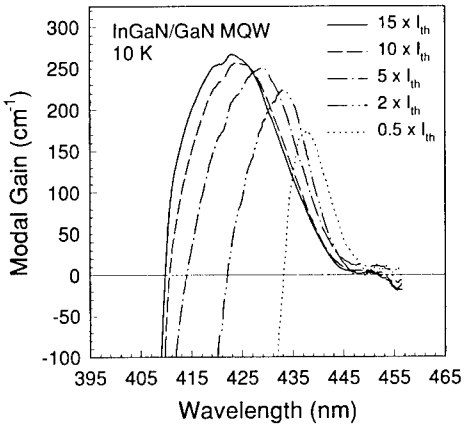


Figure 4: 10 K modal gain spectra of an InGaN/GaN MQW at several excitation densities. The excitation densities are given with respect to the SE threshold measured for long (~ 2.5 mm) excitation lengths.

The modal gain spectra measured by the variable-stripe method of Shaklee and Leheny[22] are shown in Fig. 4 at 10 K. The spectra were taken for L_{exc} less than 200 μm to minimize re-absorption induced distortions in the spectra. The excitation densities in Fig. 4 are given with respect to the SE threshold measured for long (~ 2.5 mm) excitation lengths. A clear blueshift in the gain peak is seen with increasing excitation. This blueshift was observed to stop for $I_{exc} > 12 \times I_{th}$. Further increases in I_{exc} resulted only in an increase in the modal gain maximum. The maxima of the gain spectra are seen to be redshifted by more than 20 nm with respect to the start of the "soft" absorption edge. The large shift in the gain maximum to higher energy with increasing I_{exc} is consistent with band filling of localized states in the InGaN active regions. We note that the fully blueshifted gain spectrum covers the entire spectral region in which SE was observed. Similar behavior was observed at room temperature.

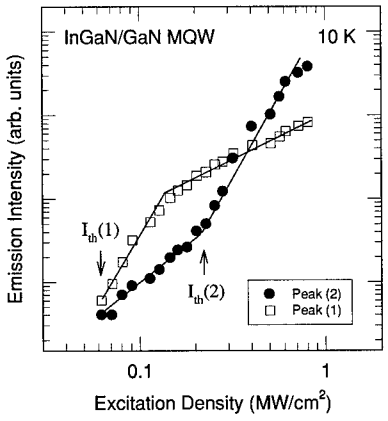


Figure 5: Emission intensity of SE peaks (1) and (2) as a function of optical excitation density at 10 K, illustrating gain competition. The excitation length is 1300 μm. The respective SE thresholds, I_{th}, of SE peaks (1) and (2) are indicated for completeness. The solid lines are given only as guides for the eye.

The dependence of the emission intensity of peaks (1) and (2) on I_{exc} is shown in Fig. 5 for L_{exc} = 1300 μm at 10 K. The emission of peak (1) increases in a strongly superlinear fashion (~ $I_{exc}^{3.8}$) until the SE threshold of peak (2) is reached, at which point it turns linear, indicating that peak (2) competes for gain with peak (1). This is most likely a result of competition for carriers or re-absorption of the emitted photons. The presence of SE peak (2) is therefore seen to be deleterious to SE peak (1). The same process is observed at room temperature and for various excitation lengths. This gain competition may limit this material's performance in high power laser diode applications, where increased driving current and/or longer cavity lengths may result in a shift in the dominant gain mechanism and a drastic change in the emission behavior.

CONCLUSIONS

In summary, the dependence of stimulated emission on excitation length in MOCVD grown InGaN/GaN MQW structures has been studied. Two distinctly different SE peaks were observed with different dependencies on excitation length. The high energy SE peak exhibits a strong redshift with increasing excitation length due to competition between an easily saturable gain mechanism and a background absorption tail. The lower energy SE peak does not exhibit this re-absorption induced redshift with increasing excitation length. The presence of the lower energy SE peak has been shown to be detrimental to the higher energy SE peak due to gain competition in the InGaN active region. This competition may prove to be an obstacle in the design of InGaN based high power laser diodes, where high current densities and/or long cavity lengths can lead to a shift in the dominant gain mechanism and a change in the emission characteristics.

ACKNOWLEDGEMENTS

This work was supported by BMDO, AFOSR, ARO, ONR, and DARPA.

REFERENCES

[1] S. Nakamura, M. Senoh, N. Iwasa, S. Nagahama, T. Yamada, and T. Mukai, Jpn. J. Appl. Phys. **34**, L1332 (1995).
[2] S. Nakamura, M. Senoh, S. Nagahama, N. Iwasa, T. Yamada, T. Matsushita, Y. Sugimoto, and H. Kiyoku, Appl. Phys. Lett. **69**, 4056 (1996).
[3] B.W. Lim, Q.C. Chen, J.Y. Yang, and M.A. Khan, Appl. Phys. Lett. **68**, 3761 (1996).
[4] Y.F. Wu, B.P. Keller, S. Keller, D. Kapolnek, P. Kozodoy, S.P. DenBaars, and U.K. Mishra, Appl. Phys. Lett. **69**, 1438 (1996).
[5] X.H. Yang, T.J. Schmidt, W. Shan, J.J. Song, and B. Goldenberg, Appl. Phys. Lett. **66**, 1 (1995). S. Bidnyk, T.J. Schmidt, Y.H. Cho, G.H. Gainer, J.J. Song, S. Keller, U.K. Mishra, and S.P. DenBaars, Appl. Phys. Lett. **72**, 1623 (1998).
[6] S. Nakamura, M. Senoh, S.I. Nagahama, N. Iwasa, T. Yamada, T. Matsushita, Y. Sugimoto, and H. Kiyoku, Appl. Phys. Lett. **70**, 1417 (1997).
[7] S. Nakamura, M. Senoh, S.I. Nagahama, N. Iwasa, T. Yamada, T. Matsushita, Y. Sugimoto, and H. Kiyoku, Appl. Phys. Lett. **70**, 2753 (1997).
[8] S. Chichibu, T. Azuhata, T. Sota, and S. Nakamura, Appl. Phys. Lett. **69**, 4188 (1996).
[9] Y. Narukawa, Y. Kawakami, M. Funato, S. Fujita, S. Fugita, and S. Nakamura, Appl. Phys. Lett. **70**, 981 (1997).
[10] A. Satake, Y. Masumoto, T. Miyajima, T. Asatsuma, F. Nakamura, and M. Ikeda, Phys. Rev. B **57**, R2041 (1998).
[11] T. Deguchi, T. Azuhata, T. Sota, S. Chichibu, M. Arita, H. Nakanishi, and S. Nakamura, Semicond. Sci. Technol. **13**, 97 (1998).
[12] E.S. Jeon, V. Kozlov, Y.K. Song, A Vertikov, M. Kuball, A.V. Nurmikko, H. Liu, C. Chen, R.S. Kern, C.P. Kuo, and M.G. Craford, Appl. Phys. Lett. **69**, 4194 (1996).
[13] Y. Narakawa, Y. Kuwakima, S. Fujita, S. Fujita, and S. Nakamura, Phys. Rev. B **55**, R1938 (1997).
[14] J.S. Im, S. Heppel, H. Kollmer, A. Sohmer, J. Off, F. Scholz, and A. Hangleiter, Proc. 2nd Int. Conf. Nitride Semicond., Tokushima, Japan, 228 (1997).
[15] S. Keller, A.C. Abare, M.S. Minsky, X.H. Wu, M.P. Mack, J.S. Speck, E. Hu, L.A. Coldren, U.K. Mishra, and S.P. DenBaars, Materials Science Forum **264-268**, 1157 (1998). B.P. Keller, S. Keller, D. Kapolnek, W.N. Jiang, X.-F. Wu, H. Masui, X.H. Wu, B. Heying, J.S. Speck, U.K. Mishra, and S.P. DenBaars, J. Electron. Mater. **24**, 1707 (1995).
[16] T.J. Schmidt, Y.H. Cho, G.H. Gainer, J.J. Song, S. Keller, U.K. Mishra, and S.P. DenBaars, Appl. Phys. Lett. **73**, 560 (1998).
[17] T.J. Schmidt, Y.H. Cho, G.H. Gainer, J.J. Song, S. Keller, U.K. Mishra, and S.P. DenBaars, Appl. Phys. Lett. **73**, 1892 (1998).
[18] M. Kuball, E.S. Jeon, Y.K. Song, A.V. Nurmikko, P. Kozodoy, A. Abare, S. Keller, L.A. Coldren, U.K. Mishra, S.P. DenBaars, and D.A. Steigerwald, Appl. Phys. Lett. **70**, 2580 (1997).
[19] G. Mohs, T. Aoki, M. Nagai, R. Shimano, M. Kuwata-Gonokami, and S. Nakamura, Proc. 2nd Int. Conf. Nitride Semicond., Tokushima, Japan, 234 (1997).
[20] S. Nakamura, MRS Internet J. Nitride Semicond. Res. **2**, Art. 5 (1997).
[21] M.P. Mack, A. Abare, M. Aizcorbe, P. Kozodoy, S. Keller, U.K. Mishra, L. Coldren, and S.P. DenBaars, MRS Internet J. Nitride Semicond. Res. **2**, Art. 41 (1997).
[22] K.L. Shaklee and R.F. Leheny, Appl. Phys. Lett. **18**, 475 (1971).

INDUCTIVELY COUPLED PLASMA ETCHING OF III-NITRIDES IN Cl_2/Xe, Cl_2/Ar AND Cl_2/He

Hyun Cho [1], Y.B. Hahn[1], D.C. Hays [1], K.B. Jung [1], S.M. Donovan [1], C.R. Abernathy[1], S.J. Pearton[1] and R.J. Shul[2]

[1] Department of Materials Science and Engineering, University of Florida, Gainesville FL 32611
[2] Sandia National Laboratories, Albuquerque NM 87185

Cite this article as: MRS Internet J. Nitride Semicond. Res. 4S1, G6.56(1999)

Abstract

The role of additive noble gases He, Ar and Xe to Cl_2-based Inductively Coupled Plasmas for etching of GaN, AlN and InN were examined. The etch rates were a strong function of chlorine concentration, rf chuck power and ICP source power. The highest etch rates for InN were obtained with Cl_2/Xe, while the highest rates for AlN and GaN were obtained with Cl_2/He. Efficient breaking of the III-nitrogen bond is crucial for attaining high etch rates. The InN etching was dominated by physical sputtering, in contrast to GaN and AlN. In the latter cases, the etch rates were limited by initial breaking of the III-nitrogen bond. Maximum selectivities of ~ 80 for InN to GaN and InN to AlN were obtained.

Introduction

There have been a number of studies of high density plasma etching techniques for patterning of III-nitrides for photonic device applications such as laser diodes and light-emitting diodes (LEDs) [1-12]. Essentially all of the LEDs and a majority of the lasers are ridge wave guide structures in which the mesas are formed by dry etching [13]. Most of the previous etching studies have been focused on obtaining relatively the large etch depths (2-4μm) typical of ridge or facet heights in LEDs or laser diodes, where the final surface morphology on the field is less important. There is increasing interest in the development of GaN-based high power/high temperature electronics for power switching and transmission applications [14-18]. In these devices, the etch depth is much shallower, but smooth morphologies and high selectivities for InN over the other nitrides are required because layers based on InN will probably be used to obtain low ohmic contact resistance.

Shul et al. [1,10] first reported Inductively Coupled Plasma (ICP) etching of GaN, AlN, InN, InAlN and InGaN at low dc biases (≤ -100V) with Cl_2, CH_4/H_2, Cl_2/Ar, Cl_2/N_2 and Cl_2/H_2 plasma chemistries. They controlled the etch rates in the range of 500-1500Å/min for electronic device structures, and obtained maximum etch selectivities of ~ 6 at higher ICP source powers (850W) for InN over the other nitrides.

In this paper, the influence of the inert gas species (He, Ar and Xe) in chlorine-based ICP etching of GaN, AlN and InN was studied for various plasma parameters. The results are explained in a systematic way based on calculated ion fluxes at the sheath edge, Bohm velocity and sheath thickness. The ICP discharges are well suited for achieving controllable etch rates (500–1500Å/min) and high selectivities (up to 80) for InN over AlN and GaN, using simple Cl_2/neutral gas chemistries.

Mat. Res. Soc. Symp. Proc. Vol. 537 © 1999 Materials Research Society

Experimental

The AlN and InN samples were grown by Metal Organic Molecular Beam Epitaxy (MOMBE) on Al_2O_3 substrates at 800°C and 575°C, respectively in an Intevac Gen II system [19,20]. The GaN was grown at 1040°C on Al_2O_3 substrates by Metal Organic Chemical Vapor Deposition (MOCVD). Total layer thicknesses were ~ 1μm for the AlN and InN, and 2-3μm for the GaN.

The samples were patterned with Apiezon wax and etched in a Plasma-Therm ICP 790 system. The temperature of the back-side cooled chuck was held at 23°C. The rf chuck power was varied between 50 and 350W, and ICP source power between 300 and 1000 W. The process pressure was held constant at 5mTorr, while the total flow rate of Cl_2-additive gas was 15 standard cubic centimeter per min (sccm). Etch rates were calculated from stylus profilometry measurements of the etched samples after the removal of the mask material. The error of these measurements is approximately ±5%. The selectivity was calculated for InN over AlN and GaN.

Results and discussion

We first examined the effect of discharge composition for the three chemistries. Figures 1 shows the effect of Cl_2 concentration on etch rates of InN, AlN and GaN in Cl_2/He, Cl_2/Ar and Cl_2/Xe discharges at 5mTorr, 750W source power and 250W rf chuck power. It is seen that the effects of noble gas additives are strongly dependent on the particular III-nitride material: the highest etch rates for InN were obtained with Cl_2/Xe (Figure 1, top) and for AlN (center) and GaN (bottom) with Cl_2/He. It is also seen that etch rates of AlN and GaN were much lower in chlorine-based plasmas compared to InN. The high rates for the latter are similar to the previously reported results observed for InP where efficient ion-assisted desorption of the $InCl_x$ occurs under ICP conditions [21]. These results indicate that etch mechanism is dependent on the material bond strengths and on the particular plasma chemistry employed, and optimization of the ICP etching process is crucial for obtaining the best results.

The highest etch rates for AlN and GaN at these low bias conditions were obtained with Cl_2/He discharges. Ion fluxes and Bohm velocities at the sheath edge at 66.7% Cl_2 are, respectively, $1.59x10^{16}cm^{-2}s^{-1}$ (Cl_2/Ar), $1.84x10^{16}cm^{-2}s^{-1}$ (Cl_2/He) and $1.92x10^{16}cm^{-2}s^{-1}$ (Cl_2/Xe), and 1,740m/s (Cl_2/Xe), 2,350m/s (Cl_2/Ar) and 2,660m/s (Cl_2/He). In other words, the Cl_2/Xe discharges showed the highest ion flux at the sheath edge, while the ions created by Cl_2/He discharge have the greatest Bohm velocity. It is interesting to see that the ion fluxes and sheath edge velocities are in the same order as we expected based on ionization energy [Ar (15.76eV) > He (13.6eV) > Xe (12.13eV)] [22] and atomic mass. The predicted ion fluxes and Bohm velocities explain why the etch rates with Cl_2/Ar are the lowest, while the highest are obtained with Cl_2/He. Ions created in the Cl_2/He discharge, having the fastest velocity, arrive at the surface with higher velocities, helping activate the nitride surface for the coincident reactive chlorine neutral flux. They also provide the impetus for directional etching. In the ICP system, the sheath layer near the sample position is determined mainly by the capacitively coupled power because the sheath thickness due to the inductively coupled power is much smaller. The values of sheath thickness predicted at 66.7% Cl_2, 750W ICP and 250W rf powers are 0.62cm in Cl_2/He, and 0.44cm in Cl_2/Xe discharges. Although the heavier Xe ions are accelerated within the sheath region, the sheath thickness is not long enough for them to reach the energy carried by the fast-moving ions created by the Cl_2/He discharge. This partially explains the difference in etch rates between the different chemistries.

The effect of rf chuck power on the etch rates is shown in Figure 2. The etch rates of InN with Cl_2/Xe and Cl_2/He discharges increased up to 250 W and decreased at higher power (Figure 2, top), but increased monotonically with Cl_2/Ar as the rf power increased. The increase in etch

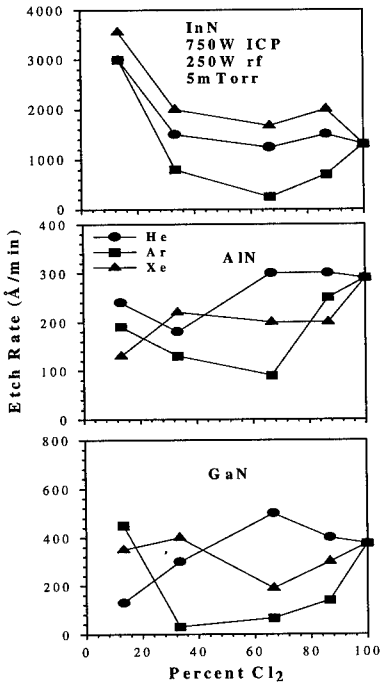


Figure 1. Effect of chlorine concentration on etch rates of InN (top), AlN (center) and GaN (bottom) with Cl_2/He, Cl_2/Ar and Cl_2/Xe plasma chemistries (750W source power, 250W rf chuck power, 5mTorr).

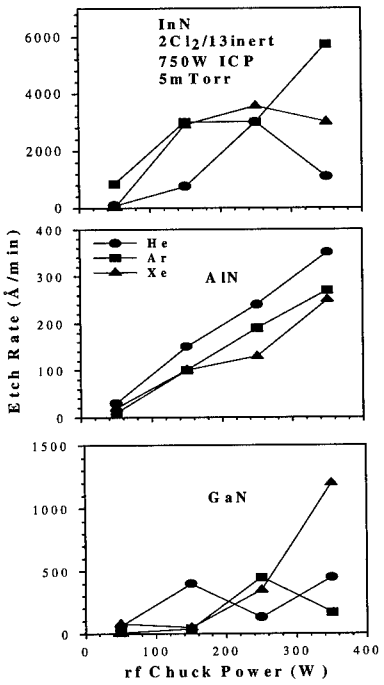


Figure 2. Effect of rf chuck power on etch rates of InN (top), AlN (center) and GaN (bottom) with $2Cl_2$/13He, $2Cl_2$/13Ar and $2Cl_2$/13Xe plasma chemistries (750W source power, 5mTorr).

rate can be attributed to enhanced sputter desorption of etch products as well as dominant physical sputtering of the InN surface. The etch rates of AlN increased monotonically as the rf power increased with all Cl_2-based discharges (Figure 2, center). However, GaN etching in Cl_2/He and Cl_2/Ar showed relatively constant etch rates with some fluctuations, and increased rapidly in the Cl_2/Xe chemistry as the rf power increased (Figure 2, bottom). Again, He and Xe additives resulted in overall better etch rates than Ar.

The monotonic increase in AlN etch is mainly due to the higher bond strength of AlN (11.52eV) compared to InN and GaN, indicating that AlN etch rate is limited by breaking the Al-N bond. In order to initiate etching, breaking the group III-nitrogen bond is crucial, since this must precede the formation of etch products. Bond energies are in the order of InN (7.72eV) < GaN (8.92eV) < AlN (11.52eV) [22]. The etch rate is also related to volatilities of the etch products. In chlorine-based plasmas, the boiling points are $AlCl_3$ (183°C) < $GaCl_3$ (201°C) < $InCl_3$ (600°C) [22]. In addition to the experimental results, from the view points of bond strength and boiling point, two conclusions may be drawn: 1) the etch rates of InN are dominated by physical sputtering, due to the relatively low bond strength, but possibly limited by desorption of etch products due to the lowest volatility of $InCl_3$ and 2) lower etch rates of GaN and AlN are limited by initial breaking of the III-nitrogen bond. The dc bias increased monotonically with increasing rf chuck power from 50 to 350W, but the ion flux at the sheath edge increased

slightly. Ion fluxes in Cl_2/He and Cl_2/Xe discharges were ~ $1.9\times10^{16}cm^2\cdot s^{-1}$ at 750W source power, while that with Cl_2/Ar was lower, ~ $1.6\times10^{16}cm^2\cdot s^{-1}$.

The effect of the rf power on ion fluxes at the sheath edge, respectively, generated by capacitive and inductive coupled discharges with chlorine-based chemistries was calculated from a simple model (Figure 3). The ion flux generated by the capacitive discharge increases substantially with increasing rf power, while that in the counterpart by the inductively coupled discharge maintains an essentially constant value. The rf power increases the ion bombarding energy, resulting in an increase in etch rate with increasing the chuck power. However, the predicted ion flux (or bulk ion density) showed that the contribution of the capacitive discharge to total ion flux in the ICP etching process is less than 2%, indicating that the main role of the chuck power is to increase the ion bombarding energy.

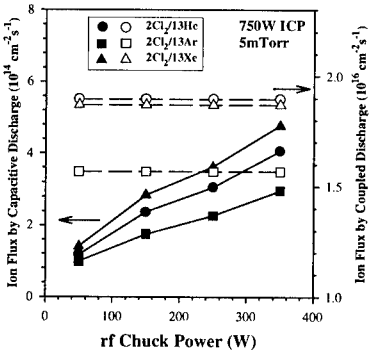


Figure 3. Effect of rf chuck power on the ion fluxes generated by capacitive discharge and inductively coupled discharge with $2Cl_2$/13He, $2Cl_2$/13Ar and $2Cl_2$/13Xe plasma chemistries (750W source power, 5mTorr).

The effect of ICP source power on etch rate is shown in Figure 4. The influence of additive noble gases was dependent on III-nitride materials: the best etch rate for InN was obtained with Cl_2/Xe (Figure 4, top), while the overall highest rates for the other materials were achieved with Cl_2/He. InN showed higher etch rates again than AlN and GaN. The etch rates of InN with Cl_2/He and Cl_2/Xe discharges increased up to 750W ICP power, and decreased at > 750W. However, the Cl_2/Ar discharge showed the highest etch rate of InN at 1000 W. AlN etch rate increased slightly with the source power, but resulted in low etch rates. GaN etch rates with Cl_2/He and Cl_2/Ar chemistries showed maxima as the source power increased, but relatively constant etch rates with Cl_2/Xe. The increase in etch rate with increasing source power is due to the higher concentration of reactive species in the plasma, suggesting a reactant-limited regime, and to higher ion flux to the substrate surface. Increased numbers of ions also make the surface more active with respect to the reactive neutrals. The decrease in etch rate with further increase of the ICP power is attributed either to lower ion energies or ion-assisted desorption of the reactive species at the substrate surface prior to etch reactions. The dc bias of the sample chuck was decreased as the ICP power increased mainly due to the increased ion density.

In order to reduce the currently high contact resistance in GaN-based heterostructure field transistors [23], and eventually heterojunction bipolar transistors, it is expected that InN-based contact layers will be necessary [24-26], in analogy to InGaAs on GaAs. In such a case, the ability to selectively etch InN relative to the other nitrides will be crucial. Figures 5 shows some selectivity data as functions of rf power in chlorine-noble discharges. As the rf power increased, the Cl_2/Ar discharge showed overall the best selectivity of InN over GaN, but the Cl_2/He chemistry yielded the lowest selectivities for InN over AlN as well as over GaN. The selectivity data obtained in this work showed overall higher selectivity characteristics for InN over GaN and AlN in Cl_2/He, Cl_2/Ar and Cl_2/Xe than that previously reported [1,12].

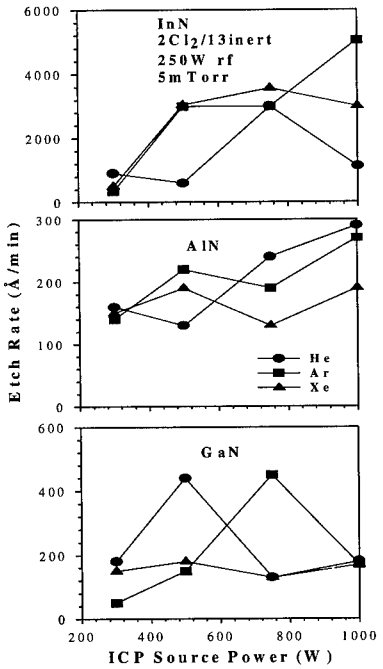


Figure 4. Effect of ICP source power on etch rates of InN (top), AlN (center) and GaN (bottom) with $2Cl_2$/13He, $2Cl_2$/13Ar and $2Cl_2$/13Xe plasma chemistries (250W rf chuck power, 5mTorr).

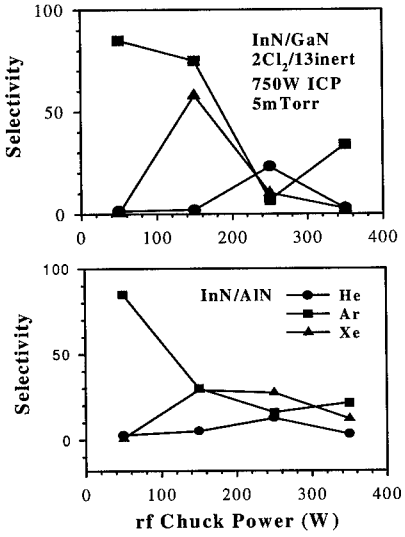


Figure 5. Effect of rf chuck power on the selectivity for InN over GaN and AlN (750W source power, 5mTorr, $2Cl_2$/13 noble gas).

Summary and conclusions

The effect of the noble gas additive to Cl_2 ICP discharges was examined for etching of GaN, AlN and InN. The etch rates were greatly affected by chlorine concentration, rf chuck power and ICP source power. The influence of the additive gases was much dependent on the particular III-nitride material, with InN showing higher etch rates than the other nitrides. Efficient breaking of the III-nitrogen bond is crucial for achieving high etch rates. The InN etching was dominated by physical sputtering because of the low volatility of $InCl_3$, while GaN and AlN etching was limited by initial breaking of the III-nitrogen bond. The contribution of the capacitive discharge to total ion flux in the ICP etching process is less than 2%, indicating that the main role of the chuck power is to increase the ion bombarding energy. The etch rates increased with increasing ICP source power due mainly to increased ion flux. Selectivities up to ~ 80 for InN over GaN and AlN were achieved.

Acknowledgements

The work at UF is partially supported by a DARPA/EPRI grant MDA-972-98-1-0006 (D. Radack / J. Melcher), while that of HC is partially supported by KOSEF. YBH gratefully acknowledges the supports of Korea Research Foundation for Faculty Research Abroad and

KOSEF through the Automation Research Center. Sandia is a multi-program laboratory operated by Sandia Corporation, a Lockheed-Martin company, for the US Department of Energy under contract DEAC-94AL-85000.

References

1. R. J. Shul, G. B. McClellan, S. A. Casalnuova, D. J. Rieger, S. J. Pearton, C. Constantine, C. Barrat, R. F. Karlicek, Jr., C. Tran, and M. Schurman, Appl. Phys. Lett., **69** 1119 (1996).
2. R. J. Shul, in GaN and Related Materials, ed. S. J. Pearton (Gordon and Breach, N. Y., 1997).
3. H. P. Gillis, D. A. Choutov, and K. P. Martin, JOM, **48** 50 (1996).
4. I. Adesida, A. Mahajan, E. Andideh, M. A. Khan, D. T. Olsen, and J. N. Kuznia, Appl. Phys. Lett., **63** 2777 (1993).
5. M. E. Lin, Z. F. Fan, Z. Ma, L. H. Allen, and H. Morkoc, Appl. Phys. Lett., **64** 887 (1994).
6. H. Lee, D. B. Oberman, and J. S. Harris, Jr., Appl. Phys. Lett., **67** 1754 (1995).
7. W. Pletschen, R. Niegurch, and K. H. Bachem, Proc. Symp. Wide Bandgap Semiconductors and Devices, **Vol. 95-21** (Electorchemcal Society, Pennington, N. J., 1995), p.241.
8. S. J. Pearton, C. R. Abernathy, and F. Ren, Appl. Phys. Lett., **64** 2294 (1994).
9. L. Zhang, J. Ramer, J. Brown, K. Zhang, L.F. Lester, and S. D. Hersee, Appl. Phys. Lett., **68** 367 (1996).
10. R. J. Shul, R. D. Briggs, S. J. Pearton, C. B. Vartuli, C. R. Abernathy, J. W. Lee, C. Constantine, and C. Barratt, Mat. Res. Soc. Symp. Proc., **449** 969 (1997).
11. H. Cho, C. B. Vartuli, S. M. Donovan, C. R. Abernathy, S. J. Pearton, R. J. Shul, and C. Constantine, J. Vac. Sci. Technol. A **16** 1631 (1998).
12. H. Cho, C. B. Vartuli, S. M. Donovan, K. D. Mackenzie, C. R. Abernathy, S. J. Pearton, R. J. Shul, and C. Constantine, J. Electron. Mat., **27** 166 (1998).
13. S. Nakamura, in GaN and Related Materials, ed. S. J. Pearton (Gordon and Breach, N. Y. 1997).
14. O. Aktas, Z. Fan, S. N. Mohammad, A. Botcharev, and H. Morkoc, Appl. Phys. Lett., **69** 25 (1996).
15. M. A. Khan, J. N. Kuznia, M. S. Shur, C. Eppens, J. Burm, and W. Schaff, Appl. Phys. Lett., **66** 1083 (1995).
16. Y. F. Wu, B. P. Keller, S. Keller, D. Kapolnek, S. D. Den Baars, and U. K. Mishra, IEEE Electron. Dev. Lett., **17** 455 (1996).
17. M. A. Khan, Q. Chen, M. S. Shur, B. T. McDermott, J. A. Higgins, J. Burm, W. Schaff, and L. F. Eastman, Elecrtron. Lett., **32** 357 (1996).
18. Y. T. Wu, S. Keller, P. Kozodoy, B. P. Keller, P. Parikh, D. Kapolnek, S. P. Denbaars, and V. K. Mishra, IEEE Electron. Dev. Lett., **18** 290 (1997).
19. C. R. Abernathy, J. Vac. Sci. Technol. A **11** 869 (1993).
20. C. R. Abernathy, Mat. Sci. Eng. Rep., R**14** 203 (1995).
21. J. W. Lee, J. Hong, and S. J. Pearton, Appl. Phys. Lett., **68** 847 (1996).
22. CRC Handbook of Chemistry and Physics, 70th Ed., eds. R. C. Weast, D. R. Lide, M. J. Astle, and W. H. Beyer (CRC Press Inc., Boca Raron, FL, 1989).
23. J. Burm, K. Chu, W. J. Schaff, L. F. Eastman, M. A. Khan, Q. Chen, J. W. Yang, and M. S. Shur, IEEE Electron. Dev. Lett., **18** 141 (1997).
24. S. M. Donovan, K. D. MacKenzie, C. R. Abernathy, S. J. Pearton, F. Ren, K. Jones, and M. Cole, Appl. Phys. Lett., **70** 2592 (1997).
25. F. Ren, C. R. Abernathy, S. J. Pearton, and P. W. Wisk, Appl. Phys. Lett., **64** 1508 (1994).
26. F. Ren, R. J. Shul, C. R. Abernathy, S. N. G. Chu, J. R. Lothian, and S. J. Pearton, Appl. Phys. Lett., **66** 1503 (1995).

FOCUSED ION BEAM ETCHING OF GaN

C. Flierl[(1)], I.H. White[(1)], M. Kuball[(2)], P.J. Heard[(3)], G.C. Allen[(3)], C. Marinelli[(1)], J.M. Rorison[(1)], R.V. Penty[(1)], Y. Chen[(4)] and S.Y. Wang[(4)]

[(1)]Department of Electrical and Electronic Engineering, University of Bristol, Bristol BS8 1TR, UNITED KINGDOM;
[(2)]H.H. Wills Physics Laboratory, University of Bristol, Bristol BS8 1TL, UNITED KINGDOM
[(3)] Interface Analysis Centre, University of Bristol, Bristol BS2 8BS, UNITED KINGDOM
[(4)]Hewlett-Packard Laboratories, Palo Alto CA 94304, USA

Cite this article as: MRS Internet J. Nitride Semicond. Res. 4S1, G6.57

ABSTRACT

We have investigated the use of focused ion beam (FIB) etching for the fabrication of GaN-based devices. Although work has shown that conventional reactive ion etching (RIE) is in most cases appropriate for the GaN device fabrication, the direct write facility of FIB etching – a well-established technique for optical mask repair and for IC failure analysis and repair – without the requirement for depositing an etch mask is invaluable. A gallium ion beam of about 20nm diameter was used to sputter GaN material. The etching rate depends linearly on the ion dose per area with a slope of $3.5 \times 10^{-4} \mu m^3/pC$. At a current of 3nA, for example, this corresponds to an etch rate of $1.05 \mu m^3/s$. Good etching qualities have been achieved with a side wall roughness significantly below 0.1μm. Changes in the roughness of the etched surface plane stay below 8nm.

INTRODUCTION

Tremendous effort has been made in recent years in developing GaN-based devices due to their wide spectrum of potential applications ranging from short-wavelength light emitters and lasers, solar-blind detectors to high temperature devices [1–4]. GaN-based devices reported to date have mostly been fabricated using reactive ion etching (RIE) [5]. RIE-etched side walls, however, often suffer from a significant surface roughness, which is a major concern, e.g., for laser diodes since optical losses in the laser end mirrors increase the threshold current. Because of the difference in the cleavage plane between GaN (1100) and the commonly used sapphire substrate (1102) it is difficult to achieve flat cleaved end mirrors. The development of improved etching techniques is therefore essential to enhance the performance of GaN-based devices [6–8]. Furthermore, it will be necessary to find etching techniques which allow the fabrication of GaN on the nanometer scale for the development of novel device structures,, e.g., for integrating laser diodes with wavelength selective electro-absorbers [7].

Focused ion beam (FIB) etching is not only the most promising technique for the fine patterning of GaN-based devices, but also for improving the quality of laser facets. A focused gallium ion beam of 5-20nm size is used in FIB to sputter material. The direct write facility of focused ion beam (FIB) etching – a well-established technique for optical mask repair and for IC failure analysis and repair – without the requirement for depositing an etch mask is invaluable. This allows the nanometer scale fabrication of nitride devices. Focused ion beam (FIB) etching

Mat. Res. Soc. Symp. Proc. Vol. 537 © 1999 Materials Research Society

has also great potential for the post-processing of devices and has been successfully applied to achieve polarization control in red GaAs-based vertical cavity surface emitting lasers (VCSELs) [9,10]. In this report, we determine basic parameters for the FIB-etching of GaN. We investigate the quality of FIB-etched GaN structures using atomic force microscopy and scanning electron microscopy.

EXPERIMENT

GaN layers, 1.2μm thick, were grown by metalorganic vapor phase epitaxy (MOCVD) on sapphire substrates. The layers were unintentionally n-doped with a carrier concentration of $6\times10^{17}cm^{-3}$ and a carrier mobility of $360cm^2/Vs$. Patterns were etched in the GaN layer using a focused gallium ion beam of 20nm diameter size. The instrument used comprises an FEI focused gallium ion gun with a magnetic sector mass analyser, a Thornley Everhard secondary electron detector and peripheral components. It enables the user to capture an image of the sample at high magnification using the scanned focused ion beam and secondary electron detector, and then to delineate or import arbitrary patterns in two dimensions to be etched into the specimen with the same beam.

Furthermore, an integrated mass spectrometer, a double-focusing electric and magnetic sector unit, can be used to provide secondary ion mass spectrometry (SIMS) analysis, and so the instrument can be employed as an analytical tool in its own right, or the SIMS detector can be used to provide end-point detection during etching, particularly on devices with multi-layered structures. The spatial resolution of the system is below 100nm at 50pA; the main component limiting the available resolution being noise and vibration. The spectral resolution of the SIMS detector is $M/\Delta M=2000$.

The fabricated samples were investigated using an atomic force microscope from TopoMetrix and a JEOL-6400 scanning electron microscope to determine the etch depth and surface roughness of the fabricated GaN structures.

RESULTS AND DISCUSSION

Square patterns of about 7μm size were etched in the 1.2μm-thick-GaN layer by FIB at different Ga-ion doses. Figure 1 displays the secondary-electron image of the specimen after

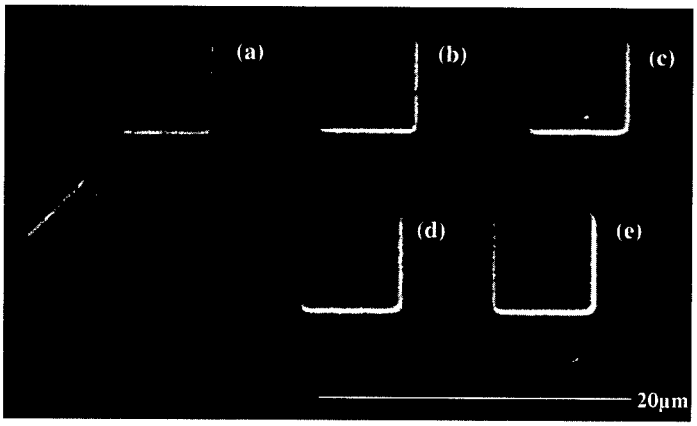


Figure 1: Focused ion beam (FIB)-etched pattern in GaN layer, fabricated using Ga-ion doses of (a) 500, (b,d) 1000, (c) 1500, and (e) $2000pC/\mu m^2$.

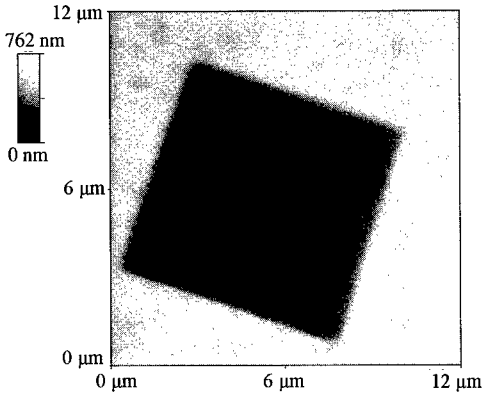


Figure 2: Atomic force microscopy (AFM) image of FIB-etched structure in GaN.

the etching, obtained while scanning the Ga-ion beam over the sample surface at a very low dose. The individual square patterns were etched with ion doses of: (a) 500pC/µm^2, (b,d) 1000pC/µm^2, (c) 1500pC/µm^2, and (e) 2000pC/µm^2. The pattern (b) and (d) were etched at a different current, 1nA and 3nA, respectively. Note that no etch mask is necessary for the etching. The pattern is written directly onto the specimen by scanning the 20nm-wide gallium ion beam over the sample surface. This direct write facility of focused ion beam (FIB) etching is illustrated by the etched arrow on the left side of Figure 1. The etched lines of the arrow are less than 1µm wide. The achievable minimal line width is only limited by the diameter of the gallium ion beam and the vibrational stability of the FIB-instrument.

Increasing the gallium-ion dose results in an increasing etch depth in the GaN layer as seen Figure 1. Atomic force microscopy (AFM) images were recorded from the various square patterns to determine the etch depth as function of ion dose. Figure 2 shows an AFM image of the etched pattern (e) of Figure 1. The determined etch depth as function of gallium ion dose per area is displayed in Figure 3. The etching rate depends linearly on the gallium-ion dose with a slope of 3.5×10^{-4}µm^3/pC. At a current of 3nA, for example, this corresponds to an etch rate of 1.05µm^3/s. We note that the etching rate shows a minor dependence on the gallium-ion currents used. Figure 3 shows the results obtained at a low gallium-ion current. Increasing the current from 1nA to 3nA at a constant dose of 1000 pC/µm^2 in Figure 1 (b,d), i.e., decreasing the etch time, results in an decrease in the etching rate by about 10-20%. The underlying mechanism is currently not known and is part of ongoing investigations.

Figure 4 shows the change in the RMS roughness of the GaN surface after etching, i.e., inside the etched square pattern in Figure 1, as function of the gallium ion dose, determined from the AFM images to evaluate the quality of the FIB etching of GaN. The RMS surface roughness increases up to gallium ion doses of 1000pC/µm^2, however, saturates at higher ion doses. Note that the RMS roughness of the GaN layer is only 8nm larger after the FIB etching at a dose of 2000pC/µm^2 than on the as-grown sample (RMS=17nm).

Figure 5 shows a scanning electron microscopy image of an edge of a deep square pattern etched by FIB at a gallium-ion dose of 3000pC/µm^2 at a current of 3nA. The image allows us to estimate the obtained side wall roughness achievable with FIB. The side wall roughness stays

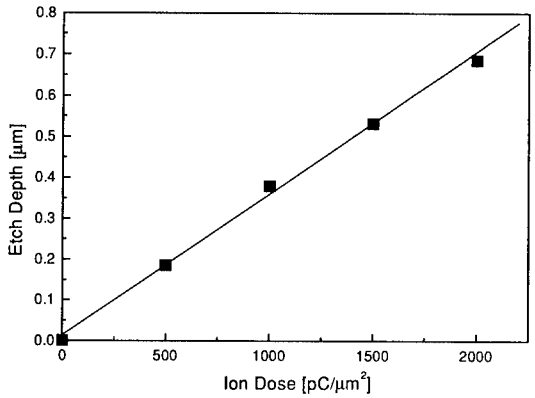


Figure 3: Etch rate as function of gallium ion dose.

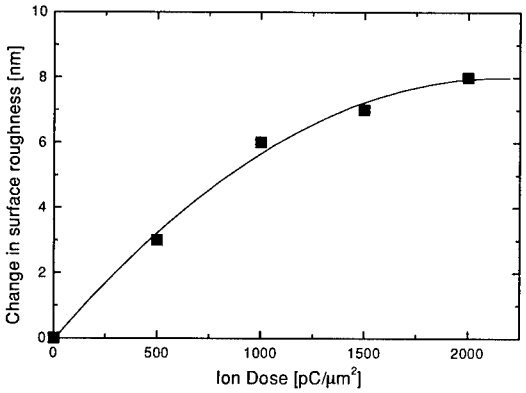


Figure 4: Change in the root mean square (RMS) of the GaN surface roughness after the FIB etching.



Figure 5: Scanning electron microscopy images of FIB-etched edge.

well below 0.1μm. This result is very promising for use of FIB etching for the fabrication of smooth GaN laser facets. Note that the pattern shown in Figure 5 was etched at a high gallium ion current. The result can even be improved by lowering the current. A large beam current results in an increased gallium beam diameter, a reduced spatial resolution and therefore a reduced etch quality. A closer examination of Figure 5 shows consistently rounded top edges (top of Figure 5). Reducing the Ga-ion current significantly improves the etching quality as indicated in Figure 1 when comparing the pattern (b) and (d) fabricated at a current of 1nA and 3nA, respectively.

The good quality of the FIB-etched GaN surfaces as well as of the side walls illustrates that FIB-etching is well suited for the fabrication of GaN-based devices. The achieved surface roughness and side wall roughness is comparable or better than etching results obtained with reactive ion etching (RIE) reported in the literature [11]. The superiority of FIB for the fabrication of GaN laser diode end facets has recently been illustrated by Mack *et al.* [8]. FIB-post-processed GaN laser diodes showed a reduction in the threshold current, i.e., reduced optical losses in the end facet mirrors. The direct write facility of FIB is invaluable for the fabrication of nanometer size features in GaN (see e.g. Figure 1).

CONCLUSIONS

We have demonstrated the great potential of focused ion beam (FIB) etching to fabricate GaN-based devices. Parameters for the FIB etching of GaN were determined. The etching rate increases linearly with ion dose with a slope of $3.5 \times 10^{-4} \mu m^3/pC$. The obtained side wall roughness stays well below 0.1μm. The direct write facility of FIB was demonstrated. Arbitrary nanometer scale features were etched in a GaN film. Since FIB etching is intrinsically a serial process, FIB etching is slower than high-density plasma etching techniques. However, the high etching quality of FIB as well as its high versatility makes FIB etching highly attractive for the post-processing of GaN-based devices where only a small area has to be modified.

ACKNOWLEDGEMENTS

We like to thank J. Mallett and J. Hart (Department of Physics, University of Bristol) for support during the atomic force microscopy and scanning electron microscopy measurements, and J.C.C. Day (Interface Analysis Centre, University of Bristol) for the development of the windows-based software package for the FIB instrument to control the etch parameters such as pixel dwell times, overall exposure to the ion beam, number of scan repetitions.

REFERENCES

[1] S. Nakamura, M. Senoh, S. Nagahama, N. Iwasa, T. Yamada, T. Matsushita, H. Kiyoku, Y. Sugimoto, T. Kozaki, H. Umemoto, M. Sano, K. Chocho, Appl. Phys. Lett. **72**, 211 (1998).

[2] Y.-K. Song, M. Kuball, A.V. Nurmikko, G.E. Bulman, K. Doverspike, S.T. Shappard, T.W. Weeks, M. Leonard, H.S. Kong, H. Dieringer, and J. Edmonds, Appl. Phys. Lett. **72**, 1418 (1998).

[3] Y.-F. Wu, B.P. Keller, S. Keller, N.X. Nguyen, M. Le, C. Nguyen, T.J. Jenkins, L.T. Kehias, S.P. DenBaars, and U.K. Mishra, IEEE Elec. Dev. Lett. **18**, 438 (1997).

[4] S. Yoshida and J. Suzuki, Jpn. J. Appl. Phys. Pt. 2 **37** 482 (1998).

[5] S. Nakamura and G. Fasol, "The blue laser diode: GaN based light emitters and lasers" (Springer, Berlin, New York, 1997).
[6] T. Ito, H. Ishikawa, T. Egawa, T. Jimbo, and M. Umeno, Jpn. J. Appl. Phys. Pt. 1 **36**, 7710 (1997).
[7] H. Katoh, T. Takeuchi, C. Anbe, R. Mizumoto, S. Yamaguchi, C. Wetzel, H. Amano, I. Akasaki, Y. Kaneko, and N. Yamada, Jpn. J., Appl. Phys. Pt. 2 **37**, 444 (1998).
[8] M.P. Mack, G.D. Via, A.C. Abare, M. Hansen, P. Kozodoy, S. Keller, J.S. Speck, U.K. Mishra, L.A. Coldren, and S.P. DenBaars, Electr. Lett. **34**, 1315 (1998).
[9] P. Dowd, P.J. Heard, J.A. Nicholson, L. Raddatz, I.H. White, R.V. Penty, J.C.C. Day, G.C. Allen, S.W. Corzine, M.R.T. Tan, Electr. Lett. **33**, 1315 (1997).
[10] L.J. Sargent, M. Kuball, J.M. Rorison, R.V. Penty, I.H. White, P. J. Heard, M. R. T. Tan, and S. Y. Wang, submitted to Appl. Phys. Lett.
[11] K.V. Vassilevski, M.G. Rastegaeva, A.I. Babanin, I.P. Nikitina, and V.A. Dmitriev, MRS Internet J. Nitride Semicond. Res. **1**, 38 (1996).

PHYSICS-BASED INTRINSIC MODEL FOR AlGaN/GaN HEMTs

Shangli Wu*, Richard T. Webster** and A. F. M. Anwar*

*Electrical and Systems Engineering Department, University of Connecticut,
Storrs, CT 06269-2157
** Electromagnetics Technology Division, Air Force Research Laboratory
Hanscom AFB, MA 01730

MRS Internet J. Nitride Semiconductor Res. 4S1, G6.58 (1999)

ABSTRACT

DC and intrinsic small signal parameters are reported for AlGaN/GaN high electron mobility transistors. The calculations are based upon a self-consistent solution of Schrödinger and Poisson's equation to model the quantum well formed in GaN. Transport parameters are obtained from an ensemble Monte Carlo simulation.

INTRODUCTION

AlGaN/GaN high electron mobility transistors (HEMTs) have recently attracted much attention with the large available band gap of the channel material (GaN) and excellent thermal properties for possible applications in high power and high temperature microwave devices.

Some of the HEMT structures reported by Binari et. al. [1-2] and Redwing et. al. [3] had appreciable two dimensional electron gas (2DEG) concentration though the AlGaN supply layer was undoped. Dangling bonds at the AlGaN/GaN heterointerface may give rise to interface charge that could explain the observed 2DEG concentration. Recently, an alternative explanation of the formation of the 2DEG concentration using the piezoelectric effect has been proposed by Asbeck et. al. [4]. However, as shown by the present authors [5] the calculation of 2DEG concentration as a function of Al mole fraction is in excellent agreement with the experimental data, even though the piezoelectric effect was not incorporated in the calculation.

The dc and small signal parameters and the rf performance can be investigated once the quantum well (QW) properties and the transport properties of the channel material are known. In this paper the dc and small signal parameters are calculated using results obtained from an exact quantum calculation modeling the QW formed at the AlGaN/GaN heterointerface along with transport data obtained from an ensemble Monte Carlo simulation. The rf performance can then be obtained by evaluating the small signal model.

THEORY

The electron concentration, n_s, in the QW formed in GaN is determined by solving the Schrödinger and Poisson's equations self-consistently [5]. The calculated average distance of the electron cloud from the heterointerface, x_{avg}, and the position of the Fermi level, E_F, are expressed by the following functional forms and are used in the evaluation of the dc and small signal parameters [6, 7, 8]:

$$x_{av} = a + b \cdot \ln(n_s) \quad (\text{Å}) \tag{1}$$

$$E_F = E_F(0) + \gamma \cdot \ln(n_s) \quad (\text{eV}) \tag{2}$$

Mat. Res. Soc. Symp. Proc. Vol. 537 © 1999 Materials Research Society

where the constants a, b, $E_{F(0)}$ and γ are determined from the results of the quantum calculation. The drain-source current I_{ds} can then be written as [5] :

$$I_{ds} = \frac{G_0|V_T|^2}{\varepsilon_0 L_1}\cdot\left(\frac{s}{2}\sqrt{s^2-p^2} - \frac{p^2}{2}\ln\left(\frac{s+\sqrt{s^2-p^2}}{p}\right)\right) + \frac{\gamma}{|V_T|}\left[\sqrt{s^2-p^2} - p\cdot\cos^{-1}\left(\frac{p}{s}\right)\right] \quad (3)$$

where $G_0 = \varepsilon Z v_s / d_{eff}$, $d_{eff} = d + \Delta d$ with d and Δd being the thickness of AlGaN layer and effective channel thickness, respectively. Z is the width of the gate and L_1 is the length of unsaturated region of the channel. The above equation incorporates the effect of the quantum well through eqs. 1 and 2 via reduced potentials, s and p. Also implicit in eq. 3 is the use of a velocity-electric field characteristic of the form $v_d = \mu_0 E/((v_s/\mu_0)^2 + E)^{1/2}$ where v_d is the drift velocity, μ_0 is the low field mobility, v_s is the saturation velocity and E is the electric field. The velocity-electric field characteristics are obtained from an ensemble Monte Carlo simulation using the following scattering mechanisms: acoustic phonon, optical phonon, intervalley, alloy, ionized impurity and piezoelectric scattering The evaluation of dc and small signal parameters follows the treatment presented in Ref. [5].

RESULTS AND DISCUSSION

The QW formed in GaN in an $Al_{0.25}Ga_{0.75}N$/GaN heterostructure is considered. The electron effective masses in GaN and AlN are assumed to be $0.19m_0$ and $0.23\ m_0$, respectively, where m_0 is the free electron mass. The electron effective mass of $Al_xGa_{1-x}N$ is obtained by a linear interpolation between the values for GaN and AlN. Based on a calculated valence band offset in $Al_xGa_{1-x}N$/GaN, it is found that the conduction band offset may be given as: $\Delta E_c = 0.75\Delta E_G$, where ΔE_G is the difference in bandgaps of GaN and $Al_xGa_{1-x}N$ [5]. The temperature dependent bandgap for GaN is given as $E_G^{GaN}(T) = 3.056 + 5.08\times10^{-4}T^2/(T-996)$ [9]. The bandgap of AlN is assumed to be 5.1 eV.

Fig.1 shows the conduction band profiles obtained by solving the Schrödinger and Poisson's equations self-consistently for 300K and 500K. On the same plot the 2DEG

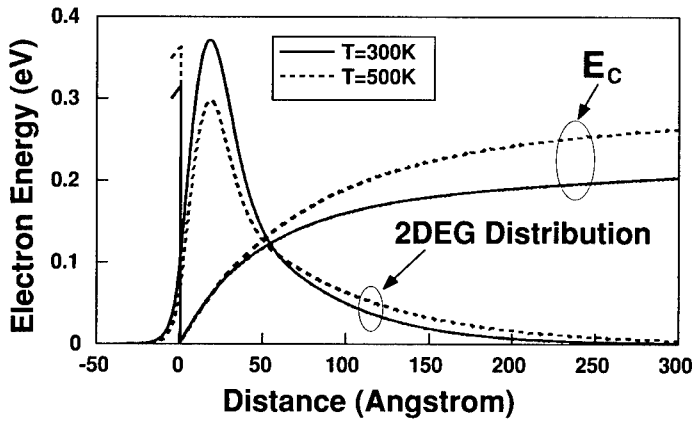


Fig. 1 Conduction band profile and 2DEG concentration at 300K and 500K.

distributions are also plotted. The plots are obtained for a 2DEG concentration of $1.8 \times 10^{12}\,cm^{-2}$ and the corresponding positions of the Fermi level are 0.092 eV and 0.052eV above the tip of the conduction band discontinuity at 300K and 500K, respectively. The conduction band profiles can be explained by the fact that n_i(300K) is 12 orders of magnitude less that n_i(500K). This difference in n_i is due to the higher effective density of states at higher temperatures and a decrease in bandgap of GaN with increasing temperature. Moreover, the conduction band offset increases from 0.313eV at room temperature to 0.361eV at 500K. Assuming fully ionized acceptors in GaN at both temperatures, the Fermi level moves closer to the intrinsic Fermi level at the higher temperature. Therefore, less band bending in GaN is required to obtain the same 2DEG concentration at 500K that at 300K. At room temperature a higher fraction of the 2DEG concentration is in the first subband due to the close proximity of the Fermi level to the first eigen energy. On the other hand, at 500K a larger separation between the first eigen energy and the Fermi level implies a lesser degree of occupation of the first subband, allowing the higher subbands to be populated.

In Fig. 2, the average distance of the electron cloud from the first heterointerface, x_{av}, and the position of the Fermi level, E_F, with respect to the tip of the conduction band are plotted as a function of the 2DEG concentration, n_s. At room temperature for $n_s > 1 \times 10^{11}\ cm^{-2}$, x_{av} and E_F can be expressed by the following relationships:

$$x_{av} = 1740 - 104 \log_{10}(n_s)\ \text{Å} \quad (4)$$

$$E_F = -5.232 + 0.4363 \log_{10}(n_s)\ \text{eV} \quad (5)$$

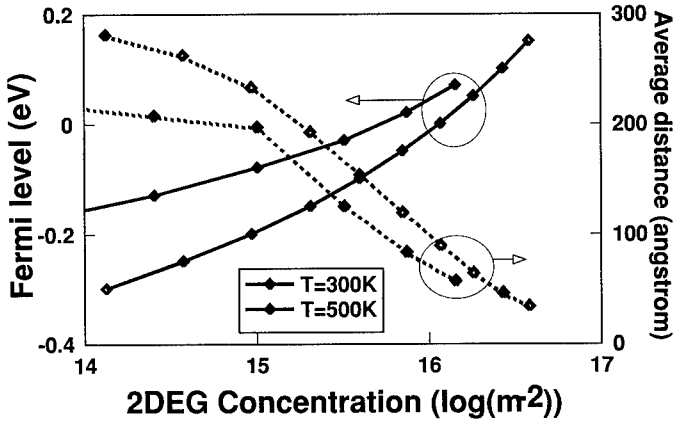


Fig. 2 x_{av} and E_f as a function of the 2DEG concentration.

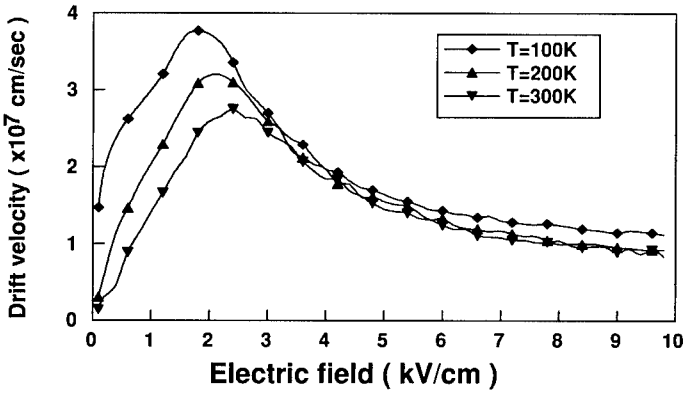


Fig. 3 Velocity-electric field characteristics for undoped GaN with temperature as a parameter.

The simulated electron drift velocity is plotted in Fig. 3 as a function of applied electric field in undoped bulk GaN with temperature as a parameter. A peak velocity of 2.6×10^7 cm/s is obtained at a field strength of 145 kV/cm for undoped GaN at room temperature . The position of the peak velocity moves from 140 kV/cm at 100K to 170 kV/cm at 500K. It is interesting that the low field mobility increases as the temperature is lowered, whereas, the saturation velocity does not show such a pronounced temperature dependence. This can be explained by noting that the low field mobility, which is dominated by acoustic phonons and polar optical phonon absorption, shows improvement due to the suppression of these scattering process at lower temperatures. The high field transport on the other hand, is dominated by polar optical phonon emission and intervalley scattering, both of which have a weak lattice temperature dependence. The room temperature low field mobility, μ, obtained from the initial slope of the velocity field curves, changes from 590 $cm^2/V\text{-}s$ at 1×10^{17} cm^{-3} to 440 $cm^2/V\text{-}s$ at 1×10^{19} cm^{-3} for GaN. The

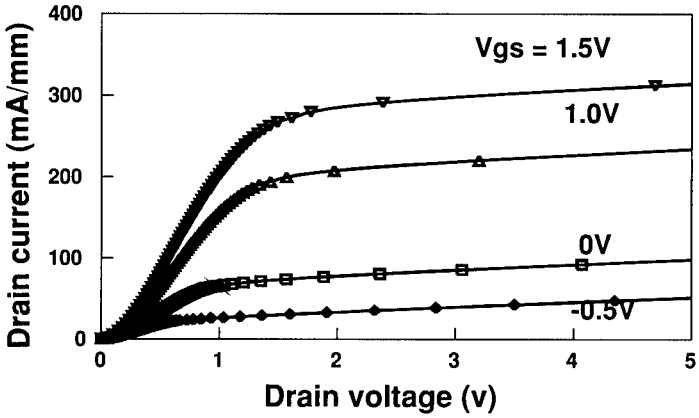


Fig. 4 DC current-voltage characteristics of AlGaN/GaN HEMT.

simulations show that the temperature dependence of the low field mobility for a doping level of 1×10^{17} cm^{-3} can be given as $\mu(T) = 1156 - 2.75T + 0.002T^2$ $cm^2/V\text{-}s$. With increasing doping the peak in the low field mobility decreases and shifts towards higher temperature. This behavior is attributed to the strong influence of ionized impurity scattering.

The current voltage characteristics of a 1.2 μm x 20μm $Al_{0.25}Ga_{0.75}N$/GaN HEMT at room temperature are plotted in Fig. 4. A low field mobility of 600 $cm^2/V\text{-}s$ and a saturation velocity of $1x10^7$ cm/s are assumed for the undoped GaN channel. The AlGaN epilayer thickness is assumed to be 220 Å. The threshold voltage is calculated to be -3.75 V, and the barrier potential, φ_b =1.1eV.

In Fig. 5, the saturation drain current and the transconductance of a 1.2 μm x 20 μm gate HEMT are plotted as a function of the gate-source potential at V_{ds}=2.0V. A transconductance of 100 mS/mm is obtained at V_{gs} =2.0 V. In Fig 5 (b), the small signal gate capacitance and the drainresistance are shown. These small signal parameters predict a maximum unity current gain cutoff frequency, f_T, of 12 GHz at room temperature that reduces to 10 GHz at 500K.

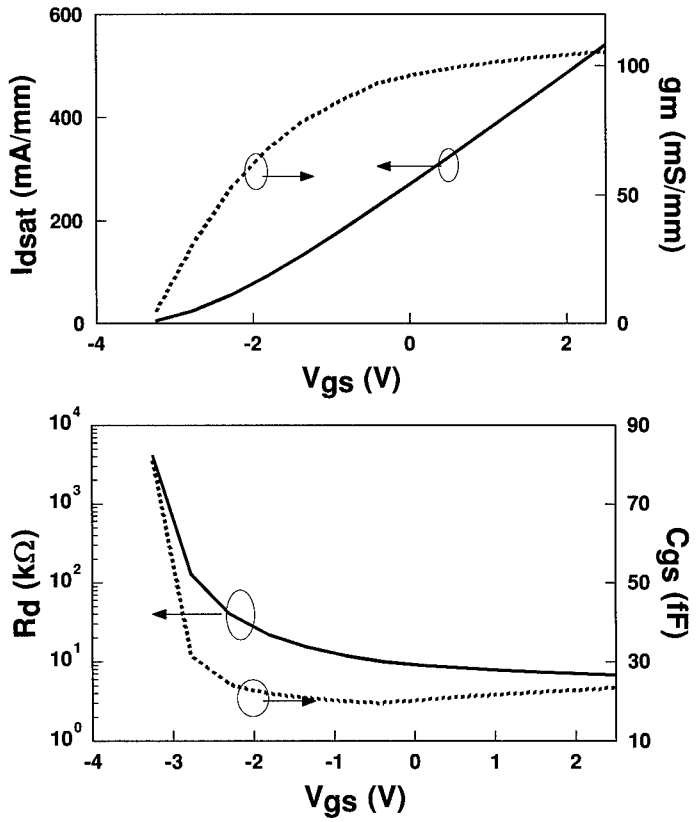


Fig. 5 (a) Saturation drain current and transconductance (b) drain resistance and gate-source capacitance are plotted as a function of gate bias.

CONCLUSION

A physics based intrinsic model for AlGaN/GaN HEMTs has been presented. The model is based a self-consistent solution the Schrödinger and Poisson's equations as well as channel material transport properties obtained from a Monte Carlo simulation. The resulting small signal model predicts a high transconductance of 100 mS/mm with a unity current gain cutoff frequency of 12 GHz. Transistors with these characteristics will be useful in microwave applications at high temperatures.

ACKNOWLEDGMENTS

The authors acknowledge support from the Air Force Office of Scientific Research and the Expert Science and Engineering Program under Air Force Research Laboratory contract number F30602-97-C-0199. This work was supported in part by a grant of High Performance Computer (HPC) time from the DOD HPC Center, Air Force Aeronautical Systems Center (ASC), Cray C90.

REFERENCE

[1].S. C. Binari, J. M. Redwing, G. Kelner and W. Kruppa, Electron. Lett., vol. 33, No. 3, p. 242, 1997.
[2].S. C. Binari, Electrochem. Soc. Proc., 95-21, p. 136, 1995.
[3].J. M. Redwing, M. A. Tischler, J. S. Flynn, S. Elhamri, M. Ahoujja, R. S. Newrock and W. C. Mitchel, Appl. Phys. Lett., vol. 69, p. 963, 1996
[4].P. M. Asbeck, E. T. Yu, S. S. Lau, G. J. Sullivan, J. Van Hove and J. Redwing, Electron. Lett., p. 241, Aug. 1997.
[5].R. T. Webster and A.F.M. Anwar, MRS Proc. vol. 428, p.929, 1997.
[6].M. A. Khan, Q. Chen, M. S. Shur, B. T. Dermott and J. A. Higgins, IEEE Electron Dev. Lett., vol. 17, No.7, p. 325, 1996.
[7].M. S. Shur and M. A. Khan, MRS Bull., p. 44, Feb., 1997
[8].J. M. Redwing, M. A. Tischler, J. S. Flynn, S. Elhamri, M. Ahoujja, R. S. Newrock and W. C. Mitchel, Appl. Phys. Lett., vol. 69, p. 963, 1996
[9].S. Strite and H. Morkoc, J. Vac. Sci. Technol., vol. B 10, No. 4, p. 1237, 1992.

ENSEMBLE MONTE CARLO STUDY OF ELECTRON TRANSPORT IN BULK INDIUM NITRIDE

E. Bellotti *, B. Doshi *, K. F. Brennan * and P. P. Ruden **

*School of ECE, Georgia Tech, Atlanta, GA 30332, kbrennan@ece.gatech.edu
** Dept. of ECE, University of Minnesota, Minneapolis, MN 55455

Cite this article as: MRS Internet J. Nitride Semicond. Res. 4S1, G6.59 (1999)

ABSTRACT

Ensemble Monte Carlo calculations of electron transport at high applied electric field strengths in bulk, wurtzite phase InN are presented. The calculations are performed using a full band Monte Carlo simulation that includes a pseudopotential band structure, all of the relevant phonon scattering agents, and numerically derived impact ionization transition rates. The full details of the first five conduction bands, which extend in energy to about 8 eV above the conduction band minimum, are included in the simulation. The electron initiated impact ionization coefficients and quantum yield are calculated using the full band Monte Carlo model. Comparison is made to previous calculations for bulk GaN and ZnS. It is found that owing to the narrower band gap in InN, a lower breakdown field exists than in either GaN or ZnS.

INTRODUCTION

Wide band-gap semiconductors are becoming of increasing importance in many emerging optoelectronic and electronic device applications. Among these applications are ultraviolet (UV) photodetectors, blue and UV light emitters, and high frequency, high power electronic devices. Of the emerging wide band-gap semiconductors, the most promising candidates for power field effect transistors, FETs, are SiC and the III-nitrides. It is well known that SiC or GaN based transistors offer significantly higher maximum output power than comparable structures made from GaAs or Si [1,2]. Owing to their relatively wide and direct energy band-gap, the III-nitride semiconductors are in addition particularly useful for UV and blue-light photonic detectors and emitters. The III-nitrides offer an additional advantage since heterostructures can be made from these materials. Along with GaN, the InN ternary alloy, InGaN, has found application in a variety of heterostructure based opto-electronic devices. In spite of its potential application, little information is available about the transport properties of InGaN or its constituent binary materials, InN and GaN. Some progress has been made on GaN [3-10], but only a single limited study of electron transport in InN [11] has yet been performed.

It is the purpose of this paper to present the first theoretical study of the high field electronic transport properties of bulk InN. The calculations are performed using a full band, ensemble Monte Carlo simulation that includes a numerical formulation of the interband impact ionization transition rate [12]. The electron initiated impact ionization coefficients are calculated as a function of applied electric field strength.

Mat. Res. Soc. Symp. Proc. Vol. 537 © 1999 Materials Research Society

MODEL DESCRIPTION

The band structure of InN used within the Monte Carlo simulation is calculated using the empirical pseudopotential method. Though ab initio methods have been applied to the study of InN [13], the empirical pseudopotential method is employed herein since it offers a computationally efficient and reasonably accurate accounting of the band structure. The band structure derived from the pseudopotential model is shown in Figure1.

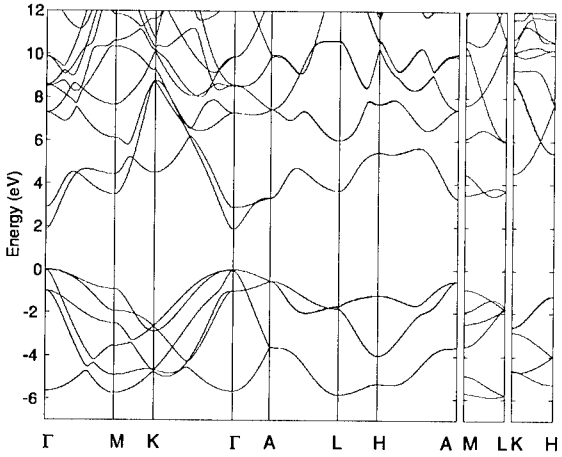


Fig. 1 Calculated pseudopotential band-structure of wurtzite InN

Electron-phonon and impurity scattering form the other principal input into the Monte Carlo model. Polar-optical, acoustic phonon, ionized impurity, and piezoelectric scattering are included for electron energies below 0.9 eV. The acoustic phonon scattering is formulated inelastically. Above 0.9 eV, only polar optical, deformation potential and impact ionization scatterings are included. This choice is made to avoid using intervalley scattering explicitly since the intervalley deformation potentials are unknown. By substituting a general deformation potential scattering mechanism in place of the many intervalley mechanisms, the parametrization can be greatly reduced. Therefore, only one isotropic deformation potential scattering mechanism based on the realistic density of states is employed at electron energies greater than 0.9 eV. The coupling constant for this deformation potential scattering is determined by matching the low energy and high energy rates at 0.9 eV. The material parameters used to calculate the scattering rates are collected in Table I. The interband impact ionization transition rate is computed numerically from the pseudopotential band structure using a wave-vector dependent dielectric function following the approach of Kolnik et al. [12]. The wave-vector dependent rate is computed on a 924 point grid for the first five conduction bands within the irreducible wedge of the first Brilloiun zone. The total transition rate is then determined by averaging the wave-vector dependent rate over constant energy surfaces.

Table I. Bulk material parameters used in the phonon scattering rate calculations for wurtzite type InN.

Parameter	Value
Lattice constant (Å) [14]	a=3.54 c=5.7
Low frequency dielectric constant [14]	15.4
High frequency dielectric constant [14]	8.4
Energy band gap (eV) [15]	1.86
Longitudinal Sound velocity (cm/s) [14]	$6.24\ 10^5$
Transverse Sound velocity (cm/s) [14]	$2.55\ 10^5$
Density (g cm^{-3}) [14]	6.81
Effective mass at Γ (m^*/m_0) [15]	0.11
Nonparabolicity at Γ (eV^{-1}) [15]	0.419
Intravalley acoustic deformation potential (eV) [14]	7.1
Optical phonon energy at Γ (eV) [14]	0.089
Piezoelectric coupling constant K^2_{av} [16]	0.0652

CALCULATED RESULTS

The ionization coefficients are calculated using the Monte Carlo simulator. It is well known that the ionization coefficients depend strongly on the high energy phonon scattering rate. Unfortunately, little information about the high energy scattering rates is known even for the most studied semiconductors. The high energy electron-phonon scattering rate is dominated by deformation potential scattering. Deformation potential scattering is, to lowest order, isotropic and proportional to the final density of states. The deformation potential scattering rate is generally calculated assuming a single, constant, energy independent coupling constant whose value is ascertained by comparison of the Monte Carlo coefficients to experimental data. In the present situation, no experimental information about the ionization coefficients exists so no comparison to experimental data is possible. Instead, we select a baseline value for the deformation potential constant such that the high and low energy scattering rates match at 0.9 eV as mentioned above. By varying the deformation potential constant from this baseline value, the sensitivity of the ionization coefficients to the choice of the scattering rate can be assessed.

The calculated ionization coefficients for fields applied along the (110) and (001) directions in bulk InN are plotted in Figure 2. The solid curves shown in Figure 2 correspond to the calculated coefficients using the baseline phonon scattering rate.

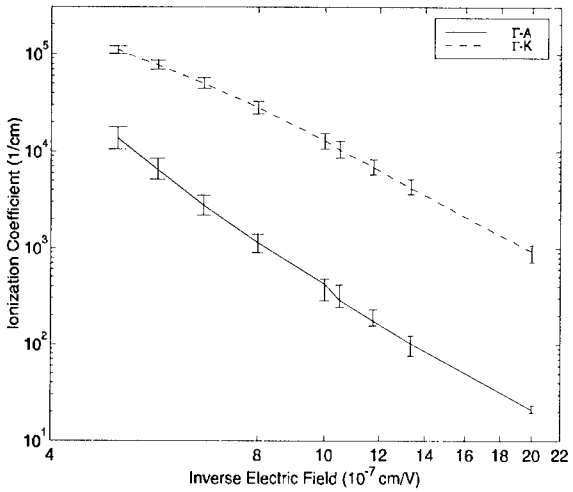


Fig.2 Calculated impact ionization coefficients for wurtzite InN

There exists a substantial anisotropy in the ionization coefficients. Notice that the ionization coefficients are significantly lower for an applied field along the (001) direction than along the (110) direction. Since the present model assumes an isotropic high energy phonon scattering rate, the anisotropy in the ionization coefficients most likely is due to differences in the band structure along these two directions. Inspection of the band structure shows that the first two conduction bands are well separated from the third and higher bands except near the K point. For fields applied along the (110) direction, the electrons can readily drift to states from which they can be scattered into the third and higher conduction bands. The ionization transition rate is substantially larger within the third and higher conduction bands than within the first or second bands. Therefore, when an electron transfers into the third or higher bands, it is highly likely to undergo an impact ionization event. Conversely, when the field is applied along the (001) direction, the electrons cannot directly drift to states from which they can transfer into the third and higher conduction bands. Given the large separation of the energy bands along this direction far fewer electrons, on average, then will transfer into the third and higher bands. As a result, the ionization coefficients are substantially lower for an applied field along the (001) direction.

The top end of the error bars shown in Fig.2 represents the variation of the ionization coefficient for a 5% decrease in the high energy scattering rate. The bottom end of the error bars represents the variation of the ionization coefficient for a 5% increase in the high energy scattering rate. The total variation of the ionization coefficient is of the order of ~25% in the (110) direction and ~45% in the (001) direction. As is

generally observed, the ionization coefficient is highly sensitive to variations in the scattering rate.

It is useful to further characterize the relative hardness of the threshold energy. A hard threshold implies that upon reaching the minimum energy for which an ionization event occurs, a carrier soon suffers an impact ionization event. Most semiconductor materials seem to exhibit relatively soft thresholds, i.e., the carriers drift to energies substantially above the minimum necessary for an ionization event before impact ionizing. The character of the threshold can best be ascertained from the quantum yield. The quantum yield is defined as the average number of impact ionization events caused by a high energy injected carrier until its kinetic energy relaxes below the ionization threshold through scattering and/or impact ionization. The calculated quantum yield for electrons in InN is shown in Figure 3. As can be seen from Fig. 3, a substantial number of carriers survive to energies of 5.5 – 6 eV, nearly three times the energy gap, before suffering an impact ionization event. This is an indication of a relatively soft threshold, significantly softer than that of either GaN [7] or ZnS[17].

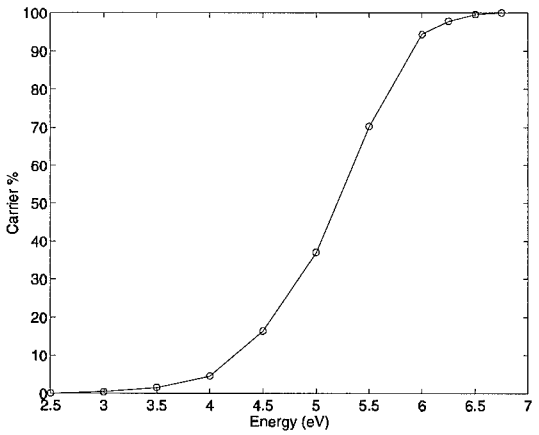


Fig.3 Calculated quantum yield for wurtzite InN as a function of the energy.

CONCLUSIONS

This paper presents the first study of high field electron transport in bulk, wurtzite InN. Theoretical results based on a full band, ensemble Monte Carlo model are presented. It is found that there exists a substantial anisotropy in the ionization coefficients, with the rate for fields applied along the (001) direction significantly less than for the (110) direction. It is further found that the threshold is relatively soft, significantly softer than either GaN or ZnS.

ACKNOWLEDGEMENTS

This work was sponsored in part through a subcontract to Georgia Tech and the University of Minnesota from the Office of Naval Research MURI program at UCSB and

by the National Science Foundation through a joint contract to the University of Minnesota and Georgia Tech, (ECS-9811366). The work at Georgia Tech was also supported by NORTEL through grant E21-5D7, and by the Office of Naval Research through contract E21-K19.

References

[1] C. Weitzel, L. Pond, K. Moore, and M. Bhatnagar, Proc. Int. Conf. on Silicon Carbide, III-Nitrides and Related Materials, Aug 31- Sept. 5, 1997, Stockholm, Sweden.
[2] K. Shenai, R. S. Scott, and B. J. Baliga, IEEE Trans. Electron Dev. **36**, 1811 (1989).
[3] M. A. Littlejohn, J. R. Hauser, and T. H. Glisson, Appl. Phys. Lett. **26**, 625 (1975).
[4] B. Gelmont, K. Kim, and M. Shur, J. Appl. Phys. **74**, 1818 (1993).
[5] N. S. Mansour, K. W. Kim, and M. A. Littlejohn, J. Appl. Phys. **77**, 2834 (1995).
[6] J. Kolnik, I. H. Oguzman, K. F. Brennan, R. Wang, P. P. Ruden, and Y. Wang, J. Appl. Phys. **78,** 1033 (1995).
[7] J. Kolnik, I. H. Oguzman, K. F. Brennan, R. Wang, P. P. Ruden, J. Appl. Phys. **81**, 726 (1997).
[8] I. H. Oguzman, J. Kolnik, K. F. Brennan, R. Wang, T.-N. Fang, and P. P. Ruden, J. Appl. Phys. **80**, 4429 (1996).
[9] I. H. Oguzman, E. Bellotti, J. Kolnik, K. F. Brennan, R. Wang, and P. P. Ruden, J. Appl. Phys. **81**, 7827 (1997).
[10] J. D. Albrecht, R. P. Wang, P. P. Ruden, M. Farahmand, and K. F. Brennan, J. Appl. Phys. **83,** 4777 (1998).
[11] S. K. O'Leary, B. K. Foutz, M. S. Shur, U. V. Bapkar, and L. F. Eastman, J. Appl. Phys. **83**, 826 (1998).
[12] J. Kolnik, I. H. Oguzman, K. F. Brennan, R. Wang, and P. P. Ruden, J. Appl. Phys. **79**, 8838 (1996).
[13] W. R. L. Lambrecht and B. Segall, *Properties of the Group III Nitrides,* edited by J. E. Edgar (INSPEC, IEE, London, 1994).
[14] V. W. Chin, T. L. Tansley, and T. Osotchan, J. Appl. Phys. **75**, 7365 (1994).
[15] Y.C. Yeo, T. C. Chong, and M.F. Li, J. Appl. Phys. **83**, 1429 (1998).
[16] B. K. Ridley, *Quantum Processes in Semiconductors,* (Oxford, Oxford Univ. Press, 1982) p.123.
[17] E. Bellotti, K. F. Brennan, R. Wang, and P. P. Ruden, J. Appl. Phys. **83,** 4765 (1998).

PHONON DYNAMICS AND LIFETIMES OF AlN AND GAN CRYSTALLITES

Leah Bergman*, Dimitri Alexson*, Robert J. Nemanich*, Mitra Dutta**, Michael A. Stroscio**, Cengiz Balkas***, Robert F. Davis***,

*Department of Physics, North Carolina State University, Raleigh, NC 27695-8202
**U. S. Army Research Office, P. O. Box 12211, Research Triangle Park, NC 27709-2211
***Department of Materials and Science Engineering, North Carolina State University, Raleigh

Cite this article as: MRS Internet J. Nitride Semicond. Res. 4S1, G6.65(1999)

ABSTRACT

The quasi-LO and quasi-TO modes of AlN crystallite were investigated. The analysis indicates that the Raman mode behavior concurs with Loudons' model of mode-mixing in wurtzite (WZ) structure crystals which is due to the long-range electrostatic field. Phonon-lifetimes of GaN and AlN crystallites were studied via Raman lineshape. It was found that the low energy E2 mode lifetime is about an order of magnitude longer than that of the other modes, and that impurities impact significantly the phonon-lifetimes.

INTRODUCTION

Due to the long range electrostatic field associated with LO phonons, various types of interactions are possible in WZ semiconductors. Among them is the interaction between polar modes belonging to different symmetry groups which results in the creation of new mixed-symmetry phonons, referred to as quasi modes [1-2]. The first part of this paper presents a study of the LO and TO quasi modes in AlN crystallite which originate from the interaction of phonons belonging to the A1 and E1 symmetry groups; the study focuses on the mode-selection rules and mode-frequency calculations as well as on the Raman technique which enables the observation of the quasi-modes [3]. The second part of the paper focuses on Raman analyses of the lifetimes of phonons in GaN and AlN crystallites [4]. The lifetime analyses indicate that the phonon lifetimes in AlN as well as in GaN fall into two main time regimes: a relatively long time of the low energy E2 mode, which will be referred to as E2(low), and the much shorter times of the high energy E2 mode (referred to as E2(high)) and the E1(TO), A1(TO), and A1(LO) modes. The lifetime shortening due to impurities was also studied: the lifetimes of the Raman modes of an AlN crystallite which contains about two orders of magnitude more Si and C impurities relative to the concentration of the high quality crystallite were found to be 50 % shorter.

RESULTS AND DISCUSSION

The theory developed by Loudon formulates that in uniaxial materials the polar phonon characteristics may be affected via two interaction mechanisms: one due to the long range electrostatic field, and the other due to the short range field which exhibits the anisotropy of the vibrational force constants [2]. The phonon dynamics and thus the Raman spectra depend on which of the two mechanism is the dominant interaction.

For the case where the long range electrostatic field is the dominant mechanism, the interaction of the polar phonons with the long range electrostatic field may result in a significant frequency separation between the group of the TO phonons relative to that of the LO phonons. Moreover, the TO phonons belonging to different symmetry are grouped together in a relatively narrow frequency range; the same holds for the LO phonons. One consequence of the dominant electrostatic field interaction is that under certain propagation and polarization conditions, phonons of mixed A1 and E1 symmetry character exist and can be observed in the Raman spectra. These mixed symmetry modes are termed quasi-LO and -TO modes. The frequencies

Mat. Res. Soc. Symp. Proc. Vol. 537 © 1999 Materials Research Society

of such quasi modes are predicted by the theory to be between the values of the pure-A1 and the pure-E1 for each of the LO and the TO bands. Alternatively, for the case where the short range interatomic forces are dominant, the LO-TO splitting will be small and in this case the TO and LO mode of each symmetry group will occur in a relatively narrow band.

In AlN the E1(TO) and A1(TO) Raman frequencies are grouped together in ~60 cm^{-1} frequency range, the E1(LO) A1(LO) in ~20 cm^{-1} range, and the LO-TO group-splitting is ~220 cm^{-1}. The frequency scheme of AlN thus implies the dominance of the long range electrostatic force interaction. The mode-mixing in AlN may occur if the propagation direction (q-vector) of the quasi-polar phonons, their polarization LO, and one of their two TO's, lie in the plane which spans between the c and the a_1 (or a_2) crystallographic axes [1]. This plane is referred as to the mixing plane. For example, the pure-A1 phonon has a c-direction polarization while the pure-E1 phonon is polarized in the basal plane; thus a quasi-phonon with the q-vector between the c and the a_1 axes would exhibit a mixed polarization of A1-E1 symmetry. When the q-vector lies along the crystallographic axes or in the a_1-a_2 plane only pure phonons are observed in the spectra.

In this study we observed the AlN quasi-TO and -LO modes by rotating the crystallite relative to the laboratory coordinate system as schematically depicted in Figure 1. In the figure, the X, Y, and Z are the axes of the fixed coordinate laboratory system (where X is out of the paper plane), while the c, a_1 and a_2 are the axes of the rotating coordinate system of the crystal (where a_2 is out of the paper plane and is coincided with the X-axis), and N is the normal to the crystallite surface (and is coincided with the a_1-axis). The AlN crystallite was rotated through an angle θ about the X-axis such that the quasi-phonon propagation direction, the q-vector (**q**), as well as its LO and one of its two TO components lay in the mixing c-a_1 plane (the other TO is along the X-axis). The micro-Raman spectra was acquired in a back scattering geometry from the Y-axis for various values of θ.

In order to investigate the polarization conditions upon which the quasi modes appear in the spectra, the Raman tensors, R_θ, of the rotating crystal (relative to a fixed X, Y, Z laboratory coordinate system) are calculated via the rotational transformation equation [5]: $R_\theta = T_X R T_X^{-1}$ where T_x is the rotation matrix about the X-axis. The Raman tensors of the WZ structure take the form:

$$A1_c(\theta) = \begin{pmatrix} h & 0 & 0 \\ 0 & h\cos^2\theta + b\sin^2\theta & b\sin\theta\cos\theta - h\sin\theta\cos\theta \\ 0 & b\sin\theta\cos\theta - h\sin\theta\cos\theta & h\sin^2\theta + b\cos^2\theta \end{pmatrix}$$

$$E1_X(\theta) = \begin{pmatrix} 0 & d\sin\theta & d\cos\theta \\ d\sin\theta & 0 & 0 \\ d\cos\theta & 0 & 0 \end{pmatrix} \qquad E1_{a_1}(\theta) = \begin{pmatrix} 0 & 0 & 0 \\ 0 & 2d\sin\theta\cos\theta & d\left(\cos^2\theta - \sin^2\theta\right) \\ 0 & d\left(\cos^2\theta - \sin^2\theta\right) & -2d\sin\theta\cos\theta \end{pmatrix}$$

$$E2(\theta) = \begin{pmatrix} 0 & f\cos\theta & -f\sin\theta \\ f\cos\theta & 0 & 0 \\ -f\sin\theta & 0 & 0 \end{pmatrix} \qquad E2(\theta) = \begin{pmatrix} f & 0 & 0 \\ 0 & -f\cos^2\theta & f\cos\theta\sin\theta \\ 0 & f\cos\theta\sin\theta & -f\sin^2\theta \end{pmatrix} \qquad (1)$$

The tensors describe the in-crystal projections, due to the rotation, of the incident and scattered polarization of the light. Moreover, for each polar mode the direction of the polarization is indicated in the subscripts: A1 is polarized along the c axis while E1 is polarized along a_1 and a_2, the latter which coincides with the X-axis ($E1_X$). The polarization direction of the polar modes, like the Raman tensors, can be expressed in terms of the laboratory coordinate system; however, it is not necessary for the present study. For θ=0 the crystal coordinate system coincides with that of the laboratory (a_1=Y and c=Z, see Fig. 1), and Eq. 1 takes the usual form [1-2].

For the first set of experiments we chose the Raman setup such that the incident light is polarized along the X-axis and the scattered light has both X and Z polarization directions,

expressed in Porto notation [6] as: $Y\left(X\ \frac{X}{Z}\right)\overline{Y}$. This choice of polarization implies that the XX and the XZ components of each of the Raman tensors will contribute a Raman signal provided they are not zero. Figure 2 presents the Raman spectra for this setup for rotations: $\theta = 0°$, 35°, and 70°. Inspection of Eq.1 indicates that the E2 mode should appear in the spectra since the XX and the XZ components of its tensors are not zero; our spectra display the E2 mode at 655 cm^{-1}. This mode is non-polar and as such no change in frequency is expected as a function of the rotation. The XZ component of the $E1_x$ is non-zero, and although the q-vector of the mode lies in the a-c mixing plane its polarization is not: it is in the X-direction (TO component) and thus no symmetry mixing is expected. This analysis indicates that the spectra should exhibit the pure-E1(TO) with no change of frequency upon rotation. The pure-E1(TO) in our spectra is at 669 cm^{-1} and is independent of rotation.

Next we investigated the A1 mode which contributes a signal to the Raman spectra via the non-zero value of its XX tensor component. The pure-A1 mode has solely c-polarization; however, upon rotating the crystal quasi modes are created for which their TO and LO components have a c-polarization component of A1 symmetry as well as an a_1-polarization component of E1 symmetry. This situation is schematically depicted in the inset to Figure 1. In the figure, the TO component of the quasi-mode lies in the mixing plane and is composed of A1 and E1 polarization symmetry components; the quasi-TO mode will have mostly A1 symmetry for q-vectors near the a-axis and mostly E1 symmetry for q-vectors near the c-axis. The frequency of the quasi-TO, according to Loudons' theory, should be between the frequency of the pure-A1(TO) mode and that of the pure-E1(TO) mode [2]. As can be seen in Figure 2, the frequency of the A1(TO) mode shifts from its pure value at 608 cm^{-1} towards that of the E1(TO) mode as a function of the rotation angle: for $\theta=35°$ the peak of the quasi-TO is at 614 cm^{-1} and for $\theta=70°$ is at 620 cm^{-1}. The spectrum of $\theta=70°$ exhibits a small peak of the pure-A1(TO) and is attributed to an internal reflection.

The frequencies of the quasi-TO can be calculated via the relation [1-2]

$$\omega^2_{Q(TO)} = \omega^2_{E1(TO)}\cos^2(90-\beta) + \omega^2_{A1(TO)}\sin^2(90-\beta) \qquad (2)$$

where β (see Fig. 1) is the propagation angle of the q-vector of the quasi-phonon ($\mathbf{q}$) in the crystallite, and is related to the angle of rotation, θ, via Snell's law and the momentum-conservation law of the Raman scattering effect as is discussed next. The conservation law states that in the scattering medium $\mathbf{q} = \mathbf{k}_i - \mathbf{k}_s$ where $\mathbf{k}_i$ and $\mathbf{k}_s$ are wavevectors of the incident and scattered photons respectively [2]. Thus, for our backscattering geometry the q-vector lies along the same path as that of the incident and scattered photons. To find the angle, β, of that path the index of refraction has to be taken into account via Snell's law: $n_1\sin\theta=n_2\sin\beta$, where for air $n_1=1$ and for AlN $n_2=2.2$ which is the accepted value in the visible range and of negligible anisotropy [7]. Our calculations yield a value of $\beta=15°$ for the rotation $\theta=35°$, and from Eq. 2, $\omega_{Q(TO)} = 612\ cm^{-1}$, a value which concurs with our experimental finding of 614 cm^{-1}. For the 70° rotation, $\beta=25°$ and $\omega_{Q(TO)} = 619\ cm^{-1}$, a value which is similar to the experimental result of 620 cm^{-1}.

Lastly we investigated the quasi-LO Raman mode. In order to observe this mode the incoming polarization of the light was set at the Z-direction such that the Raman geometry was $Y\left(Z\ \frac{X}{Z}\right)\overline{Y}$. This Raman geometry enables the observation of the quasi-LO modes since the ZZ component of the $E1_{a_1}$ Raman tensor is non-zero for $\theta>0$ as is indicated by Eq. 1. In this configuration the q-vector of the phonon as well as its polarization directions lie in the mixing plane. Figure 3 presents the Raman spectra of the quasi-LO mode for $\theta=15°$, 35°, and 70°, and the pure A1(LO) mode at $\theta=90°$; the Raman peak positions are at 913 cm^{-1}, 912 cm^{-1}, 908 cm^{-1}, and 890 cm^{-1} respectively. Taking into account the index of refraction and utilizing the equation for the quasi-LO frequencies [1-2],

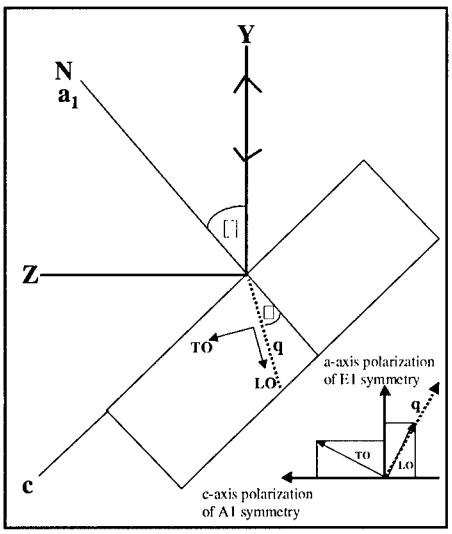


Fig. 1. The experimental setup. The laboratory system: X (out of the paper), Y, and Z. The rotating crystal system: c, a_1. N is the normal and θ is the rotation angle about the X-axis, β is the angle of refraction and defines phonon propagation. The dashed line represents the phonon q-vector the arrows are its LO and TO components. The Raman spectra was acquired in a back scattering geometry from the Y axis.

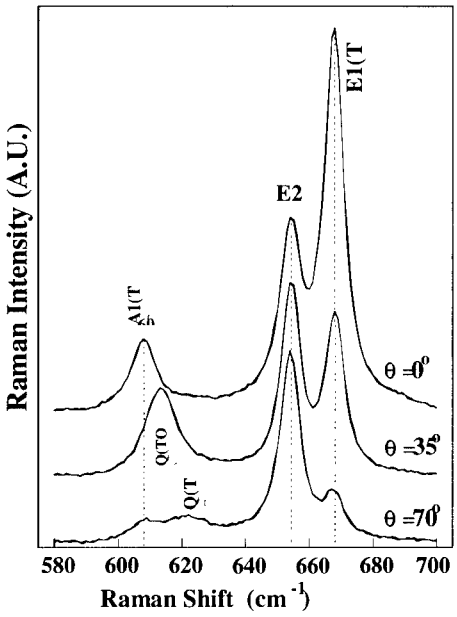


Fig. 2. The quasi-TO modes: 620, and 614 cm^{-1}. the pure A1(TO) is at 608 cm^{-1}.

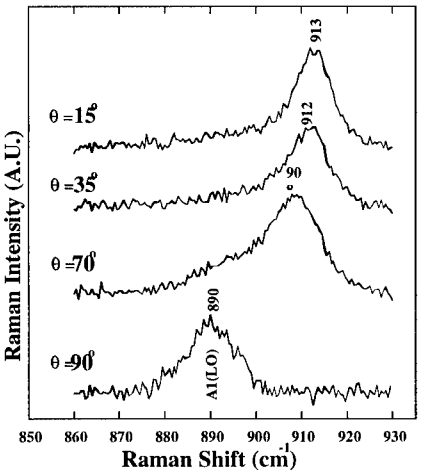


Fig. 3. The quasi-LO modes: 913, 912, and 908 cm^{-1}. The pure A1(LO) is at 890 cm^{-1}.

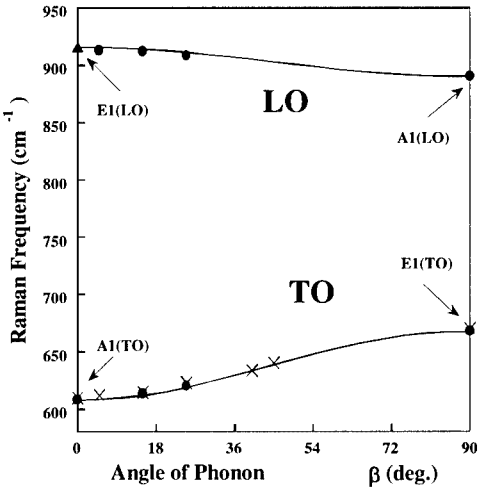


Fig. 4. The quasi-mode frequency as a function of the phonon-propagation direction. The lines represent Loudons' model, the dots our data, and the x's are from [9].

$$\omega^2_{Q(LO)} = \omega^2_{A1(LO)}\cos^2(90-\beta) + \omega^2_{E1(LO)}\sin^2(90-\beta) \quad (3)$$

where $\omega_{ad(LO)}$ is 890 cm^{-1} and $\omega_{E1(LO)}$ is 916 cm^{-1} [8], we found the calculated quasi frequencies to be 915 cm^{-1}, 914 cm^{-1}, and 911 cm^{-1}, which agree well with the above experimental values.

Figure 4 summarizes our findings. In the figure the lines denote the TO and LO quasi-frequencies calculated utilizing Loudons' model (Eqs. 2 and 3), and the dots represent our experimental values for the modes. The additional data points of the quasi-TO modes, represented by X's, are from Filippidis et al who were the first to observe the quasi-TO modes in AlN [9]; our results are in agreement with theirs. Moreover, as depicted in the figure, our study of the quasi-TO as well as the quasi-LO concur with Loudons' model, implying the presence of a long range electrostatic field which is active in the coupling of modes belonging to the different symmetry groups.

PHONON-LIFETIMES

In order to obtain the phonon-lifetime via the Raman spectral linewidth, the linewidth has to be corrected for the contribution of the instrumental bandpass broadening. In order to do so, the Raman spectra were acquired at successive slit widths ranging from 400 μm down to 100 μm; the measured linewidth-values, W_M, were plotted as a function of the slit width, W_S, and extrapolated to the zero slit-value, W_P, via the relation:

$$W_M = \sqrt{W_P^2 + \left(W_S * 9.2 * 10^{-3}\right)^2} \quad (4)$$

The second term in Eq. 4 is the instrumental bandpass, i.e., the slit width multiplied by the monochromator linear dispersion, $9.2*10^{-3}$ $cm^{-1}/\mu m$. This method yields the actual phonon linewidth, W_P, from which the phonon lifetime can be calculated.

In general, two main mechanisms control the phonon lifetimes: the phonon anharmonic interactions in which a phonon decays into other phonons, and the phonon scattering at impurity or defect centers [10-11]. The energy conservation law of the anharmonic decay requires that the energy of the decay phonon be equal to the sum of the energies of the created phonons. In the following we present a study of phonon-lifetime in two types of AlN crystallites, referred to as blue and transparent, which differ mainly in their impurity contents: the blue crystallite contains about two orders of magnitude more Si and C impurities then the transparent AlN [12].

In order to calculate the phonons lifetime via the Raman linewidths, the linewidths were plotted as a function of the slit width and a curve fit was obtained via Eq. 4. The results are presented in Fig. 5: the dots represent the data taken from the transparent AlN while the squares data from the blue crystallite. It is evident from the figure that the linewidth of all the Raman modes are strongly correlated with the impurity concentration. The values of the Raman linewidths at the zero slit width may be used to evaluate the phonons lifetime, τ, via the energy-time uncertainty relation: $\Delta E/\hbar = 1/\tau$. Where ΔE is the Raman linewidth in units of cm^{-1}, and $\hbar = 5.3*10^{-12}$ cm^{-1}-sec. Table I summarizes the results: for each sample the zero slit linewidth is presented along with the calculated lifetime of the Raman modes. Two main conclusions can be drawn from the above results: the lifetimes are correlated with the impurity concentration, and the E2(low) mode of both samples has a significantly longer lifetime than that of the E2(high), E1(TO), A1(TO), and A1(LO) modes. The lifetimes of an high quality GaN crystallite were analyzed as well; the lifetimes computed via the above described method are summarized in Table I. Similar to the AlN lifetimes, the E2(low) mode of the GaN has a significantly longer lifetime than that of the E2(high), E1(TO), and A1(TO) modes. The A1(LO) was not observed in the spectra and its absence is attributed to the plasmon damping. The relatively long lifetime of the E2(low) mode is attributed to its small anharmonic decay probability. Unlike the other modes, the energy of the E2(low) mode lies at the low energy regime of the wurtzite dispersion curve, and only the acoustical phonons are available as a channel of decay [13]. Inspection of the dispersion curves reveals that in order for the energy conservation to hold the E2(low) mode is allowed to decay into acoustical modes of very low density of state. This implies the small probability of decay and thus the long lifetime; a model calculation will be presented at a later date.

Table I. Linewidth Γ (cm^{-1}) and lifetime τ (ps)

	AlN Transp.		AlN Blue		GaN	
Mode	Γ	τ	Γ	τ	Γ	τ
E2(low)	1.2	4.4	2.6	2.0	0.5	10.1
E2(high)	6.4	0.83	12.4	0.43	3.9	1.4
E1(TO)	5.8	0.91	10.0	0.53	5.6	0.95
A1(TO)	7.0	0.76	14.4	0.37	11.6	0.46
A1(LO)	11.9	0.45	18.9	0.28		

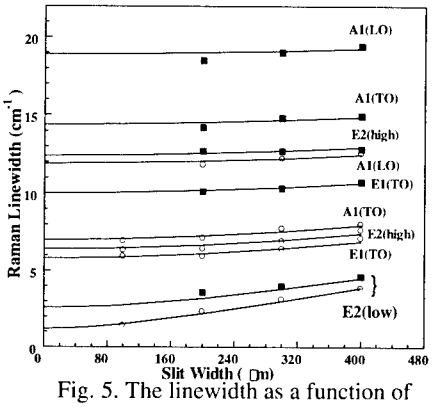


Fig. 5. The linewidth as a function of slitwidth. Data from transparent AlN: circles; blue AlN: squares.

CONCLUSIONS

The analyses indicate that the Raman mode behavior in AlN concurs with Loudons' model of mode-mixing in WZ structure which is due to the dominance of the long-range electrostatic field. Phonon-lifetimes of GaN and AlN crystallites were studied via Raman lineshape. It was established that the E2(low) mode lifetime is about an order of magnitude longer than that of the other modes, and that impurities significantly shorten the phonon-lifetimes.

ACKNOWLEDGEMENTS

The author acknowledges the National Research Council and the Army Research Office for supporting this research.

REFERENCES

1. C.A. Arguello, D.L. Rousseau, and S.P.S. Porto, Phys. Rev. **181**, 1351 (1969).
2. R. Loudon, Advan. Phys. **13**, 423 (1964).
3. L. Bergman, M. Dutta, R.J. Nemanich, and R.F. Davis, To appear in J. Appl. Phys. (1999).
4. L. Bergman, M. Dutta, M.A. Stroscio, R.J. Nemanich, and R.F. Davis, To appear in Phys. Rev.B. (1999).
5. D. A. Long , *Raman Spectroscopy*, (McGraw-Hill, New York, 1977).
6. S.P.S Porto, in *Light Scattering Spectra of Solids*, (G.B. Wright, ed. Springer-Verlag, Berlin, 1969).
7. S. Loughin, and R. H. French, *Properties of Group III Nitrides*, p. 175. Ed. J. H. Edgar, (INSPEC, London, 1994).
8. L.E. McNeil, M. Grimsditch, and R.H. French, J. Am. Ceram. Soc. **76**, 1132 (1993).
9. L. Filippidis, H. Siegle, A. Hoffmann, C. Thomsen, K. Karch, and F. Bechstedt, Phys. Stat. Sol. **B198**, 621 (1996).
10. P.G. Klemens, Phys. Rev. **148**, 845 (1966).
11. K.T. Tsen, D.K. Ferry, A. Botchkarev, B. Sverdlov, A. Salvador, and H. Morkoc, Appl. Phys. Lett. **72**, 2132 (1998).
12. C.M. Balkas, Z. Sitar, T. Zheleva, L. Bergman, R.J. Nemanich, and R.F. Davis. J. Crys. Growth **179**, 363 (1997).
13. J.C. Nipko, and C.K. Loong, Phys. Rev. **B57**, 10550 (1998).

Part VII

LEDs, UV Detectors, and Optical Properties

SYMMETRY OF ELECTRONS AND HOLES IN LIGHTLY PHOTO-EXCITED

InGaN LEDs

T.A. Kennedy,* E.R. Glaser,* W.E. Carlos,* P.P. Ruden** and Shuji Nakamura***

*Naval Research Laboratory, Washington, DC 20375, kennedy@bloch.nrl.navy.mil
**University of Minnesota, Department of Electrical and Computer Engineering, Minneapolis, MN 55455
***Nichia Chemical Industries Ltd., Department of Research and Development, Tokushima, JAPAN

Cite this article as: MRS Internet J. Nitride Semicond. Res. 4S1, G7.4(1999)

ABSTRACT

The symmetry of the recombining electrons and holes in lightly photo-excited InGaN LEDs revealed through ODMR is related to the physical structure, band structure and defects present. Calculations of the electron-g within the $k \cdot p$ formalism give the average shift from the free-electron value for GaN but are not fully reconciled with the anisotropy. This theory is also extended to InGaN alloys for both pseudomorphic and relaxed layers. The average shift is close to the experimental values for the green LED. The strongly reduced hole anisotropies seen experimentally are explained by a recently published theory for acceptors in GaN.

INTRODUCTION

Advances in nitride materials have led to the development of state-of-the-art LEDs in the visible range and lasers in the near uv [1]. While the success of these nitride devices has been remarkable, there is a need for an improved understanding of the recombination process. Interest at the moment is focused on the influence of the spontaneous polarization, the piezoelectric effect arising mismatch-induced strain and the potential fluctuations associated with the tendency in InGaN alloys toward phase separation. Numerous studies of these effects have been published. Among the optical characterizations are studies of photoluminescence, photoluminescence excitation and photoluminescence decay [1-5]. These studies reveal the effects of charge separation of the electron and hole in the growth direction and localization of the carriers or excitons by potential fluctuations in the growth plane.

Optically detected magnetic resonance (ODMR) has recently been observed in green and extra-blue InGaN single-quantum well diode structures [6]. The distinct electron and hole resonances denote significant charge separation in the lightly photo-excited structures. Analysis of the frequency dependence of the ODMR for magnetic-dipole microwave transitions gives long lifetimes [7]. The ODMR technique is particularly valuable since the g-factors directly reflect the symmetry of the recombining electron and hole. This symmetry reveals the detailed structure determining the electron- and hole-states.

This paper explores the link between the symmetry as revealed by ODMR and the vertical and lateral structure of the InGaN LED. Theories for the g-factor of electrons and localized holes are presented, extended and compared with experiment. For the electron, the present extensions of the theory are still inadequate to achieving a good understanding of the data. For the hole, new spectral data is presented and discussed using a recent theory for acceptors in GaN [8]. The analysis shows that the hole states are affected by strong in-plane strain.

Mat. Res. Soc. Symp. Proc. Vol. 537 © 1999 Materials Research Society

SYMMETRY OF THE ELECTRON

The g-factor for a conduction electron in a direct-gap semiconductor can be calculated using ***k•p*** theory [9]. The g-values for GaN were calculated within a cubic approximation [10]. It is necessary to include both the valence bands and the upper conduction bands in order to achieve agreement with experiment. The experiments in InGaN LEDs show changes in the average g-factor and in the anisotropy of the g-factor[6]. Hence it is necessary to extend the calculations to include the wurtzitic crystal fields, the changes in band structure in moving from GaN to the InGaN alloy, and effects due to the quantum well and differing barrier layers. The following paragraphs address these issues.

First, the anisotropic g-tensor for electrons in wurtzitic GaN is calculated. Two sets of band parameters were chosen [11]. The first is a "best" set from a mix of theory and experiment within a quasi-cubic approximation. The second is a full set of calculated values. The energy differences , crystal-field and spin-orbit splittings and interband matrix elements are shown in Fig. 1 and collected in Table 1. For coupling between the lowest conduction band and the uppermost valence band, the expressions for the g-factors are

$$\frac{g_{\parallel}}{g_0} - 1 = \frac{-P^2}{2}\left\{\frac{1}{E_0 - E_A} - \frac{\gamma_1^2}{E_0 - E_B} - \frac{\left(1-\gamma_1^2\right)}{E_0 - E_C}\right\} \qquad \text{and} \qquad (1a)$$

$$\frac{g_{\perp}}{g_0} - 1 = \frac{-P^2}{2}\left\{\frac{1}{E_0 - E_B} - \frac{1}{E_0 - E_C}\right\}\sqrt{2}\cdot\gamma_1\sqrt{1-\gamma_1^2} \qquad (1b)$$

where

$$\gamma_1 = \frac{\gamma}{\sqrt{\gamma^2 - 1}}\ , \qquad \gamma = \frac{\Delta_1 - \Delta_2 + \sqrt{\left(\Delta_1 - \Delta_2\right)^2 + 8\Delta_3^2}}{2\sqrt{2}\Delta_3} \qquad \text{and} \qquad (2)$$

$$E_A = \Delta_1 + \Delta_2 \qquad E_B = \frac{1}{2}\left\{\left(\Delta_1 - \Delta_2\right) + \sqrt{\left(\Delta_1 - \Delta_2\right)^2 + 8\Delta_3^2}\right\} \qquad (3)$$

$$E_C = \frac{1}{2}\left\{\left(\Delta_1 - \Delta_2\right) - \sqrt{\left(\Delta_1 - \Delta_2\right)^2 + 8\Delta_3^2}\right\}$$

Similarly, the contributions from the upper conduction bands were calculated using the same equations with the upper conduction band parameters replacing the valence band contributions. The contributions from both bands add and are of the same magnitude. The resulting total g-factors are given in Table 2 for both the "best" parameters and the calculated parameters. The

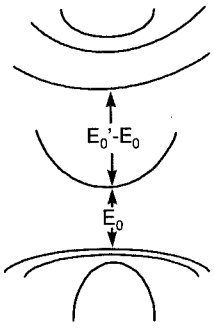


Figure 1. Band structure for wurtzitic nitrides.

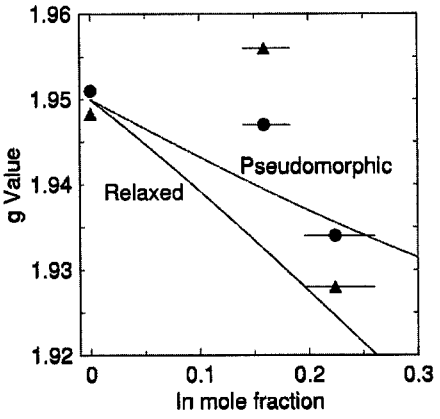


Figure 2. Electron g-factors in InGaN. The dashed lines are calculated for relaxed and pseudomorphic layers. The circles are $g_{\parallel}$ and the triangles $g_{\perp}$.

average shift from the free-electron g-factor is predicted well. The anisotropy is of the right order but with differing signs: disagreeing with experiment for the "best" parameters but with the right sense for the calculated parameters. Thus the anisotropy in wurtzitic GaN depends in a delicate way on the band parameters.

Table 1. Band parameters used in the ***k•p*** calculations.

	E_0	Δ_1	Δ_2	Δ_3	P^2	E_0'	Δ_1'	Δ_2'	Δ_3'	P'^2
Best GaN	3.5eV	10 meV	6.3 meV	(6.3 meV)	22.5 eV	9.015 eV	-0.406 eV	0.112 eV	(0.112 eV)	9 eV
Calculated GaN		36 meV	5.0 meV	5.9 meV						
InN	1.89 eV	43 meV	0.3 meV	0.3 meV	22.5 eV	7.91 eV		0.284 meV	0.284 meV	9 eV

Table 2. Electron g-values in wurtzitic GaN.

	$g_{\parallel}$	$g_{\perp}$
Experiment	1.9510	1.9483
Best	1.952	1.953
Calculated	1.955	1.954

In previous work the g-values have been calculated for In-mole fractions up to 0.4 [6,7]. The calculations were done for unstrained alloys assumed to be cubic. Here these calculations are improved by incorporating the recent results for the energy-gap dependence on alloy composition [12]. The new relationship allows a comparison of the g-factors with calculations for both pseudomorphic and fully relaxed InGaN.

The new calculations were done by combining the gap equation with a $\boldsymbol{k \cdot p}$ calculation within a quasi-cubic approximation. The equation for the energy gap is

$$E_G = 3.42 (1 - x) + 1.89 x - b x (1 - x), \quad (4)$$

where the bowing parameter, b, is 2.6 eV for a pseudomorphic layer and 3.8 eV for a fully relaxed layer. Since the original estimates for x for the green and extra-blue diodes were made with a bowing parameter of 1 eV, these need to be revised. The green changes from 0.43 to 0.22 and the extra-blue from 0.3 to 0.16. The band parameters for InN are shown in Table 1. The interband matrix elements are taken from GaN. E_0' and Δ_2' are scaled from GaN using the ratio of the values of atomic transitions. Δ_1 and Δ_2 for InN are taken from first-principles calculations [13]. For the pseudomorphic layers, strain introduces a Δ_1 by a deformation potential taken also from the first-principles calculations. Δ_1, Δ_2, Δ_2' and E_0' are then scaled to different In mole fractions by a virtual crystal approach. The g-shifts versus mole-fraction obtained in this way needed to be scaled by 15 % to match at GaN.

The calculated g-factors versus mole fraction for both relaxed and pseudomorphic layers are plotted along with the data in Fig. 2. The experimental values for the green diode, expected to be relaxed, fall close to the calculated values. However, the g-values for the extra-blue diode lie substantially above the calculated lines. From the reversal in anisotropy for this structure and its lower mole-fraction, the extra-blue diode is expected to be pseudomorphic. Thus while the calculation approximates the g-factors for the green diode, other interactions must be important for the extra-blue diode.

The next step in this analysis is to consider the effect of the quantum well potential. Theories have been developed for other heterostructure systems [14]. The strain, confinement and piezoelectric effect present in the InGaN LED structure certainly provide enough interactions to produce the reversal in symmetry observed experimentally. Hence, it does seem likely that a clear understanding of the symmetry of the electronic state can be deduced from the experimental data.

SYMMETRY OF THE HOLE

The g-factors for an acceptor in a wide-bandgap semiconductor have been calculated [8] for an acceptor including both Coulomb and central-cell potentials. Formulation of the problem in k-space avoids a divergence at the origin. The calculation is first done in a spherical approximation with only the Coulomb and central-cell potentials. The Coulomb interaction gives a binding energy of 200 meV. The crystal field is introduced as a strain in the [111] direction which corresponds to a crystal-field splitting of 37 meV. Spin-orbit interaction is then added to produce a splitting of 12 meV. This reproduces the conditions in GaN with perfect crystal structure and leads to highly anisotropic g-values. Since previous ODMR studies of acceptors in GaN revealed g-tensors which are only weakly anisotropic [15,16], the authors then consider an additional strain which lowers the symmetry at the acceptor from axial to rhombic and produces a reduction in the g-anisotropy. The authors attribute the reduction in symmetry to the Jahn-Teller effect but the symmetry lowering could arise from other sources.

The results of this theory can be summarized by considering the g-factors as a function of the symmetry-lowering strain energy (See Fig. 3). For an acceptor in purely axial symmetry $g_\parallel$ is -3.3 and $g_\perp$ is 0. In-plane strain becomes important as its associated energy becomes comparable to the spin-orbit splitting of 12 meV. For large in-plane strain, the g-tensor becomes less anisotropic and reverts to the free-electron value of 2.00.

When all the luminescence is collected from the green LED, the g-tensor for the hole is $g_{\|}$ =2.08 (1) and $g_{\perp}$ = 1.996 (3)[6]. The anisotropy is strongly reduced from that expected for holes in purely axial symmetry. Using filters, a spectral study has been performed which reveals that the $g_{\|}$ changes for emission at different energies (See Fig. 4). In the study, long-pass filters were used to detect all the emission across the green band and the emission from the lower-energy half of the band. A subtraction reveals the part characteristic of the upper energy-range with $g_{\|}$ = 2.20 and the one filter gives the lower range with $g_{\|}$ = 2.09. There is a direct correlation between decreasing energy and decreasing g-value. This may arise in part from a changing hole g-factor with changing In-concentration. However, the character of the hole may also be changing. Since a deepening in energy is expected with increasing in-plane strain, the reduction in anisotropy with energy may also arise from increased in-plane strain.

In summary, the g-tensor for holes in lightly photo-excited InGaN reveals states which differ from those of the band edge and those for bound holes in purely axial symmetry. The binding could arise from either an acceptor or a fluctuation in composition of the alloy. The theory which describes the changes in g-tensor for different values of in-plane strain provides a solid framework to interpret the data. Spectral studies of the g-factor show that the anisotropy decreases with decreasing emission-energy. Compositional change and greater non-axial strain produce the reduction in anisotropy. These results are consistent with the behavior of acceptors in other semiconductors [17].

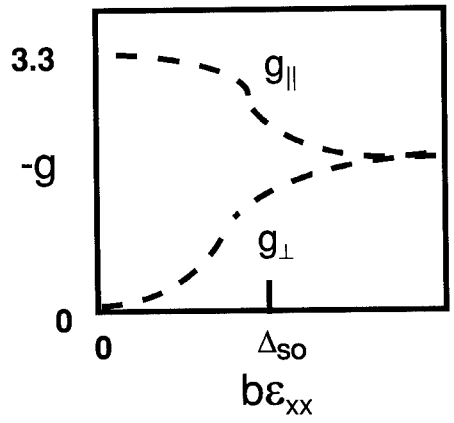


Figure 3. Hole g-factors in GaN versus the energy associated with an in-plane strain. The measure of the energy is the spin-orbit splitting.

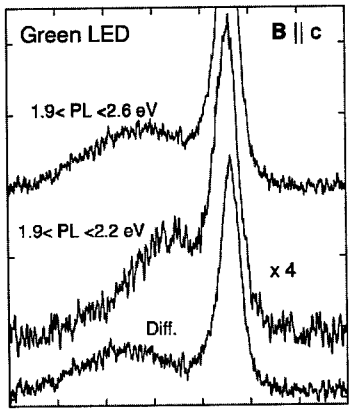


Figure 4. Spectral decomposition of the ODMR for the Green LED. The two experimental curves are subtracted to give the difference spectrum.

SUMMARY

The symmetry of the g-factors of recombining electrons and holes in InGaN is related to the band structure and local perturbations of that structure. For GaN, the average g-factor for electrons can be deduced from known band parameters but the anisotropy is difficult to calculate. Improved calculations are made for both pseudomorphic and relaxed InGaN. Again the anisotropy is beyond the current calculations. The hole g-anisotropy is strongly reduced from that for the band edge. A recent theory for acceptors in GaN demonstrates the experimental features and reconciles them with strong in-plane strain.

ACKNOWLEDGEMENTS

The work at NRL was supported by ONR. We thank I. Merkulov for helpful conversations. PPR thanks W.R.L. Lambrecht for unpublished GaN band structure data.

REFERENCES

1. Nakamura and Fasol, *The Blue Laser Diode* (Springer, Berlin, 1997).
2. K.P. O'Donnell, T. Breitkopf, Hl.Kalt, W. Van Der Stricht, I. Moerman, P. Demeester and P.G. Middleton, Appl. Phys. Lett. **70**, 1843 (1997).
3. S.F. Chichibu, A.C. Abare, M.S. Minsky, S. Keller, S.B. Fleischer, J.E. Bowers, E. Hu, U.K. Mishra, L.A. Coldren, S.P. DenBaars and T. Sota, Appl. Phys. Lett. **73**, 2006 (1998).
4. Yong-Hoon Cho, G.H. Gainer, A.J. Fischer, J.J. Song, S. Keller, U.K. Mishra and S.P. DenBaars, Appl. Phys. Lett. **73**, 1370 (1998).
5. T.J. Schmidt, Yong-Hoon Cho, G.H. Gainer, J.J. Song, S. Keller, U.K. Mishra and S.P. DenBaars, Appl. Phys. Lett. **73**, 1892 (1998).
6. E.R. Glaser, T.A. Kennedy, W.E. Carlos, P.P. Ruden and S. Nakamura, Appl. Phys. Lett. **73**, 3123 (1998).
7. W.E. Carlos, E.R. Glaser, T.A. Kennedy and Shuji Nakamura, J. Electron Mater., to be published.
8. A.V. Malyshev, I.A. Merkulov and A.V. Rodina, Phys. Solid State **40**, 917 (1998).
9. C. Hermann and C. Weisbuch in *Optical Orientation*, F. Meier and B.P. Zakharchenya, editors (North Holland, Amsterdam, 1984), p. 463.
10. W.E. Carlos, J.A. Freitas, Jr., M. Asif Khan, D.T. Olson and J.N. Kuznia, Phys. Rev. B **48**, 17,878 (1993).
11. Kwiseon Kim,Walter R.L. Lambrecht, Benjamin Segall and Mark van Schilfgaarde, Phys. Rev. B **56**, 7363 (1997).
12. C. Wetzel, T. Takeuchi, S. Yamaguchi, H. Katoh, H. Amano and I. Akasaki, Appl. Phys. Lett. **73**, 1994 (1998).
13. Su-Huai Wei and Alex Zunger, Appl. Phys. Lett. **69**, 2719 (1996).
14. E.L. Ivchenko and A.A. Kisilev, Sov. Phys. Semicond. **26**, 827 (1992).
15. M. Kunzer, J. Baur, U. Kaufmann, J. Schneider, H. Amano and I. Akasaki, Solid-State Electron. **41**, 189 (1997).
16. E.R. Glaser, T.A. Kennedy, K. Doverspike, L.B. Rowland, D.K. Gaskill, J.A. Freitas, Jr., M. Asif Khan, D. T. Olson, J.N. Kuznia and D.K. Wickenden, Phys. Rev. B **51**, 13,326 (1995).
17. T.N. Morgan, *Proceedings of the Tenth International Conference on the Physics of Semiconductors* (U.S. Atomic Energy Commission, 1970), p. 266.

FABRICATION OF SMOOTH GaN-BASED LASER FACETS

D. A. Stocker,* E. F. Schubert,* K. S. Boutros,** J. M. Redwing**

*Center for Photonics Research, Boston University, Boston, MA 02215
**Epitronics, Phoenix, AZ 85027

Cite this article as: MRS Internet J. Nitride Semicond. Res. 4S1, G7.5 (1999)

ABSTRACT

A method is presented for fabricating fully wet-etched InGaN/GaN laser cavities using photoenhanced electrochemical wet etching followed by crystallographic wet etching. Crystallographic wet chemical etching of n- and p-type GaN grown on c-plane sapphire is achieved using H_3PO_4 and various hydroxides, with etch rates as high as 3.2 μm/min. The crystallographic GaN etch planes are {0001}, $\{10\bar{1}0\}$, $\{10\bar{1}\bar{1}\}$, $\{10\bar{1}\bar{2}\}$, and $\{10\bar{1}3\}$. The vertical $\{10\bar{1}0\}$ planes appear perfectly smooth when viewed with a field-effect scanning electron microscope (FESEM), indicating a surface roughness less than 5 nm, suitable for laser facets. The etch rate and crystallographic nature for the various etching solutions are independent of conductivity, as shown by seamless etching of a p-GaN/undoped, high-resistivity GaN homojunction.

INTRODUCTION

Most post-growth processing of the III-nitrides is currently done by dry plasma etching.[1,2] There are several disadvantages to dry etching, including the generation of ion-induced damage[3] and difficulty in obtaining smooth etched sidewalls, which are required for lasers. The typical root-mean-square (RMS) roughness of sidewalls produced by dry etching is on the order of 50 nm,[4,5] although recently surfaces with an RMS roughness as low as 4-6 nm have been reported.[6] Photoenhanced electro-chemical (PEC) wet etching has also been demonstrated for etching of GaN.[7-10] PEC etching has the advantage of low surface damage and low equipment cost, but a method for producing smooth vertical sidewalls by this method has not yet been found. Recently, a two-step process including crystallographic wet chemical etching has been demonstrated for n-type GaN.[11] This process involves one conventional etching step, such as dry etching or PEC etching, followed by a second, crystallographic wet etching step. The two-step process provides smooth surfaces and can be used to create undercut, overcut, or vertical sidewalls.

EXPERIMENT

The first of the two etching steps in the crystallographic etching process is used to establish the *etching depth*, and it can be performed by several common processing methods, including dry etching, PEC etching, and cleaving. This first step is required because the c-plane {0001} is impervious to all chemical agents investigated,[12,13] except at defect sites where etch pits occur.[14,15] In the second step the semiconductor sample is immersed in a hot chemical etchant that is able to crystallographically etch GaN. This etching step can produce smooth crystallographic surfaces, and the resulting etching planes are controlled by varying the orientation of the first step and the chemical agents and temperature of the second step. The etch

Mat. Res. Soc. Symp. Proc. Vol. 537 © 1999 Materials Research Society

rates and crystal planes observed for all chemicals used in this work are summarized in Table I. The etching planes listed in this table are those that appear during the etch.

In all cases the etch rate in the "vertical" [0001] direction is immeasurably small, but etching occurs "horizontally," i.e., normal to [0001]. Because the c-plane is impervious to all of the chemicals used in this study, no etch mask is required for the crystallographic etching step; the c-plane itself acts as a mask. An etch mask may be necessary, however, if long etching times are used, to prevent the development of etch pits at defect sites. For this purpose we have successfully used both titanium masks annealed at 900°C for 30 seconds in a nitrogen atmosphere and nickel masks annealed at 650°C for 2 minutes in a nitrogen atmosphere.

RESULTS

The $\{10\bar{1}0\}$ plane shown in Fig. 1 was produced by etching in 10% KOH by weight dissolved in ethylene glycol at 170°C. This plane has been examined using a high resolution field-effect scanning electron microscope (FESEM) with a resolution of 5 nm at 2.5 kV, and the surface appears perfectly smooth. This indicates that wet chemical etching may be a valuable tool for producing high-quality laser facets with reflectivities close to the ideal for a perfectly smooth surface.[16]

For this etching method to be useful for fabricating pn-junction laser diodes, the dependence of etch rate and surface morphology on doping must be determined. A scanning electron microscope (SEM) image of p-type GaN after anisotropic wet etching in molten KOH at a temperature of 195°C is shown in Fig. 2. Only the top portion of the epilayer is doped p-type; the lower 1 μm is undoped. The seamless morphology of the surface displayed in Fig. 2 indicates that the change in doping does not affect the etch plane or the etch rate. The quality of the crystallographically etched surfaces is generally lower in the p-type material than in

Table I: Etch rates and observed etching planes for various chemicals

Chemical	Temperature (°C)	Etch Rate (μm/min)	Etching Planes Observed
Acetic Acid (CH_3COOH)	30	< 0.001	None
Hydrochloric Acid (HCl)	50	< 0.001	None
Nitric Acid (HNO_3)	81	< 0.001	None
Phosphoric Acid (H_3PO_4)	108 – 195	0.013 – 3.2	$\{10\bar{1}\bar{2}\}$,$\{10\bar{1}3\}$
Sulphuric Acid (H_2SO_4)	93	< 0.001	None
Potassium Hydroxide (KOH), molten	150 – 247	0.003 – 2.3	$\{10\bar{1}0\}$,$\{10\bar{1}\bar{1}\}$
50% KOH in H_2O	83	< 0.001	None
10 – 50% KOH in Ethylene Glycol (CH_2OHCH_2OH)	90-182	0.0015 – 1.3	$\{10\bar{1}0\}$
50% NaOH in H_2O	100	< 0.001	None
Tetramethylammonium Hydroxide (TMAH)	76	0.013	$\{10\bar{1}\bar{2}\}$
Tetraethylammonium Hydroxide (TEAH)	91	0.007	$\{10\bar{1}\bar{2}\}$
20% NaOH in Ethylene Glycol	178	0.67 – 1.0	None

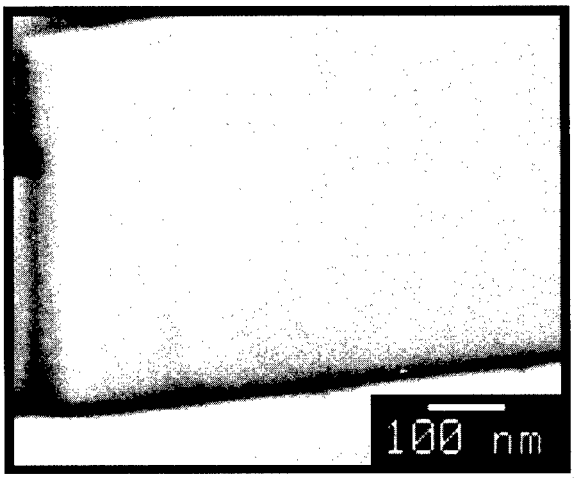


FIG. 1: High-resolution field-effect SEM image of a vertical $\{10\bar{1}0\}$ plane etched in n-GaN by KOH dissolved in ethylene glycol at a temperature of 170°C.

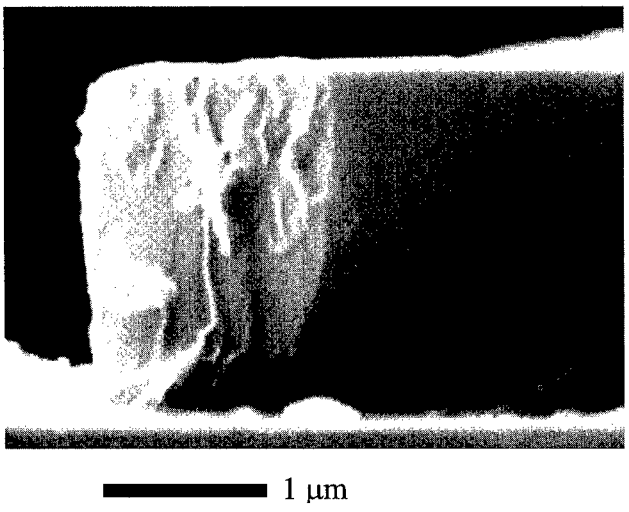


FIG. 2: SEM image of a $\{10\bar{1}0\}$ surface made by crystallographic wet etching in molten KOH at 195°C. The upper portion of the epilayer is p-GaN, while the lower 1 μm is highly resistive GaN.

the n-type material; in many cases, the only distinct crystal plane left after etching is the c-plane. The reason for this difference is unclear at the present time. It seems to be unrelated to crystal quality; the crystals are of similar quality, as indicated by x-ray rocking curve full-width-at-half-maxima of 800 - 900 arcsec and by etch pit densities on the order of 5×10^7 cm^{-2} after etching in molten KOH. The difference is also not related to the doping, since the p-type material etches seamlessly with the undoped material on which it is grown.

We are currently using photoenhanced electrochemical (PEC) etching and crystallographic wet etching to fabricate fully wet-etched laser cavities in an InGaN:Si/GaN double heterostructure. The structure consists of an initial 10-μm-thick buffer layer of GaN grown on c-plane sapphire by HVPE, and a 0.5 μm GaN bottom cladding layer, a 1000 Å $In_{0.09}Ga_{0.91}N$:Si active region, and a 2200 Å GaN top cladding layer grown by MOVPE. This is the same structure which we have previously used to demonstrate optically pumped cleaved-facet lasers.[17] Waveguide calculations reveal that the heterostructure is a single-mode waveguide with an active region confinement factor of 6%. The guided mode is confined mainly to the upper portion of the epilayers, with 50% of the intensity carried in the top 2 μm.

180-nm-thick annealed Ni masks are used to define cavities with lengths varying from 50 μm to 500 μm. The unusually thick Ni layer is used to minimize the light penetrating into the masked area during PEC etching. The edges of the masks are aligned with the ⟨1120⟩ direction of the GaN, so that the resulting PEC-etched sidewalls correspond with the {1010} plane for subsequent crystallographic etching.

The PEC etching is done under voltage biased conditions in a 0.03 M KOH solution at room temperature. During etching, the samples are clamped against a nickel bar and immersed along with a gold wire cathode in the aqueous KOH solution. Voltage and current are both monitored and a DC power supply is used to apply a bias voltage of -2 V on the anode. The bias voltage has been found to improve the uniformity of the etching process, minimizing the roughness which is commonly seen when using PEC etching with GaN. Ultraviolet illumination is provided by a 200W Hg lamp, and a silicon wafer is used as a cold mirror to reduce heating by increasing the ratio of UV to IR illumination. The time required to produce vertical sidewalls extending down to the sapphire substrate under these conditions is 4 hours. A typical PEC-etched sidewall in this material is shown in Fig. 3(a). The nickel mask is visible at the top of the image, and is allowed to remain in place throughout the subsequent crystallographic etching. As the image shows, the PEC-etched sidewall is extremely rough and has a fibrous texture, although the sapphire surface has etched cleanly. The clean sapphire surface shows the effectiveness of the bias voltage in eliminating the islands often formed on the sapphire substrate by uneven PEC etching of the GaN. Note that there are some deep holes in the top 1 μm of the structure, near the InGaN layer. These holes form during PEC etching, but the etching mechanism is not yet understood.

The sidewall produced by PEC etching is far too rough to be used as a laser facet, since the reflectivity is strongly dependent upon surface roughness.[16] Crystallographic etching in molten KOH is used to smooth the PEC-etched surface to improve the reflectivity. The series of SEM images in Fig. 3(b)-3(d) shows the effect of etching in 175°C molten KOH on the PEC-etched sidewall. The etch rate at this temperature is approximately 0.05 μm/min. The fibrous PEC-etched surface shows considerable smoothing after only 1 minute of crystallographic etching, as can be seen in Fig. 3(b). Further improvement is observed in Fig. 3(c) after three minutes of crystallographic etching. After five minutes of etching, no further smoothing occurs; the image shown in Fig. 3(d) after nine minutes of etching is very similar to images taken

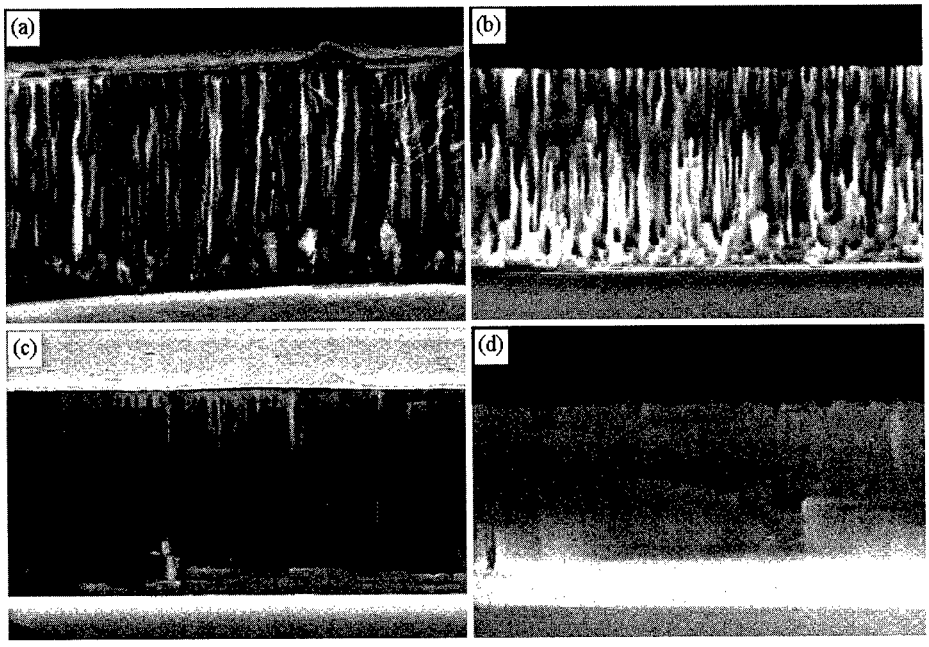


FIG. 3: Smoothing of a surface produced by photo-enhanced electrochemical (PEC) etching of an InGaN/GaN double heterostructure. The 10 μm bar underneath the figure is valid for all of the SEM images. (a) PEC-etched surface before smoothing by crystallographic etching in molten KOH at 175°C. (b) PEC-etched surface after smoothing for 1 min. (c) After smoothing for 3 min. (d) After smoothing for 9 min.

anywhere in the range of five to ten minutes. Note that the density of holes in the top 1 μm does not tend to change during crystallographic etching. Horizontal steps like those across the center of Fig. 3(d) are common features produced by crystallographic etching in KOH. These may be due to anisotropy of etch rate in the [0001] and [000$\bar{1}$] directions.

The usefulness of these wet-etched sidewalls for laser facets is currently under investigation. We believe that the horizontal steps will not have a significant effect on the reflectivity, since the waveguide confines the guided mode mostly in the upper part of the epilayers.

CONCLUSIONS

We have presented a method for fabricating fully wet-etched laser facets for GaN-based laser structures. Photoenhanced electrochemical (PEC) etching is used to produce rough vertical facets which are aligned with the $\{10\bar{1}0\}$ planes of the GaN. Crystallographic wet chemical etching is used to smooth the rough PEC-etched surfaces. The resulting facets have large areas where the roughness is less than 5 nm, the smoothest etched vertical sidewalls which have been

reported to date. The crystallographic etching used to produce the vertical $\{10\bar{1}0\}$ facets is independent of carrier concentration, which suggests its usefulness in fabricating wet-etched laser diodes.

REFERENCES

[1] J. C. Zolper and R. J. Shul, MRS Bulletin **22** (2), 36 (1997).
[2] H. P. Gillis D. A. Choutov, and K. P. Martin, JOM **48** (8), 50 (1996).
[3] F. Ren, J. R. Lothian, S. J. Pearton, C. R. Abernathy, C. B. Vartuli, J. D. MacKenzie, R. G. Wilson, and R.F. Karlicek, Journal of Electronic Materials **26**, 1287 (1997).
[4] S. Nakamura, M. Senoh, S. Nagahama, N. Iwasa, T. Yamada, T. Matsushita, H. Kiyoku, Y. Sugimoto, Jpn. J. Appl. Phys. **35**, L74 (1996).
[5] F. Binet, J. Y. Duboz, N. Laurent, C. Bonnat, P. Collot, F. Hanauer, O. Briot, R. L. Aulombard, Appl. Phys. Lett. **72**, 960 (1998).
[6] M. Kneissl, D. P. Bour, N. M. Johnson, L. T. Romano, B. S. Krusor, R. Donaldson, J. Walker, C. Dunnrowicz, Appl. Phys. Lett. **72**, 1539 (1998).
[7] M.S. Minsky, M. White, and E.L. Hu, Appl. Phys. Lett. **68**, 1531 (1996).
[8] L.-H. Peng, C.-W. Chuang, J.-K. Ho, C.-N. Huang, and C.-Y. Chen, Appl. Phys. Lett. **72**, 939 (1998).
[9] H. Lu, Z. Wu, and I. Bhat, J. Electrochem. Soc. **144**, L8 (1997).
[10] C. Youtsey, I. Adesida, L. T. Romano, and G. Bulman, Appl. Phys. Lett. **72**, 560 (1998).
[11] D. A. Stocker, E. F. Schubert, and J. M. Redwing, Appl. Phys. Lett. **73**, 2654 (1998).
[12] M. Seelmann-Eggebert, J. L. Weyher, H. Obloh, H. Zimmermann, A. Rar, and S. Porowski, Appl. Phys. Lett. **71**, 2635 (1997).
[13] C. B. Vartuli, S. J. Pearton, C. R. Abernathy, J. D. MacKenzie, F. Ren, J. C. Zolper, and R. J. Shul, Solid-State Electronics **41**, 1947 (1997).
[14] A. Shintani and S. Minagawa, J. Electrochem. Soc. **123**, 706 (1976).
[15] T. Kozawa, T. Kachi, T. Ohwaki, Y. Taga, N. Koide, M. Koike, J. Electrochem. Soc. **143**, L17 (1996).
[16] D. A. Stocker, E. F. Schubert, W. Grieshaber, K. S. Boutros, and J. M. Redwing, Appl. Phys. Lett. **73**, 1925 (1998).
[17] D. A. Stocker, E. F. Schubert, K. S. Boutros, J. S. Flynn, R. P. Vaudo, V. M. Phanse, and J. M. Redwing, Electron. Lett. **34**, 373 (1998).

UNIFORMITY AND PERFORMANCE CHARACTERIZATION OF GaN P-I-N PHOTODETECTORS FABRICATED FROM 3-INCH EPITAXY

R. Hickman II, J. J. Klaassen, J. M. Van Hove, A. M. Wowchak, C. Polley, M. F. Rosamond, P. P. Chow

SVT Associates, Inc., 7620 Executive Dr., Eden Prairie, MN 55344, rhickman@svta.com

Cite this article as: MRS Internet J. Nitride Semicond. Res. 4S1, G7.6 (1999)

ABSTRACT

Gallium nitride wafer epitaxy on large diameter substrates is critical for the future fabrication of large area UV linear or 2D imaging arrays, as well as for the economical production of other GaN-based devices. Typical group III-nitride deposition is now performed on 2-inch diameter or smaller sapphire substrates. Reported here are visible blind, UV GaN *p-i-n* photodetectors which have been fabricated on 3-inch diameter (0001) sapphire substrates by RF atomic nitrogen plasma MBE. The uniformity across the wafer of spectral responsivity and shunt resistance (R_0) for the *p-i-n* photodetectors has been characterized. Spectral responsivity and 1/*f* noise as a function of temperature exceeding 250°C will be presented for the GaN *p-i-n* photodetectors. Spectral response with >0.17 A/W at peak wavelength and having 4-6 orders of magnitude visible rejection has been achieved. 1/*f* noise typically less than 10^{-14} A/Hz$^{1/2}$ at room temperature also has been achieved with GaN *p-i-n* photodiodes. The results have been correlated with proposed models for dark current and 1/*f* noise in GaN diodes.

INTRODUCTION

Gallium nitride (GaN) and its alloys with aluminum are the most promising semiconductors for development of ultraviolet (UV) photodetectors for applications such as combustion monitoring, space-based UV spectroscopy and missile plume detection. With a direct bandgap energy of approximately 3.39 eV (366 nm), GaN is an ideal material for the fabrication of photodetectors capable of rejecting near infrared and visible regions of the solar spectrum while retaining near unity quantum efficiency in the UV. GaN is also an extremely robust semiconductor suitable for high temperature (>200°C) applications.

GaN devices are normally fabricated on sapphire substrates with diameters of two inches or less. The growth and fabrication of GaN UV photodetectors on larger diameter substrates is important for the realization of cost effective discrete detectors, linear detector arrays and 2-dimensional imaging arrays. Other reports on GaN *p-n* UV photodetectors have included 0.05 mm^2 junction area devices with 0.07 A/W peak responsivity [1], 0.04 mm^2 junction area devices [2], and 0.25 mm^2 junction area devices with 0.1 A/W peak responsivity [3]. Presented here is the first reported performance data for GaN *p-i-n* UV photodetectors with 0.59 mm^2 junction areas fabricated on 3-inch diameter substrates.

EXPERIMENT

The GaN *p-i-n* ultraviolet (UV) photodiodes were grown on (0001) basal-plane 3-inch sapphire substrates by molecular beam epitaxy (MBE) using an RF atomic nitrogen plasma source [4]. Details of the growth process have been previously reported [5-6]. The detector epitaxial layers consisted of a $5 \cdot 10^{18}$ cm^{-3} *n*-GaN layer followed by a 5000 Å intrinsic region

Mat. Res. Soc. Symph. Proc. Vol. 537 © 1999 Materials Research Society

with unintentional *n*-type doping in the 10^{15} cm^{-3} decade. The topmost epitaxial layer consisted of 2000 Å $1 \cdot 10^{18}$ cm^{-3} *p*-GaN. Mesas reaching the *n*-GaN cathode contact layer were formed by inductively coupled plasma (ICP) plasma etching with chlorine-based chemistry. Ohmic contacts to the *n*-type and *p*-type GaN were made by Ti-based and Ni-based metallizations, respectively. All of the GaN *p-i-n* UV detectors were fabricated with an optical detection area of 0.5 mm^2 and a *p-i-n* junction area of 0.59 mm^2, which is considerably larger (>12.5 times) than other GaN *p-n* detectors reported with noise measurements [1-3].

Shunt resistance and spectral responsivity data were collected using on-wafer probing. The shunt resistance was determined by the linear trace of the current-voltage (IV) characteristic from -10 mV to +10 mV. The spectral responsivities of the UV photodiodes were measured in photovoltaic mode (zero bias) using a 75 W xenon arc lamp chopped at 700 Hz and filtered by a 1/8 meter monochromator set to a 5 nm bandpass. The power of the monochromatic light was measured with a calibrated, NIST traceable, silicon photodiode and then focused onto the 3" GaN wafers resting on a micropositioner stage. The GaN *p-i-n* diode photocurrent was amplified, and the power spectral density in a 1 Hz bandwidth at the modulation frequency was monitored with a FFT spectrum analyzer. Measurements of incident power and photodiode current were made in 10 nm intervals.

For high temperature testing, individual GaN *p-i-n* photodiodes chips were diced from the wafers and mounted on a heated stage. All measurements were performed in an oxidizing, open air environment. The temperature dependent spectral responsivities were performed as described above. The 1/*f* noise measurements were performed with both the dice and heated stage mounted in an enclosure designed to suppress electromagnetic interference. For 1/*f* measurement, the signal from a battery powered, transimpedance amplifier-photodiode circuit was input into the FFT. The operational amplifier in the circuit was specified with a 1 kHz input noise current of 0.16 $fA/Hz^{1/2}$, and the minimum noise power density of the measurement setup was approximately $4 \cdot 10^{-24}$ A^2/Hz.

RESULTS

All GaN UV photodector responsivity measurements reported here were obtained with the devices operating in the unbiased, photovoltaic mode. Shown in Figure 1 is a 25°C spectral responsivity curve for a UV photodetector with 0.194 A/W peak responsivity and 4 orders of

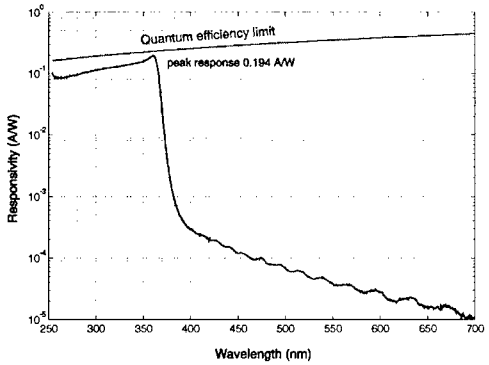


Fig. 1: Typical GaN *p-i-n* UV photodetector unbiased spectral response.

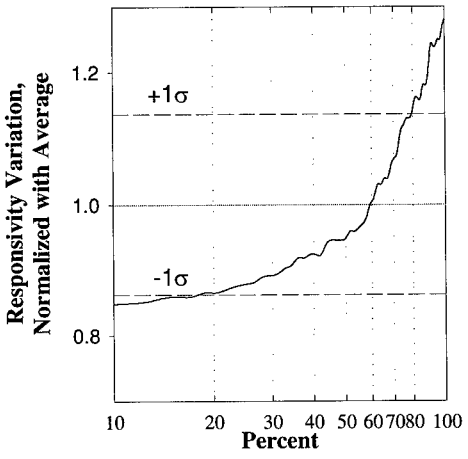


Fig. 2: Variation plot of unbiased peak responsivity normalized with the mean value.

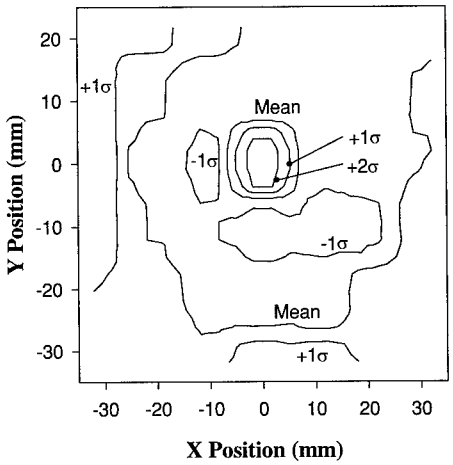


Fig. 3: Mean normalized unbiased peak responsivity contour plot for UV photodetectors verses position on a 3-inch GaN *p-i-n* wafer.

magnitude visible rejection. The statistical distribution of the photodetector devices on a 3" wafer is illustrated with the variation plot in Figure 2. The peak responsivity variation was normalized by the average of all functioning devices, and as a result of a very high yield, the single wafer data set numbered in the thousands. The standard deviation, $\pm 1\sigma$, of the peak spectral responsivity was calculated to be $\pm 13\%$ of the average peak responsivity. Therefore, a 3-inch GaN epitaxial wafer of UV photodetectors with 0.17 A/W peak responsivity would yield devices within the $\pm 1\sigma$ deviation range with 0.15-0.19 A/W peak responsivity. 60% of the UV photodetectors on the 3-inch GaN epitaxial wafer functioned within the $\pm 1\sigma$ range. Further, nearly all of the UV photodetectors, with the exception of electrically shorted failed devices, functioned within the $\pm 2\sigma$ range.

The 2-dimensional (2D) data for the normalized peak responsivity is presented in the contour plot of Figure 3. A diameter of more than 60 mm, or greater than 2 inches, enclosed a circle representing a large number of photodectors with peak responsivities that were near the average of the wafer set. Small patches of devices with peak responsivities between the mean and -1s were present without any identifiable or expected pattern. An unexpected result was the increasing peak responsivity of the devices near the wafer edge. The 2D distribution of the shunt resistance, which has a strong influence on noise and sensitivity but not on responsivity, was more varied. The contour plot of Figure 4 illustrates the shunt resistance pattern, normalized by the mean, of the GaN *p-i-n* photodetectors on the 3-inch wafer. Higher shunt resistance (up to 3 times the mean) detectors were positioned in the wafer center, and photodetectors with lower shunt resistance (as little as 0.2 times the mean) were distributed around the wafer edge. The majority of the GaN photodetectors exhibited a shunt resistance that was within the same decade of one another.

The high temperature spectral responsivity of a randomly selected GaN UV photodetector chip, previously fabricated and diced from a different wafer lot, is presented in Figure 5. No significant increase in visible responsivity was detectable above the noise level of

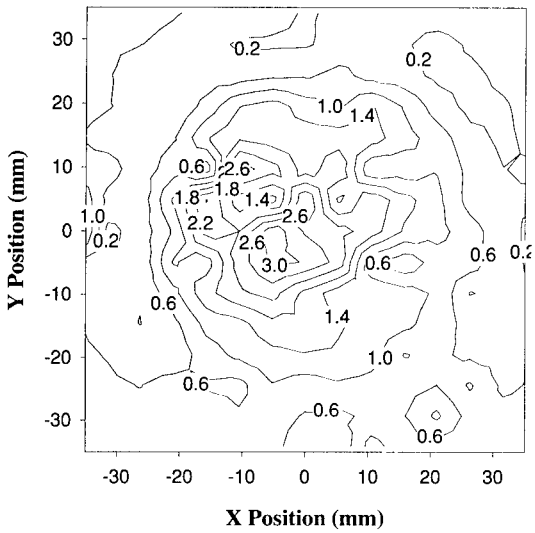


Fig. 4: Contour plot of mean normalized UV photodetector shunt resistance on a 3-inch GaN *p-i-n* wafer.

the test setup as the device temperature increased from 25°C to 300°C. The peak responsivity shifted with the bandgap edge from 359 nm at 25°C, to 365 nm at 150°C, to 372 nm at 300°C. The GaN UV photodetector chip fully recovered the 25°C spectral responsivity characteristic after being tested at 300°C in the oxidizing environment of open air. The slight differences in spectral responsivity magnitudes are within the error of the high temperature test setup which experienced focusing and position perturbations during measurement as a result of thermal expansion.

The temperature dependent $1/f$ noise characteristics for the GaN *p-i-n* photodetectors are presented in Figures 6 and 7. In Figure 6, the noise power density in photovoltaic mode is plotted over the frequencies including 100 Hz to 1 kHz at temperatures ranging from 25°C to 300°C. A measurable $1/f$ noise signal was not present until the photodetector reached 150°C, and an room temperature extrapolation of the GaN *p-i-n* photodetector noise power density at 100 Hz is presented in Figure 7. Based on the fit shown, the room temperature noise power density for the GaN *p-i-n* photodetectors, with a 0.59 mm^2 junction area, was approximately $3.0 \cdot 10^{-30}$ A^2/Hz ($1.7 \cdot 10^{-15}$ $A/Hz^{1/2}$ noise current density) at zero bias.

Johnson noise, equal to the formula $4kT/R_0$, cannot fully explain the zero bias presence of the $1/f$ noise in the GaN UV photodetectors at higher temperatures. The $1/f$ noise power density, which is normally modeled by a relation including the dark current, suggests the presence of a thermally generated dark current in the photodetectors at zero bias. At temperatures as high as 300°C, thermocouple voltages and/or thermally ionized electron-hole pairs may yield diffusion and recombination in the *p-i-n* junction under equilibrium. Additional characterization and comparison with theory are required to fully explain the high temperature noise characteristics of the GaN devices.

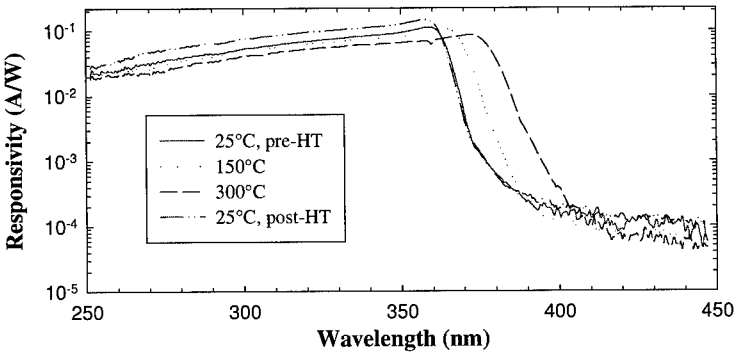


Fig. 5: Temperature dependent, unbiased spectral responsivity for GaN UV photodetector chips up to 300°C.

CONCLUSIONS

UV photodetectors with an optically active surface area of 0.5 mm^2 and a junction area of 0.59 mm^2 have been fabricated on 3-inch diameter GaN *p-i-n* epitaxial wafers and characterized for the first time. Wafer maps of photodetector peak responsivity indicated that more than 60% of all the GaN UV photodetectors performed within the $\pm 1\sigma$ statistical range, which corresponded to a ±13% deviation from the average peak responsivity. The remaining UV photodetectors on the 3" GaN epitaxial wafer were distributed within the $\pm 2\sigma$ range. Further, the vast majority of GaN UV photodetectors were characterized with shunt resistances that were within one decade of each other.

High temperature testing of the GaN *p-i-n* photodetectors up to 300°C indicated no significant increase in visible spectral responsivity or short term degradation. The room temperature spectral responsivity of the GaN photodetectors was fully recovered after 300°C testing. The 300°C GaN photodetector $1/f$ noise power densities were measured to be $6.6 \cdot 10^{-19}$ and $2.1 \cdot 10^{-21}$ A^2/Hz at 100 Hz and 1 kHz, respectively. The room temperature, 100 Hz noise power density of the GaN photodetectors was extrapolated to be $3.0 \cdot 10^{-30}$ A^2/Hz ($1.7 \cdot 10^{-15}$ $A/Hz^{1/2}$ noise current density).

ACKNOWLEDGEMENT

The authors wish to acknowledge the assistance of Dr. Steve Pearton at the University of Florida, Gainesville, for performing the ICP etching of the GaN wafers.

REFERENCES

1. G. Xu, A. Salvador, A. E. Botchkarev, W. Kim, C. Lu, H. Tang, H. Morkoc, G. Smith, M. Estes, T. Dang, and P. Wolf in *Materials Science Forum, Part 2* (**264-268**, Trans Tech, Enfield, NH, 1998) pp. 1441-1444.

2. D. V. Kuksenkov, H. Temkin, A. Osinsky, R. Gaska, and M. A. Khan, in *1997 International Electron Devices Meeting Technical Digest* (IEEE, Piscataway, NJ, 1997) pp. 759-762.

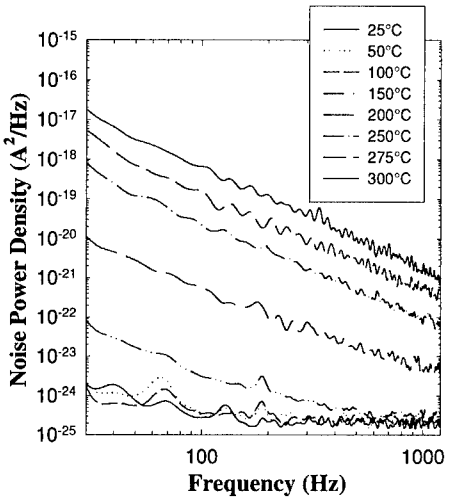


Fig. 6: Typical $1/f$ noise power density for a 0.59 mm^2 GaN *p-i-n* UV photodetector plotted at temperatures up to 300°C. The data were collected at zero bias.

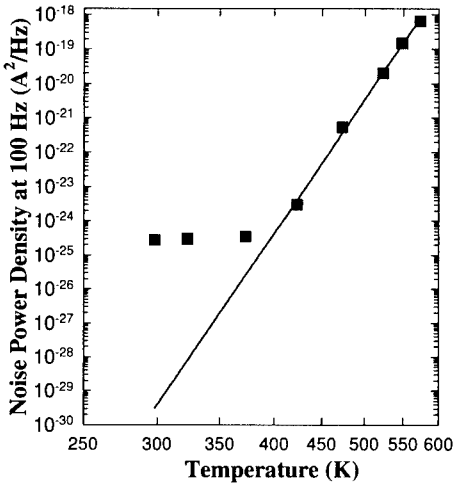


Fig. 7: The GaN *p-i-n* UV photodetector noise power density at 100 Hz. The measurements below 400 K were limited by

3. A. Osinsky, S. Gangopadhyay, R. Gaska, B. Williams, and M. A. Khan, Appl. Phys. Lett. **71** (16), 2334 (1997).

4. J. M. Van Hove, G. J. Cosimini, E. Nelson, A. M. Wowchak, and P. P. Chow, J. Cryst. Growth **150**, 908 (1995).

5. J. M. Van Hove, P. P. Chow, R. Hickman, A. M. Wowchak, J. J. Klaassen, and C. J. Polley in *III-V Nitrides*, edited by F. A. Ponce, T. D. Moustakas, I. Akasaki, and B. A. Monemar (Mater. Res. Soc. Proc. **449**, Pittsburgh, PA, 1996) pp. 1227-1231.

6. J. M. Van Hove, R. Hickman, J. J. Klaassen, and P. P. Chow, Appl. Phys. Lett. **70** (17), 2282 (1997).

MONITORING AND CONTROLLING OF STRAIN DURING MOCVD OF AlGaN FOR UV OPTOELECTRONICS

Jung Han*, M. H. Crawford, R. J. Shul, S. J. Hearne, E. Chason
J. J. Figiel, and M. Banas

Sandia National Laboratories, Albuquerque, NM 87185

Cite this article as: MRS Internet J. Nitride Semicond. Res. 4S1, G7.7 (1999)

ABSTRACT

The grown-in tensile strain, due to a lattice mismatch between AlGaN and GaN, is responsible for the observed cracking that seriously limits the feasibility of nitride-based ultraviolet (UV) emitters. We report *in-situ* monitoring of strain/stress during MOCVD of AlGaN based on a wafer-curvature measurement technique. The strain/stress measurement confirms the presence of tensile strain during growth of AlGaN pseudomorphically on a thick GaN layer. Further growth leads to the onset of stress relief through crack generation. We find that the growth of AlGaN directly on low-temperature (LT) GaN or AlN buffer layers results in a reduced and possibly controllable strain.

INTRODUCTION

Thus far the optoelectronic effort of the III-nitride community has focused primarily on InGaN-based visible light emitting devices for display and data storage applications [1]. Most of these devices were grown on sapphire substrates with thick GaN layers of 2 to 4 μms inserted for improved structural and morphological quality. (Thick n-GaN layers are also required for low-resistive electrical injection.) The active region typically consists of (higher fraction) InGaN-based quantum wells (QWs) and (lower fraction) InGaN barriers for electrical confinement. Further electrical and optical confinement is attained through the use of wide bandgap AlGaN layers (Figure 1a). Substantial lattice mismatches, however, exist among the III-nitrides; the mismatches (in the in-plane lattice constant) of InN (a ~ 0.354 nm) and AlN (a = 0.3112 nm) to the thick and presumably relaxed GaN (a = 0.3188 nm) layers are 11% compression and 2.4% tension, respectively [2]. So far most of the strain-related studies have focused on the optical [3] and structural [4] properties of thick GaN epilayers on sapphire or SiC substrates.

A simple analysis of the state of strain energy, denoted here as strain-thickness product in Figure 1c, reveals the benefit of the alternating AlGaN/InGaN heterolayers (Figure 1a) in balancing the tensile and compressive components to avoid excessive strains and to maintain a pseudomorphic growth (dashed line in Figure 1c). Recently we have reported the growth and device operation of an AlGaN/GaN QW-based UV LED on a thick GaN layer [5]. The use of various AlGaN confinement layers, in the absence of any InGaN layers (Figure 1b), results in a steep accumulation of grown-in tensile strain (solid line in Figure 1c). Indeed cracking was

* Corresponding author. Present address: Sandia National Laboratories, MS-0601, P.O. Box 5800, Albuquerque, New Mexico 87185-0601, Fax: 505-844-3211, email: jhan@sandia.gov

Mat. Res. Soc. Symp. Proc. Vol. 537 © 1999 Materials Research Society

observed during fabrication of AlGaN/GaN UV LEDs with thick AlGaN barriers (Figure 2a). The presence of cracking causes a significant variation of current-voltage characteristics among the tested devices and contributes to a large leakage current under reverse-bias conditions (Figure 2b). It is worth noting that cracking of AlGaN layers on thick GaN has been reported previously [6, 7].

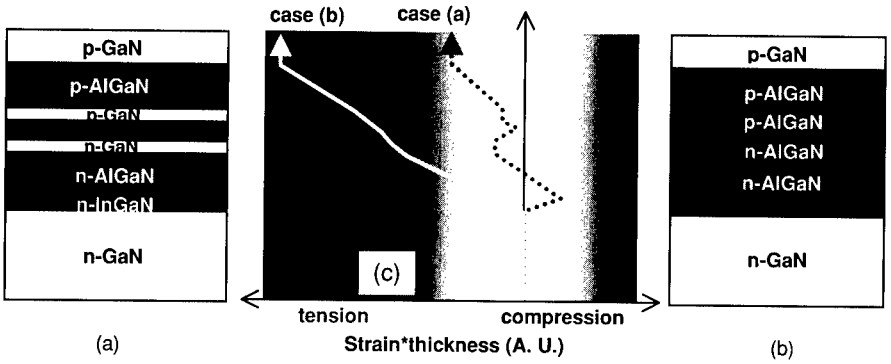


Figure 1. Schematic diagrams of a blue laser diode (a) and a UV LED (b). The indium-containing layers are labeled in blue and the AlGaN layers are colored in red. (c) Strain-thickness product along the growth direction for the structures of (a) (dashed line) and (b) (solid yellow line). InGaN layers tend to move the curve toward blue (compression) and AlGaN layers to red (tension).

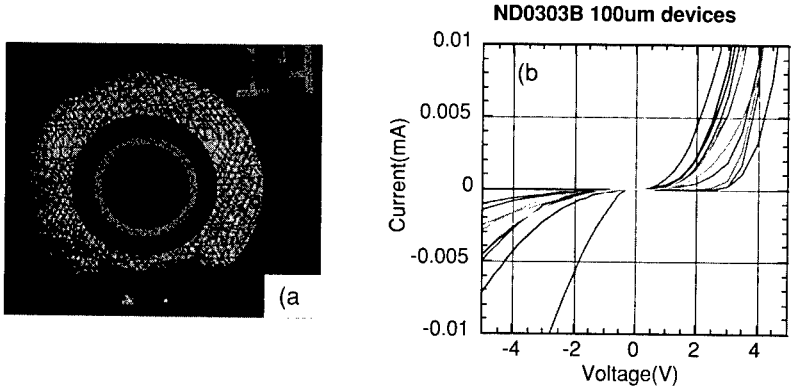


Figure 2. (a) Top view of an etched circular mesa (100 μm diameter) showing the presence of a high density of cracks. (b) Diode I-V curves taken from various devices across the same cracked sample.

An additional complication arises for AlGaN grown on sapphire, the most common substrate of choice, as the sapphire (linear thermal expansion coefficient $\alpha \sim 7.6 \times 10^{-6}\ k^{-1}$) exerts a compressive strain to the AlGaN layers ($\alpha \sim 5.6 \times 10^{-6}\ k^{-1}$) during cool down which tends to mask the grown-in tensile strain due to lattice mismatch. Most of the post-growth ex-situ strain characterizations [8-13] would in this case measure a combination of a tensile stress due to lattice mismatch and a compressive component due to thermal expansion mismatch. In an attempt to

isolate these two competing factors by directly probing the grown-in strain, we have employed an *in-situ* stress/strain monitor based on wafer-curvature measurement [14]. In this paper we will report the monitoring and subsequent control of grown-in strain of AlGaN on sapphire using different buffer layer schemes.

EXPERIMENT

A high-speed (1200 rpm), inductively heated, rotating disk reactor (RDR) was used to deposit GaN films (nominally 1-3 μm thick) onto 2" diameter, 330μm thick, (0001) sapphire wafers. Trimethylgallium, trimethylaluminum, and ammonia where used as the precursors, with hydrogen as the carrier gas. A detailed description can be found in Ref. [15]. A two-step deposition process was used. Initially, a LT buffer of GaN (~550°C) or AlN (~600°C) was grown. The buffer was then heated to 1050°C and stabilized for 1 minute prior to deposition of the high temperature (HT) layer.

Real time wafer curvature measurements were performed with a multi-beam optical stress sensor (MOSS) [16] modified for use on our reactor. To determine the wafer curvature, the divergence of an array of initially parallel laser beams is measured on a CCD camera after reflection of the array from the film/substrate surface. Changes in wafer curvature induce a proportional change in the beam spacing on the camera. This technique provides a direct measurement of the stress during deposition and is described in detail in Ref. [17].

The relation between film stress (σ_f), and substrate curvature (κ), is given by Stoney's equation [18],

$$\sigma_f h_f = \frac{M_s h_s^2}{6}\kappa , \qquad (1)$$

h_f and h_s are the film and substrate thickness, respectively and M_s is the substrate biaxial modulus. Curvature is directly proportional to the product of the film stress and film thickness ($\sigma_f h_f$), both of which vary, in general, during growth. Equation 1 can be derived by balancing the forces and bending moments in the film with those in the substrate, and assuming the film is much thinner then the substrate [18]. We also simultaneously obtain information on the surface roughness and film thickness during deposition by monitoring the intensity of one of the reflected laser beams, similar to the method described in Ref. [19].

RESULTS AND DISCUSSION

Figure 3 shows the stress-thickness product ($\sigma_f h_f$) and the reflected beam intensity as functions of growth time (see the following explanation) during growth of an AlGaN (Al~15%) layer on a 0.6 μm GaN layer grown at 1050°C. We have reported that [19] *in-situ* reflectance could provide the information of growth rate from the periodicity of Fabry-Perot interference. Such information in turn enables the conversion of time axis into film thickness (h_f). On a plot of $\sigma_f h_f$ versus h_f, the slope is simply the grown-in stress (σ_f). A positive slope on such a plot denotes a *tensile* stress throughout this paper.

A slight slope of the $\sigma_f h_f$ curve during GaN growth (in Figure 3) was observed which suggests the presence of a slight tensile stress. The grown-in stress of GaN on sapphire is the subject of another publication [14]. After a growth transition in adjusting the reactor parameters for the growth of AlGaN (an artifact of an abrupt decrease in the $\sigma_f h_f$ curve was therefore generated), a steady slope of 1.33 GPa was established which agrees well with the expected value assuming a

pseudomorphic growth. After the growth of approximately 0.6 μm of AlGaN, however, a step decrease of the $\sigma_f h_f$ curve was recorded. Tentatively this feature is designated to be the relief of grown-in tensile stress due to the occurrence of cracking. (Cracking was indeed observed from Nomarski microscopy.) One implication is that the use of a thick GaN bottom layer, a common practice shared by the InGaN-based heterostructures, could lead to a build-up of excessive tensile strain in the case of AlGaN-based heterostructures for UV optoelectronics.

Direct growth of AlGaN on sapphire via LT buffer layers becomes attractive as a means to circumvent and alleviate the mismatch-induced tension imposed inevitably by the two-dimensional growth mode (i.e. AlGaN on a HT GaN layer). In Figures 4 and 5, $\sigma_f h_f$ and reflectance versus thickness are presented for the growth of AlGaN (Al~17% in both cases) on LT GaN and AlN buffer layers, respectively, on sapphire substrates. Even though a tensile stress (0.82 GPa) was still measured for AlGaN on LT GaN buffer (Figure 4), it is interesting to note that this value is less than half of the expected stress due to the mismatch between $Al_{0.17}Ga_{0.83}N$ and GaN. One could speculate that the conventional, mismatch-induced strain constraint is somewhat relaxed under a possibly three-dimensional island growth mode.

In the case of direct growth of AlGaN on a LT AlN buffer (Figure 5), the $\sigma_f h_f$ curve first moves downward, indicative of a *compressive* stress, before assuming a relatively flat (stress free) growth mode. The origin of the compressive strain during the initial growth of $Al_{0.17}Ga_{0.83}N$ is currently under investigation. A plausible cause is that the AlN nucleation template has a smaller lattice constant than that of AlGaN. The compressive stress was estimated to be around 1.3 GPa, much less than the full mismatch between $Al_{0.17}Ga_{0.83}N$ and AlN (around 9 GPa).

CONCLUSIONS

Using a novel *in-situ* stress monitor, we measured the grown-in strain of AlGaN on various layers. It was found that AlGaN grown on a thick HT GaN layer has a tensile strain well predicated by the pseudomorphic lattice mismatch before strain relaxation occurs. Growth on a LT GaN buffer layer resulted in a relaxation of more than 50% of the coherent tensile strain. The use of a LT AlN buffer caused a compressive strain during the initial (first 0.1 μm) growth of AlGaN. The combination of LT GaN and AlN buffer schemes could lead to the control of strain during AlGaN growth for UV optoelectronics.

ACKNOWLEDGMENTS

The authors gratefully acknowledge valuable interaction with H. Amano (Meijo University, Japan). Technical assistance by T. Kerley and J. Hunter is also acknowledged. Sandia is a multiprogram laboratory, operated by Sandia Corporation, a Lockheed Martin company, for the United States Department of Energy, under contract DE-AC04-94AL85000.

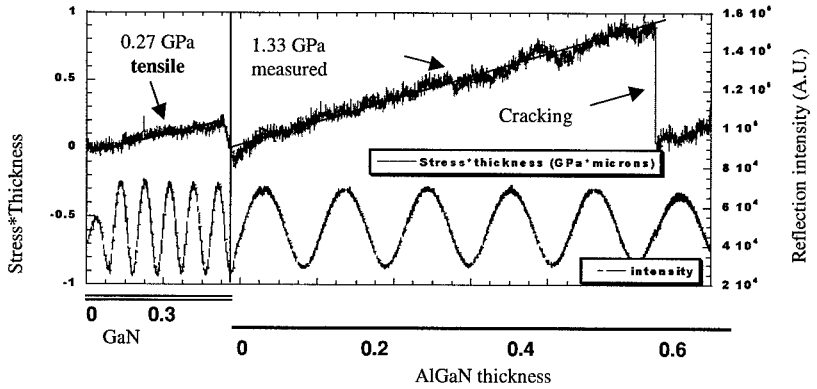


Figure 3 Stress-thickness product and reflectance versus thickness during growth of AlGaN (Al~0.15) on a 0.6 μm GaN layer

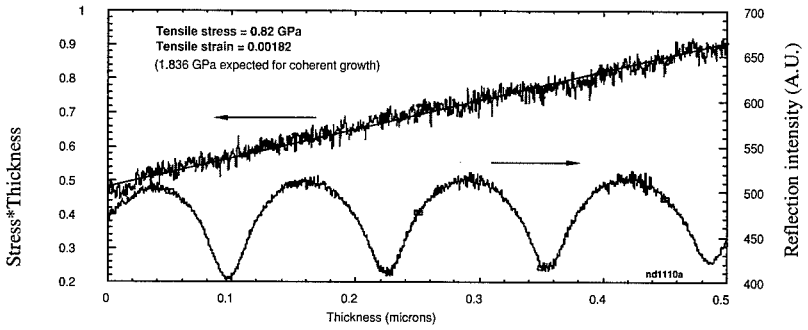


Figure 4 Stress-thickness product and reflectance versus thickness during growth of AlGaN (Al~0.17) directly on a LT GaN buffer on sapphire

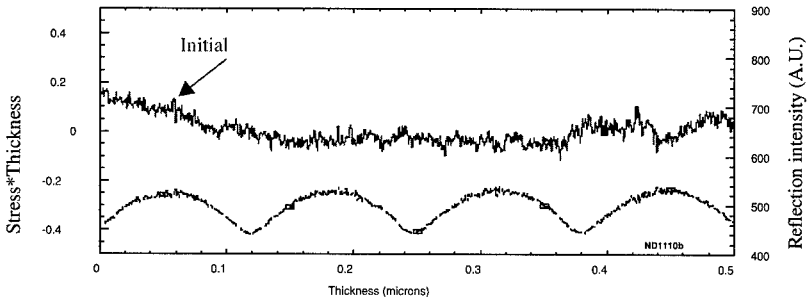


Figure 5 Stress-thickness product and reflectance versus thickness during growth of AlGaN (Al~0.17) directly on a LT AlN buffer on sapphire

REFERENCES

1. For a review, see S. Nakamura and G. Fasol, *The Blue Laser Diode*, Springer-Verlag, Berlin (1997).
2. A. Trampert, O. Brandt, and K. H. Ploog, *Gallium Nitride (GaN) I*, edited by J. I. Pankove and T. D. Moustakas, Academic Press, San Diego (1998), p167.
3. For example, C. Kisielowski, J. Kruger, S. Ruvimov, T. Suski, J. W. Ager III, E. Jones, Z. Liliental-Weber, M. Rubin, E. R. Weber, M. D. Bremser, and R. F. Davis, Phys. Rev. B 54, 17745 (1996).
4. T. Detchprohm, K. Hiromatsu, K. Itoh, and I. Akasaki, Jpn. J. Appl. Phys. 31, L1454 (1992)
5. J. Han, M. H. Crawford, R. J. Shul, J. J. Figiel, M. Banas, L. Zhang, Y. K. Song, H. Zhou, and A. V. Nurmikko, Appl. Phys. Lett, 73, 1688 (1998)
6. O. Gfrorer, T. Schlusener, V. Harle, F. Scholz, and A. Hangleiter, Mat. Res. Soc. Symp. Proc. 449, 429 (1997)
7. W. G. Perry, M. B. Bremser, T. Zheleva, K. J. Linthicum, and R. F. Davis, Thin Solid Films 324, 107 (1998).
8. W. Li, W. Ni, Appl. Phys. Lett. 68, 2705 (1996).
9. M. Leszczynski, T. Suski, H. Teisseyre, P. Perlin, I. Grzegory, J. Jun, S. Porowski, J. Appl. Phys 76, 4909 (1994).
10. T. Kozawa, T. Kachi, H. Kano, H. Nagase, N. Koide, K. Manabe, J. Appl. Phys. 77, 4389, (1995).
11. B. Skromme, H. Zhao, D. Wang, H. Kong, M. Leonard, G. Bulman, R. Molnar, Appl. Phys. Lett. 71, 829 (1997)
12. I. Lee, I. Choi, C. Lee, S. Noh, Appl. Phys. Lett. 71,1359, (1997)
13. P. Vennegues, B. Beaumont, M. Vaille, P. Gilbart, J. of Crystal Growth, 173, 249 (1997).
14. S. Hearne, E. E. Chason, J. Han, J. A. Floro, J. Figiel, J. Hunter , H. Amano, I. Tsong, Appl. Phys. Lett. 74, 356 (1999)
15. J. Han, T. B. Ng, R. M. Biefeld, M. H. Crawford, D. M. Follstaedt, Appl. Phys. Lett, 71, 3114 (1997)
16. C. Taylor, D. Barlett, E. Chason, J. A. Floro, Ind. Physicist 4, 25 (1998)
17. J. Floro, E. Chason, S. Lee, R. Twesten, R. Hwang, L. Freund, J. Elec. Mat. 26, 969 (1997)
18. M. Doerner and W. Nix, CRC Critical Reviews in Sol. State and Mat. Sci. 14, 224, (1988).
19. T. B. Ng, J. Han, R. M. Biefeld, and M. V. Weckwerth, J. Electron. Mat. 27, 190 (1998).

GENERATION RECOMBINATION NOISE IN GaN PHOTOCONDUCTING DETECTORS

M. Misra, D. Doppalapudi, A.V. Sampath, T.D. Moustakas
Department of Electrical Engineering and Center for Photonics Research, Boston University, MA 02215
P.H. McDonald
Center for Photonics Research, Boston University, MA 02215

Cite this article as: MRS Internet J. Nitride Semicond. Res. 4S1, G7.8 (1999)

Abstract

Low frequency noise measurements are a powerful tool for detecting deep traps in semiconductor devices and investigating trapping-recombination mechanisms. We have performed low frequency noise measurements on a number of photoconducting detectors fabricated on autodoped n-GaN films grown by ECR-MBE. At room temperature, the noise spectrum is dominated by 1/f noise and thermal noise for low resistivity material and by generation-recombination (G-R) noise for high resistivity material. Noise characteristics were measured as a function of temperature in the 80K to 300K range. At temperatures below 150K, 1/f noise is dominant and at temperatures above 150K, G-R noise is dominant. Optical excitation revealed the presence of traps not observed in the dark, at room temperature.

Introduction

The III-Nitrides is an important class of materials for the development of optoelectronic devices and electronic devices for operation at high speeds and high temperatures[1]. The performance of most of these devices is strongly influenced by the presence of defects and traps in the material. Several techniques, such as Deep Level Transient Spectroscopy (DLTS)[2-4], Photo Induced Capacitance Transient Spectroscopy (PICTS)[5], Thermally Stimulated Current (TSC)[6], and Thermal Admittance Spectroscopy (TAS)[7] have been used to investigate and characterize the deep defects in GaN. In this paper, we describe the technique of noise spectroscopy to study the presence of deep levels in GaN films grown on sapphire. Noise spectroscopy has been used as a tool to investigate traps in silicon[8] and III-As/P compounds, and to study the influence of the deep levels on performance of devices such as JFETs[9] and MODFETs[10, 11]. It has also been used to characterize the performance of GaN p-n junctions.[15] To the best of our knowledge, this is the first report of using noise measurements to study deep levels in GaN photoconductors.

Theory

Photoconducting detectors, typically, exhibit three types of noise: *1/f* noise which is associated with contacts and surfaces, generation-recombination (G-R) noise which is associated with the trapping and emission of charges from deep traps and thermal or Johnson noise, which is associated with the resistance of the material. Generation-recombination noise arises because the trapping and emission of charges from the deep levels causes fluctuations in the dc dark current. This excess current decays, on an average, with a time constant τ, so that the average current as a function of time t will be given as

$$i(t) = I_0 \exp\left(-t/\tau\right) \qquad (1)$$

Mat. Res. Soc. Symp. Proc. Vol. 537 © 1999 Materials Research Society

The time constant τ is a characteristic of the deep level and is related to its emission (τ_e) and capture (τ_c) time constants according to the relation[12]

$$\frac{1}{\tau} = \frac{1}{\tau_e} + \frac{1}{\tau_c} \qquad (2)$$

When the noise arises from deep levels with a well-defined time constant the observed noise spectrum has a Lorentzian shape which can be described as

$$\langle i^2 \rangle = \frac{A * \Delta f}{\left[1 + \left(f / f_0\right)^2\right]} \qquad (3)$$

where $f_0 = 1/2\pi\tau$ is the characteristic frequency associated with the time constant τ and A is the amplitude of the noise current at frequencies $f \ll f_0$, and referred to as the zero frequency noise plataeu. It is from the variation of the zero frequency plataeu value A and the time constant τ with temperature that the activation energy of deep levels can be determined. If the variation of the free carrier concentration n as a function of temperature is also known, other trap parameters such as its density, degeneracy and capture cross section can also be deduced. Furthermore, multi-level spectra can be decomposed into separate Lorentzians, such that each Lorentzian contains information of a single trap, if the Fermi level is a few kT away from the trap level and the concentration of mobile carriers is larger than the concentration of impurities[13].

The zero frequency amplitude increases as the temperature increases until the Fermi-level crosses the trap level, and then decreases rapidly.[12, 13] The temperature dependence of τ is obtained from the following relation[13],

$$\frac{1}{\tau} = \alpha n \left[B \exp\left(\frac{E_T - E_f}{kT}\right) + 1\right] \qquad (4)$$

where α is the recombination coefficient, B and E_T are the degeneracy factor and depth of the trap respectively, E_f is the dark Fermi-level, n is the free carrier concentration, k is Boltzman's constant, T is the temperature. In the low temperature limit, when the Fermi-level lies above the trap level, the exponential in Eq. (4) is small compared to unity and the characteristic time constant is virtually constant. As the temperature increases, and the Fermi-level is below the trap level, the exponential dominates, and a strong temperature dependence is observed.

In order to extract trap parameters, we followed the method derived by Copeland[12]. In brief, the method consists of combining the three temperature dependent experimentally observed parameters A, τ and n into a single function of temperature F(T), such that

$$F(T) = \frac{An^2}{\tau} \qquad (5)$$

From the slope of the plot of ln(F(T)) versus 1/T, the trap activation energy and other parameters can be determined.

Experimental Methods

Noise measurements were performed on photoconducting detectors fabricated on n-GaN films grown on c-plane sapphire by the electron cyclotron resonance microwave plasma assisted molecular beam epitaxy (ECR-MBE) method. The photoconducting detectors were fabricated by patterning interdigitated electrodes, with inter-electrode spacing ranging from 5μm to 20μm,

using standard photolithography and lift-off techniques. For the noise measurements, we studied two types of devices: (i) devices fabricated on low resistivity material ($\rho = 10^2$ohm-cm) and (ii) devices fabricated on high resistivity material ($\rho = 10^6$ohm-cm). The noise characteristics of the GaN photoconducting detectors were measured in the 10Hz to 50KHz range using a low noise current preamplifier and a signal analyzer. The device was mounted in a temperature controlled cryostat and the temperature was varied from 80K to 320K. The bias voltage on the sample varied from 0.5V to 1.5V. In order to illuminate the photoconductors, a 10mW He-Cd laser, emitting at 325nm was used.

Experimental Results

In this section, we shall illustrate (i) the effect of the position of the dark Fermi-level, (ii) the effect of optical excitation and (iii) the effect of thermal excitation on the noise characteristics of GaN photoconducting detectors.

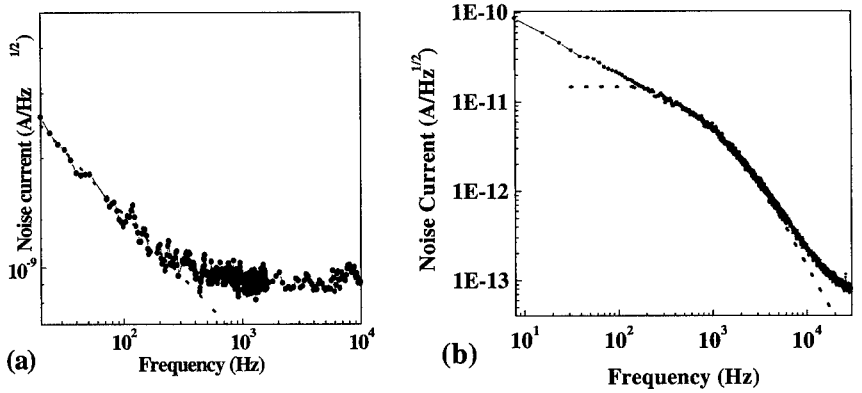


Figure 1: Noise characteristics at room temperature for GaN photoconducing detectors fabricated on (a) low resistivity material and (b) on high resistivity material. Dotted lines are (a) linear and (b) lorentzian fit to the data.

Figure 1a shows the noise spectrum at room temperature for a GaN photoconducting detector fabricated on low resistivity material. The spectrum is dominated by 1/f noise in the low frequency range (f<500Hz) and by thermal noise at higher frequencies (f >500Hz). The dark Fermi-level, at room temperature, was estimated to be 0.18eV below the conduction band. Since the noise measurement is sensitive to levels within a few kT of the Fermi-level, this measurement senses shallow traps, which typically have higher characteristic frequencies. Since the thermal noise is quite large, the G-R noise from these shallow levels is obscured at the higher frequencies. Figure 1b shows the noise spectrum for a GaN photoconducting detector fabricated on high resistivity material, measured under identical conditions. In this case, the spectrum shows 1/f noise in the 10Hz -100Hz range and a strong contribution of G-R noise in the 100Hz-10KHz range. In this case the dark Fermi-level was estimated to be 0.38eV below the conduction band edge. Thus it measures G-R noise from the deep levels, within a few kT of the Fermi-level. In addition, the thermal noise level, evident at frequencies greater than 20KHz is much lower. By fitting a

Lorentzian to the measured spectrum (dotted line), we deduced a characteristic frequency of 1.5KHz for this trap, corresponding to a characterisitic time constant of 106μs.

The effect of illumination is to excite traps throughout the gap and the traps for which the G-R noise contribution is greater than the thermal noise, will be observed. Figure 2 illustrates the noise characteristics from optically excited traps for both samples discussed earlier. We find that the low resistivity sample shows a G-R noise component with a characteristic frequency of about 1.5KHz upon optical excitation. The high resistivity device shows two G-R noise components: (i) with a characteristic frequency at 1.5KHz as seen by thermal excitation and an additional shallower level with a characteristic frequency of about 10KHz, which was not observed by thermal excitation alone at room temperature.

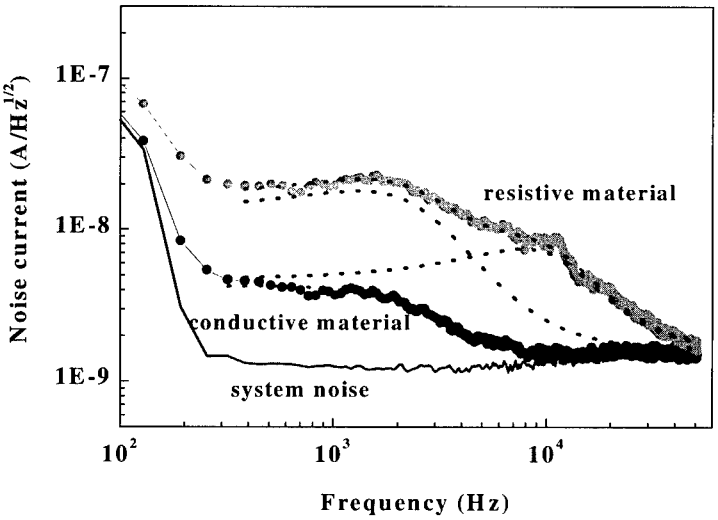


Figure 2: Noise characteristics of the GaN photoconductors when illuminated with He-Cd laser.

From the similarity in the characteristic frequency for the two samples, we may infer that the same trap level is present in both detectors and responsible for the G-R noise observed.

The temperature dependence of the noise characteristics of the high resistivity detector in the 80K to 300K range was also investigated. At temperatures below 120K, the noise spectrum was dominated by 1/f noise and thermal noise, and no G-R noise component was observable. At temperatures higher than 120K, a gradual increase in the G-R noise component was increased. An increase in the zero-frequency plataeu value and and shift in the characteristic frequency was observed. Figures 3a and 3b show the noise characteristics at 100K and 160K. The same at 300K are shown in figure 1b. In addition, we also measured the variation in the dark resistance of the detector as a function of temperature in the 80K-300K range, to obtain an independent measurement of the free electron concentration n. From the variation of A, f_0 and n, we calculated the function F(T) and estimate the depth of the trap to be 0.38eV. In addition, from the measurement of the characteristic frequency and the measurement of the free carrier concentration at room temperature, we can calculate the depth of the trap using Eq. (4).

Using this expression, with $\alpha=3x10^{-11}cm^3/s$,[14] $n=1.5x10^{15}cm^{-3}$, B=1, T=300K, we calculated the depth of the trap to be 0.4eV below the conduction band. This value is in good agreement with the observation of a deep level in the 0.4eV-0.5eV range by several researchers

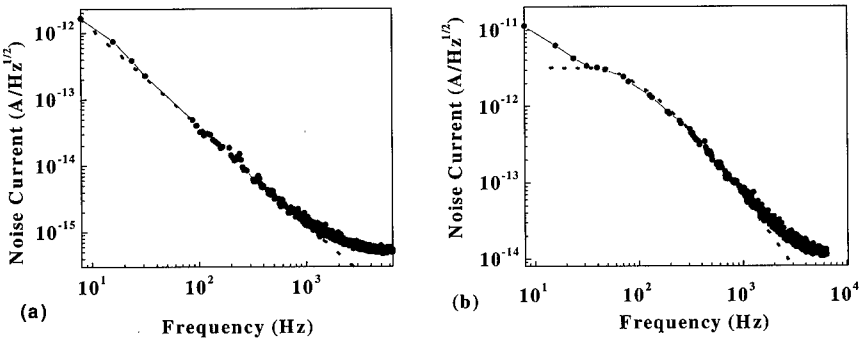


Figure 3: Noise characteristics of the resistive device at (a) 100K and (b) 160K. Dotted lines are (a) linear and (b) Lorentzian fits to the data.

using other techniques such as DLTS, PICTS and TAS, on samples grown by MOVPE[2-5] and MBE.[6] and in GaN p-n junctions operating in the forward bias, grown by MOCVD, and studied used techniques similar to those described in this paper.[15]

From the relation $\tau = 1/v_{th}Sn$, where v_{th} is the thermal velocity of electrons, we have calculated the capture cross-section to be $S= 2x10^{-19}$ cm^2, which indicates that the trap is a coulombic center. However, we believe that measurements above 300K are necessary to observe the sharp decrease in τ and A with temperature, as the Fermi-level crosses the trap level. Unfortunately, we could not measure the noise characteristics at higher temperatures, at this time, due to excessive 1/f noise in our high temperature apparatus

Conclusions

In conclusion, we have investigated the noise behavior of GaN photoconductors in the 10Hz-50KHz range and was found that it is dominated by *1/f* and thermal noise for low resistivity ($\rho=10^2$ohm-cm) devices and by G-R noise for high resistivity devices ($\rho=10^6$ohm-cm) at room temperature. A deep level was identified, with a time constant of 106μs, and its activation energy was estimated to be in the 0.3eV-0.4eV range. The capture cross-section of this trap was found to be $2x10^{-19}cm^2$, suggesting that it is a coulombic center. In addition, optical excitation revealed the presence of a similar trap in the low resistivity material, which was not seen by thermal excitation. However, noise measurements need to be performed at temperatures higher than 300K, to determine the full temperature dependence of τ and to confirm the trap properties. To the best of our knowledge, this is the first report of using noise measurements to study deep levels in GaN photoconductors.

Acknowledgements

This work was supported by DARPA through a sub-contract with Lockheed-Martin.

References

1. H. Morkoc, S. Strite, G.B. Gao, M.E. Lin, B. Sverdlov and M. Burns, J. Appl. Phys. **76**, 1363, (1994)
2. P. Hacke, H. Nakayama, T. Detchprom, K. Hiramatsu and N. Sawaki, Appl. Phys. Lett. **68**, 1362, (1996)
3. W.I. Lee, T.C. Huang, J.D. Guo and M.S. Feng, Appl. Phys. Lett. **67**, 1721, (1995)
4. W. Gotz, N.M. Johnson, R.A. Street, H. Amano and I. Akasaki, Appl. Phys. Lett. **66**, 1340, (1995)
5. A.Y. Polyakov, N.B. Smirnov, A.V. Govorkov, M. Shin, M. Skowronski and D.W. Greve, J. Appl. Phys. **84**, 870, (1998)
6. D.C. Look, Z.-Q. Fang, W. Kim, O. Atkas, A. Botchkarev, A. Salvador and H. Morkoc, Appl. Phys. Lett. **68**, 3775, (1996)
7. A. Krtschil, H. Witte, M. Lisker, J. Christen, U. Birkle, S. Einfeldt, D. Hommel, , J. Appl. Phys. **84**, 2040, (1998)
8. S.L. Jang, and G. Bosman, J. Appl. Phys. **65**, 201, (1989)
9. S. Kugler, K. Steiner, U. Seiler, K. Heime and E. Kuphal, Appl. Phys. Lett. **52**, 111, (1988)
10. J.R. Kirtley, T.N. Theis, P.M. Mooney, S.L. Wright, J. Appl. Phys. **63**, 1541, (1988)
11. S. Kugler, IEEE Trans. Electron. Dev. **35**, 623, (1988)
12. J. A. Copeland, IEEE Trans. Electron. Dev. **ED-18**, 50, (1971)
13. A.D. vanRheenen, G. Bosman, R.J. Zijlstra, Solid State Electron. 30, 259, (1987)
14. A.V. Dmitriev, A.L. Oruzheinikov, M.V. Lomonosov, MIJ-NSR 1, 46, (1996)
15. D.V. Kuksenkov, H. Temkin, A. Osinsky, R. Gaska, M.A. Khan, J. Appl. Phys. **83**, 2142, (1998)

Part VIII

Electronic Devices and Processing

GROUP-III NITRIDE ETCH SELECTIVITY IN BCl_3/Cl_2 ICP PLASMAS

R. J. Shul,[*] L. Zhang,[*] C. G. Willison,[*] J. Han,[*] S. J. Pearton,[**] J. Hong,[**] C. R. Abernathy,[**] and L. F. Lester[***]

[*]Sandia National Laboratories, Albuquerque, NM 87185-0603, rjshul@sandia.gov
[**]University of Florida, Department of Materials Science and Engineering, Gainesville, FL 32611
[***]University of New Mexico, Electrical Engineering, Albuquerque, NM

Cite this article as: MRS Internet J. Nitride Semicond. Res. 4S1, G8.1 (1999).

ABSTRACT

Patterning the group-III nitrides has been challenging due to their strong bond energies and relatively inert chemical nature as compared to other compound semiconductors. Plasma etch processes have been used almost exclusively to pattern these films. The use of high-density plasma etch systems, including inductively coupled plasmas (ICP), has resulted in relatively high etch rates (often greater than 1.0 μm/min) with anisotropic profiles and smooth etch morphologies. However, the etch mechanism is often dominated by high ion bombardment energies which can minimize etch selectivity. The use of an ICP-generated BCl_3/Cl_2 plasma has yielded a highly versatile GaN etch process with rates ranging from 100 to 8000 Å/min making this plasma chemistry a prime candidate for optimization of etch selectivity. In this study, we will report ICP etch rates and selectivities for GaN, AlN, and InN as a function of BCl_3/Cl_2 flow ratios, cathode rf-power, and ICP-source power. GaN:InN and GaN:AlN etch selectivities were typically less than 7:1 and showed the strongest dependence on flow ratio. This trend may be attributed to faster GaN etch rates observed at higher concentrations of atomic Cl which was monitored using optical emission spectroscopy (OES).

INTRODUCTION

Etch selectivity for the group-III nitrides has become important as interest in high power, high temperature electronic devices has increased. For example, the formation of low resistivity ohmic contacts or a gate recess for high electron mobility transistors (HEMTs) and heterojunction bipolar transistors (HBTs) requires accurately stopping the etch on a specific contact layer. Patterning the group-III nitride films has improved significantly despite their inert chemical nature and strong bond energies primarily due to the use of high-density plasma (HDP) etch systems. HDP etch systems operate under high plasma flux conditions which improve the III-N bond breaking efficiency and the sputter desorption of etch products from the surface. Unfortunately, the best etch results i.e. anisotropic profiles, smooth surface morphology and high etch rates, are often obtained under energetic ion bombardment conditions which can minimize etch selectivity. However, by reducing the ion energy or increasing the chemical activity in the plasma, etch selectivity can often be improved.

The chemical activity of an etch process and therefore the etch characteristics can be strongly effected by the choice of reactive source gas (Cl_2, BCl_3, $SiCl_4$, IBr, BBr_3, CH_4/H_2, ICl, CHF_3 etc.).[1-15] Table I shows the boiling points of possible etch products for group-III nitride films exposed to halogen-based plasmas. Etch rates are often limited by the volatility of the group-III halogen etch product. Therefore, chlorine-, iodine-, and bromine-based chemistries are preferred

Mat. Res. Soc. Symp. Proc. Vol. 537 © 1999 Materials Research Society

to etch Ga- and Al-containing materials due to the high volatility of the etch product as compared to fluorine-based chemistries. Chlorine-based plasmas have been the most widely used to etch Ga-containing compound semiconductors since they are less corrosive than iodine- or bromine-based plasmas and typically yield fast rates with anisotropic, smooth etch profiles. For In-containing species, etch rates obtained in room temperature chlorine-based plasmas tend to be slow with rough surfaces due to the low volatility of the $InCl_3$ etch products and preferential loss of the group-V species. However, under high plasma flux conditions the $InCl_3$ etch products are sputtered away before they can passivate the surface resulting in improved etch rates and surface morphology.[16] Also, at elevated substrate temperatures (>130°C), the volatility of $InCl_3$ etch product increases thus improving the etch results.[17-19]

Several selectivity studies have recently been reported for the group-III nitrides.[20-26] GaN:AlN and GaN:InN etch selectivities were typically < 7:1, however Smith and co-workers reported an etch selectivity > 38:1 for GaN:AlN in an inductively coupled plasma (ICP) etch system at –20 V dc-bias.[21] Plasma chemistries can have a significant effect on etch selectivities due to the differences in volatility of the etch products.[20, 24] For example, GaN:AlN and GaN:InN etch selectivities were typically > 1:1 in Cl_2-based plasmas and < 1:1 in BCl_3-based plasmas. This was attributed to higher concentrations of reactive Cl generated in Cl_2-based plasmas as compared to BCl_3-based plasmas and thus faster GaN etch rates. Alternatively, InN and AlN etch rates showed much less dependence on the Cl concentration and were fairly comparable in Cl_2 and BCl_3-based plasmas.

The use of an ICP-generated BCl_3/Cl_2 plasma has yielded a highly versatile GaN etch process with rates ranging from 100 to 8000 Å/min[27, 28] making this plasma chemistry a prime candidate for optimization of the group-III nitride etch selectivity. In this study, we will report ICP etch rates and selectivities for GaN, AlN, and InN as a function of BCl_3/Cl_2 flow ratios, cathode rf-power, and ICP-source power.

Table I. Boiling points for possible III-N etch products in halogen-based plasmas.

Etch Products	Boiling Points (°C)
$AlCl_3$	183
AlF_3	na
AlI_3	360
$AlBr_3$	263
$GaCl_3$	201
GaF_3	1000
GaI_3	sublimes 345
$GaBr_3$	279
$InCl_3$	600
InF_3	>1200
InI_3	na
$InBr_3$	sublimes
NCl_3	<70
NI_3	explodes
NF_3	-129

EXPERIMENT

The GaN films etched in this study were grown by metal organic chemical vapor deposition (MOCVD), whereas the AlN and InN samples were grown using metal organic-molecular beam epitaxy (MO-MBE). The ICP reactor was a load-locked Plasma-Therm SLR 770 which used a 2 MHz, 3 turn coil ICP source. All samples were mounted using a thermally conductive paste on an anodized Al carrier that was clamped to the cathode and cooled with He gas. The ion energy or dc-bias was defined by superimposing a rf-bias (13.56 MHz) on the sample. Samples were patterned with AZ-4330 photoresist. Etch rates were calculated from the depth of etched features measured with an Alpha-step stylus profilometer after the photoresist was removed. Depth measurements were taken at a minimum of 3 positions. Samples were ~1 cm^2 and were exposed to the plasma for 1 to 3 minutes. Run-to run repeatability was typically better than ±10% while the uniformity across the sample was typically better than ±5%. One exception was InN samples, which yielded a uniformity closer to ±25% due to the rough surface morphology of the as-grown sample. Surface morphology, anisotropy, and sidewall undercutting were evaluated with a scanning electron microscope (SEM). The root-mean-square (rms) surface roughness was quantified using a Digital Instruments Dimension 3000 atomic force microscope (AFM) system operating in tapping mode with Si tips.

Optical emission spectra (OES) were obtained for most of the plasma conditions reported in this paper. Due to limited optical access immediately above the sample surface, spectra were obtained through a window mounted on the top of the ICP plasma generation region. Consequently, the conclusions drawn from the OES results may be only qualitatively applicable to the conditions at the sample surface, especially where mean-free paths were sufficiently short to enable several collisions between the plasma generation region and the sample surface. Atomic emission intensities from Cl species were normalized by the intensity of the Ar emission at 750 nm to correct for variations in excitation efficiency under different plasma conditions.

RESULTS AND DISCUSSIONS

A characteristic OES spectra is shown in Figure 1 for an ICP-generated BCl_3/Cl_2 plasma under the following conditions; 2 mTorr chamber pressure, 125 W cathode rf-power with a corresponding dc-bias of -235 V, 500 W ICP-power, 32 sccm Cl_2, 8 sccm BCl_3, and 5 sccm Ar. Strong emission from excited neutral Cl^0 atoms was obtained at 726, 741, 755, 775, 808.3, and 837.5 nm. Strong emissions were also observed from excited Cl^+ species at 413 nm. This implied that both Cl neutrals and ions were prominent in the group-III nitride etch process whereas our earlier study showed only weak Cl^+ emission.[28] In general, etch rate data for GaN tracked with the Cl neutral and ion emission peaks while the AlN and InN etch rates were less dependent on Cl concentration.

Changes in the plasma gas composition can have a strong effect on the chemical-to-physical components of the etch mechanism and thus etch selectivity. In Figure 2 GaN, AlN, and InN etch rates are plotted as a function of $\%Cl_2$ in the BCl_3/Cl_2 ICP plasma. Plasma parameters were 2 mTorr pressure, 500 W ICP power, and 125 W cathode rf-power with corresponding dc-bias ranging from –230 to –285 V. The dc-bias initially increased as Cl_2 was added to the BCl_3/Ar plasma and then decreased at higher Cl_2 concentrations. GaN etch rates increased up to ~4390 Å/min at 80% Cl_2 due to higher concentrations of reactive Cl. This was confirmed using OES where the Cl^+ and Cl^0 emission intensity increased up to 80% Cl_2 (see Figure 3). Slower GaN

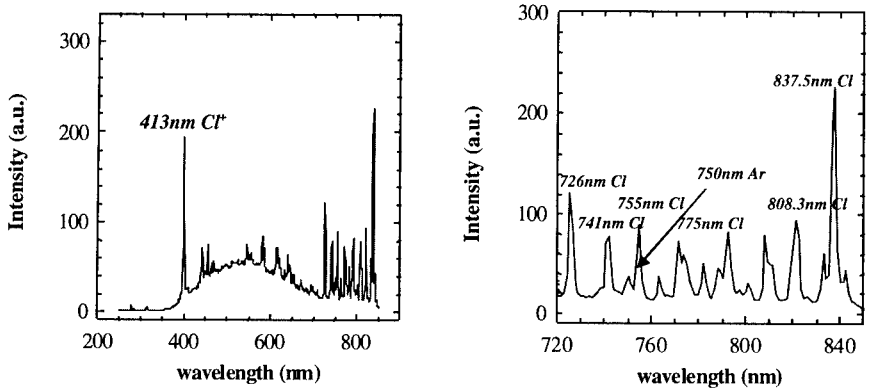


Figure 1. OES of ICP generated BCl_3/Cl_2 plasma.

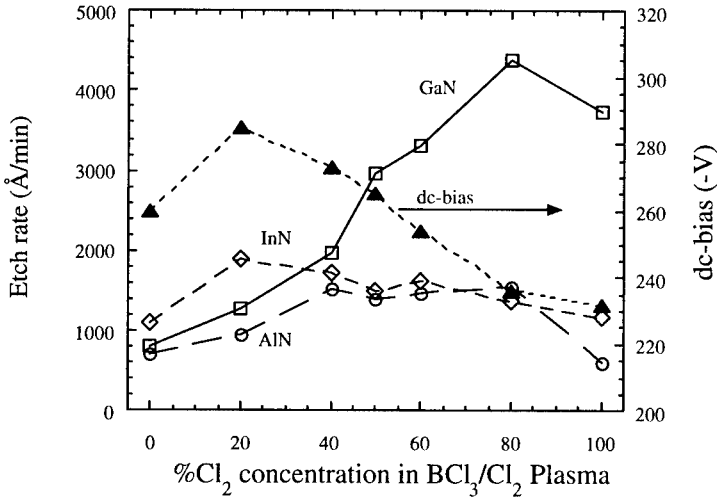


Figure 2. GaN, InN, and AlN etch rates as a function of $\%Cl_2$ in a $BCl_3/Cl_2/Ar$ ICP plasma. Plasma conditions were: 2 mTorr pressure, 500 W ICP-source power, 125 W cathode rf-power, and 25°C cathode temperature.

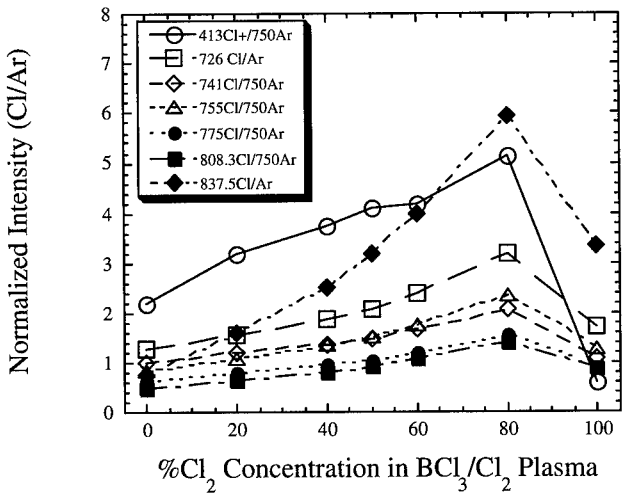


Figure 3. OES showing the increase in Cl^+ and Cl^0 emission normalized to Ar as a function of $\%Cl_2$ concentration.

etch rates observed at 100% Cl_2, were attributed to lower Cl^0 and Cl^+ emission and less efficient sputter desorption of the etch products from the surface in the absence of the heavier BCl_x ions. Lee and co-workers saw a similar trend where the maximum GaN etch rate was obtained at90% Cl_2.[14] Using OES and a Langmuir probe, they observed higher ion current densities and Cl radical densities as the $\%Cl_2$ increased.

InN etch rates initially increased as the Cl_2 concentration increased and then decreased above 20%. The AlN etch rates increased up to 40% Cl_2 concentration and then remained relatively constant. Above 50% Cl_2, InN and AlN etch rates were much slower than GaN. For InN, this may be attributed to the low volatility of the $InCl_3$ etch products, however for AlN the volatility of the $AlCl_3$ etch product is quite high. Therefore, slow AlN etch rates were attributed to their strong bond energy, 11.52 eV/atom, as compared to 8.92 eV/atom for GaN and 7.72 eV/atom for InN. The etch selectivities for GaN:AlN and GaN:InN are shown in Figure 4 as a function of %Cl concentration. In both cases the selectivities increased as the concentration of Cl_2 increased due to higher GaN etch rates. At low Cl_2 concentrations the GaN:InN selectivity was less than 1. A maximum selectivity of 6.3:1 was obtained for GaN:AlN in a pure Cl_2 plasma.

Another method of changing the chemical-to-physical component of the etch mechanism is to vary the energy of the ions which bombard the substrate surface. In Figure 5, etch rates for GaN, AlN, and InN are shown as a function of cathode rf-power (which corresponds to ion energy). Plasma etch conditions were 2 mTorr pressure, 32 sccm Cl_2, 8 sccm BCl_3, 5 sccm Ar, and 500 W ICP source power. In general, etch rates for all 3 films increased monotonically as cathode rf-power increased due to more efficient breaking of III-N bonds and sputter desorption of the etch products at higher ion energies. The decrease in etch rate for GaN at 350 W cathode rf-power may be due to sputter desorption of reactant species from the surface prior to reaction. Faster InN etch rates at higher ion energies were attributed to efficient sputter desorption of the $InCl_3$

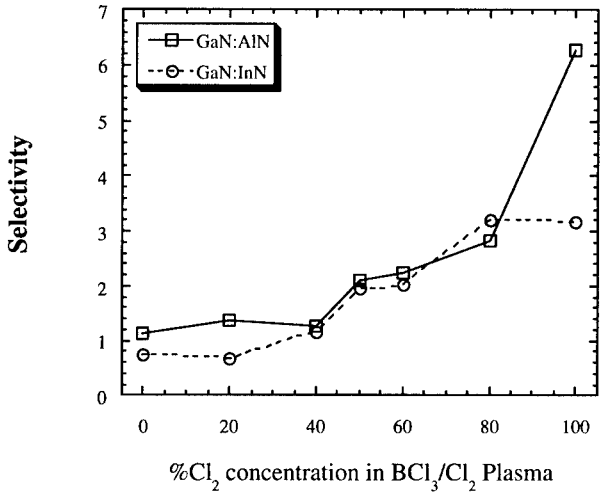


Figure 4. GaN:AlN and GaN:InN etch selectivities as a function of $\%Cl_2$ in a $BCl_3/Cl_2/Ar$ ICP plasma. Plasma conditions were: 2 mTorr pressure, ICP-source power 500 W, 125 W cathode rf-power, and 25°C cathode temperature.

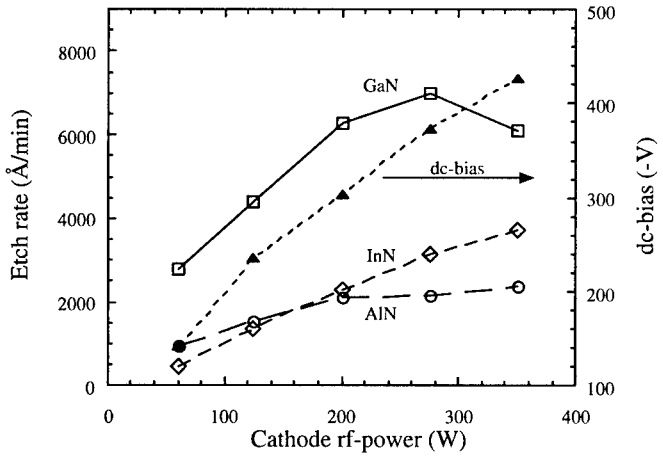


Figure 5. GaN, InN, and AlN etch rates as a function of cathode rf-power in a $BCl_3/Cl_2/Ar$ ICP plasma. Plasma conditions were: 2 mTorr pressure, ICP-source power 500 W, 32 sccm Cl_2, 8 sccm BCl_3, and 25°C cathode temperature.

etch products prior to passivation of the etch surface by the non-volatile $InCl_3$.[16] The etch-rate dependence on dc-bias did not correlate well with Cl^0 emission intensity which was somewhat scattered over the conditions studied. However, the etch rates tracked fairly well with the Cl^+ emission intensity. Etch rates were slightly slower than our earlier results[28] due to differences in the chamber conditions as well as slightly lower dc-biases under comparable cathode rf-power. The GaN:InN etch selectivity decreased as a function of cathode rf-power (see Figure 6) due to efficient sputter desorption of the $InCl_3$ at higher ion energies. The GaN:AlN etch selectivity remained relatively constant at approximately 3:1.

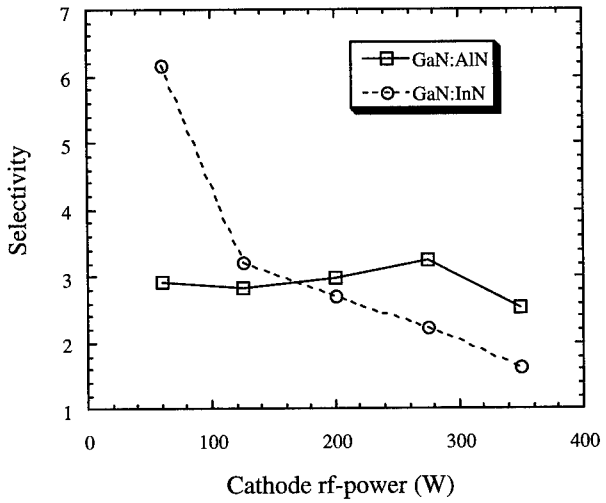


Figure 6. GaN:AlN and GaN:InN etch selectivities as a function of cathode rf-power in a BCl_3/Cl_2/Ar ICP plasma. Plasma conditions were: 2 mTorr pressure, ICP-source power 500 W, 32 sccm Cl_2, 8 sccm BCl_3, and 25°C cathode temperature.

By varying the ICP source power, the chemical (reactant neutral flux) and physical (ion flux) components of the etch mechanism can be changed. As the ion flux increases so does the efficiency of III-N bond breaking and the sputter desorption of etch products from the surface. In Figure 7, GaN, InN, and AlN etch rates are plotted as a function of ICP source power. The plasma conditions were 2 mTorr pressure, 125 W cathode rf-power with corresponding dc-bias ranging from –160 to –300 V, 32 sccm Cl_2, and 8 sccm BCl_3. For all 3 films the etch rate initially increased up to 500 W ICP source power and then stabilized and even decreased at higher powers. The decrease in etch rate may be attributed to sputter desorption of reactants from the surface before they have time to react and/or lower dc-biases (lower ion energies) observed at higher ICP power. Once again, the GaN etch results were significantly slower than those obtained in our earlier studies.[28] Etch rates tracked identically with the Cl^+ (413 nm) and the Cl^0 (837.5 nm) emission intensity as determined by OES indicating that both the physical and

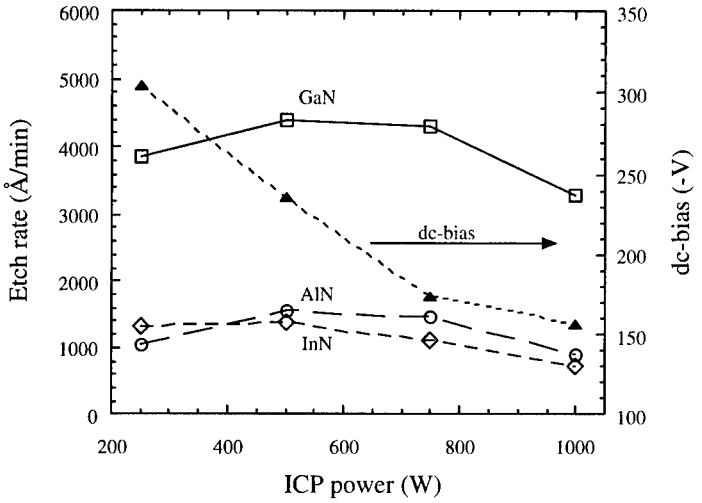


Figure 7. GaN, InN, and AlN etch rates as a function of ICP source power in a $BCl_3/Cl_2/Ar$ plasma. Plasma conditions were: 2 mTorr pressure, 125 W cathode rf-power with corresponding dc-bias ranging from –160 to –300 V, 32 sccm Cl_2, 8 sccm BCl_3, and 25°C cathode temperature.

chemical components of the etch are significant. Additional Cl^0 emission lines increased slightly with ICP source power. In Figure 8, GaN:AlN etch selectivity remained relatively constant, whereas the GaN:InN increased slightly with ICP power.

AFM was used to quantify the etched surface morphology as rms roughness for many of the plasma conditions reported in this paper. Rough etch morphology often indicates a non-stoichiometric surface due to preferential removal of either the group-III or group-V species. The rms roughness for the as-grown samples were 1.00 nm for GaN, 5.98 nm for AlN, and 239.97 nm for InN. For GaN, the surface morphology remained smooth, (< 5.1 nm) as a function of $\%Cl_2$, ICP source power, and cathode rf-power implying stoichiometric etching. RMS roughness for GaN, InN, and AlN is plotted as a function of $\%Cl_2$ concentration in Figure 9. The largest GaN rms roughness was obtained in pure BCl_3 where the physical component of the etch was greatest due to higher mass ions and then remained relatively constant at < 1.7 nm as Cl_2 was added to the plasma. The InN rms was normalized to the as-grown rms and scanned over a 40 x 40 μm area (as compared to 10 x 10 μm for GaN and AlN) due to the as-grown sample's rough surfaces. The InN surface remained relatively smooth as a function of plasma gas ratio again implying stoichiometric etching. However, the AlN rms roughness increased to a maximum of 34.2 nm at 50% Cl_2 and then smoothed out as the Cl_2 concentration increased. This trend may be attributed to the high bonding energy for AlN and demonstrates the need to balance the chemical-to-physical ratio of the etch mechanism.

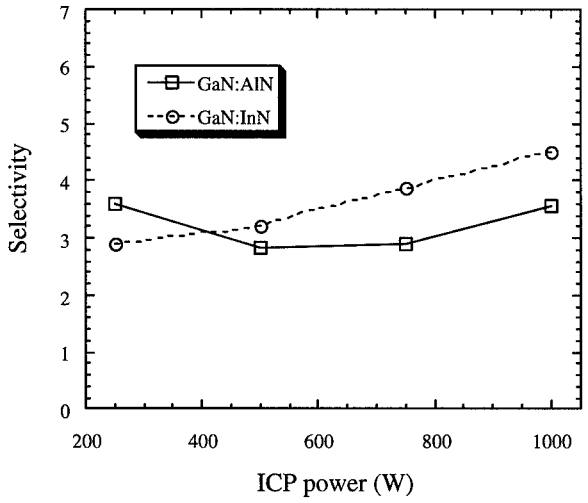


Figure 8. GaN:AlN and GaN:InN etch selectivities as a function of ICP source power in a $BCl_3/Cl_2/Ar$ plasma. Plasma conditions were: 2 mTorr pressure, 125 W cathode rf-power with corresponding dc-bias ranging from –160 to –300 V, 32 sccm Cl_2, 8 sccm BCl_3, and 25°C cathode temperature.

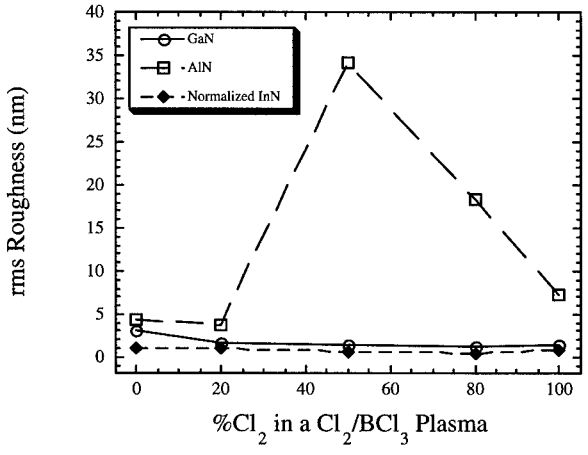
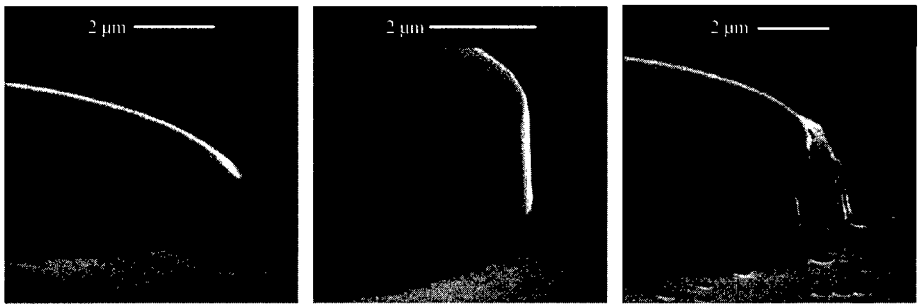


Figure 9. GaN, AlN, and normalized InN rms roughness as a function of $\%Cl_2$. ICP etch conditions were 32 sccm Cl_2, 8 sccm BCl_3, 5 sccm Ar, 500 W ICP source power, and 2 mTorr pressure.

In general, etch profiles ranged from highly anisotropic and smooth to undercut and rough dependent upon the plasma etch conditions. For example, in Figure 10, SEM micrographs are shown for GaN samples etched at a) -50, b) -150, and c) -300 V dc-bias under the following conditions; 32 sccm Cl_2, 8 sccm BCl_3, 5 sccm Ar, 500 W ICP source power, and 2 mTorr pressure. The etch anisotropy improved as the dc-bias increased from -50 to -150 V dc-bias due to the perpendicular nature of the ion bombardment energies. However, at -300 V dc-bias a tiered etch profile with vertical striations in the sidewall was observed due to erosion of the mask-edge under high ion bombardment energies. GaN etch profiles declined as either the ion energy or plasma flux increased. This was attributed to breakdown of the mask edge. For InN and AlN the range of plasma conditions yielding anisotropic smooth etching was much less than GaN. This trend may be attributed to GaN being more reactive in Cl-based plasmas, higher quality of as-grown material, low volatility of the InN etch products, or the higher bonding energy of AlN.



(a) (b) (c)

Figure 10. SEM micrographs for GaN etched at a) -50, b) -150, and c) -300 V dc-bias. ICP etch conditions were 32 sccm Cl_2, 8 sccm BCl_3, 5 sccm Ar, 500 W ICP power, and 2 mTorr pressure.

CONCLUSIONS

In summary, the BCl_3/Cl_2 plasma chemistry appears to provide a very versatile etch process for the group-III nitrides. However, the etch selectivity for GaN:AlN and GaN:InN is typically low < 7:1 as a function of $\%Cl_2$ in a Cl_2/BCl_3 plasma, ICP source power, and cathode rf-power. Selectivity seemed to improve as the concentration of reactive Cl increased due to the strong dependence of the GaN etch rate on the neutral and ion Cl flux which had very little effect on AlN and InN. Etch selectivity for the group-III nitrides was much less dependent on ion-to-neutral flux and ion energy. A wide range of plasma conditions were observed which yielded highly anisotropic etch profiles with smooth etch morphologies for GaN with a more limited range for InN and AlN.

ACKNOWLEDGMENTS

Sandia is a multiprogram laboratory operated by Sandia Corporation, a Lockheed Martin Company, for the United States Department of Energy under contract DE-ACO4-94AL85000. Two of the authors (L. F. Lester and L. Zhang) are also supported by a National Science Foundation CAREER Grant EC5-9501785.

REFERENCES

1. I. Adesida, A. Mahajan, E. Andideh, M. Asif Khan, D. T. Olsen, and J. N. Kuznia, Appl. Phys. Lett. 63, 2777 (1993).
2. M. E. Lin, Z. F. Zan, Z. Ma. L. H. Allen, and H. Morkoç, Appl. Phys. Lett. 64, 887 (1994).
3. A. T. Ping, I. Adesida, M. Asif Khan, and J. N. Kuznia, Electron. Lett. 30, 1895 (1994).
4. H. Lee, D. B. Oberman, and J. S. Harris, Jr., Appl. Phys, Lett. 67, 1754 (1995).
5. S. J. Pearton, C. R. Abernathy, F. Ren, J. R. Lothian, P. W. Wisk, A. Katz, and C. Constantine, Semicond. Sci. Technol. 8, 310 (1993).
6. S. J. Pearton, C. R. Abernathy, and F. Ren, Appl. Phys. Lett. 64, 3643 (1994).
7. R. J. Shul, S. P Kilcoyne, M. Hagerott Crawford, J. E. Parmeter, C. B. Vartuli, C. R.
8. L. Zhang, J. Ramer, J. Brown, K. Zheng, L. F. Lester, S. D. Hersee, Appl. Phys. Lett. 68, 367 (1996).
9. B. Humphreys and M. Govett, MIJNSR 1, (1996).
10. R. J. Shul, G. B. McClellan, S. A. Casalnuovo, D. J. Rieger, S. J. Pearton, C. Constantine, C. Barratt, R. F. Karlicek, Jr., C. Tran, and M. Schurman, Appl. Phys. Lett. 69, 1119 (1996).
11. C. B. Vartuli, S. J. Pearton, J. W. Lee, J. D. MacKenzie, C. R. Abernathy, and R. J. Shul, J. Vac. Sci. and Technol B15, 98 (1997).
12. C. B Vartuli, S. J. Pearton, J. D. MacKenzie, C. R. Abernathy, and R. J. Shul, J. Electrochem. Soc. 143, L246 (1996).
13. J. Hong, T. Maeda, S. M. Donovan, J. D. MacKenzie, C. R. Abernathy, S. J. Pearton, R. J. Shul, and J. Han, MIJNSR 3, 5 (1998).
14. S. J. Pearton, C. R. Abernathy, and F. Ren, Appl. Phys. Lett. 64, 2294 (1994).
15. R. J. Shul, C. I. H. Ashby, D. J. Rieger, A. J. Howard, S. J. Pearton, C. R. Abernathy, C. B. Vartuli, P. A. Barnes, and P. Davis, Mat. Res. Soc. Symp. Proc. Vol. 395, 751 (1996).
16. J. W. Lee, J. Hong, and S. J. Pearton, Appl. Phys. Lett. 68, 847 (1996).
17. C. Constantine, C. Barratt, S. J. Pearton, F. Ren, and J. R. Lothian, Electron. Lett. 28, 1749 (1992).
18. C. Constantine, C. Barratt, S. J. Pearton, F. Ren, and J. R. Lothian, Appl. Phys. Lett. 61, 2899 (1992).
19. D. G. Lishan and E. L. Hu, Appl. Phys. Lett. 56, 1667 (1990).
20. Hyun Cho, J. Hong, T. Maeda, S. M. Donovan, C. R. Abernathy, S. J. Pearton, R. J. Shul, and J. Han, J. Electron. Mats. 27, 915 (1998).
21. S. A. Smith, C. A. Wolden, M. D. Bremser, A. D. Hanser, and R. F. Davis, Appl. Phys. Lett. 71, 3631, 1997.
22. C. B. Vartuli, S. J. Pearton, J. D. MacKenzie, C. R. Abernathy, and R. J. Shul, J. Electrochem. Soc. 143, L246 (1996).
23. J. W. Lee, Hyun Cho, D. C. Hays, C. R. Abernathy, S. J. Pearton, R. J. Shul, G. A. Vawter, and J. Han, IEEE J. of Selected Topics in Quantum Electronics, 4, 557 (1998).
24. R. J. Shul, C. G. Willison, M. M. Bridges, J. Han, J. W. Lee, S. J. Pearton, C. R. Abernathy, J. D. MacKenzie, S. M. Donovan, L. Zhang, and L. F. Lester, J. Vac. Sci. Technol A16, 1621 (1998).
25. R. J. Shul, C. G. Willison, M. M. Bridges,. J. Han, J. W. Lee, S. J. Pearton, C. R. Abernathy, J. D. MacKenzie, S. M. Donovan, Mat. Res. Soc. Symp. Proc. Vol. 483, 155 (1998).
26. J. W. Lee, J. Hong, and S. J. Pearton, Appl. Phys. Lett. **68**, 847 (1996).
27. Y. H. Lee, H. S. Kim, W. S. Kwon, G. Y. Yeom, J. W. Lee, M. C. Yoo, and T. I. Kim, J. Vac. Sci. Technol. A16, 1478 (1998).
28. R. J. Shul, C. I. H. Ashby, C. G. Willison, L. Zhang, J. Han, M. M. Bridges, S. J. Pearton, J. W. Lee, and L. F. Lester, Mats. Res. Soc. Symp. Proc. 512, 487 (1998).

PATTERNING III-N SEMICONDUCTORS BY LOW ENERGY ELECTRON ENHANCED ETCHING (LE4)

H.P. Gillis*, M.B. Christopher*, K.P. Martin#, and D.A. Choutov#@

Department of Chemistry and Biochemistry, UCLA, Los Angeles, CA 90095.

#Microelectronics Research Center, Georgia Tech, Atlanta, GA 30332

@Present Address: National Semiconductor, San Jose, CA

Cite this article as MRS Internet J. Nitride Semicond. Res. 4S1, G8.2(1999)

ABSTRACT

Fabricating device structures from the III-N wide bandgap semiconductors requires anisotropoic dry etching processes that leave smooth surfaces with stoichiometric composition after transferring high-resolution patterns with vertical sidewalls. The purpose of this article is to describe results obtained by a new low-damage dry etching technique that provides an alternative to the standard ion-enhanced dry etching methods in meeting these demands for processing the III-N materials.

INTRODUCTION

The Group III nitride wide bandgap semiconductors hold the potential for important technological innovations in optoelectronics and in high power, high frequency microelectronics.[1 2 3] Blue and green Light Emitting Diodes (LEDs) are available,[4 5] and blue Laser Diodes have been reported.[6] Moreover, transistors fabricated from the III-N materials operate at much higher temperatures and under more adverse conditions than similar devices based on more familiar materials, because of the combination of wide bandgap, strong chemical bonds, and relative chemical inertness.[7] These same properties of high chemical bond energies and relative chemical inertness lead to difficulties in processing the III-N materials by standard lithographic and etching processes.[8] Since only very limited wet etching reactions have been identified for these materials,[9 10] fabrication of even large structures requires dry etching. Reactive Ion Etching (RIE) gives very slow rates and requires unusually high ion energies; the results are ion bombardment damage, modified stoichiometry in surface and near-surface

Mat. Res. Soc. Symp. Proc. Vol. 537 © 1999 Materials Research Society

regions, and a tendency toward the overcut etch profiles and trenching effects familiar in ion-dominated dry etching processes. [11 12 13 14] High-density Electron Cyclotron Resonance (ECR) microwave plasmas at modest power, sometimes accompanied by heating the sample to 200°C, produce acceptable etch rates; however, further increase of plasma power and rf bias on the sample to increase etch rate again creates ion-induced damage, alters stoichiometry, and roughens the surface.[15 16 17] Depending on plasma power and rf bias, ECR etching of GaN produces RMS surface roughness from 4 nm to 85 nm.[18] Chemically Assisted Ion Beam Etching (CAIBE), in which Ar^+ ion beams at 500 eV are directed to the etching surface through a background pressure of reactive gases, has produced vertical profiles on features 2.0 μm wide (but not on sub-micrometer features), but with N depletion at the etched surfaces.[19 20 21 22] Two recent comprehensive reviews summarize results achieved for the III-N materials with these standard *ion-enhanced* dry etching techniques and provide references to numerous specific studies.[23 24]

The difficulties faced by the ion-enhanced dry etching techniques trace largely to the need for energetic ions to overcome the strong chemical bond energies in the III-N materials. Alternative dry etching techniques that avoid energetic ions must then be considered, especially to achieve surface smoothness and selectivity between different III-N films.

A very attractive alternative is the new, low-damage dry etching technique called *Low Energy Electron Enhanced Etching (LE4)* in which electrons at energies 1-15 eV and reactive species at thermal velocities arrive at the surface. These electrons impart negligible momentum to the etching surface, and thereby avoid the ion bombardment damage intrinsic to RIE, ECR, and CAIBE, while "enhancing" the etch chemistry to give anisotropic pattern transfer. In earlier work, we demonstrated LE4 of Si(100)[25] and GaAs(100)[26] in a DC hydrogen or hydrogen/chlorine plasma with good anisotropy, high selectivity relative to the masking materials, and very smooth surfaces; the etch rate ranged from 20 $nm \cdot min^{-1}$ to 5 $\mu m \cdot min^{-1}$ depending on the reactive gas composition and temperature.

The first studies of LE4 on GaN demonstrated anisotropic pattern transfer, smooth surfaces, and stoichiometric surfaces for 1.0 μm thick films of GaN on Si(100) substrates, [27] and for 2.0 μm thick films of GaN(0001) deposited on α(6H)-SiC(0001) with a buffer layer of AlN(0001) between film and substrate.[28] Results reported here illustrate the capability of LE4 to produce anisotropic etching and smooth surfaces in samples with stacked interfaces.

EXPERIMENTAL METHODS

LE4 was conceived as a damage-free alternative to RIE and ECR for fabricating nanostructures in Si and compound semiconductors. The feasibility of LE4 was first demonstrated in UHV surface science type experiments with a beam of molecular hydrogen and a beam of low energy electrons simultaneously incident on an atomically clean, non-masked sample, with *in situ* mass spectrometry and surface spectroscopy.[29] Recently LE4 has been used to transfer a hexagonal array of 18-nm holes on a 22-nm lattice constant from a biologically derived pattern into Si(100). [30] High resolution cross-sectional transmission electron microscopy showed Si lattice fringes at the perimeter of the etched holes. TEM images of identical samples intentionally briefly ion bombarded with 2 keV Ar ions before LE4 showed an amorphous damaged layer surrounding the perimeter of the etched holes. These experiments together demonstrate that LE4 does not inflict lattice displacement damage on the substrate. For device applications, as described here, LE4 is carried out by placing the sample on the (grounded) anode of a DC glow discharge. Temperature of the sample is controlled by and measured at the sample stage. The apparatus is described in moderate detail in References 25 and 26. Typical process pressures were 2 - 10 Pa; pure chlorine, pure hydrogen, or mixtures of chlorine and hydrogen were studied, at flow rates of 10 - 30 sccm.. GaN samples were masked by deposition of a 200 nm SiO_2 film [by plasma enhanced chemical vapor deposition (PECVD)]. Patterns were defined in the oxide mask layer by standard photolithography techniques followed by either wet etching or RIE through the oxide layer.

RESULTS

Etch Profile.

Figure 1 shows an SEM image of the edges of lines 2 μm wide on a 2.5 μm thick single crystal GaN(0001) sample patterned by RIE of the oxide layer, and etched at 6.6 Pa pure chlorine and 150 $mA \cdot cm^{-2}$ discharge current. The result is highly anisotropic etching, as evidenced by straight side walls, no overcut, no trenching, and no "pedestal" at the base of the line. The etched open field areas between lines appears quite smooth in the SEM image. The samples patterned by photolithography and wet etching of the oxide layer showed mask undercutting during wet etching, which led to mask edge erosion and mask edge roughness. These imperfections in the mask were faithfully transferred to the sample during LE4, and did not show anisotropy comparable to that in Figure 1.



Fig.1. Anisotropic etching of GaN film with SiO_2 mask patterned by RIE. The sample was etched in 6.6 Pa of chlorine for 20 minutes at a current density of 150 mA/cm^2. (Ref.28)

Surface Morphology.

AFM of this sample before etching showed RMS surface roughness was 8.5 - 10 Å. After LE4, RMS surface roughness is 2.5 Å, and the difference between highest and lowest features is 2.2 nm. Nearly identical images were obtained at several locations on the etched surface. By comparison, ECR etching of GaN produces RMS surface roughness from 4 nm to 85 nm, depending on plasma power and rf bias.[31]

It is significant that LE4 smoothened the surfaces of the as-grown GaN material in these experiments. Similar experimental conditions in our earlier LE4 studies of Si(100) and GaAs(100) cited above produced measured RMS surface roughness of 2 - 3 Å after LE4, nearly identical to the values measured on the polished wafers from which the samples were cut. Under these intermediate conditions of pressure and current density, LE4 can accomplish surface polishing as well as etching. This result is not seen in ion enhanced etching, which roughens surfaces during etching. The mechanism of the smoothening process remains to be explained.

Figure 2 shows results of etching such a sample to a depth of 2.75 μm. In this case the etch passed completely through the GaN layer and the AlN buffer layer, exposing the SiC substrate. It is notable that LE4 produced reasonably anisotropic (clearly limited by the mask) and clean sidewalls and a very smooth etched surface while passing through three such disparate materials separated by two very challenging interfaces. This result suggests that LE4 processes can be designed to produce vertical, smooth, and damage-free sidewalls for edge-emitting complex multi-layer structures such as LEDs or laser diodes in which the active layer is a multi-quantum well structure.

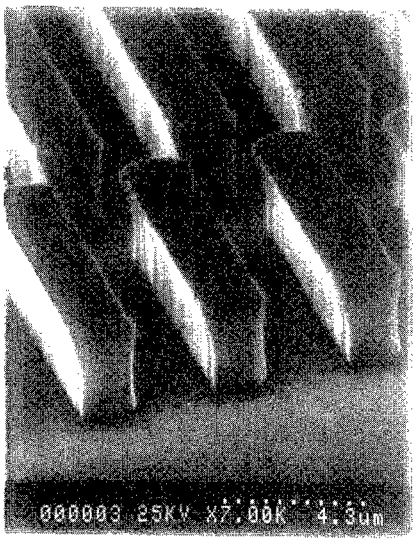


Fig.2 Deep etching of GaN film with SiO_2 mask defined by photolithography and wet etching. The sample was etched in 6.6 Pa of chlorine, with current density of 150 ma/cm^2.

Surface Composition.

Using the GaN/Si(100) samples grown by MOMBE in LE4 with pure hydrogen plasma, we qualitatively evaluated the effects of different LE4 conditions on surface composition by Auger electron spectroscopy. The lack of reliable GaN standards for comparison precludes rigorous quantitative Auger analysis, and roughness of the samples makes questionable any semi-quantitative analyses based on tabulated Auger sensitivity factors. Thus our qualitative estimates of surface composition were obtained by comparing the *relative intensities* of the gallium

$L_3M_{45}M_{45}$ line at 1068 eV and the nitrogen $KL_{23}L_{23}$ line at 384 eV measured on samples before and after etching. Within the limits of this comparison method, the stoichiometry of etched surfaces is essentially the same as for unetched samples. In other studies, this simple qualitative comparison method has shown that ion-enhanced etching processes deplete N relative to Ga at the surface.[32]

Etch Rate.

We observed a strong temperature dependence of the GaN/Si(100) etching rate in hydrogen plasma, ranging from 70 Å/min at 50°C to 525 Å/min at 250°C; details are presented in Reference 27. The Arrhenius plot is fit by a single straight line with activation energy of 160 meV. Temperature dependence of the etch rate for III-V compounds usually gives Arrhenius plots with double slopes when both group III and group V elements are solids at the process temperature, signifying the need for two independent reactions to volatilize the III and V atoms.[33] At present, we do not know the chemical identity of the actual etch products in the LE4 of GaN. But since the temperature dependence appears to determine the activation energy for a single chemical reaction, and since nitrogen does not need to form a compound to become volatile, we speculate that the products are GaH_3 or $GaCl_3$and N_2.

All GaN(0001)/SiC samples in the present study were etched in pure chlorine plasma at room temperature at moderate etch rates of 50 - 70 $nm \cdot min^{-1}$ in order to ensure controllable etch results on the thin film materials. Nonetheless, the LE4 apparatus allows the plasma current density to be increased by an order of magnitude. Besides this, according to our previous experiments on GaAs, anisotropic etching is maintained up to 30 Pa of the process pressure while the etch rate increases substantially at higher pressures due to the greater density of the reactive species. According to our estimates, it is therefore possible to achieve LE4 rates exceeding 150 $nm \cdot min^{-1}$ *at room temperature* while maintaining good etch results such as anisotropy, surface morphology and stoichiometry. Preliminary results indicate that the rate increases substantially with temperature. Quantitative studies and process optimization have yet to be carried out.

SUMMARY AND DISCUSSION

The results obtained to date indicate that, within the moderate ranges of gas pressure and current density used here, LE4 of GaN samples is intrinsically anisotropic, with the quality of etched profiles determined primarily by the quality of the SiO_2 mask material and sharpness of the mask edges. In all our studies of LE4 on Si, GaAs, and GaN samples, we have never observed trenching effects or overcut profiles, which are associated with ion-induced degradation

of the mask in ion-enhanced etching processes. This excellent result is inherently characteristic of LE4, since LE4 was developed specifically to achieve anisotropic etching without ion bombardment, in order to eliminate ion bombardment damage to both mask and substrate during etching.

Excellent anisotropy has been achieved at the same time as acceptable rate, and with no etch-induced surface roughening or degradation of surface stochiometry. The vertical, smooth, damage-free sidewalls should serve as excellent laser cavity mirrors, and the smooth, stoichiometric etched surfaces are well suited for ohmic contacts.

However, several questions remain to be studied. It is necessary to extend these results systematically to a wider variety of III-N materials (including alloys and heterostructures) grown on different substrates. Etch rate, surface roughness, etch profile, and surface composition must be explored over broad ranges of process chemistry and temperature. Since LE4 presumably proceeds via material-specific energy thresholds for electron energy transfer instead of the indiscriminate momentum transfer of ion-surface collisions, LE4 processes that are highly selective between materials can be designed. This will require careful consideration of temperature to guarantee that the necessary reactants can be adsorbed and the resulting products removed while the electron energy is in the appropriate range for a particular material.

Acknowledgements.

Financial support has been provided by the National Science Foundation (Grant No. DMR-9202879). The authors are grateful to Dr. Michael D. Bremser, Prof. Robert F. Davis, Prof. Cammy R. Abernathy, and Prof. Stephen J. Pearton for growth of samples and for numerous helpful discussions on processing III-N materials. The authors are grateful to Dr. John Vajo of Hughes Research Laboratories of Malibu, CA for the Auger analyses.

REFERENCES

[1] S. Strite, "The III-V Nitride Semiconductors for Blue Light Emission," in R. Helbig (ed.) Advances in Solid State Physics 34, Vieweg, Braunschweig/Wiesbaden, Germany, 1995. pp. 79 - 95.

[2] S. Strite and H. Morkoc, J. Vac. Sci. Technol. **B10**, 1237 (1992).

[3] S. Strite, M.E. Lin, and H. Morkoc, Thin Solid Films, **231,** 197 (1993).

[4] S. Nakamura, M. Senoh, N. Iwasa, and S. Nagahama, Jpn. J. Appl. Phys. **34,** L797 (1995).

[5] S. Nakamura, M. Senoh, N. Iwasa, S. Nagahama, T. Yamada, and T. Mukai, Jpn. J. Appl. Phys. **34,** L1332 (1995).

[6] S. Nakamura, M. Senoh, S. Nagahama, N. Iwasa, T. Yamada, T. Matsusha, H. Kiyoku, and Y. Sugimoto, Jpn. J. Appl. Phys. **35,** L74 (1996).

[7] J. Burm, W.J. Schaff, and L.F. Eastman, Appl. Phys. Lett. **68,** 2649 (1996).

[8] S.J. Pearton, J.W. Lee, J.D. MacKenzxie, C.R. Abernathy, and R.J. Shul, Appl. Phys. Lett. **67,** 2329 (1995).

[9] J.R. Mileham, S.J. Pearton, C.R. Abernathy, J.D. MacKenzie, R.J. Shul, and S.P. Kilcoyne, Appl. Phys. Lett. **67,** 1119 (1995).

[10] M.S. Minsky, A.M. White, and E.L. Hu, Appl. Phys. Lett. **68,** 1531 (1996).

[11] I. Adesida, A. Mahajan, E. Andideh, M.A. Khan, D.T. Olsen, and J.N. Kuznia, Appl. Phys. Lett. **63,** 2777 (1993).

[12] M.E. Lin, Z. Fan, Z. Ma, L. H. Allen, and H Morkoc, Appl. Phys. Lett. **64,** 887 (1994).

[13] A. T. Ping, I. Adesida, M. A. Khan, and J. N. Kuznia, Electr. Lett. **30,** 1895 (1994).

[14] S.J. Pearton, C.B. Vartuli, R.J. Shul, and J.C. Zolper, Mat. Sci. Eng. **B31**, 309 (1995).

[15] R.J. Shul, S.P. Kilcoyne, M. Hagerott Crawford, J.E. Patmeter, C.,B. Vartuli, C.R. Abernathy, and S.J. Pearton, Appl. Phys. Lett. **66,** 1761 (1995).

[16] R.J. Shul, A.J. Howard, S.J. Pearton, C.R. Abernathy, C.B. Vartuli, P.A. Barnes, and M.J. Bozack, J. Vac. Sci. Technol. **B13**, 2016 (1995).

[17] S. J. Pearton, J. W. Lee, J. D. MacKenzie, C. R. Abernathy, and R. J. Shul, Appl. Phys Lett., **67**, 2329 (1995)

[18] R.J. Shul, A.J. Howard, S.P. Kilcoyne, S.J. Pearton, C.R. Abernathy, C.B. Vartuli, P.A. Barnes, and M.J. Bozack, Electrochemical Society Proceedings, **95-6,** 209 (1995).

[19] I. Adesida, A.T. Ping, C. Youtsey, T. Dow, M.A. Khan, D.T. Olson, and J.N., Kuznia, Appl. Phys. Lett. **65,** 889 (1994).

[20] A.T. Ping, C. Youtsey, I. Adesida, M.A. Khan, and J.N.Kuznia, Jour. Electr. Mat. **24,** 229 (1995).

[21] A.T. Ping, I. Adesida, and M.A. Khan, Appl. Phys. Lett. **67,** 1250 (1995).

[22] A.T. Ping, A.C. Schmitz, M.A. Khan, and I. Adesida, Jour. Electr. Mat. **25,** 825 (1996).

[23] H.P. Gillis, D.A. Choutov, and K.P. Martin, J. of Mat. **48,** 50 (1996).

[24] R.J.Shul et al, MRS Bulletin, Spring 1998

[25] H.P. Gillis, D.A. Choutov, P.A. Steiner IV, J.D. Piper, J.H. Crouch, P. M. Dove, and K.P. Martin, Appl. Phys. Lett. **66,** 2475 (1995).

[26] H.P. Gillis, D.A. Choutov, K.P. Martin, and Li Song, Appl. Phys. Lett. **68,** 2255 (1996).

[27] H.P. Gillis, D.A. Choutov, K.P. Martin, S.J. Pearton, and C.R. Abernathy, J. Electrochem. Soc., **143**, L251 (1996).

[28] H.P. Gillis, D.A. Choutov, K.P. Martin, M.D. Bremser, and R.F. Davis, J. Electron. Mat. **26,** 301 (1997).

[29] H.P. Gillis, J.L Clemons, and J.P. Chamberlain, Jour. Vac. Sci. Technol. **B10,** 2729 (1992).

[30] T.A. Winningham, H.P. Gillis, D.A. Choutov, K.P. Martin, J.T. Moore, and K. Douglas, "Formation of Ordered Nanocluster Arrays by Self-Assembly on Nanopatterned Si(100) Surfaces," Surf. Sci. **406,** 221 (1998)..

[31] R.J. Shul, A.J. Howard, S.P. Kilcoyne, S.J. Pearton, C.R. Abernathy, C.B. Vartuli, P.A. Barnes, and M.J. Bozack, Electrochemical Society Proceedings, **95-6,** 209 (1995).

[32] R.J. Shul, A.J. Howard, S.P. Kilcoyne, S.J. Pearton, C.R. Abernathy, C.B. Vartuli, P.A. Barnes, and M.J. Bozack, Electrochemical Society Proceedings **95-6,** 209 (1995).

[33] S.J. Pearton, A.B. Emerson, U.K.Chakrabarti, E. Lane, K.S. Jones, K.T. Short, A. E. White, and T.R. Fullowan, J. Appl. Phys., **66**, 3839 (1989).

NORMAL AND INVERTED ALGAN/GAN BASED PIEZOELECTRIC FIELD EFFECT TRANSISTORS GROWN BY PLASMA INDUCED MOLECULAR BEAM EPITAXY

M. J. Murphy[a], B. E. Foutz[a], K. Chu[a], H. Wu[a], W. Yeo[a], W. J. Schaff[a], O. Ambacher[a], L. F. Eastman[a], T. J. Eustis[b], R. Dimitrov[c], M. Stutzmann[c], W. Rieger[d]

[a]School of Electrical Engineering, Cornell University, Ithaca, NY 14853
[b]Department of Materials Science, Cornell University, Ithaca, NY 14853
[c]Walter Schottky Institute, TU-Munich, Am Coulombwall, D-85748 Garching, Germany
[d]Ferdinand Braun Institute, Rudower Chaussee 5, D-12489 Berlin, Germany

Cite this article as: MRS Internet J. Nitride Semicond. Res. 4S1, G8.4(1999)

ABSTRACT

High quality Ga-face and N-face AlGaN/GaN based heterostructures have been grown by plasma induced molecular beam epitaxy. By using Ga-face material we are able to fabricate conventional heterojunction field effect transistors. Because the N-face material confines electrons at a different heterojunction, the resulting transistors are called inverted. The Ga-face structures use a high temperature AlN nucleation layer to establish the polarity. Structures from these materials, relying only on polarization induced interface charge effects to create the two-dimensional electron gases, are used to confirm the polarity of the material as well as test the electrical properties of the layers. The resulting sheet concentrations of the two dimensional electron gases agree very well with the piezoelectric theory for this materials system. Hall mobilities of the two-dimensional gases for the N-face structures are as high as 1150 cm^2/Vs and 3440 cm^2/Vs for 300 K and 77 K respectively, while the Ga–face structures yield room temperature mobilities of 1190 cm^2/Vs. Both structures were then fabricated into transistors and characterized. The inverted transistors, which were fabricated from the N-face material, yielded a maximum transconductance of 130 mS/mm and a current density of 905 mA/mm. Microwave measurements gave an f_t of 7 GHz and an f_{max} of 12 GHz for a gate length of 1 μm. The normal transistors, fabricated from the Ga-face material, produced a maximum transconductance of 247 mS/mm and a current density of 938 mA/mm. Microwave measurements gave an f_t of 50 GHz and an f_{max} of 97 GHz for a gate length of 0.25 μm. This shows that using plasma induced molecular beam epitaxy N-face and Ga(Al)-face AlGaN/GaN heterostructures can be grown with structural and electrical properties very suitable for high power field effect transistors.

INTRODUCTION

The polarity of group III-nitrides is a subject that has seen much research recently.[1] The fact that the material has wurtzite crystal symmetry means that there exists a polarity in the growth direction, yielding either Ga-face (0001) or N-face (000$\bar{1}$) material. This polarity issue has several important consequences, some of which are the differing materials properties of the different polarities as well as how the different polarities can be achieved from a growth point of view. The polarity also determines the orientation of the spontaneous and piezoelectric

Mat Res. Soc. Symp. Proc. Vol. 537 © 1999 Materials Research Society

polarization inside the material, which has drastic effects on device design. The devices under study are piezoelectric HFETs grown by Plasma Induced Molecular Beam Epitaxy (PIMBE). The transistor structures are intentionally undoped and therefore rely on polarization induced interface charge effects to create a two-dimensional electron gas (2DEG). Depending on the polarity of the material grown, the 2DEG will be confined at different interfaces. Thus by determining at which interface the electrons are confined, it is possible to probe the polarity of the layers grown. These structures are also useful for comparing the electrical quality of the different polarities. We will show that high quality N-face epitaxial layers can be deposited that are suitable for inverted transistors which can be used in high frequency applications. We will further show that PIMBE Ga-face HFETs can achieve state-of-the-art frequency response as well as excellent DC results.

EXPERIMENTAL DETAILS

The structures in this study consist of GaN/AlGaN/GaN heterostructures deposited by PIMBE. Two separate MBE machines were used to obtain this material. The N-face material, which was used to achieve the inverted HFETs, was deposited in a Tectra MBE, which uses conventional effusion cells for the Group IIIs. This system is equipped with an Oxford Applied Research CARS 25 RF plasma source. A more detailed description of the machine and the typical growth conditions can be found in Reference 2. The transistor structure using the N-face material is unintentionally n-type, therefore a 2.5 μm Mg doped buffer layer is employed. By using this compensation technique, a background doping concentration in the 10^{12} cm^{-3} range is achievable as measured by capacitance voltage profiling and Hall measurements. A 60 nm $Al_{.28}Ga_{.72}N$ layer is then deposited, followed by a 30 nm GaN top layer.

The Ga-faced layers used for conventional HFETs in this research were deposited in a turbo-pumped Varian GenII MBE which also uses conventional effusion cells for Ga and Al. The nitrogen radicals for this machine are supplied via an EPI Uni-Bulb RF plasma source. A more detailed description of the machine and the typical growth conditions can be found in Reference 3. The Ga-face device consists of a nominally 7 nm AlN nucleation layer, followed by a 1.2 μm GaN buffer layer. Unlike the aforementioned structure, this buffer layer has a background doping concentration in the 10^{12} cm^{-3} range, so no compensation is needed. This buffer layer is followed by a 20 nm $Al_{.2}Ga_{.8}N$ layer and a 2 nm GaN cap layer. It should be noted that the only way Ga-face material was achievable was through the use of the AlN nucleation layer.

Capacitance voltage profiling is used to probe the free carrier profiles of the materials grown. This profiling was done using an HP 4275A multi-frequency LCR meter and a standard mercury probe. The normal biasing range is from 0.4 to –10.0 V with 200 steps and a small signal frequency of 10 kHz is used.

THEORY

The group III-nitrides commonly occur in the wurtzite crystal structure and lack inversion symmetry along the c-axis. This asymmetry allows for the possibility of a built-in spontaneous polarization directed along the c-axis. Calculations have shown that the group III–nitrides have a strong spontaneous polarization.[4] In the case of GaN, the direction of

polarization points from the N atom to the Ga atom along the c-axis bond. As shown in Figure 1, N-faced material corresponds to N in the upper position of the (0001) bi-layer and the direction of the spontaneous polarization points toward the surface, opposite the (0001) direction. In the case of Ga-faced material, Ga occupies the top position of the (0001) bi-layer. In this case, the spontaneous polarization points toward the substrate. Strain perpendicular to the c-axis deforms the crystal and modifies the polarization. This is the piezoelectric effect. Details of the calculation of the piezoelectric polarization and induced sheet charges can be found in Reference 5. To determine the total polarization of a given epi-layer the spontaneous polarization of the relaxed material is added to the change in polarization due to the strain. A more complete treatment of our calculations including the spontaneous polarization will be found in Reference 6.

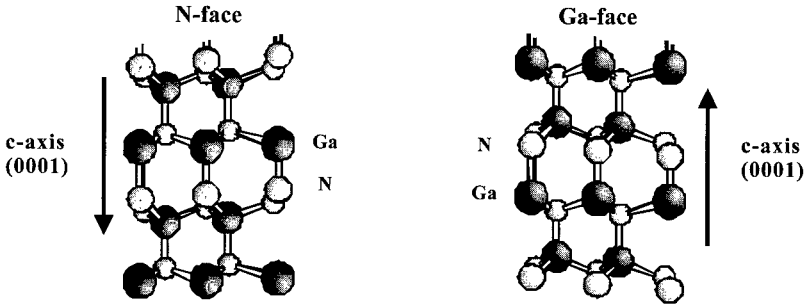


Figure 1. Schematic of the wurtzite crystal structure for the different polarities of GaN, showing the placement of the Ga and N atoms.

The polarity of the device structure, N-face or Ga-face, determines where a 2DEG will form. As can be seen in Figure 2, the total polarization (**P**) in the AlGaN is flipped for the case of differing material polarity. The spontaneous polarization of the relaxed GaN layers points in the same direction as the AlGaN layer, but is weaker. The large change in polarization from one material to the other creates a positive bound charge ($\sigma_b = \mathbf{P}_{AlGaN} - \mathbf{P}_{GaN}$) at one of the interfaces. This charge creates a strong electric field at the interface that confines electrons and a 2DEG will form. For the case of the Ga-faced material, one expects the positive bound charge and the 2DEG to be located at the lower AlGaN/GaN interface. This is the conventional HFET structure and is referred to as a "normal" structure. In contrast, the N-face material will confine the 2DEG at the upper GaN/AlGaN interface, and is referred to as an "inverted" structure. Since the location of the 2DEG can be determined through the capacitance-voltage profiling technique, the polarity of the material can be determined.

RESULTS AND DISCUSSION

While two separate machines were used to obtain the different materials, it should be noted that both machines were able to obtain N-face material without the use of the AlN nucleation layer. The superior quality of the N-face material obtained from the Tectra MBE was more suitable for devices however. It should also be noted that recent growths from the Tectra MBE confirm the ability of the AlN nucleation layer to switch the polarity of the films

deposited, and similar material properties were measured on Ga-face material from both machines.

The first structure to be studied was the inverted HFET. The measured Hall mobility for this device was 1150 cm^2/Vs at 300 K and 3440 cm^2/Vs at 77 K with a constant sheet density of 6.0×10^{12} cm^{-2}. The existence and position of the 2DEG was verified using capacitance voltage profiling. As can be seen in Figure 3, the position of the 2DEG is at the upper heterointerface, which agrees with the piezoelectric theory for N-face material. Inverted HFETs were then fabricated from this layer structure and tested. DC measurements on devices with a gate length of 1.0 μm and a gate width of 40 μm yielded a maximum transconductance of 130 mS/mm and a peak current density of 905 mA/mm. Frequency tests were then performed on the devices, from which an f_t of 7 GHz and an f_{max} of 12 GHz were obtained.

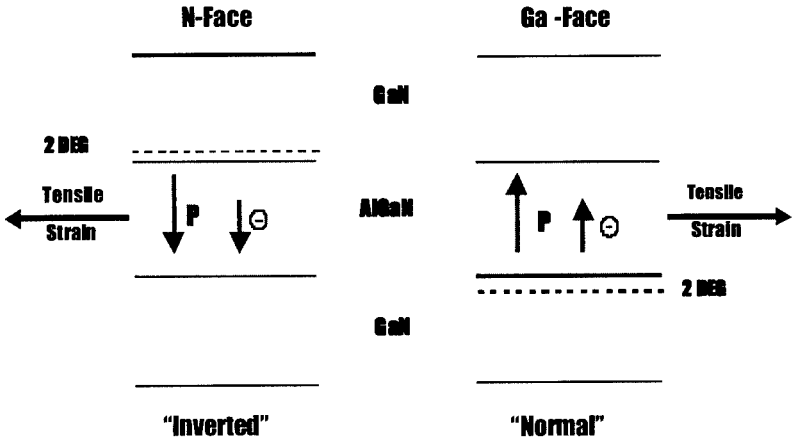


Figure 2. Schematic layer structure for GaN/AlGaN/GaN heterostructures showing both the total polarization (**P**) in the AlGaN layer and the interfaces at which the 2DEG will be confined. The N-face yields a 2DEG at the upper interface and hence is called an inverted structure, while the Ga-face confines carriers at the bottom interface and is called a normal structure.

The Ga-face material under study gave a Hall mobility of 1190 cm^2/Vs at 300 K, with a sheet density of 1.0×10^{13} cm^{-2}. Results of capacitance voltage profiling of this structure are shown in Figure 4. This data proves the existence and position of a 2DEG, only this time the confinement is at the lower heterointerface, which agrees with the piezoelectric theory for Ga-face material. Conventional HFETs were then fabricated from this material and tested, the results appear in Figure 5. DC measurements on devices with a gate length of 0.25 μm and a gate width of 100 μm yielded a maximum transconductance of 247 mS/mm and a peak current density of 938 mA/mm. With a –6 V bias applied to the gate contact, breakdown voltages as high as 60 V from source to drain were attained. Microwave measurements were then performed on the devices, from which an f_t of 50 GHz and an f_{max} of 97 GHz were obtained, as shown in Figure 5, however values of f_t as high as 60 GHz were measured for the devices with slightly smaller gate lengths.

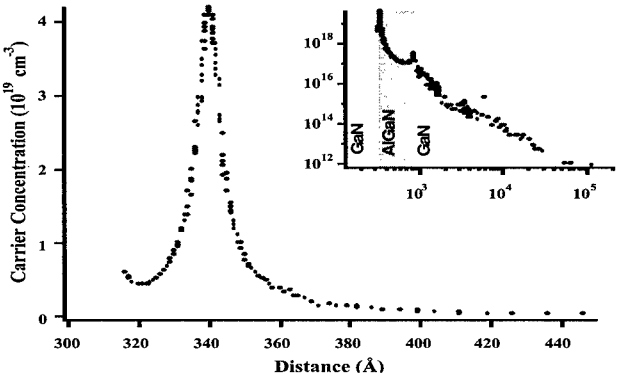


Figure 3. Capacitance voltage profile for the inverted HFET. The graphs clearly show a 2DEG that is confined at the upper interface. This agrees perfectly with the piezoelectric theory for N-face material.

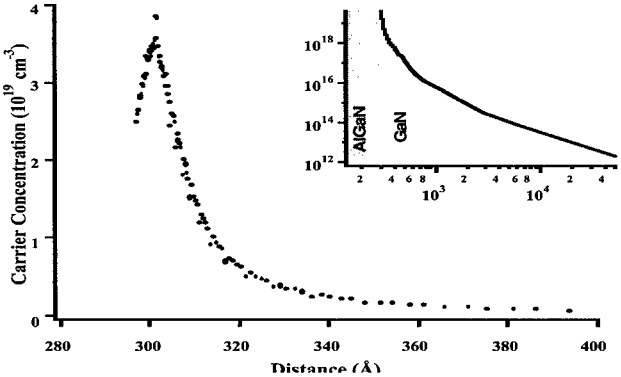


Figure 4. Capacitance voltage profile for the normal HFET. The graphs clearly show a 2DEG that is confined at the lower interface. This agrees perfectly with the piezoelectric theory for Ga-face material.

CONCLUSION

Several important issues have been covered in this research. Firstly, it has been shown that capacitance voltage profiling can be used as a tool to determine the polarity of the GaN material in question by determining at which interface the 2DEG is confined. Secondly, it has been shown that piezoelectric HFETs are possible in both polarities of (Al)GaN material. Both the N-face and Ga-face material appear to have a single polarity across the entire wafer and no evidence of inversion domain boundaries is seen by Hall measurements, C-V profiling, or device testing. While the N-face material in this study is of excellent electrical quality, it is possible to attain Ga-face material with PIMBE by utilizing an AlN nucleation layer. This Ga-face material

can be used to create state-of-the-art HFETs with frequency response that is comparable to the best attainable in (Al)GaN by MOCVD.[7]

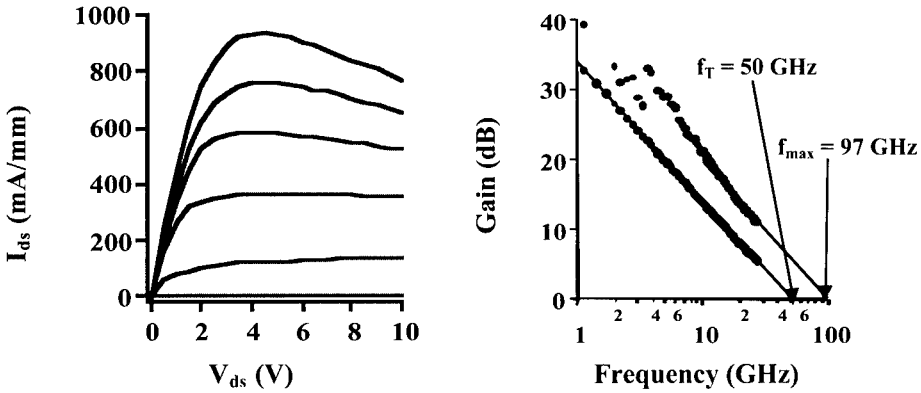


Figure 5. Results from DC and microwave measurements on a normal HFET with a gate length of 0.25 μm and a gate width of 100 μm. For the DC curves, the gate bias starts at + 1.0 V and drops by 1.0 V for each increment.

ACKNOWLEDGEMENTS

Dr. Ambacher would like to thank the Alexander von Humboldt Stiftung for a Feodor Lynen fellowship. The work done at Cornell University is supported by the Office of Naval Research under Contracts No. N00014-96-1-1223 and N00014-95-1-0926 under the direction of Dr. John Zolper. The work done at the Walter Schottky Institute was funded by the Deutsche Forschungsgemeinschaft (Stu 139/2).

REFERENCES

[1]E. S. Hellman, MRS Internet J. Nitride Semicond. Res. **3**, 11 (1998).
[2]R. Dimitrov, L. Wittmer, H. P. Felsl, A. Mitchell, O. Ambacher and M. Stutzmann, phys. stat. sol. **168**, R7 (1998).
[3]M. J. Murphy, K. Chu, T. J. Eustis, J. Smart, H. Wu, W. Yeo, W. J. Schaff, O. Ambacher, J. R. Shealy and L. F. Eastman, "MBE growth of normal and inverted two-dimensional electron gases in AlGaN/GaN based heterostructures," in print J. Vac. Sci. Tech. B.
[4]F. Bernardini, V. Fiorentini, and D. Vanderbilt, Phys. Rev. B **56**, 16 (1997).
[5]P. M. Asbeck, E. T. Yu, S. S. Lau, G. J. Sullivan, J. Van Hove, and J. Redwing, Elec. Lett. **33**, 1230 (1997).
[6]O. Ambacher, J. Smart, J. R. Shealy, N. G. Weimann, K. Chu, M. Murphy, W. J. Schaff, and L. F. Eastman "Two dimensional electron gases induced by spontaneous and piezoelectric polarization charges in N- and Ga-face AlGaN/GaN heterostructures," in print J. Appl. Phys.
[7]K. K. Chu, J. Smart, J. R. Shealy, and L. F. Eastman, SOTAPOCS, 1998.

Part IX

Quantum Dots and Processing

PIEZOELECTRIC PROPERTIES OF GaN SELF-ORGANIZED QUANTUM DOTS

B. Daudin*, F. Widmann*, J. Simon*, G. Feuillet*, J. L. Rouvière*, N. T. Pelekanos*, G. Fishman**

*Département de Recherche Fondamentale sur la Matière Condensée, CEA/ Grenoble, SPMM, 17 rue des Martyrs, 38054 Grenoble Cedex 9, France, daudin@drfmc.ceng.cea.fr
**Laboratoire de Spectrométrie Physique, UMR C5588, Université J. Fourier-Grenoble 1- CNRS, BP 87, 38402 St. Martin d'Hères Cedex, France

Cite this article as: MRS Internet J. Nitride Semicond. Res. 4S1, G9.2 (1999)

ABSTRACT

It is demonstrated that GaN quantum dots with the wurtzite structure grown by molecular beam epitaxy on AlN exhibit optical properties which, depending on the size of the dots, may be dominated by piezoelectric effects. In "large" quantum dots with an average height and diameter of 4.1 and 17 nm, respectively, the photoluminescence peak is centered at 2.95 eV, nearly 0.5 eV *below* the bulk GaN bandgap, which is assigned to a piezoelectric field of 5.5 MV/cm present in the dots. The decay time of the photoluminescence was also measured. A comparison is carried out with theoretical calculation of the radiative lifetime.

INTRODUCTION

Despite the successful realization of blue LDs by Nakamura et al., serious problems are still to be overcome, related to the lack of adapted substrate. In particular, a reduction in the number of cristallographic defects is highly desirable in order to improve the lifetime and to reduce the threshold current of the LDs. This is partly achieved through the recent development of lateral overgrowth for GaN which leads to the reduction of the dislocation density by several orders of magnitude [1]. Alternately, the realization of devices with quantum dots (QDs) in the active layer appears promising, based on the theoretical prediction of a low threshold current and of a weak temperature dependence of the threshold current [2]. Furthermore, due to the reduced size of the QDs, they are expected to be virtually perfect, with most cristallographic defects out of the dots, which should result in a decrease in non radiative recombination. It is the aim of this article to adress this point in the case of self-assembled GaN QDs, with a particular attention paid to the peculiar properties resulting from the presence of a huge piezoelectric field which is one of the most fascinating aspect of nitrides [3,4].

Mat. Res. Soc. Symp. Proc. Vol. 537 © 1999 Materials Research Society

EXPERIMENT

The samples were grown by molecular beam epitaxy (MBE) in a commercial MECA 2000 machine. The substrate was (0001) sapphire. After the nitridation step of the sapphire, a low temperature AlN layer, about 15 nm thick, was deposited followed by the growth of a 1.5 μm thick AlN buffer layer. The details of the growth procedure have been published elsewhere [5]. The GaN QDs were grown by depositing the equivalent of 3 monolayers of GaN on AlN at 700°C (Ref. 6, 7). Next, they were covered by AlN in order to smooth the surface again and the operation was repeated several times to obtain a superlattice of GaN QDs layers. The size of the dots was varied, depending on whether they were « ripened » under vacuum or not before further covering with AlN. The « large » dots were ripened under vacuum during about one minute before further capping with AlN. They were typically 4.1 ± 0. 4 nm high (17 nm diameter). The « small » unripened dots were capped with AlN with no growth interruption. They were 2.3 ± 0.2 nm high (8 nm diameter). These figures were extracted from the analysis of high resolution electron microscopy (HREM) pictures. As shown in Fig.1, analysis of the HREM pictures taken along two directions rotated by 30° allowed to conclude that the GaN quantum dots are coherently matched to the (0001) plane of AlN, then experiencing a strong biaxial stress. As a consequence of

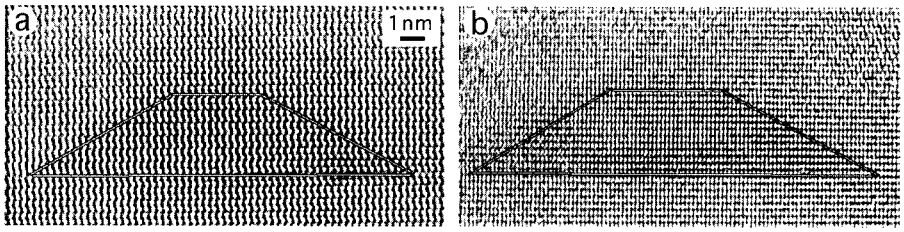


Fig.1 HREM images of the same GaN island taken along (a) the 1/3[2,-1,-1,0] and (b) the [10$\underline{1}$0] directions, differing from 30°

the biaxial stress and of the cristallographic symmetry, a strong piezoelectric field is expected to be present in the dots [3,4].

This hypothesis was confirmed by measuring the photoluminescence of the large dots. The result, plotted in figure 2, reveals that the PL peak of the large dots is observed at 2.95 eV, i.e. 0.5 eV *below* the bulk GaN energy gap.

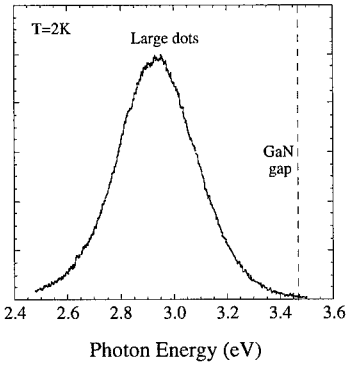


Figure 2: Photoluminescence of « large » GaN QDs

Actually, it has been shown elsewhere that the photoluminescence emission energy of GaN QDs was dramatically dependent on the QD size [8], with the « small » QDs exhibiting a PL peak centered at 3.75 eV, nearly 0.3 eV higher than the GaN bandgap. Consistent with the HREM results, this striking QD size effect was attributed to the presence of a giant piezoelectric field in the QDs along the c-axis [8]. This hypothesis was supported by PL experiments as a function of excitation power which revealed an increasing blue shift for increasing power, as an evidence of the screening of the piezoelectric field for an increased density of photocreated carriers. Finally, theoretical calculations were performed, allowing to conclude that the GaN QDs matched to the AlN matrix experience a piezoelectric field as high as 5.5 MV/cm, consistent with the experimental data available on the piezoelectric field values in GaN and related alloys [9-11].

The strong localization effects resulting from the reduced size of the GaN QDs was further confirmed by measuring the photoluminescence intensity as a function of temperature. As shown in figure 3 , it was found that, by contrast to quantum wells or Mg-doped bulk GaN, the PL intensity of large dots was practically unaffected by temperature and was even increasing slightly, as an evidence of strong localization effects.

The hypothesis of a strong piezoelectric field to account for the energy position of the PL peak of large dots was supported by optical power dependent PL spectra, the center of gravity of the PL peak being significantly blueshifted for increased power density [8]. This behaviour is typical of piezoelectric nanostructures and is due to partial screening of the piezoelectric field by the photoexcited electron-hole (e-h) pairs. In the case of large dots, a 70 meV blueshift was observed as the power density varies from 60 to 450 W/cm^2.

Further evidence of the strong piezoelectric field present in the GaN QDs is provided by PL decay measurements. The time-resolved PL experiments presented here were performed with a standard streak camera setup at T=10K

on a QD sample with 72 layers of " small " QDs. In this sample, a relatively broad QD size distribution is available as manifested by the 500meV-broad PL spectrum centered at 3.6eV. The excitation was provided by 265nm pulses of 1.5ps duration at 76MHz repetition rate, resulting from frequency-tripling a 795nm line of a picosecond Ti-Sapphire laser. Typical average power densities used in these measurements were $50W/cm^2$ and the corresponding sheet exciton density created per pulse is estimated to be about $10^{11}cm^{-2}$, which is several times smaller than the QD density. In Fig. 4, we plot by solid squares the measured PL decay times, τ_D, as a function of photon energy. On the high energy side, we observe a continuous increase of the PL decay time with decreasing photon energy. This is consistent with the picture of piezoelectric QDs, since the piezoelectric field in the larger dots is more efficient in separating the electron and hole wavefunctions and hence increases their radiative recombination time. However, as the photon energy is further decreased we observe that the PL decay times reaches a plateau not exceeding the 3.6ns. We attribute this plateau to the presence of nonradiative channels and set τ_{NR}=3.6ns. If we assume that τ_{NR} is independent of energy, then, based on the equation $1/\tau_D = 1/\tau_{NR}+1/\tau_R$, we can tentatively estimate the radiative recombination time τ_R as a function of energy. The result is plotted as open-cross squares in Fig. 4. The most striking feature is the dramatic increase in the decay time which is observed for decreasing energy. In particular, when extrapolating down to 3 eV, corresponding to « large » dots emitting in the blue range a very large decay time is expected.

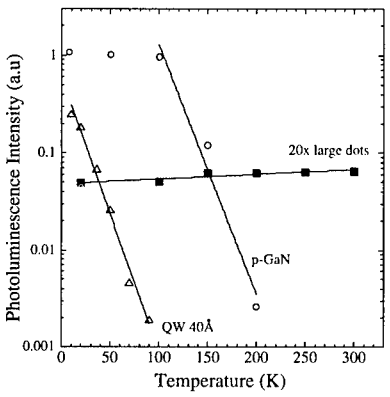


Figure 3: Temperature dependence of the photoluminescence for a) bulk GaN, b) quantum wells and c) large quantum dots

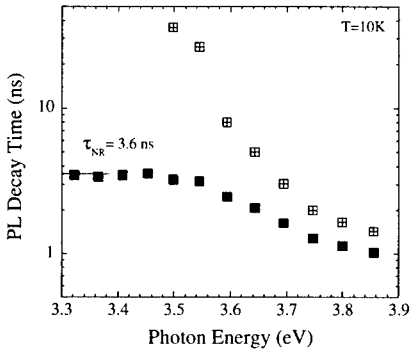


Figure 4: Photoluminescence decay time as a function of energy. Crossed squares are an estimation of τ_R deduced from the experimental data (full squares) by substracting the influence of τ_{NR}

DISCUSSION AND CONCLUSION

In an attempt to understand the above results, the influence of the piezoelectric field on the oscillator strength was investigated. We first calculated the exciton radiative lifetime τ in the bulk semiconductor using the usual approach [12,13]. It was found that in GaN τ was of the order of 25 ns. Then, in order to determine the radiative lifetime in a QD, we use the model of Ref.14, which allows to calculate the oscillator strength, and therefore the radiative lifetime, in a cubic box provided that the bulk radiative lifetime is known. For that purpose, we have defined an equivalent cubic box which has the same volume as the pyramidal QD of heigth h. The radiative lifetime τ_h without piezoelectric field was then obtained. In a further step, the piezoelectric field F was taken into account via a two-dimensional quantum well, as reported in Ref. 8. Note that this approach is meaningful as the exciton Bohr radius parallel to the quantum well is smaller than the side of the equivalent cubic box (this would not apply to very small pyramids). We then obtain the relations linking $\tau_{h,50}$, τ_h and τ, where $\tau_{h,50}$ is the radiative lifetime in a QD taking into account a piezoelectic field F = 5 MV/cm. The last step of the calculation is to link the size of the pyramid to the transition energy [8]. The final result is shown in Fig.5. The key information is that the influence of the piezoelectric field is not very important (an increase in the lifetime by a factor of about 2 at 4 eV, h = 20 Å) for a small box (large energy). By contrast, this influence is very large in a large box (an increase in the lifetime by a factor of about 200 at 3eV, h = 40Å).

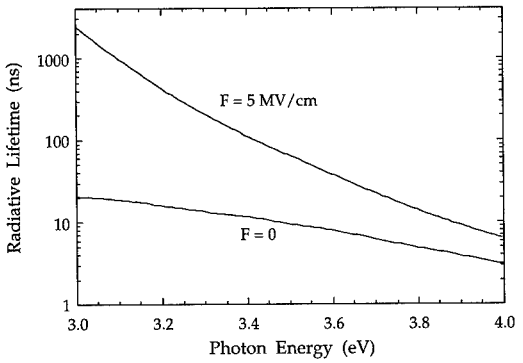


Figure 5: Theoretical calculation of the radiative lifetime in GaN QDs as a function of the photon energy, with and without piezoelectric field

In conclusion it has been experimentally and theoretically demonstrated that the optical properties of GaN quantum dots with wurtzite structure grown on AlN by MBE of GaN result from the competition between confinement and piezoelectric effects. The piezoelectric effects were found to be dominant for QD height larger than 3nm. This is a very unique situation resulting from the combined effect of the QD crystallographic symmetry (wurtzite with a [0001] growth direction) and of the huge piezoelectric coefficients specific to the nitride family. The photoluminescence decay time was theoretically calculated and found to be strongly dependent on the piezoelectric field, consistent with experimental data. Finally, these results open the way to the achievement of high efficiency blue light emitting devices with no In.

Ackowledgments: The authors are grateful to Dr. R. André for his contribution to the calculation.

REFERENCES

[1] S. Nakamura, M. Senoh, S. Nagahama, N. Iwasa, T. Yamada, T. Matsushita, H. Kiyoku, Y. Sugimoto, T. Kozaki, H. Umemoto, M. Sano, K. Chocho, Appl. Phys. Lett., **72**, 211 (1998)
[2] Y. Arakawa, H. Sakaki, Appl. Phys. Lett. **40**, 939 (1982)
[3] F. Bernardini, V. Fiorentini, D. Vanderbilt, Phys. Rev. Lett. **79**, 3958 (1997)
[4] F. Bernardini, V. Fiorentini, D. Vanderbilt, Phys. Rev. B **56**, R10024 (1997)
[5] G. Feuillet, F. Widmann, B. Daudin, J. Schuler, M. Arlery, J. L. Rouvière, N. Pelekanos, O. Briot, Mat. Sc. Engineering B **50**, 233 (1997)
[6] B. Daudin, F. Widmann, G. Feuillet, Y. Samson, M. Arlery, J. L. Rouvière, Phys. Rev. B, **56**, R7069 (1997)
[7] F. Widmann, B. Daudin, G. Feuillet, Y. Samson, J. L. Rouvière, N. Pelekanos J. Appl. Phys., **83**, 7618 (1998)
[8] F. Widmann, J. Simon, B. Daudin, G. Feuillet, J. L. Rouvière, N. T. Pelekanos, G. Fishman, Phys Rev B, in press
[9] G. Martin, A. Botchkarev, A. Rockett, H. Morkoç, Appl. Phys. Lett. **68**, 2541 (1996)
[10] Jin Seo Im, H. Kollmer, J. Off, A. Sohmer, F. Scholz, A. Hangleiter, Phys. Rev. B **57**, R9435 (1998)
[11] R. Langer, J. Simon, O. Konovalov, N.T. Pelekanos, A. Barski, M. Leszczynski, MRS Internet Journal of Nitride Semiconductor Research, **3**, 46 (1998).
[12] D.L.Dexter, in *Solid State Physics*, edited by F.Seitz and D.Turnbull (Academic, New York, 1958), Vol.6, p.353.
[13] G.W.'t Hooft, W.A.J.A. van der Poel, L.W.Molenkamp, C.T.Foxon, Phys.Rev.B **35**, 8281 (1987).
[14] R.Romestain, G.Fishman, Phys.Rev.B **49**, 1774 (1994).

FABRICATION OF SELF-ASSEMBLING AlGaN QUANTUM DOT ON AlGaN SURFACES USING ANTI-SURFACTANT

H. HIRAYAMA*, Y. AOYAGI* and S.TANAKA**

*The Institute of Physical and Chemical Research (RIKEN), 2-1 Hirosawa, Wako-shi, Saitama, 351-0198, Japan, hirayama@postman.riken.go.jp
**Hokkaido University, Kita-ku, Sapporo 060, Japan

Cite this article as: MRS Internet J. Nitride Semicond. Res. 4S1, G9.4(1999)

ABSTRACT

We report on the first artificial fabrication of self-assembling AlGaN quantum dots (QDs) on AlGaN surfaces using metal organic chemical vapor deposition (MOCVD). The AlGaN QDs are fabricated using a growth mode change from 2-dimensional step-flow growth to 3-dimensional island formation by modifying the AlGaN surface energy with Si anti-surfactant. The average lateral size and the thickness of fabricated AlGaN QDs, as determined by AFM, are approximately 20 nm and 6nm, respectively. The dot density was found to be controlled from 5×10^{10} cm^{-2} down to 2×10^{9} cm^{-2} by increasing the dose of Si anti-surfactant. We obtained the photoluminescence (PL) from AlGaN QDs embedded with $Al_{0.38}Ga_{0.62}N$ capping layers. The Al incorporation in AlGaN QDs was controllable within the range of 1-5 %.

INTRODUCTION

GaN and related nitrides are currently of great interest for the application to optical devices in the visible and ultraviolet (UV) energy range. The progress of blue laser diodes (LDs) or blue-green light-emitting diodes (LEDs) are extremely remarkable in recent years [1-3]. High-power and long-lifetime InGaN multi-quantum well lasers was already achieved[1].

AlGaN alloy is useful material for UV optical devices, because of wide bandgap direct transition emission between 3.4eV (GaN) and 6.2eV (AlN). The wide transition range of AlGaN covers the lasing wavelength range achieved by UV gas or solid state lasers, for example, XeCl(308nm) or KrF(248nm) excimer lasers, N_2(337nm), He-Cd(325nm) or SHG-Ar(257nm) lasers. UV semiconductor lasers are very attractive in comparison with gas or solid state lasers because of small size, long lifetime, high efficiency, low driving power and CW lasing operation. CW-UV lasers using AlGaN material in the near future will take the place of UV gas or solid state lasers.

For the realization of the UV semiconductor lasers, we should clear several technical barriers such as current injection through high Al content AlGaN crystals or efficient UV emission from AlGaN alloy. Especially, the realization of high optical gain in UV emission range of AlGaN alloy is most important for using it as active region of UV lasers. However, it is theoretically predicted that the reduction of the transparency carrier density is difficult in III-nitride material lasers because of a large effective mass [4] in comparison with GaAs or InP based materials.

In order to realize the high optical gain necessary in UV semiconductor lasers, the use of low dimensional quantum structures is quite useful. Optical gain enhancement using a exciton-related emission is theoretically predicted and expected even at room temperature, due to the large binding energy of exciton in GaN-related quantum dot structures [5]. It has been reported that the quantum efficiency of InGaN-based quantum well lasers is enhanced by the effect of localized excitons in nano-scale In segregated (In-rich) regions of the quantum well [6]. It is desirable to obtain a strong exciton-related emission from AlGaN quantum dot (QD) structures in order to achieve UV lasers.

Mat. Res. Soc. Symp. Proc. Vol. 537 © 1999 Materials Research Society

Recently, we have succeeded in the fabrication of self-assembling GaN and InGaN QD on AlGaN surfaces using metal organic chemical vapor deposition (MOCVD) and observed a strong photoluminescence (PL) emission from QD structures [7][8]. We also achieved optical pumping stimulated emission from GaN QDs sandwiched with AlGaN optical confinement layers[9]. The QDs were fabricated using a growth mode change from 2-dimensional step-flow growth to 3-dimensional island formation by modifying the surface energy balance of AlGaN with a Si anti-surfactant. Contrary to Stranski-Krastanov (SK) growth mode, the QD formation using this method is based on the surface energy balance. Then, this method is especially useful for the QD formation on the interfaces of small lattice mismatch system.

In this report, we demonstrate the first fabrication of self-assembling AlGaN QDs on AlGaN surfaces using MOCVD. The formation of AlGaN QDs on AlGaN surfaces is relatively difficult in comparison with the cases of GaN or InGaN QDs, because AlGaN easily forms a film on GaN or AlGaN surfaces due to large surface energy of AlGaN. The use of Si anti-surfactant was not enough to obtain a growth mode control to 3-dimensional nano-scale dot formation in high growth temperature. In addition to the use of anti-surfactant, we reduced the growth temperature of AlGaN QDs in order to control the migration of precursors on AlGaN surface, and as a result, we succeeded in the fabrication of nano-scale AlGaN QDs.

EXPERIMENTS AND DISCUSSIONS

The structures were grown, at 76 Torr on the Si-face of an on-axis 6H-SiC(0001) substrate, by a conventional horizontal-type MOVPE system. As precursors ammonia (NH_3), tetraethylsilane (TESi), trimethylaluminum (TMAl), and trimethylgallium (TMGa) were used with H_2 as carrier gas. N_2 gas was also independently supplied by a separate line and mixed with the H_2 just before the substrate susceptor. Typical gas flows were 2 standard liters per minute (SLM), 2 SLM, and 0.5 SLM for NH_3, H_2, and N_2, respectively. The molar fluxes of TMG and TMA of $Al_{0.38}Ga_{0.62}N$ growth for buffer and capping layers were 38 and 13 μmol/min, respectively. At this condition, the growth rate was approximately 2.5 μm/h. The molar fluxes of TMG and TMA of $Al_{0.05}Ga_{0.95}N$ growth for fabrication of QD structure were 7.2 and 0.47 μmol/min, respectively. The growth rate used for QD formation was approximately 0.4 μm/h. The substrate temperature during the growth was measured with a thermocouple located at the substrate susceptor.

The sample structure is shown in Fig.1. In order to achieve a surface suitable for growth of AlGaN QDs, first an approximately 400-nm-thick $Al_{0.38}Ga_{0.62}N$ buffer layer was deposited on a 6H-SiC substrate at 1140°C. The buffer layer was found to provide a step-flow grown surface as confirmed by atomic force microscopy (AFM). Prior to the $Al_xGa_{1-x}N$ dot growth, TESi was intentionally supplied for the deposition of silicon anti-surfactant modifying the surface properties at 1140°C. Then the sample was cooled to the $Al_xGa_{1-x}N$ dot growth temperature, i.e., around 900°C. The $Al_xGa_{1-x}N$ QDs were grown by a short supply of TMAl/TMGa using H_2 as carrier gas. The equivalent layer thickness, based on the growth rate, was determined to be 3 nm. This resulted in a three-dimensional nano-scale island growth which was not observed in the case without any silicon dose. Then an approximately 5-nm-thick $Al_{0.38}Ga_{0.62}N$ capping layer was grown on $Al_xGa_{1-x}N$ QDs.

In this experiment, we used relatively low growth temperature even for AlGaN QD formation in order to control the surface migration of precursors. So, we confirmed at first the atomically flat surface of AlGaN grown with low temperature. Figure 2 shows AFM views of the surface of $Al_{0.05}Ga_{0.95}N$ quantum film without using anti-surfactant grown at 900°C. A step-flow image is observed on the surface of AlGaN quantum film even in low growth temperature as seen in Fig. 2.

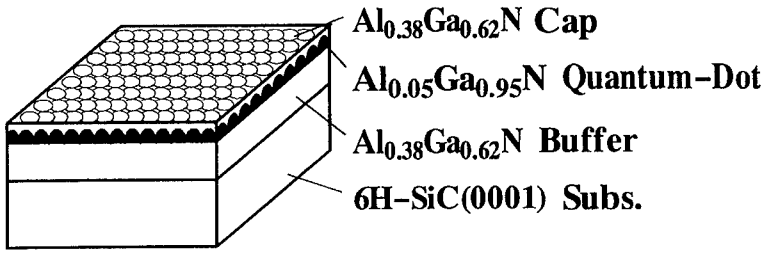


Fig.1. Schematic view of fabricated AlGaN quantum dot sample.

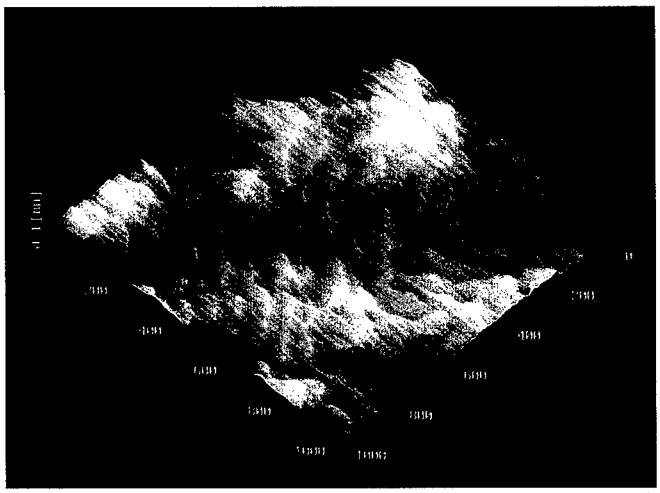


Fig.2. A Step-flow image of the surface of $Al_{0.05}Ga_{0.95}N$ quantum film grown without using anti-surfactant at 900°C observed by AFM.

Figures 3(a)-(d) show the AFM images just after the growth of $Al_{0.05}Ga_{0.95}N$ on Si deposited surfaces. The growth temperature Tg and the Si-dose amount are 1100°C and 0.04μmol, 1100°C and 0.2μmol, 900°C and 0.04μmol, and 900°C and 0.2μmol for Fig. 3(a), (b), (c) and (d), respectively. 3-dimensional growth is seen on the samples using anti-surfactant. For high growth temperature of 1100°C, we could not obtain nano-scale dot structures as shown in Fig. 3(a) and (b). We can see an network-like morphology on the grown surface for small amount of Si-dose of 0.04μmol which is enough large amount for the fabrication of GaN or InGaN nano-scale QDs. We obtained large dot structures when increasing the Si-dose amount by 5 times as seen in Fig. 3(b). In this case, the typical lateral size of the dot was 100-200nm. Therefore, the surface energy control by using Si anti-surfactant was not enough to obtain a growth mode change to 3-dimensional nano-scale QD formation for AlGaN.

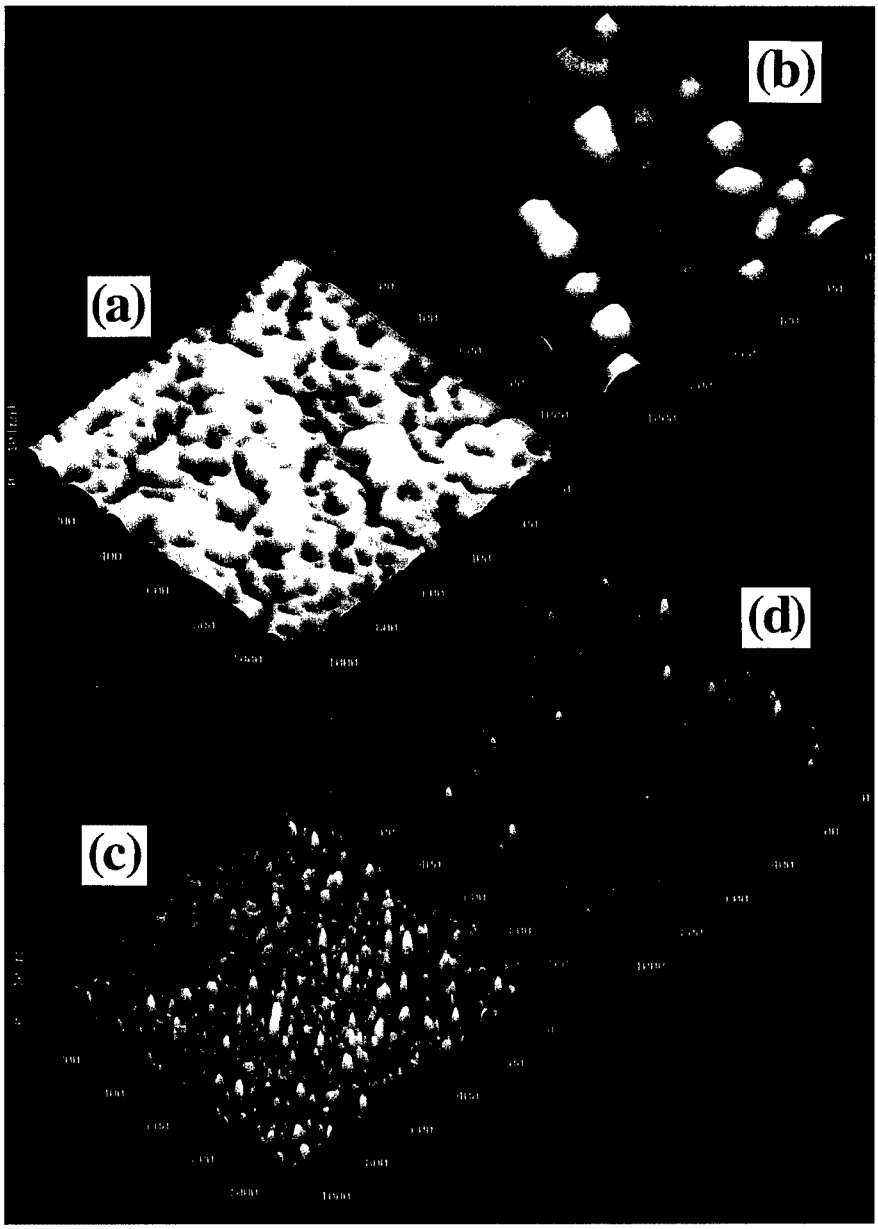


Fig. 3(a)-(d). AFM images just after the growth of $Al_{0.05}Ga_{0.95}N$ on Si deposited surfaces. The growth temperature Tg and the Si-dose amount are (a)1100°C and 0.04μmol, (b)1100°C and 0.2μmol, (c)900°C and 0.04μmol, and (d)900°C and 0.2μmol.

On the other hand, the AlGaN dot was controlled to nano-scale structure by reducing the QD growth temperature to 900°C as seen in Fig. 3(c) and (d). The average lateral size and the height of fabricated AlGaN dots grown at 900°C were estimated to be approximately 20 nm and 6 nm, respectively, by AFM views. The dot density is found to be controlled from 5×10^{10} cm^{-2} down to 2×10^{9} cm^{-2} by increasing the dose of Si anti-surfactant from 0.04μmol to 0.2μmol.

We are investigating the GaN QD formation mechanism on AlGaN surfaces in detail [10]. However, the detailed formation mechanism is still very difficult to observe. It was found from our experiment that very small amount of Si atom deposited on the steps of AlGaN (several % of mono-layer) inhibit the step-flow growth of GaN, because the Ga atom is hard to be adsorbed around Si atom. The disordering process of step-flow growth makes a state of chaotic wandering and may stimulate the transition to 3-dimensional GaN growth. We guess that Al atom is much easily to be adsorbed around Si in comparison with Ga atom, therefore, the transition to 3-dimensional growth mode is hard to occur. The successful formation of nano-scale AlGaN QDs may be due to the enhanced effect of step-flow inhibition with the reduction of Al migration on the surface.

We obtained the photoluminescence from AlGaN QDs embedded with $Al_{0.38}Ga_{0.62}N$ layers. Figure 4 shows 77K PL spectra from AlGaN QDs with capping layers fabricated at 900°C with the Si dose of 0.04μmol for various TMAl flow rate. The emission intensity was the same level as those of GaN QDs fabricated with the same growth condition. The blue shift of QD emission due to the increase of Al incorporation was observed. Al molar fraction in QDs are estimated to be 0.01, 0.03 and 0.05 for the TMAl flow rate of 0.19, 0.38 and 0.47μmol/min, respectively, taking into account the quantum confinement level shift.

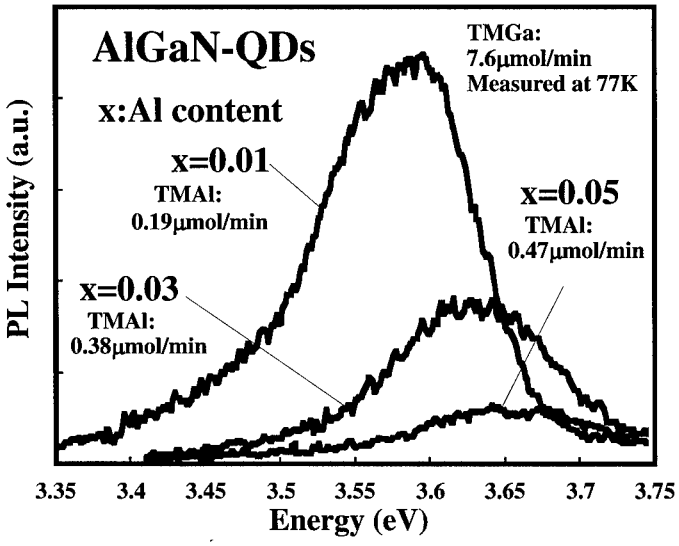


Fig. 4. 77K PL spectra from AlGaN QDs with capping layers fabricated at 900°C for various TMAl flow rate.

At this moment, the half width of the AlGaN QD emission is still large which may be mainly caused by the size fluctuation of QDs. Also the emission intensity is week for high Al content QDs. The emission intensity and size fluctuation of QD may be much improved even for high Al content QDs by increasing the growth temperature of QDs and by optimizing the growth condition of buffer and capping layer. We are now trying high temperature AlGaN QD growth by controlling the surface migration of precursors with the use of more heavy carrier gas.

CONCLUSION

We demonstrated the first artificial fabrication of self-assembling AlGaN QDs on AlGaN surfaces using low pressure MOCVD system. The AlGaN QDs were fabricated using a growth mode change from 2-dimensional step-flow growth to 3-dimensional island formation by modifying the surface energy balance of AlGaN with Si anti-surfactant. The average lateral size and the thickness of the AlGaN QDs, as determined by AFM, were approximately 20 nm and 6nm, respectively. The dot density was found to be controlled from 5×10^{10} cm^{-2} down to 2×10^{9} cm^{-2} by increasing the dose of anti-surfactant. We obtained the photoluminescence from AlGaN QDs embedded with $Al_{0.38}Ga_{0.62}N$ layers. The Al content of AlGaN QDs was controllable within the range of 1-5 %.

REFERENCES

1. S.Nakamura, M.Senoh, S.Nagahama, N.Iwasa, T.Yamada, T.Matsushita, Y.Sugimoto, and H.Kiyoku, Jpn. J. Appl. Phys., **36**, L1059 (1997).
2. S.Nakamura, T.Mukai, and M.Senoh, Appl. Phys. Lett., **64**, 1687 (1994).
3. S.Nakamura, M.Senoh, S.Nagahama, N.Iwasa, T.Yamada, T.Matsushita, Y.Sugimoto, and H.Kiyoku, Appl. Phys. Lett., **69**, 3034 (1996).
4. M.Suzuki, and T.Uenoyama, Jpn. J. Appl. Phys., **35**, 1420 (1996).
5. M.Sugawara, and K.Mukai, Ouyoubuturi **65**, 6, 614 (1996).
6. Y.Narukawa et al, Appl. Phys. Lett., **70**, 891 (1997).
7. S.Tanaka, S.Iwai, and Y.Aoyagi, Appl. Phys. Lett., **69**, 4096 (1996).
8. H.Hirayama S.Tanaka, P.Ramvall and Y.Aoyagi, Appl. Phys. Lett., **72**, 1736 (1998).
9. S.Tanaka, H.Hirayama, and Y.Aoyagi, Appl. Phys. Lett., **71**, 1299 (1997).
10. S.Tanaka and Y.Aoyagi, International Symposium on Formation, Physics and Device Application of Quantum Dots Structures, 126 (1998)

SCANNING TUNNELING MICROSCOPY STUDIES OF InGaN GROWTH BY MOLECULAR BEAM EPITAXY

Huajie Chen,* A. R. Smith,*[a] R. M. Feenstra,* D. W. Greve,** and J. E. Northrup***

*Department of Physics, Carnegie Mellon University, Pittsburgh, PA 15213
**Department of Electrical and Computer Engineering, Carnegie Mellon University
***Xerox Palo Alto Research Center, 3333 Coyote Hill Road, Palo Alto, CA 94304

Cite this article as: MRS Internet J. Nitride Semicond. Res. 4S1, G9.5 (1999)

ABSTRACT

InGaN alloys with indium compositions ranging from 0–40% have been grown by molecular beam epitaxy. The dependence of the indium incorporation on growth temperature and group III/group V ratio has been studied. Scanning tunneling microscopy images, interpreted using first-principles theoretical computations, show that there is strong indium surface segregation on InGaN. Based on this surface segregation, a qualitative model is proposed to explain the observed indium incorporation dependence on the growth parameters.

INTRODUCTION

Ternary $In_xGa_{1-x}N$ alloys are widely used in the development of GaN-based optoelectronic devices.[1] To achieve high quality layers with desired optical properties, it is important to understand and control the indium incorporation efficiency and uniformity. In conventional III-V semiconductors, surface segregation of metal species (Ga, In, or Al) is known to be an important process.[2] In this paper, we present results for the indium incorporation in InGaN during growth by molecular beam epitaxy (MBE), with the characterization performed by x-ray diffraction (XRD), Auger spectroscopy, and scanning tunneling microscopy (STM). The dependence of the indium incorporation on growth parameters is studied. STM images reveal strong surface segregation of the indium, from which a model is proposed to explain the incorporation kinetics.

EXPERIMENT

The studies described here were performed in a combined MBE/surface analysis system. The growth chamber contains gallium and indium effusion cells, an RF-plasma nitrogen source, and a reflection high energy electron diffraction (RHEED) system. Growth is performed on solvent-cleaned sapphire (0001) substrates, heated first to 700°C for 15 min, then exposed at 1050°C to the nitrogen plasma with a power level of 550 W and pressure of 7.0×10^{-5} Torr, for 30 min. First a GaN buffer layer of about 20 nm thickness is grown at 550°C using a nitrogen pressure of 1.5×10^{-5} Torr. The growth temperature is then increased to 720°C for the remainder of the GaN growth. The total thickness of GaN was in the range 200–400 nm. Following the GaN growth, the substrate temperature is lowered to 620–670°C for the InGaN deposition. Typical growth rates for the GaN and InGaN are 200 nm/h. Gallium and indium flux rates were calibrated with an *in situ* crystal thickness monitor. The substrate temperature was measured by a optical pyrometer with emissivity set to be 0.7; care was taken to ensure a clean viewport between the pyrometer and the sample. From our previous work,[3] it is known that GaN films prepared in the above manner are nitrogen polar.

Mat. Res. Soc. Symp. Proc. Vol. 537 © 1999 Materials Research Society

RESULTS AND DISCUSSION

Indium Incorporation Dependence on Growth Parameters

Several series of samples have been grown with different growth parameters. After the growth, XRD were performed to measure the indium incorporation. For the analysis of the XRD data, we assume that InGaN layer is fully strain relaxed (the thickness of InGaN is typically 200 nm), and Vegard's law applies.

First, we consider variation of the growth temperature, keeping the indium, gallium, and nitrogen flux all constant. Results are shown in Fig. 1. For the set of samples whose XRD results are shown in Fig. 1(a), the indium incident flux is about 22% of the total metal (that is, In+Ga) flux. It can be seen from the XRD data that indium incorporation decreases when the growth temperature is increased. The XRD study of the sample grown at 660°C was performed in triple axis mode to increase the resolution, while the other scans were performed with a 0.8 mm slit in front of the detector. The fringes seen in the former are the thickness fringes of the GaN layer. A summary of the temperature dependent results is given in Fig. 1(b); an additional set of data is shown there with In/(In+Ga) flux ratio of 36%. Both of the data sets show a similar dependence of the indium incorporation on growth temperature. Similar results have been observed in both MOCVD and MBE growth by other groups.[4]

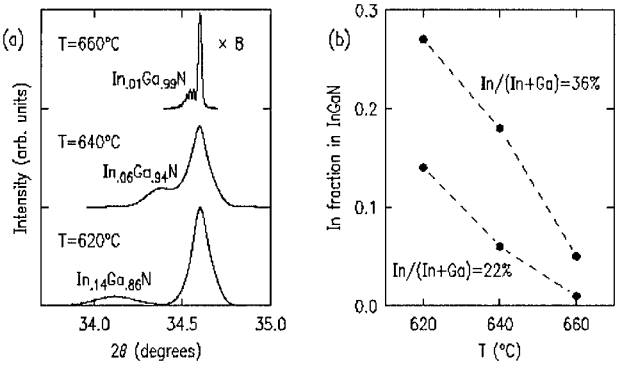


Figure 1. (a) X-ray diffraction 2θ-ω scans for a series of InGaN films grown with a In/(In+Ga) flux ratio of 22%. Indium incorporation, deduced from the x-ray results, is indicated for each film. (b) Summary of the indium incorporation dependence on growth temperature.

Let us now consider variation of the group III/group V ratio while keeping the In/Ga ratio constant. The set of samples whose results are shown in Fig. 2(a) were grown at 640°C, with the In/(In+Ga) flux ratio being about 36%. We find that when the metal flux is increased from 3.4×10^{14} $cm^{-2}s^{-1}$ to 4.4×10^{14} $cm^{-2}s^{-1}$, indium incorporation *decreases* from 23% to 8%. However, comparing the two samples grown with 2.5×10^{14} $cm^{-2}s^{-1}$ and 3.4×10^{14} $cm^{-2}s^{-1}$ metal flux, there is a small *increase* in indium incorporation with increasing metal flux. For the sample grown with 4.4×10^{14} $cm^{-2}s^{-1}$ metal flux, there is an XRD peak at 32.9°, arising from indium droplet (101) planes which are parallel to the GaN $(000\bar{1})$ planes. The results are summarized in Fig. 2(b); two additional sets of data are shown there with different growth temperatures.

Also indicated in Fig. 2(b) is a dashed line indicating the transition point between N rich and group III rich growth regimes. This transition point is obtained from studies of GaN growth in the absence of indium,[5] where a transition from rough to smooth morphology (*i.e.* spotty to streaky RHEED pattern) is found as a function of gallium flux. In the present work, using the same nitrogen pressure as for the InGaN growth and a temperature of 720°C, we find this transition gallium flux to be about 2.9×10^{14} $cm^{-2}s^{-1}$. This value varies slightly between the data sets in Fig. 2(b), because the nitrogen flux varies slightly from set to set. For the case of InGaN

growth, we find that there is no such clear transition from rough to smooth growth, so we use the transition flux determined from the GaN growth as an approximate reference. From Fig. 2(b), we see that in the nitrogen rich regime the indium incorporation increases when the metal flux is increased. In contrast, we find in the group III rich region that the indium incorporation *decreases* when the metal flux is increased. We actually have much more data in this region, and they all show the same trend. This behavior is different from what have been reported for MOCVD growth,[6] where indium incorporation consistently increases when metal flux is increased.

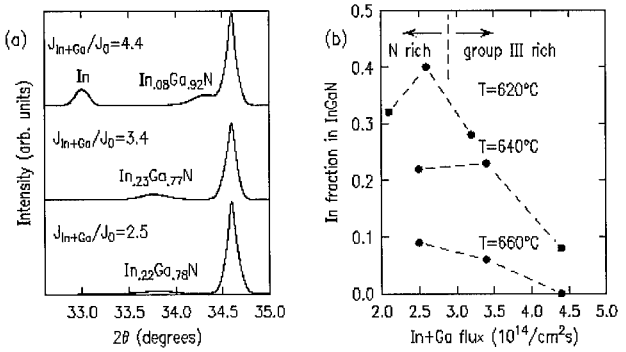


Figure 2. (a) X-ray diffraction 2θ-ω scans for a series of InGaN films grown with varying In+Ga flux, J_{In+Ga}, with $J_0 = 10^{14}$ cm^{-2}s^{-1}, at 640°C. The In/(In+Ga) flux ratio was kept constant at 36%. (b) Summary of the indium incorporation dependence on (In+Ga) flux.

Indium Surface Segregation

Figure 3 shows an STM image of an InGaN surface, prepared by growth at 670°C with In/(In+Ga) flux ratio of 20%. As mentioned earlier, the samples we studied here are nitrogen polar, in which case we know that the surface layer consists of an *adlayer* of metal atoms (gallium and/ or indium).[7] An XRD scan of this sample showed no InGaN peak, meaning that there is negligible indium incorporation in the bulk. In the middle of the STM image, there is a step, and the image shows two separate terraces. Each terrace displays two types of regions, one bright and the other dark. In this type of STM constant-current image, roughly speaking, the bright areas are higher in morphology and dark areas are lower. As can be seen from the line cut, the height difference between bright and dark area is 0.30 ± 0.05 Å. As described below, we identify the bright areas to be indium covered regions and dark areas to be gallium covered regions.

For the sample imaged in Fig. 3, Auger spectroscopy showed that there is a significant indium signal, with a In/Ga signal ratio of about 0.5. Although our Auger system is not well calibrated, so quantitative determination of surface concentration is difficult, the result certainly shows that there is a significant amount of indium on the surface. Furthermore, theoretical computations have been performed which permit the identification of the bright and dark areas in the STM image. Those results are pictured in Fig. 4. The total energy calculation is performed within the local density functional theory using first-principles pseudopotential methods for various GaN$(000\bar{1})1\times1$:Ga_yIn_{1-y} adlayer structures. The calculations are performed in a 2×2 unit cell with various numbers of In and Ga atoms in the top site. The equilibrium adlayer In-N bond length is found to be about 2.23 Å while the equilibrium Ga-N bond in the adlayer is 1.99 Å. These values are essentially independent of y. From explicit examination of charge density contours for states located near the Fermi-level, we find that the different height of the adatoms above the surface (~0.2 Å) is manifested in a corrugation in the charge density of a similar magnitude at a height of several Å above the adatoms. Based on these two reasons, and on our

previous experience on the study of GaN surface, we identify the bright regions as arising from indium atoms in the surface adlayer, and the dark regions as arising from gallium atoms in the adlayer.

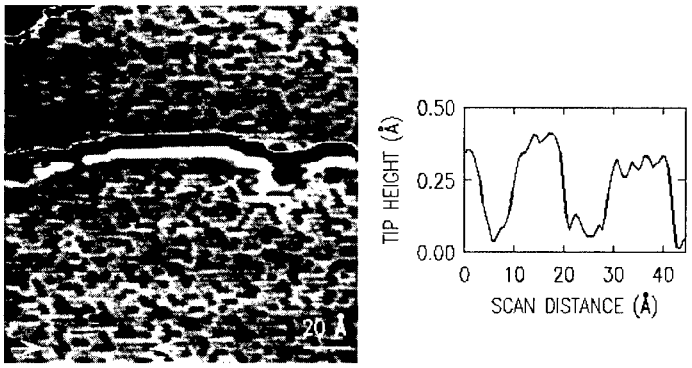


Figure 3. STM image of the InGaN(000$\bar{1}$) surface, obtained from a sample with negligible indium incorporation in the bulk. The image was acquired with sample bias voltage of -0.5 V and tunnel current of 0.075 nA. The grey scale range is 0.6 Å for each terrace. A line cut, taken at the position of the arrows in the figure, is shown on the right side of the figure.

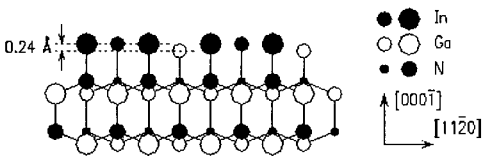


Figure 4. Schematic view of the InGaN surface in an (1$\bar{1}$00) projection, showing theoretical results for atomic positions. The surface adlayer consists of 75% In plus 25% Ga, in a 2×2 arrangement..

From the STM image of Fig. 3 it is clear that the InGaN surface is mostly covered with indium atoms, whereas for the same sample there is negligible indium incorporation in the bulk. Thus there is strong surface segregation of indium on the InGaN. We have observed similar surface segregation on other samples, including those containing significant amounts of indium in the bulk. Indium surface segregation has been attributed in large part[8] to the fact that the InN bond is weaker than the GaN bond (1.93 eV for InN and 2.24 eV for GaN).[9] In the bulk, a metal atom forms four bonds with nitrogen atoms, whereas on the surface, for N-polar InGaN, a metal atom forms only one bond with a nitrogen atom. Therefore it is energetically favorable for a gallium atom on the surface to switch sites with an indium atom in the bulk.

Model

Figure 5 illustrates the near surface region of a N-polar InGaN film, showing a typical distribution of metal atoms (indium and gallium) on the surface and in the bulk. From prior studies in the absence of indium, it is known that the surface is terminated with a monolayer of metal atoms (layer 2 in Fig. 5), and a few additional metal atoms (layer 1) may reside on top of this adlayer.[7] The population of metal atoms in layer 1 depends on how metal rich the growth is. For GaN growth, it is known that the gallium atoms in layer 1 diffuse quickly,[10,11] and the observation of step flow growth[12,13] implies that the gallium atoms (and presumably also the

nitrogen atoms) diffuse to surface steps where they incorporate. For the present case of InGaN growth, the observed surface segregation reveals that layer 2 contains mainly indium atoms. This surface composition will affect the growth in several ways. First, the atomic diffusivity will increase on an indium covered $(000\bar{1})$ surface compared with a gallium covered surface.[14] Second, a gallium atom in layer 1 may simply switch sites with an indium atom in layer 2 without diffusing to a step edge, and that particular gallium atom could possibly further switch positions with an indium atom in the bulk. Therefore the growth kinetics for Ga incorporation in InGaN growth may be different from that in GaN growth. Third, if the nitrogen source is NH_3, rather than an RF-plasma source, the decomposition rate of NH_3 may be affected by the surface metal species.

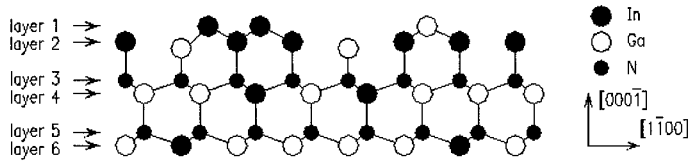


Figure 5. Schematic view of the InGaN$(000\bar{1})$ surface layers, in a $(11\bar{2}0)$ projection: layer 1, the metal adatoms residing on top of the metal adlayer; layer 2, metal adlayer on nitrogen; layers 3 and 5, nitrogen atoms; layers 4 and 6, metal atoms.

Since there is a strong surface segregation of indium atoms, the gallium atom population on the surface is small, under the condition that the growth is not overly metal rich. Then, the gallium evaporation will also be small, and most of the incident gallium flux will incorporate into the bulk. For indium atoms, the incident flux can proceed in one of several kinetic pathways. One is to be incorporated into the bulk. The second possibility is to evaporate, including evaporation from layer 2 (which is actually decomposition of InN) or evaporation from layer 1 (the rate of which depends on the numbers of atoms in that layer). We denote the concentration of indium atoms in the *ith* layer as $[In_i]$, and the rate of indium evaporation from the *ith* layer as R_{Ini}. When the metal flux is increased while keeping the nitrogen flux constant, the metal atom population in layer 1 will increase and so R_{In1} will increase to keep the metal flux in balance. When the metal flux is further increased, the layer 1 metal population is so high that metal droplets will form, which is the third pathway for the incident indium.

Based on this model, the dependence of indium incorporation on group III/group V ratio which was described in the earlier section can be explained. In the metal rich region, the maximum amount of In+Ga which can be incorporated into the bulk is limited by the active nitrogen flux. When the metal flux is increased, those additional gallium atoms will compete to go into bulk. Since there is a strong indium surface segregation, those additional gallium atoms will mostly go into bulk and kick out indium atoms, so that the indium incorporation will decrease. Excess indium atoms, formed from the increased metal flux as well as the decreased bulk incorporation, will tend to increase $[In_1]$, and so R_{In1} will increase. Thus, the excess indium will evaporate, or alternatively, it will form droplets if there is too much indium. In the nitrogen rich region, however, the number of metal atoms in layer 1 is minimal. Thus, metal evaporation proceeds mainly via R_{In2}, which is almost constant for a given temperature. Therefore with the loss of indium being constant, an increase of both indium and gallium flux while keeping their ratio constant will lead to an increase in the indium incorporation.

CONCLUSION

The dependence of indium incorporation on temperature and metal flux has been studied during MBE growth of InGaN. It is found that the incorporation decreases when the growth

temperature is increased, it decreases when the group III/group V flux ratio is increased under metal rich conditions, and it increases as a function of this flux ratio under nitrogen rich conditions. STM images show that InGaN surface is mostly covered with indium atoms, revealing a strong surface segregation of the indium. Based on this surface segregation, a model is proposed to explain the indium incorporation dependence on the growth parameters.

ACKNOWLEDGEMENTS

This work was supported by grants from the National Science Foundation, DMR–9615647, and from the Office of Naval Research, N00014-96-1-0214.

(a) Present address: Dept. of Physics and Astronomy, Ohio University, Athens, Ohio 45701.

REFERENCES

[1] S. Nakamura, M. Senoh, S.-I. Nagahama, N. Iwasa, T. Yamada, T. Matsushita, H. Kiyoku, Y. Sugimoto, T. Kozaki, H. Umemoto, M. Sano, and K. Chocho, Jpn. J. Appl. Phys., Part 2 **36**, L1568 (1997); S. Nakamura and G. Fasol, *The Blue Laser Diode* (Springer, Berlin, 1997).

[2] J.M. Moison, C. Guille, F. Houzay, F. Barthe, and M. Van Rompay, Phys. Rev. B **40**, 6149 (1989).

[3] A.R. Smith, R.M. Feenstra, D.W. Greve, M.-S. Shin, M. Skowronski, J. Neugebauer, J.E. Northrup, Appl. Phys. Lett. **72**, 2114 (1998).

[4] See for example, S. Nakamura, Microelectron. J. **25**, 651 (1994); J.M. Van Hove, P.P. Chow, A.M. Wowchak, J.J. Klaassen, R. Hickman II, and C. Polley, J. Vac. Sci. Technol. B **16**, 1286 (1998); N. Grandjean, and J. Massies, Appl. Phys. Lett. **72**, 1078 (1998).

[5] A.R. Smith, V. Ramachandran, R.M. Feenstra, D.W. Greve, A. Ptak, T. Myers, W. Sarney, L. Salamanca-Riba, M. Shin, and M. Skowronski, MRS Internet J. Nitride Semicond. Res. **3**,12 (1998).

[6] E.L. Piner, F.G. Mcintosh, J.C. Roberts, K.S. Boutros, M.E. Aumer, V.A. Joshkin, N.A. El-Masry, S.M. Bedair, and S.X. Liu, Mat. Res. Soc. Symp. Proc. **449**, 85 (1997).

[7] A.R. Smith, R.M. Feenstra, D.W. Greve, J. Neugebauer, and J.E. Northrup, Phys. Rev. Lett. **79**, 3934 (1997).

[8] J.E. Northrup, J. Neugebauer, and L.T. Romano, submitted to Appl. Phys. Lett.

[9] W.A. Harrison, *Electronic structure and the properties of solids* (Freeman, San Francisco, 1980) p 176.

[10] A.R. Smith, R.M. Feenstra, D.W. Greve, J. Neugebauer, and J.E. Northrup, Appl. Phys. A **66**, S947 (1998).

[11] T. Zywietz, J. Neugebauer, and M. Scheffler, Appl. Phys. Lett. **73**, 487 (1998).

[12] E.J. Tarsa, B. Heying, X.H. Wu, P. Fini, S.P. DenBaars, and J.S. Speck, J. Appl. Phys. **82**, 5472 (1997).

[13] A.R. Smith, V. Ramachandran, R.M. Feenstra, D.W. Greve, M.-S. Shin, M. Skowronski, J. Neugebauer, J.E. Northrup, J. Vac. Sci. Technol. A **16**, 1641 (1998).

[14] T.K. Zywietz, J. Neugebauer, M. Scheffler, and J.E. Northrup (unpublished).

Ni/Si-BASED CONTACTS TO GaN: THERMALLY ACTIVATED STRUCTURAL TRANSFORMATIONS LEADING TO OHMIC BEHAVIOR

E.Kaminska[a)], A.Piotrowska[a)], J.Jasinski[b)], J.Kozubowski[c)], A. Barcz[a)], K.Golaszewska[a)], D.B.Thomson[d)], R.F.Davis[d)], M.D.Bremser[e)].

[a)]Institute of Electron Technology, Al.Lotnikow 46, Warsaw, Poland, eliana@ite.waw.pl.
[b)]Institute of Experimental Physics, Warsaw University, Warsaw, Poland
[c)]Faculty of Material Science and Eng., Warsaw Technical University, Warsaw, Poland
[d)]Department of Material Science and Eng., NCSU, Raleigh, NC 27695-7907, USA
[e)]Aixtron, Inc., Buffalo Grove, IL 60089, USA

Cite this article as: MRS Internet J. Nitride Semicond. Res. 4S1, G9.9 (1999)

ABSTRACT

Structural transformations in Ni/Si-based contacts to GaN occurring under heat treatment have been studied using transmission electron microscopy and secondary ion mass spectrometry. Transition from non-ohmic to ohmic behavior correlates with reaction between Ni and Si, and decomposition of the initially formed interfacial Ni:Ga:N layer. Transport of dopant atoms from metallization into GaN testifies in favour of the SPR process of ohmic contact formation

INTRODUCTION

One of the key problems in GaN-based devices is a poor quality of ohmic contacts to p-GaN. The commonly adopted procedure for making ohmic contacts involves the use of high-work-function metallization schemes. These contacts convert from Schottky to ohmic-like after annealing, yielding resistivities of about $10^{-2}\Omega cm^2$ [1].

In order to reduce the contact resistivity, procedures enhancing the concentration of the active dopant in the semiconductor superficial region should be considered. To achieve that, we have adopted the idea of Sands et al. [2] of the incorporation of a dopant into the subcontact region by solid-state dissolution and subsequent regrowth (SPR). We have used Ni/Si metallization, with Mg as a dopant to produce contacts to p-GaN. For n-GaN, Si was the intended donor dopant. It has been shown that these contacts became ohmic after annealing at temperatures ranging from 400 to 600^0C, with resistivity of ~ $1*10^{-3}\Omega cm^2$ on p-type GaN with hole concentration $3*10^{17}$ cm^{-3} [3].

In order to further elucidate structural changes that take place during the formation of ohmic contacts, a study of the microstructure of Ni/Si-based contacts has been performed. We have used transmission electron microscopy (TEM) methods and SIMS. The high spatial resolution of TEM provides details about the morphology of metal/semiconductor interfaces, phase compositions and crystallographic relationships in the contact region. SIMS was applied to probe the elemental depth profiles. The question of dissimilarities in the behavior of p-type and n-type metallizations during the formation of ohmic contacts has been of special concern.

EXPERIMENTAL PROCEDURE

Contacts under investigation have been made to (0001) oriented GaN epilayers, 1-2 μm thick, grown via organometallic vapour phase epitaxy on AlN buffer layers predeposited on 6H-

Mat. Res. Soc. Symp. Proc. Vol. 537 © 1999 Materials Research Society

SiC substrates [4]. Prior to metal deposition, the samples were etched in buffered HF and in $NH_4OH:H_2O$ (1:10). The cleaning was finished in the deposition chamber by heat treatment at 400^0C for 10 min., under UHV conditions, for thermal desorption of hydrocarbon contaminants. The metallization in the form of sandwich structures Ni/Mg/Ni/Si and Ni/Si/Ni/Si for p- and n-type GaN, respectively, was deposited by e-beam evaporation. The thickness of consecutive metallization films was 25 nm/8 nm/25 nm/240 nm.

In view of a high thermal stability of GaN, contacts were fabricated in a two-step process. The first layer of nickel was evaporated onto the substrate held at 350^0C, then the sample was cooled down to room temperature, and the deposition of the metallization was completed. Finally, heat treatment was carried out in flowing N_2, at temperatures 200-400^0C for 30 min.

The microstructure of contacts was investigated by cross-sectional transmission electron microscopy (XTEM) and high resolution imaging (HREM) combined with energy dispersive x-ray spectroscopy (EDX). TEM observations were performed using a JEOL JEM 3010 microscope operating at 300 keV. A microprobe beam size of ~10 nm was used for EDX analysis.

SIMS profiling was performed in a Cameca 6F instrument with a caesium primary ion beam and detection of CsM_i^+ secondary cluster ions, which enabled the analysis with reduced matrix effects. To follow the thermally activated displacement of nickel and magnesium atoms relative to the contact interface in contacts to p-GaN, Ni-Ga and Mg-Ga cluster ions were analyzed as well. To examine the interaction between GaN and nickel in as-deposited samples, the Ni-Ga-N complex was also monitored with negative secondaries.

RESULTS

TEM micrographs of as-deposited contacts to p-and n-type GaN are presented in Fig.1(a) and Fig.2(a). Both as-deposited contacts consist of four distinct layers. In both contacts the upper Si layers are amorphous, and the intermediate Ni films are polycrystalline. No sign of reaction between these layers was observed.

The high resolution micrographs of metal/semiconductor interfaces are shown in Fig.1(b) and Fig.2(b). In p-type metallization, the Mg film is polycrystalline and, as proved by EDX analysis, accommodates some amount of Ni, while in n-type contacts, a thin film of Si in-between Ni layers, is amorphous.

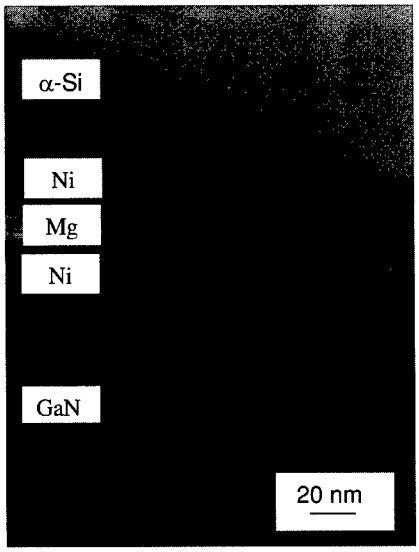
In both contacts the layer adjacent to GaN is very uniform, 20-25 nm thick, and crystalline in nature. Fourier transforms of the lattice fringes are consistent with a face-centred cubic phase with lattice parameter a=0.341 nm, which, within the resolution of our measurements, suggests Ni. In our previous publication [3] we speculated on the formation of a highly textured Ni_3Ga_2 phase. This work gives evidence for the presence of nickel. Because of the small lattice expansion for the Ni-Ga and Ni-N solid solutions [5], the incorporation of a few atomic percent of Ga and N into the Ni film is below the detection limit of the applied method.

No oxide at metal/semiconductor interface was observed.

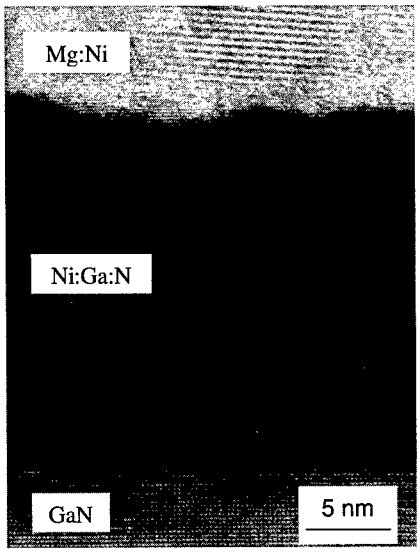
The progress of the contact reaction, as registered by SIMS, is shown in Fig.3. SIMS analysis reveals evidence for the expected interaction in as-deposited contacts between Ni and semiconductor. The Ni-Ga cluster peak, Fig.3.(a), and Ni-Ga-N complex, Fig.3.(b), apparently coincide with the superficial region of GaN.

Annealing at 350^0C, which is 50^0C below the onset of the ohmic behavior, causes migration of Mg towards the contact interface and movement of Ni in the opposite direction, Fig.3.(c). This trend is preserved after annealing at 400^0C. The concentration of Mg in the interfacial layer has further increased, while the position of Ni, which now forms only one distinct layer, coincides with that of Si, Fig.3(d).

a



b



c



Fig. 1. XTEM micrographs of p-GaN/Ni/Mg/Ni/Si contacts:
a) as-deposited contact, b) HREM lattice image of the interface of the as-deposited contact, c) contact annealed at 400°C.

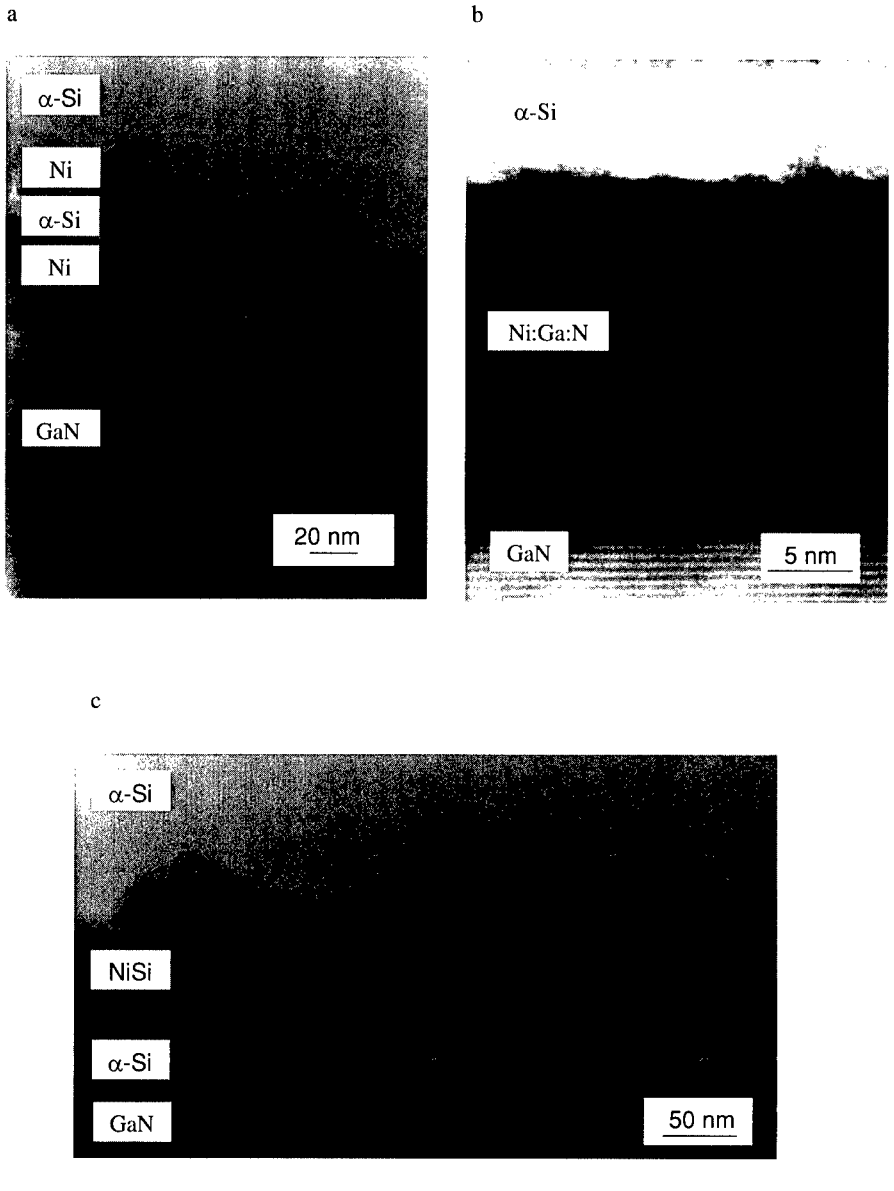


Fig. 2. XTEM micrographs of n-GaN/Ni/Si/Ni/Si contacts:
a) as-deposited contact, b) HREM lattice image of the interface of the as-deposited contact, c) contact annealed at 400°C.

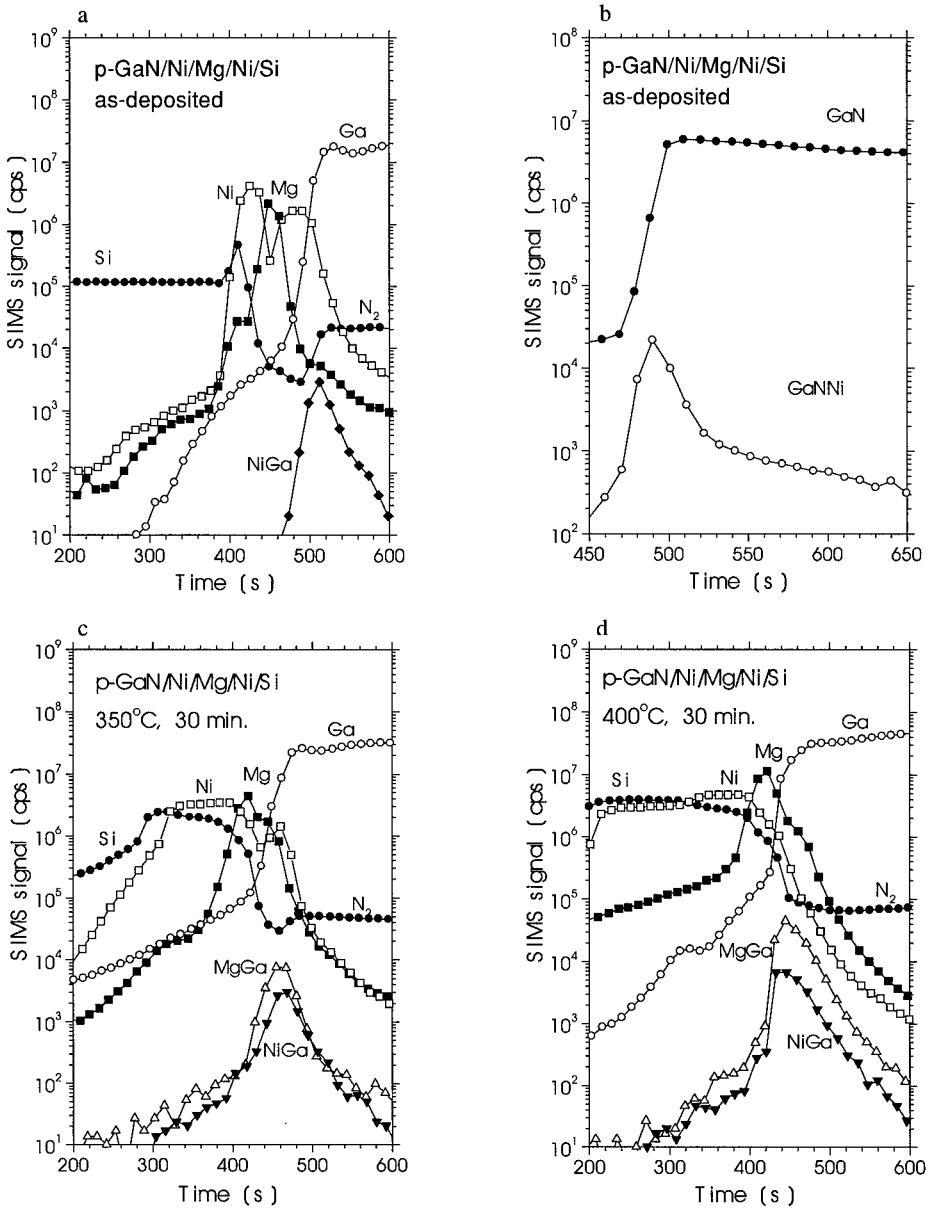


Fig. 3. SIMS in-depth profiles for p-GaN/Ni/Mg/Ni/Si contacts:
a) and b) as-deposited contact - profiles obtained with positive and negative secondary ions, respectively, c) annealed at 350°C, d) annealed at 400°C.

The microstructures of contacts after annealing at 400^0C for 30 min. are presented in Fig.1(c) and Fig.2(c). In both contacts, amorphous planar interlayers, ~10 nm thick, are formed along the interface separating the semiconductor and the metallization. Careful EDX analysis revealed that in p-type contact this layer contains Mg, and some amount of Ni and Ga. Small crystalline voids of Ni are present throughout this film. In the n-type contact, Si is the only component of the interfacial film. The main constituent of each contact consist of nickel silicide. Excess of unreacted amorphous Si is detected in the outermost layer. The contact interfaces are sharp and abrupt.

DISCUSSION AND CONCLUSIONS

From the experimental observations of two Ni/Si-based contacts to GaN some common structural transformations are apparent. During the deposition, Ni reacts with GaN and forms a highly ordered Ni layer containing some amount of Ga and N. This reaction provides a very good oxide-free interface. Upon annealing the interfacial film decomposes, and Ni is transported toward the outer Si layer. At the same time, the dopant atoms (Mg or Si) move in the direction of the semiconductor substrate and finally form a continuous film at the interface.

As for electrical properties, the transition from non-ohmic to ohmic behavior in GaN/NiSi contact system takes place when the initial interface interlayer Ni:Ga:N decomposes as a result of Si-Ni reaction. The NiSi phase is not in direct contact with GaN when the contact become ohmic, so it can not be responsible for the ohmic behavior. On the other hand, the presence of Mg in the superficial film of the semiconductor, in the applied temperature range, can not be explained in terms of diffusion. The contact reaction is probably accompanied by a regrowth of the decomposed volume of the semiconductor. Since the semiconductor surface layer reacted with Ni is very thin, the observed ohmic behavior must be due to a few monolayers thick regrown GaN film. The growth of an amorphous layer at the surface of GaN could lower the barrier height across the metal/semiconductor interface, and thus facilitate the formation of the low-resistance contact. The interface of Ni/Si-based contacts to GaN appears to be sharp as opposed to a continuous diffuse interface, characteristic of the presently used alloyed contacts. In terms of electronic properties, interface and surface morphologies, the Ni/Si contact scheme appears to be promising for device applications.

ACKNOWLEDGEMENTS

Electron Microscope JEM 3010 used in this study was founded by the Foundation for Polish Science. This work was partially supported by the Committee for Scientific Research, grant No. PBZ 28.11/P9.

REFERENCES

1. M.Murakami, Y.Koide, Critical Reviews in Solid State and Materials Science, **23**, 1 (1998).
2. T.Sands, E.D.Marshall, L.C.Wang, J.Mater.Res. **3**, 914 (1988).
3. E.Kaminska, A.Piotrowska, A.Barcz, M.Guziewicz, S.Kasjaniuk, M.D.Bremser, R.F.Davis, E.Dynowska, S.Kwiatkowski, Mat.Res.Soc.Symp.Proc.,vol. **482**, 1077 (1998).
4. T.W.Weaks, Jr., M.D.Bremser, K.S.Ailey, E.Carlson, W.G.Perry, E.L.Piner, N.A. El-Masry, R.F.Davis, J.Mater.Res., **10**, 1011 (1996).
5. M.Hansen, K.Anderko, *Constitution of Binary Alloys*, (McGrow-Hill Book Company, Inc.,London, 1958).

Part X

Novel Growth, Doping, and Processing

IMPROVEMENT OF CRYSTALLINE QUALITY OF GROUP III NITRIDES ON SAPPHIRE USING LOW TEMPERATURE INTERLAYERS

H. Amano, M. Iwaya, N. Hayashi, T. Kashima, M. Katsuragawa, T. Takeuchi, C. Wetzel and I. Akasaki,

Meijo University, 1-501 Shiogamaguchi, Tempaku-ku, Nagoya 468-8502, Japan

Cite this article as: MRS Internet J. Nitride Semicond. Res. 4S1, G10.1 (1999)

ABSTRACT

In organometallic vapor phase epitaxial growth of group III nitrides on sapphire, insertion of a low temperature interlayer is found to improve crystalline quality of $Al_xGa_{1-x}N$ layer with x from 0 to 1. Here the effects of the low temperature deposited GaN or AlN interlayers on the structural quality of group III nitrides is discussed.

INTRODUCTION

From the late 60's to the early 70's Maruska and Tietjen [1], Pankove *et al.* [2] and Monemar [3] demonstrated the significant potential of GaN as a solid source blue light emitter. However, the difficulty in growing high crystalline quality GaN free of cracks, and in fabricating p-type GaN, have long prevented the practical application of GaN. The use of low-temperature-deposited buffer layer (LT-BL) [4,5] and the realization of p-type GaN [6,7] triggered the vast expansion of nitride research worldwide [8]. Today, bright blue light emitting diodes (LEDs), green LEDs and white LEDs based on nitrides have been commercialized, and purple, deep purple and even UV laser diodes have been fabricated. Microwave field effect transistor (FET) and solar-blind UV detectors are also available. These results are remarkable considering the 16% lattice mismatch between GaN and sapphire, which were accommodated by the LT-BL approach.

Nevertheless, GaN grown on sapphire using a LT-BL still contains high threading dislocations (TDs) densities on the order of 10^8-$10^{10}cm^{-2}$ that originate at the interface between GaN and the LT-BL and/or sapphire substrate [9,10]. TDs affect performances of several devices such as LEDs or FETs because some of the TDs act as non-radiative recombinaiton centers [11] and/or scattering centers in the transport of electrons [12].

Recently, we found that insertion of low-temperature-deposited GaN or AlN interlayers (LT-GaN IL or LT-AlN IL) between high-temperature-grown GaN (HT-GaN) layers reduces TD densities of HT-GaN [13-15]. We also found that the low temperature interlayer is effective not only for the improvement of the crystalline quality of the HT-GaN layer, but also for that of HT-AlGaN and HT-AlN.

In this study, X-ray diffraction (XRD), transmission electron microscopy (TEM) as well as microscopic observations were performed to investigate the effects of LT-ILs on the structural properties of the topmost GaN, AlGaN and AlN layers.

Mat. Res. Soc. Symp. Proc. Vol. 537 © 1999 Materials Research Society

EXPERIMENTS

Nominally undoped GaN, AlGaN and AlN layers were grown on (0001) sapphire substrates in a horizontal reactor [16]. TMGa, TMAl and ammonia were used as Ga, Al and nitrogen source gases, respectively, at around 140 Torr growth pressure.

Fig.1 schematically shows the structure of the sample used in this study. In this paper, the LT-layer between sapphire substrate and HT-GaN is called buffer layer (BL), while the LT-layer between HT-nitride is called interlayer (IL).

Just after thermal annealing of the sapphire (0001) substrate in a hydrogen flow at 1,150°C, the graphite susceptor was cooled down to 500°C in order to deposit either a LT-AlN BL or a LT-GaN BL on the sapphire substrate. The thickness was ~20nm. HT-GaN was grown at 1,050°C on the LT-BL. The thickness of the first HT-GaN layer was fixed at ~1 μm. The deposition conditions for LT-AlN IL or the LT-GaN IL was just the same as that for the first LT-BL. HT-nitrides were grown on top of the LT-IL. For comparison, HT-AlGaN and HT-AlN were also grown on LT-BL or on HT-GaN not covered with a LT-IL.

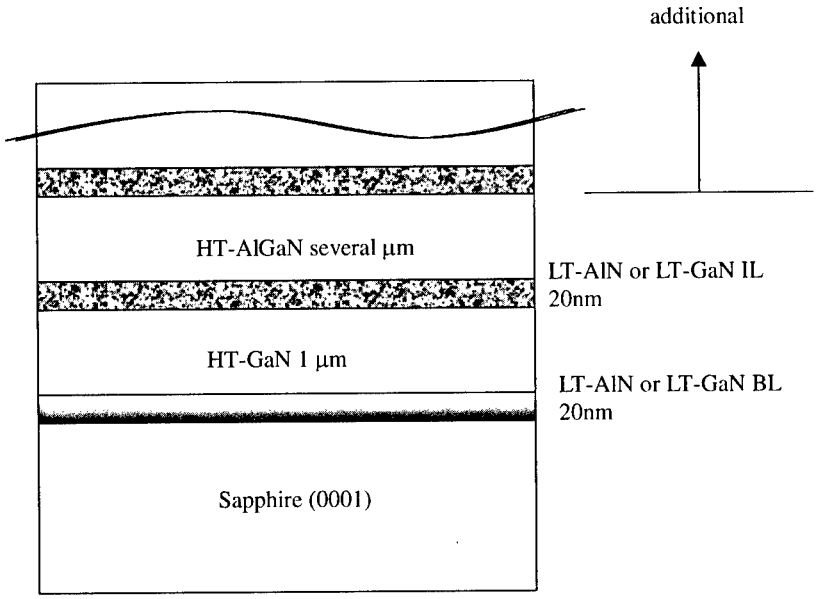


Fig. 1 Schematic drawing of the structure of the samples used in this study.

LT : low temperature
HT : high temperature
BL : buffer layer
IL : Interlayer

Plan view and cross sectional transmission electron microscopy (TEM) observations were carried out to measure the density of TDs using a HITACHI H-9000 TEM system with an acceleration voltage of 300 kV. In order to determine the density of TDs of the uppermost layer by plan view TEM, the samples were thinned from the back side. A focused ion beam technique was used to prepare the cross sectional TEM samples.

X-ray diffraction was performed by a Philips X'Pert system to characterize the crystalline quality of the samples.

RESULTS

HT-GaN/LT-IL/HT-GaN/LT-BL/Sapphire

Fig. 2 shows a multi-beam dark field cross sectional TEM image of the GaN grown by the newly developed LT-IL technique. It is clearly seen that several TDs originated at the interface between HT-GaN and the LT-AlN BL and/or sapphire were annihilated at the LT-AlN IL. In this case, LT-AlN IL was used. We confirmed that LT-GaN IL is also effective to reduce TDs.

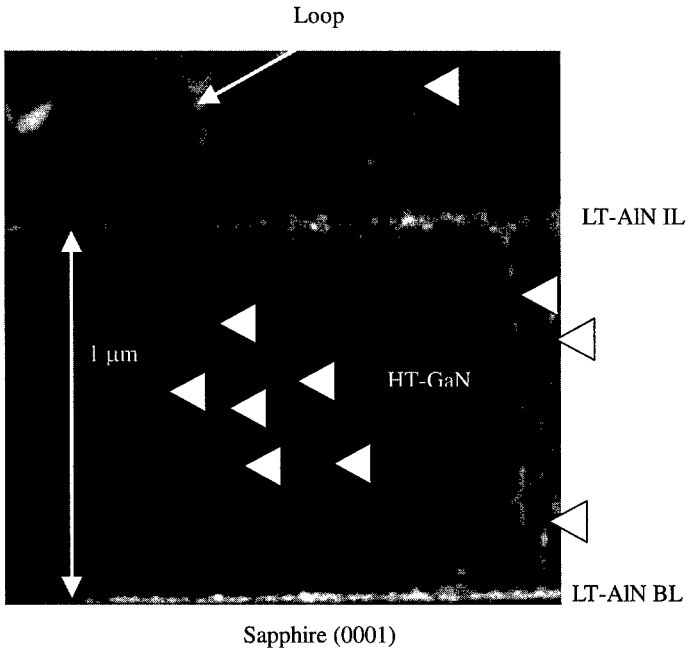
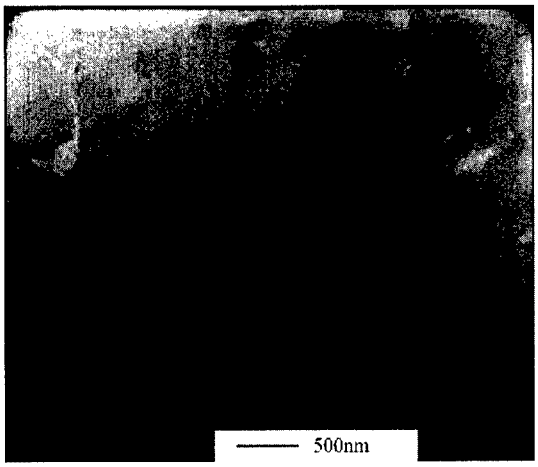
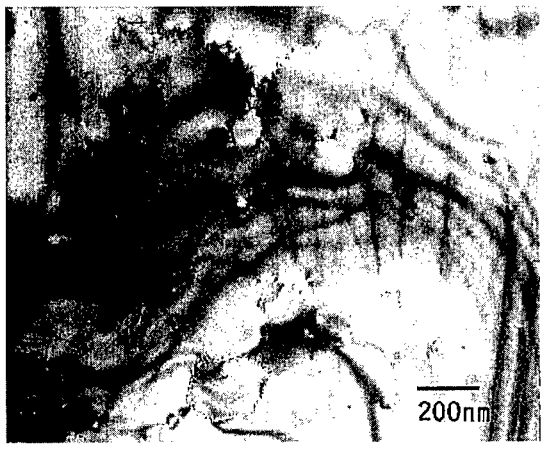


Fig.2 Multi beam dark field cross sectional TEM image of GaN grown by using a LT-AlN IL. TDs are indicated by triangles.

Fig. 3 shows the plan view TEM images of the top HT-GaN grown on sapphire (a) using five LT-AlN IL and one LT-AlN BL, and (b) using conventional one LT-AlN BL. In fig. 3 (b), plenty of TDs can be seen while in fig. 3 (a), TDs can hardly be observed.



(a)



(b)

Fig. 3 Plan view TEM□image of the uppermost HT-GaN grown (a) using five LT-AlN ILs and one LT-AlN BL, and (b) using one LT-ALN BL. Magnification is different for each image.

Fig. 4 shows the density of TDs measured by plan view TEM of the top HT-GaN layer as a function of number of LT-layers. A reduction in the TDs density is always observed with an increased number of LT-ILs. This result is independent of the interlayer material. In other words, both LT-AlN IL and LT-GaN IL act as TDs filters.

Comparing the LT-AlN IL and LT-GaN IL as TDs filters, they seem to show similar effects. However, in case of LT-GaN IL, the HT-GaN tends to crack when the number of IL repetition exceeds a certain value. In the case of LT-GaN ILs, a cracking network is clearly visible when the repetition exceeds 8 times. On the contrary, no cracks are observed in HT-GaN grown by using LT-AlN ILs. From in-situ stress monitoring with a multi-optical beam stress sensor system [15,17,18], it was found that HT-GaN is grown under tension, and the magnitude of tensile stress increases with increasing number of repetitions of the LT-GaN IL. Therefore, it is natural to think that cracks are generated during the growth when the tensile stress exceeds some critical value. In comparison, in the case of the LT-AlN IL, the magnitude of tensile stress during growth is almost constant irrespective of the number of repetitions of the LT-AlN IL. Details will be give elsewhere[15].

The LT-IL method is different from the thermal cyclic annealing, because in this newly developed process either GaN or AlN is deposited at low temperature. Actually, even though thermal cyclic annealing was performed, due probably to the high thermal stability of dislocations in nitrides, no improvement of the crystalline quality of HT-GaN was observed.

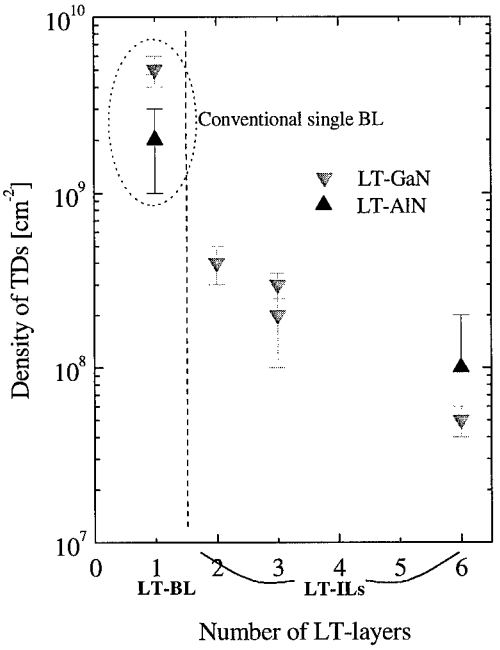


Fig. 4 Density of TDs measured by plan view TEM as a function of number of ILs. Up and down triangles show the LT-AlN and LT-GaN cases, respectively.

HT-AlGaN/LT-IL/HT-GaN/LT-BL/Sapphire

One of the advantages of the LT-IL method is that it can be applicable not only for the growth of GaN but also for the growth of Al-containing alloys. To verify this superiority of LT-IL method, HT-$Al_{0.5}Ga_{0.5}N$ or HT-AlN was grown on HT-GaN covered with LT-AlN IL. Both HT-$Al_{0.5}Ga_{0.5}N$ and HT-AlN grown on LT-GaN IL or on HT-GaN showed a cracking network as shown in figs. 5 (b) and 5 (d). On the other hand, as shown in figs. 5 (a) and (c), no cracking was observed on the surface of HT-AlN grown on a LT-AlN IL.

The improvement of the crystalline quality of HT-AlN by the use of the LT-AlN IL method was confirmed by X-ray rocking curve (XRC) measurements. As shown in fig. 6, the crystalline quality of HT-AlN grown on LT-AlN IL is far superior to that of HT-AlN grown on HT-GaN or on LT-AlN BL on sapphire. We verified the same results on the growth of HT-$Al_xGa_{1-x}N$ on LT-AlN IL within the entire composition range.

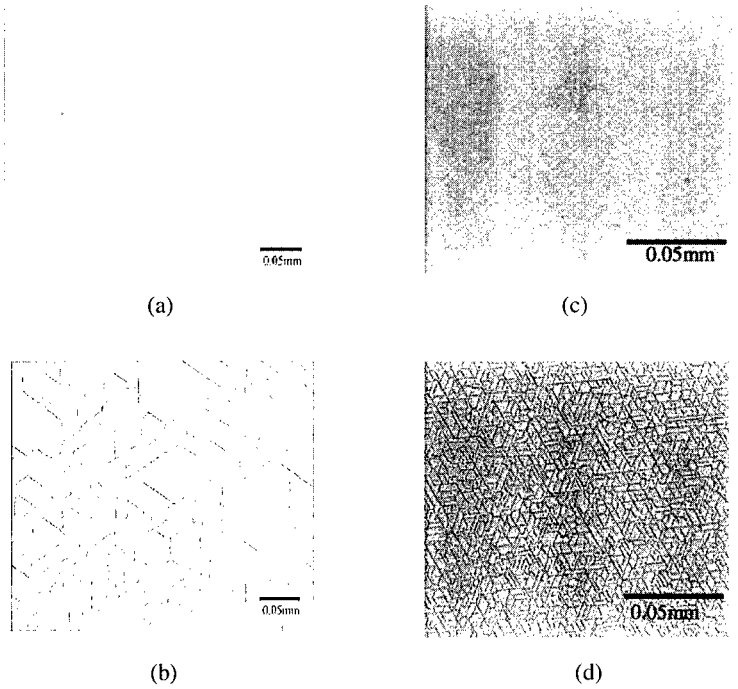


Fig. 5 Differential interference contrast micrographs of the surface of HT-$Al_{0.5}Ga_{0.5}N$((a), (b)) and HT-AlN ((c), (d)) grown on (a),(c) LT-AlN IL/HT-GaN/LT-AlN BL/Sap., and (b),(d) HT-GaN/LT-AlN BL/Sap.

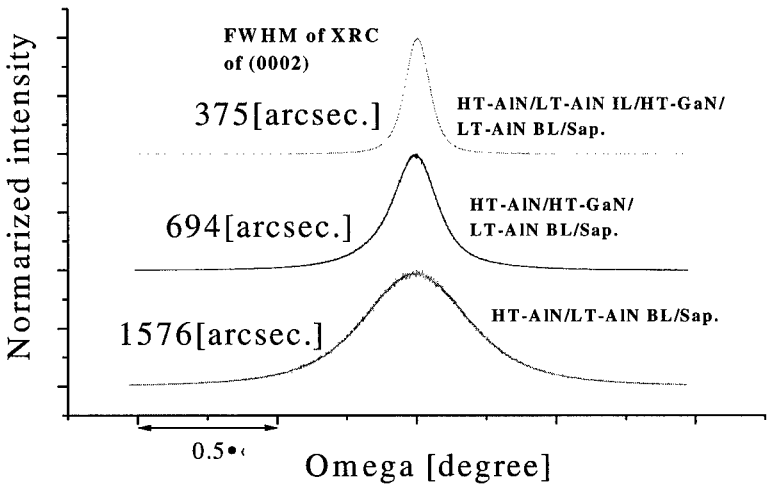


Fig. 6 FWHMs of X-ray rocking curve of (0002) diffraction from HT-AlN on (a) LT-AlN IL/HT-GaN/LT-AlN BL/Sap., (b)HT-GaN/LT-AlN BL/Sap., and (c) LT-ALN BL/Sap.

SUMMARY

The effect of the insertion of low temperature interlayers on the improvement of the crystalline quality of the upper nitride layers were investigated. The low temperature interlayer method is applicable not only for the growth of GaN, but also for the growth of high crystalline quality AlGaN including binary AlN free of cracks. Therefore, application of low temperature interlayers is not limited to the improvement of the performance of the GaN based devices, but is quite useful for the fabrication of novel devices such as distributed Bragg reflectors, vacuum UV detectors or UV emitting devices, all of which include high AlN content AlGaN layers.

ACKNOWLEDGEMENTS

This work was partly supported by the Ministry of Education, Science, Sports and Culture of Japan, (contract nos. 09450133, 09875083 and High-Tech Research Center Project), Japan Society for the Promotion of Science (JSPS) Research for the Future Program in the Area of Atomic Scale Surface and Interface Dynamics under the project of "Dynamical Process and Control of Buffer Layer at the Interface in Highly-Mismatched System".

One of the authors (H.A.) would like to thank Dr. Jung Han, Dr. Jerry A. Floro and Mr. Sean Hearne of Sandia National Laboratories for cooperative work on in-situ stress monitoring.

REFERENCES

1. H. P. Maruska and J. J. Tietjen, Appl. Phys. Lett., **15**, 327 (1969).
2. J. I. Pankove, E. A. Miller, D. Richman and J. E. Berkeyheiser, J. Lumin., **4**, 63 (1971).
3. B. Monemar , Phys. Rev. **B10**, 676 (1974).
4. H. Amano, N. Sawaki, I. Akasaki and Y. Toyoda, Appl. Phys. Lett. **48**, 353 (1986).
5. S. Nakamura, T. Mukai and M. Senoh: J. Appl. Phys. **71**, 5543 (1992).
6. H. Amano, M. Kito, K. Hiramatsu, N. Sawaki and I. Akasaki, Jpn. J. Appl. Phys., **28**, L2112 (1989).
7. S. Nakamura, M. Senoh and T. Mukai, Jpn. J. Appl. Phys., **30**, L1708 (1992).
8. I. Akasaki, Proc. Mater. Res. Soc. **482**, 3 (1998).
9. S. D. Lester, F. A. Ponce, M. G. Craford and D. A. Steigerwald, Appl. Phys. Lett., **66**, 1249 (1995).
10. X. J. Ning, F. R. Chien, P. Pirouz, J. W. Yang and M. A. Khan, J. Mater. Res., **11**, 580 (1996).
11. T. Sugahara, H. Sato, M. Hao, Y. Naoi, S. Kurai, S. Tottori, K. Yamashita, K. Nishino, L. T. Romano and S. Sakai, Jpn. J. Appl. Phys., **37**, L398 (1998).
12. L. Eastman, K. Chu, W. Schaff, M. Murphy and N. G. Weimann, Internet J. of Nitride Semiconductor Re, **2**, 17 (1997).
13. M. Iwaya, T. Takeuchi, S. Yamaguchi, C. Wetzel, H. Amano and I. Akasaki, Jpn. .J. Appl. Phys. **37**, L316 (1998).
14. M. Iwaya, N. Hayashi, T. Takeuchi, T. Kashima, M. Katsuragwa, H. Kato, S. Yamaguchi, C. Wetzel, H. Amano and I.Akasaki, Jpn. J. Appl. Phys. (to be submitted).
15. H. Amano, M. Iwaya, T. Kashima, M. Katsuragawa, I. Akasaki, J. Han, S. Hearne, J. A. Floro, E. Chason and J. Figiel, Jpn. J. Appl. Phys., **37**, (1998)L1540.
16. K. Hirosawa, K. Hiramatsu, N. Sawaki and I. Akasaki, Jpn. J. Appl. Phys., **32**, L1039 (1993).
17. J. Floro, E. Chason, S. Lee, R. Twesten, R. Hwang and L. Freud, J. Electron. Mater., **26**, 969 (1997).
18. S. Hearne, E. Chason, J. Han, J. Floro, J. Figiel, J. Hunter, H. Amano and I. Tsong, Appl. Phys. Lett., (to be published).

GaN HOMOEPITAXY FOR DEVICE APPLICATIONS

M. Kamp*, C. Kirchner*, V. Schwegler*, A. Pelzmann*, K.J. Ebeling*,
M. Leszczynski**, I. Grzegory**, T. Suski**, S. Porowski**

* Dept. of Optoelectronics, University of Ulm, 89069 Ulm, GERMANY,
Tel.: +49-731-5026050, Fax: +49-731-5026049, e-mail: markus.kamp@e-technik.uni-ulm.de
** High Pressure Research Center, Warsaw, POLAND

Cite this article as: MRS Internet J. Nitride Semicond. Res. 4S1, G10.2(1999)

Abstract

Epitaxial growth on GaN single bulk crystals sets new standards in GaN material quality. The outstanding properties provide new insights into fundamental material parameters (e.g. lattice constants, exciton binding energies, etc.) being not accessible by heteroepitaxial growth on sapphire or SiC. With MOVPE and MBE we realized unstrained GaN layers with dislocation densities about six orders of magnitude lower than in heteroepitaxy. Those layers revealed an exceptional optical quality as determined by a reduction of the photoluminescence linewidth from 5 to 0.1 meV and a reduced XRD rocking curve width from 400 to 20 arcsec.

Only recently, progress in surface preparation allowed morphologies of the layers suitable for device applications. We report on InGaN/GaN MQW structures as well as the first GaN *pn*- and InGaN/GaN double heterostructure LEDs on GaN single bulk crystals. Those LEDs are twice as bright as their counterparts grown on sapphire. In addition they reveal an improved high power characteristics, which is attributed to an enhanced crystal quality and an increased *p*-doping. Time resolved electroluminescence measurements proof that band/band recombination is the dominant emission mechanism for the InGaN/GaN LEDs.

Introduction

Due to its excellent optical and electrical properties, GaN attracts worldwide attention for devices and fundamental research. The wide direct bandgap, the high luminescence efficiency and the thermal, mechanical, and chemical robustness make group III-nitride semiconductors the superior material system for optoelectronic devices in the UV to visible range. Despite exceptional progress, group III-nitrides technology still suffers from mismatched heteroepitaxial growth. Mismatch in lattice constants and thermal expansion coefficients between substrate (mostly sapphire or SiC) and epitaxial layer inhibit perfect crystal formation, resulting in 10^9 to 10^{10} threading dislocations per cm^2.

Homoepitaxial growth of GaN has proven its tremendous potential to achieve superior material quality resulting in extremely narrow photoluminescence (PL) linewidths [1],[2] and a reduction of the dislocation densities by six orders of magnitude. These material qualities can only be attained using a substrate which is identical in crystal structure, lattice parameter and thermal expansion coefficient. Under those conditions, two-dimensional layer-by-layer growth can be obtained and the generation of dislocations can be inhibited. Additional process steps such as nitridation and nucleation layers, mandatory in heteroepitaxy of GaN, are no longer required, thus significantly simplifying the growth process. Besides the fundamental advantages of homoepitaxy, GaN substrates have a high thermal conductivity facilitating high power applications. Since they are electrically conductive, too, they provide additional freedom for the device design (e.g. vertical current transport) and simplify the device processing. Beside above

Mat. Res. Soc. Symp. Proc. Vol. 537 © 1999 Materials Research Society

mentioned advantages, GaN substrates are of particular interest for GaN-based blue laser, since simple facet cleaving [3] becomes feasible and the far field pattern will be improved due to the relative high index of refraction of the GaN substrates. These outstanding properties justify the enormous endeavor conducted at several laboratories on the growth of single crystal GaN substrates [4],[5],[6]. Even when the effort for those substrates is probably too high for mass products such as LEDs, it might be worth for high power laser applications.

Experimental

Substrate preparation

The GaN substrates have been grown in a high-temperature high-pressure process where the GaN is formed at N_2 pressures up to 20 kbar and at temperatures up to 1600°C from atomic nitrogen dissolved in a Ga melt. At a growth rate of approximately 100 µm/h perpendicular to the c-plane, the wurtzite crystals are grown up to areas of some 100 mm^2 at a thickness of about 200 µm. Undoped crystals used in this study reveal an flat (000-1) surface (i.e. N-polarity) and a rough (0001) surface (i.e. Ga-polarity), following E. Hellman's convention on the orientation [7]. The (000-1) surface can be mechano-chemically polished to achieve an atomically flat surface. The initial roughness of the (0001) side requires a polishing for device quality growth. Due to the chemically inertness of the (0001) surface this can only be achieved by mechanical polishing.

The crystal quality of the GaN substrates is excellent as indicated by x-ray rocking curve measurements [8]. Using $CuK\alpha_1$ radiation, linewidths of 20 arcsec are obtained for the (0002) reflex. The excellent structural properties are also pointed out by very low dislocation densities ranging from 10^3 - 10^5 cm^{-2}. The optical quality however is poor, near-bandgap excitonic transitions are not visible, weak PL at 380 nm and at 530 nm is observed at room temperature (RT).

Epitaxial growth

The homoepitaxial growth of GaN is performed in a horizontal, RF heated, water cooled quartz MOVPE reactor (AIXTRON AIX 200 RF) operated at low pressures. Trimethylgallium (TMGa), Trimethylindium (TMIn), Trimethylaluminum (TMAl), ammonia (NH_3), silan (SiH_4) and bis-cyclopentadienylmagnesium (Cp_2Mg) are used as precursors, hydrogen is used as carrier gas. The one side polished GaN substrates (approximately 8x6 mm^2 in size) were heated to 1060°C under a steady flow of ammonia to avoid surface degradation. During growth, the flow rates of NH_3 and TMGa were kept at 2.0 slm and 17 µmol/min, respectively. The Cp_2Mg flow rate was 90 nmol/min for *p*-type doping. After growth, thermal annealing under nitrogen ambient at 750°C was performed for 5 min to obtain *p*-type conductivity.

Characterization

Photoluminescence measurements at RT and 4 K are performed using a HeCd laser ($\lambda = 325$ nm) with an excitation density of approx. 10 mW/mm^2. X-ray diffraction (XRD) with $CuK\alpha_1$ radiation is used to characterize the structural quality of the binary layers as well as the composition of the ternary ones. Hall measurements of the epitaxial layers are inhibited by the highly conductive GaN substrate.

Devices

LEDs are fabricated taking advantage of the vertical device structure. Ni/Au contacts (50/200 nm) are evaporated as *p*-contacts. Dicing is achieved by simple cleaving, since layer and substrate are identical in their crystal structure and orientation. Subsequently, the devices are mounted on a copper plate using silver glue as backside contact material (*n*-type). The LEDs are

characterized by *I-V* measurements, their output power, and their electroluminescence spectra under cw- as well as ns-short-pulse-excitation.

Results and Discussion

Surface orientation and preparation

Both orientations (N-polarity (000-1) and Ga-polarity (0001)) of undoped single crystal substrates have been investigated in this study. Figure 1 compares the photoluminescence of GaN layers grown under identical conditions on GaN substrates of both orientations.

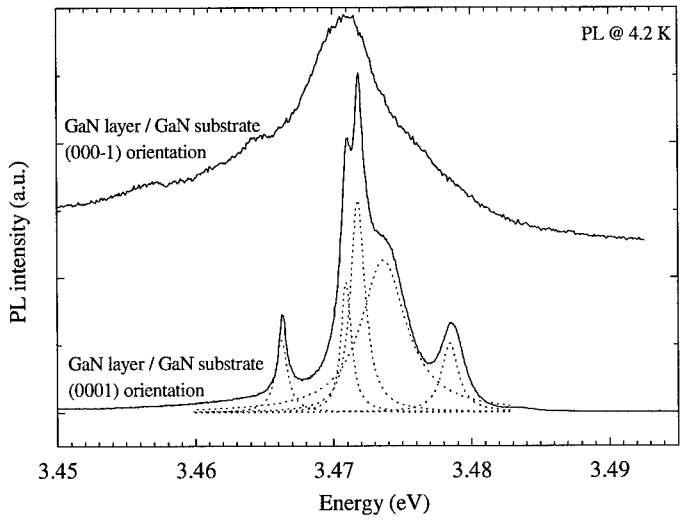


Fig 1.: Photoluminescence of epitaxial GaN layers (MBE) on (000-1)- and (0001)-oriented GaN substrates. Linewidth is as low as 0.5 meV for the (0001)-orientation.

At a PL linewidth of approx. 2 meV the material quality of the epitaxial layer grown on (000-1) oriented substrates compares favorably to heteroepitaxial growth. However, the properties of epitaxial films deposited on (0001) oriented substrates are clearly superior. Due to the outstanding material quality achieved on the (0001) oriented substrates (0.5 meV for the bound excitons in this MBE grown layer), this orientation has been used for the subsequently described work. The differences between both orientations can be traced back to the significantly different free surface energies of the orientations. From ab-initio calculations it is determined that the free surface energy of the (000-1) surface is significantly higher than the one of the (0001) surface [9]. From this point, the (0001) orientation provides a more stable surface with a lower probability of dopant incorporation [10].

For the following experiments the Ga-terminated side was mechanically polished to remove the initial roughness of the (0001) surface. This process, however, is known to create sub-surface damage which interferes with high quality epitaxial growth on such treated substrates. In conventional III-V technology, this damage is chemically removed, an approach

not accessible for the nitrides, as there is no suitable etchant known. Therefore, chemically assisted ion beam etching (CAIBE), a dry etching technique where the physical and chemical components of the etching process can be controlled fairly independently, is used to remove residual sub-surface damage. For direct comparison one half of a sample is CAIBE treated, whereas the other part is left unetched. Therefore, the substrate surface is partially coated with photoresist, acting as an etch mask. Argon and chlorine gas are used as physical and chemical etching components, respectively. Within 10 minutes an etch depth of approx. 300 nm was achieved using an ion energy of 400 eV which is reduced to 100 eV towards the end to minimize the ion damage. Nevertheless, the process is supposed to create an ion damage up to a depth of 8 Å. Since the etch rate depends only weakly on the chlorine flux, the process is regarded to be dominated by the physical component, i.e. sputtering. Figure 2a shows a SEM micrograph of a homoepitaxial GaN layer grown on a substrate which has been treated as described above.

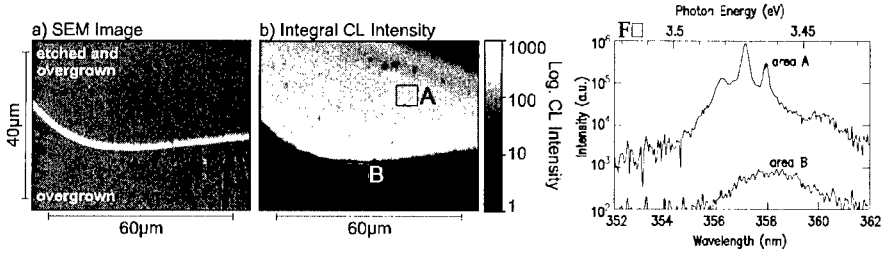


Fig 2.: SEM image (2a), corresponding cathodoluminescence (CL) intensities (2b) and local CL spectra (2c) obtained from an epitaxial GaN layer grown on partially CAIBE treated (0001)-oriented GaN substrates. CL by F. Bertram, T. Riemann, and J. Christen (Univ. Magdeburg).

The micrograph depicts the surface of a MOVPE grown GaN film just at the borderline between the etched and overgrown part (upper part) and the overgrown part which was not previously etched (lower part). The CAIBE-etched part of the sample reveals a significantly improved surface topology with almost no visible scratches, trenches, or holes. Figure 2b shows the corresponding CL intensity distribution of the same region of the sample. On the etched part, the intensity variation is almost negligible. In contrast, the area being not etched yields only weak CL signals (1000 times less in intensity) which also fluctuate locally. The comparison of the local CL spectra reveals large differences. The measured linewidth of the spectrum taken from the etched region (fig. 2a, area A) is ten times narrower than that of the non-etched region (fig. 2a, area B). However, the narrow CL spectra obtained from area A are still clearly resolution limited by the employed setup. The following mechanism is proposed to be responsible for the observations [11]. After mechanical polishing, the bulk GaN substrates reveal a smooth and mirror-like surface, however, sub-surface damage is induced by the polishing. By heating the substrates to growth temperature under ammonia during the MOVPE process, the damage becomes obvious revealing the observed trenches and scratches in the surface (fig. 2a, lower part). This experimental finding can be understood by dissociation and subsequent desorption of the damaged GaN. Eventually, during the heat up phase of the MOVPE growth, the substrate temperature of about 1100°C becomes high enough to achieve chemical etching (dissociation) under NH^3 even of non-deteriorated GaN layers [12]. Whenever CAIBE is applied before annealing, the originally mirrorlike surface morphology is kept mirrorlike during the mostly physical etching process and thereby transferred into the undisturbed part of the substrate. However, ion-beam induced damage is created by the CAIBE process. This damage,

nevertheless, is distributed homogeneously over the sample surface. During annealing in the MOVPE system this damage will dissociate revealing an almost perfect and smooth surface. Excess metallic Ga left on the surface is desorpt due to the exceptional high growth temperature of the group III-nitrides.

The necessity of the CAIBE treatment for devices based on single crystal substrates can best be seen in Fig. 3 showing evaporated Ni/Au metal contacts on a GaN *pn*-junction LED in an area without (Fig. 3a) and with prior CAIBE treatment (Fig 3b). The region of the device which was not CAIBE-treated reveals deep trenches as described earlier. Since the depths of the trenches is above the typical thickness of the *p*-GaN layer any metallization covering the sidewalls of the trenches will short circuit the *pn*-junction of the device.

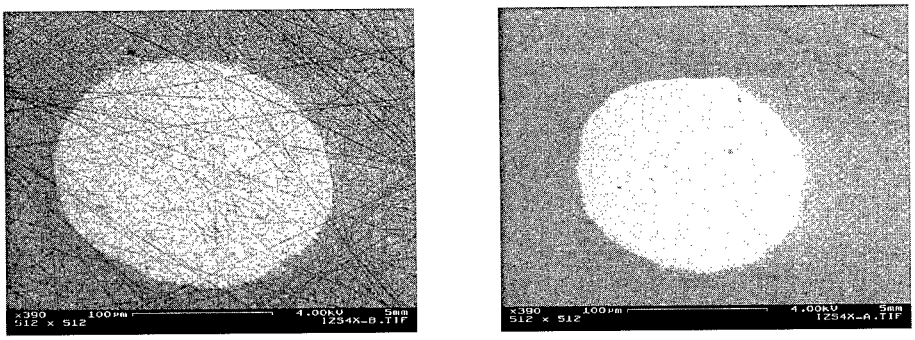


Fig. 3: SEM micrograph of the surface of a homoepitaxial GaN *pn*-junction LED with evaporated Ni/Au metal contacts, without (3a) and with (3b) CAIBE treatment prior to growth (different areas of the same sample).

Binary and ternary layer properties

Homoepitaxial GaN layers with outstanding properties have been achieved using above described CAIBE technique (Fig. 4). PL at 4.2 K reveals free excitons A, B, C as well as excited states of those excitons, where the identification is verified by reflectance measurements included in the figure. The linewidth of the bound excitons (3.464 – 3.474 eV) is as low as 0.1 meV.

The structural quality of the homoepitaxial GaN layers is extremely high as indicated by the narrow linewidth of approx. 20 arcsec ((0002) reflex), revealing the low dislocation density and the negligible mosaicity of the GaN layers grown on single crystal GaN substrates. A minor lattice mismatch of approx. $\Delta a/a \approx 10^{-4}$ between layer and substrate is due to the high carrier concentration of the substrates [8]. The outstanding xray data confirm that homoepitaxial growth conserves or even improves the excellent structural quality and low dislocation density of the GaN substrates, as expected

Ternary III-N compounds have been investigated as building blocks for double-heterostructure- (DH) and MQW-LEDs. The PL of 50 nm thick InGaN layers is shown in Fig 5. For comparison the PL of a heteroepitaxially layer grown under identical conditions (but employing a nucleation layer) is included. The observed shift in the emission wavelength can be understood by a different surface temperature between the highly heat conductive and partially

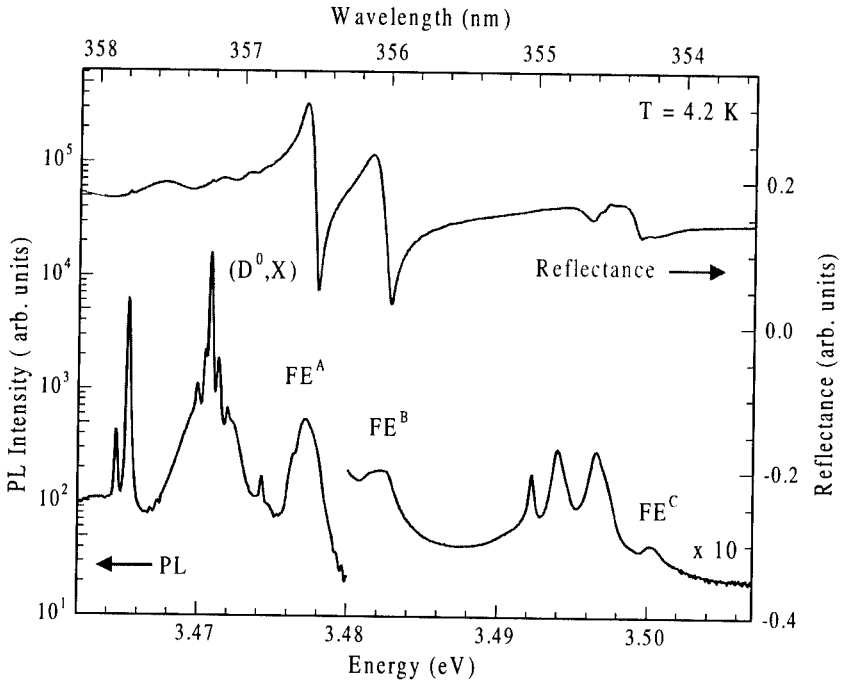


Fig. 4: High resolution photoluminescence (log. scale) and reflectance (lin. scale) of a 2 µm epitaxial GaN layer grown on CAIBE treated (0001)-oriented GaN substrates. Measurements by K. Kornitzer, K. Thonke, and R. Sauer (Univ. Ulm, Dept. of Semiconductor Physics).

absorbing GaN substrate and the sapphire. This causes a higher surface temperature for the GaN substrates at a nominally identical susceptor temperature, leading to a reduced In incorporation and the observed slightly lower emission wavelength. Fig 6. reveals a analogously comparison for InGaN/GaN (3nm/3nm) multiple quantum well structures.

Light emitting diodes

Initial LED structures have been homotype *pn*-junction LEDs. Only the regions of the device which underwent a CAIBE treatment yield functional devices, as becomes obvious from Fig. 3. The EL of those devices is depicted in Fig. 7 for various current densities. The LEDs show an intense, single peak emission at about 420 nm wavelength with a linewidth of 60 nm for low currents. UV emission is not observed even under the highest current densities. It is remarkable that the emission wavelength is constant at approx. 425 nm up to current densities of 3000 kA/cm^2. As was initially pointed out by S.Nakamura et al. for GaN *pn*-junction LEDs this is a clear indicative of the high quality of the *p*-type material obtainable by homoepitaxial growth [13]. With increasing free hole concentration, the PL transition at 425 nm is found to increase in intensity [14],[15]. Only a very high density of those recombination centers can guarantee an emission at 425 nm in EL even under high current densities. Once the injected carriers outnumber these recombination centers the surplus carriers recombine under emission of UV light at about 380 nm [16]. The EL obtained from heteroepitaxial LEDs grown on sapphire under identical conditions is also included for comparison (dashed line).

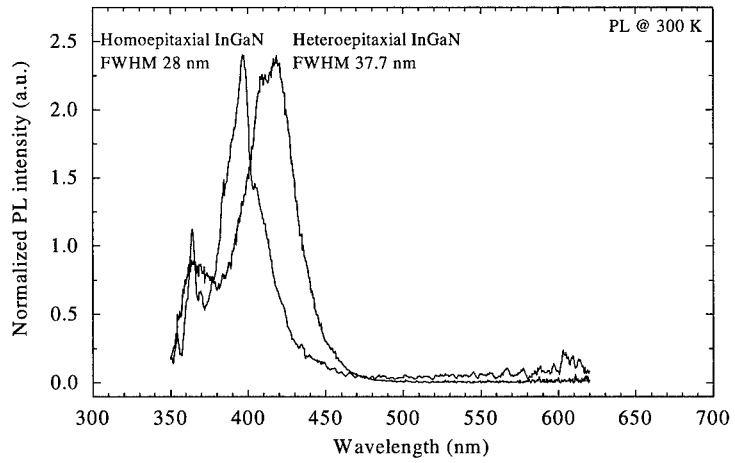


Fig. 5: Room temperature photoluminescence of approx. 50 nm InGaN layers grown on GaN- and sapphire-substrates, respectively.

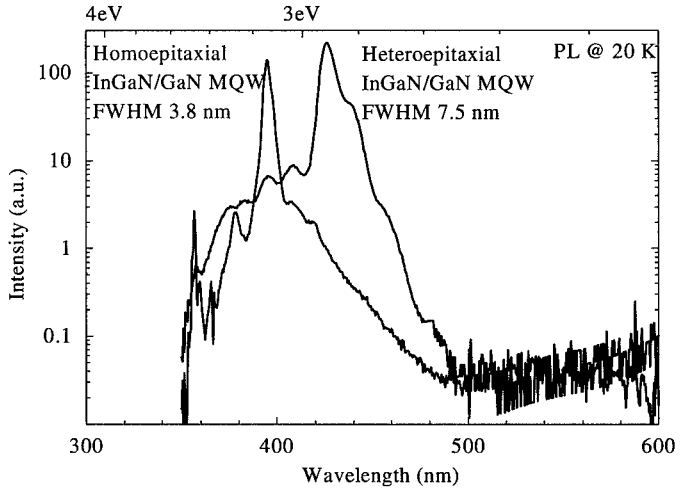


Fig. 6: Photoluminescence of InGaN/GaN (3nm/3nm) multiple quantum well structures grown on GaN- and sapphire-substrates, respectively (20 K).

The heteroepitaxial devices reveal a clear shift towards shorter wavelengths which is attributed to an inferior quality of the *p*-material at the *pn*-junction. Furthermore, the homoepitaxial LED is approx. twice as bright as their counterpart on sapphire.

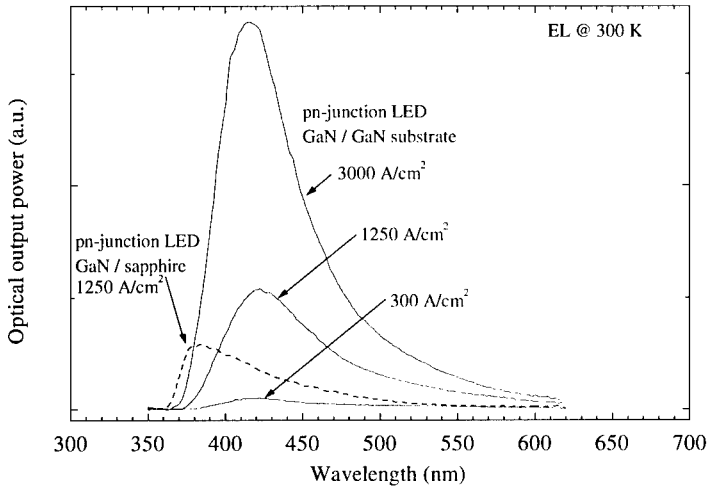


Fig. 7: Electroluminescence (EL) of a GaN homojunction *pn*-LED grown on GaN substrate. Emission spectra at various current densities. At a given current density, the homoepitaxial devices are twice as bright as comparable LEDs grown on sapphire (dashed line).

In addition to above homojunction LEDs, first InGaN/GaN DH-LEDs have been fabricated using single bulk crystal substrates. The EL of those devices is depicted in Fig. 8. Even at low current densities of 6 A/cm^2 decent EL is observed revealing a significant lower density of non-radiative recombination centers than in their on-sapphire-grown counterparts. Time resolved EL is measured to reveal the recombination mechanisms (Fig. 9) [17]. A single exponential decay with a time constant as low as 1 ns clearly identifies band/band recombination to be the dominant emission mechanism, since defect- as well as DAP-related electroluminescence transitions, as localized states, reveal a two order of magnitudes longer decay time (about 100 ns) [18].

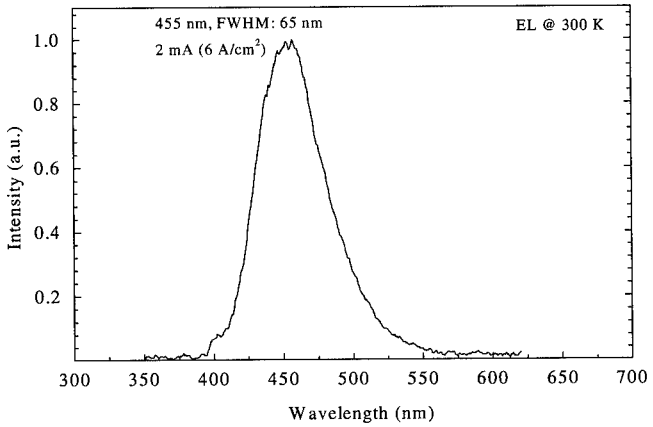


Fig. 8: Electroluminescence (EL) of a InGaN/GaN DH-LED grown on GaN substrate. Excellent EL is achieved at low current densities, revealing a low density of non-radiative defects.

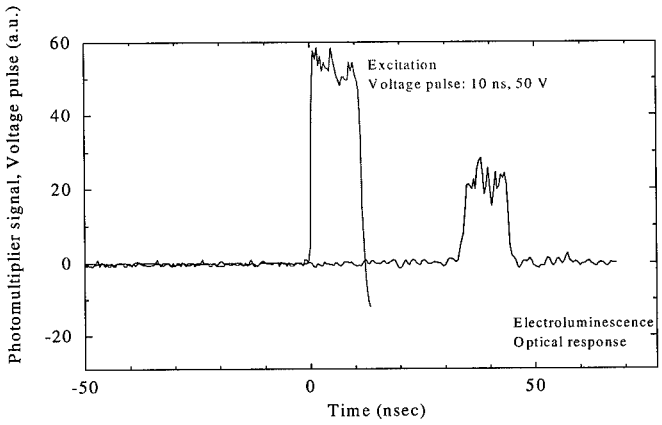


Fig. 9: Time resolved electroluminescence (EL) of a InGaN/GaN DH-LED grown on GaN substrate. Depicted is the EL after short-pulse-excitation at 50 V for 10 ns (pulse being also depicted). Exponential decay time is as short as 1 ns indicating band/band recombination. The pulse-signal delay of 35 ns is caused by the experimental setup.

The current through the LED as depicted in Fig. 10 is obviously limited by the series resistance (i.e. contact and sheet resistances) of the devices, which can be deduced to about 1 kΩ from the currents at high voltages (U_D larger than a few $(nk_BT)/q$). The voltage drop at the series resistance is most likely caused by the imperfect housing of the LEDs, since the devices have

just been glued to a metal base using silver glue. The current then is then passed through the 200 – 300 μm thick substrate of the vertical device. Further improvements are expected using a more elaborated contact and housing technology.

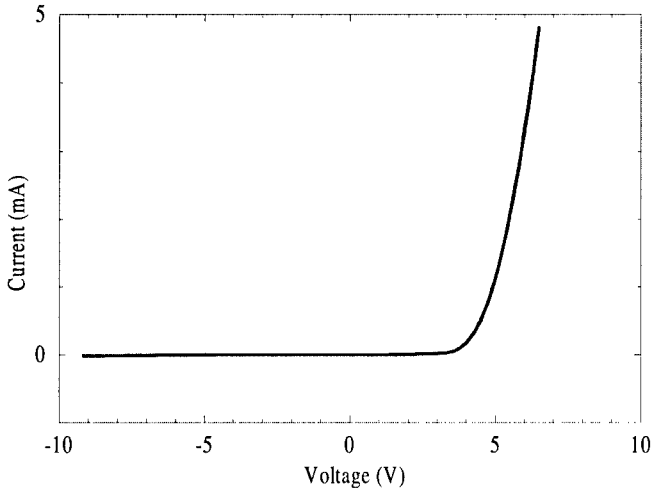


Fig. 10: Current/voltage characteristics of a GaN InGaN/GaN DH-LED. The curve reveals a good breakdown behavior and turn-on-voltage but still a rather high series resistance. The later is probably originated by contributions from the silver glue (*n*-contact metal) and the 200 - 300 μm thick *n*-layer (i.e. mostly the substrate).

Summary

After introduction of a CAIBE dry-etching step GaN layers with outstanding optical qualities and excellent morphologies have been achieved on bulk GaN single crystal substrates. Thick InGaN layers as well as InGaN/GaN MQWs are clearly superior to their counterparts grown on sapphire. Homoepitaxial GaN LEDs reveal single-peak blue emission at 420 nm, with a linewidth of 60 nm. The excellent quality of the homoepitaxial LEDs grown on GaN substrates is revealed by a comparison with heteroepitaxially LEDs on sapphire. The homoepitaxial devices are twice as bright as the LEDs grown on sapphire. This and the wavelength shift of the LED on sapphire are indications for a higher hole concentration of the homoepitaxial device. First InGaN/GaN DH-LEDs have been fabricated and reveal excellent electroluminescence at 455 nm even at low current densities, indicating a low density of non-radiative defects. Time resolved EL measurements performed on those devices clearly evince band/band recombination to be the dominant mechanism in those devices.

Acknowledgments

Several researchers severely contributed to this work, including M. Schauler, F. Eberhard, S. Menzel, and P. Unger from Dept. of Optoelectronics, F. Bertram, T. Riemann, and J. Christen from Univ. Magdeburg (CL measurements), K. Kornitzer, K. Thonke, and R. Sauer from Univ. Ulm, Dept. of Semiconductor Physics (high resolution PL measurements and reflectance). The

authors gratefully acknowledge their valuable contributions as well as financial support by the German Federal Ministry of Education, Science, Research and Technology (BMBF) under contract no. 01 BM 419 / 9 and the Volkswagen Foundation.

References

[1] M. Mayer, A. Pelzmann, M. Kamp, K.J. Ebeling, H. Teisseyre, G. Nowak, M. Leszczynski, I. Grzegory, M. Bockowski, S. Krukowski, S. Porowski, G. Karczewski, Jpn. J. Appl. Phys. Part 2, Vol. 36, L1634-L1636 (1997).

[2] J. Baranowski, S. Porowski, Proc. 23rd Int. Conf. on the Physics of Semiconductors, Berlin 1996, edited by M. Scheffler and R. Zimmermann (World Scientific, Singapore 1996) vol. 3, (1996).

[3] S. Nakamura, M. Senoh, S. Nagahama, N. Iwasa, T. Yamada, T. Matsushita, H. Kiyoku, Y. Sugimoto, T. Kozaki, H. Umemto, M. Sano, K. Chocho, Appl. Phys. Lett. 73, 832 (1998).

[4] J. Karpinski, J. Jun and S. Porowski: J. Crystal Growth 66, 1-10 (1984).

[5] T. Detchprohm, H. Amano, K. Hiramatsu and I. Akasaki: J. Crystal Growth 128, 384-390 (1993).

[6] S. Sakai, S. Kurai, K. Nishino, K. Wada, H. Sato and Y. Naoi: Mat. Res. Soc. Symp. Proc. 449, 15-22 (1997).

[7] E. Hellman, *MRS Internet J. Nitride Semicond. Res.* ***3***, 11(1998).

[8] M. Leszczynski, H. Teisseyre, T. Suski, I. Grzegory, M. Bockowski, J. Jun, S. Porowski, K. Pakula, J.M. Baranowski, C.T. Foxon, T.S. Cheng, Appl. Phys. Lett. 69 (1), 73-75 (1996).

[9] T. Zywietz, J. Neugebauer, M. Scheffler,J. Northrup, Chris G. Van de Walle, *MRS Internet J. Nitride Semicond. Res.* ***3***, 26(1998).

[10] M. Leszczynski, B.K. Meyer, unpublished.

[11] M. Schauler, F. Eberhard, C. Kirchner, V. Schwegler, A. Pelzmann, M. Kamp K.J. Ebeling, F. Bertram, T. Riemann, J. Christen, M. Leszczynski, I. Grzegory, T. Suski, S. Porowski, accepted for Appl. Phys. Lett.

[12] Yu. Makarov, Yu. Karpov, private communication.

[13] S. Nakamura, T. Mukai and M. Senoh: Jpn. J. Appl. Phys. 30 No. 12A, L1998-L2001 (1991).

[14] U. Kaufmann, M. Kunzer, M. Maier, H. Obloh, A. Ramakrishnan, B. Santic, P. Schlotter, Appl. Phys. Lett. 72 (11), 1326-1328 (1998).

[15] S. Haffouz, B. Beaumont, M. Leroux, M. Laugt, P. Lorenzini, P. Gibart, L.G. Hubert-Pfalzgraf, MRS Internet J. Nitride Semicond. Res. 2, 37(1997).

[16] F. Calle, E. Monroy, F.J. Sánchez, E. Muñoz, B. Beaumont, S. Haffouz, M. Leroux, P. Gibart, MRS Internet J. Nitride Semicond. Res. 3, 24(1998).

[17] V. Schwegler, C. Kirchner, M. Kamp K.J. Ebeling, M. Leszczynski, I. Grzegory, S. Porowski, submitted to Appl. Phys. Lett.

[18] F.S. Choa, J.Y. Fan, P.L. Liu, J. Sipior, G. Rao, G.M. Carter, Y.J. Chen, Appl. Phys. Lett. 69 (24), 3668-3670 (1996).

DOPING OF AlGaN ALLOYS

Chris G. Van de Walle,[*] C. Stampfl,[**] J. Neugebauer,[**] M. D. McCluskey,[*,a] N. M. Johnson[*]

[*]Xerox Palo Alto Research Center, 3333 Coyote Hill Road, Palo Alto, CA 94304
[**]Fritz-Haber-Institut der Max-Planck-Gesellschaft, Faradayweg 4-6, D-14 195 Berlin-Dahlem, Germany

Cite this article as: MRS Internet J. Nitride Semicond. Res. 4S1, G10.4 (1999)

ABSTRACT

Nitride-based device structures for electronic and optoelectronic applications usually incorporate layers of $Al_xGa_{1-x}N$, and *n*- and *p*-type doping of these alloys is typically required. Experimental results indicate that doping efficiencies in $Al_xGa_{1-x}N$ are lower than in GaN. We address the cause of these doping difficulties, based on results from first-principles density-functional-pseudopotential calculations. For *n*-type doping we will discuss doping with oxygen, the most common unintentional donor, and with silicon. For oxygen, a *DX* transition occurs which converts the shallow donor into a negatively charged deep level. We present experimental evidence that oxygen is a *DX* center in $Al_xGa_{1-x}N$ for $x>\sim0.3$. For *p*-type doping, we find that compensation by nitrogen vacancies becomes increasingly important as the Al content is increased. We also find that the ionization energy of the Mg acceptor increases with alloy composition *x*. To address the limitations on *p*-type doping we have performed a comprehensive investigation of alternative acceptor impurities; none of the candidates exhibits characteristics that surpass those of Mg in all respects.

INTRODUCTION

Significant theoretical and experimental attention has been devoted to doping of GaN: which dopants to use, how to increase doping efficiency, what sources of compensation may occur, etc. For practical electronic and optoelectronic devices, however, it is essential to be able to control not just doping of GaN, but also of AlGaN alloys. For instance, AlGaN alloys form the thick cladding layers in nitride-based injection lasers, and the resistivity of these layers plays a major role in the device characteristics. Most research to date has indicated that AlGaN alloys are more difficult to dope than pure GaN, and the ability to dope AlGaN alloys significantly decreases with increasing Al content.

Several experimental studies have indicated a decrease in *n*-type conductivity of $Al_xGa_{1-x}N$ with increasing *x*. Koide *et al.*[1] reported a decline in free electron concentration for $x>0.2$. For unintentionally *n*-type doped AlGaN, Lee *et al.*[2] reported a rapid decrease in conductivity for $x>0.4$. McCluskey *et al.*[3] found a significant decrease in conductivity for $x>0.3$ in unintentionally doped AlGaN samples; they were able to attribute the unintentional conductivity to oxygen. McCluskey *et al.* also found that intentional doping with silicon produced highly conductive material for $x=0.44$. Bremser *et al.*[4,5] also achieved intentional *n*-type doping with silicon up to $x=0.42$, but for $x>0.42$ addition of Si resulted in highly resistive films.

[a] Present address: Department of Physics, Washington State University, P.O. Box 642814, Pullman, WA 99164-2814

Mat. Res. Soc. Symp. Proc. Vol. 537 © 1999 Materials Research Society

The decrease in doping efficiency with increasing Al content is even more dramatic for *p*-type AlGaN. While *p*-type doping of pure GaN was originally a problem, those difficulties have largely been overcome due to the use of the Mg acceptor and the understanding of the role of hydrogen.[6,7] For $Al_xGa_{1-x}N$, however, Bremser *et al.*[4,5] reported a failure to achieve *p*-type conductivity with Mg doping for $x>0.13$. Other studies have also found a decrease in achievable hole concentration when the Al content of the AlGaN alloy is increased.[8,9,10]

Useful information about the doping characteristics of nitride semiconductors can be obtained by performing first-principles calculations. We previously performed comprehensive studies of doping in *n*-type[11,12] and *p*-type[6,7,13] GaN. In order to address doping of AlGaN, we have first performed comprehensive studies of native defects and dopant and impurities in AlN.[14] Many useful results for AlGaN alloys can be obtained by "interpolating" between the binary compounds.

First-principles calculations for native defects in AlN[14,15,16] have yielded conclusions similar to those for GaN: self-interstitials and antisites are high in energy—with the exception of the Al interstitial in *cubic* AlN, which is a triple donor and could act as a compensating center in *p*-type material. The nitrogen vacancy is a high-energy defect in *n*-type AlN, but has a relatively low energy in *p*-type AlN. The behavior of V_{Al} is similar to V_{Ga} in GaN, but because of the larger band gap of AlN the formation energy of V_{Al} becomes significantly lower than V_{Ga} for Fermi-level positions high in the gap. The consequences of the behavior of these defects for doping will be explored in subsequent sections.

Our results identify two mechanisms that can reduce the *n*-type doping efficiency: (i) in the case of doping with oxygen (the most common unintentional donor), a *DX* transition occurs which converts the shallow donor into a negatively charged deep level[3,17]; and (ii) cation vacancies (V_{Ga} or V_{Al}) act as triple acceptors and increase in concentration with alloy composition x. For *p*-type doping, we find that (i) nitrogen vacancies act as compensating centers and are more easily formed in AlN than in GaN; and (ii) the ionization energy of the Mg acceptor increases with alloy composition x.

The large ionization energy of Mg (around 200 meV) poses severe limitations on the ability to dope GaN, and this problem increases with increasing Al content in AlGaN alloys. It would be highly desirable to identify other *p*-type dopants that do not suffer from the limitations imposed by Mg. We have performed extensive investigations for a wide range of candidate acceptor species, addressing criteria such as solubility, ionization energy, and potential compensation due to interstitial configurations of the acceptor impurity; the results of this investigation will be discussed in the section on *p*-type doping.

METHODOLOGY

Our first-principles calculations are based on density-functional theory within the local density approximation (LDA) and using the pseudopotential-plane-wave method.[18,19] We employ a supercell approach and use a tight-binding initialization scheme for the electronic wave functions.[20] Supercells containing 32 atoms were used to study the zinc-blende phase, and up to 96 atoms for the wurtzite phase. An energy cutoff of 40 Ry was used for AlN, with two or three special **k** points in the irreducible part of the Brillouin zone. The pseudopotentials were created using the scheme of Troullier and Martins.[21]

The formation energy of a defect in charge state q is expressed as

$$E^f(q) = E^{\text{tot}}_{defect}(q) - \sum_X n_X \mu_X + qE_F \qquad (1)$$

where $E^{\text{tot}}_{defect}(q)$ is the total energy of the defect and n_X and μ_X are the number and chemical potential of atoms of species X, respectively. E_F is the Fermi energy which is set to zero at the va-

lence-band maximum. In evaluating the chemical potentials, which depend on the experimental growth conditions, we assume thermal equilibrium: $\mu_{Ga} + \mu_N = \mu_{GaN}$ for GaN, and $\mu_{Al} + \mu_N = \mu_{AlN}$ for AlN. For convenience, we will display results for metal-rich conditions: μ_{Ga} is put equal to the energy of bulk Ga, or μ_{Al} is put equal to the energy of bulk Al. N-rich conditions would correspond to the chemical potential μ_N being determined by the energy of an N_2 molecule. The chemical potentials for the impurity species (O, Si, and Mg) are fixed by invoking equilibrium with Ga_2O_3, Si_3N_4, and Mg_3N_2. For Li, Na, K, Be, Zn, and Ca, the chemical potentials of Li_3N, Na, K, Be_3N_2, Zn_3N_2, and Ca_3N_2 were used. Formation energies for general values of the chemical potential can always be obtained by referring back to Eq. (1).

RESULTS FOR *N*-TYPE DOPING

Our first-principles studies[11] as well as those of others[15,22] have shown that the formation energy of the nitrogen vacancy in *n*-type GaN is too large for this defect to occur in any appreciable concentrations. We obtain similar results for the nitrogen vacancy in AlN. Figure 1 displays formation energies for native defects and donor impurities relevant for *n*-type AlN. For each defect we only show the line segment corresponding to the charge state that gives rise to the lowest energy at a particular value of E_F. The change in slope of the lines therefore represents a change in the charge state of the defect [see Eq. (1)]. Figure 1 applies to the zinc-blende phase and shows E_F spanning the theoretical (*GW*) band gap for zinc-blende AlN,[23] which is larger than the LDA band gap in our calculations (3.15 eV). Results for the wurtzite phase are very similar.

Figure 1 clearly shows that the formation energy of the nitrogen vacancy is significantly higher than that of oxygen and silicon, which behave as shallow donors. This indicates that the nitrogen vacancy is not the dominant center responsible for the *n*-type conductivity of $Al_xGa_{1-x}N$.

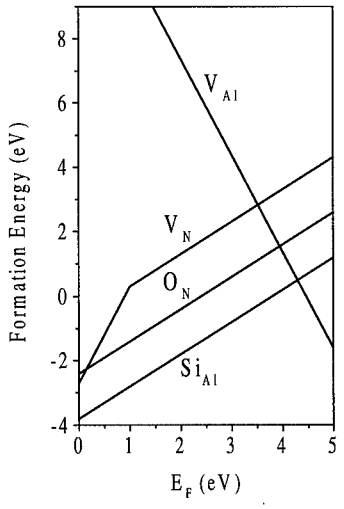


Figure 1: Formation energies as a function of Fermi level for defects and impurities relevant for *n*-type AlN, obtained from first-principles calculations for the zinc-blende phase, and assuming Al-rich conditions.

Unintentional doping – oxygen

Nitrogen vacancies were traditionally thought to be responsible for the large background *n*-type conductivity in GaN. In 1994 we proposed that not the nitrogen vacancy but oxygen and silicon impurities are responsible for unintentional *n*-type conductivity in GaN.[12] Oxygen had been proposed as a potential source of *n*-type conductivity in GaN as early as 1983.[24] Still, the prevailing conventional wisdom, attributing the *n*-type behavior to nitrogen vacancies, proved hard to overcome. Recent experiments have confirmed that unintentionally doped *n*-type GaN samples contain silicon or oxygen concentrations high enough to explain the electron concentrations. Götz *et al.*[25,26] reported electrical characterization of intentionally Si-doped as well as unintentionally doped samples, and concluded that the *n*-type conductivity in the latter was due to silicon. They also found evidence of another shallow donor with a slightly higher activation energy, which was attributed to oxygen. Secondary-ion mass spectroscopy (SIMS) on hydride vapor phase epitaxy (HVPE) material also shows levels of oxygen or silicon in agreement with the electron concentration determined by electrical measurements.[26]

Contaminating impurities may have many sources: water is the main contaminant of NH_3, the most frequently used source in metal-organic chemical deposition (MOCVD). The fact that even high-purity (99.999%) NH_3 can be a significant source of oxygen contamination was documented in the case of InGaN growth by Piner *et al.*[27] Fortunately, purification can remove most of the water. In MBE, oxygen may enter as a contaminant in the nitrogen source gas; or it may be due to the quartz lining of certain components, for instance plasma sources. We note that Götz *et al.*[26,28] and Look and Molnar[29] have pointed out potential pitfalls in extracting information about dopant concentrations and ionization energies from Hall-effect measurements. Experiments on unintentionally doped HVPE-grown layers indicated the presence of a thin, highly conductive layer near the interface with the sapphire substrate. This layer acts as a parasitic, parallel conduction path. Götz *et al.*[26] suggested oxygen contamination may be responsible for the high conductivity of this layer.

The activation energy of oxygen has been determined from variable-temperature Hall effect measurements[30] to be 29 meV for a donor concentration $N_D=1\times10^{18}$ cm^{-3}. This activation energy decreases with increasing donor concentration. Götz *et al.* also reported that the total oxygen concentration (measured by SIMS) was significantly higher than the donor concentration. We suggest that such additional oxygen may occur in the form of Ga_2O_3 precipitates.

Hydrostatic pressure offers a very useful tool to explore the cause and behavior of *n*-type conductivity in GaN.[31,32] Freeze-out of carriers was reported under application of hydrostatic pressure greater than 20 GPa. These findings can be explained by the behavior of oxygen, which undergoes a transition from a shallow to a deep *DX* center in wurtzite GaN under pressure.[17,32,33] The stable shallow center at the *equilibrium* volume of GaN corresponds to oxygen at the substitutional nitrogen site. The *DX* geometry corresponds to an oxygen atom moving off the substitutional position along the [0001] direction. This geometry becomes stable under hydrostatic pressure. The associated induced electronic state is a highly localized deep level. In the *DX* configuration the defect is negatively charged, i.e., it is a deep acceptor, and will therefore trap free carriers. The stability of the localized deep *DX* state is attributed to interactions between the negatively charged oxygen impurity and a third-nearest-neighbor cation along the *c* axis: we have proposed that a Coulombic attraction is the driving force for the large lattice relaxation that stabilizes the *DX* geometry.[17] In the zinc-blende structure, these third-nearest-neighbor atoms occur in different positions in the lattice; the formation of the *DX* configuration is correspondingly suppressed in the zinc-blende phase.

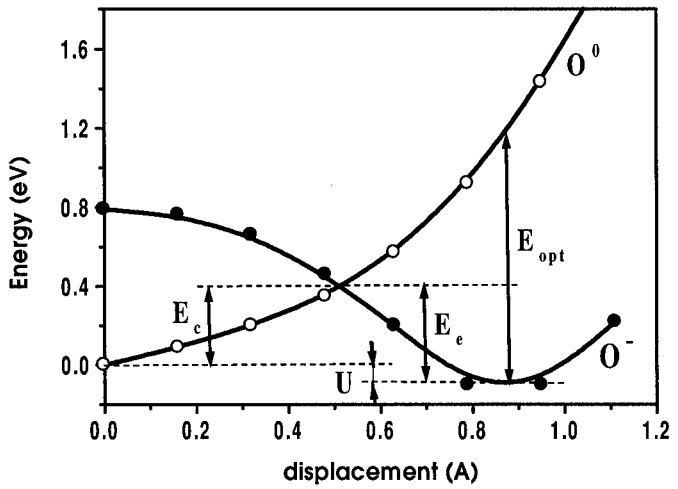


Figure 2: Configuration coordinate diagram for oxygen displacements along [0001] in AlGaN, based on first-principles calculations for GaN:O and AlN:O. E_{opt} is the optical ionization energy; E_c and E_e are the capture and emission barriers.

Alloying with AlN increases the band gap of GaN in a similar way to hydrostatic pressure. *DX* center formation is therefore also expected to occur in $Al_xGa_{1-x}N$. Indeed, our computational studies showed that the *DX* configuration is the stable state for the oxygen impurity in wurtzite (but not zinc-blende) AlN.[17] Figure 2 shows a configuration coordinate diagram for oxygen displacements in AlGaN. The data points were obtained from first-principles calculations for oxygen in GaN and in AlN, based on an interpolation for the case where the *DX* configuration is 0.1 eV lower in energy than the substitutional donor.

The configuration coordinate diagram is characteristic of a metastable center: for zero displacement, the impurity is located on the substitutional site and behaves as a shallow donor. However, a second minimum occurs in the diagram, corresponding to a large displacement of the impurity (close to 1 Å) and a different (negative) charge state. For $x<0.3$, this second minimum is higher in energy than the on-site, shallow-donor configuration. However, for $x>0.3$, the second minimum becomes lower in energy, as illustrated in Fig. 2. The *DX* state is then the lowest-energy state of the system; however, electrons can be emitted out of the *DX* state, and since there is a barrier (E_c) to capturing them again, one expects to observe persistent photoconductivity, at least at low temperatures. The mechanism to release electrons out of the *DX* state can be either thermal (with an activation energy E_e) or optical, with a threshold E_{opt}.

Experimental confirmation for this model has come from Hall effect and persistent photoconductivity measurements on unintentionally doped AlGaN samples with Al content up to $x=0.39$.[3] The samples were MOCVD grown, with a thickness of 1 μm, and Al concentrations were determined by x-ray diffraction, assuming relaxed layers and Vegard's law. Concentrations of Si and oxygen impurities were measured by SIMS. Unintentionally doped AlGaN showed

oxygen concentrations of approximately 10^{19} cm^{-3} and silicon concentrations of 10^{18} cm^{-3}, indicating that the conductivity of the samples was due to oxygen. Variable-temperature Hall effect measurements showed a freezeout of the free electrons with decreasing temperature, characterized by an activation energy that increased with Al concentration in the alloy. The activation energy E_{DX} was determined by exponential fits to the Hall effect data. The decrease in the free electron concentration can be explained by an increase in E_{DX}. This increase in the donor binding energy is consistent with a deep *DX* level which becomes stable (has a lower energy than the conduction-band minimum) for $x>0.27$, in good agreement with the theoretical prediction. This result is also consistent with the experiments on GaN:O under pressure: the band gap of GaN at 20 GPa is approximately 0.8 eV higher than at ambient pressure, and a similar increase in band gap is found when alloying with AlN with x between 0.3 and 0.4.

Persistent photoconductivity is a direct manifestation of metastability, characteristic of centers with a large difference in lattice relaxation between two metastable states. Persistent photoconductivity was observed in $Al_xGa_{1-x}N$ epilayers with $x\geq0.39$ at temperatures below 150 K. The persistent photoconductivity decreases with time, because oxygen centers return from the shallow to the deep state. In doing so, they need to surmount the barrier (Fig. 2). The temperature range in which this transition was observed was between 120 and 150 K; this is consistent with the barrier E_c of about 0.4 eV emerging from our calculations.

To measure the optical cross section of absorption for the *DX* centers, the photocurrent was measured for photon energies from 1.0 to 1.5 eV. An optical threshold of about 1.3 eV was found, again in good agreement with the theoretical prediction shown in Fig. 2.

While the observation of persistent photoconductivity is one of the distinguishing features of metastable *DX* centers, it should be pointed out that observations of persistent photoconductivity are not *necessarily* indicative of the presence of *DX*-like centers. Various groups have reported persistent photoconductivity in *n*-type GaN.[34,35] Those observations show photoconductivity at room temperature, while our observations for *DX* centers only show photoconductivity for temperature below 150 K. In addition, the optical absorption threshold was found to be greater than 2 eV, again inconsistent with the observations for *DX* centers. The behavior observed in Refs. 34 and 35 may be due to other types of point defects, or to the presence of defective regions near extended defects.

For oxygen, we must conclude that it cannot be used as a shallow donor in $Al_xGa_{1-x}N$ with $x>0.3$. Even if another donor impurity is used (such as silicon, see below) that does not exhibit *DX* behavior, the presence of oxygen in the layer could be detrimental to *n*-type conductivity: indeed, once oxygen undergoes the *DX* transition it behaves as an acceptor, and therefore counteracts the electrical activity of other donors. Control of oxygen incorporation in $Al_xGa_{1-x}N$ with high Al content is therefore essential.

Doping with Silicon

Silicon is almost universally used for intentional *n*-type doping of GaN, AlGaN, and InGaN. Silicon doping is typically achieved by flowing SiH_4 during MOCVD growth, or using a solid Si source in MBE. The formation energies shown in Fig. 1 show that the formation energy of silicon is quite low in AlN, and therefore it is readily incorporated in AlN as well as in GaN. The activation energy of silicon in GaN derived from variable-temperature Hall effect measurements[25,30] is 17 meV for $N_D=3\times10^{17}$ cm^{-3}. As pointed out in the case of oxygen, the ionization energy is sensitive to the concentration of the dopant.

Our calculations for silicon in GaN under pressure, and in AlN, indicate that silicon donors do not exhibit the *DX* transition.[17] The difference with oxygen can be understood on the basis of the different location in the lattice. While oxygen substitutes on a *nitrogen* site, silicon sits on a

substitutional *cation* site. In that position, the third nearest neighbor is a *nitrogen* atom. In the *DX* state, the silicon would become negatively charged, and would thus experience a Coulomb repulsion from the third-nearest-neighbor anion; this repulsion suppresses the *DX* formation. Silicon was indeed experimentally found to remain a shallow donor in GaN under pressure up to 25 GPa.[32] For $Al_xGa_{1-x}N$ alloys with x=0.44 we found that intentional doping with silicon resulted in a free-electron concentration close to the silicon concentration (8×10^{18} cm^{-3}, as measured by SIMS). It was also found, however, that even in the intentionally Si-doped sample a background of oxygen was present (at a level of 3×10^{18} cm^{-3}). Those oxygen atoms can still undergo the *DX* transition, effectively becoming compensating centers. It is important, therefore, to suppress oxygen incorporation when growing Si-doped $Al_xGa_{1-x}N$ with high x.

The negative impact of unintentional oxygen incorporation on the conductivity of Si-doped AlGaN is a likely explanation for the experimental observations of Polyakov *et al.*[36,37] They found that the free electron concentration decreases with increasing Al content of the alloy. The increase in Al content also led to an increase in the density of defects with energy levels deeper than silicon, leading to increased difficulty in *n*-type doping of the alloy. Polyakov *et al.* also reported persistent photoconductivity in their samples. The observations of Polyakov *et al.* can be consistently explained by assuming that oxygen is unintentionally incorporated, a possibility that was recognized by Polyakov *et al.* The decrease in electron concentration for $x \geq 0.3$ is then due to the formation of oxygen *DX* centers; in the negatively charged *DX* state, oxygen effectively acts as an acceptor, compensating the *n*-type conductivity introduced by the Si donors. The characteristics of the persistent photoconductivity (capture and emission barrier, and optical ionization energy) are consistent with those obtained for oxygen *DX* centers[3] and in our first-principles calculations (see Fig. 2).

Unintentional incorporation of oxygen may also explain the decrease in *n*-type conductivity in Si-doped $Al_xGa_{1-x}N$ for x>0.42 observed by Bremser *et al.*[4,5] We should point out, however, that even in the absence of oxygen a compensation mechanism may occur, namely due to cation vacancies. In GaN, compensation of Se donors by Ga vacancies was observed by Yi and Wessels.[38] The calculated defect formation energy for the Al vacancy is shown in Fig. 1, for Al-rich conditions in AlN. For *n*-type conditions (E_F high in the gap), silicon donors will suffer from some degree of compensation by triply ionized Al vacancies. The behavior of V_{Al} is similar to V_{Ga} in GaN,[11] but because of the larger band gap of AlN the formation energy of V_{Al} in AlN becomes significantly lower than that of V_{Ga} in GaN for Fermi-level positions high in the gap. Cation vacancies thus become an increasingly important source of donor compensation as the Al content x is increased in Al_xGa_xN.

RESULTS FOR *P*-TYPE DOPING

Magnesium has emerged as the *p*-type dopant of choice for GaN. Still, the hole concentration that can be achieved is lower than desired, particularly for applications such as high *p*-type doping near metal contacts for improved Ohmic contact behavior. In addition, the hole concentration that can be achieved with Mg doping has been observed to decrease rapidly with increasing Al content x in $Al_xGa_{1-x}N$.[5,8,9,10] Magnesium exhibits no tendency to form deep levels (so called *AX* levels, analogous to *DX* for donors),[33] thus ruling out a shallow-deep transition as the source of the drop in hole concentration. We also found, for Mg in GaN, that incorporation of Mg on interstitial sites, or on nitrogen sites, is energetically unfavorable.[39] The main issue limiting the hole concentration achievable with Mg in GaN is the solubility.

Our calculations for the Mg acceptor in AlN indicate that its ionization energy (0.4 eV) is higher than in GaN (0.2 eV), as can be seen from Fig. 3 (the ionization energy corresponds to the Fermi level positions where the formation energies of Mg^0 and Mg^- are equal). This increase in

the ionization energy leads to a decrease in doping efficiency. Based on an analysis of temperature-dependent Hall data Tanaka *et al.* found the Mg activation energy to be 35 meV deeper in $Al_{0.08}Ga_{0.92}N$ than in GaN.[8] Assuming linearity, this would make the Mg acceptor in AlN 0.44 eV deeper than in GaN.

Compensation by native defects is another important mechanism that may contribute to the decline in hole concentrations. Fig. 3 shows that two defects with low formation energies may inhibit successful *p*-type doping of $Al_xGa_{1-x}N$, namely the nitrogen vacancy and the cation interstitial. The cation interstitial has a low formation energy in zinc-blende material, but is much higher in energy in wurtzite. The nitrogen vacancy has a strikingly lower formation energy in AlN than in GaN, and it may play an important role in *p*-type GaN and AlGaN. The formation energy of the nitrogen vacancy is too high for it to be incorporated in *n*-type GaN, but as can be seen from Fig. 3, this formation energy becomes significantly lower in *p*-type material. During MOCVD growth the formation of nitrogen vacancies is suppressed because hydrogen also behaves as a compensating donor, and has a lower formation energy.[7] Still, a certain concentration of nitrogen vacancies will be incorporated, and we propose that these vacancies are at least partially responsible for the decreased doping efficiency of Mg when the Al content is raised in $Al_xGa_{1-x}N$ alloys.

For certain values of the Fermi level, some formation energies in Figs. 1 and 3 become negative; one may wonder about the physical meaning of negative formation energies. Inspection of the plots, however, will make clear that physically meaningful positions of the Fermi level will always produce positive formation energies. Indeed, the Fermi energy is determined by the condition of charge neutrality; for Fermi-level positions far from the band edges, this requires having equal numbers of positively and negatively charged defects or impurities (if they are singly charged). The Fermi level will therefore be pinned near the point where the formation energies of the dominant donor and acceptor are equal. The plots then show that this value of the Fermi level corresponds to positive formation energies.

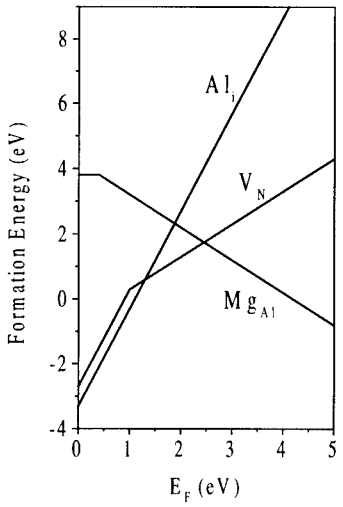


Figure 3: Formation energies as a function of Fermi level for defects and impurities relevant for *p*-type AlN, obtained from first-principles calculations for the zinc-blende phase, and assuming Al-rich conditions. We note that the formation energy of Al_i is significantly higher in *wurtzite* AlN.

The nitrogen vacancy (V_N) behaves as a donor which can donate one, two, or three electrons. Only the V_N^+ and V_N^{3+} charge states are found to be stable; the V_N^{2+} state is unstable, presenting a so-called negative-*U* effect. This behavior is similar to that calculated for nitrogen vacancies in GaN.[40] However, the +/3+ transition level occurs at a higher position in the band gap in the case of AlN (around 1 eV). Because the formation energy decreases much faster with decreasing Fermi level in the 3+ charge state, the nitrogen vacancy becomes much more favorable for low Fermi-level positions in AlN.

The +/3+ transition is characterized by a large lattice relaxation.[40] Defects with large lattice relaxations are often responsible for persistent photoconductivity (as we saw in the case of oxygen *DX* centers). The presence of nitrogen vacancies may therefore be responsible for the observed persistent photoconductivity effects in *p*-type GaN.[41,42,43] The nitrogen vacancy may also give rise to the blue lines (around 2.9 eV) commonly observed by photoluminescence in Mg-doped GaN.[33,43,44,45,46] The appearance and disappearance of photoluminescence (PL) lines during post-growth annealing of Mg-doped layers grown by MOCVD[47,48] may be related to the interactions of hydrogen with nitrogen vacancies. Complexes between hydrogen and nitrogen vacancies can form during growth[43]; the calculated binding energy of the V_NH^{2+} complex, expressed with respect to interstitial H in the positive charge state, is 1.56 eV. Dissociation of this complex, producing isolated nitrogen vacancies, may explain the behavior of PL lines during annealing for acceptor activation.[43]

Alternative Acceptors

Despite the successes achieved with Mg, *p*-type doping levels in GaN and AlGaN alloys are lower than desirable for low-resistance cladding layers and Ohmic contacts. Achieving higher hole concentrations with Mg as the dopant has proved difficult. It would therefore be desirable to identify acceptors that are superior to Mg.

The performance of an acceptor can be judged on the basis of three main criteria: (i) solubility; (ii) stability against compensation by other configurations of the acceptor dopant (e.g., interstitials); and (iii) depth of the acceptor level (ionization energy). Each of these aspects can be addressed on the basis of results obtained from first-principles calculations. The *solubility* of a substitutional acceptor corresponds to the equilibrium concentration of the impurity in the lattice, which is determined by the formation energy. The formation energy of the impurity in configurations other than the substitutional site determines the likelihood of incorporation on those sites. Interstitial configurations tend to be favorable for elements with a small atomic radius, such as Li or Be.

Previous theoretical investigations[13,49,50] have not produced any candidate with characteristics exceeding those of Mg in all respects. Our own results show that the column-II acceptors perform noticeably better than those from column I; the latter suffer from poor solubility. Lithium also suffers from incorporation on interstitial sites, where it acts as a donor. Among column-II acceptors, Ca and heavier elements also have high formation energies and hence poor solubility. The calculated ionization energies for Zn and Ca are larger than for Mg. The smallest column-II element, Be, has a solubility comparable to Mg. Its calculated ionization energy is slightly smaller than Mg, but the difference is within the error bar of the computation and hence not conclusive.[50] Because it is a small atom, Be may suffer from incorporation on interstitial sites, where it acts as a donor, thus causing self-compensation.

Experimental work on acceptors other than Mg has been very limited. Bergman *et al.* used photoluminescence (PL) to derive an ionization energy of 0.34 eV for Zn.[51] Doping with Zn has not resulted in *p*-type conductivity, presumably due to the large ionization energy of the Zn acceptor. Experimental results about Be are inconclusive: Brandt *et al.* have reported high levels

of *p*-type doping using Be in MBE, provided oxygen is present as a co-dopant.[52,53] This result is difficult to understand based on equilibrium thermodynamics, as pointed out by Bernardini *et al.*[50] Other work has indicated Be indeed acts as an acceptor; results about the ionization energy are based on luminescence, with Salvador *et al.* finding a relatively large ionization energy (250 meV),[54] Ronning *et al.* finding 150 meV,[55] and Sánchez *et al.* deriving a much smaller value (90 meV).[56]

To our knowledge, experimental studies of other acceptor impurities have only been performed using ion implantation (see, e.g., Ref. 57). Unfortunately, implantation damage is very difficult to remove by annealing in GaN, due to the hardness of the lattice and the low diffusivity. The presence of implantation defects then makes it difficult to reliably assess the properties of the implanted acceptors, and in our opinion no conclusive results have been obtained.

CONCLUSIONS

We have reported a comprehensive investigation of impurities and defects in AlN and GaN, from which we have drawn conclusions about the limitations on doping in $Al_xGa_{1-x}N$ alloys. Our first principles calculations indicate that the *DX* behavior of oxygen and compensation by the cation vacancy are responsible for the decrease in *n*-type conductivity in $Al_xGa_{1-x}N$ with increasing x. With respect to *p*-type doping of $Al_xGa_{1-x}N$, our results show that the nitrogen vacancy becomes an increasingly dominant compensating center as x increases. We also observe an increase in the Mg ionization energy with increasing Al content. Investigations of a wide range of potential alternative acceptors show that none emerge as being superior to Mg; Be may be a possibility, but could suffer from compensation by Be interstitials.

ACKNOWLEDGMENTS

We acknowledge fruitful collaborations with D. P. Bour, M. Kneissl, W. Walukiewicz, and W. Götz. This work was supported in part by DARPA under agreement no. MDA972-96-3-0014. C. Stampfl and J. Neugebauer gratefully acknowledge support from the DFG (Deutsche Forschungsgemeinschaft).

REFERENCES

[1] Y. Koide, H. Itoh, N. Sawaki, I. Akasaki, and M. Hashimoto, J. Electrochem. Soc., **133**, 1956 (1986).
[2] H. G. Lee, M. Gershenzon, B. L.Goldenberg, J. Elec. Mat. **20**, 621 (1991).
[3] M. D. McCluskey, N. M. Johnson, C. G. Van de Walle, D. P. Bour, M. Kneissl, and W. Walukiewicz, Phys. Rev. Lett. **80**, 4008 (1998).
[4] M. D. Bremser, W. G. Perry, T. Zheleva, N. V. Edwards, O. H. Nam, N. Parikh, D. E. Aspnes, and R. F. Davis, MRS Internet J. Nitride Semicond. Res. **1**, 8 (1996).
[5] M. D. Bremser, W. G. Perry, N. V. Edwards, T. Zheleva, N. Parikh, D. E. Aspnes, and R. F. Davis, Mat. Res. Soc. Symp. Proc. **395**, 195 (1996).
[6] J. Neugebauer and C. G. Van de Walle, Phys. Rev. Lett. **75**, 4452 (1995).
[7] J. Neugebauer and C. G. Van de Walle, Appl. Phys. Lett. **68**, 1829 (1996).
[8] T. Tanaka, A. Watanabe, H. Amano, Y. Kobayashi, I. Akasaki, S. Yamazaki, and M. Koike, Appl. Phys. Lett. **65**, 593 (1994).

[9] M. Katsuragawa, S. Sota, M. Komori, C. Anbe, T. Takeuchi, H. Sakai, H. Amano, and I. Akasaki, J. Cryst. Growth **189/190**, 528 (1998).
[10] M. Suzuki, J. Nishio, M. Onomura, and C. Hongo, J. Cryst. Growth **189/190**, 511 (1998).
[11] J. Neugebauer and C. G. Van de Walle, Phys. Rev. B **50**, 8067 (1994).
[12] J. Neugebauer and C. G. Van de Walle, in *Proceedings of the 22nd International Conference on the Physics of Semiconductors* (World Scientific, Singapore, 1995), p. 2327.
[13] J. Neugebauer and C. G. Van de Walle, in *Proceedings of the 23rd International Conference on the Physics of Semiconductors* (World Scientific, Singapore, 1996) p. 2849.
[14] C. Stampfl and C. G. Van de Walle, Appl. Phys. Lett. **72**, 459 (1998).
[15] T. Mattila and R. M. Nieminen, Phys. Rev. B **54**, 16676 (1996).
[16] T. Mattila and R. M. Nieminen, Phys. Rev. B **55**, 9571 (1997).
[17] C. G. Van de Walle, Phys. Rev. B **57**, R2033 (1998).
[18] R. Stumpf and M. Scheffler, Computer Phys. Commun. **79**, 447 (1994)
[19] M. Bockstedte, A. Kley, J. Neugebauer, and M. Scheffler, Comp. Phys. Commun. **107**, 187 (1997).
[20] J. Neugebauer and C. G. Van de Walle, Mater. Res. Soc. Symp. Proc. **408**, 43 (1996).
[21] N. Troullier and J. L. Martins, Phys. Rev. B **43**, 1993 (1991).
[22] P. Boguslawski, E. L. Briggs, and J. Bernholc, Phys. Rev. B **51**, 17255 (1995).
[23] A. Rubio, J. L. Corkhill, M. L. Cohen, E. Shirley, and S. G. Louie, Phys. Rev. B **48**, 11810 (1993).
[24] W. Seifert, R. Franzheld, E. Butter, H. Sobotta, and V. Riede, Cryst. Res.& Technol. **18**, 383 (1983).
[25] W. Götz, N. M. Johnson, C. Chen, H. Liu, C. Kuo, and W. Imler, Appl. Phys. Lett. **68**, 3144 (1996).
[26] W. Götz, J. Walker, L. T. Romano, and N. M. Johnson, Mat. Res. Soc. Symp. Proc. **449**, 525 (1997).
[27] E. L. Piner, M. K. Behbehani, N. A., El-Masry, J. C. Roberts, F. G. McIntosh, and S. M. Bedair, Appl. Phys. Lett. **71**, 2023 (1997).
[28] W. Götz, L. T. Romano, J. Walker, N. M. Johnson, and R. J. Molnar, Appl. Phys. Lett. **72**, 1214 (1998).
[29] D. C. Look, and R. J. Molnar, Appl. Phys. Lett. **70**, 3377 (1997).
[30] W. Götz, R. S. Kern, C. H. Chen, H. Liu, D. A. Steigerwald, and R. M. Fletcher, Mater. Sci. and Engin. B (in press).
[31] P. Perlin, T. Suski, H. Teisseyre, M. Leszczynski, I. Grzegory , J. Jun, S. Porowski, P. Boguslawski, J. Bernholc, J. C. Chervin, A. Polian, and T. D. Moustakas, Phys. Rev. Lett. **75**, 296 (1995).
[32] C. Wetzel, T. Suski, J. W. Ager III, E. R. Weber, E. E. Haller, S. Fischer, B. K. Meyer, R. J. Molnar, and P. Perlin, Phys. Rev. Lett. **78**, 3923 (1997).
[33] C. H. Park and D. J. Chadi, Phys. Rev. B **55**, 12 995 (1997).
[34] M. T. Hirsch, J. A. Wolk, W. Walukiewicz, and E. E. Haller, Appl. Phys. Lett. **71**, 1098 (1997).
[35] A. E. Wickenden, G. Beadie, D. D. Koleske, W. S. Rabinovich, and J. A. Freitas, Jr., Mat. Res. Soc. Symp. Proc. **449**, 531 (1997).
[36] A. Y. Polyakov, M. Shin, J. A. Freitas, M. Skowronski, D. W. Greve, and R. G. Wilson, J. Appl. Phys. **80**, 6349 (1996).
[37] A. Y. Polyakov, N. B. Smirnov, A. V. Govorkov, M. G. Mil'vidskii, J. M. Redwing, M. Shin, M. Skowronski, D. W. Greve, and R. G. Wilson, Solid-State Electronics **42**, 627 (1998).
[38] G.-C. Yi, and B. W. Wessels, Appl. Phys. Lett. **69**, 3028 (1996).

[39] J. Neugebauer and C. G. Van de Walle, Proc. Mater. Res. Soc. Symp. **395**, 645 (1996).
[40] J. Neugebauer and C. G. Van de Walle, in Festkörperprobleme/Advances in Solid State Physics, Vol. **35,** edited by R. Helbig (Vieweg, Braunschweig/Wiesbaden, 1996) p. 25.
[41] J. Z. Li, J. Y. Lin, H. X. Jiang, A. Salvador, A. Botchkarev, and H. Morkoç, Appl. Phys. Lett. **69**, 1474 (1996).
[42] C. Johnson, J. Y. Lin, H. X. Jiang, M. A. Khan, C. J. and Sun, Appl. Phys. Lett. **68**, 1808 (1996).
[43] C. G. Van de Walle, Phys. Rev. B **56**, R10 020 (1997).
[44] M. Leroux, B. Beaumont, N. Grandjean, P. Lorenzini, S. Haffouz, P. Vennéguès, J. Massies, and P. Gibart, Mat. Sci. Engin. B. **50**, 97 (1997).
[45] U. Kaufmann, M. Kunzer, M. Maier, H. Obloh, A. Ramakrishnan, B. Santic, and P. Schlotter,. Appl. Phys. Lett. **72**, 1326 (1998).
[46] F. Calle, E. Monroy, F. J. Sánchez, E. Muñoz, B. Beaumont, S. Haffouz, M. Leroux, and P. Gibart, MRS Internet J. Nitride Semicond. Res. **3**, 24 (1998).
[47] S. Nakamura, N. Iwasa, M. Senoh, and T. Mukai, Jpn. J. Appl. Phys. **31**, 1258 (1992).
[48] W. Götz, N. M. Johnson, J. Walker, D. P. Bour, and R. A. Street, Appl. Phys. Lett. **68**, 667 (1996).
[49] V. Fiorentini, F. Bernardini, A. Bosin, and D. Vanderbilt, in *Proceedings of the 23rd International Conference on the Physics of Semiconductors*, edited by M. Scheffler, and R. Zimmermann (World Scientific, Singapore, 1996), p. 2877.
[50] F. Bernardini, V. Fiorentini, and A. Bosin, Appl. Phys. Lett. **70**, 2990 (1997).
[51] P. Bergman, G. Ying, B. Monemar, and P. O. Holtz, J. Appl. Phys. **61**, 4589 (1987).
[52] O. Brandt, H. Yang, H. Kostial, and K. H. Ploog, Appl. Phys. Lett. **69**, 2707 (1996).
[53] K. H. Ploog and O. Brandt, J. Vac. Sci. Technol. A. **16,** 1609 (1998).
[54] A. Salvador, W. Kim, Ö. Aktas, A. Botchkarev, Z. Fan, and H. Morkoç, Appl. Phys. Lett. **69**, 2692 (1996).
[55] C. Ronning, E. P. Carlson, D. B. Thomson, and R. F. Davis, Appl. Phys. Lett. **73**, 1622 (1998).
[56] F. J. Sánchez, F. Calle, M. A. Sánchez-García, E. Calleja, E., Muñoz, C. H. Molloy, D. J. Somerford, F. K. Koschnick, K. Michael, and J. M. Spaeth, MRS Internet J. Nitride Semicond. Res. **3**, 19 (1998).
[57] J. W. Lee, S. J. Pearton, J. C. Zolper, and R. A. Stall, Appl. Phys. Lett. **68**, 2102 (1996).

ETCH PROCESSING OF III-V NITRIDES

Charles R. Eddy, Jr.
Boston University
Electrical & Computer Engineering Dept.
8 Saint Mary's Street, Boston, MA 02215-2421

Cite this article as: MRS Internet J. Nitride Semicond. Res. 4S1, G10.5(1999)

ABSTRACT

As III-V nitride devices advance in technological importance, a fundamental understanding of device processing techniques becomes essential. Recent works have exposed various aspects of etch processes. The most recent advances and the greatest remaining challenges in the etching of GaN, AlN, and InN are reviewed. A more detailed presentation is given with respect to GaN high density plasma etching. In particular, the results of parametric and fundamental studies of GaN etching in a high density plasma are described. The effect of ion energy and mass on surface electronic properties is reported. Experimental results identify preferential sputtering as the leading cause of observed surface non-stoichiometry. This mechanism provides excellent surfaces for ohmic contacts to n-type GaN, but presents a major obstacle for Schottky contacts or ohmic contacts to p-type GaN. Chlorine-based discharges minimize this stoichiometry problem by improving the rate of gallium removal from the surface. In an effort to better understand the high density plasma etching process for GaN, in-situ mass spectrometry is employed to study the chlorine-based high density plasma etching process. Gallium chloride mass peaks were monitored in a highly surface sensitive geometry as a function of microwave power (ion flux), total pressure (neutral flux), and ion energy. Microwave power and pressure dependencies clearly demonstrate the importance of reactive ions in the etching of wide band gap materials. The ion energy dependence demonstrates the importance of adequate ion energy to promote a reasonable etch rate ($\geq$ 100-150 eV). The benefits of ion-assisted chemical etching are diminished for ion energies in excess of 350 V, placing an upper limit to the useful ion energy range for etching GaN. The impact of these results on device processing will be discussed and future needs identified.

INTRODUCTION

The family of nitride semiconductors has undergone amazing growth and development in the last decade and is now poised to play a pivotal role in a wide range of advanced semiconductor devices. This family, comprised of the binary semiconductors InN, GaN, and AlN and their ternaries, is now being applied in light emitting diodes that emit from UV to the amber regions of the visible electromagnetic spectrum and to blue lasers. Aside from these landmark optoelectronic device realizations, nitride semiconductors are also undergoing extensive research and development efforts for application in high frequency, high temperature, and high power microelectronic devices. In practically all of these applications, the ability to pattern the nitride semiconductor is required.

As a result of many of the properties that make nitride semiconductors attractive in the aforementioned electronic and optoelectronic device applications, they have proven notoriously difficult to etch. This situation has placed energetic pattern transfer processes in the lead for

Mat. Res. Soc. Symp. Proc. Vol. 537 © 1999 Materials Research Society

nitride device development. It has also placed some restriction on acceptable masking materials for lithography – with more robust silicon dioxide and nitride often being chosen over photoresist. These requirements for etch processing of the nitrides clearly differentiates them from silicon, gallium arsenide and indium phosphide, the only semiconductors with reasonably well understood etch processes. As a result, considerable research and development will be required to realize production-quality etch processes for the nitrides.

In this work, the progress in developing etch processes for the nitrides is reviewed and the remaining etch process issues are identified. The review starts with a brief overview of wet etching techniques and then moves on to cover the more prominent ion-assisted etching techniques. The first ion assisted technique addressed is the conventional reactive ion etching processes. The review then moves on to discuss the bulk of nitride etching efforts where high density plasmas have been employed. Also in this section, detailed results of experiments investigating the damage resulting from and the fundamentals of high density plasma etching will be discussed. The highlights of these efforts are then summarized and the most important remaining issues identified.

WET ETCHING METHODS

As a result of their high bond energies, group III nitrides typically are not etched by wet etching methods. The efforts to date are well reviewed in a recent chapter by Pearton and Shul[1]. Wet etchants are generally only successful on poor quality nitride films deposited by sputtering or reactive evaporation. For these poor quality films both acid and base solutions are moderately successful at elevated temperatures. If such films are first annealed to improve their quality, etch rates drop by up to an order of magnitude. For single crystal nitrides it is very difficult to find reliable, effective wet etchants. For single crystal GaN and InN there are no wet etchants that are effective under 80°C. For AlN, however, photoresist developer and strong KOH solutions are effective at lower temperatures.

Since standard wet etches are largely ineffective, there have been a number of efforts examining assisted wet etching techniques. The most successful has been photoelectrochemical etching of n-GaN grown on SiC. A description of the apparatus is given elsewhere [2], but is basically electrochemical etching in KOH under broad area illumination from a Hg arc lamp. The above bandgap light creates electron-hole pairs that in n-GaN provides a hole flux to the surface where the holes assist in the chemical attack. The technique is not effective for p-GaN as holes are unable to reach the surface due to the specific band bending in the material [2]. Highly anisotropic, high rate (>3000Å/min) etching is achieved at room temperature in 0.04 M KOH with 50mW/cm^2 light intensity (measured at 365 nm). The process becomes diffusion limited in these solutions for light intensities greater than 20mW/cm^2 [3]. Very smooth surfaces are achievable (1.5nm roughness vs. 0.3 nm as-grown) with 0.02 M KOH solutions at 40mW/cm^2 light intensities at 365nm. The smoothness is a very sensitive function of the molarity of the solution [4]. These same solutions have recently been used as a threading and mixed dislocation identification tool for counting low defect density GaN (such as lateral epitaxially overgrown films) with the same high degree of sensitivity on the molarity of the solution [5].

DRY ETCHING METHODS

Reactive Ion Etching

Conventional reactive ion etching (RIE) using parallel plate electrodes and capacitively coupled 13.56 MHz plasma generation power has long been the primary technique for pattern transfer in silicon and gallium arsenide device technologies. In these reactors the plasma density and energy of impinging ions on the substrate are tightly coupled with higher applied rf powers resulting in higher densities and energies. Low damage etch processing using RIE is possible in the Si and GaAs systems with low applied rf power levels. Despite the associated drop in density, etch rates remained reasonable due to the low binding energy of these semiconductors. In the nitrides, with their much higher binding energies, this is not the situation as a quick review of research efforts will show.

The results of a representative set of studies on RIE of the III-V nitrides are summarized in Table I. The bulk of RIE efforts have centered on the application of halogen chemistries (predominantly chlorine) and have involved high coupled rf powers[6-10]. This is consistent with higher plasma densities and high dc bias levels or ion energies. In all cases nitride etch rates are seen to increase monotonically with increasing rf power and decrease with increasing pressure – signifying the importance of the ion driven or physical component to the etch process. Demonstrated etch rates have maximum values of ~1000Å, with the notable exception of GaN in Cl_2 chemistries. Most of these works have been performed with resist masks that were relatively thick in order to withstand the high ion energies used in processing. Under such conditions etch selectivities between the mask material and the nitride are low. These conditions are also likely to result in considerable surface damage to the nitride. Halogen-based chemistries give higher etch rates than methyl based chemistries, except for InN, which is consistent with arsenide semiconductor processing observations. A final note, is that processing with Si-containing precursors can render the nitride surface Si-doped. This generates the need for post-etch processing to recover the original nitride surface properties.

Based upon these efforts, the application of RIE to pattern transfer processing in the III-V nitrides faces considerable difficulties. Primarily, the rates are very low prohibiting application to the etching of light emitting diode and laser diode structures due to the required depth of the etch. Furthermore, the high ion energies required to achieve even these modest rates have

Table I. Summary of select RIE efforts in the III-V nitrides.

Plasma Chemistry	Bias or Power Density	Etch Rates [Å/min]	Masking Material	Comments	Ref
CHF_3	100-500W	50-200(GaN)	Shipley1813	6k-9k Å resist, 100 mTorr	6
C_2ClF_5	"	"	"	"	6
BCl_3	0.3-0.9 W/cm^2	150-730(AlGaN)	Ni	AlGaN/Ni selectivity = 4/1	7
$SiCl_4/SiF_4$	-400 V	500 (GaN)		Smooth, anisotropic	8
Cl_2/Ar	450 W	2800 (GaN) 200 (AlN) 200 (InN)	Resist		9
$CH_4/H_2/Ar$	450W	400 (GaN) 350 (AlN) 300 (InN)	Resist		9
$HBr/H_2/Ar$	-400V	400-600 (GaN)	AZ5214,Ni/ SiO_2		10

serious negative consequences for surface damage and for selectivities between mask and substrate and heterojunction layers. These consequences place substantial challenges to the application of RIE in nitride device processing.

High Density Plasma Etching

General Overview of Efforts

High density plasma reactors have a significant advantage over the reactive ion etching reactors of the previous section – the ion density or plasma density can be de-coupled from the bias applied to the substrate. This permits the high ion flux densities that data from RIE experiments have shown enhances nitride etch rates, but with low, adjustable ion energies (>20 eV). This characteristic enables higher selectivity in the etch process and lower damage levels to the semiconductor surface while maintaining reasonable etch rates.

The family of high density plasma reactors essentially consists of electron cyclotron resonance (ECR) microwave plasma sources and inductively coupled plasma (ICP) sources. However, it is appropriate to include magnetically enhance reactive ion etching (MERIE) systems because of the similarities in the discharges in terms of plasma density.

The efforts to etch III-V nitrides using high density plasma sources are summarized in Table II. As can be seen, the etch rates achieved with these methods is nearly an order of magnitude higher than in conventional RIE methods. The bulk of these efforts have involved halogen based chemistries including chlorine- [11-17], iodine- [18], and bromine-based [14,17] chemistries. There have also been efforts in mixed halogen chemistries such as ICl [19] and CCl_2F_2 [17]. Based upon successful application to the etching of other III-V compound semiconductors, methyl-based chemistries have also been investigated [14,17]. The fastest etch rates are generally achieved at high microwave powers in halogen based chemistries. The ICl chemistry has produced the fastest reported etch rates for all three nitrides: 1.3μm/min for GaN, 1.15μm/min for InN, and 7000Å/min for AlN (notably, at a bias of –275 V).

Because of the ion driven nature of the etch process for the nitrides achievement of vertical sidewalls in etched features is mostly dependent on the robustness of the mask material. When the mask is sufficiently robust to the etch process, perfectly vertical sidewalls are achieved. When the mask is eroded by the etch process the features are overcut and critical dimensions are compromised. A remaining challenge is the introduction of a controlled degree of isotropy to the process. This is important in the fabrication of field effect and bipolar junction devices which require conformal, uniform metal gate deposition over etch steps to avoid a reduction in the breakdown voltage of the device.

High selectivity between the nitrides is important in the processing of heterojunction structures used in lasers, field effect, and bipolar junction transistor devices. The maximum selectivities reported to date are as follows: GaN/InN ~11 in an ECR Cl_2/Ar plasma at low bias, GaN/AlN ~6 in an ECR ICl/Ar plasma at high bias, and InN/GaN ~6.5 in an ECR CH_4/H_2/Ar plasma at low bias[19]. These levels are generally 5-10 times smaller than desired for heterojunction device processing. Thus, improved etch selectivities are another area in need of substantial research and development efforts.

Table II. Summary of select High Density Plasma Etching Efforts in the III-V Nitrides.

Chemistry	Technique	Etch Rate (Å/min)	Source Power (Watts)	Bias (Volts)	Ref
BCl_3	MERIE	3500(GaN)	0.5W/cm^2	-75	11
$SiCl_4$	ECR	960(GaN)	300W	-280	12
Cl_2	ICP	4000(GaN)	500W	-250	13
		2000(AlN)			
		2200(InN)			
Cl_2	ICP	1200(GaN)	1500W	-100	14
		200(AlN)	1500W		
		4800(InN)	1000W		
BCl_3	ICP	3000(GaN)	500W	-250	13
		2200(AlN)			
		2600(InN)			
Cl_2/BCl_3	ICP	8500(GaN)	600W	-120	15
$Cl_2/CH_4/H_2$	ECR	2340(GaN)	850W (170°C)	-180	16
		960(AlN)			
		2300(InN)			
HI/H_2	ECR	1100(GaN)	1000W	-150	18
		1250(AlN)			
		1000(InN)			
HBr/H_2	ECR	900(GaN)	1000W	-150	18
		700(AlN)			
		200(InN)			
ICl	ECR	13000(GaN)	1000W	-275	19
		7000(AlN)			
		11500(InN)			
CCl_2F_2	ECR	300(GaN)	200W	-250	17
		90(AlN)			
		90(InN)			
CH_4/H_2	ECR	75(GaN)	200W	-300	17
		25(AlN)			
		100(InN)			
CH_4/H_2	ICP	1250(GaN)	500W	-225	14
		200(AlN)			
		1250(InN)			

Damage Studies

In addition to the above considerations, one of the most critical figures of merit for etch processing of devices is the damage imparted to the remaining semiconductor. To date, most reports on etch damage in the III-V nitrides have centered on topographic or stoichiometric changes imparted to the surface [13,20-23]. In these representative reports, smooth etched surfaces are identified as generally achievable, with the exception of "etch pit" formation on the surfaces of nitride films grown on basal plane sapphire [13]. Smooth sidewall surfaces are also reported to be contingent upon a robust mask – erosion of the mask edges leads to striations in the sidewall in these high fidelity processes [13].

Although such damage reports are important to the development of low damage processes for the nitrides, it is the effect of etch processing on the electronic properties of nitride surfaces that is essential to the creation of high quality devices. Despite this importance there have been far fewer reports on electronic damage [24-29]. The general conclusions from these efforts are that

high density plasma etching renders the n-type GaN surface less conductive (due primarily to mobility reduction) and semi-insulating GaN surfaces n-type conducting and that the degree of conduction enhancement or degradation is a strong function of incident ion energy and mass. This result is often beneficial to ohmic contacts to n-type GaN, but presents a challenge for reproducible ohmic contacts to p-type GaN or Schottky contacts to either extrinsic type. This result is consistent in InN-based semiconductors where ion energies > 300 eV resulted in a reduction in carrier concentrations – presumably the result of deep trap introduction [27]. As with other III-V compound semiconductors hydrogen has been shown to passivate shallow dopants in the nitrides [30,31].

We have performed detailed experiments on ECR plasma etching damage in n-type GaN (Si-doped to mid 10^{18} cm^{-3}) and highly resistive GaN films grown by MOCVD on sapphire [29]. The GaN wafers used in this study were grown by metal organic chemical vapor deposition (MOCVD) on c-plane (0001) oriented sapphire substrates. The surface of the sample was smooth (~ 5 nm rms roughness by atomic force microscopy) and the thickness of the layers was 2-3 μm. The wafers were cut into ~ 0.4 cm^2 samples and the individual samples were evaluated using Hall measurements before and after exposure to the etching environment. Electron beam evaporated W/10%Ti alloy thin films deposited on the corners of the samples served as both ohmic contacts and as etch masks. Semi-insulating GaN film resistances were determined by I-V measurements using removable liquid Ga/In eutectic contacts. Etch depths were measured with a Tencor AlphaStep 250 stylus profilometer.

All plasma etching was performed in an electron cyclotron resonance microwave plasma reactive ion etching system described previously [32]. In these experiments, the total pressure was held at 1mTorr while total flows of 12.8 sccm, 9.6 sccm, 6.8 sccm and 9.0 sccm were used for $CH_4/H_2/Ar$ (2.8/6.8/3.2 flow fractions), CH_4/H_2 (2.8/6.8), H_2 and Cl_2 chemistries, respectively. Microwave powers of 300-400W and 200W were used for hydrogen-containing and chorine-based chemistries, respectively. The capacitively coupled, rf-induced dc bias level of the substrate platen ranged from -150 V to -400 V (corresponding to rf power densities from 0.8 W/cm^2 to 3.4 W/cm^2) for all of the studies performed here. The substrates were placed 32 cm downstream of the position of the electron cyclotron resonance condition, defined by the on-axis location of the 875 G magnetic field intensity contour.

Rapid thermal annealing experiments were performed to evaluate the response of electrical parameters to annealing treatments. In these experiments, the wafer is placed face down on a Si wafer with the GaN surface in contact with the smooth Si surface. Annealing was performed in flowing N_2 gas. The sample was first annealed at 400°C for 30 sec and then a room temperature Hall measurement was performed. The annealing was continued at higher temperatures in 100°C increments, each of 30 sec duration. After each anneal the electrical parameters were determined.

In these efforts, we've found that 'etching' in inert gas plasmas renders the surface of n-type films more resistive and that the degree of resistivity is dependent on ion energy and mass – heavier ions (Ar) at higher energies (400 eV) resulting in the most resistive films. The resistivity increase is largely attributed to a drastic decrease in the mobility. Similar observations are made on GaN films etched in $CH_4/H_2/Ar$ ECR plasmas. Films etched at 300 eV in hydrogen shown only modest increases in resistivity, and decreases in mobility. Films etched in Cl_2 ECR plasmas etched at the fastest rates (>2000Å/min) and showed no change in the surface electrical properties. Supporting results of surface stoichiometry (Auger Electron Spectroscopy) and topography (Atomic Force Microscopy and Scanning Electron Microscopy) show that heavily damaged surfaces are well decorated with 'etch pits' (Figure 1) and are gallium rich (with pre-etch Ga:N ratios of 2 and post-etch ratios of 3.2). This damage could be annealed away with rapid thermal anneals of 120 sec duration at temperatures as low as 450°C. These observations

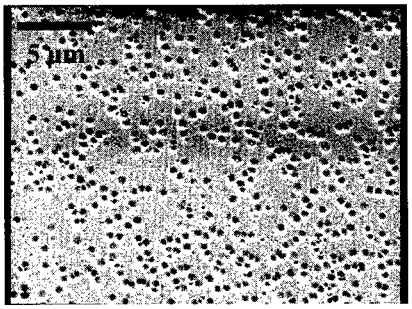


Figure 1. SEM micrograph of GaN surface morphology after 20 min. exposure to 150 eV Ar ions.

support a combination of preferential sputtering and compensating defects. Preferential sputtering increases the depth of disorder to ~ 2000Å. The addition of a strong chemical component, as in Cl_2 etching, reduces the disorder by removing it at a rate comparable to its introduction leaving the surface effectively undamaged. Similar dependencies on etch gas, ion mass, and ion energy are observed in highly resistive films (undoped, $R_o > 10^8$ Ω) except that the surfaces were rendered more n-type conducting.

Fundamentals of Nitride Etching Studies

We've also performed preliminary studies investigating the fundamentals of etching of GaN in an effort to understand the etching process in terms of process conditions most suited to ion-assisted etching at minimal damage levels. These studies have involved the use of mass spectrometric sampling through the substrate platen with and without the substrate present. Studies without the substrate were performed to evaluate the make-up of the incident plasma flux as a function of process conditions (pressure and microwave power) [33]. Studies with un-patterned GaN films (grown by MOCVD on sapphire) were performed to evaluate the rate of etch product formation as a function of variations in the plasma flux and the incident ion energy. The sampling technique has been shown to be extremely sensitive to the surface chemistry and, therefore, provides an unambiguous sampling of surface chemistry through monitoring of etch products that evolve from the surface [34,35].

The $GaCl_2$ etch products at 139 ($^{69}Ga^{35}Cl_2$), 141 ($^{69}Ga^{35}Cl^{37}Cl$ and $^{71}Ga^{35}Cl_2$), 143 ($^{71}Ga^{35}Cl^{37}Cl$, $^{69}Ga^{37}Cl$), and 145 ($^{71}Ga^{37}Cl_2$) are used to monitor the etch product formation rate as a function of changes in the plasma/surface interaction region. As microwave power is increased from 300-600 W, Figure 2, we see a monotonic increase in the mass peak intensities of the etch products with a particular jump between 400 and 450 W. Flux characterization measurements show that for > 300 W microwave power the flux is nearly fully dissociated, consistent with other reports. For > 400 W microwave power, the flux is dominated by Cl^+ and Ar^+. Figure 3 shows the dependence of etch product formation on the process pressure. We see a dramatic decrease in the mass peak intensities of the etch products as pressure is increased from 0.25 to 2 mTorr. Over this same pressure range, flux characterizations show that the ion fraction of the flux drops rapidly to background levels at 2 mTorr as the pressure is increased and that neutral species rise monotonically over this pressure range with Cl_2 and Ar domination for pressures > 1mTorr.

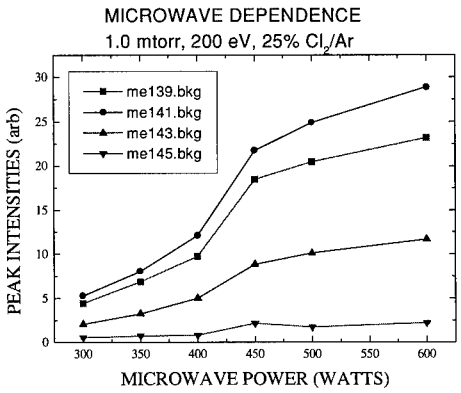


Figure 2. Variation in etch product mass intensities with coupled microwave power.

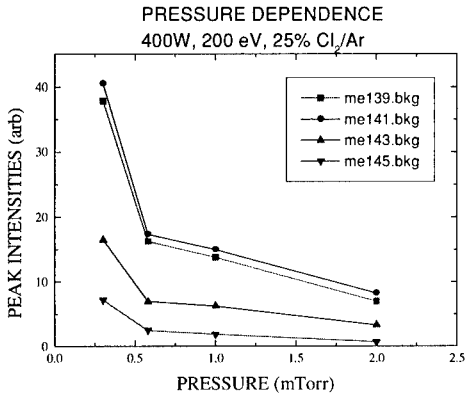


Figure 3. Variation in etch product mass intensities with process pressure.

Taken together, these observations with variations in process conditions indicate a clear need for a high ion and atomic chlorine fluxes at the substrate to promote reasonable etch rates, this requires process conditions of high microwave powers and low process pressures. These requirements should be met with care, however, as they will reduce selectivity. The pressure requirement is well aligned with the highly anisotropic nature of etch processing at these pressures due to increased directionality of incident ions. Both requirements further support high density plasma tools as the tool of choice for nitride etch processing.

The critical parametric dependence for understanding the driving force behind surface chemistry in these etch processes is the dependence of etch product formation rate on incident ion energy. Figure 4 shows the dependence of the $GaCl_2$ mass peak intensities on incident ion energy, as determined by the level of the capacitively coupled rf bias power. As can be seen in the figure, there is effectively no etching of GaN for ion energies up to 75-100 eV. Above that level, the etch product formation rate begins to slowly increase up to energies of 200 eV, indicative of ion-assisted product formation. This ion-assist is substantially enhanced for ion energies in the 200-350 eV range as

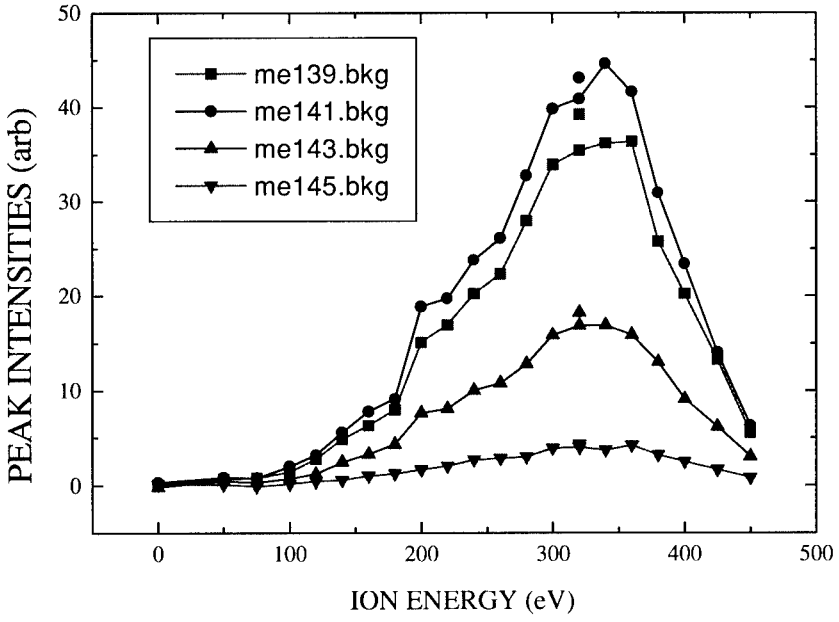


Figure 4. Variation in etch product mass intensities with substrate bias.

the product mass peak intensities increase rapidly over this range. For ion energies greater than 350 eV there is a considerable decrease in the product mass peak intensities, almost to background levels by 450 eV. Over this same range of energies, we have seen and others have shown that the GaN etch rate continues to increase. Combining these observations, we see that at 350 eV the etch process transitions from the desired ion-assisted chemistry to physical sputtering. The best results are therefore expected when the ion energy is in the range from 150-350 eV. Excellent anisotropy can be expected over this entire range, while the higher end of this range will give faster etch rates with poor selectivity and high damage levels and the lower end of the range will give better selectivities and lower damage levels.

SUMMARY & FUTURE DIRECTIONS

Various plasma-based etching techniques for III-V nitrides have been reviewed. Conventional reactive ion etching techniques using a capacitively-coupled parallel plate geometry are capable of etching the nitrides, but etch rates are very low even at relatively high ion energies (400 eV). This situation has serious negative implications on selectivity and damage, but demonstrates the importance of ions to the etching process in the III-V nitrides. As a whole, high density plasma etching has many advantages for etch processing of the nitrides. Etch rates approaching 1μm/min are being realized in chlorine-based chemistries. Perfect anisotropy is possible due to the strong ion dependence of the etching mechanism. The limit on anisotropy is the robustness of the mask material, if the mask erodes the profiles will be overcut. A remaining challenge is the introduction of some degree of controlled isotropy to the process for device technologies requiring rounded trench bottoms. Etch selectivity between the nitrides is quickly becoming a daunting issue, also a result of the strong ion dependence of the etching mechanism. Maximum selectivities are 6-10 and higher selectivities are desired for ease of processing heterojunction devices, particularly the microelectronic versions. Etch damage to GaN surfaces is strongly influenced by ion energy and mass. This is partially attributed to preferential sputtering of nitrogen. The addition of a chemical component to the etch greatly reduces the effect by rapidly removing the residual gallium from the surface. Fundamental studies in high density plasma etching have shown that GaCl product formation, presumably the limiter - although the true limitation is likely the breaking of the GaN bond to permit formation of GaCl - is most efficient for Cl, Cl^+ dominated plasma fluxes to the substrate. This is consistent with high plasma powers and low pressures. These studies have also shown that the most effective ion-assisted etching is for incident ion energies in the 150-350 eV range.

ACKNOWLEDGEMENTS

The author wishes to acknowledge the efforts of Drs. Bela Molnar, Darrin Leonhardt, Vasgen Shamamian, and James Butler for their substantial efforts in the damage and fundamental experiments reported here. I also wish to acknowledge the support of the Office of Naval Research.

REFERENCES

1 S.J. Pearton and R.J. Shul in *Gallium Nitride I*, J. Pankove and T.D. Moustakas Eds., Semiconductor and Semimetals Series, Vol. 50, P. 103, Academic Press, New York, NY (1998).

2 C. Youtsey, I. Adesida and G. Bulman, Electronics Lett. **33**, 245 (1997).

3 C. Youtsey, I. Adesida and G. Bulman, Appl. Phys. Lett. **71**, 2151 (1997).

4 C. Youtsey, I. Adesida, L.T. Romano and G. Bulman, Appl. Phys. Lett. **72**, 560 (1998).

5 C.Youtsey, L.T. Romano and I. Adesida, Appl. Phys. Lett. **73**, 797 (1998).

6 H. Lee, D.B. Oberman and J.S. Harris, Jr., *Appl. Phys. Lett.* **67**, 1754 (1995).

7 W.C. Hughes, W.H. Roland, Jr., M.A.L. Johnson, J.W. Cook, Jr. and J.F. Schetzina, in *Gallium Nitride & Related Materials*, F.A. Ponce, R.D. Dupuis, S. Nakamura and J.A. Edmond eds., MRS Proc. Vol. 395, p. 757, Materials Research Society, Pittsburgh, PA (1996).

8 I. Adesida, A. Mahajan, E. Andideh, M. Asif Khan, D.T. Olsen and J.N. Kuznia, *Appl. Phys. Lett.* **63**, 2777(1993).

9 C.B. Vartuli, J.D. MacKenzie, J.W. Lee, C.R. Abernathy, S.J. Pearton and R.J. Shul, *J. Appl. Phys.* **80**, 3705 (1996).

10 A.T. Ping, I. Adesida, M. Asif Khan and J.N. Kuznia, *Electronics Lett.* **30**, 1895 (1994).

11 G.F. McLane, L. Casas, S.J. Pearton and C.R. Abernathy, *Appl. Phys. Lett.* **66**, 3328 (1995).

12 L. Zhang, J. Ramer, J. Brown, K. Zheng, L.F. Lester and S.D. Hersee, *Appl. Phys. Lett.* **68**, 367 (1996).

13 R.J. Shul, C.G. Willison, M.M. Bridges, J. Han, J.W. Lee, S.J. Pearton, C.R. Abernathy, J.D. MacKenzie, S.M. Donovan, L. Zhang, and L.F. Lester, *J. Vac. Sci. Technol. A* **16**, 1621 (1998).

14 H. Cho, C.B. Vartuli, S.M. Donovan, C.R. Abernathy, S.J. Pearton, R.J. Shul, C. Constantine, *J. Vac. Sci. Technol. A* **16**, 1631 (1998).

15 Y.H. Lee, H.S. Kim, G.Y. Yeom, J.W. Lee, M.C. Yoo and T.I. Kim, *J. Vac. Sci. Technol. A* **16**, 1478 (1998).

16 R.J. Shul, S.P. Kilicoyne, M. Hagerott Crawford, J.E. Parmeter, C.B. Vartuli, C.R. Abernathy and S.J. Pearton, *Appl. Phys. Lett.* **66**, 1761 (1995).

17 S.J. Pearton , C.R. Abernathy and F. Ren, *J. Vac. Sci. Technol. A.* **11**, 1772 (1993).

18 S.J. Pearton, C.R. Abernathy and C.B. Vartuli, *Electronics Lett.* **30**, 1985 (1994).

19 C.B. Vartuli, S.J. Pearton, J.D. Mackenzie, C.R. Abernathy and R.J. Shul, *J. Electrochem. Soc.* **143**, L246 (1996).

20 S.J. Pearton, C.R. Abernathy, F. Ren and J.R.. Lothian, *J. Appl. Phys.* **76**, 1210 (1994).

21 G.F. McLane, S.J. Pearton and C.R. Abernathy, in *Wide Bandgap Semiconductors And Devices*, PV 95-21, p. 204, The Electrochemical Society Proceedings, Pennington, NJ (1995).

22 R.J. Shul, A.J. Howard, S.J. Pearton, C.R. Abernathy and C.B. Vartuli, in *Wide Bandgap Semiconductors And Devices*, PV 95-21, p. 217, The Electrochemical Society Proceedings, Pennington, NJ (1995).

23 R.J. Shul, A.J. Howard, S.P. Kilcoyne, S.J. Pearton, C.R. Abernathy, C.B. Vartuli, P.A. Barnes and M.J. Bozack, in *Proceedings 22nd SOTAPOCS*, PV 95-6, p. 209, The Electrochemical Society Proceedings, Pennington, NJ (1995).

24 C.R. Eddy, Jr. and B. Molnar in *Gallium Nitride & Related Materials*, F.A. Ponce, R.D. Dupuis, S. Nakamura And J.A. Edmond Eds., MRS Proc. Vol. 395, p. 745, Materials Research Society, Pittsburgh, PA (1996).

25 B. Molnar, C.R. Eddy, Jr. and K. Doverspike, *J. Appl. Phys.* **78**, 6132 (1995).

26 A.T. Ping, A.C. Schmitz, I. Adesida, M. Asif Khan, Q. Chen and J.W. Yang, *J. Electron. Mater.* **26**, 266 (1997).

27 S.J. Pearton, J.W. Lee, J.D. MacKenzie, C.R. Abernathy and R.J. Shul, *Appl. Phys. Lett.* **67**, 2329 (1995).

28 H.Ishikawa, S. Kobayashi, Y. Koide, S. Yamasaki, S. Nagai, J. Umezaki,M. Koike and M. Murakami, *J. Appl. Phys.* **81**, 1315 (1997).

29 C.R. Eddy, Jr. and B. Molnar, to appear in *J. Electron. Mater.*, March 1999 issue.

30 M.S. Brandt, N.M. Johnson, R.J. Molnar, R. Singh and T.D. Moustakas, *Appl. Phys. Lett.* **64**, 2264 (1994).

31 S. Nakamura, T. Mukai, M. Senoh and N. Iwasa, *Jpn. J. Appl. Phys.* **31**, L139 (1992).

32 C.R. Eddy, Jr., E.A. Dobisz, J.R. Meyer and C.A. Hoffman, J. Vac. Sci. Technol. A **11**, p. 1763 (1993)

33 C.R. Eddy, Jr., D. Leonhardt, S.R. Douglass, B.D. Thoms and J.E. Butler, J. Vac. Sci. Technol. A **17**, 38 (1999).

34 C.R. Eddy, Jr., O.J. Glembocki, D. Leonhardt, V.A. Shamamian, R.T. Holm, B.D. Thoms, J.E. Butler, and S.W. Pang, *J. Electron. Mater.* **26**, 1320 (1997).

35 D. Leonhardt, C.R. Eddy, Jr., V.A. Shamamian, R.T. Holm, O.J. Glembocki and J. E. Butler, *J. Vac. Sci. Technol. A* **16**, 1547 (1998).

DAMAGE-FREE PHOTO-ASSISTED CRYOGENIC ETCHING OF GaN AS EVIDENCED BY REDUCTION OF YELLOW LUMINESCENCE

J. T. Hsieh, J. M. Hwang and H. L. Hwang
Institute of Electronic Engineering, National Tsing-Hua University, Hsinchu, 300, Taiwan, R.O.C.
W. H. Hung
Synchrotron Radiation Research Center, Hsinchu, 300, Taiwan, R.O.C.

Cite this article as: MRS Internet J. Nitride Semicond. Res. 4S1, 10.6 (1999)

ABSTRACT

Damage-free etching of GaN by Cl_2, assisted by an ArF (193 nm) excimer laser, is demonstrated. At low temperatures, photo-assisted etching can provide a better etch rate and largely improve the surface morphology and quality. AFM results show that the etched GaN surface is obtained with a root-mean-square roughness of 1.7 nm. As compared with the photoluminescence spectra of photoelectrochemical wet etched GaN, the photo-assisted cryogenic etching is proved to be a damage-free dry etching technique.

INTRODUCTION

GaN and related substrates have good thermal stability and excellent chemical inertness because of their strong bond strengths. This has made it difficult to develop controlled etch processes to successfully realize III-nitride based devices. Most of the previous work has been directed toward mesa formation in UV/blue/green laser diodes, where etch depths are relatively large (2-4 •m) and the final surface morphology is relatively unimportant. Most attention is paid to a smooth vertical facet. On the other hand, the etching requirements for high power/high temperature electronics are quite different. With shallower etch depths, the fabrication of these devices is on retaining smooth surface morphologies and obtaining high etch selectivity for one material to another. In the past, chemically assisted ion beam etching (CAIBE)[1], reactive ion etching (RIE)[2] and inductively coupled plasma (ICP)[3] etching techniques have been used to etch GaN and related compounds. Despite high etch rates and good anisotropy etching have been obtained from these techniques, it is difficult to produce a perfect facet and damage-free sidewall and bottom surface due to the bombardment of energetic ions.

Based on the above discussions, photo-assisted etching appears to be an alternative method to resolve these problems. Photo-induced etching is initiated as a result of direct absorption of photons by adsorbate molecules on the semiconductor substrate. Subsequently, the photo-stimulated chemical reaction occurs to form volatile products, which may desorb from the surface and are exhausted out by the pumping system to complete the etching process. Desorption of product species plays a key role in determining the etching characteristics. By cryogenic cooling of the substrate during photo-assisted etching, thermal reaction and desorption are suppressed. It provides a route for an anisotropic etching process with the damage-free surface. The advantage of etching at low temperatures also includes the fact that the sticking coefficient of Cl_2 on the substrate is increased.

In previous work, Shih et al.[4] presented a technique for cryogenic chlorine etching of GaAs. Leonard and Bedair[5] also obtained successful realization of photoassisted etching of GaN in HCl

Mat. Res. Soc. Symp. Proc. Vol. 537 © 1999 Materials Research Society

by using a 193 nm ArF excimer laser. In Leonard's experiment, HCl etchant with a base pressure of ~5×10^{-4} Torr, a sample temperature between 200 and 400 °C and a laser fluence of 1400 mJ/cm^2 were combined to produce an etch rate of 8 nm/min. In this letter we will show the preliminary results and demonstrate the improved GaN surface quality using photo-assisted cryogenic etching laser in Cl_2 ambient with an ArF excimer. Photoelectrochemical (PEC) etching experiments is also performed to compare with the results of photo-assisted cryogenic (PAC) etching.

Table I. A $L_{16}4^4$ Taguchi orthogonal design of various parameters in PAC etching.

Parameter	Laser Power (mJ)	Cl_2 pressure (mTorr)	Repetition Rate (Hz)	Temperature (°C)
1	270	0.1	1	+100
2	300	0.5	2	+25
3	210	1	4	-60
4	240	5	8	-170

EXPERIMENT

A high vacuum etching system was composed of a load lock, a preparation chamber and the main etching chamber. The main chamber was turbo pumped maintaining a base pressure of 8 x 10^{-9} Torr when the system was not in use. Cl_2 was introduced into the chamber via a leak valve doser. Liquid nitrogen was used to cool down the sample holder to 100 K. For the purpose of studying the relationship between various parameters and etch rate, a sixteen-run experiment using $L_{16}4^4$ Taguchi orthogonal design was employed. The experimental parameters in this study are listed in Table I.

The light source was a Lambda Physik LPX-200 ArF excimer laser (193 nm). The n-type GaN ($\leq 5\text{x } 10^{16}$ cm^{-3}) samples, epitaxially grown on the sapphire substrate, were purchased from CREE Corporation. Prior to the sample mounting, the samples were solvent cleaned. A stainless plate with small holes was used to serve as the overlaid mask. Before introducing the laser beam through a quartz window into the etching chamber, one reflection mirror and one focus lens of 15-cm focus length were arranged to direct the beam path. The beam output power measured in front of the quartz window was 210-300 mJ/pulse. The focus lens reduced the laser beam spot size on the substrate to 10% of its original 3 x 1 cm^2 dimensions.

For the damage identification study, PEC etched samples were prepared to compare with that obtained from PAC etching. The illumination source for PEC etching was an ORIEL 1000 W Hg lamp, which was generally operated at 600 W. To avoid the heating problem from the electrolyte absorption, a water reservoir was mounted in front of the exit window of the Hg lamp to filter out the infared radiation. The samples were clipped between a Pt electrode plate with a 4 mm hole and a Teflon holder. A Teflon mask with a 3 mm hole was used to cover and prevent the Pt electrode from UV illumination. The electrolyte was prepared by dissolving potassium hydroxide (KOH) pellets in deionized water to form a 0.02 M aqueous solution. The standard lift-off lithography technique was used to form the 100 •m square Ti metal mask that served as an ohmic contact for better photocurrent conduction.

A continuous wave He-Cd laser with $\bullet_{exc}$=325.0 nm was used in the photoluminescence (PL) mesurement. All PL spectra were recorded using a monochrometer and a photomultiplier.

RESULTS AND DISCUSSION

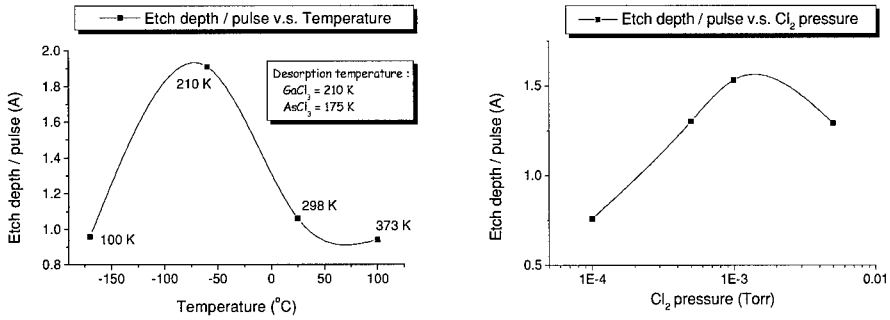


Figure 1. Etch depth/pulse as a function of (a) temperature and (b) Cl_2 pressure.

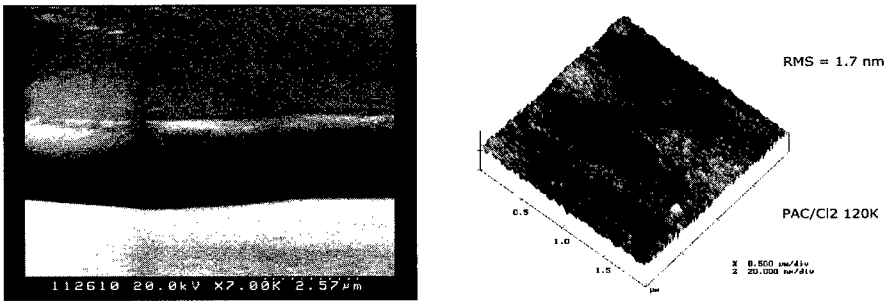


Figure 2. SEM and AFM photographs of photo-assisted cryogenic etched GaN surfaces.

Figure 1(a) shows the GaN etch rates as a function of temperature. The etch depth is measured using an alpha-step and a maximum etch rate of 84 nm/mim is obtained at 210K. As compared with Leonard and Bedair's results[5], the increased etch rate may be attributed to the higher efficiency of Cl radical production since the Cl-Cl binding energy (242.58 kJ/mol at 298 K) is smaller than that of the H-Cl (431.62 kJ/mol at 298 K).[6] In order to prevent the volatile product from residing on the surface during the course of etching, the surface must be kept above the desorption temperature to assure the etching to proceed. The etch rate also increases with the increase of laser power density. The linear dependence of the etch rate on the Cl_2 pressure is shown in Fig. 1(b). The etch rate increases with the decrease of temperature and the increase of Cl_2 pressure. This suggests that the etching process is initiated by Cl atoms photogenerated from the physisorbed chlorine layer on the substrate. At lower temperature, more molecular chlorine is condensed on the surface, which is photodissociated and reacts with the GaN substrate. However, the etch rate becomes saturated at a Cl_2 pressure of ~1mTorr and then decreases at higher pressures. The threshold of laser power density is estimated to be about 600 mJ/cm^2. No appreciable etching is observed when the substrate is exposed to Cl_2 without laser illumination or a laser illumination without Cl_2 introduction. The combination of both Cl_2 and ArF laser energy is a necessary condition to proceed the photo-assisted etching. It is also found that the ablative etching occurs at the power density of more than 1000 mJ/cm^2.

Table II. A comparison of the roughness of the etched GaN surface in the previous studies and this work.

Gas	Roughness (nm)	Etch technique	References
$Cl_2/H_2/CH_4/Ar$	65.2	ICP	10
$Cl_2/H_2/CH_4/Ar$	19.3	RIE/ECR	10
Cl_2/Ar	5.4	ICP	3
BI_3/Ar	~10	ICP	11
BBr_3/Ar	~3	ICP	11
Cl_2	~1.7	PAC	This work

As shown in Figure 2, SEM and atomic force microscopy (AFM) photographs indicate that the root-mean-square roughness of 1.7 nm can be achieved on GaN surface etched at 210 K. The surface roughness of GaN etched at low temperatures is much better than that obtained at room temperature. It can be inferred that the higher sticking coefficient of Cl_2 at low temperatures helps to etch the substrate more efficiently. Compared with the results using RIE/ECR-RIE/ICP dry etching techniques, photo-assisted cryogenic etching produces the smoothest surface. Table II lists some roughness data reported in the previous studies using other etching techniques and conditions.

Figurs 3(a) shows the room temperature PL spectrum of PAC etched GaN surfaces. The 3.41 eV peak is attributed to the near-band-edge emission and the 1.705 eV peak is its second harmonic conterpart. A broad yellow luminescence (YL) is observed for the GaN surface etched at room temperature, which is centered at 2.2 eV. But it does not appear at the GaN surface etched at low tempertures. For further investigation on this broad band emission, PL spectra of PEC etched GaN surfaces are shown in Figure 3(b). All PEC etched surfaces show a broad band emission and its relative intensity increases with the increase of the UV radiation power. On the GaN surface etched under the irradiation of 700 W UV, the peak shifts from 3.41 eV to the lower energy. The origin of yellow luminescence has attracted much attention and several mechanisms have been proposed. Neugebauer and Van De Walle[7] investigated the native vacancy defect and vacancy-impurity complexes and suggested that the main defect source is attributed to V_{Ga} (Ga vacancy) forming an acceptor-like defect level. From the first–principle calculation, they concluded that V_{Ga} is easier to form due to its lower formation energy and is possibly the origin of YL. During the photo-assisted etching of GaN, Ga is removed as volatile $GaCl_x$ products via a photo-stimulated reaction while N is most likely removed as a free atom. This process creates a Ga-deficient surface and results in the acceptor-like native defect, namely, gallium vacancy that is the origin of YL as proposed by Neugebauer and Van De Walle. The use of cryogenic temperatures for the substrate increases the range of usable molecular adsorbates and suppresses unwanted thermally active reactions that normally occur at room temperature. Hence, the defect center is largely reduced and no YL band is observed on the photo-assisted cryoetched GaN surfaces. On the other hand, Minsky et al.[8] proposed that the PEC etching of GaN occurs through the oxidative decomposition, in which photogenerated holes assist the oxidation and the subsequent dissolution of the semiconductor into aqueous solution. Youtsey et al.[9] postulated that the oxidation reaction, $2GaN + 6h^+ \rightarrow 2Ga^{3+} + N_2$, is responsible for the decomposition of GaN. While in our wet etching condition, we tentatively conjecture that YL may result from deep level V_{Ga} and V_{Ga}-O_N defect-impurity complexes. During the PEC etching, the oxidation reaction takes away Ga and N atoms (V_{Ga} and V_N) and incorporates O atoms into N sites to form the V_{Ga}-O_N

complexes, in which UV irradiation provides the enough formation energy. However, further experimental studies are needed to confirm this conjecture.

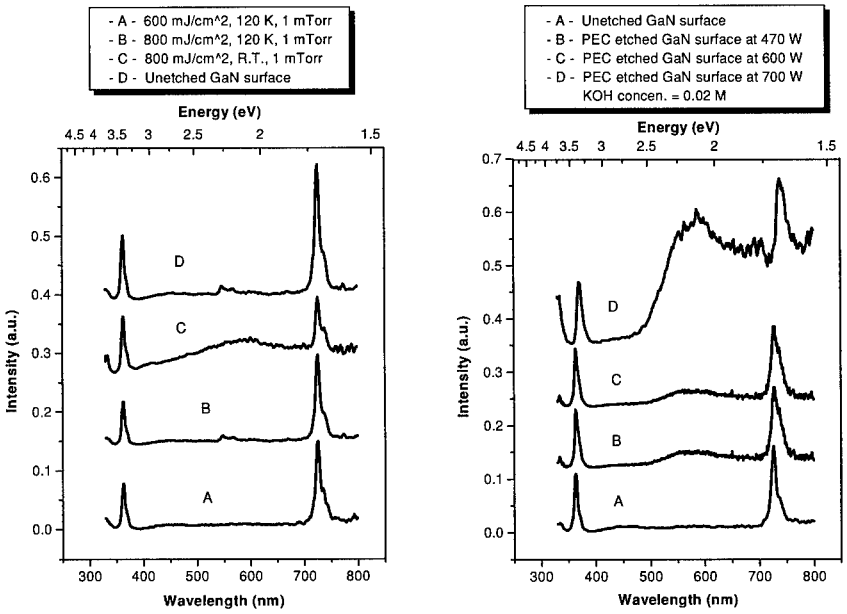


Fig. 3. PL spectra of (a) cryogenic photo-assisted and (b) photoelectrochemical etched GaN.

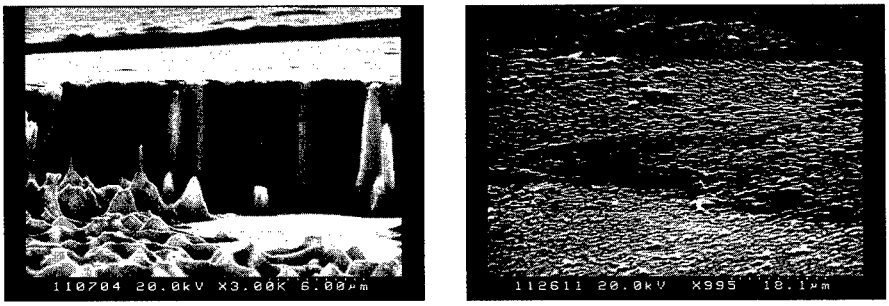


Fig. 4(a) SEM picture of photoelectrochemical etched $In_{0.25}Ga_{0.75}N$ at the elevated temperature in the KOH electrolyte with magnetic stirring. (b) SEM picture of photoelectrochemical etched GaN after a photo-assisted post-treatment. The post-treatment was conducted under 1 mTorr Cl_2 at R.T., with a laser power of 240 mJ/pulse and a repetition rate of 8Hz for 10 mins.

We have also employed PAC and PEC techniques to etch InGaN samples. Like the GaN substrate, PAC etching of InGaN can produce a smooth vertical sidewall. But in the PEC etching, an indium oxide layer grows during etching and causes to slower the etching process. After

stirring the electrolyte at the elevated temperature, we can continue the etching process and obtain a vertical sidewall as shown in Figure 4(a). It is also found that whiskers is formed on the GaN surface after PEC etching[12]. A post-treatment by Cl_2 dry etching under the laser illuminaton, followed by PEC etching, can obtain a much improved smooth surface as shown in Figure 4(b).

CONCLUSIONS

In this study, PAC and PEC techniques are used to etch GaN and InGaN. The photo-assisted cryogenic etching technigue can produce smooth and vertical sidewall features and resolve the yellow luminescence problem. Photoelectrochemical etching of GaN at room temperature is hindered by the formation of indium oxide. After stirring the KOH electrolyte at the elevated temperature, the vertical sidewall features can be achieved. The post-treatment of PEC etched GaN under a Cl_2 ambient with the excimer laser illumination provides an alternative to obtain vertical and smooth etched surfaces.

ACKNOWLEDGEMENT

Financial support was provided by the Opto-Electronics and System Laboratories, Industrial Technology Research Insitute and National Science Council of Republic of China (Contract No. NSC 87-2215-E-007-031). The author would like to acknowledge the Material Science Research Center at National Tsing Hua University for the support of excimer laser.

REFERENCES

[1] A. T. Ping, A. C. Schmitz, M. Asif Khan and I. Adesida, J. Electronic Materials **25**, 825 (1996).
[2] S. J. Pearton, C. B. Vartuli, R. J. Shul and J. C. Zolper, Mater. Sci. Eng. **B31**, 309 (1995).
[3] H. Cho, C. B. Vartuli, S. M. Donovan, J. D. Mackenzie, C. R. Abernathy, S. J. Pearton, R. J. Shul, and C. Constantine, J. Electronic Material **27**, 166 (1998).
[4] M. C. Shih, M. B. Freiler, R. Scarmozzino and R. M. Osgood, Jr., J. Vac. Sci. Technol. **B13**, 43 (1995).
[5] R. T. Leonard and S. M. Bedair, Appl. Phys. Lett. **68**, 794 (1996).
[6] D. R. Lide, CRC Handbook of Chemistry and Physics (Boca Raton: CRC press, 1992), p. 9-129.
[7] J. Neugebauer and C. G. Van De Walle, Appl. Phys. Lett. **69**, 503 (1996).
[8] M. S. Minsky, M. White, and E. L. Hu, Appl. Phys. Lett. **68**, 1531 (1996).
[9] C. Youtsey, I. Adesida and G. Bulman, Appl. Phys. Lett. **71**, 2151 (1997).
[10] R. J. Shul, G. B. McClellan, S. J. Pearton, C. R. Aberbathy, C. Constantine and C. Barratt, Electronics Letters, **32**, 1408 (1996).
[11] H. Cho, J. Hong, T. Maeda, S. M. Donovan, C. R. Abernathy, S. J. Pearton, R. J. Shul, and J. Han, MRS Internet J. Nitride Semicond. Res. 3, 5 (1998).
[12] C. Youtsey, L. T. Romano and I. Adesida, Appl. Phys. Lett. **73**, 797 (1998).

FOCUSED ION BEAM MICROMACHINING OF GaN PHOTONIC DEVICES

Irving Chyr and A. J. Steckl

Nanoelectronics Laboratory, University of Cincinnati
Cincinnati, Ohio 45221-0030 USA, a.steckl@uc.edu

Cite this article as: MRS Internet J. Nitride Semicond. Res. 4S1, G10.7 (1999)

ABSTRACT

Ga^+ and Au^+ focused ion beams (FIB) are used to micromachine GaN films. The GaN micromachining has been studied at energies from 30-90 keV, incident angle from 0-30°, and number of repetitive scans from 10 to 50 scans. Trenches milled in GaN have vertical and smooth side-walls and very smooth bottoms. The micromachining rate was found to be fairly independent of ion dose, ranging from 0.4 to 0.6 $\mu m^3/nC$ for Ga^+ and 1 to 2 $\mu m^3/nC$ for Au^+. This translates into an effective yield of of 6-7 atoms/ion for Ga^+ and 21-26 atoms/ion for Au^+. This represents the highest direct FIB removal yield reported to date. We have also investigated the micromachining of GaN substrate material: c-face sapphire. Using FIB Ga^+, sapphire has an effective yield of ~2-2.5 atoms/ion, or approximately 1/3 of the GaN sputtering yield. For the materials investigated, we found the sputtering yield to be inversely proportional to the strength of the material chemical bond. We also describe the application of the FIB μmachining technique to the fabrication of small period Distributed Bragg Reflector (DBR) mirrors for a short cavity GaN laser structure.

INTRODUCTION

GaN and its alloys are of great interest for visible and UV light emitting devices because of their applications for displays, scanners, printers, optical disks, etc. Recently, commercialized laser diodes[1] have been announced using GaN-based structure grown on sapphire and SiC substrate. Most of the research and development to date is focused on GaN grown on sapphire substrates because of good crystal quality. However, there still remain some fabrication issues concerning sample preparation and processing. In particular, suitable cavity and high reflectivity mirror facets are hard to obtain by conventional processing procedures due to the large misalignment[2] between sapphire and GaN-based materials. Currently, facets are formed by either the cleaving method[3] (which cannot provide lower roughness on the sidewalls), or by dry plasma etching[4] (which generates high ion-induced damage and smooth etched sidewalls). Therefore, it is important to find a simple and efficient processing technique in order to fabricate low mirror loss and mode selection of laser diodes.

Conventional edge-emitting semiconductor lasers fabricated by cleaving result in the low mirror reflectivity in the range of ~0.3-0.4. Even though there are distributed feedback (DFB) or distributed Bragg reflector (DBR)[5,6] in the ends of the laser cavity, the overall mirror reflectivity still remains low. Recently several research groups[7,8,9] reported an alternative method to increase the mirror reflectivity of semiconductor lasers by introducing a short (but deep) stack of DBR grating consisting of multilayers of semiconductor materials and air. This is attractive

Mat. Res. Soc. Symp. Proc. Vol. 537 © 1999 Materials Research Society

since the large refractive index difference between semiconductor materials and air provides a very high reflectivity and reduces the length of cavity at the same time.

The Focused Ion Beam (FIB) technique has been applied to many aspects of microelectronic device fabrication. In particular, FIB is successfully used in the areas of micromachining[10] and ion-induced mixing[11], with applications to photonic components such as waveguides, mirrors, gratings and laser cavity in the GaAs/AlAs and InP materials systems. Recently, there are several groups[12,13] who have applied FIB micromachining to produce flat and smooth mirror facets for GaN laser diodes. Nonetheless, no quantitative analysis of GaN micromachining has been reported to date. In this paper, we present the results on FIB micromachining of GaN and related substrates under various experimental parameters of energy, incident angle and scan strategy. We also apply FIB micromachining for the fabrication of GaN laser with short-period cavity with semiconductor/air DBR mirrors.

EXPERIMENT

Liquid metal ion source (LMIS) of Ga^+ and Au^+ were used with the MBI (MicroBeam Inc.) NanoFab 150 system of FIB. This system has two sets of electrostatic lenses and E×B mass separation. The total emission current was typically set at 3 μA for Ga^+ and 15 μA for Au^+. The target current of Ga^+ was ~170 pA for measuring milling rate, ~220pA for fabricating the waveguides and ~22 pA for grating fabrication. The Au^+ target current was ~185 pA for measuring milling rate. The total dose used in the experiments for the milling rate analysis reported here was kept constant at $1\times10^{18}cm^{-2}$. We used $2.5\times10^{18}cm^{-2}$ for waveguide and gratings. Multiple number of scans with FIB, ranging from 10, 20 and 50, are made to achieve this dose. The GaN micromilling was investigated using Ga^+ ions with energy ranging from 30 to 70 keV, and Au^+ ions from 30 to 90 keV, respectively. The ion beam angle of incidence was varied between 0° (normal incidence) and 30° for Ga^+, while Au^+ is incident to the normal surface of GaN.

The primary GaN material used for milling experiments was grown by hydride vapor phase epitaxy (HVPE) on sapphire substrates. The GaN film was relatively thick (~20μm) which allowed for milling experiments to be performed without encountering any substrate effects. However, since in practice thinner GaN layers are grown on various substrates for fabricating devices, we have investigated the FIB Ga^+ milling for the primary substrate material: c-face sapphire. We fabricated the waveguides and gratings on GaN (thickness = 2 μm), grown on sapphire by MOCVD.

Scanning electron microscopy (SEM) was used to observe the structures of laser cavity, mirror facets, and gratings on GaN samples. Another useful instrument to measure the depth profiles of milled pattern is the Atomic Force Microscope (AFM), which measures detailed information in the milling depth, side-wall angles and roughness of surface and bottom of the GaN pattern. AFM images and data were obtained by using Nanoscope II and Dimension 3100 systems from Digital Instruments.

RESULTS

Fig. 1(a) shows an SEM microphotograph of a GaN pattern micromilled using 90kV Au^+ FIB with a dose of $1\times10^{18}cm^{-2}$, at normal incidence, and 10 FIB scans. The total area of the pattern FIB-micromilled into GaN is 200 μm^2, which requires approximately 30-35 min exposure for a $1\times10^{18}\,cm^{-2}$ dose. The milling depth of GaN experiments ranged between ~0.6 to 1 μm for Ga^+, and ~2.3 to 3 μm for Au^+. The "writing" strategy is that of serpentine scan,

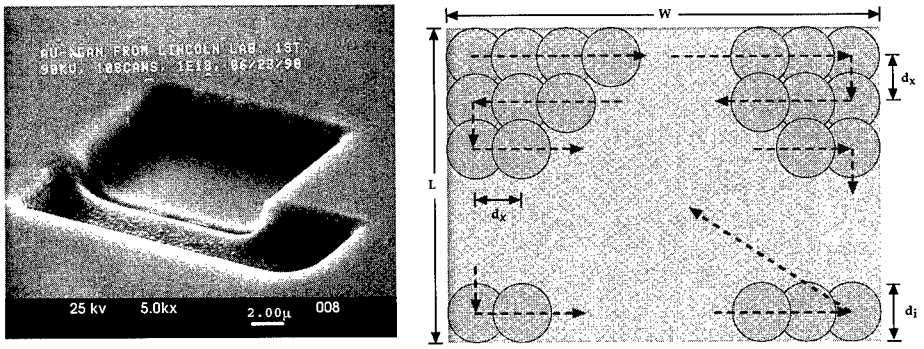


Fig. 1 The Ga^+ FIB micromachined pattern: (a) SEM photograph of GaN pattern micromachined using 90kV Au^+ FIB with a dose of $1\times10^{18}cm^{-2}$, at normal incidence, and 10 scans; (b) schematic diagram of serpentine scan.

illustrated in Fig. 1(b), where the scan direction is reversed after each pass to minimize redeposition effects. A sharply defined milled region is obtained, with a uniform depth, a smooth milled surface, and with minimum redeposition of material. A deeper trench is observed where the two rectangles of the pattern have a slight overlap.

In Fig. 2, we compare the Ga^+ milling rate as a function of off-axis angle from the normal target surface at different energy from 30 to 70 keV and 10 FIB scans. We found that the milling rate increases with the Ga^+ incident angle in all cases. For the normal angle (i.e. 0°), increasing the ion energy results in an increasing the milling rate. For 15° and 30° the incident angles, the milling rate is weakly independent of ion energy. Fig. 3 shows the effect of changing the number of scans on the milling rate for various incident angles at a fixed ion energy of 50 keV. The milling rate is independent of FIB scans at 0°. For angles of 15° and 30°, the milling rate becomes larger as the number of FIB scans increases. A similar effect was also observed at 30 and 70 keV.

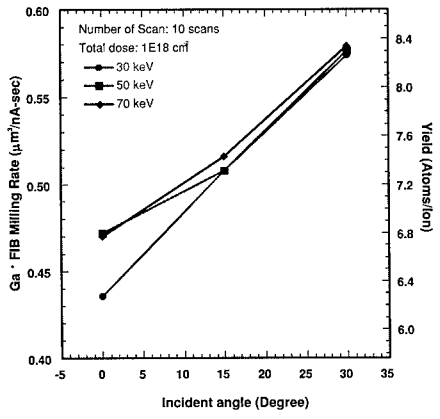


Fig. 2 Ga^+ milling rate of GaN versus angle of incidence for different energies in 10 FIB scans. (total dose: $1\times10^{18}cm^{-2}$)

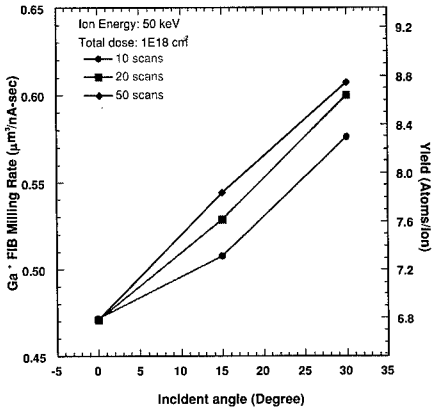


Fig. 3 Ga^+ milling rate of GaN versus angle of incidence for different scan conditions at 50 keV. (total dose: $1\times10^{18}cm^{-2}$)

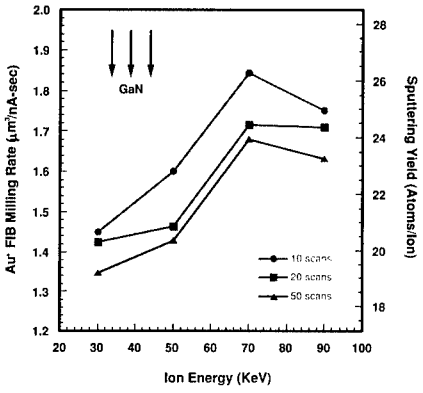


Fig. 4 Au^+ milling rate of GaN versus ion energy for different scan conditions in the normal incidence. (total dose: $1\times10^{18}cm^{-2}$)

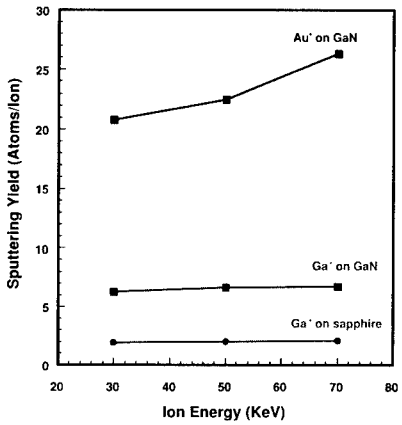


Fig. 5 Comparison of Ga^+ and Au^+ milling rate of GaN and sapphire as a function of ion energy. (total dose: $1\times10^{18}cm^{-2}$, normal incidence, 10 scans)

The milling rate of Au^+ ions for energies from 30 to 90 keV and different repetitive scans under the condition of normal incident angle (0 degree) is observed in Fig. 4. The milling rate increased with ion energy increasing from 30 to 70 keV, decreased at 90 keV. For Au^+ ion, the physical limitation of milling rate is at 70 keV. The reason is that for most of ion energy over 70 keV, the ions will be implanted into the target instead of milling the target. The increase of scan speed (i.e. number of scans) reduces the milling rate for all energies. In Fig. 5, we compare the sputtering yield of Au^+ ions for GaN with Ga^+ ion for GaN and sapphire. As expected, the Au^+ ion which is heavier than Ga^+ ion has a much higher sputtering yield. For example, the sputtering yield of Au^+ ion at conditions of 70 keV and 10 FIB scans is 26 atoms/ion, which is almost 4 times larger than Ga^+ ion under the same conditions. The drawbacks of Au^+ FIB milling add more redeposition on the side-wall and a wider beam diameter. From Fig. 1(a), we can see that there is some redeposition on the side-wall and bottom surface of the milled pattern. The Ga^+ sputtering yield of GaN is about 3 times larger than that of sapphire substrate. The fact that the GaN milling rate is always higher than sapphire is of assistance in terminating the milling process without removing excessive amounts of substrate material. We have observed that an increase in scan speed causes a decrease in sputtering yield of Au^+ ions at normal incidence, which is similar to the same result with Ga^+ ions shown in Fig. 3.

We have applied FIB milling to the fabrication of short cavity lasers which utilize air/semiconductor DBR grating mirrors. With this DBR structure, the mirrors formed by grating structures can offer better reflectivity than conventional cleaved mirrors. In Fig. 6, we show the SEM photographs for the DBR gratings and short cavity laser structures fabricated in GaN using Ga^+ ion FIB micromachining. The cavity length is 120 μm and the cavity width is 18 μm, shown in Fig. 6(a). The DBR grating shown in Fig. 6(b) is a 5th order grating, with a grating period of 675 nm and spacing of 200 nm. The SEM photographs indicate that FIB is a very precise technique for the fabrication of DBR gratings and other optoelectronic and photonic applications in GaN.

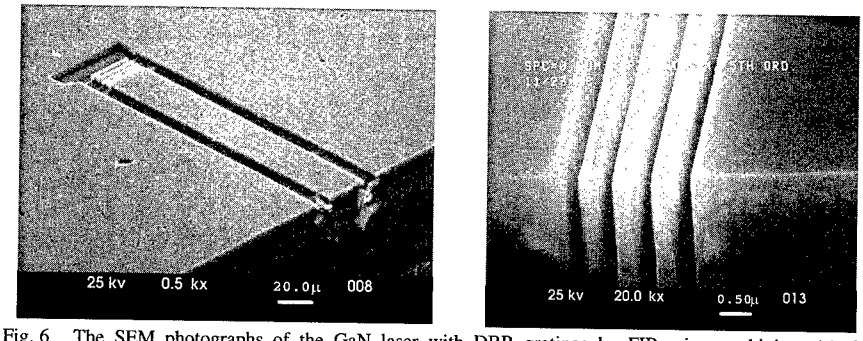


Fig. 6 The SEM photographs of the GaN laser with DBR gratings by FIB micromachining: (a) the overview of laser structure, cavity length is 120 μm; (b) the 5th order grating structure, the period is 675 nm and spacing is 200 nm..

CONCLUSION

In conclusion, we have reported the Ga^+ and Au^+ FIB micromachining characteristics of GaN. We have compared the milling rate and sputtering yield of GaN by two potential ion species, Ga^+ and Au^+, under various experimental conditions (ion energy, numbers of FIB scans, angle of incidence). The high FIB milling rate of GaN (significantly higher than that of common sapphire substrate) has positive implications for future fabrication of GaN devices. We also demonstrated that FIB micromachining has the capability to fabricate DBR gratings in order to obtain better reflectivity for laser diodes. We believe that FIB micromachining is a very promising technique for GaN laser fabrication. The authors gratefully acknowledge the HVPE GaN material provided by R. Molnar and the support of this work by MRL/NSA.

REFERENCES

[1] S. Nakamura, T. Mukai, and M. Senoh, Appl. Phys. Lett. **64**, 1678 (1994).

[2] J. Edgar, J. Mater. Res. **7**, 235 (Jan. 1992).

[3] M. A. Khan, D. T. Olson, J. M. Van Hove, and J. N. Kuznia, Appl. Phys. Lett. **58**, 1515 (1991).

[4] F. Binet, J. Y. Duboz, N. Laurent, C. Bonnat, P. Collot, F. Hanauer, O. Briot, and R. L. Aulombard, Appl. Phys. Lett. **72**, 960 (1998).

[5] G. M. Smith, J. S. Hughes, M. L. Osowski, D. V. Forbes, and J. J. Coleman, Electron. Lett. **30**, 30 (1990).

[6] D. Hofstetter, H. P. Zappe, J. E. Epler, and J. Söchtig, Electron. Lett. **30**, 1858 (1990).

[7] T. Baba, M. Hamasaki, N. Watanabe, P. Kaewplung, A. Matsutani, T. Mukaihara, F. Koyama, and K. Iga, Jpn. J. Appl. Phys. Part 1, **35**(2B), 1390 (1996).

[8] Y. Yuan, T. Brock, P. Bhattacharya, C. Caneau and R. Bhat, IEEE Photonics Technol. Lett., **9**(7), 881 (1997).

[9] T. F. Krauss, O. Painter, A. Scherer, J. S. Roberts, and R. M. De La Rue, Opt. Eng., **37**(4), 1143 (1998).

[10] L. R. Harriott and H. Temkin, Chapter 6 in *Integrated Optoelectronics*, edited by M. Dagenais, R. F. Leheny, and J. Crow, (Academic Press, New York, 1995).

[11] A. J. Steckl, P. Chen, H. E. Jackson, A. G. Choo, X. Cao, J. T. Boyd, and M. Kumar, J. Vac. Sci. Technol. B**13**, 2570 (1995).

[12] T. Ito, H. Ishikawa, T. Egawa, T. Jimbo, M. Umeno, Jpn. J. Appl. Phys. Part 1, **36**(12B), 7710 (1997).

[13] H. Katoh, T. Takeuchi, C. Anbe, R. Mizumotos, S. Yamaguchi, C. Weitzel, H. Amano, I. Akasaki, Y. Kaneko, N. Yamado, Jpn. J. Appl. Phys. Part 2, **36**(4B), L444 (1998).

Part XI

Rare-Earth Doping and Optical Emission

LUMINESCENCE FROM ERBIUM-DOPED GALLIUM NITRIDE THIN FILMS

J. M. Zavada‡, Myo Thaik*, U. Hömmerich*, J. D. MacKenzie**, C. R. Abernathy**, F.Ren**, H. Shen***,, J. Pamulapati***, H. Jiang†, J. Lin†, R.G. Wilson†

‡U.S. Army European Research Office, London, UK NW1 5TH; *Hampton University, Department of Physics, Research Center for Optical Physics, Hampton, VA 23668; **University of Florida, Department of Materials Science and Engineering, Gainesville, FL 32611; ***U.S. Army Research Laboratory, Adelphi, MD, 20783; Kansas State University, Department of Physics, Manhattan, KN; †Consultant, Stevens Ranch, CA 91381
E-mail: jzavada@army.ehis.navy.mil

Cite this article as: MRS Internet J. Nitride Semicond. Res. 4S1, G11.1 (1999)

ABSTRACT

The III-V nitride semiconductors appear to be excellent host materials for optical device applications involving thin films doped with rare earth atoms. In particular, GaN epilayers doped with Er ions have shown a highly reduced thermal quenching of the Er luminescence intensity from cryogenic to elevated temperatures. The remarkable thermal stability of the light emission may be due to the large energy bandgap of the material, as well as to the optical inactivity of material defects in the GaN film. In this paper we present recent developments concerning the luminescence characteristics of Er-doped GaN thins films. We have used two methods for doping GaN films with Er ions, ion implantation and in-situ incorporation during gas source metal-organic molecular beam epitaxy (MOMBE). Bandedge (at ~ 0.34 μm) and infrared (at ~ 1.54 μm) photoluminescence (PL) spectra have been measured for both types of Er-doped GaN films. Considerably different emission spectra have been observed depending upon the incorporation method and the heat treatment procedure. In situ Er-doped GaN layers have been processed into hybrid light emitting devices and emission spectra at 1.54 μm have been measured.

Erbium in Semiconductors and Thermal Quenching

The optical properties of rare earth ions in insulating materials have been extensively studied for applications in solid state lasers and optical fiber amplifiers [1]. Solid state lasers, such as Nd^{3+}:YAG, are based on the 4f intra-subshell transitions of the rare earth trivalent ions (RE^{3+}) which exhibit a very stable lasing wavelength and minimum temperature dependence. Because of these characteristics, such lasers have found widespread applications in laboratory and military systems. Er-doped silica fibers are being used for amplification of optical signals in wavelength division multiplexing (WDM) communication systems operating at 1.54 μm and Pr-doped fibers are being developed for use at 1.3 μm [2].

Investigations of the optical properties of rare earth-doped III-V semiconductors have begun relatively recently. Beginning with the work of Ennen et al. in 1983 [3], the luminescence of rare earth ions in III-V compound semiconductors has received considerable attention. The main goal of this work has been to develop electrically pumped optical sources and amplifiers for use in optical communication systems. Studies of rare earth ions in a variety of different semiconductors have been conducted [4,5,6]. Due to the importance of the 1.54 μm region for optical communications, Er has been the main rare earth element to be investigated.

Mat. Res. Soc. Symp. Proc. Vol. 537 © 1999 Materials Research Society

Favennec et al. studied the dependence of the emission intensity of the Er^{3+} ions on the bandgap of the host semiconductor and on the sample temperature [7]. Several different semiconductors were implanted with Er^{+} ions and the emission intensity was measured at different temperatures. It was found that the intensity decreased at higher temperatures. This thermal quenching of the emission intensity was more severe for the smaller bandgap materials, such as Si and GaAs. The wide bandgap II-VI compounds, such as ZnTe and CdTe, exhibited the least temperature dependence.

Since the wider bandgap semiconductors lead to less thermal quenching of the Er^{3+} emission, the III-V nitride alloys appear to be especially promising host materials for rare earth doping. These alloys have a bandgap ranging from 1.9 eV for InN to 3.4 eV for GaN and 6.2 eV for AlN. However, due to a lack of a lattice matched substrate, present III-V nitride epilayers contain a high density of dislocation defects and various impurity elements. Nevertheless, very encouraging results have been obtained with Er-doped III-V nitride materials.

Erbium Doping Methods

Several different methods have been used for incorporating Er atoms into III-V semiconductor materials, mainly ion implantation and epitaxial growth. Each method presents certain advantages as well as difficulties. Apparently, there are no reports of Er incorporation into these semiconductor materials during bulk growth or by diffusion. Ion implantation has been widely used in processing integrated electronic circuits and optoelectronic devices. Because this method is a non-equilibrium process, it is not limited by solubility constraints or by surface chemistry. Wilson et al. [8] were the first to introduce Er into GaN and AlN materials using ion implantation. They observed strong infrared luminescence centered at 1.54 μm. However, co-implantation with O and subsequent furnace annealing was needed to achieve this luminescence. Subsequently, several other research groups used ion implantation to dope III-N semiconductors with Er atoms [9,10,11].

Three different methods of epitaxial growth have been used successfully for doping III-N semiconductors with Er atoms: gas source Gen II metal-organic molecular beam epitaxy (MOMBE) [12]; hydride vapor phase epitaxy (HVPE) [11], and solid source molecular beam epitaxy (MBE) [13]. However, with each of these techniques, there have been difficulties incorporating Er atoms into the epilayers and obtaining optically active centers. The maximum concentration of Er in these epilayers has been on the order of 10^{19} cm^{-3}. Nevertheless, high quality epilayers, doped with Er ions, have been achieved and good luminescence characteristics have been observed.

Optical Excitation Spectroscopy

Photoluminescence (PL) spectroscopy has been the main optical technique used to characterize the emission of Er-doped III-N semiconductor materials. This technique involves optical excitation of the Er^{3+} ions and measurement of the spectrum of the light emission as a function of intensity and energy. In a simplified view, optical excitation, at above-bandgap energy, leads to creation of electron-hole pairs. Some of the electron-hole pairs may transfer energy to the Er^{3+} ions, exciting the 4f-electrons to higher energy states and resulting in optical emission. Most of the PL measurements of Er-doped semiconductors have involved use of a laser operating at an energy above that of the bandgap of the host semiconductor. This corresponds to an indirect excitation of the Er^{3+} ions by electron-hole pairs. A few experiments have been carried out in

which the Er^{3+} ions have been excited directly by the optical pump radiation [14]. In this case, the Er^{3+} ions are excited directly by the optical pump, with the energy of the laser radiation equal to that of one of the higher energy states of the Er^{3+} ion. Defects and impurities in the material serve as non-radiative recombination centers which can reduce the light emission. Recent studies [15,16] have shown that defects can also serve as absorption centers transferring below-bandgap optical energy to the Er^{3+} ions, resulting in emission at 1.54 μm. The exact mechanism for transferring optical energy to the Er^{3+} ions, either through electron-hole pairs or by defects is not well understood at present.

We performed a series of experiments to determine the thermal quenching of luminescence in an Er-doped GaN films [15]. The GaN films, which were grown on sapphire substrates, were co-implanted at room temperature with Er and O ions. The Er^{3+} emission in the region of 1.54 μm was measured over a range of temperatures from 13 - 550 K. For temperature-dependent measurements between 15 and 300 K, the Er-implanted GaN sample was placed onto a cold finger of a closed-cycle helium refrigerator. For measurements above 300 K, a home-made heating element was used. The sample was excited with above-bandgap radiation, using a HeCd laser operating at 325 nm, and with below-bandgap radiation from an Ar laser operating at 488 nm. In Fig. 1 (a) are shown the high-resolution PL spectra at 300 and 550 K of the sample pumped with above-bandgap excitation. There were only minor changes in the PL spectra between 300 and 550 K. The full width half maximum (FWHM) of the PL spectrum at 300 K was ~ 80 nm, suggesting inhomogeneous broadening of the emission. This broadening indicated that the Er^{3+} ions occupy a range of sites, with slightly different atomic configurations, in the GaN host. The integrated PL intensity of the luminescence was found to be nearly constant over the entire range of measurement temperatures, see Fig. 1 (b). Relative to its value at 15 K, the integrated PL intensity at 550 K decreased by only about 10 %.This remarkable temperature stability of the Er^{3+} luminescence is the best reported data from any Er-doped semiconductor,

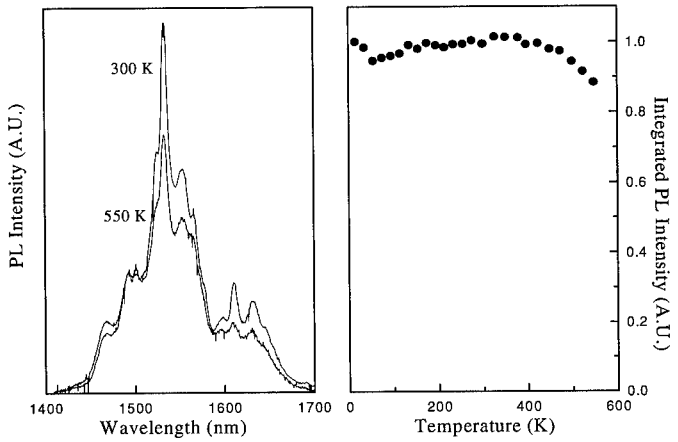


Figure 1: (a) High-resolution Er^{3+} PL spectra, taken at 300 and 550 K, of an Er-implanted GaN sample using above-bandgap excitation. (b) The integrated PL intensity measured between 15 and 550 K

including Er-doped SiC [17]. In a chathodoluminescence study of Er+O co-implanted GaN films, Qiu et al. found that the integrated intensity decreased by less than 5 % as the temperature was raised from 6K to 300 K [18]. These results demonstrate that Er-doped GaN is an attractive material for high temperature optoelectronic applications.

In Fig. 2 (a) are shown the high-resolution PL spectra at 300 and 550 K of the sample with below-bandgap excitation. This excitation method corresponds to pumping the Er^{3+} ions through the broad, defect-related, absorption band. There were significant changes in the PL spectrum between 300 and 550 K. In addition, above-bandgap and below-bandgap excitation resulted in considerably different PL spectra as shown in Figs. 1 (a) and 2 (a). Depending upon the excitation method, different subsets of Er^{3+} ions are excited leading to distinct PL spectra. The full width half maximum (FWHM) of the PL spectrum at 300 K was ~ 50 nm, which was narrower than that in Fig. 1 (a). There was also a large change in the integrated PL intensity over the range of measurement temperatures, as indicated in Fig. 2 (b). Relative to its value at 15 K, the integrated PL intensity at 550 K decreased by about 50 %. While this behavior is not as good as the data shown in Fig. 1 (b), this reduced thermal quenching is still better than that reported from any other Er-doped III-V semiconductor.

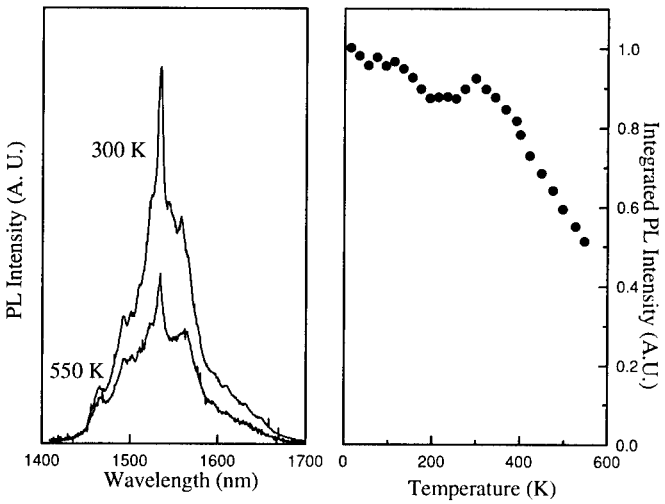


Figure 2: (a) High-resolution Er^{3+} PL spectra, taken at 300 and 550 K, of an Er-implanted GaN sample using below-bandgap excitation. (b) The integrated PL intensity measured between 15 and 550 K.

We have measured bandedge PL spectra for both the GaN films implanted with Er and for the GaN films doped with Er during MOMBE growth. In general, there is little or no PL signal after implantation. With annealing, under a N ambient, there is a slight recovery of the bandedge PL signal. However, even after annealing at 950 C, the Er-implanted films contain highly defective surface regions with only weak PL signals. Hansen et al. reported similar results with Er-implanted GaN films [10]. These data are consistent with studies by Zolper et al. on Si-implanted

GaN films [19]. Higher annealing temperatures are required before a significant recovery of the bandedge PL signal occurs. In contrast, there was a strong bandedge PL signal from the GaN films doped with Er during MOMBE growth. The PL spectra had a peak at 3.28 eV which is quite different from the PL spectra from undoped GaN films.

Light Emitting Device

Recently, we have demonstrated a hybrid light emitting device in which an Er-doped III-V nitride film is optically pumped by a green InGaN LED to produce emission at 1.54 μm. In these experiments, a Nichia InGaN LED, with a peak emission at 520 nm was used to excite the Er^{3+} ions in a GaN film, grown on sapphire by MOMBE. The epoxy bubble of the InGaN LED was cut and polished to provide a flat surface near the LED top contact. The GaN film/sapphire sample was place in close proximity to the LED, as shown in the inset in Fig. 3. The spectrum of the Er-related luminescence is also shown in this figure. While the emission at 1.54 μm is weak, the spectrum is similar to that in Fig. 2 (a). A green InGaN LED was used in this hybrid device, since

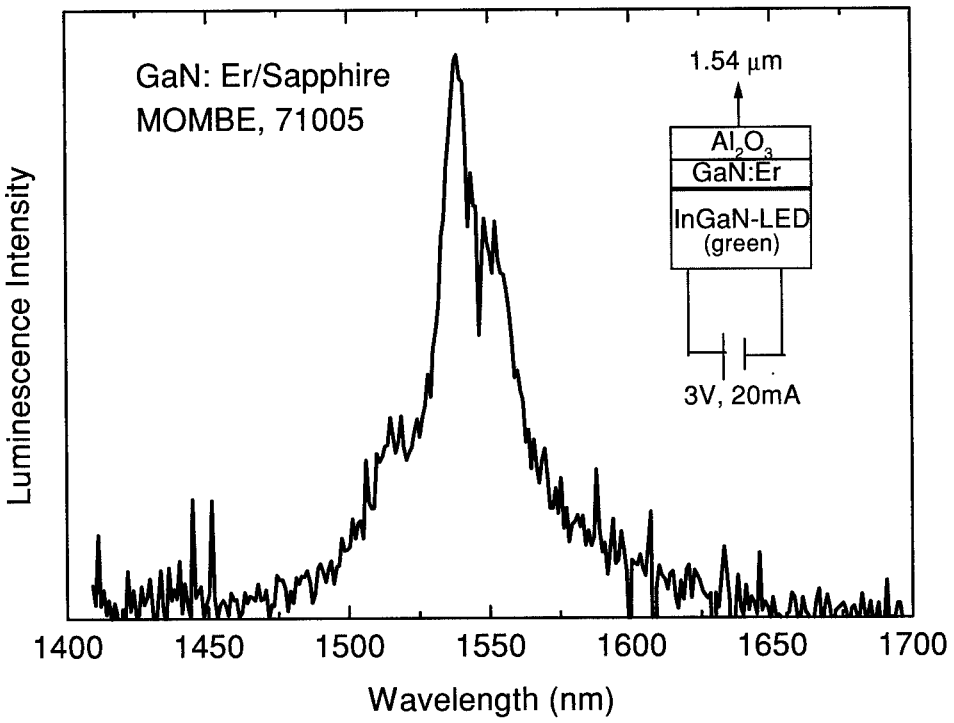


Figure 3: Temperature dependence of the integrated PL intensity from in-situ Er doped GaN for above and below gap excitation.

a absorption spectrum for the film indicated a strong absorption in this region, both with the sharp line transition at 525 nm and with the broad defect-related absorption. The luminescence at 1.54 μm was collected through the sapphire substrate. While the resulting emission at 1.54 μm was

weak, in comparison with the PL studies, it does demonstrate that the electroluminescence of an InGaN LED can be used to excite the Er centers in a GaN film. Furthermore, a monolithic semiconductor device, in which an Er-doped GaN film is grown directly on top of an InGaN LED structure, appears feasible. Questions concerning overall efficiency and light collection schemes need to be further addressed.

Summary

Considerable progress has been made in the past ten years in understanding the optical properties of Er-doped III-V semiconductors. Luminescence of Er^{3+} ions in many III-V semiconductors has been observed. A number of experiments have shown that the use of wide gap semiconductors, such as the III-V nitrides, reduces the thermal quenching of the Er^{3+} luminescence. However, difficulties remain concerning the incorporation of Er atoms in the III-V nitride materials and the proper processing conditions necessary for optical activation. Experimental evidence indicates that the Er atoms occupy a variety of sites within the III-N crystal. Furthermore, different Er centers yield different emission spectra and different thermal quenching characteristics. Due to the intense current research in III-V nitride semiconductors for blue light emission, major improvements in the crystal quality and in the processing technology of these materials are very likely to occur. Such advances will assist efforts to develop devices based on III-V nitride semiconductors doped with Er ions, making possible a new class of optoelectronic components for optical communication and display systems.

REFERENCES

1. W. Koechner, *Solid State Laser Engineering,* Springer Verlag, 3rd Ed. (1992).
2. E. Desurvire, J. R. Simpson, and P. C. Becker, Opt. Lett., **12**, 888 (1987).
3. H. Ennen, J. Schneider, G. Pomrenke, and A. Axmann, Appl. Phys. Lett. **43** 943 (1983).
4. *Rare Earth Doped Semiconductors I* , Materials Research Society Proceedings, Vol. **301** (G. S. Pomrenke, P. B. Klein and D. W. Langer, eds.) (1993).
5. J. M. Zavada and D. Zhang, Solid-St. Electron. **38** 1285 (1995).
6. *Rare Earth Doped Semiconductors I* , Materials Research Society Proceedings, Vol. **422** (S. Coffa, A. Polman, and R. N. Schwartz, eds.) (1996).
7. P. N. Favennec, H. L'Haridon, M. Salvi, D. Moutonnet, and Y. L. Guillou, Electron. Lett., **25,** 718 (1989).
8. R. G. Wilson, R. N. Schwartz, C. R. Abernathy, S. J. Pearton, N. Newman, M.Rubin, T. Fu, and J. M. Zavada, Appl. Phys. Lett. **65** 992 (1994).
9. J. T. Torvik, R. J. Feuerstein, J. I. Pankove, C. H. Qiu, and F. Namavar, Appl. Phys. **69** 2098 (1996).
10. S. Kim, S. J. Rhee, D. A. Turnbull, E. E. Reuter, X. Li, J. J. Coleman, and S. G. Bishop, Appl. Phys. Lett. **71** 231 (1997).
11. D. M. Hansen, R. Zhang, N.R. Perkins, S. Safvi, L. Zhang, K. L. Bray, and T. F. Keuch, Appl. Phys. Lett. **72** 1244 (1997).
12. J. D. MacKenzie, C. R. Abernathy, S. J. Pearton, U. Hömmerich, X. Wu, R. N. Schwartz, R. G. Wilson, and J. M. Zavada, Appl. Phys. Lett. **69** 2083 (1996).
13. A. J. Steckl and R. Birkhahn, Appl. Phys. Lett. **73** 1701 (1998).
14. J. T. Torvik, R. J. Feuerstein, C. H. Qiu, M. W. Leksano, F. Namavar, and J. I. Pankove, Mat. Res. Soc. Symp. Proc. **422** 199 (1996).

15. Myo Thaik, U. Hömmerich, R. N. Schwartz, R. G. Wilson, and J. M. Zavada, Appl. Phys. Lett. **971** 2641 (1997).
16. S. Kim, S. J. Rhee, D. A. Turnbull, E. E. Reuter, X. Li, J. J. Coleman, S. G. Bishop, and P. B. Klein, Appl. Phys. Lett. **71** 2662 (1997).
17. W. J. Choyke, R. P. Devaty, L. I. Clemen, M. Yoganathan, G. Pensl, and Ch. Hassler, Appl. Phys. **65** 1668 (1994).
18. C. H. Qiu, M. W. Leksono, J. I. Pankove, J. T. Torvik, R. J. Feuerstein, and F. Namavar, Appl. Phys. **66** 562 (1995).
19. J. C. Zolper, M. H. Crawford, J. S. Williams, H. H. Tan and R. A. Stall, Nucl. Instrum. and Methods B 127/128 467 (1997).

RBS LATTICE SITE LOCATION AND DAMAGE RECOVERY STUDIES IN GaN

E. Alves*, M.F. DaSilva*, J.C. Soares*, J. Bartels**, R. Vianden**, C.R. Abernathy***, S.J. Pearton***

*ITN, Sacavém, Portugal

**ISKP, University of Bonn, D-53115 Bonn, Germany, vianden@iskp.uni-bonn.de

***Dept. Materials Science and Engineering, University of Florida, Gainesville, FL, USA

Cite this article as: MRS Internet J. Nitride Semicond. Res. 4S1, G11.2 (1999)

Abstract

Erbium was implanted with 160 keV at doses between $5x10^{14}$ and $5x10^{15}$ at/cm^2 into (0001) epitaxial GaN on sapphire and annealed at various temperatures between 600° and 1000° C. The RBS/Channeling technique was used to analyze the damage recovery during different annealing steps and to determine the lattice location of the implanted Er. For a sample implanted with $5x10^{14}$ and annealed for 30 min at 600° C a complete overlap of the Er and Ga angular scans across the <0001> axis was observed, indicating that 100% of Er occupies substitutional sites. Measurements along the $<10\bar{1}1>$ channel show that Er is located on Ga sites. The damage recovery was slightly better for the samples co-implanted with the same dose of Oxygen in an overlapping profile (E=25 keV). However, a complete recovery of the damage caused by the implantation was not achieved. Samples implanted with higher Er and O doses ($5x10^{15}$ at/cm^2) and at the same energies as above were annealed at 600° for 30 min and at 900°, 1000° C for 120 s using a proximity cap. The higher dose caused an almost complete amorphisation of the surface layer. After annealing indications of epitaxial regrowth were observed, however, the substitutional fraction remains substantially lower and the damage recovery is less complete.

Introduction

GaN and other wide gap nitrides are materials with a large potential for high temperature electronics and optoelectronics applications. However, for the integration of GaN into circuits an adequate structuring technique is necessary. At present, the standard technique for selectively doping semiconductors and thus creating device structures is ion implantation. It unavoidably introduces damage to the crystal which has to be annealed in order to achieve electrically or optically active doping. Whereas in standard semiconductors like Si these procedures are well understood the situation in GaN is more complicated. The strong bonding of this material on one hand ensures a high resistance to lattice damage and amorphisation on the other hand it considerably hampers the epitaxial regrowth on the underlying undamaged crystal lattice after an implantation. It is therefore interesting to study the behavior of impurities after implantation as well as the general recovery of the GaN lattice. In the present study the lattice location of Er implanted in GaN and the possible influence of coimplanted Oxygen on the Er behavior was investigated. Doping of GaN with Er during growth or by implantation has been intensively studied mainly in photoluminescence measurements [1, 2] due to the potential application of this impurity in optoelectronics. The intra 4f shell transitions at a wavelength of 1.54 μm, which coincides with a minimum in loss in silica optical fibers, makes Er an interesting, optically active ion in devices such as lasers, optical amplifiers and optically pumped glass fibers [3].

Mat. Res. Soc. Symp. Proc. Vol. 537 © 1999 Materials Research Society

Experiment

Samples were cut from high quality (0001) GaN epilayers of 4μm thickness grown by the MOCVD technique on sapphire substrates at the University of Florida. In some cases also commercially available material (CREE, 1.5μm) was used. The unintentional n-type background doping was of the order of 10^{16} cm^{-3}. The GaN samples were implanted at room temperature with doses of D = $5x10^{14}$ Er^+/cm^2 and $5x10^{15}$ Er^+/cm^2 at an energy of 160 keV. The measured implantation range (R_p) was about 40 nm in agreement with TRIM95 [4] calculations. Some samples were further implanted with Oxygen with the same doses, respectively. The energy of the O ions was chosen to be 25 keV in order to obtain an overlap of the O and Er profiles. After the implantation all samples were annealed between graphite strips at various temperatures under flowing nitrogen using another GaN sample as a proximity cap.

RBS/channeling studies were performed with a 1 mm diameter collimated beam of 2 MeV He^+ ions. The backscattered particles were detected at 140° and 180°, with respect to the beam direction, using silicon surface barrier detectors located in the standard IBM geometry and with resolutions of 13 and 16 keV, respectively. The angular scans were carried out using a two-axis goniometer and, in order to avoid radiation effects due to the analyzing beam, a fresh spot for each measurement was used. To reduce the pile-up effect which would degrade the sensitivity for the Er signal, the beam current was kept below 2 nA. Full angular scans of the axial directions were recorded for the <0001> and <10$\bar{1}$1> axes. The experimental results were compared to computer simulations which were carried out using a Monte Carlo code [5]. The wurtzite structure, not part of the original code, was incorporated in order to simulate the GaN angular curves.

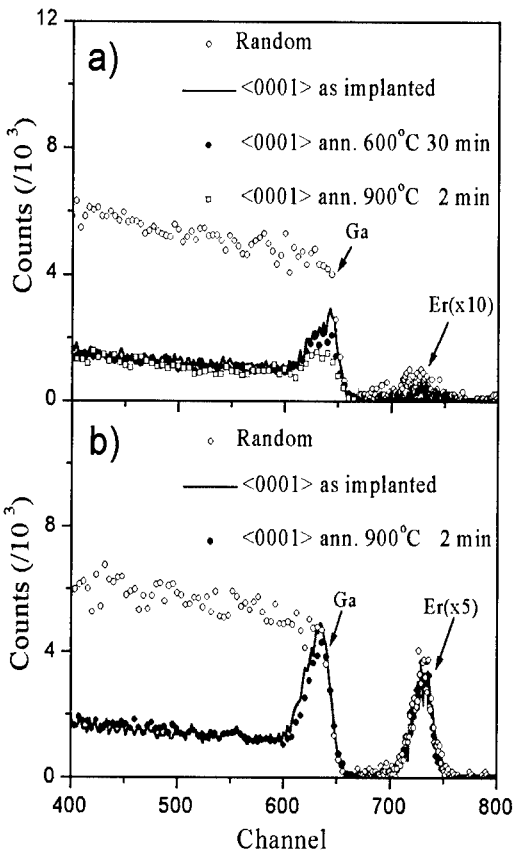


Figure 1: Random and <0001> aligned RBS spectra for GaN samples implanted with two different doses of Er ions after annealing at different temperatures. a) D = $5x10^{14}$ Er^+/cm^2, b) D = $5x10^{15}$ Er^+/cm^2

Results

A. Damage annealing

Figure 1 shows the random and <0001> aligned RBS spectra of the samples (CREE, 1.5 μm) implanted with $5x10^{14}$ cm^{-2} (Fig. 1a) and

$5x10^{15}$ cm^{-2} (Fig. 1b). As can be seen the amount of damage created by the implantation of the higher dose is just enough to produce an overlap of the random and aligned spectra in the whole implanted region (55nm). This result, also observed in other semiconductors, is an indication of the amorphisation of this region. In the present case it allows to conclude that a dose of D = $5x10^{15}$ Er^{+}/cm^{2} at 160 keV is just above the threshold dose for the amorphisation of GaN at 293 K. This is slightly lower than in the case of Si implantation into GaN [6] but, due to the higher mass of Er, not unexpected. Essentially the same features were observed in the samples coimplanted with oxygen.

A mild annealing at 600°C for 30 min reduces the damage in the 4 μm thick sample almost to the virgin level (of χ_{min} = 2%), whereas in the 1.5 μm sample implanted with the lower dose of Er only a slight decrease of the damage is observed (Fig. 1a). The same annealing procedure has little effect on the damage of the samples implanted with $5x10^{15}$ ions/cm^{-2} (Fig. 1b). For both Er doses the results show that the coimplantation of O does not influence the recovery process significantly at this temperature. A further small decrease of the damage peak in all the samples after annealing at 900° C can be observed (Fig. 1b). The small narrowing of the Ga peak in figure 1b indicates that some epitaxial regrowth of the amorphous layer occurs at this temperature. Further regrowth takes place at 1000° C yielding values of χ_{min} = 12% and χ_{min} = 60% for the sample with the lowest and the highest dose, respectively. An extension of the annealing time at 1000° C to 30 min leads to an increase of the Ga surface peak for the samples with the lowest Er and O doses, probably as a consequence of surface decomposition. During the whole annealing program the Er profile in both Er + O implanted samples remained unchanged. A different behavior is observed for the samples implanted with Er only. Here at the highest annealing temperatures the Er peak shows a narrowing towards the surface whereas the damage peak is reduced similarly to the other samples. This can be taken as an indication that the presence of Oxygen in the vicinity of the Er impurity contributes to the stabilization of Er in substitutional positions. Generally the results illustrate the difficulty to anneal the damage completely, even for low implantation doses.

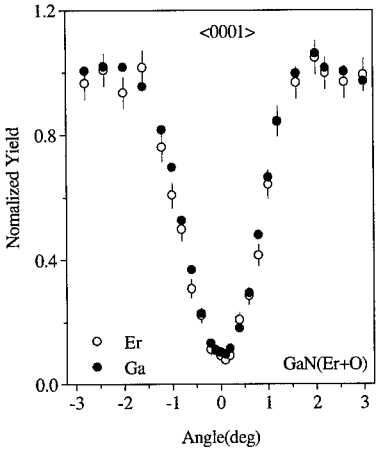


Figure 2: Angular scan through the <0001> axis of the GaN wurtzite lattice for a sample (Univ. Florida) implanted with Er and O at a dose of $5x10^{14}$ cm^{-2} each and annealed at 600° C for 30 min.

B. Lattice location

Angular scans through the <0001> axis immediately after the lower dose implantations show minimum yield values of 40% for the samples implanted with Er and Er + O. For these measurements the Ga window was set from 20 to 80 nm, incorporating all the Er implanted depth region. The corresponding Er scans show a complete overlap with the Ga scans indicating that Erbium is subjected to exactly the same disorder caused by the implantation as the Ga sublattice.

In figure 2 a detailed angular scan through the <0001> axis for the sample grown at Florida University implanted with $5x10^{14}cm^{-2}$ Er + O after implantation and a mild annealing for 30 min at 600°C is shown. The temperature was chosen because it is easily reached with conventional annealing set-ups. A minimum yield of χ_{min} = 10% is derived which can be compared to the minimum yield of a virgin sample of χ_{min} = 2%. Again the Er and Ga curves fully overlap which is an indication that Er is occupying a Ga site. The large fraction of Er in substitutional sites after the 600° C annealing step agrees well with a hyperfine interaction study on the incorporation of the transition metal Hf into GaN after implantation [7]. Also there it was observed that the implantation damage around the Hf impurity was annealed to a large extent at 600° C. This effect was attributed mainly to the restoration of the N sublattice.

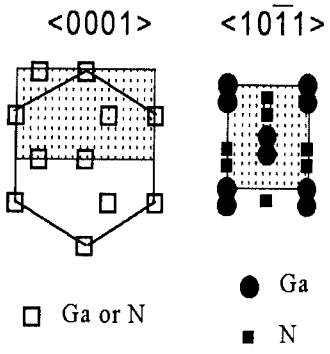


Figure 3: Projections of the atomic position of Ga and N in the GaN wurtzite lattice as seen along the <0001> and the <10$\bar{1}$1> axes.

In samples obtained from CREE the 600° C annealing step produces a decrease of 10% in the number of atoms in substitutional sites for the sample containing only Er while for the sample coimplanted with O no changes were observed. The annealing at 900°C leads to a further reduction of the substitutional fraction and a narrowing on the bottom of the angular curve of Er for the Er implanted sample while for the sample coimplanted with O Er remains in the Ga site. The observed narrowing could be due to the association of Er with defects, which lead to a slight displacement of the Er atoms from the ideal substitutional positions.

The assumption made above that Er is located on the Ga sites could be proven by a scan across the <10$\bar{1}$1> axis. Contrary to the <0001> axis, where we have mixed rows of Ga and N, in the <10$\bar{1}$1> direction we have pure Ga and N rows as depicted in figure 3. The different atomic numbers of Ga and N result in different steering potentials for the respective rows leading in turn to angular scans with very different widths as can be seen from the simulated curves shown in figure 4. Simulations or the <0001> axis with an average potential of the mixed Ga + N rows yield just one width. By varying the fraction of Er atoms in Ga and random sites it was tried to reproduce the experimental data. The best agreement was obtained (continuous curve in Fig. 4) by assuming that 70% of the Er atoms are in regular Ga sites of the lattice with the rest at random positions. The random fraction takes into account the still damaged or not perfectly regrown regions of the lattice. A comparison of the O co-implanted to the samples implanted only with Er but subjected to the same annealing procedures indicate that the presence of O stabilizes the Er in the Ga sites probably through the formation of Er-O complexes similar to the ones observed in Si and GaAs co-doped with Er and O [8, 9].

Conclusions

After implantation into epitaxial GaN and annealing Er is incorporated to more than 70% into substitutional Ga sites. The threshold dose for the amorphisation of the GaN films studied is close to $5x10^{15}$ Er^+/cm^2, a relatively high value compared with other III-V compounds. The implantation damage in lightly damaged samples ($D = 5x10^{14}$ cm^{-2}) starts to anneal at 600°C. However, an increase of the annealing temperature up to 900°C is not enough to remove the damage completely. At this temperature the thickness of the amorphous layer is reduced, indicating the occurrence of some epitaxial regrowth. The presence of low doses of O in the implanted layer does not influence the annealing process significantly but increases the amount of Er in Ga sites after the annealing at 900°C. At the highest annealing temperatures the presence of O seems to stabilize the Er in substitutional lattice position.

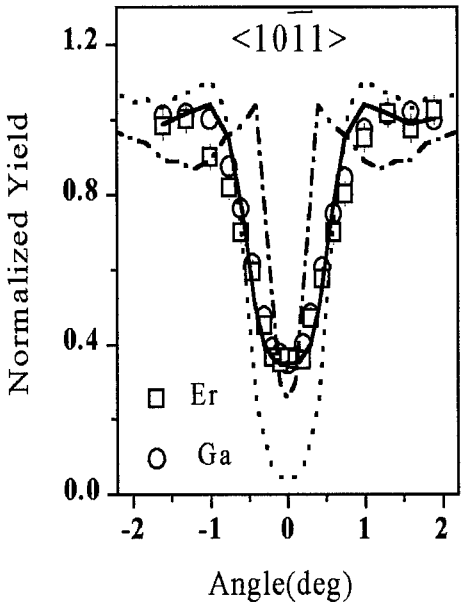


Figure 4: Angular scan through the <10$\bar{1}$1> axis for the sample implanted with $5x10^{14}$ cm^{-2} Er+O after annealing at 900°C. The dotted and the dash-dotted curve are the angular scans expected for Ga and N, respectively. The symbols are the data points obtained for Er and Ga and the solid line represents the result of a simulation assuming 70% of the Er impurities in substitutional Ga positions.

Acknowledgment

This work was partially supported by the EC under contract no: CHRX-CT93-0363 and at the University of Florida through ARO grant no. DAAH04-95-1-0026.

References

[1] D.H. Hanssen, R. Zhang, N.R. Perkins, S. Savfi, Z. Zhang, K.L. Bray, T.F. Kuech, Appl. Phys. Lett. 72 (1998) 1244

[2] M. Thaik, U. Hömmerich, R.N. Schwartz, R.G. Wilson, J.M. Zavada, Appl. Phys. Lett. 71 (1998) 2641

[3] A. Polman, J. Appl. Phys. 82 (1997) 1

[4] J.P. Biersack and L.G. Haggmark, Nulc. Instr. & Meth. 174 (1980) 257

[5] P.J.M. Smulders and D.O. Boerma, Nucl. Instr. Meth. B29 (1987) 471

[6] H.H. Than, J.S. Williams, J. Zou, D.J.H. Cockayne, S.J. Pearton, J.C. Zolper and R.A. Stall, Appl. Phys. Lett. 72 (1998) 1190

[7] J. Bartels, K. Freitag, J.G. Marques, J.C. Soares and R. Vianden, Hyp. Int. (1998) in press

[8] J.T. Torvick, R.J. Feuerstein, C. Qiu, M. Leksono, J. Pankove, F. Namavar, Mater. Res. Soc. Symp. Proc. 422 (1996) 199.

[9] A. Polman,G.N.van den Hoven, J.S.Custer, J.H.Shin, R.Serna, P.F.A. Alkemade, J. Appl. Phys. 77 (1995) 1256-1262.

VISIBLE AND INFRARED RARE-EARTH ACTIVATED ELECTROLUMINESCENCE FROM ERBIUM DOPED GaN

M. Garter*, R. Birkhahn*, A. J. Steckl* and J. Scofield**

*Nanoelectronics Laboratory, University of Cincinnati
Cincinnati, Ohio 45221-0030 USA, a.steckl@uc.edu

**Air Force Research Laboratory, Wright-Patterson AFB, OH 45433

Cite this article as: MRS Internet J. Nitride Semicond. Res. 4S1, G11.3 (1999)

ABSTRACT

Room temperature visible and IR light electroluminescence (EL) has been obtained from Er-doped GaN Schottky barrier diodes. The GaN was grown by molecular beam epitaxy on Si substrates using solid sources (for Ga and Er) and a plasma source for N_2. Transparent contacts utilizing indium tin oxide were employed. Strong green light emission was observed under reverse bias due to electron impact excitation of the Er atoms. Weaker emission was present under forward bias. The emission spectrum consists of two narrow green lines at 537 and 558 nm and minor peaks at 413, 461, 665, and 706 nm. There is also emission at 1000 nm and 1540 nm in the IR. The green emission lines have been identified as Er transitions from the $^2H_{11/2}$ and $^4S_{3/2}$ levels to the $^4I_{15/2}$ ground state. The IR emission lines have been identified as transitions from the $^4I_{11/2}$ and $^4I_{13/2}$ levels to the $^4I_{15/2}$ ground state. EL intensity for visible and IR light has a sub-unity power law dependence on bias current. An external quantum efficiency of 0.1% has also been demonstrated under a reverse bias current of 3.85 mA.

INTRODUCTION

The recent groundbreaking work[1] by Nakamura in GaN based LEDs and laser diodes has resulted in shorter wavelength semiconductor visible light emission. At the same time novel work is being conducted using rare earth elements as sources of light emission. Results based on glasses[2,3] are exciting for display, memory and discrete device technologies. Rare-earth (RE) doped Silicon based devices[4,5,6,7,8,9] have improved so that room temperature emission is now possible. III-V semiconductors doped with rare-earth elements have also been used[10,11,12,13,14,15,16,17,18] and have advantages compared to narrow bandgap materials[19]. The advantage of Nakamura's devices is their extremely high quantum efficiency[1] (~5%), whereas RE doped devices offer multiple color emission, wavelength-limited only by the RE element(s) chosen and not by the band gap energy of the semiconductor. Our recent work now indicates the possibility of combining the advantages of these two very different approaches in order to realize highly efficient full color displays in a single semiconductor host or very simple discrete devices

Mat. Res. Soc. Symp. Proc. Vol. 537 © 1999 Materials Research Society

using RE-doped GaN. We have recently reported strong visible (green) RE-activated PL from in-situ Er-doped GaN grown by MBE on sapphire[20] and on Si[21] substrates. The same strong green RE-activated emission was also observed[22] in EL from simple Al Schottky diodes on GaN:Er and from more sophisticated devices using indium tin oxide(ITO) transparent contacts. In this paper we report on the performance characteristics of Er-doped GaN LEDs emitting in both the visible and IR regions.

EXPERIMENT

The GaN:Er light emitting devices can be operated in two different ways. One way is to use both top side contacts, which consist of patterned indium tin oxide (ITO), for both positive and negative electrodes. Under reverse bias, the smaller, emitting electrode is negative and the larger electrode is positive. The devices can also be operated by making an ohmic contact to the backside of the Si. This method is interesting because current actually flows across the GaN/Si heterojunction. The devices behave very similarly in both modes and all data presented here were taken using top-side contacts.

The Er-doped GaN was grown using a Riber MBE-32 system on 2 inch p-Si (111) substrates and on 2 inch sapphire. Solid sources were used to supply the Ga and Er fluxes, while an STVA RF-plasma source supplied atomic nitrogen. Prior to MBE growth, the Si substrate was cleaned in acetone, methanol and DI water, followed by HF to remove all native oxide. After insertion into the MBE chamber, a thin, low temperature GaN buffer layer was first grown followed by a GaN:Er layer. The GaN layers were grown at a substrate temperature between 700- 750°C. The ITO contacts were formed using RF-sputtering in conjunction with a lift-off process. The ITO target had a composition of 90% In_2O_3 and 10% SnO_2. The sputtering was performed at 5 mTorr with 133 W of RF power, resulting in –183 volts of DC bias. Under these conditions, the deposition rate was ~70 Å/min. The ITO film was ~4200 Å thick and had a sheet resistance of 30 Ω/square as-deposited. Subsequent annealing in a nitrogen atmosphere for 2 minutes at 450 °C reduced the sheet resistance to ~5.5 Ω/square with transmission of ~92% at a wavelength of 537 nm and ~3% at 1.5 μm. Electroluminescence data were collected using either an Acton Research spectrometer or an Ocean Optics fiber optic spectrometer. Optical power measurements were made using a Newport 1818-SL/CM optical power meter. All measurements reported were made at room temperature.

RESULTS

Fig. 1 shows a photograph of a GaN:Er LED in operation using a standard probe station. In this photo, negative bias is being applied to the green light emitting electrode, resulting in a current of 19 mA. The device shown here is fairly large (2 mm radius) because it was designed to

make spectral data collection using an optical fiber more practical. An optical fiber can be placed in the immediate vicinity of the device, while still leaving enough room for an electrical probe tip. The emission intensity and color is uniform across the diode and the emitted light is easily seen in a normally lit room. Fig. 2 shows the difference in spectral shape between a commercial GaP-based device and our GaN:Er device. Notice that the conventional GaP LED is shifted more toward the yellow end and has an FWHM of 30 nm. By comparison, the GaN:Er green device has an FWHM of 5-6 nm and emits in the middle of the green range. The GaP LED was biased at 2 mA and the GaN:Er device was biased at 10 mA during these measurements. The peaks represent the actual signal intensity. Minor peaks at 413 nm and 665 nm are also present in the GaN:Er device spectrum. Fig. 3 shows the IR emission spectrum from a GaN:Er device biased at 75 volts and 19 mA. We have identified the 1.5 μm radiation preiously.[23] The 1 μm peak corresponds to a transition from $^4I_{11/2}$ to the $^4I_{15/2}$ ground state. It has an FWHM of ~25 nm. The visible and IR optical power emitted and detected from a GaN:Er LED are plotted as a function of bias current in Fig. 4. The visible optical power at the detector has a sub-unity power law dependence on bias current over the measurement range, reaching a value of 212 nW at 19 mA. The IR optical power.

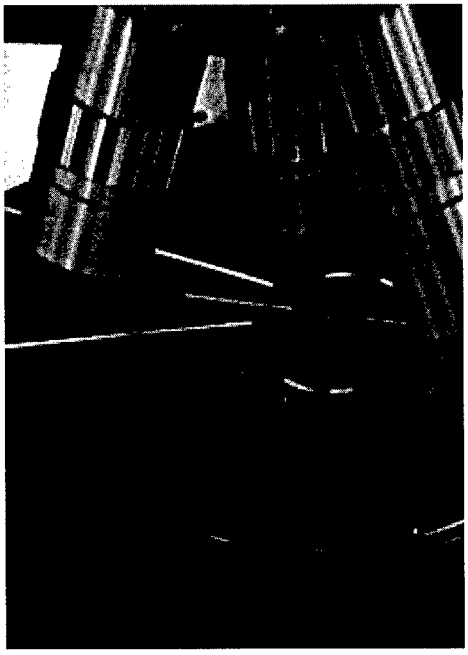


Fig. 1 Photograph of visible rare-earth-activated emission from ITO/GaN:Er device.

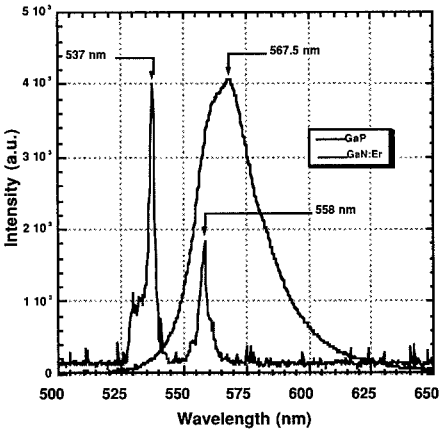


Fig. 2 Emission spectrum in the visible range from a commercial green GaP-based LED vs. our GaN:Er device.

also increases with a power law dependence over the measurement range reaching a value of 12.3 nW at 19 mA. It is important to note that the ITO electrodes for these experiments were optimized for green light, but the transmission in the IR can be increased by processing the ITO differently. The ITO layer transmits about 3% of the IR light emitted and about 92% of the visible green light

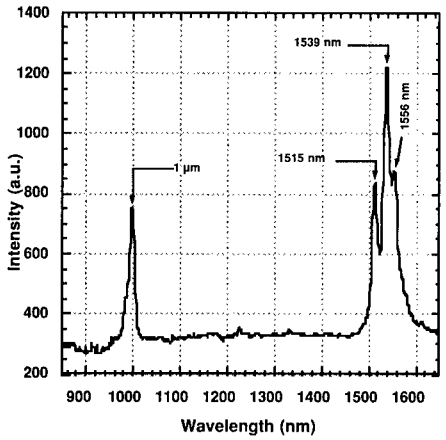


Fig. 3 Rare-earth activated emission spectra in the IR range from an ITO/GaN:Er device.

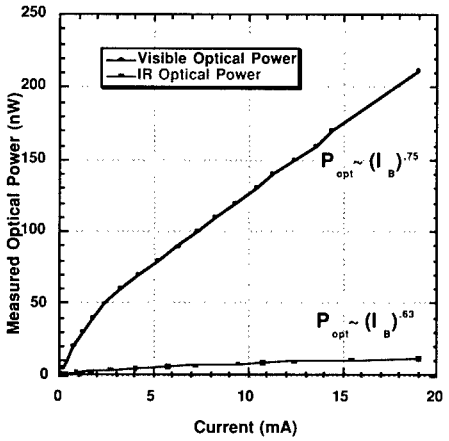


Fig. 4 Visible and IR optical power as a function of bias current.

With this in mind, our devices probably emit slightly more IR light than visible light, however, the ITO absorbs most of the IR light. During these measurements, a Si photodetector was placed 2.0 cm above the device. Assuming a point source of radiation, and uniform hemispherical emission, the visible optical power generated at the device is estimated to be 5.33 μW for 10 mA of applied reverse bias. Under these conditions, the external quantum efficiency at 537 nm is estimated to be 0.012%. However, a maximum external quantum efficiency of 0.1% has been reached for a GaN:Er device grown on sapphire. This device was operated at 155 Volts and 3.85 mA, and it was also used to take the data presented in Fig. 5. Fig. 5 summarizes the EL peaks that we have observed to date. The number of observable peaks increases with increasing applied power. The following peaks have been observed during EL of GaN:Er: 413, 461, 537, 558, 665, 671, 706, 1000, 1515, 1539, 1555nm. The EL peaks at 537 and 558 nm are dominant in the visible range and correspond to transitions from the $^2H_{11/2}$ and the $^4S_{3/2}$ to the $^4I_{15/2}$ ground state. It is interesting to note that the 706 nm line probably corresponds to a transition from the $^4F_{7/2}$ to the $^4I_{13/2}$ state instead of the normal ground state. This is the only intermediate transition we have observed. In addition, it is interesting that the $^4I_{9/2}$ (~1.55 ev above the ground state) level, a common transition in other host materials, is not observed in our material.

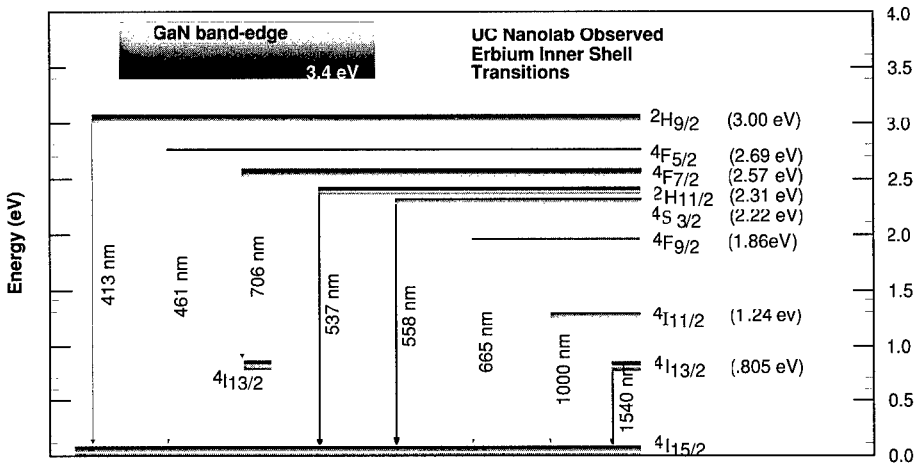


Fig. 5 Summary of the observed atomic energy levels of Rare-earth-activated emission in the visible and IR range from an ITO/GaN:Er device.

SUMMARY

In summary, we have reported visible and IR rare-earth-activated electroluminescence of Er-doped GaN. The use of ITO as a contact provides a fast and easy way to make devices, and also increases the amount of visible light output from the device. Both IR and visible EL peaks show narrow linewidths. Our devices transmit appreciably more visible than IR light, however the use of ITO as a contact material is not ideal for IR light emission under the specific conditions that the ITO was deposited. Future work will focus on reducing the operating voltage and increasing the external quantum efficiency of the devices. This work was supported in part by a BMDO/ARO contract (L. Lome and J. Zavada) and AASERT grants. The authors would like to acknowledge the support and encouragement of J. Zavada. Equipment support was provided by an ARO URI grant and the Ohio Materials Network.

REFERENCES

[1] S. Nakamura and G. Fasol, *The Blue Laser Diode*, Springer Verlag, Berlin (1997), p. 215.

[2] E. Downing, L. Hesselink, J. Ralston and R. Macfarlane, Science **273**, 1185 (August 1996).

[3] A.C. Tropper, J.N. Carter, R.D.T. Lauder, D.C. Hanna, S.T. Davey, and D. Szebesta, J. Opt. Soc. Am. B **11** (5), 886 (May 1994).

[4] H. Ennen, G. Pomrenke, A. Axmann, K. Eisele, W. Haydl, and J. Schneider, Appl. Phys. Lett. **46** (4), 381 (February 1985).

[5] G. Franzo and F. Priolo, Appl. Phys. Lett. **64**, 2235 (April 1994).

[6] B. Zheng, J. Michel, F. Y. G. Ren, L. C. Kimerling, D. C. Jacobson, and J. M. Poate, Appl. Phys. Lett. **64**, 2842 (May 1994).

[7] S. Lombardo, S. U. Campisano, G.N. van den Hoven, and A. Polman, J. Appl. Phys. **77**, 6504 (June 1995)

[8] C. X. Du, W. X. Ni, K. B. Joelsson, and G. V. Hansson, Appl. Phys. Lett. **71**, 1023 (August 1997).

[9] S. Coffa, G. Franzo, and F. Priolo, MRS Bulletin, 25 (April 1998).

[10] R. G. Wilson and R. N. Schwartz, C. R. Abernathy and S. J. Pearton, N. Newman, M. Rubin, and T. Fu, J. M. Zavada, Appl. Phys. Lett. **65** (8), 992 (August 1994).

[11] S. Kim, S. J. Rhee, D. A. Turnbull, E. E. Reuter, X. Li, J. J. Coleman, and S. G. Bishop, Appl. Phys. Lett. **71** (2), 231 (July 1997).

[12] S. Kim, S. J. Rhee, D. A. Turnbull, X. Li, J. J. Coleman, and S. G. Bishop, Appl. Phys. Lett. **71** (18), 2662 (November 1997).

[13] D. M. Hansen, R. Zhang, N. R. Perkins, S. Safvi, L. Zhang, K. L. Bray, and T. F. Kuech, Appl. Phys. Lett. **72** (10), 1244 (March 1998).

[14] E. Silkowski, G. S. Pomrenke, Y. K. Yeo and R. L. Hengehold, Physica Scripta T69, 276 (1997).

[15] J. T. Torvik, C. H. Qiu, R. J. Feuerstein and J. I. Pankove, F. Namavar, J. Appl. Phys. **81** (9), 6343 (May 1997).

[16] C. H. Qiu, M. W. Leksono, and J. I. Pankove, J. T. Torvik and R. J. Feuerstein, F. Namavar, Appl. Phys. Lett. **66** (5), 562 (January 1995).

[17] J. M. Zavada and D. Zhang, Solid-State Electron. **38**, 1285 (1995).

[18] J. T. Torvik, R. J. Feuerstein, J. I. Pankove, C. H. Qiu, and, F. Namavar, Appl. Phys. Lett. **69**, 2098 (September 1996).

[19] J. M. Zavada, M. Thaik, U. Hommerich, J.D. Mackenzie, C. R. Abernathy, Electrochem. Soc. **98-1**, 193rd Meeting, Abstract no. 535, (Spring 1998).

[20] A. J. Steckl and R. Birkhahn, Appl. Phys. Lett. **73** (12), 1700 (1998).

[21] R. Birkhahn and A. J. Steckl, Appl. Phys. Lett. **73** (14), 2143 (1998).

[22] A. J. Steckl, M. Garter, R. Birkhahn, J. Scofield, Appl. Phys. Lett. **73** (17), 2450 (1998).

[23] M. Garter, J. Scofield, R. Birkhahn, A.J. Steckl, Appl. Phys. Lett. **74** (Jan. 11, 1998).

PHOTOLUMINESCENCE AND PHOTOLUMINESCENCE EXCITATION SPECTROSCOPY OF *IN SITU* Er-DOPED AND Er-IMPLANTED GaN FILMS GROWN BY HYDRIDE VAPOR PHASE EPITAXY

S. KIM,* X. LI,* J. J. COLEMAN,* R. ZHANG,** D. M. HANSEN,** T. F. KUECH,** S. G. BISHOP*

*Microelectronics Laboratory, University of Illinois at Urbana-Champaign, Urbana, IL 61801
**Department of Chemical Engineering, University of Wisconsin, Madison, WI 53706

Cite this article as: MRS Internet J. Nitride Semicond. Res. 4S1, G11.4 (1999)

ABSTRACT

Photoluminescence (PL) and photoluminescence excitation (PLE) spectroscopy have been carried out at 6K on the 1540 nm $^4I_{13/2} \rightarrow {}^4I_{15/2}$ emission of Er^{3+} in *in situ* Er-doped and Er-implanted GaN grown by hydride vapor phase epitaxy (HVPE). The PL and PLE of these two different Er-doped HVPE-grown GaN films are compared with Er-implanted GaN grown by metal organic chemical vapor deposition (MOCVD).

In the *in situ* Er-doped HVPE-grown GaN, the lineshape of the broad PLE absorption bands and the broad PL bands is similar to that in Er-doped glass. The PL spectra of this *in situ* Er-doped sample are independent of excitation wavelength, unlike the PL of the Er-implanted GaN. These PL spectra are quite different from the site-selective PL spectra observed in the Er-implanted GaN, indicating that the seven different Er^{3+} sites existing in the Er-implanted MOCVD-grown GaN are not observed in the *in situ* Er-doped HVPE-grown GaN. Four of the seven different Er^{3+} sites observed in the Er-implanted MOCVD-grown GaN annealed at 900 °C under a flow of N_2 are present in the Er-implanted HVPE-grown GaN annealed at 800 °C in an NH_3/H_2 atmosphere.

INTRODUCTION

Photoluminescence (PL) and photoluminescence excitation (PLE) spectroscopy have been performed to study the different structural configurations (sites or centers) on which Er^{3+} ions are incorporated in Er-doped GaN and to investigate their excitation mechanisms [1-7]. Our previous study of site-selective PL and PLE spectroscopy in Er-implanted samples of GaN grown by metal organic chemical vapor deposition (MOCVD) that were annealed at 900 °C under a flow of N_2 revealed the existence of seven different Er^{3+} sites [3]. Six of these Er^{3+} PL sites are attributed to complexes of Er atoms with defects and impurities. Only one of the seven sites can be pumped by direct 4*f* absorption; the concentrations of the other sites are too low to allow excitation by direct 4*f* absorption. These results raise an obvious question concerning the generality or uniqueness of the Er^{3+} centers observed in GaN. That is, are these multiple, selectively excited, discrete Er^{3+} sites or centers unique to Er-implanted MOCVD-grown GaN subjected to specific post-implantation annealing conditions, or are they also present in Er-doped GaN synthesized by other growth, doping and annealing procedures?

Site-selective PL and PLE spectroscopies used in our previous work are applied in this study to Er-implanted hydride vapor phase epitaxy (HVPE)-grown GaN annealed at 800 °C in an NH_3/H_2 atmosphere and *in situ* Er-doped HVPE-grown GaN [7] to see if any of the seven different Er^{3+} sites observed in Er-implanted MOCVD-grown GaN exist in these samples. The

Mat. Res. Soc. Symp. Proc. Vol. 537 © 1999 Materials Research Society

PLE and PL of these two different HVPE-grown samples are compared here first with the Er-implanted MOCVD-grown sample and then the differences and similarities among the site-selective PLE and PL spectra of these three different Er-doped GaN films are discussed in detail.

EXPERIMENTAL PROCEDURE

The GaN films were doped *in-situ* with Er in a horizontal HVPE reactor during growth. A peak Er concentration of 2 x 10^{19} ions/cm^3 was achieved in this *in situ* Er-doped GaN at a thickness of 1000 nm [7]. The GaN films grown on sapphire by HVPE were implanted with a dosage of 2 x 10^{14} ions/cm^2 at 300 keV. The peak concentration of Er is 5.3 x 10^{19} ions/cm^3 at a depth of 33 nm [7]. These Er-implanted HVPE-grown GaN films were annealed in a conventional tube furnace at 800 °C for 30 minutes in a flowing NH_3/H_2. For comparison, the GaN films grown on sapphire by atmospheric pressure MOCVD were implanted with a dosage of 4 x 10^{13} ions/cm^2 at 280 keV [1-4]. The peak concentration of Er is 2 x 10^{18} ions/cm^3. Post-implantation annealing was carried out in a conventional tube furnace at 900 °C for 30 minutes under a continuous flow of nitrogen gas.

6K PL spectroscopy was carried out on the three different Er-doped GaN samples. The PL spectra were excited by a variety of sources including a tunable titanium-doped sapphire laser, a HeNe laser, an Ar ion laser, a Xe lamp dispersed by a double grating monochromator, and a HeCd laser. The PLE spectra were obtained with a xenon lamp dispersed by a double grating monochromator or with a tunable titanium-doped sapphire laser. All of the PLE spectra were corrected for the spectral response of the tunable excitation systems. The luminescence was analyzed by a 1-m single grating monochromator and detected by a cooled Ge PIN detector. Samples were cooled to liquid helium temperature in a Janis Supervaritemp Cryostat.

RESULTS AND DISCUSSION

Figure 1 shows the PL spectra obtained at 6 K under excitation by 515 nm light ("green-pumped") from *in situ* Er-doped and Er-implanted GaN grown by HVPE. The PL spectrum taken for Er-implanted MOCVD-grown GaN under the same experimental conditions is also shown for comparison. All three PL spectra exhibit the 1540 nm band characteristic of the $^4I_{13/2} \rightarrow {}^4I_{15/2}$ transitions of Er^{3+} and broad background PL bands on which the Er-related PL bands are superimposed. In the PL of the *in situ* Er-doped GaN (Fig. 1a), the broad PL bands have different lineshapes and peak positions from those of the damage-induced broad-band PL observed in the Er-implanted MOCVD-grown GaN (Fig. 1c) [4]. Since these bands have not been observed in undoped HVPE-grown GaN, they are apparently

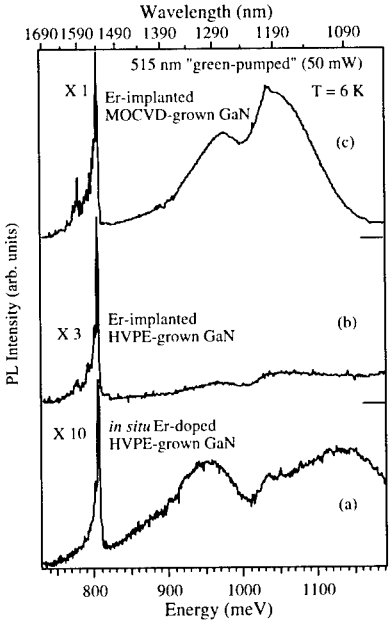


Fig. 1. The Er^{3+} PL spectra and the broad defect PL bands (pumped by 515 nm light).

induced by the *in situ* doping during growth. In the PL spectrum of the Er-implanted HVPE-grown GaN (Fig. 1b), the damage-induced broad-band PL is barely observable.

Figure 2 displays the PLE spectra of the three different Er-doped samples obtained by detecting the integrated Er^{3+} PL intensity while scanning the wavelength of the xenon lamp-double monochromator excitation system. The PLE spectrum 2(a) of the *in situ* Er-doped sample exhibits relatively narrow absorption bands attributable to direct optical excitation of the intra 4*f*-shell transitions of Er^{3+}, and an exponential absorption tail just below the 3.5 eV band gap. The exponential energy dependence of the below-gap absorption tail is reminiscent of the Urbach absorption edge that characterizes the band edge of disordered materials such as chalcogenide glasses [8] or highly doped crystalline semiconductors [9]. This PLE spectrum does not show the broad, mid-gap defect- or impurity-related absorption bands that are observed in the PLE spectra 2(b) and 2(c) of the Er-implanted samples. The absorption peaks seen at 378, 400, 445, 487, 521, 543, 651, 796, and 970 nm in the PLE spectrum 2(a) are attributed to $^4I_{15/2} \rightarrow {}^4G_{11/2}$, $^4I_{15/2} \rightarrow {}^4H_{9/2}$, $^4I_{15/2} \rightarrow {}^4F_{3/2,5/2}$, $^4I_{15/2} \rightarrow {}^4F_{7/2}$, $^4I_{15/2} \rightarrow {}^4H_{11/2}$, $^4I_{15/2} \rightarrow {}^4S_{5/2}$, $^4I_{15/2} \rightarrow {}^4F_{9/2}$, $^4I_{15/2} \rightarrow {}^4I_{9/2}$, and $^4I_{15/2} \rightarrow {}^4I_{11/2}$ Er^{3+} intra 4*f*-shell transitions, respectively [5,6,10]; some of these PLE bands were reported in Refs. 5 and 6 to be observed in Er-implanted GaN and *in situ* Er-doped AlN grown by molecular-beam epitaxy (MBE). In contrast, the PLE spectra 2(b) and 2(c) obtained from the Er-implanted HVPE- and MOCVD-grown samples, respectively, show only the broad, defect- or impurity-related absorption bands that are not attributable to Er^{3+}. These absorption bands are characteristic of the implanted films only, suggesting that some of the broad absorption bands in the PLE spectra 2(b) and 2(c) are associated with defects or defect-impurity complexes created during the implantation and annealing procedures [1,3].

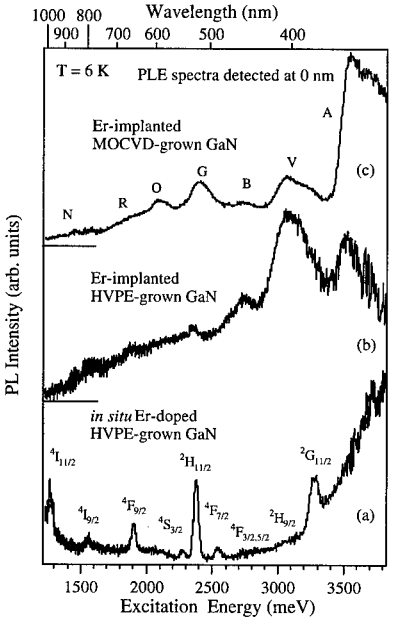


Fig. 2. The PLE spectra obtained by detecting the integrated Er^{3+} PL intensity.

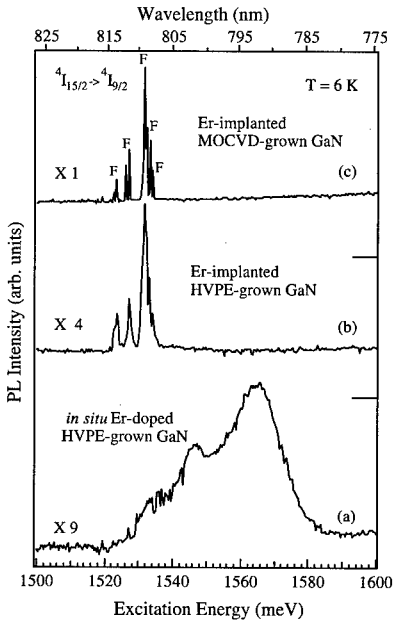


Fig. 3. The $^4I_{15/2} \rightarrow {}^4I_{9/2}$ 4*f* shell Er^{3+} PLE spectra.

The high-resolution PLE spectra (Fig. 3) obtained in the 775-825 nm spectra range with the tunable Ti-doped sapphire laser exhibit PLE peaks assigned to direct $^4I_{15/2} \rightarrow {}^4I_{9/2}$ $4f$ shell absorption. The absorption bands seen in the PLE spectrum (Fig. 3a) of the *in situ* Er-doped sample are much broader and their peak positions are shifted to the shorter wavelength region, compared to the Er-implanted samples. Note that the PLE spectrum of the MOCVD-grown GaN in Fig. 3c shows five pairs of sharp peaks, indicative of a single type of Er^{3+} center or site. The loss of the sharp structure in the PLE spectrum of the *in-situ* Er-doped GaN sample indicates that the Er dopants in this sample occupy sites located in disordered regions of the material. The disordered or "amorphous" character of the Er^{3+} centers' structural environments gives rise to site-to-site variations in the magnitude and symmetry of the crystal fields experienced by the Er^{3+} ions that are responsible for the spectral broadening of the Er^{3+} $4f$ PLE bands [8,9]. Additional evidence for disorder in the structural environment of the Er dopants in the GaN doped during growth is provided by the broad Urbach absorption edge in the near-band edge PLE spectrum of Fig. 2a, which contrasts strongly with the relatively sharp band edge absorption features observed in the PLE spectra of the Er^{3+} emission in Er-implanted samples of GaN (see, for example, Fig. 2c). Furthermore, the 1540 nm Er^{3+} PL bands from the *in situ* Er-doped sample shown in Figs. 1a, 5a, and 7a all have a broadened line shape more characteristic of Er dopants in glasses [8], than the sharply structured 1540 nm Er^{3+} PL bands of the Er-implanted GaN samples shown in Figs. 1b and c, 5b and c, 6a and b, and 7b and c.

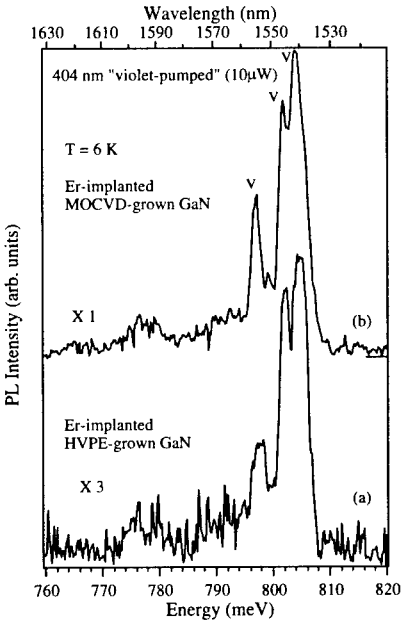


Fig. 4. The "violet-pumped" PL spectra as excited by violet light (404 nm).

The PLE spectrum of the Er-implanted HVPE-grown GaN in Fig. 3b exhibits sharp-structured peaks having the same peak positions as those in the Er-implanted MOCVD-grown GaN (Fig. 3c). A careful comparison between these two PLE absorption bands reveals that the PLE peaks in the HVPE-grown one are broader, compared to the MOCVD-grown one. The broadening of the sharp $^4I_{15/2} \rightarrow {}^4I_{9/2}$ $4f$ shell absorption peaks in the Er-implanted, HVPE-grown sample is apparently attributable to the fact that the concentration (5.3×10^{19} ions/cm^3) of the implanted Er^{3+} ions is larger than that (2×10^{18} ions/cm^3) in the Er-implanted MOCVD-grown sample; a similar broadening of the sharp absorption peaks was observed in the PLE spectrum of MOCVD-grown GaN implanted with 10^{15} Er ions/cm^2 at 350 keV reported in Ref. 11. While the sharpness of the PLE peaks in the PLE spectrum of the Er-implanted MOCVD-grown GaN indicates that isolated Er ions on Ga atomic positions are on identical, high-quality sites in this material [4], the spectral broadening of the direct $4f$ PLE absorption peaks for the Er-implanted HVPE-grown sample implies moderate site-to-site variation in the crystal field.

The seven distinct optically active Er^{3+} centers observed previously in the Er-implanted MOCVD-grown GaN annealed at 900 °C (Ref. 3) have been labeled on the basis of their excitation wavelengths, as follows: above-gap (A), blue (B), orange (O), red (R), near-IR (N), $4f$

(F) and violet (V). This labeling system has been used to identify the PLE absorption bands associated with the selective excitation of these Er^{3+} centers in the PLE spectra in Figs. 2c and 3c. Figures 4, 5, and 6 show the "violet-pumped", "blue-pumped", and "red-pumped" PL spectra excited by 404, 458 and 633 nm light, respectively, that correspond with the similarly labeled PLE bands in Fig. 2c [4]. The "violet-pumped" PL spectra presented in Fig. 4 demonstrate that the PL peaks in the "violet-pumped" PL spectrum of the Er-implanted HVPE-grown GaN are the same as those in the Er-implanted MOCVD-grown GaN, while there was no Er^{3+} emission from the *in situ* Er-doped GaN when excited by 404 nm (violet) light. In Fig. 5, the broadened PL peaks in the "blue-pumped" PL spectrum of the *in-situ* Er-doped sample do not correspond to the B-labeled PL peaks associated with the "blue" Er^{3+} site observed in the Er-implanted MOCVD-grown sample, but the PL of the Er-implanted HVPE-grown sample includes both the B- and A-labeled PL peaks. The "red-pumped" PL spectra in Fig. 6 show that while the 633 nm light excites the R (red)-labeled Er^{3+} emission as well as the B-, A-, N-, and O-labeled bands in the Er-implanted MOCVD GaN sample (Fig. 6b), only the B-labeled PL peaks are observable in the PL of the Er-implanted HVPE-grown sample (Fig. 6a), and no ~1540 nm emission is excited from the *in situ* Er-doped GaN.

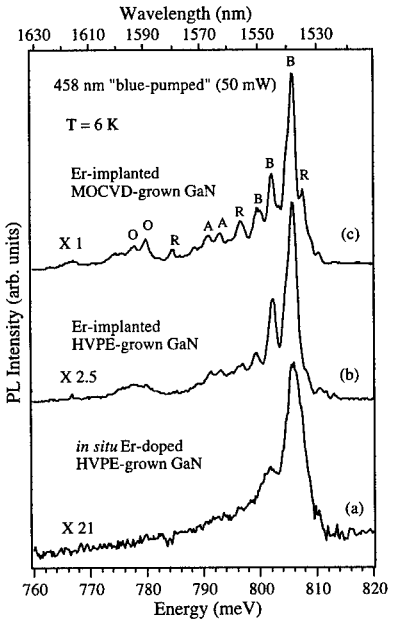


Fig. 5. The "blue-pumped" PL spectra as excited by blue light (458 nm).

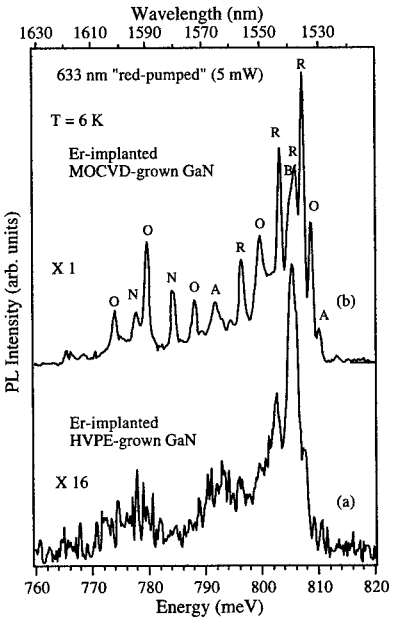


Fig. 6. The "red-pumped" PL spectra as excited by red light (633 nm).

The "4*f*-pumped" PL spectra in Fig. 7 were excited by 809 nm light that corresponds to direct Er^{3+} 4*f*-band absorption. Significantly, the "4*f*-pumped" PL spectrum of the Er-implanted HVPE-grown GaN (Fig. 7b) shows sharply-structured PL peaks that are nearly identical in peak energy and relative intensities to those of the Er-implanted MOCVD-grown GaN PL spectrum of Fig. 7c. This indicates that most of the Er atoms in the Er-implanted HVPE-grown GaN occupy

a single type of high-concentration, isolated Er^{3+} center, that can only be excited by direct 4*f*-band absorption, and that this is the same high-concentration Er^{3+} center previously observed by direct 4*f*-band pumping in Er-implanted MOCVD-grown GaN [3,4]. In contrast, 4*f* pumping of the Er^{3+} dopants in the *in-situ* Er-doped GaN excites a broad 1540 nm PL spectrum (Fig. 7a) that is identical to the "green-pumped" PL spectrum (Fig. 1a) and the "blue-pumped" PL spectrum (Fig. 5a) for this sample, clearly demonstrating the absence in the *in-situ*-doped material of the multiple, selectively excited, discrete Er^{3+} sites or centers that are observed in the Er-implanted GaN. The broad 4*f*-pumped Er^{3+} PL spectrum confirms our earlier suggestion that the Er dopants in the *in-situ*-doped sample occupy sites located in disordered regions of the material and therefore experience site-to-site variations in the crystal field.

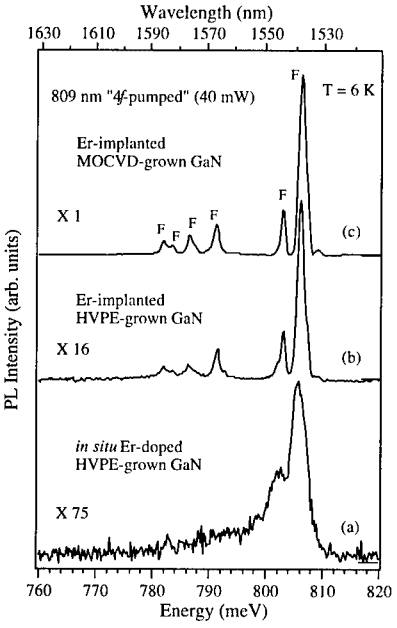


Fig. 7. The "4*f*-pumped" PL spectra as excited by 809 nm light.

CONCLUSIONS

Site-selective PLE and PL spectroscopy have been carried out at 6K on the 1540 nm $^4I_{13/2} \rightarrow {}^4I_{15/2}$ emission of Er^{3+} in *in situ* Er-doped and Er-implanted GaN grown by HVPE. The PLE and PL spectra of these two different Er-doped HVPE-grown GaN films are compared in this study with Er-implanted GaN grown by MOCVD to see if the multiple, selectively excited, discrete Er^{3+} sites or centers observed in our previous studies of Er-implanted GaN are present in Er-doped GaN synthesized by other growth, doping and annealing procedures.

The PLE and PL spectroscopy of this study reveal that four of the seven different Er^{3+} sites observed in Er-implanted MOCVD-grown GaN annealed at 900 °C under a flow of N_2 are present in Er-implanted HVPE-grown GaN annealed at 800 °C in an NH_3/H_2 atmosphere. In contrast, the *in situ* Er-doped HVPE-grown GaN exhibits a single, broad ~1540 nm Er^{3+} PL spectrum whose lineshape is independent of excitation wavelength. This broad Er^{3+} PL spectrum, which is reminiscent of emission from an Er-doped glass, prompts the suggestion that the Er dopants in the *in-situ*-doped sample occupy sites located in disordered regions of the material characterized by site-to-site variations in the crystal field.

ACKNOWLEDGMENTS

This work was supported by NSF under the Engineering Research Centers Program (ECD 89-43166), DARPA (MDA972-94-1-004), and the JSEP (0014-90-J-1270).

REFERENCES

1. S. Kim, S. J. Rhee, D. A. Turnbull, E. E. Reuter, X. Li, J. J. Coleman, and S. G. Bishop, Appl. Phys. Lett. **71**, 231 (1997).
2. S. Kim, S. J. Rhee, X. Li, J. J. Coleman, and S. G. Bishop, Appl. Phys. Lett. **71**, 2662 (1997).
3. S. Kim, S. J. Rhee, X. Li, J. J. Coleman, and S. G. Bishop, Mater. Res. Soc. Symp. Proc. **501**, to be published (1998).
4. S. Kim, S. J. Rhee, X. Li, J. J. Coleman, and S. G. Bishop, J. Electron. Mater., **27**, 246 (1998).
5. M. Thaik, U. Hommerich, R. N. Schwartz, R. G. Wilson, and J. M. Zavada, Appl. Phys. Lett. **70**, 2641 (1997).
6. X. Wu, U. Hommerich, J. D. MacKenzie, C. R. Abernathy, S. J. Pearton, R. N. Schwartz, R. G. Wilson, and J. M. Zavada, Appl. Phys. Lett. **70**, 2126 (1996).
7. D. M. Hansen, R. Zhang, N. R. Perkins, S. Safvi, L. Zhang, K. L. Bray and T. F. Kuech, Appl. Phys. Lett. **72**, 1244 (1998).
8. D. A. Turnbull and S. G. Bishop, J. Non-Cryst. Solids., **223**, 105 (1998).
9. N. F. Mott and E. A. Davis, *Electronic Processes in Non-Crystalline Materials*, (Clarendon Press, Oxford, 1979), p. 273.
10. F. Gan, *Laser Materials*, (World Scientific, New Jersey, 1995), p. 220.
11. J. T. Torvik. C. H. Qui, R. J. Feuerstein, J. I. Pankove, F. Namavar, J. Appl. Phys. **81**, 6343 (1997).

OPTICAL CHARACTERIZATION OF ERBIUM DOPED III-NITRIDES PREPARED BY METALORGANIC MOLECULAR BEAM EPITAXY

U. Hömmerich*+, J. T. Seo*, Myo Thaik*, J. D. MacKenzie**, C. R. Abernathy**, S.J. Pearton**, R.G. Wilson†, J. M. Zavada‡
*Hampton University, Department of Physics, Research Center for Optical Physics, Hampton, VA 23668
**University of Florida, Department of Materials Science and Engineering, Gainesville, FL 32611
†Consultant, Stevenson Ranch, CA 91381
‡U.S. Army European Research Office, London, UK, NW1 5
+ E-mail: hommeric@gprc.hamptonu.edu

Cite this article as: MRS Internet J. Nitride Semicond. Res. 4S1, G11.6 (1999)

ABSTRACT

We are currently engaged in a systematic study of the optical properties of Er doped III-nitrides prepared by metalorganic molecular beam epitaxy (MOMBE). Under below-gap excitation it was observed that GaN: Er samples with [O]~10^{20} cm^{-3} and [C]~10^{21} cm^{-3} luminesce at 1540 nm with an intensity of more than two orders of magnitude greater than samples with low oxygen and carbon concentrations (< 10^{19} cm^{-3}). Associated with the different oxygen and carbon concentrations were different thermal quenching behaviors and below-gap absorption bands. Interestingly, for above-gap excitation only small differences in absolute Er^{3+} PL intensity and quenching behavior were observed for samples of varying O and C content. Initial lifetime studies were performed and showed a rather unusual short decay time of ~100 μs at room temperature. In order to gain more insight in the Er^{3+} PL, a comparison of the integrated PL intensity and lifetime was performed for the temperature range 15-500K. The result reveals that the Er^{3+} PL quenches above room temperature due to the onset of non-radiative decay and the reduction in excitation efficiency. All samples were also investigated for visible luminescence. Red luminescence was observed from GaN: Er on sapphire substrates under below-gap excitation.

INTRODUCTION

Rare earth doped semiconductors have been studies for more than a decade because of the possibility to develop compact and efficient electroluminescence devices.[1,2,3,4] Trivalent Erbium ions (Er^{3+}) are of special interest because they exhibit an atomic-like transition at 1540nm, which corresponds to the low-loss window of silica-based optical fibers. Electroluminescence devices based on Er doped Si and GaAs were reported, however, their efficiency was too low for practical applications.[3,4] An important step forward in the field of Er doped semiconductors was the observation that the room-temperature Er^{3+} photoluminescence (PL) intensity strongly depends on the bandgap of the host materials. It was found that for larger bandgap energy, there is less detrimental temperature quenching of Er^{3+} PL occurring.[5,6] Therefore, doping Er^{3+} ions into wide gap semiconductors is a promising approach to overcome the thermal quenching of Er^{3+} PL. Consequently, current research efforts focus on studying Er^{3+} doped into wide bandgap semiconductors such as SiC and GaN.[7,8] First results on the observation of 1.54 μm photoluminescence from Er implanted GaN and AlN were reported by Wilson et al.[9] Subsequently, other research groups reported results of photoluminescence, cathodoluminescence, and electroluminescence (EL) studies of Er implanted GaN. [10,11,12,13] The goal for practical device applications is to incorporate Er^{3+} ions during epitaxial growth. Doping during growth has several advantages over ion implantation including the absence of implantation damage, unlimited layer thickness, and a more homogenous doping profile. In-situ Er doping of AlN using metalorganic molecular beam expitaxy (MOMBE) was first reported by MacKenzie et

Mat. Res. Soc. Symp. Proc. Vol. 537 © 1999 Materials Research Society

al. in 1996.[14] This work was followed by the first demonstration of in-situ Er doping of GaN.[15] Recently, Hansen et al. reported results of in-situ doped GaN: Er prepared by hydride vapor phase growth.[16] Visible PL and EL from GaN: Er grown by molecular beam epitaxy have been reported.[17,18] Even though encouraging strong Er^{3+} PL results were obtained, initial infrared electroluminescence studies of GaN: Er have shown rather poor efficiencies.[19,20] In order to optimize the material preparation for developing more efficient 1.54 μm devices, it is crucial to understand the incorporation and excitation mechanisms of Er^{3+} ions in III-Nitrides. More specifically, it will be important to identify the Er^{3+} sites that are excited efficiently through electrical injection of electron-hole pairs and to optimize their concentration in the GaN host.[12] In this paper we present new spectroscopic results focusing on the 1.54 μm PL from MOMBE grown Er doped GaN. Results of temperature dependent PL intensity, lifetime, and excitation studies will be shown and discussed for samples with varying oxygen and carbon content. In addition, we will also report some initial results on visible luminescence studies.

EXPERIMENTAL PROCEDURES

The Er doped GaN films were grown by MOMBE in an INTEVAC Gas Source Gen II on In-mounted (100) Si or (0001) Sapphire substrates. The GaN films were preceded by a low temperature AlN buffer (T_g=425 °C). A 0.2 μm undoped GaN spacer was deposited prior to the growth of GaN: Er. Triethylgallium (TEGa), Dimethylethylamine alane (DMEAA), and thermally-evaporated 8N Ga metal provided the group III fluxes. A shuttered effusion oven with 4N Er was used for solid source doping. Reactive nitrogen species were provided by a SVT radio frequency plasma source. Due to the incorporation of carbon and oxygen from residual ether in TEGa, the C and O background observed in TEGa derived GaN were ~$10^{21}$$cm^{-3}$ and ~10^{20} cm^{-3}, respectively, as determined by SIMS measurements. GaN grown using thermally-evaporated 8N pure Ga as the group III source had oxygen and carbon backgrounds of less than 10^{19} cm^{-3}.[21]

PL measurements were performed using either the broad-band visible (457-514nm) or uv (333.6-363.8nm) outputs of an argon-ion laser for excitation. The luminescence spectra were recorded using a 1-m monochromator equipped with a liquid-nitrogen cooled Ge detector. Visible PL studies employed a thermo-electric cooled photomultiplier tube. The signal was processed using lock-in technique. The samples were cooled on the cold-finger of a two-stage closed-cycle refrigerator. High temperature PL studies were carried out using a homemade heating element, which had a temperature accuracy of ±5°C. Luminescence lifetime data were taken with a fast response Ge detector and averaged using a digitizing oscilloscope. PLE studies were carried out using an argon pumped dye laser or and a Nd: YAG/Optical Parametric Oscillator system.

RESULTS AND DISCUSSION

a) Er^{3+} PL intensity and spectra

Figure 1 shows the room-temperature, infrared PL spectra of Er doped GaN on Al_2O_3 prepared by MOMBE. No significant spectral differences were observed for Er doped GaN on Sapphire or Si substrates. For comparison, the Er^{3+} PL spectra of AlN: Er (MOMBE) and Er implanted GaN are also shown in figure 1.[9,14] All samples were excited with the 363-366.8nm UV output of an Argon-Ion laser. UV excitation was chosen to simulate carrier-mediated Er^{3+} excitation as in GaN: Er electroluminescence devices. All samples showed characteristic Er^{3+} PL centered at 1.54 μm, which can be assigned to the intra-4f Er^{3+} transition $^4I_{13/2}$--->$^4I_{15/2}$. The Er^{3+} PL spectra from in-situ Er doped GaN and AlN are very similar. They exhibit nearly featureless spectra (25-35nm @FWHM) suggesting a homogenous distribution of Er sites as typically

observed from Er doped glasses.[22,23] Er peaks located at 1.517μm, 1.540μm, 1.548μm, and 1.555 μm are either due to Stark splittings and/or multiple Er sites. The overall spectral width of the Er^{3+} PL from Er implanted GaN was significantly larger (100nm@FWHM) than that observed from Er doped GaN and AlN. Moreover, Er implanted GaN exhibits a more sharply structured Er^{3+} PL than the in-situ Er doped III-Nitride samples. Based on previously published data [9,10,11,12,13], the more complex and broad Er^{3+} PL seems to be characteristic for Er implanted GaN samples and is due to a combination of different Er sites and Stark splittings of Er ions in low symmetry sites. For example, Kim et al. identified up to 4 Er sites in Er implanted GaN grown by MOCVD.[12] The authors demonstrated that it was possible to selectively excite these four sites by three different below-gap absorption processes and through direct intra-4f excitation. Important for future device development was the observation that only a small fraction of incorporated Er^{3+} ions are excitable through carrier-mediated processes.[24] Time-resolved PL studies of in-situ Er doped AlN (MOMBE) have indicated the existence of at least two different classes of Er^{3+} sites with distinct lifetime and excitation schemes.[25] These results underline that it is crucial to identify the incorporation and excitation mechanism of Er^{3+} in different sites in order to optimize the material preparation for device applications.

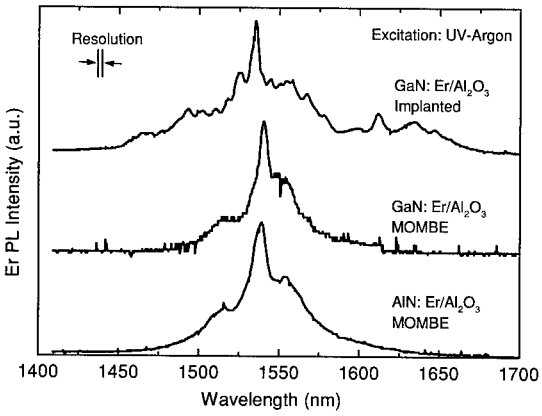


Figure 1: Room-temperature Er^{3+} PL spectra of Er implanted GaN and in-situ Er doped GaN and AlN.

Figure 2 depicts a comparison of the absolute Er^{3+} PL intensities of GaN: Er (MOMBE) for below and above-gap excitation at room-temperature. Under below-gap excitation, GaN: Er (TEGa) with high oxygen and carbon background ([O]~$10^{20}cm^{-3}$, [C]~$10^{21}cm^{-3}$) showed an Er^{3+} PL peak intensity two orders of magnitude larger than GaN: Er (Ga) with low O and C backgrounds (<$10^{19}cm^{-3}$). It is interesting to note that also GaN: Er/Si showed strong 1.54μm PL at room temperature, which makes this material attractive for integration with Si based optoelectronics.[21] Drastic improvements of the absolute Er^{3+} PL intensity have been observed for Er and oxygen codoped Si and GaAs. The enhanced 1.54μm PL was attributed to an increased concentration of optically active Er^{3+} ions and a more efficient Er^{3+} PL excitation.[26,27,28,29,30] Our results for below-gap Er^{3+} excitation in GaN suggest that the incorporation of O and C introduces beneficial mid-gap states that provide efficient energy transfer pathways for Er^{3+} in GaN. Support for this idea was obtained from photoluminescence excitation (PLE) studies shown in figure 3. In

PLE the effectiveness of stimulating 1.54 μm Er^{3+} PL is measured as a function of excitation wavelength. The PLE spectra of GaN: Er/Si (TEGa) reveal that the incorporation of high O and C backgrounds leads to a broad PLE band extending over the entire visible region (~400-800 nm). The GaN: Er (Ga) sample with low C and O content did not show this broad PLE band, but direct intra-4f Er transitions (see e.g. ~525nm). Therefore, the visible output from an Argon-Ion laser leads to a significantly more efficient excitation of Er^{3+} in GaN:Er/Si (TEGa) than in GaN: Er/Si (Ga).

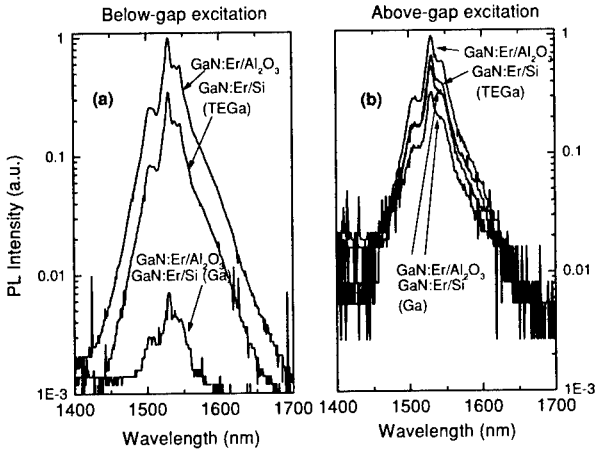


Figure 2: Comparison of Er^{3+} PL intensity from Er doped GaN (MOMBE) for a) below-gap and (b) above-gap excitation (300K).

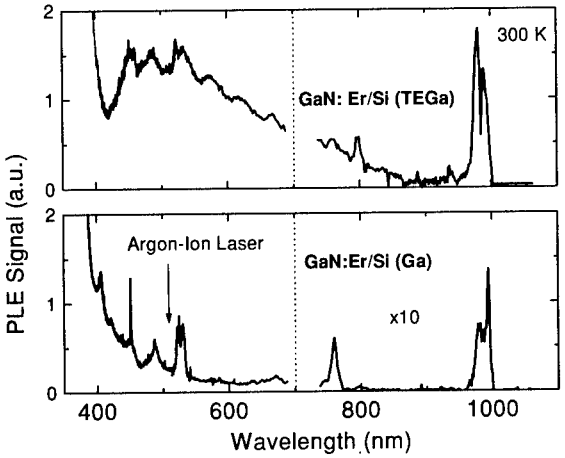


Figure 3: PLE of GaN: Er/Si samples with varying oxygen and carbon content. The incorporation of high oxygen and carbon backgrounds (upper graph) leads to a broad Er^{3+} excitation band covering the entire visible region.

Under above-gap excitation (figure 2b) all GaN: Er (MOMBE) samples showed a greatly reduced Er^{3+} PL intensity relative to below-gap excitation, independent of carbon and oxygen concentration. A similar PL reduction was reported for Er implanted GaN.[31] It is somewhat surprising that under above-gap excitation the Er^{3+} PL intensities of samples with high oxygen and carbon backgrounds is only roughly twice as strong as the Er^{3+} PL observed from low O and C contents. These observations suggest that either only a fraction of optically active Er^{3+} ions are excited and/or the excitation efficiency is reduced under above-excitation. Moreover, it also indicates that high oxygen and carbon concentrations do not necessary lead to an enhanced luminescence for carrier-mediated Er^{3+} excitation. More work is necessary to address this issue in more detail.

b) Er PL quenching and lifetime

Figure 4 shows the integrated Er^{3+} PL intensity of Er doped GaN samples for the temperature range from 15-500K. The Er^{3+} PL was excited either with the broad-band visible (Fig. 4a) or uv (Fig. 4b) outputs of an Argon ion laser corresponding to below and above-gap Er^{3+} excitation. Under below-gap excitation a significantly different Er^{3+} PL quenching behavior was observed for samples with varying O and C contents (see Figure 4a). As was previously observed for Er and oxygen codoped Si and GaAs, GaN: Er samples with high O and C concentrations showed a significantly reduced Er^{3+} PL quenching compared to samples with low C and O backgrounds.[26,27,28,29,30] Between 15K and room-temperature samples with high O and C backgrounds showed Er^{3+} PL quenching of only ~20%, whereas the 1.54μm luminescence from low O and C concentration samples decreased by ~90% over the same temperature range. At higher temperatures also the O and C rich samples showed an enhanced Er^{3+} PL quenching and the luminescence decreased to roughly 10% of their low temperature value at 500K. Under above-gap excitation the situation was different. As shown in Fig. 4(b) hardly any difference in Er^{3+} PL quenching behavior was observed for samples with varying oxygen/carbon content. As mentioned above, the oxygen and carbon concentration does not greatly effect the carrier-mediated Er^{3+} excitation. Up to room temperature the Er^{3+} PL decreased for all four samples by less than 50% relative to its low temperature value. When heating the samples above room temperature, we observed a steady decrease of the Er^{3+} PL with increasing temperature. At 550 K, the Er^{3+} PL from all samples had decreased by nearly 90% of its low temperature value.

To gain more insight in the observed Er^{3+} PL quenching, we performed initial luminescence lifetime studies on the two oxygen and carbon rich samples, GaN: Er/Si (TEGa) and GaN:Er/Sapphire (TEGa). These samples showed the strongest Er^{3+} PL signal, which allowed us to carry out lifetime studies for the entire range 15-500 K. It was observed that the Er^{3+} PL decay curves were non-exponential which provides further support for the existence of a wide distribution of Er^{3+} sites. To describe the luminescence decay an average lifetime $<\tau>$ was used:

$$<\tau>=\frac{\int I(t)tdt}{\int I(t)dt} \qquad (1)$$

where I(t) is the luminescence decay curve and t is the time.[32,33] The low temperature lifetime of both samples was found to be ~130μs and decreased to ~100μs at room temperature. At 500K the lifetime had shortened to ~50μs. These lifetimes are significantly shorter than previously reported lifetimes for Er implanted GaN, which were in the order of 1-2ms.[10,16] It is possible that the short lifetimes are due to a higher oscillator strength of Er^{3+} transitions in MOMBE grown samples compared to Er implanted GaN. In order to confirm this explanation direct absorption measurements of intra-4 Er transitions are necessary. It is also conceivable that the Er^{3+} lifetimes

are shortened due intra-4f non-radiative decay or cooperative processes such as upconversion or energy migration.[34] Power dependent lifetime studies, however, did not show any change in lifetime with increasing excitation density suggesting that the later processes are not dominant in GaN:Er.

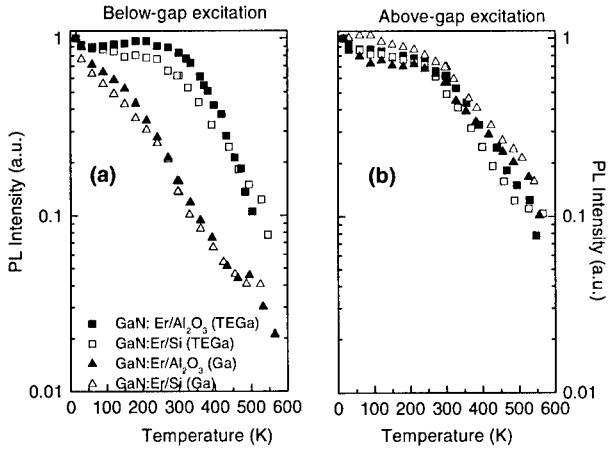


Figure 4: Temperature dependence of the integrated PL intensity from in-situ Er doped GaN for above and below gap excitation.

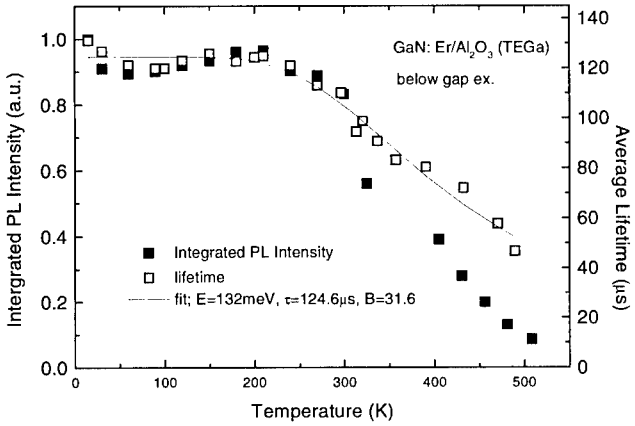


Figure 5: Comparison of the temperature dependence of Er^{3+} intergrated PL and lifetime for in-situ Er doped GaN.

It is instructive to compare the temperature dependence of PL intensity and lifetime as shown in figure 5. In the following discussion it is assumed that the Er^{3+} PL intensity is proportional to the number (or concentration) of excited Er ion (N_{Er}^{*}) and the radiative decay rate (w_{rad}). Under steady state condition and low pump power intensities the Er^{3+} PL signal can be written as:

$$I_{PL} = C \cdot \frac{I_p}{hc} \cdot \lambda_p \cdot \sigma_{ex} \cdot N_{tot} \cdot w_{rad} \cdot \tau \qquad (2)$$

where C is a constant, I_p is the pump intensity, λ_p is the pump wavelength, σ_{ex} is the excitation cross-section defined as the product of pump efficiency and absorption cross-section, N_{tot} is the total Er concentration, w_{rad} is the radiative decay rate, and τ is the luminescence lifetime. Under the assumption that the radiative decay rate and total Er concentrations are temperature independent, the Er^{3+} PL quenching at higher temperatures can be explained by either the onset of nonradiative deexcitation processes reducing the Er^{3+} lifetime and/or by a decrease of the excitation efficiency.

The comparison of the temperature dependent Er^{3+} PL intensity and lifetime enables one to separate the above mentioned Er^{3+} PL quenching mechanism. As can be inferred from figure 5, the Er^{3+} lifetime follows the change in integrated PL intensity very closely up to room temperature. This means that between 15 and 300K the small decrease in Er^{3+} PL intensity is due to nonradiative decay. Above room-temperature the lifetime changes less than the integrated Er^{3+} PL intensity. This suggests that Er^{3+} PL quenching occurring above room temperature is not only due nonradiative deexcitation, but also due to a reduction in excitation efficiency. Nearly the same Er^{3+} PL intensity and lifetime behavior was observed for GaN:Er/Si (not shown). Similar to other Er doped semiconductor systems, we assume that the excited Er ion can decay either through emission of a 1.54 μm photon or through non-radiative energy transfer processes to the host (also referred to as "backtransfer" [28,35]). It is further assumed that internal Er^{3+} quantum efficiency does not change with temperature. The change in lifetime is then described by a thermally activated nonradiative decay process, which is controlled by Boltzmann's law:

$$\frac{1}{\tau} = \frac{1}{\tau_{rad}}\left(1 + B \cdot \exp\left(-\frac{E}{kT}\right)\right) \qquad (3)$$

where τ_{rad} is the radiative lifetime, E is the thermal activation or threshold energy for non-radiative decay, and B is a constant. Fitting equation 3 to the lifetime data shown in figure 5 gives the following parameter values: τ_{rad}= 124.6μs, B=31.6, and an activation energy E=132meV. The fit result suggests the existence of a defect-related level close to Er^{3+}, which acts as a particular effective channel for nonradiative energy transfer between Er^{3+} and the host. The deexcitation of Er ions through some mid-gap level has been discussed before for Er doped Si and GaAs. In the backtransfer model as proposed by Takahei et al.[28], the existence of an Er-related level provides the possibility of energy backtransfer where excited Er ions transfer an excited carrier back to the defect level followed by a thermalization into the conduction band. This model for the deactivation of excited Er^{3+} ions may also be relevant for GaN:Er, however, no experimental evidence for an Er-related defect level has yet been reported. A more detailed comparison of the Er^{3+} lifetimes of GaN: Er samples with varying oxygen and carbon content is in progress and promises to provide deeper insight in the Er excitation and deexcitation mechanisms.

c) visible PL from GaN: Er

Very recently green luminescence was observed from GaN: Er grown by solid source molecular beam epitaxy under above-gap excitation.[36] Narrow lines centered at 537nm and 558nm were identified to be due to the intra-4f Er transitions $^2H_{11/2} \rightarrow {}^4I_{15/2}$ and $^4S_{3/2} \rightarrow {}^4I_{15/2}$. Subsequently the same authors reported green electroluminescence from Er doped GaN Schottky barrier diodes.[37] In figure 6 we show the visible PL spectra of GaN: Er/Sapphire prepared by MOMBE.

We observed no green emission lines from any of the investigated samples under below (488nm) or above-gap (325nm) excitation. Interestingly, however, for below-gap excitation we observed a broad red luminescence band, which showed sharp structure at around 665 nm and 690 nm. This emission was not found for the GaN: Er/Si samples. Preliminary studies indicated that the peaks at 665 nm and 690 nm had lifetimes in the millisecond range. The peak at 665 nm is assigned to the $^4F_{9/2} \rightarrow {}^4I_{15/2}$ transition of Er^{3+} ions, whereas the origin of the 690 nm peak is not yet know. The data suggest that the 690 nm line is a pure electronic transition (no-phonon line) accompanied by a vibronic sideband at around 720 nm. A more detailed study is currently being undertaken to identify the origin of the red luminescence from GaN:Er/Sapphire.

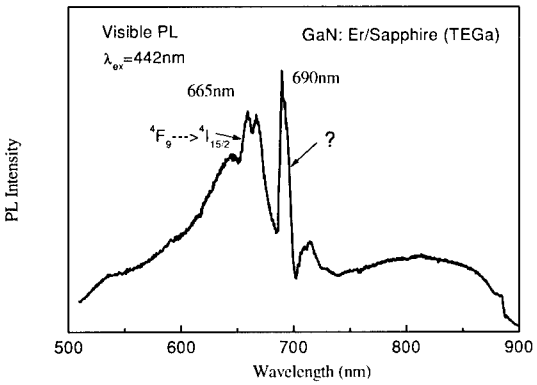


Figure 6: Visible PL spectrum of GaN: Er/Sapphire for below-gap excitation at room-temperature.

SUMMARY

We presented new results on the 1.54 μm luminescence properties of GaN: Er grown by MOMBE. It was observed that high oxygen and carbon concentrations (~10^{20} cm^{-3}) enhance the 1.54μm Er^{3+} PL intensity and reduce the Er^{3+} PL quenching under below-gap excitation. Moreover, PLE studies revealed that oxygen/carbon introduces a broad below-gap PLE band, which provides an efficient pathway for Er^{3+} excitation. A direct comparison of the temperature dependence of Er^{3+} PL intensity and lifetime suggests that both nonradiative decay and a decrease in excitation efficiency reduce the Er^{3+} PL. Under above-gap excitation the absolute Er^{3+} PL intensity from all samples was greatly reduced and only a weak PL dependence on the oxygen and carbon concentration was observed. The weak above-gap Er^{3+} PL suggests that the efficiency of electroluminescence devices (forward biased LED's) based on currently available materials will be rather low. More materials engineering will be necessary to optimize the 1.54μm Er^{3+} PL from GaN: Er. Initial results of visible luminescence studies were also presented. It was found that only under below-gap excitation GaN:Er on sapphire emits red luminescence peaking at 665 and 690 nm. The 665 nm line was assigned to an intra-4f Er^{3+} transition, whereas the origin of the 690 nm line is not yet known. More detailed studies on the luminescence properties of GaN: Er are in progress in will be presented in a forthcoming paper.

ACKNOWLEDGMENTS

We would like to thank George Ofori-Boudu and Jakeithia Preajan for the help with some PL experiments. The authors from Hampton University acknowledge financial support by NASA through Grant NCC-1-251 and the Army Research Office through Grants DAAH04-96-1-0089 and DAAG55-98-1-0112. The work at the University of Florida was supported by ARO grant DAAH04-96-1-0089.

REFERENCES

[1] R. L. Bell, J. Appl. Phys. Comm. **34**, 1563 (1963).
[2] H. Ennen, U. Kaufmann, G. S. Pomrenke, J. Schneider, J. Windschif, and A. Axmann, J. Crystal Growth **64**, 165 (1983).
[3] G. S. Pomrenke, P. B. Klein, and D. W. Langer, Rare Earth Doped Semiconductors, Material Research Society Symposium Proceedings, Vol. 301, Material Research Society, Pittsburg, 1993.
[4] S. Coffa, A. Polman, and R.N. Schwartz, Rare Earth doped Semiconductors II, Materials Research Society Symposium Proceedings, Vol. 422, Material Research Society, Pittsburgh, PA, 1996.
[5] P. N. Favennec, H.L. Haridon, M. Salvi, D. Moutonnet, and Y. Le Guillou, Electr. Lett. **25**, 718 (1989).
[6] A.J. Neuhalfen and B.W. Wessels, Appl. Phys. Lett. **60**, 2657 (1992).
[7] W. J. Choyke, R. P. Devaty, L. L. Clemen, M. Yoganathan, G. Pensl, and Ch. Hässler, Appl. Phys. Lett. 65, 1668 (1994).
[8] J. M. Zavada and D. Zhang, Solid-State Electronics, Vol. **38**, No.7, 1285 (1995).
[9] R. G. Wilson, R. N. Schwartz, C. R. Abernathy, S. J. Pearton, N. Newman, M. Rubin, T. Fu, and J. M. Zavada, Appl. Phys. Lett. **65**, 992 (1994).
[10] C.H. Qui, M. W. Leksono, J. I. Pankove, J. T. Torvik, R. J. Feuerstein, and F. Namavar, Appl. Phys. Lett. **66**, 562 (1995).
[11] E. Silkowski, Y.K. Yeo, R. L. Hengehold, B. Goldenberg, and G. S. Pomrenke, MRS Proceedings, Vol. **422**, 69 (1996).
[12] S. Kim, S. J. Rhee, D. A. Turnbull, E. E. Reuter, X. Li, J. J. Coleman, and S. G. Bishop, Appl. Phys. Lett. **71**, 231 (1997).
[13] Myo Thaik, U. Hömmerich, R. N. Schwartz, R. G. Wilson, and J.M. Zavada, Appl. Phys. Lett. **71**, 2641 (1997).
[14] J. D. MacKenzie, C. R. Abernathy, S. J. Pearton, U. Hömmerich, X. Wu, R. N. Schwartz, R. G. Wilson, J. M. Zavada, Appl. Phys. Lett. **69**, 2083 (1996).
[15] J. D. MacKenzie, C. R. Abernathy, S. J. Pearton, U. Hömmerich, X. Wu, R. N. Schwartz, R. G. Wilson, J. M. Zavada, J. Cryst. Growth **175/176**, 84 (1997).
[16] D.M. Hansen, R. Zhang, N. R. Perkins, S. Safvi, L. Zhang, K.L. Bray, and T. F. Kuech, Appl. Phys. Lett **72**, 1244 (1998).
[17] A. J. Steckl and R. Birkhahn, Appl. Phys. Lett. **73**, 1701 (1998).
[18] A. J. Steckl, M. Garter, R. Birkhahn, and J. Scofield, Appl. Phys. Lett. **73**, 2450, (1998).
[19] J. T. Torvik, R. J. Feuerstein, C. H. Qui, J. I. Pankove, and F. Namavar, J. Appl. Phys. **69** 2098 (1996).
[20] H. Shen, J. Pamulapati, J. D. Mackenzie, F. Ren, C. R. Abernathy, and J. M. Zavada, MRS Fall Meeting 1998, paper G11.5.
[21] J. D. MacKenzie, C. R. Abernathy, S. J. Pearton, U. Hömmerich, J. T. Seo, R. G. Wilson, and

J. M. Zavada, Appl. Phys. Lett. **72**, 2710 (1998).
[22] W. J. Miniscalco, J. of Lightwave Techn. **9**, 234 (1991).
[23] B. J. Ainslie, J. of Lightwave Techn. **9**, 220 (1991).
[24] S. J. Rhee, S. Kim, X. Li, J. J. Coleman, and S. G. Bishop, Mat. Res. Soc. Symp. Proc., Vol. **482**, 667 (1998).
[25] X. Wu, U. Hömmerich, J. D. MacKenzie, C. R. Abernathy, S. J. Pearton, R. N. Schwartz, R. G. Wilson, and J. M. Zavada, Appl. Phys. Lett. **70**, 2126 (1997).
[26] J. L. Benton, D.J. Eaglesham, M. Almonte, P.H. Citrin, M. A. Marcus, D.L. Adler, D. C. Jacobson, and J. M. Poate, Mat. Res. Soc. Symp. Proc., Vo. **301**, 119 (1993).
[27] S. Coffa, F. Priolo, G. Franzo, V. Bellani, A. Carnera, C. Spinella, Phys. Rev. B, **48**, 11782 (1993).
[28] K. Takahei, A. Taguchi, J. Appl. Phys. 74, 1979 (1993).
[29] J. Michel, J.L. Benton, R.F.Ferrante, D.C. Jacobson, D.J.Eaglesham, E.A. Fitzgerald, Y.H. Xie, J.M. Poate, and L.C. Kimmerling, J. Appl. Phys. **70**, 2672 (1991).
[30] S. Coffa, F. Priolo, G. Franzo, V. Bellani, A. Carnera, and C. Spinella, Mat. Res. Soc. Symp. Proc., Vol. **301**, 125, 1993.
[31] J. T. Torvik, R. J. Feuerstein, C. H. Qui, J. I. Pankove, and F. Namavar, Mat. Res. Soc. Symp. Proc., Vol. **482**, 579, 1998.
[32] J. Fernandez, R. Balda, M. A. Illarramendi, G. F. Imbusch, J. Lumin. **58**, 294 (1994).
[33] L. J. Andrews, A. Lempicki, and B. C. McCollum, J. Chem. Phys. **74**, 5526 (1981).
[34] G. N. van den Hoven, Jung H. Shin, A. Polman, S. Lombardo, and S. U. Campisano, J. Appl. Phys. **78**, 2642, 1995.
[35] P. G. Kik, M. J. A de Dood, K. Kikoin and A. Polman, Appl. Phys. Lett. **70**, 1721 (1997).
[36] R. Birkhahn and A.J. Steckl, Appl. Phys. Lett. **73**, 2143 (1998).
[37] A. J. Steckl, M. Garter, R. Birkhahn, and J. Scofield, Appl. Phys. Lett. **73**, 2450, (1998).

OPTICAL AND STRUCTURAL PROPERTIES OF AlGaN/GaN QUANTUM WELLS GROWN BY MOLECULAR BEAM EPITAXY

Nicolas Grandjean*, Jean Massies*, Mathieu Leroux*, Marguerite Laügt*, Pierre Lefebvre**, Bernard Gil**, Jacques Allègre**, Pierre Bigenwald ***

* Centre de Recherche sur l'Hétéro-Epitaxie et ses Applications - CNRS
Rue B. Grégory, Sophia Antipolis, F-06560 Valbonne, France.
** Groupe d'Etude des Semiconducteurs - CNRS - Université Montpellier II.
Case Courrier 074. 34095 Montpellier Cedex 5, France.
*** LPM - Université d'Avignon - 33, rue Pasteur. 84000 Avignon, France.

Cite this article as: MRS Internet J. Nitride Semicond. Res. 4S1, G11.7 (1999)

ABSTRACT

AlGaN/GaN quantum well (QWs) were grown on (0001) sapphire substrates by molecular beam epitaxy (MBE) using ammonia as nitrogen precursor. The Al composition in the barriers was varied between 8 and 27 % and the well thickness from 4 to 17 monolayers (MLs, 1ML = 2.59Å). X-ray diffraction (XRD) experiments are used to investigate the strain state of both the well and the barriers. The QW transition energy are measured by low temperature photoluminescence (PL). A large quantum confined Stark effect is observed leading to QW luminescence much lower than the emission line of the GaN buffer layer for well width above a certain critical thickness. The built-in electric field responsible for such a phenomenon is deduced from fit of the PL data. Its magnitude is of several hundred kV/cm and increases linearly with the Al composition.

INTRODUCTION

The III-V nitride compounds have demonstrated their peculiar aptitude for producing light from the green to UV spectral range [1]. As for the case of other optoelectronic devices based on arsenide, phosphide or antimonide compounds, quantum wells (QWs) are currently used in the active region of nitride based light emitting diodes and laser diodes [1]. However, there is still only a few reports on the physical properties of nitride QWs compared to what is known about the prototypical system AlGaAs/GaAs. This is especially the case when considering the AlGaN/GaN QWs [2-8] though they appear very promising for extending the applications of nitrides to the far UV spectral region owing to the large direct band gap of AlN (6.2 eV/200 nm). It has been already shown that a large internal electric field of several hundred kV/cm takes place in the wurtzite AlGaN/GaN QWs [2-8]. Both piezoelectric and spontaneous polarization must be considered to account for the polarization field inside the quantum structure. Actually, spontaneous polarization has been theoretically considered because of the expected huge influence on the properties of AlGaN/GaN heterostructures [9,10].

In this paper, we report on AlGaN/GaN QWs grown by MBE on c-plane sapphire substrates. Their structural properties have been checked by XRD and their optical properties by low temperature PL. The Al composition of the AlGaN barriers was ranged between 8 and 27% and

Mat. Res. Soc. Symp. Proc. Vol. 537 © 1999 Materials Research Society

the well thickness increases from 4 to 17 MLs. The internal electric field was deduced by fitting the PL data using a self-consistent envelope function calculation, including excitonic effects.

EXPERIMENTS

The growth of GaN and AlGaN layers are carried out in a Riber 32 P MBE system. Both reflection high-energy electron diffraction (RHEED) and laser reflectivity facilities are available *in situ*. The substrate is c-plane sapphire back-coated with Mo for heating. NH_3 is used as nitrogen precursor. Ga and Al elements are evaporated by a double filament cell and a cold-lip cell, respectively. A few µm of GaN is deposited at 820°C before growing the QWs structures which are separated by 100Å-thick AlGaN barriers. The Al mole fraction is measured *in situ* by the RHEED intensity oscillation technique [11]. The PL experiments are performed at 10 K. Two excitation sources are used, either a HeCd laser (10 mW) or a frequency-doubled Ar^+ laser (244 nm/40mW).

RESULTS AND DISCUSSIONS

The quality of the quantum heterostructures is strongly dependent on the surface morphology. Fig. 1 shows the surface observed by scanning electron microscopy after the growth of a 10 period $Al_{0.11}Ga_{0.89}N$/GaN multi(M)-QW structure. Despite the standard grain-like structure of the GaN film, the roughness is rather low. Indeed, the rms roughness measured on a $3x3\mu m^2$ scan area by atomic force microscopy is only 3 nm. This value falls down to 0.2nm for $100x100\ nm^2$ scan which is consistent with the observation of RHEED intensity oscillations attesting a 2D layer by layer growth mode. This point constitutes a key issue for achieving AlGaN/GaN QWs with sharp interfaces, but also for measuring *in situ* the Al mole fraction in the AlGaN barriers.

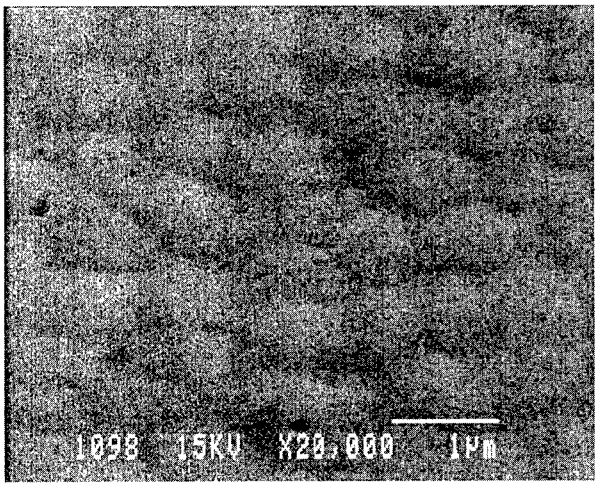


Figure 1: scanning electron micrograph of a multi-quantum well sample grown on sapphire.

Fig. 2 displays the intensity variation of the specular beam intensity recorded during the growth of $Al_{0.1}Ga_{0.9}N$ at 600 °C. The period corresponds to the growth of 1 ML and allows one directly determining the growth rate. From the difference with the growth rate of pure GaN, we can measure the Al mole fraction ($x = (r_{AlGaN}-r_{GaN})/r_{AlGaN}$). It should be noted that in order to avoid the flux transient which takes place just after opening the Ga and Al shutters, and which may affect the measurements, a careful procedure has been followed: taking advantage of the stability of GaN at 600°C without ammonia, a general shutter is intercalated between the cells and the sample, and is only opened when the Ga and Al fluxes are stabilized. The data in Fig. 2 correspond to such a procedure. Thick AlGaN layers (1 µm) have been grown and energy dispersive x-ray (EDX) has been used to determine the Al mole fraction. The discrepancy between RHEED and EDX determinations is within one percent.

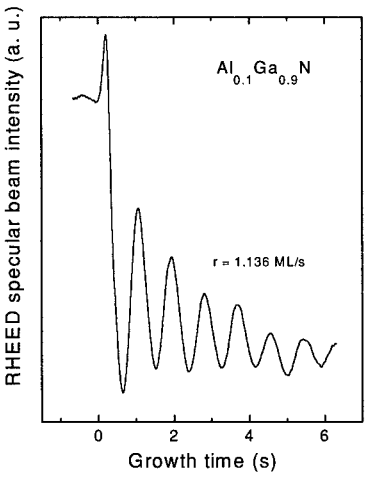


Figure 2: RHEED intensity oscillations recorded during AlGaN growth.

The 10 K PL spectra of AlGaN layers with different Al mole fractions are shown in Fig. 3. The peak linewidth increases with the Al composition together with the Stokes-shift between PL and reflectivity. This indicates that a degradation of the crystal quality occurs. Actually, AlGaN barriers have been grown keeping the same growth parameters than GaN (growth temperature 820°C), while it is obvious that high Al content AlGaN layers should be grown at higher temperature.

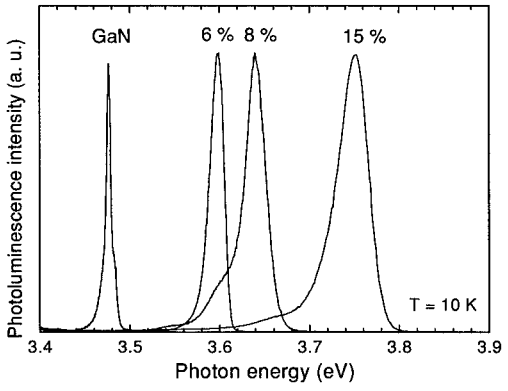


Figure 3: PL spectra of AlGaN layers with different Al mole fraction.

The structural properties of the quantum heterostructures have been checked by XRD reciprocal space mapping, as shown for instance in Fig. 4 for a MQW sample. This sample consists of 10 periods of GaN(6 MLs)/AlGaN(19MLs) deposited on a 2 μm-thick GaN template. Fig. 4 shows that $Al_{0.11}Ga_{0.89}N$ barriers are pseudomorphically strained onto the GaN template. Both the value of a and c lattice constants (3.189_2 Å and 5.185_5 Å, respectively) and the position of the A free exciton (3.478 eV) indicate that the GaN thick buffer layer is nearly relaxed. AlGaN barriers are thus under tensile stress. This point has to be kept in mind for the following part which concerns the origin of the built-in electric field in AlGaN/GaN Qws.

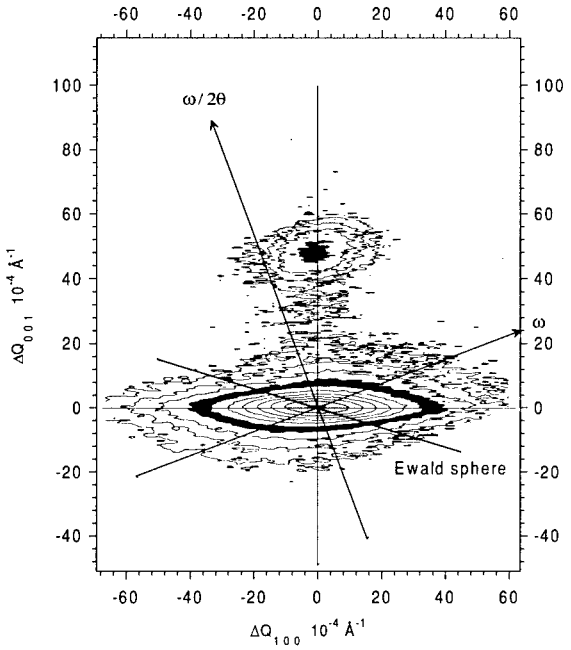


Figure 4: XRD reciprocal space mapping of a 10xGaN(6 MLs)/$Al_{0.11}Ga_{0.89}N$(19 MLs) MQW

Let us turn now towards the optical properties of AlGaN/GaN based quantum structures. Fig. 5 displays the 10 K PL spectra of two samples containing four QWs of different thicknesses with Al composition in the AlGaN barriers of 13% (a) and 27% (b), respectively. The thickness of the barriers is 100Å. For the Al composition of 13% (Fig. 5(a)), the PL energy of the 17 ML wide well is much lower than the GaN band gap. This is a consequence of a quantum confined Stark effect due to a strong internal electric field in the quantum structure. This effect is reinforced in Fig. 5(b) for an Al mole fraction in the barriers of 27%. The 26 meV splitting of the PL line of the 16 MLs wide QW in Fig. 5(b) could correspond to a well thickness fluctuation of 1 ML taking into account a built-in electric field of 1 MV/cm. The values of the internal electric field have been deduced from fitting PL energies with a self-consistent envelope function model including the electric field [7]. They are plotted in Fig. 6 as a function of the Al composition in the barriers from 8 to 27%. The field is shown to vary linearly with Al content, extrapolating to zero for pure GaN. It is larger than 1MV/cm for an Al content of 27%.

Let us discuss the strength and origin of the internal field. First, we mention that for an Al content in the barriers in the 10-15% range, Fig. 6 shows that the field is in the 400-600 kV/cm range. This is in agreement with the results of other authors, who also studied AlGaN/GaN heterostructures with similar barrier compositions [5-8,12]. Second, as exemplified in Fig. 4, we are dealing with strained AlGaN barriers on nearly relaxed GaN. This means that the piezoelectric effect occurs in our samples mainly in the barrier, and not in the well (as in the typical case of (111) grown GaAs/GaInAs QWs for instance). Moreover, following Bernardini et al. [9,10], we ascribe the Stark effect in our samples to the difference in total (piezoelectric and spontaneous) polarization between well and barrier materials. In that case, the resulting electric field in the well (for infinite barriers, which is not the case of our samples) is given by $F = (P_b - P_w)/\varepsilon\varepsilon_0$, where P_b and P_w are the total polarization in the barrier and the well, respectively. Note that with the above definition of the electric field, the effect of a biaxial compressive strain in GaN is the same as that of a biaxial tensile strain in AlGaN barriers (apart from a small difference due to the slight differences of material constants and that of deformation potentials). When using the theoretical piezoelectric constants and spontaneous polarization values [10], field magnitudes at least a factor of 2 larger than those deduced from figure 6 are obtained. The values are still too large when taking into account the effect of finite barrier width [7]. Apart from the uncertainties in the physical parameters used, reasons for the discrepancies could be the crystal quality (the high dislocation density in GaN/Al_2O_3 samples may influence the strain field), but also partial screening of the polarization field due to the residual n-type doping level of GaN (and AlGaN), in the 10^{17} cm^{-3} range.

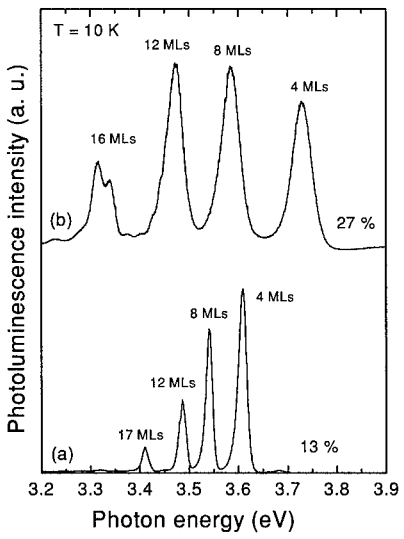


Figure 5: PL spectra of QW structures

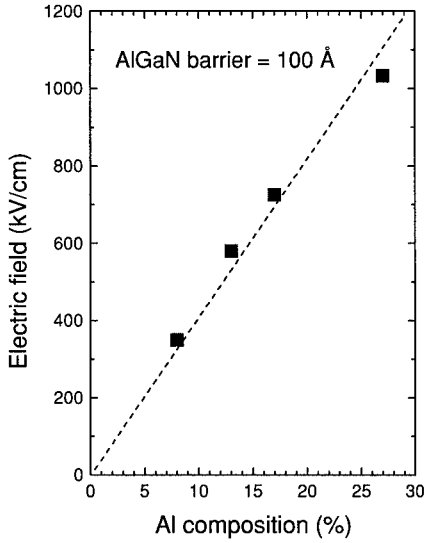


Figure 6: electric field *versus* the Al content

CONCLUSIONS

AlGaN/GaN quantum wells of various widths have been grown by molecular beam epitaxy on c-plane sapphire substrates with different Al contents in the barriers. The QW transition energies deduced from low temperature photoluminescence exhibit a quantum confined Stark effect due to strong internal electric fields which can reach 1 MV/cm for only 25 % of Al content. This electric field is found to vary linearly with the Al mole fraction, at least up to $x \approx 0.3$. A conclusion of this study is that, due to the balance between the blue shift due to quantum confinement (increasing with Al content in the barrier), and red shift due to the Stark effect (also increasing with Al content), only GaN well thicknesses lower than $\approx$ 11 MLs ($\approx$ 30 Å) yield transition energies larger than the GaN band gap, at least in the range of barrier thicknesses and AlGaN compositions studied in this work.

ACKNOWLEDGEMENTS

This work was supported in part by E.C. Contract No. BPR-CT96-0334 'ANISET'

REFERENCES

[1] S. Nakamura and G. Fasol, 'The Blue Laser Diode', Springer - Berlin (1997)

[2] R. Niebuhr, K.H. Bachem, D. Behr, C. Hoffman, U. Kaufmann, Y. Lu, B. Santic, J. Wagner, M. Arlery, J.L. Rouvière and H. Jürgensen, Mat. Res. Soc. Symp. Proc. **449**, 769 (1997).

[3] M. Smith, J.Y. Lin, H.X. Jiang, A. Khan, Q. Chen, A. Salvador, A. Botchkarev and H. Morkoç, Mat. Res. Soc. Symp. Proc. **449**, 829 (1997).

[4] N. Grandjean and J. Massies, Appl. Phys. Lett., **73**, 1260 (1998).

[5] J.M. Im, H. Kollmer, J. Off, A. Sohmer, F. Scholz and A. Angleiter, Mat. Res. Soc. Symp. Proc. **482**, 513 (1998)

[6] J.S. Im, H. Kollmer, J. Off, A. Sohmer, F. Scholz, and A. Hangleiter, Phys. Rev. B **57**, R9435 (1998)

[7] M. Leroux, N. Grandjean, M. Laügt, J. Massies, B. Gil, P. Lefebvre, and P. Bigenwald, Phys. Rev. B **58**, R13371 (1998)

[8] P.Lefebvre, J.Allègre, B.Gil, H.Mathieu, P.Bigenwald, N.Grandjean, M.Leroux and J.Massies, Phys. Rev. B, *to be published.*

[9] F. Bernardini, V. Fiorentini and D. Vanderbilt, Phys. Rev. B **56**, R10024 (1997)

[10] F. Bernardini and V. Fiorentini, Phys. Rev. B **57**, R9427 (1998)

[11] N.Grandjean and J.Massies, Appl. Phys. Lett. **71**, 1816 (1997)

[12] T.Honda, T.Miyamoto, T.Sakaguchi, H.Kawanishi, F.Koyama and K.Iga, J. Cryst. Growth **189/190**, 644 (1998)

DEFECT LUMINESCENCE IN HEAVILY Mg DOPED GaN

M. A. Reshchikov*, G.-C. Yi, and B. W. Wessels

Department of Materials Science and Engineering and Materials Research Center
Northwestern University, Evanston, IL, 60208

Cite this article as: MRS Internet J. Nitride Semicond. Res. 4S1, G11.8 (1999)

ABSTRACT

Behavior of the photoluminescence band at about 2.8 eV in heavily Mg doped GaN has been studied at different temperatures and excitation intensities. The 2.8 eV band is attributed to donor–acceptor transitions involving a Mg acceptor. The large blue shift of the band with increasing excitation intensity is explained by variation in the contribution of close and distant pairs to the luminescence. The red shift of the band with increasing temperature under high excitation intensity conditions results from thermal release of carriers from close pairs. The thermal activation energy of the deep donor, about 0.4 eV, is determined from the quenching of the 2.8 eV luminescence band at high temperatures.

INTRODUCTION

High concentrations of magnesium acceptors are required to obtain conductive p-type GaN because of its large activation energy. In heavily Mg doped GaN a broad photoluminescence (PL) band around 2.6-2.95 eV (referred hereafter as the 2.8 eV band) dominates the PL spectrum [1-11]. The nature of the defect responsible for this band and even the type of optical transitions involved remain unclear. The most widely accepted model is that the PL is due to an optical transition from the conduction band to a deep defect with a level at about 0.5-0.55 eV above the valence band [2-6]. Recently, it was proposed that the 2.8 eV PL band involves an optical transition from a deep donor to the shallow Mg acceptor [7]. Up to now there is no definite evidence supporting one particular model. The main distinguishing feature of the 2.8 eV band, a large blue shift with increasing excitation intensity, may be explained by several models [5-8]. In the donor-acceptor pair (DAP) model, the shift is attributed to saturation of emission from distant DAP due to their longer lifetime [7,8]. Alternatively, formation of impurity bands [5,6] or potential fluctuations [6] have been considered as possible reasons for the observed shift.

Indeed, large potential fluctuations due to randomly distributed charged impurities are expected in heavily doped semiconductors [12]. Free carriers in compensated material are localized in potential wells and optical transitions have many similar features to that of the DAP type transitions [13]. The similarities in behavior of the DAP emission and the band-assisted transitions in heavily doped semiconductor with potential wells complicate assignment of PL bands.

In this work we investigated the 2.8 eV PL band in heavily doped GaN at different temperatures and excitation intensities. The results of the study support the deep donor-acceptor pair assignment of this PL. The large measured shifts of the 2.8 eV band with variation of temperature or excitation intensity originate from varying contribution of emission from close and distant pairs.

Mat. Res. Soc. Symp. Proc. Vol. 537 © 1999 Materials Research Society

EXPERIMENTAL RESULTS

The Mg-doped GaN epilayers were grown on c-plane sapphire by metal-organic vapor phase epitaxy. The samples are either semi-insulating or p-type with resistivity as low as 3 Ω·cm at room temperature. PL was excited by cw He-Cd laser (325 nm) and analyzed by Spex grating monochromator with Hamamatsu photomultiplier tube. Excitation power density (P_{exc}) was varied over the range 10^{-5}-27 W/cm^2 by means of neutral density filters. The sample temperature was varied from 13 to 380 K using a closed cycle helium cryostat.

A broad band with a peak near 2.8 eV has been observed in the PL spectra of the studied samples. In some samples another PL band with a maximum near 3.2 eV was noted as a shoulder or separate peak. The position of the 2.8 eV band depended strongly on excitation intensity (Fig. 1). At low temperature the total blue shift of the band with increasing excitation power amounted to 0.23 eV. The peak position shifted largely at high excitation density and was nearly independent of excitation rate in the low excitation limit. At room temperature the PL band shifted about 0.10 eV over the same excitation intensity range (Fig. 1). The shape of the band remained almost independent of excitation intensity for the samples with small overlap with the 3.2 eV band. A typical change in the PL spectrum is shown in Fig. 2. We attribute the observed dependence of the PL spectrum with excitation to changes in contributions of emission from close and distant pairs in the case of deep DAP transitions. The DAP transition rate for a pair with a separation R has the approximate form [13,14]

$$W(R) = W_0 \exp\left(-\frac{2R}{a_B}\right) \tag{1}$$

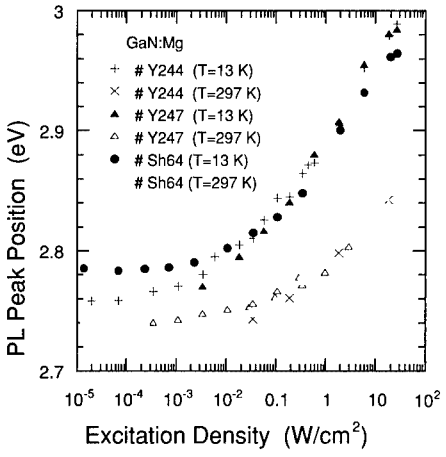


Fig. 1. Dependence of the 2.8 eV PL peak position on excitation power density at 13 and 297 K for three GaN:Mg samples.

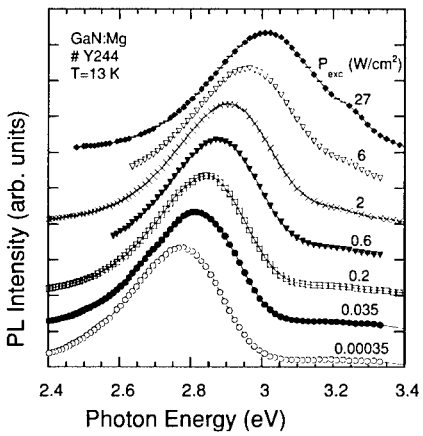


Fig. 2. PL spectra of the semi-insulating GaN:Mg sample # Y244 at different excitation intensities.

where a_B is the largest Bohr radius for the bound carriers. The radiative lifetime increases exponentially with increasing R according to Eq. (1). At high excitation intensity, PL from distant pairs saturates due to their longer lifetime and transitions between close pairs dominate. The PL energy corresponding to a transition between a pair with separation R is given by

$$E_{PL}(R) = E_g - (E_A + E_D) + \frac{e^2}{\varepsilon R} \tag{2}$$

where E_g is the band gap, E_A and E_D are the acceptor and donor binding energies, e is the electronic charge, and ε is the low frequency dielectric constant. The last term is due to the Coulomb interaction between charged donor and acceptor. As a result of strong Coulomb interaction between close pairs, the PL band blue-shifts with increasing excitation intensity. Saturation of the band shift in the low excitation limit may be explained by the fact that transitions between pairs with more than average separation are highly unlikely because of their small fraction and the low probability of such transitions.

For a high excitation intensity the 2.8 eV band red-shifted significantly with increasing temperature whereas at low excitation intensity its position remained almost unchanged up to 100 - 200 K (Fig. 3). This behavior also may be explained by the DAP nature of this band. The Coulomb interaction between close pairs may be very strong [14] and the resultant ionization energy will decrease sufficiently enough for thermal release of the trapped carriers. As a result, the high-energy portion of the spectrum begins quenching at lower temperatures and the PL band undergoes a red shift. However at a low excitation rate, emission from comparatively distant pairs dominates and the red shift is reduced. This effect has been previously observed in Si doped with donors and acceptors having similar activation energies [15]. The observed temperature-induced red shift is just the reverse of the well-known blue shift for DAP emission for shallow donors and acceptors [13]. In the latter case the blue shift is due to thermal escape of electrons from the shallow donor which is more favorable for the long-lived distant pairs contributing to the low-energy part of a spectrum. The observed red shift of the 2.8 eV band with increase in temperature can not be attributed to potential fluctuations since the red shift caused by the potential fluctuations should increase with a decrease of excitation rate [13].

The temperature dependence of the PL intensity for the 2.8 eV band is shown in Fig. 4. The 2.8 eV PL band quenches at temperatures above 200-250 K with an activation energy E_D of about 0.3-0.4 eV, observed for all samples. The quenching is attributed to thermal release of electrons from deep donor to the conduction band. In the inset of Fig. 4 the calculated dependence of the PL intensity is shown using the following expression

$$I(T) = I_0\left(1 + A\exp\left(-\frac{E_D}{kT}\right)\right)^{-1} \tag{3}$$

where A is a constant, assumed to be temperature independent for simplicity. We attribute the discrepancy between calculated curve and the experimental data to the distribution of donor energies due to the Coulomb interaction with the charged acceptors. The higher the excitation intensity, the higher the contribution of the close pairs characterized by the stronger Coulomb interaction. Thermalization of electrons to the conduction band from the donors of these close pairs results in the beginning of thermal quenching of PL at lower temperatures, see the inset of Fig. 4.

The lifetime of the 2.8 eV PL has been estimated to be 10^{-5} sec at low temperature from the time-resolved measurements. The decay of the PL is non-exponential. These results are also consistent with the DAP model for the 2.8 eV PL band.

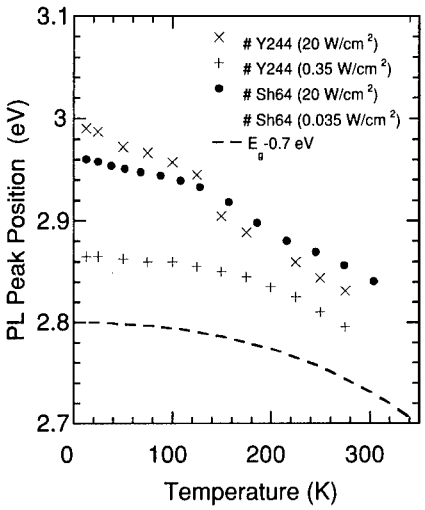


Fig. 3. Variation of the 2.8 eV PL peak position with temperature. Variation of the gap width is shown shifted by 0.7 eV for convenience.

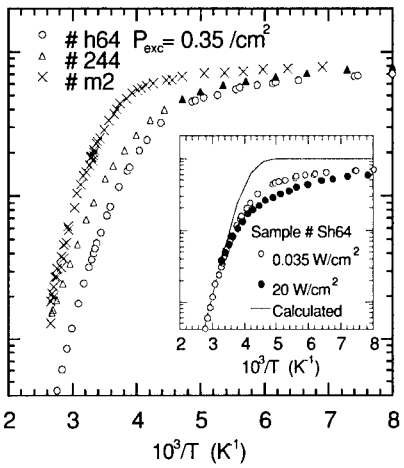


Fig. 4. Intensity of the 2.8 eV PL band versus reverse temperature. The inset shows the $I\ (T^{-1})$ dependence at low and high excitation intensities in comparison with the calculated from Eq. (3) dependence ($A = 1.5\times10^7$; $E_D = 0.35$ eV).

DISCUSSION

The 2.8 eV PL band appears at high concentrations of Mg (10^{19}–10^{20} cm^{-3}) [1,2,6,7,10] which correspond to a mean separation between impurities of about 15–30 Å. The close location of pair components results in a high probability for DAP type transitions in spite of the strong localization of the wave-functions for electron and hole bound to the deep defects. The Coulomb interaction energy for an average separation between acceptor and donor is estimated to be ~ 0.1–0.15 eV by taking R = 10–15 Å (corresponds to acceptor concentration of ~10^{19} cm^{-3}) in Eq. (2). Supposing that saturation of the PL band peak position in the low excitation limit (at 2.75–2.78 eV in Fig. 1) corresponds to transitions between DAP having an average separation, and taking E_g = 3.5 eV and E_A = 0.2 eV, we calculated E_D = 0.6–0.7 eV for the isolated deep donor. The actual position of the donor level in heavily doped GaN depends essentially on the location of the nearest charged acceptor, shown schematically in Fig. 5.

The potential fluctuations, expected for heavily doped semiconductors [12], should not strongly affect the deep DAP emission. Indeed, the higher the magnitude of the potential fluctuation, the larger its size [12], and optical transition between defects separated by about 10–15 Å may be considered as almost vertical in the scale of the long-range fluctuations.

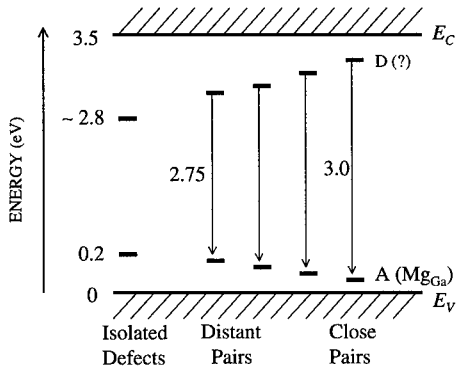


Fig. 5. Schematic diagram showing optical transitions in heavily Mg doped GaN

The values of radiative lifetime for the 2.8 eV band found in this study (about 10 μsec) and by Seitz et al. [11] (about 0.2 msec) are consistent with DAP emission. Similar lifetimes were observed for the deep DAP in ZnSe (about 0.1 msec) [14].

The question of the nature of donor responsible for the compensation of Mg in GaN is open. The nitrogen vacancy (V_N), which has a low formation energy in p-type GaN, is one possibility. However the vacancy is expected to have the +/3+ energy level not far from the valence band [16]. It is possible that the donor is formed from a complex defect. Kaufmann et al. suggested that Mg_{Ga} and mobile V_N form a complex $Mg_{Ga}V_N$ that acts as a donor [7]. The identification of this defect requires further investigations.

CONCLUSIONS

A large blue shift of the 2.8 eV PL band with increasing excitation intensity has been observed in Mg doped GaN. This effect, as well as the observed red shift of the band with increasing temperature at high excitation rate, is explained by variation in contributions of emission from close and distant pairs to the PL band. The 2.8 eV band is attributed to transitions from the compensating deep donor to the shallow Mg acceptor. Thermal quenching of the 2.8 eV band begins at $T > 200$ K with an apparent activation energy of about 0.4 eV. The observed quenching is attributed to the thermalization of trapped electrons from the deep donor state to the conduction band.

ACKNOWLEDGEMENTS

The authors thank F. Shahedipour at the Electronic and Photonic Materials Group and Ian Ferguson at EMCORE for providing p-type GaN samples. This work was supported by the National Science Foundation GOALI Program, under grant number ECS-9705134.

REFERENCES

* On leave from A. F. Ioffe Physico-Technical Institute of Russian Academy of Sciences, St. Petersburg, Russia.

1. H. Amano, M. Kitoh, K. Hiramatsu, I. Akasaki, J. Electrochem. Soc., **137**, 1639 (1990).
2. A. K. Viswanath, E. Shin, J. I. Lee, S. Yu, D. Kim, B. Kim, Y. Choi and C.-H. Hong, J.Appl. Phys. **83**, 2272 (1998).
3. H. P. Maruska, D. A. Stevenson and J.I. Pankove, Appl. Phys. Lett. **22**, 303 (1973).
4. S. Nakamura, N. Iwasa, M. Senoh, and T. Mukai, Jpn. J. Appl. Phys. **31**, Pt. 1, 1258 (1992).
5. M. Smith, G. D. Chen, J. Y. Lin, H. X. Jiang, A. Salvador, B. N. Sverdlov, A. Botchkarev, H. Morkoc, and B. Goldenberg, Appl. Phys. Lett. **68**, 1883 (1996).
6. E. Oh, H. Park and Y. Park, Appl. Phys. Lett **72**, 70 (1998).
7. U. Kaufmann, M. Kunzer, M. Maier, H. Obloh, A. Ramakrishnan, B. Santic, and P. Schlotter, Appl. Phys. Lett. **72**, 1326 (1998).
8. L. Eckey, U. Von Gfug, J. Holst, A. Hoffmann, B. Schineller, K. Heime, M. Heuken, O. Schön, and R. Beccard, J. Cryst. Growth **189/190**, 523 (1998).
9. J. M. Myoung, K. H. Shim, C. Kim, O. Gluschenkov, K. Kim, S. Kim, D. A. Turnbull, and S.G. Bishop, Appl. Phys. Lett. **69**, 2722 (1996).
10. W. Götz, N. M. Johnson, J. Walker, D. P. Bour, and R. A. Street, Appl. Phys. Lett. **68**, 667 (1996).
11. R. Seitz, C. Gaspar, T. Monteiro, E. Pereira, M. Leroux, B. Beaumont, and P. Gibart, *Materials Science Forum* **258-263**, 1155 (Trans. Tech. Publications, Switzerland, 1997).
12. B. I. Shklovskii and A. L. Efros, *Electronic Properties of Doped Semiconductors* (Springer, Berlin, 1984), pp. 53-73, 253-313.
13. A. P. Levanyuk, V. V. Osipov, Usp. Fiz. Nauk **133**, 427 (1981) [Sov. Phys. Usp. **24**, 187 (1981)].
14. F. C. Rong, W. A. Barry, J. F. Donegan, and. G. D. Watkins, Phys. Rev. B **54**, 7779 (1996); W. A. Barry and G. D. Watkins, *ibid.*, 7789 (1996).
15. A. S. Kaminskii and Ya. E. Pokrovskii, Fiz. Tekh. Poluprovodn. **3**, 1766 (1969) [Sov. Phys. Semicond. **3**, 1496 (1970)].
16. C. G. Van de Walle, C. Stampfl and J. Neugebauer, J. Cryst. Growth **189/190**, 505 (1998).

AUTHOR INDEX

Abernathy, C.R., G6.33.1, G6.39.1, G6.40.1, G6.56.1, G8.1.1, G11.1.1, G11.2.1, G11.6.1
Adesida, I., G1.4.1
Ager III, J.W., G3.15.1
Akasaki, I., G2.5.1, G3.26.1, G3.66.1, G5.4.1, G10.1.1
Aksenov, I., G3.4.1
Albrecht, J.D., G6.6.1, G6.35.1
Albrecht, M., G4.11.1
Alexson, D., G6.65.1
Allègre, J., G3.69.1, G11.7.1
Allen, G.C., G6.57.1
Alves, E., G11.2.1
Amano, H., G2.5.1, G3.26.1, G3.66.1, G5.4.1, G10.1.1
Ambacher, O., G5.5.1, G8.4.1
Ancona, M.G., G6.35.1
André, R., G3.19.1
Andreev, A.D., G6.45.1
Angus, J.C., G3.23.1
Anwar, A.F.M., G6.7.1, G6.58.1
Aoyagi, Y., G3.74.1, G9.4.1
Argoitia, A., G3.23.1
Arunmozhi, G., G3.76.1
As, D.J., G2.3.1, G3.14.1, G3.24.1
Ashmawi, W.M., G3.38.1
Aspnes, D.E., G3.78.1
Auner, G.W., G3.7.1
Auret, F.D., G6.12.1, G6.13.1

Babcock, S.E., G3.56.1
Baca, A.G., G6.9.1
Bachem, K-H., G2.8.1
Bae, I-T., G3.11.1
Bailey, J., G3.40.1
Balkas, C., G6.65.1
Banas, M., G7.7.1
Barcz, A., G9.9.1
Barrière, S., G3.59.1
Barski, A., G3.19.1
Bartels, J., G11.2.1
Bartram, M.E., G3.68.1, G6.9.1
Batchelor, A.D., G3.2.1, G3.78.1
Beach, R.A., G3.77.1, G6.26.1
Beaumont, B., G6.12.1, G6.13.1
Bedair, S.M., G3.22.1
Behr, D., G2.8.1
Bellotti, E., G6.6.1, G6.59.1
Benamara, M., G4.6.1
Berding, M.A., G5.1.1
Bergman, J.P., G2.5.1
Bergman, L., G6.65.1
Bertram, F., G3.26.1, G3.33.1
Bhat, I., G3.76.1
Bidnyk, S., G6.44.1 G6.48.1, G6.54.1
Bigenwald, P., G3.69.1, G11.7.1
Binari, S.C., G6.35.1
Birkhahn, R.H., G3.80.1, G11.3.1
Birkle, U., G3.57.1, G5.6.1
Bishop, S.G., G3.67.1, G4.8.1, G11.4.1
Bliss, D., G3.40.1
Boleslawski, M.P., G3.62.1, G4.7.1
Botchkarev, A., G3.3.1, G6.5.1
Böttcher, T., G3.33.1
Bour, D.P., G2.2.1, G3.15.1, G3.42.1
Bouthillette, L., G3.8.1, G3.40.1
Boutros, K.S., G7.5.1
Bozdog, C., G5.9.1
Bozlee, B.J., G6.15.1
Braski, D.N., G3.79.1
Bremser, M.D., G3.78.1, G6.42.1, G9.9.1
Brennan, K.F., G6.6.1, G6.59.1
Bridger, P.M., G3.77.1
Briot, O., G6.28.1
Broser, I., G2.3.1
Brown, J.D., G4.3.1, G5.2.1, G5.10.1
Bruno, G., G3.12.1
Bulman, G., G1.4.1
Bunea, G.E., G6.41.1
Burkhardt, W., G3.24.1
Busch, J., G3.24.1
Buyanova, I.A., G3.78.1, G5.4.1
Bykhovski, A.D., G1.6.1

Callahan, M., G3.40.1
Campion, R.P., G4.11.1
Cao, X.A., G6.33.1, G6.39.1
Capezzuto, P., G3.12.1
Carlos, W.E., G7.4.1
Carlson, E.P., G3.17.1, G3.38.1, G4.9.1
Carter, C.B., G3.13.1
Chan, M.C.Y., G6.25.1
Chang, K.L., G3.44.1
Chang, Y.A., G6.49.1
Chason, E., G7.7.1
Chaudhuri, J., G3.39.1, G3.79.1
Chen, A-B., G5.1.1
Chen, H., G9.5.1
Chen, K.L., G4.7.1
Chen, W.M., G5.4.1
Chen, Y., G6.49.1, G6.57.1
Cheng, T.S., G4.11.1
Chichibu, S.F., G2.7.1
Chiu, S-Y., G6.7.1
Cho, H., G6.40.1, G6.56.1
Cho, H.K., G3.49.1
Cho, Y-H., G2.4.1, G6.44.1, G6.48.1, G6.54.1
Choi, J.Y., G3.49.1
Choi, S.C., G3.49.1
Choutov, D.A., G8.2.1
Chow, P.P., G7.6.1
Chow, W.W., G3.3.1
Christen, J., G3.14.1, G3.26.1, G3.33.1, G3.71.1
Christmann, T., G3.26.1
Christopher, M.B., G8.2.1

Chtchekine, D.G., G6.47.1
Chu, K., G8.4.1
Chua, S.J., G6.47.1
Chuang, R.W., G6.42.1
Chyr, I., G10.7.1
Cingolani, R., G1.2.1, G3.50.1
Cole, M.W., G6.39.1
Coleman, J.J., G4.8.1, G11.4.1
Colì, G., G3.50.1
Coltrin, M.E., G6.9.1
Cook, Jr., J.W., G4.3.1, G5.2.1, G5.10.1
Crawford, M.H., G6.9.1, G7.7.1
Creighton, J.R., G3.68.1
Culbertson, J.C., G3.70.1

Dalfors, J., G2.5.1
Dalmasso, S., G3.59.1
DaSilva, M.F., G11.2.1
Daudin, B., G9.2.1
Davis, R.F., G3.2.1, G3.17.1, G3.37.1, G3.38.1, G3.78.1, G4.9.1, G6.65.1, G9.9.1
Demangeot, F., G6.28.1
DenBaars, S.P., G2.4.1, G2.7.1, G4.5.1, G6.25.1. G6.44.1, G6.54.1
Dickens, C.S., G3.61.1
Dimitrov, R., G8.4.1
Dmitriev, V.A., G6.53.1
Donaldson, R.M., G2.2.1
Dong, Z.J., G6.42.1
Donovan, S.M., G6.40.1, G6.56.1
Doppalapudi, D., G7.8.1
Doshi, B., G6.59.1
Dovidenko, K., G6.43.1, G6.46.1
Drews, A.R., G3.7.1
Dunham, S.T., G6.41.1
Dunnrowicz, C., G2.2.1
Dupuis, R.D., G4.6.1
Dutta, M., G6.65.1
Dyck, J.S., G3.23.1

Eastman, L.F., G8.4.1
Ebeling, K.J., G10.2.1
Eddy, Jr., C.R., G10.5.1
Edgar, J.H., G3.39.1, G3.79.1
Edmond, J.A., G4.3.1, G5.10.1
Edwards, N.V., G3.78.1
Einfeldt, S., G3.33.1, G3.57.1, G5.6.1
Eiting, C.J., G4.6.1
Eizenberg, M., G6.39.1
El-Masry, N.A., G3.22.1, G4.3.1, G5.10.1
Elsner, J., G3.29.1, G6.3.1
Eustis, T.J., G8.4.1
Exarhos, G.J., G6.15.1

Feenstra, R.M., G9.5.1
Fehrer, M., G5.6.1
Feng, Z.C., G6.47.1
Ferguson, I., G6.47.1
Feuillet, G., G9.2.1
Figiel, J.J., G7.7.1
Fini, P.T., G4.5.1
Fischer, A.J., G6.54.1
Fishman, G., G9.2.1
Fleischer, K., G3.30.1
Fleming, J.G., G3.72.1
Flierl, C., G6.57.1
Follstaedt, D.M., G3.72.1
Fong, W.K., G6.4.1, G6.5.1
Foutz, B.E., G8.4.1
Foxon, C.T., G4.11.1
Frabboni, S., G3.50.1
Frandon, J., G6.28.1
Frauenheim, Th., G3.29.1, G6.3.1
Frey, T., G2.3.1
Fu, M., G6.33.1
Fujita, Shigeo, G6.31.1
Fujita, Shizuo, G6.31.1
Fuke, S., G6.23.1
Funato, M., G6.31.1

Gaffey, B., G3.44.1
Gainer, G.H., G2.4.1
Gao, Y., G3.53.1
Garter, M., G11.3.1
Gaska, R., G1.6.1
Ge, W.K., G6.4.1
Gehrke, T., G3.2.1, G3.17.1, G3.37.1, G3.38.1, G4.9.1
Gerthsen, D., G3.50.1
Gfrörer, O., G6.20.1
Gherasimova, M., G3.44.1
Gibart, P., G6.12.1, G6.13.1
Gil, B., G1.2.1, G3.69.1, G11.7.1
Gilliland, G.D., G6.47.1
Gillis, H.P., G8.2.1
Glaser, E.R., G7.4.1
Godlewski, M., G3.19.1
Goeldner, A., G3.26.1
Golaszewska, K., G9.9.1
Goodman, S.A., G6.12.1, G6.13.1
Gorla, C., G3.60.1
Gorman, R.J., G3.70.1
Grandjean, N., G3.59.1, G3.69.1, G6.28.1, G11.7.1
Greve, D.W., G9.5.1
Griffin, J., G3.61.1
Grossner, M.T., G3.23.1
Grudowski, P.A., G4.6.1
Grzegory, I., G4.11.1, G10.2.1
Guggi, D., G3.50.1
Guido, L.J., G3.44.1
Gulino, D.A., G3.53.1
Guo, H.J., G6.33.1
Gutierrez, R., G3.29.1
Gutowski, J., G5.6.1

Haberern, K.W., G4.3.1
Hahn, Y.B., G6.56.1
Haller, E.E., G3.15.1
Han, J., G3.72.1, G5.8.1, G6.9.1 , G6.33.1, G6.40.1, G7.7.1, G8.1.1
Hangleiter, A., G6.20.1
Hansen, D.M., G4.7.1, G11.4.1
Harris, M., G3.40.1

Hartlieb, P.J., G3.17.1
Haugk, M., G3.29.1
Hayashi, N., G10.1.1
Hayman, C.C., G3.23.1
Hays, D.C., G6.56.1
Headley, T.J., G5.8.1
Heard, P.J., G6.57.1
Hearne, S.J., G7.7.1
Heggie, M.I., G3.29.1
Henry, A., G3.16.1
Henry, R.L., G3.70.1, G6.35.1
Herres, N., G2.8.1
Hickman II, R., G7.6.1
Higgins, R., G3.53.1
Hills, C.R., G5.8.1
Hiramatsu, K., G3.1.1, G4.1.1
Hirayama, H., G3.74.1, G9.4.1
Hiroyama, Y., G3.9.1
Hirsch, L., G3.59.1
Hirsch, M.T., G5.5.1
Ho, W.Y., G6.4.1, G6.5.1
Hoffmann, A., G2.3.1, G3.26.1, G3.57.1
Hofstetter, D., G2.2.1, G3.42.1
Holst, J., G2.3.1
Holtz, P.O., G2.5.1
Hommel, D., G3.33.1, G3.57.1, G5.6.1
Hömmerich, U., G11.1.1, G11.6.1
Honda, T., G6.2.1
Hong, J., G8.1.1
Hong, M-H., G3.23.1
Hsieh, J.T., G10.6.1
Hsieh, K.C., G3.44.1
Huang, C., G3.7.1
Hudgins, R., G3.80.1
Hung, W.H., G10.6.1
Hwang, H.L., G10.6.1
Hwang, J.M,. G10.6.1
Hwang, Y.G., G6.3.1

Ibbetson, J.P., G4.5.1
Iga, K., G6.2.1
Ignatiev, C., G3.39.1, G3.79.1
Ikenaga, Y., G6.31.1
Ikossi-Anastasiou, K., G6.35.1
Im, J.S., G6.20.1
Ingerly, D.B., G6.49.1
Itoh, H., G3.1.1
Ivanov, I.G., G3.16.1
Iwasa, N., G1.1.1
Iwaya, M,. G10.1.1
Iyechika, Y., G4.1.1

Jasinski, J., G9.9.1
Jiang, H-X., G1.2.1, G3.3.1, G3.79.1, G11.1.1
Jiang, W., G6.15.1
Johnson, M.A.L., G4.3.1, G5.2.1, G5.10.1
Johnson, N.M., G3.15.1, G3.42.1, G10.4.1
Jones, R., G3.29.1
Jones, R.L., G3.40.1
Joshkin, V., G6.43.1
Juergensen, H., G6.42.1
Jun, J., G3.42.1
Jung, K.B., G6.56.1

Kalinina, E.V., G6.53.1
Kaminska, E., G9.9.1
Kamp, M., G10.2.1
Kaschner, A., G3.57.1
Kash, K., G3.23.1
Kashima, T., G10.1.1
Katsuragawa, M., G10.1.1
Kawaguchi, Y., G4.1.1
Kawanishi, H., G6.2.1
Kawasaki, M., G6.23.1
Keller, S., G2.4.1, G4.5.1, G6.44.1, G6.54.1
Kelly, M., G5.5.1
Kennedy, T.A., G7.4.1
Khan, F., G1.4.1
Kim, H.S., G3.3.1
Kim, J-H., G3.49.1
Kim, S., G11.4.1
Kim, W., G6.5.1
Kirchner, C., G10.2.1
Kirchner, V., G5.6.1
Kirfel, O., G5.5.1
Klaassen, J.J., G7.6.1
Kneissl, M., G2.2.1, G3.42.1
Koeck, F.A., G5.10.1
Koinuma, H., G6.23.1
Kolbas, R.M., G5.2.1
Koleske, D.D., G3.70.1, G6.35.1
Kollmer, H., G6.20.1
Kompan, M.E., G6.14.1
Konenkova, E.V., G6.14.1
Kong, H.S., G4.3.1, G5.10.1
Konovalov, O., G3.19.1
Korakakis, D., G4.11.1
Kordesch, M.E., G3.23.1
Koschnick, F.K., G6.12.1, G6.13.1
Kovarsky, A.P., G6.53.1
Koyama, F., G6.2.1
Kozubowski, J., G9.9.1
Krasinski, J., G6.48.1
Kriegseis, W., G3.24.1
Krishnamurthy, S., G5.1.1
Krtschil, A., G3.14.1, G3.71.1
Krusor, B.S., G3.42.1
Kuball, M., G6.28.1, G6.57.1
Kuech, T.F., G3.56.1. G3.62.1, G3.67.1, G4.7.1, G11.4.1
Kunzer, M., G2.8.1

Lambrecht, W.R.L., G1.2.1, G6.8.1, G6.11.1
Langer, R., G3.19.1
Lantier, R., G3.50.1
Lau, S.S., G1.5.1
Laügt, M., G3.59.1, G11.7.1
Lee, B.K., G3.80.1
Lee, D.S., G3.80.1
Lee, H.J., G3.49.1
Lee, H.P., G6.42.1
Lee, S.M., G6.3.1
Lee, Y.H., G6.3.1
Lefebvre, P., G3.69.1, G11.7.1

Leroux, M., G3.59.1, G3.69.1, G11.7.1
Lester, L.F., G8.1.1
Leszczynski, M., G10.2.1
Li, E.H., G6.25.1
Li, J.B., G3.25.1
Li, L.Y., G3.39.1
Li, X., G4.8.1, G11.4.1
Liang, S., G3.60.1
Liliental-Weber, Z., G1.5.1, G4.6.1
Lim, K.Y., G3.49.1
Limpijumnong, S., G6.8.1, G6.11.1
Lin, J.Y., G1.2.1, G3.3.1, G3.79.1, G11.1.1
Lindström, J.L., G5.4.1
Linthicum, K.J., G3.2.1, G3.17.1, G3.37.1, G3.38.1, G4.9.1
Lischka, K., G2.3.1, G3.14.1, G3.24.1
Lisker, M., G3.14.1, G3.71.1
Little, B.D., G2.4.1, G6.48.1
Litton, C.W., G3.40.1
Look, D.C., G3.40.1
Losurdo, M., G3.12.1
Lothian, J.R., G6.39.1
Lu, D.Q., G4.7.1
Lu, L.W., G6.4.1
Lu, Y., G3.60.1
Lübbers, M., G3.24.1
Lüth, H., G3.50.1

MacKenzie, J.D., G11.1.1, G11.6.1
Madsen, L.D., G3.16.1, G3.78.1
Maeda, T., G4.1.1
Maier, M., G2.8.1
Mao, Z., G3.13.1
Marchand, H., G4.5.1
Marinelli, C., G6.57.1
Martin, K.P., G8.2.1
Maruska, P.H., G3.8.1
Massies, J., G3.59.1, G3.69.1, G11.7.1
Mathieu, H., G3.69.1
Matushita, T., G1.1.1
McCluskey, M.D., G3.15.1 G3.42.1, G10.4.1
McDonald, P.H., G7.8.1
McGill, T.C., G3.77.1, G6.26.1
McKernan, X., G3.13.1
McPherson, S.A., G3.13.1, G6.48.1
Mehregany, M., G4.9.1
Meyer, B.K., G3.24.1, G3.26.1
Michler, P., G5.6.1
Millecchia, M.R., G3.10.1
Mimkes, J., G3.24.1
Mishra, U.K., G2.4.1, G4.5.1, G6.44.1, G6.54.1
Misra, M., G7.8.1
Missert, N., G6.9.1
Mitev, P., G3.44.1
Mitha, S., G3.44.1
Miyake, H., G3.1.1, G4.1.1
Monemar, B., G2.5.1, G3.16.1, G3.78.1, G5.4.1
Morkoç, H., G1.2.1, G3.3.1, G6.5.1
Moustakas, T.D., G6.41.1, G7.8.1
Mukai, T., G1.1.1
Munzel, M., G5.5.1
Murphy, M.J., G8.4.1
Muth, J.F., G4.3.1, G5.2.1
Myers, S.M., G3.73.1, G5.8.1
Myers, T.H., G3.10.1

Nagahama, S., G1.1.1
Nakada, Y., G3.4.1
Nakamura, S., G1.1.1, G2.7.1, G7.4.1
Nambu, S., G4.1.1
Narayan, J., G6.43.1, G6.46.1
Nemanich, R.J., G6.65.1
Neubauer, B., G3.50.1
Neugebauer, J., G10.4.1
Norris, P.E., G3.8.1
Northrup, J.E., G9.5.1
Novikov, S.V., G4.11.1

Obloh, H., G2.8.1
Off, J., G3.71.1, G6.20.1
Ohnishi, T., G6.23.1
Ohtomo, A., G6.23.1
Ohtsuka, K., G6.23.1
Ohuchi, Y., G3.1.1
Okagawa, H., G3.1.1
Oktyabrsky, S., G6.43.1, G6.46.1
Okumura, H., G3.4.1
O'Reilly, E.P., G6.45.1

Pamulapati, J., G3.60.1, G11.1.1
Pantelides, S.T., G5.3.1
Parisi, J., G5.5.1
Park, D-C., G6.31.1
Park, J., G4.6.1
Parker, C.A., G3.22.1
Paskova, T., G3.16.1
Paul, A.J., G3.22.1
Pearton, S.J., G5.9.1, G6.33.1, G6.39.1, G6.40.1, G6.56.1, G8.1.1, G11.2.1, G11.6.1
Pelekanos, N.T., G3.19.1, G9.2.1
Pelzmann, A., G10.2.1
Pennycook, S.J., G6.33.1
Penty, R.V., G6.57.1
Perkins, N.R., G3.56.1
Petersen, G.A., G5.8.1
Phillips, M.R., G3.30.1
Piner, E.L., G3.22.1
Ping, A.T., G1.4.1
Piotrowska, A., G9.9.1
Piquette, E.C., G3.77.1, G6.26.1
Polley, C., G7.6.1
Porezag, D., G6.3.1
Porowski, S., G1.3.1, G4.11.1, G10.2.1
Pozina, G., G2.5.1
Provencio, P., G3.72.1
Przbylinska, H., G5.9.1
Ptak, A.J., G3.10.1

Qiao, D., G1.5.1

Raevskii, S.D., G6.14.1
Rajagopal, P., G3.2.1, G3.37.1, G3.38.1
Ralph, S.E., G6.47.1
Ramakrishnan, A., G2.8.1

Rashkeev, S.N., G6.11.1
Razeghi, M., G6.46.1
Reboredo, F.A., G5.3.1
Redwing, J.M., G7.5.1
Reeber, R.R., G3.18.1
Rehder, E., G3.56.1
Ren, F., G6.39.1, G6.40.1, G11.1.1
Renucci, M.A., G6.28.1
Reshchikov, M.A., G11.8.1
Reuter, E.E., G3.67.1
Reynolds, D.C., G3.40.1
Rieger, D.J., G6.33.1
Rieger, W., G8.4.1
Riemann, T., G3.33.1
Rizzi, A., G3.50.1
Roberts, J.C., G3.22.1
Robins, L.H., G3.22.1
Romano, L.T., G1.4.1., G2.2.1, G3.42.1
Ronning, C., G3.17.1
Rorison, J.M., G6.57.1
Rosamond, M.F., G7.6.1
Rouvière, J.L., G9.2.1
Ruden, P.P., G6.6.1, G6.35.1, G6.59.1, G7.4.1
Rudloff, D., G3.33.1
Ruterana, P., G3.59.1
Ruvimov, S., G1.5.1
Ryder, P.L., G3.33.1

Sakaguchi, T., G6.2.1
Saleh, A., G3.80.1
Sampath, A.V., G7.8.1
Sawaki, N., G4.1.1
Schaff, W.J., G8.4.1
Schetzina, J.F., G4.3.1, G5.2.1, G5.10.1
Schikora, D., G2.3.1, G3.24.1
Schmidt, T.J,. G6.44.1, G6.54.1
Scholz, F., G3.71.1, G6.20.1
Schöttker, B., G2.3.1, G3.14.1, G3.24.1
Schowalter, L.J., G3.76.1
Schubert, E.F., G7.5.1
Schurman, M.J., G6.47.1
Schwall, D., G3.40.1
Schwegler, V., G10.2.1
Scofield, J., G11.3.1
Seager, C.H., G5.8.1
Segall, B., G6.8.1
Seifert, O.P., G5.5.1
Sekhar, J.A., G6.33.1
Selke, H., G3.33.1
Senoh, M., G1.1.1
Seo, J.T., G11.6.1
Seong, T-Y., G3.11.1
Sernelius, B.E., G2.5.1
Shan, W., G3.15.1
Sharma, A.K., G6.43.1
Shen, B., G4.7.1
Shen, H., G3.60.1, G11.1.1
Shenai, K., G1.2.1
Sher, A., G5.1.1
Shih, R., G6.42.1
Shul, R.J., G6.33.1, G6.39.1, G6.40.1, G6.56.1, G7.7.1, G8.1.1
Shur, M.S., G1.6.1
Shusterman, Y., G3.76.1
Siegle, H., G3.57.1
Simon, J., G3.19.1, G9.2.1
Simonsmeier, T., G3.24.1
Singh, R.K., G6.33.1
Slack, G.A., G3.76.1
Smith, A.R., G9.5.1
Smith, S.A., G3.38.1
Smith, T.P., G4.9.1
Soares, J.C., G11.2.1
Solov'ev, V.A., G6.53.1
Sone, H., G4.1.1
Song, C.Y., G5.9.1
Song, J.J., G2.4.1, G6.44.1, G6.48.1, G6.54.1
Sota, T., G2.7.1
Spaeth, J-M., G6.12.1, G6.13.1
Spear, J., G3.44.1
Speck, J.S., G4.5.1
Spencer, M.G., G3.61.1
Stampfl, C., G10.4.1
Stavola, M., G5.9.1
Steckl, A.J., G3.80.1, G10.7.1, G11.3.1
Steude, G., G3.26.1
Stinespring, C.D., G3.10.1
Stocker, D.A., G7.5.1
Strauf, S., G5.6.1
Stroscio, M.A., G6.65.1
Strunk, H.P., G4.11.1
Stutzmann, M., G5.5.1, G8.4.1
Sullivan, G.J., G1.5.1
Sumiya, M., G6.23.1
Surya, C., G6.4.1, G6.5.1
Suscavage, M., G3.40.1
Suski, T., G3.42.1, G10.2.1
Sutandi, A., G6.35.1
Svedberg, E.B., G3.16.1
Swider, W., G4.6.1

Tadatomo, K., G3.1.1
Takeuchi, T., G3.66.1, G10.1.1
Tamura, M., G3.9.1
Tanaka, M., G6.23.1
Tanaka, S., G9.4.1
Thaik, M., G11.1.1, G11.6.1
Thevuthasan, S., G6.15.1
Thompson, M.P., G3.7.1
Thomsen, C., G3.57.1
Thomson, D.B., G3.2.1, G3.17.1, G3.37.1, G3.38.1. G4.9.1, G9.9.1
Thornton, R.L., G2.2.1
Tong, K.Y., G6.4.1, G6.5.1
Toth, M., G3.30.1
Tracy, K.M., G4.9.1
Tsang, K-O., G6.25.1
Tu, C.W., G3.11.1
Twigg, M.E., G3.70.1

Uenoyama, T., G2.9.1

Van de Walle, C.G., G10.4.1
Van Hove, J.M., G7.6.1

van Schilfgaarde, M., G5.1.1
Vennéguès, P., G3.59.1
Vianden, R., G11.2.1

Wada, K., G2.7.1
Wagner, J., G2.8.1
Wagner, Mt., G5.4.1
Walukiewicz, W., G3.15.1
Wampler, W.R., G3.73.1, G5.8.1
Wang, K., G3.18.1
Wang, R., G3.76.1
Wang, S-Q., G3.40.1
Wang, S.Y., G6.57.1
Wang, Y.T., G3.25.1
Washburn, J., G4.6.1
Watkins, G.D., G5.9.1
Weber, W.J., G6.15.1
Webster, R.T., G6.58.1
Wei, C.H., G3.39.1, G3.79.1
Weinstein, M.G., G5.9.1
Wessels, B.W., G11.8.1
Wetzel, C., G3.66.1, G10.1.1
White, I.H., G6.57.1
Wickenden, A.E., G3.70.1, G6.35.1
Widmann, F., G9.2.1
Willan, C.C., G6.9.1
Willison, C.G., G8.1.1
Wilson, R.G., G3.80.1, G5.9.1, G6.33.1, G11.1.1, G11.6.1
Wilson, S., G3.61.1
Witte, H., G3.14.1, G3.71.1
Wolford, D.J., G6.47.1
Wowchak, A.M., G7.6.1
Wraback, M., G3.60.1
Wu, H., G8.4.1
Wu, S., G6.7.1, G6.58.1
Wu, X.H., G4.5.1

Xie, Z.Y., G3.39.1, G3.79.1
Xiong, F.F., G6.42.1
Xu, D.P., G3.25.1

Yakimova, R., G3.16.1
Yamaguchi, M., G4.1.1
Yang, G.M., G3.49.1
Yang, H., G3.25.1
Yang, N., G3.23.1
Yang, W., G3.13.1, G6.48.1
Yeo, W., G8.4.1
Yi, G-C., G11.8.1
Yip, P.W., G3.8.1, G3.40.1
Yoshimoto, M., G6.23.1
Youtsey, C., G1.4.1
Yu, L.S., G1.5.1
Yu, Z., G4.3.1, G5.2.1, G5.10.1

Zavada, J.M., G3.80.1, G11.1.1, G11.6.1
Zeitouny, A., G6.39.1
Zeng, K.C., G3.79.1
Zhang, L., G8.1.1
Zhang, Ling, G3.56.1, G3.62.1, G4.7.1,
Zhang, R., G3.62.1, G3.67.1, G4.7.1, G11.4.1
Zhao, Y., G3.11.1
Zheleva, T.S., G3.38.1, G4.9.1
Zheng, L.X., G3.25.1
Zheng, Y.D., G4.7.1
Zhilyaev, Y.V., G6.14.1
Zhou, M., G3.56.1
Zhu, L.D., G3.8.1
Ziemer, K.S., G3.10.1
Zolper, J.C., G6.33.1, G6.39.1
Zorman, C.A., G4.9.1
Zou, A.Q., G6.42.1
Zubrilov, A.S., G6.53.1

SUBJECT INDEX

absorption coefficient, G5.2.1
activation
  energy, G6.40.1
  of acceptors, G6.31.1
active nitrogen, G3.10.1
AFM, G3.7.1
ALE, G5.6.1
AlGaN, G1.5.1, G3.26.1, G3.74.1, G5.2.1, G6.20.1, G7.7,1, G10.1.1, G10.4.1
  alloy, G9.4.1
alloys, G6.8.1
AlN, G3.7.1, G3.56.1, G3.72.1, G6.65.1, G10.1.1
aluminum nitride, G3.2.1, G3.61.1, G3.76.1
ambient gas, G3.1.1
ammonia, G3.68.1
anisotropy, G8.2.1
anneal, G3.42.1
annealing, G6.31.1
anti-surfactant, G9.4.1
Ar, G6.56.1
armchair, G6.3.1
Auger, G3.79.1
  electron spectroscopy, G3.4.1
AZ400K solution, G6.40.1

band structure, G6.8.1 , G6.11.1
bandgap bowing, G6.8.1
base transit time, G6.7.1
BGaN, G3.79.1
birefringence, G6.11.1
blue, G1.1.1
  LEDs, G6.4.1
boron contamination, G3.10.1
bowing, G2.8.1
breakdown, G7.9.1
buffer, G3.72.1
bulk GaN substrates, G4.11.1

c-GaN, G2.3.1
c-InGaN, G2.3.1
carbon, G3.67.1, G5.6.1
carrier confinement, G6.2.1, G6.20.1
cathodoluminescence, G3.30.1
characteristic temperature, G6.2.1
CL, G4.3.1, G4.8.1
Cl2-based chemistries, G6.56.1
coaxial impact collision ion scattering spectroscopy (CAICISS), G6.23.1
combustion synthesis, G3.45.1
compensation, G5.6.1
complex-coupled, G2.2.1
composition, G2.8.1
compositional
  fluctuations, G3.33.1
  inhomogeneity, G3.22.1
computational materials science, G5.1.1
conductivity, G11.9.1
confined exciton, G2.7.1
contact resistance, G6.42.1
cryogenic, G10.6.1
crystal
  growth, G3.18.1
  structure, G6.43.1
crystallographic, G7.5.1
cubic
  GaN, G3.9.1, G3.24.1
  phase, G3.25.1

damage, G10.5.1
deep levels, G5.5.1, G7.8.1
defect(s), G3.13.1, G4.6.1, G6.12.1, G6.13.1, G6.28.1
degradation, G6.28.1
delta-doping, G3.49.1
detectors, G7.8.1
device(s), G10.2.1
  fabrication, G6.57.1
DFB laser, G2.2.1
diffusion(-), G3.42.1, G11.9.1
  limited, G6.40.1
dislocations, G1.4.1, G3.72.1
dissociation, G6.47.1
DLTFS, G6.4.1
DLTS, G6.12.1, G6.13.1
domains, G3.16.1
donor-acceptor pair, G11.8.1
doping, G3.57.1, G5.6.1, G6.20.1, G10.4.1, G11.2
DX center, G10.4.1

edge energy, G6.3.1
effect annealing, G6.15.1
effective bandgap inhomogeneity, G2.7.1
elective etching, G3.38.1
electric
  field, G11.7.1
    in quantum wells, G2.7.1
electrical, G3.7.1
electrically injected, G2.2.1
electroluminescence, G6.4.1, G11.3.1, G11.5.1
electroreflection, G3.66.1
ellipsometry, G3.12.1
ELO, G4.3.1, G4.8.1, G6.9.1
epilayers, G3.15.1
epitaxial
  lateral overgrowth, G4.1.1, G6.9.1
  ZnO, G3.60.1
epitaxy, G3.61.1, G3.72.1
Er, G3.80.1, G11.4.1
Er-doped, G11.5.1
erbium, G3.80.1, G11.1.1, G11.2.1, G11.3.1, G11.6.1
etch selectivity, G6.56.1, G8.1.1

etching, G1.4.1, G7.5.1
  damage, G8.2.1
  fundamentals, G10.5.1
exciton, G6.47.1
excitonic recombination, G3.26.1
extended defects, G3.29.1

facet, G7.5.1
FET, G6.35.1
finite element model, G3.18.1
flicker noise, G6.4.1, G6.5.1
fluctuations, G2.5.1
focused ion beam, G10.7.1
  etching, G6.57.1
Franz-Keldysh effect, G3.66.1

g-factors, G7.4.1
Ga, G3.68.1
  desorption, G3.70.1
  droplet formation, G3.70.1
gain, G2.3.1, G2.6.1, G6.54.1
GaInN, G3.66.1, G6.20.1
gallium nitride (GaN), G1.3.1, G1.5.1, G2.8.1, G3.2.1, G3.4.1, G3.10.1, G3.12.1, G3.13.1, G3.15.1, G3.16.1, G3.19.1, G3.23.1, G3.26.1, G3.29.1, G3.37.1, G3.38.1, G3.39.1, G3.40.1, G3.45.1, G3.49.1, G3.53.1, G3.62.1, G3.67.1, G3.68.1, G3.72.1, G3.73.1, G3.77.1, G3.80.1, G4.1.1, G4.3.1, G4.5.1, G4.6.1, G4.7.1, G4.8.1, G4.11.1, G5.1.1, G5.4.1, G5.5.1, G5.6.1, G5.8.1, G5.9.1, G5.10.1, G6.2.1, G6.3.1, G6.4.1, G6.5.1, G6.7.1, G6.9.1, G6.12.1, G6.13.1, G6.15.1, G6.23.1, G6.26.1, G6.28.1. G6.33.1, G6.39.1, G6.47.1, G6.48.1, G6.53.1, G6.57.1, G6.58.1, G6.65.1, G7.2.1, G7.5.1, G7.6.1, G7.8.1, G7.9.1, G9.5.1, G9.9.1, G10.1.1, G10.2.1, G10.6.1, G10.7.1, G11.1.1, G11.2.1, G11.3.1, G11.4.1, G11.5.1, G11.8.1
  decomposition, G3.70.1
  defect structure, G3.30.1
  doping p-type defects, G5.3.1
GaN(0001), G3.68.1
GaN/AlGaN MQWs, G3.3.1
GaN/AlGaN QWs, G11.7.1
GaNAs, G3.11.1, G3.44.1
GaNP, G3.11.1
group-III nitrides, G8.1.1
growth, G3.23.1, G3.77.1
  chemistry, G3.62.1
  kinetics, G6.9.1
  mechanisms, G6.9.1

HBT, G6.7.1
He(-), G6.56.1
  ion, G6.12.1
heterostructure(s), G3.2.1, G6.29.1, G6.35.1
high(-)
  electron mobility transistor, G6.58.1
  pressure solution growth, G1.3.1
  temperature processing, G6.28.1
holography, G2.2.1
homoepitaxy, G10.2.1
hot electrons, G5.1.1
HVPE, G3.16.1, G4.1.1, G4.7.1
hydride vapor phase epitaxy, G4.7.1
hydrogen, G3.1.1, G3.68.1, G3.70.1, G3.73.1, G5.8.1, G5.9.1, G6.31.1

ICP etching, G8.1.1
implantation, G3.17.1
indium
  gallium nitride, G3.22.1, G9.5.1
  nitride, G6.59.1
inductively coupled plasma etching, G6.56.1
influence of the additive gas (He), G6.56.1
InGaN, G1.1.1, G2.5.1, G2.6.1, G2.7.1, G2.8.1, G2.9.1, G3.15.1, G3.22.1, G3.25.1, G3.33.1, G3.59.1, G5.10.1, G6.7.1, G6.25.1, G7.4.1, G9.5.1, G10.6.1
  laser, G6.45.1
in situ RBS/channeling, G6.15.1
interface effects, G5.5.1
interfacial reaction, G6.28.1
intermixing, G3.42.1, G6.25.1
inversion domains, G6.46.1
ion channeling, G3.73.1, G3.76.1
ion implantation, G5.8.1, G5.9.1, G6.33.1, G6.53.1

KOH, G6.40.1

laser, G1.1.1, G6.2.1, G7.5.1
  diode(s), G2.6.1, G6.48.1
  gain, G6.45.1
lasing, G6.48.1
lateral
  epitaxial overgrowth, G4.5.1
  epitaxy, G3.37.1, G3.38.1
  overgrowth, G4.8.1, G6.48.1
lattice location, G11.2.1
LE4, G8.2.1
LED(s), G1.1.1, G2.8.1, G3.59.1, G5.10.1, G7.4.1, G10.2.1
lifetimes, G6.65.1
light emitting diode(s), G6.29.1, G6.42.1, G7.2.1, G11.6.1
local
  vibration, G5.4.1
  vibrational modes, G3.57.1
localized
  exciton, G2.7.1
  state(s), G2.6.1, G2.9.1
low temperature, G7.2.1
  interlayer, G10.1.1
luminescence, G3.33.1, G6.29.1, G11.1.1

magnesium, G10.4.1
MBE, G3.59.1, G3.77.1, G3.80.1, G4.3.1, G5.6.1, G5.10.1, G6.5.1, G6.26.1, G11.7.1

metal(-)
contact, G6.49.1
semiconductor contact, G9.9.1
metalorganic
chemical vapor deposition, G3.49.1, G4.5.1
vapor phase epitaxy, G4.7.1
metastable states, G5.5.1
Mg, G11.9.1
doped GaN, G3.24.1
MgO, G6.8.1
microstructure(s), G3.38.1, G6.48.1
mobility, G6.6.1, G8.4.1
MOCVD, G2.8.1, G3.8.1, G3.25.1, G3.39.1, G3.44.1, G3.53.1, G3.61.1, G3.68.1, G3.72.1, G3.74.1, G7.7.1, G7.9.1
modeling, G3.53.1
MODFETs, G6.5.1
molecular beam epitaxy, G3.10.1, G4.11.1, G8.4.1, G9.5.1
Monte Carlo, G6.6.1, G6.7.1, G6.59.1
MOVPE, G3.1.1, G3.37.1, G3.38.1, G3.56.1, G3.62.1, G4.1.1, G4.3.1, G4.7.1, G5.10.1, G6.42.1, G10.2.1
growth, G3.70.1
MQW(s), G3.15.1, G6.25.1
multiple quantum wells, G7.2.1
multi-quantum-well, G3.74.1

nanotubes, G6.3.1
NaOH, G6.40.1
NiIn, G6.49.1
nitridation of, G3.12.1
GaAs, G3.4.1
sapphire, G3.10.1
nitride(s), G1.4.1, G3.18.1, G3.68.1 G6.29.1, G6.54.1
MBE, G3.50.1
semiconductors, G1.2.1
nitrogen(-), G3.1.1, G3.70.1
deficient GaN, G6.43.1
metastables, G3.10.1
noise, G7.8.1
power density, G7.6.1
nonlinear optics, G6.11.1
non-stationary transport, G6.7.1

ODMR, G7.4.1
offsets, G6.8.1
ohmic contact, G1.5.1, G6.39.1, G6.49.1, G9.9.1
OMVPE, G3.76.1, G4.9.1
optical
absorption, G3.22.1
anisotropy, G3.60.1
gain, G2.9.1
modulator, G3.60.1
pumping, G6.48.1
quenching, G5.5.1
optically-detected-magnetic-resonance, G5.9.1
ordering, G3.11.1
overgrowth epitaxy, G4.6.1
oxide, G3.45.1
oxygen, G5.4.1, G6.26.1, G10.4.1

p-n junction, G6.53.1, G7.2.1
p-type GaN, G6.31.1
pendeo-epitaxy, G3.2.1, G3.37.1, G3.38.1, G4.9.1
phase separation, G3.11.1, G3.22.1
phonons, G6.65.1
photo-assisted, G10.6.1
photoconductivity, G5.5.1
photoconductors, G7.8.1
photodetectors, G7.6.1, G7.9.1
photoelectrochemical, G1.4.1
etching of $In_xGa_{1-x}N$, G6.40.1
photoluminescence (PL), G3.17.1, G3.24.1, G3.40.1, G3.50.1, G3.59.1, G3.66.1, G3.67.1, G3.79.1, G5.4.1, G6.25.1, G6.47.1, G7.2.1, G11.4.1, G11.6.1, G11.7.1, G11.8.1, G11.9.1
excitation (PLE), G3.22.1, G3.67.1, G11.4.1
red, G3.67.1
yellow, G3.67.1
photoreflectance, G3.7.1
photoreflection, G3.66.1
physics-based modeling, G6.58.1
picosecond time-resolved PL, G3.3.1
piezoelectric, G3.3.1, G3.19.1, G8.4.1
effect(s), G3.69.1
field, G3.66.1, G6.20.1, G7.2.1
polarization, G2.7.1
plasma etching, G10.5.1
polarity, G3.77.1, G6.23.1, G6.43.1, G6.46.1, G8.4.1
pressure, G3.15.1, G3.70.1
proton, G6.12.1
pyramids, G6.48.1

quantum
dot(s), G6.45.1, G9.4.1
confined Stark effect, G7.2.1
well(s) (QWs), G2.5.1, G2.9.1, G3.19.1 G3.42.1, G3.59.1, G3.66.1, G6.20.1, G6.29.1, G6.54.1

radiation effects, G6.15.1
Raman, G6.65.1
scattering, G6.28.1
spectroscopy, G3.22.1, G3.57.1
rapid thermal processing, G6.33.1
rare earth, G11.3.1
doping, G3.80.1
recombination, G2.5.1, G7.4.1
red, G1.1.1
photoluminescence, G3.67.1
redistribution, G6.33.1
refractive index, G5.2.1
remote plasma-MOCVD, G3.12.1
residual
donor, G5.4.1
stress, G3.18.1

rf(-), G3.77.1
  plasma, G3.10.1
RHEED, G3.4.1, G3.7.1, G11.7.1
Rutherford backscattering, G3.76.1, G11.2.1

SAE, G4.8.1
SAG, G3.1.1
sapphire, G3.77.1
scanning tunneling microscopy, G9.5.1
Schottky
  barrier diodes, G6.13.1
  contact, G1.5.1
screening, G2.5.1, G6.20.1
selective
  area
    epitaxy, G4.8.1
    growth, G4.1.1
  growth, G3.13.1, G3.37.1, G3.38.1, G4.6.1
self(-)
  assembling formation, G9.4.1
  compensation, G5.6.1
SEM, G4.3.1
semiconductor, G3.2.1
  alloys, G3.44.1
SHS, G3.45.1
Si, G3.49.1, G3.72.1, G4.9.1
  doped GaN, G3.24.1
  substrate, G3.9.1
SiC, G3.7.1, G3.9.1, G4.9.1
  surface preparation, G3.50.1
silicon, G10.4.1
  carbide, G3.61.1
  substrate, G3.53.1
SIMS, G3.17.1, G3.24.1
single
  crystal substrates, G10.2.1
  crystalline $ZnGeN_2$, G3.8.1
6H-SiC, G3.39.1, G3.79.1
smoothening, G8.2.1
spatial resolution, G3.33.1
spontaneous polarization, G2.7.1, G3.69.1
sputter deposition, G6.13.1
Stark effect, G3.66.1
stimulated emission, G6.54.1
STM, G9.5.1
strain, G3.26.1, G3.57.1, G6.20.1, G7.7.1
  energy, G6.3.1
stress, G7.7.1
structural
  characterization, G3.8.1
  properties, G3.16.1, G3.50.1, G4.5.1
substrate(s), G3.23.1, G3.40.1, G3.76.1
sulphide solution, G6.14.1
surface(s), G3.68.1, G3.77.1, G6.14.1, G6.26.1
  etching, G3.39.1
  morphology, G6.23.1
  structure, G4.5.1
susceptor geometry, G3.53.1
symmetry, G7.4.1

tailored substrates, G4.9.1
TEM, G3.11.1, G3.59.1, G4.6.1, G6.43.1, G6.46, G10.1.1
temperature effect, G3.7.1
thermal
  annealing, G6.25.1
  effects, G6.35.1
  stability, G6.28.1
thick layers, G3.16.1
thin films, G3.13.1, G5.5.1, G6.46.1
3rd order grating, G2.2.1
III nitrides, G6.46.1, G6.56.1, G6.59.1
3x3, G6.26.1
III-V nitrides, G3.2.1
tight-binding total energy method, G6.3.1
time-resolved photoluminescence, G3.69.1
transistor, G8.4.1
transmission electron microscopy, G3.9.1, G3.38.1
transport, G5.1.1, G6.6.1
  modeling, G6.9.1
  properties, G6.59.1
treatment, G6.14.1

ultraviolet (UV), G7.6.1,
  lasers, G3.74.1, G9.4.1
  photo-assisted etching, G6.40.1

vibrational spectroscopy, G5.9.1

W mask, G4.1.1
wavelength dispersive X-ray spectrometry, G3.30.1
wide bandgap nitrides, G8.2.1

Xe, G6.56.1
XPS, G6.26.1
X-ray diffraction, G3.17.1
XRD, G2.8.1, G3.7.1, G11.7.1

yellow photoluminescence, G3.67.1

zigzag, G6.3.1
zinc oxide, G3.40.1
ZnGeN2, G6.11.1
ZnO, G3.40.1, G6.8.1